

AD-A135 034

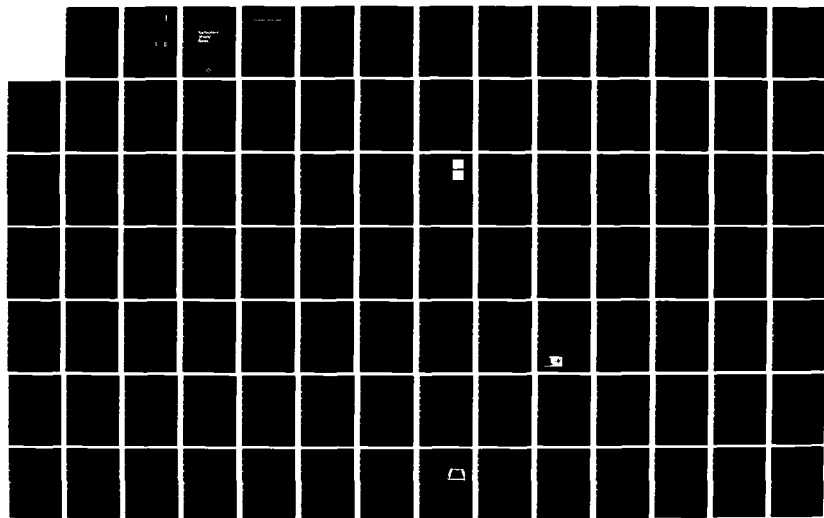
SYMPOSIUM ON TURBULENT SHEAR FLOWS (4TH) HELD AT
KARLSRUHE UNIVERSITY (GERMANY FR) 12-14 SEPTEMBER 1983
(U) KARLSRUHE UNIV (GERMANY F R) SEP 83

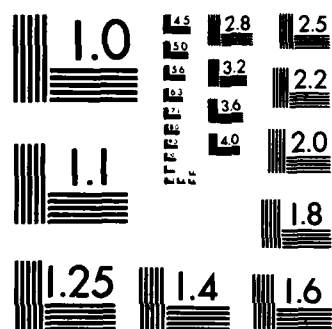
1/7

UNCLASSIFIED

F/G 20/4

NL





MICROCOPY RESOLUTION TEST CHART
NATIONAL BUREAU OF STANDARDS-1963-A

PHOTOGRAPH THIS SHEET

A135034

DTIC ACCESSION NUMBER

II

LEVEL

I

INVENTORY

Fourth Symposium on Turbulent Shear
Flows. Held at the Univ. of Karlsruhe, FR Germany
DOCUMENT IDENTIFICATION 12-14 Sept. '83

DISTRIBUTION STATEMENT A

Approved for public release
Distribution Unlimited

DISTRIBUTION STATEMENT

ACCESSION FOR	
NTIS	GRA&I
DTIC	TAB
UNANNOUNCED	
JUSTIFICATION	
BY	
DISTRIBUTION /	
AVAILABILITY CODES	
DIST	AVAIL AND/OR SPECIAL
A/3	

DISTRIBUTION STAMP

DTIC
ELECTE
NOV 22 1983
D

DATE ACCESSIONED



83 11 18 026

DATE RECEIVED IN DTIC

PHOTOGRAPH THIS SHEET AND RETURN TO DTIC-DDA-2

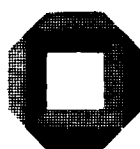
A 135034

FOURTH SYMPOSIUM ON

turbulent shear flows

APPROVED FOR PUBLIC RELEASE
DISTRIBUTION UNLIMITED

September 12-14, 1983



Karlsruhe, F.R. Germany

FOURTH SYMPOSIUM ON

turbulent shear flows

Organizing Committee

L. J. S. BRADBURY

Mechanical Engineering Department
University of Surrey
Guildford, Surrey, UK

F. DURST

Chair of Fluid Mechanics
Erlangen – Nürnberg
8520 Erlangen
F. R. Germany

B. E. LAUNDER

Department of Mechanical Engineering
University of Manchester
Institute of Science and Technology
Manchester, M60 1QD, UK

F. W. SCHMIDT

Department of Mechanical Engineering
The Pennsylvania State University
University Park, PA 16802, USA

J. H. WHITELAW

Department of Mechanical Engineering
Imperial College
London SW7 2BX, UK

APPROVED FOR PUBLIC RELEASE
DISTRIBUTION UNLIMITED

PREFACE

This volume contains the papers to be presented at the 4th Symposium on Turbulent Shear Flows held at the University of Karlsruhe, in Germany in the period September 12-14, 1983. The meeting continues the series of biennial international symposia launched at the Pennsylvania State University in 1977 and continued at Imperial College, London in 1979 and at University of California, Davis 1981. The aim of the Symposium, like that of its predecessors, has been to provide a forum for airing new developments across the multitude of activities that comprise turbulence research in the 1980's. The papers, which provide the formal record of the meeting, were selected following review of each of the 190 extended abstracts offered for the meeting by two members of the Advisory Committee. The assistance thus provided by the Committee, whose membership appears in the Symposium programme, is most warmly appreciated. The final composition and format of the meeting was set by a Papers' Committee consisting of L.J.S. Bradbury, F. Durst, H. Leuckel, and M. McDonald with the assistance of Frank W. Schmidt as secretary.

The Organizing Committee wishes to acknowledge financial support kindly provided by the National Science Foundation, European Office of Aerospace Research Development (USAF), U.S. Army Research, Development and Standardization Group, Office of Naval Research and in cooperation with American Society of Mechanical Engineer's Heat Transfer and Fluid Engineering Division.

L.J.S. Bradbury	F.J. Durst	B.E. Launder
F.W. Schmidt	J.H. Whitelaw	
Organizing Committee		

SESSION 1 - INTERNAL BOUNDARY LAYERS

H. McDonald - Chairman

- Second-order closure for the calculation of compressible wall bounded flows with an implicit Navier-Stokes solver 1.1
D. Vandromme, H.H. Minh, J.R. Viegas,
M.W. Rubesin, W. Kollmann
- Prediction of wall-bounded turbulent flows with an improved version of a Reynolds-stress model 1.7
M. Prud'homme and S. Elghobashi
- Rough- and smooth-walled shear flows 1.13
A.E. Perry, K.L. Lim, S.M. Henbest, M.S. Chong
- Further spectral analysis of smooth-walled pipe flow 1.18
A.E. Perry, S.M. Henbest, M.S. Chong
- The development of a large scale structure in the rod gap region for turbulent in-line flow through closely spaced rod arrays 1.23
J.D. Hooper

SESSION 2 - EXTERNAL 2-D BOUNDARY LAYERS

W. Reynolds - Chairman

- On the structure of turbulent boundary layers at different Reynolds numbers 2.1
J. Andreopoulos, F. Durst, J. Jovanovic
- Optical measurements of the transport properties in a highly cooled turbulent boundary layer at low Reynolds number n.r.
S. Eriksen, S.L.K. Wittig, K.P. Rud

Scrutinizing the k- ϵ -model under adverse pressure gradient conditions	2.8
W. Rodi and G. Scheuerer	
The behaviour of a compressible turbulent boundary layer under incipient separation conditions	2.15
K.C. Muck and A.J. Smits	
A universal velocity distribution and turbulence properties in the shear flow on a rotating cylinder in a quiescent fluid	2.21
I. Nakamura, Y. Ueki, S. Yamashita	

SESSION 3 - 3-D FLOWS

P.N. Joubert - Chairman

Calculation of ship boundary layers	3.1
V.C. Patel, O.P. Sarda, A. Shashahan	
Secondary current in a straight channel flow and the relation to its aspect ratio	3.8
H. Nakagawa, I. Nezu, A. Tominaga	
Some effects of rotation on turbulent boundary layers	3.14
H.T. Witt, J.H. Watmuff, P.N. Joubert	
Computer simulation of the time varying velocity field in the viscous wall region	3.21
C. Nikolaides and T.J. Hanratty	
Three dimensional vortex dynamics near a wall	3.25
H. Viets, R.J. Bethke, D. Bougine	

SESSION 4 - NUMERICAL SCHEMES AND COMPUTATIONS

G. Krause - Chairman

Calculated scalar dissipation in two-dimensional flows W.T. Ashurst, A.R. Kerstein, E. Effelsberg, N. Peters	4.1
Large eddy simulations of a wall-bounded turbulent jet flow and of a homogeneous shear flow F. Baron and D. Laurence	4.7
Stability of similarity solutions by two-equation models of turbulence W. Stüttgen and N. Peters	4.13
Computation of turbulent flow over a backward-facing step N.N. Mansour, J. Kim, P. Moin	n.r.
A use of sensitivity analysis in k- ϵ turbulent round jet modeling F. Raiszadeh and H.A. Dwyer	4.20

SESSION 5 - WAKES

E. Naudascher - Chairman

Structural features of the near region of an asymmetric turbulent wake M. Shokr, J.F. Keffer, J.G. Kawall	5.1
An investigation of Reynolds stress structures in plane turbulent wakes G. Fabris and A. Nakayama	5.7
Organized structures in wakes and jets - an aerodynamic resonance phenomenon? W. Koch	5.13

	<u>Page</u>
Turbulent boundary layer-wake interaction E.P. Tsiolakis, E. Krause, U.R. Müller	5.19
Effect of side walls of wind-tunnel on turbulent wake behind two dimensional bluff body M. Takeuchi and T. Okamoto	5.25
Experimental investigation of the turbulent structure of vortex wakes O. Leuchter and J.L. Solignac	5.31
Statistical characteristics of the turbulent wake behind an intersecting cruciform circular cylinder H. Osaka, H. Yamada, I. Nakamura	5.37

SESSION 6 - CURVED FLOWS

M.M. Gibson - Chairman

The influence of a spoiler on the development of a highly curved turbulent wall jet U. Hartmann	6.1
Computation and turbulence closure models for shear flows in rotating curved bodies M. Pouagare and B. Lakshminarayana	6.6
The effect of rotation on turbulence structure J. Kim	6.14
Turbulent momentum and heat transport in flow through a 180° bend of square cross section S.M. Chang, J.A.C. Humphrey, R.W. Johnson, B.E. Launder	6.20
Flow in sigmoid diffusers of moderate curvature J. Rojas, J.H. Whitelaw, M. Yianneskis	6.26

Effects of streamline curvature on laminar and turbulent wakes 6.32

H.S. Koyama

Experiment on turbulent boundary layers over a concave surface - Effects of introduction of curvature - 6.38

T. Shizawa and S. Honami

SESSION 7 - JETS

W. Rodi - Chairman

Measurements in a turbulent rectangular free jet 7.1

W.R. Quinn, A. Pollard, G.F. Marsters

Measurements in two-dimensional jets and plumes 7.7

M.S. Chandrasekhara and B.R. Ramaprian

On a forced elliptic jet 7.13

E. Gutmark and C.M. Ho

Confined jets in a diverging duct 7.18

G. Binder and K. Kian

An experimental study of the mixing of a jet into a cross flow using heat as a passive scalar 7.24

J. Andreopoulos

SESSION 8 - FREE SHEAR AND PERIODIC FLOWS

T.J. Hanratty - Chairman

Investigation of a plane mixing layer 8.1

S.V. Sherikar and R. Chevray

Velocity, vorticity, and strain rate measurements at the entraining boundary of a large plane shear layer	n.r.
J.F. Foss and C. L. Klewicki	
Numerical study of the phenomenon of turbulence suppression in a plane shear layer	8.6
M. Nallasamy and A.K.M.F. Hussain	
Hysteresis of turbulent stresses in a wall flow subjected to periodic disturbances	8.12
K. Hanjalić and N. Stošić	
Periodic turbulent shear flows	8.18
B.R. Ramaprian, S.W. Tu, A.N. Menendez	
SESSION 9 - FUNDAMENTALS I	
J. Mathieu - Chairman	
Parameterization of turbulent transport in swirling flows I. - theoretical considerations	9.1
D. Ettestadt and J.L. Lumley	
Effects of rotation on isotropic turbulence	9.7
B. Aupoix, J. Cousteix, J. Liandrat	
Two-point closures as a subgrid scale modeling for large eddy simulations	9.13
J.-P. Chollet	
Study of subgrid models for sheared turbulence	9.18
J.-P. Bertoglio and J. Mathieu	
A spectral model for the calculation of homogeneous turbulent flows	9.23
Y. Yassour and M. Wolfshtein	

	<u>Page</u>
Some developments in the application of renormalisation methods to turbulence theory W.D. McComb and V. Shanmugasundaram	9.30
A new look on turbulent shear flow S.I. Cheng	9.37

SESSION 10 - REACTING FLOWS

W. Leuckel - Chairman

Turbulent premixed combustion in a boundary layer M. Champion and P.A. Libby	10.1
Lagrangian models for turbulent combustion R. Borghi and E. Pourbaix	10.7
Simultaneous measurement of velocity and scalars in a turbulent nonpremixed flame by combined laser Doppler velocimetry and laser Raman scattering R.W. Dibble and R.W. Schefer	10.13
Nonequilibrium chemistry in an isothermal turbulent flow N. R. Mudford and R.W. Bilger	10.19
Assessment of various turbulence models for turbulent round diffusion jets with combustion F.C. Lockwood and P. Stolakis	10.25
A model for flame extinction in turbulent flow S. Byggstøl and B.F. Magnussen	10.32

SESSION 11 - GEOPHYSICAL FLOWS

J.C. André - Chairman

Transition from a horizontal turbulent buoyant jet to a mixing layer: An entrainment model G.H. Jirka	11.1
Katabatic wind in opposing flow D.R. Fitzjarrald	11.5
Turbulence structure in stratified turbulent shear flow horizontally discharged at water surface A. Murota and K. Nakatsuji	11.12
Elliptical turbulence in the atmosphere D. Schertzer and S. Lovejoy	11.18

SESSION 12 - TWO PHASE FLOWS

P. Humphrey - Chairman

Turbulent flow of incompressible mixtures M.C. Roco and C.A. Shook	12.1
Spray modelling in high turbulent swirling flow M.M. Elkotb, O.M.F. Elbahar, M.M.M. Abou-Elail	n.r.
A two-equation turbulence model for two-phase jets S. Elghobashi, T. Abou-Arab, M. Rizk, A. Mostaffa	12.9
Experimental results concerning separated two-phase flow around a circular cylinder F. Hara and Y. Kawamoto	12.15

SESSION 13 - OPEN FORUM

B.E. Launder and J.H. Whitelaw - Chairmen

SESSION 14 - FUNDAMENTALS II

J. Lumley - Chairman

- A comparison of triple-moment temperature - velocity correlations in the asymmetric heated jet with alternative closure models 14.1
I. Dekeyser and B.E. Launder
- The effect of mechanical strain on the dissipation rate of a scalar variance n.r.
S.E. Elghobashi and J.C. LaRue
- Higher order derivative correlations of velocity and temperature in isotropic and sheared numerical turbulence 14.9
R.M. Kerr
- Reynolds stress closure model for conditional variables 14.13
J. Janicka and W. Kollmann
- The asymptotic development of nearly homogeneous turbulent shear flow 14.18
U. Karnik and S. Tavoularis

SESSION 15 - EXPERIMENTAL TECHNIQUES

L. Bradbury - Chairman

- A computational Preston tube method 15.1
W. Nitsche, R. Thünker, C. Haberland

Measurements of the wall shear stress in boundary-layer flows	15.7
M. Acharya and M.P. Escudier	
A comparison between hot-wire and pulsed-wire measurements in turbulent flows	15.12
P. Dengel and J.-D. Vagt	
A multipoint detection method to identify coherent temperature fronts in a turbulent boundary layer over a rough surface	15.17
A.J. Chambers, R.A. Antonia, L.W.B. Browne, M.R. Raupach	
A new diagnostic technique for simultaneous, time-resolved measurements of concentration and velocity in simple turbulent flow systems	15.22
W.M. Pitts, B.J. McCaffrey, T. Kashiwagi	

SESSION 16 - COHERENT STRUCTURES

A.K.M.F. Hussain - Chairman

Transition to turbulence in a spherical gap	16.1
K. Bühler and J. Zierep	
A perspective view of the plane mixing layer	16.7
J. Jimenez, M. Cogollos, L.P. Bernal	
Axial coherence functions of circular turbulent jets based on an inviscid calculation of damped modes	16.13
P. Plaschko	
A model of the excitation of orderly structures in a shear layer	16.17
D.W. Bechert	

Large-scale coherent structure and far-field jet noise K.B.M.Q. Zaman	16.23
--	-------

SESSION 17 - HEAT TRANSFER

L. Back - Chairman

Verification of the extended gradient diffusion model by measurements of the mean and fluctuating temperature fields in sodium flow downstream of a multi-bore jet block L. Krebs and K. Bremhorst	17.1
The interference of multiple line sources in grid turbulence Z. Warhaft	17.6
Diffusion behind a line source in grid turbulence M.S. Anand and S.B. Pope	17.11
Modelling of scalar transport in homogeneous turbulent flows W.P. Jones and P. Musonge	17.18
The structure of turbulence in a natural convection boundary layer R. Cheesewright and A. Dastbaz	17.25
Heat transfer mechanism and associated turbulence structure in the near-wall region of a turbulent boundary layer Y. Iritani, N. Kasagi, M. Hirata	17.31
The statistics of the passive scalar field in an axisymmetric turbulent wake B.A. Kolovandin, Yu.M. Dmitrenko, S.I. Gabrilovich	17.37

SESSION 18 - RECIRCULATING FLOWS

R. Adrian - Chairman

- Turbulence measurements related to heat transfer in an axisymmetric confined jet with laser Doppler anemometer 18.1
K. Suzuki, S. Ida, T. Sato
- LDA-measurements and some theoretical aspects of separated flows 18.7
D. Geropp and A. Leder
- Mass and momentum turbulent transport experiments with confined coaxial jets 18.14
B.V. Johnson and J.C. Bennett
- Turbulent flow downstream of a backward-facing step 18.20
J.O. Ilegbusi and D.B. Spalding
- Improvements to the k- ϵ model for calculations of turbulent recirculating flow 18.26
A.M. Gooray, C.B. Watkins, W. Aung

SESSION 19 - RECIRCULATING FLOWS II

R. Dumas - Chairman

- Streamline curvature effects in confined isothermal recirculating flow fields behind an axisymmetric bluff body: numerical calculations with the k- ϵ turbulence model 19.1
L. Krishnamurthy and S.O. Park
- An experimental investigation of the turbulent shear flow downstream of a normal flat plate with a long splitter plate-modification of a flow model 19.7
R. Ruderich and H.H. Fernholz

Unsteady measurements in separated-and-reattaching
flows

19.13

R. Hillier, M.E.M.P. Latour, N.J. Cherry

Velocity field around a disk

19.19

D.F.G. Durão and F.C. Firmino

The turbulent structure of swirling flow in a sudden
expansion

19.25

W.L.H. Hallett and R. Günther

SESSION 1 - INTERNAL BOUNDARY LAYERS

H. McDonald - Chairman

SECOND ORDER CLOSURE FOR THE CALCULATION OF COMPRESSIBLE WALL BOUNDED FLOWS WITH AN IMPLICIT NAVIER-STOKES SOLVER

Dany Vandromme
(Universite de Lille, France)

Hieu Ha Minh
(Institut de Mecanique des fluides de Toulouse, France)

John R. Viegas
(NASA Ames Research Center, USA)

Morris W. Rubesin
(NASA Ames Research Center, USA)

Wolfgang Kollmann
(University of California, Davis, USA)

ABSTRACT

A second order closure has been implemented in a two-dimensional implicit Navier-Stokes solver for high Reynolds number compressible flows with integration to the wall. Modification to existing models were necessary to improve the skin friction, recovery factor and the distribution of kinetic energy and anisotropy in an adiabatic flat plate boundary layer in $M=3$ flow.

1] INTRODUCTION

The ultimate goal of this work is to develop a second-order closure model for compressible turbulent boundary layers which is capable of predicting the behavior within a shock-wave, boundary layer interaction. Because such a flow often results in boundary-layer separation, concurrent with its development, it is necessary to incorporate the model into an efficient numerical solution scheme capable of solving the averaged, compressible Navier-Stokes equations.

Although second order closure models have been derived for compressible fluids in the past, Wilcox and Rubesin (1980), Dussauge (1981), Varma et al. (1974) and Bonnet (1982), in the current work it was decided to rederive the conservation and turbulence model equations based on the pioneering incompressible flow models of Launder, Reece, and Rodi (1975) and Hanjalic and Launder (1976). The primary reasons for this rederivation were to clarify the contributions to the turbulence of the large divergence of velocity that occurs in compressible flows with the rapid pressure changes characteristic of shock waves, to consider the effects of non-zero mean fluctuating quantities that result from mass-weighted averaging, Favre (1965), and to permit integration to the surface. The latter point is emphasized in this paper. In the near wall region, the model of Hanjalic and Launder (1976), which was developed for use with two-equation modeling, is generalized to accept both the normal and shear Reynolds stresses that are dependent variables in the current work.

The numerical method used in this study is based on the work of MacCormack (1971) and (1981).

Only results applicable to flow over an adiabatic flat plate, without pressure gradient, in a $M=3$ airstream will be presented here. These results demonstrate the ability of the model to provide the surface parameters of skin friction coefficient and recovery factor and the profiles of both the mean flow properties and the individual Reynolds stresses throughout the boundary layer. It is believed a good representation of the Reynolds stresses in the near wall region will be critical in the application of the current methods to the prediction of the onset of separation.

II] BASIC EQUATIONS AND NUMERICAL METHOD

The numerical method used in this study is the new implicit scheme of MacCormack (1981). This method represents an implicit extension of an explicit method also developed by MacCormack (1971). The new method contains two stages.

In the first stage, MacCormack's explicit predictor-corrector scheme is used. Here, the finite difference equations approximate the governing fluid flow equations to second order accuracy in space and time, but are subject to restrictive explicit stability criteria. The second stage removes these stability conditions by numerically creating an implicit form of the finite difference equations. This new method is unconditionally stable and can be made second order accurate for most flows. The MacCormack algorithm utilizes the vector form of the set of equations that is

$$\frac{\partial U}{\partial t} + \frac{\partial F}{\partial x} + \frac{\partial G}{\partial y} = H \quad (1)$$

For two-dimensional flows with Favre averaging and second-order modeling, the components of the dependent variable vector are represented by

$$U = \begin{bmatrix} \rho \\ \rho u \\ \rho v \\ \rho E \\ \rho \tilde{u} \\ \rho \tilde{v} \\ \rho \tilde{u}^2 \\ \rho \tilde{v}^2 \\ \rho \tilde{u} \tilde{v} \\ \rho \tilde{\epsilon} \end{bmatrix} \quad (2)$$

Note that in the present analysis, the heat flux vector is not treated with a field equation because first-order closure is applied to the total energy equation needed to establish the temperature field. This was done for computational efficiency, but it is not believed to introduce significant error under the adiabatic conditions of interest in the present work.

Consistent with Eq.(1) and the dependent variable vector of Eq.(2), the conservation equations are written in the following forms.

The continuity of mass is

$$\frac{\partial \bar{\rho}}{\partial t} + \frac{\partial}{\partial x_k} (\bar{\rho} \tilde{u}_k) = 0 \quad (3)$$

where the repeated index k represents the x and y terms in Eq.(1), respectively.

When fluctuations in viscosity are ignored, the momentum in the i 'th direction is represented by

$$\frac{\partial}{\partial t}(\bar{\rho} \tilde{u}_i) + \frac{\partial}{\partial x_k} (\bar{\rho} \tilde{u}_i \tilde{u}_k + \bar{P} \delta_{ik} - \bar{\mu} \tilde{S}_{ik} + \bar{\rho} \tilde{u}_i \tilde{u}_k) = 0 \quad (4)$$

where the strain tensor in the viscous term is approxi-

$$\tilde{S}_{ik} \approx \tilde{S}_{ik} = \frac{\partial \tilde{u}_i}{\partial x_k} + \frac{\partial \tilde{u}_k}{\partial x_i} - \frac{2}{3} \delta_{ik} \frac{\partial \tilde{u}_j}{\partial x_j} \quad (5)$$

In Eq.(5), the mean values of the mass weighted fluctuating velocities, though non-zero in Favre averaging, have been neglected in the low Reynolds number terms.

When fluctuating thermal conductivity and viscosity are neglected, the total energy equation becomes

$$\begin{aligned} \frac{\partial}{\partial t}(\bar{\rho} \tilde{E}) + \frac{\partial}{\partial x_k} \left[(\bar{\rho} \tilde{E} + \bar{P}) + \bar{\rho} \tilde{u}_i \tilde{u}_k \tilde{u}_i \right. \\ \left. + \frac{1}{2} \bar{\rho} \tilde{u}_i \tilde{u}_i \tilde{u}_k + \gamma C_v \bar{\rho} \tilde{u}_i \tilde{u}_k - \lambda \frac{\partial \tilde{T}}{\partial x_k} \right. \\ \left. - \bar{\mu} (\tilde{S}_{ik} \tilde{u}_i + \tilde{S}_{ik} \tilde{u}_k + \tilde{S}_{ik} \tilde{u}_i + \tilde{S}_{ik} \tilde{u}_k) \right] = 0. \end{aligned} \quad (6)$$

To solve Eqs.(3) to (6), it is necessary to evaluate simultaneously the Reynolds stresses, $\bar{\rho} \tilde{u}_i \tilde{u}_k$, the turbulent diffusion of kinetic energy, $\frac{1}{2} \bar{\rho} \tilde{u}_i \tilde{u}_i \tilde{u}_k$, the turbulent heat flux, and the averages of the fluctuating velocities, $\bar{\rho} \tilde{u}_i$ or their gradients. The exact equations for the Reynolds stresses in mass-weighted average variables written in divergence form are

$$\begin{aligned} \frac{\partial}{\partial t}(\bar{\rho} \tilde{u}_i \tilde{u}_k) + \frac{\partial}{\partial x_j} \left[\bar{\rho} \tilde{u}_j \tilde{u}_i \tilde{u}_k + \bar{\rho} \tilde{u}_i \tilde{u}_k \tilde{u}_j + \delta_{ij} \overline{\tilde{u}_k \tilde{u}_k} \right. \\ \left. + \delta_{ik} \overline{\tilde{u}_j \tilde{u}_j} - \bar{\mu} \tilde{u}_i \tilde{S}_{kj} - \bar{\mu} \tilde{u}_k \tilde{S}_{ij} \right] \\ = -\bar{\rho} \tilde{u}_i \tilde{u}_j \frac{\partial \tilde{u}_k}{\partial x_j} - \bar{\rho} \tilde{u}_k \tilde{u}_j \frac{\partial \tilde{u}_i}{\partial x_j} + \bar{\rho} \left(\frac{\partial \tilde{u}_i}{\partial x_k} + \frac{\partial \tilde{u}_k}{\partial x_i} \right) \\ - \tilde{u}_i \frac{\partial \bar{P}}{\partial x_k} - \tilde{u}_k \frac{\partial \bar{P}}{\partial x_i} + \bar{\mu} \left(\tilde{S}_{ij} \frac{\partial \tilde{u}_k}{\partial x_j} + \tilde{S}_{kj} \frac{\partial \tilde{u}_i}{\partial x_j} \right) \end{aligned} \quad (7)$$

These equations are modeled by extending the incompressible flow models of Launder, Reece, and Rodi (1975) and Hanjalic and Launder (1976) to compressible conditions by introducing Favre averaging, reintroducing the non-zero divergence terms that were eliminated in the original models, and accounting for the non-zero mass weighted fluctuating velocities, Rubesin (1976). Further, some of the modeling decisions in Hanjalic and Launder (1976) relating the values of the Reynolds stresses to the kinetic energy in their two-equation model can be avoided here since these stresses are computed individually in the present work.

The modeled Reynolds stress equations are

$$\begin{aligned} \frac{\partial}{\partial t}(\bar{\rho} \tilde{u}_i \tilde{u}_j) + \frac{\partial}{\partial x_k} \left[\bar{\rho} \tilde{u}_k \tilde{u}_i \tilde{u}_j - \bar{\mu} \frac{\partial \tilde{u}_i \tilde{u}_j}{\partial x_k} \right. \\ \left. - C_0 \bar{\rho} \frac{1}{2} \tilde{u}_i \tilde{u}_i \frac{\partial \tilde{u}_j}{\partial x_k} \right] \\ = R_{ij} - \frac{C_0 + 2}{11} (R_{ij} - \frac{2}{3} \delta_{ij} P) - \frac{3C_0 + 2}{11} (D_{ij} - \frac{2}{3} \delta_{ij} D) \\ - \frac{10C_0 + 2}{11} \bar{\rho} \tilde{S}_{ij} - C_1 \bar{\rho} \frac{1}{2} (\tilde{u}_i \tilde{u}_j - \frac{2}{3} \delta_{ij} \tilde{u}_k \tilde{u}_k) \\ + \left[C_2 \bar{\rho} \frac{1}{2} (\tilde{u}_i \tilde{u}_j - \frac{2}{3} \delta_{ij} \tilde{u}_k \tilde{u}_k) + C_3 (R_{ij} - D_{ij}) + C_4 \bar{\rho} \tilde{u}_k \left(\frac{\partial \tilde{u}_i}{\partial x_j} + \frac{\partial \tilde{u}_j}{\partial x_i} - \frac{2}{3} \delta_{ij} \frac{\partial \tilde{u}_k}{\partial x_k} \right) \right. \\ \left. + \frac{1}{2} \frac{\partial \tilde{u}_k}{\partial x_i} \bar{\rho} \tilde{u}_j \tilde{u}_k + (1 - f_0) \frac{2}{3} \delta_{ij} \tilde{u}_k \tilde{u}_k \right] - \tilde{u}_i \frac{\partial \bar{P}}{\partial x_j} - \tilde{u}_j \frac{\partial \bar{P}}{\partial x_i} \end{aligned} \quad (8)$$

$$\text{where } P = D = -\bar{\rho} \tilde{u}_j \tilde{u}_j \frac{\partial \tilde{u}_k}{\partial x_k} \quad \tilde{u}_i = \frac{\tilde{u}_i \tilde{u}_i \tilde{u}_i}{(\tilde{u}_i \tilde{u}_i) C_p \tilde{T}} \\ R_{ij} = -\bar{\rho} (\tilde{u}_i \tilde{u}_k \frac{\partial \tilde{u}_j}{\partial x_k} + \tilde{u}_j \tilde{u}_k \frac{\partial \tilde{u}_i}{\partial x_k}) \quad D_{ij} = -\bar{\rho} (\tilde{u}_i \tilde{u}_k \frac{\partial \tilde{u}_k}{\partial x_j} + \tilde{u}_j \tilde{u}_k \frac{\partial \tilde{u}_k}{\partial x_i})$$

The turbulence is scaled with the dissipation of kinetic energy, $\tilde{\epsilon}$, given by the equation

$$\begin{aligned} \frac{\partial}{\partial t}(\bar{\rho} \tilde{\epsilon}) + \frac{\partial}{\partial x_k} \left[\bar{\rho} \tilde{\epsilon} \tilde{u}_k - (\bar{\mu} + C_\epsilon \bar{\rho} \frac{1}{2} \tilde{u}_i \tilde{u}_i) \frac{\partial \tilde{\epsilon}}{\partial x_k} \right] = \\ - C_\epsilon \bar{\rho} \frac{1}{2} \tilde{u}_i \tilde{u}_i \frac{\partial \tilde{u}_k}{\partial x_k} - C_\epsilon \bar{\rho} \tilde{u}_k \tilde{S}_{ij} \left[\tilde{\epsilon} - 2 \nu \left(\frac{\partial \tilde{u}_k}{\partial x_k} \right)^2 \right] \\ + C_\epsilon \bar{\mu} \frac{1}{2} \tilde{u}_i \tilde{u}_i \left(\frac{\partial \tilde{u}_k}{\partial x_j} \frac{\partial \tilde{u}_j}{\partial x_k} \right) - C_\epsilon \bar{\rho} \tilde{u}_k \frac{\partial \tilde{\epsilon}}{\partial x_k} \end{aligned} \quad (9)$$

Although not used in the present application, note the presence of a pressure gradient term that is introduced by the compressibility.

Finally, the total energy equation is modeled in first order, and becomes

$$\begin{aligned} \frac{\partial}{\partial t}(\bar{\rho} \tilde{E}) + \frac{\partial}{\partial x_k} \left[(\bar{\rho} \tilde{E} + \bar{P} + \frac{1}{2} \bar{\mu} \frac{\partial \tilde{u}_i}{\partial x_i}) \tilde{u}_k + (\bar{\rho} \tilde{u}_i \tilde{u}_k - \bar{\mu} \tilde{S}_{ik}) \tilde{u}_i \right. \\ \left. - C_5 \bar{\rho} \frac{1}{2} \tilde{u}_i \tilde{u}_i \frac{\partial}{\partial x_k} (\tilde{u}_i \tilde{u}_i) - \bar{\mu} \frac{\partial}{\partial x_k} \left(\frac{\tilde{u}_i \tilde{u}_i}{2} + \frac{\tilde{u}_i \tilde{u}_i}{2} \right) \right. \\ \left. - (C_6 \bar{\rho} \frac{1}{2} \tilde{u}_i \tilde{u}_i + \delta_{ik} \frac{1}{2} \nu) \frac{\partial \tilde{\epsilon}}{\partial x_k} \right] = 0 \end{aligned} \quad (10)$$

The modeling coefficients used in these equations are given in table I.

The computations were performed in a rectangular computation domain that was located downstream of the leading edge of the flat plate. The boundary conditions at the upstream edge of the computation domain were determined from the output of a boundary-layer code that contains the Wilcox and Rubesin turbulence model. This model, as a special case, uses the Launder, Reece, and Rodi model for the pressure rate of strain terms in homogeneous flow, but without the near wall modification, and accounts for compressibility by use of the local mean density and non-zero dilatation in the definition of the mean strain rate. The scaling parameter in this model is the square of the dissipation rate per unit of kinetic energy. The model also contains some near wall, or low Reynolds number, modifications to allow integration to the surface that are equivalent to, but different from, those used by Hanjalic and Launder (1976). These differences of the model in the boundary-layer code and the one used here causes a sudden departure from the upstream boundary conditions to occur in the computations. The size of this departure, however, is very small and it extends into the computation zone by only about two streamwise mesh spacings. This "mismatch" of models affects the overall results to such a small extent that it does not warrant "renormalizing" the upstream conditions by the results of the present calculations a short distance into the computational domain.

The boundary conditions at the surface are set to

$$\begin{aligned} \tilde{U} = \tilde{V} = 0 \quad \frac{\partial \bar{P}}{\partial y} = 0 \quad \frac{\partial \tilde{T}}{\partial y} = 0 \\ \tilde{u}'' = \tilde{v}'' = \tilde{w}'' = \tilde{u}' \tilde{v}' = 0 \quad \frac{\partial \tilde{\epsilon}}{\partial y} = 0 \end{aligned}$$

The boundary conditions at the "top" of the computational domain are set to $\tilde{u}'' = \text{constant}$, with all of the other dependent variables set to a zero derivative in the normal direction.

The downstream boundary conditions for all the dependent variables are zero derivatives in the streamwise direction.

III] RESULTS AND DISCUSSION

The computations presented here are confined to the evaluation of the turbulent boundary layer on an adiabatic flat plate, with zero axial pressure gradient, in an airstream at $M=3$. The purpose of these calculations was to examine the applicability of extending turbulence models derived for incompressible flows to conditions where compressibility or the variation of mean properties is significant. Under these zero axial pressure gradient conditions, however the pressure gradient terms in Eqs.(8) and (9) essentially vanish so that the modeling of terms such as u'' cannot be tested here. In addition, modifications of the full Reynolds stress equations to account for locally low Reynolds numbers and to permit integrations to the surface are developed so as to yield results consistent with near-wall experimental data, Eckelmann (1974), Kreplin and Eckelmann (1979).

It is often difficult in the solution of complex flow fields that require the Navier-Stokes equations to separate the effects of the basic solution algorithm and the necessarily limited mesh configuration from those of the turbulence model. To enable us to distinguish the contributions of these effects, a boundary layer code utilizing the same turbulence model as in the Navier-Stokes code was also employed. This boundary layer code uses a modified version of the Patankar and Spalding method, and is described in detail by Vandromme (1980). The initial profiles used with the boundary layer code are identical to those described above for the Navier-Stokes code. In addition to helping verify the numerics of the Navier-Stokes code, the speed of the boundary layer code enabled it to be a most useful tool to guide and test turbulence model modifications prior to their introduction into the more time consuming Navier-Stokes code.

In the computations that follow the boundary layer code employed 128 mesh points across the computational domain. In contrast, the Navier-Stokes code employed only 32 mesh points across its computational domain. The mesh spacing in both codes is exponentially stretched from a fine spacing near the surface, to resolve the region where very rapid changes in the mean velocity occur, to a relatively coarse mesh in the outer flow where the velocity is asymptotically approaching a constant value. Prior to selecting these meshes, tests indicated that results obtained with the boundary-layer code did not deviate significantly from those presented here when as many as 200 mesh points were used across its computational domain. Similarly 50 mesh points were tried with the Navier-Stokes code and found to yield insignificant differences in the results. Consequently, the more economical 128 and 32 mesh point configurations perpendicular to the surface were selected for the boundary-layer and Navier-Stokes codes, respectively, for the calculations shown in this work. In the flow direction, the boundary-layer code selects its own mesh spacing, while the Navier-Stokes code utilized a mesh spacing which corresponded to about one-half the boundary layer thickness at the inflow boundary. Experience with other Navier-Stokes codes has shown this streamwise resolution to be adequate for an accurate solution of an equilibrium boundary layer flow, Viegas and Horstmann (1978).

The first case calculated employed the modeling coefficients recommended by Launder, Reece, and Rodi (1975), Hanjalic and Launder (1976), and Gibson and Launder (1976). These are shown in table I. The results of the calculations with this model referred to as the standard model are shown in Figs. 1 to 9. The first two figures show the mean velocity profiles in the near-wall and wake portions of the boundary layer. To account for compressibility, the mean velocity in both figures was transformed according to the relation

$$u_+ = \int_0^u \sqrt{\frac{\rho}{\rho_w}} du \quad (11)$$

These figures show the transformed mean velocity profiles calculated with both the Navier-Stokes (N.S.) and the boundary layer (B.L.) codes at a station where the local Reynolds number based on momentum thickness is 10. Fig. 1 is plotted in "law of the wall" coordinates, when y^+ is defined in terms of wall properties. The computed results from the two codes are in close agreement over most of the boundary layer and behave in the generally expected manner. The computed results fit the $u^+ = y^+$ curve near the surface, and then blend gradually to a logarithmic behavior that has a smaller slope and higher level than the straight line which represents the normal logarithmic "law of the wall". The values of skin friction found from the two codes are included on the figure and agree within 3.5%, but are about 13.5% lower than that evaluated from the Karman-Schoenherr skin-friction law modified according to the van Driest II transformation, van Driest(1951). Only about half of the excess of the computed velocity in the logarithmic region can be explained by the relative skin friction results. The calculated recovery factor was $r=0.85$.

Fig. 2 shows the transformed mean velocity profiles in the bulk of the boundary layer. For reference, the solid line represents the extension of Coles' "law of the wake", to compressible flow through the use of Eq.(11), Hopkins, Keener, Polek and Dwyer (1972). The agreement between the results from the boundary layer and Navier-Stokes codes over this major portion of the boundary layer, is very good. These results appear to be fuller than the "law of the wake", and only about half the fullness can be attributed to the lower predicted skin friction.

Fig. 3 shows a comparison between the calculated values of the normal Reynolds stresses, from both codes, and data from the experiments of Klebanoff(1955) and Robinson, Seegmiller, and Kussay(1983). These experimental results are referred to on the figure as KLEB and LASR, respectively. The Klebanoff experiment was conducted over a large flat plate at a speed sufficiently low so that the air acted as an incompressible fluid. In contrast, the Robinson et al. experiment was in an airstream of $M=3$, along a circular cylinder. The coordinates chosen for this figure collapses these different data reasonably well, suggesting that mass weighting of Reynolds stress accounts quite well for the effects of compressibility. This correlation of the experimental data implies that it is also permissible to compare $M=3$ calculations with data from experiments with incompressible fluids. As with the mean velocity results, the Navier-Stokes and boundary-layer codes agree. In comparison with the experimental data, the computed results for u and v are generally low in the inner portion of the boundary layer and high over the outer 80%, or so, of the boundary layer. The calculated v is slightly higher than the data over the entire boundary layer. Note that in this figure, and in subsequent figures, the abscissa, y/δ , is based on the mean momentum boundary layer thickness corresponding to each individual case. This allows observing, in this figure, the extent of the Reynolds stress profiles relative to their velocity thickness for each case.

Figs. 4 and 5 represent the turbulence kinetic energy, or $1/2$ the trace of the Reynolds stress tensor, in the near wall region and over the bulk of the boundary layer, respectively. The small differences in the Navier-Stokes and boundary layer results are not considered significant, when consideration is given to the stiffness of the Reynolds stress equations and the differences in the mesh resolution utilized in the two codes. The data of Eckelmann (1974), Kreplin and Eckelmann (1979) and of Klebanoff (1955) on these and subsequent figures are represented by the symbols identified by KREP and KLEB, respectively. Fig. 4 shows the extent to which these calculated results underpredict the kinetic energy of the turbulence for $y^+ < 250$ (this corresponds to about the limit of the useful range of comparisons with the wall coordinates for this case). Conversely, Fig. 5 shows that a significant over prediction of the level of kinetic energy occurs over the remaining bulk of the boundary layer. Fig. 5 also shows that the calcu-

lated turbulence kinetic energy thickness corresponds well with the measured thickness when each is compared to their respective mean velocity boundary layer thicknesses.

Figs. 6 and 7 show the shear stress distribution in the boundary layer, again in coordinates appropriate to the near-wall region and over the bulk of the boundary layer. Again the Navier-Stokes and boundary layer solutions are in reasonably good agreement. In the wall region, up to a $y^+ = 100$, the shear stress fits the experimental data exceedingly well, much better than would have been expected from the kinetic energy distribution shown in Fig. 4. This good agreement assures that the sublayer and buffer regime, where as much as 60% of the momentum change in the boundary layer can occur, are well represented by this model. In the main part of the boundary layer, the shear stress exceeds the experimental data by as much as 50%, which is consistent with the behavior of the kinetic energy, indicated in Fig. 5. As with the kinetic energy, the calculated shear stress thickness is consistent with the thickness of the mean flow boundary layer. This is not surprising since the shear stress intimately affects the mean motion.

Finally, the ratio of the local shear stress to turbulence kinetic energy are shown in Figs. 8 and 9 for the bulk of the boundary layer and the near wall region, respectively. It is observed from Fig. 8 that this ratio remains essentially constant and equal to 0.34 over most of the boundary layer. This value essentially agrees with the value reported by Bradshaw (1967), but is about 10% higher than the Klebanoff data plotted on the figure. The differences between the results from the Navier-Stokes and boundary layer calculations near the outer edge of the boundary layer are explainable by the large differences in the mesh spacing of the two computer codes. In Fig. 9, this ratio is shown in comparison with the near wall data of Kreplin and Eckelmann and of Klebanoff. Again the differences of the computed results can be attributed to the mesh differences. It is noted that the computed results retain their value of close to 0.3 much closer to the surface than the experimental data. The high calculated values of the ordinate in the region of $y^+ < 100$ reflects the results shown on Figs. 4 and 6. There the calculated kinetic energy of turbulence was significantly lower than the measured values whereas the calculated shear stress represented the data well. The high values of the Kreplin and Eckelmann data closest to the surface are believed to be unreal as the ratio is expected to approach zero linearly with the distance from the surface.

The computed results shown on the previous figures were indicated to be essentially independent of the particular computer code and/or the computational mesh employed. Thus, they represent a reliable test of the turbulence model for flow of an airstream at $M=3$ over a flat plate in a zero pressure gradient. This test shows qualitative agreement with experiment but overall the turbulence model is in need of quantitative improvement before it should be applied to more complex flows that may be very dependent on the normal stresses.

Some of the weaknesses of the standard model are manifest in the following mean results: (1) The local skin friction is about 10.5 to 13.5% lower than expected. (2) The recovery factor is 0.85 instead of the required 0.89 or 0.9. (3) The mean velocity profile is somewhat fuller than expected. These mean results are caused by the standard model characteristics which yield: low values of the kinetic energy of turbulence near the surface, but values that are high for $y^+ > 0.15$; too little anisotropy near the surface, too high a value of anisotropy over $y^+ > 0.15$; values of the turbulent shear stress that are quite good near the surface, but high in the region when $y^+ > 0.1$. These inconsistencies, in the standard model suggest it would be inadequate for use for more complex flows such as might occur when severe pressure gradients exist and where a knowledge of the normal stresses are important. The failures of this model to give good normal Reynolds stress results is disquieting for it is just for flows where the normal stress might be important, such as where separation and attachment occur, that

the Reynolds stress model would be expected to be most useful and more accurate than less complex models of turbulence (eg. k -models).

To improve the results based on the standard model, modifications were made to some of the modeling coefficients. These are indicated in table I under the title "new". The reasoning underlying these changes is given below.

To improve the anisotropy in the vicinity of the surface, the coefficient f_1 (see table I) was introduced to reduce C_1 , the coefficient of the return to isotropy terms of Eq. 8. The values of the constants in f_1 were selected to produce an enhancement of the anisotropy in the near wall region but without yielding unrealistic values of the normal stresses at the onset of the fully turbulent region. A 25% increase in the exponent of f_1 over the value 2.0 was found to violate realizability there. With these modifications to C_1 , further improvements in the anisotropy near the surface were still required. It was decided then to modify the coefficients C_3 , C_4 and C_5 in the "near wall" correction to the pressure rate of strain correlation term of Eq. 8. During the derivation of the values of these coefficients, it was found that values based on the normal and shear stresses from a consensus of experimental data (Launder et al. (1975)), did not agree exactly with the values of C_3 , C_4 and C_5 indicated in Launder et al. (1975). The values derived in the present work are shown in table I. It was found these new coefficients, themselves, improved the anisotropy, but the results still showed too low a kinetic energy in the near wall region.

It was decided then to emphasize the improvement in the kinetic energy, before further optimizing the anisotropy. This was attempted through changes in the dissipation rate equation. It was reasoned that enhanced diffusion, i.e. increased C_ϵ , would reduce ϵ in the near wall region and increase it in the outer part of the boundary layer, and that this would in turn increase k near the surface and lower it in the outer part of the boundary layer as would be required from the behavior of k related to that shown in Fig. 4 and 5. As expected, the combined effect was the movement of the peak of the k curve towards the surface. The change in C_ϵ was accompanied by a change in C_μ to maintain the customary log-law relationship, see Eq. (31) of Launder et al. (1975). Also, since k was too low near the wall, f_μ served no purpose in the present model and was set to unity. With these changes to the dissipation equation, it was found that better skin friction results were obtained from changing C_3 from 2.0 to 1.0.

The results of these combined changes to the turbulence model are shown in Figs. 10 through 18. Fig. 10 shows improved skin friction and agreement with the law of the wall over the standard model. Although not shown, it was found that the skin friction coefficient showed similar agreement with the theoretical value after the initial "mismatch" in flow conditions discussed above decayed. It is interesting that use of the same diffusion coefficient, C_ϵ , in the total energy equation now resulted in a temperature recovery factor equal to 0.88 in close agreement with experimental results. It is believed that the enhanced anisotropy in the near wall region that reduces v led to this result. Fig. 11 shows that the mean velocity profile in the outer portion of the boundary layer is essentially unchanged by the turbulence model modifications.

The effects of the model modifications can be seen most clearly in the behavior of the Reynolds stresses and kinetic energy. From a comparison of Figs. 3 and 12, it is observed, in the very near wall region, that the modified model yields higher u and w , and lower v . The latter is remarkably consistent with the experimental data, whereas the u and w are still lower than the data. Further out in the boundary layer the v is still in good agreement with the data, whereas the u and w still rise above their corresponding experimental values, though not as high as the standard model.

Figs. 13 and 14 show that the new distribution of the turbulent kinetic energy in the vicinity of the surface and over the bulk of the boundary layer conform better with the experimental data than the standard model.

The expected changes in k by the alteration of the modeling coefficients in the dissipation equation discussed earlier occurred, but there is still room for improvement. Similar improvements did not occur in the uv curves shown in Figs. 15 and 16. The change in Fig. 17 is not very dramatic. Figure 18, which emphasizes the behavior of uv/k in the near wall region, however shows astonishing improvement over the standard model.

IV CONCLUSIONS

A second order closure has been implemented in a 2-D implicit Navier-Stokes solver for high-Reynolds-number compressible flows.

The basic Launder, Reece, and Rodi (1975) and Hanjalic and Launder (1976) models have been rederived and modified to include compressibility effects and, especially, to allow integration of all the equations to the wall. Although the basic equations are applicable to complex compressible flows, to emphasize the modeling required to extend the computations to the surface accurately, the calculations were confined to the simpler case of flow over an adiabatic flat plate in a $M=3$ airstream where transformed incompressible flow data could be utilized for guidance of the turbulence modeling. To avoid ambiguities regarding the influence of the numerics, the identical turbulence model introduced in the Navier-Stokes code was also implemented in a boundary layer code. Both codes employed common upstream boundary conditions. It was found that 32×32 mesh point computations in the Navier-Stokes code yielded comparable results to those given by the boundary layer code with 128 crosswise mesh points.

When a model was used that was the logical combination of the methods of Launder, Reece, and Rodi (1975) and Hanjalic and Launder (1976) it was found that both the Navier-Stokes and boundary layer codes could be integrated to the surface, but that the results were not satisfactory in all respects. In particular, deficiencies were noted in the predicted anisotropy and the kinetic energy throughout the boundary layer and in the shear stress in the outer part of the boundary layer. These deficiencies were reflected in fairly small, but significant, errors in the mean velocity profiles and the surface quantities of skin friction and recovery factor. The model was then modified by (1) damping the Rotta return to isotropy term, (2) adjusting the near-wall pressure rate of strain terms of the Launder, Reece, and Rodi (1975), (3) modifying the turbulent diffusion of the dissipation rate, and (4) altering the coefficient in the Hanjalic and Launder (1976) dissipation rate equation needed there to permit integrations to the surface. These turbulence model modifications produced excellent values of skin friction and recovery factor, and maintained reasonably good velocity profiles in the wake region. The anisotropy and kinetic energy results, while better than those of the standard model, are still in need of improvement, as is also the shear stress in the wake region of the boundary layer. Finally, the new model yields results of $\langle uv \rangle / k$ very near the surface that are in remarkable agreement with the transformed experimental data.

Although the model improvements suggested in this paper have resulted in what is believed to be limited success, it is not clear that further improvement can be made unambiguously at this time. The modelling changes performed here were guided by experimental data obtained in incompressible flows that were extended to the conditions of the $M=3$ test case through the use of local density or a van Driest like transformation. The magnitude of the error of this approach could not be assessed from the widely scattered existing compressible flow data, Fernholz, Finley, and Mikulla (1981). Fine tuning of the turbulence model may have to wait for more extensive experiments utilizing more accurate instrumentation such as Robinson, Seegmiller, and Kussoy (1983).

Coef.	Eq. NO	Std	New	comment
C1	8	1.500	1.500	
f1	8	1.000	*	
C2	8	0.400	0.400	
C3	8	0.125	0.1597	
C4	8	0.015	0.0133	
C5	8	0.000	0.0041	
Cs'	8,10	0.250	0.250	
Ce1	9	1.280	0.675	
Ce2	9	1.800	1.800	
fe	9	**	1.000	
Ce3	9	2.000	1.000	
Ce4	9	0.000	0.000	fl. pl. only
Cse	10	0.313	0.313	
fs	8	***	***	

* : $f1 = \exp(-2.0/(1.0 + Ret/30.0))$
 ** : $fe = 1.0 - 0.222 \exp(-(Ret/6.0))$
 *** : $fs = 1.0/(1.0 + Ret/10.0)$

Table I : modeling coefficients and functions

BIBLIOGRAPHY

- Bonnet J. P., 1982, "Etude theorique et experimentale de la turbulence dans un sillage supersonique". Thesis for Doctor of Physical Sciences, University of Poitiers, France.
- Bradshaw P., Ferriss D. H. and Atwell N. P., 1967, "Calculation of boundary layer development using the turbulent energy equation". J.F.M. vol 28, p593.
- Dussauge J. P., 1981, "Evolution de Transferts Turbulents dans une Detente Rapide, en Ecoulement Supersonique". Thesis for Doctor of Physical Sciences, University of Aix-Marseille II.
- Eckelmann H., (1974), "The structure of the viscous sub-layer and the adjacent wall region in a turbulent channel flow". JFM vol 65, pp 439-459
- Favre A., (1965), "Equations des gaz turbulents compressibles". Journal de Mecanique, vol 4, n 3
- Fernholz, H. H., Finley, M. A. and Mikulla, V., 1981, "A Further Compilation of Compressible Boundary Layer Data with a Survey of Turbulent Data". AGARDograph-AG-263
- Gibson, M. M. and Launder, B. E., 1976, "On the Calculation of Horizontal, Turbulent, Free Shear Flows Under Gravitational Influence." Journal of Heat Transfer, Transactions of the ASME, vol 98, serie C, n 1, pp 81-87.
- Hanjalic, K. and Launder, B. E., 1976, "Contribution Towards a Reynolds-Stress Closure for Low Reynolds number turbulence" J. Fluid Mech., Vol. 74, Part 4, pp. 593-610.
- Klebanoff, P. S., 1955, "Characteristics of Turbulence in a Boundary Layer with Zero Pressure Gradient". NACA Rept. 1247.
- Kreplin, H. and Eckelmann, M., 1979, "Behavior of the Three Fluctuating Velocity Components in the Wall Region of a Turbulent Channel Flow". Phys. Fluids, Vol. 22, pp. 1233-1239.
- Launder, B. E., Reece, G. J., and Rodi, W., 1975, "Progress in the Development of a Reynolds-stress Turbulence closure" J. Fluid Mech., vol. 68, Part 3, pp. 537-566.
- MacCormack, R. W., 1971, "Numerical Solution of the Interaction of a Shock Wave with a Laminar Boundary Layer", Lecture Notes in Physics, Springer-Verlag, 8, 151.
- MacCormack, R. W., 1981, "A Numerical Method for Solving the Equations of Compressible Viscous Flow", AIAA-81-0110, AIAA 19th Aerospace Sciences Meeting, St. Louis, Missouri, Jan. 12-15.
- Robinson S. K., Seegmiller H. L. and Kussoy M. I., 1983, "Hot-wire and laser Doppler anemometer measurements in a supersonic boundary layer". AIAA paper-83-1723, Danvers, Massachusetts.
- Rubens, M. W., 1976, "A One-equation Model of Turbulence For Use with the Compressible Navier-Stokes Equations" NASA TMX-73,128.
- Van Driest E. R., 1951, "Turbulent boundary layer in compressible fluids" J. Aero. Sci. vol 8, p145.

Vandromme D., 1980, "Turbulence modelling in variable density flow" PhD Thesis, University of Brussels, Belgium

Varma A. K., Beddini R. A., Sullivan R. D. and Donaldson C. du P., (1974), "Application of an invariant second-order closure model to compressible shear layers". AIAA paper 74-592.

Viegas, J. R., and Horstman, C. C., 1978, "Comparison of Multiequation Turbulence Models for Several Shock Separated Boundary-Layer Interaction Flows". Paper 78-1165 AIAA 11th Fluid and Plasmadynamics Conference, Seattle, Wash, July 10-12.

Wilcox, D. C. and Rubesin, M. W., 1980, "Progress in Turbulence Modeling for Complex Flow Fields Including Effects of Compressibility" NASA Technical Paper 1517.

This study was sponsored by the National Aeronautics and Space Administration through a grant (NASA-HCC2-186) to University of California, Davis, California. The authors would like to express their appreciation to this agency for its support for this work.

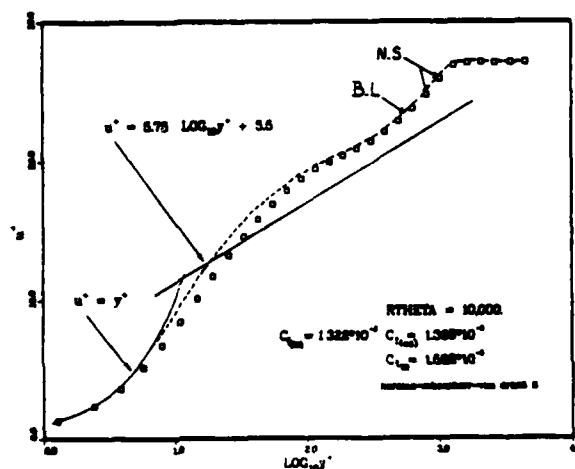


Fig. 1. Velocity profile (standard model).

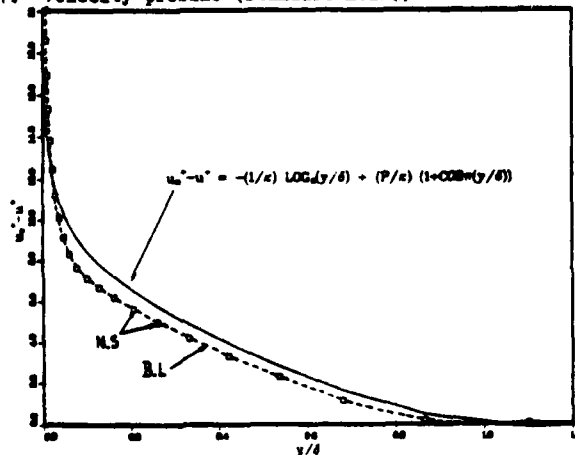


Fig. 2. Defect velocity profile (standard model). (compressible effects included).

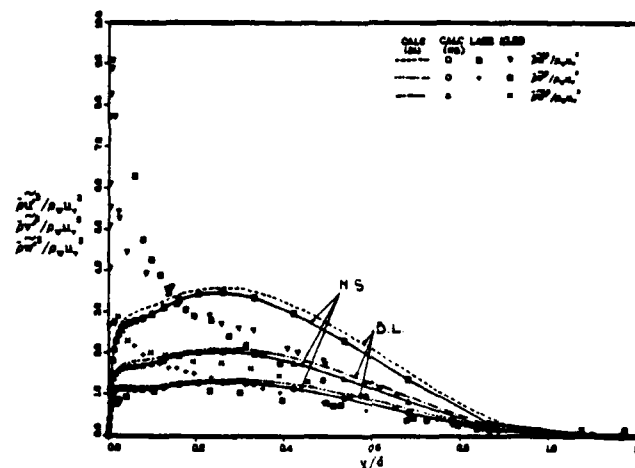


Fig. 3. Normal stress distribution (standard model).

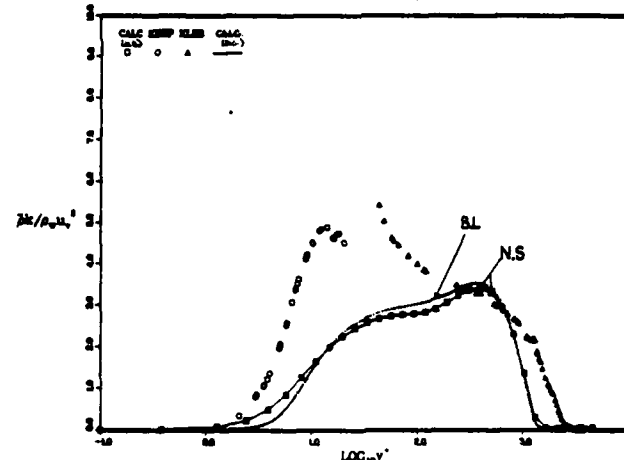


Fig. 4. Turbulent kinetic energy (standard model).

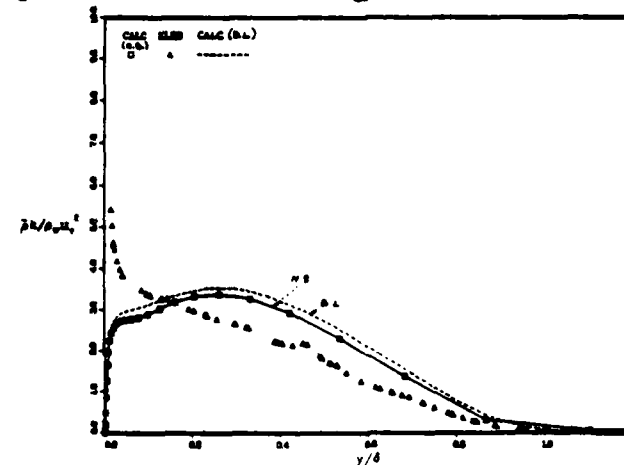


Fig. 5. Turbulent kinetic energy (standard model).

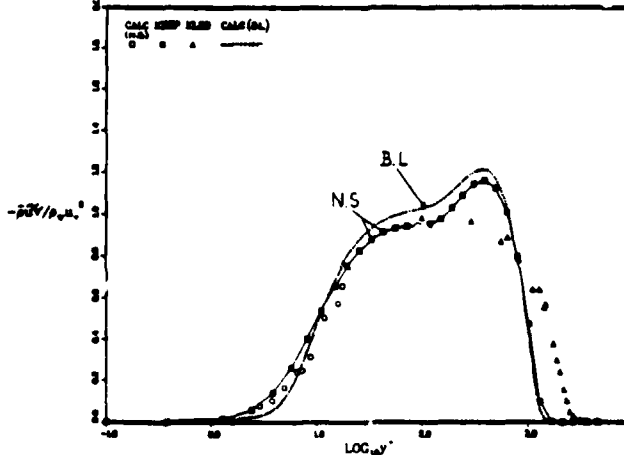


Fig. 6. Turbulent shear stress (standard model).

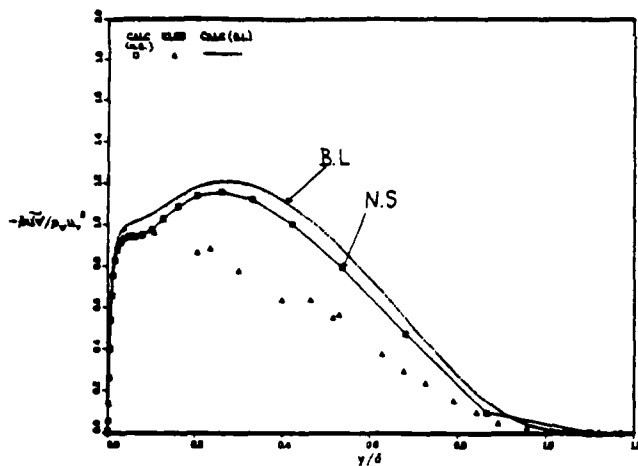


Fig. 7. Turbulent shear stress (standard model).

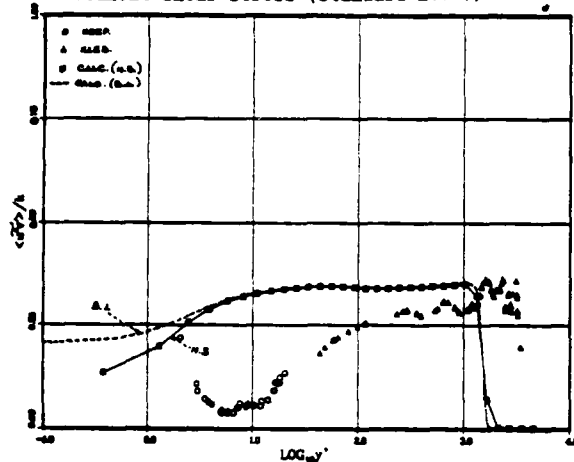


Fig. 8. Turbulence ratio (standard model).

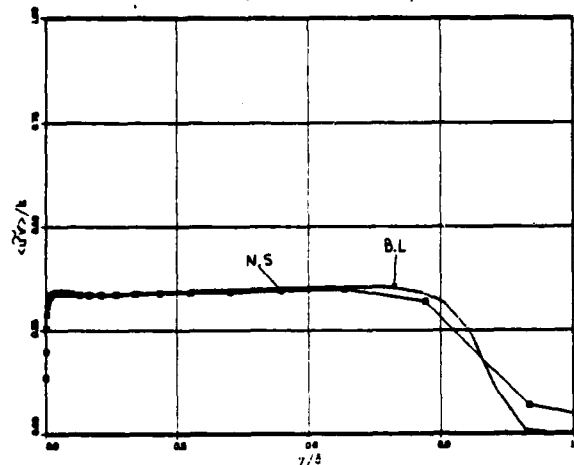


Fig. 9. Turbulence ratio (standard model).

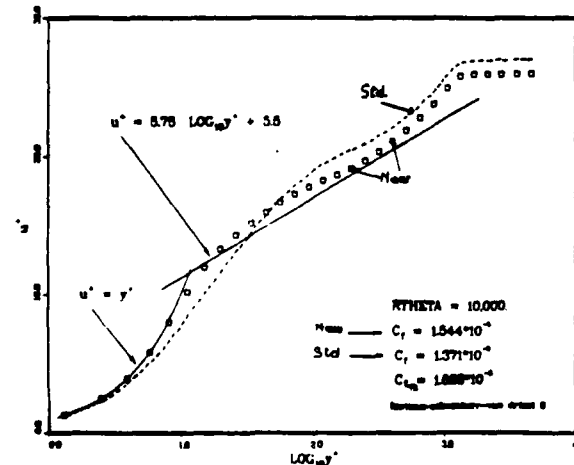


Fig. 10. Velocity profile.

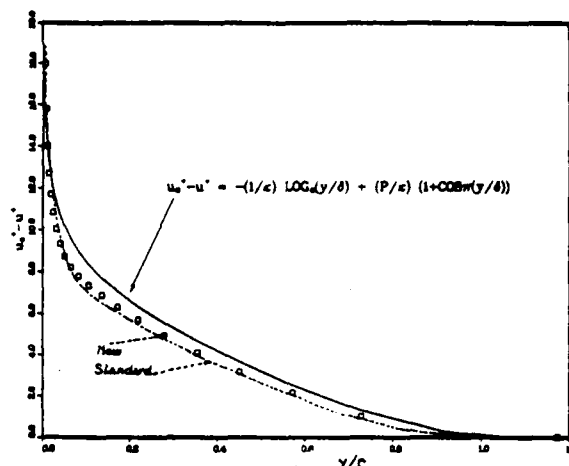


Fig. 11. Defect velocity profile. y/δ (compressible effects included)

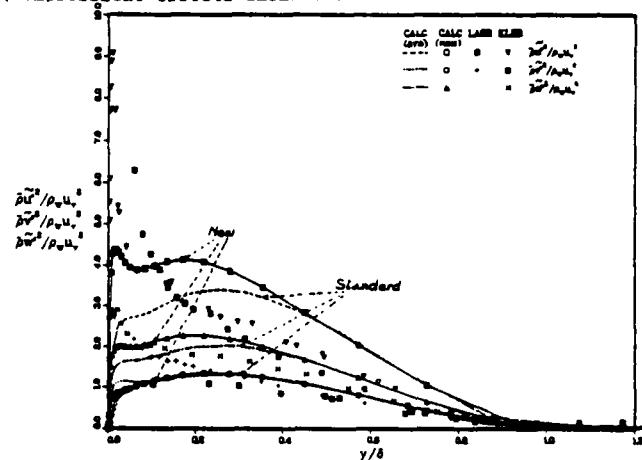


Fig. 12. Normal stress distribution.

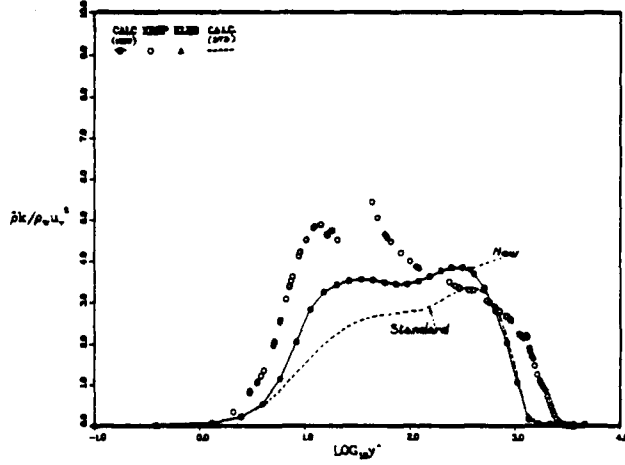


Fig. 13. Turbulent kinetic energy.

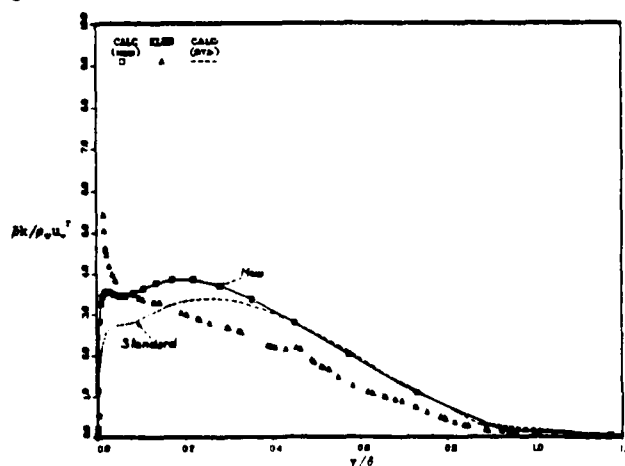


Fig. 14. Turbulent kinetic energy.

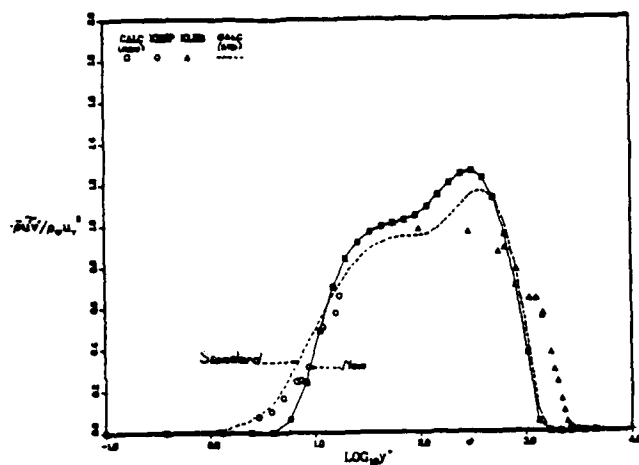


Fig. 15. Turbulent shear stress.

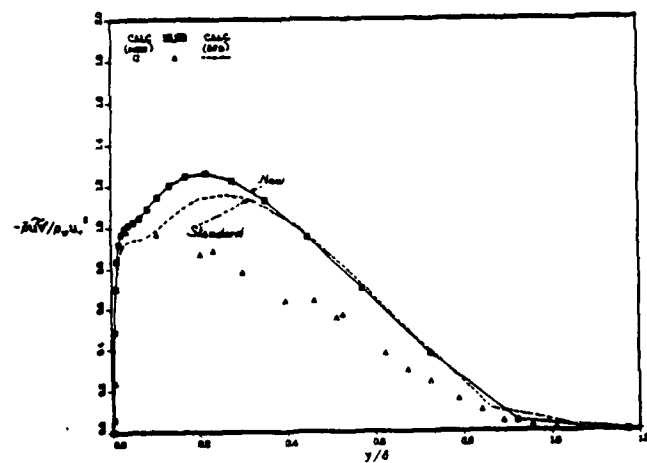


Fig. 16. Turbulent shear stress.

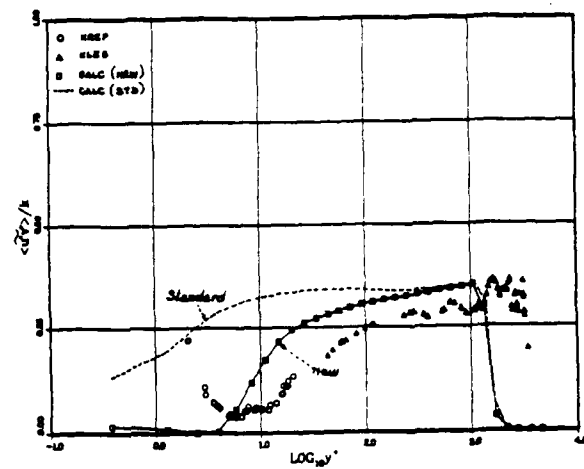


Fig. 17. Turbulence ratio.

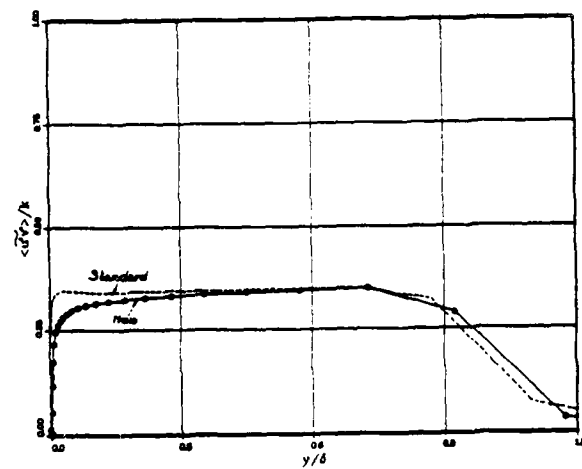


Fig. 18. Turbulence ratio.

PREDICTION OF WALL-BOUNDED TURBULENT FLOWS WITH AN IMPROVED VERSION OF A REYNOLDS-STRESS MODEL

M. Prud'homme and S. Elghobashi
Mechanical Engineering Department
University of California, Irvine
Irvine, California 92717

ABSTRACT

The paper proposes some improvements to the modeled transport equations of the Reynolds stresses $\overline{u_i u_j}$ and the turbulence energy dissipation rate ϵ introduced by Launder, Reece and Rodi (1975) and Hanjalic & Launder (1976). Special attention is given to modeling the pressure - strain correlation near solid walls and the treatment of the boundary conditions for ϵ .

Predictions obtained with the proposed model are compared with measurements of confined flows with and without recirculation.

INTRODUCTION

The Reynolds-stresses model proposed by Launder, Reece & Rodi (1975) was shown to predict many flows with reasonable accuracy such as jets, mixing layers, symmetric and asymmetric channel flows. Later, Pope & Whitelaw (1976) predicted near wake flows using both the $k-\epsilon$ model and the Launder et al. model (hereinafter called LRR) and found the latter to yield significantly better results. However, the LRR model is a high Reynolds number model which does not account for the influence of viscosity on the various transport processes of $\overline{u_i u_j}$ and ϵ . Regions adjacent to solid walls where steep velocity gradients exist and viscous effects are important were avoided in the computations of LRR and Pope & Whitelaw (1976). Instead surface boundary conditions were transferred to points within the fluid removed from the near-wall region by the so-called wall functions. Thus the LRR model is restricted to unconfined flows or wall bounded flows where universal wall functions are sufficiently well established.

To alleviate these shortcomings, Hanjalic & Launder (1976) (hereinafter called HL) proposed a version of LRR's model valid for low Reynolds number regions as well. This allowed for calculations up to the wall itself in situations where wall functions were inaccurate or unavailable. They tested their model in flows where boundary-layer approximations were valid but unfortunately they did not solve for all the turbulent stresses. They relied instead on the fact that $uv/u^2 v^2$ was nearly constant over the wall region to obtain a simplified closure in boundary layer form involving only k , uv , ϵ and U as unknown quantities, where U and u denote the mean and fluctuating velocity in a direction parallel to the wall, and v the fluctuating velocity normal to the wall. As expected the HL model did not predict the wall region satisfactorily when we tested it in channel flows. For example the friction coefficient C_f was over predicted by up to 50%, the maximum value of k was under predicted by 40%, and the anisotropy of the components of k , i.e. u^2, v^2, w^2 was poorly reproduced. The need to correct these defects motivated our search for an improved Reynolds stress model.

In the present work viscous effects on the diffusive transport of $\overline{u_i u_j}$ and ϵ are explicitly accounted for, and a new approximation of the pressure-strain correlation near solid walls is proposed. The dissipation terms in the transport equations for $\overline{u_i u_j}$ are modified and some constants appearing in the model reevaluated. Also we discuss the wall boundary condition for the ϵ equation since its correct prescription is of paramount importance in obtaining an accurate solution.

Closure of the Transport Equations

The Stress Transport Equations. The Reynolds-stresses $\overline{u_i u_j}$ in an incompressible turbulent flow are governed by an exact equation derived using the Navier-Stokes equation (see Tennekes & Lumley, 1972) written as

$$\begin{aligned} d(\overline{u_i u_j})/dt = & - (\overline{u_j u_k} \overline{U_{i,k}} + \overline{u_i u_k} \overline{U_{j,k}}) \\ & + (\overline{p/\rho}) (\overline{u_{i,j}} + \overline{u_{j,i}}) \\ & + \{ \nu (\overline{u_{i,j}})_{,k} - \overline{u_i u_j u_k} - (\overline{p/\rho}) (\overline{\delta_{jk} u_i} + \overline{\delta_{ik} u_j}) \}_{,k} \\ & - 2\nu \overline{u_{i,k} u_{j,k}} \end{aligned} \quad (1)$$

where $d(\overline{u_i u_j})/dt$ represents the substantial derivative of $\overline{u_i u_j}$, \overline{p} denotes the instantaneous fluctuation of pressure about the mean value, ρ stands for the fluid density and ν is the kinematic viscosity. The comma-suffix notation indicates differentiation with respect to spatial coordinates and upper case letters denote time-mean quantities. The stress production term (I) (written as P_{ij} hereinafter) can be evaluated exactly within the frame of a full second order closure and so does the molecular diffusion term (first term in III). The remaining terms in (I) can only be approximated as functions of the mean velocities and Reynolds stresses in order to achieve closure.

Hanjalic & Launder (1972) evaluated $\overline{u_i u_j u_k}$ (Second term in III) by starting with an exact transport equation for $\overline{u_i u_j u_k}$, employing the quasi-Gaussian assumption for the distribution of the correlation, and neglecting both the convection and diffusion contributions to get

$$\begin{aligned} - \overline{u_i u_j u_k} = & c_s (k/\epsilon) (\overline{u_i u_k} \overline{u_{j,l}})_{,l} \\ & + \overline{u_j u_l} (\overline{u_k u_l})_{,i} + \overline{u_k u_l} (\overline{u_i u_l})_{,j} \end{aligned} \quad (2)$$

Cornack, Leal & Seinfeld (1978) proposed a complicated 4-parameter expression instead of that given in (2) (obtained from Lumley's (1973) rational closure scheme) but recommended (2) for actual computations. However it is the gradient of $\overline{u_i u_j u_k}$ that appears in (1) and contributes to the turbulent diffusion of $\overline{u_i u_j}$. Now the gradient of the right side of (2) in the x_k -direction can be approximated to a first order by the gradient of the last term on that side and neglecting the other two. This turbulent diffusion is strongly damped by fluid viscosity near a wall as the scales become progressively smaller, and thus a damping function of the Van Driest type suggests itself. Therefore we use the approximation

$$-(\overline{u_i u_j u_k})_{,k} = [c_s(k/\epsilon) f_u \overline{u_k u_l} (\overline{u_i u_j})_{,l}]_{,k} \quad (3)$$

where

$$f_u = \exp[-3.4(1 + R_\epsilon/50)^{-2}] \quad (4)$$

and $R_\epsilon = k^2/\nu \epsilon$ is the turbulence Reynolds number. The damping function f_u has been employed by Launder & Sharma (1974) in conjunction with the $k-\epsilon$ turbulence model and is adopted for the present work after experimentation with many other such functions (see Patel, Rodi & Scheuerer 1981) as the most compatible with the rest of our model.

The pressure diffusion term (last term in III) is neglected, first following HL (1972) recommendations based on measurements in asymmetric channel flow (see also Hinze 1975), second because very little is known about it.

Term (IV) in (1) is modeled as

$$\epsilon_{ij} = \frac{2}{3} \epsilon \delta_{ij} + \overline{u_i u_j} (\epsilon/k) f_s (1 - \delta_{ij}) \quad (5)$$

where the summation convention does not apply and f_s is given by (HL)

$$f_s = (1 + R_\epsilon/10)^{-1} \quad (6)$$

This form (5) provided a better representation of the anisotropy of u^2, v^2, w^2 near the wall than HL's original proposal

$$\epsilon_{ij} = \epsilon [\frac{2}{3} (1 - f_s) \delta_{ij} + f_s \overline{u_i u_j} / k] \quad (7)$$

which promotes isotropy in the wall region by splitting ϵ among the normal stresses in proportion to the ratios $\overline{u_i u_j} / k$. Corrsin and Fournier (1982) have shown that ϵ_{ij} can have negative regions even though ϵ must always be positive at each point in space, therefore neither (5) nor (7) can be regarded as anything more than first-order approximations.

Term (II) of (1) was modeled by LRR as

$$\begin{aligned} (p/\rho)(\overline{u_{i,j} + u_{j,i}}) &= -c_1(\epsilon/k)(\overline{u_i u_j} - \frac{2}{3}k\delta_{ij}) \\ &- \frac{(c_2 + 8)}{11} (P_{ij} - \frac{2}{3}P\delta_{ij}) \\ &- \frac{(30c_2 - 2)k(U_{i,j} + U_{j,i})}{55} - \frac{(8c_2 - 2)(D_{ij} - \frac{2}{3}P\delta_{ij})}{11}, \end{aligned} \quad (8)$$

where c_1 and c_2 are constants, $P = \frac{1}{2} P_{ii}$ and

$$D_{ij} = -(\overline{u_i u_k} u_{k,j} + \overline{u_j u_k} u_{k,i}) \quad (9)$$

Lumley (1978) pointed out that c_1 is not strictly a constant. Chung & Adrian (1979) based a turbulence model on Lumley's proposal but it did not seem to perform better than LRR's model. Speziale (1980) criticized the right-hand side of (8) for not being invariant under a time-dependent change of frame while the left-hand side is. He proposed an expression, quadratic in $\overline{u_i u_j}$, involving four constants that have yet to be evaluated. However, we feel that his argument is not well supported for two reasons, first the exact

Navier-Stokes equations themselves are not invariant under time-dependent rotations, second Hanjalic & Launder (1972) have shown that expressions involving products of Reynolds stresses can not satisfy all the requirements of homogeneous turbulence. Therefore we adopt (8) as our model.

The constants c_1 and c_2 are evaluated using the nearly homogeneous shear flow data of Champagne et al. (1970) where U_1 varies linearly with x_2 . One merely substitutes (8) into (1) and neglects convection and diffusion, assuming $P = \epsilon$. This yields algebraic expressions for the Reynolds stresses

$$\begin{aligned} \overline{u^2}/k - 2/3 &= \frac{(8 + 12c_2)}{33c_1} \quad (= .03) \\ \overline{v^2}/k - 2/3 &= \frac{(2 - 30c_2)}{33c_1} \quad (= -.18) \\ \overline{w^2}/k - 2/3 &= \frac{(-10 + 18c_2)}{33c_1} \quad (= -.12) \end{aligned} \quad (10)$$

The experimental values shown between parentheses in (10), are very closely matched by $c_1 = 1.17$, $c_2 = .3$. Rotta (1951) showed that, under certain conditions of homogeneity, the pressure-strain term could be expressed as:

$$(p/\rho)(\overline{u_{i,j} + u_{j,i}}) = \phi_{ij,l} + a_{lj}^{mi} U_{l,m} \quad (11a)$$

where $\phi_{ij,l}$ is a triple correlation of the fluctuating velocities while a_{lj}^{mi} is a fourth-order tensor which should satisfy some kinematic constraints. LRR modeled this tensor as a linear combination of Reynolds stresses in order to derive (8). For an axisymmetric homogeneous flow it can be shown that

$$a_{11}^{22} = 2/3k, \quad a_{22}^{22} = 1/3k, \quad a_{33}^{22} = k \quad (11b)$$

using integral forms for the components of a_{lj}^{mi} . On the other hand, LRR's linear representation yields

$$\begin{aligned} a_{11}^{22} &= \left(\frac{46 - 30c_2}{55}\right) k = .67k \\ a_{22}^{22} &= \left(\frac{18 + 5c_2}{55}\right) k = .35k \\ a_{33}^{22} &= \left(\frac{46 + 25c_2}{55}\right) k = .97k \end{aligned} \quad (11c)$$

Leslie (1980) questioned the validity of (8) and recommended a simplified expression which does not allow for anisotropy between v and w on grounds that (11c) is incompatible with (11b) if one uses $c_2 = .4$ as suggested by LRR. However, using the new value ($c_2 = .3$) the agreement is acceptable between (11b) and the calculated values in (11c).

To account for the anisotropy of the normal stresses near a solid wall we modify (8) by adding to it a wall effect term $\phi_{ij,w}$ defined as

$$\phi_{ij,w} = c_3(P_{ij} - D_{ij}) \exp(-c_4 k^{1/2} s/\nu) \quad (12)$$

where s represents the distance from the wall. The constant c_3 is given in terms of c_1 and c_2 by substituting the modified (8) into (2). For the near wall region in a fully developed channel flow we can assume $P = \epsilon$, neglect the convection and diffusion contribution, and assume the exponential in (12) to be equal to one for small values of s . There results after simplification

$$\begin{aligned} \frac{\overline{u^2}}{k} - \frac{2}{3} &= \frac{2(1 - B_1 + c_3) + 2/3(B_1 + B_3) - 2/3}{c_1} = .51 \\ \frac{\overline{v^2}}{k} - \frac{2}{3} &= \frac{-2(B_3 + c_3) + 2/3(B_1 + B_3) - 2/3}{c_1} = -.42 \end{aligned}$$

$$\frac{\overline{w}^2}{k} - \frac{2}{3} = \frac{2/3(B_1 + B_3) - 2/3}{c_1} = -0.12 \quad (13)$$

with

$$B_1 = \frac{c_2 + 8}{11}, \quad B_3 = \frac{8c_2 - 2}{11} \quad (14)$$

The experimental values in parentheses (see LRR) in the first two cases show that the streamwise stress component is larger and the transverse component smaller than in the free shear layer. The reader will notice that ϕ_{33} vanishes implying that w^2 is not affected by the wall's presence (13); this is not strictly true (see LRR) but still is a good approximation. From (13), (14) one obtains

$$c_3 = \frac{(c_2 + 8)}{11} + .315c_2 \quad (15)$$

The value of the constant c_4 which actually controls the wall shear stress was adjusted to 0.003 to match the data of Kreplin & Eckelmann (1979). The procedure followed in the neighborhood of a corner is described below.

Assume that (a) and (b) (Figure 1) are located on the wall far away from the corner in a symmetric fashion, thus

$$\phi_{ij,w} = c_3(P_{ij} - D_{ij}) f(s_1, s_2) \quad (16a)$$

where

$$f(s_1, s_2) = \exp(-c_4 k^{1/2} s_1 / v) + \exp(-c_4 k^{1/2} s_2 / v) \quad (16b)$$

and

$$\begin{aligned} \phi_{11,w} &= 2c_3 \overline{uv} (v, x, -u, y) f(s_1, s_2) \\ \phi_{22,w} &= 2c_3 \overline{uv} (u, y, -v, x) f(s_1, s_2) \\ \phi_{12,w} &= c_3 [(u^2 - v^2) u, y + (v^2 - u^2) v, x] f(s_1, s_2) \end{aligned} \quad (17)$$

Therefore (17) reduces to:

$$\begin{aligned} \phi_{11,w}^a &= -2c_3 (\overline{uv} u, y)_a \\ \phi_{22,w}^a &= -\phi_{11,w}^a \\ \phi_{12,w}^a &= c_3 [(u^2 - v^2) u, y]_a \end{aligned} \quad (18)$$

at point a, and to:

$$\begin{aligned} \phi_{11,w}^b &= 2c_3 (\overline{uv} v, x)_b \\ \phi_{22,w}^b &= -\phi_{11,w}^b \\ \phi_{12,w}^b &= c_3 [(v^2 - u^2) v, x]_b \end{aligned} \quad (19)$$

at point b.

From symmetry considerations we must have:

$$\begin{aligned} \overline{u}_a^2 &= \overline{v}_b^2, \quad \overline{v}_a^2 = \overline{u}_b^2, \quad \overline{uv}_a = -\overline{uv}_b \\ (u, y)_a &= -(v, x)_b \end{aligned} \quad (20)$$

And by substituting (20) in either (18) or (19) we get

$$\begin{aligned} \phi_{11,w}^a &= \phi_{22,w}^b \\ \phi_{22,w}^a &= \phi_{11,w}^b \\ \phi_{12,w}^a &= -\phi_{12,w}^b \end{aligned} \quad (21)$$

as expected. Equations (16a) and (16b) will be employed to predict pipe and channel step flows.

The Energy Dissipation Rate Equation. An exact equation for the transport of ϵ can be derived from the Navier-Stokes equations, after straightforward, but tedious, manipulations the result may be written as

$$\begin{aligned} d\epsilon/dt &= -2v \overline{u_{i,k} u_{i,l} u_{k,l}} - 2(\overline{u_{i,k} u_{i,l}})^2 \\ &\quad - (\overline{u_k} \epsilon + \frac{2v}{\rho} \overline{u_{k,l} p_{,l}} - v \epsilon_{,k})_{,k} \\ &\quad - 2v(\overline{u_{i,l} u_{i,k}} + \overline{u_{l,i} u_{l,k}}) u_{i,k} - 2v \overline{u_{i,l} u_{i,l}} u_{i,k,l} \end{aligned} \quad (22)$$

This equation can not be modeled as closely as (1) because it is difficult to take each term on the right-hand side separately and develop a suitable approximation to replace it. Instead (22) has to be modeled in a global fashion, valid for high Reynolds numbers, namely

$$\begin{aligned} d\epsilon/dt &= c_\epsilon [(k/\epsilon) \overline{u_k u_l} \epsilon_{,l}] \\ &\quad + c_{e1} P \epsilon / k - c_{e2} \epsilon^2 / k \end{aligned} \quad (23)$$

and then develop a low Reynolds number counterpart. The low Reynolds number form of the ϵ equation we employ is essentially the one proposed by HL. We will therefore state the result directly and refer the reader to HL for the steps of the derivation. The modeled transport equation for ϵ is

$$\begin{aligned} d\epsilon/dt &= [v \epsilon_{,k} + c_3 (k/\epsilon) \overline{u_k u_l} f_{u,l} \epsilon_{,l}] + c_{e1} \epsilon P / k \\ &\quad - c_{e2} f_\epsilon \epsilon \tilde{\epsilon} / k + 2v(k/\epsilon) f_u \overline{u_{i,k} u_{i,l}} u_{i,j} u_{l,k} \end{aligned} \quad (24)$$

where

$$\tilde{\epsilon} = \epsilon - 2v(k^{1/2}/l)^2 \quad (25)$$

and

$$f_\epsilon = 1 - \alpha \exp(-R_\epsilon^2/36) \quad (26)$$

Equation (24) differs from the final proposal of HL in that we have retained the viscous diffusion term and introduced the function f_u . Also the constants c_{e1} , c_{e2} , α were re-evaluated. First c_{e2} is set equal to 1.9 c_{e2}^* in order to match the data of Warhaft & Lumley (1978) for homogeneous decaying grid turbulence. Then we consider the fact that in the final period of decay (i.e. $R_\epsilon \rightarrow 0$) one must have $(c_{e2} f_\epsilon - 1) = 0.4$ (see HL) whence $\tilde{\alpha} = 1 - 1.4/c_{e2} = .263$. Finally c_{e1} was set equal to 1.45 in order to be consistent with the value of c_ϵ of .15 determined by LRR.

BOUNDARY CONDITIONS

Boundary conditions must be specified for U, V, u, v , and ϵ along the boundaries of the solution domain as the equations governing these quantities are elliptic. In all the flows considered, the following boundary conditions were used for U, V, u, v , and ϵ . The values of the dependent variables are specified at the inlet to the flow domain whereas their gradients vanish at the exit plane. At the axis of symmetry, $v = uv = 0$, while the gradients of the remaining variables are set to zero. All variables are set to zero at a solid wall, except

$$\epsilon_{\text{WALL}} = 2\nu k^{1/2} \quad (27)$$

To specify ϵ at a solid wall in the manner indicated above is, of course, entirely equivalent to setting $\epsilon = 0$ (see Eq. (25)). In fact many workers (Jones, Launder 1972, Hassid-Poreh 1978, Chien 1982) have developed low Reynolds number turbulence models solving transport equations for k and ϵ with $k = \epsilon = 0$ at the wall. Computational advantages were always stated as the reason for employing ϵ instead of ϵ even though the definition of ϵ varied among authors. We attempted to solve for ϵ rather than ϵ but the resulting wall shear stress was too high and the u, u , peaked closer to the wall than observed and the profile of ϵ was unrealistic in the buffer and laminar layers. Therefore we use Eqn (27) as our boundary condition for ϵ where the gradient $k^{1/2}$ is evaluated from a quadratic interpolation polynomial

NUMERICAL SOLUTION PROCEDURE

The elliptic transport equations of U, u, u , and ϵ are solved by a finite difference procedure based on the SIMPLER algorithm of Patankar (1981). Two discretization schemes were employed, the hybrid scheme of Spalding (1972) and QUICK of Leonard (1979). The sensitivity of the solution to the choice of the scheme will be discussed in the following section.

RESULTS AND DISCUSSION

Non-Recirculating Flows

The results presented in this section are for fully developed flow conditions in plane (channel) or axial (pipe) configurations. No mention will be made of the discretization scheme used to obtain them since the fully-developed profiles of U, ϵ and u, u are insensitive (within $\pm 1\%$) to a change of discretization scheme. However the choice of the discretization scheme does affect the predictions in the developing region. The major differences arise from the choice of either the QUICK or hybrid scheme for U equations. The differences will be slight when one switches from one scheme to another for the turbulent quantities alone.

The flow Reynolds numbers (based on duct width or diameter and section-averaged velocity) varied from 7×10^3 to 1.2×10^5 . Non-uniform grids were employed for the calculations using from 25 to 33 cross-stream nodes and 12 in the axial direction. The grid independence of the predictions was thoroughly tested by using 23, 33, 40, and 50 cross-stream nodes for channel flow at $Re = 4 \times 10^4$. The coarsest grid solution was everywhere within 3-4% of the next one and the discrepancy becomes insignificant afterwards. Typical runs required about 100 CPU seconds for execution on a CDC 7600 computer to yield a converged solution using hybrid scheme for all variables. When QUICK was used for all variables, the execution took 10% more time per iteration although the number of iterations required remained the same. Pipe and channel flows were used to test the functions f and f , mentioned earlier (eqs. (4), (6)) against other possible forms. The performance of each function was judged on the basis of how well the calculations could predict the wall shear stress, the peak value of each u, u , and its location as well as the linearity of the mean velocity profile in the laminar sublayer.

Figure 2 shows the skin friction coefficient for pipe flow over a medium range of Reynolds numbers. The agreement with the data of Lawn (see Ha-Minh, 1976) is very good.

Figure 3 shows the normalized mean velocity U^+ versus Y^+ for a pipe flow at $Re = 10^5$. The transition from the laminar sublayer (linear) velocity profile to the logarithmic profile is smooth, with a Von Karman's constant of about .4.

Figure 4 shows the normal stresses for channel flow at $Re = 21800$. The agreement with the data of Laufer

(1951) is very good for u^2 whereas v^2 and w^2 are overpredicted near the wall.

Recirculating Flows

Two flows were predicted: first a sudden expansion (1:15) in a channel for $Re = 40300$, second a sudden expansion (.375:1) in a pipe for $Re = 72000$ (based on the small sectional average velocity and diameter). For both flows, the various profiles upstream of the step were allowed to feel the effects of the adverse pressure gradient by using a short inlet section with fully developed profiles at its entrance. Strictly speaking, this inlet section should be a few duct diameters long but we kept it only to a small fraction of the diameter for economical reasons. However, our experience and others (Ha-Minh 1976) show that the influence of the inlet boundary conditions fades rapidly beyond one duct diameter downstream of the step due to the intense mixing that takes place in the recirculation region.

Figure 5 shows the predicted mean velocity profiles for the channel step. The hybrid scheme was used for all the variables with a 33×33 non-uniform grid using 15 nodes across the short inlet section. The computing time was about 10 minutes. The agreement with the data of Smyth (1979) is satisfactory except near the wall.

Figure 6 shows the predicted normal stresses u^2, v^2, w^2 at two locations downstream of the step. There is good agreement with the data everywhere except near the axis of symmetry. However the data of Smyth appear to be consistently too high near the axis, even far downstream in the fully-developed region (see Laufer's data). Calculations were repeated with a 40×50 grid which resulted in an extremely slow convergence and the final results were within 3% of those of the 33×33 grid.

Figure 7 shows the predicted mean velocity profiles for pipe step flow using both QUICK and hybrid schemes for the momentum equations and the hybrid for the other equations with a 34×37 non-uniform grid. The ability of the QUICK scheme to reduce false diffusion effects is obvious when the predictions are compared with the experimental data of Ha-Minh (1976). The last two figures (8,9) compare the predicted uv and u^2 profiles with the data of Ha-Minh. While uv is well predicted, u^2 is underpredicted by about 14% near the centerline.

CONCLUDING REMARKS

Some promising results have been obtained in wall-bounded non-recirculating and recirculating flows with a full Reynolds stresses closure. Computer time and storage requirements are within practical limits.

In recirculating flows, the accuracy of the predictions strongly depend on the ability of the finite-differencing scheme used for the momentum equations in reducing numerical diffusion errors.

REFERENCES

- Champagne, F.H. Harris, V.G. & Corrsin, S., 1970, "Experiment on nearly homogeneous shear flow," J. Fluid Mech., 41, 81.
- Chien, K.Y., 1982, "Predictions of channel and boundary-layer flows with a low Reynolds number turbulence model," AIAA Journal, 20, 33.
- Chung, M.K. & Adrian, R.J., 1979, "Evaluation of variable coefficients in second order turbulence models," 2nd Symp. on Turbulent Shear Flows, Imperial College, London.
- Cormack, D.E., Leal, L.G., Seinfeld, J.H., 1978, "An evaluation of mean Reynolds stress turbulence models: The triple velocity correlation," J. Fluids Engineering, 100, 47.

Corrsin, S., Fournier, J. L., 1982, "On viscous dissipation rates of velocity component kinetic energies," *Phys. Fluids*, 25, 583.

Ha-Minh, H. 1976, "Décollement provoqué d'un écoulement turbulent incompressible," D.Sc. thesis, Institut National Polytechnique de Toulouse.

Hanjalic, K. & Launder, B.E., 1972, "A Reynolds stress model of turbulence and its application to thin shear flows," *J. Fluid Mech.*, 52, 609.

Hanjalic, K. & Launder, B.E., 1976, "Contribution towards a Reynolds-stress closure for low-Reynolds-number turbulence," *J. Fluid Mech.*, 74, 593.

Hassid, S., Poreh, M., 1978, "A turbulent energy model for flows with drag reduction," *J. Fluids Engineering*, 100, 107.

Hinze, O., 1975, "Turbulence," 2nd edition, McGraw-Hill, New York.

Jones, W.P. & Launder, B.E., 1972, "The prediction of laminarization with a two-equation model of turbulence," *Int. J. Heat Mass Transfer*, 15, 301.

Kreplin, H.P., Eckelmann, H., 1979, "Behavior of the three fluctuating velocity components in the wall region of a turbulent channel flow," *Phys. Fluids*, 22, 1233.

Laufer, J., 1951, "Investigation of turbulent flow in a two-dimensional channel," NACA Report 1053.

Launder, B.E., Reece, G.J. & Rodi, W., 1975, "Progress in the development of a Reynolds-stress turbulence closure," *J. Fluid Mech.*, 68, 537.

Launder, B.E. & Sharma, B.I., 1974, "Application of the energy-dissipation model of turbulence to the calculation of flow near a spinning disc," *Lett. Heat Mass Transfer*, 2, 1.

Leslie, D.C., 1980, "Analysis of a strongly sheared, nearly homogeneous turbulent shear flow," *J. Fluid Mech.*, 98, 435.

Leonard, B.P., 1979, "A stable and accurate convective modelling procedure based on quadratic upstream interpolation," *Comp. Math. in Appl. Mech. & Eng.*, 19, 59.

Lumley, J.L., 1978, "Computational modelling of turbulent flows," *Adv. Appl. Mech.*, 18, 123.

Patankar, S.V., 1981, "A calculation procedure for two-dimensional elliptic situations," *Numerical Heat Transfer*, 4, 409.

Patel, V.C., Rodi, W. & Scheuerer, G., 1981, "Evaluation of turbulence models for near-wall and low-Reynolds number flows," Third Symposium on turbulent shear flows, U.C. Davis.

Pope, S.B. & Whitelaw, J.H., 1976, "The calculation of near-wake flows," *J. Fluid Mech.*, 73, 9.

Smyth, R., 1979, "Turbulent flow over a plane symmetric sudden expansion," *J. Fluids Engineering*, 101, 349.

Spalding, D.B., 1972, "A novel finite-difference formulation for differential expressions involving both first and second derivatives," *Int. J. Num. Methods Eng.*, 4, 551.

Speziale, C.G., 1980, "Closure relations for the pressure-strain correlation of turbulence," *Phys. Fluids*, 23, 459.

Tennekes, H. & Lumley, J.L., 1972, "A first course in turbulence," MIT-Press, Cambridge, Mass.

Warhaft, Z. & Lumley, J.L., 1978, "An experimental study of the decay of temperature fluctuations in grid-generated turbulence," *J. Fluid Mech.*, 88, 659.

ACKNOWLEDGEMENTS

This work has been supported by a National Science Foundation grant number CME-8018407. The authors wish to express their thanks to Mrs. Verna Bruce for her expert typing and patience.

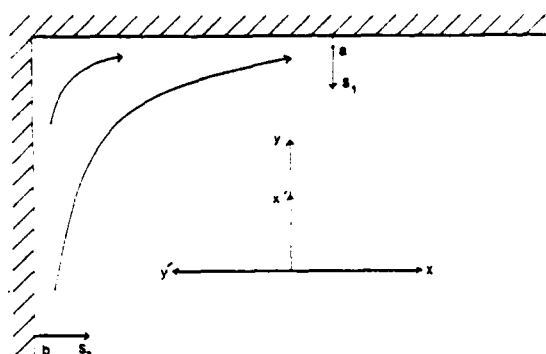


Figure 1 Flow in a corner

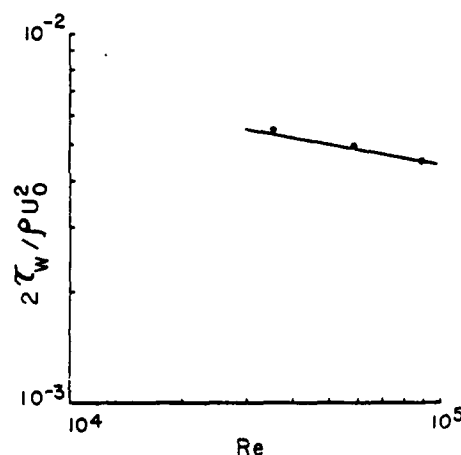


Figure 2 Skin friction coefficient for pipe flow
•, Data of Lawn (1970), — Predictions

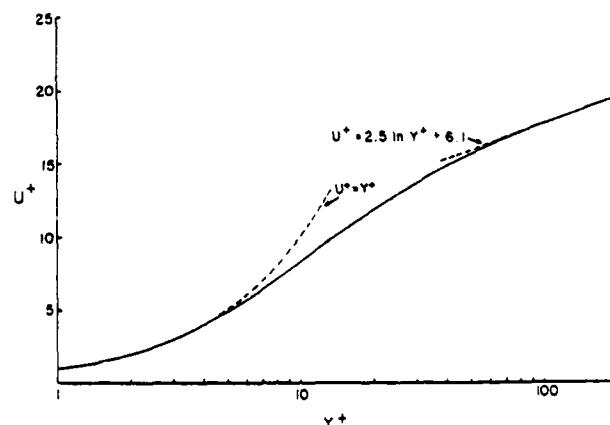


Figure 3 Predicted mean velocity for fully-developed pipe flow, $Re = 100000$

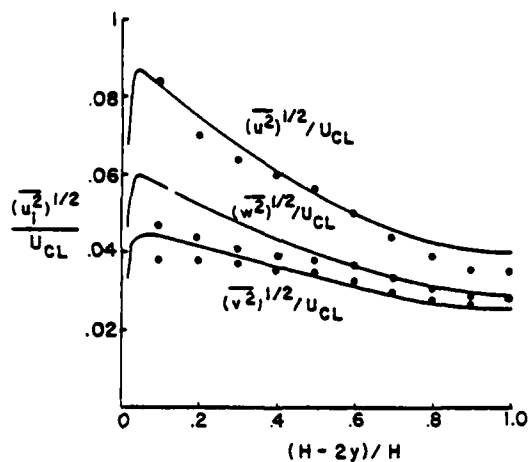


Figure 4 Normal stresses for fully-developed channel flow, $Re = 21800$
 •, Data of Laufer (1951), — Predictions

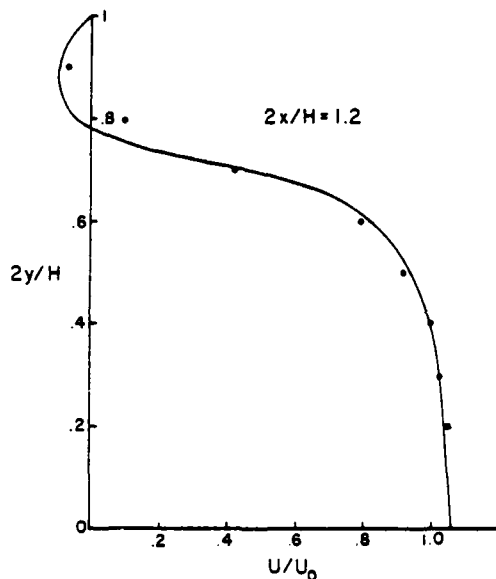


Figure 5 Mean velocity for channel step flow, $Re = 40300$
 •, Data of Smyth (1979), — Predictions

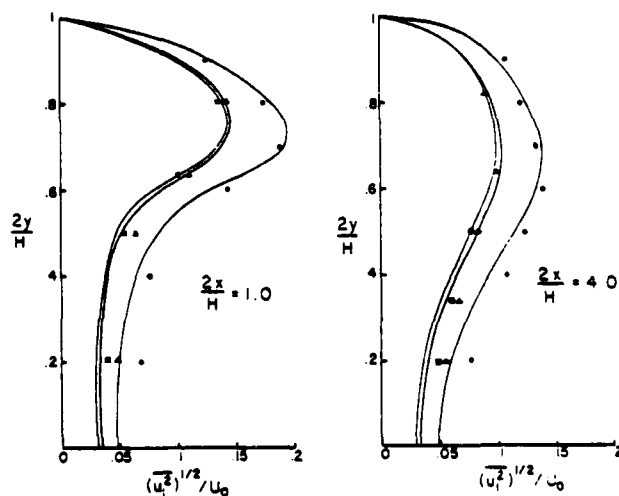


Figure 6 Normal stresses for channel step flow, $Re = 40300$, •, $(u^2)^{1/2}/U_0$, ▲, $(w^2)^{1/2}/U_0$, ■, $(v^2)^{1/2}/U_0$, Smyth (1979), — Predictions

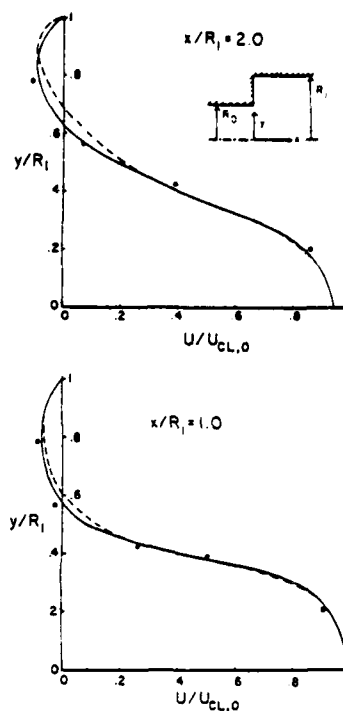


Figure 7 Mean velocity for pipe step flow, $Re = 72000$
 —, QUICK, --- Hybrid, •, Data of Ha-Minh

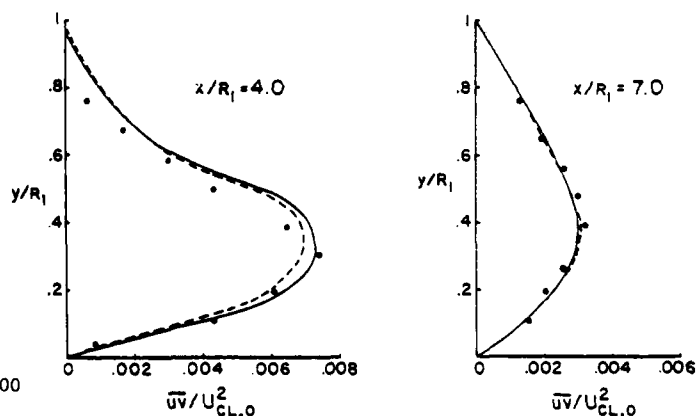


Figure 8 Turbulent shear stress for pipe step flow, $Re = 72000$. Notations as in Figure 7

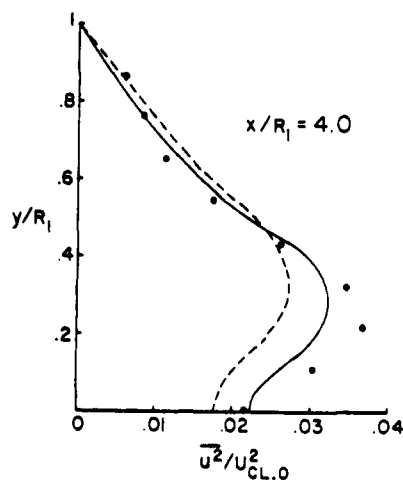


Figure 9 Normal stress for pipe step flow, $Re = 72000$
 Notations as in Figure 7

ROUGH- AND SMOOTH-WALLED SHEAR FLOWS

by

A.E. Perry, K.L. Lim, S.M. Henbest & M.S. Chong
Mechanical Engineering Department
University of Melbourne
Parkville, Victoria, Australia. 3052

Abstract

Measurements of Reynolds shear stress profiles on rough and smooth walls have been carried out and the deduced wall shear stresses are compared with "mean-velocity-profile similarity law" techniques. Agreement was obtained for smooth walls but considerable discrepancy occurred on rough walls. It appears that the problem is caused by excessive changes in the instantaneous velocity vector angle relative to the hot-wires in a flow over a rough wall and this situation is predicted by a "hairpin vortex" model for wall turbulence. The problem was cured by increasing the included angle of the X-wires and also by "flying" the probe through the flow.

Introduction

One of the major difficulties concerning research on rough wall boundary layers is the problem of determining the skin friction coefficient. Unlike smooth walls there is no firmly established wall similarity law and so there are no methods equivalent to the Clauser chart or Preston tube techniques. Further difficulties arise since we do not know the "effective origin" of the mean velocity profile, i.e. the apparent position of $z=0$ relative to the roughness elements, where z is the distance normal to the surface. The surface skin friction coefficient can in principle be determined in a number of ways, all of which are either highly inaccurate or are difficult to carry out successfully. One method is the use of the von Kármán momentum integral equation which is known to be highly sensitive to any three dimensionality of the flow and also has the undesirable feature of requiring streamwise derivatives of various mean flow quantities. Determination of derivatives of experimental data is a highly inaccurate process. Perry, Schofield & Joubert (1969) determined the skin friction of two-dimensional strip roughness by measuring the form drag of pressure tapped roughness elements. Another method which presents itself is the use of the Hama (1954) velocity defect law which has yet to be verified by an independent method. This technique (outlined later) is a variation of the "wake alignment" method of Perry and Joubert (1963). Yet another method is to measure the Reynolds shear stress distribution using hot-wire anemometry. This latter method is the main subject of this paper and its use has presented many unforeseen difficulties. Mulhearn (1977) attempted to use this method for flow over a bed of rocks and discovered that the indicated Reynolds shear stress fell off as the wall was approached. Such behaviour cannot be explained by viscous stresses since the mean strain rate is too small. Such a fall off was anticipated by Perry, Schofield & Joubert (1969). Their explanation was that above a periodic array of two dimensional roughness elements there must exist a zone close to the elements where the temporal mean velocity

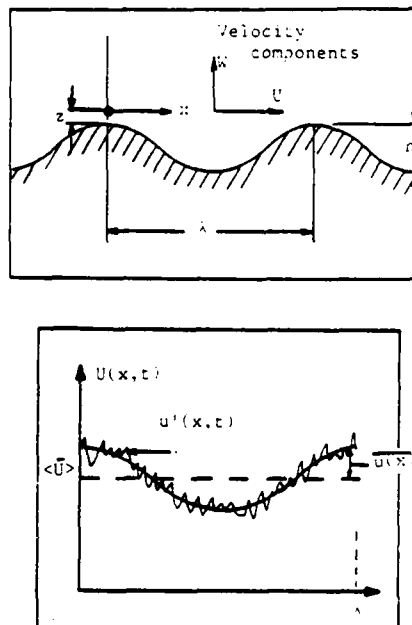


Figure 1. Geometry of the wavy wall and definition of various flow quantities.

field has a periodic variation with streamwise distance. Figure 1 defines the various relevant quantities. The instantaneous velocities for a given z are

$$U(x, t) = \langle \bar{U} \rangle + \bar{u}(x) + u'(x, t)$$

where

$$\langle () \rangle = \frac{1}{\lambda} \int_0^\lambda () dx \quad \text{and} \quad \bar{()} = \frac{1}{T} \int_0^T () dt$$

and by definition

$$\frac{1}{\lambda} \int_0^\lambda \bar{u}(x) dx = 0$$

$$\frac{1}{T} \int_0^T u'(x, t) dt = 0 \quad \text{for } T \rightarrow \infty$$

Similarly

$$W(x,t) = \overline{W} + \overline{w(x)} + w'(x,t)$$

and \overline{W} is assumed to be zero close to the wall. If the effective wall shear stress, τ_0 , has negligible streamwise gradient, and if the pressure gradient is sufficiently small, then

$$\tau_0 = -\rho \overline{u'(t,x)w'(t,x)} = -\rho \overline{u(x)w(x)} \quad (2)$$

For the rough surfaces tested here, it has been found that $u'(t,x)w'(t,x)$ was invariant with x for the smallest z/h values attainable with the X-wire probe. Therefore,

$$\tau_0 = \overline{ou'(t)w'(t)} = -\rho \overline{u(x)w(x)} \quad (3)$$

The first term is the Reynolds shear stress as determined by a stationary X-wire probe and the second term represents the contribution to the momentum transport by the "standing wave" above the elements. This could explain why the first term in equation (3) drops off as we approach the boundary since it is expected that the second term would increase.

The Wavy Wall

Figure 2 shows a typical Reynolds shear stress profile above a wavy wall in a zero pressure gradient. The boundary layer thickness was 150mm, the height of the waves was 17mm and the wavelength was 77mm. The fall off of Reynolds shear stress is obvious.

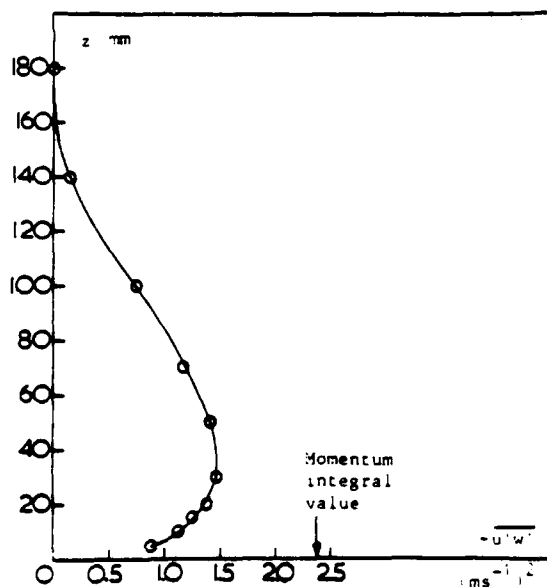


Figure 2. Typical Reynolds shear stress profile above a wavy wall in a zero pressure gradient.

Figure 3 shows some typical plots of $\overline{u(x)}$ and $\overline{w(x)}$ which were measured using a "flying" X-hot wire probe mounted on an air bearing sled. The air bearing sled is described in Perry & Watmuff (1981) and Watmuff, Perry & Chong (1983). The Reynolds stress profile was taken with a stationary X-wire probe. It can be seen that $\overline{u(x)}$ and $\overline{w(x)}$ attenuate as we move away from the wall and that they are approximately 90 degrees out of phase. This means that the spatial average would be negligible and calculations confirmed this. Hence the fall off in Reynolds shear stress must be explained in some other way.

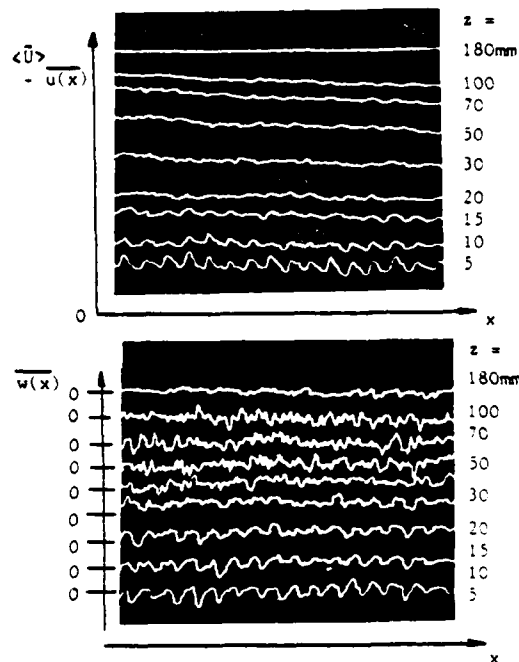


Figure 3. Plots of $\overline{u(x)}$ and $\overline{w(x)}$ above a wavy wall using a "flying" hot-wire.

Mesh Roughness and Smooth Wall Measurements

It was decided to measure the Reynolds stress above a three-dimensional mesh type roughness in a zero pressure gradient. The size and geometry of this roughness is shown in figure 4(a) and a typical boundary layer thickness was 90mm. Figure 4(b) shows a typical Reynolds shear stress profile. The wall shear stress determined using the Hama velocity defect law is also shown. For this case it agrees with the von Kármán momentum integral shear stress prediction. For many other cases not covered here this agreement was poor (about $\pm 20\%$).

In the Hama velocity defect method of determining the local skin friction coefficient C_f , the effective origin of the wall $z=0$, and the skin friction coefficient C_f are systematically adjusted such that the mean velocity profile is forced to collapse onto the law given by

$$\frac{U_1 - U}{U_1} = f(n), \text{ where } U_1 \text{ is the free stream velocity,}$$

$$\text{where for } n < .15, f(n) = -\frac{1}{.41} \ln(n) + 2.309$$

$$\text{and } .15 < n < 1.0, f(n) = 9.6(1-n)^2$$

$$\text{where } n = z/\delta_H, \quad \delta_H = \frac{6}{C_1} \sqrt{\frac{2}{C_f}} \quad (4)$$

$$\text{and } C_1 = \int_0^1 f(n)dn = 3.3715$$

where δ^* is the boundary layer displacement thickness and U_1 is the wall shear velocity.

From figure 4 it can be seen that large discrepancies exist between the values of wall shear stress predicted by the Reynolds shear stress profile and that predicted by the Hama velocity defect law. It was therefore decided to check the X-wires, anemometers and calibration techniques by measuring flow over a smooth wall immediately after the rough wall measurements. The Clauser chart method can be used to

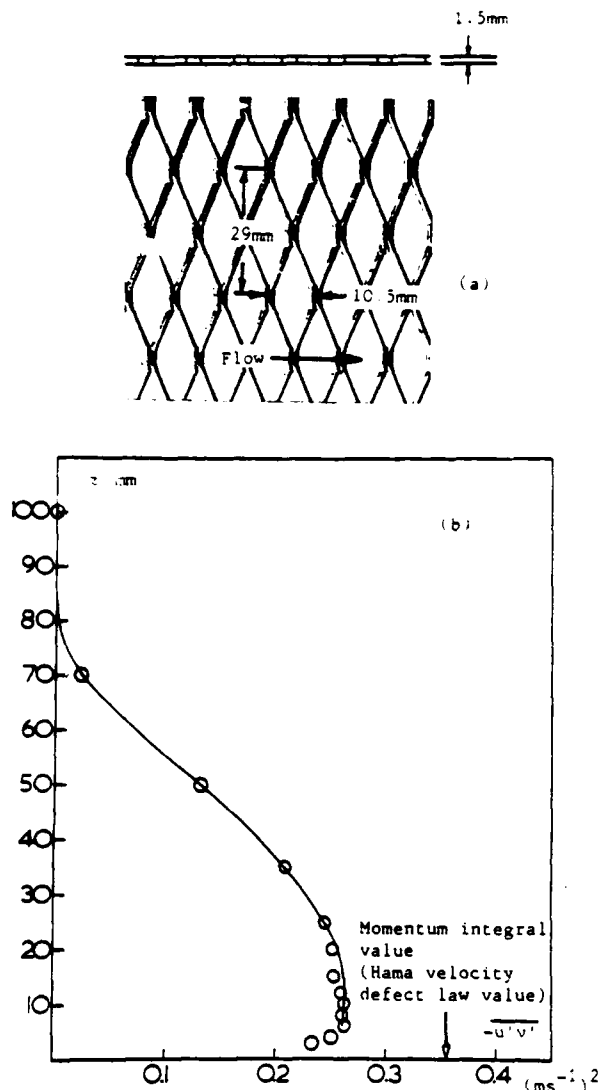


Figure 4. (a) Size and geometry of mesh roughness. (b) Typical Reynolds shear stress profile above a three-dimensional mesh type roughness.

obtain the wall shear stress for the smooth wall. This can be compared with the shear stress obtained by extrapolation of the Reynolds shear stress to the wall, (Clauser, 1954). Excellent agreement was obtained. The smooth wall plate which covered the mesh roughness was then quickly removed and measurement of the rough wall Reynolds stress profile was repeated using the same wires, anemometers and hot-wire calibration. The same incorrect profile, as was obtained in the previous runs, was obtained to high accuracy.

It was then thought that the spatial resolution of the X-wires was not fine enough and that this limitation could be a cause of the discrepancy. This, however, would imply that the eddy structures above a rough surface are finer than those above a smooth surface. This is unlikely. As a check, the profiles were repeated using shorter wire filaments which were spaced closer together but the resulting profiles were close to the previous ones, indicating that spatial resolution was not the cause of the discrepancy.

Effect of Velocity Vector Wedge Angles

Errors in the measurement of Reynolds shear stress may be caused by an excessive "wedge angle" θ . This is the included angle which the instantaneous velocity

vector approaching the wires undergoes during measurements. This should be kept below β , the included angle of the wires (see figure 5). Large velocity components v' normal to the plane of the X-wires will also cause errors. If θ exceeds β , any measurements taken will be ambiguous and completely erroneous.

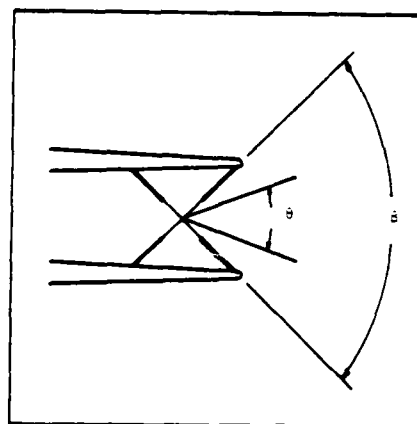


Figure 5. Hot wire filaments showing included wire angle and velocity wedge angle.

One of the major differences between flow over a rough surface and flow over a smooth surface is that for a given $(U\delta_H)/\nu$ (where δ_H is a length scale defined in equation (4) and ν is the kinematic viscosity of the fluid) the local mean velocity at a given z/δ_H is much lower on a rough surface.

In fact,

$$\left(\frac{\bar{U}}{U_\tau}\right)_R = \left(\frac{\bar{U}}{U_\tau}\right)_S - \left(\frac{\Delta U}{U_\tau}\right) \quad (5)$$

where $\Delta U/U_\tau$ is the Hama (1954) roughness function. The suffix R signifies a rough surface and the suffix S signifies a smooth surface. Furthermore, if we assume that the eddies above a rough surface are similar to those above a smooth surface, i.e. they follow the same scaling laws as postulated by Perry & Chong (1982), then, if we are at a distance z above the boundary, eddies of scale z contribute mainly to the Reynolds stress at z (the attached eddy hypothesis of Townsend, 1976). If we assume that their characteristic velocity scales with U_τ , then one can compute some likely velocity signatures for the velocity components that a X-wire probe might experience close to a boundary. This was done by applying the Biot-Savart law to the hairpin or Λ -vortex model of Perry & Chong in a manner similar to that described in another paper presented at this conference (see Perry et al.). The vortex shape was the same and parameters were adjusted to give $(u'w')/U_\tau = O(1)$. Computations were then carried out for different values of $\Delta U/U_\tau$ and the signatures were fed into a computer program which simulated our hot wire anemometry system and calibration scheme. In spite of the fact that our calibration scheme takes into account wire response non-linearities, (this method is explained in detail in Perry (1982) pp. 122-127) significant errors occurred in the inferred velocities under certain flow conditions. The X-wire filaments were modelled using the Champagne et al. (1967) cosine cooling law. Figure 6 shows the results of the inferred Reynolds stresses for different values of \bar{U}/U_τ . These computations are equally valid for smooth walls. Several simplifying assumptions were incorporated in the analysis, the main one being that we are only considering one hierarchy of eddy scales. Hence, figure 6 is meant only to show trends. If more hierarchies were included, the errors would be larger. Errors in the inferred Reynolds stress occurred only when the angle of the velocity vectors approaching the X-wires were large. Under these

conditions the effect of v' was also important. Figure 6 also show the results with and without v' present and it can be seen that its effect is large. Also shown in the figure are the differences in inferred Reynolds stress when the hot-wire included angle is altered from 90 degrees to 120 degrees. A significant improvement can be seen.

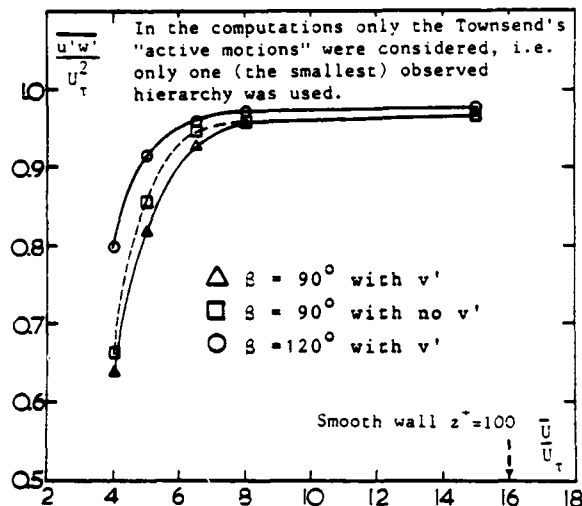


Figure 6. Computed errors in the measurement of Reynolds shear stress due to "wedge angle" effect and the effect of v' .

Experimental results also show that the X-wires with the larger included angle β gave significantly smaller error. It would therefore appear necessary to keep the velocity vector wedge angles somewhat lower than the hot-wire included angle and also somehow reduce the effect of v' if a correct Reynolds shear stress is to be measured.

Further computations agreed very well with simple tests that were carried out by shaking a calibrated set of X-wires with a dynamic calibrator in the free stream. This imposed accurately known Reynolds stresses on the hot-wires. The wedge angles of the velocity vectors could also be calculated accurately and the wedge angle at which the measurement of Reynolds stress started to break down could be observed. This is shown in figure 7.

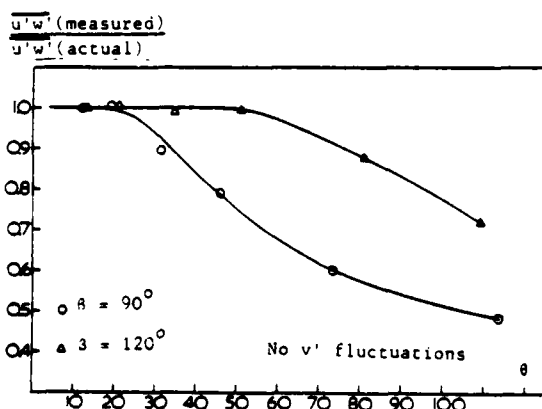


Figure 7. Breakdown of Reynolds shear stress measurements due to excessive "wedge angle".

Figure 8 shows the various measured Reynolds shear stress profiles above the mesh roughness close to the wall where $\overline{U}/U_\tau = 4$. It can be seen that the indicated Reynolds stress increased by increasing the included hot-wire angle from 90 degrees to 120 degrees. To reduce the wedge angle of the velocity vectors even

further and to reduce the effect of the v' fluctuations, it was decided to "fly" the X-wire probe through the flow so as to increase the bias velocity relative to the probe.

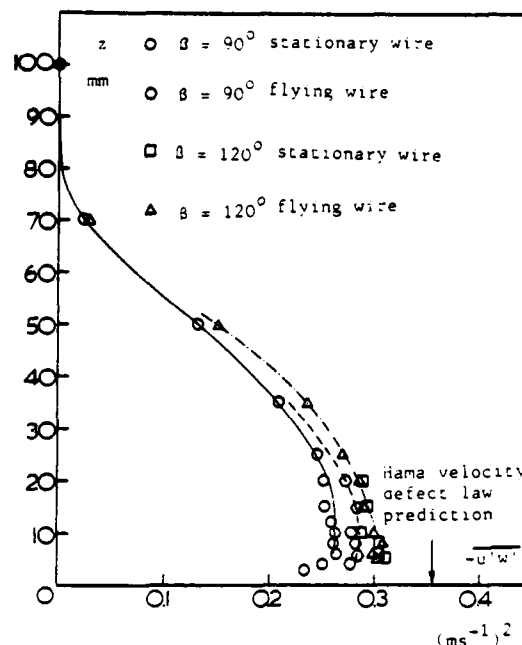


Figure 8. Reynolds shear stress profiles measured above a mesh type roughness using 90 degree and 120 degree wires. Measurement were taken with the hot-wire probe stationary and "flying".

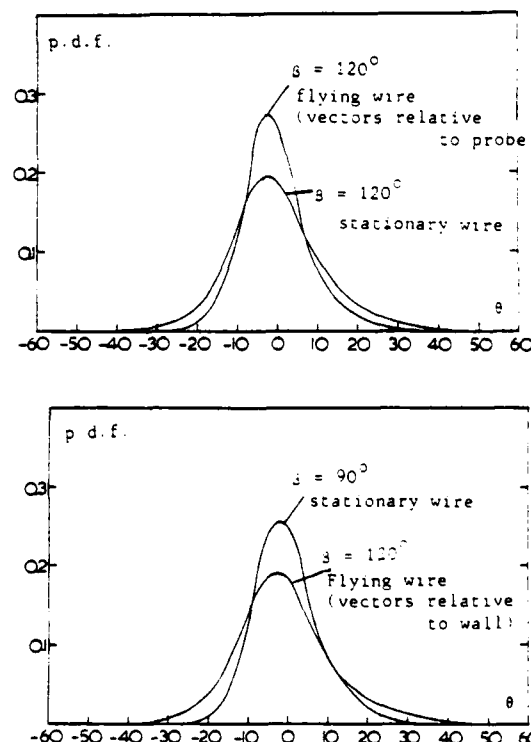


Figure 9. Histograms of wedge angles of velocity vectors inferred from X-wires.

The flying hot-wire air bearing sled system mentioned earlier was used and this imposed an additional \bar{U}/U_τ of 2.5. Figure 8 also shows how the inferred Reynolds stresses increase for both the 90 degree and 120 degree X-wires. Data was sampled in bursts over a length of 100mm of streamwise distance and three hundred sled passes were required for adequate convergence of the Reynolds stress data at each level. Figure 9 shows histograms of the wedge angles of the velocity vectors as inferred by the X-wires for each of the four cases described. The highest Reynolds stress approaches the Hama velocity defect law prediction and the profile has the expected shape for a zero pressure gradient boundary layer. The 120 degree X-wire seems to be insensitive to bias velocity and so the authors contend that the stationary 120 degree X-wires were giving approximately correct value.

In the flying hot-wire experiments, the contribution from the "standing waves" was computed for the mesh roughness. Its contribution was found to be negligible.

Conclusion

Excessive changes in the angle of the instantaneous velocity vector relative to the X-wire probes causes significant errors in inferred Reynolds shear stresses on a rough wall. The validity of the Hama velocity defect law for zero pressure gradient layers on rough surfaces is still in some doubt and needs further work.

Acknowledgements

The authors wish to acknowledge the financial assistance of the Australian Research Grant Scheme and The Australian Institute of Nuclear Science and Engineering.

References

- Champagne, F.H., Sleicher, C.A. & Wehrmann, O.H. 1967a Turbulence measurements with inclined hot-wires. Part 1. *J. Fluid Mech.*, 28, 153-176.
- Champagne, F.H., Sleicher, C.A. & Chao, J.L. 1967b Turbulence measurements with inclined hot-wires. Part 2. *J. Fluid Mech.*, 28, 177-182.
- Clauser, F.H. 1954 Turbulent boundary layers in adverse pressure gradients. *Jour. Aero. Sci.*, 21, 91.
- Hama, F.R. 1954 Boundary layer characteristics for smooth and rough surfaces. *Trans. SNAME*, 62.
- Mulhearn, P.J. 1977 Turbulent flow over a very rough surface. 6th Australasian Hydraulics and Fluid Mechanics Conference, Adelaide, Australia.
- Perry, A.E. & Joubert, P.N. 1963 Rough-wall boundary layers in adverse pressure gradients. *J. Fluid Mech.*, 17, 193-211.
- Perry, A.E., Scholfield, W.H. & Joubert, P.N. 1969 Rough wall turbulent boundary layers. *J. Fluid Mech.*, 37, 383-413.
- Perry, A. E. & Watsuff, J.H. 1981 The phase-averaged large-scale structures in three-dimensional turbulent wakes. *J. Fluid Mech.*, 103, 33-51.
- Perry, A.E. & Chong, M.S. 1982 On the mechanism of wall turbulence. *J. Fluid Mech.*, 119, 173-217.
- Perry, A.E. 1982 Hot-Wire Anemometry. Clarendon Press.
- Townsend, A.A. 1967 The Structure of Turbulent Shear Flow. 2nd. Ed. Cambridge University Press.
- Watsuff, J.H., Perry, A.E. & Chong, M.S. 1983 A flying hot-wire system. To appear in *Experiments in Fluids*.

FURTHER SPECTRAL ANALYSIS OF SMOOTH-WALLED PIPE FLOW

by

A.E. Perry, S.M. Henbest and M.S. Chong
Mechanical Engineering Department
University of Melbourne.

Abstract

Using the attached eddy hypothesis of Townsend (1976) and the model of wall turbulence proposed by Perry & Chong (1982) the spectra of streamwise velocity fluctuations and normal velocity fluctuations were derived. These were compared with measured experimental data. The agreement between the experimental data and the deduced scaling laws is encouraging.

Introduction

Perry & Chong (1982) proposed a model for wall turbulence which was based on Townsend's (1976) attached eddy hypothesis. Using the observations of Head and Bandyopadhyay (1981) as a guide, wall turbulence was modelled as a "forest" of hair-pin or "A" shaped vortices attached to the boundary. The vortex filaments originate from viscous sublayer material.

It was proposed that a range of scales of geometrically similar "forests" exist and that each "forest" or hierarchy has the same characteristic velocity scale (which is the wall shear velocity U_τ). The length scales of the hierarchies range from the scale of the smallest eddies at the wall which have the Kline (1967) scaling δ_v to the largest scale which is taken to be the pipe radius or the boundary layer thickness Δ . Two different probability density functions (p.d.f.'s) of hierarchy scales were tested. One was a discrete distribution with the scales going in a geometric progression and the other was a continuous distribution and was of inverse power law form as assumed by Townsend (1976). It was found that both distributions give much the same result. How the hierarchies are formed is not understood. Nevertheless, such a model gives the correct mean flow velocity distribution. Also using the velocity signatures generated by such an ensemble of vortex filaments with the aid of the Biot-Savart law, it appears that the correct spectral distribution for the streamwise velocity fluctuations u_1 is obtained. The power spectral density for u_1 is characterized by a flat region at low wavenumbers which asymptotes into a -1 power law which then asymptotes into an exponential-like curve at high wavenumbers. Perry & Chong's (1982) analysis was rather crude and the velocity fluctuations u_2 normal to the wall were not considered. This paper outlines a more refined approach to the problem and presents some new data. This new work adds considerable weight to the validity of the theory presented by Perry & Chong.

Spectra and Eddy Intensity Functions

The analysis of Perry & Chong (1982) was rather crude. The velocity signatures from an isolated vortex "rod" with solid body rotation surrounded by irrotational fluid were used to obtain an ensemble

averaged power spectral density for u_1 for a given hierarchy. These densities were then summed up for varying numbers of hierarchies. The resulting spectra appeared to have the correct functional forms when compared with the experimental results of Perry & Abell (1975, 1977) for flow in a smooth-walled pipe.

More refined models are currently being considered by the authors. Unfortunately these are analytically intractable and so numerical methods have to be used. Figure 1 shows an isolated A-vortex at a boundary with its image vortex. This will be taken to be a "representative eddy" for a given hierarchy.

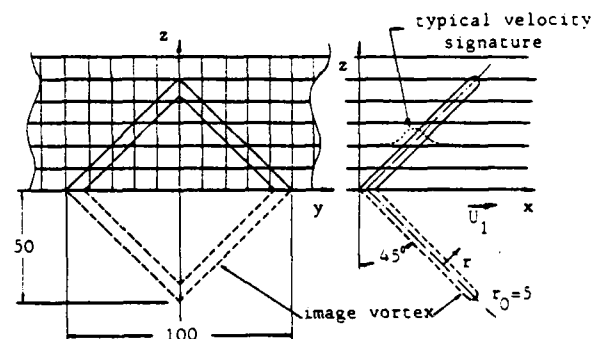


FIGURE 1. A "representative eddy" with streamwise "cuts".

The proportions of the eddy are shown together with the streamwise "cuts" along which u_1 , u_2 and u_3 velocity signatures are generated using the Biot-Savart law. A Gaussian distribution of vorticity is assumed for the vortex "rods" which is

$$\Omega \sim \exp[-(r/r_0)^2/2] \quad (1)$$

where Ω is the modulus of the vorticity at radius r and r_0 is a length scale of the vorticity distribution. (Throughout this paper \sim means 'proportional to' or 'scales with'). The square of the modulus of the Fourier transforms of the u_1 , u_2 and u_3 signatures of this isolated A-vortex is determined and ensemble averaged over each value of z . We obtain $F_{ij}(k, z, \delta)$ where k is the streamwise wavenumber and δ is the height of the eddy representative of the hierarchy under consideration. Given that in each hierarchy the average longitudinal and lateral spacings each scale with δ .

then the power spectral density $\phi_{ii}(k_1 z)$ for the u_i signatures is given by

$$\phi_{ii}(k_1 z) \sim \int_{\delta_1}^{\Delta_E} F_{ii}(k_1 z, z/\delta) p_H(\delta) d\delta \quad (2)$$

where $\phi_{ii}(k, z)$ is the energy per unit non dimensional wavenumber k, z, δ_1 is the scale of the smallest eddies (i.e. the Kline scaling given earlier) and $p_H(\delta)$ is the pdf of hierarchy scales. Δ_E is the length scale of the largest hierarchy and this should scale with the shear layer thickness or pipe radius. Assuming a continuous distribution of hierarchy scales then

$$p_H(\delta) \sim \frac{1}{\delta} \quad (3)$$

as used by Townsend. Also it can be shown that

$$\int_0^\infty F_{ii}(k_1 z, z/\delta) d(k_1 z) \sim I_{ii}(z/\delta) \quad (4)$$

where $\phi_{ii}(z/\delta)$ is the Townsend eddy intensity function (Townsend 1976, pp 153-155). The authors have not yet included the effect of vortex stretching mentioned by Perry & Chong (1982) but the results so far indicate that the spectra for u_i fluctuations are much the same as given by the crude analysis of Perry & Chong. Also the spectra for the u_2 and u_3 fluctuations are much the same in functional form as the u_1 fluctuations if we consider only one hierarchy. Figure 2 shows sketches of the eddy intensity functions.

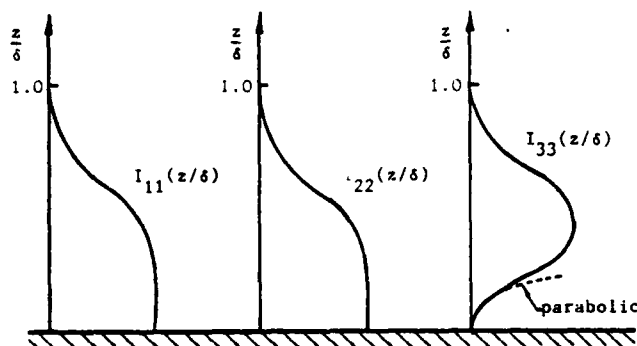


FIGURE 2. Eddy intensity functions.

It should be noted that I_{11} and I_{22} are similar in shape but I_{33} has a different shape as a consequence of the boundary conditions at the wall. Thus we would expect that spectra for u_3 fluctuations to differ considerably from the u_1 and u_2 spectra.

From work carried with simple discrete pdf's (as used by Perry & Chong) the authors expect that equations (2), (3) and (4) and figure 2 will lead to the various spectral similarity regions for u_1 fluctuations as shown in figure 3.

The "outer flow" similarity law is given by

$$\frac{\phi_{11}(k_1 \Delta_E)}{U_\tau^2} = g_{11}(k_1 \Delta_E) ; k_1 \leq \frac{M}{z} \quad (5)$$

where $\phi_{ii}(k, \Delta_E)$ is the energy per unit non-dimensional wavenumber k, Δ_E . For a given large scale flow geometry G_{11} is a universal function. M is a universal constant for all smooth wall flow regions.

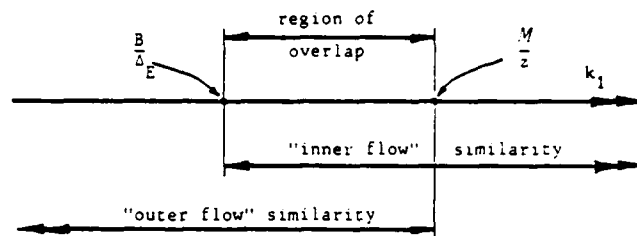


FIGURE 3. Spectral similarity regions for u_1 fluctuations.

The "inner flow" similarity law is given by

$$\frac{\phi_{11}(k_1 z)}{U_\tau^2} = g_{11}(k_1 z) ; k_1 \geq \frac{B}{\Delta_E} \quad (6)$$

where g_{11} is universal for a smooth wall provided $\delta_1 \ll z^2 \ll \Delta_E$ and B is a constant for a given large scale flow geometry.

Perry and Abell (1977) referred to the motions given by equation (6) as the "universal wall motions". As can be seen from figure 3, there exists a region of overlap between equations (5) and (6). It can be shown by dimensional arguments that in this region the equations are of the form

$$\begin{aligned} \frac{\phi_{11}(k_1 \Delta_E)}{U_\tau^2} &= \frac{A_{u1}}{k_1 \Delta_E} \\ \frac{\phi_{11}(k_1 z)}{U_\tau^2} &= \frac{A_{u1}}{k_1 z} \end{aligned} \quad (7)$$

which corresponds to the inverse power law region of the spectrum for u_1 fluctuations mentioned earlier. This inverse power law distribution is a consequence of having a sufficiently large range of hierarchy scales.

A similar behaviour can be shown for the spectra for u_2 fluctuations by virtue of the fact that I_{11} and I_{22} are of similar shape. However, for the spectra of the u_3 fluctuations, only one region of similarity exists, i.e.

$$\frac{\phi_{33}(k_1 z)}{U_\tau^2} = h_{33}(k_1 z) \quad (8)$$

for all k, z . The reason for this differing behaviour can be seen from figure 4.

As seen in figure 4(a), a hot-wire probe distant z from the wall "sees" u_1 fluctuations from all eddies whose height δ is of order z and above. Eddies smaller than z are not "seen" by the probe and they do not contribute to the spectrum. Therefore, the resulting spectrum is made up of contributions of all eddies whose scale fall in the range z to Δ_E . On the other hand, as shown in figure 4(b) a probe "sees" u_3 fluctuations only from eddies whose scale is of order z . In the former case we see many hierarchies whereas in the latter we see approximately one hierarchy.

Figure 5 shows the various spectra collapsed according to the various similarity laws mentioned above.

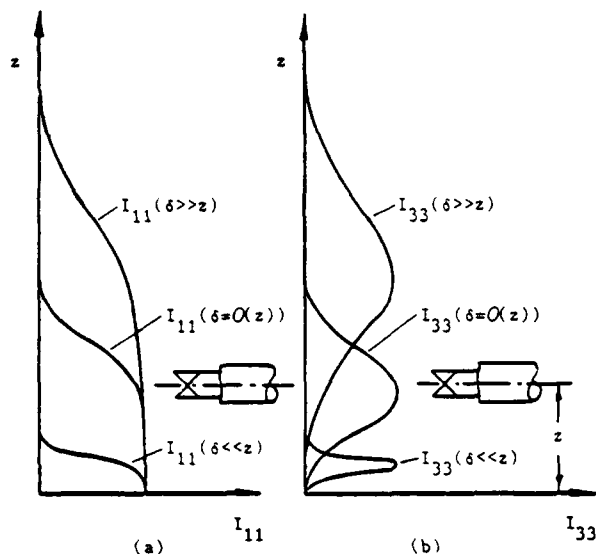


FIGURE 4. (a) I_{11} for various values of δ .
(b) I_{33} for various values of δ .

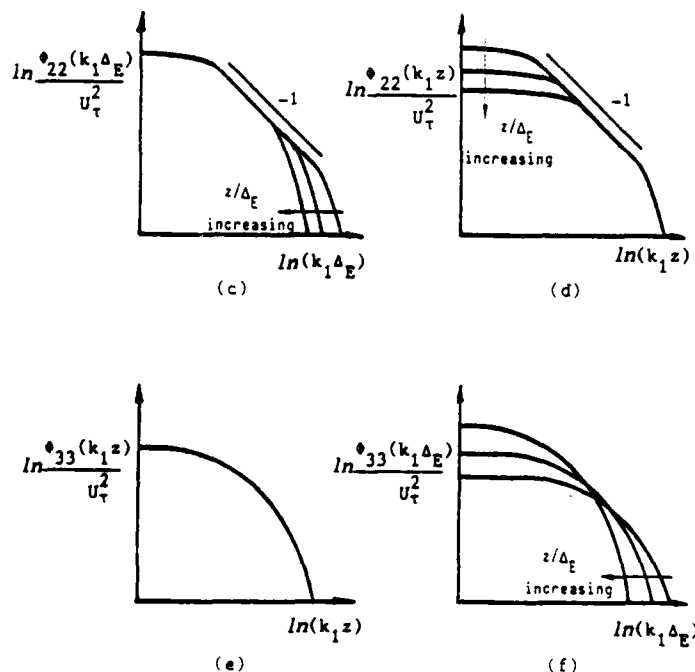
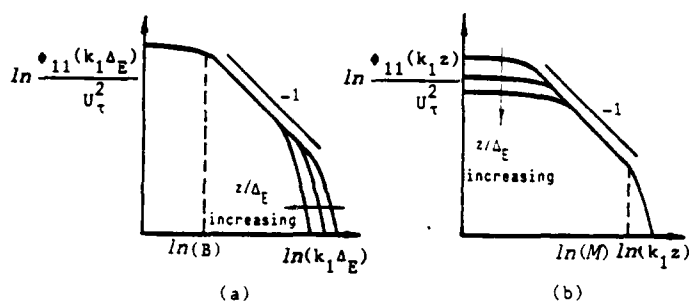


FIGURE 5. "Inner flow" and "outer flow" scaling for u_1 , u_2 and u_3 spectra for various values of z/Δ_E .

Experimental Results

Figure 6(a) shows the u_1 fluctuation results obtained in a smooth-walled pipe using a 1.26 mm long normal wire.

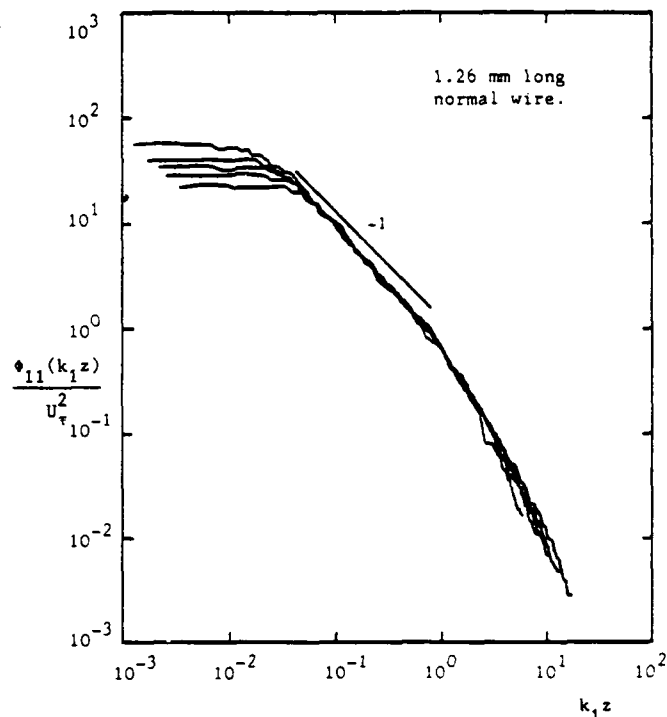


FIGURE 6. (a) "Inner flow" scaling for u_1 spectra for various values of z/Δ_E .
 $Re=200,000$ ($2\Delta_E U_0/\nu$) and
 $140U_0/\nu \leq z \leq 0.14\Delta_E$.
1.26 mm long normal wire.

Using "inner flow" scaling, one expects the spectra to collapse to an inverse power law and asymptote to an exponential-like curve at high wavenumbers and to "peel-off" from the inverse power law at low wavenumbers for differing values of z/Δ_E , as shown in figure 5(b). The results in figure 6(a) appear to behave correctly at low and moderate $k_1 z$; however, at high $k_1 z$ they "peel-off" for varying values of z/Δ_E . The smaller the value of z/Δ_E , the earlier the "peel-off" occurs. It appears that as z/Δ_E decreases, the contribution to the spectrum from the smaller hierarchies, whose scale is of order z , decreases and these hierarchies seem to "disappear". One possible reason for the "missing" hierarchies is the spatial resolution limit of the normal wire. This is strongly supported from the data in figure 6(b) where a 0.39 mm long normal wire was used. One can see some of the "missing" small scale hierarchies have emerged and the data now collapses more convincingly at high wavenumbers and the spectral distribution correlates better with figure 5(b). Figure 7 shows this data using "outer flow" scaling. The collapse at low wavenumbers has improved and the spectra appear at low wavenumbers to correlate better with the scheme shown in figure 5(a).

$+ U_0$ is the centerline velocity and ν is the kinematic viscosity of the fluid.

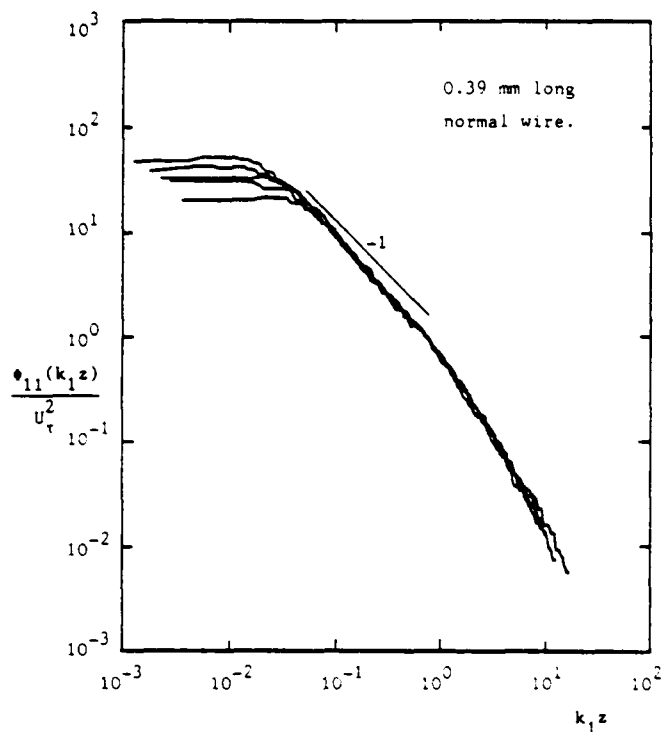


FIGURE 6. (b) "Inner flow" scaling for u_1 spectra for various values of z/Δ_E .
 $Re=200,000$; 0.39 mm long normal wire and $140U_\tau/\nu \leq z \leq 0.14\Delta_E$.

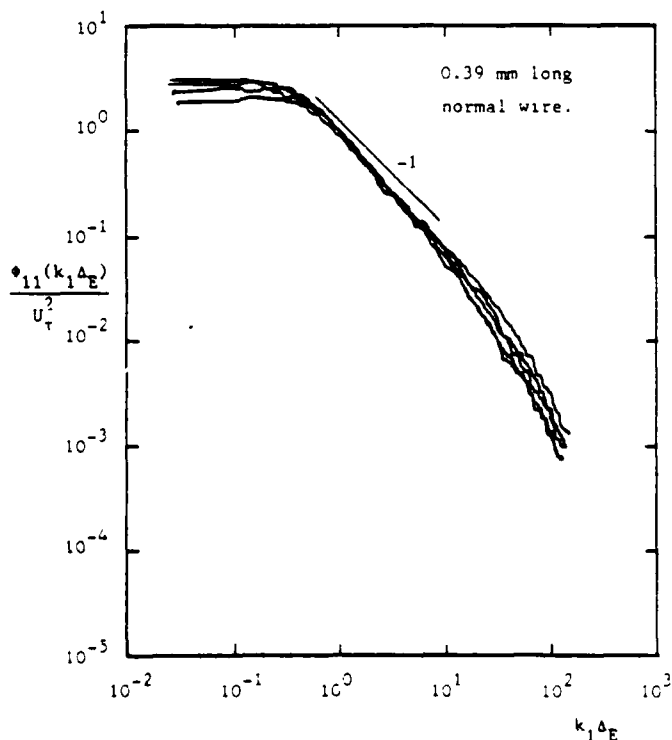


FIGURE 7. "Outer flow" scaling for u_1 spectra for various values of z/Δ_E .
 $Re=200,000$; 0.39 mm long normal wire and $140U_\tau/\nu \leq z \leq 0.14\Delta_E$.

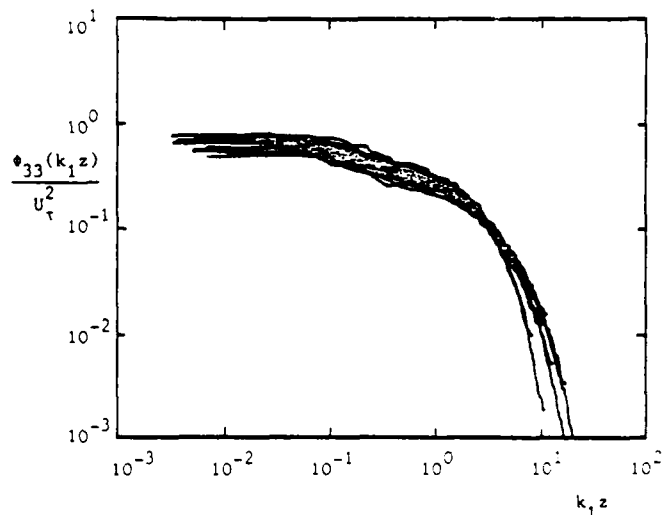


FIGURE 8. "Inner flow" scaling for u_3 spectra for various values of z/Δ_E .
 $Re=75,000$ to $200,000$ and $140U_\tau/\nu \leq z \leq 0.14\Delta_E$.

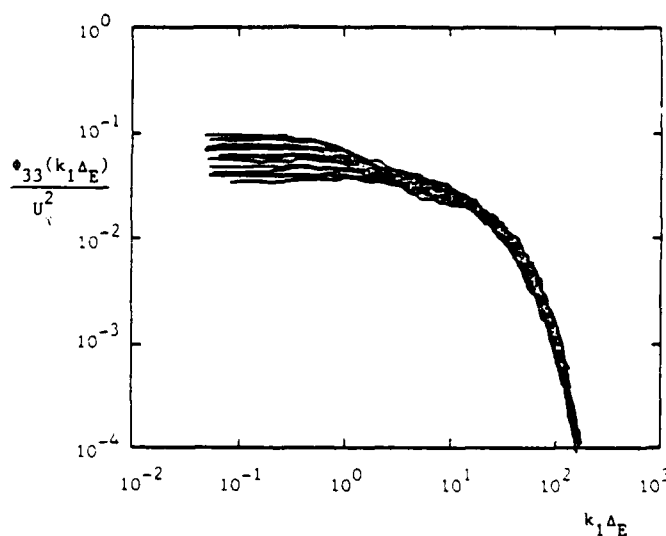


FIGURE 9. "Outer flow" scaling for u_3 spectra for various values of z/Δ_E .
 $Re=75,000$ to $200,000$ and $140U_\tau/\nu \leq z \leq 0.14\Delta_E$.

Figures 8 and 9 show the u_3 fluctuation spectra according to "inner flow" and "outer flow" similarity scaling. It can be seen that a more uniform collapse occurs using "inner flow" scaling and that the spectral shape is characteristic of one hierarchy, (i.e. no inverse power law occurs). However, at high wavenumbers the spectra successively "peel-off" earlier for decreasing values of z/Δ_E . Once again, this is most probably a spatial resolution effect. As z/Δ_E decreases the scale of the X-wires increases relative to the scale of the hierarchy which contributes to u_3 fluctuations, which is of order z (see figure 4(b)), and the "observed" contribution to the u_3 spectra at high wavenumbers decreases. The authors propose that if the scale of the X-wires was significantly reduced, the spectra obtained would collapse to a universal curve for

all k, z as shown in figure 5(e).

Unfortunately no u_2 results have yet been obtained for pipe flow.

Broad-band Turbulence Intensity Distributions

The broad-band turbulence intensity distributions can be found either from the eddy intensity functions of Townsend or by integrating the spectra using the functional relations given earlier.

Using the eddy intensity functions

$$\frac{\overline{u_i^2}}{U_\tau^2} \sim \int_{\delta_1}^{\Delta_E} I_{ii}(z/\delta) \frac{1}{\delta} d\delta \quad (9)$$

Townsend has shown that if $\delta_1 \ll z \ll \Delta_E$ and if $I_{11}(0)$ and $I_{22}(0)$ are finite and

$$I_{33}(z/\delta) \sim (z/\delta)^2 \text{ as } (z/\delta) \rightarrow 0$$

(these are the inviscid boundary conditions assumed in the model) then

$$\begin{aligned} \frac{\overline{u_1^2}}{U_\tau^2} &= B_{u1} - A_{u1} \ln\left(\frac{z}{\Delta_E}\right) \\ \frac{\overline{u_2^2}}{U_\tau^2} &= B_{u2} - A_{u2} \ln\left(\frac{z}{\Delta_E}\right) \\ \frac{\overline{u_3^2}}{U_\tau^2} &= K_{33} \end{aligned} \quad (10)$$

where A_{u1} and A_{u2} and K_{33} are universal constants for a smooth wall and B_{u1} and B_{u2} depend on the large scale external flow geometry. Here Δ_E is taken to be the pipe radius. As mentioned earlier, the spectral scaling scheme given earlier also leads to equation (10). Figure 10 shows the broad-band results and the correlations in the turbulent wall region (i.e. $zU_\tau/\nu \geq 140$ and $z/\delta \leq 0.14$). The correlations given by equation (10) look encouraging.

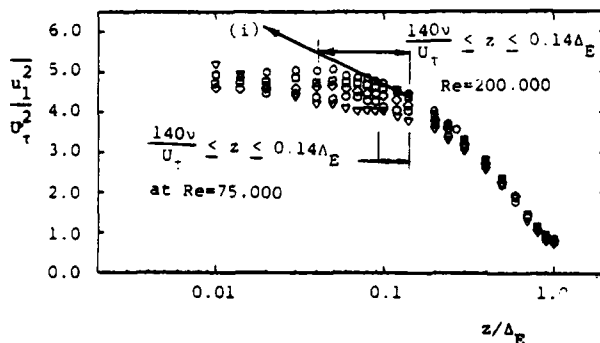


FIGURE 10. (a) $\overline{u_1^2}/U_\tau^2$ versus z/Δ_E . Symbols for figures 10 (a) and (b) are :
 $Re=200,000$ - \circ ; $175,000$ - \square ;
 $150,000$ - \diamond ; $125,000$ - \triangle ;
 $100,000$ - \ominus ; $75,000$ - ∇ .
 Equation to (i) is given by

$$\frac{\overline{u_1^2}}{U_\tau^2} = 2.64 - 0.90 \ln\left(\frac{z}{\Delta_E}\right)$$

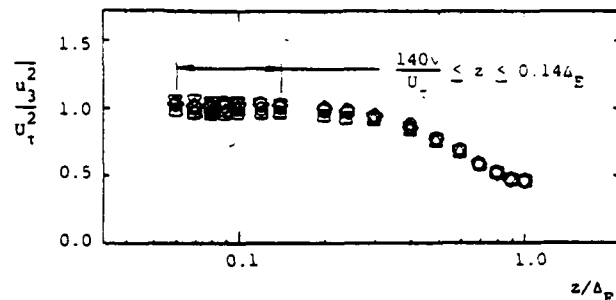


FIGURE 10. (b) $\overline{u_3^2}/U_\tau^2$ versus z/Δ_E . Symbols as for figure 10(a).

The values of $A_{u1}=0.9$, $B_{u1}=2.64$ and $K_{33}=1.0$ were obtained independently from spectra. The authors suspect that the low Reynolds number break down in figure 10(a) occurs because the condition $\delta_1 \ll z \ll \Delta_E$ is violated, since as the Reynolds number decreases, the scale δ_1 of the smallest eddies increases. Also, very close to the wall, spatial resolution problems becomes important.

Conclusions

By comparing spectra for streamwise velocity fluctuations and normal velocity fluctuations in the "constant stress layer" close to the wall (i.e. in the wall similarity region defined by $zU_\tau/\nu \geq 140$ and $z/\Delta_E \leq 0.14$) the attached eddy hypothesis is strongly confirmed and so also is the idea that there exists a range of scales of geometrically similar eddies with a characteristic velocity scale given by U_τ .

References

- HEAD, M.R. & BANDYOPADHYAY, P. 1981 New aspects of turbulent boundary-layer structure. *J. Fluid Mech.* 107, 297-337.
- KLINE, S.J., REYNOLDS, W.C., SCHRAB, F.A. & RUNSTADLER, P.W. 1967 The structure of turbulent boundary layers. *J. Fluid Mech.* 30, 741-773.
- PERRY, A.E. & ABELL, C.J. 1975 Scaling laws for pipe flow turbulence. *J. Fluid Mech.* 67, 257-271.
- PERRY, A.E. & ABELL, C.J. 1977 Asymptotic similarity of turbulent structures in smooth- and rough-wall pipes. *J. Fluid Mech.* 79, 785-799.
- PERRY, A.E. & CHONG, M.S. 1982 On the mechanism of wall turbulence. *J. Fluid Mech.* 119, 173-217.
- TOWNSEND, A.A. 1976 "The structure of turbulent shear flow". 2nd edn. Cambridge University Press.

THE DEVELOPMENT OF A LARGE SCALE STRUCTURE IN THE ROD GAP REGION FOR
TURBULENT IN-LINE FLOW THROUGH CLOSELY SPACED ROD ARRAYS

J.D. Hooper
CSIRO Mineral Physics Division
Lucas Heights Research Establishment
Private Mail Bag 7, Sutherland, NSW.
Australia 2232

ABSTRACT

Experimental studies of developed axial single-phase flow through closely spaced rod arrays have shown, with reducing p/d ratio, the development of high axial and azimuthal turbulence intensities in the rod gap region. Associated with this is the existence of very high levels of the azimuthal Reynolds shear stress component either side of the rod gap centre. Spatial correlation analysis of the three turbulent velocity components has shown a large scale coherent and almost periodic structure in the rod gap region. The structure is markedly different to the currently accepted secondary flow model.

INTRODUCTION

Secondary flows, induced by gradients of the Reynolds stresses in a plane normal to the duct axis, are present in developed single-phase turbulent flow through ducts not having a rotational symmetry axis. For the large arrays of heat generating rods used in nuclear power reactors, such secondary flows have been assumed to have considerable significance, as they serve to decrease the azimuthal variation of the local rod surface heat transfer coefficient. The detection of V and W in rod arrays is experimentally difficult. Kjellstrom (1974) used an air rig with a triangular rod array test section spaced at a p/d ratio of 1.217, and measured the mean velocity distribution, wall shear stress variation, and five of the six Reynolds stresses. Although secondary flow velocity components of the order of 1% of the local axial velocity were reported, they were not symmetrical and indicated a circulation around one rod of the array. Trupp and Azad (1975) used air as the working fluid in a triangular array spaced at three p/d ratios, 1.50, 1.35 and 1.20. Secondary flow cells were not directly measured. Rowe (1973) used a laser-Doppler anemometer with water as the working fluid in a square-pitched rod array spaced at two p/d ratios, 1.250 and 1.125. The mean axial velocity distribution and two of the Reynolds stress components were measured. Multiple secondary flow cells for the repeated symmetry areas of one subchannel were deduced from the axial turbulence intensity distribution, without direct experimental measurement. A study by Carajilescov and Todreas (1975) of a triangular array spaced at a p/d ratio of 1.123, using water as the working fluid and a laser-Doppler anemometer as the measurement system, again failed to directly resolve secondary flow cells.

The experiments of Rehme (1979, 1982a, 1982b) in a square-pitched rod array bounded by a rectangular duct and using air as the working fluid have shown a progressive increase in the axial and azimuthal turbulence intensity in the rod gap region as the rod to rod or rod to wall distance (p/d or w/d ratio) is reduced. This extensive experimental series covers

the p/d range 1.036, 1.071, 1.15 and 1.40, and the w/d range 1.026, 1.048, 1.071 and 1.118 (1982b). The very high axial and azimuthal turbulence intensities present in the rod gap region for the closest rod to rod or wall spacings lend some doubt as to the accuracy of the hot wire small signal approximations. However, a consistent trend noted in the series is the development of very high levels of the azimuthal Reynolds shear stress in the rod gap region as the p/d or w/d ratio are reduced, with no direct measurements of secondary flow.

A similar study in a symmetrical square-pitch rod array (Hooper (1980)) for two p/d ratios (1.194 and 1.107) showed the same increase in the axial and azimuthal turbulence intensity as the rod spacing was reduced. There was little evidence of any non-zero secondary flow components V and W . The mechanism whereby the high axial and azimuthal turbulence intensities develop in the rod gap region was unresolved.

2. EXPERIMENTAL RIGS

The results from two experimental studies are discussed. One duct represented the interior region of a symmetrical square-pitch rod array spaced at a p/d ratio of 1.107 (Hooper (1980)). The other test-section is the rig used in the Rehme (1982a) study.

2.1 Symmetrical Square-pitch Rod Array. The six rod cluster forming a symmetrical test section, figure 1, was intended to model the fluid mechanics in the interior of a large square-pitch rod array. The rod diameter was 140 mm, and the test section length 9.14 m. The ratio of the test section length to hydraulic diameter was 128. This was shown to be sufficient to ensure developed flow conditions.

Air was the working fluid, and hot-wire anemometry was used to determine the direction of the mean velocity vector and all six components of the Reynolds stresses. A rotated inclined wire probe was estimated to be capable of detecting secondary flow velocities greater than 1% of the local axial U .

2.2 Wall Bounded Square-pitch Array. The central part of the test section, consisting of four rods equidistant from the walls of an enclosing rectangular duct, is shown by figure 2. The rod diameter was 157.5 mm and the minimum rod to wall distance for all four rods (g) was 11.35 mm, with a rod gap width 5.7 mm. The test section averaged hydraulic diameter d_h was 45.6 mm, and the test section length 7.0 m. The non-linearized bridge output signals from constant temperature hot wire anemometer bridges were high pass filtered at 0.1 Hz, and directly recorded on F.M. tape.

In contrast to the rod centered cylindrical

co-ordinate system used by Rehme (1982a), a cartesian co-ordinate system centered in the rod gap (fig.2) was used. The subchannel averaged Reynolds number of the study was 7.60×10^4 .

3. EXPERIMENTAL RESULTS - SYMMETRICAL SQUARE-PITCH ROD ARRAY

Complete experimental data of the mean axial velocity distribution, wall shear stress variation and the magnitude of the six Reynolds stresses over the Reynolds number range 22.6 to 207.6×10^3 is given by Hooper et. al (1983).

The axial momentum equation for turbulent flow through the rod cluster, resolved in a cylindrical coordinate system centered on an inner rod of the array is :

$$\rho \frac{DU}{U\tau} = -\frac{\partial P}{\partial z} + \mu \nabla^2 U - \frac{\rho}{r} \frac{\partial(rUV)}{\partial r} - \frac{\rho}{r} \frac{\partial UV}{\partial \theta} \quad (1)$$

For developed flow conditions, derivatives of the mean velocity and Reynolds stresses in the axial direction (z) are zero. As shown by Wood (1981) the above equation may be integrated radially from the rod wall for a fixed traverse angle. The viscous term is of negligible magnitude except in the viscous sublayer at the rod surface, where $\mu \frac{\partial U}{\partial r}$ is equal to $\tau(\theta)$.

The integral momentum equation is :

$$\rho \int_R^{R+y} r \left(V \frac{\partial U}{\partial r} + \frac{W}{r} \frac{\partial U}{\partial \theta} \right) dr = -\frac{\partial P}{\partial z} \cdot \left(\frac{y^2}{2} + \frac{2Ry}{2} \right) - R \tau(\theta) - \rho \overline{uv} \cdot (y + R) - \rho \int_R^{R+y} \frac{\partial \overline{uw}}{\partial \theta} dr \quad (2)$$

The right hand terms of equation(2) are known or may be numerically calculated, allowing an estimation of the significance of V and W to the axial momentum balance. The high contribution of the azimuthal shear stress $-\rho \overline{uw}$ to the balance for the rod gap region is indicated by figure 3, for a Reynolds number of 46.3×10^3 . Wood (1981) has shown, using the data from Hooper (1980) and a notional single cell of secondary flow for the 0 to 45° symmetry zone, that the maximum level of V for the 0° traverse is 0.25% of U , the peak level of the local axial velocity. Hooper and Rehme (1983) using different assumptions for V , showed V to be not greater than 0.1% of U at 0° .

These low estimated levels of V are in agreement with the experimental data for the extended Reynolds number study (Hooper et. al(1983)), where no non-zero V or W measurements were made to $\pm 1\%$ of U .

4. EXPERIMENTAL RESULTS - WALL BOUNDED SQUARE-PITCH ARRAY

The association of increasingly high axial and radial turbulence intensities in the rod gap, and the generation of higher levels of the azimuthal Reynolds shear stress near to the gap centre as the p/d ratio is reduced does not appear to be related to increasing or even measurable secondary flow components. This is shown by the lack of significant V and W measurements in the rod gap (1979, 1982a) in the extensive Rehme studies (1982b). In an attempt to resolve the fluid mechanism whereby high turbulent kinetic energy is transported to or generated in the gap region, a two probe spatial correlation study was made for the Rehme (1982a) test section at the same Reynolds number.

4.1 Direct Reproduction of u,v,w. The turbulent velocity components for two points in the rod gap, point 2 located at (x,y) co-ordinates $(0, -10 \text{ mm})$ and

point 4 at $(0,10 \text{ mm})$ are shown in figures 4a and b. The time record length of 0.1 seconds is far less than the time used to compute the correlation functions. However, there is clearly shown to be a considerable large scale structure in the axial velocity fluctuations at both locations for the $x-z$ plane. The mean axial velocity U at these locations was 20.5 m s^{-1} , and the peak excursion of the axial turbulence component U is approximately 25% of this value.

The turbulence component along the x axis, v , is seen to be considerably reduced in magnitude, with little evidence of the large scale structure of the axial component. The lack of a large scale structure and reduced intensity for v in the rod gap is not surprising, as the narrow gap width must dampen and restrict velocity fluctuations normal to the rod surface.

The velocity component along the y axis, w , is seen in figure 4b to have an almost periodic large scale structure. The magnitude of the velocity fluctuations in w is at least equivalent to u . There is more fine scale turbulence superimposed on the transverse or w component than u , however. The large scale structure of w is clearly correlated across the rod gap centre-line. The presence of a large scale, energetic and periodic momentum exchange process through the rod gap is strongly suggested by figure 4b.

4.2 Cross-correlation Coefficients Within

One Subchannel. In order to resolve the extent of penetration of the large scale structure present in the rod gap into the subchannel, the cross-correlation coefficients between u , v and w were measured along the y axis. A fixed hot wire probe 1 was located at (x, y) coordinates at $(0,10 \text{ mm})$ and probe 2 moved along the y axis between this location and $(0,55 \text{ mm})$. An unfiltered analog signal processing system was used to generate the results shown by figure 5.

The axial velocity component u is seen to be significantly correlated for a considerable distance from the rod gap area. The furthest data point, corresponding to a y_2 value of 55 mm , is in the same region reached by a radial traverse at 35° . The results of Rehme (1982a) show a significant reduction here in the axial turbulence intensity.

The transverse turbulent velocity component w , directed towards the rod gap, is also well correlated over the same distance. The x axis or v component of the turbulence is seen to have no significant cross-correlation for the whole traverse length.

4.3 Auto-correlation Functions.

The auto-correlations of the axial and transverse turbulent velocity components were computed for the rod gap region along the y axis, with the fixed probe at $y = -10 \text{ mm}$ (location 2). The moving probe was placed at locations 1,3 and 4, corresponding to y values of 0.5 and 10 mm . A digital analysis method was used, with antialiasing filters set at 736 Hz .

The axial velocity component u shows little evidence of a periodic function for the rod gap centre, as shown by figure 6a. However, away from the x axis symmetry line, the axial component of turbulence does show a damped periodic response, with a cyclic frequency of 92 Hz (figure 6b). This frequency is repeated in all the periodic auto- and cross-correlation functions measured (Hooper and Rehme 1983) and represents an average frequency of the cyclic momentum interchange process for the 100 second time records used in the computation.

The transverse turbulent velocity component w shows a periodic response at all locations for the auto-correlation. Figure 6c is typical, with strong evidence of the 92 Hz . Further spatial correlations of u and w are given by Hooper and Rehme (1983). The cross-correlation functions for the transverse velocity component were shown to be highly correlated for all rod gap locations. This is significant, as secondary flow cells would not be expected to cross the x axis, a symmetry boundary of the duct.

4.4 Reynolds shear stress $-\rho u'w'$. It has been demonstrated experimentally (Section 3) that this component is antisymmetric with respect to the x axis. An examination of the cross-correlation function for these turbulent velocity components at the rod gap centre, figure 7a, and at locations 2 and 4 on either side of the x axis, figures 7b,c, shows the high magnitude of this Reynolds stress component to be associated with the cyclic fluctuation centered at 92 Hz. Although it is difficult to talk of the phase of a signal that is jittering in both amplitude and frequency (figure 4b), figures 7a,b,c suggest that the change of sign of $-\rho u'w'$ is connected to a phase shift between u and w. The functions were calculated for 100 sec., a sufficiently long record to give reasonable statistical accuracy, and without recourse to any of the conditional sampling techniques.

5. DISCUSSION

The spatial extent of the high correlation coefficients for both the axial and transverse turbulent velocity components, and the auto- and cross-correlation functions computed for the rod gap region, support the existence and demonstrate the extent of the periodic intersubchannel momentum exchange process for the wall subchannel test section. The peak value of the transverse turbulent velocity component in the rod gap region is approximately 25% of the local axial velocity, a level at least one order of magnitude higher than possible level of secondary flow components.

It is necessary to consider whether the highly correlated large scale, in terms of the rod gap width, turbulent structure present in the study for a p/d ratio of 1.036 is characteristic of developed rod bundle turbulent flow at low p/d ratios, or may be traced to another physical phenomenon.

Bradshaw (1982) has suggested the possibility of an acoustic resonance effect; the rig length of 7 m is close to a half wavelength for the resonance frequency noted by Section 4.3. A possible indication that the phenomenon is not linked to an acoustic resonance is the demonstration that the resonant frequency is Reynolds number dependent. It has not yet been possible to test this in the Kehme (1982a) test section. However, two as yet unpublished studies (Hofman 1982), using flow visualization to resolve the fluid structure in closely spaced rod arrays, do answer this question. Both experiments used water as the working fluid and aluminium powder as the flow visualization particles. Both studies clearly showed the presence of the large scale turbulent structure in the rod gap, an effect that became more marked as the gap width was reduced. For a fixed test-section geometry, it was also shown that the cyclic frequency was Reynolds number dependent. The scale of the rigs was considerably smaller than the air test sections of Sections 3 and 4, and it should be noted that the ratio of the speed of sound in water to air at 20°C is 4.4 : 1. The test section length was one order of magnitude less than the acoustic resonance wavelength.

Another possible source of the fluid structure in the rod gap is a mechanical vibration of the rods, coupled to the fluid. Thompson (1982) noted that if the rods vibrate laterally, the fluid in the gap will be transported with them as a virtual mass effect. Accelerometer studies have shown negligible rig vibration, with no correlation to the turbulent velocity components. A further possible acoustic source is in the pressure noise generated by the rig blower. However, the study of the symmetrical four-rod array (Hooper (1980)) showed the mean and turbulent flow structure to be insensitive to changes in the blower pressure noise of approximately two orders of magnitude. It is therefore considered probable that a large scale coherent structure in the rod gap region is a characteristic feature of rod bundle turbulent flow at low p/d ratios. The origin of this structure is likely to be a cyclic pressure field between adjacent subchannels. As noted by Bradshaw (1982) an incompressible flow instability is possible. If the mass flow axially along one subchannel decreases, the

axial pressure gradient for this channel will also decrease, leading to a pressure difference between it and the surrounding subchannels. Phase lags may make this an unstable situation, leading to vortex shedding in the rod gap region.

6. CONCLUSIONS

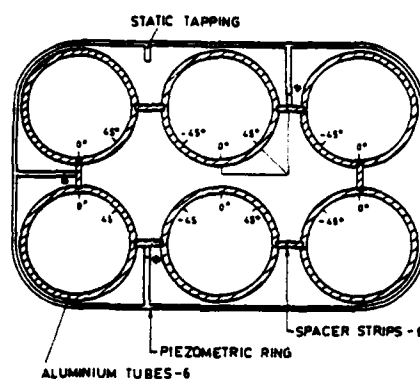
A most significant feature of developed single phase flow through closely spaced rod bundles is the development of a large scale fluid structure in the rod gap region. The structure is almost periodic in frequency for high Reynolds number flows, and develops high levels of the transverse turbulent velocity component through the rod gap. The role of secondary flows, induced by gradients of the Reynolds stresses in an axial plane, appears to be minimal in this process.

ACKNOWLEDGEMENT

The support of Prof. K. Kehme in making possible my year's secondment to the KfK is gratefully acknowledged. The assistance of Mr Mensinger in the experimental work is acknowledged, as is the work of Mr W.J. Crawford of the A.A.E.C. The digitization work was made possible through the assistance of Dr Váth of the INR Noise Laboratory.

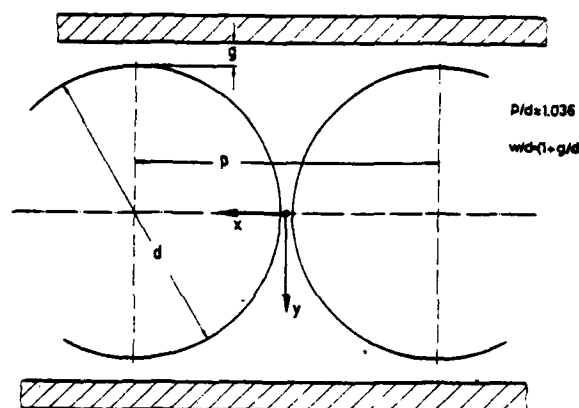
REFERENCES

1. Bradshaw, P., 1982, Private Communication Department of Aeronautics, Imperial College, London.
2. Garajilesco, P. and Todreas, N.E. 1975, "Experimental and analytical study of axial turbulent flows in an interior subchannel of a bare rod bundle", Paper HT/51, A.S.M.E. Winter annual meeting.
3. Hofman, G., 1982, Private Communication, IIRs, Kernforschungszentrum Karlsruhe.
4. Hooper, J.D., 1980, "Developed single phase turbulent flow through a square pitch rod cluster", Nucl. Engng. Des. Vol 60.
5. Hooper, J.D., Wood, D.H. and Crawford, W.J., 1983, "Developed single phase turbulent flow through a square pitched rod cluster for an extended range of Reynolds numbers", Aus. Atomic Energy Report E.558.
6. Hooper, J.D. and Kehme, K., 1983, "The structure of single-phase turbulent flow through closely spaced rod arrays", KfK Report 3467.
7. Kjellström, B., 1974, "Studies of turbulent flow parallel to a rod bundle of triangular array", Atkiesbolaget Atomenergi, Report AE-487.
8. Kehme, K., 1979, "The structure of turbulent flow through subchannels of rod bundles", A.S.M.E. Winter Annual Meeting.
9. Kehme, K., 1982a, "Strömungsuntersuchungen im Wandkanal eines Stabbündels", (p/d = 1.036, w/d = 1.072), KfK Report 3361.
10. Kehme, K., 1982b, "Experimental investigations of turbulent flow in gaps of rod bundles", LAHR 2nd International Specialists meeting on thermal-hydraulics in LMFBR rod bundles, Rome.
11. Rowe, D.S., 1973, "Measurements of turbulent velocity, intensity and scale in rod bundle flow channels", B.N.W.L.-1736.
12. Thompson, J.J., 1982, Private Communication, Nuclear Engineering, University of N.S.W. Australia.
13. Trupp, A.C. and Azad, K.S., 1975, "Turbulent flow in triangular rod bundles", Nuc. Engng. Des. Vol. 32.
14. Wood, D.H., 1981, "The equations describing secondary flow in cylindrical polar coordinates", University of Newcastle T.N.-F.M. 61, Australia.



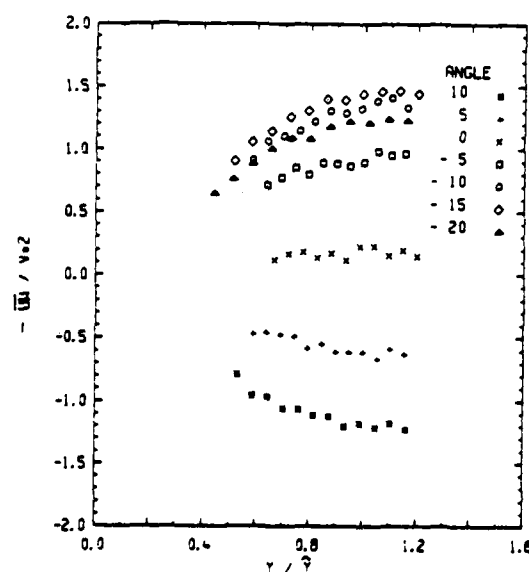
Symmetrical square-pitch rod array

Figure 1



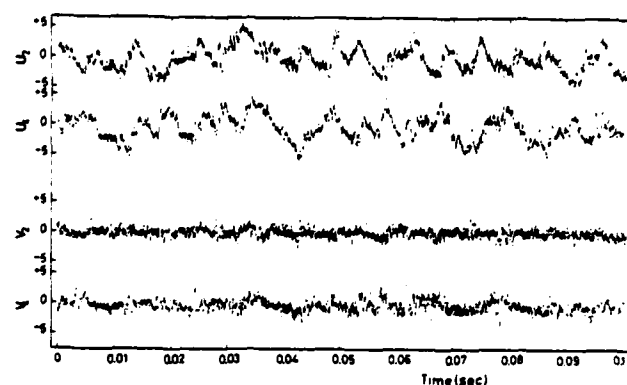
Wall bounded square-pitch array

Figure 2



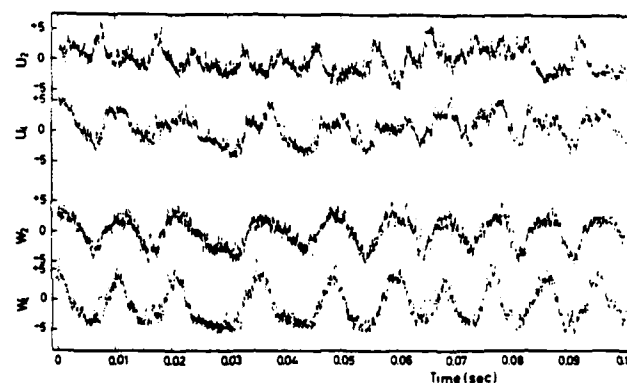
Azimuthal component of Reynolds shear stresses in the rod gap

Figure 3



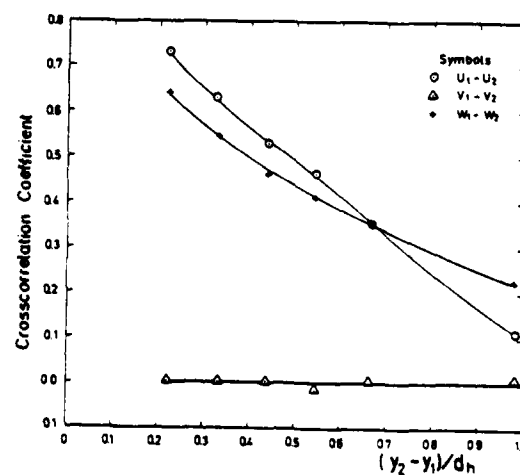
Turbulent velocity components u, v (m s^{-1})

Figure 4a



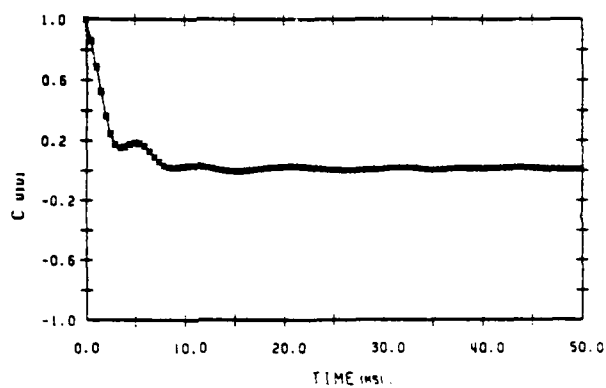
Turbulent velocity components u, w (m s^{-1})

Figure 4b



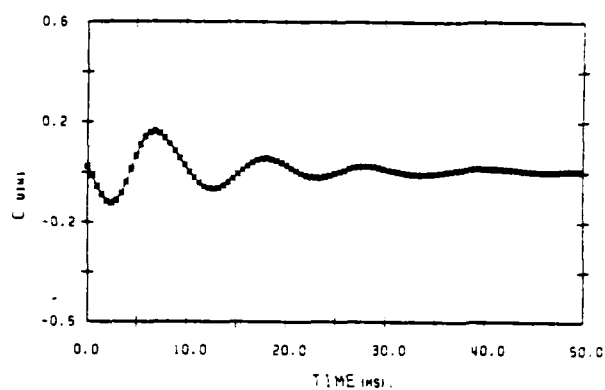
Spatial cross-correlation coefficient u, v, w within one subchannel of the wall bounded square-pitch array.

Figure 5



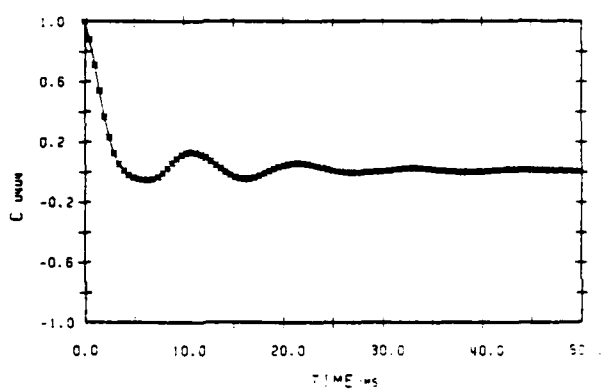
Axial turbulent velocity u auto-correlation,
location 1

Figure 6a



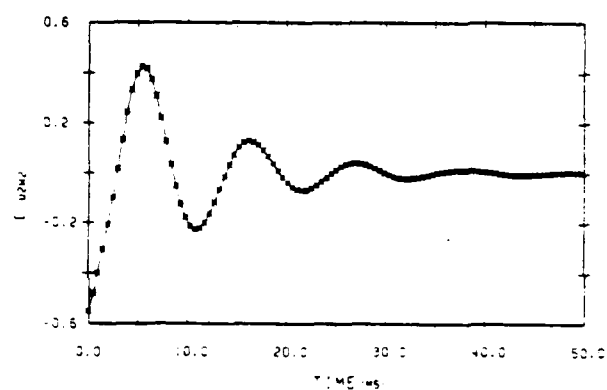
Cross-correlation function C_{uw} ,
location 1

Figure 7a



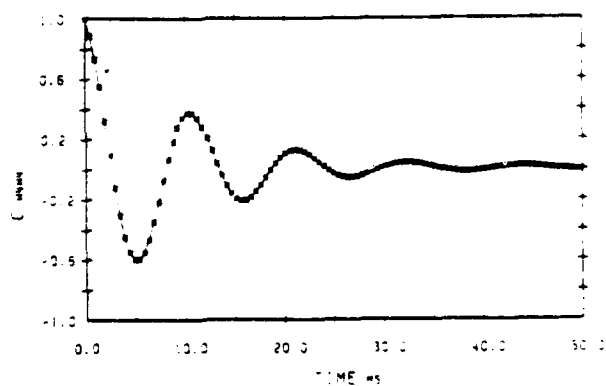
Axial turbulent velocity u auto-correlation,
location 4

Figure 6b



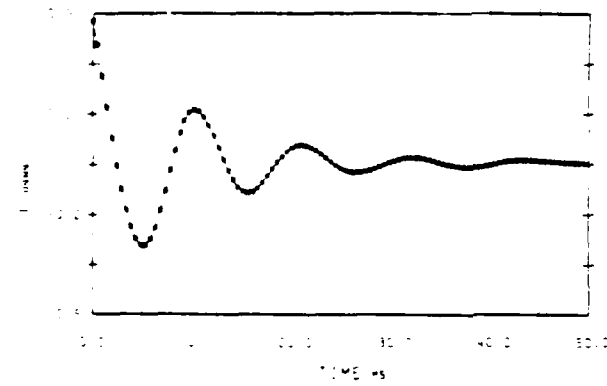
Cross-correlation function C_{uw} ,
location 2

Figure 7b



Transverse turbulent velocity w
auto-correlation, location 4.

Figure 6c



Cross-correlation function C_{uw} ,
location 4

Figure 7c

SESSION 2 - EXTERNAL 2-D BOUNDARY LAYERS

W. Reynolds - Chairman

ON THE STRUCTURE OF TURBULENT BOUNDARY LAYERS AT DIFFERENT REYNOLDS NUMBERS

by

J. Andreopoulos*, F. Durst**, J. Jovanovic***

- * Sonderforschungsbereich 80, Universität Karlsruhe
Kaiserstraße 12, D-7500 Karlsruhe, FRG
- ** Lehrstuhl für Strömungsmechanik, Universität Erlangen-Nürnberg
Egerlandstraße 13, D-8520 Erlangen, FRG
- *** Boris Kidric Institute for Nuclear Sciences
P.O.Box 522, Beograd, Yugoslavia

ABSTRACT:

The present paper summarizes experimental results obtained by means of hot-wire anemometry. Measurements are provided for boundary layer flows at various Reynolds numbers. Measurements of mean flow properties are given and results obtained via conditional sampling are provided. The employment of a hot-wire temperature wake sensor allowed relevant information on the cross velocity fluctuations to be obtained in regions very close to the wall.

1. INTRODUCTION:

Turbulent wall boundary layers have been extensively studied by many research workers of fluid mechanics and a vast amount of information has become available on mean and fluctuating flow properties as well as spectral information from which turbulence length scales were deduced. Quantitative information like this formed the basis of turbulence model development and the development of prediction procedures for turbulent flows. It has occasionally been claimed, however, that boundary layer information is only available at low Reynolds numbers whereas turbulence models embrace assumptions that are usually attributed to flows at high Reynolds numbers. Hence, questions have arisen regarding the influence of Reynolds number on the properties of wall boundary layers.

In recent years, coherent flow structures, present in wall bounded flows, have gained the attention of experimentalists and it has been claimed that they control the development of wall boundary layers and all major contributions to the Reynolds shear stress. Complications occur in studying these structures because of their double nature; the large scale structure which is Reynolds number independent and the wall structure for which complete scaling laws are not yet available. Questions arise whether scaling laws obtained for low Reynolds number flows, mostly studied by previous authors, can be extrapolated to higher values.

It has been the aim of the authors' work to provide partial answers to the aforementioned questions. In which way their work is related to that of other research workers, is given by Andreopoulos et al. (1983) where detailed information on the authors' experimental results are presented. Below only a summary is provided.

2. EXPERIMENTAL ARRANGEMENT

The present investigations were performed in the closed circuit wind tunnel of the Institut für Hydromechanik of the Universität Karlsruhe, details of which are provided by Ermshaus and Naudascher (1977). It consists of a well designed settling chamber with wire meshes followed by contraction with an area ratio of 10:1 entering into an 8 m long working section. The cross sectional shape of the wind tunnel is octagonal with an internal diameter of 1.5 m. The entire roof of the working section is adjustable to permit flow investigations at zero longitudinal pressure gradient. This experimental condition can be achieved without influencing the low turbulence intensity in the free-stream which was approximately 0.06 % at 40 m/sec.

A flat plate made of formica was installed horizontally inside the tunnel section 30 cm from the tunnel floor. The total length of the plate was 6 m and it was supported by strong vertical bars mounted over the entire plate length. It avoids plate deflections due to static pressure differences. The plate material was chosen to avoid hot-wire corrections close to the wall and was suggested in a theoretical and experimental study performed by Bhatia et al. (1982) which explains the actual mechanism of the increased heat transfer from hot-wires close to walls. The study showed that heat losses due to wall proximity are negligible if highly heat-insulating wall materials are employed.

The traversing mechanism for the hot-wire probes was installed inside the wind tunnel and had an automatic, externally driven position control. The driving unit consisted of a stepping motor which permitted precise relative positioning of the hot-wire in the three directions of a cartesian coordinate system with a step size of 25 μ m in each direction. For measurements in close proximity of the wall, the relative motion of the probe was also checked independently by means of a comparator clock of 1 μ m positioning accuracy. The absolute position of the wire from the wall surface was obtained through an additional position calibration performed in still air outside the wind tunnel. This calibration was performed on the top of a wall consisting of the same material as the flat plate inside the wind tunnel. It was found that the hot-wire anemometer output voltage was a function of wire distance from the wall as shown in Fig. 1. The actual wire position in this distance calibration was obtained with a precision microscope with a traverse for the scaled objective lens system having a traverse accuracy of 2 μ m. The measurements inside the tunnel were started without any flow and the starting wire position was obtained using the position calibration information of Fig. 1.

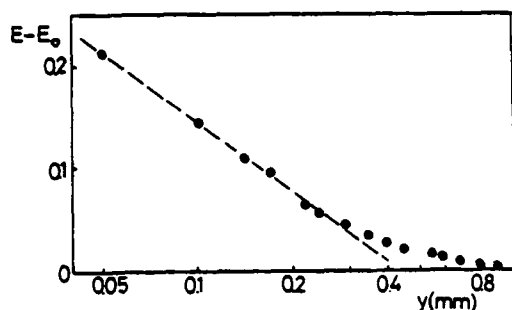


Fig. 1: Calibration curve for the determination of absolute distance of the hot-wire location from the wall

Special care was taken to position the prongs of the probe parallel to the wall in order to approach the surface as close as possible and to minimize flow disturbances by the wire prongs and probe support. At higher flow velocities the hot-wire probes were inclined with respect to the wall surface by up to about 5° in order to permit measurements inside the viscous sub-layer of the flow; this region becomes thinner as the Reynolds number of the flow increases.

Streamwise velocity measurements were performed with standard hot-wire anemometer equipment consisting of a DISA P05 gold-plated boundary layer probe operated with a DISA 55M01 constant temperature anemometer. The over-heating ratio for the hot-wire was 1.8, and the wire was calibrated for this value in the range 0.3 m/s - 40 m/s using the modified DISA 55D90 calibration equipment described by Braun and Tropea (1979) together with a Baratron 3 mmHg pressure transducer. In addition to measurements with single hot-wire probes, the present investigations also incorporated simultaneous measurements of two velocity components, the longitudinal component and the component perpendicular to the wall. To obtain both velocity components at small distances to the wall, a small hot-wire, temperature-wake sensor was employed as described by Durst and Ermshaus (1977). This sensor measures the magnitude of the instantaneous velocity vector with the help of a $5 \mu\text{m}$ diameter hot-wire located at the front end of a three wire probe shown in Fig. 2.

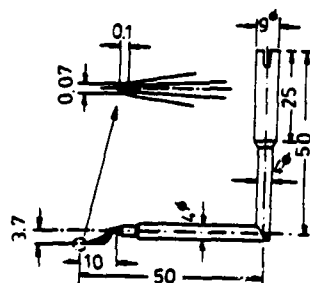


Fig. 2: Hot-wire, temperature wake sensor

This wire is followed by two parallel $2 \mu\text{m}$ diameter temperature sensors employed to measure the direction of the temperature wake. Having the magnitude of the instantaneous velocity vector and its direction relative to the wall, permits the instantaneous velocity components U and V to be computed. However, as already explained by Durst and Ermshaus (1977), the sensor design has to be matched to the flow field under investigation and the present sensor is limited to applications in the velocity range of 1.5 m/s to 7.0 m/s approx.

In the present experiments, the front hot-wire was operated in the bridge of a hot-wire anemometer (DISA 55M01) employed in its constant temperature mode. The two temperature wires were driven by two DISA 55M20 systems operated as constant current anemometers. The heating current to each wire was approximately 1mA in all ex-

periments. All anemometers were carefully checked prior to their employment in the present investigations.

The hot-wire temperature-wake sensor required careful calibration and this was performed in the centre part of the wind tunnel employed in the present study. The probe inclination to the flow direction was altered in steps of 5° and the voltage difference of the two temperature wires was measured as the calibration signal for the flow direction. Calibration had to be formed for various flow velocities as indicated in Fig. 3 which shows two typical calibration curves for $U = 1.42 \text{ m/s}$ and 7.43 m/s . Both calibration curves indicate deviations from the theoretically expected nearly linear response, see Durst and Ermshaus (1977), due to small imperfections in manufacturing the probe. To obtain the actual flow angle in the measurements, linear interpolation was employed, as indicated in Fig. 3, utilizing the calibration data. In the data reduction scheme, see Andreopoulos (1980), the dependence of the hot-wire signal on the flow parallel to the wire was not considered and calibrations for this velocity component did not need to be performed.

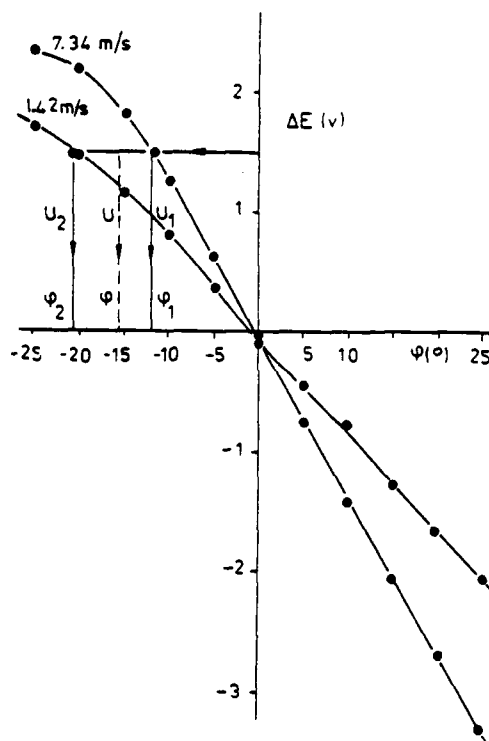


Fig. 3: Calibration curve and interpolation scheme for evaluation of the temperature wake sensor signals

Within the centre part of the wind tunnel, the front wire of the hot-wire temperature-wake sensor was also calibrated insitu yielding the anemometer output voltage as a function of the adjusted flow velocity. The anemometer voltage turned out to be a function of the probe inclination to the flow direction. It is for this reason that the hot-wire part of the sensor had also to be calibrated for velocity direction yielding results as indicated in Fig. 4.

All measurements, including the calibration data, were recorded on-line by a data acquisition system based on a Hewlett Packard 5451C Fourier Analyser. Prior to storing and/or recording the data, the output of the anemometers was first low-pass filtered at 10 kHz and then digitized and recorded on magnetic tapes. For the actual measurements signals between 20 sec and 40 sec total length were taped at each measuring point with the recording length being dependent on the flow velocity and the measuring location from the wall. The sampling rate for the data was chosen to be between 5 to 20 kHz

depending on the Reynolds number of the flow. These sampling rates ensured the high frequency components of the velocity fluctuations to be retained in the signal records. The taped signals were subsequently analysed employing special soft-ware programs written for the UNIVAC 1108 digital computer of the Universität Karlsruhe. The stored signals were also converted into velocities and restored on tapes for further processing.

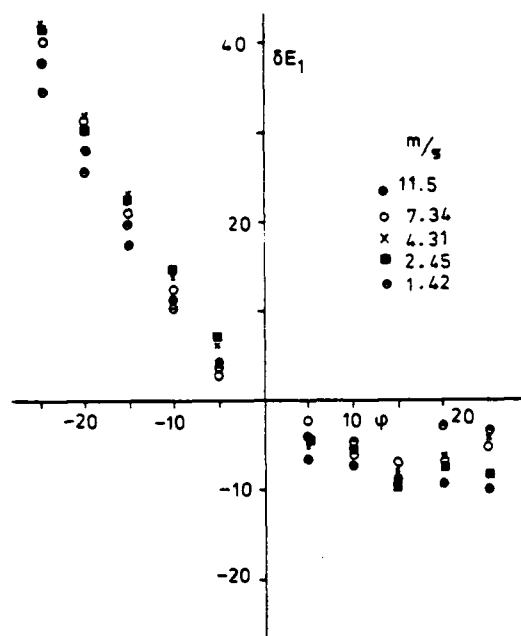


Fig. 4: Angle dependence of signal from front wire of the temperature wake sensor

3 EXPERIMENTAL RESULTS

3.1 Conventional Averaged Flow Properties

The authors' investigation embraced various Reynolds numbers that are given in Table 1 together with properties of the boundary layers investigated.

In this table U_∞ is the free stream velocity, u_τ the friction velocity, δ the boundary layer thickness, δ^* the displacement thickness, θ the momentum thickness, H its shape factor, R_θ the Reynolds number based on momentum thickness and c_f the friction factor.

U_∞ m/s	U_τ m/s	δ mm	δ^* mm	θ mm	H	R_θ	$c_f \times 10^2$
6.33	0.25	73.9	11.3	8.6	1.312	3624	0.3119
10.89	0.40	67.7	9.9	7.6	1.303	5535	0.2698
22.61	0.81	88.1	11.0	8.5	1.292	12436	0.2566
28.79	0.99	81.2	10.6	8.3	1.284	15406	0.2364

Table 1: Integral properties of investigated boundary layers at various Reynolds numbers

The data in table 1 were obtained by numerical integration of Pitot tube measurements. The shear stress information was obtained from direct slope measurements of hot-wire anemometers. This information was compared with friction factors obtained from Clauser plots (1954) of the mean velocity data and Preston tube measurements using Patel's calibration curve (1965).

The authors' mean velocity measurements are given by Andreopoulos et al. (1983). They yielded no Reynolds number dependence of the sub-layer region when normalized with wall variables. Inside the buffer region and the log region of the normalized velocity distribution, a Reynolds number dependence was observed. The additive constant of the log law fitted to the authors' data slightly decreased with increasing Reynolds number.

Figure 5 shows the Reynolds number dependence of the rms-values of the longitudinal velocity fluctuations. Data are presented in normalized quantities with wall variables as normalizing parameters. Within the sub-layer ($y^+ \leq 5$) no Reynolds number dependence of the rms-values of longitudinal log velocity fluctuations is observed. In the buffer region ($5 \leq y^+ \leq 50$) a strong Reynolds number dependence is observed showing a decrease in magnitude with Reynolds numbers up to approximately $Re_\theta = 10^3$. For higher Reynolds numbers, a universal distribution appears to be reached which extends into the log law region of the flow. It is worth noting that the decrease of the (u'/u_τ) -values with Reynolds number within the buffer region of the flow, is in general agreement with measurements by Laufer (1950), Comte-Bellot (1965) and Zanic (1972) obtained in channel flows.

The skewness and flatness factors of the velocity fluctuations are presented in Fig. 6 and 7. These figures indicate some interesting features of near-wall flows reflected by the shape of the distribution of skewness and flatness factors of the streamwise

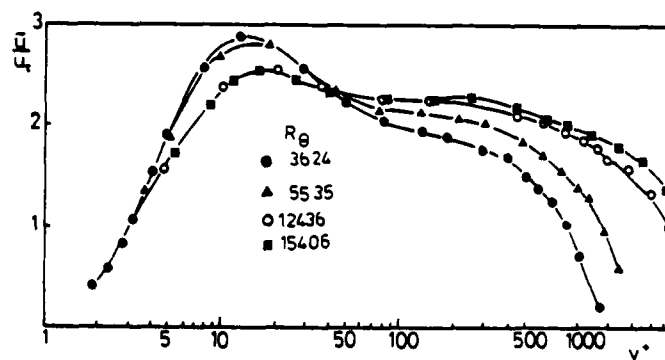


Fig. 5: Non-dimensionalized rms-values of the longitudinal velocity fluctuations

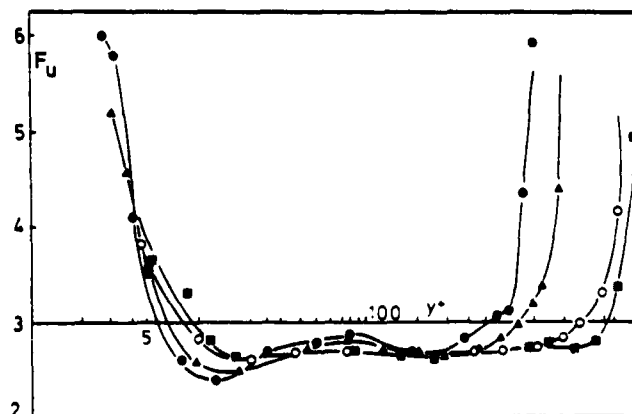


Fig. 6: Distribution of flatness factor of the longitudinal fluctuations. Symbols as in figure 5

velocity components in the viscous sublayer. This information is completed by the skewness factor for the cross velocity component provided in Fig. 8. High values of skewness factors S_{S_V} close to the wall, but with opposite signs, and high values of flatness factors F_U can be related to the intermittent flow structure inside the viscous sublayer. The present measurements of higher order moments are in close agreement with data presented by Gupta and Kaplan (1972) but differ slightly from those of Kreplin and Eckelmann (1979) and even more from those of Kutateladze and Khabakhpasheva (1978). In the region where the log law mean velocity profile holds, all the data show that the skewness and flatness factors are only slightly different to those of Gaussian velocity probability density distributions for both high and low Reynolds number flows.

The difference in the flow structure of low and high Reynolds number boundary layers is illustrated by the differences in the skewness distribution S_V . According to Kline (1967) this quantity is connected to the width of the streak filaments which are produced close to the wall and slowly lift up, and oscillate and finally break up forming the second stage of the so-called bursting process. For low Reynolds number flows, it is well known, see Kline et al. (1967), that the most probable location of this violent break-up process is located around the region of maximum turbulence intensity, e.g. at $y^+ \approx 15$. For the low Reynolds numbers the present data show that $y^+ \approx 15$ the skewness factor changes sign, the flatness factor distribution shows a minimum, and the skewness factor of the normal velocity component reaches its maximum positive value. Fig. 8 shows that for high Reynolds numbers the skewness S_V is not changing signs throughout the entire buffer region. Whether this finding is an indication that the intermittent, coherent flow structures, well documented for boundary layer flows at low Reynolds numbers, e.g. see Willmarth (1977), have disappeared, cannot be deduced from these data but changes in the structure of the flow are likely to occur.

The authors have also carried out measurements of shear stress distribution and other properties of the boundary layers they investigated. These are given by Andreopoulos et al. (1983).

3.2 Conditional Averaged Flow Properties

A considerable amount of experimental work has become available on coherent structures in the close wall region of turbulent boundary layer flows. Qualitative information resulted from various visualization investigations, e.g. see Kline et al. (1967), and more quantitative results from conditionally sampled studies, e.g. see Blackwelder and Kaplan (1976), Wallace et al. (1977) and Zanic (1974). Although these studies have been concerned with low Reynolds number boundary layers and have utilized similar experimental and data acquisition techniques, they have resulted in partially contradicting results as far as the properties of coherent structures in the immediate wall vicinity are concerned. This can be attributed to the experimental difficulties that exist to obtain reliable data in this flow region. Nevertheless, existing results are sufficiently consistent to give a clear physical description of the basic mechanisms of turbulence self-maintenance in the near wall region of a turbulent boundary layer. Information that is missing relates to structural changes with Reynolds number.

There have been a number of different proposals to detect the occurrence of coherent structures in the vicinity of the wall of a turbulent boundary layer, e.g. see Kovaszny (1978). The authors decided to employ for their work the widely accepted, well documented detection technique of Blackwelder and Kaplan (1976) which utilizes the amplitude of the short time averaged, local streamwise fluctuating velocity:

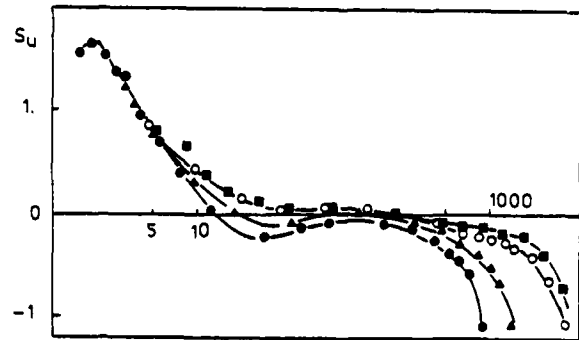


Fig. 7: Distributions of skewness factor of the longitudinal velocity fluctuations. Symbols as in figure 5

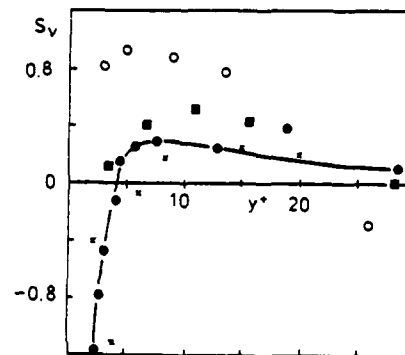


Fig. 8: Distribution of skewness factor of the cross flow velocity fluctuations in the near wall region. Symbols: o, Kutateladze et al. (1978); ■, Kreplin et al. (1979); x, Gupta et al. (1972); ●, present measurements $R_0 = 3624$

$$\hat{u}(t) = \frac{1}{T} \int_{t-T/2}^{t+T/2} u(t) dt$$

which generates the intermittency function characterizing the occurrence of flow structures. The "function" produces a logical one whenever the variants of the above digitally filtered signal, e.g. exceeds a value $K \bar{u}^2$ where K is the so-called threshold parameter and \bar{u}^2 the rms-value of the longitudinal velocity fluctuation. Although this detection scheme has two independent arbitrary parameters, the integration time T and the threshold level K , Blackwelder and Kaplan (1976) have shown that their detected coherent flow events are only a weak function of T and their channel shapes turned out to be independent of the threshold parameter K . Following their findings, the parameter T and K given in Table 2 were chosen for the conditional sampling analysis carried out by the authors.

U_∞ m/s	R_0	U_τ m/s	T^+	K
6.33	3624	0.25	10	1.20
10.89	5535	0.41	11.21	1.05
22.61	12436	0.81	13.12	1.00
28.79	15406	0.99	13.07	1.04

Table 2: Integration time and threshold values used in the conditional sampling techniques

Utilizing the detection schemes characterized in Table 2, the authors obtained conditionally averaged mean velocity values. These are presented by Andreopoulos et al. (1983). In this section, only the data obtained for the distribution of the mean bursting interval are reported. These data are shown in Fig. 9 where non-dimensional values are normalized with inner layer variables. The data show that the most probable location of the detected organized structures in the buffer region i.e. in the region $5 \leq y^+ \leq 50$, where the normalized averaged bursting interval reaches its minimum value. However, a comparison of the data for different Reynolds numbers does not suggest scaling with wall variables to be appropriate. It is worth noting that the data in Fig. 9 are already corrected for the probe size influence utilizing a correction reported by Blackwelder and Haritonidis (1981). Applying probes with small non-dimensional sensor length, Blackwelder and Haritonidis found that the bursting interval scaled with inner rather than outer flow variables. Employing their suggested correction for the wire length influence,

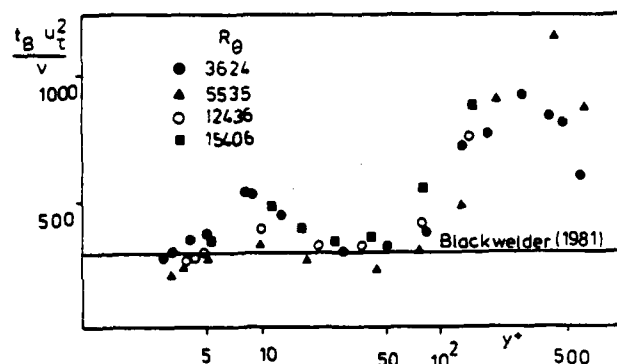


Fig. 9: Distribution of non-dimensional mean bursting interval normalized with inner variables

the authors' data did not yield a unique distribution for all Reynolds numbers.

It must be pointed out that sweeps ($u > 0, v < 0$) have been observed to have larger spanwise length scales than those of ejections and therefore be less affected by spatial averaging. Plotting the same data scaled with outer variables did not result in a single distribution. Many other investigators suggest as possible time scale the geometrical mean between the outer and inner scales, i.e. $[\nu/u_\tau^2 \theta/u_\theta]^{1/2}$

Alfredsson and Johansson (1982) argued that this mixed scale is an estimate of the time scale of small eddies. However, this time scale which is found by Afzal (1982, 1973) to be a scale for the overlapping region between the inner and the intermediate layer in a boundary layer, found to work no better than the inner or outer scalings. The main point of the results plotted in Fig. 9 is the enormous variation of the bursting time intervals across the boundary layer which partly explains the extremely large scatter in the results of various investigations which have been put together and reviewed by Hirata et al. (1982). It is also interesting to mention that the present scheme does not discriminate further the events to sweeps or ejections. Close to the wall where no sweeps are present, the results reasonably agree with those obtained by other investigators and are only weakly dependent on y^+ . Further out, ejections and sweeps are present and the time interval increases and drops again at the edge of the buffer region.

If the accurate determination of the interval bursting depends on the threshold values k , integration time T and on the spanwise length of the probe, the shape of the structures seems to be quite independent of all these factors.

The influence of Reynolds numbers on the shape of the flow structure is most pronounced in the buffer layer and the log law region. This is seen from Figs. 10 and 11 which reveal that the high speed inrush of fast fluid gains in intensity when compared with the injection phase, as the Reynolds number increases. Considering that the skewness factor S is related to the difference between the magnitude of the maximum and minimum value of the velocity inside the detected patterns, see Chen (1974), the results in Figs. 10 and 11 are in agreement with the measurements of the skewness factor of the longitudinal velocity fluctuations.

The detection scheme of Blackwelder and Kaplan (1976) was also applied to the three wire probes which the authors applied to obtain close wall information. Figs. 11 and 12 show the flow patterns deduced from the longitudinal and cross flow velocity fluctuations, respectively. Fig. 13 presents their product indicating which part of the pattern contributes to the production of Reynolds shear stress. The figure shows that the measured contributions are very similar to those reported in the literature.

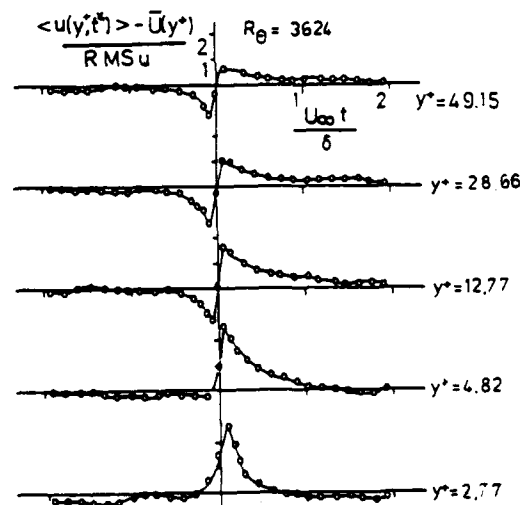


Fig. 10: Conditionally averaged fluid patterns of intermittent events near the wall, $R_\theta = 3624$

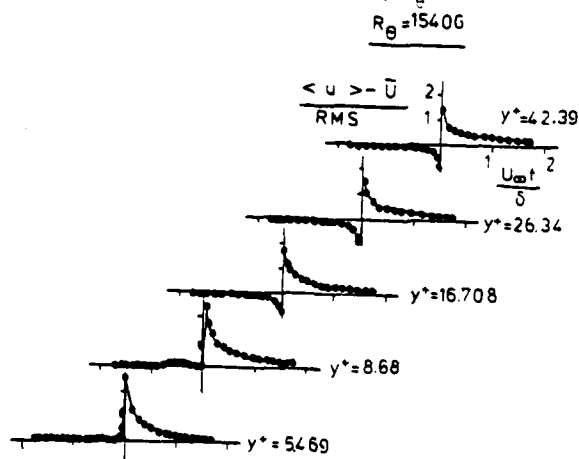


Fig. 10: Conditionally averaged fluid patterns of intermittent events near the wall, $R_\theta = 15406$

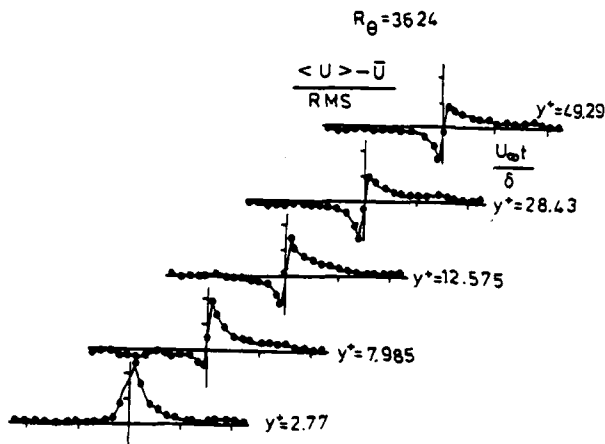


Fig. 11: "Shapes" of conditionally averaged fluid patterns obtained with three-wire probe

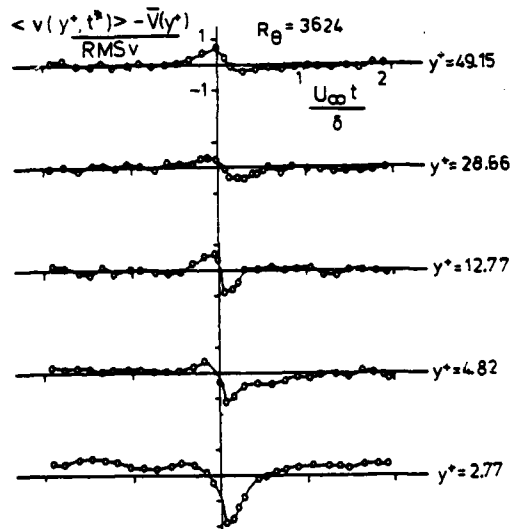


Fig. 12: "Shapes" of conditionally averaged fluid patterns obtained with three-wire probe

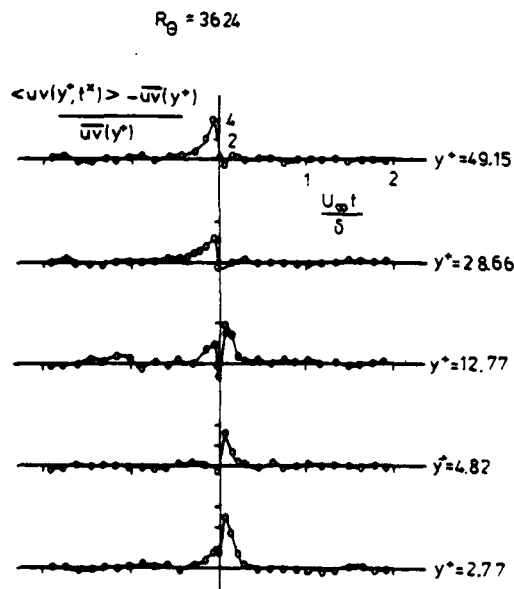


Fig. 13: "Shapes" of conditionally averaged fluid patterns obtained with three-wire probe

4. CONCLUSIONS AND FINAL REMARKS

The near wall region of a zero pressure gradient turbulent boundary layer has been investigated and found that the correlations of the turbulent velocity fluctuations depend on Reynolds numbers up to approximately $R_\theta = 10^4$. Beyond this value, the rms-value of the longitudinal velocity fluctuations approached a level where the Reynolds number dependence becomes negligible.

Based on the detection scheme proposed by Gupta and Kaplan (1972), conditionally sampled measurements have been carried out which have yielded information on flow features that are usually referred to as flow structures. These remained present up to the highest investigated Reynolds number. Although the shapes of the averaged structures change with Reynolds number when scaled with outer variables, the major features of the conditionally averaged signals remain. These reflect the well-known inrush and ejection of the bursting cycle. The simultaneous measurements of the u' and v' components have also permitted to quantify the contributions of the ejections and inrushes to the production of the Reynolds stresses down to $y^* = 2.7$.

For a long time it has been debated whether the mean time between bursts (or events) scales with inner or outer variables. All definitions of the mean time between events contain a good deal of subjectivity. Scaling this mean time interval with inner and outer variables and plotting these data as a function of y^* has not yielded the expected independence of the distributions from Reynolds number. Although existing knowledge on boundary layer flows suggests that this quantity should scale with inner variables, the present data could not confirm this. They indicate, however, that regardless the scaling the mean time between events varies across the boundary layer. It seems plausible that this time interval should be further distinguished as the time between similar events i.e. between inrushing events or ejections and not generally on the time between events.

REFERENCES

- Afzal, N. (1982) "Fully developed turbulent flow in a pipe: An intermediate layer" *Ingenieur-Archiv* 52, 355 - 377.
- Afzal, N. and Jainik, K. (1973), "Analysis of turbulent pipe and channel flows at moderately large Reynolds numbers," *J. Fluid Mech.* 61, 23 - 31.
- Alfredsson, P.H. and Johansson A.V. (1982) "Time scales for turbulent channel flow", *R. Inst. Tech., Stockholm, Rep TRITA-MEK-82-11*.
- Andreopoulos, J. (1980) "Digital techniques and computer programs for hot-wire data processing", *Rpt. SFB 80/ME/181, Universität Karlsruhe*.
- Andreopoulos, J., Durst F., Jovanovic, J. and Zarić, Z. (1983) "Influence of Reynolds number on characteristics of turbulent wall boundary layers", to appear in *Experiments in Fluids*.
- Blackwelder, R.F. and Kaplan, R.E. (1976), "On the wall structure of the turbulent boundary layer", *J. Fluid Mech.* 70, 89 - 112.
- Blackwelder, R.F. and Haritonidis, H.J. (1981), "The bursting frequency in turbulent boundary layers", *Private communication*.
- Bhatia, J.C., Durst, F. and Jovanovic, J. (1982), "Corrections of hot-wire anemometer measurements near walls", *J. Fluid Mech.* 122, 411 - 431.

Bruun, H.H. and Tropea, C. (1979), "The SFB 80 nozzle calibration facility", Rpt SFB 80/M/141, Universität Karlsruhe.

Chen, C.H.P., (1974), "The large scale motion in a turbulent boundary layer: A study using temperature contamination", Ph.D. Dissertation, University of Southern California.

Clauser, F.H. (1954) "Turbulent boundary layers in adverse pressure gradients", J. Aero. Sci. 21, 91.

Comte-Bellot, G. (1965), "Ecoulement turbulent entre deux parois parallèles", Service de documentation scientifique et technique, No. 4101, Paris.

Durst, F. and Ermshaus, R. (1977), "Hot-wire wake sensors for simultaneous two-dimensional velocity measurements", Proceeding of XVII-Congress of IAHR, Baden-Baden, FRG.

Ermshaus, R. and Naudascher, E. (1977), "Der Niedergeschwindigkeitskanal des Instituts für Hydromechanik an der Universität Karlsruhe", Zeitschrift für Weltraumforschung 1, 419 - 425.

Gupta, A.K. and Kaplan, R.E., (1972), "Statistical characteristics of Reynolds stress in a turbulent boundary layer", Phys. Fluids 15, 981 - 985.

Hirata, M., Tanaka, H., Kawamura, H. and Kasagi, N. (1982), "Heat transfer in turbulent flows", 7th International Heat Transfer Conference, München, FRG.

Kline, S.J., (1967), "Observed structure features in turbulent and transitional boundary layers", Fluid mechanics of internal flow, Ed. by Gino Sovran Elsevier Pub. Co.

Kline, S.J., Reynolds, W.C., Schraub, F.A. and Runstadler, W.P., (1967), "The structure of turbulent boundary layers", J. Fluid Mech. 30, 741 - 773.

Kovaszny, L., (1978), "Measurements in intermittent and periodic flow", Proceedings of the Dynamic Flow Conference, Marseille 1978.

Kreplin, H. and Eckelmann, H. (1979), "Behaviour of the three fluctuating velocity components in the wall region of a turbulent channel flow", Phys. Fluids 22, 1233 - 1239.

Kutateladze, S.S. and Khabakhpasheva, E.M. (1978), "Structure of wall boundary layer (forced flow, thermal convection)", Academy of Sciences of the UDSSR, Siberian Branch, Institute of Thermodynamics, Novosibirsk, UDSSR.

Laufer, J., (1950), "Investigation of turbulent flow in a two-dimensional channel", NACA TN2 123.

Patel, V.C. (1965), "Calibration of the Preston tube and limitations on its use in pressure gradients", J. Fluid Mech. 23, 185 - 208.

Wallace, J., Brodkey, S.R. and Eckelmann, H. (1977), "Pattern-recognized structures in bounded turbulent shear flows", J. Fluid Mech. 83, 673 - 693.

Willmarth, W.W., (1977), "Survey on new measurements of turbulence structure near the wall", Phys. Fluids Supplement, Vol.20, No. 10, Part II, 9-21.

Zarić, Z., (1972), "Wall turbulence studies", Advances in Heat Transfer, 8, 285 - 350.

Zarić, Z., (1974), "Etude statistique de la turbulence pariétale", Rep. Boris Kidric Institute, Beograd.

SCRUTINIZING THE k - ϵ -MODEL UNDER ADVERSE PRESSURE GRADIENT CONDITIONS

W. Rodi
University of Karlsruhe,
Karlsruhe, FRG

G. Scheuerer
University of Erlangen-Nürnberg,
Erlangen, FRG.

ABSTRACT

The k - ϵ -model and a one-equation model have been used to predict adverse pressure gradient boundary layers. While the one-equation model gives generally good results, the k - ϵ -model reveals systematic discrepancies, e.g. too high skin friction coefficients, for these relatively simple flows. These shortcomings are examined and it is shown by an analytical analysis for the log-law region that the generation term of the ϵ -equation has to be increased to conform with experimental evidence under adverse pressure gradient conditions. A corresponding modification of the ϵ -equation was employed in the present investigation and resulted in improved predictions. However, for strongly decelerated flows additional tuning of the empirical constants was necessary to obtain satisfactory predictions.

INTRODUCTION

One of the conclusions of the 1980-81 AFOSR-HTTM-Stanford Conference on Complex Turbulent Flows was that the effects of adverse pressure gradients on shear layers were not predicted very well by most turbulence models. This conclusion applies not only to the simple mixing-length approach, but especially to the two-equation and Reynolds-stress-equation models, employing a transport equation for a characteristic turbulence length scale. Indeed it is vexing to see the now widely used k - ϵ -turbulence model to be seriously in error for relatively simple adverse pressure gradient equilibrium boundary layers. The differences between this model and existing data manifest themselves mainly in consistently overpredicted skin friction values and a tendency of the calculated flow to remain attached where experiments indicate already separation. The poor predictions can be traced to the fact that the length scale determined by the ϵ -equation rises steeper near the wall than in the case of zero pressure gradient, while experimental data suggest that the length-scale gradient is virtually independent of the pressure

gradient over a wide range. For this reason, one-equation models using an empirical length-scale specification yield much better predictions for adverse pressure gradient boundary layers than does the k - ϵ -model.

Adverse pressure gradient shear layers are of great practical interest, as they occur on aerofoils, turbomachinery blading or in diffusers. The Evaluation Committee of the Stanford Conference suggested therefore that special attention be focussed on acquiring a higher predictive ability for these flows. In particular, it would be desirable to improve the accuracy of the k - ϵ -model which has been found to work well in a large variety of other flow situations. The purpose of the present paper is to trace in detail the reasons for the poor performance of the k - ϵ -model when applied to decelerated boundary layers and, based upon this knowledge, to modify the model such that it leads to improved predictions for these flows.

A few suggestions for modifying the k - ϵ -model have been published, which aimed at the ϵ -equation. Hanjalic and Launder (1980) pointed out the special role that irrotational straining plays in the spectral transport from the large, energy-containing to the small dissipating eddies. The generation term in the modelled ϵ -equation involves in its most general form both rotational and irrotational strain rates. In order to bring the irrotational part into prominence, Hanjalic and Launder (1980) multiplied this term by a larger empirical coefficient than the rotational term. For decelerated flows, the modification gives rise to larger ϵ -values, thereby reducing the length scale and also the shear stress τ_{puv} . This model has been used in the present investigation. It will be shown to yield a remarkable improvement for moderate pressure gradients but to fail for strong decelerations.

Another modification suggested by Hanjalic and Launder (see Launder, 1982) is to replace the constant C_ϵ in the diffusion term of the ϵ -equation by a function of the ratio of production to dissi-

pation of kinetic energy. According to Launder (1982), however, this modification improves the model calculations only to a minor extent. Launder (1982) further suggested to limit the growth of L by simply increasing the computed values of ϵ to yield $L = 2.5y$ whenever the computed values give rise to larger length scales. This suggestion is certainly a rather crude measure that is not really consistent with the concept of a two-equation model. In summary, none of the model extensions suggested is satisfactory, and the basic failure of the k - ϵ -model to yield the observed universal near-wall length scale gradient also under adverse pressure-gradient conditions still lacks an explanation.

In the present paper, the shortcomings of the k - ϵ -model in adverse pressure-gradient situations are investigated systematically. First, calculations with the one equation turbulence model proposed by Norris and Reynolds (1975) and the low-Reynolds-number version of the k - ϵ -model of Lam and Bremhorst (1981) are compared for two equilibrium adverse pressure-gradient boundary layers. While the one-equation model yielded good overall agreement with the data, the k - ϵ -model reveals the known discrepancies. In order to trace the reasons for these an analytical analysis was carried out for the log-law region which shows that the set of empirical coefficients in the ϵ -equation, which have been determined by reference to zero pressure gradient boundary layers, are not compatible with the experimental observations in decelerated flows. Finally, an improved model is suggested and applied that uses Hanjalic and Launder's (1980) modified ϵ -equation in connection with an algebraic stress model.

MATHEMATICAL MODELS

The mathematical models used in the present investigation employ the usual continuity and momentum equation for two-dimensional shear layers (see e.g. Patel et al, 1983) together with a turbulence model. Calculations have been carried out with the following turbulence models: the standard- k - ϵ -model (Launder and Spalding, 1974), the low-Reynolds-number version of the k - ϵ -model by Lam and Bremhorst (1981), denoted LB, and the one-equation-model given by Norris and Reynolds (1975) and denoted NR. With the standard k - ϵ -model the viscous near wall zone was bridged by wall-functions, see Launder and Spalding (1974), where the velocity at the first grid node is linked to the wall shear stress by the logarithmic law of the wall. For the LB- and NR-model calculations, the no-slip-condition was employed at the wall. In the freestream, the variation of the external velocity inferred from data served as boundary condition.

The Standard- k - ϵ -Model

The k - ϵ -model calculates the shear stress with the eddy viscosity hypothesis in the following way:

$$-\overline{uv} = \nu_t \frac{\partial u}{\partial y}; \quad \nu_t = c_\mu \frac{k^2}{\epsilon} \quad (1)$$

where k is the turbulent kinetic energy, ϵ is its dissipation rate and c_μ is an empirical constant. The local values of k and ϵ are determined from transport equations, which read

$$U \frac{\partial k}{\partial x} + V \frac{\partial k}{\partial y} = \frac{\partial}{\partial y} \left(\frac{\nu_t}{\sigma_k} \frac{\partial k}{\partial y} \right) + P_k - \epsilon \quad (2)$$

$$U \frac{\partial \epsilon}{\partial x} + V \frac{\partial \epsilon}{\partial y} = \frac{\partial}{\partial y} \left(\frac{\nu_t}{\sigma_\epsilon} \frac{\partial \epsilon}{\partial y} \right) + \frac{\epsilon}{K} (c_{\epsilon 1} P_k - c_{\epsilon 2} \epsilon) \quad (3)$$

The term P_k is the production rate of k and is given by

$$P_k = -\overline{uv} \frac{\partial U}{\partial y} - (\overline{u^2} - \overline{v^2}) \frac{\partial U}{\partial x} \quad (4)$$

The second (underlined) term in equation (4) which involves the irrotational strain rate $\partial U / \partial x$ is neglected in the models introduced here but will be needed when an improved model is suggested below. For the empirical constants the values $\{c_\mu, c_{\epsilon 1}, c_{\epsilon 2}, \sigma_k, \sigma_\epsilon\} = \{.09, 1.44, 1.92, 1, 1.3\}$ given for instance by Rodi (1980) have been adopted. As near-wall boundary conditions values of k and ϵ at the first grid node are related to the wall shear stress by assuming local equilibrium in the k -equation, see Launder and Spalding (1974).

The Low-Reynolds-Number k - ϵ -Model (LB)

The low-Reynolds-number version resolves the flow field down to the wall and hence accounts directly for viscous effects. To this end the empirical constants c_μ , $c_{\epsilon 1}$, and $c_{\epsilon 2}$ are multiplied by functions f_μ , f_1 , f_2 which involve the molecular viscosity.² The exact formulae may be found in Rodi et al (1982) and are not repeated here.

The One-Equation-Model (NR)

In the one-equation-model of Norris and Reynolds (1975) the eddy viscosity concept (eqn. 1) is used as well, however with a different function f_ν . This model calculates only the turbulent kinetic energy k from a transport equation, whereas the dissipation rate is now obtained from

$$\epsilon = \frac{k^{3/2}}{L} \left(1 + \frac{c_\epsilon}{k^{1/2} L / \nu} \right) \quad (5)$$

where L is prescribed algebraically in the form of a ramp distribution like in the mixing-length approach

$$L = c_D \min \{ \kappa y, \lambda \delta \} \quad (6)$$

and σ is the boundary layer thickness. The empirical constants c_μ , c_D , c_ϵ , κ , λ have the values .084, .156, 13.2, .41, .085. It should be noted that the same transport equation for k is used as in the LB-two-equation model. In all cases the resulting set of equations is solved with an adapted version of the GENMIX-code described by Spalding (1977). Computational details may be found in Rodi et al (1982).

RESULTS AND DISCUSSION

Comparison of NR- and LB-Predictions

In this section the results obtained with the LB-model and the NR-model are compared for two experimental situations investigated by Andersen et al (1972). The first relates to a zero pressure gradient (ZPG) boundary layer and the second to an equilibrium adverse pressure gradient (APG) boundary layer. In these experiments, the freestream velocity was varied according to the $U \sim x^m$ and the test conditions refer to $m = 0.0$ and $m = -0.20$. At $x = 2.08$ m, where the bulk of the comparison with the calculations was made, momentum-thickness-Reynolds numbers of 2900 and 4100 were achieved, so that viscous effects were negligible to first order.

Fig. 1 shows the computed skin friction coefficients $c_f = 2\tau_w/\rho U_e^2$.

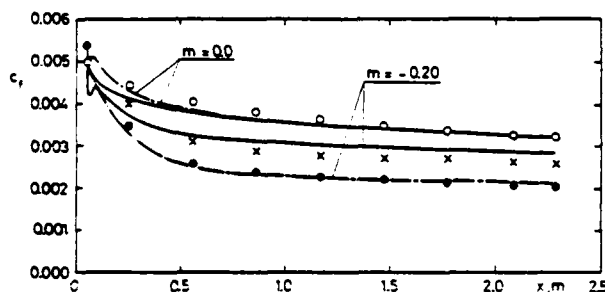


Fig. 1: Comparison of model predictions and experimental c_f -values; data: \circ $m = 0.0$, \bullet $m = -0.20$; predictions: — LB, — NR, x standard k- ϵ -model

In the ZPG-case the LB- and NR-model produce almost identical c_f -values which are in excellent agreement with the data, at least for $x > 1.5$ m. While the NR-model simulates the influence of the adverse pressure gradient on c_f satisfactorily, the LB-model yields markedly too high c_f -values for this case. At the last measurement station the differences amount to 40%, which is clearly unacceptable for boundary layer calculations. To shed some light on this behaviour Fig. 2 compares the computed velocity profiles with the data at $x = 2.08$ m. The NR-model gives an

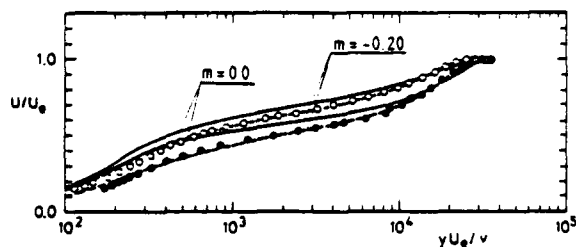


Fig. 2: Mean velocity profiles at $x = 2.08$ m; key as for Fig. 1

excellent representation of the velocity distribution for both, the ZPG and APG case. For the ZPG-case the LB-model overpredicts the velocities somewhat especially in the near wall region ($y^* = yU_e/\nu < 1000$)

somewhat, but still gives the correct c_f -values. For the APG condition the discrepancies become more severe: the k- ϵ -model predictions do not respond sufficiently to the deceleration in the viscous near wall zone and display too rapid an increase of the velocity, which is almost as strong as for the ZPG-flow. This increase in the near-wall region leads to an overprediction of the velocity in the log-law and outer part of the boundary layer.

The corresponding shear stress distributions are presented in Fig. 3 which shows clearly that the poor performance of the k- ϵ -model is caused by an overprediction of the shear stress. While both tur-

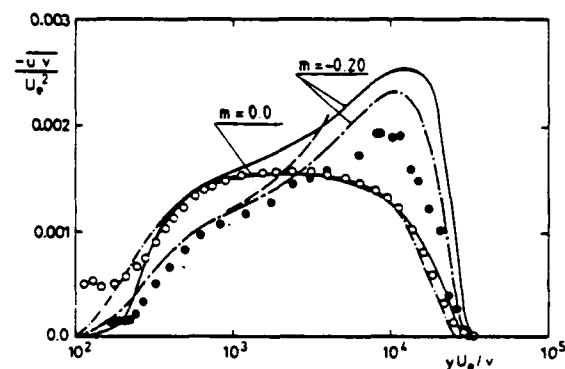


Fig. 3: Shear stress profiles at $x = 2.08$ m; key as for Fig. 1.

bulence models yield shear stress profiles in very good agreement with the data for the ZPG-flow, differences become apparent for the decelerated flow. Again it is the one-equation model which gives a very good representation of the shear stress distribution near the wall and overpredicts the shear-stress peak in the outer zone only slightly. The discrepancies displayed by the two-equation model are more important: this shows virtually no response to the pressure gradient in the immediate vicinity of the wall ($y^* < 1000$) and produces a steep increase of the shear stress. Accordingly, the measured data are considerably overpredicted in this region and the high level is maintained further outwards in the boundary layer. However, the predicted slope $\partial \overline{uv} / \partial y$ (which in fact enters the momentum equation) is similar to the measured one. Fig. 3 also shows \overline{uv} according to equation (7)

$$\frac{-\overline{uv}}{U_e^2} = \frac{c_f}{2} - Ky^* - \frac{c_f}{2} \frac{1}{Ky^*} \quad (7)$$

which may be derived from the momentum equation upon neglect of the convective terms. The acceleration parameter K is defined as $K = \nu dU/dx/U^2$. Relation (7) can be seen to provide a fair approximation to the data in the log-law region.

According to equation (1) the shear stress $-\rho \overline{uv}$ in the k- ϵ -model is calculated from the turbulent kinetic energy k , its dissipation rate ϵ and the local velocity gradient $\partial U/\partial y$; it is therefore interesting to see how these quantities are influenced by the pressure gradient. The non-dimensionalized velocity gradient is plotted in Fig. 4. At the wall this quan-

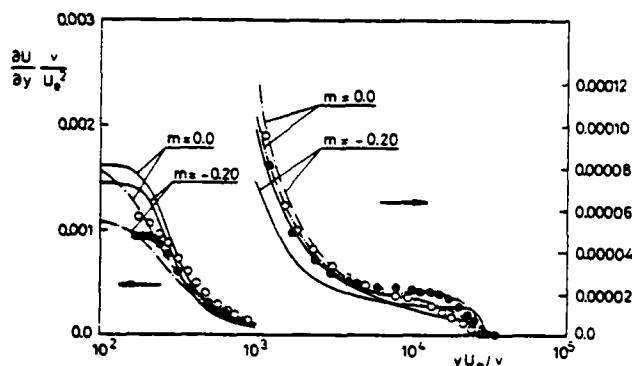


Fig. 4: Velocity gradients at $x = 2.08$ m; key as for Fig. 1.

tity reduces to $c_s/2$ and the c_s -behaviour is therefore reflected directly in the near wall zone, i.e. the one-equation model shows a stronger response to the deceleration. Further away from the wall the computed and also the measured gradients become similar in magnitude for both ZPG and APG cases and reveal the typical y^+ -behaviour. It is important to note that, except very close to the wall the gradients predicted with the k - ϵ -model are smaller than those obtained with the NR-model so that they cannot be responsible for the overprediction of the shear stress.

The predicted profiles of the turbulent kinetic energy k are compared with the data in Fig. 5. The distributions for

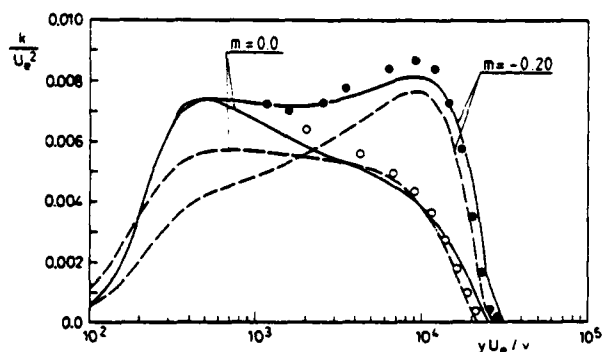


Fig. 5: Turbulent kinetic energy at $x = 1.78$ m; key as for Fig. 1.

ZPG-flow are discussed first. The calculations with the LB- and NR-model agree only in the log-law and outer part ($y^+ > 3000$) of the boundary layer and reproduce the data quite well in this region. Near the wall, however, the computed profiles differ considerably. Due to probe limitations there are unfortunately no measurements available in this region. The calculations presented by Patel et al (1983) show however, that the LB-model predictions fit very well existing data in the peak-region ($y^+ \approx 500$) while the one-equation model gives clearly too low k -values. Therefore, the two-equation model mimics reality better for the ZPG-flow. When an adverse pressure gradient is applied, this model produces an almost identical near wall increase and displays a reaction only beyond

$y^+ = 800$. On the other hand, the NR-one-equation model yields a distinctly different behaviour for the two pressure gradient conditions insofar as it gives a much slower rise in the vicinity of the wall for the APG-case. In the log-law region the existing data are better fitted by the k - ϵ -model, while in the outer zone both models produce similar k -distributions in good agreement with the data. It appears therefore that the main differences between the two models and also discrepancies with the data originate from the region very close to the wall ($y^+ \approx 1000$). The fact that the NR-model predicts a reduction of k in this region under the influence of an adverse pressure gradient, while the LB-model does not, can be explained by the relative change of production of k , P_k , and dissipation ϵ . Figs. 6 and 8 below, will show that in the NR-calculations, P_k is reduced more than ϵ by the deceleration while both are reduced by approximately the same amount in the LB-calculations.

The third quantity that determines the shear stress in the k - ϵ -model is the dissipation rate ϵ . Its variation with wall distance is depicted in Fig. 6. The

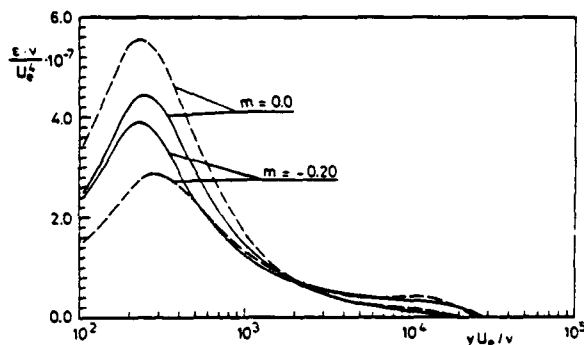


Fig. 6: Dissipation rate of turbulent kinetic energy at $x = 1.78$ m, key as for Fig. 1.

first feature to notice is that for the ZPG-case the LB- and NR-models yield similar shapes but substantially different peak-values for the ϵ -profiles. It has been demonstrated by Patel et al (1983) that it is again the two-equation model that simulates existing data better. In the log-law region, both curves behave similar. For the decelerated flow both models yield a reduction in ϵ . It may seem somewhat surprising that this reduction is much stronger in the case of the one-equation model as one might expect that this would lead to an increase of the shear stress (according to eqn. (1)), which is not the case (see Fig. 3). In fact UV actually decreases because the fall in ϵ is more than offset by the parallel decrease of k shown in Fig. 5.

A more instructive picture emerges when k and ϵ are combined to yield the length-scale $L = k^{3/2} / \epsilon$, whose distribution is plotted in Fig. 7. For the one-

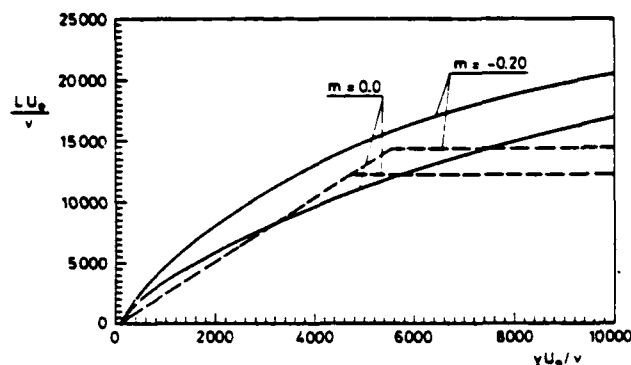


Fig. 7: Turbulence length scales at $x = 2.08$ m; key as for Fig. 1.

equation model the near-wall distribution is prescribed independently of the pressure gradient and is given by eqn. (6). In the most important near-wall and log-law regions this variation is reproduced to a good approximation by the k - ϵ -model for the ZPG-case. In the APG-case a steeper increase of the length scale results, which is mainly caused by the fact that too high k -levels persist near the wall.

As was mentioned already, the high k -values are due to the dissipation rate ϵ being too small relative to the production P_k shown in Fig. 8, and this may be traced

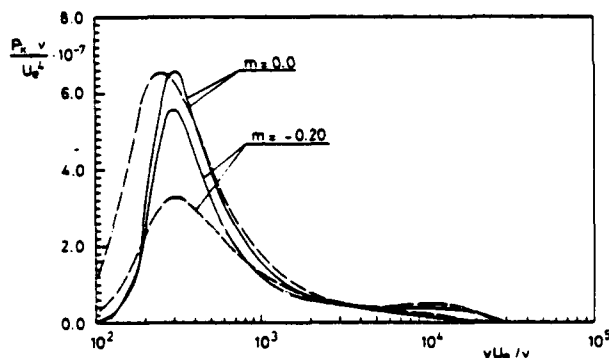


Fig. 8: Production rates of turbulent kinetic energy k at $x = 2.08$ m; key as for Fig. 1.

to the production of ϵ being too small. The word "relative" is very important here for, as can be seen from Fig. 6, the ϵ -values predicted by the LB-model are actually larger than those resulting from the NR-model (for the APG-flow). In any case, an increase in ϵ would directly reduce \overline{uv} and L via eqn. (1) but what is much more important, would reduce also k and hence again \overline{uv} and L . Further, according to eqn. (4), P_k would decrease which would also act to reduce k and finally \overline{uv} . Due to the strong interlinkage and feedback, a relatively small increase in the production of ϵ can have a significant effect on the predictions.

Analysis

The results presented above have clearly demonstrated that the poor performance of the k - ϵ -model under APG-conditions

can be traced to the ϵ -equation. It will now be shown by an analytical analysis for the log-law region that the empirical coefficients used in this equation are not really compatible with experimental observations in decelerated flows. In order that the k - ϵ -model is consistent for ZPG-flow the constants in the ϵ -equation must satisfy the following condition:

$$c_{\epsilon 1} = c_{\epsilon 2} - \frac{\kappa^2}{\sigma_{\epsilon} \sqrt{c_u}} \quad (8)$$

To obtain this relation from the ϵ -equation (3) the following assumptions have been invoked: i) the convection of ϵ is negligible, ii) the local shear stress $-\overline{uv}$ is approximately equal to u_1^2 , iii) the production of k balances the dissipation rate and iv) the logarithmic law of the wall applies. A corresponding relation is now derived for APG-flows. Assumption i) is kept, while the shear stress is now approximated by equation (7) which involves an explicit dependence on the pressure gradient. Experiments have shown that the logarithmic law of the wall prevails even under APG-conditions, so that the log-law is retained to describe the variation of U . The final assumption is that the near-wall length scale is independent of the pressure gradient and is described (as in the one-equation model) by

$$L = \frac{\kappa}{c_L} y \quad (9)$$

For $c_L = 0.09$ and $\kappa = 0.41$ this yields the experimentally observed variation $L = 2.5y$. When these conditions are inserted into the ϵ -equation and k is eliminated via a structural coefficient

$$a_1 = \frac{-\overline{uv}}{k} = c_L^{1/2}$$

independent of the pressure gradient (as found experimentally by Bradshaw, 1967) the following relation results:

$$c_{\epsilon 1} = c_{\epsilon 2} \left[\frac{-\overline{uv}}{u_1^2} - \frac{\kappa^2}{\sigma_{\epsilon} c_L^{1/2}} + \frac{\kappa^2}{\sigma_{\epsilon} c_L^{1/2}} \right] \quad (10)$$

$$\left[\frac{3}{2} \frac{dP/dx}{-\overline{uv}/y} - \frac{3}{4} \frac{(dP/dx)}{(-\overline{uv}/y)} \right]$$

The variation of the shear stress $-\overline{uv}$ in the log-law region is given by eqn. (7). From this it can be seen that $-\overline{uv}/u_1^2$ rises (above unity) with increasing adverse pressure gradient so that $c_{\epsilon 1}$ also has to be increased in order that the ϵ -equation be consistent with experimental observations entering the derivation of (10). The bracketed term in (10) has a similar, but smaller effect on $c_{\epsilon 1}$. In the calculations presented above, $c_{\epsilon 1}$ as determined from the ZPG-formula (8) was used, and hence it is not surprising that the APG observations were not recovered.

Test of Model Improvements

From the preceding two subsections two features become obvious: The first is that the disagreement with the data for APG-flows originates mainly from the viscous near wall region. Computations were therefore carried out also with the standard k - ϵ -model in which this region is bridged by wall functions. The second feature, which may be delineated from the

preceding discussion is that an increase in the generation rate of ϵ may lead to a better simulation of APG-boundary layers. As the direct application of eqn. (10) did not prove successful for this purpose, calculations were carried out with the model of Hanjalic and Launder (1980). In this model the irrotational contribution to the production P is retained (underlined term in eqn. (4)), but in the ϵ -equation this contribution is multiplied with a constant $c_{\epsilon 3}$ instead of $c_{\epsilon 1}$ multiplying the rotational part. The modified ϵ -equation reads

$$\begin{aligned} U \frac{\partial \epsilon}{\partial x} + V \frac{\partial \epsilon}{\partial y} &= \frac{\partial}{\partial y} \left(\frac{\nu_t}{\sigma_\epsilon} \frac{\partial \epsilon}{\partial y} \right) - c_{\epsilon 1} \frac{\epsilon}{k} \overline{uv} \frac{\partial U}{\partial y} - \\ &- c_{\epsilon 3} (\overline{u^2} - \overline{v^2}) \frac{\partial U}{\partial x} - c_{\epsilon 2} \frac{\epsilon^2}{k} \end{aligned} \quad (11)$$

The empirical constant $c_{\epsilon 3}$ was given the value 4.44. For decelerated flows both production terms are positive and enhance the values of k and ϵ respectively, the latter having the desired effect. Due to the relatively large value of $c_{\epsilon 3}$ (compared with $c_{\epsilon 1} = 1.44$), the modified k - ϵ -model becomes much more sensitive to deceleration than the standard model. As the k - ϵ -model does not provide values of $\overline{u^2}$ and $\overline{v^2}$ explicitly, Hanjalic and Launder (1980) suggested to relate these quantities empirically to the turbulent kinetic energy via $(\overline{u^2} - \overline{v^2}) = 0.33 k$. In the present investigation a more refined approach was also examined in which $\overline{u^2}$ and $\overline{v^2}$ were calculated from an algebraic stress model (ASM). In the ASM the convective and diffusive transport of $\overline{u^2}$ and $\overline{v^2}$ is set proportional to the transport of k which is nothing but $P_k - \epsilon$. With this assumption modelled Reynolds-stress equations were simplified to algebraic relations for the normal stresses $\overline{u^2}$ and $\overline{v^2}$ which depend on the ratio P_k/ϵ and the wall distance. The actual ASM-expressions are given in Rodi and Scheuerer (1982).

The three models just described were first applied to the moderately decelerated flow used previously as test case (experiments of Andersen et al, 1972). Relative to the LB-prediction the standard k - ϵ -model gives already an improved prediction of c_f (see Fig. 1). This is achieved by the fact that at least at one point in the logarithmic zone (where the wall functions are specified), the velocity is forced to have the "correct" value. However, there is still substantial disagreement with the data. The Hanjalic-Launder-model on the other hand yielded very good agreement with the data and the resulting c_f -variation coincides with the NR-curve in Fig. 1. This is true for both versions of this model, i.e. the one with constant structural coefficients $\overline{u^2}/k$ and $\overline{v^2}/k$ and the other one involving the ASM expression.

A different picture evolved for a case with stronger deceleration (experiments of East et al, 1979), in which the flow was on the verge of separation. The c_f -values obtained for this test case are depicted in Fig. 9. The LB-model produces

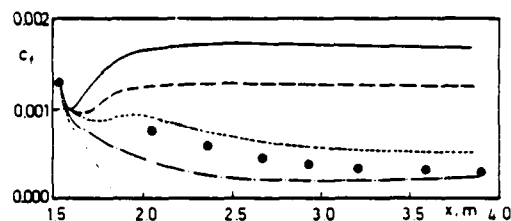


Fig. 9: Skin friction coefficient for the experiments by East et al (1979); data: \bullet ; predictions: — LB, — NR, --- standard k - ϵ , Hanjalic-Launder model, -.-.- Hanjalic-Launder model with ASM.

completely unacceptable c_f -values and the standard k - ϵ -model using wall functions leads to only minor improvements. An acceptable overall agreement is obtained with the NR-model. It is surprising, however, that the Hanjalic-Launder-model, which worked satisfactorily for the Andersen-flow, predicts for this case separation shortly after the start of the computation. This can be traced to the fact that for highly retarded flows velocity gradient $\partial U/\partial x$ becomes very large in the outer region of the boundary layer, so that too much ϵ is produced by the irrotational term in the equation. The high ϵ -values created in this way, reduce the shear stress so much that the flow cannot remain attached and displays the behaviour shown in Fig. 9. The use of the ASM gave only a slightly better prediction, insofar as the point of separation moved further downstream. This is related to the feature that the difference $(\overline{u^2} - \overline{v^2})$ as predicted by the ASM approaches zero faster than k which is used in the original Hanjalic-Launder model. A reasonable simulation of the experimental data could be obtained only when the value of the empirical coefficient $c_{\epsilon 3}$ was reduced to 2.5. The curve resulting from such a calculation is shown in Fig. 9. It should be added that this change in $c_{\epsilon 3}$ had only negligible effect on the predictions for the experiment of Andersen et al (1972).

CONCLUSION

The present investigation allows the following conclusions. The k - ϵ -turbulence model gives consistently too high c_f -values when applied to decelerated boundary layers. It was shown that this originates from too steep an increase of the turbulent kinetic energy k and consequently the shear stress $-\overline{uv}$ near the wall. This steep increase is caused by ϵ -values which are too small relative to the production rate of k and contribute therefore directly via the eddy viscosity relation and indirectly via the resulting higher k -values to the described behaviour. An analytical treatment has shown that an enhancement of the ϵ -generation in adverse pressure gradient situations is necessary in order to correct this feature. A modification of the ϵ -equation to this effect, proposed by Hanjalic and Launder (1980), was employed and refined by combining it with an algebraic stress model. It yielded good predictions for moderately decelerat-

ed flows. However, situations with strong adverse pressure gradients could only be simulated by adjusting one empirical constant ($c_{\epsilon_3} = 2.5$). This modified two-equation model yielded good results for the fairly wide range of deceleration investigated. Finally, the one-equation model used for comparison purposes produced excellent results for all test cases.

ACKNOWLEDGEMENTS

The authors are grateful to Miss A. Messner for her expert typing of the manuscript. The calculations were performed at the RRZE Erlangen.

BIBLIOGRAPHY

Andersen, P.S., Kays, W.M., Moffat, R.J., 1972, "The Turbulent Boundary Layer on a Porous Plate: An Experimental Study of the Fluid Mechanics for Adverse Free-Stream Pressure Gradients", Rept.-No. HMT-15, Stanford Univ., Dept. Mech. Eng., Thermosc. Div., Stanford, CA.

Bradshaw, P., 1967, "The Turbulence Structure of Equilibrium Boundary Layers" J. Fluid Mech., 29, 625.

East, L.F., Sawyer, W.G., Nash, C.R., 1979, "An Investigation of the Structure of Equilibrium Turbulent Boundary Layers", Techn. Report 79040, RAE, Farnborough.

Hanjalic, K., Launder, B.E., 1980, "Sensitizing the Dissipation Equation to Irrotational Strains", J. Fluids Eng., 102, 34.

Lam, C.K.G., Bremhorst, K.A., 1981, "Modified Form of the $k-\epsilon$ Model for Predicting Wall Turbulence", J. Fluids Eng., 103, 456.

Launder, B.E., 1982, "Second Moment Closure: Methodology and Practice", Ecole d'Eté d'Analyse Numérique - Modélisation Numérique de la Turbulence, Clamart, France.

Launder, B.E., Spalding, D.B., 1974, "The Numerical Computation of Turbulent Flow", Comp. Meth. in Appl. Mech. and Eng., 3, 269.

Norris, L.H., Reynolds, W.C., 1975, "Turbulent Channel Flow with a Moving Wavy Boundary", Rept.-No. FM-10, Stanford Univ., Dept. Mech. Eng., Stanford, CA.

Patel, V.C., Rodi, W., Scheuerer, G., 1983, "Evaluation of Turbulence Models for Near-Wall and Low-Reynolds Number Flows", subm. to AIAA-J.

Rodi, W., 1980, "Turbulence Models and their Application in Hydraulics", International Association for Hydraulic Research Publ.

Rodi, W., Celik, I., Demuren, A.O., Scheuerer, G., Shirani, I., Leschziner, M.A., Rastogi, A.K., 1982, Proc., 1980-81 AFOSR-HTTM-Stanford Conference on Complex Turbulent Flows, ed. S.J. Kline, B.J. Cantwell, G.M. Lilley, Vol. III, 1495.

Rodi, W., Scheuerer, G., 1982, "Calculation of Curved Shear Layers with Two-Equation Models of Turbulence", Rept. SFB 80/T/211, Univ. Karlsruhe.

THE BEHAVIOUR OF A COMPRESSIBLE TURBULENT BOUNDARY LAYER UNDER INCIPIENT SEPARATION CONDITIONS

K. C. Muck and A. J. Smits
Gas Dynamics Laboratory,
Mechanical and Aerospace Engineering Department
Princeton University
Princeton, NJ 08544

ABSTRACT

This paper presents an experimental study of a turbulent boundary-layer/shock-wave interaction. The interaction was generated by a two-dimensional compression corner, and the flow was on the point of separating. Measurements were made using both normal and inclined hot wires, and the data include measurements of the longitudinal mass-flow fluctuation intensity and the mass-weighted Reynolds shear stress.

INTRODUCTION

When a shock wave interacts with a turbulent boundary layer, the boundary layer properties experience a sudden, severe perturbation. The resulting distortion of the mean flow properties has been clearly documented, and considerable data appear to be available (see, for instance Fernholz and Finley, 1977). In contrast, direct measurements of the turbulent stresses are still rather scarce and sometimes of dubious quality (see, for example Fernholz and Finley, 1981). Nevertheless, high quality turbulence measurements in a wide range of interactions are urgently required; calculation methods for shock-wave/boundary-layer interactions have generally not performed well, and only if accurate and extensive turbulence data become available will better turbulence models be developed.

At the Gas Dynamics Laboratory at Princeton University, we hope to fulfill partially this need by studying the behaviour of turbulence in a range of compression corner flows. The corners are two-dimensional, and the flows range from fully attached to fully-separated. The mean flow behaviour was extensively documented by Settles (1975) and Settles et al (1979), and, using these results, four corner angles were selected for detailed turbulence measurements: 8° , 16° , 20° , and 24° .

In the current contribution, we present measurements in the 16° corner interaction, which, at a freestream Mach number of 2.87 corresponds to incipient separation (Settles et al, 1976). The measurements were made using hot wire anemometry, and both normal and inclined wires were used. The data therefore include longitudinal mass-flow fluctuations $(\rho u)^{1/2}$ as well as measurements of the mass-weighted Reynolds shear stress $(\rho u)^{1/2} v'$. To gain further insight into the turbulence structure, the longitudinal velocity fluctuation intensity, u'^2 , and the correlation $u'v'$ were deduced using Morkovin's "Strong Reynolds Analogy."

We begin by describing the apparatus and experimental conditions, and follow this with a presentation and discussion of the results. A summary of the conclusions is given in the final section.

This work was supported by NASA Headquarters under Grant NAGW-240, monitored by Drs. Clint Brown and Gary Hicks.

APPARATUS AND EXPERIMENTAL TECHNIQUES

The wind tunnel

The experiment was performed in the Princeton University high Reynolds number 20 cm x 20 cm supersonic blow-down tunnel (see Fig. 1). The tunnel was operated at a stagnation pressure of $6.9 \times 10^5 \text{ N/m}^2$, the wall conditions were near adiabatic and the freestream rms mass-flow turbulence level was about 1%. The upstream boundary layer developed in a region of essentially zero pressure gradient along the tunnel floor. Immediately prior to the interaction, the boundary layer thickness was about 28 mm and the Reynolds number based on the momentum thickness was approximately 77,600 (see Table 1).

The test model

The test model was a two-dimensional ramp with a corner angle of 16° . The width was 15.24 cm, and side fences were installed to isolate the corner flow from the tunnel wall boundary layers (see Fig. 1). The measurement stations are shown in Fig. 2.

Hot-wire anemometry

A DISA 55M 10 constant-temperature anemometer was used for the turbulence measurements. In an effort to improve the quality of these measurements, the authors recently undertook a critical study of hot-wire techniques in supersonic flows (Smits et al, 1983, and Smits and Muck, 1983) which resulted in a substantial improvement in both normal and inclined wire measurement accuracy.

The probes were constructed using 50 μm diameter tungsten wire with an active length of $0.8 \sim 1.0 \text{ mm}$, and they were operated at overheats of $1.0 \sim 1.3$. At these high overheat ratios, the contribution due to the temperature fluctuations was small and it was therefore neglected. For the incoming boundary layer the uncertainties in $(\rho u)^{1/2}/(\rho u)^{1/2}_{\text{ref}}$ were -10% to $+19\%$, and for $(\rho u)^{1/2} v'/(\rho u^2)_{\text{ref}}$

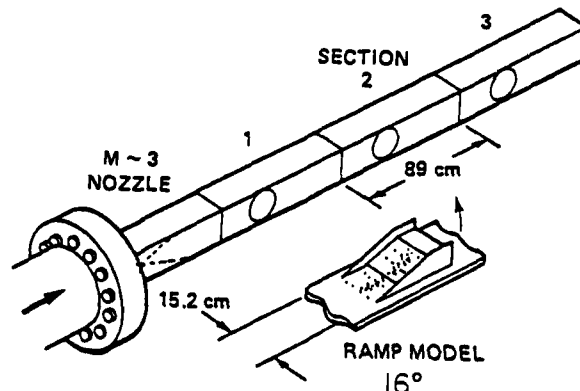


Figure 1. Sketch of the 20 x 20 cm high Reynolds number channel and test model installation.

these were -32% to $+21\%$ (see Smits et al, 1983, and Smits and Muck, 1983). In addition, these estimates may be used as an indication of the measurement accuracy downstream of the interaction. It is important to note, however, that the results are only reliable where the local normal Mach number exceeds 1.2 since the calibration was not extended into the transonic regime. This restriction applies in particular to the inclined wire measurements, and it may explain why the Reynolds shear stress levels in a supersonic boundary layer are often suspiciously low near the wall.

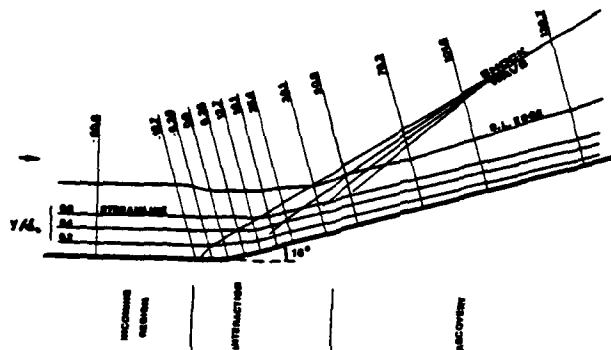


Figure 2. The 16° two-dimensional compression corner flow field with indicated locations of the measuring stations. All dimensional units are in mm.

RESULTS AND DISCUSSION

Mean flow

The properties of the incoming boundary layer at a position -51 mm upstream of the corner are summarized in Table 1. A shadowgram of the interaction region is given in Fig. 3, and the distributions of static pressure and skin friction coefficient are shown in Fig. 4.

The pressure distribution indicates a considerable upstream influence. As measurements by Dolling and Murphy (1983) in a similar configuration suggest, this upstream influence is actually caused by large, low frequency oscillations in the shock location. This observation may have important consequences for the interpretation of the turbulence behaviour.

Downstream of the corner the pressure gradient decreases, and the pressure eventually reaches the inviscid level, as expected. There is no evidence of flow three-dimensionality, and the surface streak patterns observed by Settles (1975) did not reveal the presence of any longitudinal Taylor-Görtler-like vortices. (These vortices are commonly observed in subsonic boundary layers under the action of concave streamline curvature.)

The skin friction coefficient indicates that the separation zone, if it exists, is extremely small. Downstream of the corner the skin friction coefficient increases rapidly; this increase continues even after the pressure gradient has fallen to zero, and the level actually overshoots the equilibrium value (shown on the right-hand-side of Fig. 4b).



Figure 3. Shadowgram of the shock wave/boundary layer interaction.

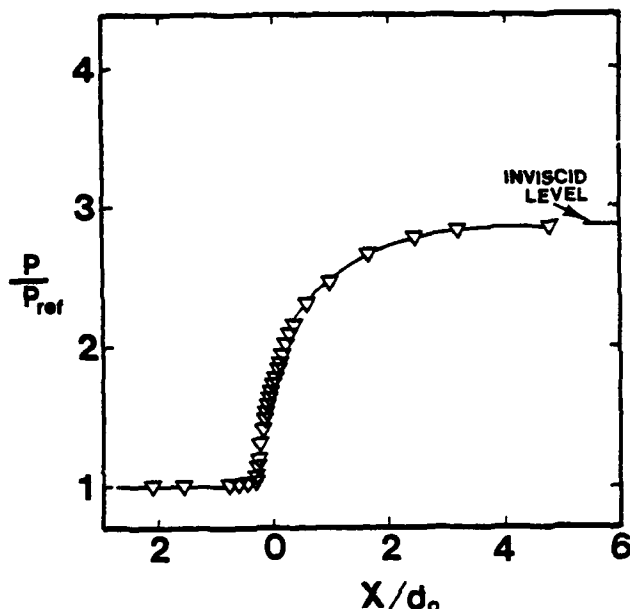


Figure 4(a). Surface pressure distribution (from Settles et al, 1979).

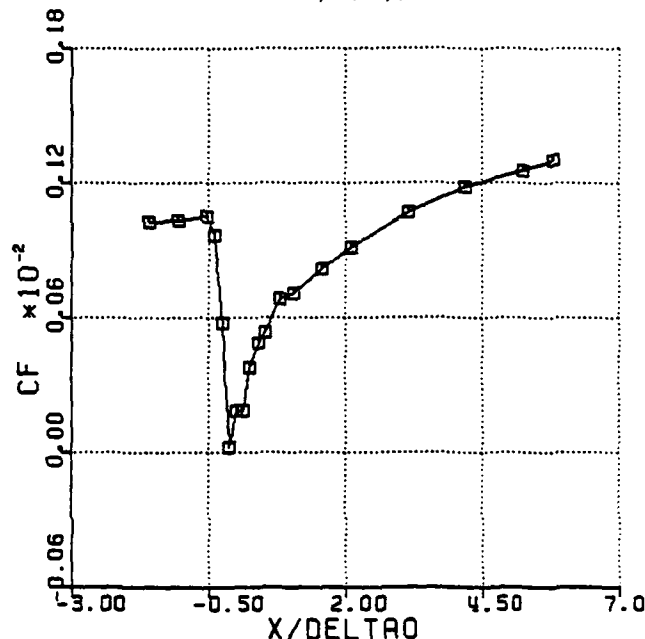


Figure 4(b). Distribution of the local skin-friction coefficient (from Settles et al, 1979).

Turbulence measurements

Normal wire results. The rms mass-flow fluctuation level $\langle (ou)' \rangle$ is shown in Fig. 5. The freestream mass flow rate $(\rho U)_{ref}$ and the upstream boundary layer thickness δ_0 were used to non-dimensionalize the results, and these scales were chosen simply because it is not clear what scaling variables are appropriate within the interaction region. Figure 5 therefore presents information on the behaviour of the absolute mass-flow fluctuation level. Where applicable, the point at which the local normal Mach number equals 1.2 is shown in the figure; note that measurements below this point must be treated cautiously.

The most obvious feature of the turbulence behavior is the large increase in the level of $\langle (ou)' \rangle$. The initial rise occurs as the flow passes through the interaction zone and results in a doubling of the turbulence level, but what is in some ways more surprising is the continued rise of $\langle (ou)' \rangle$ within the "recovery" zone. At the furthest downstream station, the peak value of

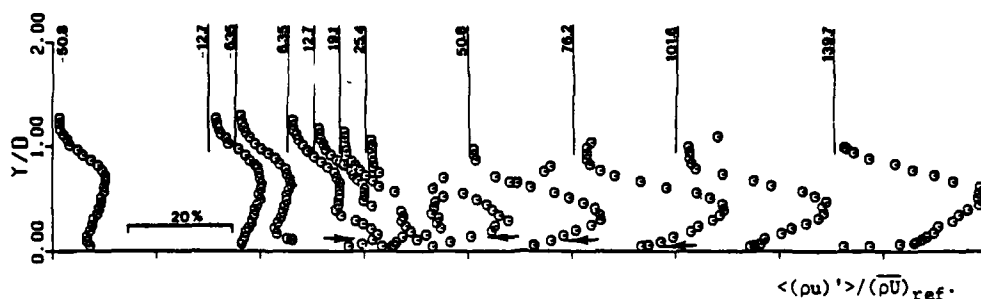


Figure 5. Profiles of the rms longitudinal mass flow fluctuations $\langle \rho u \rangle' / \langle \rho u \rangle_{ref}$.

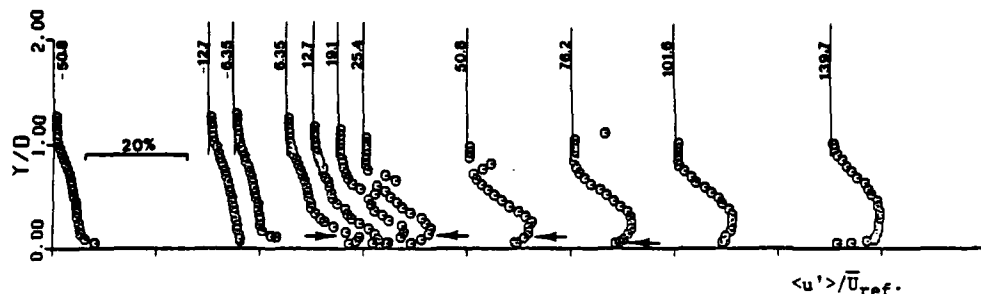


Figure 6. Profiles of the rms longitudinal velocity fluctuation $\langle u \rangle' / \bar{u}_{ref}$.

$\langle \rho u \rangle'$ actually reaches a level 2.8 times the upstream value. A similar, but smaller amplification was observed in the 8° corner flow (Hayakawa et al, 1982).

To investigate the approximate behavior of the rms velocity fluctuation intensity $\langle u \rangle'$, we assumed that Morkovin's (1962) "Strong Reynolds Analogy" could be applied in this flow. In other words, we assumed that,

$$\sqrt{\frac{\rho'^2}{\rho}} = (\gamma-1) M_a^2 \sqrt{\frac{u'^2}{\bar{u}^2}}$$

Thus,

$$\frac{\overline{u'^2}}{\bar{u}_{ref}^2} = \frac{\overline{\rho'^2}}{\bar{\rho}_{ref}^2} \frac{\overline{u'^2}}{\bar{u}_{ref}^2} \left\{ 1 + 2R_{ou}(\gamma-1) M_a^2 + [(\gamma-1) M_a^2]^2 \right\}^{-1}$$

where

$$R_{ou} = \frac{\overline{\rho'^2}}{\bar{\rho}_{ref}^2} \frac{\overline{u'^2}}{\bar{u}_{ref}^2}$$

R_{ou} was taken to be a constant across the boundary layer and equal to 0.8 (Dussauge and Gaviglio, 1981). Although these assumptions are always somewhat questionable in highly disturbed flows, even approximate information regarding the velocity fluctuations is valuable. The results are shown in Fig. 6.

The initial behavior of $\langle u \rangle'$ is broadly similar to the behavior of $\langle \rho u \rangle'$ in that there is a sudden increase in $\langle u \rangle'$ within the interaction zone. Downstream, in contrast to the increase observed in $\langle \rho u \rangle'$, the level of $\langle u \rangle'$ reaches a plateau and eventually begins to decrease.

Inclined wire results. The mass weighted Reynolds shear stress $\overline{(\rho u)'v'} / (\overline{\rho u^2})_{ref}$ is shown in Fig. 7. Before discussing these results, the accuracy and limitation of the hot-wire technique should be considered.

It is becoming increasingly clear that one of the major limitations on using inclined hot-wires in low Mach number supersonic flows is the requirement that the instantaneous normal Mach number should be greater than 1.2 (Smits and Muck, 1982). Within the transonic range,

the hot-wire behavior changes drastically, and a sharp fall-off occurs in the inferred turbulence intensity. For this reason, results for which the normal Mach number is below 1.2 are expected to be in error and should be used cautiously. It should be noted that it is possible, with due caution, to use the shear stress at the wall as a guide for interpreting the results near the surface.

Consider now the results shown in Fig. 7. The behavior of $\overline{(\rho u)'v'}$ is obviously rather different from that displayed by $\overline{(\rho u)^2}$. In passing through the interaction region, $\overline{(\rho u)'v'}$ increases by as much as 16 times, whereas $\overline{(\rho u)^2}$ increases by less than 10 times over the same distance. In additional contrast, $\overline{(\rho u)'v'}$ decreases significantly further downstream.

To determine the behavior of the turbulent shear stress $\tau = \overline{\rho u'v'}$, we again assumed that the "Strong Reynolds Analogy" could be applied. That is,

$$\tau / \tau_w = \frac{\overline{\rho u'v'}}{\rho_w u_\tau^2} = \frac{2}{c_f} \frac{\overline{\rho u^2}}{\rho_{ref} \bar{u}_{ref}^2} \frac{1}{[1 + (\gamma-1) M_a^2]} \frac{\overline{(\rho u)'v'}}{\bar{\rho} \bar{u}^2}$$

where the subscript "w" indicates values at the wall. In the case of the undisturbed, upstream boundary layer (see Fig. 8), the results agree closely with Sandborn's "best fit", which does not prove that the data are accurate, but does give some confidence in our method.

Although the behavior of the Reynolds stress $\overline{\rho u'v'}$ is interesting, the behavior of the kinematic shear stress $\overline{u'v'}$ is in some ways even more interesting. The distinction is useful because the equations of motion can be written in different ways. When dealing with compressible flows, there is always a choice between using either mass-weighted quantities or kinematic quantities. By separating the density variations from the velocity fluctuations, the turbulence behavior in supersonic flows can be described in terms familiar to workers in subsonic flows, and this approach is valuable when we wish to emphasize the effect of compressibility on the turbulence behavior (see, for example, Bradshaw, 1974). Here, we have chosen to present only the results for the kinematic stress $\overline{u'v'}$, and these results are shown in Fig. 9.

The streamwise trend displayed by $\overline{u'v'}$ is similar to that observed for $\overline{(\rho u)'v'}$; a sudden increase immediately downstream of the shock wave is followed by a more gradual rise which then levels off and subsequently begins to decrease. The magnitude of the increase in $\overline{u'v'}$,

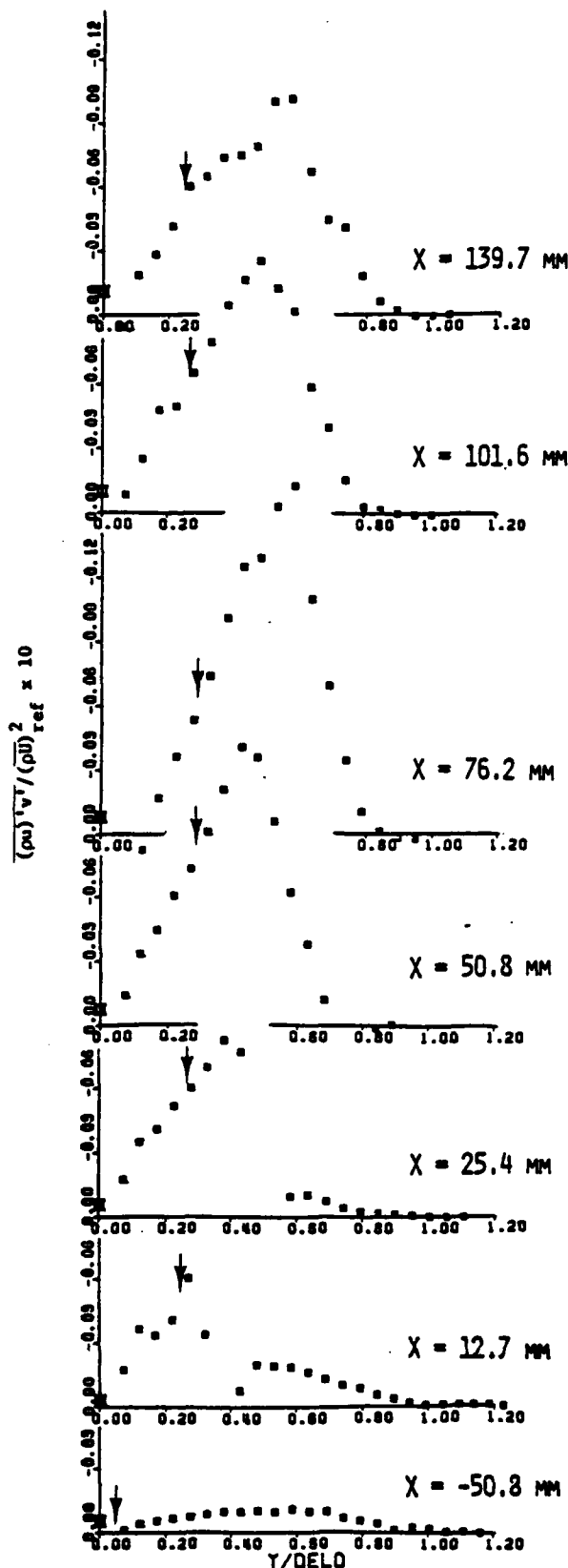


Figure 7. Profiles of the mass weighted Reynolds shear stress $(\rho u'v')/(\rho U^2)_{ref}$. The arrows indicate the locations at which the mean local normal Mach number is 1.2. The values given at $y = 0$ were taken from the mean flow data.

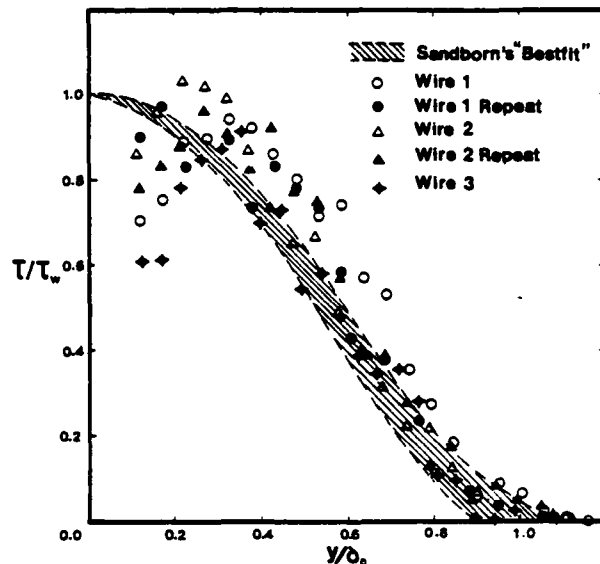


Figure 8. Profiles of the Reynolds shear stress normalized by the surface shear stress, τ/τ_w for different wires at the upstream station ($x = -50.8$ mm). Wire 1 was used for all the measurements presented in this paper. The region of "best fit" is taken from Sandborn (1974).

however is considerably smaller than the observed increase in $(\rho u')^2$. At $x = 76$ mm, for instance, $u'v'$ has increased by a factor of 2.6 whereas $(\rho u')^2$ increased about 16 times. At the same station, the corresponding amplification factors for u'^2 and $(\rho u')^2$ were 4 and 8 respectively, which suggests a considerable change in the turbulence structure.

For instance, the ratio $-u'v'/u'^2$ can be taken as a structure parameter. In the undisturbed boundary layer at $x = -51$ mm, this ratio has a value of about 0.25 (at $y/\delta_0 = 0.6$), which agrees well with the value commonly quoted for incompressible boundary layers (see Townsend, 1976, p.107). Through the interaction zone, the ratio $u'v'/u'^2$ increases to about 0.35, although it must be stated that the measurements of $u'v'$ in this region are probably not too reliable. Downstream in the recovery region, however, this ratio decreases significantly, and it reaches a value of 0.16~0.18 at the furthest downstream station ($x = 140$ mm). A similar trend was observed by Smits et al (1979) in a subsonic boundary layer subjected to an impulse in concave curvature. It is interesting to note that in the present experiment, where both curvature and compressibility effects are important, the turbulence appears to respond in a similar fashion.

CONCLUSIONS AND FINAL DISCUSSION

All the turbulence parameters considered in this study, including $(\rho u')^2$, u'^2 , $(\rho u')^2$ and $u'v'$ have shown a similar trend. All of these parameters increase through the interaction over a distance which corresponds approximately to the region of non-zero pressure gradient and the increases are not insignificant; amplification factors vary from 2.6 to 16. It was observed that the turbulence at the furthest downstream station is still far from equilibrium, and it appears that the relaxation process is very slow. In addition, the turbulence structure is considerably distorted by the interaction. For instance, the ratio $u'v'/u'^2$ first increases by about 40% and then decreases by approximately the same amount.

To interpret these results, we can begin by considering the theoretical work of Zang, et al (1982) and

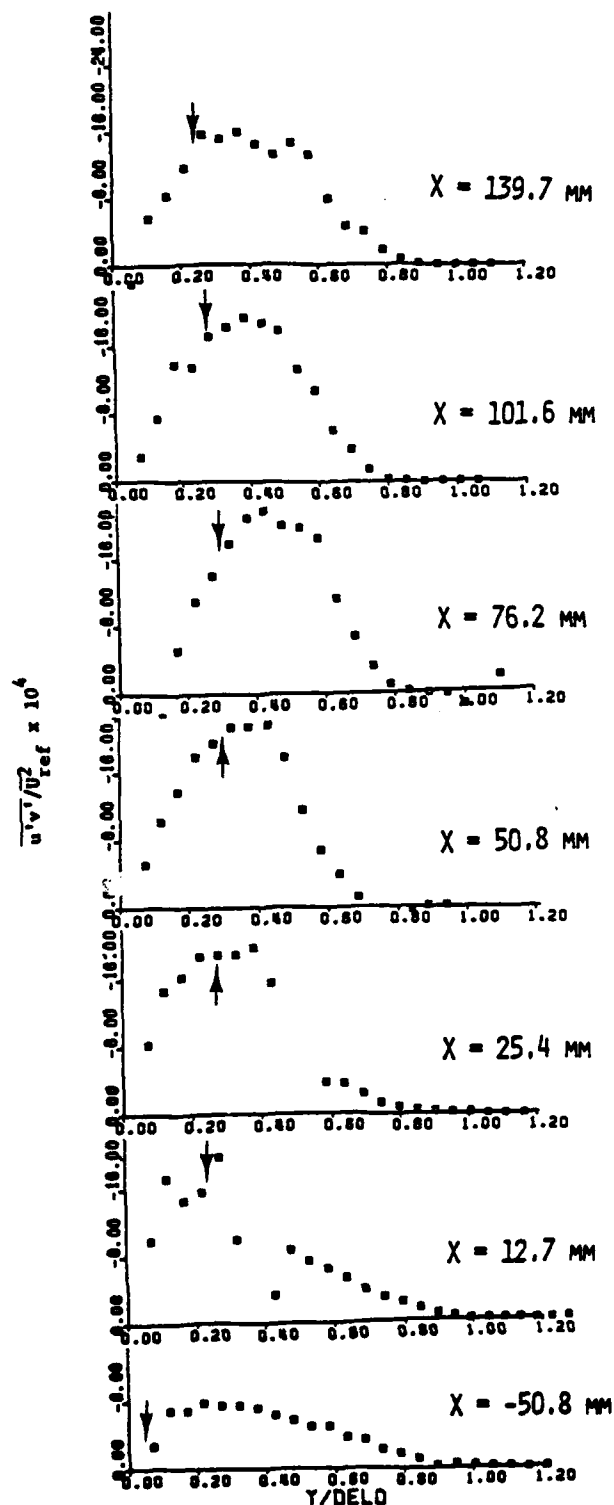


Figure 9. Profiles of the kinematic shear stress $(u'v')/U_{ref}^2$. The arrows indicate the locations at which the mean local normal Mach number is 1.2.

Anyiwo and Bushnell (1982). Using the two-dimensional Euler equations, these authors showed that several possible turbulence amplification or generation mechanisms may occur during an interaction between a plane shock wave and an incident turbulence field. These mechanisms include (1) direct amplification, (2) "generation" of turbulence from incident acoustic and entropy fluctuations, and (3) "focussing" caused by distortions of the shock front.

When a shock wave interacts with a turbulent boundary layer, however, the flow field is rather different from the ideal case considered by these authors. The shock wave within the boundary layer spreads out into a system of instantaneous compression waves (see, for instance, Fig. 3) which are unsteady and appear to be in constant, low frequency motion (Dolling and Murphy, 1982). As Zang et al (1982) point out, the direct conversion of mean flow energy into turbulence by shock oscillation can serve as a powerful turbulence amplification mechanism. In our particular experiment, however, it does not appear that shock oscillation is an important amplification mechanism. This conclusion is based on the results given in Figs. 5 and 6; the amplification begins very close to the mean shock location, and if shock oscillation was important we would expect to see a greater upstream influence.

Of the other three mechanisms, the first two are probably more important than the third (Anyiwo and Bushnell, 1982). We can consider these two mechanisms together for our purposes, and simply call them "compressibility" effects. The choice of the name is deliberate. In any shock-wave/boundary layer interaction the compression occurs over some distance and it is difficult to identify a precise shock front. We tentatively suggest, therefore, that what we call compressibility effects are similar to the compressibility effects identified by Bradshaw (1973, 1974) in supersonic boundary layers subjected to adverse pressure gradients. If we can ignore viscous effects associated with the compression waves, the question appears to be more a matter of degree rather than a fundamental difference in kind.

The interaction zone may perhaps be viewed simply as a region of impulsively applied pressure gradient. The physical mechanism by which turbulence is amplified across an interaction zone can then be identified as a change in the cross-sectional area of fluid elements, caused by the compression. A useful measure of the strength of the interaction is given by the integral of the divergence of the velocity field over the time it acts, and this is approximately equal to $\theta_p = (1/\gamma) \ln(p_2/p_1)$, where p_2/p_1 represents the pressure rise across the shock wave (Hayakawa, et al, 1982).

In the case of a compression corner, the streamlines experience concave longitudinal curvature as they pass through the interaction zone. Concave curvature is an unstable extra strain rate in that it causes turbulence levels to increase (Bradshaw, 1973), and therefore it must be considered as an additional amplification mechanism. We can similarly characterize the strength of the curvature effect by evaluating the integral of the extra strain rate over the time it acts, and we find that this is equal to the total turning angle θ_c (Smits et al, 1979).

For the present experiment, $\theta_p \approx 0.74$ and $\theta_c \approx 0.28$ which suggests that the effects of compressibility outweigh the effects of curvature, if no interaction between these effects occurs.

We have remarked that the turbulence structure appears to be significantly distorted by the interaction. This observation is in accord with the analysis presented by Debieve et al (1980). By using an approach based on rapid distortion theory, and by modelling the shock wave as a discontinuity, they showed that the shock wave rotates the Reynolds stress tensor. As a consequence, a structure parameter such as $u'v'/u'^2$ must change, and their analysis predicts an increase, as observed in our

measurements. The subsequent decrease indicates that this analysis apparently breaks down in the recovery region.

A final note should be added regarding the time-dependent response of the turbulent motions. It seems highly likely that the full impact of the distortion is not felt until some distance downstream of the interaction zone. At first sight, the results do not show evidence of such a lagged response. This aspect of the turbulence behavior, however, is under further investigation.

Re_{∞}/m	$6.3 \times 10^7/m$
$M_{a_{\infty}}$	2.87
P_o	$6.9 \times 10^5 \text{ N/m}^2$
T_w/T_o	1.04
δ_o	28.0 mm
δ_{ref}^*	6.7 mm
θ_{ref}	1.3 mm

TABLE 1: Incoming flow conditions. The boundary layer parameters were taken at $x = -51 \text{ mm}$. The thickness δ_o is defined as the distance where the mass flow rate reaches 99% of the freestream value.

REFERENCES

- Anyiwo, J. C. and Bushnell, D.M., 1982, "Turbulence Amplification in Shock-Wave Boundary Layer Interaction," AIAA J., Vol. 20, pp. 893-899.
- Bradshaw, P., 1973, "Effects of Streamline Curvature on Turbulent Flow," AGARDograph 169.
- Bradshaw, P., 1974, "The Effect of Mean Compression or Dilatation on the Turbulent Structure of Supersonic Boundary Layers," J. Fluid Mech., Vol. 63, pp. 449-464.
- Dolling, D. S. and Murphy, M., 1982, "Wall Pressure in a Supersonic Separated Compression Ramp Flow Field," AIAA Paper 82-0986.
- Dussauge, J. P. and Gaviglio, J., 1981, "Bulk Dilatation Effects on Reynolds Stress in the Rapid Expansion of a Turbulent Boundary Layer at Supersonic Speed," Proc. Third Symp. on Turbulent Shear Flows, Univ. of Calif., Davis, pp. 2.33.
- Fernholz, H. H. and Finley, P. J., 1977, "A Critical Compilation of Compressible Turbulent Boundary Layer Data," AGARD-AG-223.
- Fernholz, H. H. and Finley, P. J., 1981, "A Further Compilation of Compressible Boundary Layer Data with a Survey of Turbulence Data," AGARD-AG-263.
- Hayakawa, K., Smits, A. J. and Bogdonoff, S. M., 1982, "Hot-Wire Investigation of an Unseparated Shock-Wave/Turbulent Boundary Layer Interaction," AIAA Paper No. 82-0985.
- Morkovin, M. V., 1962, "Mecanique de la Turbulence," Favre, A. Ed., C.N.R.S., Paris, pp. 367-380.
- Sandborn, V. A., 1974, "A Review of Turbulence Measurements in Compressible Flow," NASA TM X-62,337.
- Settles, G. S., 1975, "An Experimental Study of Compressible Turbulent Boundary Layer Separation at High Reynolds Numbers," Ph.D. Thesis, Aerospace and Mechanical Sciences Department, Princeton University, Princeton, NJ.
- Settles, G. S., Bogdonoff, S. M. and Vas, I. E., 1976, "Incipient Separation of a Supersonic Turbulent Boundary Layer at High Reynolds Numbers," AIAA J., Vol. 14, pp.50-56.
- Settles, G. S., Fitzpatrick, T. J. and Bogdonoff, S. M., 1979, "Detailed Study of Attached and Separated Compression Corner Flow Fields in High Reynolds Number Supersonic Flow," AIAA J., Vol. 17, pp. 579-585.
- Smits, A. J., Young, S.T.B. and Bradshaw, P., 1979, "The Effect of Short Regions of High Surface Curvature on Turbulent Boundary Layers," J. Fluid Mech., Vol. 94, pp. 209-242.
- Smits, A. J., Hayakawa, K. and Muck, K. C., 1983, "Constant Temperature Hot-Wire Anemometer Practice in Supersonic Flows, Part I: The Normal Wire," Experiments in Fluids, Vol. 1, pp. 83-92.
- Smits, A. J. and Muck, K. C., 1983, "Constant Temperature Hot-Wire Anemometer Practice in Supersonic Flows, Part II: The Inclined Wire," AIAA Paper No. 83-0508, and Experiments in Fluids (submitted).
- Townsend, A. A., 1976, "The Structure of Turbulent Shear Flow," Cambridge University Press.
- Zang, T. A., Hussaini, M. Y. and Bushnell, D. M., 1982, "Numerical Computations of Turbulence Amplification in Shock Wave Interactions," AIAA Paper No. 82-0293.

A UNIVERSAL VELOCITY DISTRIBUTION AND TURBULENCE PROPERTIES IN THE SHEAR FLOW ON A ROTATING CYLINDER IN A QUIESCENT FLUID

Ikuo NAKAMURA*, Yoshinori UEKI** and Shintaro YAMASHITA*

* Department of Mechanical Engineering, Nagoya University, Nagoya, Japan

** Department of Mechanical Engineering, Nagano Technical College, Nagano City, Japan

ABSTRACT

Discussion is given on a universal velocity distribution in the shear layer induced by a spinning cylinder in an infinite still fluid and a novel semi-logarithmic law different from that of the conventional two-dimensional turbulent boundary layer is derived. Experiments have been performed for various Reynolds numbers extending from 4.5×10^4 to 7.8×10^5 and the mean and fluctuating velocity fields have been measured. The novel universal velocity distribution law obtained is verified by these measurements. Extremely unstable nature of this flow is inferred from the profile of Richardson number calculated from the measured mean velocity. The averaged velocity distribution exhibits the existence of two types of power law regions where $U \propto 1/r^2$ and $U \propto 1/r$, but a notice should be paid that the flow is still turbulent in the $1/r$ -region. The same scaling law can be applied for the turbulent field and the similar distributions of various turbulent quantities are obtained irrespective to the value of Reynolds number. The statistical parameters are used to depict the flow field. Especially the intermittency distribution suggests that the entrained ambient fluid enters deep into the rotating shear layer.

NOMENCLATURE

- a = Radius of the cylinder
- C_f = $-2 \tau_w / \rho U_w^2$, Skin friction coefficient
- D = $2a$, Diameter of the cylinder
- P = Static pressure
- r = Radial distance
- $q^2/2$ = $(u^2 + v^2 + w^2)/2$, Turbulent energy
- Re = $U_w D / \nu$, Reynolds number
- U, V, W = Mean velocity components in the x -, y - and z -directions
- u_τ = $\sqrt{-\tau_w / \rho}$, Friction velocity
- u, v, w = Fluctuating velocity components in the x -, y - and z -directions
- u', v', w' = RMS values of u, v and w , respectively
- x, y, z = Cylindrical coordinates, x : Peripheral direction, y : Axial distance, z : Radial distance from the cylinder surface
- ω = Angular velocity of the cylinder
- τ = Shear stress

Subscript

- w = At the cylinder surface

INTRODUCTION

It is well known that the streamline curvature has an appreciable effect on the structure of turbulent shear flow even if the radius of its curvature is considerably larger than the length scale in a problem [1]. Many types

of turbulent shear flows having a curved streamline have long been of special interest from the fact that they show various characteristics which cannot be inferred from the knowledge of the flat-plate turbulent boundary layer. Perhaps one of the simplest types is the turbulent shear flow induced by a rotating cylinder in a quiescent fluid filling infinite space. In this flow, the mean rate of deformation is $dU/dr = U/r$, and the mean vorticity is $dU/dr + U/r$; the flow has the extra rate of strain $-U/r$ according to Bradshaw [2]. Or it may be said that the flow has the extra vorticity.

Although numerous studies have been performed on the flow between concentric rotating cylinders, there is surprisingly little research on the limiting case in which the outer cylinder diameter tends to infinity. Among the experimental studies in particular can be cited the torque measurement by Theodorsen and Regier [3], the measurement of velocity distribution by Thom [4], and the flow visualization in the near-wall region and the velocity measurement by Kasagi and Hirata [5]. The experiment on turbulence properties is insufficient. The mean flow structure, especially the universal velocity distribution on a rotating cylinder, was discussed by Fujimoto [6] and Dorfmann [3], and recently, in case of concentric rotating cylinders, by Smith and Townsend [8]. These discussions, however, contradict one another in basic ideas, and none of them seems to be conclusive at least for the present authors.

In this study, first consideration is given to a universal velocity distribution law in the turbulent shear flow on a rotating cylinder in a quiescent fluid, and then experiments on the mean flow velocity distribution and turbulence properties are presented. Discussion is undertaken on the mean flow field, and turbulence structure: i.e., the fluctuating velocity and Reynolds stress distributions, the turbulent energy budget, the probability density distributions of the fluctuating velocities, and the auto- and space correlations of turbulence.

SIMILARITY PROFILE OF MEAN FLOW

Because of the simplicity of the flow geometry, the universal velocity distribution law is expected to hold at high Reynolds numbers. There is an opinion that the same logarithmic law as in the flat-plate flow should be valid in the turbulent shear flow on a cylinder spinning in an infinite space. Kasagi and Hirata [5] applied their mean flow data to the usual two-dimensional law of the wall, but the data did not fit the two-dimensional law except in the viscous sublayer. Smith and Townsend [8] have also used the two-dimensional logarithmic law to express the measured mean velocity distribution of the turbulent shear flow in concentric rotating cylinders. These data are considerably scattered and not conclusive about the law of the wall.

Earlier, Fujimoto considered the velocity distribution of this flow [6]. Assuming the same mixing length hypothesis as the flat-plate flow, $\tau = -\rho \ell^2 (dU/dz)^2$ where $\ell = \kappa z$, and the constant moment of the shear force across the

layer, i.e., $\tau r^2 = \tau_w a^2$, he derived

$$U/u_\tau = (1/\kappa)[(r/a)\ln(1+a/z) - 1]. \quad (1)$$

However, this expression could not depict the present experimental velocity profiles.

Dorfmann deduced a universal velocity distribution law of the turbulent flow in concentric rotating cylinders, assuming $\tau = \rho \nu_T r \partial(U/r)/\partial r$ where $\nu_T = \kappa_D \sqrt{\tau/\rho} z$ is an eddy viscosity. If the radius of the outer cylinder tends to infinity in this law, the expression for the velocity distribution on the rotating cylinder in a quiescent fluid can be obtained. Dorfmann did not show this velocity distribution but it is easily obtained in defect law form as

$$(a/r)U/u_\tau = -(1/\kappa_D)[\ln(1-a/r) + a/r + C]. \quad (2)$$

The mean flow structure must be influenced by the effect of streamline curvature. As will be shown later, the extra rate of strain in this flow is small only in the vicinity of the wall and not negligible in fully turbulent region near the wall corresponding to the logarithmic region in the flat-plate flow. Although the considerations of Fujimoto and Dorfmann deserve credit for attempting to establish a universal velocity distribution law instead of the two-dimensional conventional law, they are incomplete; their basic idea or assumptions are open to question.

The equation of mean velocity in the peripheral direction is integrated to be (e.g., Ref. [9]),

$$-u_\tau r^2 + \nu r^3 d(U/r)/dr = \text{const.}, \quad (3)$$

or

$$r^2 \tau = a^2 \tau_w = -a^2 \rho u_\tau^2. \quad (4)$$

Equations (3) and (4) are identical with those for the peripheral velocity component in the near wall region of the flow on a rotating cylinder in an axial uniform stream [10]. Therefore, basically the same, but more precise, discussion on the mean flow near the wall can be made as in the section 4.4.2 of Ref. [10] where the law of the wall and the logarithmic law different from two-dimensional laws are derived. For convenience a brief description is given as follows.

Introducing a dimensionless argument z^* defined by

$$dz^*/dr = u_\tau a^3/\nu r^3, \quad (5)$$

Eq. (3) is transformed as

$$d(aU/ru_\tau)/dz^* - r^2 u_\tau^2/a^2 u_\tau^2 = 1. \quad (6)$$

We may expect the solution of Eq. (6) to be

$$aU/ru_\tau = F(z^*), \quad (7)$$

or the law of the wall, if such exists, corresponding to the two-dimensional law should read as

$$[U_w - (a/r)U]/u_\tau = F(0) - F(z^*) = f(z^*). \quad (8)$$

Under the condition of $z^* = 0$ at $r = a$, the integration of Eq. (5) yields

$$z^* = (u_\tau a/\nu)(r^2 - a^2)/2r^2. \quad (9)$$

In the viscous sublayer where the Reynolds stress can be neglected, the velocity profile becomes

$$[U_w - (a/r)U]/u_\tau = z^* = (u_\tau a/\nu)(r^2 - a^2)/2r^2. \quad (10)$$

This expression is a special one included in the general expression of the law of the wall, Eq. (8).

In the fully turbulent region outside the sublayer, a universal velocity distribution is obtained as

$$[U_w - (a/r)U]/u_\tau = A \log_{10}[(u_\tau a/\nu)(r^2 - a^2)/2r^2] + B, \quad (11)$$

which is different from a two-dimensional turbulent boundary layer with respect to the wall variable. Moreover, the values of the constants A and B are different from those of the flat-plate flow, as will be shown later. Equation (11) can be deduced from the assumption of the existence of the overlap region where both the law of the wall

(8) and a defect law in outer layer, which may be expressed

$$aU/ru_\tau = g(r/a, \delta/a), \quad (12)$$

are valid; or it can also be obtained from the assumption that the eddy viscosity is scaled by the relevant coordinate $\nu z^*/u_\tau = a(r^2 - a^2)/2r^2$.

EXPERIMENTAL APPARATUS

Two kinds of cylinders $D = 2a = 300$ mm and 80 mm are rotated between two end plates standing 880 mm apart from each other. The cylinders are made from aluminum alloy and have smooth surfaces. Probes used are conventional I and X hot-wire probes and a static pressure probe. Care was taken to minimize the effect of the prong wake on the hot-wire output. The hot-wire signal was calibrated in a wind-tunnel. The speed of the thick cylinder rotation was varied from $N = 480$ rpm to 2500 rpm, and that of the thin cylinder attained 5000 rpm maximum. The corresponding Reynolds number Re is 1.5×10^5 to 7.8×10^5 in the thick cylinder and up to 1.1×10^5 in the thin cylinder.

RESULTS AND DISCUSSION

Secondary flow observed was weak and the mean velocity profile U/U_w obtained at three different sections in the axial direction showed a clear two-dimensionality. Thus, it can be said that the flow fields in the central section of the cylinder concerned in the present study are not influenced significantly by the secondary flow.

Wall Shear Stress

The most important factor for describing turbulent wall flow is the wall shear-stress τ_w . Theodorsen and Regier [3] measured torque exerted on various rotating cylinders, and Dorfmann [7] proposed a semi-empirical formula for skin friction coefficient c_f . In the present study

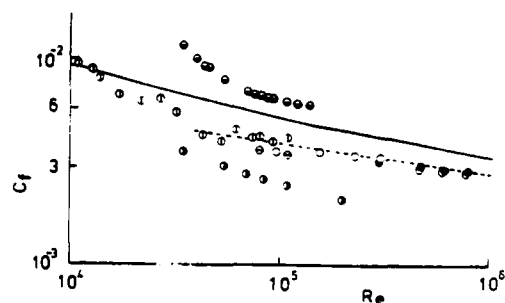


Fig. 1 Skin friction coefficient estimated both from the Reynolds stress (\bullet and \circ , for cylinders $D=300$ mm and 80 mm, respectively) and from the mean velocity gradient (\circ and \bullet , for these cylinders, respectively). —, Dorfmann [7]; ---, Eq. (13); \bullet , Thom [4]; \circ , Smith & Townsend [8].

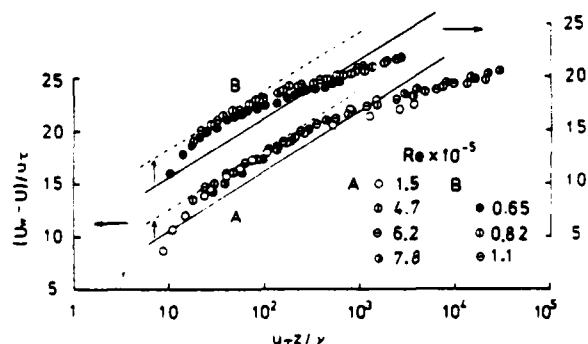


Fig. 2 Logarithmic plots according to the two-dimensional law of the wall. A, thick cylinder ($D=300$ mm); B, thin cylinder ($D=80$ mm); the same designation will be used in the following figures.

τ_w was estimated both from the measurement of Reynolds stress \overline{uw} , and from the value of the mean velocity gradient measured in the vicinity of the cylinder surface.

Figure 1 shows a comparison of c_f obtained by various investigators. In this experiment the values of c_f obtained from \overline{uw} and from the mean velocity gradient near the wall agree well. The dotted line in Fig. 1 is drawn according to the equation:

$$1/\sqrt{c_f} = 3.09 \log_{10}(\text{Re}\sqrt{c_f}/2) + 4.79. \quad (13)$$

This expression is derived from Eq. (11) in an analogy to Dorfmann's formula [Eq. (14)] with the numerical coefficients determined by the mean velocity distribution discussed in the next section. The difference between the distribution of the present data and the solid line, the resistance formula of Dorfmann [7], is appreciable. The plots of the wall shear stress from the torque measurements of Theodorsen and Regier [3] on which the Dorfmann's formula is based exhibited appreciable scatter within the range of the Reynolds number shown in this figure. Smith and Townsend [8] have measured the mean velocity in turbulent flow between two concentric rotating cylinders. In the figure, the skin friction coefficient at the inner cylinder estimated by the present authors from their mean velocity profiles with the outer cylinder at rest is also presented.

For laminar flow between the two concentric rotating cylinders the exact solutions of the Navier-Stokes equation exist, and when the outer cylinder is at rest the wall shear stress on the inner cylinder becomes $\tau_w = -2\mu\omega a'^2/(a'^2 - a^2)$ where a' is the radius of the outer cylinder. In case of a single cylinder rotating in an infinite fluid ($a' \rightarrow \infty$) it becomes $\tau_w = -2\mu\omega$, i.e., smaller than that of concentric cylinders. It is natural to expect that, for turbulent flow too, the wall shear stress for a single rotating cylinder is smaller than for concentric rotating cylinders. Thus, although the skin friction coefficient of Smith and Townsend estimated by the present authors may have considerable error, the value of Dorfmann's formula seems too high and open to doubt; it is needless to mention the higher value of Thom's results [4]. The results of this measurement are more reasonable. Moreover, the various quantities of the mean flow and turbulent fields in this experiment were found to be better arranged by using the wall shear stress obtained here than Dorfmann's formula.

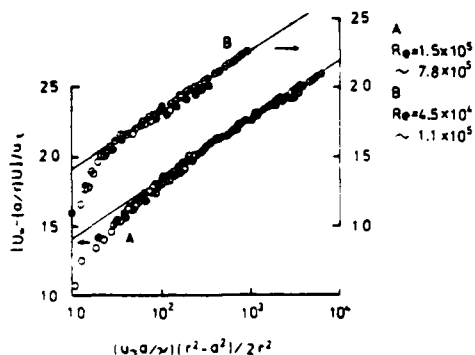


Fig. 3 Logarithmic velocity distribution according to Eq. (11) with $A=4.2$ and $B=9.8$.

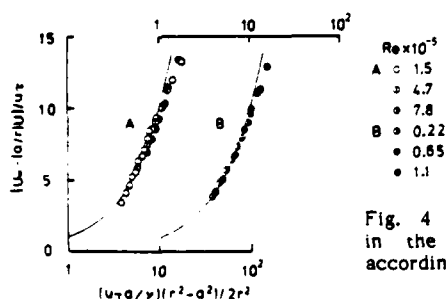


Fig. 4 Velocity profiles in the viscous sublayer according to Eq. (10).

Universal Velocity Distribution

Figure 2 shows the logarithmic plots of the velocity distribution in this experiment according to the two-dimensional logarithmic velocity distribution law, u_τ being estimated as in the previous section. The measured velocity profiles do not collapse into the lines of the two-dimensional law, and, moreover, the velocity profiles have almost no portions parallel to these lines. It is clear that the two dimensional logarithmic law is invalid in this turbulent shear flow; the validity of this law is diminished with the increasing effect of the streamline curvature.

If $\delta_s \ll a$ where δ_s is the thickness of the viscous sublayer, it may be legitimate to assume a linear velocity profile in the sublayer. Joining this profile with Eq. (2) at the outer edge of the sublayer, putting $\delta_s = \alpha\nu/u_\tau$, yields $C = -\kappa_D(U_w/u_\tau - \alpha) - 1 + \ln(u_\tau a/\alpha\nu + 1)$ for the first approximation. Dorfmann assumed $\kappa_D = 0.4$, the same value as in the flat-plate flow, and estimated $\alpha = 7.5$ using the data of the flow between concentric rotating cylinders. Using these values he obtained a semi-empirical formula for the resistance:

$$1/\sqrt{c_f} = 4.07 \log_{10}(\text{Re}\sqrt{c_f}/2) - 0.6. \quad (14)$$

This distribution is already shown in Fig. 1 by a solid line.

The present data plotted according to Eq. (2) showed fairly scattering and the experimental evaluation yields $\kappa_D = 0.5 \sim 0.6$ and $\alpha = 13 \sim 15$, quite different from those of Dorfmann.

Equation (2) is rewritten

$$[U_w - (a/r)U]/u_\tau = (1/\kappa_D)[\ln(1-a/r) + a/r] + \alpha + (1/\kappa_D)[\ln(1+u_\tau a/\alpha\nu) - 1]. \quad (15)$$

The plots of the present data on the basis of Eq. (15) exhibited a high dependence on the Reynolds number though fairly wide ranges of the straight line portions in the velocity profiles could be discerned.

We have derived the universal velocity distribution law, Eq. (11), for the turbulent shear flow on a rotating cylinder in a quiescent fluid; this expression is considered most reasonable among various expressions proposed so far because of the consistency in the procedure of the derivation as well as in the basic assumptions. The experimental results are plotted in Fig. 3 on the basis of Eq. (11) with $A = 4.2$ and $B = 9.8$. This figure reveals that the data are satisfactorily expressed by this universal logarithmic velocity distribution, independent of the Reynolds number for the first approximation. It should be noted that the value of the gradient of the line, i.e., $A = 4.2$, has been determined in an experiment of the turbulent boundary layer on a thin cylinder rotating in an axial uniform stream [11]. It can be supposed that the shear layer structure of these two flows are similar. The velocity distribution in the viscous sublayer is presented in Fig. 4 according to Eq. (10). This figure reveals the validity of the estimation of the wall shear stress from the mean velocity gradient near the wall.

The defect law, Eq. (12), becomes

$$aU/u_\tau = -A \ln[1-(a/r)^2] + C', \quad (16)$$

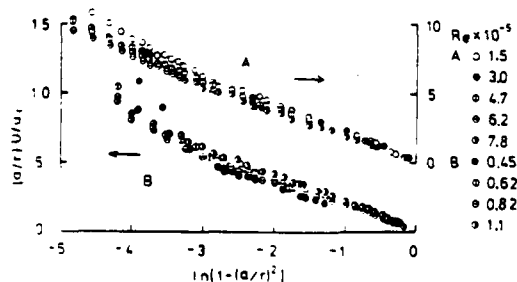


Fig. 5 Logarithmic plots of the velocity profiles according to defect law representation, Eq. (16).

in the overlapping region of the wall layer and the outer layer. Here C' is a function of δ/a . Figure 5 shows the measured velocity profiles plotted according to Eq. (16). The functional relationship of Eq. (12) and Eq. (16) may be considered reasonable.

A gradient Richardson number [1]

$$Ri = 2S(1+S), \quad (17)$$

where $S = (U/r)/(dU/dr)$, is a parameter relevant to turbulent structure in curved flows and utilized by many researchers. The minimum value of Ri is -0.5 ; in this case it turns out to be $U \propto 1/r^2$ from the definition of S . The profiles of Ri obtained from the present data are shown in Fig. 6 and are always negative; in a certain range of r , they take a minimum value -0.5 , suggesting that this flow is extremely unstable.

Figure 7 shows how the velocity profiles relate to the power of r . Here $U^* = U/u_\tau$ and $r^* = ru_\tau/\nu$. The two distinct regions of $U \propto 1/r^2$ and $U \propto 1/r$ are noted. As shown in Fig. 5, even the velocity distribution in the outermost part of the layer behaves logarithmically as

$$(a/r)U/u_\tau \sim \ln[(r^2 - a^2)/r^2]. \quad (18)$$

Far from the wall, the right-hand side of Eq. (18) is expanded as

$$\ln[(r^2 - a^2)/r^2] = -(a/r)^2 - (1/2)(a/r)^4 - \dots \quad (19)$$

Therefore we can obtain $U \propto 1/r$ in the outermost part of the turbulent shear layer. Here it should be noted that the flow in the region of $U \propto 1/r$ is not laminar but turbulent. In fact, the present experiment reveals that the value of u'/U is nearly constant in this region; the fluctuating velocities are damped outward together with the mean velocity.

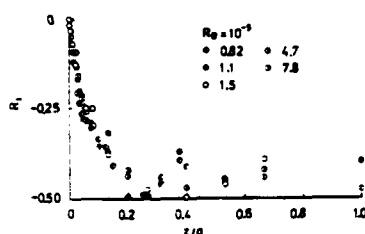


Fig. 6 Distribution of Richardson number.

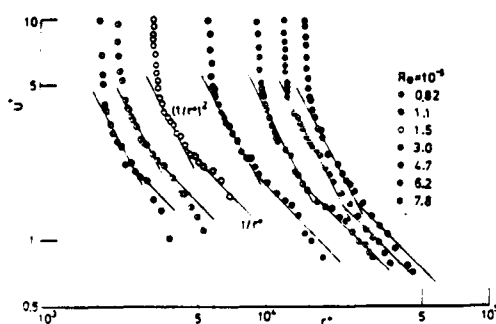


Fig. 7 Velocity profiles related to the power of r .

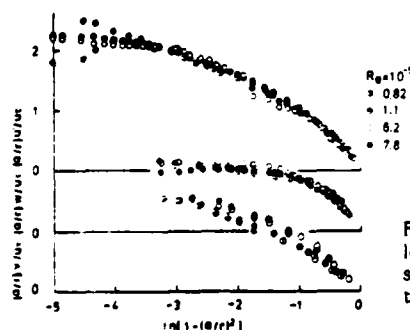


Fig. 8 Fluctuating velocity profiles using the same scaling law as the mean velocity.

The rate of strain of this flow is

$$dU/dr - U/r = (dU/dr)(1-S). \quad (20)$$

The term U/r can be regarded as the extra rate of strain to the flat-plate flow. If $|S| \ll 1$, the flow can be reasonably approximated by the two-dimensional flat-plate flow; on the other hand, when S is not very small, the two-dimensional treatment for this flow is not valid. In the whole region of the present shear layer, except near the wall, the magnitude of S is not small; the role of the extra rate of strain in this flow is very important.

Turbulent Field

The measured distributions of the RMS fluctuating velocity components u' , v' and w' , and the turbulent energy are shown in Figs. 8 and 9, respectively, using the same scaling law as the mean velocity distribution. Except in the near-wall region, each of the data falls along one single curve. The value of u'/U was increased gradually with the distance from the wall and had a nearly constant value 0.4 in the region of $U \propto 1/r$; it is conjectured that there is a noticeable error in the turbulence quantities measured in the outermost region. In this region the existence of the large eddy structure of vortex motions is anticipated, and there possibly exist instantaneous reverse flows. Figure 10 shows the distribution of the Reynolds stress multiplied by r^2 . The constancy of the torque of the shear force acting at any cylindrical surface required from Eq. (3) is well satisfied in the fully turbulent region. The value of the wall shear stress presented in Fig. 1 is estimated from the extrapolation of the distribution of \overline{uwr}^2 , and its accuracy seems to be reliable. It can be thought that the flow around a cylinder spinning in an infinite fluid is, far from the wall, the same as in the potential flow field with the velocity $U \propto 1/r$ induced by a vortex filament. Although the present experiment shows the existence of the region $U \propto 1/r$, the flow in this region is turbulent and not a usual potential flow.

Balances of Mean Momentum and Turbulent Energy

The balance of the equation in the peripheral direction is shown in Fig. 10. The radial mean momentum equation has a complex nature and may be significant for investigation of the balance of the equation. To avoid the differentiation of the experimental data, we integrate the equation, and the following is obtained:

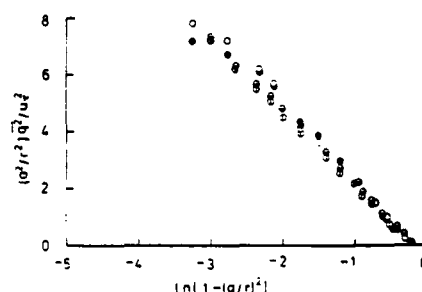


Fig. 9 Turbulent energy distribution.

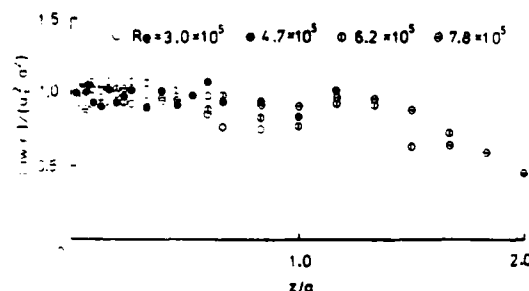


Fig. 10 Reynolds stress distribution multiplied by r^2 .

$$(P_e - P) / \rho U_w^2 + (\overline{w_e^2 - w^2}) / U_w^2 + \int_{a+z}^{a+\delta} \frac{(\overline{w^2 - u^2})}{r U_w^2} dr = \int_{a+z}^{a+\delta} \frac{(U/U_w)^2 (1/r) dr}{2} \quad (21)$$

Figure 11 shows the terms appearing in the above equation estimated on the basis of the experimental data. The normal stress term clearly shows its importance in the balance of the radial mean momentum.

The equation for the turbulent kinetic energy $q^2/2$ is

$$\overline{uwr} \partial(U/r) / \partial r + (1/r) \partial[r(q^2/2 + p/\rho)w] / \partial r + \epsilon = 0, \quad (22)$$

where ϵ stands for the viscous dissipation of the turbulent energy. The turbulent energy budget is plotted in Fig. 12. Here the dissipation was measured directly, that is, estimated from $(du/dt)^2$, and the diffusion term was obtained by difference. The production and dissipation are large in the near-wall region and almost in equilibrium. The

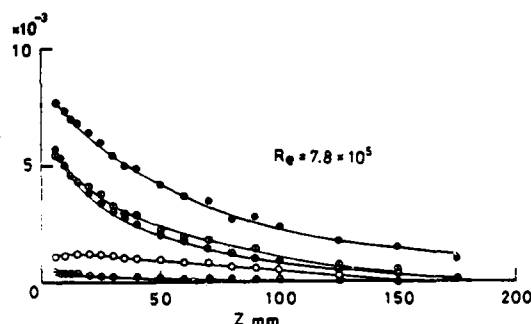


Fig. 11 Balance of the momentum equation in the radial direction. \bullet , left-hand side of Eq. (21); \circ , right-hand side of Eq. (21). The first, second and third terms on the left-hand side of Eq. (21) are plotted by the symbols \bullet , \circ and \bullet , respectively.

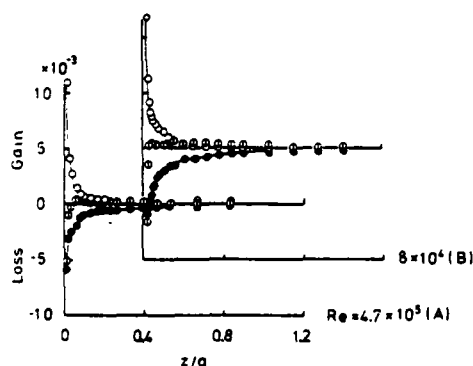


Fig. 12 Turbulent energy budget.

- \circ , production: $-(a/U_w^3) \overline{uwr} \partial(U/r) / \partial r$;
- \bullet , diffusion: $-(a/U_w^3) r \partial[r(q^2/2 + p/\rho)w] / \partial r$;
- \bullet , dissipation: $-a\epsilon/U_w^3$.

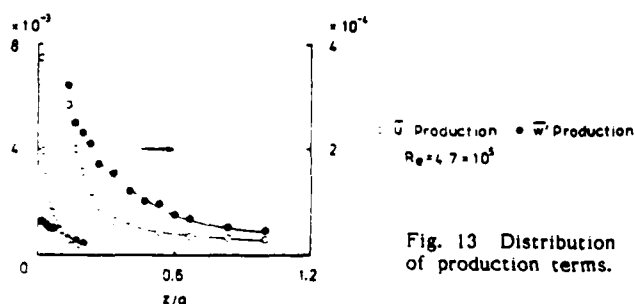


Fig. 13 Distribution of production terms.

advection is absent in this flow, and the diffusion in the outer part of the layer is of the same order as the dissipation. The turbulent energy production shown in Fig. 12, by which the mean flow energy is converted directly into u-fluctuation, is divided into two parts: the production term for w-energy which extracts the energy from u-fluctuation, and the net production term for u-energy which is a residual of the turbulent production from the mean flow energy minus the production for the w-energy. Figure 13 shows the variation of these production terms. Near the wall the u-production is much larger than the w-production, and in the middle region of the shear layer the latter is larger than the former. The flux Richardson number is anticipated large in absolute value in this region.

Statistical Properties of Turbulence

Measured probability density functions of u- and w-fluctuations are presented in Figs. 14 a and b, respectively. Since the probe used to measure the probability density function of w was a conventional X-probe, it was impossible to obtain the profiles of $P(w)$ in the vicinity of the rotating surface. The probability density function of u-fluctuation has a nearly Gaussian profile in the near wall region and it shows a rather positively skewed distribution in the outer layer. The profile of $P(w)$ is positively skewed in the region of $z = 5 \sim 60$ mm. Although it has a large kurtosis in the outer layer, the skewness is relatively small in that region. It is remarkable that $P(w)$ shows an almost similar profile throughout the layer.

The profiles of $P(u)$ in the outer layer suggest that the probability of realization generating negative fluctuation is great due to the entrainment of the quiescent fluid outside of the layer and intermittent ejection of the energetic fluid from the inner layer. Also, the profile of $P(w)$ exhibits a corresponding peak at the negative side of w. In this turbulent shear flow, which may also have a super layer, the turbulent region is confined within a statistically definite cylindrical region. The turbulent shear layer is expected to entrain the fluid outside the layer, so the same amount as with the entrained fluid should escape from the rotating turbulent region (i.e., some type of reverse transition should occur).

According to the proposal of Townsend [9], the intermittency γ can be inferred from the values of kurtosis

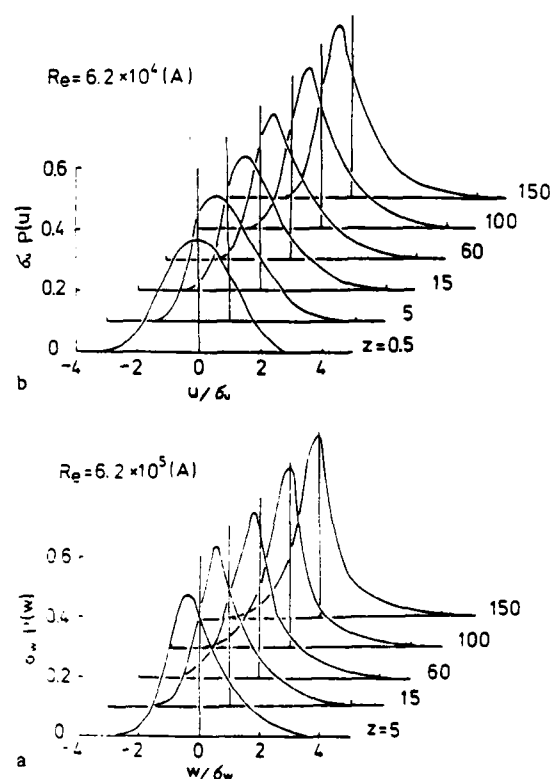


Fig. 14 a, b Distribution of the probability density functions of u- and w-fluctuations.

and skewness. Figure 15 presents the distribution of γ calculated by this method. The distribution of γ of the present flow deviates extraordinarily from that of the flat-plate flow which is designated by a broken line in the figure. The flow on the flat plate exhibits a complete turbulent character in the inner region, but in the shear layer developing on the rotating cylinder in a quiescent fluid, the value of γ attains unity in the very vicinity of the rotating surface as seen from the figure. This probably corresponds to the reverse transition phenomenon as mentioned above, and future measurements using conditionally sampling method will clarify the structure.

A series of auto-correlation coefficients of u-fluctuation is shown in Fig. 16. Although it shows no appreciable negative value in the region of $z = 0.5 \sim 5$ mm, a rather large negative coefficient appears at the large time delay in the outer layer which may be explained by assuming big eddies in that part of the layer. Also, the spatial structure of the big eddy exhibits itself in the distribution of transverse space-correlation coefficient with zero time delay as presented in Fig. 17. In the near wall region, correlated flow field is narrower than that of the outer layer, where it may be said that the representative eddy size is about 60 ~ 70 % of the cylinder radius.

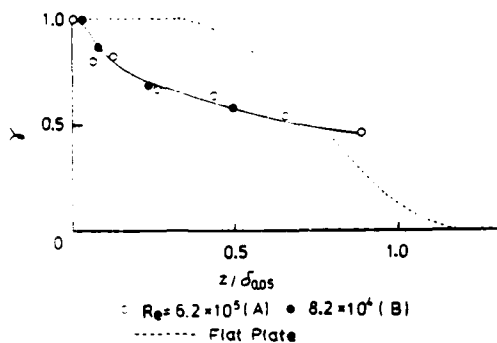


Fig. 15 Intermittency factor.

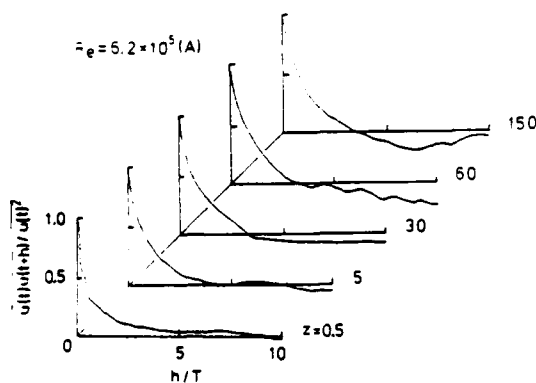


Fig. 16 Profiles of auto-correlation coefficients of u-fluctuation.

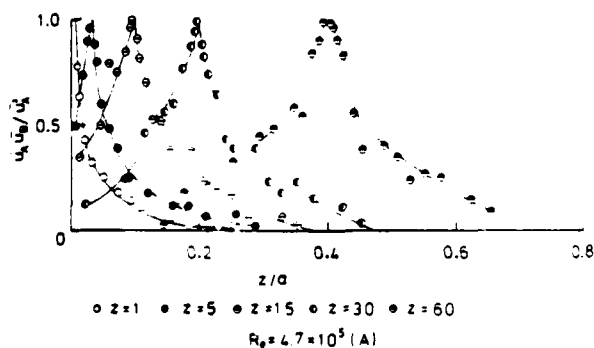


Fig. 17 Distribution of transverse space-correlation coefficients of u-fluctuation.

CONCLUDING REMARKS

Measurements have been performed with regard to the mean and fluctuating velocity fields induced by a rotating cylinder in an infinite quiescent fluid for nine kinds of Reynolds numbers. The results are as follows.

(1) Discussion of mean velocity field was undertaken, and a novel universal velocity distribution law differing from the usual two-dimensional flow was confirmed.

(2) Also, the mean velocity exhibits two regions where it shows power laws proportional to $1/r^2$ and $1/r$, respectively. The flow field is still turbulent in the $1/r$ region.

(3) The turbulent fluctuating velocity field can be well correlated according to the same scaling law as the mean velocity.

(4) The momentum balance shows the important role of the normal stresses in the radial direction. The turbulent energy budget has also been clarified.

(5) Correlations and probability density functions of the fluctuating velocity components have been measured and discussed. The intermittency distribution gives an indication of completely different turbulent structure from that of the conventional flat-plate flow.

ACKNOWLEDGEMENT

The authors wish to express their appreciation to Mr. H. Kanda of the Department of Mechanical Engineering, Nagoya University, for his technical assistance.

REFERENCES

1. Bradshaw, P., 1969, "The analogy between streamline curvature and buoyancy in turbulent shear flow", *J. Fluid Mech.*, 36(1), 171-191.
2. Bradshaw, P., 1973, "Effects of streamline curvature on turbulent flow", AGARDograph, No. 169.
3. Theodorsen, T. & Regier, A., 1944, "Experiments on drag of revolving disks, cylinders, and streamline rods at high speeds", NACA Rep., No. 793.
4. Thom, D., 1931, A.R.C. R. & M., No. 793.
5. Kasagi, N. & Hirata, S., 1975, "Transport phenomena in near-wall region of turbulent boundary layer around a rotating cylinder", ASME Pub., 75WA/HT.
6. Fujimoto, B., 1938, *Japan J. Mech. Eng.*, 41(257), 776, in Japanese.
7. Dorfmann, L.A., 1963, *Hydrodynamic Resistance and the Heat Loss of Rotating Solids*, 171, Oliver and Boyd.
8. Smith, G.P. & Townsend, A.A., 1982, "Turbulent Couette flow between concentric cylinders at large Taylor numbers", *J. Fluid Mech.*, 123, 187-218.
9. Townsend, A.A., 1976, *The Structure of Turbulent Shear Flow*, 2nd ed., 393, Cambridge University Press.
10. Furuya, Y., Nakamura, I. & Yamashita, S., 1978, "The laminar and turbulent boundary layers on some rotating bodies in axial flows", *Mem. Fac. Eng., Nagoya Univ.*, 30(1), 1-58.
11. Nakamura, I., Yamashita, S., Sawaki, Y. & Watanabe, T., 1981, "Three-dimensional turbulent boundary layer on a spinning thin cylinder in an axial uniform stream", 3rd Symposium on Turb. Shear. Flows, ed. Bradbury, L.J.S., et. al., U. C. Davis, California, USA, 2.7.

SESSION 3 - 3-D FLOWS

P.N. Joubert - Chairman

CALCULATION OF SHIP BOUNDARY LAYERS

by

V.C. PATEL, O.P. SARDA and A. SHAHSHAHAN

Iowa Institute of Hydraulic Research
The University of Iowa
Iowa City, Iowa 52242, USA

ABSTRACT

Two problems related to ship boundary layers are considered. The first is the generalization of an established three-dimensional boundary-layer calculation method to treat arbitrary hulls. This is used to study the influence of strong transverse hull curvatures and sharp keels by comparisons with experimental data on double models. The second is concerned with the boundary layer along the intersection of the free surface with the hull. A simple method is presented and used to demonstrate the phenomenon of local wave-induced separation.

INTRODUCTION

As evidenced by the SSPA-ITTC Workshop (Larsson, 1981) and the EUROVISC Workshop (Hirschel et al., 1983), many methods have been developed for the calculation of three-dimensional boundary layers, and efforts to improve them are continuing. It appears that the manner in which the body geometry and the initial and boundary conditions are handled play a critical role in determining the success of a method, the influence of the turbulence model being swamped by other uncertainties.

Boundary layers on ship hulls differ from those in aerodynamics in at least three respects:

- (1) Although the boundary layer remains thin over a large portion of the hull, it thickens rapidly over the stern leading to a region of strong viscous-inviscid interaction even in the absence of separation. Thus, it is necessary to establish the limits of first-order boundary-layer theory and identify the critical parameters responsible for the evolution of the thick boundary layer.
- (2) Ship hulls often contain extensive regions of large transverse surface curvature, e.g. along the shoulders of flat-bottomed full-form tankers, and slope discontinuities, e.g. along a sharp keel. Although these are excluded in boundary-layer theory, their effect is usually ignored in practical calculations.
- (3) The boundary layer on the hull is influenced by the free-surface waves which, in turn, depend upon the Froude number. Of the many methods available for the calculation of hull boundary layers, a few integral methods have been used at nonzero Froude numbers, but none takes into account the special features of the flow at the free surface, namely the vanishing of the velocity component normal to the free surface, local damping of turbulence in that direction and gradients of the piezometric head associated with the wave elevation.

This paper is concerned with these three aspects of

ship boundary layers.

Part I considers the boundary-layer development on two double models of simple ship hulls for which extensive data have been obtained recently. One of these is an elongated ship-like body whose vertical cross-section is everywhere elliptic, with an axes ratio of 3:1. Although there are no sharp edges, the transverse radius of curvature at the keel is large. The wind-tunnel measurements of Groves et al. (1982) over the stern of this model show strong viscous-inviscid interaction and therefore provide an opportunity to test the limits of thin boundary-layer theory. The second hull is a mathematical form, known as the Wigley hull, whose vertical and horizontal cross-sections are parabolas. It has been used extensively in ship hydrodynamics to test various theories for wave resistance and to compare measurements in different towing tanks. Also, it is one of four hulls selected by the International Towing Tank Conference for the Cooperative Experimental Program which seeks to establish a firm data base from measurements in towing tanks. The sharp wedge-shaped keel of this model raises a basic question about the boundary conditions to be imposed there and their influence on the solution. A similar problem also arises at the waterline when double-body calculations are performed for practical hull forms since the sloping sides of the hull then imply a wedge at the waterline plane of symmetry. The recent water-channel measurements of Hatano and Hotta (1982) over the stern of a double Wigley model are used to assess this aspect.

Part II of the paper is concerned with the boundary layer at the intersection of the wavy free surface with the hull. This is a preliminary study in which attention is focussed on the flow at the free surface. A suitable coordinate system for arbitrarily prescribed waves is first identified. The assumption of small deflections of the free surface across the boundary layer then leads to the usual small-crossflow approximations and enables the boundary layer along the wave profile to be calculated independently of the flow below the free surface. Calculations performed for the Wigley hull and a two-dimensional surface-piercing strut at different Froude numbers show interesting wave-related phenomena.

PART I. BOUNDARY LAYERS ON DOUBLE MODELS (SARDA AND PATEL)

1.1 Calculation Method

The numerical method adopted for the double-hull calculations is that of Nash and Scruggs (1976) which has been developed further by Patel and Choi (1980). The three-dimensional boundary-layer equations are solved using the ADI finite-difference scheme. The turbulence model is based on the turbulent kinetic-

energy equation, a prescribed length-scale distribution and the assumption that the directions of the stress and rate-of-strain vectors are coincident. Laminar as well as turbulent boundary layers can be calculated, transition being simulated by activating the turbulence model along a prescribed transition line. The equations are solved numerically up to the wall without using any wall functions. The numerical scheme and the turbulence model have been tested quite extensively in earlier applications (Patel and Choi, 1980; Patel and Baek, 1983) in laminar, turbulent and transitional boundary layers on bodies of revolution at incidence.

Due to the simple geometries of the axisymmetric bodies considered previously, it was possible to use analytical, orthogonal, body-fitted coordinates. In the present application to arbitrary ship hulls, greater generality is achieved by first dividing the hull surface into panels which are not necessarily orthogonal. As shown in Figure 1, the number of panels is fixed in the girthwise direction but the spacing is arbitrary in both directions. Thus, the geometry treatment is quite similar to that in some of the well known potential-flow calculation methods. Although the global coordinates are not orthogonal, the boundary-layer equations are solved in a locally orthogonal system. This is achieved by making a conical development for each element as sketched in Figure 1 and described in detail by Nash and Scruggs (1976).

1.2 The Elliptic Hull

The coordinates of this body are tabulated in Groves et al. (1982). Its major dimensions are shown in Figure 2. The potential-flow pressure distribution used for the boundary-layer calculations was determined by the method of Dawson and Dean (1972) and provided by Dr. Huang of the DTNSRDC.

The boundary-layer calculations were performed with several different step sizes to ascertain grid independence of the solutions. The results discussed here were obtained with 179 axial steps and 20 girthwise steps over the half body below the minor axis, as shown in Figure 2. Plane-of-symmetry conditions were applied along $\theta = 0^\circ$ and 180° and therefore the boundary layer along the keel ($\theta = 90^\circ$) is calculated as a part of the interior solution. The calculations were started a short distance downstream of the nose, using stagnation-point velocity profiles, and transition was imposed at 3 percent of the body length. As in the experiments of Groves et al., the length Reynolds number is 6×10^6 .

Since the measurements were restricted to the stern region $0.719 < X/L < 0.954$, the performance of the calculation method over a large part of the body cannot be assessed. The present solutions showed no unusual features and, in particular, did not indicate any forebody separation around $X/L = 0.04$ and $\theta = 75^\circ$, as had been predicted by Groves et al. using the method of Cebeci et al. (1978). However, as expected from the circumferential pressure gradients, the boundary layer over the forebody thickens along the waterline ($\theta = 0^\circ$ and 180°) and the divergence of the flow along the keel ($\theta = 90^\circ$) maintains a relatively thin boundary layer there. Over the rear, this situation is reversed and the boundary layer over the keel thickens. Eventually, the continued convergence of the external flow into the keel leads to a region of flow divergence near the wall, and the convergence of the near-wall flow from both sides produces a maximum boundary-layer thickness in the vicinity of $\theta = 80^\circ$. As shown in Figure 3, this is already evident at the most upstream measurement station, $X/L = 0.719$. Continuation of the solutions further downstream leads to a rapid growth of the boundary layer along $\theta = 80^\circ$. However, as Figure 4 shows, the predicted velocity profiles elsewhere remain in satisfactory agreement with the measurements. Figures 3 and 4 also indicate that the measured turbulent kinetic energy is considerably smaller than that predicted in the thick boundary layer region. While this may be attributed to the inadequacy of the turbulence model, it is felt that the local breakdown of the calculations around $\theta = 80^\circ$

is due to a strong viscous-inviscid interaction. This is evident from Figure 5 which shows marked departures of the measured pressure distribution from that predicted by potential-flow solutions downstream of $X/L = 0.81$.

The present solutions show the same qualitative features as those of Patel and Baek (1983) on a spheroid at incidence and, as noted there, it is unlikely that the use of the measured pressure distribution would lead to a dramatic improvement in the agreement. The observed disagreements result from a general breakdown of the first-order boundary-layer theory rather than the limitations of any one component of the calculation method.

1.3 The Wigley Parabolic Hull

The coordinates of this body are given by

$$\frac{y}{b} = \pm (1 - \frac{x^2}{L^2})(1 - \frac{z^2}{d^2}) \quad (1)$$

where (x, y, z) are Cartesian coordinates with the origin at the centroid, and the length ($L = 2x$), beam ($2b$), draft (d) ratio is 10:1:0.625 (see Figure 6). Calculations were performed at a length Reynolds number of 8×10^5 , corresponding to the water-channel experiments of Hatano and Hotta (1982).

The potential-flow pressure distribution was calculated using the centerplane source-distribution method of Miloh and Landweber (1980). In the boundary-layer calculations, plane-of-symmetry conditions were imposed along the waterline ($z = 0$) and along a line a short distance above ($z/d = 0.987$) the sharp keel. Laminar flow initial conditions were provided just downstream of the bow, transition was imposed at 5 percent of body length, and 8 unequally-spaced girthwise steps, in the domain $0 < z/d < 0.987$, and 89 axial steps, were used.

Here also, the available data is restricted to the stern and the near wake, $0.9 < X/L < 1.1$ and consequently the performance of the method can be judged only by comparisons of the calculations with the data in this region. From the velocity and turbulent kinetic-energy profiles at $X/L = 0.9$, shown in Figure 7, it is clear that the calculated velocity profiles are in reasonable agreement with measurements except at the keel, where measurements along the local surface normal and in the plane of symmetry (i.e., along the wedge bisector) indicate a thinner viscous layer. Thus, the assumption of a plane of symmetry condition a short distance from the keel is not realistic and since the streamlines diverge from this region and converge into the waterline ($z = 0$) such a boundary condition contaminates the solution over the entire girth. For example, the increasing under prediction of the boundary layer thickness at $X/L = 1.00$ (Figure 8) at all three girthwise positions away from the keel is presumably due to an insufficient crossflow from the assumed boundary condition along the keel.

Although the surface pressure distribution was not measured, the disagreement in the measured and calculated edge velocities, particularly at $X/L = 1.00$, is indicative of local viscous-inviscid interaction. However, the velocity profiles measured with two different orientations of the hot-film probe were somewhat different and therefore definitive conclusions could not be reached in this regard from the comparisons with the set of measured values that are shown here.

As in the case of the elliptic hull, the experimental turbulent kinetic energy is lower than predicted. Also, at $X/L = 1.00$, the measurements show a pronounced peak near the surface and this is followed by a region of nearly constant values. This feature has been observed also in measurements in thick stern boundary layers on other hull forms. A review of this and other characteristics of thick boundary layers has been made by Patel (1982).

PART II. BOUNDARY LAYER AT THE HULL-WAVE INTERSECTION (SHAHSHAHAN AND PATEL)

II.1 Coordinates and Equations

Consider a hull whose surface is given by $y = \pm f(x, z)$ in the Cartesian coordinates (x, y, z) with origin at midships at the undisturbed waterline, as shown in Figure 9. Denote the intersection of the wave with the hull by $z = g(x)$. This wave profile is assumed to be known either from experiment or inviscid-flow theory.

For the hull boundary layer along this wave, we choose an orthogonal coordinate system (ξ, η, ζ) , in which ξ is measured along the wave, η is normal to the hull and ζ is normal to the free surface; see Figure 9.

The physical requirement of zero velocity normal to the free surface implies that within the boundary layer the free surface will be distorted and does not coincide with the η coordinate. However, within the approximations of first-order boundary-layer theory, this distortion can be related to a fictitious crossflow velocity in the ζ direction. Thus, to a first approximation, we assume that the boundary layer along the free surface can be calculated by the small-crossflow equations (see Nash and Patel, 1972):

$$U \frac{\partial U}{\partial \xi} + V \frac{\partial U}{\partial \eta} - \frac{U}{h_\xi} \frac{\partial U}{\partial \xi} + \frac{\partial}{\partial \eta} (\overline{UV}) - \nu \frac{\partial^2 U}{\partial \eta^2} = 0 \quad (2)$$

$$\frac{1}{h_\xi} \frac{\partial U}{\partial \xi} + \frac{\partial V}{\partial \eta} + k_{31} U = 0 \quad (3)$$

$$\begin{aligned} & \frac{U}{h_\xi} \frac{\partial W}{\partial \xi} + V \frac{\partial W}{\partial \eta} + k_{31} W U + k_{13} (U_e^2 - U^2) \\ & + \frac{\partial}{\partial \eta} (\overline{VW}) - \nu \frac{\partial^2 W}{\partial \eta^2} = 0 \end{aligned} \quad (4)$$

where (U, V, W) are the components of mean velocity in the (ξ, η, ζ) directions, \overline{UV} and \overline{VW} are the Reynolds stresses and ν is kinematic viscosity. U_e , the velocity in the ξ direction outside the boundary layer is related to the wave elevation $g(x)$ via the Bernoulli equation:

$$U_e^2 = U_\infty^2 - 2g_0 g \quad (5)$$

where g_0 is the acceleration due to gravity and U_∞ is the stream velocity or ship speed.

The metric coefficients h_ξ , h_η and the coordinate curvatures

$$k_{13} = \frac{1}{h_\xi h_\eta} \frac{\partial h_\xi}{\partial \zeta}, \quad k_{31} = \frac{1}{h_\eta h_\xi} \frac{\partial h_\eta}{\partial \xi} \quad (6)$$

can be related to the hull geometry $f(x, z)$ and the wave profile $g(x)$ using the method of Miloh and Patel (1973) as follows:

$$\begin{aligned} h_\xi^2 &= (1 + f_x^2) + 2f_x f_z g' + (1 + f_z^2) g'^2 \\ h_\eta^2 &= (1 + f_x^2) h'^2 + 2f_x f_z h' + (1 + f_z^2) \\ k_{13} &= - \frac{g'' + D^2(f_z - g'f_x)(f_{xx} + 2g'f_{xz} + g'^2 f_{zz})}{Dh_\xi^3} \\ k_{31} &= - \frac{-h'' + D^2(h'f_z - f_x)(h'^2 f_{xx} + 2h'f_{xz} + f_{zz})}{Dh_\eta^3} \end{aligned} \quad (7)$$

where $D \equiv (1 + f_x^2 + f_z^2)^{-1/2}$

$$\text{and } h' = - \frac{g' + (f_x + g'f_z) f_z}{1 + (f_x + g'f_z) f_x} \quad (8)$$

Equation (8) expresses the orthogonality of ξ and ζ directions.

II.2 Solution Procedure and Results

The small-crossflow approximation uncouples the ξ -momentum equation (2) and the continuity equation (3) from the ζ -momentum equation (4). Hence (2) and (3) can be solved for U and V , and then the crossflow W can be determined from (4). Here, the equations have been solved by the Crank-Nicolson method of Chang and Patel (1975). For turbulent flow, the Reynolds stresses are obtained from the two-layer eddy-viscosity model and transition is simulated by an intermittency function (see Cebeci and Smith, 1974).

Figure 10 shows the wave profiles measured by Shearer and Cross (1965) on a towing-tank model of the Wigley hull (eq. (1) for $z < 0$, $y = b$ for $z > 0$) at three Froude numbers. Calculations were performed along each of these waves by starting with the Blasius solution a short distance from the bow and imposing transition at 5 percent of the length where the models were fitted with tripping devices.

The distributions of the wall shear-stress presented in Figure 11 clearly indicate the influence of the waves. The strong wave system at $Fr = 0.348$ produces a marked oscillation in the stress distribution. Note that the usual procedure of double-body calculations would result in a single unrealistic prediction. These calculations also indicate that there is no separation at the free surface in the range of Froude numbers considered. Thus, the influence of Froude number on the viscous resistance is felt primarily through the changes in the friction distribution and the wetted surface area. Finally, Figure 12 shows the variation of the crossflow angle across the boundary layer at three streamwise positions along the wave for $Fr = 0.348$. As noted earlier, these may be regarded as a measure of the deflection of the free surface through the boundary layer. The three locations have been selected to show the influence of the free-surface curvature which is concave at $x = 2.58$ ft, convex at $x = 15.64$ ft and contains an inflexion point at $x = 9.85$ ft. It is seen that the surface deflections are well correlated with the curvature changes. However, the deflections are small since the body is slender and the waves are not very steep.

The second example is that of a two-dimensional 1.26 ft. long airfoil-like strut which was used by Chow (1967) to demonstrate wave-induced separation. Figure 13 shows the calculated two-dimensional flow pressure distribution in an unbounded stream, converted to a "wave elevation" using equation (5), and the free-surface profiles measured at two Froude numbers with the strut mounted vertically, piercing the free surface, in a hydraulic flume. According to Chow, the strut was designed to avoid separation in an unbounded stream, i.e., at large depths. However, he observed localized separation in the free surface experiments just beyond the wave troughs (at $x = 0.59$ ft. for $Fr = 0.26$ and at $x = 0.83$ ft. for $Fr = 0.43$) although the flow remained attached at greater depths. Unfortunately, no further information is available to guide the boundary-layer calculations beyond these flow-visualization results.

In view of the low Reynolds numbers in these experiments, the calculations were performed with the stagnation-point profile at the bow, and transition was assumed to take place at the pressure minimum in the two-dimensional case and at the first wave trough in the case of the free surface. The corresponding distributions of the wall shear-stress coefficient are shown in Figure 14. The results for two-dimensional flow indicate no separation, as noted by Chow. However, separation is predicted at $x = 0.69$ ft. for $Fr = 0.26$ and $x = 0.92$ ft. for $Fr = 0.43$, in qualitative agreement with the observations. Although the agreement can be improved by manipulating the transition location, we believe the present calculations are sufficient to demonstrate the phenomenon of local separation under the influence of steep free-surface waves.

CONCLUSIONS

The two double-body calculations presented in Part I indicate that the coordinate system used to describe arbitrary ship forms is satisfactory. Both demonstrate that the present method can be used to calculate the boundary-layer development over a large part of the hull. The prescription of the initial conditions and transition do not appear to present any special difficulties for the examples presented.

Comparisons with the data over the two sterns show that the calculation method yields satisfactory results in regions where the boundary layer remains thin. The method breaks down in an area near the keel of the elliptic stern due to strong viscous-inviscid interaction. On the parabolic stern, this interaction is weak and confined to a smaller region near the trailing edge but the solution is sensitive to the plane-of-symmetry boundary conditions applied near the sharp keel. Since, in both cases, there is no catastrophic failure of the method, it is of interest to develop practical criteria which can be used to abandon first-order boundary-layer calculations and adopt more general solution procedures for the flow over the stern. Calculations need to be performed for other hull forms in order to establish such criteria.

In Part II we have demonstrated not only the feasibility of performing boundary-layer calculations along the intersection of a prescribed wave with an arbitrary hull, but also the possibility of local separations induced by steep waves. Such separations, when present, would imply a strong interaction between the viscous and wave resistance components, in addition to the influence of the wave system on the frictional resistance. Although the experimental evidence is rather meagre, the theory suggests that strong bow waves may provoke an early separation with quite important consequences in towing-tank tests and in the study of scale effects.

The generalized geometry treatment used in Part I enables the specification of boundary conditions along an arbitrary free surface. The methodology of Part II can therefore be incorporated to develop a three-dimensional boundary-layer calculation method for ship hulls at non-zero Froude numbers. Such a study is in progress. However, a major stumbling block at the present time is the lack of a reliable inviscid-flow method that can be used to predict the wave profiles and the corresponding hull pressure distribution with the accuracy required for boundary-layer calculations.

ACKNOWLEDGEMENTS

This research was sponsored by the General Hydromechanics Research Program of the Naval Sea Systems Command, administered by the David W. Taylor Naval Ship Research and Development Center under Contract No. N00014-82-K0200. Partial support for the study reported in Part II was also provided by the Office of Naval Research under Contract No. N0014-82-K0069. The authors are grateful to Dr. T.T. Huang of the DTNSRDC for providing the potential-flow calculations for the elliptic hull, and to Professor Hatano and Dr. Hotta of Hiroshima University for the data on the Wigley hull.

REFERENCES

- Cebeci, T. and Smith, A.M.O. (1974) "Analysis of Turbulent Boundary Layers", Academic Press, New York.
- Cebeci, T., Chang, K.C. and Kaups, K. (1978) "A General Method for Calculating Three-Dimensional Laminar and Turbulent Boundary Layers on Ship Hulls", McDonnell Douglas Corp., Report MDC J7998. Also, Proc. 12th Sym. on Naval Hydrodynamics, Washington, pp. 188-208, 1979.
- Chang, K.C. and Patel, V.C. (1975) "Calculation of Three-Dimensional Boundary Layers on Ship Forms", Iowa Institute of Hydraulic Research, The University of Iowa, IHR Report No. 178.

Chow, S.K. (1967) "Free-Surface Effects on Boundary-Layer Separation on Vertical Struts", Ph.D. Dissertation, The University of Iowa.

Dawson, C. and Dean, J. (1972) "The XYZ Potential flow Program", Naval Ship Research and Development Center, NSRDC Report 3892.

Groves, N.C., Belt, G.S. and Huang, T.T. (1982) "Stern Boundary-Layer Flow on a Three-Dimensional Body of 3:1 Elliptic Cross-Section", David Taylor Naval Ship Research and Development Center, Report DTNSRDC-82/022.

Hatano, S. and Hotta, T. (1982) "Turbulence Measurements in the Thick Boundary Layer and Near Wake of a Three-Dimensional Body", Hiroshima University, personal communication.

Hirschel, E.H. et al. (1983) Proc. EUROVISC Workshop on Three-Dimensional Boundary Layers, Berlin, 1 April 1982. To be published by Springer-Verlag.

Larsson, L. (Ed.) (1981) "Proceedings of the SSPA-ITTC Workshop on Ship Boundary-Layers 1980", Swedish Maritime Research Center, SSPA, Report No. 90.

Miloh, T. and Landweber, L. (1980) "Ship Centerplane Source Distribution", J. Ship Research, Vol. 24, pp. 8-23.

Miloh, T. and Patel, V.C. (1973) "Orthogonal Coordinate Systems for Three-Dimensional Boundary Layers, with Particular Reference to Ship Forms", J. Ship Research, Vol 17, pp. 50-58.

Nash, J.F. and Scruggs R.M. (1976) "An Implicit Method for the Calculation of Three-Dimensional Boundary Layers on Fuselage Configurations", Lockheed Georgia Transonic Technology Report LG76ER0199.

Nash, J.F. and Patel, V.C. (1972) "Three-Dimensional Turbulent Boundary Layers", SBC Tech. Books, Atlanta.

Patel, V.C. and Choi, D.H. (1980) "Calculation of Three-Dimensional Laminar and Turbulent Boundary Layers on Bodies of Revolution at Incidence", Turbulent Shear Flow 2, Springer-Verlag, pp. 199-217.

Patel, V.C. and Baek, J.H. (1983) "Calculation of Boundary Layers and Separation on a Spheroid at Incidence", Proc. 2nd Sym. Numerical and Physical Aspects of Aerodynamic Flows, Cal. State Uni., Long Beach.

Patel, V.C. (1982) "Some Aspects of Thick Three-Dimensional Boundary Layers", Proc. 14th Sym. on Naval Hydrodynamics, Ann Arbor.

Shearer, J.R. and Cross, J.J. (1965) "The Experimental Determination of the Components of Ship Resistance for a Mathematical Model", Trans. Royal Inst. Nav. Arch., Vol. 107, pp. 459-473.

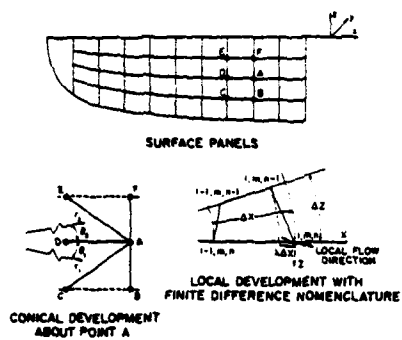


FIGURE 1. GEOMETRY REPRESENTATION.

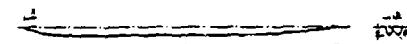


FIGURE 2. THE 3:1 ELLIPTIC HULL. $L = 3.07 \text{ m}$, $B = 0.242 \text{ m}$, $D = 0.0809 \text{ m}$.

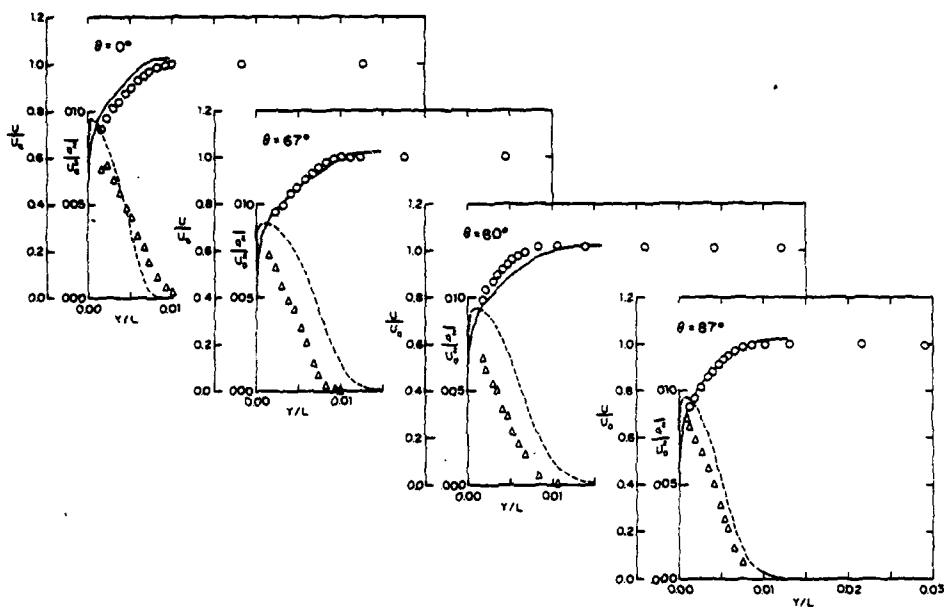


FIGURE 3. ELLIPTIC HULL: VELOCITY AND TURBULENT KINETIC-ENERGY PROFILES AT $X/L = 0.719$

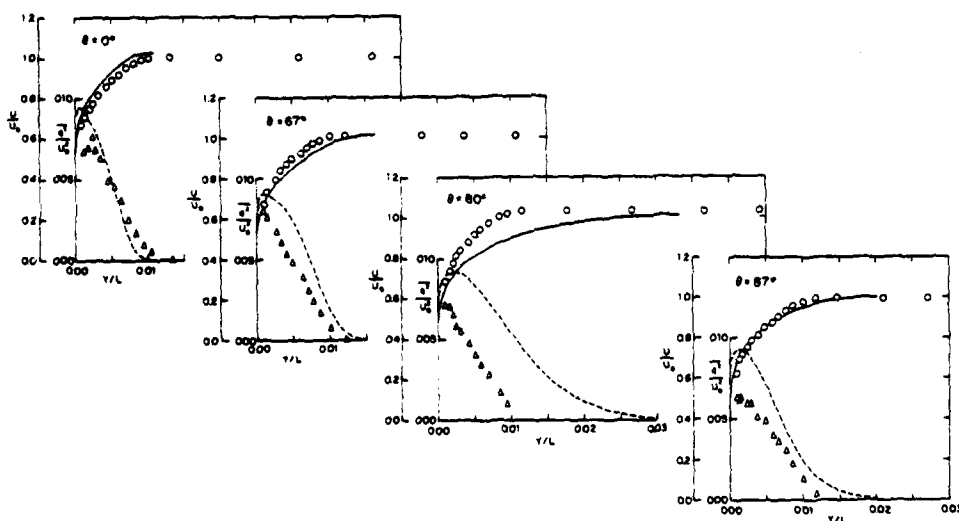


FIGURE 4. ELLIPTIC HULL: VELOCITY AND TURBULENT KINETIC-ENERGY PROFILES AT $X/L = 0.810$.

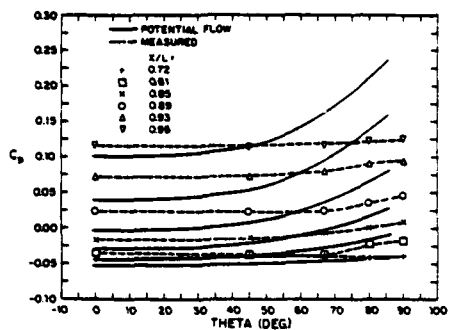
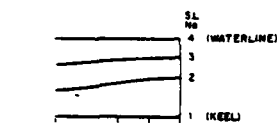


FIGURE 5. ELLIPTIC HULL: POTENTIAL-FLOW AND EXPERIMENTAL PRESSURE DISTRIBUTIONS OVER THE STERN



SCHEMATIC OF THE WIGLEY HULL



INVISCID STREAMLINES ON STERN OF WIGLEY HULL FROM DATA OF HATANO AND NOTTA

FIGURE 6 THE WIGLEY PARABOLIC HULL

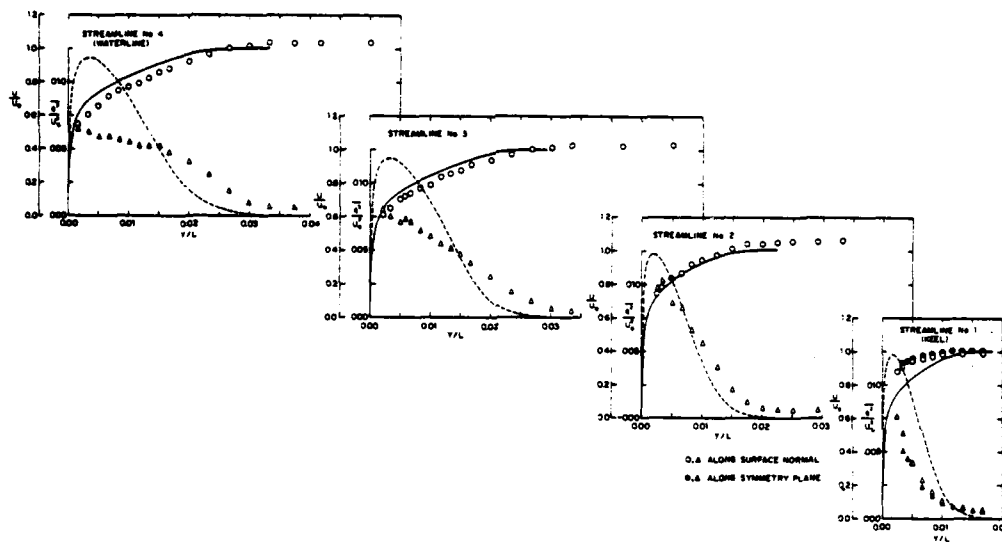


FIGURE 7 PARABOLIC HULL: VELOCITY AND TURBULENT KINETIC-ENERGY PROFILES AT $x/L = 0.90$

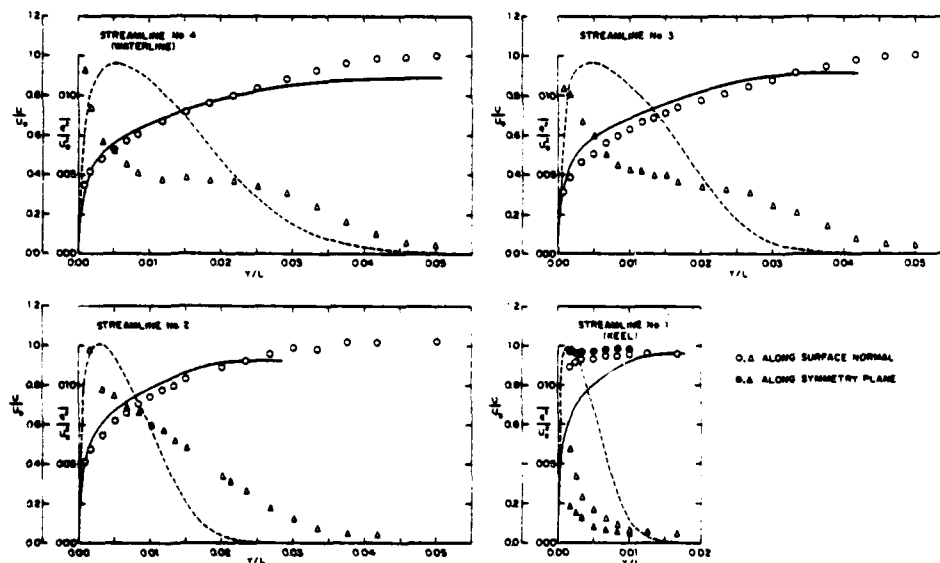


FIGURE 8. PARABOLIC HULL: VELOCITY AND TURBULENT KINETIC-ENERGY PROFILES AT $x/L = 1.00$

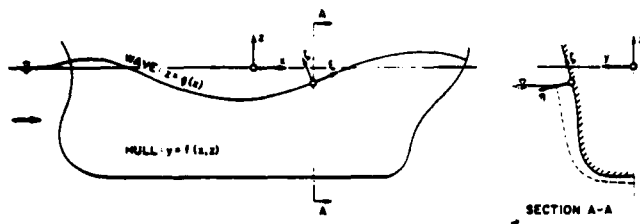


FIGURE 9. SHIP (x, y, z) AND BOUNDARY LAYER (ξ, η, ζ) COORDINATES.

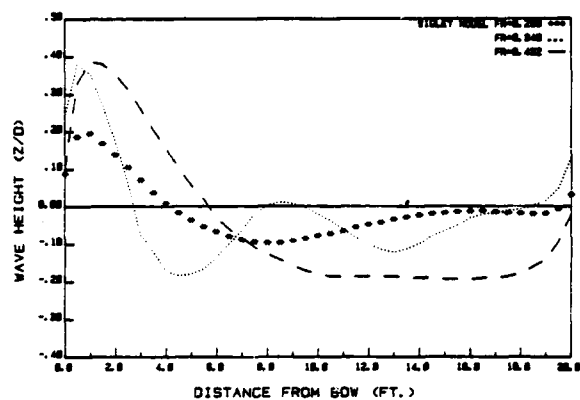


FIG. 10 WAVE PROFILES ON THE WIGLEY HULL

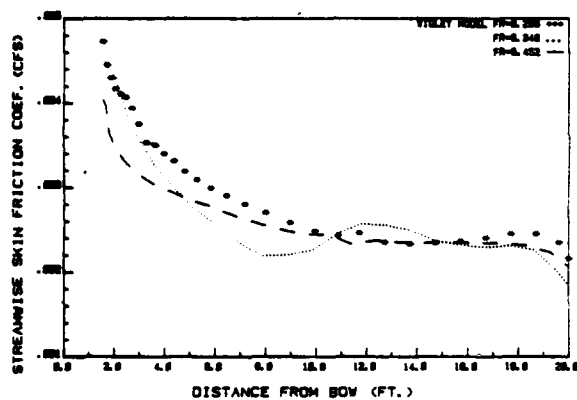


FIG. 11 SKIN-FRICTION COEF. ALONG THE WAVES, WIGLEY HULL

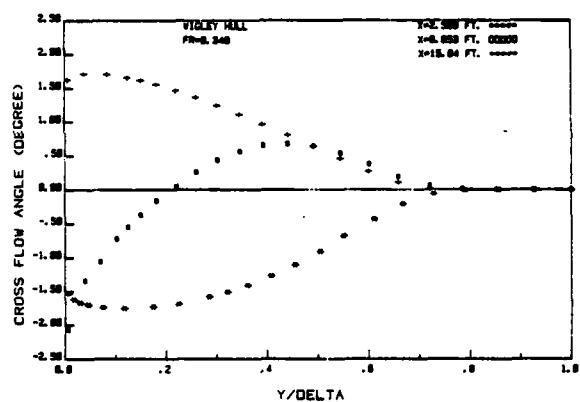


FIG. 12 CROSS FLOW ANGLES ACROSS THE BOUNDARY LAYER

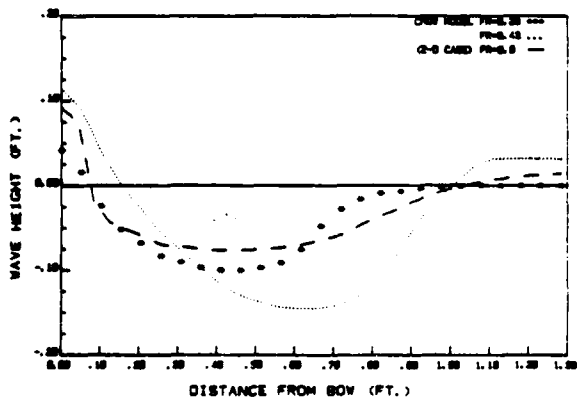


FIG. 13 PRESSURE DISTRIBUTION & WAVES ON A 2-D STRUT

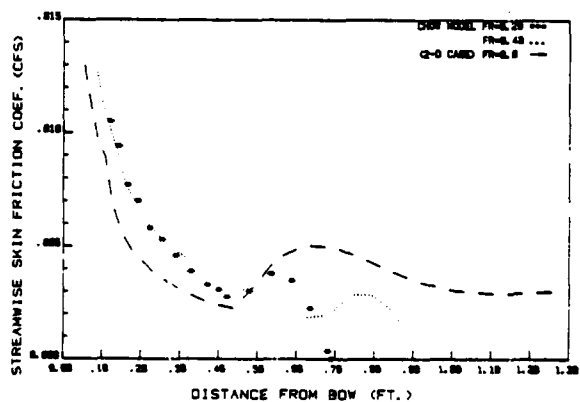


FIG. 14 SKIN FRICTION COEFFICIENT ON THE STRUT

SECONDARY CURRENTS IN A STRAIGHT CHANNEL FLOW AND THE RELATION TO ITS ASPECT RATIO

H. Nakagawa

I. Nezu *

Department of Civil Engineering
Kyoto University
Kyoto 606, Japan

and

A. Tominaga

Department of Civil Engineering
Gunma University
Kiryu, Gunma 376, Japan.

ABSTRACT

The initiation and maintenance mechanism of multi-cellular secondary currents in a straight wide-river is quite unknown at present. This study investigated experimentally the existence of secondary currents over a flat bed by varying the aspect ratio of channel. It was suggested strongly that an initiation of cellular secondary currents may be motivated by the mutual interaction between the secondary currents and the sand bed.

INTRODUCTION

Many river engineers have hitherto suggested that there might exist cellular secondary currents in a straight wide-river. Vanoni(1946) pointed out that the spanwise distribution of sediment concentration varied periodically in wide open channel, and he inferred that this fact might have been caused by cellular secondary currents. Matthes(1947) envisaged that there might exist a strong upward-current, like a tornado, near the river bed, and also that it developed up to the free surface and then became a so-called 'boil' which was observed as a vortex-ring-like swollen water surface.

Kinoshita(1967) found by means of aerial stereoscopic survey (Cameron effect) of flood rivers that a boil became a low-speed zone and, at both spanwise sides with the spacing of twice the flow depth h , high-speed zones were formed. He suggested then that there might exist cellular secondary currents in a straight river which had a pair of counter-rotating streamwise vortices with a vortex diameter of about h (see Fig. 1). After the flood had gone, Karcz(1973) found, on the other hand, that longitudinal ridges and troughs which are called 'sand ribbons' were formed periodically on the river bed. Thus, he suggested an existence of cellular secondary currents.

On the basis of these suggestions, Fig. 1 envisages a behaviour of river flow. An investigation of cellular secondary currents, i.e. three-dimensional flow patterns, is very important in hydraulic engineering, as well as in basic hydromechanics, because they might cause three-dimensional sediment transport and bed forms in river. However, the initiation and maintenance mechanisms of cellular secondary currents in a straight wide-channel are quite unknown at present.

We(1982) have firstly measured cellular secondary currents in straight open-channel flow (Case K: the channel width $B=30$ cm, the flow depth $h=4.0$ cm, the average bulk velocity $U_m=32.0$ cm/s, the Reynolds number $Re=U_m h/\nu=1.3 \times 10^4$ and the Froude number $Fr=0.51$), by making use of the X-type hot-films (DISA 55R61). Longitudinal ridge elements of 8 m

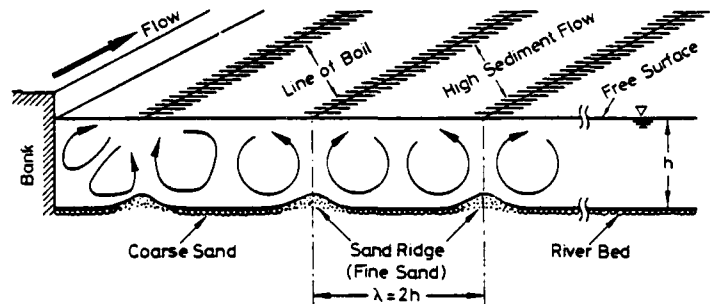


Fig. 1. Envisaged flow-pattern of multi-cellular secondary currents in a straight wide river.

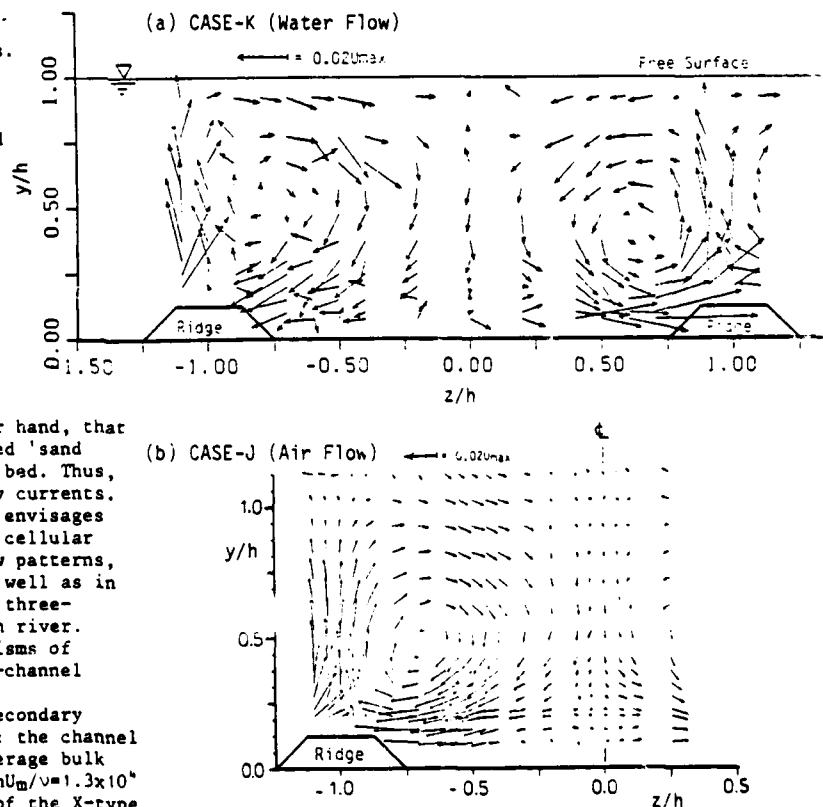


Fig. 2. Comparison of cellular secondary currents in (a) water-flow with those in (b) air-flow. Both the Reynolds numbers are nearly equal to 1.3×10^4 .

*) Presently Alexander von Humboldt fellow, Inst. of Hydromechanics, Univ. of Karlsruhe, Karlsruhe, West Germany

long with a 45°-trapezoid cross section of 5 mm thick and 20 mm wide were attached onto the smooth channel bed in the spanwise spacing of $\lambda=2h=8$ cm. This simulated the longitudinal ridges and troughs of river bedform, i.e. sand ribbons, as shown in Fig. 1. Fig. 2(a) shows the flow pattern of cellular secondary currents (V, W) obtained experimentally. A pair of cellular secondary currents is seen clearly. Speaking roughly, the upflow (V>0) and downflow (V<0) appear over the ridge and trough, respectively, and they behave as a circular vortex motion in which the diameter is equal to h and the position of the circular center is nearly equal to $y/h=0.5$. The upflow is stronger rather than the downflow, and the secondary currents are larger near the bed than near the free surface. These features support well the flow mechanism envisaged by Kinoshita (1967) and Karcz (1973). It should be noticed that, although the velocity $\sqrt{V^2 + W^2}$ of the secondary currents is within only 5% of the maximum mainstream velocity U_{max} , its experimental values show comparatively large scatters. The experimental values of the turbulence quantities indicated also large scatters. We have then judged that it was fairly difficult to examine the equations of mean vorticity, mean flow energy and turbulent energy experimentally and to discuss the maintenance mechanism of cellular secondary currents even qualitatively.

Next, we (1983 a) could measure more accurately all three components of the velocity in air duct flow (Case J: the half vertical width h of the duct, which corresponds to the flow depth, is $h=4.0$ cm, $U_m=5$ m/s and $Re=1.3 \times 10^4$), by making use of X hot-wires. In order to simulate sand ribbons on the bed, the same longitudinal ridge elements as used in water experiment of Fig. 2(a) were attached onto both the lower and upper bottoms of the duct. Fig. 2(b) shows the flow pattern of secondary currents in air flow. It should be noticed that the relative magnitudes of the secondary currents normalized by U_{max} are roughly equal to each other in both Case J (air duct) and Case K (water channel) except for near the free surface, in spite of the large difference between their absolute values, i.e. $U_{max}=540$ cm/s (Case J) and $U_{max}=35$ cm/s (Case K). We must emphasize here that the intensity of secondary currents is surely strengthened near the free surface by its existence in comparison of Fig. 2(a) with Fig. 2(b). However, the flow patterns of cellular secondary currents are similar to each other in both cases. Hence, we can conclude that Case J makes a good reproduction of cellular secondary currents in open channel flow which is shown in Fig. 1. Then, its turbulent structure was examined through the equations of vorticity and mean flow energy. As the results, the Reynolds stress term, $(\partial^2/\partial x^2 - \partial^2/\partial y^2)vw$, is nearly balanced with the production term of vorticity, $\partial^2/\partial y \partial z (\bar{v}^2 - \bar{w}^2)$, in most of the cell structure. The wall shear stress becomes larger on the troughs than on the ridges. A more detailed discussion is given in our recent paper (1983 a).

Such a spanwise non-homogeneity of flow may cause secondary currents, or the reverse may be true. However, an initiation mechanism of cellular secondary currents and sand ridges over a uniformly flat channel bed is quite unknown at present. Three possibilities of this initiation mechanism are considered, as follows:

- (1) The aspect ratio $\alpha \equiv B/h$ of channel must be selected as an even number, irrespective of wall properties. It is only a kind of eigen-value problem.
- (2) An initiation of cellular secondary currents is motivated by the mutual interaction between the secondary currents and the sand bed.
- (3) An existence of free surface motivates cellular secondary currents.

On the basis of our preliminary water flow experiments (1982, 83 b) and the numerical calculations of Naot-Rodi (1982) who took the effect of free surface into account, we can attain a hypothesis that the existence of free surface is not an essential cause of cellular secondary currents, but it only promotes their intensity near the free surface, as seen in Fig. 2.

In the light of the above, the present study is to investigate the existence of secondary currents over a flat solid bed by varying the aspect ratio $\alpha \equiv B/h$ of channel and to examine their initiation mechanism. That is, we will examine experimentally which of (1) and (2) has a more possibility.

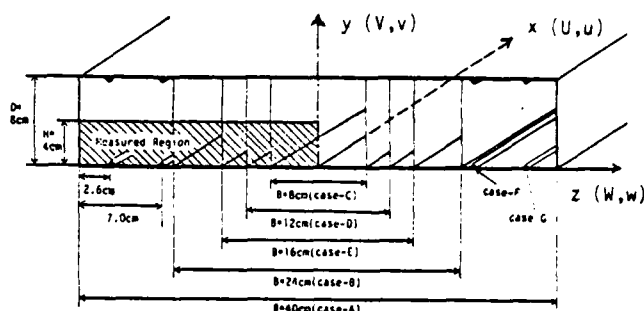


Fig. 3. Test section of the channel and its coordinate system.

APPARATUS AND PROCEDURE

Experiments were conducted in a straight channel 6m long with a rectangular cross section of 8 cm x 40 cm (see Fig. 3). Air was delivered to the channel by a centrifugal fan by way of a 40 cm-square settling chamber 165 cm in length and a contraction section 100 cm in length. In order to promote the development of flow, rough sandpapers were attached onto both lower and upper bottoms at the entrance of channel, and the test section was set up at 5 m downstream from its entrance. Two partition plates of 8 cm wide and 6 m long were set into the channel as both side-walls, and thus the spanwise width B of channel could be changed arbitrary (see Fig. 3).

The half vertical width h of channel which corresponds to the flow depth of open channel, was fixed to be 4.0 cm. In this experiments, the aspect ratio $\alpha \equiv B/h$ was chosen to be equal to 10 (Case A), 6 (Case B), 4 (Case E), 3 (Case D) and 2 (Case C), as shown in Fig. 3. Of course, Case C is a square-cross channel. The maximum mainstream velocity U_{max} was fixed to be 7.1 m/s, in all cases. The Reynolds number $Re \equiv 4RU_m/\nu$ (R is the hydraulic radius) became equal to $(3-5) \times 10^4$.

In order to examine in detail the turbulent structure of secondary currents, the velocity measurements were done at about 300 measuring points in the 1/4 cross section of y-z plane, as shown in Fig. 3. Two velocity pairs of (u,v) and (u,w) could be measured accurately by X-type hot-wires (DISA 55P61). The hot-wire signals were recorded in digital form by using an AD-converter, with the sampling size $N=20,000$ and the sampling frequency $f=2,000$ Hz. Then, some statistical analyses were carried out by a large digital computer at the Data Processing Center, Kyoto University.

EXPERIMENTAL RESULTS AND DISCUSSION

Mean Primary Velocity

Fig. 4 shows the contours of the iso-velocity of the mean primary velocity $U(y,z)$ normalized by U_{max} in the square channel (Case C). For a comparison, the previous data of Melling & Whitelaw (1976) are shown at the right side of Fig. 4. They could measure water flows in a square channel by making use of a Laser-Doppler anemometer (LDA). The present hot-wire data coincide fairly well with their LDA data, although the distributions of the latter are a little more peaked than those of the former. This difference may be due to the shorter channel length of Melling & Whitelaw (i.e. 147R, compared with 250R for the present experiment). The iso-velocity lines bulge outwards along the corner bisector. This indicates that the square channel flow is three-dimensional in all cross section.

Fig. 5 shows the variations of $U(y,z)$ against the spanwise direction, z. The value of $U(z)$ at the center elevation of $y/h=1.0$ for both Cases A and B increases firstly with z/h and then attains a constant. That is to say, the central zone of $|z/h| < 3$ (Case A; $B/h=10$) and 1 (Case B; $B/h=6$) is considered to be a two-dimensional flow. As defined later, the diameter ℓ_2 of the bottom vortex of the secondary current is shown in Fig. 5. It should be noticed that the spanwise variation of $U(z)$ has a somewhat minimum value at the position of $(1-2)h$ farther from the side-wall, that is, in the bottom-vortex. As mentioned later, this minimum position corresponds to the position of an upflow of secondary current and a minimum wall shear stress. This result is one of the most important features

when an initiation mechanism of cellular secondary currents is investigated.

Secondary Currents (Longitudinal Vortex)

Fig. 6(a)-(e) are vector descriptions of the mean velocity V and W of secondary currents for all cases. A secondary current towards the corner of the channel is recognized clearly in all cases. The maximum value of the secondary current velocity $U_s \equiv \sqrt{V^2 + W^2}$ is nearly equal to $0.015U_{max}$, which is in a good agreement with the result of Melling & Whitelaw (1976). This value is, however, smaller than the magnitude of the multi-cellular secondary currents which were shown in Fig. 2.

This well-known secondary current (we call it 'corner secondary flow') flows along the corner bisector, i.e. 45° -line, irrespective of the aspect ratio B/h , and it produces only a pair of longitudinal vortices. One vortex over the corner bisector is called 'side-vortex', and the other vortex under the bisector is called 'bottom-vortex'. Of course, in the square channel of Case C, the side- and bottom-vortices are well symmetrical with each other in regard to the bisector.

The pattern of the side-vortex is completely confined by the side wall and thus it is seldom affected by the aspect ratio $\alpha = B/h$ of channel. On the other hand, the bottom-vortex is much affected by the aspect ratio α . As α increases, the size of the bottom-vortex becomes larger and then tends to attain a constant. In order to evaluate the size of the bottom-vortex, the position of the vortex center and the vortex-diameter are defined as horizontal distances l_1 and l_2 , respectively, from the side-wall. l_1 and l_2 could be determined easily from Fig. 6, although the vortex-diameter l_2 was evaluated roughly. These experimental data are shown in Fig. 7, together with the corresponding Case-name. When α is smaller than 2, a side-vortex in the case of $\alpha > 2$ can be regarded as a bottom-vortex by the exchange of B for h . The vortex-diameter l_2 increases linearly with the aspect ratio α when $\alpha \leq 3$. However, when $\alpha > 3$, its increase is much suppressed, and then l_2 tends to attain a constant, i.e. $l_2/h \approx 2$. The distance l_1 of the vortex center is nearly equal to a half of l_2 . Also, the elevation of the vortex center attains a half depth, i.e. $y/h = 0.5$, with an increase of the aspect ratio α .

We must emphasize here that multi-cellular secondary currents observed in Figs. 1 and 2 cannot be recognized in the central zone of Cases A and B. This indicates that cellular secondary currents are produced directly neither by the corner secondary flow, nor by the variation of the aspect ratio. That is to say, the initiation mechanism (1) of cellular secondary currents mentioned in the Introduction is considered to be minor possibility.

Friction Velocity (Wall Shear Stress)

Firstly, we have examined the law of the wall, i.e. the log-law, which is described by

$$U/U_* = 5.75 \log (U_* y/\nu) + 5.5 \quad (1)$$

The friction velocity U_* can be evaluated by the least-square method so that the experimental values of U for $U_* y/\nu < 0$ may coincide with Eq. (1). An example of these velocity distributions is plotted in Fig. 8 for Case A. Except for very near the side-wall (i.e. Run 25), the mean primary velocity $U(y)$ agrees very well with Eq. (1). A good agreement could be also obtained for the other cases. That is, the log-law is satisfied near the bed irrespective of the existence of corner secondary flow, although the side-wall effect appears farther from the bed and near the side-wall. Therefore, the friction velocity U_{*2} could be easily evaluated from the log-law, and its spanwise distributions are shown in Fig. 9.

Next, we have developed a new method by which the friction velocity can be evaluated directly. A single-sensor hot-wire was set precisely at $y = 2$ mm from the wall instead of a Preston-tube, and its output voltage E was calibrated carefully by the friction velocity U_* which was obtained from the pressure gradient $\partial P/\partial x$ of the channel flow, i.e. $U_* \equiv \sqrt{R \cdot \partial(-P/\rho)/\partial x}$. Then, the Calib-

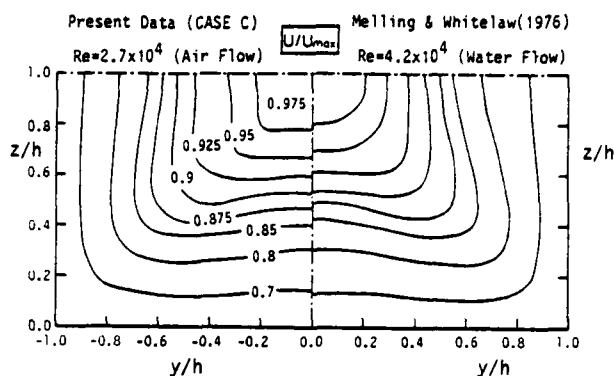


Fig. 4. Comparison of the present hot-wire data of $U(y,z)$ -isovet lines with the LDA data by Melling & Whitelaw.

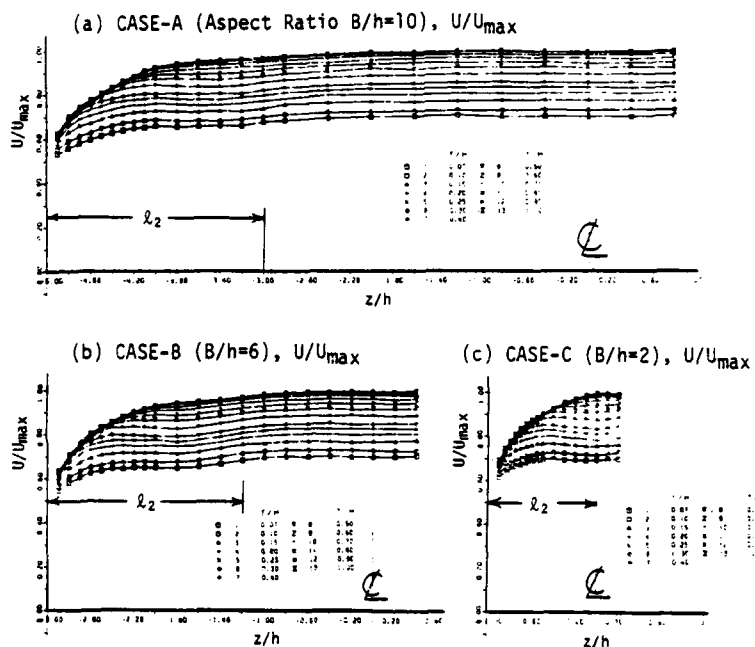


Fig. 5. Variations of mean primary velocity $U(y,z)$ against the spanwise direction, z .

ration curve between E and U_{*1} could be described very well by

$$E^2 - E_0^2 = A \cdot U_{*1}^n \quad (2)$$

in which E_0 is the output voltage at $U_{*1} = 0$, and A and n are the calibration coefficients.

By using the calibration curve of Eq. (2), the spanwise distributions of the friction velocity U_{*1} could be obtained directly, and they are shown in Fig. 9. The experimental values of U_{*1} and U_{*2} are normalized by their spanwise average values \bar{U}_{*1} and \bar{U}_{*2} , respectively, in Fig. 9. Then, $\bar{U}_{*1}/\bar{U}_{*2}$ was equal to 0.98, 0.98 and 0.96 for Cases A, B and C, respectively. Both the distributions of U_{*1} and U_{*2} coincide well with each other for all cases. This indicates the validity of the above-mentioned evaluation methods of the friction velocity.

For the square channel of Case C, the peak of the friction velocity appears not at the channel center $z=0$, but at the position of $|z|=0.5h$. In the same manner, the friction velocity attains a mild but important peak at the position of $1.2h$ for Case A and $0.8h$ for Case B from the side-wall. And then, it decreases somewhat and increases again in the central zone where a two-dimensional flow is established as shown in Figs. 5 and 6. Fig. 9 shows also the experimental curves obtained by Leutheusser (1963). He could measure the friction velocity by making use of a Preston-tube for the same aspect ratios as Cases B and C. The present values are in a good agreement with his data.

This mild peak and valley distribution of the fric-

tion velocity in the bottom-vortex whose size is l_2 , could be also observed in open-channel flow by the authors (1983 a), although the amplitude of peak/valley was somewhat larger in open-channel than in closed channel. The same feature of the friction velocity has been recently found by Knight et al. (1982) in both open and closed channels.

It should be noticed that the valley region of U_* at the position of $(1-2)h$ from the side-wall corresponds to the upflow ($V > 0$) region of the bottom-vortex which is produced by the corner secondary flow. In multi-cellular secondary currents shown in Fig. 2, the authors (1982, 83 a) have also found the same noticeable feature that the friction velocity or wall shear stress is depressed at the place where an upflow ($V > 0$) occurs, while it is promoted at the place where the downflow ($V < 0$) occurs.

Turbulence Characteristics

We have analyzed the distributions of turbulence intensities u' , v' and w' , and also Reynolds stress $-\overline{uv}$ and $-\overline{uw}$ for all cases.

Turbulence Intensities.

The present experimental data of u' , v' and w' in the square channel have agreed well with many previous data. For example, Fig. 10 shows the contours of turbulence intensity u'/U_{\max} in the square channel, and its corresponding contours of the primary mean velocity have been already indicated in Fig. 4. Surely, the present distribution of u'/U_{\max} is in a good agreement with the result of Melling & Whitelaw (1976), although there are a little quantitative differences between the two. The contour lines of u' are symmetric with each other in regard to the corner bisector, and they bulge more strongly towards the corner than the contour lines of the primary mean velocity U . This suggests that the turbulence intensities are affected more strongly by the corner secondary flow than the primary mean velocity is affected, and vice versa. A close interrelation between the turbulence characteristics and the secondary currents can be explained by the vorticity equation (e.g. see our paper (1983 a)). The contour lines of v' and w' showed a good anti-symmetric distribution with each other in regard to the corner bisector for the square channel, which can be easily obtained by its boundary condition. They also bulged towards the corner, although their bulges were smaller than that of u' .

Even when the aspect ratio α became greater than 2, the turbulence intensities u' , v' and w' showed a similar distribution to those of the square channel ($\alpha=2$), i.e. Fig. 10, in the side-wall zone whose size is l_2 , as shown in Fig. 7. In the central zone where

$$|z|/h \leq (B/2 - l_2)/h \approx (\alpha-4)/2 \quad (3),$$

u'/U_* , v'/U_* and w'/U_* indicated a two-dimensional distribution and they agreed well with the results of Laufer (1951) which were obtained at $z=0$ for the aspect ratio of $\alpha=24$.

Reynolds Stresses. Fig. 11 is the vertical distributions of $-\overline{uv}/U_{\max}^2$ for Case A. They indicate a linear distribution in the central zone, i.e. $|z|/h < 3$ from Eq. (3), and thus a two-dimensional turbulent structure can be recognized here again. The values of $-\overline{uv}$ deviate somewhat upwards from this linear distribution in the upflow ($V > 0$) region of $|z|/h=3.0-3.6$, and then they deviate downwards from it due to the side-wall effect. This deviation is,

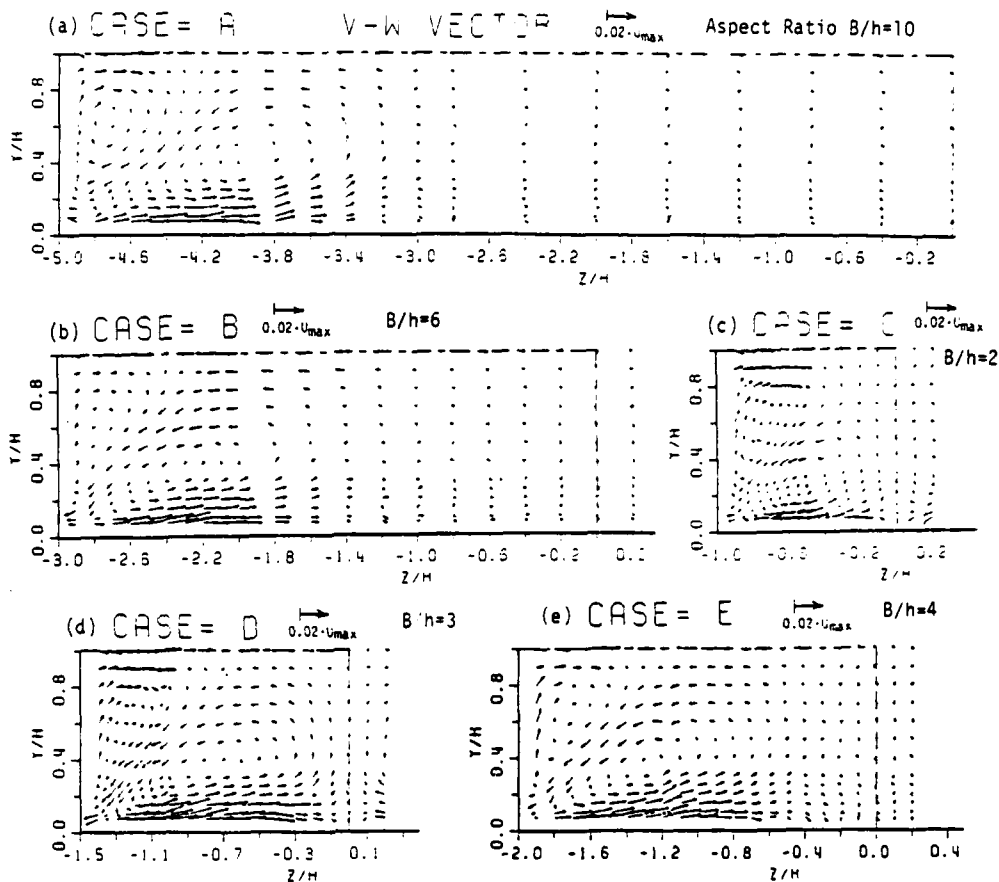


Fig. 6. Vector descriptions of the secondary currents (V, W) for all cases.

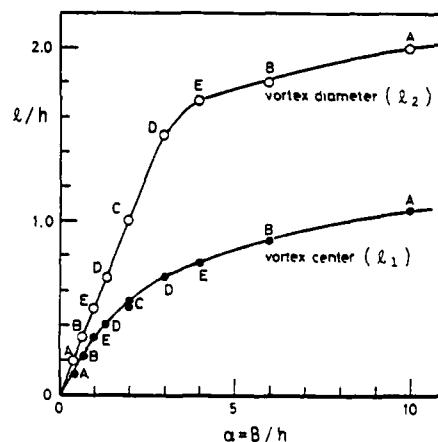


Fig. 7. Size of the bottom-vortex.

however, very small near the boundaries of $y/h=0$ and 1, although it becomes largest near the half depth of $y/h=0.5$. Therefore, this feature suggests an interrelation between such a deviation of $-\overline{uv}$ and a vertical mean velocity V .

Fig. 12 shows an example of the spanwise distribution of $-\overline{uw}/U_{\max}^2$. Of course, $-\overline{uw}$ should be equal to zero if any secondary current does not exist. This feature is satisfied well in the central zone of $|z| < h$, which is obtained from Eq. (3) for Case B. It should be noticed that the gradient of $-\overline{uw}$ against z is positive, i.e. $\partial(-\overline{uw})/\partial z > 0$, in the upflow ($V > 0$) region of $|z|/h=1.4-2.0$ (see Fig. 6). This feature could be also obtained in the multi-cellular secondary currents of Fig. 2. Then, the authors (1983 a) verified that the loss of mean flow energy convected by the upflow was nearly balanced with the gain of energy done by the transverse Reynolds stress $-\overline{uw}$.

Vorticity. Figs. 13 and 14 show the contours of the turbulence intensity difference $(\overline{w^2} - \overline{v^2})$ and the streamwise vorticity $\xi \equiv (\partial w / \partial y - \partial v / \partial z)$, respectively, for Case A. The production term $\partial^2(\overline{v^2} - \overline{w^2}) / \partial y \partial z$ of vorticity is not at all equal to zero in the side-wall zone, and as the result it produces the vorticity ξ only in this zone, as seen in Fig. 14. As has been expected in Fig. 6, it is understood from Fig. 14 that the intensity of the bottom-vortex is stronger than that of the side-vortex. On the other hand, in the central zone of $|z|/h < 3$, the vorticity is nearly equal to zero.

To sum up, cellular secondary currents are not produced in the central zone of solid smooth channel with the aspect ratio $\alpha = B/h > 4$.

Preliminary Experiment on Initiation Mechanism of Cellular Secondary Currents

The above-mentioned fact suggests strongly that an initiation of multi-cellular secondary currents of Fig. 1 is motivated directly neither by the existence of side wall, nor by the existence of free surface. The former produces originally the corner secondary flow, while the latter strengthens its flow near the free surface (1983a).

Therefore, we must search the initiation mechanism

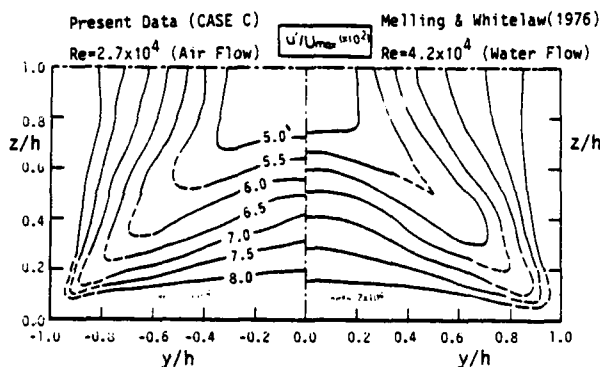


Fig. 10. Comparison of the present hot-wire data of u' -isolines with the LDA data obtained by Melling & Whitelaw (1976).

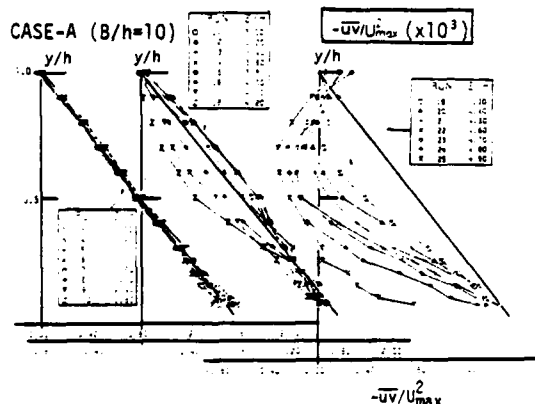


Fig. 11. Distributions of the Reynolds stress $-\overline{uv}$ against the vertical direction, y , for Case A.

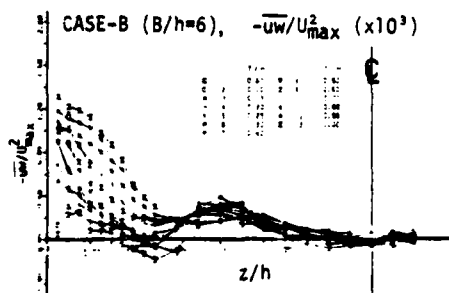


Fig. 12. Distributions of the transverse Reynolds stress $-\overline{uw}$ against the spanwise direction, z , for Case B.

CASE-A (Aspect Ratio $B/h=10$)

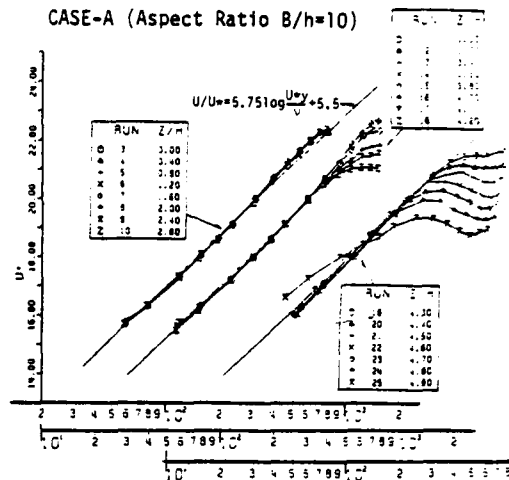
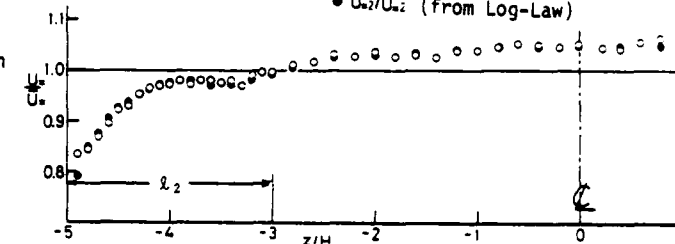
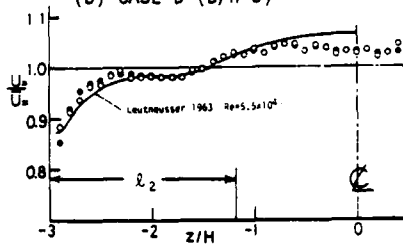


Fig. 8. Law of the wall, i.e. Log-law as a parameter of spanwise direction in the channel of $B/h=10$.

(a) CASE-A ($B/h=10$) $\circ U_w/\overline{U}_w$ (from Pressure Gradient)
 $\bullet U_w/\overline{U}_w$ (from Log-Law)



(b) CASE-B ($B/h=6$)



(c) CASE-C ($B/h=2$)

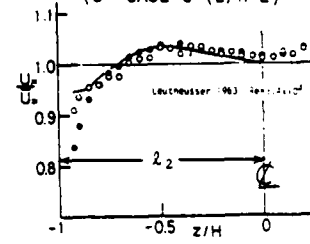


Fig. 9. Variations of friction velocity $U_w(z)$ against the spanwise direction, z .

CASE-A ($B/h=10$), $(\overline{w^2} - \overline{v^2})/U_{max}^2 \times 10^3$

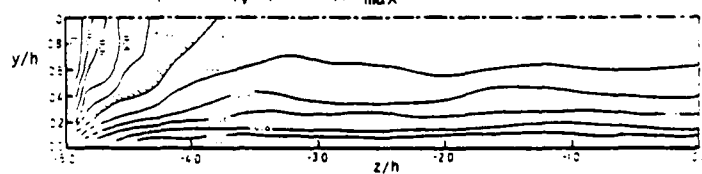


Fig. 13. Iso-lines of $(\overline{w^2} - \overline{v^2})/U_{max}^2$ in the channel of $B/h=10$.

CASE-A ($B/h=10$), $\xi h/U_{max} \times 10$

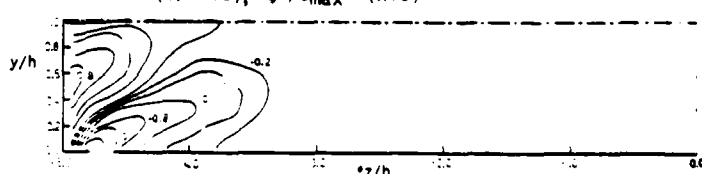


Fig. 14. Iso-lines of the streamwise vorticity ξ in the channel of $B/h=10$.

of cellular secondary currents anywhere. Then, we found an important feature in the spanwise distribution of the wall shear stress $\tau_0 = \rho U_*^2$, as mentioned previously. That is, U_* attains a mild peak in the side-wall zone of air duct, as seen in Fig. 9. This feature was also recognized in open channels by Knight et al. (1982) and the authors (1983 a). Thus, it is considered that this variation of U_* is created by the corner secondary flow. If the channel is composed of a movable flat-bed, the sediment transport varies spanwisely in the side-wall zone, and as the result a first pair of longitudinal sand ridge and trough may be produced. Of course, the peak zone of U_* is scoured to become a trough. Sands on the trough are swept out both downstream (by U) and at the side of the trough (by W), and then they are gathered to form a sand ridge.

In order to simulate this situation and verify the validity of this initiation mechanics, we have conducted two experiments of Cases F and G, in which a longitudinal rod with a triangular cross section of the height $k=0.088h$ was attached as a first longitudinal ridge onto the bed of the channel with the aspect ratio $B/h=10$ (Case A), as shown in Fig. 3. In Case F, the longitudinal rod was set at the position of the minimum wall shear stress, which could be obtained from Fig. 9(a). For a comparison with Case F, its rod of Case G was set at the position of the maximum downflow ($V<0$), which could be obtained from Fig. 6(a). The condition of Case F corresponds to the formation of a first longitudinal sand ridge.

Fig. 15 shows the vector descriptions of the secondary currents (V,W) for Cases F and G. Its ridge height k is comparatively small, but a large variation of the flow patterns is recognized in comparison with Fig. 6(a). For Case F, a strong upflow ($V>0$) is created over the ridge, and a new pair of cellular secondary currents appear on each side of the ridge. In correspondence to it, the wall shear stress varied spanwisely, and in turn it was suggested that this renewed variation of wall shear stress might produce a second pair of longitudinal ridge and trough. As seen in Case F, the flow pattern of the secondary currents over the ridge is similar to that of the cellular secondary currents of Fig. 2, although the vortex at the right side of the ridge is yet weaker than the vortex at its left side, probably because of the absence of a second longitudinal ridge. On the other hand, Case G indicates a comparatively complicated flow pattern. It should be noticed that the side-vortex of this case disappears due to the existence of the longitudinal rod, as contrasted with Cases A and F. This suggests that, if the longitudinal ridge is set on the bottom near the corner, the corner secondary flow is depressed or destroyed by its ridge.

From the above results, it is considered that an initiation of cellular secondary currents is motivated by the mutual interaction between the secondary currents and the sand bed. The wall shear stress τ_0 has a mild peak in the side-wall zone, due to the existence of the corner secondary flow which is caused by the non-homogeneity of turbulence, i.e. $\partial^2(\overline{v^2} - \overline{w^2})/\partial y \partial z \neq 0$ as shown in Fig. 13. This peak and valley of τ_0 produces a spanwise variation of the sediment transport and then a first longitudinal sand ridge is formed. In turn, this sand ridge creates a pair of cellular secondary currents. And then, these currents produce a second sand ridge. After this mutual interaction, a fully developed and hydrodynamic equilibrium state of the flow and the bedform will be established in the whole cross section of channel, as shown in Figs. 1 and 2. Although the aspect ratio of channel is not an essential cause of these initiation, a final configuration of the flow and the bedform will be re-arranged self-consistently by the aspect ratio. Also, the existence of free surface may promote this interaction process, but it does not seem to produce cellular secondary currents originally.

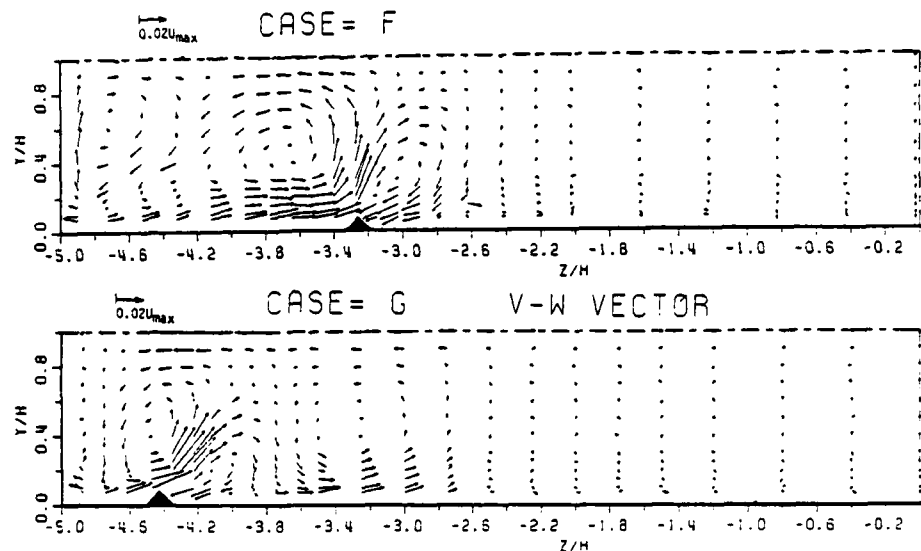


Fig. 15. Vector descriptions of the cellular secondary currents (V,W) in the channel with a first longitudinal ridge element.

CONCLUDING REMARKS

In this paper we have investigated the existence of secondary currents over a smooth solid bed by varying the aspect ratio of channel, and then examined their initiation mechanism. The main findings obtained from the above are as follows:

- (1) The present data of the turbulent structure in square channel coincide well with the previous data obtained by Melling & Whitelaw (1976) and the others.
- (2) A pair of longitudinal vortices, i.e. corner secondary flow, appear only in the side-wall zone.
- (3) The size of the vortex over the corner bisector becomes constant irrespective of the aspect ratio B/h , while the size of the vortex under its bisector increases with B/h and then it approaches a constant.
- (4) Cellular secondary currents are not produced in the central zone of solid channel with $B/h > 4$.
- (5) The bed shear stress attains a mild peak in the side-wall zone.

Among the above results, (5) is the most important feature to explain an initiation mechanism of the cellular secondary currents which are observed in straight alluvial channel flow. A sand bed of alluvial channel will be scoured initially at the position where the bed shear stress attains a peak in the side-wall zone. As the result, a longitudinal sand ridge will be produced. In turn, a new cellular secondary current will be created in the neighbourhood by this sand ridge. Eventually, cellular secondary currents will be produced in all the cross section of channel, by these mutual interaction of the flow and the bedform.

Therefore, more detailed investigations will be necessary in water flow, in order to examine such a hypothesis of the initiation mechanism of cellular secondary currents and also the effects of the free surface (Froude number) and the bed roughness on it.

REFERENCES

- Karcz, I. (1973), *Fluvial Geomorphology* (ed. M. Morisawa) pp. 149-173.
- Kinoshita, R. (1967), *Photographic Surveying*, vol.6, pp.1-17 (in Japanese).
- Knight, D.W., Patel, H.S., Demetriou, J.D. and Hamed, M.E. (1982), *Euromech 156*, Istanbul.
- Laufer, J. (1951), *NACA, Tech. Notes*, No. 1053.
- Leutheusser, H.J. (1963), *ASCE, HY-3*, vol.89.
- Matthes, G.H. (1947), *Trans. Amer. Geophy. Union*, vol.28, pp. 255-265.
- Melling, A. and Whitelaw, J.H. (1976), *J. Fluid Mech.*, vol.78, pp.289-315.
- Nakagawa, H., Nezu, I. and Ooishi, Y. (1982), *JSCE, II*.
- Nakagawa, H. and Nezu, I. (1983 a), submitted to *ASCE*.
- Nakagawa, H., Nezu, I., Tominaga, A. and Wakai, T. (1983 b) *Proc. 27th Japanese Conf. on Hydraulics*, pp.591-596.
- Naot, D. and Rodi, W. (1982), *ASCE, HY-8*, vol.108, p.948.
- Vanoni, V.A. (1946), *Trans. ASCE*, vol.111, pp.67-133.

SOME EFFECTS OF ROTATION ON TURBULENT BOUNDARY LAYERS

by

H.T. WITT, J.H. WATMUFF and P.N. JOUBERT
Mechanical Engineering Department
University of Melbourne

ABSTRACT

Turbulence measurements are presented for low Reynolds number turbulent boundary layers developing in a zero pressure gradient. The effects of rotation on these layers are examined and a comparison is made with zero rotation results.

INTRODUCTION

The present investigation in the University of Melbourne Rotating Wind Tunnel is a continuation of the work presented by Watmuff, Witt and Joubert (1983). It was shown that mean velocity profiles measured in a boundary layer rotating about a spanwise axis, were effected by the rotation from the buffer region outwards. The data were empirically described in terms of a logarithmic law with altered constants. These constants were shown to scale with an Ekman number formed by $\Omega\nu/u_\tau^2$. The experimental arrangement is shown in Fig. 1.

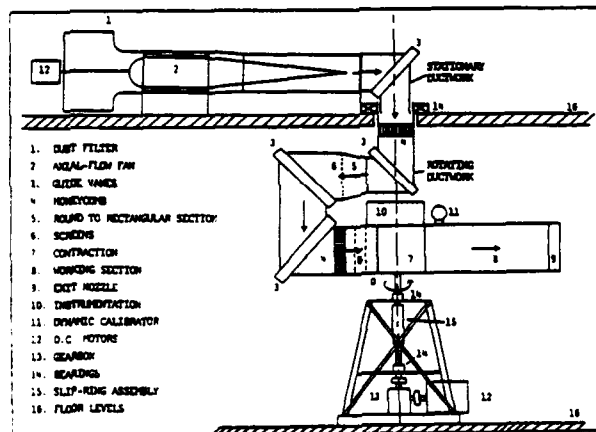


Fig.1 Experimental arrangement.

While the previous work was done mainly with pressure probes and only a few profiles were measured with hot-wires, now all profiles have been taken with normal hot-wires in order to reveal the effect of rotation on turbulence quantities.

HOT-WIRE ANEMOMETRY

The anemometers used were of the constant temperature type, as described by and Perry and Morrison (1971a) and Perry (1982). The wires were made of Wollaston wire with an etched length of about 1mm and a platinum core of about 5 μ m. The distance between wires in X-wire probes was between 0.3 and 0.7mm.

In the case of crossed-wires the output voltages were matched by suitable analogue addition and subtraction of the voltages to produce signals E_u and E_v

that were optimally sensitive to u and v , respectively. The adjustments were made when shaking the wires, first in the streamwise direction, then in the cross-stream direction. The wires were then calibrated dynamically by shaking them sinusoidally following Perry and Morrison (1971b) and Morrison, Perry and Samuel (1972). This technique evaluates the system sensitivities directly without relying on any assumed heat transfer laws or measured wire angles.

For small perturbation it is assumed that

$$\frac{\partial u}{\partial E_u} = \frac{u_{rms}}{e_{u,rms}}, \quad \frac{\partial v}{\partial E_v} = \frac{v_{rms}}{e_{v,rms}}$$

where u_{rms} is the rms value of the velocity perturbation. If the turbulence intensity at a point in the layer where a measurement is taken is low (less than 10% say) linearity of the hot-wire voltages can be assumed, i.e. the sensitivity is constant for the full perturbation, being equal to the sensitivity at its mean value.

To eliminate one source of error in measuring in regions with high turbulence intensity, such as when taking a profile close to a wall, the signals were passed through an analogue lineariser, based on the following considerations.

The sensitivities $\partial u/\partial E_u$ and $\partial v/\partial E_v$, determined by the above mentioned sinusoidal shaking technique, can be approximated with great accuracy by second order polynomials,

$$\partial u/\partial E_u = B + 2CE_u + 3DE_u^2$$

and

$$\partial v/\partial E_v = R + SE_v + TE_v^2$$

where the constants are evaluated by least squares curve fit. Integration of these expressions gives

$$E_{u,lin} = u(E_u) = A + BE_u + CE_u^2 + DE_u^3$$

$$E_{v,lin} = v(E_u, E_v) = P + QE_u + (R + SE_v + TE_v^2)E_u$$

i.e. the linear output voltages $E_{u,lin}$ and $E_{v,lin}$ are generated by passing the matched voltages E_u and E_v through an analogue circuit that generates the desired polynomials. The constants of integration are derived from static data points.

After the lineariser the quantities $E_{u,lin}$, $E_{v,lin}$, $e_{u,lin}$, $e_{v,lin}$ are measured by an analogue circuit, typically integrated over a period of 30 seconds. The averaged quantities are then fed into a computer for data reduction.

The main reason for processing the data with analogue circuits is that it allows much faster data acquisition than sampling the hot-wire voltages with A/D converters connected to digital computers. Because of the 'spiky' nature of the anemometer voltages it is necessary to take a very large number of discrete samples before convergence is achieved when digital data

acquisition is used. In the authors' opinion analogue data processing has become very attractive in recent years, due to improvements in reliability and accuracy of modern electronic computational circuits.

The effect of using a lineariser versus assuming that the sensitivity is constant for (small) perturbations around a mean velocity is shown in Figs. 2 and 3. It is seen that the mean velocity profiles differ appreciably for the two methods only close to the wall, i.e. in the buffer region and early logarithmic region where turbulence intensity is high and excursions from the mean are large, a small difference is discernible. The turbulence intensity is seen to be about 5% higher at the peak when linearity is assumed when compared to using the lineariser.

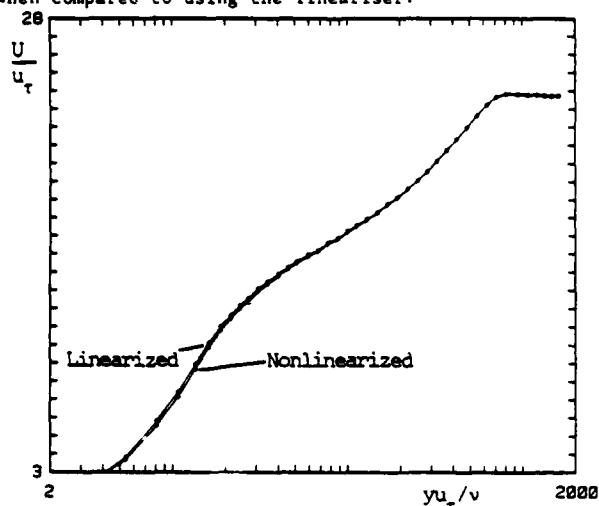


Fig. 2 Mean velocity profiles measured with normal hot-wire, with and without lineariser.

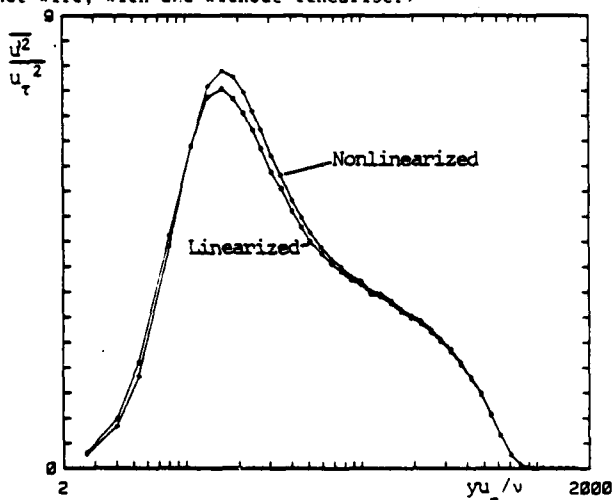


Fig. 3 Streamwise turbulence intensity measured with and without lineariser.

COMMENTS ABOUT OTHER EXPERIMENTAL TECHNIQUES

To obtain good collapse of data close to the wall it is necessary to determine the wall distance with great accuracy. This was done by viewing the wires in a microscope with a graticule in the eyepiece. The arrangement is seen in Fig. 4 and a typical photograph of the view, without graticule, is shown in Fig. 5.

It is estimated that the wire can be placed with an accuracy of about 0.01mm. Also it can be checked whether the wire is parallel to the wall - and some wires with a bow that is considered too large are rejected.

Very close to the wall, however, even a small bow in the wire makes it difficult to say exactly where the effective centre of the wire is, so that profiles measured with two different wires may not collapse exactly in this region.

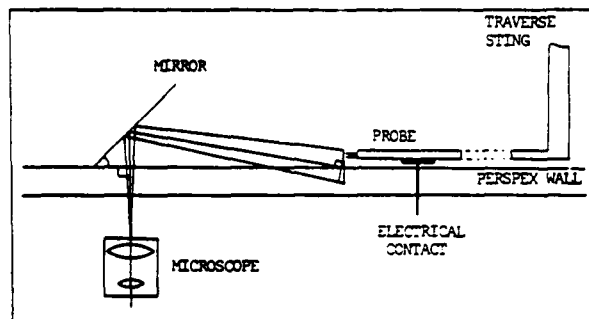


Fig. 4 Optical arrangement to determine wall distance.



Fig. 5 Hot-wire and its reflection in the wall.

When the tunnel is spinning the probe is slightly deflected, of the order of 0.2mm, due to centrifugal forces. The wall distance can still be determined with great accuracy, however, because of a small electrical button that is set up to just touch the probe when the wall distance is the same as that with the tunnel stationary. This contact also revealed that vibrations of the probe were small, of the order of 0.02mm when the tunnel is rotating.

The same optical system was used to check that the Preston tube always was flush against the wall.

All the following results have been reduced with the wall distance as measured with the microscope and with the shear velocity as measured with a Preston tube calibrated in the smooth-walled pipe described in Henbest (1983). The pipe calibration was within about 0.5% of Patel's (1965) calibration over most of the range except for very low Reynolds numbers. No alterations at all were done to y or u_τ to achieve smoother data.

COMPARISON OF MEAN VELOCITY PROFILES MEASURED WITH PITOT TUBES AND HOT WIRES

Before seriously considering the turbulence quantities, a comparison was made between mean velocity profiles obtained with a Pitot tube and a hot-wire, (refer Fig. 6) for the tunnel stationary. The agreement is seen to be excellent except in the buffer region where no attempt of carrying out a wall correction on the Pitot tube data has been made. The hot-wires also show a wall effect, only much closer to the wall, refer Fig. 7. The data follow the trend as reported by Alcaraz and Mathieu (1975). After the wire left the electric button the mean velocity, as indicated by the wire, fell before rising, while the turbulence intensity rose all the time.

Occasionally a profile did not agree with Pitot tube results and a calibration afterwards revealed that there had been drift, so the data were rejected.

When the tunnel was rotated the mean velocity profiles still showed reasonable agreement with Pitot tube results, the largest deviation occurring in the destabilised layer, where deviations of up to a few percent were encountered, (see Fig. 8). This could be caused by errors accumulated in the iterative process

used to determine the static pressure distribution, following the procedure outlined by Johnston et al., (1972).

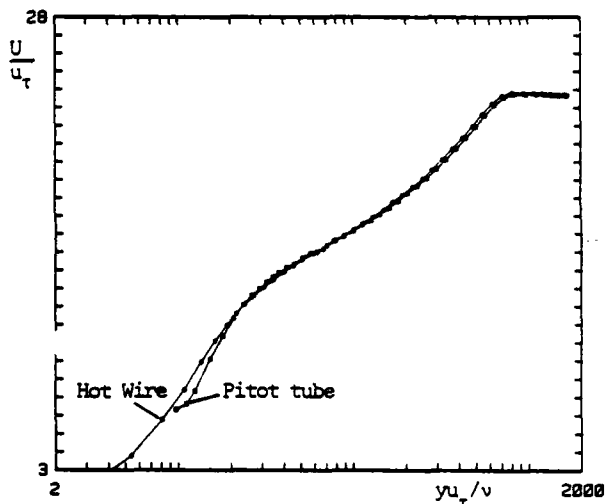


Fig. 6 Mean velocity profiles measured with Pitot tube and hot-wire, tunnel stationary.

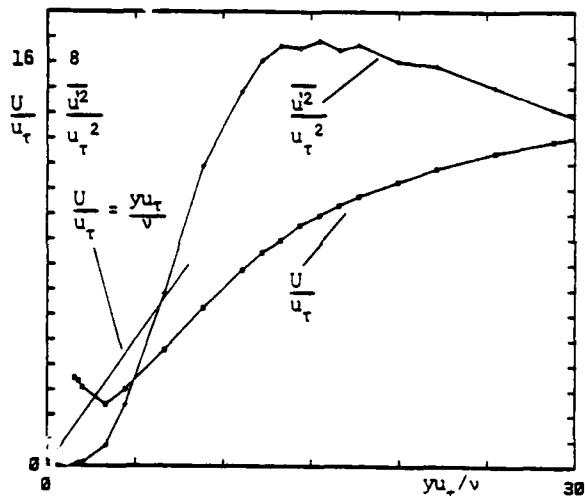


Fig. 7 Wall effect on mean velocity and streamwise turbulence intensity measured with hot-wire.

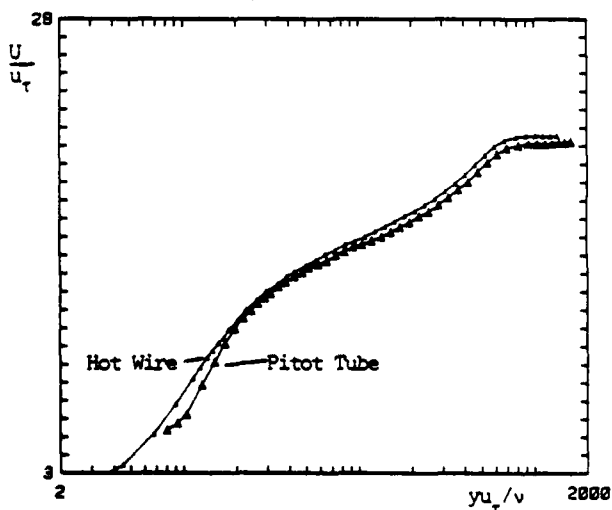


Fig. 8 Mean velocity profiles measured with Pitot tube and hot-wire, tunnel rotating, destabilised layer (leading edge).

RESULTS OBTAINED WITH NORMAL HOT-WIRES

The effect of rotation at each streamwise station on the streamwise turbulence intensity, non-dimensionalised with wall variables, is shown in Figs. 9a-f. As expected the destabilised layer shows a higher and the stabilised layer shows a lower streamwise turbulence intensity in the outer region than the corresponding zero rotation case. At each station the inner region of the intensity profiles (yu_t/v less than 16) is the same for the stationary, destabilised and stabilised cases with the peak value occurring at the same location. Close to the trip wire the three profiles are still very similar for a long way into the region where the mean velocity data shows apparent logarithmic variation with wall distance, (Watmuff et al. (1983)).

The streamwise development of the streamwise turbulence intensity versus $\log yu_t/v$ is shown in Figs. 11a-c. In spite of the accurate determination of wall distance the \pm are some profiles that stand out in the region close to the wall. This is caused by the difficulty in determining the effective wall distance for wires close to the wall where even a small bow causes some uncertainty.

For the stationary and stabilised cases, from the wall out to values of yu_t/v of about 40 or 50, the profiles vary very little with streamwise distance and free stream velocity.

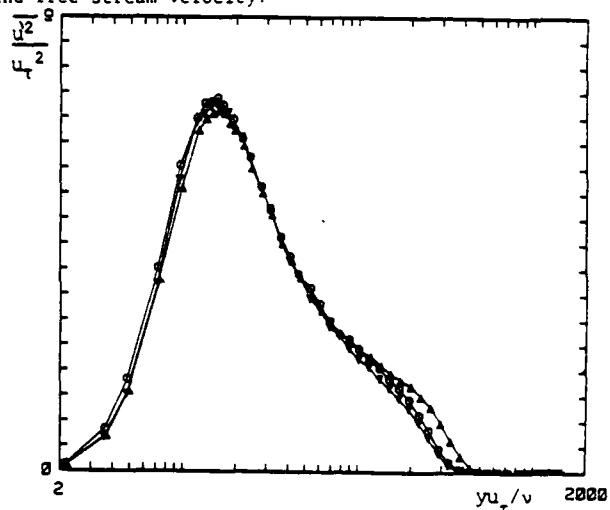


Fig. 9a Non-dimensionalised streamwise turbulence intensity, free stream velocity $U_\infty = 7.5$ m/s, distance downstream from trip wire $x = 0.30$ m, station 1, $Re = 610$ in zero rotation layer.

\circ = zero rotation layer
 Δ = destabilised layer, $\Omega = 1$ rev/sec
 ∇ = stabilised layer, $\Omega = 1$ rev/sec

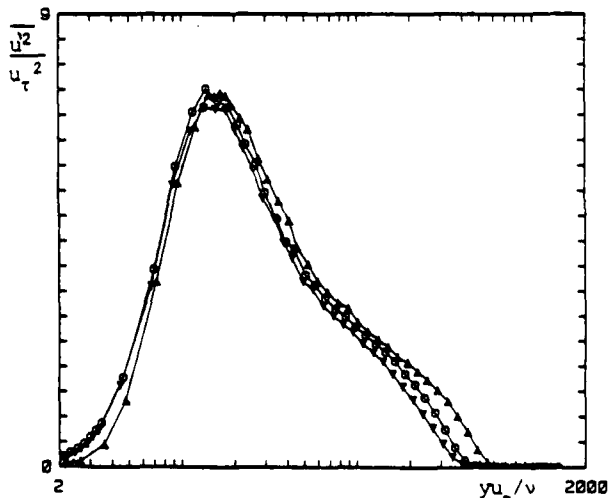


Fig. 9b Same as Fig. 9a, $x = 0.53$ m, station 2, $Re = 830$ in zero rotation layer.

The streamwise development for the stationary profiles against y/δ (where δ is the boundary layer thickness) is shown in Fig. 10. The profiles look very similar to each other but show a definite pattern with streamwise development.

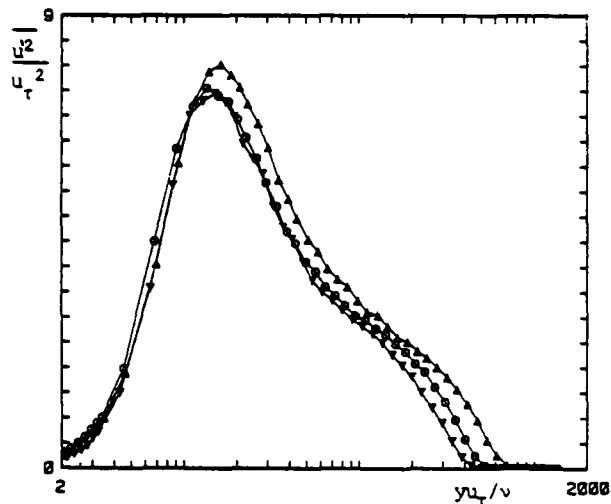


Fig. 9c Same as Fig. 9a, $x = 0.76\text{m}$, station 3, $R_\theta = 1100$ in zero rotation layer.

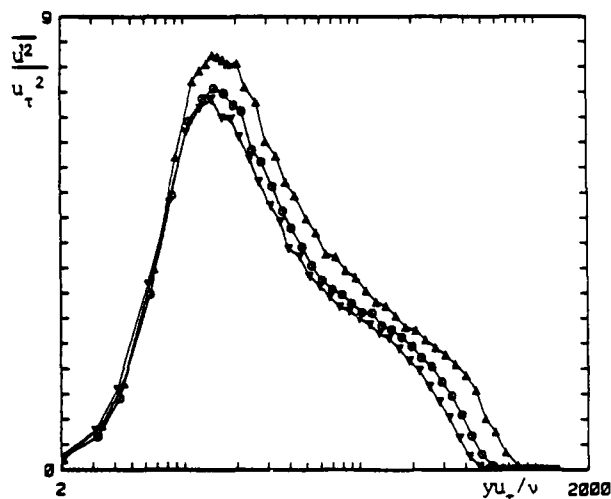


Fig. 9d Same as Fig. 9a, $x = 0.98\text{m}$, station 4, $R_\theta = 1300$ in zero rotation layer.

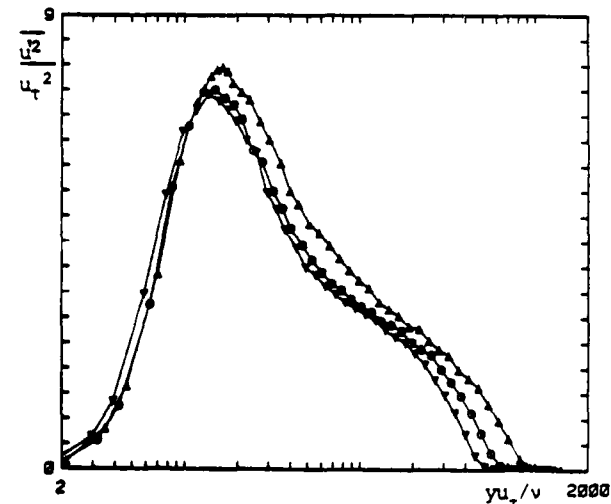


Fig. 9e Same as Fig. 9a, $x = 1.21\text{m}$, station 5, $R_\theta = 1500$ in zero rotation layer.

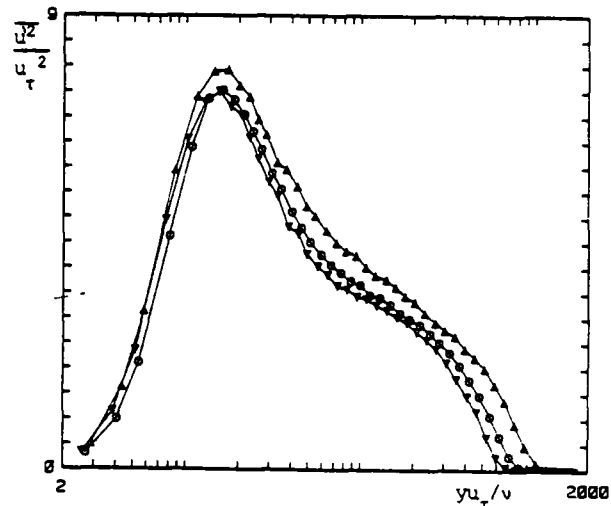


Fig. 9f Same as Fig. 9a, $U_m = 10\text{m/s}$, $x = 1.21\text{m}$, station 5, $R_\theta = 2000$, in zero rotation layer.

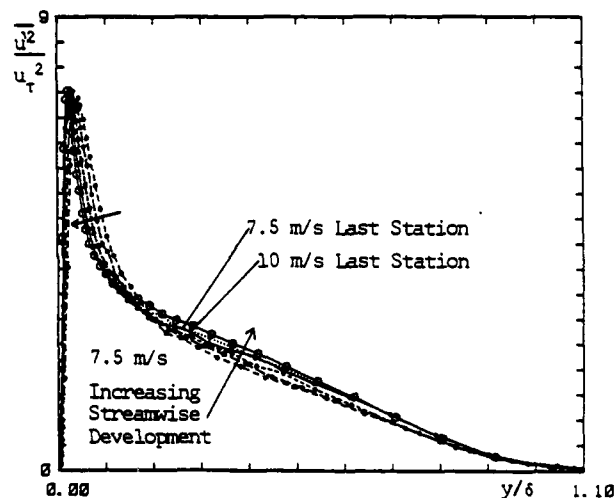


Fig. 10 Non-dimensionalised streamwise turbulence intensity versus wall distance non-dimensionalised with boundary layer thickness. Development with increasing streamwise distance, 7.5 m/s, last station at 10 m/s.

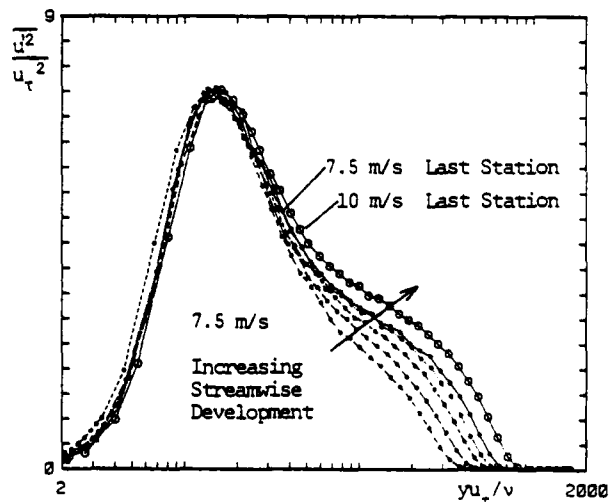


Fig. 11a Streamwise turbulence intensity for zero rotation layers. Development with streamwise distance at 7.5 m/s and last station at 10 m/s.

In the destabilised layers the influence of rotation is seen to have an effect into the region below the peak values. There is an apparent increase in the peak values with increasing streamwise distance until the last few profiles, which have similar values. In particular the last two stations at 7.5 m/s are almost identical, which may indicate full layer development. It should be noted, that Watmuff et al. (1983), reported that the skin friction coefficient for the destabilised layers showed large spanwise variations. These variations were observed to be smaller close to the centreline where the profiles were taken, nevertheless there could be some uncertainty in the value of u_τ .

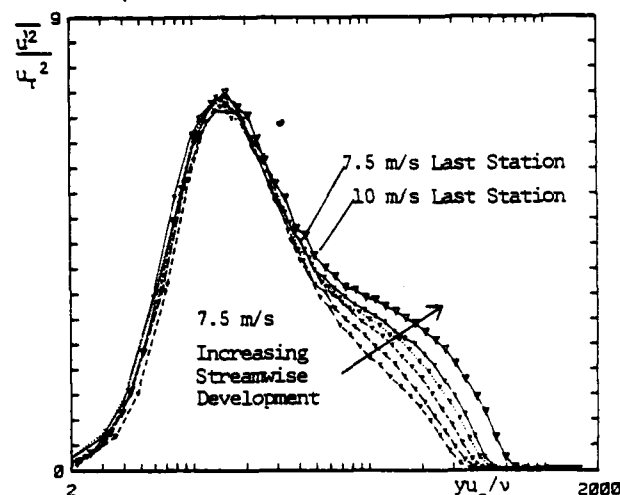


Fig. 11b Same as Fig. 11a, for stabilised layers.

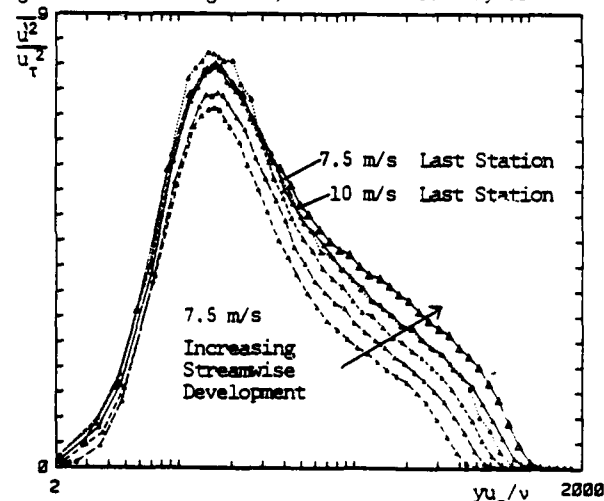


Fig. 11c Same as Fig. 11a, for destabilised layers.

PROFILES OFF THE CENTRELINE

As mentioned above, large periodic spanwise variations of the skin friction coefficient occur in the destabilised layers for positions away from the centreline. Since the aim was to look at the effect of rotation alone, all the above profiles were taken on the centreline to avoid the complication of additional effects such as Taylor-Goertler vortices. As a matter of interest, a few profiles were taken off the centreline in the destabilised layer, namely at positions corresponding to a maximum and a minimum skin friction position and at an intermediate position.

The mean velocity profiles, see Fig. 12, are seen to look entirely different from the profiles measured on the centreline. While it was found that profiles for rotating layers had no region where the usual logarithmic law of the wall with the constants 0.41 and 5.0 fitted the data, there was always an often quite large region where some straight line could be fitted.

In the profiles obtained at a skin friction maximum and at the intermediate position, however, there does not appear to be any linear region at all. The profile at the skin friction maximum shows very little wake component, the profile at the intermediate position is nearly the same except for a slightly larger wake. The

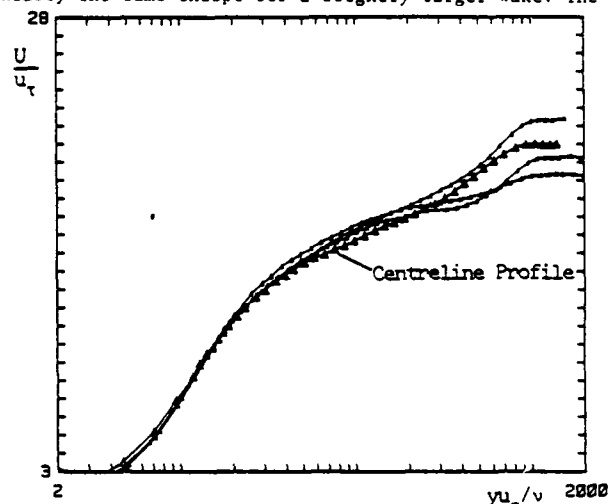


Fig. 12 Off centreline velocity profiles, destabilised layer, obtained with a normal hot wire, $x = 1.21m$, $U_\infty = 7.5$ m/s, compared to centreline profile. $U_\infty/u_\tau = 22.4$, $U_\infty/u_\tau = 20.2$, $U_\infty/u_\tau = 19.2$

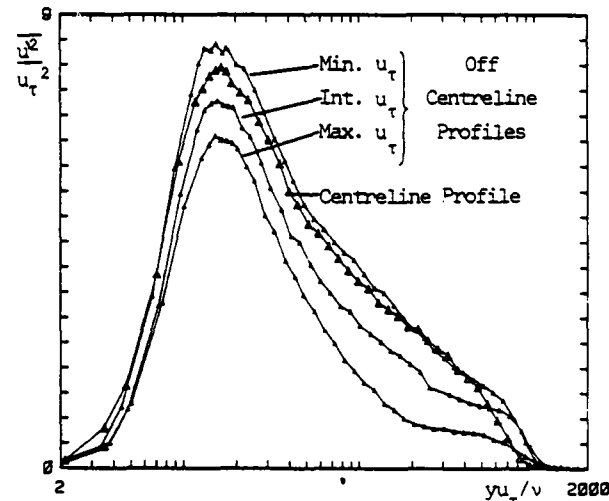


Fig. 13a Streamwise turbulence intensity corresponding to mean velocity profiles shown in Fig. 12.

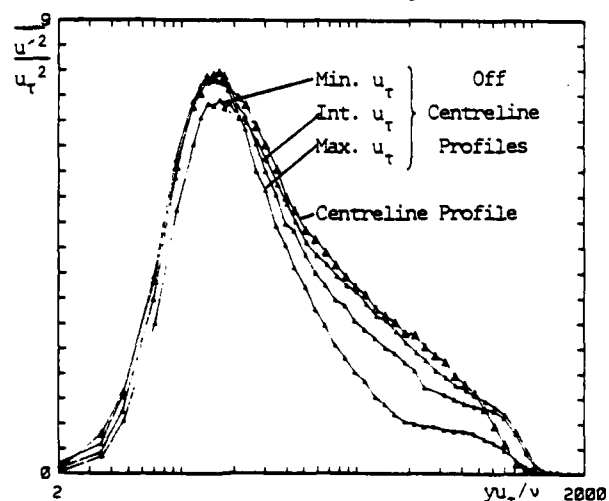


Fig. 13b Same as Fig. 13a, with mean value of u_τ used to non-dimensionalise data.

profile at the skin friction minimum has a fairly long section that appears linear and it shows a large wake.

The turbulence profiles are shown in Fig. 13a, together with the profile measured on the centreline. Here the off-centreline profiles have been non-dimensionalised with the local value of the friction velocity u_τ and it can be seen that there is a large variation between them. The same data is shown in Fig. 13b, non-dimensionalised with the centreline value of the friction velocity (which is close to the mean value) and it can be seen that the data shows less variation from the wall out to yu_τ/ν of about 40 or 50. This raises the question of what value of u_τ should be used to reduce data when there are spatial variations of this parameter.

X-WIRE RESULTS

Presently profiles are being taken with crossed-wire probes. The mean velocity profiles agree very well with those obtained with normal hot-wires, see Fig. 14. The streamwise turbulence intensity seems to be somewhat higher than that measured with the normal wire, see Fig. 15. This is not surprising, however, since the distance of the effective centre of a X-wire from the wall is less well defined than the wall distance of a normal hot-wire.

The transverse turbulence intensity and the Reynolds stress for a few experiments in the stationary duct are presented in Figs. 16 and 17. It is seen that the repeatability is very high. It is noted, however, that the non-dimensionalised Reynolds stress close to the wall is lower than expected. Assuming that there is a small region of constant shear stress in the layer from the wall outwards, in this region we would expect to find the non-dimensionalised Reynolds shear stress $u'v'/u_\tau^2$ to be close to unity value provided viscous stresses are negligible. In the region of validity of the logarithmic law of the wall the viscous component of the shear stress is less than 4%. At higher free stream velocities, i.e. higher Reynolds numbers, our measured values tend to increase closer to the unity value, see Figs. 18, 19 and 20. Here some earlier cursory results are shown at three different free stream velocities, for the stabilised, destabilised and stationary cases. These results were taken without using the lineariser and there is greater uncertainty in the wall distance. In all cases the Reynolds stress appears to be constant in the region where the mean velocity profiles show apparent logarithmic variation with wall distance. Watmuff et al. (1983) showed that this region was considerably larger for the destabilised layers and smaller for the stabilised layers when compared to the zero rotation case. The Reynolds stress profiles are consistent with this observation. At each free stream velocity the profiles effected by rotation have values close to the zero rotation result close to the wall, within the experimental uncertainty.

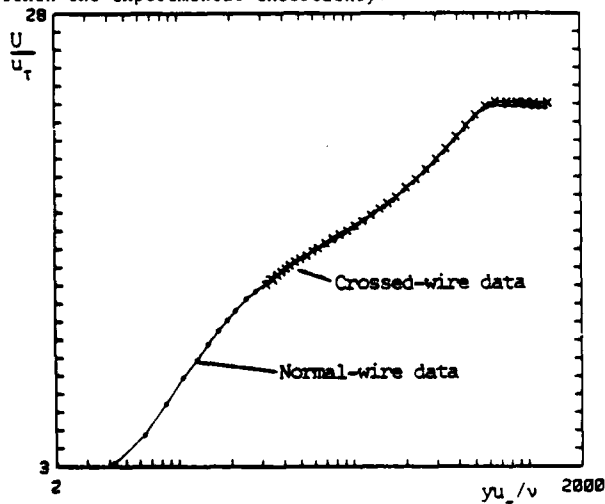


Fig. 14 Comparison of mean velocity profiles, normal wire and X-wire. $U_\infty = 7.5$ m/s, $x = 1.21$ m, $Re = 1500$.

The results may indicate some low Reynolds number effects. As there is a lack of reliable data in this form for low Reynolds number boundary layers, the authors are not sure whether this is a real phenomenon in the flow or whether it is a property of the probe or instrumentation under these conditions.

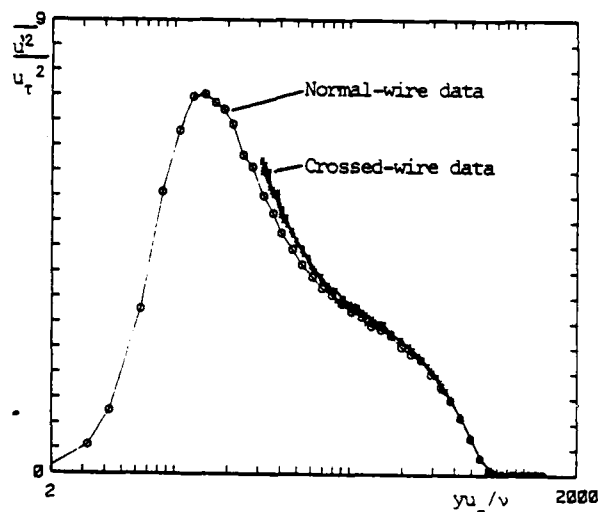


Fig. 15 Streamwise turbulence intensity obtained on 5 different occasions with X-wire probe.

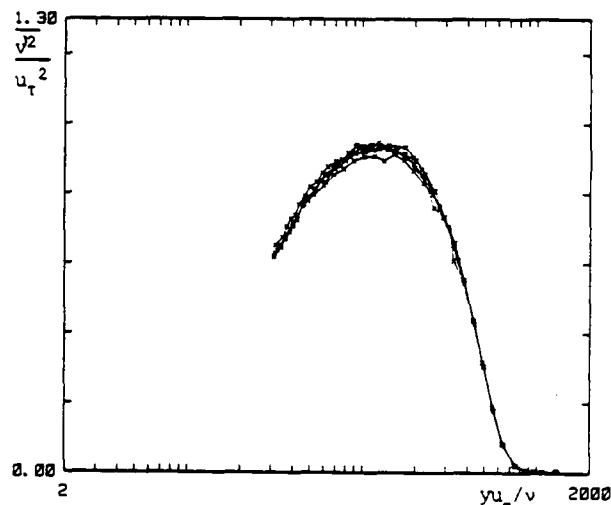


Fig. 16 Turbulence intensity normal to the wall, on 5 different occasions, corresponding to Fig. 15.

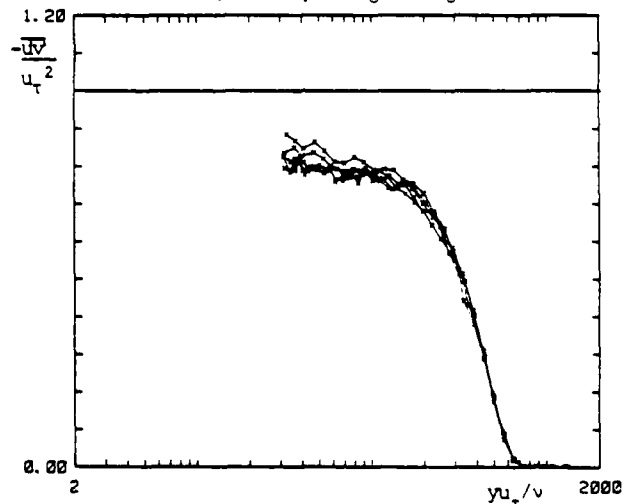


Fig. 17 Non-dimensionalised Reynolds stress obtained on 5 different occasions, corresponding to Fig. 15.

As far as instrumentation is concerned the matched hot-wire voltages were on two occasions simultaneously calibrated and processed by our analogue system and with an on-line digital computer, using a non-linear hot-wire voltage inversion program. Similar trends in the data were observed.

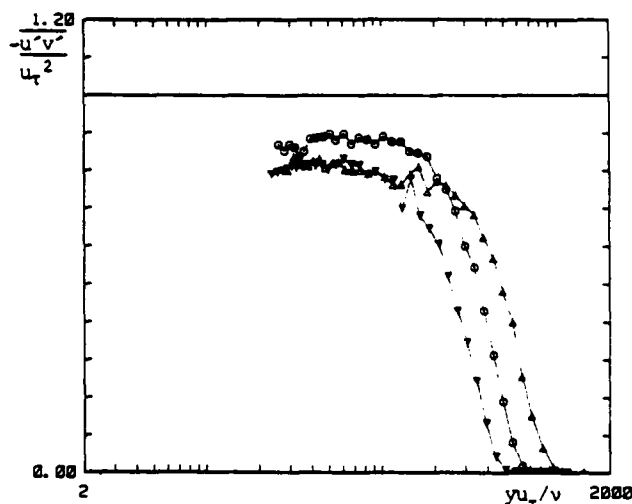


Fig. 18 Reynolds stress, no lineariser, $U_{\infty} = 7.5$ m/s, $x = 1.21$ m, symbols as in Fig. 9a.

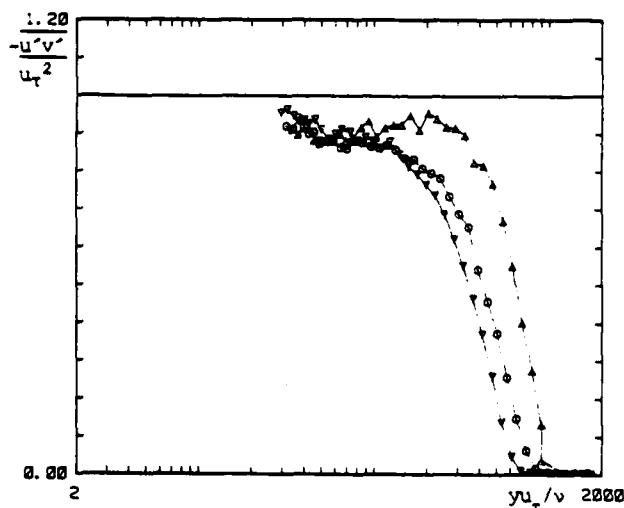


Fig. 19 Same as Fig. 18, $U_{\infty} = 10$ m/s.

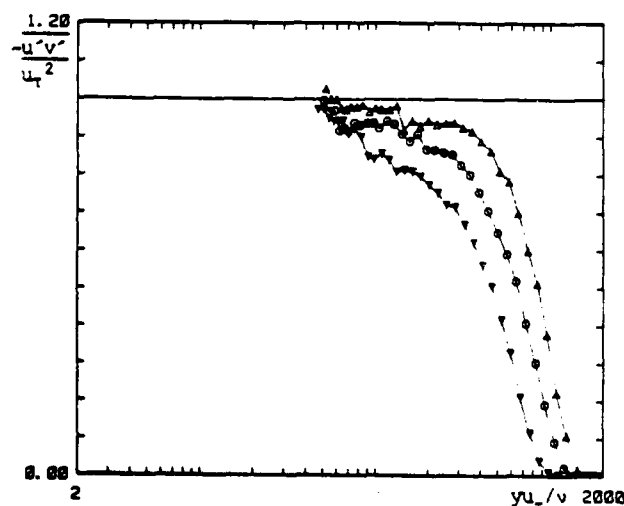


Fig. 20 Same as Fig. 19, $U_{\infty} = 15$ m/s.

CONCLUSIONS

The low Reynolds number zero rotation and stabilised boundary layer streamwise turbulence intensity data show good collapse and agreement with each other in the inner region, independent of streamwise development and free stream velocity when plotted in wall coordinates. The results for the destabilised layers do not exhibit this collapse, but rather indicate a variation with streamwise development for a considerable distance. The lack of agreement could be due in part to the spanwise variation in skin friction coefficient. The off-centreline results (where the skin friction coefficient shows large spanwise variations) have similar values in the inner region if the mean value of the friction velocity is used to non-dimensionalise the data.

The crossed-wire data for zero rotation do not asymptote to the expected value of $\overline{u'v'}/u_{\tau}^2 = 1$ in the inner region at low free stream velocities. The authors find that the asymptotic value is approached as the free stream velocity is increased. This may indicate a low Reynolds number effect in the flow but may very well be due to an effect on the crossed-wire probe or the Preston tube. In spite of this anomaly our zero rotation data are very repeatable and indicate a region of constant shear stress. The authors believe that any error would be of similar magnitude for the rotating profiles so that our data are likely to show the correct trend. At each free stream velocity the profiles effected by rotation have values close to the zero rotation results near the wall, within experimental uncertainty. There also appears to be a region of constant shear stress corresponding to the region of apparent logarithmic variation of mean velocity with wall distance reported by Watmuff et al. (1983).

REFERENCES

- Alcaraz, A. and Mathieu, J., 1975, "Mesure des vitesses moyennes pres d'une paroi par anemometrie a fil chaud", C.R. Acad. Sci. Paris, Series A, T. 280, No 11, 737-740.
- Henbest, S.M., 1983, "The Structure of Turbulent Pipe Flow", Thesis submitted for the degree of Doctor of Philosophy, University of Melbourne.
- Johnston, J.P., Halleen, R.M. and Lezius, D.K., 1972, "Effects of Spanwise Rotation on the Structure of Two-Dimensional Fully Developed Turbulent Channel Flow", J. Fluid Mech., 56, 533-557.
- Morrison, G.L., Perry, A.E. and Samuel, A.E., 1972, "Dynamic Calibration of Inclined and Crossed Hot-Wires", J. Fluid Mech., 52, 465-474.
- Patel, V.C., 1965, "Calibration of the Preston Tube and Limitations on its Use in Pressure Gradients", J. Fluid Mech., 23, 185-208.
- Perry, A.E. and Morrison, G.L., 1971a, "A Study of the Constant-Temperature Hot-Wire Anemometer", J. Fluid Mech., 47, 577-99.
- Perry, A.E. and Morrison, G.L., 1971b, "Static and Dynamic Calibrations of Constant-Temperature Hot-Wire Systems", J. Fluid Mech., 47, 765-77.
- Perry, A.E., 1982, "Hot-Wire Anemometry", Clarendon Press Oxford.
- Watmuff, J.H., Witt, H.T. and Joubert, P.N., 1983, "Effect of Spanwise Rotation on Two-Dimensional Zero Pressure Gradient Turbulent Boundary Layers", IUTAM Symposium, Structure of Complex Turbulent Shear Flow, Marseille 1982, Springer-Verlag.

COMPUTER SIMULATION OF THE TIME VARYING
VELOCITY FIELD IN THE VISCOUS WALL REGION

$$(0 < y^+ < 40)$$

by

Christos Nikolaidis and Thomas J. Hanratty

University of Illinois
Urbana, Illinois 61801
U.S.A.

ABSTRACT

A simple model for the flow oriented eddies in the viscous wall region is explored which assumes them to be associated with spanwise velocity fluctuations at the edge of the viscous wall region ($y^+=40$) which are homogeneous in the flow direction and have a period in the z -direction equal to the observed streak spacing ($\lambda^+=100$). The velocity field calculated by solving the unaveraged Navier Stokes equations agrees with measurements. This agreement suggests that the model correctly describes the production of turbulent kinetic energy close to the wall. Furthermore, an interesting selection process is observed whereby the fluctuating streamwise velocity field close to the wall does not respond to all of the frequencies of the velocity fluctuations in a plane perpendicular to the direction of the mean flow.

INTRODUCTION

A number of studies in recent years have shown that turbulent flow close to a solid boundary is dominated by coherent structures which are greatly elongated in the direction of the flow (Laufer, 1975). These structures have been found to be associated with the production of Reynolds stress and, therefore, with the production of turbulent kinetic energy. This paper summarizes progress made in this laboratory to develop a model for these wall eddies. The basic approach is to solve for the time varying velocity field in the viscous wall region ($0 < y^+ < 40$) by solving the unaveraged Navier Stokes equations. An important aspect of this work is to explore the effects of various boundary conditions at $y^+=40$ on the dynamics of the viscous wall region. The immediate purpose is to establish a representation of a shear flow close to a wall which is consistent with measurements of the turbulence quantities in the fluid and at the wall. The ultimate goal is to develop an understanding of the process by which turbulent energy is produced close to the wall and how this process is affected by changes in the flow conditions.

The calculation is motivated by the idealized model of the wall eddies developed by Sirkar and Hanratty (1970) and, later, by Fortuna (1971). Flow close to the wall is pictured to be dominated by a secondary flow homogeneous in the streamwise direction of the type shown in Figure 1a. The secondary flow brings high momentum fluid from the region outside the viscous wall region, transfers momentum to the wall and brings low momentum fluid away from the wall. These structures would thus be characterized by a spanwise variation of the components of the velocity gradient in the spanwise, s_z , and in the streamwise, s_x , directions of the type shown in Figures 1b and 1c. Measurements by Lee, *et al.* (1970) support this model in that they show the spatial phase relation between s_x and s_z indicated in Figures 1b and 1c.

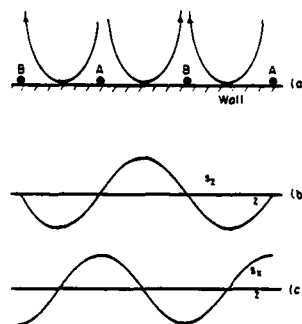


Figure 1.

Idealized coherent
eddy structure

The basic notion of the Sirkar and Fortuna model is that the wall structures are coupled with spanwise velocity fluctuations at the outer edge of the viscous wall region. Recent measurements by Hogenes (1979) and Lau (1980) provide support for this picture. In these studies, simultaneous measurements of the velocity gradient at multiple locations on the wall and of the velocity field at multiple locations in the fluid were made. In this way, flow patterns away from the wall could be correlated through conditional sampling techniques with coherent structures detected from the measurements of the velocity gradient at multiple wall locations. Hogenes and Hanratty (1982) analyzed the experimental data of Hogenes and found that the $\lambda^+=100$ wall eddies, as characterized by their spanwise velocity signature at the wall, are controlling the fluctuations of the streamwise velocity component in the viscous wall region. An analysis of Lau's data by Nikolaidis *et al.* (1983) showed that these eddies are strongly coupled with spanwise flows at $y^+=40$. The calculation of auto- and cross-correlation coefficients of the streamwise and spanwise components of the velocity also revealed a high degree of coherency throughout the viscous wall region.

NUMERICAL COMPUTATIONS

Our initial effort at modeling the wall eddies has been reported by Hatzivramidis and Hanratty (1979). In this work, the time varying Navier Stokes equations were solved using a boundary condition for the spanwise component of the velocity at $y^+=40$, which is periodic in the spanwise direction ($\lambda^+=100$) and which is periodic in time ($T^+=100$ =period between bursts). The fluctuating velocity in the streamwise direction at $y^+=40$ was taken to be zero. The results have encouraged us to pursue this type of modeling further.

AD-A135 034

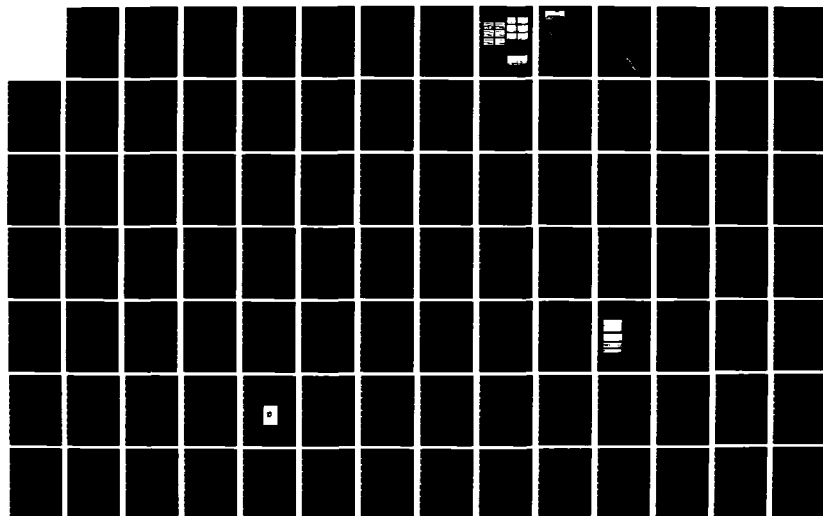
SYMPOSIUM ON TURBULENT SHEAR FLOWS (4TH) HELD AT
KARLSRUHE UNIVERSITY (GERMANY FR) 12-14 SEPTEMBER 1983
(U) KARLSRUHE UNIV (GERMANY F R) SEP 83

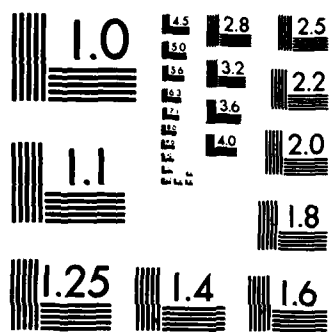
2/7

UNCLASSIFIED

F/G 20/4

NL





MICROCOPY RESOLUTION TEST CHART
NATIONAL BUREAU OF STANDARDS-1963-A

Our more recent work is an improvement over the effort by Hatziaivramidis in that more realistic outer boundary conditions are sought. The most notable change is the use of randomly varying velocities at the outer boundary.

Because of the assumption of homogeneity in the flow direction the following simplified form of the Navier-Stokes equations is used:

$$\frac{\partial v}{\partial t} + v \frac{\partial v}{\partial y} + w \frac{\partial v}{\partial z} = -\frac{1}{\rho} \frac{\partial p}{\partial y} + \nu \left(\frac{\partial^2 v}{\partial y^2} + \frac{\partial^2 v}{\partial z^2} \right) \quad (1)$$

$$\frac{\partial w}{\partial t} + v \frac{\partial w}{\partial y} + w \frac{\partial w}{\partial z} = -\frac{1}{\rho} \frac{\partial p}{\partial z} + \nu \left(\frac{\partial^2 w}{\partial y^2} + \frac{\partial^2 w}{\partial z^2} \right) \quad (2)$$

$$\frac{\partial U}{\partial t} + v \frac{\partial U}{\partial y} + w \frac{\partial U}{\partial z} = \nu \left(\frac{\partial^2 U}{\partial y^2} + \frac{\partial^2 U}{\partial z^2} \right) \quad (3)$$

$$\frac{\partial v}{\partial y} + \frac{\partial w}{\partial z} = 0 \quad (4)$$

Equations (1), (2) and (4) are first solved in order to determine the flow in the y - z plane. By eliminating the pressure gradient between (1) and (2), and by defining a stream function to satisfy (4), the following vorticity-stream function formulation is obtained for the v - w velocity field:

$$\frac{\partial \zeta}{\partial t} + v \frac{\partial \zeta}{\partial y} + w \frac{\partial \zeta}{\partial z} = \nu \left(\frac{\partial^2 \zeta}{\partial y^2} + \frac{\partial^2 \zeta}{\partial z^2} \right) \quad (5)$$

$$\nabla^2 \psi = \zeta \quad (6)$$

where $v = -\frac{\partial \psi}{\partial z}$, $w = \frac{\partial \psi}{\partial y}$ and $\zeta = \frac{\partial w}{\partial y} - \frac{\partial v}{\partial z}$.

Equations (5) and (6) are solved for ψ and ζ and the values of v and w thus obtained are used in (3) to solve for the streamwise velocity field.

The boundary conditions at the wall are the no-slip conditions: $v=0$, $w=0$, $U=0$ at $y=0$. At the sides of the computational domain ($z=0$, $\lambda/2$) the spanwise component of the velocity is taken to be zero whereas the normal and streamwise velocity components are assumed to attain extrema: $w=0$, $\frac{\partial v}{\partial z}=0$, $\frac{\partial U}{\partial z}=0$ at $z=0$, $\lambda/2$. At the upper boundary ($y=y_0$) of the computational domain the prescription of boundary conditions is a more difficult task. These boundary conditions specify the interaction between the wall layer and the outer flow and thus influence greatly the calculated features of the viscous wall region. Hatziaivramidis and Hanratty used the following conditions at $y=y_0$: $w = \hat{w}_L \cos \frac{2\pi x}{\lambda} \sin \frac{2\pi z}{\lambda}$, $\frac{\partial w}{\partial y} = 0$. The zero tangential stress condition was motivated by experimental measurements at $y^+=40$, which show that $\frac{\partial w^2}{\partial y} = w \frac{\partial w}{\partial y} = 0$ and the notion that the flow at $y^+=40$ is well-mixed and superimposed on the wall layer.

More recently, a number of other boundary conditions have been explored for the outer boundary. It was found that the $\frac{\partial w}{\partial y} = 0$ condition is not a good representation of the flow at $y^+=40$. Non zero tangential stresses in combination with strong spanwise flows are found to be necessary for providing the right behavior of the correlation function between w at $y^+=40$ and $s_z = \frac{\partial w}{\partial y}|_{y=0}$ at the wall, as calculated by Nikolaides, *et al.* (1983).

The following set of boundary conditions is used in the present work:

$$w = w_L(t) \sin \frac{2\pi z}{\lambda}, \quad v = v_L(t) \cos \frac{2\pi z}{\lambda}$$

$$\text{and} \quad U = U_L + u_L(t) \cos \frac{2\pi z}{\lambda} \quad \text{at } y = y_0.$$

The terms $w_L(t)$, $v_L(t)$ and $u_L(t)$ are specified from measurements of $w(t)$, $v(t)$ and $u(t)$ at $y^+=40$. They are selected in such a way that

$$\overline{v_L(t) w_L(t)} = 0 \quad \text{and} \quad \frac{\overline{u_L(t) v_L(t)}}{\sqrt{u_L^2} \sqrt{v_L^2}} = 0.4.$$

The amplitude is adjusted so that the spatially and time averaged values of the squares of the fluctuating velocities at $y^+=40$ agree with measurements. The above conditions provide for non-zero $\frac{\partial w}{\partial y}$ and for large values of the fluctuating vorticity ζ .

The differential equations are solved by the ADI finite difference scheme to get the time varying velocity field. The calculation is continued until a stationary randomly varying field is obtained. The time step and the mesh-spacing for the numerical calculations were selected as follows: $\Delta t^+=1$, $\Delta z^+=2$, $\Delta y^+=1.25$ where $+$ denotes quantities normalized with wall variables.

DISCUSSION

The most striking feature of the results is the production of large magnitude streamwise velocity fluctuations within the viscous wall region. This process seems to be selective in that only low frequency velocity fluctuations in the plane perpendicular to the flow direction are effective in producing streamwise turbulence. Evidence for this selection process comes from an examination of the trajectories of inertia-free fluid particles within the wall region.

COMPUTER SIMULATION OF THE TIME VARYING
VELOCITY FIELD IN THE VISCOUS WALL REGION

$$(0 < y^+ < 40)$$

by

Christos Nikolaides and Thomas J. Hanratty

University of Illinois
Urbana, Illinois 61801
U.S.A.

ABSTRACT

A simple model for the flow oriented eddies in the viscous wall region is explored which assumes them to be associated with spanwise velocity fluctuations at the edge of the viscous wall region ($y^+=40$) which are homogeneous in the flow direction and have a period in the z -direction equal to the observed streak spacing ($\lambda^+=100$). The velocity field calculated by solving the unaveraged Navier Stokes equations agrees with measurements. This agreement suggests that the model correctly describes the production of turbulent kinetic energy close to the wall. Furthermore, an interesting selection process is observed whereby the fluctuating streamwise velocity field close to the wall does not respond to all of the frequencies of the velocity fluctuations in a plane perpendicular to the direction of the mean flow.

INTRODUCTION

A number of studies in recent years have shown that turbulent flow close to a solid boundary is dominated by coherent structures which are greatly elongated in the direction of the flow (Laufer, 1975). These structures have been found to be associated with the production of Reynolds stress and, therefore, with the production of turbulent kinetic energy. This paper summarizes progress made in this laboratory to develop a model for these wall eddies. The basic approach is to solve for the time varying velocity field in the viscous wall region ($0 < y^+ < 40$) by solving the unaveraged Navier Stokes equations. An important aspect of this work is to explore the effects of various boundary conditions at $y^+=40$ on the dynamics of the viscous wall region. The immediate purpose is to establish a representation of a shear flow close to a wall which is consistent with measurements of the turbulence quantities in the fluid and at the wall. The ultimate goal is to develop an understanding of the process by which turbulent energy is produced close to the wall and how this process is affected by changes in the flow conditions.

The calculation is motivated by the idealized model of the wall eddies developed by Sirkar and Hanratty (1970) and, later, by Fortuna (1971). Flow close to the wall is pictured to be dominated by a secondary flow homogeneous in the streamwise direction of the type shown in Figure 1a. The secondary flow brings high momentum fluid from the region outside the viscous wall region, transfers momentum to the wall and brings low momentum fluid away from the wall. These structures would thus be characterized by a spanwise variation of the components of the velocity gradient in the spanwise, s_z , and in the streamwise, s_x , directions of the type shown in Figures 1b and 1c. Measurements by Lee, *et al.* (1970) support this model in that they show the spatial phase relation between s_x and s_z indicated in Figures 1b and 1c.

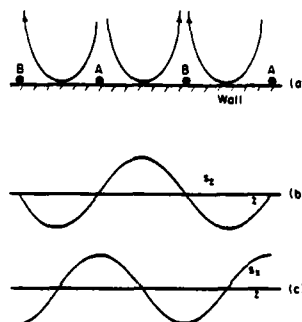


Figure 1.

Idealized coherent
eddy structure

The basic notion of the Sirkar and Fortuna model is that the wall structures are coupled with spanwise velocity fluctuations at the outer edge of the viscous wall region. Recent measurements by Hogenes (1979) and Lau (1980) provide support for this picture. In these studies, simultaneous measurements of the velocity gradient at multiple locations on the wall and of the velocity field at multiple locations in the fluid were made. In this way, flow patterns away from the wall could be correlated through conditional sampling techniques with coherent structures detected from the measurements of the velocity gradient at multiple wall locations. Hogenes and Hanratty (1982) analyzed the experimental data of Hogenes and found that the $\lambda^+=100$ wall eddies, as characterized by their spanwise velocity signature at the wall, are controlling the fluctuations of the streamwise velocity component in the viscous wall region. An analysis of Lau's data by Nikolaides *et al.* (1983) showed that these eddies are strongly coupled with spanwise flows at $y^+=40$. The calculation of auto- and cross-correlation coefficients of the streamwise and spanwise components of the velocity also revealed a high degree of coherency throughout the viscous wall region.

NUMERICAL COMPUTATIONS

Our initial effort at modeling the wall eddies has been reported by Hatzivramidis and Hanratty (1979). In this work, the time varying Navier Stokes equations were solved using a boundary condition for the spanwise component of the velocity at $y^+=40$, which is periodic in the spanwise direction ($\lambda^+=100$) and which is periodic in time ($T^+=100$ =period between bursts). The fluctuating velocity in the streamwise direction at $y^+=40$ was taken to be zero. The results have encouraged us to pursue this type of modeling further.

Calculated profiles of the mean velocity and Reynolds stress are shown in Figure 2. It is noted that

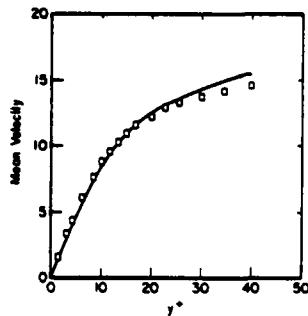
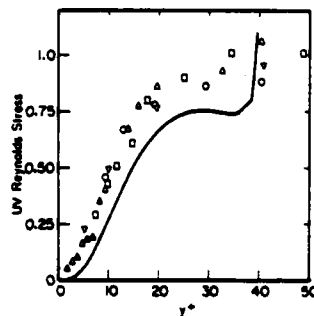


Figure 2a.
Mean streamwise
velocity profile

Figure 2b.
Reynolds
stress



good agreement with measurements is obtained. This supports the notion that $\lambda^+ = 100$ wall structures are producing almost all of the Reynolds stress in the viscous wall region. The calculated values of the intensity, the skewness and the flatness factor of the streamwise velocity fluctuations are shown in Figures 3 and 4. Good qualitative agreement with experiment is noted. The calculated statistical properties of the streamwise velocity fluctuations are not changed much in the region $y^+ < 20$, if the boundary condition at y_0 on \bar{U} is taken to be $\bar{U} = \bar{U}_L$, rather than what is given by (5). This indicates that essential features shown in Figures 3 and 4 are not due to the superimposed $u_L(t)$ at y_0 but are associated with the secondary flow.

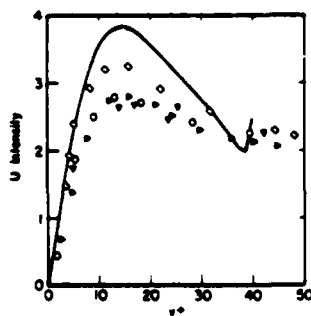


Figure 3a.
Intensity of
streamwise
velocity
fluctuations

Figure 3b.
Intensity
of lateral
velocity
fluctuations

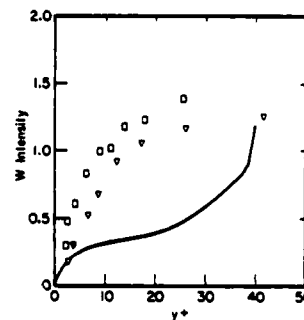
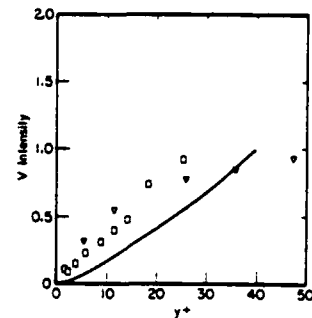


Figure 3c.
Intensity
of spanwise
velocity
fluctuations

The calculated profile of \bar{v}^2 , shown in Figure 3, is in reasonable agreement with experiment data, but shows values which are small very close to the wall. A possible explanation for that is the neglect of the $\frac{\partial U}{\partial x}$ term in the model. It is to be noted that better agreement is obtained if a lower frequency v signal is used at the outer boundary. The calculated profile of \bar{w}^2 , shown in Figure 3, is not in good agreement with measurements. Up to $y^+ = 5$ the agreement is satisfactory but from $y^+ = 5$ up to $y^+ = 40$ very low values of \bar{w}^2 are obtained. It is to be remarked again that the same behavior (with somewhat higher values of \bar{w}^2) is obtained if a lower frequency w signal is employed at $y = y_0$. We believe that this behavior is associated with the representation of the flow at $y^+ = 40$ with a single harmonic in z . The dominant eddy pattern for a single harmonic is a vortical structure whose center (eye) lies within the region $15 < y^+ < 40$. The presence of the eye of the eddy pattern is responsible for the low calculated values of w in this region.

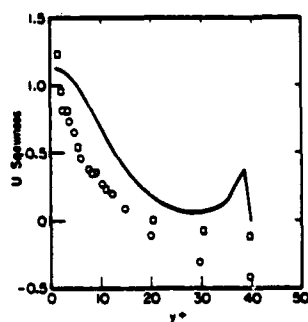
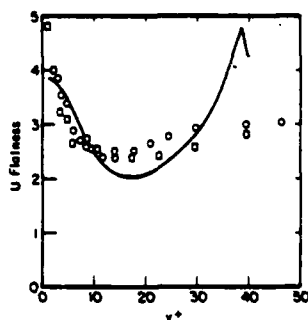


Figure 4a.
Skewness of
u velocity
fluctuations

Figure 4b.
Flatness of
u velocity
fluctuations



We have explored the effect of changing the scale of the velocity fluctuations at the upper boundary on the calculated intensity profiles. Better agreement for the $(\overline{u^2})^{1/2}$ profile is obtained if some energy of the spanwise fluctuations is attributed to scales larger than $\lambda^+=100$. The only problem with this approach is that the resulting s_z patterns at the wall do not agree well with measurements obtained at this laboratory. We are currently investigating the effect of including small scale velocity fluctuations on the computed dynamics and will report on this work at the meeting.

REFERENCES

1. Laufer, J., 1975, Annual Review of Fluid Mechanics, 7, 307.
2. Sirkar, K. K., and Hanratty, T. J., 1970, J. Fluid Mech., 44, 589.
3. Fortuna, G., 1971, Ph.D. Thesis, University of Illinois, Urbana.
4. Lee, M. K., Eckelman, L. D., and Hanratty, T. J., 1970, J. Fluid Mech., 66, 17.
5. Hogenes, J.H.A., 1979, Ph.D. Thesis, University of Illinois, Urbana.
6. Lau, K. K., 1980, Ph.D. Thesis, University of Illinois, Urbana.

7. Hogenes, J.H.A., and Hanratty, T. J., 1982, J. Fluid Mech., 124, 363.
8. Nikolaides, C., Lau, K. K., and Hanratty, T. J., 1983, J. Fluid Mech., (to be published).
9. Hatzivramidis, D. T., and Hanratty, T. J., 1979, J. Fluid Mech., 95, 655.

THREE DIMENSIONAL VORTEX DYNAMICS NEAR A WALL

Hermann Viets*
College of Engineering
West Virginia University
Morgantown, WV 26506 U.S.A.

Richard J. Bethke** and David Bougine***
Department of Engineering
Wright State University
Dayton, Ohio 45435 U.S.A.

ABSTRACT

The three dimensional deformation of an artificially generated line vortex near a flat wall is examined by means of flow visualization and quantitative conditioned sampling of a hot wire anemometer. The vortex is observed to undergo a very rapid deformation from the rectilinear form to a hairpinlike shape. Similar shapes have been observed in the case of driven flows in laminar boundary layers. In the present case the vortices are driven by a rotor configuration of larger scale than the boundary layer thickness.

INTRODUCTION

The dynamics of vortex structures has been of interest to many researchers for a variety of reasons. Much of the early interest was analytical and motivated by the ability to model the structure in terms of inviscid hydrodynamics. The ideal vortex structures were even employed at one point as a model for atomic structure and successfully predicted some of the earlier observations of atomic physics. Multiple vortex interactions were also computed and in some cases stability analyses were performed to reveal potential naturally occurring vortex configurations. Of course the most successful application of inviscid vortex structures to predict an observed phenomena is the well known Karman Vortex Street analysis. Karman (1911) was able to predict, by actually computing the effect of a number of vortices on each other, that only a very specific spacing of vortices would yield a stable configuration.

Most of the early vortex analyses and experiments concerned free vortices (i.e. those removed from wall boundaries). This allowed the structure to be treated inviscidly. Most of these vortex structures were ring vortices and have been reviewed by Zaroodyny (1973).

The dynamics of vortex ring motion has been analyzed inviscidly by Arms and Hama (1965). An experimental and analytical treatment was performed by Viets and Sforza (1972) who employed a viscous model due to Rankine (1858). More recent fully viscous analyses are due to Widnall (1975) and Saffman (1978) and have been reviewed by Saffman and Baker (1979).

The objective of the present paper is to examine the three dimensional vortex dynamics near a wall. The

methods employed for the prediction of vortex dynamics far from a wall will be directly applicable if one is willing to model the wall in an inviscid fashion. Then the inviscid wall would amount to a plane of symmetry in the analysis.

VORTEX NEAR A WALL

The initial studies of vortex structure near a wall were driven by the interest in boundary layer transition. The initial stability predictions of Tollmien (1929) and later Schlichting (1935) were verified by the classical experiment of Schubauer and Skramstad (1947) who employed an electromagnetically oscillating ribbon in a laminar flow. The magnitude and frequency of the oscillation were controlled as well as the Reynolds number of the flow. The results, in terms of a stability diagram, are very well predicted by Tollmien's (1929) analysis.

Perhaps more interesting, from the point of view of vortex dynamics in the vicinity of a wall, is the structure of the unsteady flow produced near the surface. As calculated by Schlichting (1968) for a neutral (i.e. neither growing nor decaying) disturbance, the closed streamlines exhibit a vortex-like structure which is convected in the streamwise direction. This structure has been named Tollmien-Schlichting waves. Some excellent photographic evidence of this structure behind a driven oscillating ribbon of the type employed by Schubauer and Skramstad (1947) has been obtained by Wortmann (1977).

The deformation process of a straight vortex line of the Tollmien-Schlichting type has been conceptualized by Hinz (1975). The vortex distorts slightly and this small distortion is amplified by the self-induced velocity distribution setup by the vortex. The region of highest curvature of the vortex has the highest self-induced velocity. Thus the loop in the vortex is propelled fastest from the wall and thus finds itself in a higher streamwise velocity region. The loop is then convected faster in the streamwise direction than the straight portion deeper within the boundary layer and the vortex filament is stretched until, by a mechanism which is not fully understood, it is said to "burst". This mechanism is currently being called into question as the actual process leading to boundary layer transition. Some recent evidence indicates that the initially turbulent region (or "spot") is actually composed of numerous vortex filaments instead of a single deformed vortex. However, from the present point of view of vortex dynamics near a wall, the model still offers a rational deformation process in a boundary layer.

Various investigators have attempted to model the transition process both analytically and experimentally. Coles and Barker (1975) produced a turbulent spot by causing a disturbance in a laminar boundary layer with

* Professor and Associate Dean, Currently Professor and Dean of Engineering, University of Rhode Island, Kingston, RI, 02881.

** Associate Professor.

*** Research Assistant.

an intermittent jet perpendicular to the wall. The two dimensional slice through the spot looked very much like a convected vortex. Another investigation of a synthetic turbulent spot was performed by Haritonidis, Kaplan and Wygnanski (1978). A spark trip was employed and vortex-like structures were found in the boundary layer.

A viscous vortex model which results in the on-going production of new vorticity, was developed by Doligalski, Smith and Walker (1980). In this model, the existence of the vortex caused an erupting of fluid from the wall region which then curls up and produces a vortex structure of like sign.

Although it appears probable that the turbulent spot is not composed of a single vortex but rather a number of vortices, the dynamics of single vortices are required to treat the multiple vortex problem. In addition, the question of vortex deformation near a wall is of interest in relation to the energization of wall layers and the characteristics of unsteady flows. As will be discussed, the rotor device employed in the current investigation has been successfully applied to various situations where unsteady flow was found to have a beneficial effect.

Thus the objective of the study is to identify the deformation of an initially rectilinear vortex structure near a wall. The two techniques employed in the study are flow visualization and conditioned sampling of a hot wire anemometer signal. The scale of the experiment is greater than the scale of the boundary layer thickness.

THE FLOWFIELD GEOMETRY

Various techniques are possible to generate the initially rectilinear vortex. The vibrating ribbon employed by Schubauer and Skramstad (1947) is one possibility which has been discussed. However, in the present experiment, the objective is to operate at a larger scale than the previous vibrating ribbon experiments. Another possibility is a technique employed by Francis et. al. (1979) in their study of vorticity generated on the upper surface of an airfoil. In that case, the basic mechanism is a plate, positioned perpendicularly to the surface. The plate alternately extends from and retracts into the surface. Each time the plate is extended it creates a recirculation region behind itself. This region is shed and convected downstream each time the plate is retracted into the surface.

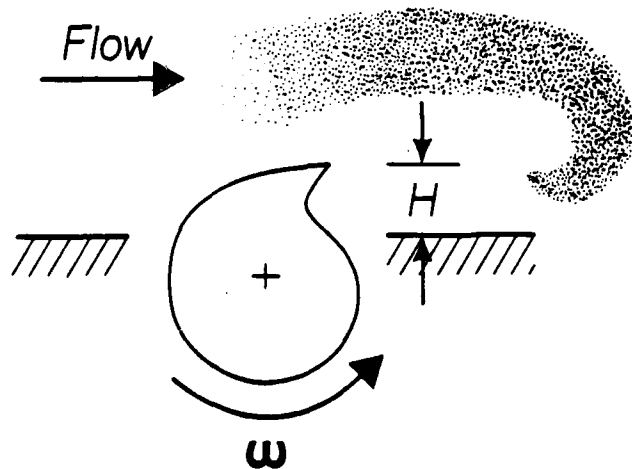


Figure 1. Schematic of the vortex flow generated by a cam shaped rotor.

From the present point of view, it is desirable to have control over the strength of the vorticity produced and thus the flat plate is declined in favor of the rotor geometry shown in Figure 1. The rotor has a discontinuity in its radius at the cusp shape. The

mean flow is from left to right. If the rotor turns in a counterclockwise direction, the rotor tip appears periodically above the surface. Each time the cusp tip is exposed to the mean flow, a transverse vortex (turning in the clockwise direction) is produced, lying parallel to the surface and perpendicular to the mean flow. The strength of the vortex so produced is proportional to the relative velocity between the rotor tip and the mean flow. Thus control over the vortex strength can be achieved by simply changing the rotational speed of the rotor, including the possibility of turning the rotor in a clockwise direction.

The rotor geometry in Figure 1 has been employed to study the vorticity produced as a quasi-two-dimensional structure in Viets, et. al. (1981b). Only center line data was taken.

In addition to a detailed examination of the vortex structure produced by the rotor, the geometry has been applied to various problems, including the control of the flow over an airfoil, avoiding separation over a rearward facing ramp, driving the flow in a dump combustor and studying the properties of convected structures. These problems are discussed in the References. Each of the potential applications will be strongly affected by the three dimensional nature of the vortex flow and thus the dynamics of this structure must be understood and predictable.

FLOW VISUALIZATION RESULTS

a. The choice of rotor speed.

The visualization of the flowfield is accomplished by the use of entrained kerosene vapor. The kerosene is vaporized by slowly dripping it on an inclined heated flat plate where it is vaporized and forced through a series of tubes which end at the inlet to the wind tunnel. Here the vapor is entrained into the tunnel, yielding the streaklines of the flowfield.

The initial study of the centerline plane was conducted at a rotor speed of 3000 rpm (in the counterclockwise direction) resulting in a velocity ratio of 2.0 relative to the freestream velocity. There are two problems with the 3000 rpm results from the point of view of studying the three dimensional vortex structure. One is that the vortex scale is large, making it difficult to follow the details of the rather diffuse vortex. The second is that the vortices are relatively closely spaced, being only one transverse scale apart. This might create some problems in detecting influence of one vortex on another. For these reasons it was determined that a lower frequency would be preferable. In addition, a well formed vortex was desired which led to the study illustrated in Figure 2, where the rotor is turning in a clockwise direction, as denoted by the negative sign. The angle θ is measured clockwise from the rotor position when the cusp is directly above the axis.

At a phase angle of $\theta = 30^\circ$ the rotor position is such that the cusp point is rotated 30° from the upright position. For various rotational speeds between -600 and -3000 rpm, the flowfields are shown in Figure 2. In each case it is clear that a vortex rotating in the clockwise direction is produced, indicating that the freestream velocity, nominally 12 m/sec, is greater than the tip speed of the cusp shape. A possible exception is the case at -3000 rpm where the vortex is very weak or non-existent since the tip speed is approximately equal to the nominal freestream velocity.

From Figure 2, the choice of a rotational speed is made. The objective is a well formed vortex with a scale that is reasonable for the tunnel scale. A rotational speed of -1600 rpm is chosen on this basis, resulting in a velocity ratio of .5 between the tip speed and freestream velocity.

b. Vortex generation.

In order to illustrate the vortex generation process employing the rotor turning in the clockwise di-

rection, Figure 3 shows the flowfield for various phase angles. At zero degrees the curling up of the smoke streaklines behind the cusp shape is clear. A secondary frequency is evident on the smoke line and may be related to an instability of the flow. As the phase angle increases, the vortex moves downstream and at a phase angle of 45° the vortex interacts with the corner of the downstream plate behind the rotor. By a phase angle of 67.5° the vortex is more clearly defined and by 90° the vortex is no longer evident. This is the first indication of the three-dimensionality of the flow, since the plane in which the photographs are taken is not the centerline of the tunnel but rather a plane closer to the far wall.

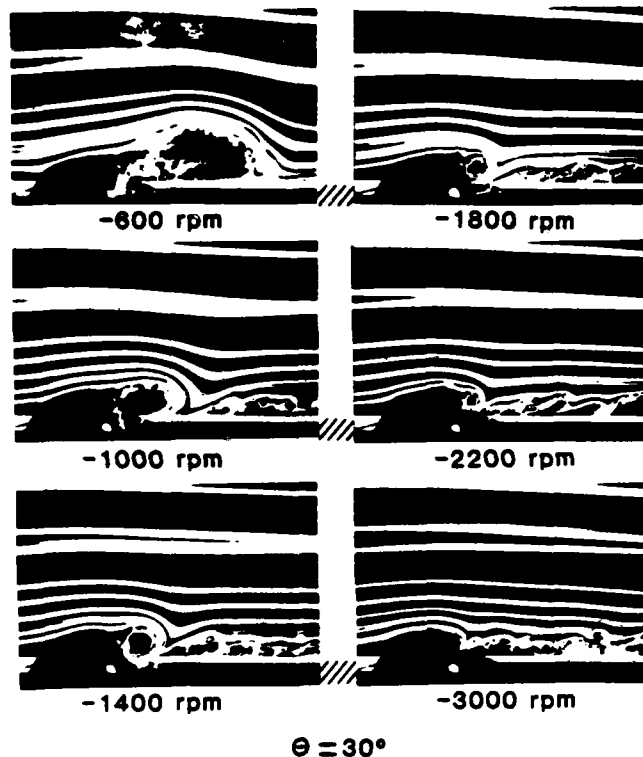


Figure 2. Formation (at $\theta = 30^\circ$) of the vortices formed at various rotor speeds, all in the clockwise direction.

The data planes considered in the present investigation are shown in Figure 4. In addition to the centerline plane, there are planes at five and ten centimeters to either side of the centerline. The photographs of Figure 3 are taken in plane -4 (four rotor step heights from the centerline). The reason that the vortex seems to disappear into a cloud of smoke at a phase angle of 90° is simply that the vortex axis has shifted to an orientation more nearly perpendicular to the wall. Farther downstream additional planes are examined including those labeled +1 (+ one step height from the centerline) and +3.5 (3.5 step heights from the centerline).

c. Visualization in various planes.

The phase angle $\theta = 120^\circ$ is chosen to illustrate the three dimensionality of the vortex structure in Figures 5 and 6. The flowfield in the centerline plane of the tunnel is shown in Figure 5 where a discrete vortex may be identified at $X = 6$. In the next figure, the same flowfield is shown in the off axis planes. At the outermost planes, ($Z = +4$), the effect of the vortex is much reduced in scale and even the smaller structures are located much closer to the wall than is the case in the centerline plane.

d. Three dimensional structure.

To characterize the typical deformation process of the initially rectilinear vortex, the portion near the centerline rises more rapidly off the wall than those elements away from the centerline. The effect is to produce a horseshoe-like shape of vortex with the ends

of the horseshoe on the wall or attached to vortex elements that still have some of the rectilinear character and remain parallel to the wall as shown in Figure 7. As the following data will show, these vortex elements may be found by flow visualization, but they become progressively more difficult to locate in a quantitative fashion.

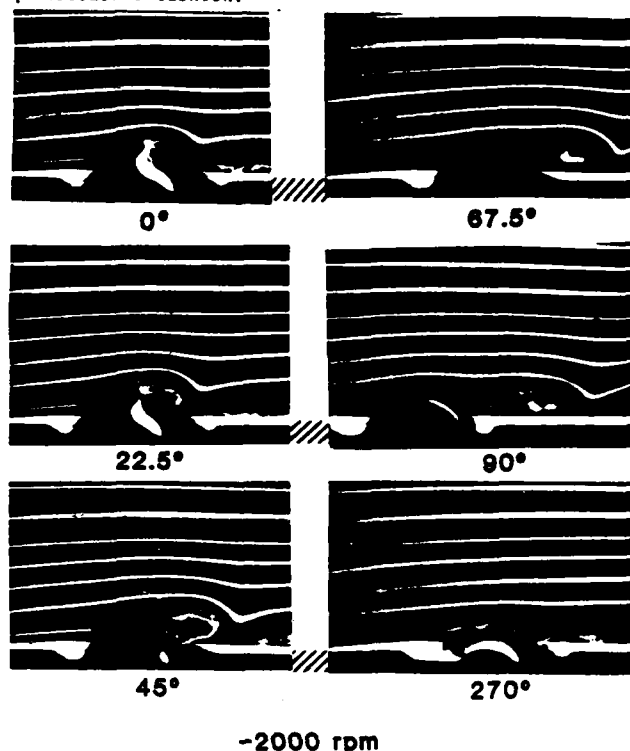


Figure 3. Vortex formation at various phase angles.

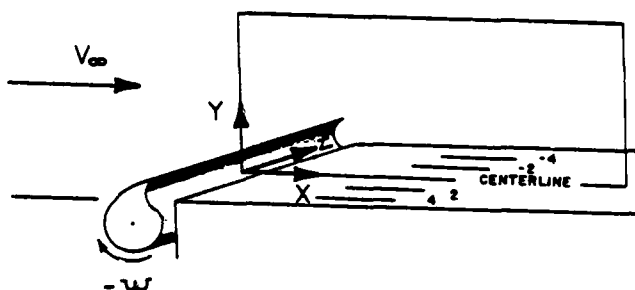


Figure 4. Experimental schematic.

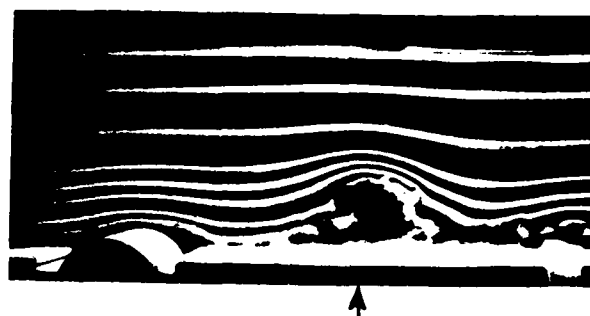


Figure 5. Flow visualization in the $Z = 0$ centerline plane with the phase angle $\theta = 120^\circ$.

The general deformation shown in Figure 7 based on flow visualization is similar to that in a transitioning laminar boundary layer, but the scales are entirely different. It is interesting to note, however that the dynamic character of the vortices is apparently not dependent upon the different scales.

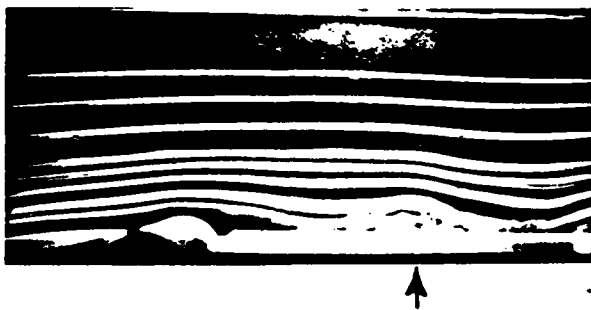


Figure 6. Flow visualization in the $\bar{Z} = +4$ plane with the phase angle $\theta = 120^\circ$.

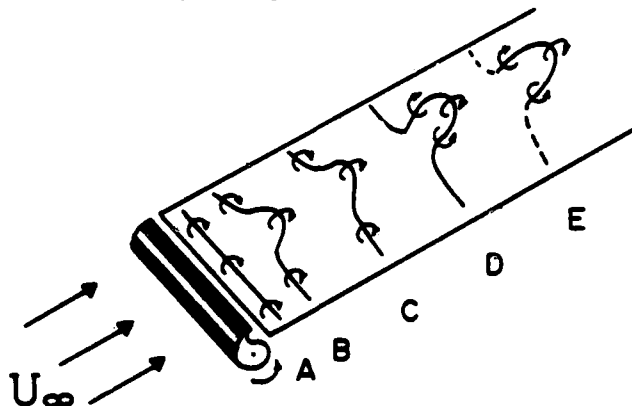


Figure 7. Schematic of the vortex deformation based on the flow visualization results.

When the flow visualization illustrated in Figures 5 and 6 is repeated for various phase angles of the vortex generator, the vortex structures can be identified and the position of the vortices plotted in space at various times. In this way the trajectories of the vortices can be identified and compared to the schematic of Figure 7.

The vortex trajectories identified by flow visualization in the centerline plane and the $\bar{Z} = +4$ planes is shown in Figure 8. The circular data points indicate the centerline trajectory while the square symbols refer to the trajectories in the outer planes. The phase angles corresponding to each data point are so indicated. The centerline portion of the vortex rises very rapidly while the outer portions of the vortex rise very little. The resulting shape is very similar to that of Figure 7. The only difference is that the vortex loops in Figure 7 are inclined in the streamwise direction while the implication of Figure 8 is that the loops are relatively perpendicular to the wall. This difference is simply due to the scale of the boundary layer relative to the scale of the vortex height above the plate. If the scales are comparable, the vortex rises into a higher velocity region and the uppermost portions of the vortex are convected downstream at a higher velocity than the lower portion. Thus the resulting structure will be inclined in the downstream direction. In the present case, the boundary layer thickness is small compared to the vortex scale, being less than a fourth of the height of the vortex generator. Thus the vortex deforms but is convected as a relative unit. Additional experiments currently underway will include the effect of a varying boundary layer thickness, including the case where the rotor generator is entirely submerged in the boundary layer.

QUANTITATIVE RESULTS

The quantitative flowfield data was obtained by a Flow Corporation (now Datametrics) Model 900 constant temperature hot wire anemometer in conjunction with a pair of Thermo Systems, Inc. linearizers. In order to obtain the instantaneous velocity field, the hot wire

data is conditioned by the circuitry shown schematically in Viets, Piatt and Ball, (1981b). The position of the rotor is determined by a magnetic pickup and this information is used to allow the circuitry to accept or reject the hot wire signal. Only those signals generated at a given phase position are accepted. Thus the entire flowfield at any phase angle can be obtained and specific examples are analyzed in this section to verify and quantify the results of the flow visualization.

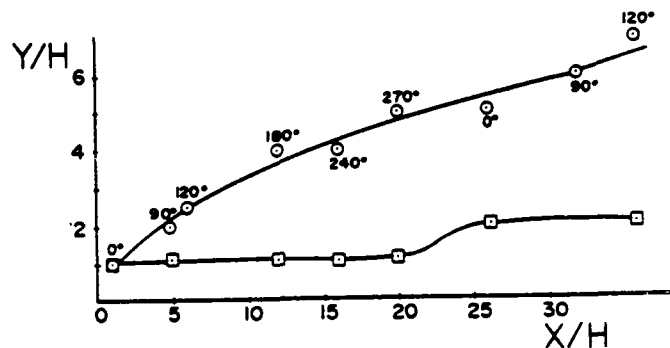


Figure 8. Vortex trajectories in the centerline plane (O) and in the $\bar{Z} = +4$ plane (square).

In order to identify a convected vortex structure, a coordinate frame moving with that structure may first be found. In that new coordinate frame, the structure will be very apparent and can be found with little difficulty. However the difficulty is to find the correct coordinate frame.

Bethke and Viets (1980,1983) have identified two alternate methods to identify convected vortex structures. The first is based on discrete Fourier transformations while the second involves the decomposition of the flow into fundamental structures. An example of the application of the latter technique is shown in an upcoming section.

a. Quantitative flow structure, $\theta = 120^\circ$.

According to the flow visualization results of Figure 8, the centerline plane shows evidence of a vortex structure at an \bar{X} location of approximately 6. Searching the conditioned sampling data at this streamwise location results in the structure shown in Figure 9. This structure is, of course, only evident in a coordinate frame moving with the vortex. This frame was identified by employing the decomposition technique of Bethke and Viets (1983) and then subtracting the streamwise velocity from the flowfield to reveal the form of the structure. Thus the flowfield of Figure 9 reveals a vortex structure approximately located at $\bar{X} = 5.5$, $\bar{Y} = 2$. In fact this position agrees well with the results of the flow visualization is seen in the composite of both hot wire and flow visualization results in Figure 10.

b. Quantitative flow structure, $\theta = 240^\circ$.

Moving farther downstream, the flow visualization results have identified a vortex at approximately $\bar{X} = 16$. In the composite plot of Figure 11, the local vortex structures identified in the three planes are shown. The vortex shape again verifies the results of flow visualization. In particular, the vortex is shown to be practically perpendicular to the plane of the wall. It is anticipated that the presence of a relatively thick boundary would cause the vortex structure to be inclined in the streamwise direction. This aspect is currently under investigation.

Data is available in the intermediate plane between planes 1 and 3.5 ($\theta = 240^\circ$) in Figure 12. Examination of that velocity field (at a distance of $\bar{Z} = 2$ from the centerline) reveals no vortex structure. Of course, in order for the vortex to be continuous from point D to point E in Figure 10, it must also pass through this plane. The discrepancy is resolved in

Figure 12 where the vortex is shown to penetrate the intermediate $\bar{Z} = 2$ plane at such an acute angle, that the vortex signature is lost. The inclined vortex does not yield the typical pattern and as the angle between the vortex and the plane decreases, the scale of the signature goes to zero.

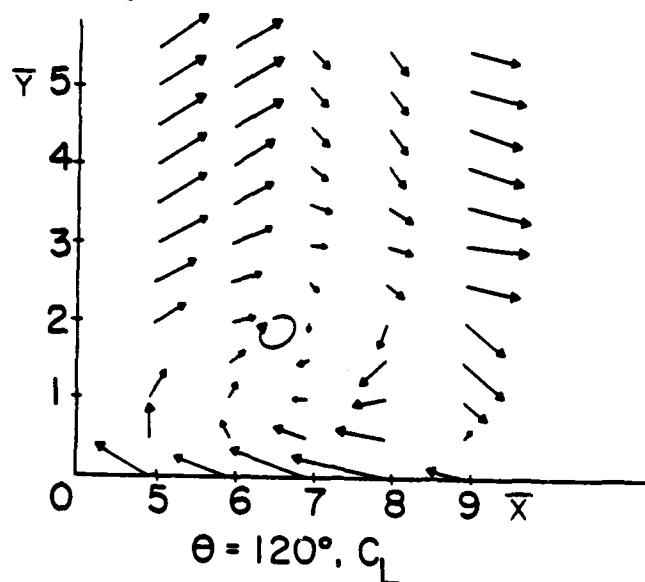


Figure 9. Velocity field $\theta = 120^\circ$, centerline plane.

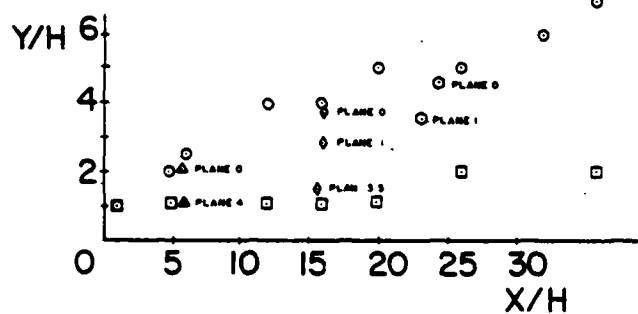


Figure 10. Vortex trajectories with quantitative data at $\theta = 0^\circ$ (O); $\theta = 120^\circ$ (Δ) and $\theta = 240^\circ$ (\Diamond). Data (O) and (\square) are flow visualization from Figure 19.

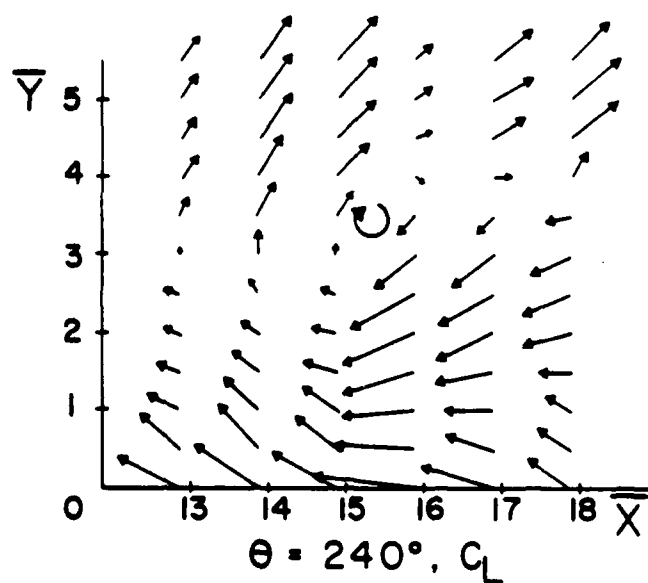


Figure 11a.

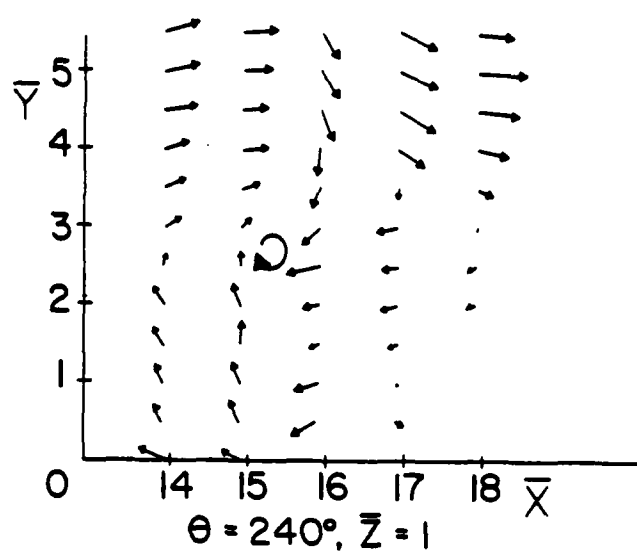


Figure 11b.

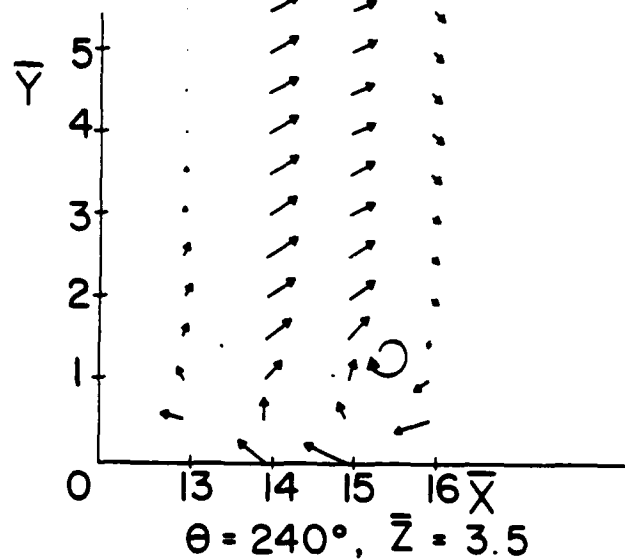


Figure 11c.

Figure 11. Vortex structures found in three planes,, $Z = 0; 1; 3.5$.

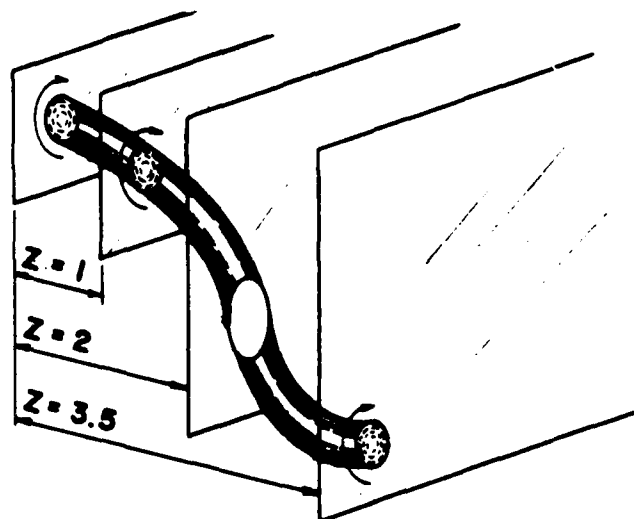


Figure 12. Schematic of vortex intersection with planes.

c. Quantitative flow structures $\theta = 0^\circ$.

At the 0° phase angle, the vortex is in the creation process and is therefore too small and close to the rotor to be found by this technique. The next appearance of the vortex at 0° phase is at $\bar{x} = 25$, according to the flow visualization results. From the quantitative point of view, vortex structures are found in planes $\bar{z} = 0$ and $\bar{z} = 1$ as shown in Figure 10. At larger distances from the centerline plane, the signature of the vortex is so weak as to be indistinguishable with this technique.

Thus the vortex structure has formed a configuration twice as high above the flat plate as its width.

CONCLUSIONS

The three dimensional flowfield structure revealed by the flow visualization results and the conditioned sampling hot wire results are summarized in Figure 7. The initially rectilinear vortex deforms very rapidly as it is convected downstream. Initially there is some evidence that the vortex lines extend out to the walls of the tunnel. However, farther downstream the connection is tenuous and it is possible that the vorticity lines end on the surface of the flat plate instead of the wind tunnel walls.

It is probable that the single deformed vortex is due to the end conditions on the wind tunnel walls. That is, if the rotor were infinitely long, the initially rectilinear vortex would still deform into a similar pattern as that in Figure 7 and that the pattern would be repeated with a certain scale length determined by the stability of the rectilinear vortex to an applied disturbance. In the present experimental case, the applied disturbance is the end walls which supply a boundary layers which cause the vortex ends to move downstream more slowly than the vortex center. This initial deformation then progresses into the shapes observed. The aspect ratio of the deformed vortex (i.e. its height above the plane/distance between the legs perpendicular to the plate) is approximately two at a position 30 generator heights downstream.

ACKNOWLEDGEMENT

The effort reported here was funded by the Air Force Office of Scientific Research under Grant No. AFOSR-81-0025 monitored by Capt. (Dr.) M. S. Francis. The contribution of Mont Ball in the construction of the apparatus and acquiring the data is much appreciated.

REFERENCES

- Arns, R.J. and Hama, F.R., 1965, "Localized Induction Concept on a Curved Vortex and Motion of an Elliptical Vortex Rings", *Phys. Fluids*, 8, 553-559.
- Bethke, R.J. and Viets, H., 1980, "Data Analysis to Identify Coherent Flow Structures", AIAA Paper No. 80-1561.
- Bethke, R.J. and Viets, H., 1983, "Identification of Convected Flow Structures by Decomposition Techniques", AIAA Paper No. 83-0048.
- Coles, D. and Barker, S.J., 1978, "Some Remarks on a Synthetic Turbulent Boundary Layer", in *Structure and Mechanisms of Turbulence 1*, Lecture Notes in Physics, 75, 234-247.
- Francis, M.S., Keese, J.E., Lang, J.D., Sparks, G.W., Jr., and Sisson, G.E., 1979, "Aerodynamic Characteristics of an Unsteady Separated Flow", AIAA, 17, 1332-1339.
- Haritonidis, J.H., Kaplan, R.E. and Wygnanski, I., 1980, "Interaction of a Turbulent Spot with a Turbulent Boundary Layer Flows", in *Viscous Flow Drag Reduction* (G.R. Bough Ed.), Progress in Astro. and Aero., 72, 47-72.
- Hinze, J.O., *Turbulence*, 1975, Second Edition, McGraw-Hill.
- Karman, Th. Von, 1911, "Über den Mechanismus des Widerstandes, den ein bewegter Körper in einer Flüssigkeit erfährt", *Göttingen Nachrichten, Mathematisch-Physikalische Klasse*, 509-511.
- Rankine, W.J.M., 1858, *Manual of Applied Mechanics*, C. Griffen and Co., London, 1st Edition.
- Saffman, P.G. and Baker, G.R., 1978, "The Number of Waves on Unstable Vortex Rings", *J. Fluid Mech.*, 84, 625-639.
- Saffman, P.G. and Baker, G.R., 1979, "Vortex Interactions", *Fluid Mech.*, 11, 96-122.
- Schlichting, H., 1968, *Boundary Layer Theory*, Sixth Edition, McGraw-Hill.
- Schubauer, G.B. and Skramstad, H.K., 1947, "Laminar Boundary Layer Oscillations and Stability of Laminar Flow", *J. Aero. Sci.*, 14, 69-78.
- Tollmien, W., 1929, "Über die Entstehung der Turbulenz" 1, *Mitteilung, Nachr. Ges. Wiss. Göttingen, Math. Phys.*, 21-44 (Also NACA TM 609, 1931).
- Viets, H., 1979, "Coherent Structures in Time Dependent Flow", NATO/AGARD CP-271.
- Viets, H. and Piatt, M., 1981a, "Induced Unsteady Flow in a Dump Combustor", in *Combustion in Reactive Systems* (Bowen, Manson, Oppenheim, and Soloukhin, eds.), AIAA Prog. in Astro. & Aero., 76, 611-624.
- Viets, H., Piatt, M. and Ball, M., 1981b, "Boundary Layer Control by Unsteady Vortex Generation", *Wind Eng. and Ind. Aero.*, 7, 135-144.
- Viets, H., Piatt, M. and Ball, M., 1981, "Forced Vortices Near a Wall", AIAA Paper 81-02565.
- Viets, H., Piatt, M. and Ball, M., 1979, "Unsteady Wing Boundary Layer Energization", AIAA Paper 79-1631.
- Viets, H. and Sforza, P.M., 1972, "Dynamics of Bi-laterally Symmetric Vortex Rings", *Phys. Fluids*, 15, 230-240.
- Widnall, S.E., 1975, "The Structure and Dynamics of Vortex Filaments", *Ann. Rev. Fluid Mech.*, 7, 141-165.
- Wortmann, F.X., 1977, "The Incompressible Fluid Motion Downstream of Two Dimensional Tollmien-Schlichting Waves", AGARD/NATO CP224 on Laminar-Turbulent Transition.
- Zaroodny, S.J., 1973, "Revised Theory of Vortex Rings—a simplified review of the state of the art", U.S. Ballistic Research Laboratory, BRL MR 2305.

SESSION 4 - NUMERICAL SCHEMES AND COMPUTATIONS

G. Krause - Chairman

CALCULATED SCALAR DISSIPATION in TWO-DIMENSIONAL FLOWS[†]

Wm T. Ashurst, A. R. Kerstein, E. Effelsberg* and N. Peters*

Sandia National Laboratories
Livermore, California 94550

*Institut für Allgemeine Mechanik
RWTH Aachen, Germany

ABSTRACT

Convection and diffusion of a conserved scalar is calculated in a two-dimensional mixing layer using the discrete vortex method. Scalar dissipation, the square of the scalar gradient, is calculated along various scalar isolines. The dissipation distribution is found to be approximately lognormal with parameters that can be described by a laminar diffusion model which has lognormally-distributed stretching of the mixing layer interface.

INTRODUCTION

For turbulent diffusion flames with fast chemistry, Bilger (1979) has formulated a conserved scalar quantity which has proven useful for predicting burning rates in jets, and which is also applicable to planar mixing layers and other geometries. These predictions involve averages over the joint distribution of the scalar and the scalar dissipation, defined as the square of the scalar gradient. The probability density function (pdf) of the scalar is readily measured, but the pdf of the dissipation and its correlation with the scalar are relatively inaccessible experimentally or theoretically. In some cases it has been assumed that these two quantities are statistically independent, an unverified assumption with significant impact on predictions.

We have directly calculated, in a stochastic fashion, the pdf of the dissipation in some model flows which have application to lift-off of turbulent jet diffusion flames. The pdf of dissipation is an input to the recent analysis by Janicka and Peters (1982) of lift-off heights. Their model, which uses assumed functional forms for the pdf's of the scalar and the dissipation in transport equations for the scalar pdf, is in good agreement with experimental lift-off data in the first ten jet diameters. When they adopt the alternative assumption of statistical independence between the scalar and its dissipation, large disagreements with experimental jet results are obtained, indicating sensitivity to assumptions concerning the correlation of the scalar and the dissipation. Since all versions of their model involve a number of assumptions, the results of our computations will aid in the validation of

the assumptions concerning the pdf's of the scalar and the dissipation.

In the same analysis, Janicka and Peters found that, for the region beyond twenty diameters, the various calculations underpredict the lift-off height by almost a factor of two. Their models also do not explain the blow-off at forty diameters for a methane jet. They believe that blow-off is caused by the passage of a large coherent structure that carries the flame stabilization region downstream. Thus, they feel that blow-off predictions will require time-dependent analysis. Our computational approach can be applied to this regime, and our current calculations represent the start of such time-dependent work.

According to Yule (1973) and Petersen (1978) the large coherent ring vortex that forms at the jet nozzle undergoes transitions to smaller three-dimensional structures within the first ten diameters of the jet (actual location depending on Reynolds number). This was determined by the loss of azimuthal correlation of velocity fluctuations. However, experimental work by Dimotakis *et al.* (1981) indicates that unreacted, entrained fluid may be found on the jet axis at substantial distances downstream. Their results are inconsistent with gradient diffusion models, suggesting the influence of coherent structures on flame blow-off.

At this time we have not done a full three-dimensional jet calculation. Earlier work (Ashurst, 1981) of a single vortex ring shows promise in its agreement with experiment in the number of waves formed by nonlinear instabilities. A complete jet calculation is a huge task. Therefore, we focus our efforts on a small volume of fluid and abstract from detailed calculations the statistics that can be incorporated into pdf analyses.

METHOD

The numerical method is the same as used by Ashurst and Barr (1981) in their conserved scalar calculations. A short description of the method will be given here. The two-dimensional velocity field is determined by a Lagrangian calculation of the motion of discrete vorticity. In the previous work the vorticity was distributed randomly in a square; in these calculations the vorticity is distributed such that it simulates a mixing layer. The discrete vortex method was

[†]Work partially supported by U. S. Department of Energy, Office of Basic Energy Sciences.

calibrated with the simulation of the spatially developing mixing layer (Ashurst, 1979). In the current problem the vorticity is randomly distributed along the y axis in the middle of the square. Initially the conserved scalar Z is zero for positive x and unity for negative x . So, this small volume of fluid simulates the edge of a diffusion jet. Free boundaries are used in the x -direction and periodic boundaries are used in the y direction. The mixing layer develops in time rather than in space. The total circulation is unity, which produces a velocity difference of unity across the layer. The scalar transport and diffusion are calculated with an Eulerian grid (80-by-80 mesh cells in the square) using Zalesak's flux-corrected transport scheme (1979). The numerical diffusion is ten times less than the assumed diffusion coefficient D of $0.0025 L^2/\tau$ where L is the square edge length and τ is a reference time unit. Because of the initial random vortex locations, the time development of the nonlinear growth requires ensemble averaging. The observation time is limited by the initial conditions and by the boundary conditions. The initial conditions of a step change in the scalar value result in a rapidly changing scalar field at early times. Therefore, we must wait until transients decay before gathering statistics. The finite system size limits the large scale growth and so we must stop gathering statistics before finite-size effects predominate. The statistics thus gathered are used to calculate the scalar dissipation χ , and its pdf. We calculate $\chi (= 2D(\nabla Z)^2)$ along selected scalar isolines and accumulate the quantity $l_Z/\sqrt{\chi}$ where l_Z is the arc length of the isoline in the mesh cell. This achieves the desired volumetric weighting.

RESULTS

The averaging time period, selected according to the above criteria, is the interval between 1.3 and 1.5τ . Figure 1 presents scalar contours at time 1.3τ for several different initial conditions of the random number seed. The contours are drawn by using bilinear interpolation of the scalar values. The discrete vorticity (200 vortices used) is shown by its velocity vector, scaled so that the largest vortex velocity is drawn with length $0.1L$ (the left-hand corners of the square are shown with lines of this length). The vorticity coalescence is apparent. From left to right, the contour lines have scalar values of $0.99, 0.5, 0.2, 0.15, 0.10, 0.05$ and 0.01 . We have also calculated isoline values between 0.2 and 0.5 in increments of 0.05 , but have not shown them in these plots for clarity.

Figure 2 presents scalar dissipation pdf's for several scalar values between 0.05 and 0.50 . These are ten-run averages. Notice that as scalar value increases, i.e., as one approaches the center of the mixing layer from outer edge, the distribution of χ continues to spread over a wider range. Thus, there is a definite correlation between the scalar and its gradient.

By definition, a random variable is lognormal if its logarithm is governed by the Gaussian distribution. Therefore, the cumulative distribution function of $\ln \chi$ will be a straight line on probability paper if χ is lognormal. In Figure 3, we show the data for scalar values of 0.05 and 0.5 . The linearity does indicate that the dissipation is lognormal. For χ lognormal, the standard deviation, σ of the $\ln \chi$ distribution is inversely proportional to the slope of the line, and the mean value, μ of $\ln \chi$ corresponds with the 50 percent point. Figure 3a is representative of the data for the small scalar values that we have calculated, $Z \leq 0.3$. Figure 3b shows

that the scalar of 0.5 has more departure from lognormality at large dissipation values. However, the calculated curve does resemble a straight line over a four e-fold range of χ . Table I presents the mean and variance, σ^2 values of the χ pdf's for each calculated scalar isoline. These lognormal parameters are determined from two estimates: 1) from the $\ln \chi$ distribution, and 2) from the χ distribution using the relations $\sigma^2 = \ln(\overline{\chi^2}/\bar{\chi}^2 + 1)$ and $\mu_Z = \ln \bar{\chi} - \sigma^2/2$. If the data are exactly lognormal, then the two methods would yield the same parameter values. While the mean values are approximately the same for all scalar values, the variances are quite different at large scalar value. For a scalar value of 0.5 , the mean and variance values from the $\ln \chi$ distribution are not very different from estimates obtained by drawing a straight line on the probability plot; 7 percent change in mean value and 24 percent in variance. Thus, we consider the data in Figure 2 to be lognormal for low scalar values, below 0.35 , but to depart from lognormality for the higher values.

However, in this inhomogeneous mixing layer, we do not obtain the statistical independence between the scalar and the dissipation of scalar fluctuations assumed by Bilger. In other work, we have studied the dissipation in a two-dimensional system where the vorticity is distributed in a uniform manner and the boundary conditions are periodic in both directions. In those results we do find that the scalar and the dissipation are statistically independent, within calculational uncertainty. Lognormality is also exhibited and the calculated dissipation agrees with Kolmogorov's third hypothesis: the variance decreases as the averaging volume is increased.

ANALYSIS

The following analysis, which we call the lognormal stretching model, accounts for the observed dependence of the scalar and its dissipation seen in Figure 2. We start with a one-dimensional diffusion equation with initial conditions of a step discontinuity, approximately the same as our numerical initial conditions for the scalar. The laminar time-dependent solution is given by the complementary error function

$$Z = \frac{1}{2} \operatorname{erfc}(\eta)$$

where η is the similarity coordinate for laminar diffusion, proportional to the square root of the product of time and the diffusion coefficient. Given the scalar profile, the instantaneous scalar dissipation rate is

$$\chi(Z, t) = \frac{1}{2\pi t} \exp(-2\eta^2(Z))$$

where η is a function of Z , given by the previous equation. To generalize this one-dimensional result to our flow field, the gradient must be modified by any stretching that occurs parallel to the original discontinuity. Let s be the measure of stretching and multiply χ by s . Now, assume that the η coordinate and the amount of stretching are statistically independent. Then we can accomplish an easy transformation between probabilities based on (η, s) and those based on (χ, Z) . The Jacobian of the transformation is

$$J(\eta, s) = -\exp(-3\eta^2)/(2\pi^{3/2}).$$

In addition to the independence between the stretching, s , and the similarity coordinate, η , we also assume the stretching to have a lognormal distribution

$$P_s(s) = \frac{1}{s\sigma\sqrt{2\pi}} \exp\left[-\frac{1}{2\sigma^2}(\ln s - \mu_s)^2\right].$$

The standard definition of the marginal distribution yields the dissipation distribution as

$$P_\chi(\chi|Z) = \frac{P_{Z\chi}(Z, \chi)}{P_Z(Z)}.$$

Using the transformation

$$P_{Z\chi}(Z, \chi) = \frac{P_\eta(\eta) P_s(s)}{|J(\eta, s)|}$$

and

$$P_\eta(\eta) = \frac{P_Z(Z)}{\left|\frac{\partial \eta}{\partial Z}\right|} = \frac{P_Z(Z)}{\sqrt{\pi} \exp(\eta^2)},$$

upon substitution, we see that the $P_Z(Z)$'s cancel and obtain a lognormal distribution for χ

$$P_\chi(\chi|Z) = \frac{1}{\chi\sigma\sqrt{2\pi}} \exp\left[-\frac{1}{2\sigma^2}(\ln \chi - \mu_Z)^2\right]$$

but with a Z dependence given as

$$\mu_Z = \mu_s - \ln(2\pi) - 2\eta^2(Z)$$

where the inverse of the complementary error function defines the η , Z relation

$$\eta(Z) = \operatorname{erfc}^{-1}(2Z).$$

The result is that the assumption of a lognormal stretching and statistical independence between stretching and the similarity coordinate leads to a statistical dependence between the scalar and its dissipation. But the dissipation is lognormal and has the simple scalar dependence predicted by the lognormal stretching model, as shown in Table I. The pdf's in Figure 2 can, for scalar values of 0.3 and less, be approximated by one lognormal distribution with a variance of $\sigma^2 = 0.38$ and a mean of $\mu_s = 0.1$, if the mean parameter μ_Z is calculated as given above. However, for scalar values greater than 0.3, μ_s is not constant, but this is the range of scalar values in which the pdf's depart from lognormality as previously shown by the inconsistent estimates for σ^2 , see Table I. We note, that for combustion applications with hydrocarbon fuels, the range of conserved scalar values used to describe the combustion zone fall within the range of values where the lognormal stretching model is a good approximation.

There appears to be a discrepancy in μ_s for the scalar value of 0.01. The model initial conditions assume a step discontinuity, whereas in the numerical calculation, the scalar change from zero to one was spread over two grid cells. It is possible that these initial differences are important at the leading edge of the diffusion "wave" in this transient solution. However, the more likely explanation is the lack of resolution in the calculated value. The gradient histogram is accumulated in bins whose width is independent of the scalar value.

The number of nonempty bins is, for increasing scalar value: 3, 59, 179, 321, 452, 499 and the remainder greater than 500. Thus, the pdf of χ for $Z = 0.01$, discretized into only three nonempty bins, is not considered as very precise.

CONCLUSIONS

We have found that the joint pdf of the scalar and the scalar dissipation, calculated in a two-dimensional mixing layer using the discrete vortex method, is well characterized at the edge of the layer by a simple model which we call the lognormal stretching model. The key feature of this model is the assumption that stretching transverse to a one-dimensional diffusion solution is lognormal and independent of the scalar value. For combustion applications, the scalar values of interest lie on the outer edge of the shear layer where three-dimensional effects may not be too important (depending on Reynolds number). Thus, our results can be used in the region near a jet nozzle when the diffusion flame has lifted-off the nozzle. It will be interesting to perform new calculations which include chemical reaction and the resulting velocity perturbation due to chemically induced volume expansion.

REFERENCES

- Ashurst, W. T., 1979, "Numerical Simulation of Turbulent Mixing Layers via Vortex Dynamics," in *Turbulent Shear Flows I*, edited by F. Durst et al. (Springer-Verlag, Berlin) pp. 402-413.
- Ashurst, W. T., 1981, "Vortex Ring Instability," *Bulletin of the American Physical Society*, 26, p. 1267.
- Ashurst, W. T. and Barr, P. K., 1981, "Lagrangian-Eulerian Calculation of Turbulent Diffusion Flame Propagation," in *Proceedings of the Third Symposium on Turbulent Shear Flows*, University of California at Davis, pp. 3.44-3.49, Sept. 1981.
- Bilger, R. W., 1979, "Effects of Kinetics and Mixing in Turbulent Combustion," *Combustion Science and Technology*, 19, pp. 89-93; see also "Turbulent Reacting Flows," Edited by Libby, P. A. and Williams, F. A., Springer-Verlag Series of Topics in Applied Physics, Volume 44, 1980.
- Dimotakis, P. E., Broadwell, J. E. and Howard, R. D., 1981, "Experiments on Chemically Reacting Turbulent Jets," *Bulletin of the American Physical Society*, 26, p. 1284.
- Janicka, J. and Peters, N., 1982, "Prediction of Turbulent Jet Diffusion Flame Lift-off Using a P.D.F. Transport Equation," presented at the Nineteenth Symposium (International) on Combustion, Haifa, Israel, August 1982.
- Petersen, R. A., 1978, "Influence of Wave Dispersion on Vortex Pairing in a Jet," *Jour. Fluid Mech.* 89, pp. 469-496.
- Yule, A. J., 1978, "Large-scale Structure in the Mixing layer of a Round Jet," *Jour. Fluid Mech.* 89, pp. 413-432.
- Zalesak, S. T., 1979, "Fully Multidimensional Flux-Corrected Transport Algorithms for Fluids," *J. Computational Physics*, 31, pp. 335-362.

JOBNUM 22 NSTEP 200 TIME 1.35 MAX VEL 0.41



JOBNUM 23 NSTEP 200 TIME 1.35 MAX VEL 0.43



CONTOURS OF SCALAR

JOBNUM 24 NSTEP 210 TIME 1.30 MAX VEL 0.47



CONTOURS OF SCALAR

JOBNUM 25 NSTEP 200 TIME 1.32 MAX VEL 0.41



Figure 1. Representative scalar contours and vorticity locations at time 1.37. The rotation is counterclockwise, so flow is down on the left side of the layer and up on the right side with a velocity difference of unity across the layer. The vorticity is shown by its velocity vectors, scaled so that the maximum

has length $0.1 L$. The left-hand corners of the square are drawn with lines of length $0.1 L$. From left to right in each plot the scalar contour values are 0.99, 0.5, 0.2, 0.15, 0.10, 0.05 and 0.01.

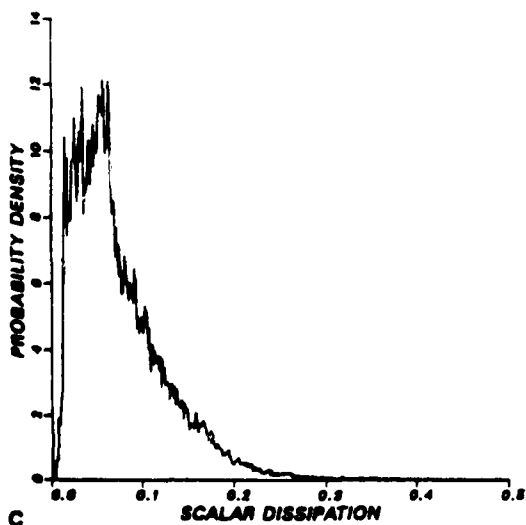
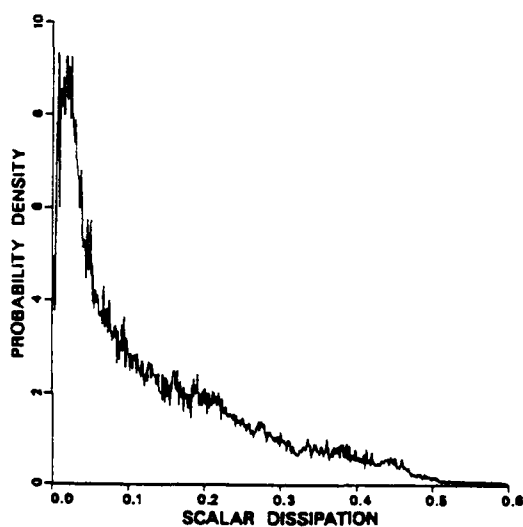
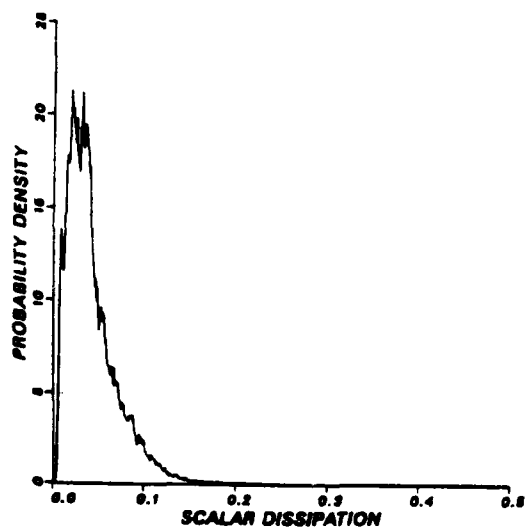
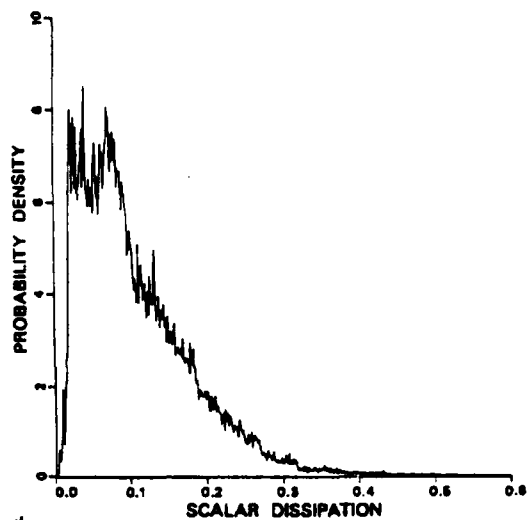
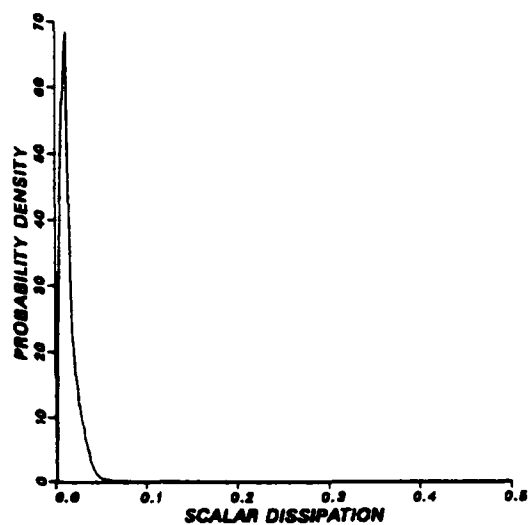


Figure 2. Probability distribution function of scalar dissipation $\chi\tau$, as a function of scalar value in the mixing layer, where τ is the reference time unit. The scalar values are 0.05, 0.10, 0.15, 0.20 and 0.50 for a) through e) respectively. Notice the larger spreading associated with the larger scalar value.

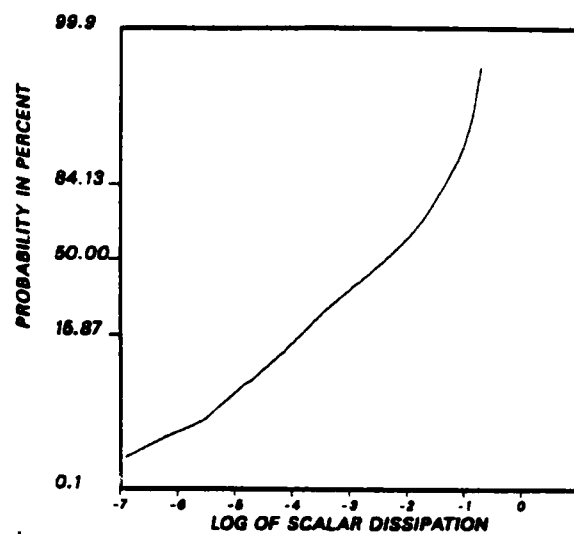
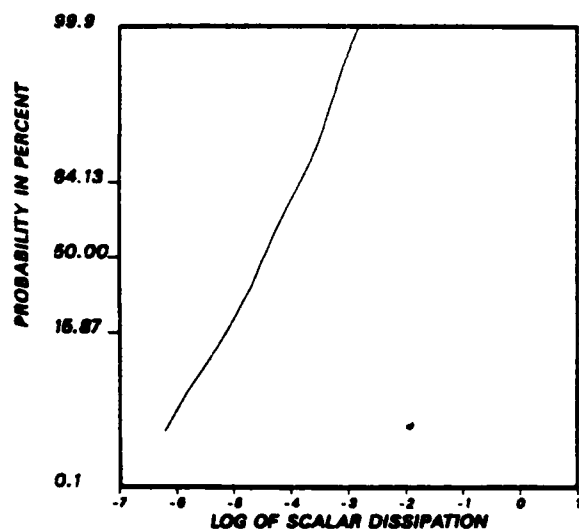


Figure 3. Representative probability plots in which a straight line indicates a lognormal distribution, the scalar value is: a) 0.05 and b) 0.5. For low scalar values, the two ways of estimating the lognormal parameters have reasonable agreement whereas at large scalar values the estimate from the χ distribution would have a much smaller slope than the straight-line region in b).

TABLE I

ESTIMATED LOGNORMAL PARAMETERS FOR SCALAR DISSIPATION

Z	σ^2	from $\ln \chi$		σ^2 ^b	from χ	
		μ_Z	μ_s ^a		μ_Z ^c	μ_s ^a
0.01	0.27	-7.30	-0.051	0.38	-7.33	-0.078
0.05	0.43	-4.51	0.039	0.35	-4.48	0.066
0.10	0.49	-3.42	0.056	0.37	-3.39	0.093
0.15	0.52	-2.85	0.062	0.38	-2.80	0.110
0.20	0.55	-2.49	0.060	0.38	-2.43	0.110
0.25	0.60	-2.25	0.041	0.38	-2.19	0.110
0.30	0.69	-2.12	-0.007	0.39	-2.03	0.082
0.35	0.86	-2.09	-0.100	0.41	-1.96	0.024
0.40	1.20	-2.19	-0.290	0.45	-2.00	-0.098
0.45	1.35	-2.35	-0.490	0.52	-2.12	-0.270
0.50	1.53	-2.57	-0.740	0.61	-2.32	-0.480

^a $\mu_s = \mu_Z + \ln(2\pi) + 2\eta^2(Z)$, mean of $\ln s$ distribution

^b $\sigma^2 = \ln(\overline{\chi^4}/\overline{\chi^2}^2 + 1)$, variance of $\ln \chi$ distribution

^c $\mu_Z = \ln \overline{\chi} - \sigma^2/2$, mean of $\ln \chi$ distribution

LARGE EDDY SIMULATIONS OF A WALL-BOUNDED TURBULENT JET FLOW AND OF HOMOGENEOUS SHEAR FLOW

F. BARON - D. LAURENCE

ELECTRICITE DE FRANCE
LABORATOIRE NATIONAL D'HYDRAULIQUE

6, quai Watier, 78400 CHATOU (FRANCE)

ABSTRACT

A numerical code solving time dependant Navier-Stokes equations in three dimensions is used to compute the large scale fluctuations of a turbulent flow induced by a jet in a cavity and of a homogeneous shear flow. Results are compared with experiment.

INTRODUCTION

Large Eddy Simulations (LES) have often been performed on simple flow configurations which allows representation by means of Fourier or Tchebycheff functions. The aim of this work was to test this approach with a numerical code operating in physical space, in the case of a complex industrial flow. It is believed that with the increasing computer performances, L.E.S. might soon overstep the scholar field and compete, in the engineering field, with classical high order closures whose costs and complexity are rapidly increasing.

I. MEASUREMENTS IN THE CUBIC BOX.

A turbulent water jet with mean velocity $U_0 = 24$ cm/s enters the domain (a cubic box with sides $a = 50$ cm) through the square window F, (sides $b = 15$ cm), hence the Reynolds number : $Re = 36.000$. The jet impinges the opposite wall, recirculates and progressively moves towards the exit window F_2 in the lower half of the box. Flow visualisations are made by taking pictures by means of plane light beams, and measurements are made by laser doppler anemometry. Comparisons are made in the vertical plane going through the centers of both inlet and outlet windows (fig. 1).

II. NUMERICAL CODE

Large Scale Components

The splitting of the instantaneous velocity field U_i into a large scale component \bar{U}_i and a subgrid fluctuation is achieved by a filtering operation.

$$\bar{U}_i(\underline{x}, t) = \int G(\underline{x} - \underline{x}') U_i(\underline{x}', t) d\underline{x}'$$

$$U_i'(\underline{x}, t) = U_i - \bar{U}_i$$

The filtered Navier-Stokes equations are then :

$$\begin{cases} \frac{\partial \bar{U}_i}{\partial t} + \frac{\partial}{\partial x_j} (\bar{U}_i \bar{U}_j) = -\frac{1}{\rho} \frac{\partial \bar{P}}{\partial x_i} \\ \quad - \frac{\partial}{\partial x_j} [(L_{ij} + S_{ij} - \nu \frac{\partial \bar{U}_i}{\partial x_j})] \\ \frac{\partial \bar{U}_i}{\partial x_j} = 0 \end{cases}$$

The subgrid stresses $S_{ij} = \overline{U_i' U_j'} + \overline{U_i' U_j} + \overline{U_i U_j'}$ are modelled by a turbulent viscosity ν_T , and the large scale strain-rate tensor \bar{D}_{ij} :

$$S_{ij} = -2 \nu_T \bar{D}_{ij} + \frac{1}{3} S_{ii} \delta_{ij}, \quad \bar{D}_{ij} = \frac{1}{2} \left(\frac{\partial \bar{U}_i}{\partial x_j} + \frac{\partial \bar{U}_j}{\partial x_i} \right)$$

where ν_T is given by Smagovinsky's model /1/

$$\nu_T = C_s \lambda^2 (\bar{D}_{ij} \cdot \bar{D}_{ij})^{1/2}$$

C_s being a constant, and λ a characteristic length of the mesh cell.

The "Leonard Stress" $L_{ij} = \overline{U_i U_j} - \bar{U}_i \bar{U}_j$ is important if one uses a formal filter which is wide in comparison with the mesh step. But this would imply a very large number of grid points. We preferred to let G be the inherent filtering effect of the finite difference scheme, and in this case, the assumed value of the "Leonard Stress" was found to fall within round-off errors of the numerical scheme, and thus was neglected /2/.

Numerical Resolution of Equations

Following Chorin's pattern /3/, the $(n+1)^{th}$ time step is computed in three steps :

Advection of Momentum

$$\frac{\partial U_i}{\partial t} + U_j \frac{\partial U_i}{\partial x_j} = 0$$

The equation is solved by a three-dimensional characteristics method. U_i is constant along the curvilinear (sub-steps of Δt) characteristic $\bar{M}(t)$:

$$\frac{d\bar{M}}{dt} = \bar{U}^n$$

$$\bar{x} = \bar{M}(t^{n+1})$$

$$\bar{x}_0 = \bar{M}(t^n)$$

$$\bar{U}_i(\bar{x}) = \bar{U}_i^n(\bar{x}_0)$$

The location \bar{x}_0 not being a node point, $U_i^n(\bar{x}_0)$ is interpolated using a weighted average of Taylor developments centered on the 9 node points of the 3D cell containing \bar{x}_0 . (32 point interpolation).

Diffusion of Momentum

$$\frac{\bar{U}_i - \tilde{U}_i}{\Delta t} = \frac{\partial}{\partial x_j} (2(\nu + \nu_T) \tilde{D}_{ij})$$

This equation is solved by a successive over relaxation (SOR) scheme.

Continuity and Pressure

The pressure p^{n+1} enables U_i^{n+1} to be divergence free :

$$\begin{cases} U_i^{n+1} - \tilde{U}_i = \frac{1}{\rho} \frac{\partial p^{n+1}}{\partial x_i} \\ \frac{\partial U_i^{n+1}}{\partial x_i} = 0 \end{cases}$$

Pressure p^{n+1} is first computed on a staggered grid through the Poisson equation :

$$\frac{\partial \tilde{U}_i}{\partial x_i} = \frac{\Delta t}{\rho} \frac{\partial^2 p^{n+1}}{\partial x_i^2}$$

which is solved by a Gauss-Seidel iterative method with over relaxation. Then, the new velocity is obtained by adding the pressure gradient.

Boundary Conditions

Entrance : $U^{n+1} = U_0(t)$ given

Exit : no condition, advection is assumed to be dominant. Normal velocity component is set to zero.

Walls : A relationship between tangential velocity and shear stress is derived from the logarithmic law of the wall. This is a crude assumption for instantaneous velocities which does not simulate wall turbulence production, but the dominant feature in the cubic box was assumed to be turbulence production in the shear layer of the jet. Large Eddy Simulation of wall effects is studied as a separated research topic.

Continuity step

With the previous boundary conditions on velocity, the following Neuman condition is valid for pressure :

$$\frac{\partial p^{n+1}}{\partial n} = 0 \quad (n : \text{normal to the boundary}).$$

III. RESULTS.

III.1. Turbulent flow in the cubic cavity

3-D k - ϵ Model

Computations using a k - ϵ Model [3] are introduced here as an extension of experimental results which do not, as yet, cover the entire 3D domain, and because the set of boundary conditions used in the Large Eddy Simulation do not allow direct comparison with experience.

The 3D k - ϵ Model is a classical one, and will not be detailed here. The numerical scheme is similar to the one described previously. Source and sink terms of the k, ϵ equations are accounted for in the diffusion step.

Comparisons with available experimental data validate this extension. The mean velocity field in the vertical plane through the jet axis is in good agreement (fig. 2). Turbulent kinetic energy in the same plane is plotted against experimental results in figure 3. Correct values are found in the jet shear layer. Higher order interpolation was proved to be necessary for the advection of energy from these very narrow production zones.

Large Eddy Simulation

Using the previous (experimental) set of boundary conditions at the entrance failed to exhibit any production of turbulence. Since this production was expected in the shear layers of the jet, it is believed that this region was too narrow in comparison with the mesh. Therefore, the uniform velocity profile at the jet entrance was changed into a triangular profile which enables the spread of the shear layer throughout the whole jet cross-section. (See fig. 5).

Turbulence triggering was not done by initial conditions but through boundary conditions at the jet entrance, since advection is dominant. Data recording is started once statistical quantities have reached a steady state (500 time steps). Turbulent variables are computed over 420 time steps (steps 500 to 920) on the $41 \times 41 \times 48$ mesh (101.6 10^3 variables).

Turbulent energy k ($k = 5 \cdot 10^{-3} \text{ m}^2/\text{s}^2$) is carried by the entering jet. In the first attempt, this energy was distributed over an equilibrium time spectrum discretized by time Fourier series. This type of fluctuating motion, having no spatial correlation, exhibited a decrease in turbulent energy while crossing the first half of the box.

Another computation was performed, in which turbulent field was calculated in the direct upstream from the box entrance and advected by the entering jet.

A 3D space energy spectrum was chosen, length scales in the streamwise direction being larger than in the cross-stream directions. This is used to compute a turbulent field in Fourier space, compatible with the L.E.S. code's continuity equation as was done for the homogeneous shear case.

This last precaution prevents a decrease of turbulent energy over the first 3 or 4 cells after the entrance owing to pressure smoothing effects.

In the vertical plane (fig. 4), the large scale turbulent energy compares quite well with the results of the k - ϵ computation (with triangular velocity profile at the entrance), it exceeds the value $10^{-2} \text{ m}^2/\text{s}^2$ at the end of the shear layer. The ability of the LES to increase the turbulent energy by a factor 20 from its boundary value was found to depend more on the length scales than on the total energy of the turbulent structures imposed at the entrance.

The jet flapping phenomenon which was observed in the experimental set-up was also reproduced by LES as can be seen on film or on fig. 5.

Fig. 6 shows again instantaneous flow patterns in the vertical planes across the jet. Unsteady large eddies are more visible since they scale with the rather small mean velocities in these planes.

III.2. Large Eddy Simulation of Homogeneous Shear Flow

Definition of the flow.

An homogeneous and isotropic turbulent flow defined in an infinite space is suddenly submitted (time $t = 0$) to

an uniform mean shear $s = \frac{d\langle U_1 \rangle}{dx_3}$ (fig. 7).

The resulting evolution of the flow - still homogeneous but anisotropic - is entirely given by s and the initial spectrum. In the case presented here the value of the mean shear is $s = 46.8 \text{ s}^{-1}$.

Spatial periodicity

The infinite space required by homogeneity is assumed to be correctly represented by spatial periodicity in the 3 directions, as long as the largest scales do not exceed half a spatial period.

In the mean shear direction x_3 , spatial periodicity has to be combined with a translation along the mean flow direction x_1 . To deal with this problem, the neighbouring virtual domains in x_3 direction are staggered at each time step in the mean flow direction (fig. 7).

Initial condition

The initial energy spectrum is taken from COMTE-BELLOT

and CORRSIN's experiments /5/ on grid turbulence.

Following ROGALLO /6/, we then define in Fourier Space a velocity field that fits the given spectrum and verifies continuity equation as it is discretized in the finite-difference scheme of the code.

This point leads to a continuity equation

$$k' \cdot \tilde{u}(k') = 0$$

of classical form, except that k' is a complex vector function of the "current" wavenumber vector k .

That initial condition is discretized on 32 wavenumbers in each directions :

$$k = \pm n \frac{2\pi}{L} \quad (1 \leq n \leq 16)$$

L being the length of the computational domain.

Inverse Fourier transform given then an initial condition discretized on the 32^3 mesh points of the physical domain of computation.

Results.

Using the homogeneous properties of the flow, the statistical operator $\langle \rangle$ used here is a spatial averaging over the 32^3 mesh points of the domain for a single run (that is for a single set of initial phases). Although the right sample for such an averaging should be a large number of runs, this classical method is acceptable for the one-point correlations presented here.

Figure 8 shows the evolution of the Reynolds tensor diagonal terms. Its trend is in good agreement with TAVOULARIS and CORRSIN's /7/ experimental results : $\langle u_1^2 \rangle$ is fed by the mean flow while $\langle u_2^2 \rangle$ takes energy from the latter through pressure strain correlation terms (fig. 9).

Figure 10 shows the evolution of the $\langle u_1^2 \rangle$ equation terms ; the rate of change $\frac{d\langle u_1^2 \rangle}{dt}$ is negative at $t = 0$

(decaying turbulence) and increases to reach positive values. The production term starts from zero and increases with $\langle u_1 u_3 \rangle$. This correlation $\langle u_1 u_3 \rangle$ has a non-zero interaction term and a sudden change in pressure-strain correlation due to its rapid (linear) part (fig. 11). $\langle u_1 u_3 \rangle$ tends toward an asymptotic value.

The projection of instantaneous velocity field on the two planes normal to the principal axes of the strain-rate tensor (fig. 12) illustrates the stretching of the vorticity along one axis and the contraction along the other.

CONCLUSION

As can be seen in the homogeneous shear case, LES performs well, provided that the computation of the large scales extends down to the equilibrium range. If not, one must abandon the Smagorinsky model for some higher order model allowing for two way energy transfer (drain and backscatter). This was not the case in the LES of the turbulent cavity but still, interesting phenomena such as jet flapping were reproduced. It shows that LES gives much more information than classical closures. This should be even more so in LES with heat fluctuations which are presently being undertaken. A model for turbulence production at the wall on a coarse mesh is also being studied, since again, a turbulent viscosity model does not apply here.

REFERENCES

- /1/ Smagorinsky J. : General circulation experiments with the primitive equations. I. the basic experiments Mon. Weather Rev., 91, 99 (1963).
- /2/ Benque J.P. : Modélisation d'écoulements turbulents isothermes. Report EDF-LNH N° HEO41/78.12 (1978).
- /3/ Chorin A.J. : The numerical solution of the Navier-Stokes equations for an incompressible fluid. Bull. Ann. Math. Soc. 73 (1967).
- /4/ Viollet P.L. : Turbulent mixing in a two layer stratified shear flow, report EDF LNH 041/80.04. (1980)
- /5/ Comte-Bellot G., Corrsin S. : Simple Eulerian time correlation of full - and narrow - band velocity signals in grid-generated, isotropic turbulence, J. Fluid Mech (Vol. 48, part 2 (1971)).
- /6/ Rogallo R.S. : Numerical experiments in homogeneous turbulence. NASA Technical memorandum 81315 (1981).
- /7/ Tavoularis S., Corrsin S. : Experiments in Nearly Homogeneous Turbulent Shear Flow with a Uniform Mean Temperature Gradient, Parts 1 and 2. J. Fluid. Mech., vol. 104, pp. 311-367 (1981).

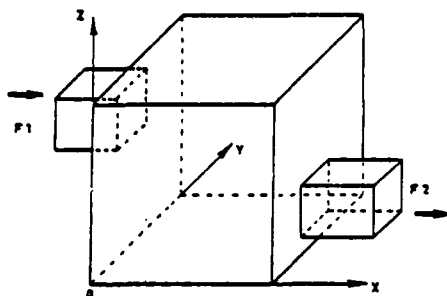


Fig. 1 : Experimental setup

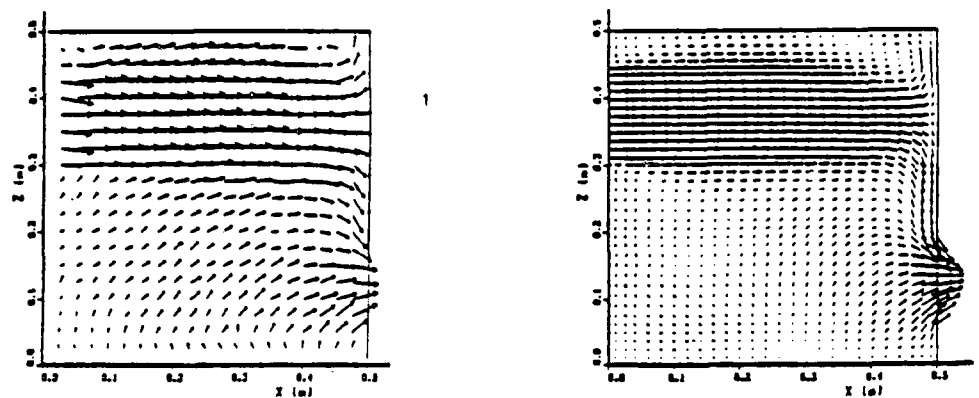


Fig. 2 : Mean velocity in the vertical plane.
1 Experiment, 2 $k-\epsilon$ computation

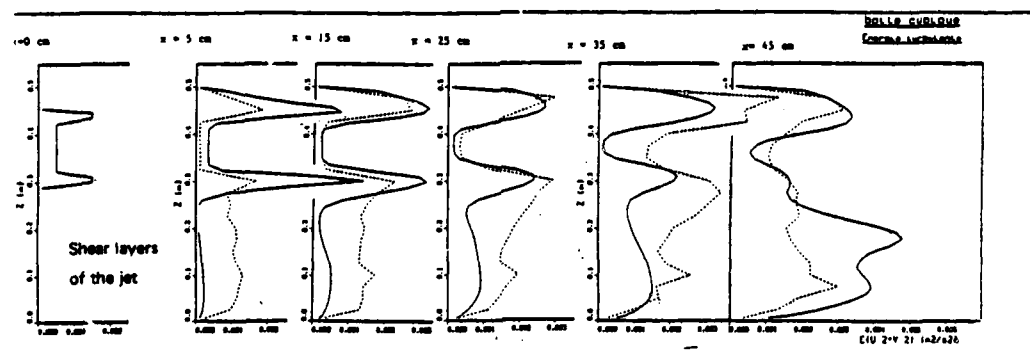


Fig. 3 : Turbulent kinetic energy, — measurements, - - - $k-\epsilon$ model

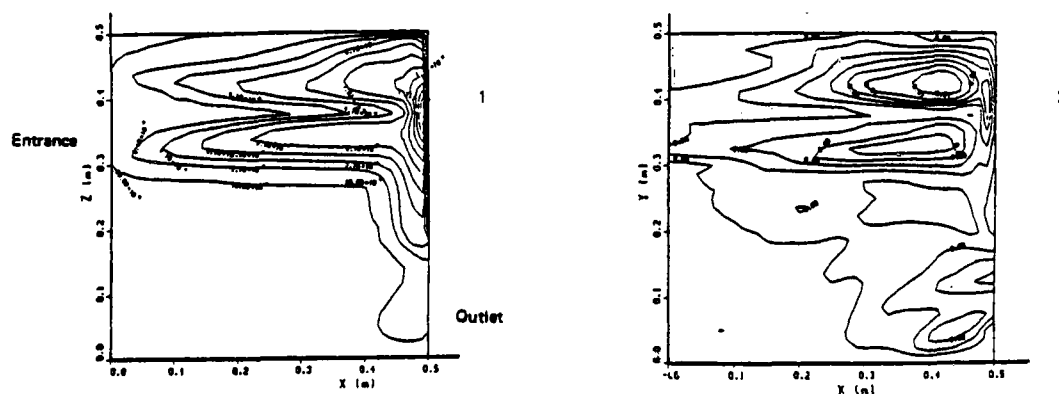


Fig. 4 : Turbulent kinetic energy : 1 $k-\epsilon$, 2 LES.

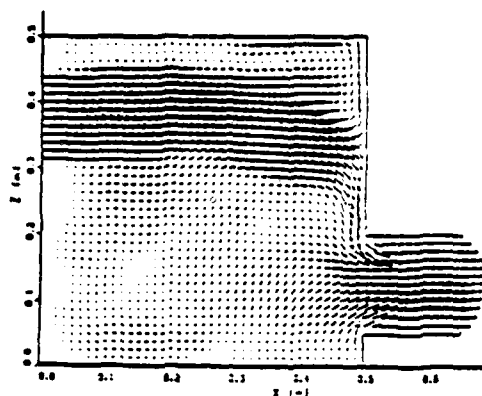
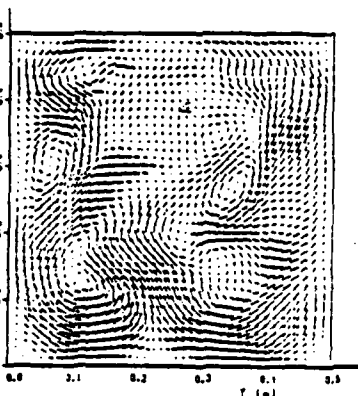
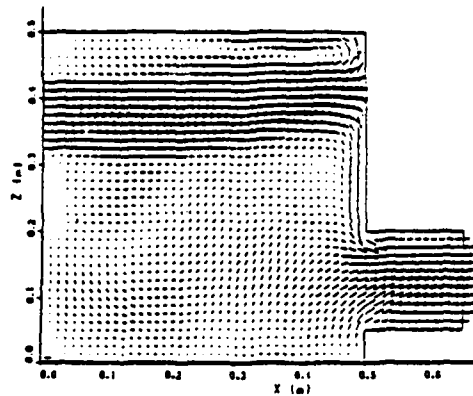


Fig. 5 : Instantaneous velocities, same vertical plane, different times.



Cross
sections
of jet

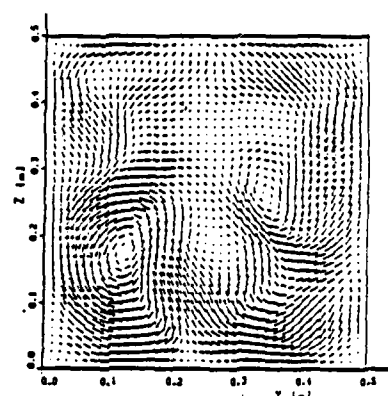


Fig. 6 : Instantaneous velocities. Vertical plane in the middle of the box, perpendicular to the jet.

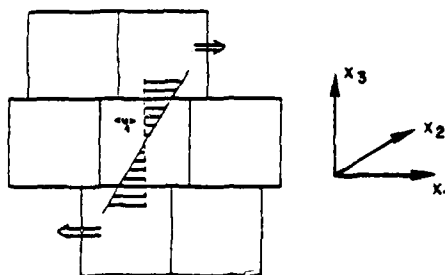


Fig. 7 : Homogeneous shear. Definition of the axes and sketch of staggered periodicity.

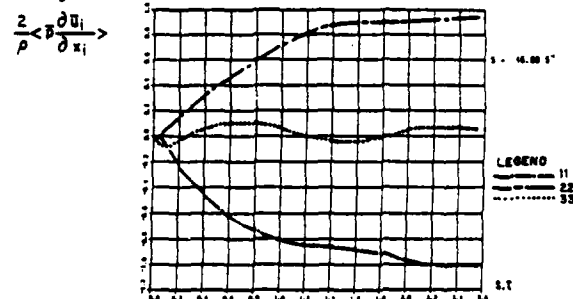


Fig. 9 : Homogeneous shear. Evolution of pressure-strain correlation tensor diagonal terms.

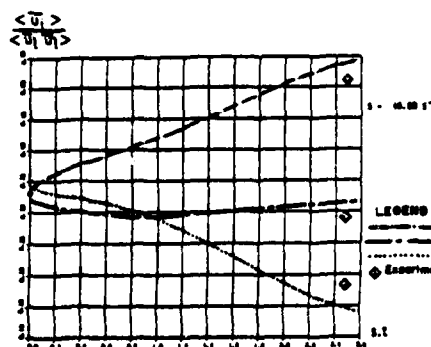


Fig. 8 : Homogeneous shear. Evolution of Reynolds tensor diagonal terms. Comparison with TAVOULARIS and CORRSIN // experiments.

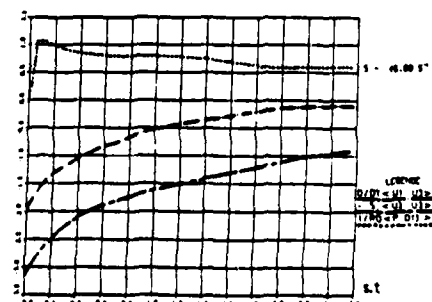


Fig. 10 : Homogeneous shear. Evolution of the $\langle u_i u_j \rangle$ equation terms.

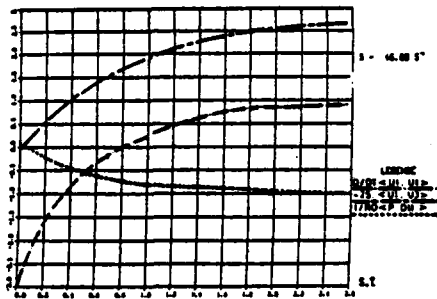


Fig. 11 : Homogeneous shear. Evolution of the $\langle u^2 \rangle$ equation terms.

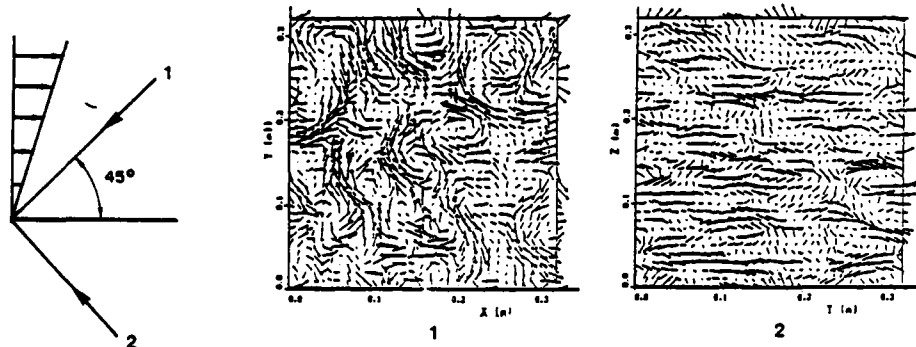


Fig. 12 : Homogeneous shear. Instantaneous velocity field projected normally to the principal axes of the strain-rate tensor.
1 - Plane normal to stretching axis
2 - Plane normal to contraction axis

STABILITY OF SIMILARITY SOLUTIONS BY TWO-EQUATION MODELS OF TURBULENCE

W. Stüttgen and N. Peters

Institut für Allgemeine Mechanik
RWTH Aachen, West-Germany

ABSTRACT

The stability of the similarity solution of a turbulent round jet with zero outer velocity is investigated. Two solutions of the equations with different modelling constants are analysed. One is Jones' and Launder's $k-\epsilon$ model and the other is Rotta's $k-l$ model. The l -equation is transformed into the form of an ϵ -equation in order to permit the comparison of the different constants of the models. In addition, an equation for the turbulent viscosity is derived.

The mathematical properties of the equations are discussed. It is shown that in the limit of vanishing laminar viscosity the parabolic equations degenerate to a form which exhibits discontinuities and has a wave-like solution. This property is discussed by comparison with Zeldovich's thermal waves.

The similarity equations are derived. The stiffness of the equations is shown by an asymptotic expansion around the limit "production equals dissipation". The similarity solution is obtained by a shooting technique. A linear and a non-linear stability analysis of the similarity solution is performed. The linear perturbation of this solution yields by a discretisation technique at least one eigenvalue with a positive real part, showing unstable solutions. The non-linear solution is performed by solving the non-similar equations with a finite difference method. Here the modified Rotta-model appears to be more stable than the $k-\epsilon$ -model.

INTRODUCTION

It is widely known that numerical integration techniques using two-equation models of turbulence exhibit severe stability problems. It is also observed that the reduction of step size does not avoid the stability problems but rather increases them. It seems that a certain amount of numerical damping is necessary to obtain stable solutions. In free shear flows of the boundary layer type the problem is sometimes circumvented by solving the governing equations in a transformed coordinate system where the normalized stream function varying between 0 and 1 appears as independent normal coordinate /1/. This technique is not applicable to elliptic flows with arbitrary boundary conditions, where the equations must be solved in the physical plane. When the boundary conditions have to be applied at large distances from the region of main turbulence production, for instance with a jet flow into a chamber, stable numerical solutions are very difficult to obtain.

There appears to be a disproportion between the large number of numerical applications of two-equation models of turbulence and of more fundamental investigations into their mathematical structure. These equations are, of course, highly non-linear and are generally solved in at least two space dimensions. In this paper we will point out certain properties of the equations which will lead to disasters in numerical computations, if they are overlooked. It is the purpose of the paper to show that the stability difficulties are not likely to originate from numerical schemes but are a property of the equations.

GOVERNING EQUATIONS

As a test case the steady turbulent flow of a round jet into a stagnant atmosphere is considered. Using the boundary layer approximations the governing equations for the mean velocities and the turbulent kinetic energy are written

Continuity

$$\frac{\partial(ur)}{\partial x} + \frac{\partial(vr)}{\partial r} = 0 \quad (1)$$

Momentum

$$ur \frac{\partial u}{\partial x} + vr \frac{\partial u}{\partial r} = \frac{\partial}{\partial r} \left[(v_t + \nu) r \frac{\partial u}{\partial r} \right] \quad (2)$$

Turbulent kinetic energy

$$ur \frac{\partial k}{\partial x} + vr \frac{\partial k}{\partial r} = \frac{\partial}{\partial r} \left[\frac{(v_t + \nu)}{Pr_k} r \frac{\partial k}{\partial r} \right] + r v_t \left(\frac{\partial u}{\partial r} \right)^2 - r \epsilon \quad (3)$$

The kinetic energy equation was first derived by Prandtl /2/. It contains as unknown quantities the turbulent viscosity v_t and the turbulent dissipation ϵ . Prandtl has shown that both can be related to at least one additional quantity, a turbulence length scale l by

$$v_t = c_1 \sqrt{k} l, \quad \epsilon = c \frac{k^{3/2}}{l} \quad (4)$$

Later, Rotta /3/ developed a balance equation for l on the basis of an equation for a point correlation function. His more recent formulation has the form /4/

$$\begin{aligned}
u r \frac{\partial k l}{\partial x} + v r \frac{\partial k l}{\partial r} = & \\
\frac{\partial}{\partial r} \left[\frac{(v_t + v)}{Pr_l} r \left(l \frac{\partial k}{\partial r} + \alpha_L k \frac{\partial l}{\partial r} \right) \right] & \\
+ r \left[v_t \frac{\partial u}{\partial r} \left(\zeta_1 l \frac{\partial u}{\partial r} + \zeta_3 l^3 \left(\frac{2}{r} \frac{\partial u}{\partial r} + \frac{\partial^2 u}{\partial r^2} \right) \right) \right. & \quad (5) \\
+ \frac{\partial}{\partial r} (v_t \frac{\partial u}{\partial r}) \zeta_2 l^3 \left(\frac{1}{r} \frac{\partial u}{\partial r} + \frac{\partial^2 u}{\partial r^2} \right) & \\
\left. - r c_l c k^{3/2} - r c_2 k l \frac{\partial u}{\partial x} \right] &
\end{aligned}$$

where

$$\begin{aligned}
c &= c_1^3 = 0.165, \quad c_2 = 1, \quad c_l = 0.8 \\
Pr_l &= c_1/k_q = 0.6856, \quad k_q = 0.8, \quad \alpha_L = 0.387 \\
\zeta &= 0.98, \quad \zeta_2 = 1.2, \quad \zeta_3 = -1.5
\end{aligned}$$

Alternatives to a length scale equation are equations for ϵ or v_t . An extensively tested and widely used model is the k - ϵ model by Jones and Lauder /5/. For sufficiently large turbulent Reynolds numbers the ϵ -equation is written as

$$\begin{aligned}
u r \frac{\partial \epsilon}{\partial x} + v r \frac{\partial \epsilon}{\partial r} = \frac{\partial}{\partial r} \left(\frac{(v_t + v)}{Pr_\epsilon} r \frac{\partial \epsilon}{\partial r} \right) & \\
+ r c_{\epsilon 1} v_t \frac{\epsilon}{k} \left(\frac{\partial u}{\partial r} \right)^2 - r c_{\epsilon 2} \frac{\epsilon^2}{k} & \quad (6)
\end{aligned}$$

where

$$\begin{aligned}
v_t &= c_D \frac{k^2}{\epsilon}, \quad c_D = c_1 c = 0.09 \\
c_{\epsilon 1} &= 1.44, \quad c_{\epsilon 2} = 1.92 \\
Pr_k &= 1.0, \quad Pr_\epsilon = 1.3
\end{aligned}$$

Using the algebraic relation between l , ϵ and k , Rotta's l -equation can be cast into the same form as the ϵ -equation, where the following additional terms appear on the r.h.s.

$$\begin{aligned}
(\text{add. terms}) = & \\
- r c_{\epsilon 3} v_t \frac{k^2}{\epsilon} \frac{\partial u}{\partial r} \left(\frac{\partial^3 u}{\partial r^3} + \frac{2}{r} \frac{\partial^2 u}{\partial r^2} \right) & \\
- r \zeta_{22} v_t \frac{\partial}{\partial r} \left(v_t \frac{\partial u}{\partial r} \right) \left(\frac{1}{r} \frac{\partial u}{\partial r} + \frac{\partial^2 u}{\partial r^2} \right) & \quad (7) \\
- c_{\epsilon 4} \frac{\epsilon}{k} \frac{\partial}{\partial r} \left[(v_t + v) r \frac{\partial k}{\partial r} \right] - r c_{\epsilon 5} v_t \frac{\epsilon}{k^2} \left(\frac{\partial k}{\partial r} \right)^2 & \\
+ r c_{\epsilon 6} v_t \frac{1}{k} \frac{\partial k}{\partial r} \frac{\partial \epsilon}{\partial r} - r c_{\epsilon 7} v_t \frac{1}{\epsilon} \left(\frac{\partial \epsilon}{\partial r} \right)^2 & \\
+ c_2 \epsilon \frac{\partial u}{\partial x} &
\end{aligned}$$

where

$$\begin{aligned}
Pr_k &= Pr_l = 0.6856, \quad Pr_\epsilon^* = Pr_l/\alpha_L = 1.77, \\
c_{\epsilon 1} &= 5/2 - \zeta = 1.52, \quad c_{\epsilon 2} = 5/2 - c_l = 1.70, \\
c_{\epsilon 3}^* &= \zeta_3 c^2 = -0.041, \quad \zeta_{22} = c^{2/3} \zeta_2 = 0.361, \\
c_{\epsilon 4}^* &= (1+3\alpha_L/2)/Pr_l - 5/(2Pr_k) = -1.34 \\
c_{\epsilon 5}^* &= 3(1+3\alpha_L/2)/(2Pr_l) = 3.4579 \\
c_{\epsilon 6}^* &= (1+3\alpha_L/2)/Pr_l + 5/(2Pr_\epsilon^*) = 3.716 \\
c_{\epsilon 7}^* &= 2/Pr_\epsilon^* = 1.13
\end{aligned}$$

The occurrence of higher order velocity derivatives in this equation leads to additional numerical difficulties. It is consistent with the assumption of a single length scale l and a single time scale k/ϵ to replace the velocity derivative by using the assumption production equals dissipation in the turbulence energy equation

$$\epsilon = v_t \left(\frac{\partial u}{\partial r} \right)^2 \quad (8)$$

leading to

$$\frac{\partial u}{\partial r} = \frac{1}{c^{2/3}} \frac{\epsilon}{k} \quad (9)$$

Then the first two terms in Eq. (7) are to be replaced by

$$- c_{\epsilon 3} v_t \frac{\partial \epsilon}{\partial r} + (c_{\epsilon 3} - \zeta_{22}) v_t \frac{\epsilon}{k} \frac{\partial k}{\partial r}$$

and the constants change to

$$\begin{aligned}
Pr_\epsilon &= Pr_\epsilon^*/(1 + Pr_\epsilon^* c_{\epsilon 3}) = 0.985 \\
c_{\epsilon 3} &= c^{2/3} \zeta_3 = -0.451 \\
c_{\epsilon 4} &= c_{\epsilon 4}^* - c_{\epsilon 3} = -0.890 \\
c_{\epsilon 5} &= c_{\epsilon 5}^* + 4 c_{\epsilon 3} - \zeta_{22} = 1.292 \\
c_{\epsilon 6} &= c_{\epsilon 6}^* + 5 c_{\epsilon 3} - \zeta_{22} = 1.099 \\
c_{\epsilon 7} &= c_{\epsilon 7}^* + c_{\epsilon 3} = 0.678
\end{aligned}$$

It is seen that the modified Rotta model and the k - ϵ -model differ only slightly in the common constants Pr_ϵ , $c_{\epsilon 1}$ and $c_{\epsilon 2}$ but that the Rotta model contains additional terms. Voges /6/ has compared the Rotta model with other two-equation models of turbulence, including the k - ϵ -model, in their capability to "postdict" the boundary layer data of the 1968 - Stanford Conference /7/. He shows that it is in particular the last term in Eq. (7) which causes considerable deficiencies. If c_2 is set zero, the predictive power of the Rotta model is similar to that of the k - ϵ -model.

The third choice is an equation for v_t rather than one for l or ϵ . Defining

$$\lambda = \frac{k^2}{\epsilon}, \quad v_t = c_D \lambda \quad (10)$$

and using again the algebraic relation between v_t , ϵ and k one obtains an equation for λ

$$\begin{aligned}
u r \frac{\partial \lambda}{\partial x} + v r \frac{\partial \lambda}{\partial r} = \frac{\partial}{\partial r} \left[\frac{(v_t + v)}{Pr_\lambda} r \frac{\partial \lambda}{\partial r} \right] & \\
+ r (2 - c_{\epsilon 1}) v_t \frac{\lambda}{k} \left(\frac{\partial u}{\partial r} \right)^2 - r (2 - c_{\epsilon 2}) k & \\
+ c_{\lambda 4} \frac{\lambda}{k} \frac{\partial}{\partial r} \left((v_t + v) r \frac{\partial k}{\partial r} \right) & \\
+ r c_{\lambda 5} v_t \frac{\lambda}{k^2} \left(\frac{\partial k}{\partial r} \right)^2 & \quad (11) \\
+ r c_{\lambda 6} v_t \frac{1}{k} \frac{\partial k}{\partial r} \frac{\partial \lambda}{\partial r} & \\
+ r c_{\lambda 7} v_t \frac{1}{\lambda} \left(\frac{\partial \lambda}{\partial r} \right)^2 & \\
+ c_{\epsilon 3} v_t \frac{\lambda}{k} \left(\frac{\partial k}{\partial r} - \frac{k}{\lambda} \frac{\partial \lambda}{\partial r} \right) & \\
+ v_t \zeta_{22} \frac{\lambda}{k} \frac{\partial k}{\partial r} &
\end{aligned}$$

where $c_2 = 0$ has been introduced and the constants are

$$c_{\lambda 4} = 2/Pr_k - 2/Pr_e + c_{e4} = -0.004$$

$$c_{\lambda 5} = c_{e5} + 4 c_{e7} - 2 c_{e6} - 2/Pr_e = -0.227$$

$$c_{\lambda 6} = c_{e6} - 4 c_{e7} + 4/Pr_e = 2.45$$

$$c_{\lambda 7} = c_{e7} - 2/Pr_e = -1.35, Pr_\lambda = Pr_e$$

(The numerical values are for the Rotta model).

Finally, a general relation between the constants can be obtained by requiring that the universal law at the wall should be satisfied. From

$$u = u_\tau \left(\frac{1}{\kappa} \ln \frac{y u_\tau}{\nu} + c \right) \quad (12)$$

where $\kappa = 0.4$ is von Kármán's constant and Eq. (8) follows $k = u_\tau^2/c_2^{2/3}$, $\lambda = \kappa u_\tau y/c_D$ and from Eq. (11) one obtains

$$c_{e2} - c_{e1} + \kappa^2 c^{-2/3} (c_{e7} - 1/Pr_e) = 0 \quad (13)$$

This equation will be used to determine c_{e7} in the modified Rotta model.

WAVE-LIKE SOLUTIONS

A certain class of non-linear diffusion equations are known to degenerate, if the diffusion coefficient depends non-linearly on the solution and vanishes at a boundary at infinity. A well-known example of an equation from this class is the so called 'Porous Media Equation'

$$\frac{\partial v}{\partial t} = \frac{\partial^2 v^m}{\partial x^2}, \quad m > 1 \quad (14)$$

or the 'Thermal Wave Equation' of Zeldovich /8/

$$\frac{\partial T}{\partial x} = a \frac{\partial}{\partial x} \left(T^n \frac{\partial T}{\partial x} \right), \quad n > 0 \quad (15)$$

with the boundary condition $v, T \rightarrow 0$ as $x \rightarrow \infty$. Eqs. (14) or (15) have solutions with peculiarities in the form of discontinuous derivatives. The mathematical theory for such degenerate parabolic equations has been developed in /9/ - /13/. For instance, the solution of Eq. (15) with a constant temperature T_0 on the boundary $x = 0$ has the form as shown in Fig. 1 (cf. /8/, p. 673). It is a thermal wave front with a front coordinate x_f proportional to $(a T_0^n t)^{1/2}$ and a propagation velocity proportional to $(a T_0^n / t)^{1/2}$.

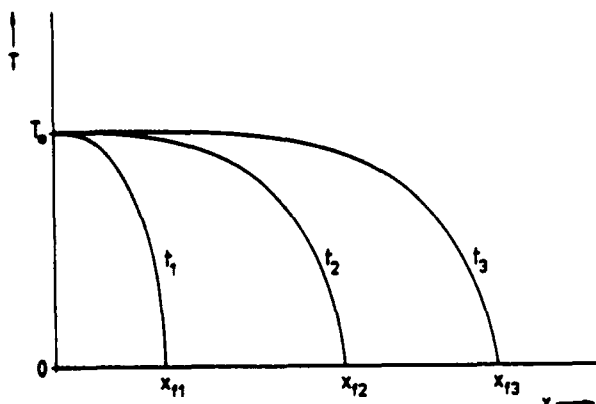


Fig. 1: Schematic solution of Zeldovich's thermal wave

Ahead of the front the temperature remains undisturbed. This is in contrast to the solution of the classical linear heat conduction equation, where the propagation velocity is infinite.

The λ -equation turns into a form very similar to Eq. (15) for $\nu \rightarrow 0$ if the boundary $\lambda = 0$ is applied at $r \rightarrow \infty$. It is easily verified that in this case the undisturbed solution $\lambda = 0$ satisfies the equation. One may therefore expect a discontinuous derivative to develop at a finite radius r_f . The existence of a discontinuity in free shear flows for $\nu \rightarrow 0$ is in fact well known for Prandtl's mixing length model (Schlichting /14/ p. 680) and Rotta's k - λ -model /4/. For finite but small values of ν this discontinuity is smeared out. However, if the boundary conditions are applied at large values of r and ν is small, the degenerate character of the equation may lead to severe stability problems. It seems that in many numerical calculations the generated numerical viscosity rescues the situation.

THE SIMILARITY SOLUTION

We introduce the similarity coordinates

$$\xi = (x + x_0)/d, \quad \eta = yr/(\xi d) \quad (16)$$

and the stream function

$$\psi = d v_{\text{tref}} \xi F(\xi, \eta) \quad (17)$$

where v_{tref} is related to the spreading parameter γ , the nozzle diameter d , the nozzle exit velocity u_0 and the non-dimensional center line decay of the velocity $a = d(u_c/u_0)/d\xi$ as

$$v_{\text{tref}} = u_0 d a / \gamma^2 \quad (18)$$

The continuity equation is satisfied by

$$uv = \partial \psi / \partial r, \quad vr = -\partial \psi / \partial x \quad (19)$$

Introducing these definitions into the momentum equation, one obtains for the non-dimensional velocity $U = u/u_c = F_\eta/\eta$

$$\xi \left(U \frac{\partial F}{\partial \xi} \eta - \frac{\partial F}{\partial \xi} \frac{\partial U}{\partial \eta} \right) - \frac{\partial}{\partial \eta} (F U) = \frac{\partial}{\partial \eta} \left(C \eta \frac{\partial U}{\partial \eta} \right) \quad (20)$$

Here the Chapman-Rubesin parameter

$$C = (v_t + \nu)/v_{\text{tref}} = \Lambda + c_v \quad (21)$$

contains contributions from the turbulent as well as the laminar viscosity. Since $u_0 d / v_{\text{tref}}$ is typically 70 in a round jet, c_v is of the order 70/Re.

In the similarity region ($\partial/\partial \xi = 0$) this equation can be integrated once using the boundary conditions $F = 0$, $U = 1$ as $\eta = 0$ and $U \rightarrow 0$ as $\eta \rightarrow \infty$ to obtain

$$-F U = C \eta \frac{\partial U}{\partial \eta} \quad (22)$$

Introducing the non-dimensional quantities

$$\kappa = \kappa \xi^2 / (b u_0^2), \quad \Lambda = \lambda / (u_0 d c) = c_D \lambda / v_{\text{tref}} \quad (23)$$

one obtains for the turbulent kinetic energy and the turbulent viscosity the equation

$$F_\eta \left(\xi \frac{\partial \kappa}{\partial \xi} - 2\kappa \right) - \left(F + \xi \frac{\partial F}{\partial \xi} \right) \frac{\partial \kappa}{\partial \eta} = \frac{\partial}{\partial \eta} \left(\frac{C \eta}{Pr_k} \frac{\partial \kappa}{\partial \eta} \right) + \eta E_1 \Lambda \left(\frac{\partial U}{\partial \eta} \right)^2 - \eta E_2 \frac{\kappa^2}{\Lambda} \quad (24)$$

with $E_1 = a^2/b$, $E_2 = b/(ac)$

$$\begin{aligned}
E F_n \frac{\partial \Delta}{\partial \eta} - (F + E \frac{\partial F}{\partial \eta}) \frac{\partial \Delta}{\partial \eta} \\
= \frac{\partial}{\partial \eta} \left(\frac{C_n}{Pr_\lambda} \frac{\partial \Delta}{\partial \eta} \right) + n E_1 (2 - c_{e1}) \frac{\Delta^2}{\kappa} \left(\frac{\partial U}{\partial \eta} \right)^2 \\
- n E_2 (2 - c_{e2}) \kappa + c_{\lambda 4} \frac{\Delta}{\kappa} \frac{\partial}{\partial \eta} \left(C_n \frac{\partial \kappa}{\partial \eta} \right) \\
+ n c_{\lambda 5} \frac{\Delta^2}{\kappa^2} \left(\frac{\partial \kappa}{\partial \eta} \right)^2 + n c_{\lambda 6} \frac{\Delta}{\kappa} \frac{\partial \kappa}{\partial \eta} \frac{\partial \Delta}{\partial \eta} \\
+ n c_{\lambda 7} \left(\frac{\partial \Delta}{\partial \eta} \right)^2 + c_{e3} \frac{\Delta^2}{\kappa} \left[\frac{\partial \kappa}{\partial \eta} - \frac{\kappa}{\Delta} \frac{\partial \Delta}{\partial \eta} \right] - \zeta_{22} \frac{\Delta^2}{\kappa} \frac{\partial \kappa}{\partial \eta}
\end{aligned} \quad (25)$$

With the boundary conditions

$$\begin{aligned}
\eta = 0 : \quad \kappa = 1, \quad \partial \kappa / \partial \eta = 0 \\
\Delta = 1, \quad \partial \Delta / \partial \eta = 0 \\
\eta \rightarrow \infty : \quad \kappa \rightarrow 0, \quad \Delta \rightarrow 0.
\end{aligned} \quad (26)$$

The system of ordinary differential equations obtained in the similarity region has to satisfy two more boundary conditions than necessary. It therefore represents an eigenvalue problem for two parameters, for instance E_1 and E_2 related to the center line decay coefficients b and c . In the numerical method, however, it was found necessary to prescribe E_1 and consider E_2 and c_{e2} as eigenvalues.

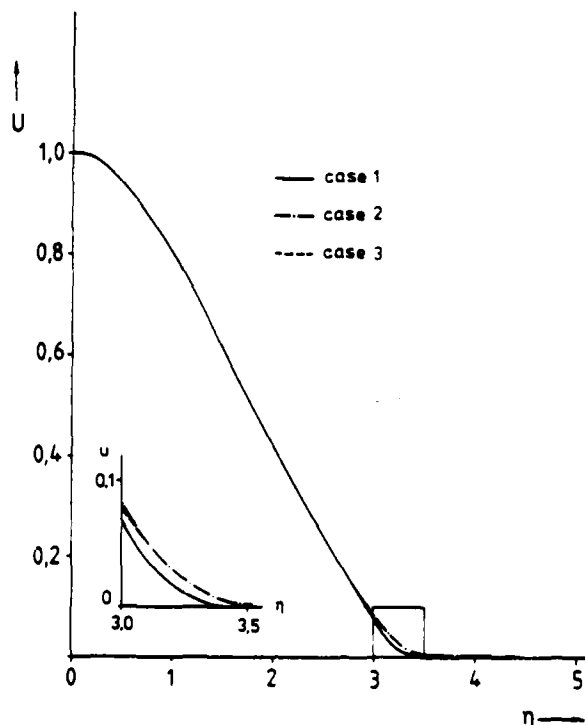


Fig. 2: Similar solution of the axial velocity

TABLE 1

	Pr_ϵ	Pr_κ	c_λ	c_{e1}	c_{e2}	c_{e3}	$c_{\lambda 4}$
case 1	1.3	1.0	0.04	1.44	1.885	0	0
case 2	1.3	1.0	0.0575	1.44	1.892	0	0
case 3	1.01	0.685	0.05	1.52	1.878	-0.449	-0.395
	$c_{\lambda 5}$	$c_{\lambda 6}$	$c_{\lambda 7}$	ζ_{22}	E_1	E_2	
case 1	-1.538	3.077	-1.538	0	9.566	2.149	
case 2	-1.538	3.077	-1.538	0	9.566	2.127	
case 3	-1.644	3.806	-1.66	0.363	9.566	1.967	

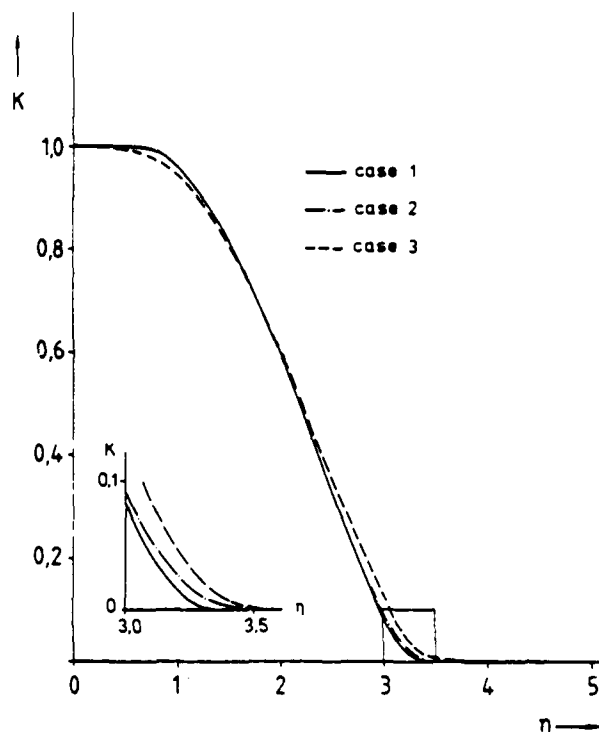


Fig. 3: Similar solution of the kinetic energy of turbulence

The similarity equations were solved by a multiple shooting method using a program package developed by Burlisch and Stoer (cf. /15/). The outer boundary condition was imposed at $\eta=6$. In particular the solution for the $k-\epsilon$ model was extremely difficult to obtain. This is seen by considering the limit $\eta \rightarrow \infty$ with $\kappa = 0$ prescribed. Then the diffusion term and the term containing the coefficient c_{e7} balance and one obtains in the limit $c_v = 0$

$$\Delta \sim (\eta - \eta_f) \frac{1}{c_{e7} Pr_\epsilon} \quad \text{for the Rotta model}$$

and

$$\lambda \sim \exp \eta \quad \text{for the } k-\epsilon \text{ model.}$$

For $c_{e7} > 0$ the Rotta model shows the discontinuity at η_f discussed in the preceding paragraph, while the $k-\epsilon$ model shows an increase to infinity as $\eta \rightarrow \infty$.

The stiffness of the equations can also be seen by considering the asymptotic limit of large values of E_1 with $E_2/E_1 = 0$ (1). This limit is justified for large η by the fact that $\partial U / \partial \eta$ is small and E_1 is of order ten. Then to leading order there results from the k -equation the approximation Eq. (8). The same limit, applied to the ϵ -equation yields a value of ϵ which is c_{e1}/c_{e2} times that obtained from the k -equation. This contradiction can only be resolved by requiring that c_{e1}/c_{e2} differs from one only by an amount of order $O(E_1^{-1})$, which is at least not evident. The existence of two competing fix-points for large E_1 adds certainly to the numerical difficulties posed by the $k-\epsilon$ -model.

Typical profiles for both models are shown in Fig. 2-4. The region, where the profiles decay to zero, has been blown up in these figures. The corresponding sets of parameters are given in Table 1. Using Eqs. (18) and (23) as well as the momentum integral

$$I = \int_0^\infty U^2 \eta \, d\eta = \gamma^2 / (8a^2) \quad (27)$$

the spreading parameter and the decay coefficients were obtained from

$$\gamma = \sqrt{\frac{a}{c c_D}}, \quad a = \sqrt{\frac{E_1 E_2}{1.8 c_D}}, \quad b = \frac{E_2}{1.8 c_D},$$

$$c = \frac{b}{E_2 a}$$

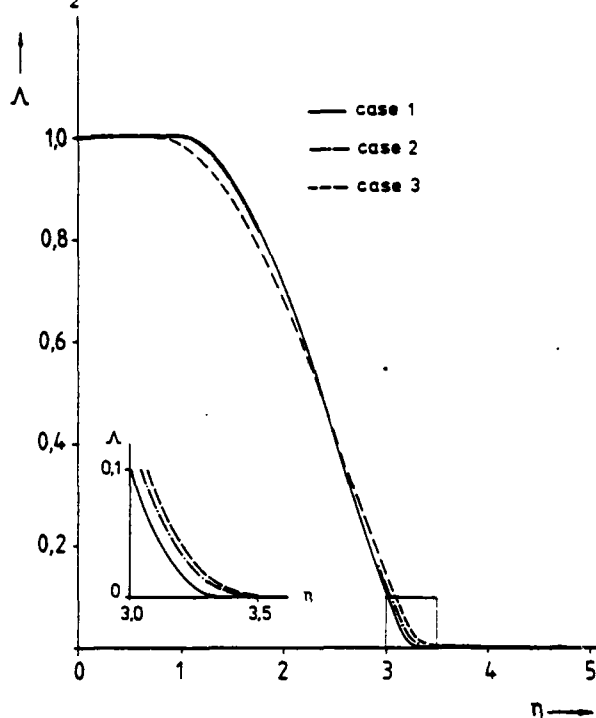


Fig. 4: Similar solution of the turbulent viscosity

A GLOBAL STABILITY ARGUMENT

In this paragraph we want to develop a global stability argument which will be useful for the interpretation of the subsequent stability results. We will only consider the $k-\epsilon$ model and write the ϵ -equation for the normalized quantity

$$E = \epsilon c d \xi^4 / (b^2 u_0^3) \quad (28)$$

as

$$F_\eta \left(E \frac{\partial E}{\partial \xi} - 4 E \right) - (F + E \frac{\partial F}{\partial \xi}) \frac{\partial E}{\partial \eta} = \frac{\partial}{\partial \eta} \left(\frac{C_\eta}{Pr_\epsilon} \frac{\partial E}{\partial \eta} \right) + \eta c_{\epsilon 1} E_1 \kappa' \left(\frac{\partial U}{\partial \eta} \right)^2 - \eta c_{\epsilon 2} E_2 \frac{E^2}{\kappa} \quad (29)$$

We assume $U = U_s(\eta)$ and $F = F_s(\eta)$ to be independent of ξ and introduce for κ_s and E small perturbations around the similarity solution

$$\begin{aligned} \kappa &= \kappa_s(\eta) + \kappa'(\xi, \eta) \\ E &= E_s(\eta) + E'(\xi, \eta) \\ C &= C_s(\eta) + C'(\xi, \eta) \end{aligned} \quad (30)$$

where $C' = 2\kappa' \kappa_s / E_s - E' \kappa_s^2 / E_s^2$. Introducing these into Eqs. (24) and (28) yields the perturbation equations

$$\begin{aligned} \frac{\partial (\eta U_s \kappa')}{\partial \ln \xi} - 2 \eta U_s \kappa' - F_s \frac{\partial \kappa'}{\partial \eta} &= \frac{\partial}{\partial \eta} \left(\frac{C_s \eta}{Pr_\epsilon} \frac{\partial \kappa'}{\partial \eta} \right) + \frac{\partial}{\partial \eta} \left(\frac{C' \eta}{Pr_\epsilon} \frac{\partial \kappa_s}{\partial \eta} \right) \\ &+ \eta E_1 C' \left(\frac{\partial U_s}{\partial \eta} \right)^2 - \eta E_2 E' \end{aligned} \quad (31)$$

$$\begin{aligned} \frac{\partial (\eta U_s E')}{\partial \ln \xi} - 4 \eta U_s E' - F_s \frac{\partial E'}{\partial \eta} &= \frac{\partial}{\partial \eta} \left(\frac{C_s \eta}{Pr_\epsilon} \frac{\partial E'}{\partial \eta} \right) + \frac{\partial}{\partial \eta} \left(\frac{C' \eta}{Pr_\epsilon} \frac{\partial E_s}{\partial \eta} \right) \\ &+ \eta c_{\epsilon 1} E_1 \kappa' \left(\frac{\partial U_s}{\partial \eta} \right)^2 \\ &- \eta c_{\epsilon 2} E_2 \left(2 \frac{E' E_s}{\kappa_s} - \frac{\kappa' E_s^2}{\kappa_s^2} \right) \end{aligned} \quad (32)$$

In order to simplify the analysis we introduce the approximation (justified by the similarity solution) that κ_s may be set equal to E_s and that

$$\left(\frac{\partial U_s}{\partial \eta} \right)^2 = \kappa \frac{E_2}{E_1} \quad (33)$$

where κ is a constant of order one to be estimated from the similarity solution. Integrating over the equations and introducing the definitions

$$\begin{aligned} I_1 &= \int_0^\infty \eta U_s \kappa' d\eta, \quad I_2 = \int_0^\infty \eta \kappa' d\eta \\ I_3 &= \int_0^\infty \eta U_s E' d\eta, \quad I_4 = \int_0^\infty \eta E' d\eta \end{aligned} \quad (34)$$

the diffusion terms and part of the convective terms drop out and one obtains with $\kappa'(0) = \kappa'(\infty) = E'(0) = E'(\infty) = 0$ the equations

$$\begin{aligned} \frac{\partial I_1}{\partial \ln \xi} - I_1 &= E_2 (2\kappa I_2 - (1+\kappa) I_4) \\ \frac{\partial I_3}{\partial \ln \xi} - 3 I_3 &= E_2 [(c_{\epsilon 1} \kappa + c_{\epsilon 2}) I_2 - 2 c_{\epsilon 2} I_4] \end{aligned} \quad (35)$$

Since U_s is always positive, it lies within the accuracy of the previous assumptions to relate I_1 with I_2 and I_3 with I_4 by $I_2 = m I_1$, $I_4 = m I_3$ with m slightly larger than one. Then one obtains a solvable system of two linear ordinary differential equations with the solution

$$I_1 = A_1 \xi^\mu, \quad I_3 = A_3 \xi^\mu \quad (36)$$

where μ is complex with a real part

$$\text{Real}(\mu) = 2 + E_2 m (\kappa - c_{\epsilon 2}) \quad (37)$$

Typical values are $E_2 = 1.8$, $m = 1.2$, $\kappa = 1.0$ and $c_{\epsilon 2} = 1.9$ leading to an approximately vanishing real part of μ and therefore to marginal instability. Small changes in the parameters would influence the stability of the solution considerably.

THE STABILITY ANALYSIS

A large number of numerical calculations was performed with different combinations of parameters used. The linear stability analysis consisted in perturbing all similar profiles including F and U in the form of Eq. (30) and discretising the resulting perturbation equation by using finite difference formulas to obtain a matrix eigenvalue problem of the form

$$Ax = \mu Bx$$

when x is the vector of $F_i, U_i, \kappa_i, \Delta_i (i=2, \dots, n-1)$. Here $n = 17$ was the number of mesh points of the discretisation.

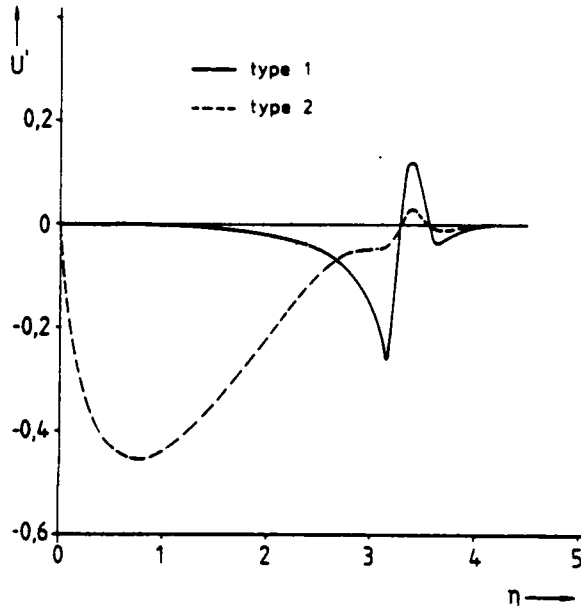


Fig. 5: Unstable eigenvectors of the case 1 velocity profile

The eigenvalue problem was solved using a standard package and the resulting eigenvalues were analysed. All results showed at least one positive eigenvalue and were therefore unstable. The eigenvectors corresponding to the positive eigenvalues were also analysed. It was found that there existed two typical shapes of the eigenvectors. As an example, in the k - ϵ model calculation case 1 with $c_\lambda = 0.04$ two real positive eigenvalues (out of 60), $\mu_1 = 4.361$ and $\mu_2 = 1.218$, were found. The corresponding eigenvectors are shown in Figs. 5 - 7. The first type eigenvectors belonging to μ_1 are small for $\eta < 2$ but blow up at around $\eta = 3.1$ with an oscillatory behaviour for larger η . The largest amplification of the instability occurs clearly in the region where the profiles decay to zero. The second type eigenvectors corresponding to the second eigenvalue have a maximum for $\eta < 2.0$ and decay with small oscillations to large η . Only the second type was observed in all calculations. It was found that the eigenvalues corresponding to the first type increased strongly with decreasing c_λ while the second type eigenvalues were independent of c_λ . For instance, in the k - ϵ model calculation case 2 with $c_\lambda = 0.0575$ the type 1 instability had vanished and only one positive eigenvalue was found with an eigenvector of type 2. The same situation is found in the Rotta model calculation, case 3. An inspection of the steady profiles shows a more rapid change in the derivatives around $\eta = 3.1$ in case 1 than in the outer two cases. We

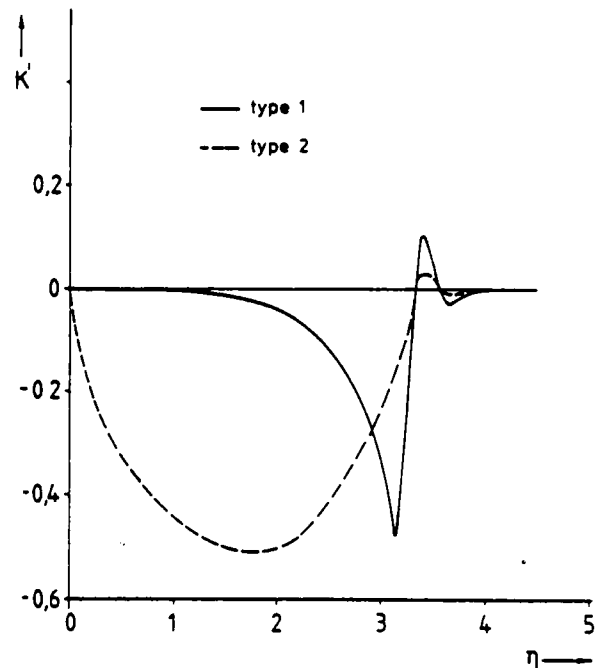


Fig. 6: Unstable eigenvectors of the case 1 kinetic energy profile

therefore believe that the type 1 instability originates from the wave-like character of the solution. This is supported by the fact that it disappears with increasing c_λ . The other, the remaining instability, seems to correspond to the global instability analysed in the preceding paragraph. It originates essentially from the different power law of the centerline decay of k and ϵ ($k_c \sim \xi^{-2}$, $\epsilon_c \sim \xi^{-4}$) which leads to the first term in Eq. (37).

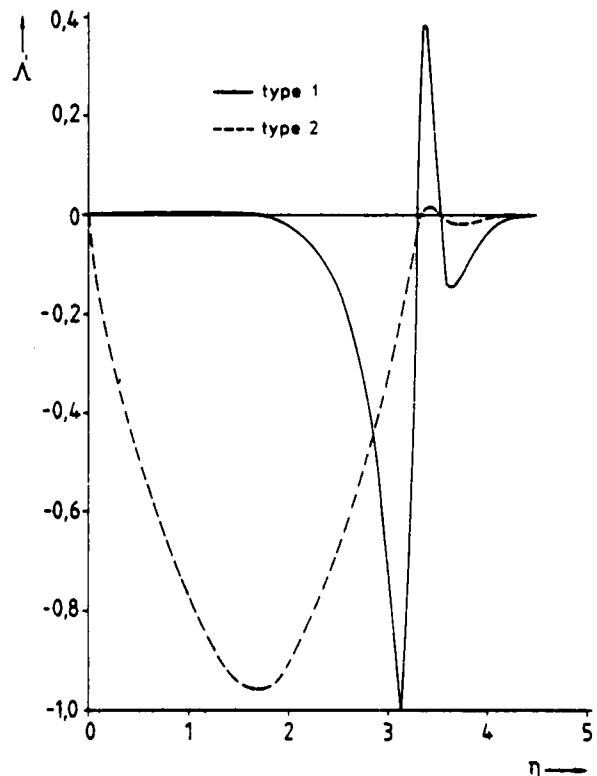


Fig. 7: Unstable eigenvectors of the case 1 turbulent viscosity profile

A non-linear stability analysis was performed by inserting the similarity solution as initial profiles into the Eqs. (20), (24)-(25) which were solved using a finite difference method with 400 spatial net points. The outer boundary condition was imposed at $\eta = 6$. It was found that the solution blows up very rapidly for all $k-\epsilon$ model calculations including case 1 and 2, while it stays essentially stable for many Rotta model calculations including case 3. It seems that in the latter case the instability is damped by non-linear effects. This should not lead to the conclusion that the Rotta model is always stable, even though it may be a candidate for calculations, where the $k-\epsilon$ model shows severe stability problems.

CONCLUSIONS

Two types of instabilities have been identified in free turbulent shear flow calculations. The first type results from the wave-like character of the equations and develops in the region where the turbulence decays discontinuously to zero at the outer edge. The second type appears to be inherent to the $k-\epsilon$ model and may be attributed to the different power law decay of these two quantities. Both instabilities appear to be weak. This also explains the success of numerical damping and of special manipulations in the iteration procedure. There is no doubt, however, that a set of modelled equations that do not provide a stable solution is unsatisfactory. It seems necessary to develop special numerical techniques to take the degenerate character of the equations into account.

ACKNOWLEDGEMENTS

We gratefully acknowledge the careful preparation of the difficult manuscript by Mrs. Steinert-Lehnen. The second authors enjoyed fruitful discussions about Zeldovich's thermal waves with Prof. Dave Kassoy, Boulder, Colorado.

REFERENCES

- / 1/ Patankar, S.V. and Spalding, D.B., 1970, "Heat and mass transfer in boundary layers", Intertext Books, London.
- / 2/ Prandtl, L., 1945, "Über ein neues Formal-system für die ausgebildete Turbulenz", Nachr. Akademie der Wissenschaften Göttingen, 6-19.
- / 3/ Rotta, J., 1972, "Turbulente Strömungen", Teubner-Verlag, Stuttgart.
- / 4/ Rotta, J.R. and Vollmers, H., 1976, "Ähnliche Lösungen der Differentialgleichungen für gemittelte Geschwindigkeiten, Turbulenzenergie und Turbulenzlänge", DLR-FB 76-24.
- / 5/ Jones, J.W. and Launder, B.E., 1973, "The calculation of low-Reynolds-number phenomena with a two-equation model of turbulence", Int. J. Heat Mass Transfer 16, 119-1130.
- / 6/ Voges, R., 1978, "Berechnung turbulenter Wandgrenzschichten mit Zwei-Gleichung-Turbulenzmodellen", Dissertation TU München.
- / 7/ Kline, S.J., Morkovin, M.V., Sovran, G., Cockrell, D.J., 1968, "Proceedings: Computation of turbulent boundary layers - 1968", AFOSR-IFP-Stanford Conference.
- / 8/ Zeldovich, Ya.B. and Raizer, Yu.P., 1967, "Physics of snock waves and high-temperature hydrodynamic phenomena, Vol. II, Academic Press, New York.
- / 9/ Aronson, D.G., 1969, "Regularly properties of flows through porous media", SIAM J. Appl. Math. 17, 461-467.
- /10/ Aronson, D.G., 1970, "Regularity properties of flows through porous media: A counter-example", SIAM J. Appl. Math. 19, 299-307.
- /11/ Aronson, D.G., 1970, "Regularity properties of flows through porous media: The interface", Arch. Rational Mech. Anal. 54, 573-392.
- /12/ Peletier, L.A., 1971, "Asymptotic behaviour of solutions of the porous media equation", SIAM J. Appl. Math. 21, 542-551.
- /13/ Knerr, B.F., 1977, "The porous media equation in one dimension", Trans.Amer.Math. Soc. 234, 381-415.
- /14/ Schlichting, H., 1965, "Grenzschicht-Theorie, Braun-Verlag, Karlsruhe.
- /15/ Stoer, J. and Burlisch, R., 1978, "Einführung in die Numerische Mathematik", Springer-Verlag, Berlin.

A USE OF SENSITIVITY ANALYSIS IN k-ε TURBULENT ROUND JET MODELING

F. Raizadeh and Harry A. Dwyer

Department of Mechanical Engineering
University of California, Davis
Davis, California 95616

INTRODUCTION

For more than a decade, researchers have been calculating with the use of k-ε turbulence models a wide variety of flow fields. In many applications these calculations are considered routine; however, a close inspection will reveal that it takes considerable experience to write and make useful a computer program to solve any given physical problem. The source of many of these difficulties is that the equations are not derived from exact principles, and it is possible that they may not approach proper limits or that the boundary and initial conditions are not well defined. Even with these difficulties it is very important that this level of modeling be improved since k-ε modeling does yield both a length and time scale for turbulence. Also, in many applications such as three-dimensional flow or flow with chemical reaction there is a need to limit the number of equations to be solved to a minimum.

It is the present author's belief that there is a need to apply sensitivity analysis to k-ε turbulence modeling. Sensitivity analysis allows for a unique and systematic understanding of how the model depends on its parameters for a given flow. With this type of information, improvements and extensions can be carried out in a scientific way, and there will be less of a chance of different parameters being changed by different investigators in order to arrive at the same physical result. In the present paper, sensitivity analysis has been applied to turbulent round jet flows with and without variable density. This flow is particularly interesting since it is one of the most important failures of the k-ε model and because of the key role that the round jet plays in mixing devices and diffusion flames.

There have been many proposed model "constant" variations [1-3] which have been applied in order to achieve the proper spreading rate of the round jet with the k-ε model. It will be shown from the present results that almost all of the constants could have been used because of the conservation of momentum property of the jet, and the fact that the length scale is approximately constant across the jet. These results imply that there is no unique way of correcting the flow and that other flows, together with the round jet, will have to be found in order to obtain a more universal set of model parameters or even functions.

BASIS ANALYSIS

The transport equations and k-ε equations which are applicable to a variable density round jet flow and which are formulated in terms of mass weighted or Favre averages are given as

Continuity Eqn.

$$\frac{\partial}{\partial x} (\bar{\rho} u) + \frac{\partial}{\partial y} (\bar{\rho} v) + \frac{\partial \bar{\rho}}{\partial y} m = 0$$

Momentum Eqn.

$$\frac{\partial}{\partial x} (\bar{\rho} u^2) + \frac{\partial}{\partial y} (\bar{\rho} uv) + \frac{\partial uv}{\partial y} m = \frac{1}{y^m} \frac{\partial}{\partial y} \left[y^m (u + u_t) \frac{\partial u}{\partial y} \right]$$

Species Eqn.

$$\frac{\partial}{\partial x} (\bar{\rho} uc) + \frac{\partial}{\partial y} (\bar{\rho} vc) + \frac{\partial cv}{\partial y} m = \frac{1}{y^m} \frac{\partial}{\partial y} \left[y^m \left(u + \frac{u_t}{\sigma_c} \right) \frac{\partial c}{\partial y} \right]$$

k-Eqn.

$$\frac{\partial}{\partial x} (\bar{\rho} uk) + \frac{\partial}{\partial y} (\bar{\rho} vk) + \frac{\partial vk}{\partial y} m = \frac{1}{y^m} \frac{\partial}{\partial y} \left[y^m \left(u + \frac{u_t}{\sigma_k} \right) \frac{\partial k}{\partial y} \right] + \mu_t \left(\frac{\partial u}{\partial y} \right)^2 - \bar{\rho} \epsilon$$

ε - Eqn.

$$\frac{\partial}{\partial x} (\bar{\rho} u\epsilon) + \frac{\partial}{\partial y} (\bar{\rho} v\epsilon) + \frac{\partial v\epsilon}{\partial y} m = \frac{1}{y^m} \frac{\partial}{\partial y} \left[y^m \left(u + \frac{u_t}{\sigma_k} \right) \frac{\partial \epsilon}{\partial y} \right] + C_1 \frac{\epsilon}{k} \mu_t \left(\frac{\partial u}{\partial y} \right)^2 - \frac{C_2}{k} \bar{\rho} \epsilon^2$$

Eq. of State

$$\bar{\rho} = \frac{P_0}{T_0} \times \frac{1}{R_1 C_1 + R_2 C_2}$$

Turbulent Stress Eqn.

$$\mu_t = C_\mu k^2 / \epsilon$$

where u and v are the mean primary and transverse velocities, k and ϵ the kinetic energy and dissipation rate in the flow, C_μ , C_1 , and C_2 the major empirical constants of the model, C concentration of the jet specie, $\bar{\rho}$ the local density of the fluid, and x and y the respective coordinates of u and v . The actual calculations were carried out in a coordinate system which expanded with the jet. This coordinate system is

$$\xi = x$$

$$\eta = \sigma y / x$$

A procedure for the application of sensitivity analysis to the above system of equations is to differentiate the system of equations with respect to that parameter. The resulting transformed equation for a sensitivity variable such as $\bar{U} = \partial u / \partial u_t$ is

Momentum Sensitivity Eq.

$$\begin{aligned} \frac{\partial}{\partial \epsilon} (\bar{R}u^2 + 2\bar{\rho}u\bar{U}) - \frac{\bar{\rho}y}{x} \frac{\partial}{\partial \eta} (\bar{R}u^2 + 2\bar{\rho}u\bar{U}) \\ + \frac{\sigma}{x} \frac{\partial}{\partial \eta} (\bar{R}uv + \bar{\rho}u\bar{v} + \bar{\rho}u\bar{v}) + \left(\frac{\bar{R}uv + \bar{\rho}u\bar{v} + \bar{\rho}u\bar{v}}{y} \right) m \\ = \frac{1}{y} \left(\frac{\sigma}{x} \right)^2 \frac{\partial}{\partial \eta} \left(y^m \frac{\partial u}{\partial \eta} \right) + \frac{1}{y} \left(\frac{\sigma}{x} \right)^2 \frac{\partial}{\partial \eta} \left([u + u_c] y^m \frac{\partial \bar{U}}{\partial \eta} \right) \end{aligned}$$

From the remaining transport equations of the system come the other independent equations needed to solve for the complete set of sensitivity variables which are:

$$\bar{E} = \frac{\partial \epsilon}{\partial u_c} \quad \bar{v} = \frac{\partial v}{\partial u_c} \quad \bar{R} = \frac{\partial \rho_A}{\partial u_c} \quad \bar{K} = \frac{\partial k}{\partial u_c}$$

For most applications, it is convenient to present the sensitivity results in terms of normalized sensitivity coefficients which can be interpreted directly in terms of percentage changes. A typical "percent" sensitivity coefficient is

$$U_{u_c} = \frac{\partial u}{\partial u_c} \frac{u_c}{u}$$

and the majority of the results will be presented in this form except in those cases where the normalization variables are zero. It should also be pointed out that the mathematical nature of the sensitivity equations is identical to the original equations and that the same numerical method can be used for both systems of equations. The physical transport equations were solved with an implicit marching scheme which employed iteration for the nonlinear turbulent transport, while the linear sensitivity equations were solved with the same implicit method but without iteration.

RESULTS

The results will be presented so that the influence of variable density will appear as a parameter in the figures. The round jet flow has been calculated with a co-flowing stream and with the following density ratios between the co-flowing stream (ρ_c) and the jet flow (ρ_j)

$$\frac{\rho_c}{\rho_j} = 1, 2, 4, 8$$

The density ratio of case eight is very close to that of a hydrogen diffusion flame and the results obtained do have implications for this flow.

Shown in Figure (1) are four velocity profiles at identical locations ($x/D = 40$) downstream with the same initial conditions except for the variable density. These profiles have been calculated with the "standard" [4] model constants without any correction for the round jet. The density profiles are shown in Figure (2) for the same locations, and all of the calculations are far enough downstream so that the influences of initial conditions are a minimum on the turbulent transport coefficients. Typical distributions for the turbulent viscosity, μ_t , and the turbulent kinetic energy, k , are shown in Figures (3) and (4), and it should be pointed out that zero gradient boundary conditions have been employed. Also, in order to limit the influence of turbulent transport outside of the jet boundaries, a standard intermittency factor correction [5] has been applied to μ_t . This correction had very little influence on the jet spreading rate, but did effectively cut off turbulent transport for turbulent Schmidt numbers less than one outside the jet boundaries. (Note: A turbulent Schmidt number of .7 has been used in the species equation for all of the calculations in Figures (1) through (4).)

Sensitivity coefficients to the parameter C_μ are shown in Figures (5) through (9) for the variables u , k , ϵ , $\bar{\rho}$, and $\bar{\rho}u$. The velocity sensitivities in Figure (5) are relatively small and are strongly influenced by the conservation of momentum property of the jet. These results can be interpreted in the following way. An increase in C_μ tends to increase turbulent viscosity, μ_t , which causes a decrease in velocity at the centerline and a negative sensitivity coefficient. However, since jet momentum must be conserved, the velocity in the outer part of the jet must increase. The same logic can be applied to the u velocity sensitivities for any parameter of the $k-\epsilon$ model, and the numerical results verify this conclusion. Therefore, the u velocity sensitivity distribution is almost the same form when any constant is varied to obtain a correct spreading rate, and it is very difficult to arrive at an appropriate reason for model failure.

It is rather surprising that the influence of the large density variation does not cause a much larger change in the structure of the model. This lack of sensitivity to density variation can be easily seen in Figures (6) and (7) where the sensitivity distributions of k and ϵ are shown. Even though the values of the sensitivity coefficients are much larger, the influence of variable density contribution is rather weak. The sensitivity coefficient for $\bar{\rho}$, Figure (8), does show a variable density influence and this combined with a Schmidt number less than one causes the sensitivity coefficient for $\bar{\rho}u$, Figure (9), to show a very strong density dependence. The change in the sign of the sensitivity coefficient for $\bar{\rho}u$ at the boundaries is indicative of the overshoot and undershoot behavior that this variable can exhibit in variable density flows.

The sensitivity coefficients for the parameter C_μ are well behaved, but the same cannot be said for the parameter C_1 appearing in the ϵ equation. Shown in Figures (10) through (13) are the C_1 sensitivities for the variables u , k , μ_t , and $\bar{\rho}u$. The two major changes in these results compared to the C_μ results are the much larger values of sensitivity coefficients and the very large sensitivities near the boundaries. The sensitivity coefficients for k and μ_t are extremely large and unphysical at the boundaries. Also, at the boundaries there does seem to be substantial density influence on the model, and it seems highly unlikely that the $k-\epsilon$ model will give a good length and time-scale prediction at jet boundaries. For many applications where the outer flow is essentially quiescent this may not pose a problem; however, if there are important turbulent characteristics in the outer flow, it is doubtful whether the $k-\epsilon$ model will do a realistic job. Both the sensitivity coefficients for u and $\bar{\rho}u$ show a similar behavior to C_μ but with opposite sign and much larger values. Again, all of the characteristics can be easily explained by conservation of jet momentum and a Schmidt number less than one.

During the past few years it has been proposed [6] that turbulent Schmidt numbers much less than one are needed to describe scalar transport with the $k-\epsilon$ model. In order to test this hypothesis, sensitivity analyses with C_1 have been performed for a Schmidt number of .7 and .25 in Figures (14) and (15) for the mean velocity and density variables. In a qualitative sense, the results in these figures show that the structure of the model is the same at the two different Schmidt numbers since it is difficult to discern any noticeable changes. Since these results have been carried out for an 8/1 density ratio, there must be quantitative differences in ρ and u sensitivities if the conservation properties of the jet are to be satisfied. In general, it can be said that the C_1 sensitivities are low for the lower Schmidt numbers because of the very high turbulent diffusivities associated with this condition. Under these conditions, the flow is more dominated by the diffusivity rather than the constants in the ϵ equation.

Another interesting situation for the application of sensitivity analysis is the initial profiles or conditions of the round jet. The primary reasons are due to the fact that, in most situations, the initial conditions are not well known and also that the round jet decays very quickly. In the present calculations,

the initial mean velocity profile was assumed flat with a thin cosine transition profile, while the k and ϵ profiles were determined from the assumption of production equals dissipation. Typical mean velocity profiles are shown in Figure (16) at a distance of approximately 8 diameters downstream from the inlet and for a 8/1 density ratio, while the sensitivity coefficients of u and μ_t to C_1 are given in Figures (17) and (18). The u sensitivities are similar to positions downstream; however, the μ_t sensitivities are very large and probably unphysical. This is particularly true at the boundary of the jet, and it should be recommended that the k - ϵ model be used only with caution near the jet boundaries. Also, it seems from the very high values of μ_t sensitivities in the initial region, that physical phenomena, such as flame blow-off which depends on the initial profiles, be predicted by k - ϵ models with a large measure of caution. These types of profiles represent situations far from the flows chosen to determine the model empirical constants, and with the large sensitivity coefficients it is highly unlikely that the predictions will be accurate.

CONCLUSIONS

It has been shown that sensitivity analyses can be used to systematically understand the structure of the k - ϵ model applied to a complex flow. In the application of sensitivity analysis to the round jet flow, it has been found that the flow is strongly dominated by the jet conservation of momentum property. All sensitivity coefficients relating to density and velocity show similar behavior because of the conservation constraint, and almost all of the parameters of the model can be used to some degree to correct the round jet spreading rate. The major results of the investigation are:

- (1) Density variation has a surprisingly weak influence on the structure of the k - ϵ model, and there were no major qualitative changes in the behavior of the sensitivity coefficients with density variation except near the jet boundary.
- (2) At the jet boundaries, the k - ϵ model yields very high sensitivity coefficients for k and ϵ to the parameters appearing in those equations. These large sensitivities do not seem to be physically correct and it seems very questionable whether the model can be used with confidence at the boundary locations.
- (3) Near the initial region of a round jet flow the k - ϵ model is very sensitive to the parameters on which it depends. This sensitivity occurs throughout the entire jet and is maximum at the boundary. Because of the rapid decay rate of the round jet, this fact could have a large influence in many practical situations which depend strongly on initial conditions.
- (4) The round jet is not a good flow to tune k - ϵ model constants because of the very strong constraint of jet conservation of momentum. All model constant variations which predict an almost flat length scale variation across the jet can be used to predict a proper spreading rate. Therefore, the proper k - ϵ model which will predict the correct round jet flow must be found from a variation of the round jet or another flow.

REFERENCES

1. Pope, S.B., 1970, "An Explanation of the Turbulent Round-Jet/Plane-Jet Anomaly," *AIAA J.*, 16(3), 279.
2. McGuirk, J.J., and Rodi, W., 1977, "The Calculation of Three-Dimensional Free Jets," *Symposium on Turbulent Shear Flow*, Pennsylvania State Univ.
3. Morse, A.P., 1977, "Axisymmetric Turbulent Shear Flows With and Without Swirl," Ph.D. Thesis, London University, England.

4. Launder, B.E., and Spalding, D.B., 1974, "The Numerical Computation of Turbulent Flow," *Computer Methods in Applied Mechanics and Engineering*, 3, 269.
5. Corrsin, S., and Kistler, A.L., 1954, *NACA Tech. Notes* 3133.
6. Jones, W.P., and Whitelaw, J.H., 1982, "Calculation Methods for Reacting Turbulent Flows: A Review," *Combustion and Flame*, 48, 1.

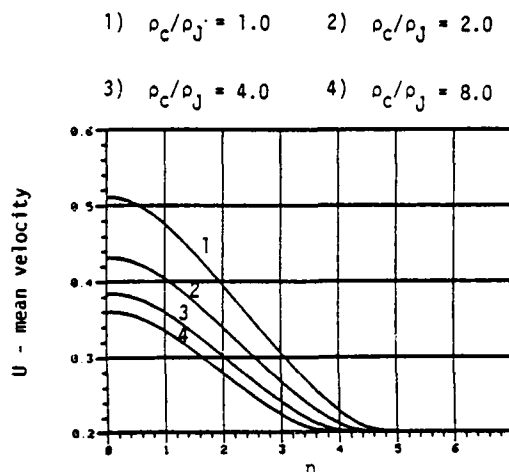


Figure 1. Round jet mean velocity profiles for different density ratios

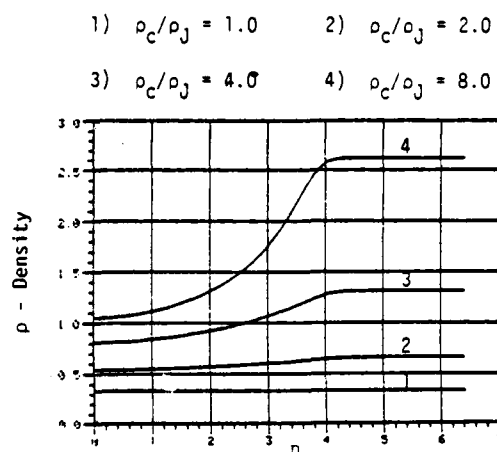


Figure 2. Round jet density distribution for different density ratios

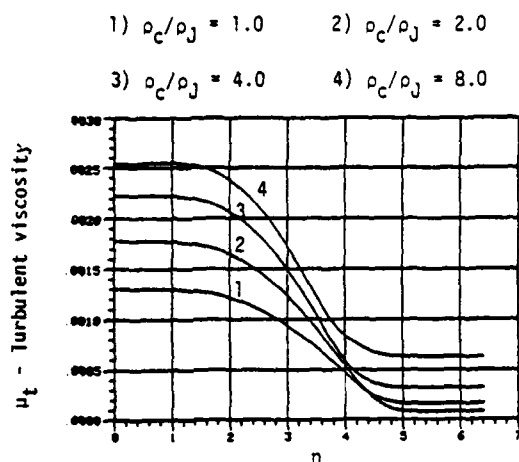


Figure 3. Round jet turbulent viscosity distribution for different density ratios

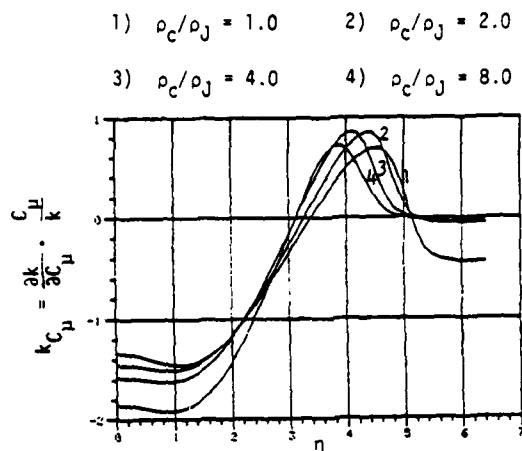


Figure 6. Turbulent kinetic energy sensitivity to C_μ for different density ratios

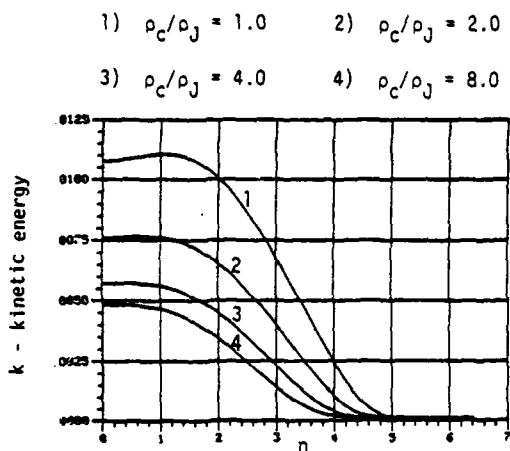


Figure 4. Round jet turbulent kinetic energy distribution for different density ratios

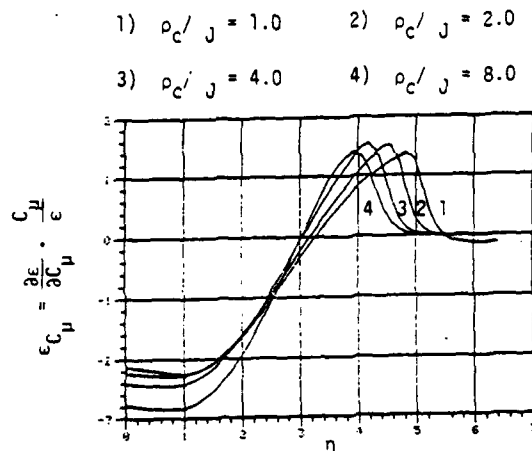


Figure 7. Turbulent dissipation sensitivity to C_μ for different density ratios

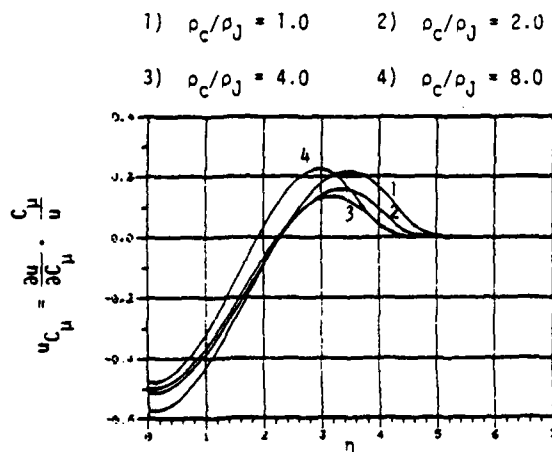


Figure 5. Primary velocity sensitivity to C_μ for different density ratios

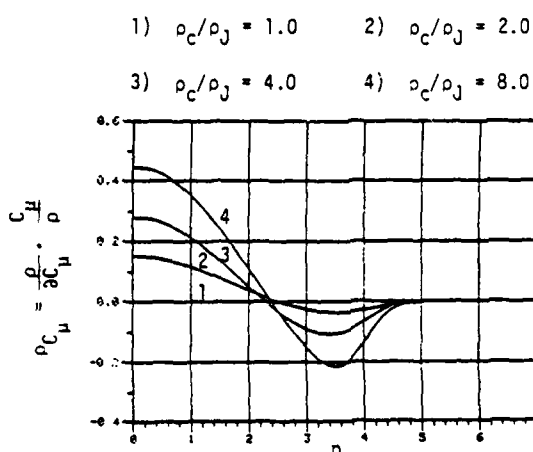


Figure 8. Density sensitivity to C_μ for different density ratios

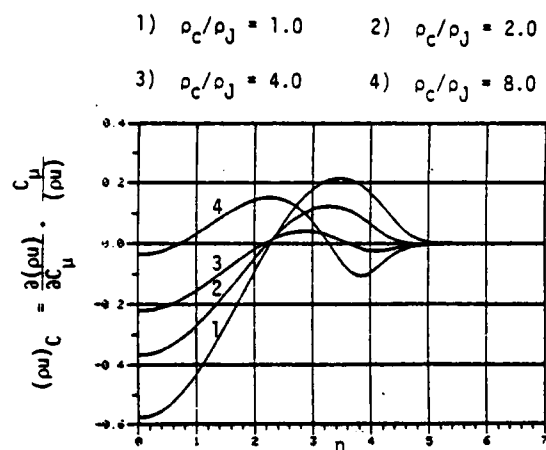


Figure 9. Mass flow sensitivity to C_1 for different density ratios

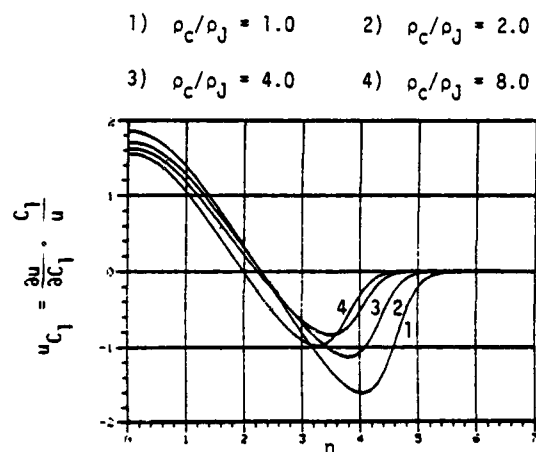


Figure 10. Primary velocity sensitivity to C_1 for different density ratios

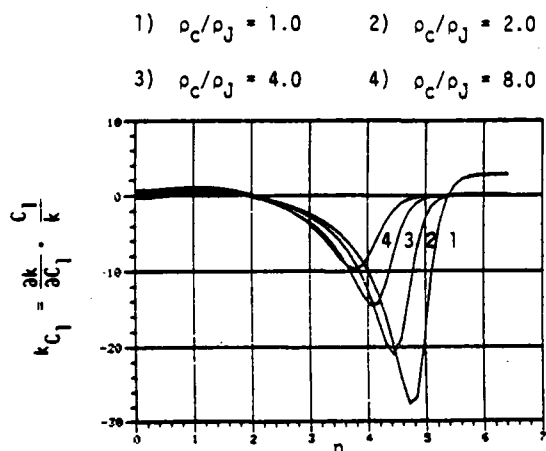


Figure 11. Turbulent kinetic energy sensitivity to C_1 for different density ratios

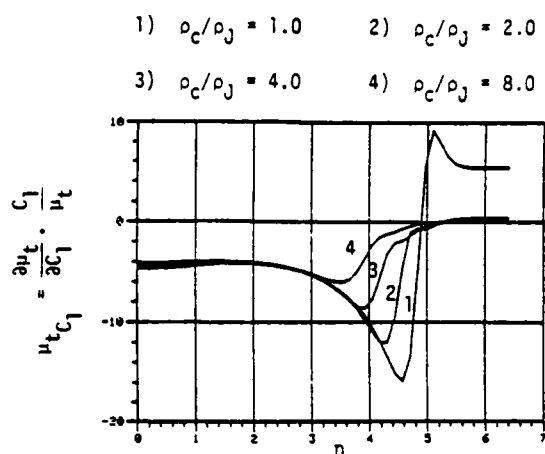


Figure 12. Turbulent viscosity sensitivity to C_1 for different density ratios

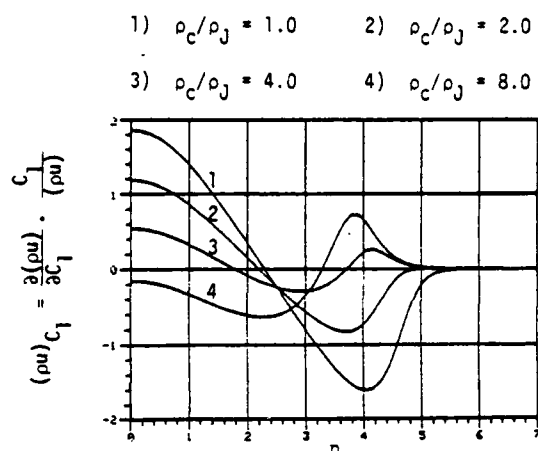


Figure 13. Mass flow sensitivity to C_1 for different density ratios

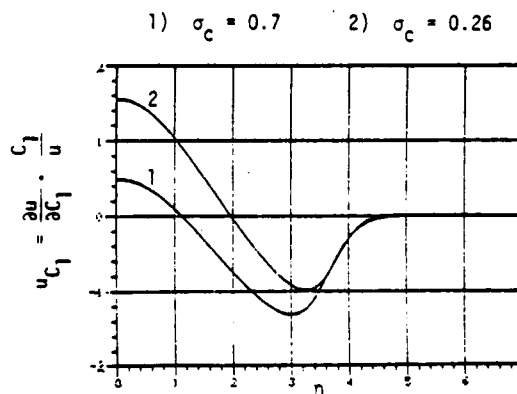


Figure 14. The effect of Schmidt number on primary velocity sensitivity to C_1

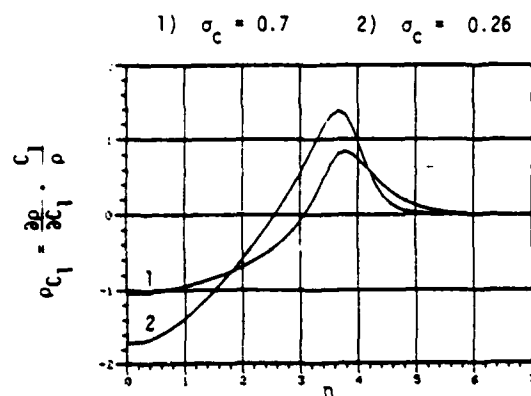


Figure 15. The effect of Schmidt number on density sensitivity to C_1

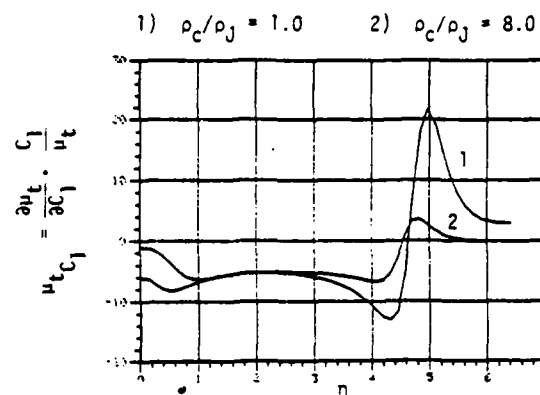


Figure 18. Upstream viscosity sensitivity to C_1 for different density ratios

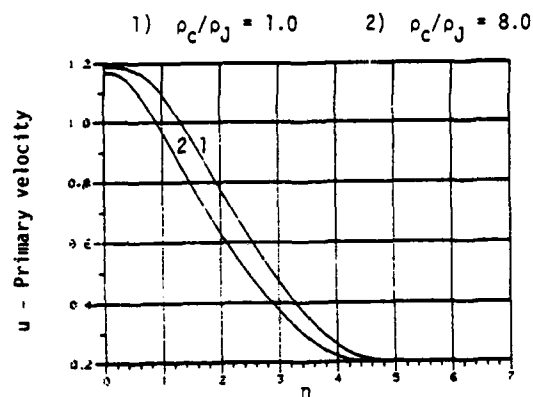


Figure 16. Round jet upstream mean velocity profiles for 2 different density ratios

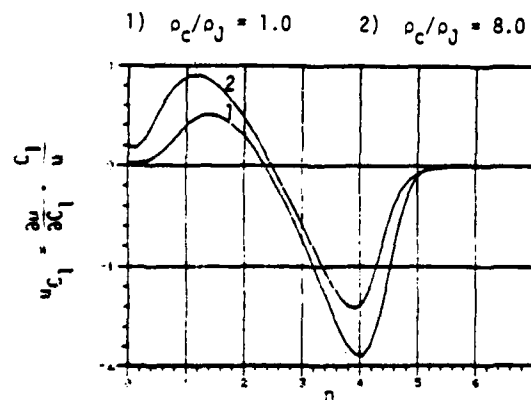


Figure 17. Upstream velocity sensitivity to C_1 for different density ratios

SESSION 5 - WAKES

E. Naudascher - Chairman

STRUCTURAL FEATURES OF THE NEAR REGION OF AN ASYMMETRIC TURBULENT WAKE

M. Shokr⁺, J.F. Keffer⁺⁺ and J.G. Kawall⁺⁺

⁺Atmospheric Environment Services, Ontario, CANADA

⁺⁺Department of Mechanical Engineering
University of Toronto, Toronto, CANADA

ABSTRACT

Statistical properties of the turbulent/non-turbulent interfaces in the near region of an asymmetric wake generated by a pair of closely-spaced, unequal-diameter cylinders have been determined by means of digital image analysis of cine flow visualization pictures of the flow. The results, comprising moments, burst rates, correlations and auto-spectra, indicate that the lower interface of the flow, which is associated with the large cylinder, has markedly steeper slopes, on the average, than the upper interface and its motion is considerably less random than that of the latter. Moreover, they establish that a "Kármán vortex street", centred in the lower part of the wake and with a characteristic frequency corresponding to a Strouhal number significantly less than that pertaining to the symmetric cylinder generated wake, is produced.

NOMENCLATURE

- D_1 - lower cylinder diameter, mm.
- D_2 - upper cylinder diameter, mm.
- D - equivalent diameter equal to $(D_1 + D_2)/2 + L$, mm.
- E - auto-spectrum, s.
- F - flatness factor.
- f - burst rate, Hz.
- f_0 - burst rate at the mean interface position, Hz.
- L - spacing between cylinder centres.
- N - number of cine picture frames.
- n - frequency, Hz.
- n_s - vortex shedding frequency, Hz.
- S - skewness factor.
- t - time, s.
- U_1 - free-stream velocity, ms^{-1} .
- x - streamwise coordinate.
- Y - instantaneous lateral interface position, mm.
- \bar{Y} - mean value of Y , mm.
- y - lateral coordinate, or instantaneous lateral interface position relative to \bar{Y} , mm.
- y' - root-mean-square value of Y , mm.
- z - spanwise coordinate.
- α - reference variable.
- β - reference variable.
- Δt - time interval between cine pictures frames, s.
- ρ - auto- or cross-correlation function.
- τ - time lag, s.
- ϕ - instantaneous interface slope, equivalent to $\partial Y/\partial x$.
- $\bar{\phi}$ - mean value of ϕ , deg.
- ϕ' - instantaneous interface slope relative to $\bar{\phi}$.
- ϕ'' - root-mean-square of ϕ .

Subscripts

- U - upper.
- L - lower.
- y - position.
- ϕ - slope.

INTRODUCTION

Recent experimental results (e.g., see Keffer, Kawall, Giralt and Béguier, 1979) have shown that the turbulent transport mechanism associated with certain "asymmetric" turbulent shear flows is fundamentally different from that associated with classical "symmetric" flows, viz, wakes and jets with symmetrical mean profiles, and mixing layers and boundary layers with monotonically-varying mean profiles. Such asymmetric flows have been found to contain well-defined localized regions within which the net production of turbulence kinetic energy (or its thermal equivalent) is negative. One such flow is the turbulent wake generated by a pair of closely-spaced, unequal diameter circular cylinders, which was first studied experimentally by Palmer and Keffer (1972).

In a review paper on negative production, Béguier, Giralt, Fulachier and Keffer (1977) suggested that the existence of the negative production zone in the Palmer-Keffer wake was linked to the presence of "Kármán vortex street" (KVS) activity, i.e., the quasi-periodic occurrence of relatively highly-organized motion, or coherent structures, within the near region of this flow. We note that Diaz, Gavalda, Kawall and Giralt (1982) have found zones of negative production in the case of a wake produced by a rotating circular cylinder, as did Gavalda, Diaz, Giralt, Kawall and Keffer (1983) in the more complicated situation of a wake generated by a pair of closely-spaced, equal diameter circular cylinders, one of which is rotating. In both instances, the results indicate that the occurrence of these zones is related to KVS activity.

In an effort to gain further insight into the structure of the Palmer-Keffer asymmetric wake, Shokr and Keffer (1982) analysed cine flow visualization pictures of the near region of this flow, using a digital image processing technique. Specifically, they measured the lateral positions of the upper and lower turbulent/non-turbulent interfaces of the flow as functions of time, for several streamwise locations, and hence, determined various interface statistics. In the present work, we have carried out an extended analysis of the aforementioned cine pictures in order to obtain additional quantitative information on the interfaces. In particular, we have determined a number of statistical properties of the interface slopes. It should be pointed out that these properties cannot be readily obtained by means of either hot-wire anemometry or laser-Doppler anemometry.

EXPERIMENTAL DETAILS

The flow visualization pictures employed herein were obtained from the Institut de Mécanique Statistique de la Turbulence (IMST), Marseille. The flow, a definition sketch of which is shown in Fig. 1, was generated by means of two cylinders of diameters $D_1 = 20$ mm and $D_2 = 12$ mm mounted horizontally in the IMST flow

visualization water tunnel. The axes of the cylinders were separated in the lateral direction by a distance, L , of 23 mm so that the quantity $(D_1 + D_2)/2 + L$, which is defined as the equivalent diameter, D , was 39 mm. This particular cylinder configuration resulted in a relatively strong "source interaction", as in the case of the Palmer-Keffer experiments. The free stream velocity was 0.17 ms^{-1} , which produced a Reynolds number based on D of 7,000. Approximately 1,000 frames and a time interval between successive frames of $1/12 \text{ s}$ were used in the analysis, and results pertaining to five selected downstream locations (i.e., x/D values) were computed.

The pictorial information was digitized, and the resulting digital data were processed by means of a Bausch and Lomb Omnicon digital image analysis system, in conjunction with an IBM 3033 computer, at the University of Toronto. The turbulent and non-turbulent regions within the pictures were identified, and the upper and lower interface positions relative to the centreline of the flow, Y_U and Y_L , and the upper and lower interface slopes, ϕ_U ($\approx \partial Y_U / \partial x$) and ϕ_L ($\approx \partial Y_L / \partial x$), were then measured as functions of time for the selected x/D values. (The technique used to determine $Y_{U,L}$ and $\phi_{U,L}$ is described by Shokr and Keffer, 1982.)

INTERFACE STATISTICS

The statistical properties of $Y_{U,L}$ and $\phi_{U,L}$ that were examined in the present work are as follows.

- (1) The first four moments of $\phi_{U,L}$, which are given by

$$\overline{\phi_{U,L}^m} = \frac{1}{N} \sum_{i=1}^N \phi_{U,L}^m(t_i), \quad m = 1, 2, 3, 4.$$

In this expression, N represents the number of frames used; $t_i = (i-1)\Delta t$, where Δt is

the time interval between frames; $m = 1$ yields the upper and lower mean interface slopes, $\bar{\phi}_U$ and $\bar{\phi}_L$; $m = 2$ yields the root-mean-square (RMS) values,

$$\phi'_{U,L} = \sqrt{\overline{\phi_{U,L}^2}},$$

where $\phi = \bar{\phi} - \bar{\phi}$; $m = 3$ yields the skewness factors,

$$S_{U,L} = (\overline{\phi^3} / \phi'^3)_{U,L};$$

and $m = 4$ yields the flatness factors,

$$F_{U,L} = (\overline{\phi^4} / \phi'^4)_{U,L}.$$

- (2) The burst rate, \hat{f} , which represents the average frequency of occurrence of turbulent bursts (or zones) at a given point in the flow, and is equal to one-half the average frequency at which the interface crosses that point. We note that if Y and ϕ are uncorrelated Gaussian random variables then \hat{f} will be given by

$$\hat{f} = \hat{f}_0 \exp(-y^2/2y'^2),$$

where \hat{f}_0 is the burst rate at the mean interface position, \bar{Y} .

- (3) The autocorrelation function, which is given by

$$\rho(\tau_j) = \left[\frac{1}{(N-j)} \sum_{i=1}^{N-j} a(t_i) a(t_{i+j}) \right] / a'^2,$$

where $\tau_j = j\Delta t$, $j = 0, 1, 2, \dots, J$, $J \ll N$, a denotes y or ϕ , and a' is the RMS value of a .

- (4) The auto-spectrum, $E(n)$, which is defined as

$$E(n) = \int_{-\infty}^{\infty} \rho(\tau) \exp(-i2\pi n\tau) d\tau.$$

- (5) The cross-correlation function, which is given by

$$\rho_{\alpha\beta}(\tau_j) = \begin{cases} \left[\frac{1}{(N-j)} \sum_{i=1}^{N-j} \alpha(t_i) \beta(t_{i+j}) \right] / \alpha' \beta', & \text{for } \tau_j \geq 0, \\ \left[\frac{1}{(N-j)} \sum_{i=1}^{N-j} \beta(t_i) \alpha(t_{i+j}) \right] / \alpha' \beta', & \text{for } \tau_j < 0, \end{cases}$$

where α and β denote y_U and ϕ_U , y_L and ϕ_L , or y_L and y_U .

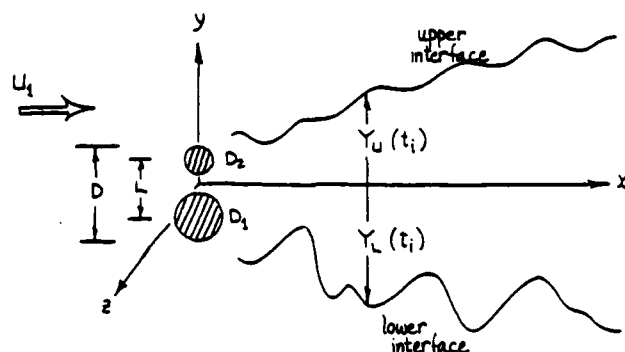


Fig. 1. Definition sketch.

RESULTS AND DISCUSSION

The streamwise variations of the mean values, the RMS values, the skewness factors and the flatness factors of the upper and lower interface slopes are presented in Figs. 2, 3, 4 and 5, where it is seen that these quantities all remain essentially constant as x/D increases. One can infer from the results for the mean values (Fig. 2) that, on the average, (a) both interfaces are fairly flat, $|\bar{\phi}_U|$ and $|\bar{\phi}_L|$ being less than 13° , and (b) the slopes of the lower interface, associated with the large cylinder (see Fig. 1), are significantly steeper than those of the upper interface, $|\bar{\phi}_L|$ being roughly twice as large as $|\bar{\phi}_U|$. These inferences are consistent both with visual observations of the cine film, which reveal that the intermittent bulges in the lower part of the wake are larger than those in the upper part, and with the results for the mean interface positions, \bar{Y}_U and \bar{Y}_L (see Shokr and Keffer, 1982), which show that \bar{Y}_L spreads more rapidly than does \bar{Y}_U - so that the rate of entrainment of potential fluid is greater across the steeper lower interface.

Figure 3 demonstrates that the RMS values of the upper and lower interface slopes, ϕ'_U and ϕ'_L , are more or less the same. The magnitude of these quantities is approximately 45° , which, together with the fact that both $|\bar{\phi}_U|$ and $|\bar{\phi}_L|$ are less than 13° , leads to the conclusion that interface folding does not occur to any significant extent (or equivalently, that the interface positions are single-valued functions). This is, in fact, the case, as evidenced by visual observations of the cine film. The skewness factors of both the upper slopes and the lower slopes, S_U and S_L (Fig. 4), deviate significantly from zero, and $|S_L|$ is consistently greater than $|S_U|$. Hence, it follows that the interface bulges are asymmetric in shape, the more so in the case of the lower interface. The upper and lower flatness factors, F_U and F_L (Fig. 5), are essentially equal, and their magnitude is roughly 2.0, so that these results reinforce the

above conclusion that interface folding is negligible in the present situation.

Normalized upper and lower burst rate distributions pertaining to the various x/D locations examined here are depicted in Fig. 6. The scatter associated with these results is seen to be large. Nonetheless, because the extent of the scatter depends upon N (the number of frames used), decreasing as N increases, we can conclude that the burst rate profiles for the present flow are self-similar. Furthermore, it appears that the upper profiles tend to follow the Gaussian curve; the lower burst rate profiles, however, deviate markedly from this curve. It is interesting to note that the intermittency factor profiles (see Shokr and Keffer, 1982) display a similar trait: the upper profiles conform to the Gaussian distribution function, but the lower profiles show little agreement with this function. The implication here is that in the near region of the wake, the process governing the motion of the upper interface (i.e., the fluctuations of its lateral position) is predominantly Gaussian in nature, whereas that governing the motion of the lower interface is not.

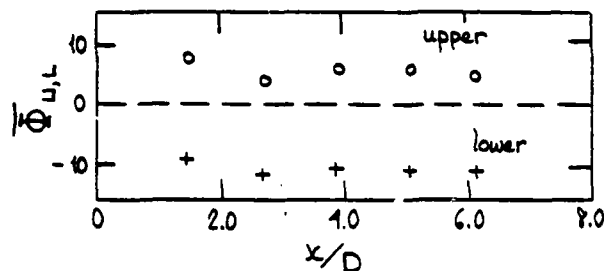


Fig. 2. Mean values of interface slopes.

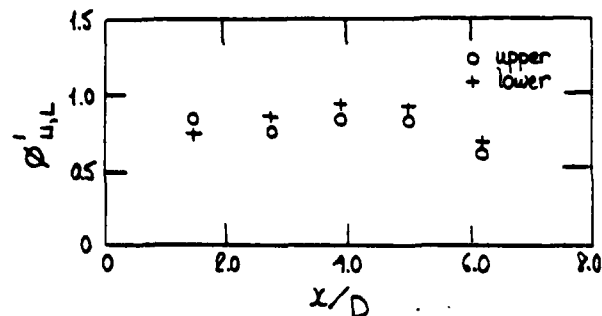


Fig. 3. RMS values of interface slopes.

In Figs. 7 and 8, we present upper and lower interface-position and interface-slope autocorrelation functions pertaining to $x/D = 3.875$, and in Figs. 9 and 10 the corresponding auto-spectra. As can be seen, the autocorrelation functions display distinct regular oscillations, establishing the presence of quasi-periodic coherent structures within the flow. The oscillations do not occur, however, until τ exceeds certain limiting values, and they decay (albeit slowly) with increasing τ . It is clear that a "Kármán vortex street" (KVS), somewhat similar to the KVS within the symmetric cylinder-generated wake, exists within the asymmetric wake; moreover, the process that gives rise to this KVS is not strictly periodic but rather is randomly modulated, as in the case of the symmetric wake (see Budny, Kewall and Keffer, 1979). Notice that the lower autocorrelations exhibit a more pronounced oscillatory behaviour than do the upper autocorrelations, suggesting that the KVS is centred in the lower part of the flow. The auto-spectra (Figs. 9 and 10) serve to show that

this is, in fact, so - the dominant peaks in these spectra, which correspond to the oscillations in the autocorrelations, being both larger and noticeably sharper in the case of the lower spectra than in the case of the upper spectra. Evidently, the frequency at which the aforementioned peaks are centred is the nominal frequency at which vortices are shed from the two cylinders (n_s). This frequency yields a Strouhal number ($n_s D/U_1$) of 0.14, which is significantly less than that associated with the symmetric wake (viz, 0.21).

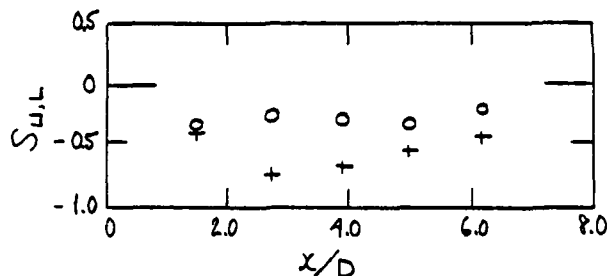


Fig. 4. Skewness factors of interface slopes.

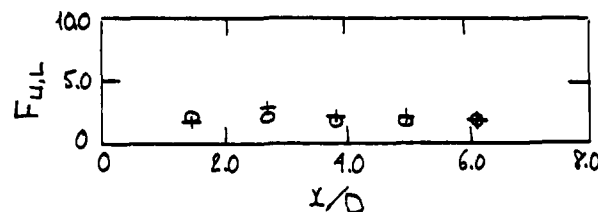


Fig. 5. Flatness factors of interface slopes.

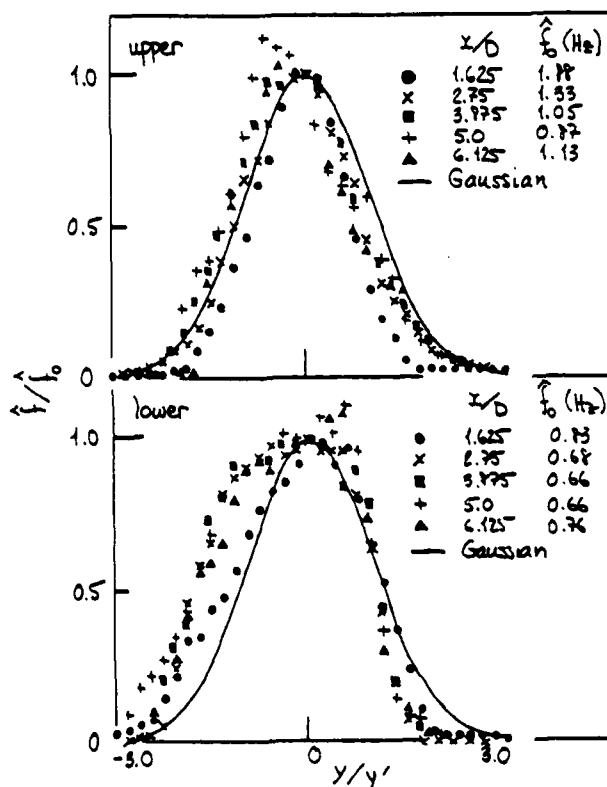


Fig. 6. Burst rate distributions.

It is interesting to note that whereas the upper spectra display only a single peak centred at n_s - the "fundamental", the lower spectra display several "harmonics" as well as the "fundamental". This trait is also exhibited by the auto-spectra of hot-wire signals from the upper and lower parts of the asymmetrical wake, that were measured by Palmer and Keffer (1972). It is interesting to note as well that a comparison of the interface-position auto-spectra and the interface-slope auto-spectra (Figs. 9 and 10) suggests that the interface slope, $\phi(t)$, is closely related to the time derivative of the interface position, $\partial y(t)/\partial t$, inasmuch as the auto-spectra of $\phi(t)$ are more sensitive to the KVS activity than are the auto-spectra of $y(t)$.

On the basis of the above results, we can regard the motion of the upper and lower interfaces in the near region of the flow as comprising a large-scale quasi-periodic component (caused by KVS activity) and a small-scale random component, with the former dominating the motion of the lower interface, once the KVS is well-established, and the latter dominating the motion of the upper interface. This picture is consistent both with the fact that the values of \bar{f}_0 pertaining to the upper interface are everywhere larger than those pertaining to the lower interface (Fig. 6), and with visual observations of the ciné film which reveal that the upper interface contains numerous small random convolutions, while the lower interface contains relatively few such convolutions.

Figure 11 depicts the upper and lower cross-correlation functions of the interface position and the interface slope for $x/D = 3.875$. It is clearly evident from this Figure that the random components of $y(t)$ and $\phi(t)$ are uncorrelated, which implies, in the light of the foregoing results, that these components are uncorrelated Gaussian random variables, and hence, are statistically independent. (The fact that the burst rate and intermittency factor profiles pertaining to the lower interface deviate from the Gaussian models can be attributed to the relatively strong effect of the quasi-periodic components of $y_L(t)$ and $\phi_L(t)$.) We note that

in the case of the upper interface, there is a phase difference between $y(t)$ and $\phi(t)$ of about 90° , the cross-correlation function being approximately zero at $\tau = 0$, and in the case of the less random lower interface, this phase difference is somewhat greater than 90° , the value of the cross-correlation function lying between zero and its minimum value. These cross-correlation results, therefore, lend support to the view that there is a strong relationship between ϕ and $\partial y/\partial t$. Indeed, with respect to the upper interface, this relationship may be taken as: $\partial y/\partial t = U_c \phi(t)$, where U_c is a characteristic (local) bulge convection velocity. It may be remarked that if this relationship holds, then for sufficiently small Δt , U_c will be given by, $(\Delta y^2/\phi \Delta y/\Delta t)$, where

$$\Delta y = y(t + \Delta t) - y(t).$$

In Fig. 12, we present the cross-correlation functions of the upper and lower interface positions for selected x/D locations in the near region of the flow. These results establish, not surprisingly, that as in the case of the symmetric wake (see Budny et al, 1979), only the quasi-periodic components of the interface positions on opposite sides of the centreline of the flow are correlated. Furthermore, they demonstrate that these components are not 180° out-of-phase as they are for the symmetric wake, since the minimum values of the correlations do not occur at $\tau = 0$. This is a consequence of the KVS being centred in the lower part of the wake, and implies that the coherent structures comprising the KVS are not arranged as in the classic KVS configuration. Finally, it should be noted that the peak values of the cross-correlation curves vary with x/D , increasing initially for x/D less than about 5, then decreasing as x/D increases beyond 5. From this, in conjunction with the fact that \bar{f}_0 pertaining to both the

upper interface and the lower interface decreases initially then increases as x/D increases from 1.625 to 6.125 (see Fig. 6), we conclude that the KVS is well-established by x/D equal to about 4, so that its formation takes place within a streamwise distance of about $3D$

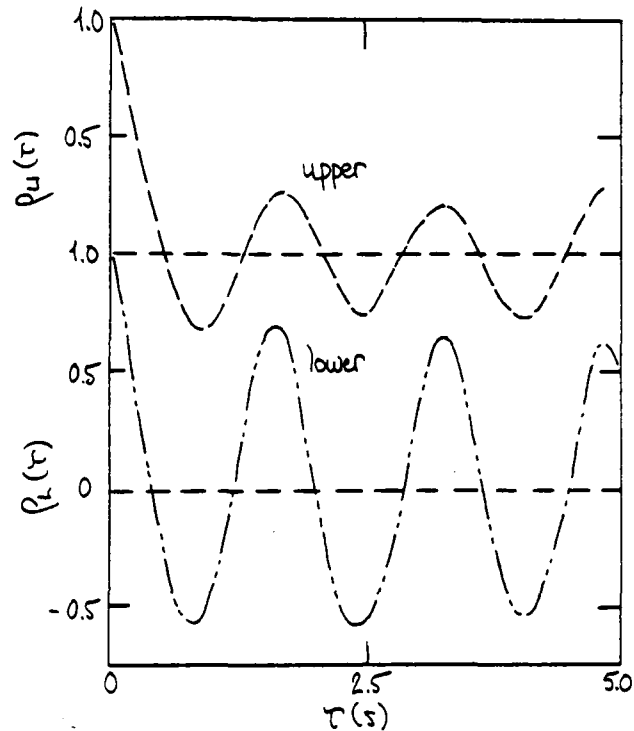


Fig. 7. Autocorrelations of interface positions, $x/D = 3.875$.

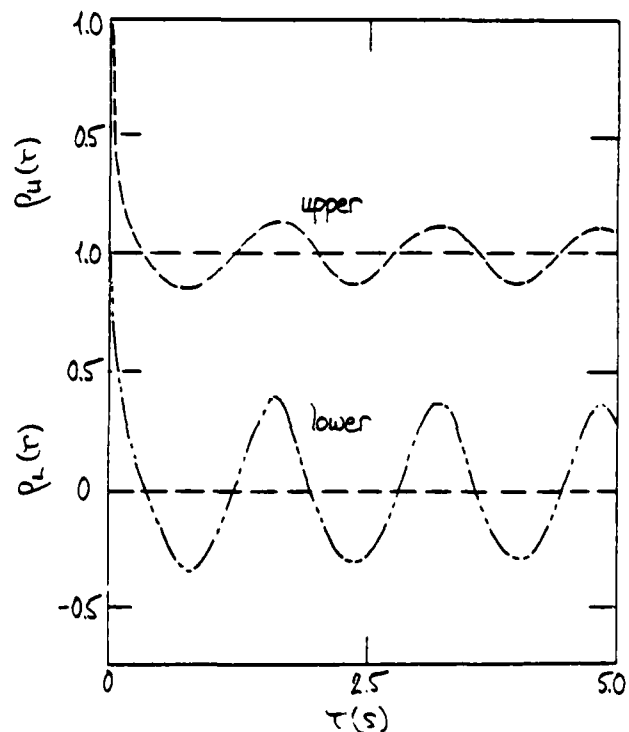


Fig. 8. Autocorrelations of interface slopes, $x/D = 3.875$.

from the cylinders, and that it starts to decay for x/D in excess of about 5.

SUMMARY AND CONCLUDING REMARKS

The present findings indicate that large vortices shed from the lower (large) cylinder coalesce with or entrain small vortices shed from the upper cylinder and thus form coherent structures that are significantly larger than the large vortices. This "vortex-merging" process is rapid (taking place within about $3D$), more or less stable and quasi-periodic, and results in the occurrence of a "Kármán vortex street" (KVS) with a characteristic frequency corresponding to a Strouhal number considerably less than 0.21 and centred in the lower part of the wake. In consequence, the lower interface is, on the average, considerably steeper than the upper interface and its motion is significantly less random than that of the latter. It is probable that such a "skewed" KVS is indirectly responsible for the existence of the zones of negative production detected in the asymmetrical wake by Palmer and Keffer (1972).

ACKNOWLEDGEMENT

This research was supported by the Natural Sciences and Engineering Research Council of Canada through Grant A-2746 and the Atmospheric Environment Services of Canada. The cine film was produced by the Institut de Mécanique Statistique de la Turbulence, Marseille.

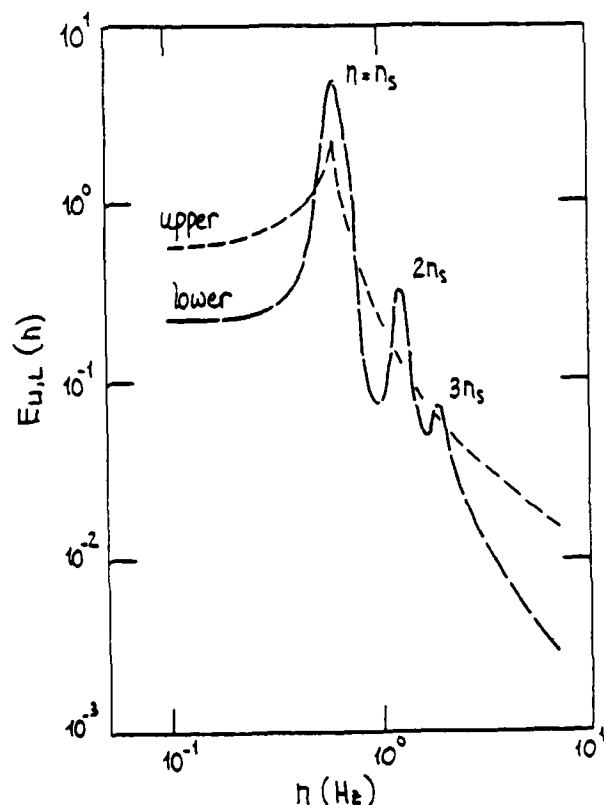


Fig. 9. Auto-spectra of interface positions, $x/D = 3.875$.

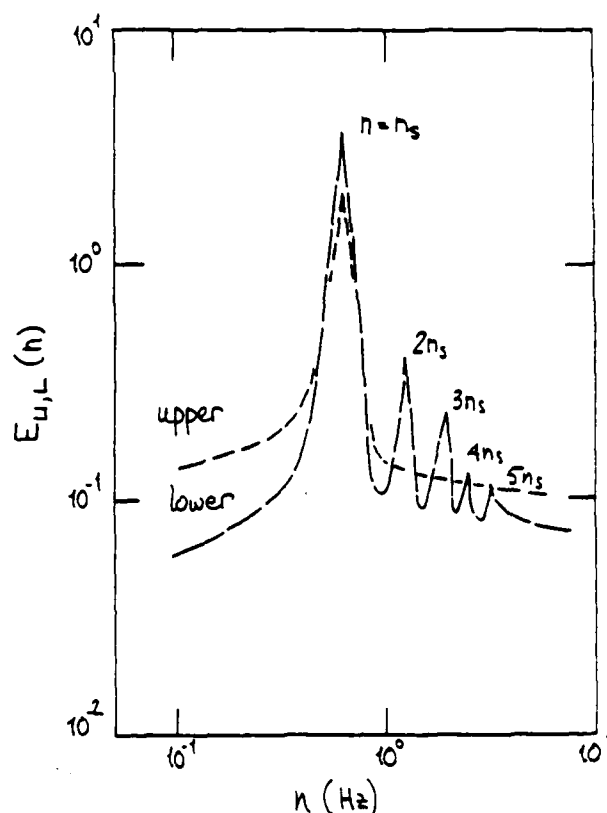


Fig. 10. Auto-spectra of interface slopes, $x/D = 3.875$.

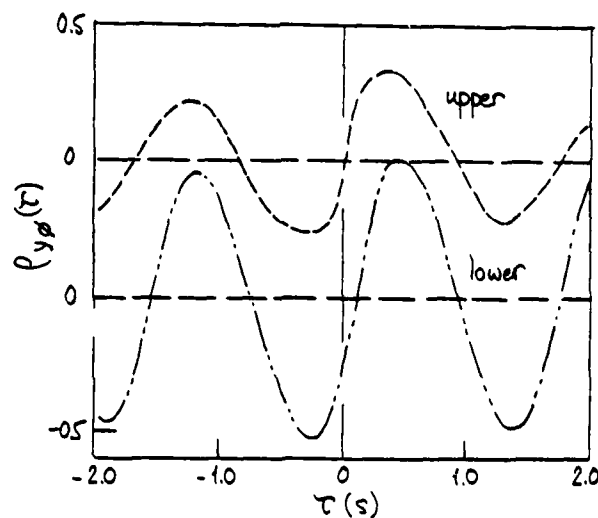


Fig. 11. Cross-correlations of interface positions and slopes, $x/D = 3.875$.

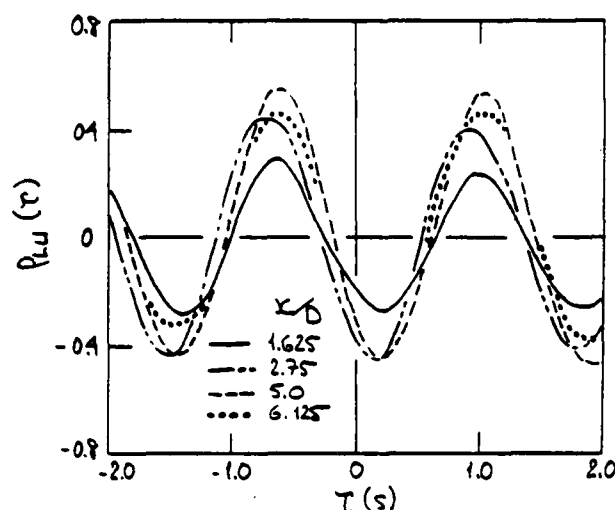


Fig. 12. Cross-correlations of interface positions.

REFERENCES

- Béguier, C., Giralt, F., Falachier, L. and Keffer, J.F., 1977, "Negative Production in Turbulent Shear Flows", Lecture Notes in Physics, 76, 22, Springer-Verlag.
- Budny, R.S., Kawall, J.G. and Keffer, J.F., 1979, "Vortex Street Evolution in the Wake of a Circular Cylinder", 2nd Symp. on Turb. Shear Flows, London.
- Diaz, F. Gavalda, J., Kawall, J.G. and Giralt, F., 1982, "Interpretation of the Complex Turbulent Flow Generated by a Rotating Circular Cylinder", Structure of Complex Turbulent Shear Flow, IUTAM Symp., Marseille, 175, Springer-Verlag.
- Gavalda, J., Diaz, F., Giralt, F., Kawall, J.G. and Keffer, J.F., 1983, "Analysis of the Wake Generated by the Interaction of a Rotating Cylinder and a Stationary Cylinder", to be submitted to J. Fluid Mech.
- Keffer, J.F., Kawall, J.G., Giralt, F. and Béguier, C., 1979, "Analysis of Turbulent Structures in Complex Shear Flows", 2nd Symp. on Turbulent Shear Flows, London.
- Palmer, M.D. and Keffer, J.F., 1972, "An Experimental Investigation of an Asymmetric Turbulent Wake", J. Fluid Mech., 53, 593.
- Shokr, M. and Keffer, J.F., 1982, "Digital Image Analysis of a Complex Turbulent Wake", Structure of Complex Turbulent Shear Flow, IUTAM Symp. Marseille, 165, Springer-Verlag.

AN INVESTIGATION OF REYNOLDS STRESS STRUCTURES
IN PLANE TURBULENT WAKES

G. Fabris

Illinois Institute of Technology, Chicago, Illinois

A. Nakayama

California State University, Long Beach, California

ABSTRACT

Instantaneous $u-v$ signals in the turbulent far wake of a cylinder have been analysed using an extended "quadrant analysis" in order to investigate the Reynolds stress structure and the features of large eddies. The results indicate that the region between the location of maximum shear and the edge of the wake is similar to the outer layer of boundary layers and bursts of slow moving flow ejecting outward contribute the most to the Reynolds shear stress. In the wake centerline region, fast moving fluid crossing the centerline contributes significantly but with opposite sign. There is a special type of flow near the centerline: flow moving upstream along the centerline slower than the mean velocity. This type of motion does not contribute to the shear stress but contains kinetic energy.

INTRODUCTION

The Reynolds stress ($-\overline{uv}$) in a turbulent shear flow is the key quantity in the mutually linked mechanisms of production of turbulent kinetic energy and transfer of momentum. It is well established that large eddies contribute the most to the Reynolds stress perhaps in an orderly quasi-periodic manner.

Features of these large eddies have been studied during the last decade using flow visualization and conditional sampling techniques. In the case of boundary layers¹⁻¹⁰ and pipe flow¹¹ quantification of features of the violent eddies has been made using so-called "quadrant analysis" in which "events" in the sequence of bursting mechanism were identified by the signs and magnitudes of the instantaneous u and v velocity components.

In the case of turbulent wakes, mechanism of the governing large eddies is not as clear. Gerrard¹² discussed observations of large-scale motions in wakes and concluded that most questions about growth and characteristics of these motions remain unanswered. As early as in 1947 Townsend¹³ concluded one of his classical wake papers with the statement "the jet structure (large eddies) can only be surmised at present, and many interesting questions remain to be answered. It is possible that useful information may be obtained from measurements of quadruple velocity products of the form u^2v^2 ... In this way more exact information about jet (turbulent burst) widths and rates of development could be collected and clearer understanding of the details of the motion attained." There appears to be no follow up to date on this visionary suggestion though Bradshaw et al.¹⁴ demonstrated how revealing is to study v^2u^2 in an axisymmetric jet. Recent studies of wakes behind cylinders by Townsend¹⁵ and Wlezian¹⁶ suggest patterns of large eddies resembling those of Karman vortex street.

Present work is an attempt to investigate large structures in fully-developed cylinder wake making use of the quadrant analysis. This method classifies the instantaneous motion by directions in which the flow is temporarily moving and whether the particular motion contributes substantially to the Reynolds stress. It may be contrasted with the conditional sampling measurements of the near wake of a flat plate made by Andreopoulos and Bradshaw¹⁷ who discriminated the instantaneous flow based on the origin of fluid and whether the fluid has mixed up with the other fluid coming from the other side of the plate (discrimination conditioned on temperature threshold). The method employed in here might prove to be more suitable studying interacting shear layers than the temperature tagging. Namely the heat has tendency of rapid diffusion into unheated turbulent flow permitting unambiguous conditional sampling only in the near interaction region. It is believed that the quadrant analysis may shed new light on instantaneous Reynolds stress mechanisms especially in the wake central region. The conventional Reynolds stress is low and changes sign in this region providing no information about the underlining physics.

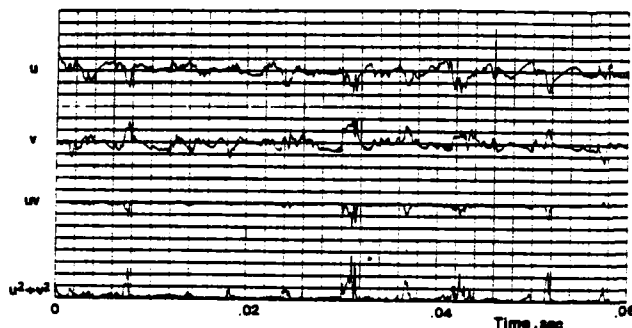
CONDITIONAL AMPLITUDE ANALYSIS

Instantaneous $u-v$ Signals and Structure of Turbulence

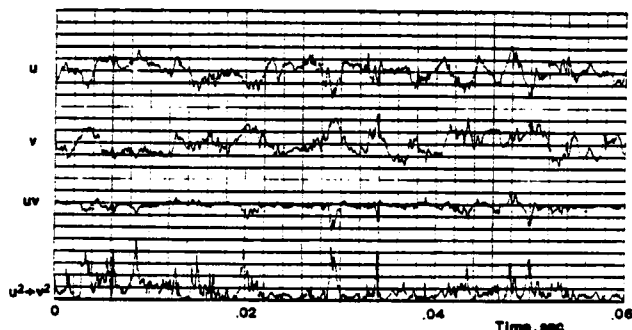
Measurements of instantaneous $u-v$ signals were made using a hot-wire probe with x-array sensors at 500 diameters downstream of a circular cylinder of diameter of 1/16 in. in an otherwise uniform flow of speed of 50 fps. Signals were analysed by digital methods by sampling and digitizing them at 20 kHz.

Fig 1 displays simultaneous instantaneous traces of u , v , uv and u^2+v^2 quantities. The figures are ordered starting with the intermittent wake edge and ending at the centerline. Structure of turbulence appears to be much more deterministic than in the pipe flow¹¹. Existence of occasional large uv bursts is evident. At the wake edge the large excursions are one sided almost exclusively due to the slow moving fluid (negative u) ejecting outward (positive v). As the centerline is approached the uv peaks are more and more double sided with both negative and positive contributions to \overline{uv} . While this is expected, careful examination of u , v and uv traces also indicates that, at the maximum-shear location and at the centerline, some of the large negative excursions of uv signals are due to fast moving fluid (positive u) moving towards the centerline. These two types of motions contributing to \overline{uv} are similar to the "ejections" and "sweeps", respectively, in boundary layers². They may correspond to the downstream and upstream sides of a large vortex-like structure seen in smoke pictures of Wlezian¹⁶ or the Karman vortex street like pattern discussed by Townsend¹². At the centerline there is an ambiguity in the sense that positive v may

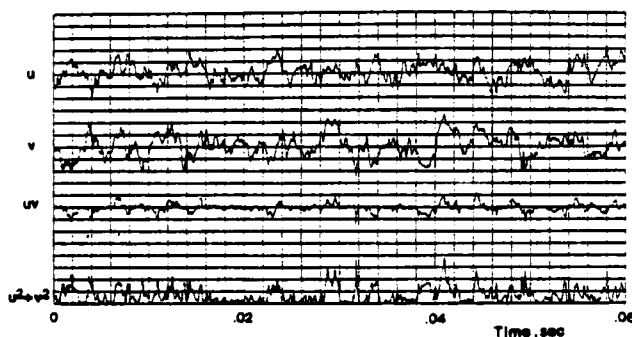
mean either moving towards the centerline or away from the centerline. Similar ambiguity has been noted by Sabot and Comte-Bellot¹¹ near the centerline of a pipe flow. However, if they are associated with large scale motion, it is likely that when (large) positive v occurs with positive u it is due to a large eddy belonging to the lower half of the wake sending fast moving fluid towards and through the centerline, while when positive v is associated with negative u it is the returning of such fluid originated from the upper half. These events are generally called "interactions" in the quadrant analysis of boundary layers.



(a)



(b)



(c)

Fig 1. Instantaneous u , v , uv and $u^2 + v^2$ Traces; (a) near the wake edge, (b) at the maximum-shear, (c) at the centerline.

The accompanying $u^2 + v^2$ traces reveal that they contain occasional "bursts" with no corresponding high excursions in the uv signal, indicating only one of u or v has high values. This is seen more clearly near the centerline and they are mainly associated with flows downstream along the centerline. Townsend¹⁵ observed recently that eddies contributing most to the shear stress are significantly different in shape and in orientation from those predominantly contributing to turbulent energy. For this reason these events are also depicted and analysed in here. The above analysis is limited of course and may even be biased in the sense that the spanwise velocity component is not included. However it does imply certain characteristics and some orderliness of the large-scale motion.

Classification of Events

For the reasons mentioned in the preceding section the following quantitative analysis has been attempted. As in the quadrant analysis of boundary layer flows the instantaneous motion was classified into different events based on the signs and magnitudes of the instantaneous u and v . Fig 2 illustrates the classification of the events in the instantaneous u - v plane. The method is close to the one introduced originally by Lu and Willmarth². Events containing significant Reynolds stress of either sign are identified by condition

$$uv > Hu'v'$$

where u' and v' are the rms intensities and H is a parameter. These events correspond to regions 1, 2, 3 and 4. In order to depict and analyse the energy containing eddies that do not contribute to the Reynolds stress, the "hole" ($uv < Hu'v'$) was subdivided by the circle

$$u^2 + v^2 = 2Hu'v'$$

to identify such events.

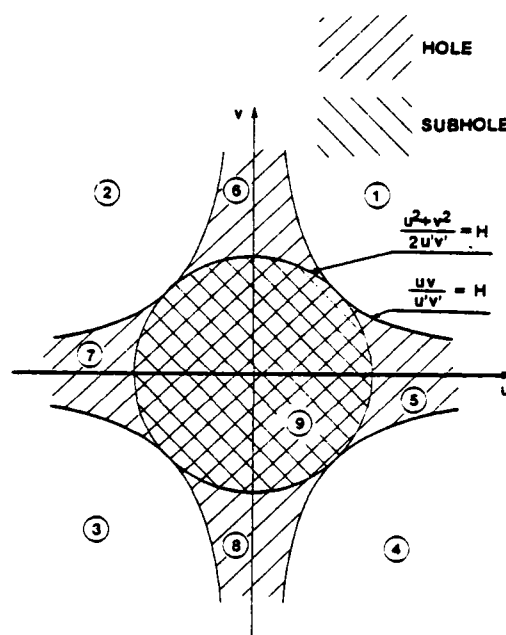


Fig 2. Classification of the Events in the u - v Plane.

Although this flow differs from boundary layers we call the event represented by region 4 "sweep" and region 2 "ejection" since former is likely to be the sweep of recently entrained potential flow, while the latter is likely to be the ejection of fully turbulent eddy originating in the wake central region. We also call the regions 1 and 3 "interactions", with a reservation near the centerline where the interactions can be sweeps penetrating through the centerline or ejections originating on one side emerging into the other side of the wake. The events represented by regions 5, 6, 7 and 8 are called respectively the turbulence moving downstream, outwards, upstream and inwards. The region 9, called subhole, represents motions that do not contribute appreciably to either the Reynolds stress or the turbulent kinetic energy.

Time Fractions

First part of the analysis consists of an investigation of the effects of the threshold level H on time fractions the u - v trace spent in different regions (events). The fraction of time spent regions 1 through 4, hole and subhole are shown in Fig 3(a) and Fig 3(b), as function of H for near-maximum-shear location and the wake center respectively.

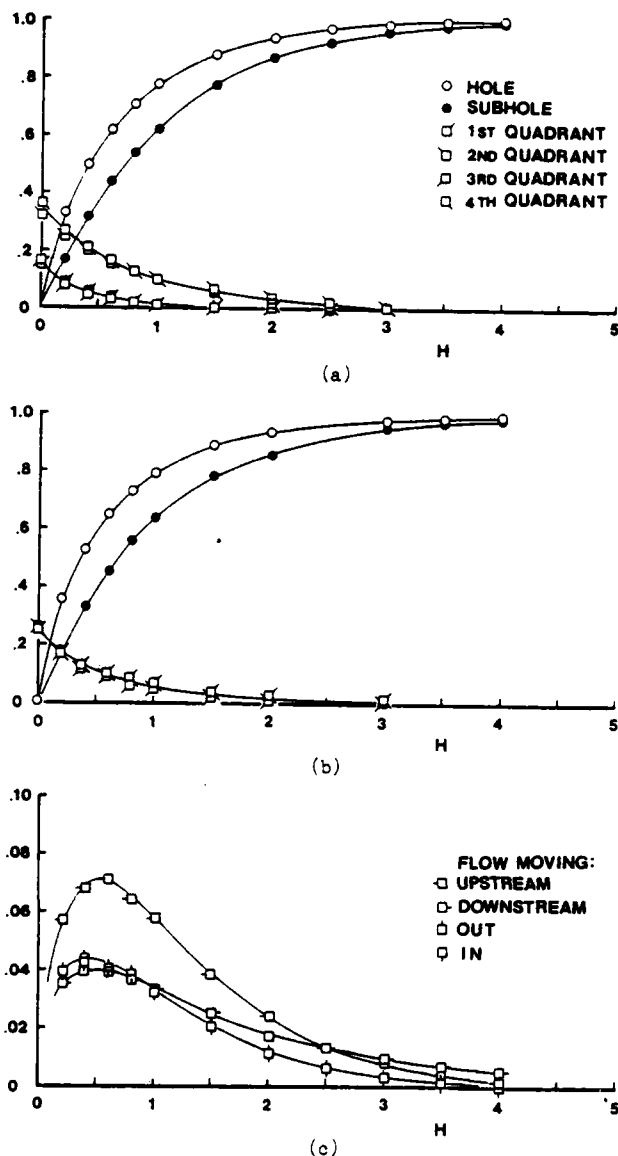


Fig 3. Fractions of Time Occupied by the Events at: (a) the maximum-shear, (b) the centerline, (c) by subregions at the center line.

Most of the quadrant analysis studies of boundary layers do not provide values of this quantity except the paper by Brodkey et al.³ where it is given as function of y for $H=0$ only. Levels of these quantities shown in Ref 3 are very close to the present results at $H=0$. Lu and Willmarth² reported fraction of time spent in the hole at several locations in the boundary layer. Again the level and shape are quite similar. The ejection-like motions and the sweep-like motions take almost equal time at the maximum-shear location. It should be noted, however, that the curve for ejections cross the curve for sweeps at about $H=1.0$ and the former is higher than the latter at $H>1.0$. Although not shown the data taken at positions between the wake edge and the maximum-shear location indicate that the cross-over points exist at at progressively smaller H values as the edge is approached. It is reasonable to say that in this region the ejection-like motions are likely to be fully turbulent eddies originating probably in the wake central region while the sweep-like motions are likely to be recently entrained potential flow. Diminishing contributions of sweeps with increasing threshold H indicate that they are considerably less violent than ejections. The first and third quadrant can be

considered either the interaction-type motions or sweeps and ejections associated with large structure on the other side of the wake. At the maximum-shear position these motions take considerably smaller fraction of time than the ejections and sweeps and become negligible at about $H=1.5$. At the wake centerline the events in all four quadrants take about equal time but the fast moving motions (first and fourth quadrants) appear to be more violent.

The fraction of time spent in the regions inside the hole but outside the subhole (regions 5, 6, 7 and 8) is not negligible. The distributions are shown in Fig 3(c) for the wake centerline only in order to show that the fluid moving upstream takes nearly twice as much time as other modes of motions. At the maximum-shear location time fractions of fluid moving in the upstream and downstream directions are almost the same, while at the near-edge position downstream eruptions dominate these energy containing motions with small contributions to the shear stress.

Fractional Contributions to the Reynolds Shear Stress

Fig 4 displays the contributions to the shear stress correlation coefficient $-\overline{uv}/u'v'$ from four quadrants for $H=0$ at various positions across the wake. The total $-\overline{uv}/u'v'$ is also shown. The subscript $J=1, 2, 3$ and 4 indicates respective quadrants. The reason for showing the contributions to the shear correlation coefficient instead of the shear stress $-\overline{uv}$ is that the shear stress is zero at the centerline and near the wake edge. Since the total $-\overline{uv}/u'v'$ is nearly constant over the shear zone, the present plots are nearly proportional to the fractional contributions to $-\overline{uv}$ in that zone.

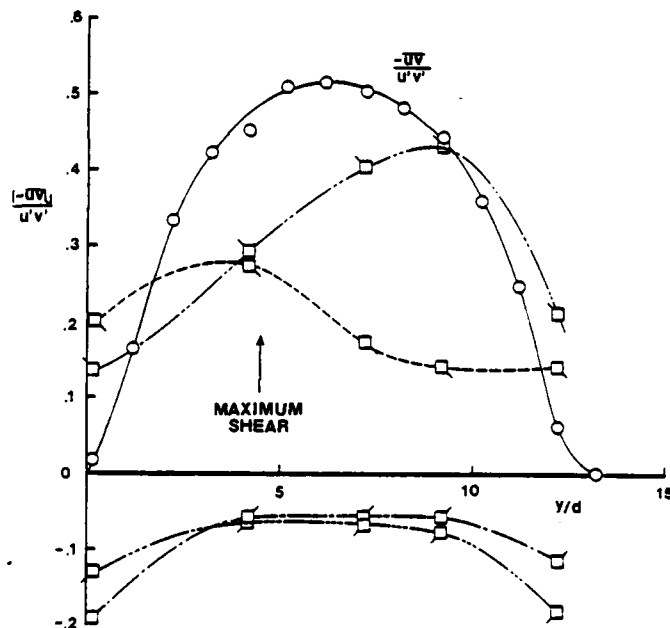


Fig 4. Contributions to the Reynolds Stress Correlation Coefficient for $H=0$.

First, Fig 4 indicates that the contribution from the ejection-like event (second quadrant) dominates in the outer half of the wake and accounts for about 80 percent of the total shear stress which is similar to the results obtained by Brodkey et al.² in the boundary layer. The contributions from sweep-like event (fourth quadrant) is generally lower but is higher in the wake central region. The events represented by the first and third quadrants which transfer momentum in the "wrong" direction account for only 20 percent in the shear zone which is only half as much as contributions of the interactions in boundary layers. This is another indication of the fact that eddies in the wake are more efficient than those in boundary layers. In the central region, as discussed earlier the first quadrant and fourth quadrant contributions balance out and the second and third quadrants are also of nearly equal magnitude. It is noted, however, that accelerated motions contribute more than the decelerated motions.

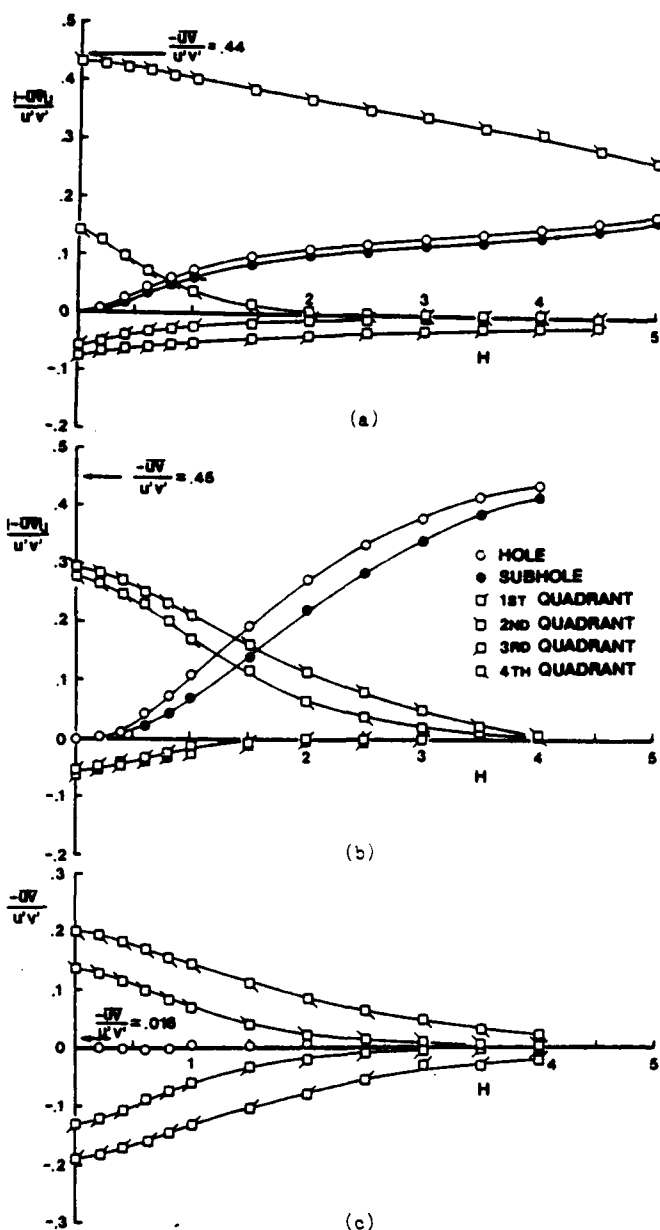


Fig 5. Contributions to the Reynolds Stress; (a) near the wake edge, (b) at the maximum-shear, (c) at the center line.

Figs 5(a), (b) and (c) show variation of the contributions by different events as function of H . Fig (a) is for a position near the edge, (b) is for the maximum-shear location and (c) is for the wake centerline. These diagrams can be directly compared with those for outer part of boundary layers² and the pipe flow¹¹. The boundary layer data appear to fit between the near-wake-edge data of Fig 5(a) and maximum-shear position shown in Fig 5(b). Near the wake edge there are surprisingly large contributions from very violent eddies moving out and very small contributions from the sweep-like events which are likely to be potential. This was expected from the instantaneous traces of u , v , and uv , but Fig 5(a) confirms this quantitatively. At the maximum-shear location the ejection-like events and sweep-like events contribute most and almost equally significant while the interactions have very small contributions and are negligible at about $H=2$. It is interesting to observe that at the centerline the fast moving fluid (first and fourth quadrants) contributions to the shear at high H are even larger than the ejections and sweep-like events do at the maximum-shear location. It suggests that these may be quite violent motions that cancel out in most of the conventional averages.

As expected the contributions from the region between the hole and the subhole is very small. Though not shown, our data do indicate that the individual contributions are small and the canceling between the different subregions (5, 6, 7 and 8) is not the reason for this.

Fractional Contributions to the Kinetic Energy

Fractional contributions to $u^2 + v^2$ (representative of the turbulent kinetic energy) at the position of maximum shear are shown in Fig 6(a). Trends are similar as for the Reynolds stress shown on Fig 5(a). Fig 6(b) offers the same contributions at the wake centerline. Significance of the regions within the hole but outside of the subhole is now more apparent with the wide difference between the curves for the hole and subhole. The contributions from the sub-hole regions (5, 6, 7 and 8) are further displayed on Fig 6(c). By far the most contributing subregion is 7 where the streamwise velocity is lower than the mean and the lateral velocity is small.

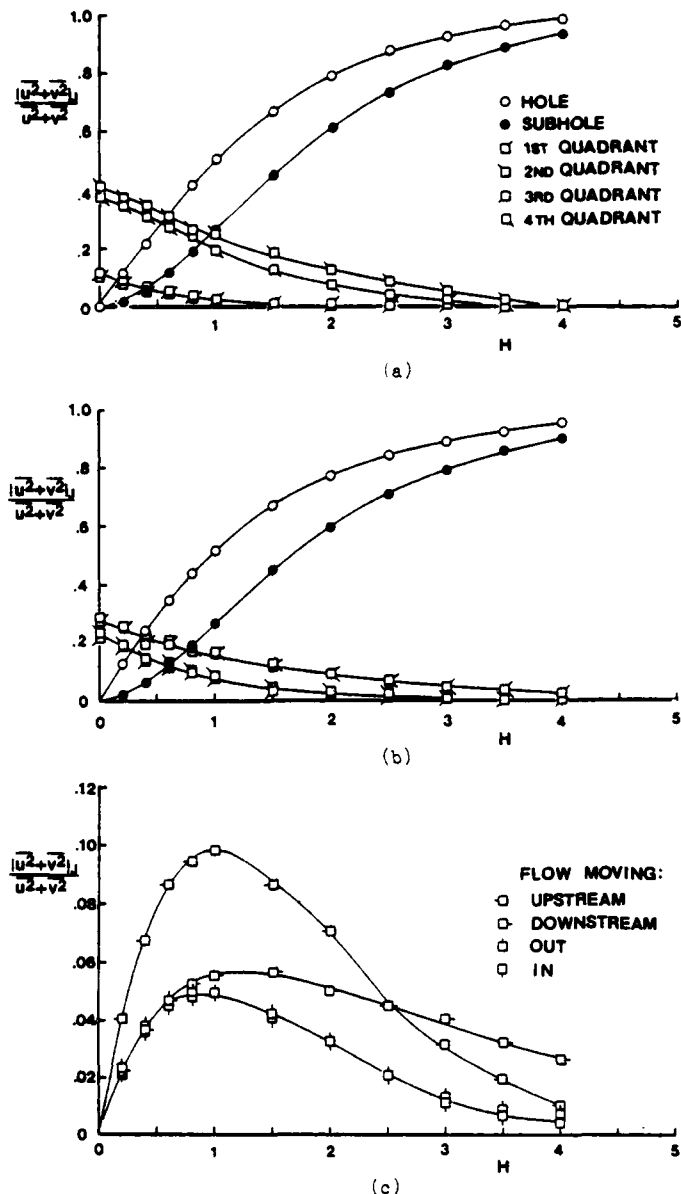


Fig 6. Contributions to $u^2 + v^2$; (a) at the maximum-shear, (b) at the center line, (c) at the center line from subregions.

Conditional Velocities of the Events

Conditional mean velocities U_c and V_c for four events (1, 2, 3 and 4) at the position of maximum shear and the centerline are given in Fig 7(a) and (b), respectively. The values are connected by equal H lines. This diagram is very informative of flow directions and intensities of different events. Points on the graph indicate the average direction and the magnitude of velocity in the $x-y$ plane of all the motions in appropriate events with the instantaneous Reynolds stress larger than $Hu'v'$. The plot for the maximum-shear location reveals that in general ejection-like and sweep-like motions are stronger than interaction-type motions. However, this tendency is less pronounced if averaged over large Reynolds stress carrying motions (large H). The figure for the wake centerline shows that faster moving motions (first and fourth quadrants) are stronger.

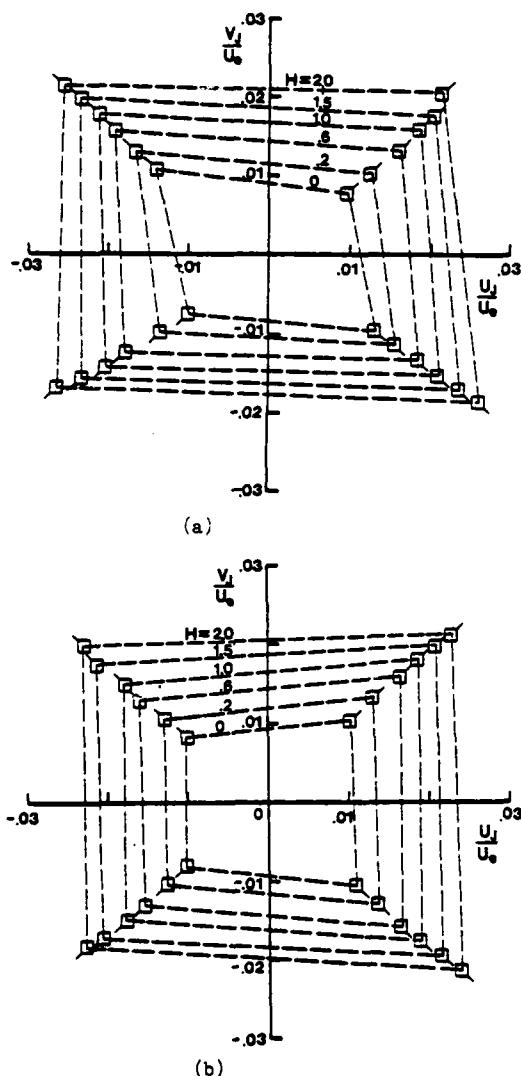


Fig 7. Conditional Velocities of the Events; (a) at the maximum-shear, (b) at the centerline.

Durations and Intervals

Lu and Willmarth² and Sabot and Comte-Bellot¹¹ determined the periods of duration of and intervals between large bursts and sweeps in the boundary layer by taking a characteristic value of H determined from the plots of contributions to uv from different events. On the other hand Brodkey et al³ considered $H=0$ only. We have tried an approach similar to the former to obtain information on the durations and intervals of various events.

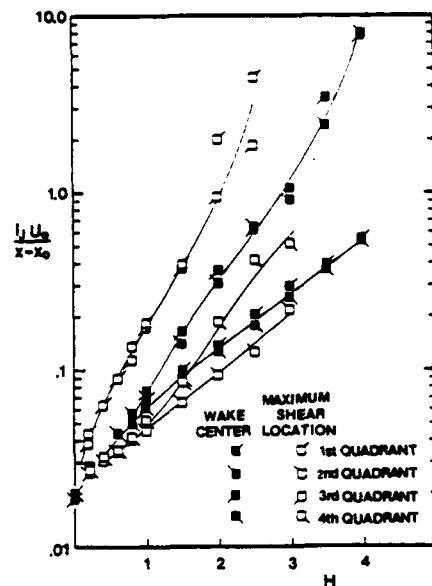


Fig 8. Mean Interval between Large Bursts; open symbols at the maximum-shear, closed symbols at the centerline.

Fig 8 is a plot of mean intervals between consecutive occurrences of events of the same type at the location of maximum shear and the wake centerline. They are normalized by the similarity variable for time, $(x-x_0)/U_\infty$, where x_0 is the virtual origin of the wake taken here as $x_0=-40D$. The trend is very similar to that given by Lu and Willmarth² in the sense that the intervals depend very strongly on H . At the location of maximum shear the ejection-like event occurs most frequently and the interaction type motions least frequently. If $H=3$, for which the contributions to $-uv$ from interactions become negligible at this position, is taken as a characteristic threshold the mean interval between the ejection-like events is $0.2(x-x_0)/U_\infty$. The characteristic interval between sweep-like events is about $0.5(x-x_0)/U_\infty$. The ratio is not very different from that of the boundary layer. At the wake centerline, the flow symmetry requires that the events associated with quadrants one and four occur at the same frequency and those of quadrants two and three also occur at the same rate. The diagram shows that the events associated with flow moving downstream (quadrants one and three) occur much more often than those moving upstream. Fig 5(c) indicates that $H=3$ may also be taken as a characteristic threshold for determining the frequency of violent events moving faster than the mean velocity. It is slightly larger than that for the ejections at the maximum shear location.

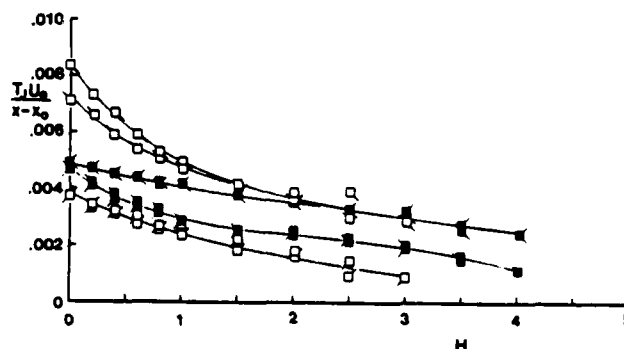


Fig 9. Mean Period of Large Burst; symbols as on Fig 8.

Fig 9 shows averages of durations of the ejections and sweeps. The durations, as in the boundary layers, exhibit a slow variation over a range of H . The durations of fast moving events at the wake center are very close to the durations of sweep and burst event at the maximum-shear position. The durations of slow moving events are shorter than these but longer than the interaction type motions at the locations of maximum shear. This implies that the larger structure near the centerline is consisting more of sweeps coming from both sides of the centerline than of the structures that develop into ejection-like motions. The upstream moving flow has shorter durations and is smaller scaled. These events are moving streamwise slower than the mean flow along the centerline can be named "old turbulence" being convected along the central region of the wake. This fluid was entrained a long time ago.

SUMMARY

The instantaneous u-v signals in the far wake of a cylinder have been analysed using an extension of the quadrant analysis method which is often employed to investigate bursting phenomena in boundary layers. Considerable qualitative and quantitative features of the large and violent eddies in the wake of a cylinder were obtained by this method. The present analysis, even without clear visualization of large structures in the wake, by sorting the instantaneous signal on the basis of Reynolds stress contribution does show structures similar to boundary layers in the shear zone and a kind of coexistence of two opposite-sided large structures and smaller scaled "old turbulence" near the centerline. Future work which incorporates other type of conditioning together with the present quadrant type analysis will further clarify the Reynolds stress structure in the far wake.

REFERENCES

- 1 Willmarth, W. W. and Lu, S. S., 1972, *J. Fluid Mech.* 55, 65.
- 2 Lu, S. S. and Willmarth W. W., 1973, *J. Fluid Mech.* 60, 481.
- 3 Brodkey, S. R., Wallace, M. J. and Eckelmann, H., 1974, *J. Fluid Mech.* 63, 209.
- 4 Wallace, M. J., Brodkey, S. R. and Eckelmann, H., 1977, *J. Fluid Mech.* 83, 673.
- 5 Eckelmann, H., Nychas, S. G., Brodkey, R. S. and Wallace, J. M., 1977, *Phys. Fluids* 20, 3225.
- 6 Wallace, J. M. and Brodkey, S. R., 1977, *Phys. Fluids* 20, 351.
- 7 Kreplin, P. H. and Eckelmann, H., 1979, *Phys. Fluids* 22, 1233.
- 8 Panton, R. L., Goldman, A. L., Lowery, R. L. and Reischman, M. M., 1980, *J. Fluid Mech.* 97, 299.
- 9 Raupach, R. M., 1981, *J. Fluid Mech.* 108, 363.
- 10 Nakagawa, H. and Nezu, I., 1977, *J. Fluid Mech.* 80, 99.
- 11 Sabot, J. and Comte-Bellot, G., 1976, *J. Fluid Mech.* 74, 767.
- 12 Gerrard, J. H., 1981, *Proc. of the Third Symp. of Turb. Shear Flows*, 11.13.
- 13 Townsend, A. A., 1947, *Proc. Roy. Soc. A* 197, 124.
- 14 Bradshaw, P., Ferris, D. H. and Johnson, R. F., 1964, *J. Fluid Mech.* 19, 591.
- 15 Townsend, A. A., 1979, *J. Fluid Mech.* 95, 515.
- 16 Wlezian, R., 1981, Ph. D. thesis, Illinois Institute of Technology.
- 17 Andreopoulos, J., and Bradshaw, P., 1980, *J. Heat Transfer* 102, 755.
- 18 Fabris, G., 1979, *J. Fluid Mech.* 94, 673.

W. Koch

DFVLR/AVA Institute for Theoretical Fluid Mechanics
D - 3400 Göttingen
F. R. Germany

ABSTRACT

An attempt is made to determine the shedding frequency of the flow past blunt edged plates by computing the natural frequencies of the system. The flow is split into a steady viscous part which is modelled and an unsteady inviscid part which defines a resonance condition. According to linear theory this resonance condition requires a bifurcation of the instability eigenvalue which provides a surprisingly good estimate of the shedding frequency if a realistic mean wake model is employed.

INTRODUCTION

Periodic aerodynamic phenomena associated with the flow about bluff bodies range from noise generation to buffeting and have been investigated for a long time due to their considerable practical importance. Not only bluff bodies but also slender airfoils and turbomachinery blades show periodic vortex shedding as demonstrated for example by Heinemann et al. (1976). These unsteady phenomena may lead to structural damage if the frequency lies close to a resonant frequency of the structure. Therefore a reliable theoretical prediction of the shedding frequency and amplitude with the intended goal of controlling them is of paramount interest. Despite extensive efforts and significant advances this still remains a largely unresolved problem.

Starting with the earliest observations by Strouhal (1878) and Rayleigh (1879) the theoretical treatment reached a first culmination with von Kármán's (1911) famous vortex-street theory. However as pointed out by Roshko (1954) the theory is incomplete in so far as it cannot by itself relate the vortex-street dimensions and velocities to the blunt-body dimension and free-stream velocity. Roshko also demonstrated that the whole problem depends crucially on the near wake immediately behind the obstacle. The need for additional empirical relations or assumptions, cf. Fathy et al. (1977), appears to be connected with the need for a better understanding of the basic mechanism of vortex formation. Wake oscillator models as well as discrete vortex models, see for example the review by Sarpkaya (1979), considerably advanced our knowledge but could not explain the physical mechanism completely.

The discovery that large scale coherent structures also play a central role in the development of various turbulent shear flows, see for example Roshko (1976), increased the interest in these periodic flow phenomena even further. From several observations it appears that the basic physical mechanism underlying many of these different discrete frequency phenomena might be qualitatively similar. A very instructive experiment of Parker (1966) as well as several examples out of a large class of time periodic flows in which a resonant condition, a feedback mechanism or structural elasticity controls highly organized flow oscillations, cf. the review by Rockwell & Naudascher (1979), suggest that the observed periodic phenomena in unforced and unobstructed flows may

also be due to aerodynamic resonance.

To a certain degree this aerodynamic resonance hypothesis is just a logical step in a development starting with the theory of shear layer stability. Considering the shear layer as a linear oscillator the main goal of stability theory is to identify the propagation and growth characteristics of the normal modes in dependence of certain parameters, mathematically leading to an eigenvalue problem. The next step, physically simplified by a forced oscillator, is concerned with the question of how certain modes are excited by externally imposed disturbances. This so-called *receptivity problem* received increased attention in the past few years, cf. Tam (1978), and is formulated mathematically as a boundary-value problem. From the receptivity problem it is only a small step to the *resonance problem* that is to find that externally imposed forcing frequency which induces the largest response of the system. If such resonances do exist it appears quite plausible to assume that any occurring discrete frequency phenomena would be sustained easiest near such resonant frequencies.

Therefore the present paper attempts to explore this aerodynamic resonance approach by determining the natural frequencies of a simple model problem. Since the prediction of the so-called Parker mode frequencies by means of linearized theory led to excellent results, cf. Koch (1983), it was hoped that the same might be true for the present problem even though the amplitudes can only be determined via nonlinear theory.

STEADY MEAN WAKE-FLOW MODELS

Before one can proceed with the analysis several simplifying assumptions have to be introduced. Following the traditional approach in stability theory each quantity is considered to be composed of a value for a specified steady mean flow plus an unsteady periodic fluctuation. Linear theory is employed for the latter assuming that fluctuating amplitudes are small compared with mean-flow quantities; products and squares of perturbation quantities are neglected. This leads to the well known nonuniform validity of the linear solution. However, assuming that the fastest growing disturbance in the linear regime will also dominate the subsequent nonlinear flow development the resonance frequency obtained from the linear analysis should provide a fairly good approximation of the spectral characteristics.

The first task is the specification of the steady mean flow. Theoretically it can be obtained by solving the steady Navier-Stokes equations numerically or by extracting properly averaged profiles from experiment. Since neither one is available the basic mean flow is modelled by employing the quasi-parallel flow assumption. The particular model profile is characterized by certain parameters but does not depend explicitly on the streamwise coordinate. However, by changing the parameters it should be possible to model actual wakes at any streamwise station reasonably well. This parallel-flow assumption is realistic for the high Reynolds number wakes be-

hind blunt edged plates investigated here. High Reynolds number wake flows have the added advantage that the large scale disturbances are practically unaffected by viscosity allowing an inviscid treatment. For comparison with actual wind tunnel tests as well as for computational convenience two symmetrically located side walls which move with the mean flow are introduced parallel to the plate.

Wake models of increasing complexity are considered. The simplest model is the vortex-sheet model in which the wake is formed by two infinitely thin vortex sheets enclosing a zero mean flow wake. This model is limited to approximating low frequency wakes where the particular profile does not matter. Nevertheless it is very instructive for studying the proper classification of the occurring waves and provides fairly good low frequency initial values for more realistic wake eigenvalue calculations. Skipping the next simple broken line profiles, wake modelling is continued with continuous profiles. Such a wake can be described for example by combining two hyperbolic-tangent shear-layer profiles which are frequently used in stability theory. One writes

$$\frac{U(y)}{U_\infty} = 1 + \frac{1}{2} \left\{ \tanh \left(\frac{y-y_w}{\delta_w} \right) - \tanh \left(\frac{y+y_w}{\delta_w} \right) \right\} \quad (1)$$

where U_∞ is the constant free stream velocity, $y_w = d/2 + \delta^*$ is the shear-layer displacement and δ_w is a measure of the steepness of the profile. All geometric variables are nondimensionalized by a reference length L_{ref} , for example the channel height in which case $h=1$. Prescribing the parameters y_w and δ_w specifies a particular wake profile which may be associated with that streamwise position in the actual wake at which the measured mean wake profile comes closest to this model profile. However it should be stressed that for the present resonance calculation the association of a specified profile with a particular x-position is not required. Figure 1 shows the velocity variation (1), with $\delta_w=0$ identifying the limiting case of the vortex-sheet model.

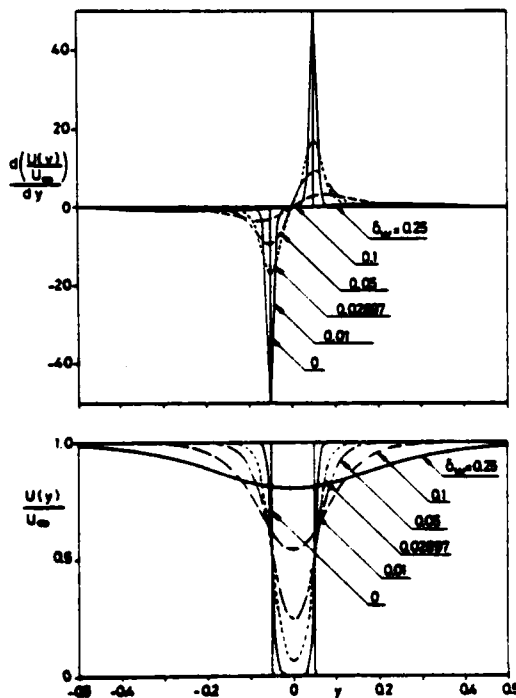


FIGURE 1. HYPERBOLIC-TANGENT WAKE MODEL: STEADY MEAN WAKE VELOCITY AND VORTICITY AS FUNCTION OF δ_w FOR $d/h = 0.1$, $\delta^*/d = 0$.

The main weakness of the ordinary hyperbolic-tangent wake model (1) is that the oncoming boundary layer is modelled only very crudely and that at least at the initial stage, the wake has constant displacement thickness instead of the more realistic constant momentum thickness. These two points can be remedied to a certain extent by

combining two modified hyperbolic-tangent shear-layer profiles introduced by Michalke (1969)

$$\frac{U(y)}{U_\infty} = 2 - \left[\frac{1 - \tanh \left(\frac{y-y_w}{\delta_w} \right)}{2} \right]^{\frac{1}{m}} - \left[\frac{1 - \tanh \left(\frac{y+y_w}{\delta_w} \right)}{2} \right]^{\frac{1}{m}} \quad (2)$$

For $m=1$ the ordinary hyperbolic-tangent profile (1) is recovered while for $m \rightarrow \infty$ boundary-layer like profiles are obtained for which the corresponding boundary-layer displacement thickness δ^* is related to the boundary-layer momentum thickness θ_s by $\delta^* = 2\theta_s$. An example of the corresponding wake profiles is shown in Figure 2.

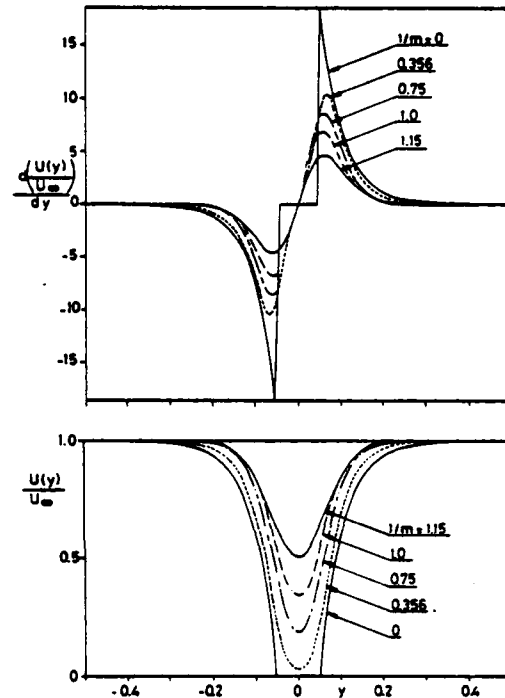


FIGURE 2. MODIFIED HYPERBOLIC-TANGENT WAKE MODEL: STEADY MEAN WAKE VELOCITY AND VORTICITY AS FUNCTION OF $1/m$ FOR $d/h = 0.1$, $\delta^*/d = 0.7$.

UNSTEADY THEORY FOR CONTINUOUS MEAN WAKES

Formulation of the Wiener-Hopf Equation

Extracting the harmonic time dependence $\exp(i\omega t)$ the fluctuating pressure p_0 is nondimensionalized

$$p_0(x_0, y_0, t) = \rho_\infty a_\infty^2 p'(x, y) \exp(i\omega t)$$

where a_∞ and ρ_∞ denote the constant free stream speed of sound and density. The governing equation

$$(iK + M \frac{\partial}{\partial x}) \left\{ \nabla^2 p' - [iK + M \frac{\partial}{\partial x}]^2 p' \right\} - 2 \frac{dM}{dy} \frac{\partial^2 p'}{\partial x \partial y} = 0 \quad (3)$$

is obtained by linearizing about the prescribed mean wake quantities. $K = \omega L_{ref}/a_\infty$ denotes the Helmholtz number and $M(y) = U(y)/a_\infty$ is the mean wake Mach number.

For continuous mean wake profiles the parallel-flow assumption requires a nonphysical penetration of the flow into the plate annihilating whatever one gains by solving for the physically exact boundaries. Therefore one may simplify the problem even further but retain the essential physics by investigating wakes around duct like "hollow" plates. Experimentally, usually sound waves or oscillations of the plate or oncoming flow are used to introduce periodic forcing, compare for example Graham & Maull (1971). Here acoustic excitation is introduced from the inside of the duct, as depicted in Figure 3, similar to the situation frequently used in jet noise investigations. While the prescribed mean wake profile $M(y)$ is allowed to violate the viscous boundary condition on the plates at $y = \pm d/2$, the inviscid perturbation solution has to satisfy the boundary condition of vanishing normal

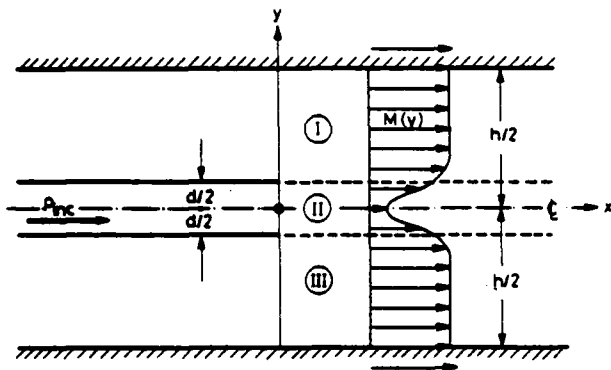


FIGURE 3. UNSTEADY MODEL PROBLEM.

velocity along all solid walls. The mathematical formulation is completed by imposing the radiation condition and a physically realistic edge condition for $x = 0$, $y = \pm d/2$ which will be discussed later.

The specified basic mean wake is symmetric in the y -direction such that symmetric and antisymmetric pressure disturbances can be separated. Here only the physically more relevant antisymmetric problem is dealt with explicitly such that $p'(x, y=0) = 0$. Furthermore the problem is formulated in terms of the diffracted field $p(x, y)$ by subtracting the incoming disturbance $p_{inc}(x, y) = -\hat{p}(y)\exp(i\beta^+x)$ in region II, i.e. $0 \leq y \leq d/2$. At least for a certain frequency range a spatially amplified instability wave is expected and one circumvents the associated mathematical difficulties as usual by temporarily considering K complex, i.e. $K = |K|\exp(i\delta)$ with δ near $-\pi/2$, assuring that then even the instability wave is damped.

For the mathematical solution of the model problem the Wiener-Hopf technique, cf. Noble (1958), may be used. In applying Jones' method of formulation the known boundary conditions are supplemented by unknown functions $\Delta p(x)$ and $w(x)$ such that the validity of the boundary conditions is extended from $x = -\infty$ to $x = +\infty$

$$\frac{\partial p}{\partial y}(x, y = \frac{h}{2}) = 0, \quad -\infty \leq x \leq +\infty \quad (4)$$

$$p(x, y = \frac{d}{2} + 0) - p(x, y = \frac{d}{2} - 0) = \begin{cases} \Delta p(x), & x < 0 \\ p_{inc}(x, y = \frac{d}{2}), & x > 0 \end{cases} \quad (5)$$

$$\frac{\partial p}{\partial y}(x, y = \frac{d}{2}) = \begin{cases} 0, & x < 0 \\ w(x), & x > 0 \end{cases} \quad (6)$$

$$p(x, y = 0) = 0, \quad -\infty \leq x \leq +\infty \quad (7)$$

Now the Fourier transformation, defined by

$$\bar{p}(y; \xi) = \int_{-\infty}^{\infty} p(x, y) e^{-i\xi x} dx$$

is taken of equation (3). This results in

$$\frac{d^2 \bar{p}}{dy^2} - \frac{2\xi dM/dy}{K + \xi M} \frac{d\bar{p}}{dy} + [(K + \xi M)^2 - \xi^2] \bar{p} = 0, \quad (8)$$

the general solution of which may be expressed in terms of two linearly independent solutions

$$\bar{p}(y; \xi) = A(\xi)f(y; \xi) + B(\xi)g(y; \xi).$$

The validity of this solution is limited to the strip of holomorphy determined mainly by the decay behavior of p for $x \rightarrow \pm\infty$ with complex K . Additional singularities occur at the singular points $\xi = -K/M(y)$, $0 \leq y \leq h/2$, of the differential equation (8) and are responsible for a continuous contribution to the otherwise discrete fre-

quency spectrum.

Taking the Fourier transformation of the boundary conditions (4) to (7) the following definitions are introduced

$$\bar{\Delta p}(\xi)_{\oplus} = \int_{-\infty}^0 \Delta p(x) e^{-i\xi x} dx$$

$$\bar{w}(\xi)_{\ominus} = \int_0^{\infty} w(x) e^{-i\xi x} dx$$

$$\bar{p}_{inc}(y = \frac{d}{2}; \xi) = -\frac{i\hat{p}(y = d/2)}{\xi - \beta^+}, \quad \text{Im } \xi < \text{Im } \beta^+.$$

The integration functions A, B can be eliminated by means of the Fourier transformed boundary conditions (4), (6) and (7) and choosing $f(y)$ and $g(y)$ such that in region I $\partial f^{(1)}/\partial y(y = h/2) \equiv 0$ and in region II $g^{(2)}(y = 0) \equiv 0$. Substitution into the remaining Fourier transformed boundary condition (5) results in the Wiener-Hopf equation, valid in the strip of holomorphy,

$$\bar{\Delta p}(\xi)_{\oplus} + \bar{w}(\xi)_{\ominus} \mathcal{K}(\xi) = \frac{i\hat{p}(y = d/2)}{\xi - \beta^+} \quad (9)$$

with the corresponding kernel function

$$\mathcal{K}(\xi; K, M) = \frac{g^{(2)}(\frac{d}{2}) \frac{df^{(1)}}{dy}(\frac{d}{2}) - f^{(1)}(\frac{d}{2}) \frac{dg^{(2)}}{dy}(\frac{d}{2})}{\frac{df^{(1)}}{dy}(\frac{d}{2}) \cdot \frac{dg^{(2)}}{dy}(\frac{d}{2})}.$$

Formal Solution of the Wiener-Hopf Equation

The detailed solution of the Wiener-Hopf equation (9) is complicated by the general form of the functions $f(y)$ and $g(y)$ depending on the chosen mean wake profile $M(y)$. However for our purpose it suffices to proceed formally. All one needs to know is the kind of zeros and singularities of the kernel function. Guided by the properties of the vortex-sheet kernel one can state that there are an infinite number of in general simple zeros in the upper and lower half plane of ξ . These zeros are associated with the eigenvalues in the downstream part $x > 0$ of the channel and include the instability eigenvalue μ_{inst} . For complex K , with δ near $-\pi/2$, μ_{inst} is located in the upper half plane but may move to the lower half plane for $\delta \rightarrow 0$. In addition the so-called "critical layer" singularity lies in the upper half plane. On the other side there exist an infinite number of in general simple poles which correspond to the eigenvalues in the upstream part $x < 0$. Therefore the multiplicative factorization can be performed formally

$$\mathcal{K}(\xi) = \mathcal{K}(\xi)_{\oplus} \cdot (1 - \xi/\mu_{inst}) \hat{\mathcal{K}}(\xi)_{\ominus}$$

where each part is zeroless, holomorphic and decays algebraically for $|\xi| \rightarrow \infty$ in the corresponding half plane indicated by the subscript \oplus or \ominus . The instability eigenvalue μ_{inst} is explicitly included in the \ominus -function. Dividing (9) by $\mathcal{K}(\xi)_{\oplus}$ the RHS term can be decomposed additively by writing

$$\frac{1}{\xi - \beta^+} \frac{1}{\mathcal{K}(\xi)_{\oplus}} = \frac{1}{\xi - \beta^+} \left\{ \frac{1}{\mathcal{K}(\xi)_{\oplus}} - \frac{1}{\mathcal{K}(\beta^+)_{\oplus}} \right\} + \frac{1}{\xi - \beta^+} \frac{1}{\mathcal{K}(\beta^+)_{\oplus}}.$$

Separating the terms holomorphic in the upper and lower half plane the usual arguments of the Wiener-Hopf method are used to equate both parts to one and the same entire function. This entire function is fixed by the edge conditions. Guided by the solution of the vortex-sheet problem which requires the application of a Kutta condition this entire function is set identically equal to zero also for the continuous profile $M(y)$. This at once determines $\bar{w}(\xi)_{\ominus}$ and hence the linear solution in the whole field. Upon Fourier inversion it is evident

that for $\delta \rightarrow 0$ and $|K|$ in the unstable frequency range the whole downstream solution is dominated by the contribution of the instability eigenvalue

$$v(x) \sim \frac{\hat{p}(y=d/2) u_{\text{inst}} \exp(i u_{\text{inst}} x)}{(u_{\text{inst}} - \delta^*) \hat{K}(u_{\text{inst}}) \hat{K}(\delta^*)} \quad (10)$$

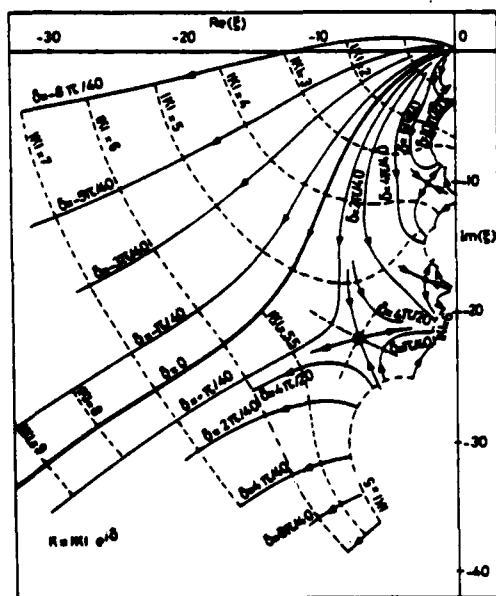
Now the whole effort centers around finding a condition for which a non-trivial solution exists if the amplitude $\hat{p}(y=d/2)$ of the forcing wave vanishes. Formally this is only possible if numerator and denominator vanish simultaneously. In (10) this implies that u_{inst} either equals δ^* or that it coalesces with one of the zeros of $\hat{K}(\xi)$ leading to a double eigenvalue or bifurcation of the instability eigenvalue.

For attenuating modes such an eigenvalue bifurcation is known to occur resulting in the so-called *Cremer optimum impedance condition* for maximal sound attenuation in acoustically lined ducts, cf. Cremer (1953) or Zorumski & Mason (1974). However for $\delta \rightarrow 0$ and $|K|$ in the unstable frequency range u_{inst} lies in the lower half plane while δ^* and all zeros of $\hat{K}(\xi)$, representing attenuated waves propagating in the downstream direction, lie in the upper half plane. Therefore in our case the only possibility for the existence of a non-trivial solution is that u_{inst} bifurcates in the lower half plane thereby coalescing with an eigenvalue of an upstream propagating wave. That this is indeed possible has already been demonstrated by Mattingly & Criminale (1972) for incompressible wakes. Therefore the remaining task is to find possible bifurcation points of the spatially amplified instability eigenvalue in the lower half plane of ξ . For this purpose the nonlinear eigenvalue problem consisting of the homogeneous complex differential equation (8) together with the homogeneous boundary conditions $\hat{p}(y=0)=0$ and $d\hat{p}/dy(y=h/2)=0$ is solved numerically by a fourth-order variable step size complex Runge-Kutta procedure and the results are presented in the next section.

NUMERICAL RESULTS

Results for Vortex-Sheet Wake Model

The solution according to the vortex-sheet model is unstable for all frequencies and a numerical search showed in general no bifurcation of the instability eigenvalue for real K . However, admitting complex K , corresponding to attenuation or amplification in time, several bifurcation points were found as shown in the example of Figure 4 for antisymmetrical excitation. Of particular interest is the specially marked bifurcation



Results for Hyperbolic-Tangent Wake Model

In this investigation time-periodic solutions are of particular interest and the parametric description of the more general wake profiles allows not only a better modelling of actual wakes but also provides more possibilities for finding a bifurcation point for real K . Indeed such a bifurcation point can be found for the hyperbolic-tangent wake model by fixing δ^*/d and varying $|K|$ and δ_w as demonstrated in Figure 6 for $\delta^*/d = 0$. Contrary to the vortex-sheet result $\delta_w = 0$, which is reshown by the thick dashed line, now the solution becomes stable above a certain frequency K . The specially marked bifurcation point in Figure 6 establishes the very specific values $\delta_w = 0.02897$ and $K = 3.2487$. The mean-wake profile corresponding to $\delta_w = 0.02897$ is shown in Figure 1 and interestingly enough represents a wake cross section

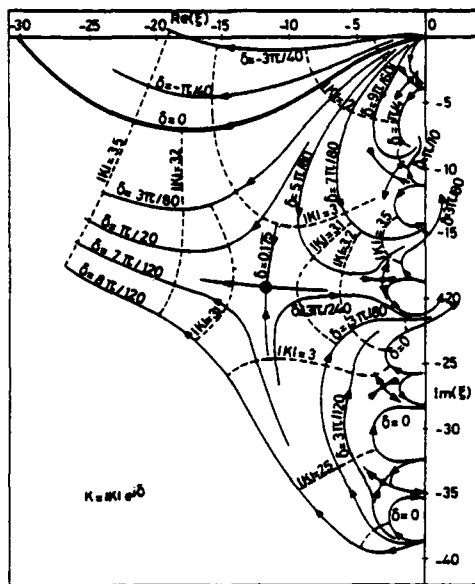


FIGURE 7. HYPERBOLIC-TANGENT WAKE MODEL: ANTISYMMETRIC EIGENVALUES AS FUNCTION OF COMPLEX K FOR $d/h = 0.1$, $M = 0.3$, $\delta^*/d = 0$, $\delta_w = 0.04$.

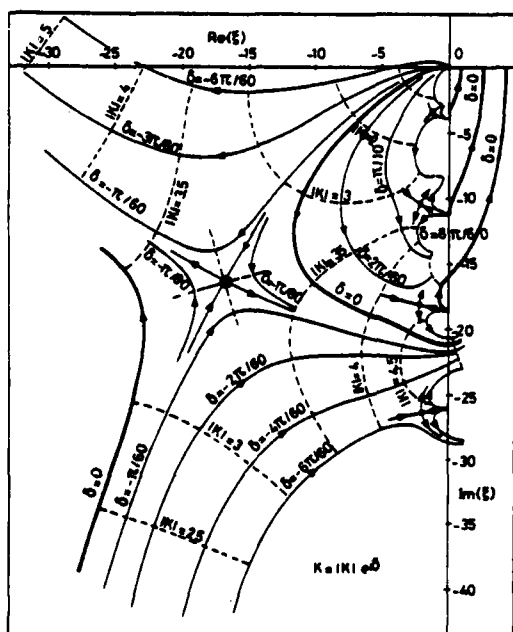


FIGURE 8. HYPERBOLIC-TANGENT WAKE MODEL: ANTISYMMETRIC EIGENVALUES AS FUNCTION OF COMPLEX K FOR $d/h = 0.1$, $M = 0.3$, $\delta^*/d = 0$, $\delta_w = 0.025$.

slightly downstream of the end of the core region. For the example of Figure 6 with $M = 0.3$ and $d/L_{ref} = 0.1$ the special value $K = 3.2487$ gives a Strouhal number $St = fd/U_\infty = 0.1729$. Figures 7 and 8 demonstrate that the bifurcation point in Figure 6 marks exactly the time-periodic transition between time-amplified and time-attenuated solutions as found previously by Mattingly & Criminale (1972). The bifurcation-point Strouhal number is plotted in Figure 9 for various values of δ^*/d as curve (A) showing only qualitative agreement with Bauer's (1961)

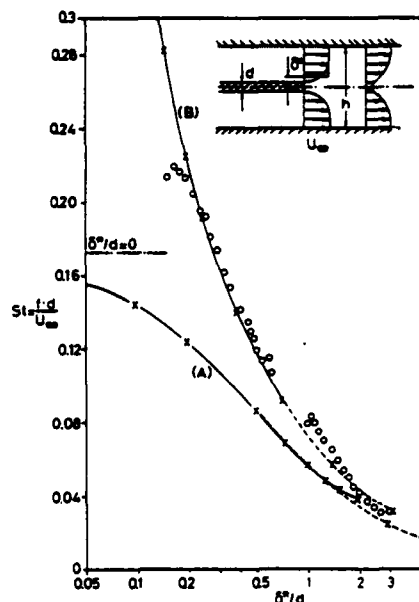


FIGURE 9. BIFURCATION POINT STROUHAL NUMBER AS FUNCTION OF δ^*/d FOR $M = 0.3$:

- (A) HYPERBOLIC-TANGENT WAKE MODEL
- (B) MODIFIED HYPERBOLIC-TANGENT WAKE MODEL
- EXPERIMENTAL RESULTS OF BAUER (1961).

experimental results. The solid line of curve (A) connects results for $d/h = 0.1$ while the dashed line connects results for $d/h = 0.01$. Obviously from a certain ratio $(2\delta^* + d)/h$ on the influence of the side walls is quite noticeable as elucidated in Figure 10.

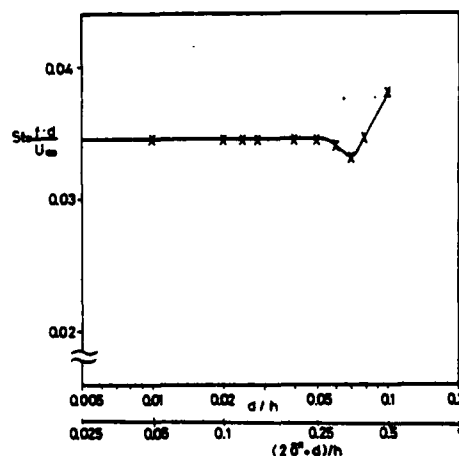


FIGURE 10. HYPERBOLIC-TANGENT WAKE MODEL: BIFURCATION POINT STROUHAL NUMBER AS FUNCTION OF d/h FOR $M = 0.3$, $\delta^*/d = 2$.

Results for Modified Hyperbolic-Tangent Wake Model

In order to achieve better quantitative agreement the same bifurcation-point search was performed for the more realistic modified hyperbolic-tangent wake model by

varying K , and $1/m$. An example is shown in Figure 11

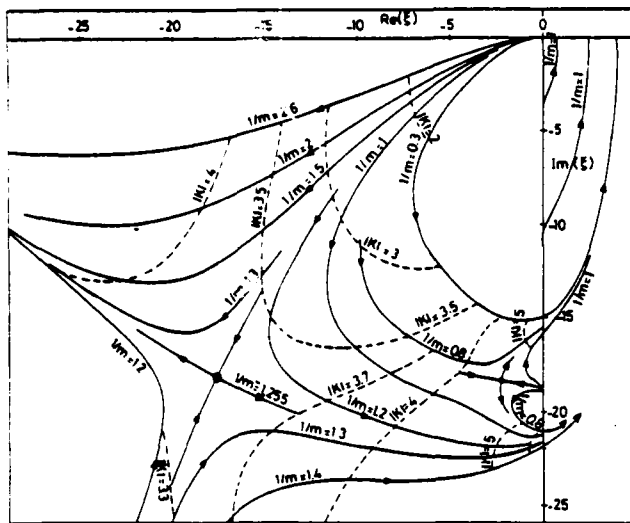


FIGURE 11. MODIFIED HYPERBOLIC-TANGENT WAKE MODEL: ANTI-SYMMETRIC EIGENVALUES AS FUNCTION OF REAL K AND $1/m$ FOR $d/h = 0.1$, $M = 0.3$, $\delta^*/d = 0.25$.

for $\delta^*/d = 0.25$ and the collected results are depicted in Figure 9 as curve (B). Contrary to the hyperbolic-tangent wake model now the bifurcation-point Strouhal number does not seem to approach a finite limiting value for $\delta^*/d \rightarrow 0$. In Figure 2 the value $1/m = 0.356$ marks the profile corresponding to the bifurcation-point condition and again indicates a wake profile slightly downstream of the end of the core region.

All theoretical results are for $M = 0.3$ while Bauer's (1961) experiments were conducted at variable but rather low Mach numbers. Therefore to convincingly back up the good agreement one has to establish that the results depend only weakly on the Mach number. This is demonstrated in Figure 12 for $\delta^*/d = 0.25$. However major

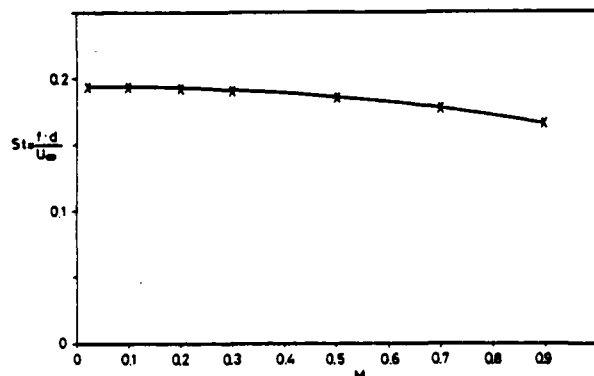


FIGURE 12. MODIFIED HYPERBOLIC-TANGENT WAKE MODEL: BIFURCATION POINT STROUHAL NUMBER AS FUNCTION OF M FOR $d/h = 0.1$, $\delta^*/d = 0.25$.

deviations from experiment occur once the boundary layer on the plate becomes transitional or turbulent. Then apparently drastically changed mean wake models are needed - exhibiting the decisive influence of the mean wake vorticity distribution.

CONCLUSION

Confirming Mattingly & Criminale's (1972) finding the wake acts like a highly tuned amplifier. At the bifurcation point condition, which appears to control the unsteady flow, the downstream propagating spatially amplified instability mode is matched exactly by an upstream propagating attenuated mode suggesting a simple feed back cycle. However, at the same time this result

clearly reveals the limits of the linear theory because the upstream propagating mode can only come from the non-linear source terms excluded in linear theory.

BIBLIOGRAPHY

- Bauer, A.B., 1961, "Vortex Shedding from Thin Flat Plates Parallel to the Free Stream", *J. Aerospace Sci.* 28, 340-341.
- Cremer, L., 1953, "Theorie der Luftschall-Dämpfung im Rechteckkanal mit schluckender Wand und das sich ergebende höchste Dämpfungsmaß", *Acustica*, 3, 249-263.
- Fathy, A., Rashed, M.I., and Lumsdaine, E., 1977, "A Theoretical Investigation of Laminar Wakes behind Airfoils and the Resulting Noise Pattern", *J. Sound Vibr.* 50, 133-144.
- Graham, J.M.R., and Maull, D.J., 1971, "The Effects of an Oscillating Flap and an Acoustic Resonance on Vortex Shedding", *J. Sound Vibr.* 18, 371-380.
- Heinemann, H.-J., Lawaczeck, O., and Bütefisch, K.A., 1976, "V.Karman Vortices and their Frequency Determination in the Wake of Profiles in the Sub- and Transonic Regimes", *Symposium Transsonicum II*, Berlin: Springer, 75-82.
- Kármán, T. von, 1911, "Über den Mechanismus des Widerstandes den ein bewegter Körper in einer Flüssigkeit erfährt", *Nachr. d. Wiss. Ges. Göttingen, Math. Phys. Kl.*, 509-517, and 1912, 547-556.
- Koch, W., 1983, "Resonant Acoustic Frequencies of Flat Plate Cascades", *J. Sound Vibr.*, 88.
- Mattingly, G.E., and Criminale, W.O., 1972, "The Stability of an Incompressible Two-Dimensional Wake", *J. Fluid Mech.*, 51, 233-272.
- Michalke, A., 1969, "The Influence of the Vorticity Distribution on the Inviscid Instability of a Free Shear Layer", *Fluid Dyn. Trans.*, 4, 751-760.
- Noble, B., 1958, "Methods Based on the Wiener-Hopf Technique for the Solution of Partial Differential Equations", London: Pergamon Press.
- Parker, R., 1966, "Resonance Effects in Wake Shedding from Parallel Plates: Some Experimental Observations", *J. Sound Vibr.*, 4, 62-72.
- Rayleigh, Lord, 1879, "Acoustical Observations", *Phil. Mag.*, Ser.5, 7, 149-162.
- Rockwell, D., and Naudascher, E., 1979, "Self-Sustained Oscillations of Impinging Free Shear Layers", *Ann. Rev. Fluid Mech.*, 11, 67-94.
- Roshko, A., 1954, "On the Drag and Shedding Frequency of Two-Dimensional Bluff Bodies", *NACA TN* 3169.
- Roshko, A., 1976, "Structure of Turbulent Shear Flows: a New Look", *AIAA J.*, 14, 1349-1357.
- Sarpkaya, T., 1979, "Vortex Induced Oscillations. A Selective Review", *Trans. ASME, J. Appl. Mech.*, 46, 241-258.
- Strouhal, V., 1878, "Über eine besondere Art der Tonerregung", *Ann. Phys. Chemie, Neue Folge*, 5, 216-251.
- Tam, C.K.W., 1978, "Excitation of Instability Waves in a Two-Dimensional Shear Layer by Sound", *J. Fluid Mech.*, 89, 357-371.
- Zorumski, W.E., and Mason, J.P., 1974, "Multiple Eigenvalues of Sound-Absorbing Circular and Annular Ducts", *J. Acoust. Soc. Am.*, 55, 1158-1165.

TURBULENT BOUNDARY LAYER-WAKE INTERACTION

E. P. Tsiolakis, E. Krause and U. R. Müller
Aerodynamic Institute of Technical University Aachen
51 Aachen, F. R. Germany

ABSTRACT

The interaction of a two-dimensional, incompressible, turbulent boundary layer on a flat plate with a plane wake of a circular cylinder was investigated experimentally and theoretically. The cylinder was positioned at various distances above the plate, with the axis normal to the free-stream direction and parallel to the surface of the plate. The time-averaged velocity components, the Reynolds stresses, the wall-pressure distribution and the wall shear stresses were measured downstream from the cylinder in the wake and in the boundary layer. Mean and fluctuating velocities were measured with hot-wire probes, conventional data reduction was used. It could be shown that the wake retains its self-preserving characteristics in the outer part and approximately in the inner layer as well. The profiles of the Reynolds stresses in the interacting part of the flow were used to deduce a mixing-length closure assumption, which was incorporated in a numerical finite-difference simulation of the relaxing boundary layer.

EXPERIMENTAL SETUP AND HOT-WIRE DATA REDUCTION

The experiment was carried out in the incompressible, two-dimensional, turbulent boundary layer on a smooth plate placed in the open test section (ϕ 1 m) of the return-circuit low-speed wind tunnel of the Aerodynamisches Institut. The flow was tripped at the leading edge with a wire of 2 mm diameter. A distance of 500 mm downstream, the boundary layer was disturbed by a circular cylinder with diameter $D = 5$ mm or 10 mm, Fig. 1. The cylinder was mounted with its axis normal to the free-stream direction and parallel to the plate at various wall distances y_c . In this paper discussion is limited to conditions, for which the cylinder ($D = 10$ mm) is fully immersed in the boundary layer ($y_c = \delta_o/2$), and for which the distance between axis and wall is equal to $y_c = 2 \delta_o$. The quantity $\delta_o = 26$ mm is the thickness of the undisturbed boundary layer at the locus of the cylinder. The details of all measurements, also including the cases $y_c = 5$ mm and 26 mm, were reported by Tsiolakis (1982). The free-stream Reynolds number per unit length was $1.8 \cdot 10^6 \text{ m}^{-1}$. Downstream of the cylinder profiles of

mean velocities and all Reynolds stresses were measured by means of miniature hot wires. The wall shear stress distribution, inferred from Preston tube measurements, and the pressure distribution, obtained from pressure taps (ϕ 1 mm) at the wall, were also described in the investigation quoted. For sake of comparison all measurements were carried out in the unperturbed boundary layer as well.

Mean and fluctuating velocities were measured by means of rotating hot wires. The influence of the magnitude and direction of the local velocity vector on the signal interpretation were taken into account in the calibration according to Müller (1982). For a hot-wire fixed coordinate system, the cooling law was described with an effective cooling velocity U_c

$$E^2/S^2 = U_c^2 = U_N^2 + k^2 U_T^2 + h^2 U_Q^2 \quad (1)$$

The velocity components normal and tangential to a hot wire in the plane of the prongs were denoted by U_N and U_T , respectively, and U_Q was perpendicular to both. The directional sensitivities k and h were determined from separate calibrations for each hot wire used, the quantity S was the constant of proportionality between the electrical output E of an analogue linearizer circuit and U_c . Transformation of the instantaneous turbulent velocities $\bar{U}_i + u_i$ of a laboratory fixed coordinate system onto the hot-wire fixed frame of reference yielded the cooling law in the form

$$E(\psi, \gamma, k, h)/S = U_c = [L(\bar{U}_i \bar{U}_j) + l(u_i) + f(u_i u_j)]^{0.5}, \quad (2)$$

where L and f contain all double velocity correlations of mean and fluctuating velocity components, respectively; the function l includes the linear fluctuation terms. With the hot-wire angle γ between wire and prong and the sensitivities k and h known, rotation of the probe around its longitudinal axis with various angles ψ yields a sufficiently large number of electrical signals for evaluating all mean velocities \bar{U}_i and the Reynolds stresses $\overline{u_i u_j}$.

As was pointed out already by Müller (1982), large scatter can result in the data reduction, if the squared time averaged signal

$$\overline{E^2}(\psi) / S^2 = \overline{L} + \overline{f} \quad (3)$$

is used to solve the corresponding set of linear equations as proposed by Durst (1971) or Acrivelllis (1979):

$$d_{ij}(\psi, y, k, h) \vec{W} = \vec{B} \quad (4)$$

with $B_i = \overline{E_i^2} / S^2$ and $\vec{W} = (\overline{U^2} + \overline{u^2}, \overline{V^2} + \overline{v^2}, \overline{w^2}, \overline{UV} + \overline{uv})$.

One reason for the scatter is the unequal order of magnitude of the terms \overline{L} and \overline{f} , with \overline{L} , in general, being much larger than \overline{f} . Another reason is that the coefficient matrix is ill-conditioned: Hadamard's criterion, see Jordan-Engeln and Reutter (1976), for an $(n \times n)$ -type matrix

$$K(d_{ij}) = |\det d_{ij}| / (a_1 a_2 \dots a_n) \quad (5)$$

with a_m being defined as the square root of the sum of all squared elements of the m -th row of d_{ij} , yielded a value of $K(d_{ij}) = 1.5 \cdot 10^{-5} \ll 1$, indicating that equation (3) cannot be used for accurate data evaluation, if the turbulence level is low. However, for high-intensity flows locally reversed velocities become significant and may falsify the hot-wire signal $\overline{E^2}$ because of rectification, Müller (1983).

In the present investigation the conventional method for calculating the Reynolds stresses from the rms-measurements of the hot-wire output was used. Root-expansion of equation (2) and time-averaging yielded

$$[\overline{E}(\psi) - \overline{E}(\psi)]^2 / S^2 = \overline{e^2}(\psi) / S^2 = a_{ij}(\psi) \overline{u_i u_j} \quad (6)$$

and

$$[\overline{e}(\psi) \pm \overline{e}(\psi + 180^\circ)]^2 / S^2 = b_{ij}(\psi) \overline{u_i u_j}.$$

For this set of equations Hadamard's condition yielded $K = 0.9978 \approx 1$ indicating a well-conditioned system.

After measuring all Reynolds stresses, the mean velocities were evaluated from equation (4) as proposed by Müller (1982), yielding an accuracy of order (u^3) compared to the conventional method, which has an inherent error of order (u^2) .

DISCUSSION OF RESULTS

Measurements

Figs. 2 and 3 show the measured mean velocities for the test cases $D = 10$ mm and $y_c = 52$ mm and 13 mm, respectively, compared to the smoothed results of the undisturbed boundary layer. The data show the spreading of the wake and the decay of the velocity defect. The near-wall region of the perturbed boundary layer recovers over a shorter distance than the outer layer. Within the downstream measuring range $20 \leq x/D \leq 86$, relative minima of the velocity profiles were only measured with the cylinder positioned outside of the boundary layer and for $y_c = 26$ mm and $x/D = 20$. Mean velocity data of boundary layer-cylinder wake interactions similar to those discussed here

were reported by Klebanoff and Diehl (1952), Clauser (1956) or Marumo et al. (1978).

The present investigation also includes measurements of the Reynolds stress tensor as shown in Figs. 4-7. For $y_c = 2 \delta_0 = 52$ mm the normal stresses are close to those of an undisturbed boundary layer ($u^2 > w^2 > v^2$) for $y \leq \delta_0/2$, Fig. 4. In the outer part of the flow the measured profiles correspond to those of Townsend (1956) obtained with a cylinder in uniform free-stream ($v^2 > w^2 > u^2$). Because of vortex shedding the v^2 -correlation is the largest one in the wake flow. The profiles of w^2 exhibit a relative minimum at $y = y_c$ which disappears at $x/D \approx 50$. At the measuring station farthest downstream ($x/D = 86$), the normal stresses measured in the wake region, Fig. 5, approach equal orders of magnitude, while in the boundary layer the turbulence structure remains unchanged. The Reynolds shear stress \overline{uv} approaches zero with increasing distance from the wall, in the outer region it has a symmetrical shape about y_c and correspondingly changes its sign. The measured results of mean velocities and Reynolds stresses for this test case with $y_c = 2 \delta_0$ indicate negligible interaction between boundary layer and wake flow. In the other example chosen for discussion, $y_c = 13$ mm (Fig. 6), boundary layer and wake do interact with each other. In contrast to the measurement discussed above, the maximum value of v^2 is reduced considerably yielding $u^2 > w^2 > v^2$. The \overline{uv} -correlation does not change its sign in this case. At $x/D = 86$, Fig. 7, the measured profiles of the Reynolds stresses are close to those of an undisturbed boundary layer except for the large values of w^2 .

For those test series, in which the profiles of the mean velocity indicate relative minima, the wall distances $y(\partial \overline{U} / \partial y = 0)$ and those of $y(\overline{uv} = 0)$ are equal and the sign of the turbulent shear stress is determined by that of the velocity gradient. Such results are consistent with gradient-type closure assumptions and therefore the mixing length distributions were evaluated. The length scale of the free shear layer was found to be constant across the wake with a magnitude being about three times the value obtained in the outer layer of the wall-bounded undisturbed shear flow. The mixing length distributions of the interacting flow of the other test cases were also evaluated; the results obtained for $y_c = 13$ mm are shown in Fig. 8. The near-wall slope $\chi = \partial l / \partial y$ decreases with increasing downstream distance ($0.8 \gtrsim \chi \gtrsim 0.5$). The average value is about 0.6. In the outer layer l/δ increases from 0.1 at $x/D = 20$ to $l/\delta \approx 0.14$ for $x/D \geq 40$. The measured near-wall and outer-layer asymptotes are substantially larger than the corresponding ones of equilibrium boundary layers, $\chi = 0.41$ and $l/\delta = 0.085$, respectively. The mixing length distributions evaluated for the test case $y_c = 5$ mm closely agree with those of Fig. 8. The same results were also obtained for the inner layer of test case $y_c = 26$ mm, while in the outer layer a constant length scale identical to that of case $y_c = 52$ mm was evaluated.

Numerical Simulation and Analysis of Self-Similarity

All flow fields investigated were simulated numerically by

solving the boundary-layer equations with an implicit finite-difference method developed at the Aerodynamisches Institut. Eddy viscosities were prescribed with a two-layer mixing-length closure assumption adjusted to the measurements. Using the smoothed velocity profiles measured at $x/D = 20$ as initial conditions and neglecting downstream pressure gradients according to the measurements of Tsiolakis (1982), good agreement between computed mean velocity profiles and experimental data was obtained. For the test case $y_c = 13$ mm, Fig. 9, the calculations show a slight overshoot in the outer layer compared to the measurements. In the transition region between law-of-the-wall and interactive flow, $y \approx 5$ mm, the measurements indicate large curvatures $\partial^2 \bar{u}_{1A} / \partial y^2$, which could not be simulated correctly in the computations. Probably a more sophisticated turbulence model would be suited better for predicting the relaxing boundary layer, though for the present flow the definition of the initial conditions is expected to give rise to problems.

The experimental data were also analyzed with regard to self-preserving characteristics of the flow. The velocity defect created by the cylinder was obtained by subtracting the mean velocity profiles of the perturbed, interacting flow from those of the undisturbed, flat-plate boundary layer, see Figs. 2 and 3:

$$\Delta \bar{u} = (\bar{u}_{FP} - \bar{u}_{1A}) \quad (7)$$

Following Schlichting (1930) and Reichardt (1942), the existence of self-similarity of the wake requires $\Delta \bar{u} \sim (x/D)^{-0.5}$ and $L \sim (x/D)^{0.5}$ as scaling laws for characteristic velocity and length scales. Therefore the maximum velocity defect $\Delta \bar{u}_{max} = \max(\bar{u}_{FP} - \bar{u}_{1A})$ as well as the outer-layer half width

$$b_{1/2} = y(0.5 \Delta \bar{u}_{max}) - y(\Delta \bar{u}_{max}) \quad (8)$$

evaluated for all test cases with $D = 10$ mm, are plotted in Fig. 10 and compared with the empirical far-field scaling laws of the investigations quoted above. Since scaling with $(x/D)^{0.5}$ approximately exists, except for $y_c = 5$ mm, the normalized velocity defect $\Delta \bar{u} / \Delta \bar{u}_{max}$ was plotted for $y_c = 52$ mm and 13 mm, e. g., in Figs. 11 and 12 versus the normalized wall distance $\eta / \eta_{1/2}$, with

$$\eta = [(y - y(\Delta \bar{u}_{max})) / D] / (x/D)^{0.5} \quad (9)$$

and

$$\eta_{1/2} = b_{1/2} / (x/D)^{0.5} \quad (10)$$

The correlations indicate that the self-preserving wake characteristics are retained for $y_c = 52$ mm and for the outer shear layer of $y_c = 13$ mm. In the interacting region of the flow, similarity exists for $-0.5 \leq \eta / \eta_{1/2} \leq 0$, but deviations become larger as $\eta / \eta_{1/2}$ approaches -1. Steep velocity gradients in the inner part of the wake region are typical for all correlations evaluated in contrast to vanishing gradients at the outer edge.

The computation of outer and inner-layer similar mean velocity profiles was carried out by assuming a constant mixing length or a constant eddy viscosity across the wake, as proposed by Schlichting (1930) and Reichardt (1942), respectively. Since both results agreed closely, discussion will be limited to the latter assumption. For a cylinder in uniform free-stream, substitution of

$$\Delta \bar{u} / \bar{u}_{\infty} = f(\eta) / (x/D)^{0.5} \quad (11)$$

into the momentum equation

$$\bar{u}_{\infty} \frac{\partial \Delta \bar{u}}{\partial x} = \hat{v}_t \frac{\partial^2 \Delta \bar{u}}{\partial y^2} \quad (12)$$

yields the similar solution

$$f/f_{max} = \exp[-\eta^2 / (4 \hat{v}_t)] \quad (13)$$

Using Reichardt's experimental far-field results for the half width ($\eta_{1/2} \approx 0.22$) and the nondimensional eddy viscosity ($\hat{v}_t = \hat{v}_t / (\bar{u}_{\infty} D) = 0.0164$), results in the profile plotted versus $\eta / \eta_{1/2}$ in Fig. 11 and in the outer half of Fig. 12. The measured correlations agree excellently with this solution, since with the measured half width being approximately $1.5 \cdot 0.22$, see Fig. 10, and with the average eddy viscosity being about $2.5 \cdot 0.0164$, the same solution for f/f_{max} versus $\eta / \eta_{1/2}$ is obtained.

The inner-layer similarity of the cylinder wake ($\eta / \eta_{1/2} \leq 0$) was analyzed by assuming the boundary layer flow to be created by a velocity defect $\Delta_1 \bar{u}$, Fig. 13. The flow of the wake of the cylinder, $\Delta_2 \bar{u}$, can be superposed in a first approximation to yield the resultant velocity defect

$$\Delta \bar{u} = \Delta_1 \bar{u} + \Delta_2 \bar{u} \quad (14)$$

Substituting $\Delta_1 \bar{u}$, approximated by

$$\frac{\Delta_1 \bar{u}}{\bar{u}_{\infty}} = \frac{f_1(\eta)}{(x/D)^{0.5}} = \frac{c \eta}{(x/D)^{0.5}} \quad \text{with } c \approx -9.5 \quad (15)$$

and

$$\frac{\Delta_2 \bar{u}}{\bar{u}_{\infty}} = \frac{f_2(\eta)}{(x/D)^{0.5}} \quad (16)$$

into the momentum equation (12), yields a differential equation for the similar profile $f_2(\eta)$ of the inner-layer. With the eddy viscosity prescribed by $\hat{v}_t \approx 0.04$ as found for all wake flows investigated, Runge-Kutta integration resulted in the profile f_2/f_{2max} plotted for $\eta / \eta_{1/2} \leq 0$ in Fig. 12; according to the measurements of Fig. 10, the half width was set to $\eta_{1/2} = 0.33$. The calculated self-similar profile reasonably approximates the measured correlations in the range $-0.5 \leq \eta / \eta_{1/2} \leq 0$. For $\eta / \eta_{1/2} \rightarrow -1$ the computed velocity gradient considerably overestimates the measured values. Obviously in the near-wall region self-similarity breaks down.

The measured profiles of the Reynolds shear stress \overline{uv} were analyzed in the same way as described for the mean velocities. In the outer-layer wake self similarity was found to correspond to that of a cylinder in uniform flow. The results obtained for

the inner-layer failed to indicate acceptable agreement between theory and experiment because of inaccuracies of the measurements and due to the coarse simplifications inherent in the theoretical similarity analysis.

CONCLUDING REMARKS

The interaction of an incompressible, two-dimensional turbulent boundary layer with a cylinder wake was investigated experimentally and theoretically. Cylinders with different diameters D were positioned at various distances y_c from the wall; the paper discusses typical results obtained from the test series with $D = 10$ mm and $y_c = \delta_0/2$ and $y_c = 2 \delta_0$ with $\delta_0 = 26$ mm being the thickness of the undisturbed boundary layer at the position of the cylinder. In addition to the wall shear stress and the pressure distributions, profiles of mean velocities and Reynolds stress tensors were measured by means of hot wires. The method of Durst (1971) or Acrivelllis (1979) for evaluating the mean and fluctuating velocities from the squared hot-wire signals was shown to yield an ill-conditioned set of equations for turbulence levels below 50 %. Therefore the conventional data reduction method based on a root-expansion of the hot-wire cooling law was used.

The results obtained from the measurements and their analysis may be summarized as follows:

- Interaction of turbulent boundary layer-wake flow occurred for the test series with $y_c \leq \delta_0/2$ as well as for $y_c = \delta_0$ in the range $y < y_c$; in the outer layer of the latter case and for $y_c = 2 \delta_0$ the wake was created by uniform free-stream.
- The mean velocities perturbed by the wake recovered over a shorter distance in the near-wall region than in the outer layer.
- At the measuring station farthest downstream ($x/D = 86$) the boundary layer had not recovered completely.
- Vortex shedding generated large velocity correlations $\overline{u^2}$, as well $\overline{w^2}$ was found to be larger than $\overline{u^2}$. The downstream relaxation reestablished the order of magnitude $\overline{u^2} > \overline{w^2} > \overline{v^2}$ typical for undisturbed boundary layers.
- The mixing length distributions determined from the measurements differed markedly from those of an undisturbed boundary layer. In the interacting flow region the near-wall slopes $\kappa = \partial l / \partial y$ decreased with increasing downstream distance ($0.8 \gtrsim \kappa \gtrsim 0.5$). The average value was about $\kappa = 0.6$. In the outer layer l/δ increased from 0.1 at $x/D = 20$ to $l/\delta \approx 0.14$ for $x/D \geq 40$. The turbulent length scale for the non-interacting wake flow was found to be constant across the shear layer with a magnitude being about two and a half times the value measured in the outer region of the undisturbed boundary layer. Consistent with a gradient-type turbulence model, the wall distances $y(\partial \bar{u} / \partial y = 0)$ agreed with $y(\bar{uv} = 0)$. At these coordinates the \bar{uv} -shear stress changed its sign.

- Numerical simulations of all flows investigated were carried out by solving the boundary-layer equations with a finite-difference method. Prescribing the eddy viscosities with a two-layer mixing-length model adjusted to the measurements, the computed mean velocities indicated good agreement with the experimental data.
- The velocity defect measured in the cylinder wake could be correlated - except for the near-wall region - in terms of similarity variables. The outer-layer correlations agreed closely with classical similarity theories, for the interacting inner-layer flow a modified similar solution was developed.

REFERENCES

- Acrivelllis, M., 1979, "Auswertung von Hitzdrahtmessungen mehrdimensionaler Strömungen beliebiger Turbulenzintensität", Habil.-Schrift TH Karlsruhe.
- Clauser, F. H., 1956, "The turbulent boundary layer", Adv. Appl. Mech., 4, 1.
- Durst, F., 1971, "Evaluation of hot-wire anemometer measurements in turbulent flows", Imperial College, Dept. of Mech. Eng. Rept. ET/TN/A/9.
- Jordan-Engeln, G. and Reutter, F., 1976, "Formelsammlung zur numerischen Mathematik mit Fortran IV-Programmen", Bibliogr.-Inst. Mannheim/Wien/Zürich, B.I.-Wissenschaftsverlag, 58.
- Klebanoff, P. S. and Diehl, Z. W., 1952, "Some features of artificially thickened fully developed turbulent boundary layers with zero pressure gradient", NACA Report 1110.
- Marumo, E., Zuzuki, K., and Sato, T., 1978, "A turbulent boundary layer disturbed by a cylinder", J. Fluid Mech., 87, 121.
- Müller, U. R., 1982, "On the accuracy of turbulence measurements with inclined hot wires", J. Fluid Mech., 119, 155.
- Müller, U. R., 1983, "A hot-wire method for high-intensity turbulent flows", 10th ICIASF, Sept. 20-23, ISL, Saint Louis, France.
- Reichardt, H., 1942, "Gesetzmäßigkeiten der freien Turbulenz", VDI-Forschungsheft, 414, 2. Auflage.
- Townsend, A. A., 1956, "The structure of turbulent shear flow", Cambridge University Press, New York.
- Tsiolakis, E. P., 1982, "Geschwindigkeiten und Reynoldssche Spannungen in einer mit einem Kreiszylinder gestörten turbulenten Plattengrenzschicht", Diss. RWTH Aachen.
- Schlichting, H., 1930, "Über das ebene Windschattenproblem", Diss. Göttingen 1930, Ing. Arch. 1, 533.

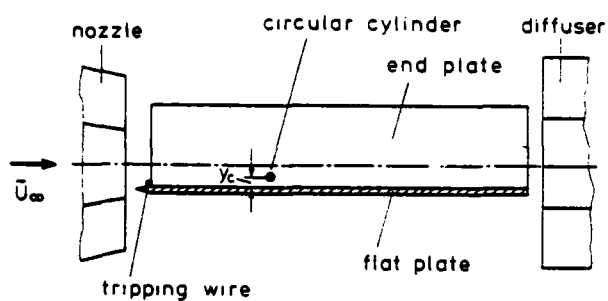


Fig. 1. Experimental setup.

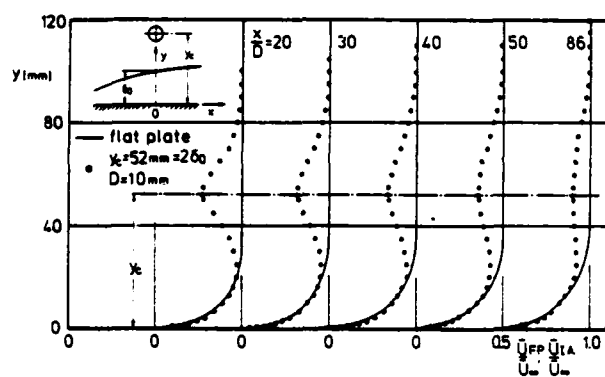


Fig. 2. Measured mean velocities of interacting flow (...) compared to undisturbed, flat-plate flow (—).

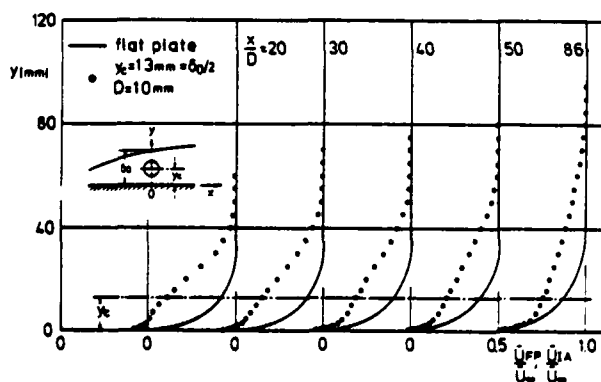


Fig. 3. Measured mean velocities of interacting flow (...) compared to undisturbed, flat-plate flow (—).

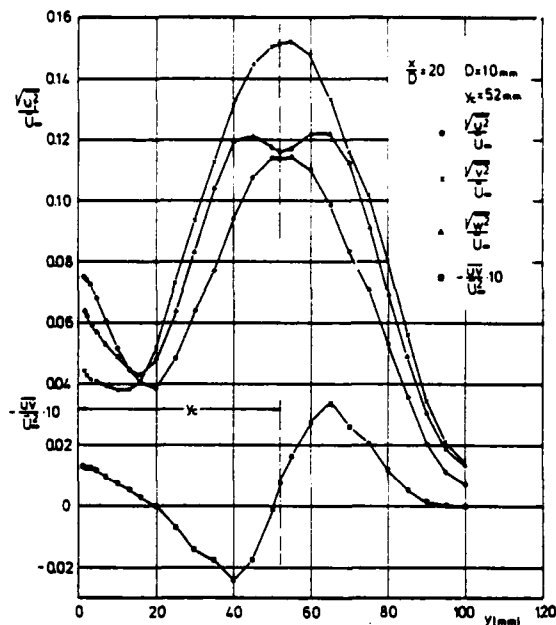


Fig. 4. Measured Reynolds stresses.

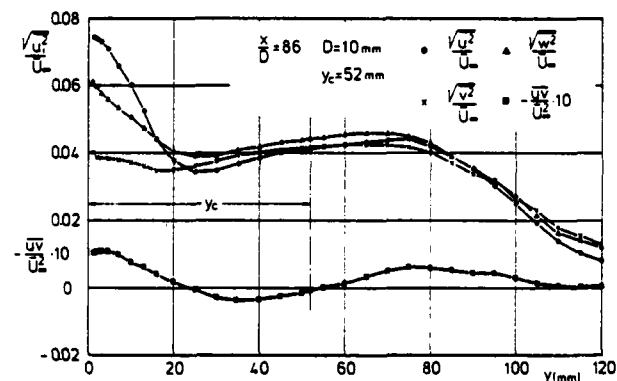


Fig. 5. Measured Reynolds stresses.

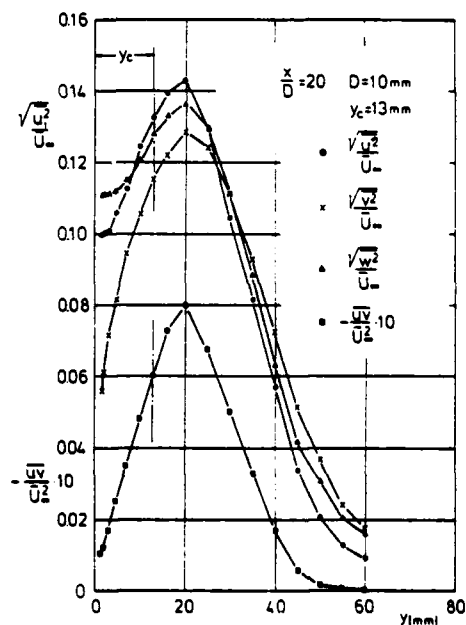


Fig. 6. Measured Reynolds stresses.

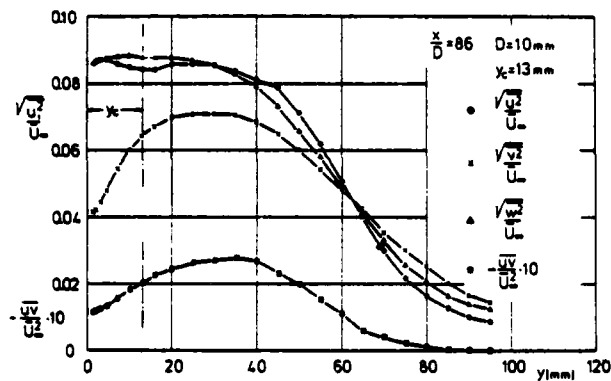


Fig. 7. Measured Reynolds stresses.

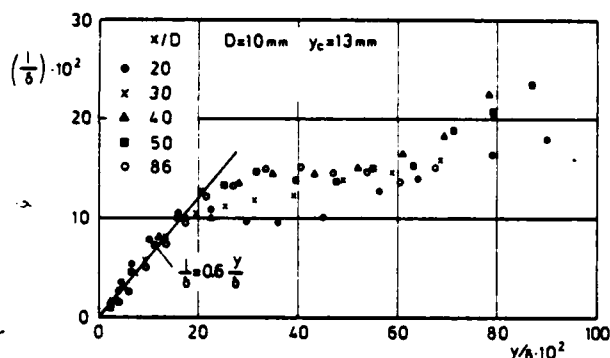


Fig. 8. Measured mixing length distributions normalized by boundary layer thicknesses.

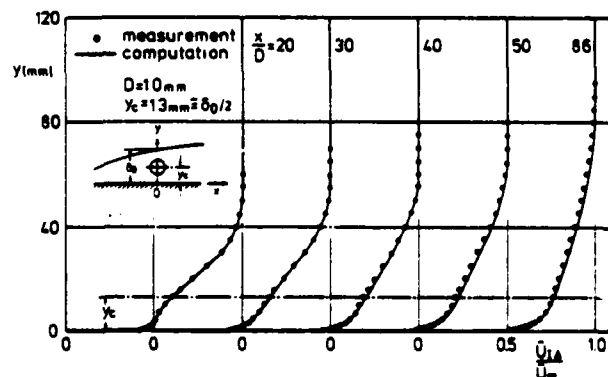


Fig. 9. Comparison of measured mean velocities with results of finite-difference solution.

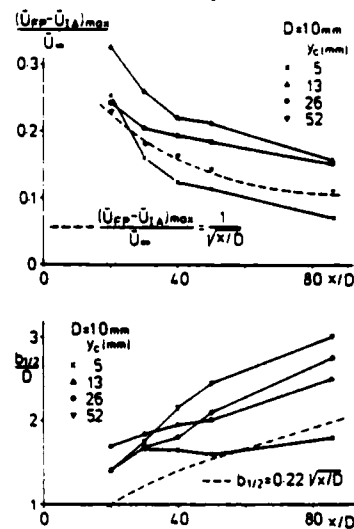


Fig. 10. Measured maximum velocity defect of cylinder wake and outer-layer half width.

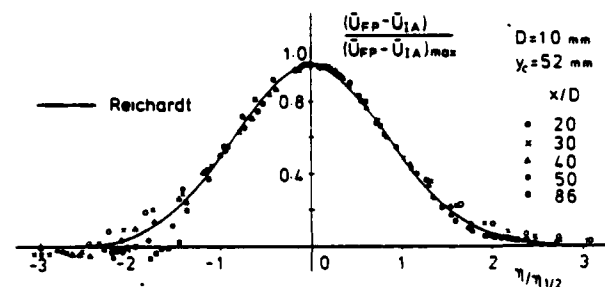


Fig. 11. Self-preservation of wake flow.

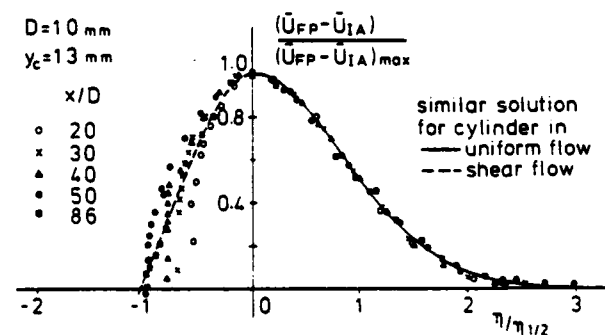


Fig. 12. Measured self-preservation of wake flow compared to similar solutions for cylinder in uniform and sheared free-stream.

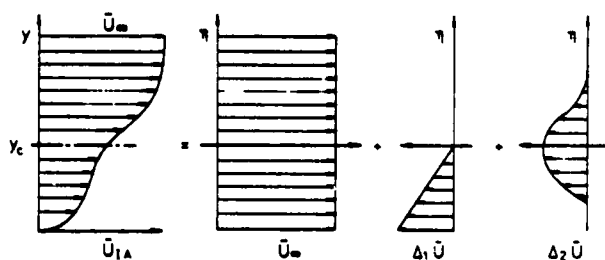


Fig. 13. Decomposition of boundary layer-wake interaction for analyzing self-similarity of wake flow.

EFFECT OF SIDE WALLS OF WIND-TUNNEL ON TURBULENT WAKE BEHIND TWO-DIMENSIONAL BLUFF BODY

Michio TAKEUCHI and Tetsushi OKAMOTO
Department of Mechanical Engineering,
Aoyama Gakuin University, Tokyo, Japan

1. ABSTRACT

This paper presents an experimental investigation of the effects of side walls of wind-tunnel on turbulent wake behind a two-dimensional flat plate. The drag of flat plate, the frequency of vortices shedding, the dimension of vortex street, the velocity and static pressure in wake and turbulence of wake behind a flat plate were measured for various distances between side walls of wind-tunnel. It is found that the drag coefficient of flat plate increases, the wake region is reduced, and turbulence of wake increases as the width of flat plate increases. And the blockage effect of side walls may be ignored when the ratio of (width of bluff body)/(distance between side walls) is less than 0.05.

2. NOTATION

x, y : coordinates with origin at center of frontal surface of flat plate (see Fig.1)
 c : width of flat plate
 H : distance between side walls of wind-tunnel
 U_0 : velocity of uniform undisturbed stream
 U : x-component of local velocity
 U_1 : x-component of velocity at outer edge of wake

u : velocity defect ($=U_1 - U$)
 u_m : maximum velocity defect
 u', v' : x- and y-component of velocity fluctuation
 b : half width of wake (value of y where $U=0.99U_1$)
 $b_{1/2}$: half width at half depth (value of y where $U=U_1/2$)
 P_0 : static pressure of uniform stream U_0
 P_s : local static pressure
 P_b : base pressure of flat plate
 C_p : pressure coefficient $= (P_s - P_0) / \frac{1}{2} \rho U_0^2$
 C_{pb} : base pressure coefficient $= (P_b - P_0) / \frac{1}{2} \rho U_0^2$
 C_d : drag coefficient
 C_{d0} : drag coefficient in case of $c/H=0$
 ρ : density of air
 ν : kinematic viscosity of air
 S : constant, ratio of mixing length l to half width of wake
 a : distance between consecutive vortices at same row
 h : distance between vortex rows
 N : frequency of vortices shedding
 St : Strouhal number $= N \cdot c / U_0$
 Re : Reynolds number $= U_0 \cdot c / \nu$

3. INTRODUCTION

Many wind-tunnel test on a building, stack, cooling tower and other structures have been conducted using relatively large models compared with the size of wind-tunnel. In those cases the blockage effects of wind-tunnel walls are involved in the test results. The authors have studied the blockage effects on the flow

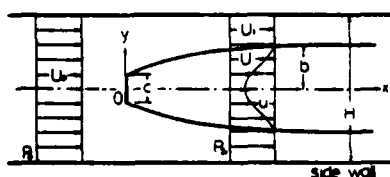


Fig1 Notations

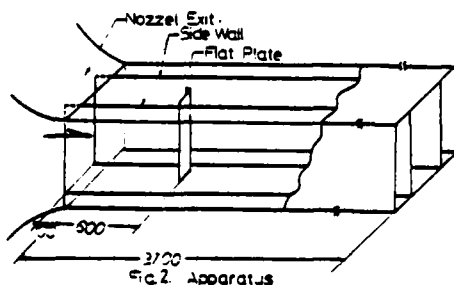
past a two-dimensional circular cylinder in previous paper⁽¹⁾. The blockage effects on the flow around a flat plate normal to a uniform stream were studied by Love⁽²⁾ and Birkhoff-Plesset-Simmons⁽³⁾, using the theory of discontinuous flow, and the wall effect on the drag was investigated by Glauert^{(4),(5)}, Fage-Johansen⁽⁶⁾ and Maskell⁽⁷⁾. In spite of those studies, however, some problems of the wake are remained to be unsolved. This paper presents an experimental investigation of the blockage effects of wind-tunnel walls on the turbulent wake behind a two-dimensional flat plate normal to a uniform stream.

4. APPARATUS AND PROCEDURE OF MEASUREMENT

The experiment was carried out in the N.P.L. type wind-tunnel having a 60×60cm working section of 310cm length. This wind-tunnel can produce a uniform stream of the velocity of 2~40m/sec and the intensity of turbulence of about 0.25%. The flat plate used in this experiment was of 25mm width, 4mm thickness and 600mm length. The rear corner of flat plate was cut off to make the sharp edge of 20 degrees⁽⁸⁾.

This flat plate was set vertically between the upper and lower walls of wind-tunnel at the distance 600mm downstream from the nozzle exit (see Fig.2). The flow in the center section may be regarded as the two-dimensional.

Two aluminum plate of 4mm thickness, 600mm width and 3,200mm length, which were used as the side walls, were mounted in the working section, as seen in Fig.2. The distance H between the side walls was varied in $c/H=0.042, 0.127, 0.213$ and 0.297 , where H was the distance corrected by reducing the displacement thickness (about 0.8mm) of the boundary layer along a side wall



from apparent distance. For all cases the inclination of the upper wall was adjusted so as to have no gradient of the static pressure in the direction of the stream.

The velocity and static pressure were measured by the Pitot-static tube of diameter 2mm, and turbulence was measured by a hot-wire anemometer of x-type probe of diameter 5μ of the tungsten wire. The rod supporting the Pitot-static tube or the hot-wire probe was mounted on a carriage moving along the rails above the working section.

Twelve pressure holes of diameter 0.3mm were bored at the surface of flat plate to measure the surface pressure. Measurements were performed in the center plane (x-y plane) of a flat plate at 17 stations of $x/c=5 \sim 80$. Since it is well-known that the drag of a flat plate normal to a uniform stream is independent of the Reynolds number when Re is greater than 1000, the test was carried out at the wind speed 20m/sec only, corresponding to $Re=3.22 \times 10^4$.

The vortex street generated in the wake behind a flat plate were observed in the water channel of length 500cm, width 38cm and depth 20cm. The flow patterns visualized by the aluminum powders floated on the water surface were photographed in cases of $c/H=0.053, 0.100, 0.200, 0.303$ and 0.400 . The velocity of the carriage having flat plates of 20mm width was 13.3cm/sec, corresponding to $Re=2.49 \times 10^4$.

5. RESULTS AND DISCUSSIONS

5.1 PRESSURE DISTRIBUTION ON SURFACE OF FLAT PLATE

The distribution of pressure on the surface of flat plate was measured in order to determine the drag, which is related to the characteristics of wake.

(a) Pressure at frontal surface

Fig.3 shows the variation of the pressure distribution on the frontal surface of a flat plate with c/H . The pressure decrease with increasing c/H , because of an increase of the velocity at the edge due to increase c/H . The pressure for case of $c/H=0.042$ agrees well with the theoretical values of Plesset et. al.⁽⁹⁾ for

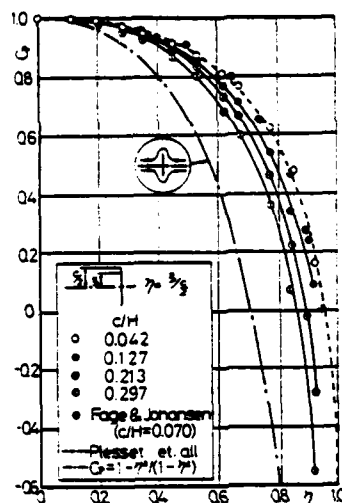


Fig.3 Distribution of pressure on front surface of flat plate

$c/H=0$, whence the pressure on frontal surface may be seen to be unaffected by the tunnel walls when $c/H < 0.042$. Moreover, the results by Fage-Johansen for case of $c/H=0.07$ are shown for the sake of comparison.

The chain line denotes the theoretical value based on the potential-flow theory, i.e. $C_p = 1 - n^2(1 - n^2)$, where $n = x/(c/2)$. The pressure distribution approaches gradually to this theoretical curve as c/H increases. The fact suggests that the wake region behind a flat plate will become narrower with increasing c/H .

(b) Base pressure

The distribution of base-pressure was almost uniform for all values of c/H . Fig.4 indicates that the base pressure coefficient decreases with increasing c/H . The result are well expressed by the equation

$$C_{pb} = 1 - 2\{1 + 0.4(c/H)\}\{1 - (c/H)\}^{-2}$$

for $c/H > 0.042$, showing a good agreement with the result of Fage-Johansen's experiment. For $c/H < 0.042$, the value of C_{pb} are almost unchanged with c/H .

5.2 DRAG COEFFICIENT

Fig.5 shows the drag coefficient determined from the surface-pressure distribution. It is found that the drag coefficient increases with increasing c/H and agrees well with the result by Fage-Johansen. Glauert⁽⁹⁾ suggested following equation of the drag coefficient :

$$C_D = C_{D0}(1 - \epsilon(c/H))^2$$

where the values of C_{D0} and ϵ are determined

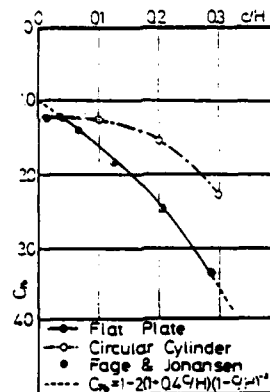


Fig.4 Distribution of base pressure of flat plate

experimentally. The present experiment gives $\epsilon = 1.11$ and $C_{D0} = 1.80$, whence

$$C_D = 1.8(1 - 1.11(c/H))^2$$

The full line in Fig.5 shows the value of C_D obtained from this equation, which agrees well with the present results except the case of $c/H=0.042$. For cases of $c/H < 0.042$, the value of C_D is 1.98.

5.3 FREQUENCY OF VORTICES SHEDDING

The frequency of vortices shedding in the wake was measured by means of a probe of the hot-wire anemometer set at the appropriate position behind a flat plate and the oscilloscope. An I-type probe of diameter 5μ of the tungsten wire was used, and the frequency of vortices shedding was determined from the photograph of signals.

The observations were performed for various values of c/H at the Reynolds number 3.22×10^4 . It is found that the frequency of vortices shedding is almost unchanged with c/H and the Strouhal number is $St = Nc/U_0 = 1.49$ so long as c/H is less than 0.297. The present result is appreciated by comparison with the result by Fage-Johansen, $St = 0.148$, in case of $c/H = 0.07$. For case of large values of c/H , Richter-Naudascher⁽¹⁰⁾ have reported that the Strouhal number for a blunt body increases in the case of large values of c/H .

5.4 VORTEX STREET IN WAKE

The vortex street in the wake behind a flat plate was photographed in the water channel. The water-channel experiment was performed at the Reynolds number 2.49×10^4 ,

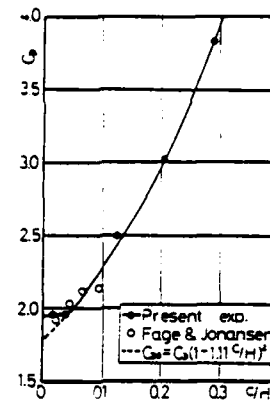


Fig.5 Drag coefficient

considering Rosenhead-Schwabe's suggestion¹⁰ that the dimension of vortex street is independent of the Reynolds number so long as Re is greater than 1000. Figs. 6-9 show the photographs of vortex street for various values of c/H . It is found from those photographs that the value of h/a decreases with increasing c/H , as shown in Fig. 10. The value of h/a in case of $c/H=0.053$ is greater than the Kármán's theoretical value, $h/a=0.281$, while h/a for a circular cylinder is close to the Kármán's value.

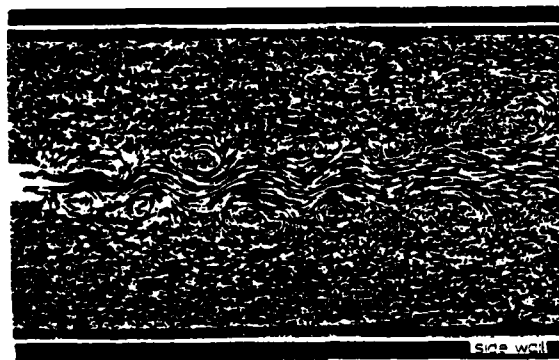


Fig. 6 Vortex street $c/H=0.053$, time exposure $1/4$ sec.

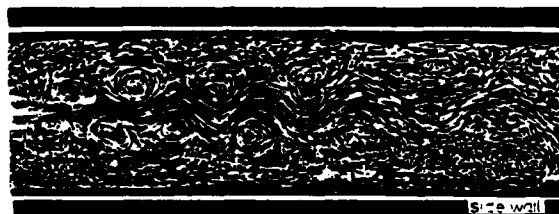


Fig. 7 Vortex street $c/H=0.100$, time exposure $1/4$ sec.



Fig. 8 Vortex street $c/H=0.200$, time exposure $1/4$ sec.



Fig. 9 Vortex street $c/H=0.303$, time exposure $1/4$ sec.

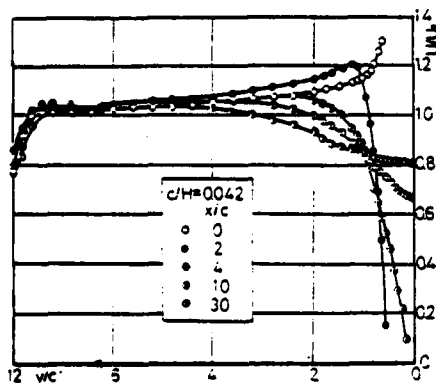


Fig. 11 Distribution of velocities for $c/H=0.042$

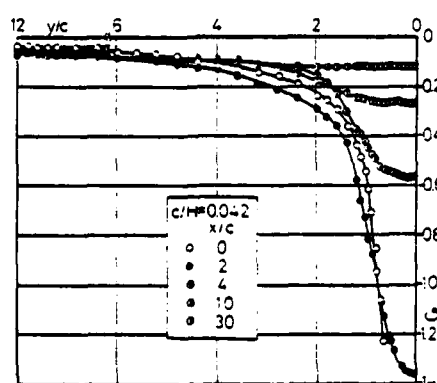


Fig. 12 Distribution of static pressures for $c/H=0.042$

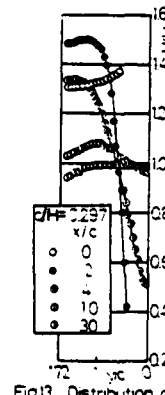


Fig. 13 Distribution of velocities for $c/H=0.297$

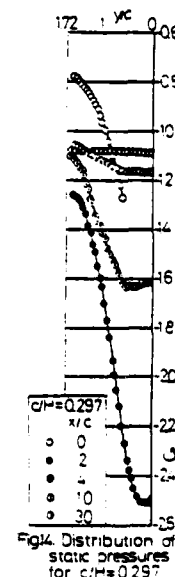


Fig. 14 Distribution of static pressures for $c/H=0.297$

5.5 VELOCITY AND STATIC PRESSURE IN WAKE

Figs. 11-14 show the distributions of velocity and static pressure for the cases of $c/H=0.042$ and 0.297 . In case of $c/H=0.042$ the velocity outside of wake is nearly $U/U_0=1.05$ and the corresponding static pressure is nearly $C_p=-0.07$. In case of $c/H=0.297$ the effect of side walls appears obviously and the wake disappears at $x/c=30$.

Fig. 15 shows the variation of velocity U_1 at the outer edge of wake with x/c . It is found that the value of U_1/U_0 varies remarkably with c/H in the near wake because of existence of vortex street, but it becomes nearly constant at the downstream distance beyond $x/c=40$.

Fig. 16 shows variation of velocity U_c and static pressure at the center of wake with x/c . It is found that the recovery of velocity is fast as c/H increases and that of static pressure is slow.

5.6 WIDTH OF WAKE

Variation of the width of wake with x/c is shown in Fig. 17, where a broken line indicates the value calculated by use of the theory of discontinuous flow for case of $c/H=0$. The width of wake becomes maximum at

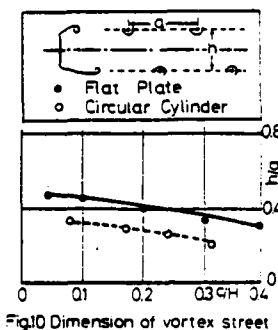


Fig. 10 Dimension of vortex street

$x/c=15.5$ for case of $c/H=0.127$, at $x/c=5.5$ for $c/H=0.213$ and at $x/c=3$ for $c/H=0.297$, and beyond the maximum point the width of wake decreases. It is found from this figure that the wake region becomes narrow with increasing c/H and it disappears at $x/c=42$ for case of $c/H=0.213$ and at $x/c=26$ for case of $c/H=0.297$.

Fig.18 shows half width $b_{1/2}$ at half depth of wake. Schlichting²³ gave following equation for half width of wake of a two-dimensional body for case of $c/H=0$, assuming that the mixing length is $l=8b$.

$$b_{1/2}=0.441/\sqrt{10}g(x/Cyc)^{1/2}$$

The present experiment for case of $c/H=0.042$ gives

$$b_{1/2}=0.269(x/Cyc)^{1/2}$$

from which the value of g is 0.193, while $g=0.179$ for a circular cylinder.

5.7 VELOCITY DEFECT OF WAKE

Fig.19 shows the velocity defect of wake at $x/c=10$ and $x/c=30$. The full line in this figure denotes the theoretical value by Schlichting in the similar profile region for case of $c/H=0$, i.e.

$$u/u_m=(1-(y/b)^2)^{1/2}$$

where u_m is the maximum velocity defect occurred at $y=0$. The velocity defect at $x/c=10$ approaches gradually to the theoretical value by Schlichting as c/H increases, but in case of $c/H=0.297$ it swells out beyond the theoretical value. The velocity defect at $x/c=30$ for case of $c/H=0.042$ is close to the theoretical value by Schlichting.

Fig.20 shows variation of the velocity defect for case of $c/H=0.042$ with x/c . The broken line in this figure indicates the theoretical value by Reichardt²⁴, i.e.

$$u/u_m=\exp(-Uoy^2/4\epsilon_0 x)$$

which is in good agreement with the present results at x/c beyond 30. Variation of the maximum velocity defect with x/Cyc is shown in Fig.21. Schlichting gave the following equation of the maximum velocity defect in the similar profile region

$$u_m/U_1=(\sqrt{10}/18g)(x/Cyc)^{-1/2}$$

The present experiment for case of $c/H=0.042$ gives

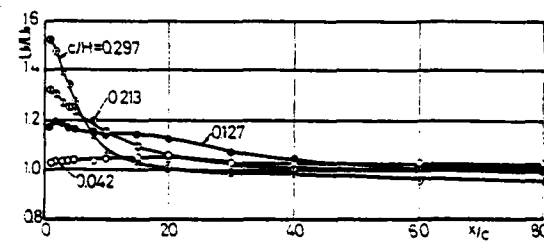


Fig.15 Velocity at outer edge of wake width

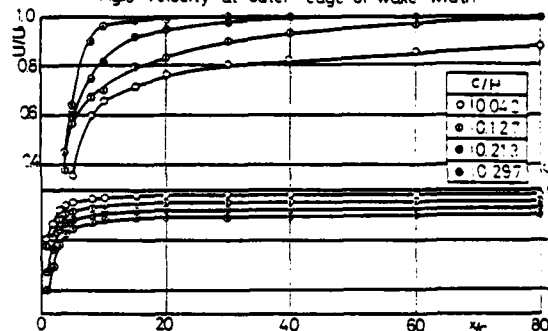


Fig.16 Velocity and static pressure at center of wake

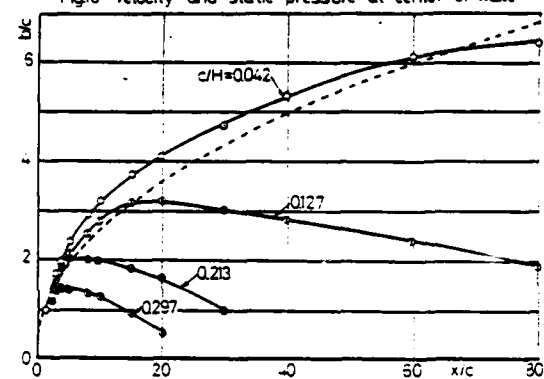


Fig.17 Width of wake

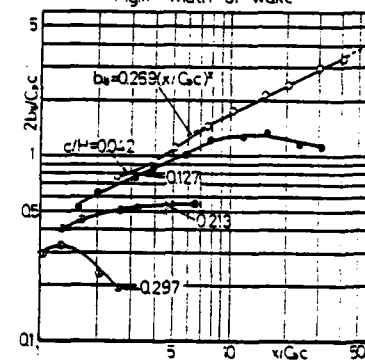


Fig.18 Half width of half depth of wake

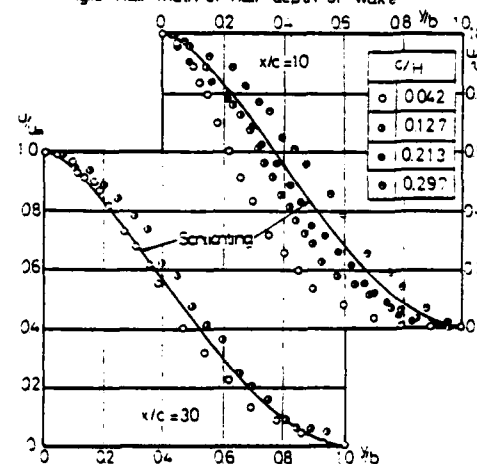


Fig.19 Similarity in velocity profile for $x/c=10$ and 30

$$u_m/U = 0.913(x/Ca_c)^{-1/2}$$

5.8 TURBULENCE IN WAKE

Fig.22 and 23 show the intensity of turbulence $\sqrt{u^2}/U$ in the x-direction and the intensity ratio $\sqrt{v^2}/\sqrt{u^2}$ for cases of $c/H=0.042$ and 0.297 respectively. For the case of $c/H=0.042$, $\sqrt{u^2}/U$ becomes maximum at the center of wake and decreases gradually to 0.25% (turbulence of main stream) with increasing y , and the turbulent intensity at the center of wake decreases as x/c increases. The value of intensity ratio disperses around the unity.

For the case of $c/H=0.297$ the intensity $\sqrt{u^2}/U$ is about 0.7% even at $x/c=30$, and there exists no region where turbulence of main stream remains.

6. CONCLUSION

Summarizing the results mentioned above, the following conclusions are obtained.

- (1) The drag coefficient of a flat plate increases with increasing c/H except the case of $c/H < 0.05$. In the case of $c/H=0.05$ the drag coefficient is 1.98.
- (2) The frequency of vortices shedding is almost unchanged with c/H and the Strouhal number is 0.149 so long as c/H is less than 0.3.
- (3) The value of h/a of vortex street decreases as c/H increases.
- (4) The wake region is reduced as c/H increases.
- (5) The x-component of intensity of turbulence in the wake increases with increasing c/H .
- (6) The effect of side walls of a wind-tunnel may be ignored when c/H is less than 0.05.

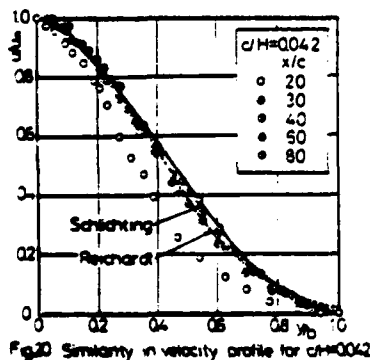


Fig.20 Similarity in velocity profile for $c/H=0.042$

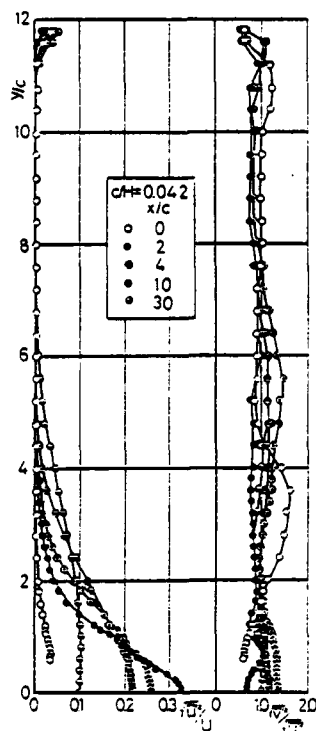


Fig.22 Turbulence in wake for $c/H=0.042$

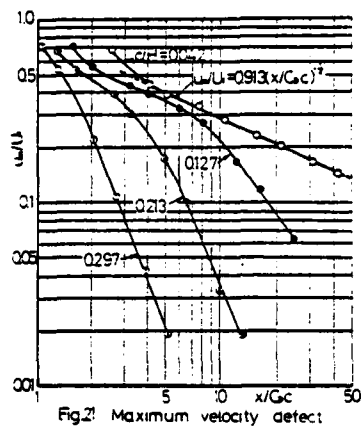


Fig.21 Maximum velocity defect

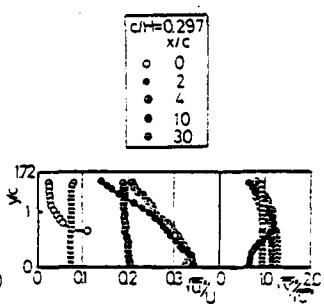


Fig.23 Turbulence in wake for $c/H=0.297$

REFERENCES

- (1) Okamoto, T. and Takeuchi, M., Bull. of the JSME., Vol.18, No.123 (1975), pp.1011-1017
- (2) Love, A.E.H., Proc. Camb. Phil. Soc., 7 (1891), 196
- (3) Birkhoff, G., Plesset, M. and Simmons, M., Quart. Appl. Math., 8 (1950), 161 and 9 (1952), 413
- (4) Glauert, H., Brit. A.R.C., R&M. 1566 (1963)
- (5) Glauert, H., Proc. Roy. Soc., A-129 (1928), 34
- (6) Page, A. and Johansen, F.C., Proc. Roy. Soc., A-116 (1927), 413
- (7) Maskell, E.C., Brit. A.R.C., R&M., 3400 (1963)
- (8) Goldstein, S., Modern Developments in Fluid Dynamics., Dover Press. (1965), 555
- (9) Plesset, M.C. and Schaffer, M., J. Appl. Phys., 19 (1948), 115
- (10) Richter, A. and Naudascher, E., J. Fluid Mech., Vol. 78 (1976), 561
- (11) Rosenhead, L., and Schabe, M., Proc. Roy. Soc., A-129 (1930), 115
- (12) Schlichting, H., Ing. Arch., 1 (1930), 533
- (13) Reichardt, H., VDI-Forsch., 414 (1942)

EXPERIMENTAL INVESTIGATION OF THE TURBULENT STRUCTURE OF VORTEX WAKES

by O. LEUCHTER and J.L. SOLIGNAC

Office National d'Études et de Recherches Aéronautiques (ONERA)
BP 72 92322 CHATILLON CEDEX

ABSTRACT

Two configurations of vertical wake flows are investigated. The first (flow A) corresponds to a double branched trailing vortex, the second (flow B) to the leading edge vortex of a delta wing. Both flows are studied in the presence of a destabilizing adverse pressure gradient leading to vortex breakdown. For various degrees of destabilization, the flow field is explored by means of a two-color laser velocimeter that yields mean velocity and Reynolds stress distributions across the flow. Breakdown is characterized by a strong deceleration of the flow near the axis of the vortex, by a significant decrease of the rotation rate in the center and consequently by a large production of turbulence. When breakdown occurs, both types of flow reveal similar characteristics of the flow structure. However, there are also significant differences, the most important being the abruptness of the breakdown phenomenon and its instability character which is much more pronounced for vortex flow B.

NOMENCLATURE

E	turbulent energy, $1/2 (\overline{u^2} + \overline{v^2} + \overline{w^2})$
K	circulation parameter, rV_θ/U_0
K_p	pressure coefficient, $(p - p_0)/q_0$
p	pressure
q	dynamic pressure
r	radial distance from the axis
U, V, W	mean velocity components in the x, y, z directions
u, v, w	fluctuating velocity components in the x, y, z directions
V_r , v_r	mean and fluctuating velocity in the radial direction
V_t , v_t	mean and fluctuating velocity in the tangential direction
x, y, z	coordinates in the streamwise, horizontal and vertical directions
α	angle of incidence
β	adverse pressure gradient parameter, $(dK_p/dx) \cdot K_0$

SUBSCRIPTS

o	reference upstream flow conditions
e	external flow conditions
a	conditions on the axis of the vortex
c	conditions in the test chamber (flow A)

INTRODUCTION

Vortical type flows play a major role in modern aerodynamics. Of special practical interest are vortex wakes generated by lifting surfaces or by rotor blades. In particular, the phenomenon of vortex bursting, that arises as a consequence of destabilization in the presence of an adverse pressure gradient, strongly affects flight qualities at high angles of incidence. Also in many other fields, rotating flows play a dominant practical role. For instance, in the field of combustion, swirling flows are commonly used to enhance mixing rates and to stabilize combustion.

A great deal of effort is presently being devoted to the development of numerical predictive methods for rotating and recirculating viscous flows. Turbulence plays a dominant role there and the success of the prediction depends strongly on the degree of accuracy of the model used in the calculations. Whilst satisfactory progress has been achieved in so far as the numerics are concerned, the progress in the field of

turbulence modeling in swirling and recirculating flows is much less satisfactory and our knowledge concerning the effects of rotation on turbulence is still incomplete and fragmentary.

Several basic research projects on vortex flows have been recently initiated at ONERA with the aim of providing a better physical understanding of the fundamental processes involved and of obtaining quantitative information concerning the structure of the mean and the turbulent field, especially under breakdown conditions. The present study, which belongs to this basic research activity, concerns two types of subsonic vortex flows: The first (flow A) corresponds to a double branched trailing vortex. This yields a quasi-axisymmetrical swirling flow configuration which has been found convenient for fundamental investigations of turbulence structure, especially under destabilizing conditions. The second (flow B) corresponds to a leading edge vortex of a delta-wing. It was used for a parametric study of the conditions under which breakdown occurs and to establish practical breakdown criteria. Flow B yields a stronger vortex and is therefore used for studying the instability features of the breakdown. In both cases, destabilization is achieved by means of an imposed positive pressure gradient.

Laser Doppler Anemometry has been extensively used in the present study. The advantages of this method lie in its non-intrusive character and in the ability of detecting the direction of the velocity, thus allowing recirculating flow regions due to breakdown to be explored accurately. Some typical results concerning the mean and the turbulent fields are presented for both types of vortex flows, especially under destabilizing conditions. Common features as well as typical differences between the two configurations are discussed.

EXPERIMENTAL ARRANGEMENTS

Flow A is generated by two identical airfoils spanning over the test section and assembled together on a slender cylindrical body, as indicated in figure 1. The two airfoils (NACA 0012 profile) have opposite incidences so that the vortex sheets issued from the blades roll-up into a double branched trailing vortex. The vortex strength can be varied by modifying the angle of attack of the airfoils. In the present study, fixed values of $\pm 12^\circ$ have been used yielding a maximal tangential velocity of $0.7 U_0$. The cylindrical test section has a diameter of 0.3 m and the upstream reference velocity is 32.5 m/s.

The positive pressure gradient in the flow is created by means of secondary suction which acts on the open part of the test section (between the locations $x = 153$ mm and $x = 287$ mm downstream the vortex generator). The pressure gradient is easily adjustable by varying the secondary mass flow rate extracted from the external test chamber. The longitudinal evolution of the static pressure in the outer part of the flow (measured at a radial distance of $r = 80$ mm) is shown in figure 2 for different aspiration rates (expressed here by the pressure coefficient K_{p_c} relative to the pressure in the test chamber). The positive pressure gradient corresponding to the middle of the open test section is expressed in terms of the non dimensional parameter $\beta = (dK_p/dx) \cdot K_0$, where the circulation parameter K_0 represents a characteristic dimension of the vortex (see Ref. [1]). The corresponding values of the pressure gradient parameter β will be given further in the text.

The longitudinal velocity in the flow is maintained constant by means of a sonic throat located downstream of the test chamber. Stable flow conditions are thus achieved even when breakdown occurs.

Flow B is generated by means of a slender delta wing (sweep angle 75°) mounted at incidence in the test section of a subsonic wind tunnel (Fig. 3). The diameter of the test section is 1 m and the free stream velocity U_0 about 15 m/s.

The vortex strength can be easily adjusted by varying the angle of attack of the wing. In the present study, an angle of 20° has been adopted yielding a maximal tangential velocity of the order of U_0 .

One of the two vortices generated by the wing enters into an air intake, the flow rate of which can be adjusted by means of moving flaps. The resulting adverse pressure gradient acting on the vortex can thus be easily varied. In the present study, the position of the flaps has been adjusted so that breakdown of the vortex occurs between the trailing edge of the wing and the air intake. The corresponding pressure gradient parameter β is of the order of 0.04.

INSTRUMENTATION

The flow field measurements presented below are obtained with a two-component laser velocimeter system developed at ONERA. It will only be briefly described here, as a more detailed description is given in Ref. [1].

The velocimeter uses a 15 W Argon laser as the light source. The laser beam is split in two beams of blue (4880 Å) and green (5145 Å) light. Both optical circuits have Bragg cell frequency shifting allowing the direction of the velocity to be detected. Seeding of the flow is generally provided by naturally occurring particles. In some extreme cases, incense smoke is employed. The system provides simultaneously the longitudinal and the vertical velocity components measured on the same (validated) particle. Statistical averages are calculated from an ensemble of at least 2000 samples. The velocimeter system operates in the forward scattering mode. The optics are mounted on rigid tables ensuring computer controlled displacements of the measuring volume along the three orthogonal axes. The visualization technique by a laser light sheet has also been used in preliminary stages of the study in order to characterize qualitatively the flow structure during the destabilizing process leading to breakdown. Examples for this kind of optical investigation can be found in Ref. [1].

RESULTS AND DISCUSSION

Flow A. In this case, the region corresponding to the open part of the test section can be easily explored by the laser velocimeter, due to the particular arrangement shown in figure 1. Horizontal and vertical explorations are made on a longitudinal cross section located at $x = 200$ mm, for the whole set of adverse pressure gradients as defined in figure 2. The corresponding values for the pressure gradient parameter β are: $\beta \approx 0, 0.008, 0.020, 0.027, 0.032$ and 0.035 . Only for the last four values are the pressure gradients strong enough to destabilize the vortex wake. Therefore, part of the results, especially those concerning the turbulent field, are limited to these four cases.

As the velocimeter measures the two velocity components U and V (longitudinal and vertical), the horizontal explorations provide for axisymmetrical flow the tangential velocity profiles and the vertical explorations, the radial ones. The comparison of the longitudinal mean and RMS velocity profiles, measured in both transverse directions y and z showed indeed that the properties of axisymmetry are well established in this flow, see Ref. [1]. It will therefore be meaningful to associate the profiles relative to the three velocity components $U(y)$, $V_r(y)$ and $V_r(z)$. Simultaneous measurements of all the three components in the same transverse direction would imply the use of a three dimensional velocimeter system. These measurements are planned for a later stage of this study with an extended version of the velocimeter.

The profiles of the three mean velocity components U , V_r and V_r , measured at the location $x = 200$ mm are given in figure 4 for the six different values of the pressure gradient parameter β .

The undisturbed configuration (no secondary aspiration, $\beta \approx 0$) yields for the longitudinal component U an almost uniform velocity profile except in the viscous core near the axis and in the external flow region where the tracks of the vortex sheets are clearly evidenced. The tangential velocity profile shows a behavior typical for a potential vortex, except in the region near the axis where viscous effects predominate. The radial component is for this case approximately zero, justifying the approximation of quasi cylindrical flow.

For a moderate compression rate ($\beta = 0.008$), the vortex wake remains stable in the sense that the U profile undergoes only a slight reduction without changing its form and that the tangential velocity profile remains approximately invariant.

For higher values of β , the flow can no longer sustain the externally imposed pressure rise and the vortex breaks down. This fact is clearly evidenced in figure 4 by the deep defect appearing in the longitudinal velocity profiles near the axis and by the concomitant decrease of the

angular velocity. The radial component remains negligibly small in the central region where the vortex is destabilized, but increases noticeably in the outer field when β grows. This is a consequence of the increasing divergence of the flow for higher aspiration rates. For the two highest values of β , the longitudinal velocity component becomes negative in the center of the wake due to the formation of a bubble with recirculation flow. The tangential component is there approximately zero.

Laser sheet visualizations have shown that the destabilization process is accompanied by a strong helical distortion of the vortex core with the helix diameter growing when the pressure gradient is increased (See Ref. [1]). This results in a strong radial expansion of the dissipative region as indicated by the velocity profiles of figure 4. High speed cinematography has revealed that this process is highly turbulent.

This fact is clearly evidenced by the profiles of the three normal stresses presented on figure 5. The rapid expansion of the turbulent zone with increasing β corresponds to that of the velocity defect appearing in the profiles of figure 4 a. The individual stresses show typical differences in so far as those relative to the tangential and to the radial velocity components tend to become rather flat for growing destabilization, whereas the longitudinal stress profiles show very distinct peaks of increasing level reaching twice that on the axis. The position of the peaks corresponds roughly to the maximum slope of the mean velocity profiles (Fig. 4a). Figure 5 shows further that the v_r^2 stresses expand further radially than the v_z^2 stresses and that on the center of the vortex the three normal stresses are of the same order of magnitude (corresponding to a RMS level with respect to U_0 of roughly 20 %).

If axial symmetry is assumed, the turbulent energy E can be deduced directly from the normal stresses of figure 5. Its distribution along the horizontal direction is given on figure 6 (with v_r^2 taken from the vertical exploration). The evolution of this quantity, which is of central importance in turbulence modeling, shows roughly the same behaviour during the destabilization process as that of the individual stresses previously discussed.

Only two of the three off-diagonal terms of the Reynolds stress tensor are available from the present laser velocimeter measurements. The longitudinal-tangential velocity correlation uv_r is obtained from the horizontal exploration, whereas the longitudinal-radial velocity correlation uv_r results from the vertical one.

The uv_r profiles of figure 7a are representative of axisymmetrical wake type flows, whereas the uv_r stresses are zero in non rotating flows. Both stresses expand radially with increasing destabilization conditions in the same manner as was shown for the normal stresses. The shear stress to energy ratio reaches, at the locations of maximum shear stress, values of about 0.3 for uv_r , and of about 0.2 for uv_r . A slight lack of axial symmetry can be observed for both quantities although the mean velocity profiles are apparently symmetric. This can be due in part to the strong mutual contamination of the two transverse components V_r and V_r if the horizontal or vertical explorations do not go exactly through the center of the vortex.

Flow B. In contrast to flow A, only one destabilized vortex configuration has been investigated. However, the measurements can be made here in a more extended domain including regions upstream and downstream of the breakdown position. Explorations have been done in the longitudinal (x) direction on the axis of the vortex wake as well as in the horizontal (y) and vertical (z) directions for several longitudinal positions.

Figure 8 shows the axial evolution of the mean velocity U and the RMS values relative to the longitudinal and transverse components. As in flow A, breakdown is characterized by a rapid decrease of the mean velocity on the axis. The initial value, about twice the free stream velocity, is much higher than in flow A. A bubble is formed downstream of the breakdown position, as evidenced by negative axial velocities.

The rapid decrease of the mean velocity is accompanied by a sharp increase of the longitudinal fluctuation intensity whereas the vertical fluctuation decreases. In the bubble both RMS values are approximately of the same magnitude (as was observed in flow A), of the order of $0.35 U_0$. The particular behaviour of both fluctuations in the breakdown region can be qualitatively explained from the joint probability density function (JPDF). Computer plotted contours of the JPDF in the U - W plane are shown in figure 9 for the three axial positions ①, ② and ③. In the upstream section ① only positive U -values occur, whereas two peaks A and A' are evident. Their symmetrical positions with respect to the U -axis suggest the existence of small fluctuations of the vortex as a whole, which could explain the relatively high level of $\sqrt{w^2}$ before breakdown.

In the breakdown region (section ②), the plots clearly show the existence of an intermittent state between two distinct flow configurations, the first corresponding to the upstream position ①, the second to the downstream position ③. This strongly intermittent state explains the high level of $\sqrt{u^2}$ shown in figure 8.

In the downstream section ③, the single peaked JPDF indicates a non intermittent state, with a negative mean value for U . Moreover, the RMS values with respect to U and W are of the same order, as shown in

figure 8. The longitudinal and vertical mean velocity profiles are given in figure 10 for the four sections ① to ④ indicated in figure 8. The vertical component can be interpreted as in flow A, as the tangential velocity provided axial symmetry is assumed. The profiles show typical evolutions for destabilized vortex flows, analogous to those shown in figure 4 for flow A. However, it must be noted, that the initial profiles (section ①, $x = 180$ mm) are quite different from those of case A : a higher overspeed on the axis for U and a flatter evolution for V_t . These characteristics are typical of Euler vortices generated by delta wings [1] [2].

The profiles of the RMS values for the three velocity components are given in figure 11. In contrast to figure 5, very high levels are obtained in the region of breakdown (section ②, $x = 230$ mm and section ③, $x = 260$ mm). This is due to the high degree of instationarity of the breakdown. Only in section ④ the profiles become more regular and qualitatively similar to those of flow A (Fig. 5).

The profiles of the velocity correlation $\overline{u v_t}$ are given in figure 12. As in figure 7, they are approximately antisymmetrical and $\overline{u v_t}$ has the same sign as V_t , except in the region near the axis. As for the RMS values, very high levels are obtained in the sections nearest to breakdown.

The formation of both vortex flows results from spirally rolling-up of the vortex sheets issued from the vortex generators. This leads to a more or less stratified structure of the flow, as can be seen from smoke visualizations, especially in undisturbed vortex configurations. A detailed exploration of section ① upstream of the breakdown position has been done in order to construct lines of equal mean and RMS values in the $y-z$ plane and to characterize the properties of axisymmetry for this flow. Figure 13 shows that the highest RMS values are located at the center of the vortex and that a ridge of locally high values prolongs the track of the wake issued from the trailing edge of the wing. The rolling up of the sheet which can be easily recognized on this figure, is similar to that given by the visualizations (see Ref. [1] and figure 14).

CONCLUDING REMARKS

The mean and turbulent velocity fields of two different vortex flows have been investigated by laser anemometry, under destabilizing conditions produced by adverse pressure gradients. The two flow configurations present close similarities so far as the general features of the destabilization are concerned : breakdown originates in both flows in the region close to the axis, with the axial velocity and the rotation rate decreasing rapidly and with a strong increase of turbulence production. Fundamental differences between the two flows lie in the internal structure of the vortex wakes as a result of the distinct generation modes, in the vortex strength which is higher with the delta-wing generator and in the abruptness of the destabilization process, which is more pronounced in flow case B. This destabilization results in a highly instable character of flow B with much higher RMS levels. The same trend can be observed from previously published results ; compare for instance Ref. [3] concerning the tip vortex and Ref. [4] for the leading edge vortex.

Flow B will be used further for studying the breakdown conditions for different flow parameters (vortex strength and adverse pressure gradient) and for working out practical breakdown criteria. The instationary character of breakdown will be more thoroughly investigated by means of conditional sampling techniques. Flow A, which is more stable, will be used for more fundamental studies of the turbulence structure and of the influence of the rotation on turbulence. The results given here for both flows should be considered only as the first step of a more exhaustive study on the general topic of turbulent flows with strong effects of rotation.

REFERENCES

- [1] SOLIGNAC, J.L. and LEUCHTER, O., "Etudes expérimentales d'écoulements tourbillonnaires soumis à des effets de gradient de pression adverse", AGARD-FDP " Aerodynamics of Vortical Type Flows in Three Dimensions", Rotterdam, April 25-27, 1983.
- [2] HALL, M.G., "A theory for the core of leading edge vortex", J. Fluid Mech., Vol. 11, 1961, pp. 209-228.
- [3] SINGH, P.I. and UBEROI, M.S., "Experiments on vortex stability", The Physics of Fluids, Vol. 19, N° 12, 1976, pp. 1858-1863.
- [4] HAYASHI, Y. and NAKAYA, T., "Flow field in a vortex with breakdown above sharp edged delta-wings", NASA TM 75. 339, 1978.

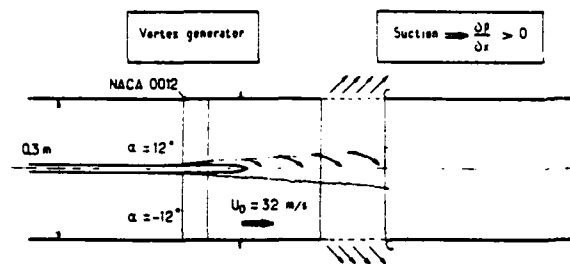


Fig. 1 - Schematic of vortex flow A.

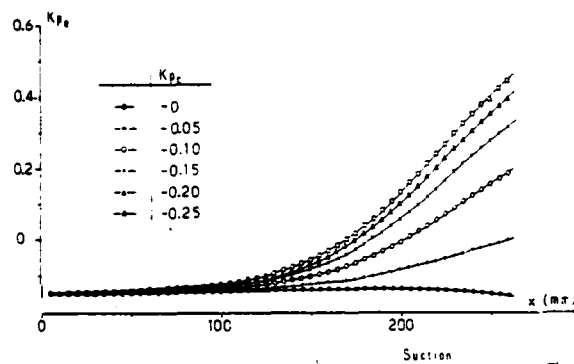


Fig. 2 - Evolution of the static pressure in the outer flow (flow A).

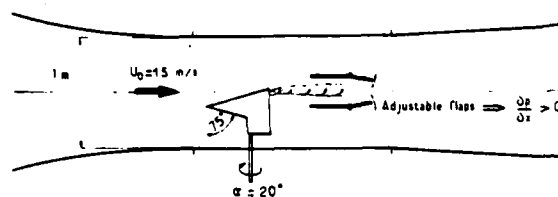


Fig. 3 - Schematic of vortex flow B.

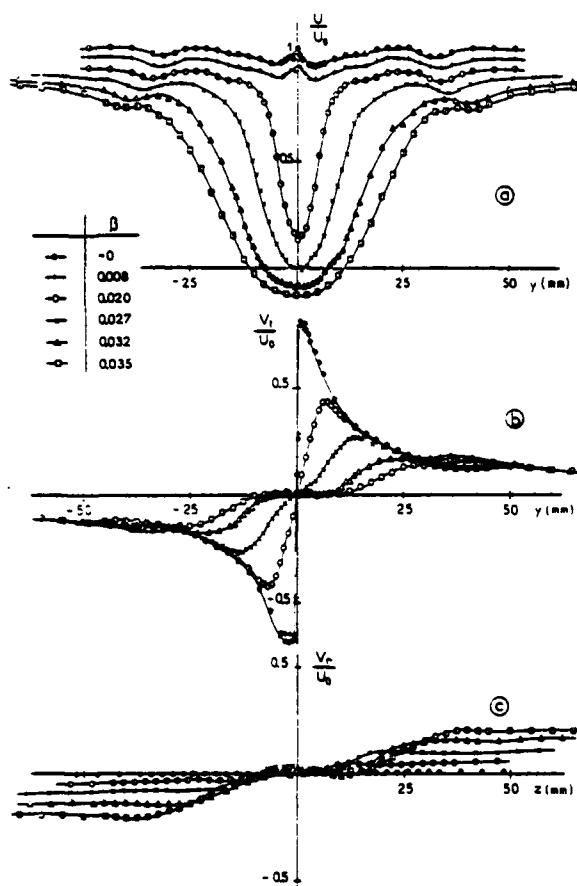


Fig. 4 - Mean velocity profiles (flow A).
a) axial component
b) tangential component
c) radial component.

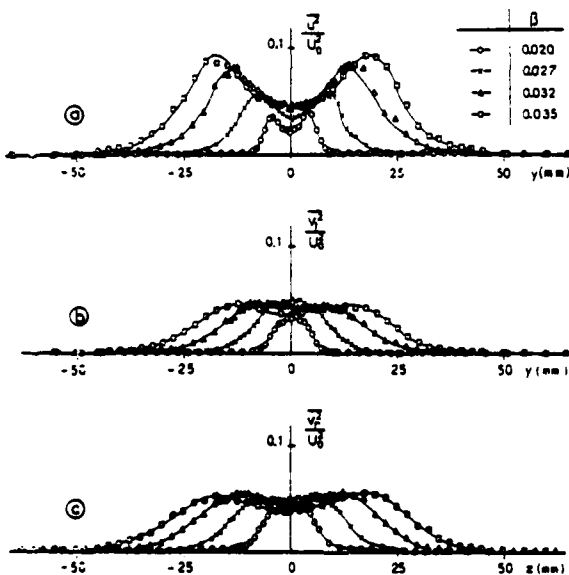


Fig. 5 - Profiles of the normal stresses (flow A).
a) axial component
b) tangential component
c) radial component.

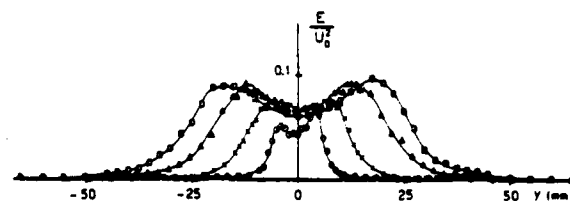


Fig. 6 - Turbulent energy profiles (flow A)

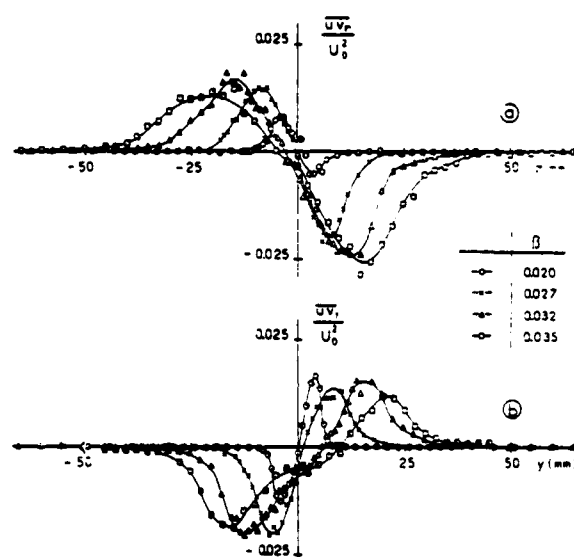


Fig. 7 - Profiles of the off-diagonal Reynolds stresses (flow A).
a) axial-radial
b) axial-tangential

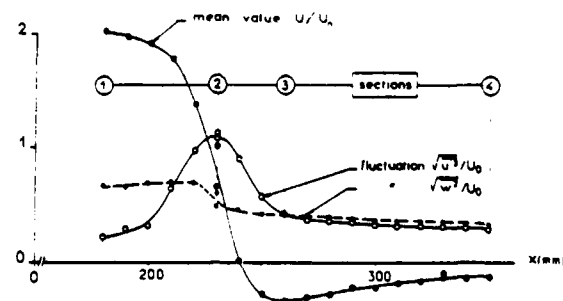


Fig. 8 - Axial evolution of the mean velocity and the RMS values (flow B).

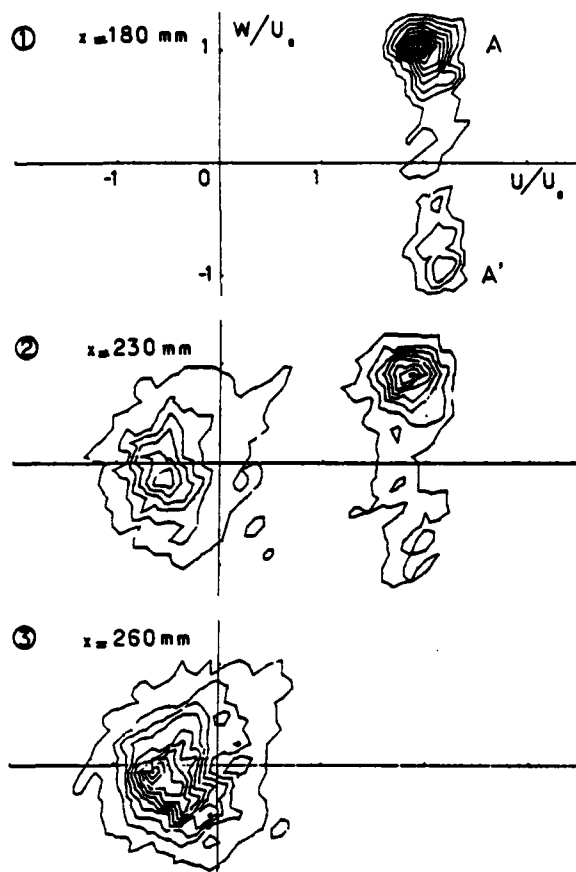


Fig. 9 - Contours of the joint probability density function (flow B).

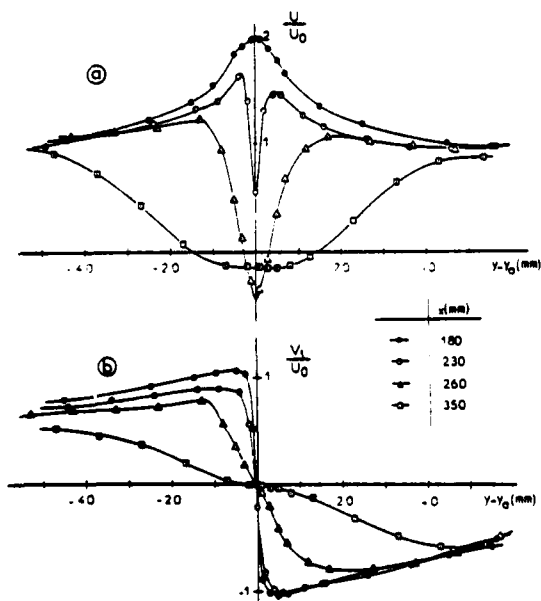


Fig. 10 - Mean velocity profiles (flow B).
a) axial component
b) tangential component.

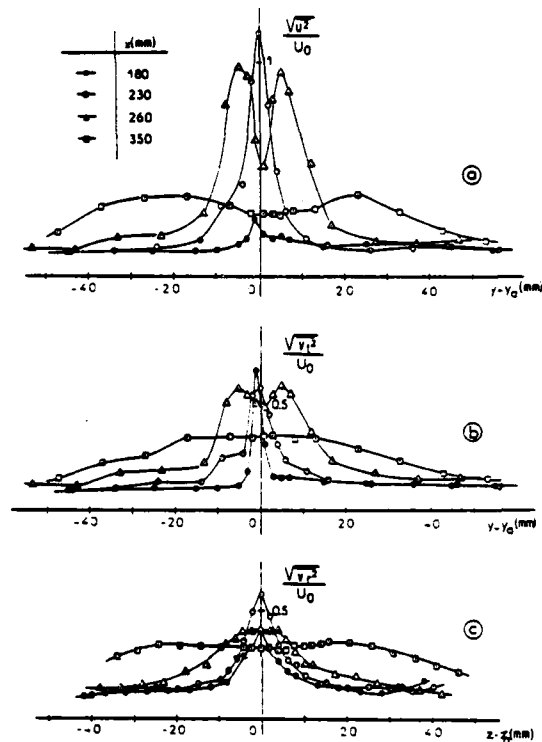


Fig. 11 - Profiles of the RMS values (flow B).

a) axial component
b) tangential component
c) radial component.

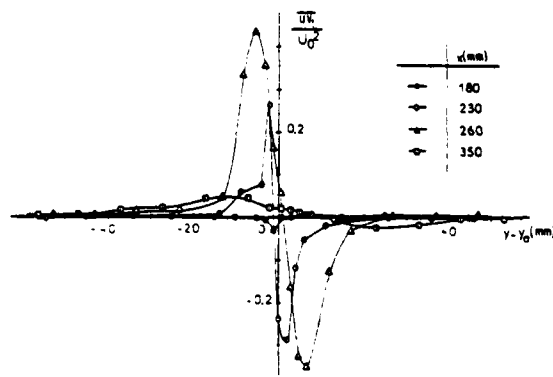


Fig. 12 - Profiles of the uv correlation (flow B).

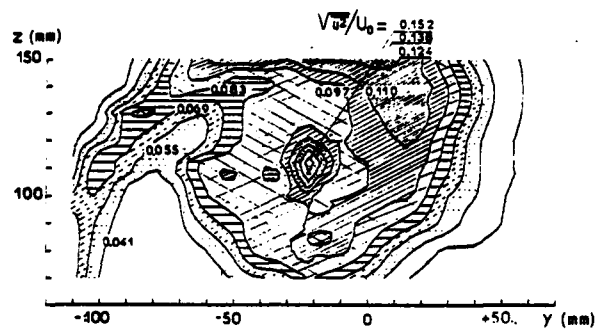


Fig. 13 — Contours of equal RMS values in the y-z plane for station ① (flow B).

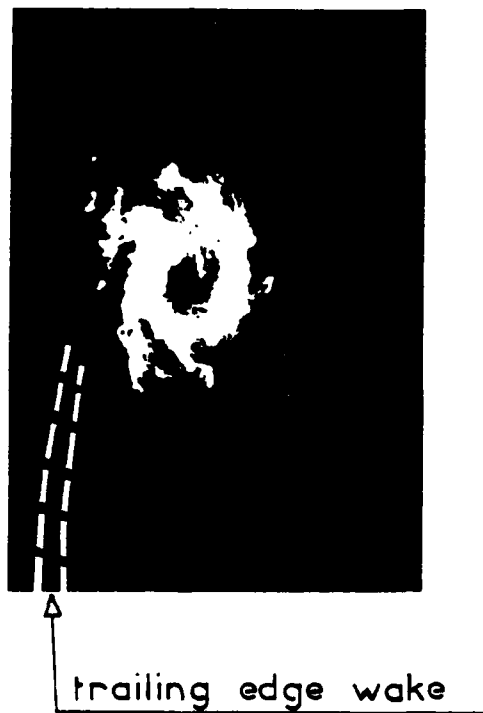


Fig. 14 — Laser sheet visualization of the vortex (flow B).

STATISTICAL CHARACTERISTICS OF THE TURBULENT WAKE BEHIND
AN INTERSECTING CRUCIFORM CIRCULAR CYLINDER

Hideo OSAKA , Hidemi YAMADA
Dept. Mech. Eng. Yamaguchi Univ., Ube, Japan
and
Ikuro NAKAMURA
Dept. Mech. Eng. Nagoya Univ., Nagoya, Japan

ABSTRACT

In order to clarify the periodic structure in the near field and the turbulent eddy structure in the far field of the intersecting cruciform circular cylinder wake, the detailed measurements have been performed on the statistical characteristics such as one-point and two-point time correlations, power spectra, triple velocity correlations and probability density profiles.

The experimental results are summarized as follows: The quasi periodicity of the fluctuating velocity appears to different degrees at the different locations in the cross section of the near wake field, and isn't found at the wake center. The turbulent large eddy structure conjectured from the contours of the space-time correlation is markedly different at each location in the cross section, and its decay rate is also slower at the center of the quasi two-dimensional region than at the wake center. The magnitude of triple velocity correlation profiles on the bisector has the same order as that of the two-dimensional wake, but some of the shapes are significantly different.

NOMENCLATURE (see Fig.1)

x : distance in the streamwise direction from the origin of the cruciform circular cylinder
 y, z : distances along two cylinder axes from the origin respectively
 y', z' : distances along the bisector of $y = z$ and normal to the bisector from the origin respectively
 r_x, r_y, r_z : distances between the fixed probe position and the moved probe position in x, y and z directions respectively
 d : diameter of circular cylinder
 b_y : half-width for the bisector
 L_u : integral length scale
 λ : Taylor's micro scale
 l_g : Kolmogorov's dissipative scale
 t : arbitrary time
 τ : time delay
 U : mean velocity in x direction
 U_1 : free stream velocity
 U_d : mean velocity defect ($U_d = U_1 - U$)
 U_{d0} : mean velocity defect at the wake center
 u, v, w : fluctuating velocity components in x, y and z directions respectively
 u', v', w' : fluctuating velocity components in y' and z' directions respectively
 $(1/2)\overline{q^2}$: turbulent kinetic energy ($\overline{q^2} = \overline{u^2} + \overline{v^2} + \overline{w^2}$)
 $R_{uu}, R_{vv}, R_{ww}, R_{u'v'}, R_{v'w'}$: one-point auto correlation coefficients of u, v, w, u', v', w' -fluctuating velocities respectively
 $R_{uv}, R_{uv'}$: one-point cross correlation coefficients between u - and v -fluctuating velocities and between u - and v' -fluctuating velocities respectively

E : power spectra of fluctuating velocity components
 S : skewness factors of fluctuating velocity components
 F : flatness factors of fluctuating velocity components
 ν : kinematic viscosity of air

INTRODUCTION

The intersecting cruciform circular cylinder which consists of two effectively long cylinders being perpendicular to one another, produces the complex flow field due to the three-dimensional interference of each intersecting cylinder wake (Fig.1). This three-dimensional flow interference is closely related to various flow fields of fluid engineering, for example the flow around heat exchanger, on-shore and off-shore structures. Damping screens formed from interwoven wires are also utilized as a means to generate isotropic turbulence.

With respect to the turbulent wake of an intersecting cylinder and two cylinders forming a cross, the mean velocity profiles were investigated by YxaoBa[1] for the turbulent wake behind an intersecting cruciform circular cylinder with the finite length. His turbulent wake approximates to the axisymmetric wake with increasing the streamwise distance. While, the pressure distribution on the surface of two circular cylinders forming a cross was measured by Zdravkovich[2], and the variation of local drag coefficient, base pressure and Strouhal number along the span of two cylinders were discussed. The strong secondary flows on the surface behind the upstream cylinder and in front of the downstream cylinder were also visualized by using the oilfilm technique.

A series of experiments on the turbulent wake behind an intersecting cruciform circular cylinder with effectively infinite length have been dealt with by present authors[3]~[5]. These results showed that the decay rate of the center line defect velocity was considerably slower than that found in either two-dimensional or axisymmetric wakes and that even far downstream the wake did not behave as a simple superposition of two perpen-

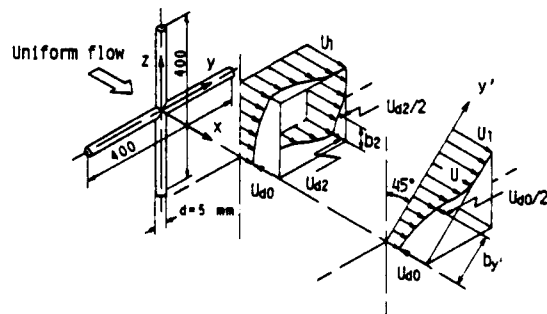


Fig.1 Configuration of flow field

dicular two-dimensional wakes, as inferred from Fig.2 [3], [4]. In addition, present authors found that the diffusion term of this wake was different from that of a two-dimensional wake for the turbulent energy budget, and that there existed the eight streamwise vortices which were symmetric with respect to the geometrical symmetric plane of this wake. Some unsolved problems of the turbulent wake behind an intersecting cruciform circular cylinder are the turbulent eddy structure, the feature of the large eddy structure and the behavior of vortex shedding from this obstacle; the former dominates the transport of momentum and the higher-order velocity correlation controls the configuration of diffusion transport, while the latter acts on the flow-induced vibration.

The aims of this paper are to examine the periodic structure of this three-dimensional wake in the near field and the detail of the turbulent eddy structure in the downstream region where the present wake is hardly affected by the pronounced periodic velocity fluctuation due to the vortices shed from the cruciform cylinder, through the measurements of various statistical quantities. The measured quantities were one-point and two-point time correlations, power spectra, triple velocity correlations and probability density profiles.

EXPERIMENTAL APPARATUS AND TECHNIQUES

The wind tunnel used in this experiment has a working section of 0.4 m square and about 4 m long [3]. The intersecting cruciform circular cylinder consists of two sufficiently long brass cylinders of 5 mm in diameter. The ratio of half length to diameter is 40. The configuration of the flow field and nomenclature are shown in Fig.1.

The measurement of the mean and fluctuating velocities of the crisscross turbulent wake under a zero-pressure gradient has been made with using a constant temperature hot wire anemometer with I-type or X-type probes. A X-type probe was used for the measurement of one-point statistical quantities such as triple velocity correlations, power spectra and probability density profiles. On the other hand for the measurement of the two-point statistical quantities such as space-time correlations between two separated points, two I-type probes were employed. The value of turbulent intensities was read directly from rms meter and the triple velocity correlations were obtained from an analogue circuit with an integrator. The difference of the output voltage of the analogue circuit to the input one was not larger than 10 % and the phase shift between the input signal and the output can't be found in the frequency band below 10 kHz. For the measurement of one- and two-point time correlations, power spectra and probability density profiles, a san-ei 7T08 digital correlator was employed. Reynolds number, $Re_d = U_1 d / \nu$ was kept to be constant at 4×10^3 for all tests.

EXPERIMENTAL RESULTS AND DISCUSSIONS

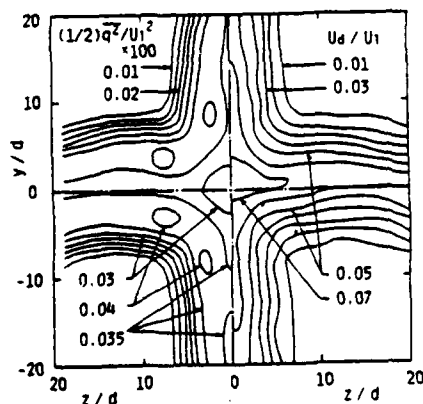


Fig.2 Contours of the mean velocity and the turbulent kinetic energy ($x/d = 298.5$)

Correlation Coefficients for near wake

It is generally known that the turbulent fluctuating velocity for near wake involved the contribution of the quasi periodic fluctuating component due to the vortex shedding from a bluff body. Fig.3 shows the auto correlation coefficients of u-fluctuating velocity at various positions in the section of $x/d = 8$. The contribution of the quasi periodic fluctuating velocity appears in graphs of R_{uu} taken both on the bisector and on the cylinder axis away from the wake center, while not at the wake center region. This suggests that the vortex lines of the vortices shed from the present cruciform circular cylinder have the shape like the broken line as described in Fig.3.

Figs.4(a) and (b) show the streamwise variation of the auto correlation coefficients along both the wake center line and the center line in the quasi two-dimensional region.

In the whole range along the wake center line the contribution of the quasi periodic fluctuating velocity can not be found. While, in the quasi two-dimensional region the periodicity in the auto correlation curve is clearly observed within the range of about $x/d = 20$. The contribution of the quasi periodic fluctuating velocity becomes also gradually smaller as x increases.

It is, usually, assumed that the rate of reduction of each fluctuating velocity component differs from one another. Fig.5 shows the auto correlation coefficients

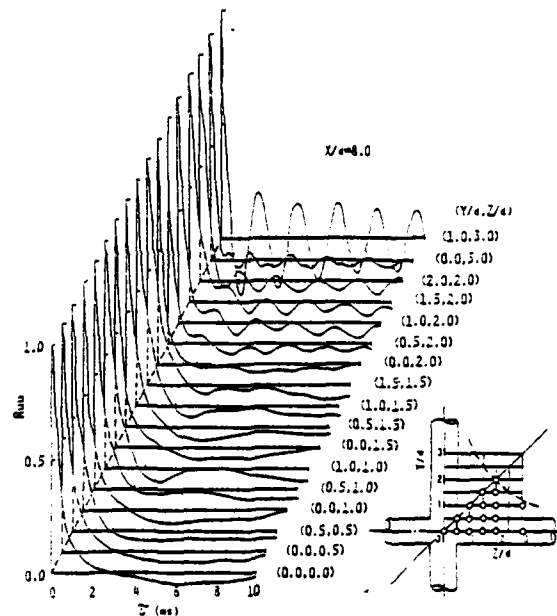


Fig.3 Auto correlation coefficients monitored at the section of $x/d = 8$

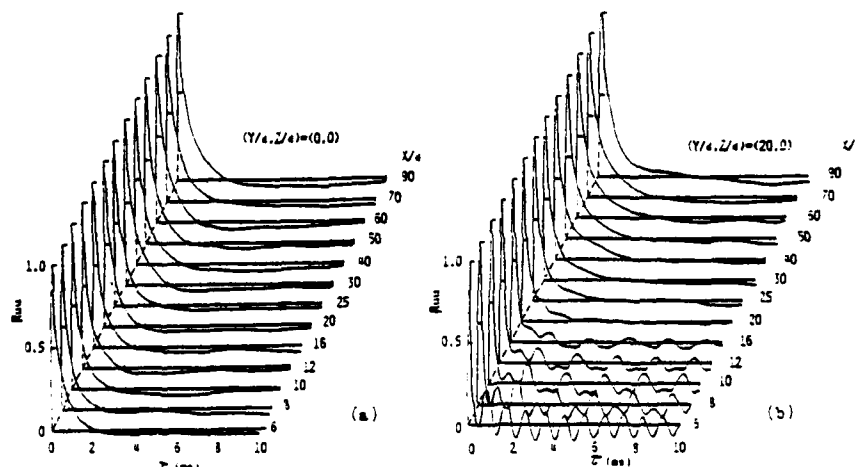


Fig.4 Streamwise variation of auto correlation coefficients; (a) along the wake center line, (b) along the center line in the quasi two-dimensional region

of u -, v - and w -fluctuating velocities at three typical locations in the section of $x/d = 30.5$. The influence due to the vortex shedding is not found for the auto correlation coefficients of u -fluctuating velocity in the entire region of this section. While, at the center in the quasi two-dimensional region far away from the wake center ($z/d = 0, y/d = 20$), the contribution due to vortex shedding can be recognized in the auto correlation coefficient of w -fluctuating velocity whose direction is perpendicular to y cylinder axis. In addition, those contributions weakly remain in the auto correlation curve of v - and w -fluctuating velocity components at the location of $y/d = z/d = 2.5$ away from the wake center along the bisector. How long distance the periodicity of v - and w -fluctuating velocity components survived clearly, has not measured, but these influences clearly disappear in the far wake region ($x/d \approx 298.5$) as described below (Fig. 11).

Turbulent Eddy Structure

As shown in Fig. 2, present authors indicated that the turbulent kinetic energy at the wake center was smaller than that on two cylinder axes [4]. It may be supposed that this result is closely related to the magnitude and the streamwise variation of the turbulent large eddy as shown in Figs. 6 and 7.

The structure of the turbulent eddy was investigated from the following space-time correlation between two locations separated by some amount of distance in x -direction,

$$R_{uu}(r_x, r_y, r_z, \tau) = \frac{u(x_0, y_0, z_0, t_0) \cdot u(x_0 + r_x, y_0 + r_y, z_0 + r_z, t_0 + \tau)}{[u^2(x_0, y_0, z_0, t_0) \cdot u^2(x_0 + r_x, y_0 + r_y, z_0 + r_z, t_0 + \tau)]^{1/2}}$$

where subscript 0 denotes the fixed probe position. The streamwise space-time correlations were measured in two cases that the fixed probe is set at the wake center and at the center of the quasi two-dimensional region in the sections of $x/d = 30.5$ and 298.5 respectively. The results are shown in Figs. 6(a), (b) and Figs. 7(a), (b). It is well known that the envelopes of correlation coefficient curves indicate the decay of turbulent eddy and they are described by some of two decay exponential curves which represent the decay of the large eddy and small one respectively [6]. Considering this concept, we may say that the decay rates of large eddy, taken as the exponential curves of slow decay, are small by one order of magnitude compared with that of small eddy at all the locations shown in figures as well as in the case of the turbulent boundary layer as well known. In addition, the decay rate of the large eddy is slower in

the downstream region than in the upstream region, and also slower at the center of the quasi two-dimensional region than at the wake center. For example, using the non-dimensional time delay $T = (U_f/b_f)\tau$ based on the local velocity U_f and the half-width b_f for the plane including the fixed probe position, the non-dimensional time delay T at which the exponential envelope for the large eddy structure takes e^{-1} is 4.81 at the wake center

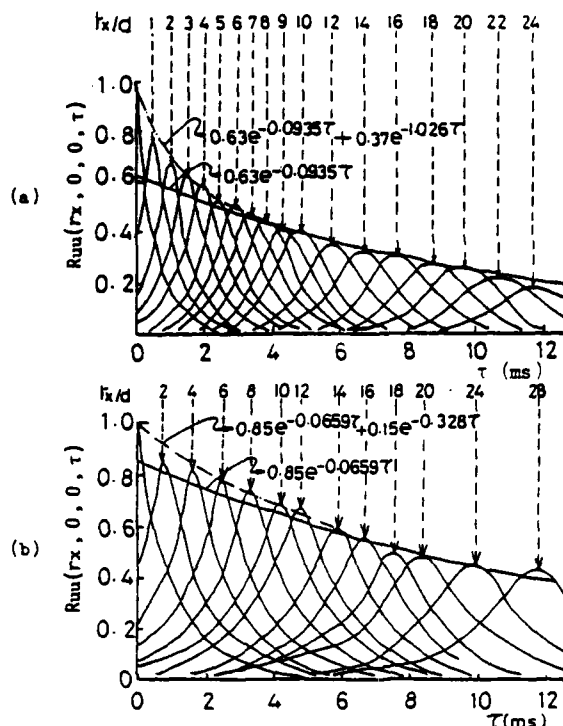


Fig. 6 Space-time correlation coefficients along the wake center line: Fixed probe position; (a) $x/d = 30.5$, (b) $x/d = 298.5$

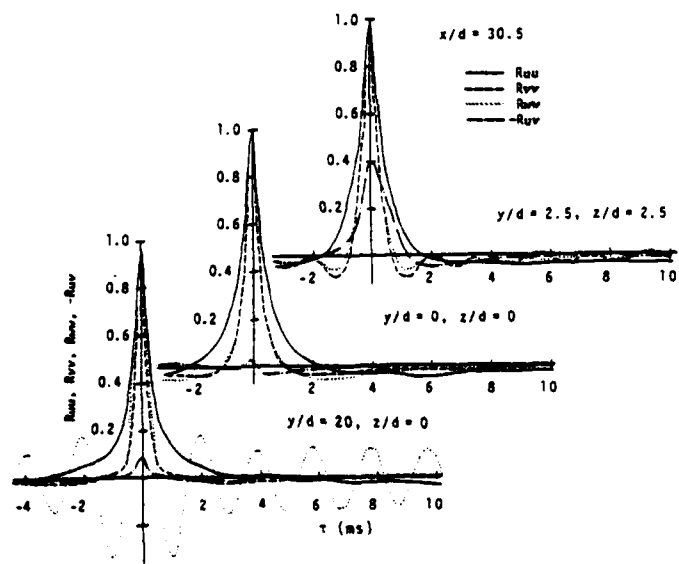


Fig. 5 Auto correlation coefficients of fluctuating velocity components at the section of $x/d = 30.5$

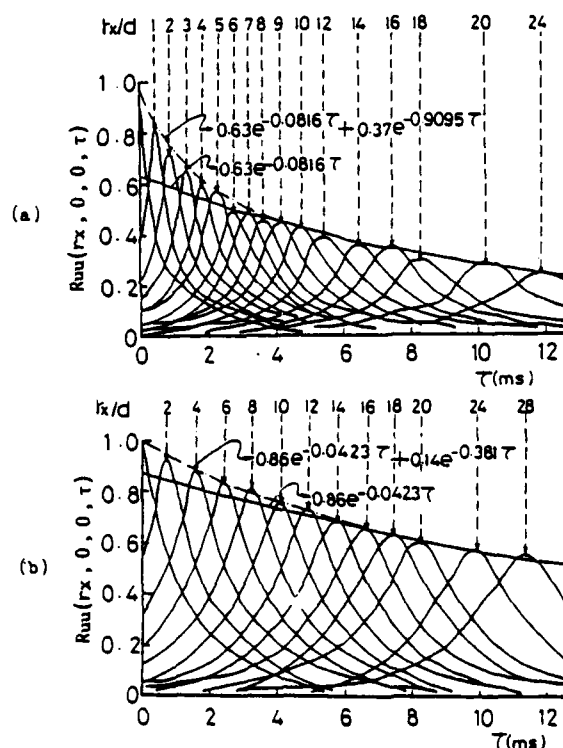
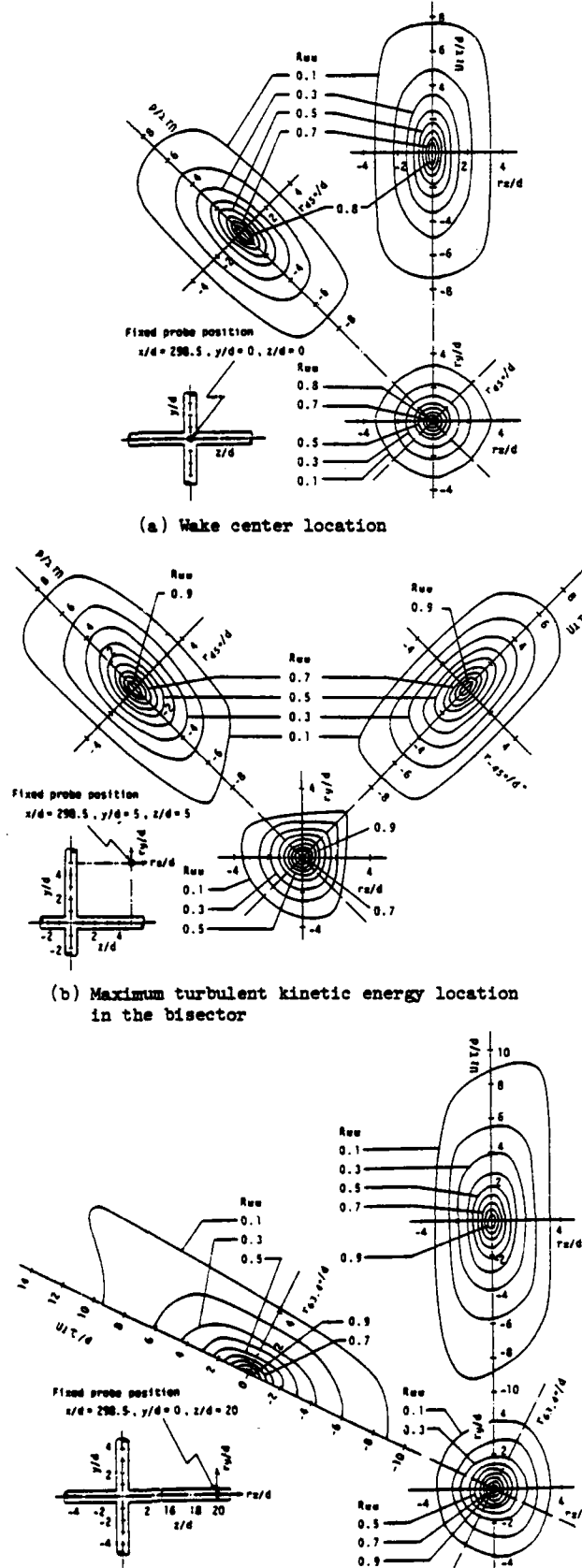


Fig. 7 Space-time correlation coefficients along the center line in the quasi two-dimensional region: Fixed probe position; (a) $x/d = 30.5$, (b) $x/d = 298.5$

and 7.58 at the center of the quasi two-dimensional region in the far downstream region of $x/d = 298.5$. It is also known that the intersection of the slowly decaying envelope curve of the correlation coefficients



(c) Center location in the quasi two-dimensional region
Fig.8 Contours of auto correlation coefficient

at $r_x = 0$ or $\tau = 0$ represents the ratio of the contribution of the large eddy structure to the total turbulent energy [6]. The contribution of the large eddy is almost equal at everywhere in the section of $x = \text{const.}$, and is larger in the downstream region than in the upstream region. This contribution is beyond 80 % in the downstream region and is almost the same value as the outer region of the turbulent boundary layer [6].

Figs.8(a) to (c) show contours of the space-time correlation, which indicate abbreviately the spatial structure of the turbulent large eddy, at the three typical locations in the section of $x/d = 298.5$. The general configuration has the shape stretched by two times in the streamwise direction to in the transverse direction as well as the one for the intermittent region in the turbulent boundary layer [7]. It is also seen that the entire scale of the turbulent eddy at the center of the quasi two-dimensional wake region is fairly large compared with those at the other locations. Furthermore, the turbulent eddy scale at $y/d = z/d = 5$ in the bisector where the turbulent kinetic energy takes the large value, is not so large as expected and this configuration has the shape such as a chestnut in the plane normal to the flow. While, at the wake center the shape of the turbulent eddy is axisymmetric and shows the spindle shape.

The magnitude of the large eddy scale is often identified by the integral length scale estimated from the streamwise auto correlation coefficient in the following manner,

$$L_u = U \int_0^{\infty} R_{uu}(\tau) d\tau,$$

where U is the local velocity. The ratio of L_u to half-width b_y in the far downstream region is shown in Fig.9. The behavior of L_u/b_y with y'/b_y is relatively mild, while the profile of L_u/b_y on the cylinder axis has the distinct kink near $y'/b_y = 1$ where the diffusion term in the turbulent kinetic energy budget contributes mightily as a gain compared with that of the other locations on the cylinder axis [5].

Fig.10 shows the profiles of the micro scale and the dissipation scale defined as

$$\lambda = (15\nu \cdot \overline{u^2}/\epsilon)^{1/2}, \quad l_\epsilon = (\nu^3/\epsilon)^{1/4},$$

respectively, where ϵ is the dissipation rate of the turbulent kinetic energy evaluated by the following equation, $\epsilon = 15\nu(\partial u/\partial t)^2/U^2$. The magnitude of the micro scale is roughly 1/3 times to the integral length scale, while the

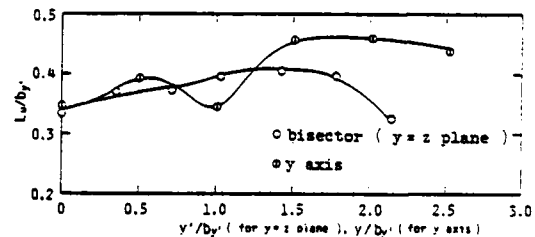


Fig.9 Integral scale profile

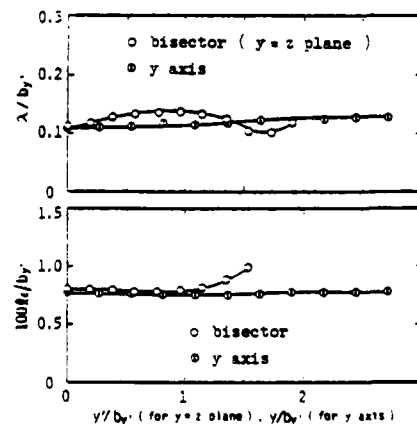


Fig.10 Micro and Dissipation scale profiles

value of the dissipation scale is extremely small. Both behaviors of the micro scale and the dissipation scale hardly vary along the bisector and the cylinder axis respectively, and the value of each turbulent scale almost equal both on the symmetric planes. It is very interesting that the spatial variation of the turbulent large eddy scale does not affect to the scale of the small eddies such as λ and λ_2 as shown in Fig.9.

The turbulent eddy structure can be understood by the one-dimensional power spectrum analysis, which is one of the simple methods. Figs.11(a) and (b) show the power spectrum of each fluctuating velocity component both on the bisector and on the cylinder axis defined as following equation,

$$\overline{\chi^2} = \int_0^\infty E_{\chi\chi}(k) dk,$$

where χ is each fluctuating velocity component and k is wave number ($k = 2\pi f/U$). The profiles of E_{uu}/u^2 have

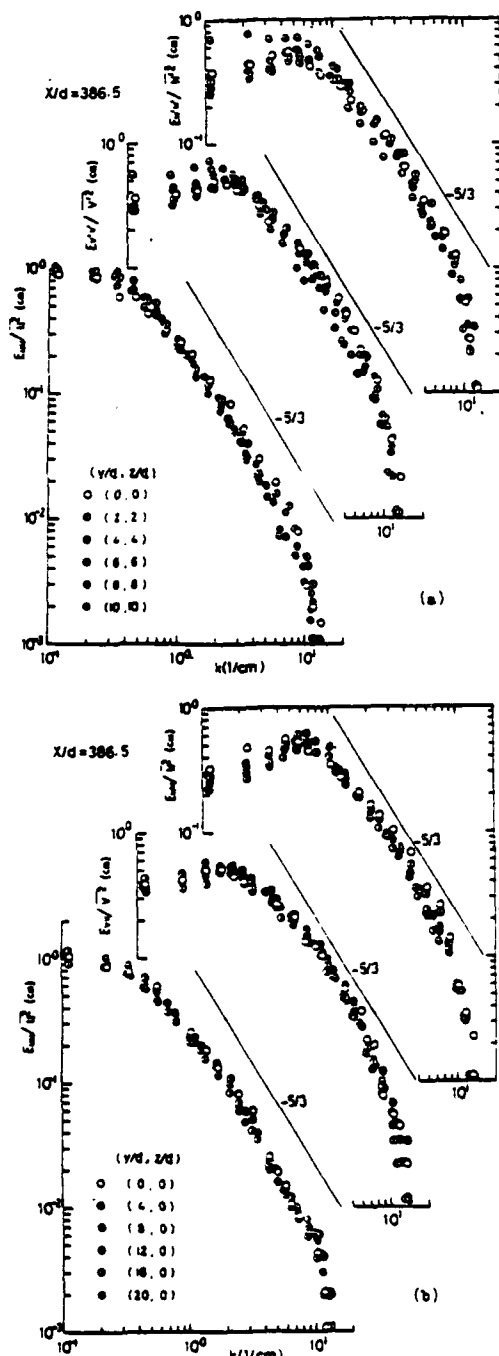


Fig.11 One-dimensional power spectrum densities of fluctuating velocity components; (a) in the bisector, (b) in the cylinder axis

almost the same shape at all locations along the bisector and the cylinder axis. The inertia subrange for the present wake exists in the range of $1 \leq k \leq 10$ which is close to that of the two-dimensional wake in $Re = 4320$ [8], and this wave number range is shifted toward the high wave number side compared with that of the outer region in the turbulent boundary layer ($0.5 \leq k \leq 5$) [9]. Both inertia subrange of E_{vv}/v^2 and E_{ww}/w^2 at all locations along the cylinder axis have the narrow range and these spectra also have the high power in the high wave number side compared with the profile of E_{uu}/u^2 . The profiles of $E_{v'v'}/v'^2$ and $E_{w'w'}/w'^2$ at any locations along the bisector have roughly the same feature as E_{vv}/v^2 and E_{ww}/w^2 described above. But, as the location approaches to the main stream, the power in the low wave number side becomes large as well as in the case of the equilibrium boundary layer [10].

Triple Velocity Correlations and Distortion of Turbulent Eddy

The significance of the diffusion term in the turbulent kinetic energy budget was pointed out for the turbulent wake behind an intersecting cruciform circular cylinder by present authors [5]. In addition, the data on the triple velocity correlation profiles may be expected to play a significant role to establish the turbulent prediction method for the three-dimensional turbulent wakes. The diffusion transport terms are estimated from the gradient of the triple velocity correlation profiles. Fig.12 shows the triple velocity correlation profiles on the bisector in the section of $x/d = 386.5$. In the figure, the results of the two-dimensional wake [11] represented by broken line are nondimensionalized by multiplying the ratio of $U_{d2}/U_{d0} = 0.7$ obtained for the present wake, and take the same order of the magnitude as those on the bisector in the present wake. This means that the magnitude of the triple velocity correlation coefficient on the bisector has the same order as that of the quasi two-dimensional region, although the velocity defect at the wake center is larger than that at the center in the quasi two-dimensional region. The positions

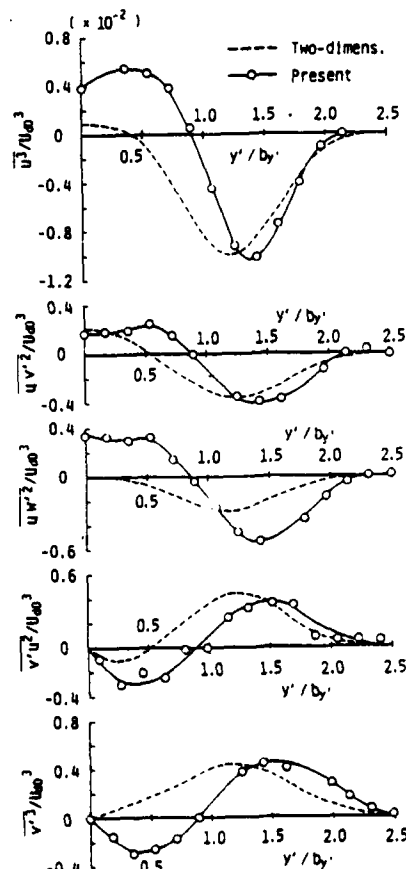


Fig.12 Triple velocity correlation profiles in the bisector

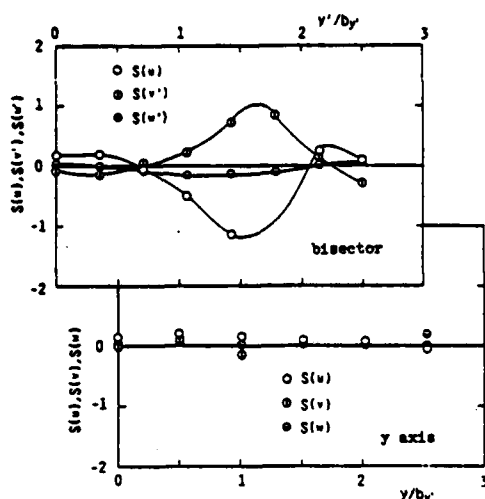


Fig.13 Skewness factor profiles in the bisector and the cylinder axis

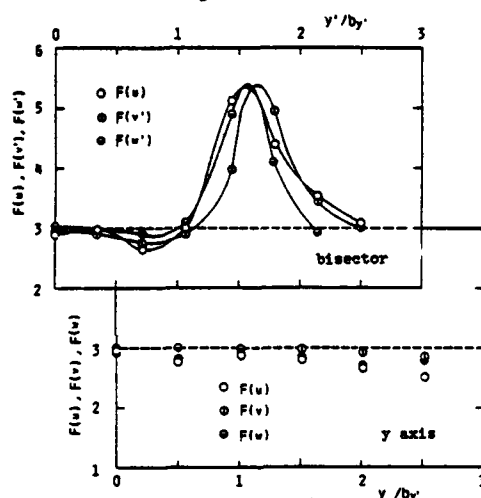


Fig.14 Flatness factor profiles in the bisector and the cylinder axis

of the maximum and minimum peaks for the every velocity correlation profile are shifted towards outer edge of the wake compared with those for the two-dimensional wake. Both profiles of $\sqrt{u^2}$ and $\sqrt{v^2}$ are markedly different from those for the two-dimensional wake respectively, but almost agree with each other on the bisector for the present wake.

Turbulent diffusion transport is associated with the distortion of the turbulent large eddy. The distortion of the eddy may exhibit itself in the profiles of the probability density function of each fluctuating velocity. Figs.13 and 14 show the skewness and the flatness factors both on the bisector and on the cylinder axis defined as following equations,

$$S(\chi) = \frac{\int_{-\infty}^{\infty} \chi^3 p(\chi) d\chi}{[\int_{-\infty}^{\infty} \chi^2 p(\chi) d\chi]^{3/2}}$$

$$F(\chi) = \frac{\int_{-\infty}^{\infty} \chi^4 p(\chi) d\chi}{[\int_{-\infty}^{\infty} \chi^2 p(\chi) d\chi]^2}$$

respectively, where $p(\chi)$ is the probability density function for each fluctuating velocity component. The values of $S(u)$ and $S(v)$ are negative and positive in the range of $y'/by' = 1 \sim 2$ respectively and then $S(w)$ is about zero everywhere on the bisector, as well as $S(u)$, $S(v)$ and $S(w)$ on the cylinder axis.

It may be, thus, said that the turbulent large eddy on the cylinder axis hardly have the spatial distortion. The flatness factors of every fluctuating velocity component on the bisector are larger than the value of three in the range of $y'/by' = 1 \sim 2$, while they are zero everywhere on the cylinder axis. The profile behavior

of the skewness and flatness factors on the bisector is roughly similar to those of the two-dimensional wake [11] as well as in the case of the mean velocity profile.

CONCLUSIONS

The turbulent eddy structure and various statistical quantities of the turbulent wake behind an intersecting cruciform circular cylinder were examined. The main results can be summarized as follows :

- (1) The quasi periodic fluctuating velocity due to the vortex shedding from a cruciform circular cylinder appears to different degrees at the different locations in the cross section, and is not found at the wake center. The magnitude of the contribution to the various turbulent quantities depends on each fluctuating velocity component.
- (2) The ratio of the turbulent kinetic energy in the large eddy to total energy is almost equal everywhere in the section of $x = \text{const.}$, but is larger in the downstream region than in the upstream region. The decay rate of large eddy is slower in the downstream region than in the upstream region, and also slower at the center of the quasi two-dimensional region than at the wake center.
- (3) The turbulent eddy structure conjectured from the contours of the space-time correlation is markedly different at each location in the cross section.
- (4) The magnitude of triple velocity correlation profiles on the bisector has the same order as that of the two-dimensional wake, but some of the shapes are significantly different. The profiles of the skewness and the flatness factors on the bisector are almost similar to those of the two-dimensional wake, while the skewness and the flatness factors are zero and three everywhere on the cylinder axis respectively.

ACKNOWLEDGEMENT

The authors wish to thank Professor Y. Kageyama for his valuable comments.

REFERENCES

- [1] Уманов, Л. Н., 1973, "СТРУКТУРА ТЕЧЕНИЯ В ТРЕХМЕРНЫХ ТУРБУЛЕНТНЫХ СЛЕДАХ", ИНЖЕНЕРНО-ФИЗИЧЕСКИЙ ЖУРНАЛ, 25, 893-898.
- [2] Zdravkovich, M.M., 1983, "Interference between two circular cylinders forming a cross", J.Fluid Mech., 128, 231-246.
- [3] Osaka, H., et al., 1983a, "The structure of a turbulent wake behind a cruciform circular cylinder. 1st report: the mean velocity field", Bull.Japan Soc.Mech.Engrs, 26, 356-363.
- [4] Osaka, H., et al., 1983b, "The structure of a turbulent wake behind a cruciform circular cylinder. 2nd report: the streamwise development of turbulent flow field", Bull.Japan Soc.Mech.Engrs, 26, 521-528.
- [5] Osaka, H., Yamada, H. and Nakamura, I., 1983c, "Three-dimensional structure of the turbulent wake behind an intersecting cruciform circular cylinder", In IUTAM Symp.on Three-Dimensional Turbulent Boundary Layers, Berlin, 29-31 March 1982. Springer-Verlag.
- [6] Blackwelder, R.F. and Kovaszny, L.S.G., 1972, "Time scales and correlations in a turbulent boundary layer", The Physics of Fluids, 15, 1545-1554.
- [7] Kovaszny, L.S.G., Kibens, V. and Blackwelder, R.F., 1970, "Large-scale motion in the intermittent region of a turbulent boundary layer", J. Fluid Mech., 41, 283-325.
- [8] Uberoi, M.S. and Freymuth, P., 1969, "Spectra of turbulence in wakes behind circular cylinders", The Physics of Fluids, 12, 1359-1363.
- [9] Klebanoff, P.S., 1955, "Characteristics of turbulence in a boundary layer with zero pressure gradient", NACA Report No.1247, 1135-1153.
- [10] Bradshaw, P., 1967, "Turbulent structure of equilibrium boundary layers", J. Fluid Mech., 29, 625-645.
- [11] Yamada, H., et al., 1980, "Multiple correlation of a two-dimensional turbulent wake", Tech. Rep. Yamaguchi Univ., 2, 341-349.

SESSION 6 - CURVED FLOWS

M.M. Gibson - Chairman

THE INFLUENCE OF A SPOILER ON THE DEVELOPMENT OF A HIGHLY CURVED TURBULENT WALL JET

U. Hartmann
Hermann-Föttinger-Institut für
Thermo- und Fluidodynamik
Technische Universität Berlin
1000 Berlin 12

ABSTRACT

A sharp edged spoiler increases the deflection angle of a curved turbulent wall jet significantly. The spoiler creates a large negative pressure gradient $\partial p/\partial x$ at the wall at the end of the channel which "relaminarizes" the turbulent wall boundary layer in this region. This effect occurs only for spoiler heights above a certain value and Reynolds numbers below a certain critical value. A discussion of the streamwise component of the turbulent Navier-Stokes equation in orthogonal cartesian coordinates for two-dimensional flow with wall boundary conditions shows that in the present case the "ordinary" turbulent wall jet separates more easily than a wall jet with a "laminar" wall region.

INTRODUCTION

If a wall jet is deflected by a curved wall or a number of straight walls, the deflection angle increases in general with the ratio of the wall radius R = constant to the height h of the nozzle or duct exit within a certain range of ratios R/h . Investigations of such flow configurations have been made for example by Köster/Löhr (1964), Fernholz (1965, 1967), Guitton (1970), Wilson/Goldstein (1976) and Alcaraz (1977). Apart from Fernholz and Köster/Löhr the authors have used configurations with ratios $R/h > 15$ which are often not suitable for technical applications which need smaller ratios. Examples are devices for the deflection of jets of aeroplane turbines for the increase of lift at take off and landing (Englar (1973), Skavdahl et al. (1974)).

If one decreases the ratio R/h to a value of about 3 the wall jet is deflected for $20^\circ - 30^\circ$ which is not sufficient for the applications mentioned above. For those cases one must use special devices to increase the deflection angle.

In the present experiment the ratio R/h is only 2.22. As Fernholz (1965) showed significant wall jet deflection can be obtained by means of a sharp-edged spoiler which is inserted at the side of the duct exit facing the curved wall (here a circular cylinder). At a certain height of the spoiler the wall jet is deflected by as much as 180° . The aim of this experiment has been to investigate the influence of the spoiler on the deflection of the wall jet and the turbulence structure of the flow which is dramatically changed in the vicinity of the wall by relaminarization for certain spoiler heights and Reynolds numbers.

TEST RIG AND PROBES

The test rig is shown in Fig. 1. The air, blown by an electronically controlled radial fan (± 1 rpm) and filtered at the air intake, passed a honeycomb and two screens and entered a slightly contracting duct with a subsequent straight section. The cylinder made from PVC had a radius of $R = 157.5$ mm, the height between the end plates was $B = 490$ mm, and the height at the duct

exit was $b = 71$ mm, providing a jet aspect ratio of 7. Three more endplates were arranged downstream in a staggered formation inside the main endplates mentioned above so that each auxiliary endplate cut off the boundary layer formed immediately upstream reducing the aspect ratio to 5 in the downstream part of the flow. A similar device was used by Guitton (1970) to suppress three-dimensional effects in the flow field (cf. section: Two-Dimensionality).

From the opposite side of the cylinder a sharp edged spoiler extended into the flow. The height of the spoiler could be varied from zero to 15 mm.

The probes used could be positioned at each point of the cylinder within an accuracy of 0.02 mm in the y-direction (Vagt/Fernholz (1979)). The mean and fluctuating velocities were measured by normal hot-wire probes and x-wire probes (driven in the CT-method) which are described in detail by Dahm/Vagt (1977) and Hartmann (1982). Wall shear stresses were measured by Preston tubes with different diameters and DISA hot films which were calibrated in a turbulent boundary layer with $\partial p/\partial x = 0$ with Preston tubes. Static wall pressures were measured by wall tappings having a diameter of 0.6 mm.

All measurements (except those described in the section: Two-Dimensionality) were performed along the line of symmetry of the cylinder. The results of the hot-wire probes were not corrected. The maximum mean velocity in the wall jet was about 25 m/s. The temperature of the flow could be held constant to $\pm 0.2^\circ$ Celsius.

RESULTS

Two-dimensionality of the flow field

As pointed out by Guitton (1970) it is very difficult to obtain a two-dimensional curved wall jet because a) the velocity - and pressure field generated by the ventilator may be dependent on the z-coordinate in the duct b) the duct end area itself has irregularities in its geometry c) the curved flow field contains secondary flows.

Measurements of mean velocity profiles at different spoiler heights, $x/h = 0.17$ and $z/B = \pm 0.16$ showed that in this region the velocity field was independent of the z-coordinate.

The wall shear stress is a good indicator for the two-dimensionality of a flow field. The pressure difference ($p_{\text{Preston}} - p_{\text{stat}}$) is a measure for the wall shear stress. These pressure differences were measured at different spoiler heights, circumferential angles and z-positions (Fig. 2). The higher the spoiler insertion is the larger is the region around the symmetry line which shows no dependence of the pressure differences on the z-position. E.g. at $S = 0$ mm this region extended at $x/h = 0.5$ from $z/B = -0.1$ to $z/B = +0.1$, at $S = 5$ mm from $z/B = -0.2$ to $z/B = +0.2$ and at $S = 10$ mm from $z/B = -0.25$ to $z/B = +0.25$. For $S = 10$ mm the flow field was two-dimensional from $z/B = -0.2$ to $z/B = +0.2$ up to angles ϕ of about 120° , whereas for $S = 5$ mm the

region of a two-dimensional flow field extended at $\varphi = 40^\circ$ only from $z/B = -0.1$ to $z/B = +0.1$. For $S = 10$ mm with a trip wire one recognizes a slight asymmetry of the flow field at $\varphi = 40^\circ$. So one may conclude that the wall jet was two-dimensional up to circumferential angles of about 120° in spanwise direction for about ± 150 mm off the line of symmetry for the most extensive investigated spoiler height $S = 10$ mm.

To support these results and to gather some data about the secondary flow in the wall jet the direction of the mean velocity vectors at wall distances of about 0.1 mm were measured for different boundary conditions (Fig. 3). For $S = 0$ mm and $x/h = 0.5$ the angle is zero in the region $-0.2 \leq z/B \leq +0.2$. That means the velocity component w is also zero. Outside of this region the vectors have a positive w for negative z/B and vice versa, which is a consequence of the beginning secondary flow. For $S = 5$ mm and $S = 10$ mm at $x/h = 0.5$ no influence of the secondary flow is obvious in this region. Only at $x/h = 1.5$ for $S = 5$ mm and $x/h = 5.78$ for $S = 10$ mm (that means at angles just upstream of the separation points of the wall jet) the measured angles have values of $\pm 8^\circ$.

Deflection angles and static wall pressures

As mentioned above the deflection angle of a curved turbulent wall jet with constant curvature and Reynolds-numbers $Re = 10^4 - 10^5$ is about 180° if the ratio R/h does not fall short of 3 - 4. In the present case the ratio R/h is 2.22 so that one expects a deflection angle of nearly zero. This may be seen from Fig. 4.

For $S = 0$ mm the deflection angles are $\varphi = 30^\circ$ in the investigated Reynolds number region. For $S = 7.5$ mm the deflection angles are $\varphi = 90^\circ$, but the behaviour of the wall jet for $S = 8.5$ mm is essential: there is a critical Reynolds number ($8 \cdot 10^4$). Below this value the deflection angle is about 180° , above this value the angle drops dramatically to about 90° . This recalls the two kinds of flow field around a cylinder, the laminar boundary layer at the cylinder below the threshold and the turbulent boundary layer above the threshold.

The behaviour of the wall jet for $S = 8.5$ mm means (for $S = 10$ mm the deflection angles are $\varphi = 180^\circ$ independent of the Reynolds Number) that it exists a drastic change of the flow field when the Reynolds number is altered, and that this is connected with the terms laminar-turbulent.

The next experiment confirms this presumption (Fig. 5). A trip wire with a diameter of 1 mm was glued on the channel surface 8 mm upstream of the cylinder. For $S = 10$ mm (the deflection angle at $Re = 10^5$ was 180° without the trip wire) the angle dropped to $\varphi = 75^\circ$. The same happened with a trip wire with a diameter of 2 mm. The condition of the near wall region of the wall jet for $S = 10$ mm and all investigated Reynolds numbers (also for $S = 8.5$ mm and $Re < 8 \cdot 10^4$) at the beginning of the cylinder was laminar which resulted in a deflection angle of 180° . The trip wires disturbed the laminar layer for $S = 10$ mm and caused the laminar-turbulent transition. The wall jet separated at about 75° independent of the diameter of the wire.

Relaminarization and wall shear stresses

The results of the foregoing experiments are: for spoiler heights $S \leq 7.5$ mm the near wall region of the wall jet at the beginning of the cylinder is turbulent. The deflection angles are $\varphi = 30^\circ$ for $S = 0$ mm and $\varphi = 95^\circ$ for $S = 7.5$ mm. For $S = 10$ mm the negative pressure gradient $\partial p/\partial x$ at the wall in the end of the channel is so large that the turbulent boundary layer relaminarizes in this region. The deflection angle is 180° . If the relaminarized boundary layer is tripped by a wire at the end of the channel ($S = 10$ mm) the deflection angle drops to about 90° . This behaviour corresponds with the dependency of the deflection angle on the Reynolds number for $S = 8.5$ mm.

Figure 6 shows the variation of the local skin friction coefficient along the cylinder surface. Note the difference between the curve for $S = 10$ mm and $S = 10$ mm with the trip wire with 1 mm diameter. For $S = 10$ mm the coefficient decreases at the beginning of

the cylinder because the acceleration of the flow field due to the spoiler (Lauder (1964)). The near wall region of the wall jet is laminar. Towards higher circumferential angles the coefficient increases because of the laminar-turbulent transition. At $\varphi = 90^\circ$ the inner boundary layer is fully turbulent and the wall shear stress begins to fall to zero.

For $S = 10$ mm with trip wire there is no region with increasing wall shear stress. The transition of the laminar wall region takes place just behind the wire. Downstream the wall shear stress continuously decreases till the separation angle is reached.

The process of the laminar-turbulent transition is clearly visible in Fig. 7. At $\varphi = 60^\circ$, $S = 10$ mm and $Re = 10^5$ there are turbulent spots in the near wall region of the wall jet which are characteristic for the transition process in a boundary layer.

Mean velocities and Reynolds stresses

Fig. 8 and 9 show the development of the mean velocity profiles along the symmetry line of the cylinder for $S = 10$ mm and $Re = 10^5$. The maximum mean velocities in the wall jet increase until $\varphi = 90^\circ$ which is a consequence of the strong acceleration of the flow due to the spoiler height. The larger the circumferential angle is the wider (normal to the wall) the wall jet becomes.

Fig. 10, 11 and 12 show the development of the intensities $\sqrt{u'^2}$, $\sqrt{v'^2}$ and $\sqrt{w'^2}$ along the symmetry line of the cylinder for $S = 10$ mm and $Re = 10^5$. From $\varphi = 10^\circ$ to $\varphi = 50^\circ$ there is only a slight increase of the levels of $\sqrt{u'^2}$ and $\sqrt{v'^2}$ near the wall, $\sqrt{w'^2}$ even decreases. This is a consequence of the relaminarization which occurs at the beginning of the cylinder. From $\varphi = 50^\circ$ to $\varphi = 110^\circ$ the three components near the wall strongly increase showing the laminar-turbulent transition (note that the variation of U_{max} with the angle φ is not so large to explain the reduction and only slight increase, respectively, of the turbulence levels from $\varphi = 10^\circ$ to $\varphi = 50^\circ$).

The outer shear layer grows rapidly along the cylinder in streamwise direction so that at $\varphi = 110^\circ$ the region of minimum intensities has nearly vanished. At $\varphi = 110^\circ$ the ratio u'^2/v'^2 is about 1 in the outer region of the wall jet. The convex curvature of the streamlines causes a higher mixing of the fluid perpendicular to the wall (see also Guittou (1970)) compared with the noncurved wall jet.

The process of relaminarization for $S = 10$ mm and $Re = 10^5$ at the beginning of the cylinder causes the strong decrease of the Reynolds shear stresses $-\rho u'v'$ in the near wall region of the wall jet (Fig. 13). For comparison the Reynolds shear stresses in the near wall region for $S = 5$ mm and $Re = 10^5$ are shown in Fig 14. There is a decrease from $\varphi = 10^\circ$ to $\varphi = 30^\circ$ too but then the shear stresses strongly increase from $\varphi = 30^\circ$ to $\varphi = 50^\circ$. This increase takes place for $S = 10$ mm from $\varphi = 50^\circ$ to $\varphi = 70^\circ$ due to the laminar-turbulent transition process.

PHENOMENOLOGICAL EXPLANATION

If the wall jet separates at about 180° there is a region along the cylinder where the pressure gradient $\partial p_w/\partial x$ is nearly zero or has only slightly positive values. For the whole wall jet the negative pressure difference normal to the wall $p_w - p_\infty$ is essential for a high deflection angle. If it is possible to maintain a large pressure difference $p_w - p_\infty$ over a large region along the cylinder the pressure forces are in equilibrium with the centrifugal forces. One may get a large deflection angle which means that the pressure gradient $\partial p_w/\partial x$ and the pressure difference $p_w - p_\infty$ are closely connected.

As shown above a large deflection angle implies the existence of a relaminarized near wall region at the beginning of the cylinder and a following laminar-turbulent transition region. The connection between the existence of these two regions and a large deflection angle may be found with the aid of the x-component of the Navier-Stokes equation in orthogonal cartesian coordinates using the boundary conditions at the wall:

$$\frac{\partial p_w}{\partial x} = \frac{\tau_w}{R} + \frac{\partial}{\partial y} \left(\mu \frac{\partial u}{\partial y} - \overline{u'v'} \right) = \frac{\tau_w}{R} + \left(\frac{\partial \tau_{m+t}}{\partial y} \right) \Big|_w$$

The pressure gradient $\partial p_w / \partial x$ must be approximately zero over a large region of the wall jet if one wants to obtain a large deflection angle. That means (see the equation) that $(\partial \tau_{m+t} / \partial y)_w$ must be negative or zero in that region because τ_w / R is always positive or can be neglected compared with the other two terms. Not only the molecular shear stress τ_m , which dominates in the near wall region, fixes the slope of τ_{m+t} at the wall ($y = 0$) but also the level of the Reynolds shear stresses in the near wall region. The higher the level of τ_t in this region is the more easily the slope of τ_{m+t} at the wall becomes positive and therefore also the pressure gradient $\partial p_w / \partial x$ becomes positive (Fig. 15). That means a quasilaminar wall region of the wall jet ($10^\circ \leq \varphi \leq 50^\circ$) where the level of Reynolds shear stresses is low favours a negative pressure gradient $\partial p_w / \partial x$ or a pressure gradient $\partial p_w / \partial x \approx 0$. If the near wall region is turbulent the increase of $|\overline{u'v'}|$ ($\varphi \geq 30^\circ$) changes the slope of τ_{m+t} at the wall which leads to a positive slope of the shear stress distribution at the wall and consequently to an adverse pressure gradient. The wall jet separates at low circumferential angles ($\varphi < 100^\circ$).

In the laminar-turbulent transition region for the relaminarized boundary layer the wall shear stresses grow significantly together with $|\overline{u'v'}|$. That means the ratio of $\tau_w / |\overline{u'v'}|_{\max}$ is kept high (well above 1) in this region so that $(\partial \tau_{m+t} / \partial y)_w$ and therefore $\partial p_w / \partial x$ is kept close to zero. Only at about $x/h = 3$ the Reynolds shear stresses change the slope of τ_{m+t} at the wall from about zero to positive and thus to an adverse pressure gradient (see Fig. 5).

If one wants to reach a high deflection angle of the wall jet for the investigated test rig one must fulfill two criteria: i) the near wall region of the wall jet at the beginning of the cylinder must be relaminarized, the Reynolds shear stresses must be very low. It is impossible to define an exact boundary between laminar and turbulent. ii) The relaminarized region of the wall jet must extend over a "sufficient" long streamwise direction so that the laminar-turbulent transition process can take place.

BIBLIOGRAPHY

Alcaraz, E., 1977, "Contribution à l'étude d'un jet plan turbulent évoluant le long d'une paroi convexe à faible courbure", Ph.D. Thesis, Université Lyon, No. d'ordre 77.37.

Dahm, A., and Vagt, J.D., 1977, "Entwicklung und Herstellung interferenzarmer Hitzdrahtsonden", HFI-Bericht 01/77, TU Berlin.

Englar, R. J., 1973, "Experimental investigation of the high velocity Coanda wall jet applied to bluff trailing edge circulation control airfoils", D.W. Taylor Nav. Ship Res. and Dev. Center, Report No. 4708.

Fernholz, H.H., 1965, "Zur Umlenkung von Freistrahlen an konvex gekrümmten Flächen (Coanda-Effekt)", Habilitationsschrift, TU Berlin.

Fernholz, H.H., 1967, "Aerodynamische Hysterese, Steuerung - und Reynoldszahl einfluss bei der Strömungsumlenkung und Ablösung an stark gekrümmten Wänden (Coanda-Effekt)", ZFW, Vol. 15, Heft 4, pp. 136-142.

Guittou, D.E., 1970, "Some contributions to the study of equilibrium and non-equilibrium turbulent wall jets over curved surfaces", Ph.D. thesis, Dep. of Mech. Eng., McGill University, Montreal.

Hartmann, U., 1982, "Wall interference effects on hot-wire probes in a nominally two-dimensional highly curved wall jet", J. Physics E: Sci. Instruments, Vol. 15, pp. 725-730.

Köster, H. and Löhr, R., 1964, "Untersuchung der Umlenkung eines ebenen Strahles durch einen Kreiszyylinder

(Coanda-Effekt)", Inst. für Aerodyn. der DVL, Braunschweig, Bericht Nr. 0272.

Launder, B.E. 1964, "Laminarization of the turbulent boundary layer by acceleration", MIT-Report Nr. 77, Gas Turb. Lab., Cambridge, Mass.

Skavdahl, H., Wang, T. and Hirst, W.J., 1974, "Nozzle development for the upper surface blown jet flap on the YC-14 airplane", Soc. of Automotive Eng., Nr. 740469.

Vagt, J.D. and Fernholz, H.P., 1979, "A discussion of probe effects and improved measuring techniques in the near-wall region of an incompressible three-dimensional boundary layer", AGARD CP 271, Turbulent Boundary Layers-Experiments, Theory and Modelling, Den Haag.

Wilson, D.J. and Goldstein, R.J., 1976, "Turbulent wall jets with cylindrical streamwise curvature", Trans. ASME, J. of Fluids Eng., Vol. 98, pp. 550-557.

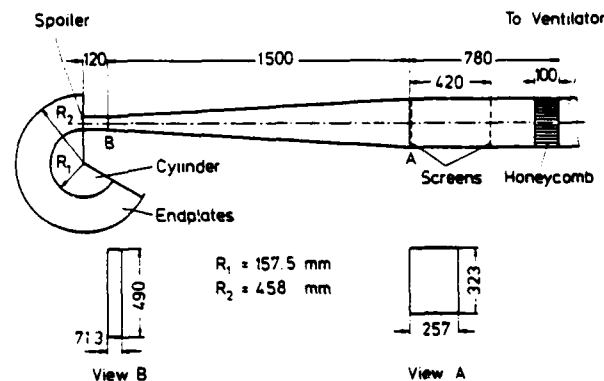


Figure 1: Test rig

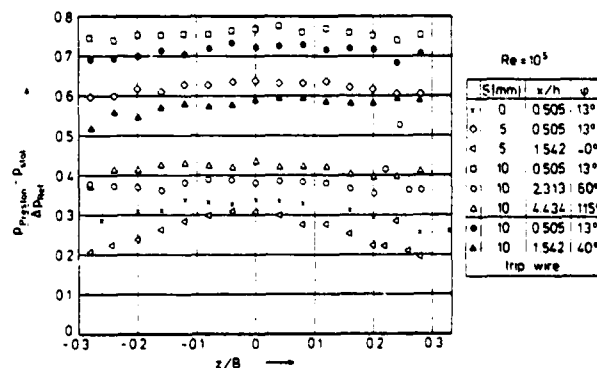


Figure 2: Preston tube readings

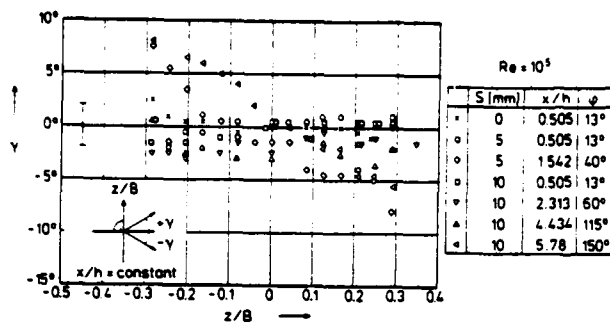


Figure 3: Angles γ between the mean velocity vector \bar{u} and symmetry line

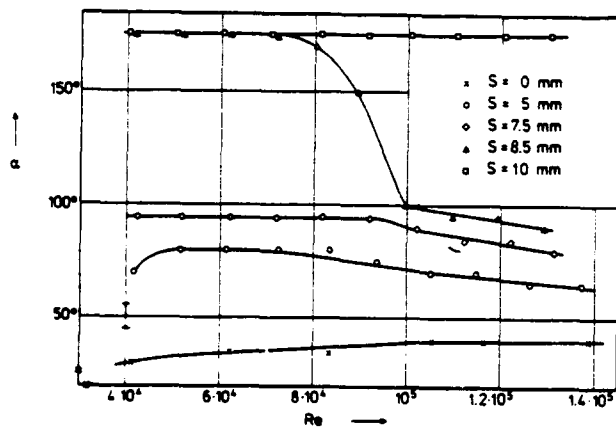


Figure 4: Deflection angles α

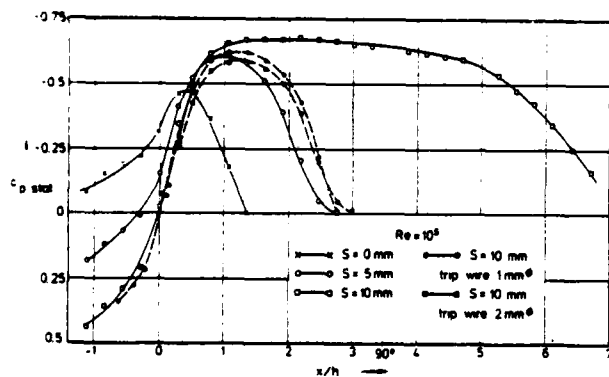


Figure 5: Static wall pressures

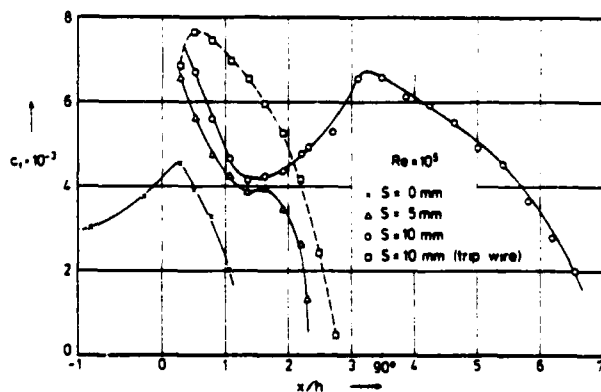
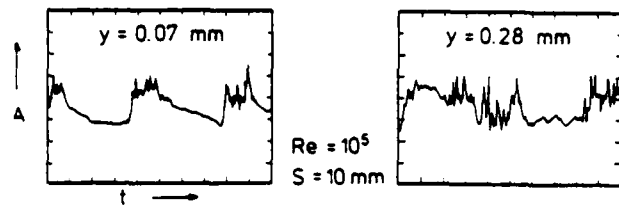


Figure 6: Local skin friction coefficients



Time scale: 2 ms/division
Amplitude scale: 200 mV/division

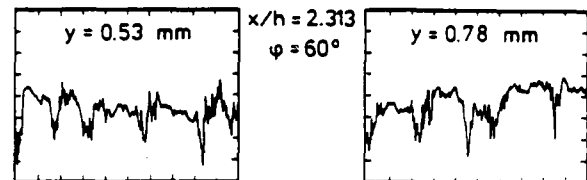


Figure 7: Linearized hot-wire signals $u'(t)$

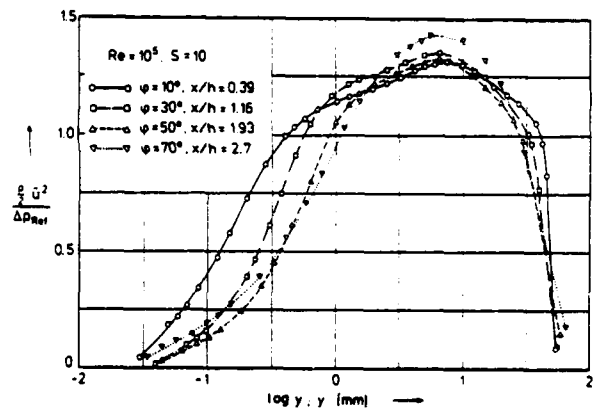


Figure 8: Mean velocity profiles

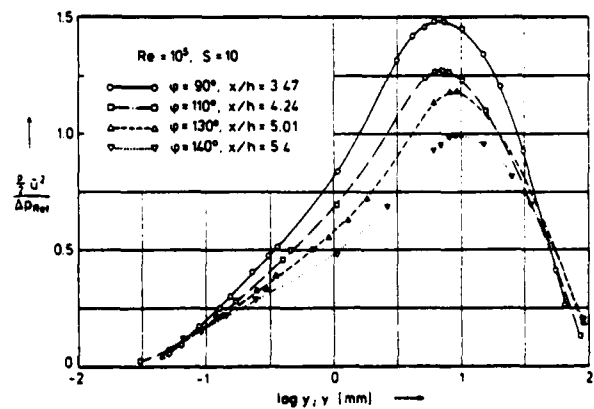


Figure 9: Mean velocity profiles

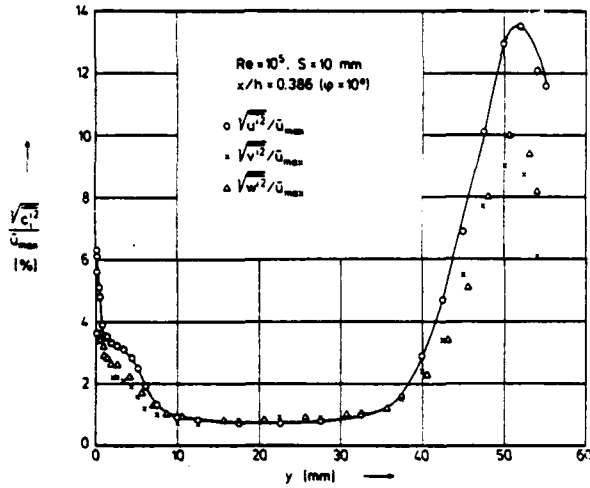


Figure 10: Turbulence levels $\sqrt{u'^2}/\bar{u}_{max}$, $\sqrt{v'^2}/\bar{u}_{max}$, $\sqrt{w'^2}/\bar{u}_{max}$

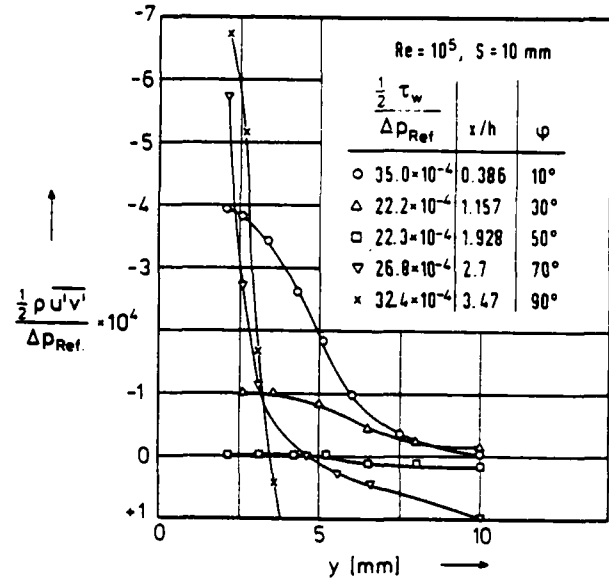


Figure 13: Reynolds shear stresses in the near wall region

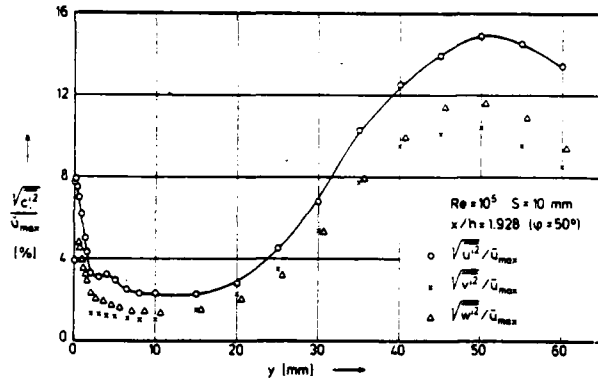


Figure 11: Turbulence levels $\sqrt{u'^2}/\bar{u}_{max}$, $\sqrt{v'^2}/\bar{u}_{max}$, $\sqrt{w'^2}/\bar{u}_{max}$

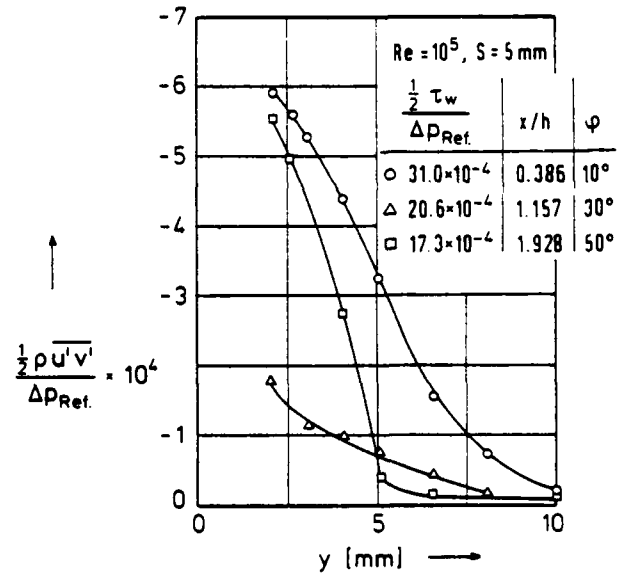


Figure 14: Reynolds shear stresses in the near wall region

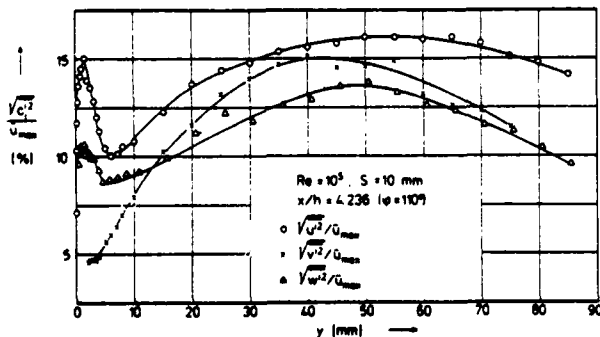


Figure 12: Turbulence levels $\sqrt{u'^2}/\bar{u}_{max}$, $\sqrt{v'^2}/\bar{u}_{max}$, $\sqrt{w'^2}/\bar{u}_{max}$

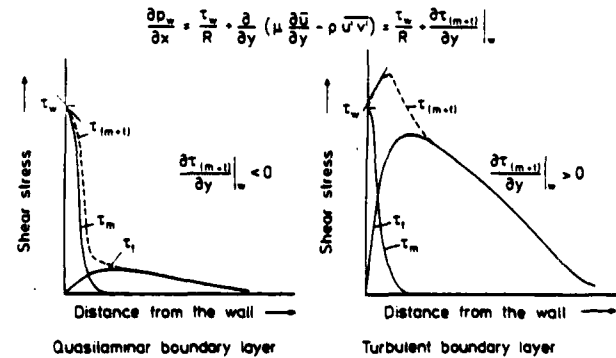


Figure 15: Shear stress profiles in the near wall region

COMPUTATION AND TURBULENCE CLOSURE MODELS FOR SHEAR FLOWS IN ROTATING CURVED BODIES

M. Pouagare and B. Lakshminarayana

Department of Aerospace Engineering
The Pennsylvania State University
University Park, PA 16802

ABSTRACT

This paper is concerned with the effects of rotation and curvature on the turbulence closure model. The $k-\epsilon$ model that includes the effects of curvature has been modified to include the anisotropy in turbulence. A space-marching algorithm which solves the parabolized Navier-Stokes equations is coupled with the turbulence closure model to predict the turbulent shear flow over a rotating cylinder and inside a rotating channel. The agreement between the predictions and available data is good. The rotation and curvature effects are predicted well.

NOMENCLATURE

D	semi-width of the two-dimensional channel
e	specific total energy = $\rho(e_1 + 0.5(U^2 + V^2 + W^2))$
e_1	specific internal energy
J	Jacobian of the coordinate transformation
k	turbulent kinetic energy
L	characteristic length; in Lohmann's experiment $L = 0.0254$ m
P_{ij}	production of $u_i u_j$
P	production of k
p	static pressure
Q	characteristic velocity
Re	Reynolds number = QL/ν
Re_T	turbulence Reynolds number = $k^2/\nu\epsilon$
Ro	rotational parameter = $2\Omega R/U_{mean}$
S	curvature Richardson number (equation 7)
T	parameter of the anisotropic eddy viscosity model (equation 17)
U, V, W	mean axial, tangential and radial components of velocity in cylindrical coordinates normalized by Q
U_c	contravariant velocity = $\xi_2 U + \xi_3 V$
$-\rho u v, -\rho u w$	Reynolds shear stress in cylindrical coordinates
U_1, U_2, U_3	velocity components in Cartesian coordinates U_1 is the principal velocity component, U_2 is normal (x_2) to the wall, U_3 is in the transverse (x_3) direction
u_1, u_2, u_3	fluctuating components of velocity in x_1, x_2, x_3 directions
$-\rho u_1 u_j$	Reynolds stresses in Cartesian coordinates
V_r^*, u^*	velocity relative to a moving wall friction velocity
x_1, x_2, x_3	Cartesian coordinates; x_1 is the main flow direction, x_2 the normal to the wall, and x_3 the cross-flow direction
y	distance from the wall
z, θ, r	cylindrical coordinates, axial, tangential and radial directions
γ	ratio of specific heats
ϵ	rate of turbulent kinetic energy dissipation
K	von-Karman constant
μ	molecular viscosity

μ_t	eddy viscosity normalized by μ
ν	molecular kinematic viscosity
ξ_1, η, ζ	body-fitted coordinates
ρ	density
Ω, Ω_p	angular velocity

Subscripts

p	quantities at the first grid point away from the wall
e	edge quantities

INTRODUCTION

There is a considerable interest at the present time in developing numerical procedures for solving the equations governing three-dimensional flows subjected to centrifugal and Coriolis forces such as those that occur on rotating curved bodies (e.g., turbomachinery blades). The analysis of such flows is very difficult due to the fact that additional effects such as Coriolis and centrifugal forces change the structure of the turbulence, thus invalidating most of the turbulence models that are presently used in computing turbulent flows on stationary bodies. Curvature and rotation of the body make the turbulence highly non-isotropic, and may affect the stability of the boundary layer.

The $k-\epsilon$ (kinetic energy-dissipation rate) model has been used successfully for over a decade for the prediction of two-dimensional flows. However, the $k-\epsilon$ model employs the isotropic eddy viscosity concept and hence it is not adequate for flows where the Reynolds stress tensor is not aligned with the mean strain tensor (e.g. 3-D boundary layers).

The objective of this paper is to modify the $k-\epsilon$ equations for rotating curved flows. An anisotropic $k-\epsilon$ model for three-dimensional thin shear layers, derived from Rotta's T-model [1], and a $k-\epsilon$ model for two-dimensional rotating flows, derived from Galmes and Lakshminarayana's algebraic Reynolds stress model [2], are proposed. The mean flow equations are solved with a space-marching algorithm for the solution of the Navier-Stokes equation developed by Govindan [3].

The modified $k-\epsilon$ equations coupled with the mean flow equations are used to predict the flow over a rotating cylinder [4] and through a rotating duct [5].

THE SPACE-MARCHING ALGORITHM

The governing equations and the numerical technique have been developed by Govindan [3] and only a brief summary will be given here. In this technique, the streamwise coordinate direction is treated as a "time-like" coordinate and the system of equations as an initial value problem in this coordinate direction. This provides a fully coupled system of equations in the

transverse plane and can be solved by fully implicit schemes.

The Navier-Stokes equations for a compressible flow in a cylindrical coordinate system (r, θ, z) can be written in non-dimensional form as

$$\frac{\partial E(q)}{\partial z} + \frac{\partial F(q)}{r \partial \theta} + \frac{\partial G(q)}{\partial r} + C(q) \frac{1}{R_e} \left[\frac{\partial A(q)}{r \partial \theta} + \frac{\partial B(q)}{\partial r} + \frac{\partial D(q)}{\partial z} + H(q) \right] \quad (1)$$

The vectors E, F, G, C contain the convective terms and A, B, D, H contain the viscous diffusion terms where the turbulence is simulated by replacing the molecular viscosity by the eddy viscosity. The dependent vector q is chosen as

$$q = [\rho, \rho U, \rho V, \rho W, \rho e_1]^T$$

where U, V, W are components of velocity in the chosen coordinate system.

Equation (1) is transformed to a body-fitted coordinate system and the flow domain mapped to a sector of a cylinder in which computations are carried out. This transformation can be described as

$$\xi = \xi(z, \theta), \quad \eta = \eta(z, \theta), \quad \zeta = \zeta(r) \quad (2)$$

where ξ is the coordinate in the streamwise direction and η and ζ are normal to it in the transverse plane. The diffusion terms in the ξ direction can be dropped in comparison to the terms in the transverse direction to make the equation parabolic in this direction and amenable to solution by a marching procedure. It can be easily shown that the form of the transformed equations can be kept similar to equation (1).

$$\frac{\partial \hat{E}}{\partial \xi} + \frac{\partial \hat{F}}{\partial \eta} + \frac{\partial \hat{G}}{\partial \zeta} + \hat{C} = \frac{1}{R_e} \left[\frac{\partial \hat{A}}{\partial \eta} + \frac{\partial \hat{B}}{\partial \zeta} + \hat{H} \right] \quad (3)$$

An example of the above flux vectors, the streamwise flux vector, is given below

$$\hat{E} = \frac{1}{J} (\xi_z E + \xi_\theta F) = \frac{1}{J} \begin{bmatrix} \rho U_c \\ \rho U U_c + \xi_z p \\ \rho V U_c + \xi_\theta p \\ \rho W U_c \\ (e + p) U_c \end{bmatrix}$$

Due to space limitations it is not possible to present all the flux vectors; they can be found in Ref. [3].

The equation of state is needed to close the system of equations (3) and is given by

$$p = (\gamma - 1) \rho e_1 \quad (4)$$

Equation (3) along with the equation of state describe the flow in the computational domain and are solved with the Linearized Block Implicit method of Briley and McDonald [6]. A brief description of the space-marching method can be found in Ref. 7. The finite difference form utilizes the Crank-Nicolson scheme.

A global pressure iteration must be implemented to converge the solution. To begin with, an approximate pressure field is prescribed and the solution marched from a known upstream initial condition. A new pressure field is obtained by using the equation of state and the solution marched again with this new pressure field. This is the technique of global pressure iteration.

This space-marching method has the following advantages over the widely used parabolic marching methods (e.g. Ref. [8]).

- (1) In the present technique, only the streamwise pressure gradient is prescribed. The pressure gradients in the cross-flow are not prescribed. It is often much easier to estimate the

streamwise pressure gradient than the pressure gradients in the cross-flow plane. Thus, the solution converges very fast in two or three sweeps of the flow field. Note that, if the first guess of the streamwise pressure gradient is the exact one, only a single pass is needed.

- (2) The cross-flow plane pressure gradients are treated implicitly and they are part of the solution. Therefore, there is no need for solving any kind of Poisson equation for the pressure in the cross-flow plane.
- (3) Unlike most of the space-marching methods the present method does not have difficulties in conserving mass since it solves the continuity equation simultaneously with the other equations of motion at each streamwise step.

It can be seen that this space-marching method avoids the two most troublesome parts of the parabolic marching methods, namely the iterative solution of the Poisson equation for the pressure and the difficulty in satisfying the conservation of mass. Therefore, it gives very accurate predictions for the velocity as well as for the cross-flow velocities. The accurate prediction of all three components of velocity is needed before attempting to draw conclusions about the performance of the various turbulence closure schemes. The turbulence closure models used are described below.

THE k- ϵ MODEL

The k- ϵ model used here was that described by Galmes and Lakshminarayana [2] and is based on the model developed by Jones and Launder [9]. To be consistent with the mean flow equations, the kinetic energy and the dissipation equations have been transformed to a body-fitted coordinate system. These equations are also marched in space, making it necessary to neglect streamwise diffusion terms. The kinetic energy and the dissipation equations can be written in a form similar to equation (3)

$$\frac{\partial \hat{E}_T}{\partial \xi} + \frac{\partial \hat{F}_T}{\partial \eta} + \frac{\partial \hat{G}_T}{\partial \zeta} + \hat{C}_T = \frac{1}{R_e} \left[\frac{\partial \hat{A}_T}{\partial \eta} + \frac{\partial \hat{B}_T}{\partial \zeta} + \hat{H}_T \right] \quad (5)$$

where

$$\begin{aligned} \hat{E}_T &= \frac{1}{J} \begin{bmatrix} \zeta_z \rho k U + \xi_z \rho k V \\ \xi_z \rho e U + \xi_\theta \rho e V \end{bmatrix} & \hat{F}_T &= \frac{1}{J} \begin{bmatrix} \eta_z \rho k U + \eta_\theta \rho k V \\ \eta_z \rho e U + \eta_\theta \rho e V \end{bmatrix} \\ \hat{G}_T &= \frac{1}{J} \begin{bmatrix} \zeta_r \rho k W \\ \zeta_r \rho e W \end{bmatrix} & \hat{C}_T &= \frac{1}{J} \begin{bmatrix} \rho k W \\ \rho e W \end{bmatrix} \\ \hat{A}_T &= \frac{1}{J} \begin{bmatrix} \eta_z^2 \mu_k \frac{\partial k}{\partial \eta} + \eta_\theta^2 \mu_k \frac{\partial k}{\partial \theta} \\ \eta_z^2 \mu_\epsilon \frac{\partial \epsilon}{\partial \eta} + \eta_\theta^2 \mu_\epsilon \frac{\partial \epsilon}{\partial \theta} \end{bmatrix} & \hat{B}_T &= \frac{1}{J} \begin{bmatrix} \zeta_r^2 \mu_k \frac{\partial k}{\partial r} \\ \zeta_r^2 \mu_\epsilon \frac{\partial \epsilon}{\partial r} \end{bmatrix} \\ \hat{H}_T &= \frac{1}{J} \begin{bmatrix} \frac{\mu_k}{\zeta} \zeta_r \frac{\partial k}{\partial \zeta} + P - \rho \epsilon R_e \\ \frac{\mu_\epsilon}{\zeta} \zeta_r \frac{\partial \epsilon}{\partial \zeta} + C_{\epsilon 1} \frac{\epsilon}{k} P - C_{\epsilon 2} (1 - C_{\epsilon 3}) \epsilon \frac{2}{k} R_e \end{bmatrix} \end{aligned}$$

where

$$\mu_k = 1 + \mu_t / c_k \quad \mu_\epsilon = 1 + \mu_t / \sigma_\epsilon$$

P represents the production of kinetic energy and is given by

$$P = \mu_t \left[2 \left[\left(\zeta_r \frac{\partial W}{\partial \zeta} \right)^2 + \left(\eta_\theta \frac{\partial V}{\partial n} + \frac{W}{\zeta} \right)^2 + \left(\eta_z \frac{\partial U}{\partial n} \right)^2 \right] + \left(\eta_z \frac{\partial W}{\partial n} + \zeta_r \frac{\partial U}{\partial \zeta} \right)^2 + \left(\eta_z \frac{\partial V}{\partial n} + \eta_\theta \frac{\partial U}{\partial n} \right)^2 + \left(\eta_\theta \frac{\partial W}{\partial n} + \zeta_r \frac{\partial V}{\partial \zeta} - \frac{V}{\zeta} \right)^2 \right] \quad (6)$$

The constants $C_{\epsilon 1}$, $C_{\epsilon 2}$, σ_k , σ_ϵ and C_c are given in Table 1. The curvature terms appear explicitly in both the source ($C_{\epsilon 1}$, S_1) and production terms (P) through the terms $1/\zeta$.

The term in the ϵ transport equation involving S accounts for the effect of streamline curvature, and it was first introduced by Sharma [10]. S is a curvature Richardson number given by

$$S = \frac{k^2}{\epsilon^2} \frac{v}{\zeta^2} \zeta_r \frac{\partial}{\partial \zeta} (\zeta V) \quad (7)$$

The eddy viscosity μ_t is given by

$$\mu_t = C_\mu \rho (k^2/\epsilon) R_e \quad (8)$$

Most researchers use a constant value for the coefficient C_μ (usually $C_\mu \approx 0.09$). In the next sections C_μ will be modified in order to account for (1) the effect of non-alignment between the shear stress and the mean strain tensors, and (2) the effect of rotation.

Table 1: Empirical Coefficients

$C_{\epsilon 1}$	$C_{\epsilon 2}$	σ_k	σ_ϵ	C_c	C_1	C_2
1.44	1.92	1	1.3	0.2	1.5	0.6

Equation (5) is only valid in regions where R_T is sufficiently high. Therefore it is not applicable in the region very close to the wall. This problem is overcome by employing wall functions. The boundary conditions for k and ϵ are applied at the first grid point away from the wall. Care is taken so that the first grid point is outside the laminar sublayer, and in the law of the wall region. It must be emphasized here that no wall function is used, unless otherwise stated, for the mean velocity and the no-slip condition is applied on the wall. Once the mean velocity profile is obtained, the friction velocity is calculated using the appropriate form of the law of the wall for each particular case. Then k and ϵ at the first point away from the wall are calculated from the relations:

$$k_p = u_*^2 / \sqrt{C_\mu} \quad (9)$$

$$\epsilon_p = u_*^3 / k y_p \quad (10)$$

where y_p is the distance of the first grid point from the wall.

Equation (5) was solved using the same method used for the Navier-Stokes equations. Rather than solving the coupled equations, each equation was solved individually. The turbulent kinetic energy equation was solved first, lagging the eddy viscosity and dissipation. Next the dissipation equation was solved using the just computed turbulent kinetic energy and lagging the dissipation. Finally, equation (8) was used to calculate the eddy viscosity using the new kinetic energy and dissipation. This procedure assumes that kinetic energy, dissipation and the eddy viscosity do not change significantly from one streamwise station to the next. Little difference was seen between predictions that solved equations (5) and (8) in one pass and predictions obtained when looping these equations several times at each streamwise station using updated

values of kinetic energy, dissipation, and eddy viscosity. This seems to justify the assumption that the set of turbulence equations for k and ϵ are not strongly coupled by the flow field. Consequently, ensuing runs only solved equations (5) and (8) once to save on computer time. Equation (3) is solved first for the mean flow quantities. Next equations (5) and (8) are solved using the just computed mean flow quantities. This procedure lags the solution of the turbulence quantities by one streamwise step.

MODIFICATION OF k - ϵ MODEL FOR ANISOTROPY

Measurements in 3-D boundary layers [11] show that the stress vector is not aligned with the mean strain vector. Therefore, an anisotropic eddy viscosity must be employed for accurate predictions. A rigorous way of deriving an anisotropic eddy viscosity is by manipulating the algebraic stress equations. The authors attempted to derive an anisotropic eddy viscosity using Rodi's [12] algebraic Reynolds stress model, which in a Cartesian coordinate system is given by

$$\frac{\overline{u_i u_j}}{k} = \frac{2}{3} \delta_{ij} + \frac{1 - C_2}{C_1} \frac{P_{ij}/\epsilon}{1 + \frac{1}{C_1} (P/\epsilon - 1)} \quad (11)$$

$$\text{where } P_{ij} = -\rho (\overline{u_i u_k} \frac{\partial U_j}{\partial x_k} + \overline{u_j u_k} \frac{\partial U_i}{\partial x_k})$$

Employing the thin shear layer assumptions, namely that $\partial U_1/\partial x_2$ and $\partial U_3/\partial x_2$ are the only important mean velocity gradients, the following expressions are derived for the two stresses $-\overline{ou_1 u_2}$ and $-\overline{ou_3 u_2}$

$$-\overline{ou_1 u_2} = \frac{\mu_{t12}}{R_e} \frac{\partial U_1}{\partial x_2} = C_{\mu 12} \frac{k^2}{\epsilon} \frac{\partial U_1}{\partial x_2} \quad (12)$$

$$-\overline{ou_3 u_2} = \frac{\mu_{t32}}{R_e} \frac{\partial U_3}{\partial x_2} = C_{\mu 32} \frac{k^2}{\epsilon} \frac{\partial U_3}{\partial x_2} \quad (13)$$

where $C_{\mu 12}$ and $C_{\mu 32}$ are functions of P , ϵ , C_1 , C_2 . One would expect that $C_{\mu 12}$ and $C_{\mu 32}$ are different giving rise to an anisotropic model. However, $C_{\mu 12}$ was found to be equal to $C_{\mu 32}$ given by

$$C_{\mu 12} = C_{\mu 32} = \frac{2}{3} (1 - C_2) \frac{C_1 - 1 + C_2 P/\epsilon}{[C_1 - 1 + P/\epsilon]^2} \quad (14)$$

This indicates that in a three-dimensional boundary layer Rodi's algebraic stress model behaves isotropically, as far as the shear stresses are concerned.

Rotta [1] showed that the non-alignment of the shear stress vector with the mean velocity gradient vector is due to the fluctuating pressure term in the turbulence transport equation. Introducing an appropriate approximation for the pressure-strain term in the stress equations he was able to derive the following expressions for $-\overline{ou_1 u_2}$, $-\overline{ou_3 u_2}$ in three dimensional boundary layers

$$-\overline{ou_1 u_2} = \alpha \frac{k^2}{\epsilon} \circ \left[\left(\frac{U_1^2 + T U_3^2}{U_1^2 + U_3^2} \right) \frac{\partial U_1}{\partial x_2} + \left(\frac{(1-T) U_1 U_3}{U_1^2 + U_3^2} \right) \frac{\partial U_3}{\partial x_2} \right] \quad (15)$$

$$-\overline{ou_3 u_2} = \alpha \frac{k^2}{\epsilon} \circ \left[\left(\frac{(1-T) U_1 U_3}{U_1^2 + U_3^2} \right) \frac{\partial U_1}{\partial x_2} + \left(\frac{U_3^2 + T U_1^2}{U_1^2 + U_3^2} \right) \frac{\partial U_3}{\partial x_2} \right] \quad (16)$$

where α is a constant and the parameter T is given by

$$T = \frac{\tan(\gamma_\epsilon - \gamma_v)}{\tan(\gamma_g - \gamma_v)} \quad (17)$$

The angles γ_v , γ_ϵ , and γ_g are angles made by the

Although Kotta's model seemed promising, it did not find wide application or success [13]. The researchers that did use it assumed that T is constant across the boundary layer thickness as well as in the streamwise direction. However, there is no reason to believe that T stays constant in the streamwise direction. In fact, it only makes sense to assume that T does change since the angles γ_t , γ_g and γ_v change in the streamwise direction. T stays constant only when the boundary layer reaches the equilibrium stage.

Comparing equations (12) and (13) with equations (15) and (16), respectively, it is evident that the desirable anisotropic eddy viscosity is obtained, with C_{112} and C_{132} given by

$$C_{u12} = \alpha \left[\frac{u_1^2 + \tau u_3^2}{u_1^2 + u_3^2} + (1-\tau) \frac{u_1 u_3}{u_1^2 + u_3^2} \frac{\partial u_3 / \partial x_2}{\partial u_1 / \partial x_2} \right] \quad (18)$$

$$C_{u32} = \alpha \left[(1-\tau) \frac{u_1 u_3}{u_1^2 + u_3^2} \frac{\partial u_1 / \partial x_2}{\partial u_3 / \partial x_2} + \frac{u_3^2 + \tau u_1^2}{u_3^2 + u_1^2} \right] \quad (19)$$

MODIFICATION OF k- ϵ MODEL TO INCLUDE EFFECTS OF ROTATION FOR A CHANNEL

flows ($P = \rho \epsilon$), their model reduces to

$$\frac{u_{1j} u_{1j}}{k} = \frac{2}{3} \delta_{1j} + \frac{R_{1j}(1 - \frac{C_2}{2}) + (P_{1j} - \frac{2}{3} \delta_{1j} P)(1 - C_2)}{C_1 P} \quad (20)$$

$$R_{ij} = -2\rho_p (\epsilon_{ipk} \overline{u_j u_k} + \epsilon_{jpk} \overline{u_i u_k})$$

Diagram illustrating the trailing vortex system. The vortex core is shown as a horizontal line. The vertical axis is labeled X_2, U_2 and the horizontal axis is labeled X_1, U_1 . The rotation is indicated by a curved arrow with angular velocity Ω . The right side of the vortex is labeled 'TRAILING SIDE' and the left side is labeled 'LEADING SIDE'.

For a two-dimensional channel flow rotating about an axis perpendicular to it (see Fig. 2) equation (20) yields (assuming the dominant velocity gradient is $\partial U_1 / \partial x_2$,

$$\frac{u_1^2}{k} = \frac{2}{3} + \frac{4\Omega u_1 u_2 (1 - \frac{C_2}{2}) + (-\frac{4}{3} u_1 u_2 \frac{\partial u_1}{\partial x_2} \chi_1 - C_2)}{C_1 (-u_1 u_2 \frac{\partial u_1}{\partial x_2})} \quad (21)$$

$$\frac{u_2}{k} = \frac{2}{3} + \frac{-4\overline{u_1 u_2}(1 - \frac{C_2}{2}) + \frac{2}{3}\overline{u_1 u_2} \frac{\partial u_1}{\partial x_2}(1 - C_2)}{C_1(-\overline{u_1 u_2} \frac{\partial u_1}{\partial x_2})} \quad (22)$$

$$\frac{\overline{u_1 u_2}}{k} = \frac{-2\Omega(\overline{u_1^2} - \overline{u_2^2})(1 - \frac{c_2}{2}) + (-\overline{u_2^2} \partial u_1 / \partial x_2)(1 - c_2)}{C_1 \varepsilon} \quad (23)$$

$$-u_1 u_2 = \frac{k^2}{\varepsilon} \left[\frac{\frac{2}{3}(1 - C_1)}{C_1} - \frac{\frac{2}{3}(1 - C_2)^2}{C_1} - \frac{\frac{2}{3}(1 - C_2)(1 - \frac{C_2}{2})}{C_1^2} + \frac{(1 - C_2)(2 - C_2)}{C_1^2} \right] \frac{\partial u_1}{\partial x_2} \quad (24)$$

where $R = \frac{-2\Omega}{\partial U_1 / \partial x_2}$.

$$-\overline{u_1 u_2} = (0.13 - 0.5R) \frac{k^2}{\epsilon} \frac{\partial u_1}{\partial x_2} \quad (25)$$

therefore, $C_1 = 0.13 - 0.5R$. (26)

$$C_1 = 0.09 - 0.5R_1 \quad (27)$$

Note that R is negative on the leading side and positive on the trailing side of the rotating channel shown in Fig. 2. Thus, $C_{y\text{leading}} > C_{y\text{trailing}}$ which means that the leading side has more turbulence than the trailing side.

trailing side, an observation confirmed by experiments. Thus, the effect of rotation can be incorporated in the k- ϵ model by using the above modified value of C_{μ} in equation (8).

Howard et al. [14] introduced the effect of rotation in the k- ϵ model by an ad hoc modification of the dissipation (ϵ) equation. They modified the constant $C_{\epsilon 2}$ by setting it equal to

$$C_{\epsilon 2} \left(1 + 0.2 \left(\frac{k}{\epsilon} \right)^2 2\Omega \frac{\partial U_1}{\partial x_2} \right) \quad (28)$$

In a later section the authors' modification (Eq. 27) will be compared with Howard's (eq. 28) in the calculation of the flow in a rotating duct.

TEST CASE 1: FLOW ON A ROTATING CYLINDER (Lohmann [4])

The anisotropic k- ϵ model as well as the standard isotropic one were tested for the flow over a rotating cylinder immersed in an axial stream. The free stream velocity was 17.53 m/sec and the boundary layer thickness at the initial station was 0.0203 m. The surface velocity was 1.411 times the free stream velocity. The radius of the rotating surface was 0.134 m. The calculation was started on the stationary part of the cylinder, 0.0127 m upstream of the location where the surface started rotating. A cylindrical coordinate system is used with U, V, W representing the axial (z), tangential (θ) and normal to the wall (r) velocity, respectively. Initial values for U, k, ϵ were needed at the initial station. U and k were obtained from the experimental data. However, ϵ had to be approximated. In order to study the effect of initial value ϵ on the solution, three different methods were used to find ϵ at the initial station:

- (1) Equation (12) was solved for ϵ

$$\epsilon = C_{\mu 12} \frac{k^2}{(-uw)} \frac{\partial U}{\partial r} \quad (29)$$

with k, $-uw$, and $\partial U/\partial r$ obtained from the data. $C_{\mu 12}$ was set equal to 0.09.

- (2) Production was assumed equal to the dissipation and the equations

$$P = \rho \epsilon R_e, \quad P = \mu_t \left(\frac{\partial U}{\partial r} \right)^2, \quad \mu_t = C_{\mu 12} \rho \frac{k^2}{\epsilon} R_e \quad (30)$$

were solved simultaneously for the unknown values of P, μ_t and ϵ .

- (3) The following equation was used

$$\epsilon = \frac{(0.3k)^{1.5}}{l/\delta} \quad (31)$$

with $l/\delta = \kappa y/\delta$ for $y/\delta \leq 0.09$

$l/\delta = 0.09$ for $y/\delta > 0.09$

where δ is the boundary layer thickness and l is the mixing length.

It was observed that all three methods of estimating ϵ yielded the same results after a few stations downstream. Therefore, the solution was independent of the initial ϵ profile, as long as it was calculated by a reasonable approximation based on physics of the flow.

The equations governing this flow were solved in a cylindrical coordinate system and thus in equations (18) and (19) the ratio $(\partial U_3/\partial x_2)/(\partial U_1/\partial x_2)$ was substituted by

$$\left[r \frac{\partial}{\partial r} (V/r) \right] / (\partial U/\partial r) \quad (32)$$

The friction velocity used in the wall-function expressions is calculated from the expressions given by Lohmann [4]

$$V_r^+ = 2.44 \ln Y_r^+ + 4.9 \quad (32)$$

where

$$V_r^+ = V_r/V_r^* \quad \text{and} \quad Y_r^+ = yV_r^*/\nu$$

with V_r the velocity relative to the moving wall.

T was set equal to 1 for the locations on the stationary part of the cylinder. It was assigned a value different than 1 at the location where the surface started rotating. For the rest of the locations it was calculated by the algorithm. Figure 3 shows the evolution of T for four different values of initial T (0.9, 0.75, 0.5, 0.25). It can be seen that after an initial adjustment region, T is found to be identical in all approaches beyond $z/L = 5$. This shows that:

- (1) The idea of leaving T free to take the value calculated by the algorithm seems to be reasonably good.
- (2) The resulting T does not depend on the initial value of T, a feature that is computationally desirable and convenient.

The fact that T is almost constant along the streamwise distance after the initial adjustment region, indicates that the boundary layer is reaching an equilibrium state.

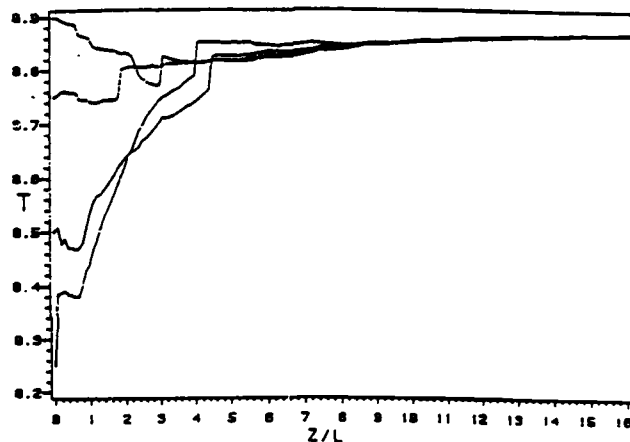


Fig. 3. Evolution of T With Axial Distance

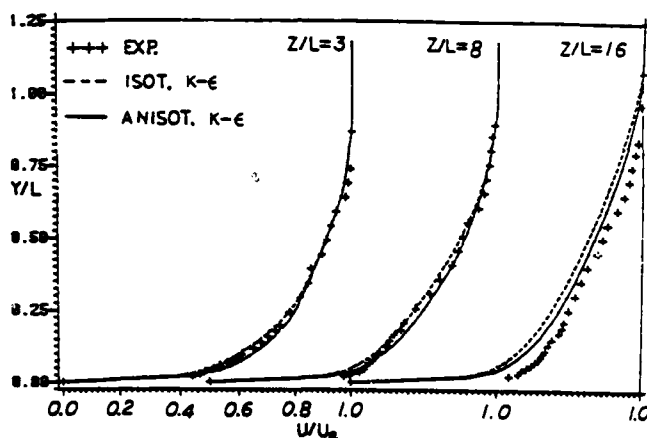


Fig. 4. Comparison Between Predicted and Experimental Axial Velocity Profiles for a Rotating Cylinder

Figures 4 to 8 show the comparison between experimental data and predictions from the isotropic and anisotropic k- ϵ model at three locations $z/L = 3, 8, 16$; $z/L = 0$ is the location where the rotation starts and l is taken equal to 1 inch = 0.0254 m. It can be seen that the predictions for U, V, k and uv have been improved by the use of the anisotropic eddy viscosity model.

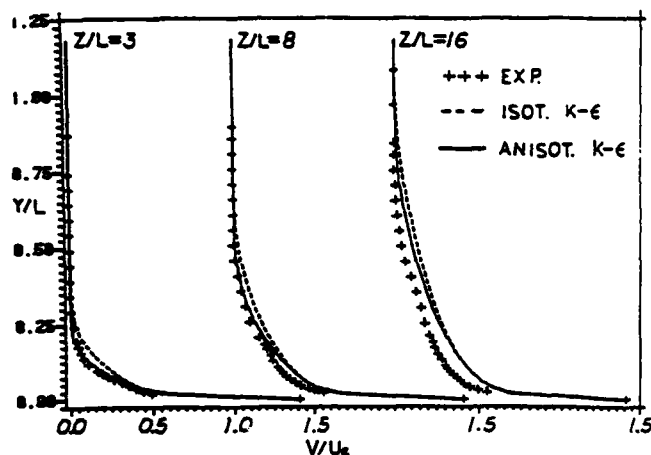


Fig. 5. Comparison Between Predicted and Experimental Tangential Velocity Profiles

The prediction of the mean velocity as well as the turbulence quantities is better than those obtained by earlier investigators [15]. The space-marching code and the modified $k-\epsilon$ turbulence closure model seem to provide good predictions of the flow field.

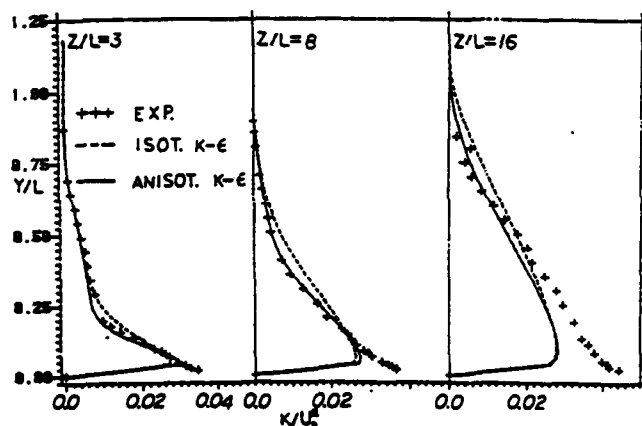


Fig. 6. Comparison Between Predicted and Experimental Kinetic Energy Profiles for Rotating Cylinder

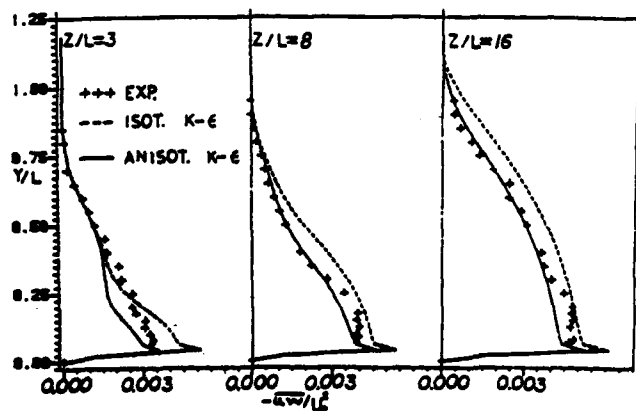


Fig. 7. Comparison Between Predicted and Experimental Streamwise Stress ($-uw$) Profiles

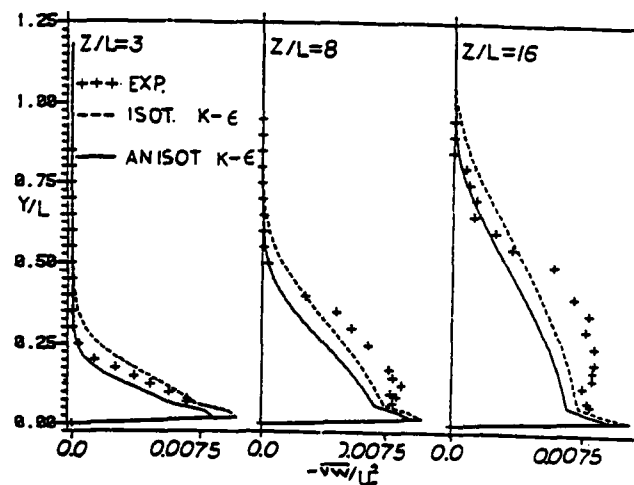


Fig. 8. Comparison Between Predicted and Experimental Tangential Stress ($-vw$) Profiles

TEST CASE 2: FLOW IN A ROTATING DUCT (Johnston [5]) - Fig. 2

The authors' computational technique and the turbulence closure were tested for the flow in a rotating duct investigated by Johnston et al. [5]. The flow was two-dimensional at the mid-span plane. The width of the duct was $2D = 0.0398$ m and the Reynolds number based on the maximum velocity was

$$Re = \frac{U_{lmax} D}{\nu} = 19000.$$

The flow was fully developed at the test section located at $x_1/D = 58$. Johnston did not provide any inlet velocity measurements and thus the inlet velocity was assumed to be uniform calculated from the total mass flow.

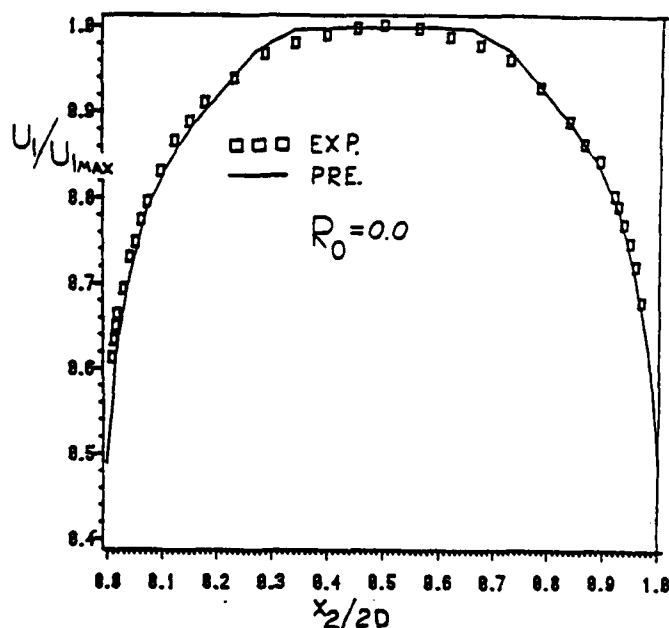


Fig. 9. Comparison Between Predictions and Experiment for the Streamwise Velocity for $R_0 = 0$

The computer code was first run for the non-rotating case. The predictions for the streamwise velocity did not compare well when the no-slip boundary condition was applied on the walls. However, when a wall slip velocity was used, the predictions were very good (Fig. 9). Following Kreskowsky et al. [16] the wall slip velocity was derived by assuming that the velocity profile is logarithmic at the first grid point away from

the wall. Therefore, the velocity gradient at the first point away from the wall is given by

$$\left(\frac{\partial u_1}{\partial x_2}\right) = \frac{u_*}{\kappa y_p} \quad (33)$$

Using a backward finite difference for equation (33), the wall slip velocity is estimated to be

$$U_{1SLIP} = U_{1p} - \frac{u_*}{\kappa} \quad (34)$$

A detailed investigation of the slip boundary condition was carried out by Gorski et al [7].

The comparison between the predicted and the measured streamwise velocity for the rotating duct ($R_o = 0.085$) is shown in Fig. 10. Even though the agreement is not as good as in the non-rotating case the qualitative effects of rotation are well predicted.

The authors' modification to the k- ϵ model (eqn. 27) gives better predictions on the trailing side than Howard's modification (eqn. 28). The latter performs slightly better on the leading side.

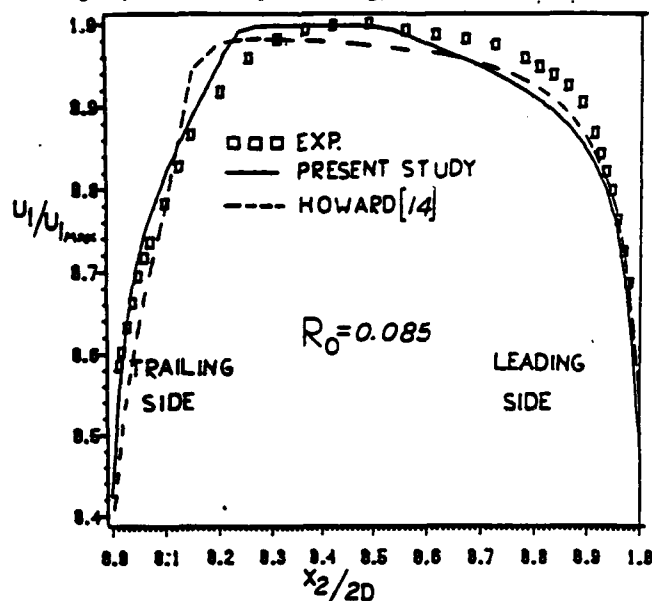


Fig. 10. Comparison Between Predictions and Experiment for the Streamwise Velocity for $R_o = 0.085$

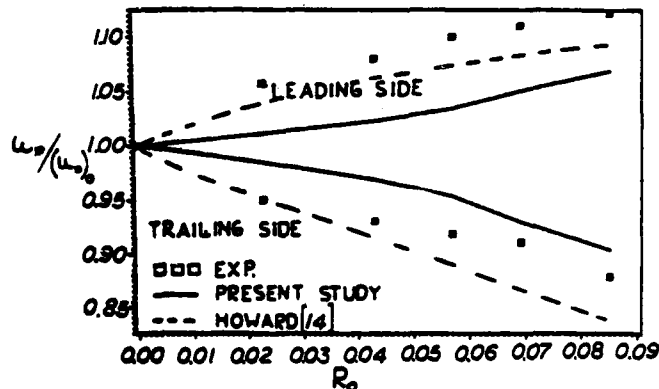


Fig. 11. Comparison Between Predicted and Experimental Values of $u_* / (u_*)_0$

Figure 11 shows the comparison between predicted and measured $u_* / (u_*)_0$ for various rotational speeds; $(u_*)_0$ is the friction velocity at $R_o = 0$. It can be seen that the models predict, qualitatively, the measured variation of u_* with R_o on both the leading

and trailing sides. Howard's model gives better results for the leading side. The author's model underestimates $|1 - u_* / (u_*)_0|$ on both sides while Howard's model overestimates $|1 - u_* / (u_*)_0|$ on the trailing side. Even though it is difficult to state which of the two models performs better, it must be emphasized that the authors' modification is derived through a procedure based on the Reynolds stress equations

CONCLUDING REMARKS

Modifications to the k- ϵ model to account for the non-alignment of the shear stress vector with the mean strain vector and for the effects of rotation have been proposed and tested. The modified T-model gave encouraging results for the flow over a rotating cylinder, but it needs further testing in more complex three-dimensional boundary layers. The study showed that the rotation effects can be accounted through the modified coefficient C_{μ} . The present study has also illustrated how the k- ϵ model can be extended, with the help of the algebraic stress equations, to account for complex phenomena.

ACKNOWLEDGMENT

This work was sponsored by the National Aeronautics and Space Administration through the Grant NSG 3266 with Dr. P. M. Sockol as the Technical Monitor. The authors wish to thank T. R. Govindan for his valuable suggestions.

REFERENCES

1. Rotta, J. C., "A Family of Turbulence Models for Three-Dimensional Thin Shear Layers," *Turbulent Shear Flows I*, Springer-Verlag, 1979.
2. Galmes, J. M. and Lakshminarayana, B., "A Turbulence Model for Three-Dimensional Turbulent Shear Flows Over Curved Rotating Bodies," AIAA Paper 83-0559, January 1983.
3. Govindan, T. R., "A Space-Marching Method for the Navier-Stokes Equations for Internal Flows," Ph.D. Thesis, Department of Aerospace Engineering, The Pennsylvania State University, 1983 (in preparation).
4. Lohmann, R. P., "The Response of Developed Turbulent Boundary Layer to Local Transverse Surface Motion," *Journal of Fluids Engineering*, pp. 354-361, Vol. 98, No. 3, September 1976.
5. Johnston, J. P., Halleen, R. M. and Lezius, D. K., "Effects of Spanwise Rotation on the Structure of Two-Dimensional Fully Developed Turbulent Channel Flow," *J. of Fluid Mechanics*, 1972, Vol. 56, Part 3, pp. 533-557.
6. Briley, W. R. and McDonald, H., "On the Structure and Use of Linearized Block Implicit Schemes," *J. Comp. Phys.*, December 1979.
7. Gorski, J. J., Govindan, T. R. and Lakshminarayana, B., "Computation of Three-Dimensional Turbulent Shear Flows," AIAA Paper 83-1733, 1983.
8. Patankar, S. V. and Spalding, D. B., "A Calculation Procedure for Heat, Mass and Momentum Transfer in Three-Dimensional Parabolic Flows," *Int. J. of Heat Mass Transfer*, 1972, Vol. 15, pp. 1787-1806.
9. Jones, W. P. and Launder, B. E., "The Calculation of Low Reynolds Number Phenomena With a Two-Equation Model of Turbulence," *J. of Heat and Mass Transfer*, Vol. 16, pp. 1119-1130, 1973.
10. Sharma, B. I., "Computation of Flow Past a Rotating Cylinder With an Energy-Dissipation Model of Turbulence," AIAA J., Vol. 15, No. 2, 1977, pp. 271-274.

11. East, L. P., "Measurements of the Three-Dimensional Incompressible Turbulent Boundary Layer Induced on the Surface of a Slender Delta-Wing by the Leading Edge Vortex," ARC RM 3768, 1973.
12. Rodi, W., "A New Algebraic Relation for Calculating the Reynolds Stresses," Z. Ange. Math. Mech., Vol. 56, 1976, pp. 219-221.
13. Cousteix, J., "Integral Method and Turbulence Models Applied to Three-Dimensional Boundary Layers," in Three-Dimensional Turbulent Boundary Layers, Ed: Fernholz, H. H. and Krause, E.; Springer-Verlag, pp. 286-297, 1982.
14. Howard, J. H. G., Patankar, S. V. and Bordinnik, R. M. "Flow Prediction in Rotating Ducts Using Coriolis-Modified Turbulence Models, J. Fluids Engineering, Vol. 102, 4, pp. 456-461, 1980.
15. Humphreys, D. A. et al., "Workshop in Three-Dimensional Boundary Layer Calculations," April 1, 1982, Berlin (to be published).
16. Kreskovsky, J. P., Briley, W. R. and McDonald, H., "Turbofan Forced Mixer-Nozzle Internal Flow Field," NASA CR-3494, 1982.

THE EFFECT OF ROTATION ON TURBULENCE STRUCTURE

John Kim
NASA Ames Research Center
Moffett Field, CA 94035

ABSTRACT

Rotating turbulent channel flow has been simulated numerically using the large-eddy-simulation technique. With a three-dimensional, time-dependent, numerical simulation of turbulence, it was possible to obtain detailed flow-field information which had not been available previously from experiments. This information was used to study the structure and statistical properties of the flow with externally imposed rotation. It was found that in agreement with experimental observations, the Coriolis force introduced by the system rotation could stabilize/destabilize turbulence. The large-scale motion observed in the experiment was also found to exist in the computed flow field.

INTRODUCTION

Understanding the turbulent flow in the blade passages of turbomachines is essential for improving the efficiency of such devices. Since the flow is periodically unsteady to an observer in a stationary frame, it is most easily analyzed in the reference frame that rotates with the blades. Analytically, the transformation between the two coordinate systems is straightforward: one only needs to add the Coriolis accelerations in the equations of motion. For incompressible flow, the centrifugal force can be included into the pressure term unless boundary conditions prohibit it. Experimentally, however, this is not an easy task since the whole test facility has to be mounted on a rotating system. Despite this difficulty, some experimental results are available in the literature because of the work done on this flow by many interested engineers who wished to improve the efficiency of turbomachines (see Johnson (1970) for an extensive review of the subject matter).

The objective of this study is to investigate the effect of rotation on the turbulence structure through a reliable numerical simulation. Recently, the large-eddy-simulation (LES) approach has shown considerable promise in investigating the physics of turbulence (e.g., Reynolds (1981), Moin and Kim (1982) (hereafter MK), Kim (1983)). In LES, the large-scale flow field is obtained by directly integrating the filtered, three-dimensional, time-dependent Navier-Stokes equations. The small-scale motions are simulated with an eddy viscosity model. Since LES can produce detailed flow structures as well as time-averaged turbulence statistics, it is possible to supplement the experimental data and to gain a better understanding of the physics of the flow field.

In this paper the numerical results obtained from simulating the flow studied experimentally by Johnson et al. (1972) (abbreviated JHL, hereinafter) are presented. Their experiment consisted of a channel on a rotating table, with the mean flow perpendicular to the rotation axis. The channel had a high aspect ratio, and the mean flow was two-dimensional in the planes

perpendicular to the rotation axis (Fig. 1). The objective of the experiment was to investigate the effects of spanwise rotation on turbulence structures. They showed that the Coriolis force introduced by the system rotation could stabilize turbulence near one of the walls (stable side) and destabilize turbulence near the other (unstable side). In addition, they observed the following three rotation-induced phenomena: (1) the reduction (increase) in the rate of bursting of wall-layer streaks in locally stabilized (destabilized) wall layers; (2) the total suppression of transition to turbulence in a stabilized layer; and (3) the development of large-scale roll cells on the destabilized side of the channel. The last two phenomena were observed only for rotation rates beyond critical values. Most of their results, however, were based on their flow-visualization work and lacked much desired quantitative information. For example, no turbulent quantities were measured: instead, they used the wall-shear velocity as a measure of the turbulence intensity close to the wall. The present investigation was undertaken with the expectation that more quantitative information with regard to the effect of rotation would benefit both the designer of turbomachinery and a turbulence modeler who would like to add such an effect into a model.

GOVERNING EQUATIONS

The dynamic equations of motion and the continuity equation for an incompressible fluid with respect to the reference frame rotating at a steady rate Ω can be written as follows:

$$\frac{\partial \mathbf{u}}{\partial t} + \mathbf{u} \cdot \nabla \mathbf{u} = -\nabla P + 2\Omega \times \mathbf{u} + \nu \nabla^2 \mathbf{u} \quad (1)$$

$$\nabla \cdot \mathbf{u} = 0 \quad (2)$$

where $\Omega = (0, 0, \Omega)$ for the present problem since the axis of the rotation is parallel to the spanwise direction, z . The second term on the right side of equation (1) is the Coriolis force due to the rotation, and the term arising from the centrifugal force is included in the pressure term; the rotation-induced centrifugal force does not play an essential role in determining the velocity field. Applying the filtering operation (Moin and Kim (1982)) to equations (1) and (2), we obtain the equations for the large-scale flow field,

$$\frac{\partial \bar{\mathbf{u}}}{\partial t} + \bar{\mathbf{u}} \cdot \nabla \bar{\mathbf{u}} = -\nabla \bar{P} + 2\mathbf{Ro} \times \bar{\mathbf{u}} + \frac{1}{\text{Re}_\tau} \nabla^2 \bar{\mathbf{u}} + \text{SGS} \quad (3)$$

$$\nabla \cdot \bar{\mathbf{u}} = 0 \quad (4)$$

where we have decomposed $\mathbf{u} = \bar{\mathbf{u}} + \mathbf{u}'$ for the large-scale and sub-grid scale components, and SGS represents the modeling term due to the sub-grid scale motions. Here, the flow variables are nondimensionalized using the channel half-width, δ , and the wall shear velocity of the

nonrotating channel flow, u_{T0} . Thus the Reynolds number and the rotation number are defined as $Re_T = u_{T0} \delta / \nu$ and $Ro_T = 2\Omega u_{T0} / \delta$ with $Ro = (0, 0, Ro_T)$.

Equations (3) and (4) are integrated numerically with the same method as MK which employs pseudospectral approximation in the homogeneous directions (i.e., streamwise and spanwise), a finite-difference approximation in the direction normal to the wall, and a semi-implicit time-advancement. The computations are carried out using $64 \times 64 \times 128$ grid points in the streamwise, normal-to-the-wall, and spanwise directions (x, y, and z, respectively). The initial field was the result of the fully developed channel flow of MK for a Reynolds number of 13,800, based on centerline velocity and channel half-width, i.e., $Re = U_c \delta / \nu = 13,800$. The same Reynolds number (corresponding to $Re_T = 640$) was used for the present work, and the Rotation number was set at $Ro = 2\Omega u_{T0} / \delta = 0.068$ (corresponding to $Ro_T = 1.47$). The same Reynolds number was used in order to compare directly the present results with the results of MK for the effect of the imposed rotation. This particular Rotation number was selected because here the flow remains turbulent at both sides of the channel and the large-scale vortical cell structures were observed on the unstable side according to the experiment of JHL.

RESULTS

Starting from the initial field, the governing equations were integrated in time until the numerical solutions reached a statistically steady state. This equilibrium state was identified by the energy balance of each of the Reynolds stress equations. Once we reached this statistical steady state, we integrated further in time to get a running-time average of the horizontally averaged turbulence quantities.

Figure 2 shows the mean velocity profile (\bar{u}) (unless otherwise stated, in this section $\langle \rangle$ indicates horizontal as well as time averaging) nondimensionalized by the centerline velocity. A profile from JHL is also plotted for comparison (the actual data were taken from a table in Halleen and Johnston (1967)). Other than the obvious experimental scatter, the agreement between the two results is very good. Both results show the asymmetry introduced by the imposed rotation. In the figure, $y/\delta = -1$ corresponds to the lower wall (unstable side with the direction of rotation as given in Fig. 1). Figure 2 shows the wall shear on the unstable side is increased whereas it is decreased on the stable side. The wall shear velocities for both sides normalized by the nonrotating channel are shown in Figure 3, together with the results from JHL for various Rotation numbers. The predicted wall shear velocity for both walls is in good agreement with the experiment. Figure 4 shows the mean-velocity profiles in wall units. The computed profiles in closed symbols show the same trend as did the experimental results from Halleen and Johnston (1967) for three different conditions (three different Rotation numbers with slightly different Reynolds numbers): both results indicate substantial deviation from the conventional log-law. It appears from the above figures that the computed results agree quite well with the experimental results.

The profiles of turbulence intensities are shown in Figure 5. Note that all intensities are nondimensionalized by the wall shear velocity of the nonrotating channel corresponding to the same Reynolds number. Also, unless otherwise stated, all the quantities presented in this section are only for resolvable or large-scale parts; the contribution from the sub-grid scales is usually negligible, except where very close to the walls. To show the effect of the rotation, turbulence intensities for the nonrotating channel are also included in the figure. This shows the increase/decrease of turbulence intensities owing to the destabilizing/stabilizing effect of the Coriolis force. On the stable side, all the turbulence intensities are decreased significantly. On the unstable side, an increase in \bar{v}_{rms} and a slight increase in \bar{w}_{rms} are noticeable. In addition, \bar{u}_{rms} decreased substantially in the region around

$-0.9 \leq y/\delta \leq -0.3$. This is because the additional terms that appear in each energy equation ($4\Omega \langle \bar{u}\bar{v} \rangle$ in $\langle \bar{u}^2 \rangle$ equation and $-4\Omega \langle \bar{u}\bar{v} \rangle$ in $\langle \bar{v}^2 \rangle$ equation) transfer energy from $\langle \bar{u}^2 \rangle$ to $\langle \bar{v}^2 \rangle$ on the unstable side where $\langle \bar{u}\bar{v} \rangle$ is negative. The opposite is true for the stable side. Thus, the Coriolis force affects turbulence intensities in such a way that, except near the walls, the components of the fluctuating velocities become more isotropic on the unstable side and more anisotropic on the stable side. An examination of the one-dimensional spectra indicates that this trend toward isotropy/anisotropy is achieved by redistributing energies in low wave numbers as shown in Figure 6.

In phenomenological turbulence modeling, one has to construct models for the correlations that appear in the governing equations for the Reynolds stresses. The terms in the equations are computed to provide the data needed to improve the effect of rotation models. Figure 7 presents the terms that appear in the energy equation. Figures 7(a) and 7(b) show the dramatic effect of the Coriolis force on each term (see Fig. 17 in MK for non-rotating channel). Note that there is no explicit dependence on the Coriolis force in the energy equation since the extra terms in the $\langle \bar{u}^2 \rangle$ and $\langle \bar{v}^2 \rangle$ equations are cancelled out. Therefore each term is implicitly affected by the rotation through the direct influence of Ω on \bar{u} and \bar{v} . We also note that on the unstable side the location of the maximum production is not changed ($y^+ \approx 15$) although the maximum magnitude is increased by about 30%. However, on the stable side, the maximum magnitude occurs at $y^+ \approx 50$ with a rather flat profile. It is also interesting to note that the dissipation term is also significantly increased/decreased to balance the increase/decrease of the production. And there is no abnormal behavior in the convection (turbulent diffusion) terms. This implies that no extra turbulence energy is being transferred from the unstable side to the stable side; rather it seems to dissipate more or less locally.

Bradshaw (1969) uses the gradient Richardson number, Ri , as a parameter of local stability describing the effect of rotation or streamline curvature on a turbulent flow. The gradient Richardson number is defined as

$$Ri = \frac{-2\Omega(\partial \bar{u} / \partial y - 2\Omega)}{(\partial \bar{u} / \partial y)^2} \quad (5)$$

For a positive Ri , local stability is enhanced; instability is enhanced with a negative Ri . The mixing length, $l = -\langle \bar{u}\bar{v} \rangle / (\partial \bar{u} / \partial y)$, is shown as a function of Ri in Figure 8. Note that the mixing length is nondimensionalized by the mixing length of nonrotating channel, l_0 . The mixing length increases with a negative Ri and decreases with a positive Ri as shown in the figure, and the "Monin-Oboukhov" formula of the type $l/l_0 = 1 - 8Ri$ is shown in the figure for $\beta = 2$ and $\beta = 4$. Also shown in the figure are the results for a higher Rotation number, $Ro = 0.21$. It should be noted that at this Rotation number the statistical steady state has just been achieved and the results are not time-averaged and must be taken with some care. Figure 8 shows β is about 2 on the unstable side and between 2 and 4 on the stable side. Bradshaw (1969) estimated (from Halleen and Johnston (1967)) β to be about 2 for the unstable side and about 4 for the stable side, while Johnston (1970) reported the data being scattered around $\beta = 4$. Although Bradshaw and Johnston used the same data, they used different approaches to get the estimate of β . Bradshaw used the deviation of the mean profile from the conventional log-law, whereas Johnston estimated directly from their measurement of mixing lengths, which involved differentiations of mean velocities.

Detailed structures of the computed flow field are investigated by examining contour plots of the instantaneous velocity, pressure, and vorticity field. To highlight the effect of rotation on turbulence structures, the results for the higher Rotation number, $Ro = 0.21$, are used in the remainder of this paper. The difference is less striking if the results for $Ro = 0.068$ were used; otherwise the same effect is observed. Figure 9 shows the contour plots of streamwise fluctuating velocity in an (x,z) plane. In all the contour

plots shown here, solid lines are for positive values and dashed lines are for negative values. The wall-layer streak structures (Kline et al. 1967) are evident in this figure. More streaks are noticeable on the unstable side (Figure 9(a)) than on the stable side. It appears from this figure that the number of streaks is directly related to the wall shear. On the unstable side there are more streaks and an increase in the wall shear; on the stable side, the opposite is true. This implies that it is possible to achieve reduction in drag by finding a way of suppressing the formation of streaks in the sublayer.

Figure 10 shows contours of streamwise vorticity in a (y, z) plane. Note that the direction of the mean flow is perpendicular to the plane and the lower wall corresponds to the unstable side. First we notice large concentrations of streamwise vorticity near the lower wall where they seem to appear as pairs of opposite signs, indicating the existence of counterrotating streamwise vortices. Also, there is evidence of large-scale vortical structures a little farther away from the wall. On the other hand, the contours on the upper wall (stable side) display relatively quiet motions without much evidence of organized structures. Figure 11 shows contour plots of turbulent shear stress in an (x, y) plane. In the lower side of the channel (unstable side), negative values contribute to the positive turbulence production; on the upper wall, positive values contribute to the production. Again, the stabilizing/destabilizing effect of the Coriolis force is evident. Also we note that the occurrence of high shear is spotty (localized in space) indicating high intermittency of the shear stress.

A computer-generated motion picture that simulated flow-visualization experiments with hydrogen-bubble wires was made to obtain a better idea of the dynamic structure of the flow. At regular intervals, particles were generated along the lines parallel to and normal to the walls. These particles were traced in time to visualize the unsteady nature of the flow field. These numerically generated bubbles clearly showed the stabilizing/destabilizing effect on the turbulence structures due to rotation. (The motion picture will be shown during the presentation at the Conference.)

In the experiment of JHL, a new type of structure was observed when the Rotation number was increased beyond 0.04; a spanwise array of large-scale vortex cells or roll cells were observed on the unstable side. The size of these roll cells was about the channel half-width. Similar large-scale vortical structures are observed in the present motion picture; a frame is shown in Figure 12 to illustrate this large-scale structure. The figure shows an end view of the structure with the mean flow perpendicular to the plane (see Fig. 13 of JHL). Particles are generated along the lines parallel to the walls located at three different y locations: $y/\delta = -0.98$, $y/\delta = -0.5$, and $y/\delta = 0.98$. Particles generated from the horizontal line at $y/\delta = -0.5$ form the shape of roll cells as they move downstream. Also shown in the figure is the formation of streaks and the ejection away from the wall on the unstable side, while all the particles on the stable side remain very close to the wall. This indicates no ejection is taking place on the upper wall during the time of the motion picture.

SUMMARY

Numerical results of rotating turbulent channel flow at Reynolds number 13,800 and Rotation number 0.068 are presented. Calculations were carried out by LES techniques using $64 \times 64 \times 128$ mesh points. The agreement of the computed mean quantities with experimental data is good. With a three-dimensional, time-dependent, numerical simulation, it is possible to obtain detailed flow-field information which had not been available from experiments. This information was used to study the structure and statistical properties of the flow field due to externally imposed rotation. All the terms that appear in the turbulent energy equation were computed. These data could be used to improve the phenomenological turbulence modeling. It was found that, in agreement with experimental observations, the Coriolis force introduced by the system rotation could stabilize/destabilize turbulence. The spacings between streaks

in the wall region were directly related to the shear stress at the wall: i.e., the small streak spacing yields high wall shear stress and vice versa. The large-scale motion observed in the experiment was also found to exist in the computed flow field.

REFERENCES

- Bradshaw, P., 1969, "The Analogy Between Streamline Curvature and Buoyancy in Turbulent Shear Flow", *J. Fluid Mech.*, 36, p. 177.
- Halleen, R. M., and Johnston, J. P., 1967, "The Influence of Rotation on Flow in a Long Rectangular Channel - An Experimental Study", Report MD-18, Department of Mech. Engineering, Stanford University.
- Johnston, J. P., 1970, "The Effects of Rotation on Boundary Layers in Turbomachine Rotors", Report MD-24, Department of Mech. Engineering, Stanford University (see also NASA Special Paper, no. 304).
- Johnston, J. P., Halleen, R. M., and Lezius, D. K., 1972, "Effects of Spanwise Rotation on the Structure of Two-Dimensional Fully Developed Turbulent Channel Flow", *J. Fluid Mech.*, 56, p. 533.
- Kim, J., 1983, "On the Structure of Wall-Bounded Turbulent Flows", to appear in *Phys. Fluids*; see also NASA TM 84313, April, 1983.
- Kline, S. J., Reynolds, W. C., Schraub, F. A., and Runstadler, P. W., 1967, "The Structure of Turbulent Boundary Layers", *J. Fluid Mech.*, 30, p. 741.
- Moin, P., and Kim, J., 1982, "Numerical Investigation of Turbulent Channel Flow", *J. Fluid Mech.*, 118, p. 341.
- Reynolds, W. C., 1981, "Simulation of Turbulent Shear Flows: What Can We Do and What Have We Learned?", Proc. of the Seventh Biennial Symposium on Turbulence, Rolla, Missouri, September 21, 1981.

AD-A135 034

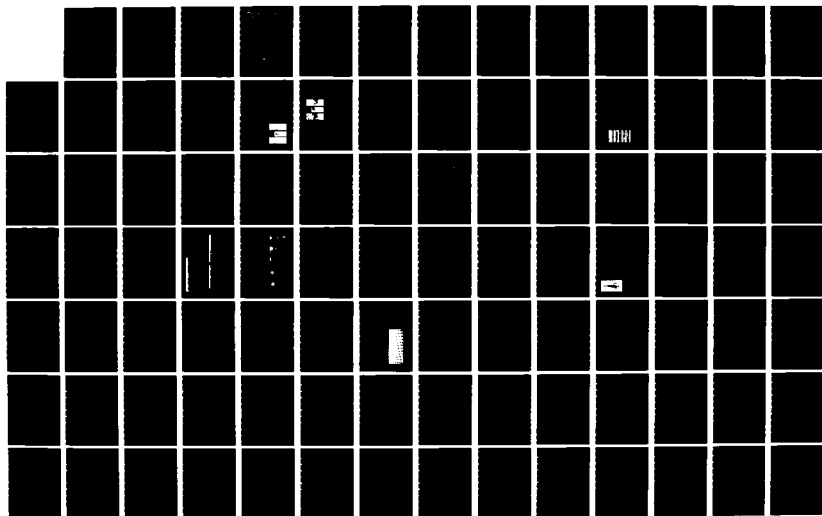
SYMPOSIUM ON TURBULENT SHEAR FLOWS (4TH) HELD AT
KARLSRUHE UNIVERSITY (GERMANY FR) 12-14 SEPTEMBER 1983
(U) KARLSRUHE UNIV (GERMANY F R) SEP 83

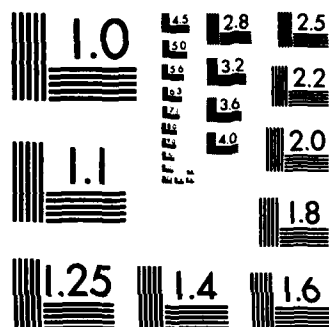
3/7

UNCLASSIFIED

F/G 20/4

NL





MICROCOPY RESOLUTION TEST CHART
NATIONAL BUREAU OF STANDARDS-1963-A

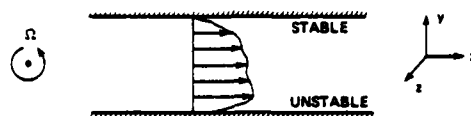


Figure 1. Turbulent flow in a rotating channel.

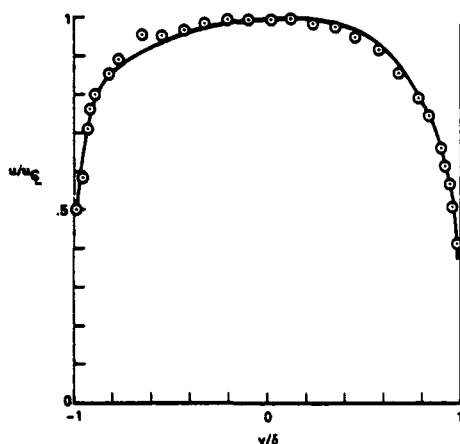


Figure 2. Mean velocity profile: \circ , Johnston et al., $Re = 6,570$ and $Ro = 0.068$; —, computation, $Re = 13,800$ and $Ro = 0.068$.

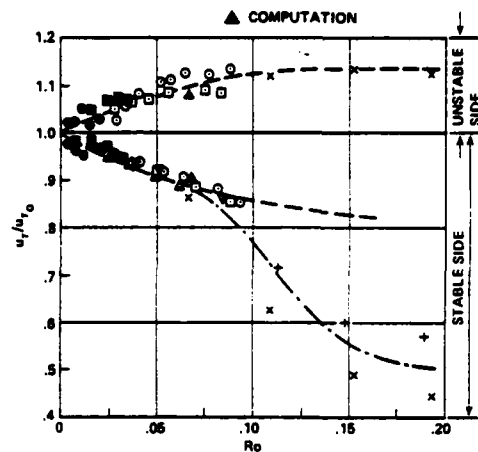


Figure 3. Wall shear velocity normalized on zero-rotation value at the same Reynolds number: Δ , present result; other symbols from Johnston et al.

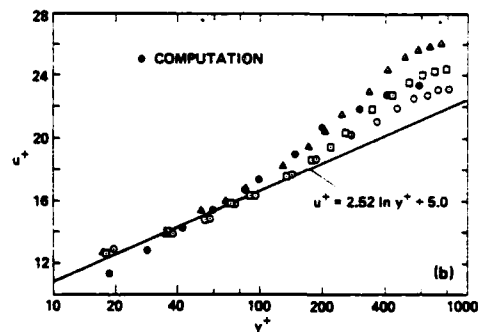
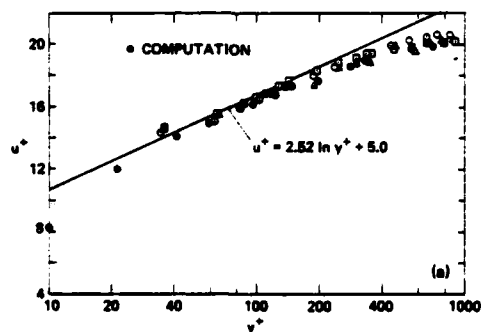


Figure 4. Mean velocity profile in wall unit: \bullet , present results; other from Johnston et al. (a) Unstable side. (b) Stable side.

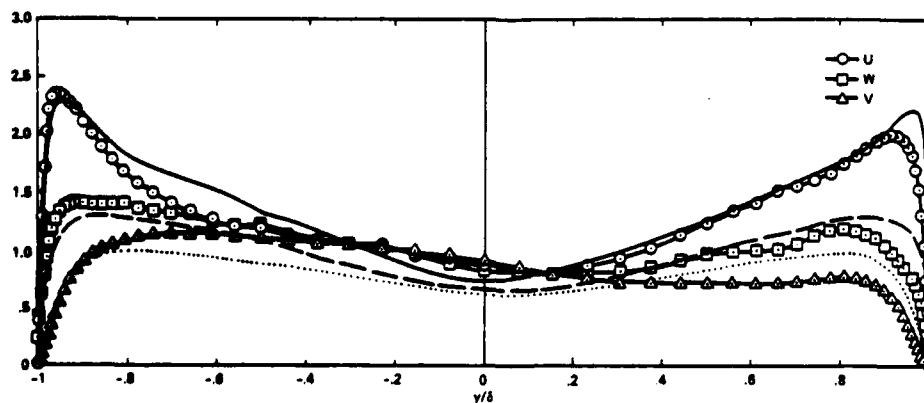


Figure 5. Profiles of turbulence intensities: \circ, Δ, \square , u, v, w for rotating channel; —, ..., —, u, v, w for nonrotating channel.

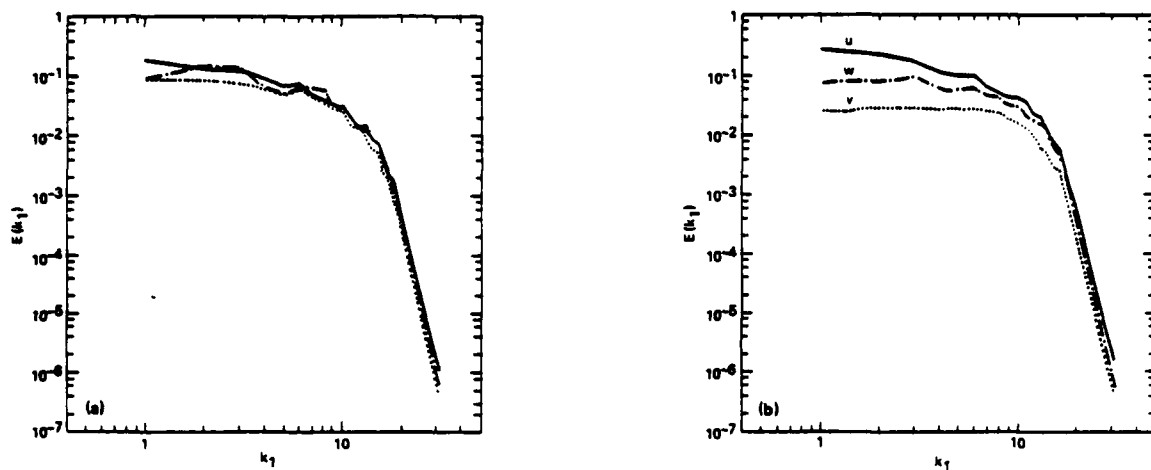


Figure 6. One-dimensional energy spectra at $y/\delta \approx 0.25$: (a) Unstable side; (b) Stable side.

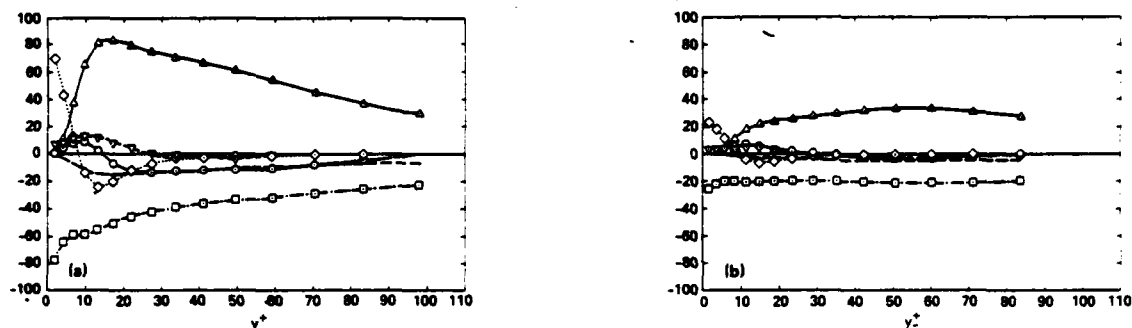


Figure 7. Energy balance for the kinetic energy equation: Δ , production; \square , dissipation; \diamond , viscous diffusion; \circ , convection; $--$, cascade; ∇ , velocity-pressure gradient. (a) Unstable side. (b) Stable side.

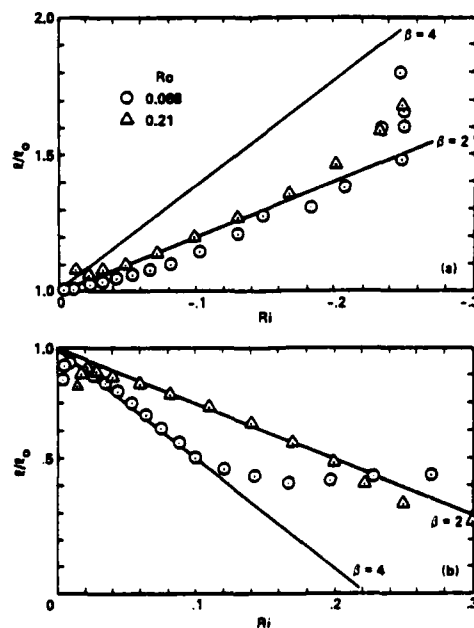


Figure 8. Mixing length as a function of the gradient Richardson number: (a) Unstable side; (b) Stable side. The straight lines represent $l/l_0 = 1 - \beta Ri$.

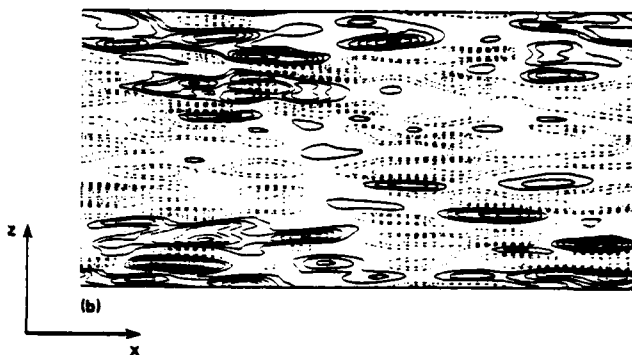
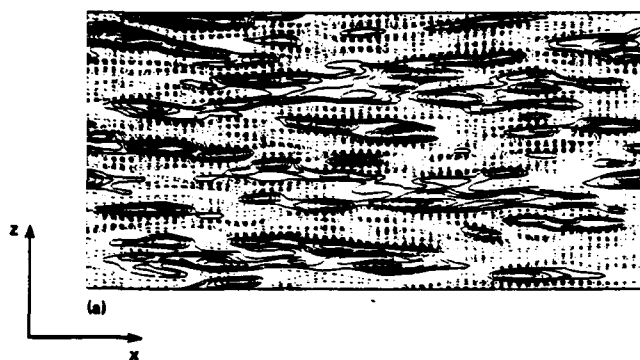


Figure 9. Contours of streamwise velocity in an (x-z) plane. (a) Unstable side, $y^+ = 12$; (b) Stable side, $y^+ = 9$.

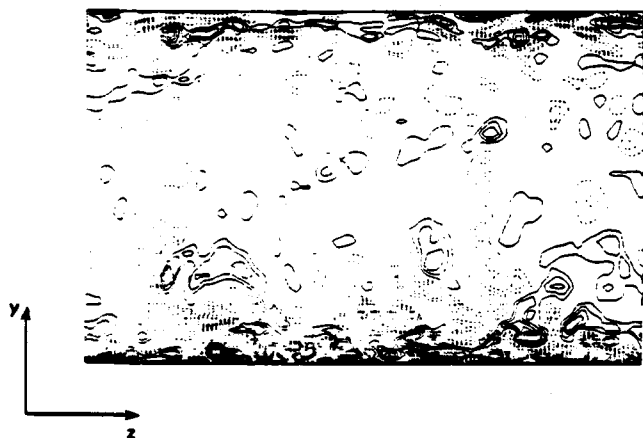


Figure 10. Contours of streamwise vorticity, ω_x , in a (y-z) plane.

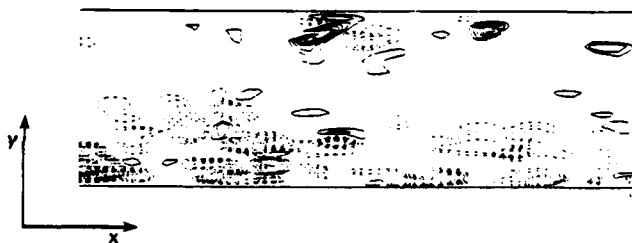


Figure 11. Contours of Reynolds shear stress in an (x-y) plane.

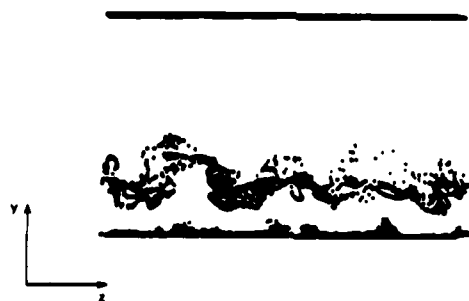


Figure 12. End view of large-scale structure in a rotating channel flow.

TURBULENT MOMENTUM AND HEAT TRANSPORT IN
FLOW THROUGH A 180° BEND OF SQUARE CROSS-SECTION

S.M. Chang J.A.C. Humphrey
Department of Mechanical Engineering,
University of California, Berkeley,
USA.

R.W. Johnson B.E. Launder
University of Manchester Institute of
Science & Technology,
Manchester, England.

ABSTRACT

The paper reports flow and heat transfer predictions of turbulent flow in passage around a 180° square-sectioned bend. The numerical results are obtained from a finite-volume discretization of the semi-elliptic form of the Navier Stokes and energy equations. The turbulent stresses are represented by the $k-\epsilon$ Boussinesq viscosity model both in its standard form and with a streamline curvature correction. Serious differences between experiment and prediction exist for both forms and suggestions are made for their origin. Heat transfer computations indicate that from 45° - 180° the secondary flow provokes at least a 2:1 circumferential variation in heat transfer coefficient around the duct perimeter and that differences of 40% between the mean heat transfer coefficient in each wall persist at least 10 diameters downstream.

1 INTRODUCTION

Computers and flow solution schemes have developed to a point where serious numerical studies of convective heat transfer in complex, 3-dimensional flows can now be made. But, for turbulent flow, what level of accuracy can one expect from such a simulation? The question is of great practical interest for if the accuracy can be relied on within the allowable tolerances the cost of computation - typically a few hundred dollars per run - will often be negligible compared with the cost of getting the information from experiment. This is the question our research on flow around 180° bends has been addressing.

The 180° -bend flow has several qualities that make it well suited as a bench-mark test case. It has very strong practical connections, especially in heat exchangers, yet its topography is relatively simple. This simplicity means that the flow boundary conditions can be easily and unambiguously reproduced by a computer; it also means that obtaining tolerably accurate numerical solutions (whatever may be the frailties of the physics) is a target within sights - though there may be argument about whether it is yet within range. It is a more challenging flow than the 90° bend that provided one of the test cases at the 1981 Stanford Conference (Kline et al, 1981, 1982) because turbulent stresses generated by the strong secondary flow have longer to act on the mean flow. Moreover, and most importantly, detailed experimental data are available (Chang et al, 1983) with which to draw comparison.

Computations of flow around the 90° square-sectioned bend adopted for the Stanford Conference have been reported by Humphrey et al (1981), McDonald (1982), Abdelmaguid et al (1982), Rodi et al (1982), Moore and Moore (1982) and Chang et al (1982); the first three employ a discretization of the full Navier Stokes equations, the last two adopt a semi-elliptic formulation

in which only the pressure field is stored over the full domain (Pratap and Spalding, 1975) and, necessarily, streamline derivatives in the momentum equations are discarded. All but McDonald's and Moore's studies employed the same mathematical model for the turbulent stress field - the $k-\epsilon$ Boussinesq viscosity model. Yet the flow patterns predicted by these schemes bear only a qualitative resemblance to each other or, for that matter, to the experimental data. The fully three-dimensional discretizations have of necessity to use a coarse grid which has severely limited the numerical accuracy available. The semi-elliptic schemes which have allowed 80 or more streamwise planes (not all, of course, in the bend itself) achieve somewhat better overall agreement with data.

The computations of Moore and Moore (1983) and McDonald (1983) extend through the viscous sublayer to the wall allowing a better numerical resolution of the near-wall region than the $k-\epsilon$ treatments (which apply "wall functions" to bridge the 5% of the flow nearest the wall). This fine-grid approach was also followed in the work of Cousteix et al (1983) for the same conference though they make only a two-dimensional inviscid calculation for the pressure field. The numerical simplification this brings is considerable since a three-dimensional marching scheme may be adopted; in view of the poor agreement obtained, however, it remains questionable whether this basis for obtaining the pressure is useful in bends of small aspect ratio with substantial curvature. Of course, more nodes near the wall means fewer elsewhere; moreover, instead of calculating the dissipation rate ϵ from a transport equation these groups obtained it via a prescribed length scale distribution - with much uncertainty as to the appropriate prescription.

In the intervening two years since computations for the Stanford Conference were made the authors have continued to give attention to curved ducts but, for reasons given earlier, to the 180° bend case.

A detailed mapping of the velocity field by laser anemometry has been made at Berkeley for the curved duct shown in figure 1. These data and preliminary numerical computations are to appear in Chang et al (1983). The present contribution provides a more refined set of computations of this flow and examines the influence of wall boundary conditions and turbulence model on the computed flow pattern. It also reports solutions of the enthalpy equation thus providing predictions of the circumferential distribution of Nusselt number around the duct perimeter.

2. SUMMARY OF NUMERICAL SCHEME

Describing Differential Equations

The stationary, turbulent, incompressible flow of fluid through a curved duct of constant rectangular cross-section is conveniently described through conservation equations in cylindrical coordinates. With coordinates x and r mapping the duct cross-section and

θ the angle of progress along the duct, the describing mean flow equations may be written:

x-momentum

$$U U_x + V U_r + (W/r) U_\theta = -\frac{1}{\rho} p_x + (2\nu U_x - \overline{u^2})_x + r^{-1} (r(\nu(U_r + V_x) - \overline{uv}))_r \quad (1)$$

r-momentum

$$U V_x + V V_r - W^2/r + (W/r) V_\theta = -\frac{1}{\rho} p_r + (\nu(U_r + V_x) - \overline{uv})_x + r^{-1} (r(2\nu V_r - \overline{v^2}))_r - 2\nu V/r^2 \quad (2)$$

θ -momentum

$$U W_x + V W_r + W W/r + (W/r) W_\theta = -\frac{1}{\rho r} p_\theta + (\nu(W_x + r^{-1} U_\theta) - \overline{uw})_x + r^{-2} (r^2(\nu(r(W/r)_r + r^{-1} V_\theta) - \overline{vw}))_r \quad (3)$$

continuity

$$V_r + V/r + r^{-1} W_\theta + U_x = 0 \quad (4)$$

enthalpy

$$U T_x + V T_r + (W/r) T_\theta = ((\nu/\sigma) T_x - \overline{uT})_x + r^{-1} (r((\nu/\sigma) T_r - \overline{vT}))_r \quad (5)$$

Here U, V and W are the mean velocity components in the x, r, θ directions, u, v, w are the correspondingly defined Reynolds stresses, T is the mean temperature and τ the temperature fluctuation. The quantities ν, ρ and σ are respectively the fluid kinematic viscosity, density and Prandtl number. The subscripts x, r and θ denote partial differentiation with respect to the space coordinate in question.

The turbulent stresses are obtained from the Boussinesq stress-strain formula which, in cylindrical coordinates, implies:

$$\begin{aligned} -\overline{u^2} &= 2\nu_T U_x - \frac{2}{3}k; \quad -\overline{v^2} = 2\nu_T V_r - \frac{2}{3}k \\ -\overline{uw} &= \nu_T(W_x + r^{-1} U_\theta); \quad -\overline{vw} = \nu_T(r(W/r)_r + r^{-1} V_\theta) \\ -\overline{uv} &= \nu_T(U_r + V_x) \end{aligned} \quad (6)$$

where, in accordance with the $k-\epsilon$ model

$$\nu_T = c_\mu k^2/\epsilon \quad (7)$$

k being the turbulence energy and ϵ its dissipation rate. These quantities are themselves found from transport equations solved simultaneously with the mean flow variables:

$$\begin{aligned} U k_x + V k_r + (W/r) k_\theta &= r^{-1} (r(\frac{\nu+\nu_T}{\sigma_k} T k_r))_r + (\frac{\nu+\nu_T}{\sigma_k} T k_x)_x \\ &+ \nu_T (2(U_x^2 + V_y^2 + r^{-2} W_\theta^2 + U_r V_x + r^{-1} U_\theta W_x + r^{-1} V_\theta W_r) \\ &+ U_x^2 + r^{-2} U_\theta^2 + V_y^2 + r^{-2} V_\theta^2 + W_x^2 + W_r^2 \\ &+ 2r^{-2} V(2W_\theta + V) - r^{-2} W(2V_\theta + 2r W_r - W)) - \epsilon \end{aligned} \quad (8)$$

$$\begin{aligned} U \epsilon_x + V \epsilon_r + (W/r) \epsilon_\theta &= r^{-1} (r(\frac{\nu+\nu_T}{\sigma_\epsilon} T \epsilon_r))_r + (\frac{\nu+\nu_T}{\sigma_\epsilon} T \epsilon_x)_x \\ &+ c_{\epsilon 1} \nu_T (2(U_x^2 + V_y^2 + r^{-2} W_\theta^2 + U_r V_x + r^{-1} U_\theta W_x + r^{-1} V_\theta W_r) \end{aligned}$$

$$\begin{aligned} &+ U_x^2 + r^{-2} U_\theta^2 + V_y^2 + r^{-2} V_\theta^2 + W_x^2 + W_r^2 \\ &+ 2r^{-2} V(2W_\theta + V) - r^{-2} W(2V_\theta + 2r W_r - W)) - c_{\epsilon 2} \epsilon^2/k \end{aligned} \quad (9)$$

The empirical coefficients are assigned the usual values optimised by Launder et al (1973):

$$c_\mu = 0.09; \quad c_{\epsilon 1} = 1.44; \quad c_{\epsilon 2} = 1.92; \quad q_k = 1.0; \quad \sigma_\epsilon = 1.22$$

The semi-elliptic truncation has been applied to all these equations in that terms containing second derivatives on θ are dropped.

The Difference Equations and their Solutions

Finite-difference forms of the transport equations were derived by integration over discretized volumes in the flow domain following broadly Pratap's (1975) guidelines. As is now customary, the velocity components and pressure are stored on a staggered mesh. Streamwise convective transport is approximated by upwind differences. In the cross-sectional plane, however, both upwind and quadratic upwind (QUICK) options are included. The latter scheme devised by Leonard (1979) has been tested by Han et al (1981) for turbulent flow in a driven cavity and found to be distinctly better than an upwind approximation. (In fact, so far as the cross-stream components are concerned, the flow around a bend is very like a driven cavity). The method of implementing the scheme in the numerical algorithm is as given by Han et al (1981).

In the course of iteration, the adjustments to the pressure field in response to mass imbalances for the control volumes surrounding each pressure node is essentially as proposed in the SIMPLE algorithm (Patankar and Spalding, 1972) except that, with the velocity field held on only two successive θ planes, reorganization is required (Pratap, 1975). At any x - y plane the U and V velocity components are solved first. The streamwise momentum equation is solved next to obtain the W velocity (displaced half a cell down-stream as a result of the 'staggering') using new values of V and U in the convective terms; finally, perturbations to the pressure field are introduced in conjunction with re-adjustments to the current-plane U - V field. This procedure is applied at all planes beginning at the upstream boundary and stepping downstream, successively overwriting 'upstream' velocities by current values. On completing such a pass over the domain the computation starts over again at the upstream end unless the residual error is small enough that convergence is signalled.

Because the computation as outlined above has had to make extensive use of upstream values (rather than current plane values) of velocity in evaluating convection coefficients and sources, a certain upstream bias is introduced into the solution if a purely marching treatment is followed. For this reason, as the computation approaches its apparent solution, it is necessary to introduce iteration on the velocity components at each step. That is to say, when current plane values have been obtained the equations are resolved using current-values as appropriate in -forming coefficients and source terms. Approximately 45 passes were needed, starting from an assumed uniform pressure field to obtain converged results; this was deemed to have been achieved when the magnitude of the mass errors summed over every cell of the domain fell below 1% of the entering mass flow. (Other studies have typically accepted mass errors of 0.5% per plane which is larger by a factor of 50 than tolerated here).

The flow field generated in the duct is symmetric about the mid-plane of the cross-section lying in the plane of the bend. Computations were thus extended over just one half of the duct, the cross-section being mapped by a 15×25 interior grid for most of the results presented here-under with the mesh expanding mildly from each wall. The computations began seven hydraulic diameters upstream of the bend and extended 11.5 downstream; this region was covered by a total of 117 streamwise planes.

Boundary Conditions

Along the symmetry plane the gradients of all but one of the dependent variables were set to zero; the value of U , the velocity normal to this plane, was made zero. On the three sides bounded by the duct wall, wall functions were employed to supply appropriate near-wall sources and sinks to the various dependent variables. Besides the 'standard' wall treatment habitually employed in codes developed by those associated with the Imperial College school (Launder and Spalding, 1974) a more elaborate version originating in the present work has been used. It is an extension of the schemes of Chieng and Launder (1980) and Johnson and Launder (1982). In relation to the present study its most significant feature is that the wall friction opposing the secondary motion is obtained independently of the streamwise velocity by performing the integration $V = \int (\tau_{yx} / \mu_{eff}) dx$

between the wall and the first node. By contrast, the IC wall treatment assumes that the resultant near-wall velocity parallel to the wall obeys the usual logarithmic law (the streamwise and cross-stream wall stress components are then obtained by resolving appropriately).

Flow inlet conditions are detailed in the next section.

3. COMPUTATIONS AND EXPERIMENT COMPARED

The experimental data providing the basis for this comparison are those reported by Chang et al (1983) for a duct in which the mean radius of the bend was 3.35 hydraulic diameters. The flow entering the bend had developed through a straight entry section of $31 D_H$ after being passed through a series of screens to promote shear layer development. Thus, while the flow had not become fully developed there was no inviscid core remaining when the flow encountered the bend. The experiments were taken at a bulk Reynolds number of 56700.

A parallel experiment at UMIST is underway which reproduces, so far as we are able to, the Berkeley test conditions. The apparatus dimensions are twice those of the Berkeley rig and since air rather than water is employed, velocities need to be increased by a factor of 8 to maintain the same Reynolds number. While the main output from the UMIST study will be convective heat transfer data it has served to provide checks on an unexpected feature of the Berkeley measurements. At 90° around the bend their streamwise velocity profile along a radial line had exhibited a pronounced double maximum. This feature while most strongly present on the plane of symmetry was still evident along the line midway between the symmetry plane and the end wall. Figure 2 compares the laser anemometer profiles reported by Chang et al (1983) with those obtained with a pair of slant hot wires at UMIST. It is seen that the double-peak feature is present in both sets of data; indeed, there is very satisfactory agreement between the two realizations of this flow.

Computations were started, as noted, seven hydraulic diameters upstream of the bend using, as initial conditions the velocity and turbulence energy profiles of Melling and Whitelaw (1976). The turbulence energy dissipation rate was assigned as: $\epsilon = k^{3/2} / \lambda$ where the length scale was assigned as the smaller of $\pi/c_u^{3/4}$ times the distance to the nearest wall or $.375 D_H$. The former is consistent with a mixing length varying as κ times the wall distance; the latter imposes a uniform length scale at distances greater than $0.15 D_H$ from any wall. It is our view that the uncertainties in initial conditions make no significant contribution to differences between experiment and computation in the bend itself. In support of this view, experiments at UMIST with a virtually fully developed flow at entry to the bend produced streamwise velocity profiles at 90° only slightly different from those shown in fig. 2.

The computed development of the streamwise and radial velocity components around the bend is shown in figures 3 and 4. Serious discrepancies between computation and measurement quickly develop. At 45° the predicted radial velocity on the centreline is somewhat too low and, as a result, the streamwise calculated profile at this position is biased towards the inside of

the bend while in the experiment the velocity peak is displaced somewhat towards the outer radius. (It appears that the experimental measurement of W_θ , the bulk mean streamwise velocity, may be too low at this position causing all the measured profiles to lie above the prediction; the differences in shape that are present are not affected by this, however). At 90° the differences are more pronounced including the very strong double peak in the measured streamwise profile and its complete absence in the predictions. The radial velocity profiles likewise display a sharp peak near the inner boundary radius that is not reproduced in the computation. Similar anomalies are present at 135° (the experimental data are at 130°) but by 180° (177° for measurements) the streamwise profiles, at any rate, are showing closer agreement; the secondary flow is still seriously in error, however.

Clearly something starts to go quite seriously wrong with the simulation fairly early on in the bend and a substantially different flow pattern is computed at 90° from that measured. In search of the cause of the differences a number of adaptations have been considered. The most recent calculations have benefited from significant mesh refinement in the near-wall region compared with an earlier set (Johnson and Launder 1983) yet the differences in the calculations are small compared with the differences between measurement and calculation. The procedure for finding the secondary wall shear stress seems a particular area of weakness and so a test was made where the wall stresses in the x-y plane were set to zero. This is clearly an incorrect hypothesis but it served to indicate whether wall stress errors could conceivably account for the large differences. The largest difference between the two practices occurs at 135° for which the primary velocity profiles are shown in figure 5. The changes produced by this step slightly improve agreement with experiment and along $2X/D_H = 0.5$ a peak in W near the inner wall is present. Nevertheless large differences remain.

It is well known that the k- ϵ model does not correctly capture the great sensitivity of real turbulence to small amounts of streamline curvature. Although this weakness is intrinsic to the use of the Boussinesq stress-strain relation, for two-dimensional curved flows it has been found possible to imitate the effect of curvature on turbulent shear stresses fairly well by introducing the following term in place of the sink $-c_\epsilon \epsilon^2 / k$ in the ϵ transport equation:

$$-c_\epsilon \frac{\epsilon^2}{k} (1 - 0.2 Ri)$$

where $Ri \equiv (k/cR)^{1/2} W(RW)_R$ is a curvature Richardson number and R is the local radius of curvature of a streamline. This is given by

$$R^{-1} = ((UV_t - VU_t)^2 + (UW_t - WU_t)^2 + (VW_t - WV_t)^2)^{1/2} / K^{3/2} \quad (10)$$

where $U_t \equiv UU_x + VU_y + WU_z$ and $K \equiv (U^2 + V^2 + W^2)^{3/2}$

In places the secondary velocity field resulting from this modification was changed by 20%; the effect on the streamwise velocity, however, was nowhere more than 3% and is thus insignificant compared with the differences here in question. This result could have been anticipated for one could not expect an empirical 'fix' on one stress component in a two-dimensional shear to be satisfactory for all the stress components in a complex three-dimensional flow.

The logical next step in improving the representation of the Reynolds stress is the introduction of an algebraic stress model of turbulence (ASM) in place of the Boussinesq stress-strain relation. Models of this type have been conspicuously successful in mimicking the effects of curvature in two-dimensional shears without the introduction of specially tuned empirical terms (e.g. Rodi et al, 1982). Unfortunately, switching from a model based on a turbulent viscosity to one where the turbulent stresses enter the calculation as sources and sinks is a severely de-stabilizing departure. At the time of writing no converged results have been obtained with the QUICK treatment of convection. With the up-wind scheme, however, convergence has been achieved though largely, we believe, because this approach brings

its own false diffusion to assist stability. Streamwise velocity profiles drawn from these results appear on figure 4 for the 90° position. The particular form of ASM adopted is that which results from applying Rodi's (1976) algebraic transport hypothesis to Gibson and Launder's (1978) second-moment closure proposals. The Gibson-Launder study which considered the case of flow past a single plane wall included terms representing the effects of pressure reflection from the rigid boundary. Here there are four walls present and their effect is assumed to be accounted for by applying a linear superposition; this extends to three-dimensions the usual two-dimensional practice. It is clear from fig. 3 that the introduction of the ASM scheme has brought no improvement in accuracy, somewhat the reverse. Based on earlier experiences with the k-ε Boussinesq model artificial diffusion introduced by upwind differencing modifies the streamwise velocity typically by amounts similar to the difference between the curves representing ASM and k-ε predictions in fig. 4 (and in the same direction). That no improvements are recorded from adopting this higher-level closure can only be said to be extremely perplexing. It is hoped that by the time of the meeting at which this work is formally presented an explanation will have emerged.

The heat transfer behaviour considered in figure 6 is that arising from using the Boussinesq k-ε model. The greatest difference between heat transfer rates on the inside and outside of the bend initially occurs at the centre plane. The secondary flow driving cold fluid towards the outer wall on this plane produces higher heat transfer levels as is typical of impingement conditions. Conversely, on the inside of the bend, the fluid adjacent to the wall has arrived there after travelling relatively slowly over a slightly greater length (due to the secondary motion). This fluid has thus been heated considerably more than that near the outer wall and heat transfer coefficients are thus lower. At 45° the ratio of the Nusselt number on the two sides is 3:1. This difference diminishes with passage around the bend as the secondary and primary flow patterns become more complex; even at 180° however the mean level of Nusselt number is 60% greater on the outer than the inner wall associated with the fact that the faster moving fluid is located near the outer wall (see fig. 3): this produces higher velocity gradients which in turn produce higher kinetic energy level.

Downstream of the bend the secondary flow decays (the maximum radial velocity is only .02 W_b at ten diameters) though the Nusselt number distribution around the duct perimeter remains strongly non-uniform. The mean level of Nusselt in the bend is some 30% higher than is found in a straight tube at the same Nusselt number.

4. CONCLUDING REMARKS

Experiments under identical flow conditions in our two institutions using different methods of measurement have confirmed that at the 90° position in a square-sectioned U-bend the streamwise velocity displays a secondary peak near the inner wall. None of our numerical simulations using relatively fine meshes and the QUICK treatment of convection has succeeded in mimicking this important flow feature. For the present we cannot offer a convincing explanation for this failure: grid refinement in the cross-sectional plane has had little influence while introducing an ASM apparently brings no benefit. There are two steps we propose to take that may bring about a marked improvement. The first is to concentrate a far greater proportion of the streamwise calculational planes in the first 90° of the bend. (The present distribution provides a virtually uniform spacing around the bend and only modest variations in the upstream and downstream tangents). The second will be to abandon, on the flat walls of the bend, the wall-function treatment. Instead, a fine mesh will be introduced, to allow computations to be carried into the viscous sublayer. In this way uncertainties as to the appropriate wall boundary condition are removed. We have found from parallel work in the round-sectioned U-bend that by assuming a radial equilibrium pressure distribution across the viscous

and buffer regions the introduction of a very fine near-wall grid has negligible effect on either convergence rates or storage requirements.

With the velocity field in such relatively poor agreement with data over most of the bend no very definitive conclusions can be drawn from the detailed heat transfer behaviour. However, results very probably give, in their overall pattern, a correct indication of the effects on heat transfer levels: i.e. at least a 2:1 ratio of heat transfer coefficients on the outer and inner curved walls of the bend; a mean level some 30% higher than in a straight duct and a strong non-uniformity in Nusselt number persisting at least 10 diameters downstream.

ACKNOWLEDGEMENTS

The work has been performed at Berkeley and UMIST under a collaborative research agreement sponsored by the US Office of Naval Research through grants NR-097-440 and NR-097-449. Additional funds for computations were provided to UCB by the Office of Fossil Energy through DOE Contract No. DE-AC03-76SF00098.

Thanks are due to Dr. T.Y. Han who during the early stages of the work contributed to the development of the numerical calculation procedure. Miss L. Towers has prepared the camera-ready typescript.

Authors' names appear alphabetically.

REFERENCES

- Abdelmeguid, A.M., Goh, S.Y., Ilegbusi, J. and Spalding, D.B. 1982. Proc. AFOSR-HTTM-Stanford Conf. on Complex Turbulent Flows, vol. III, 1521.
- Chang, S.M., Han, T. and Humphrey, J.A.C. 1982. Proc. AFOSR-HTTM-Stanford Conf. on Complex Turbulent Flows, vol. III, 1375.
- Chang, S.M., Humphrey, J.A.C. and Modavi, A. 1983. Int.J. Physico Chemical Hydrodynamics (to appear).
- Chiang, C.C. and Launder, B.E. 1980. Num. Heat Transfer 3, 189.
- Cousteix, J. et al. Proc. AFOSR-HTTM-Stanford Conf. on Complex Turbulent Flows, vol. III, 1326.
- Gibson, M.M. and Launder, B.E. 1978. J.Fluid Mech. 86, 491.
- Han, T.Y., Humphrey, J.A.C. and Launder, B.E. 1981. Comp.Meth.Appl.Engrg. 29, 81.
- Humphrey, J.A.C., Whitelaw, J.H. and Yee, G. 1981. J.Fluid Mech. 103, 433.
- Johnson, R.W. and Launder, B.E. 1983. Dept. Rep. TFD/83/2LR).
- Johnson, R.W. and Launder, B.E. 1982. Num.Heat Transfer 5, 493.
- Kline, S.J., Cantwell, B. and Lilley, G.K. 1981, 1982 (editors) Proc. 1980-81 AFOSR-HTTM-Stanford Conf. on Complex Turbulent Flows, Thermosciences Division, Stanford University.
- Launder, B.E., Morse, A., Rodi, W. and Spalding, D.B. 1973. Proc. 1972 Langley Free Shear Flows Conf. NASA SP321.
- Launder, B.E., Priddin, C.H. and Sharma, B.I. 1977. J.Fluids Engrg. 98, 763.
- Launder, B.E. and Spalding, D.B. 1974. Comp.Meth. Appl.Mech.Eng. 3, 269.
- Leonard, B.P. 1979. Comp.Meth.Appl.Mech.Engrg. 19, 59.
- McDonald, H. 1982. Proc. AFOSR-HTTM-Stanford Conference on Complex Turbulent Flows, vol. III, 1424.
- Melling, A. and Whitelaw, J.H. 1976. J.Fluid Mech. 78, 289.
- Moore, J. and Moore, J.G. 1982. Proc. AFOSR-HTTM-Stanford Conf. on Complex Turbulent Flows, vol. III, 1453.
- Pratap, S.V. and Spalding, D.B. 1975. Aero.Quart. 26, 219.
- Rodi, W. 1976. ZAMM 56, 219.
- Rodi, W. et al. 1982. Proc. AFOSR-HTTM-Stanford Conf. on Complex Turbulent Flows, vol. II, 1495.

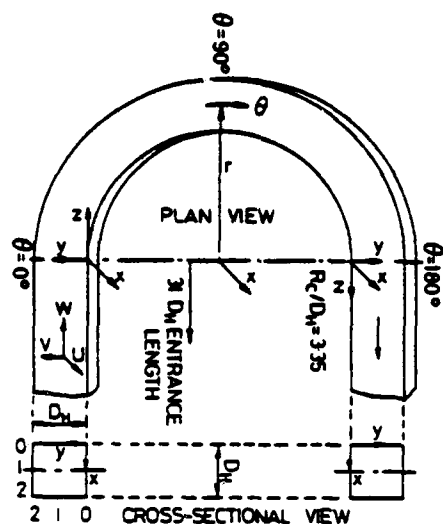


Fig. 1 The flow considered

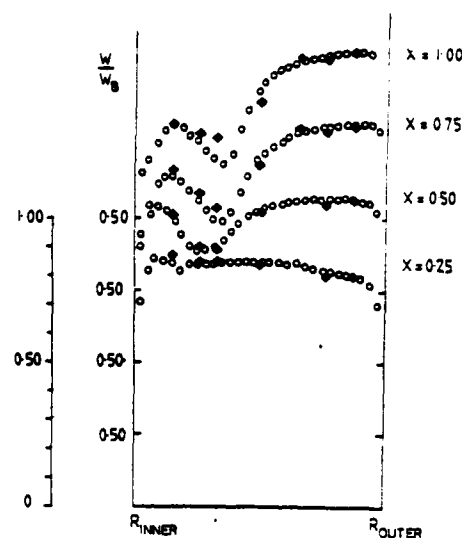


Fig. 2 Comparison of streamwise velocity profiles at 90° .
o - Berkeley data ♦ - UMIST data

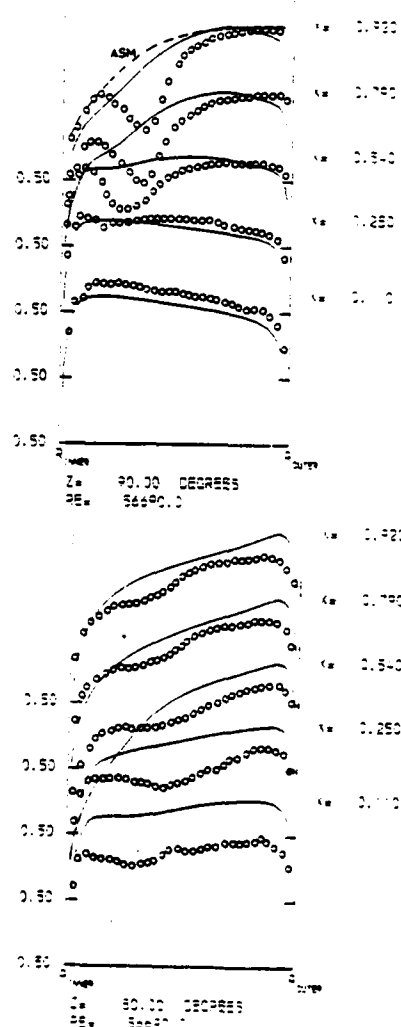
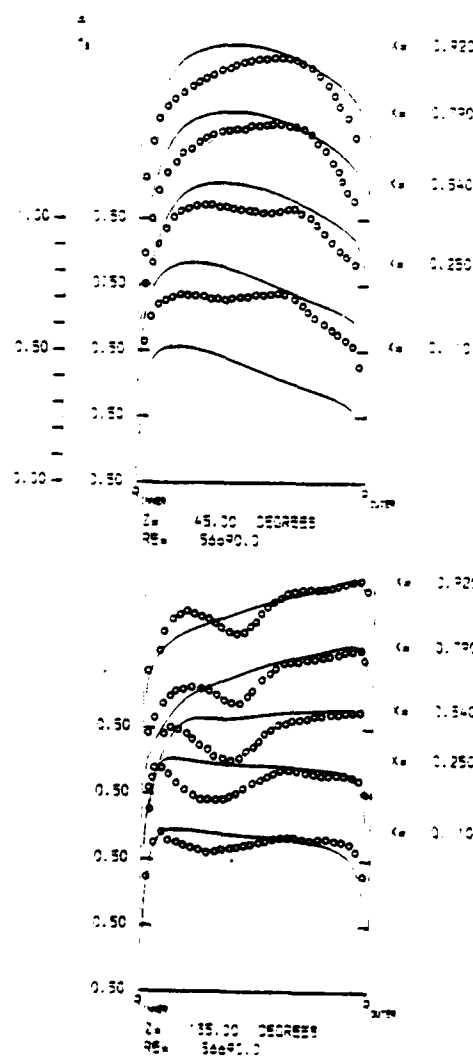


Fig. 3

Streamwise velocity profiles at 45° , 90° , 135° and 180° around the bend

o o Experiment (Chang et al 1983)
— Present predictions

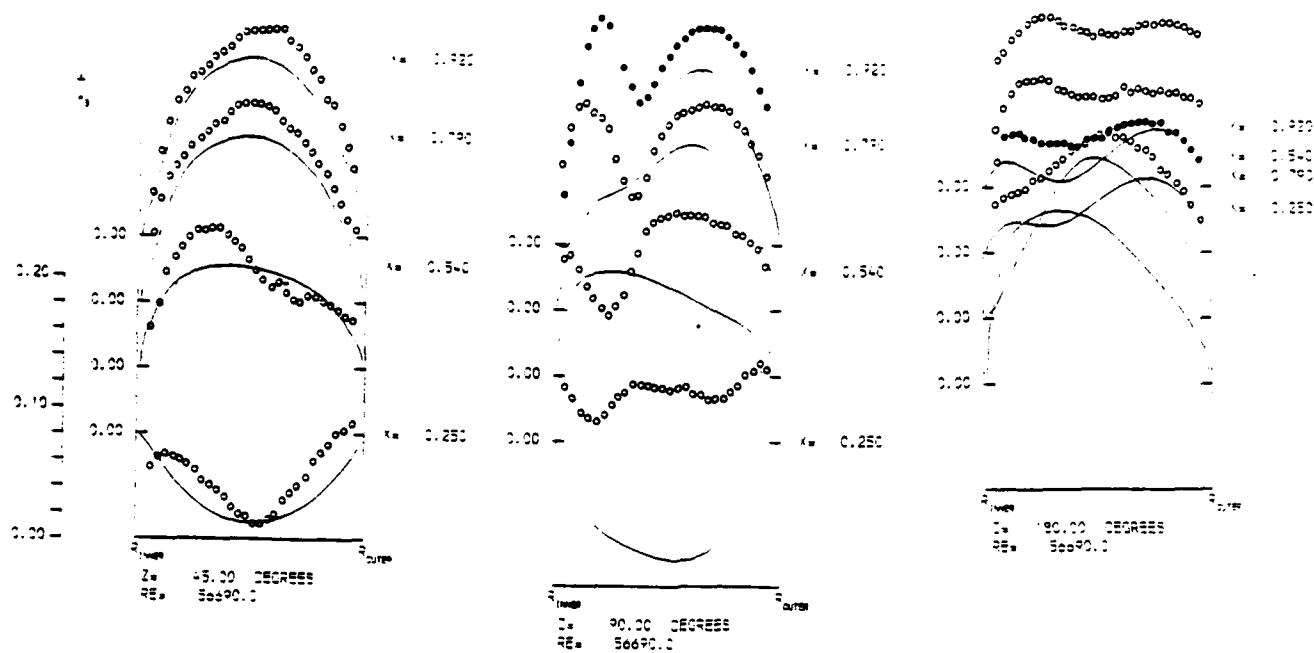


Fig. 4 Radial velocity profiles at 45°, 90° and 180° around bend

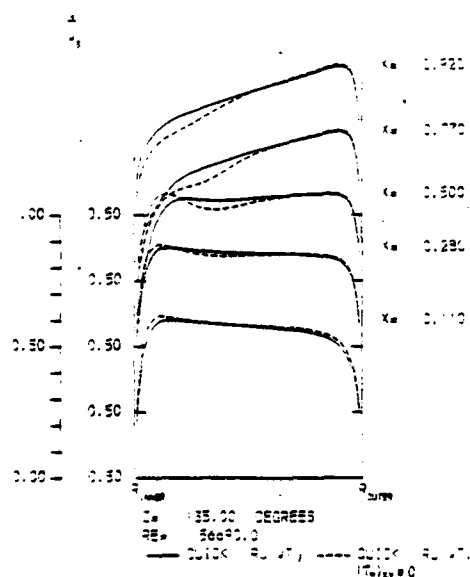


Fig. 5 Effect of removing wall shear stress opposing secondary motion

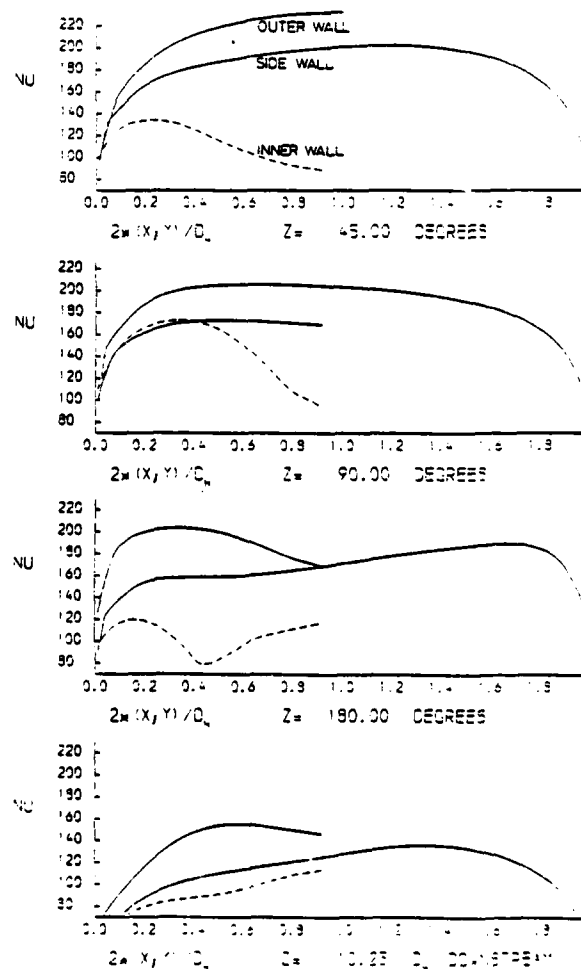


Fig. 6 Development of computed heat transfer coefficient around and downstream of bend

FLOW IN SIGMOID DIFFUSERS OF MODERATE CURVATURE

by

J. Rojas, J.H. Whitelaw and M. Yianneskis
Fluids Section, Mechanical Engineering Department
Imperial College of Science and Technology
Exhibition Road, London SW7 2BX, England

ABSTRACT

Developing laminar and turbulent flows have been measured in two diffusers with S- and C-shaped centre-lines. Small divergence angle and moderate curvature. The square inlet cross-section expanded in the plane of curvature to a rectangle with an exit-to-inlet area ratio of 1.5. Laser-Doppler anemometry was used to measure three velocity components and, in turbulent flow, the associated fluctuations and cross-correlations. Wall static pressure measurements are also reported. Flow visualisation did not reveal the presence of any recirculation regions. Pressure-driven secondary flows are present in both ducts but are generally smaller than those measured in similar ducts of uniform cross-sectioned area.

1. INTRODUCTION

Curved diffusers with S- and C-shaped centre-lines are used in a wide range of engineering situations and the present investigation was motivated by requirements of aircraft intake ducts and the need to evaluate related design procedures. Pressure-driven secondary flows occur in curved ducts and cause distortion of the flow profiles at the duct outlet with possible consequences for compressor performance. The present results quantify the effect of the secondary flows and, in conjunction with previous investigations in ducts of constant cross-sectional area (Humphrey et al. 1977, 1981; Enayet et al. 1982; McMillan, 1982 and Taylor et al. 1982a, b) allow the evaluation of the combined effects of turning and diffusing flows.

Fully-developed laminar and turbulent flows in strongly curved C-shaped ducts have been investigated by Humphrey et al. (1977, 1981), and developing flows by Taylor et al. (1982c). The results show that weaker secondary flows are present in the developing flow case, mainly due to the thinner inlet boundary layers. Enayet et al. (1982) measured the developing flow in a moderately curved 90 degree bend and found cross-stream flows with magnitudes half of those in the strongly curved duct of Taylor et al.

Experimental investigations of developing flow in S-shaped ducts of uniform cross-sectional area have been reported by Taylor et al. (1982a, b) for moderately curved, and by Bansod and Bradshaw (1972) for strongly curved S-ducts. Numerical calculations of the flow in a circular S-duct have been reported by Levy et al. (1983). The measurements of Taylor et al. show that pressure-driven secondary flows are present in the S-ducts and reach maxima of 0.22 and 0.15 of the bulk velocity in the laminar and turbulent flow regimes respectively; in the second bend of the S-ducts a secondary flow in the opposite direction to that in the first bend is established over most of the cross-section. The secondary flow generated in the first bend is sustained, however, near the outer wall of the second bend because of the sign of the local radial vorticity. There are no other investigations of doubly-curved diffuser flows known to the authors. Measurements of developing flow in a unidirectional curved diffuser of 40 degree turning angle, 1.5 area ratio and rectangular cross-section of 1.5 aspect ratio have been reported by McMillan (1982) and show secondary flow vortices similar to those encountered in bends of constant cross-sectional area, with a general deceleration of this flow pattern due to the area increase.

In the present investigation the duct cross-section at the inlet was square ($40 \pm 0.1 \times 40 \pm 0.1$ mm) and, in order to reduce the possibility of flow detachment, thin inlet boundary layers, small centre-line displacement, mild curvature and small diffusing angle (effective total

divergence angle of 2.6 degrees), were employed. The length of the diffuser itself was sufficiently short so that the flow did not become fully-developed.

The present work constitutes an extension to the previous investigations of constant area ducts and, therefore, the principal interest lies in the effect of the area expansion on the flow. A result of the non-existence of separation regions in the flow is that its calculation is amenable to marching techniques. The measurements of laminar and turbulent flows can be used to assess the numerical accuracy of calculation methods and the suitability of turbulence models respectively.

The flow configurations and the experimental apparatus and techniques are described briefly in the following section. The results from the flow measurements are presented in Section 3 and discussed in Section 4. A list of the most important findings is given in Section 5.

2. FLOW CONFIGURATION AND INSTRUMENTATION

2.1 Flow Configuration

The S-diffuser is shown in Figure 1 together with the coordinate system adopted. The test section was constructed from two 22.5 degree bends of 280mm mean radius of curvature: the cross-section of the bends expanded linearly with downstream distance on both curved surfaces to a rectangle ($40 \pm 0.1 \times 60 \pm 0.1$ mm) at the exit after 45 degrees of expansion, with an exit-to-inlet area ratio of 1.5. The ratio of the overall duct length to the centre-line displacement was 5.2. The dimensions of the upstream and downstream tangents matched closely (to within ± 0.1 mm) those of the diffuser inlet and exit, and there were no surface discontinuities at the inflexion plane or elsewhere in the duct. Apart from those related to the area expansion, all other dimensions of the test section were identical to those used by Taylor et al. (1982a). The C-shaped diffuser was assembled with the two 22.5° sectors joined so that they formed a unidirectional bend rather than the double curve of the S.

The coordinate system is also identical to that used by Taylor et al. (1982c). Streamwise distance is measured along the centre-line in hydraulic diameters of the upstream tangent ($D_H = 0.04$ m) from the inlet plane where the expansion begins. Radial distance is measured from the outer wall of the bend (inner wall of the second bend in the case of the S) and spanwise distance from the symmetry plane. The flow rate was measured by precision bore flowmeters, and experiments were made in both bends at Reynolds numbers, based on the hydraulic diameter and bulk velocity (V_b) at the upstream tangent, of 790 and 40000, corresponding to Dean numbers of 212 and 10690 for the laminar and turbulent flows respectively. Water was employed as the working fluid so that the same Reynolds numbers could be obtained at a scale much smaller than that achieved in air, and to allow a high measurement accuracy.

2.2 Laser-Doppler Velocimeter, Experimental Procedure & Accuracy

The laser-Doppler velocimeter was of the dual-beam fringe type and operated in forward scatter. Measurements were made in three directions ($0^\circ \pm 45^\circ$ to the local streamwise direction) in the $X-r$ plane at each measurement point with the beams entering through the side-wall, and the Doppler frequencies measured were resolved to provide the local streamwise (U, U and u), and radial (V, V and v) components and the uv cross-correlations. The spanwise components (W and w) were measured with the beams entering through the curved walls at $r=0$ in the $r-z$ plane. The refraction due to the curvature of the wall, although small, was accounted

for in the location of the measurement points. Frequency shifting was used only for the measurement of the spanwise component. Frequency tracking demodulation was used to process the measured Doppler frequencies. The optical and signal processing systems have been described in detail by Taylor et al (1982c), together with the sources and estimates of experimental error. In brief, systematic errors in the mean velocities are generally of the order of 1% rising to 2-3% in the regions of steep velocity gradients near the walls. The principal characteristics of the optical system are given in the Table below.

Characteristics of the optical arrangement

Focal length of imaging lens (mm)	200
Half-angle of intersection	9.3°
Fringe separation (line-pair spacing)	2µm
Number of fringes in measuring volume	86
Intersection volume diameter calculated at 1/e ² intensity (mm)	0.167
Intersection volume length calculated at 1/e ² intensity (mm)	1.357
Photomultiplier pinhole diameter (mm)	0.50
Transfer constant (MHz/ms ⁻¹)	0.510

Laser-Doppler velocity measurements were obtained in the S-diffuser at five streamwise stations within the diffuser for the turbulent flow, namely, at 0.0 (inlet plane), 1.65, 2.50, 3.85 and 5.50 (exit plane) hydraulic diameters from the entrance plane of the diffuser, and at three stations for the laminar flow, namely, at the 0.0, 2.50 and 5.50 hydraulic diameter stations. To save space, measurements in both regimes are reported at only three stations. In the C-shaped diffuser measurements were made in laminar and turbulent flow at the symmetry and exit planes only.

Wall static pressures were measured with a differential micro-manometer for the turbulent flow cases only as the pressure differences were too small for reliable measurement in laminar flow. The wall pressures were measured at six streamwise stations, located at 1.1, 2.2, 3.3 and 4.4 D_H from the diffuser inlet and at 1.0 D_H upstream of the entry and 1.0 D_H downstream of the exit. Within the diffuser, measurements were obtained at $r^*=0.0, 0.1, 0.3, 0.5, 0.7, 0.9$ and 1.0 at each station. Flow visualization was used to obtain a qualitative description of the flow. The hydrogen bubble technique and dye injection were used to determine and confirm the laminar and steady nature of the flow at the lower Reynolds number and to establish that no recirculation regions were present in either flow regime. Cine and still photography recordings were made of the flow visualization carried out with hydrogen bubbles. Measurements were made on both sides of the symmetry plane in all the flows and showed that the flows were symmetrical within the precision of the measurements.

3. RESULTS

3.1 S-Diffuser: Laminar Flow Results

Visualization of the flow revealed that the profile on the symmetry plane at the inlet is nearly symmetric at $Re=790$, but there is considerable acceleration of the flow near the outer (concave) wall and deceleration along the inner wall of the first bend by $X_H=1.1$. The same trend continues further downstream, with the velocity maximum on the symmetry plane following an almost straight path through the diffuser. In the near-wall region, visualization showed that the

secondary flow is directed towards the inner wall of the first bend, outer wall of the second bend, from $X_H=1.1$ to $X_H=4.4$ (i.e. the secondary flow due to the curvature of the first bend persists well into the second bend). After $X_H=4.4$, the flow is re-directed towards the opposite wall (at $r^*=0.0$) due to the change in the direction of the pressure gradient in the second bend.

The laminar flow velocity measurements are presented in figures 2 and 3 as streamwise component isotachs and radial component profiles, with the values normalised by the bulk velocity at the upstream tangent, $V_b=0.0198$ m/s. The boundary layer thicknesses at the diffuser inlet, defined at 0.95 of the maximum velocity, are approximately 25% of the hydraulic diameter.

The flow in the inlet plane is slightly asymmetric, with the maximum velocity located near $r^*=0.55$ in the symmetry plane. (Figure 2(i)). The radial velocities at the inlet (Figure 3(i)) are always in the same direction towards the inner wall of the first bend: the radial components in the high streamwise velocity "core" flow are small, about $0.015 V_b$, but in the boundary layer fluid near the side wall they increase to about $0.06 V_b$.

By the second measurement station, at $X_H=2.50$, the core flow is moving rapidly towards the outer wall ($r^*=0.0$) and low speed fluid accumulates near the inner wall. ($r^*=1.0$), figures 2(ii) and 3(ii). At this station, the secondary flow due to the duct curvature and the cross-flow due to the movement of the high velocity core (also observed in the flow visualization) complement each other and result in measured velocity maxima of approximately $0.4 V_b$ near the symmetry plane.

The flow at the diffuser exit (Figure 2(iii)) is characterised by an extensive low velocity region near the outer wall of the second bend. The change in the sign of $\partial U/\partial z$ at $r^*>0.5$ and $z^*<0.5$, and, therefore, in the sign of the cross-stream vorticity, results in the persistence of the secondary flow generated in the first bend near the $r^*=1.0$ wall (figure 3(iii)). Near the opposite wall and the side-wall, however, the onset of the secondary flow in the opposite direction is evident due to the curvature of the second bend.

3.2 S-Diffuser: Turbulent Flow Results

The measurements of the mean velocity components, normalised by the bulk velocity at the upstream tangent, $V_b=1.0$ m/s, are shown in figures 4 and 5. Wall pressure measurements are presented in figure 6(i) and the turbulence quantities and cross-correlations for two of the measurement stations are shown in figure 7.

The flow at the inlet to the diffuser (figure 4(i)) is similar to that in the laminar flow case: the flow is nearly symmetric with the velocity maximum located at about $r^*=0.55$, and the radial velocities (figure 5(i)) are comparable to those presented in the previous section. However, there is a much larger "core" flow region, and the boundary layer thickness at the inlet is $0.15 D_H$ for the turbulent case. There are differences also in the migration of the core flow (from $r^*=0.5$ at the inlet to $r^*=0.35$ at the exit) which is found nearer the duct centre-line at the exit than was the case in the

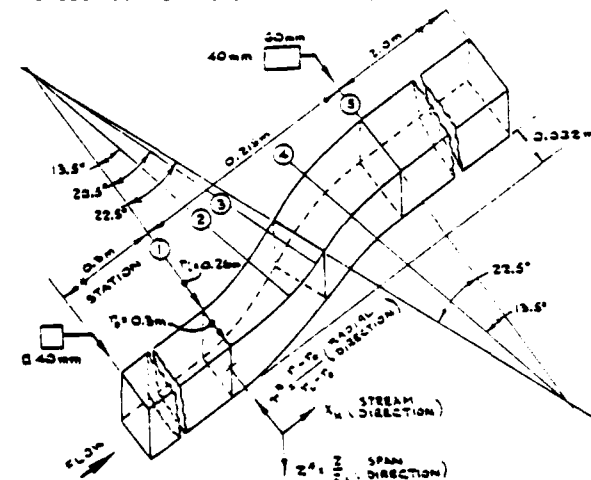


Figure 1 Flow configuration and definition of co-ordinates

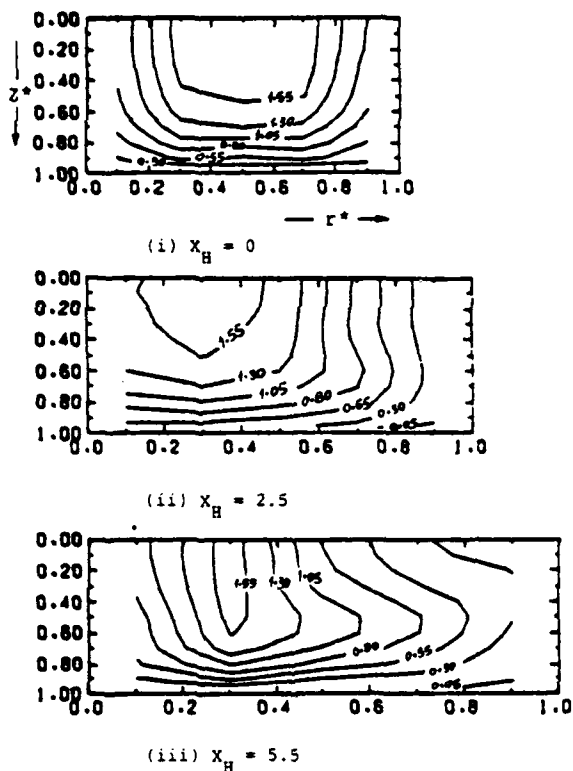


Figure 2 S-diffuser; laminar flow, isotachs of U/v_b

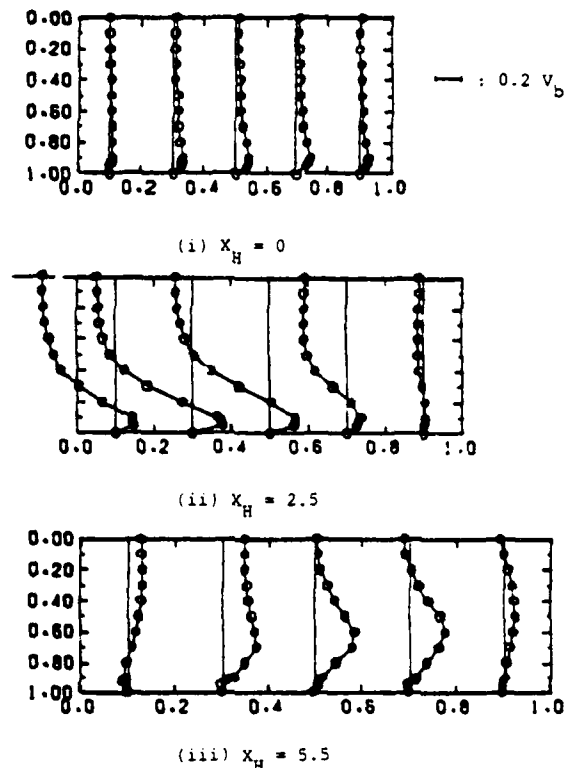


Figure 3 S-diffuser; laminar flow, profiles of V/v_b

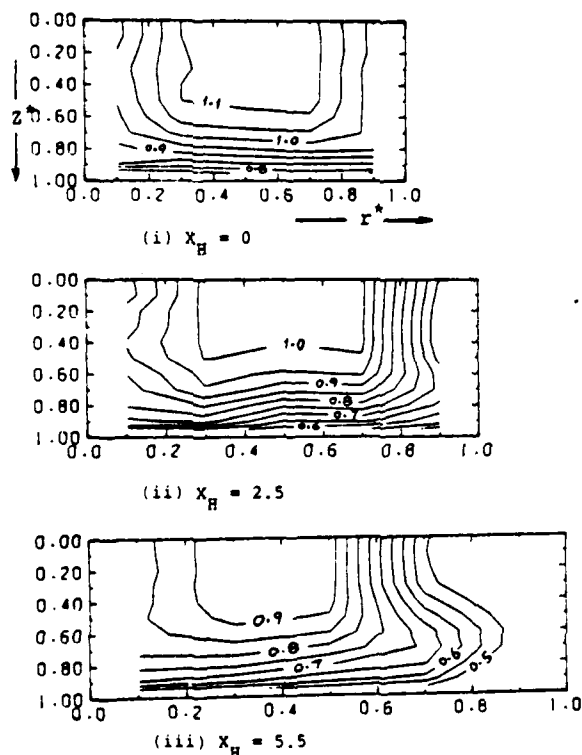


Figure 4 S-diffuser; turbulent flow, isotachs of U/v_b

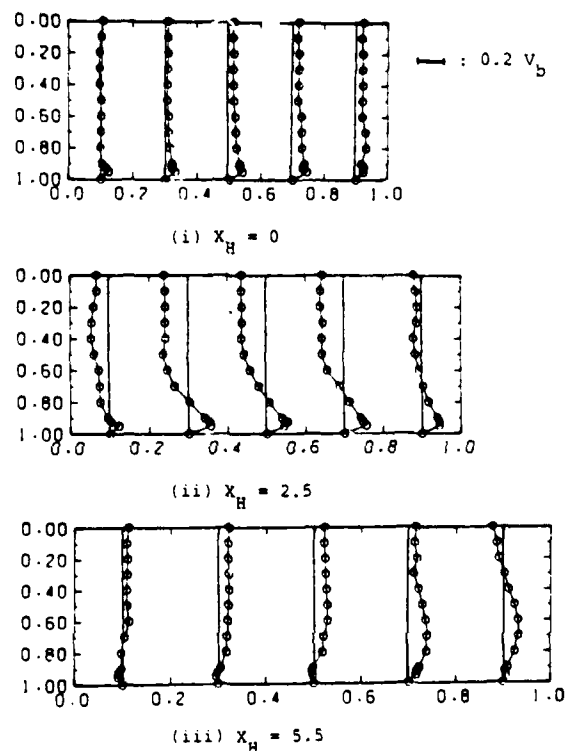


Figure 5 S-diffuser; turbulent flow, profiles of V/v_b

laminar flow. The low velocity region near the $r^*=1.0$ wall is smaller in turbulent flow and the radial velocity magnitudes (figure 5) did not exceed $0.15 V_b$. The smaller secondary flow generation is mainly attributed to the thinner inlet boundary layers, and is in accordance with the findings of Taylor et al (1982a,c).

The development of the flow in the diffuser is similar to that in the laminar flow, but with generally smaller radial velocities in the turbulent case (cf. figures 3 and 5). The persistence of the secondary flow generated in the first bend can be observed at the diffuser exit at $r^*=0.9$ (figure 5(iii)) as in the laminar case. The centre-line developments of the U , u and V and v were also measured. The diffuser centre-line is always contained within the high velocity core flow region. The variations in u and v are consequently small and U decreases with downstream distance as the diffuser area increases. The variation of V indicates the reversal of the core flow radial velocity near the inflexion plane, in an abrupt alteration of trend from decreasing to increasing magnitude.

Spanwise mean velocity components were measured at station 2, and at $0.25 D_H$ downstream of the exit plane. The spanwise profiles could be measured only up to $z^*=0.5$ because of restricted optical access near the side-walls. The spanwise velocity did not exceed $0.05 V_b$ which is significantly less than the radial component.

The wall static pressure measurements for turbulent flow are shown in figure 6(i). The pressure gradients set up by each one of the diffusing bends can be distinguished and are separated near to the inflexion plane. In the first bend, the streamwise pressure gradients are very steep away from the inner ($r^*=1.0$) wall for the first 180° of turning. The pressure recovery across the diffuser is of the order of $0.2p V_b^2$. Taking into consideration the pressure drop of $0.12p V_b^2$ measured in the constant area S-duct of Taylor et al (1982a), the total pressure recovery is comparable to those in straight diffusers of similar area expansion (Ward-Smith, 1980).

The uv cross-correlations are presented in figure 7(i) and (ii) and show a maximum of around $0.0015 V_b^2$ near the $r^*=0.0$ wall. The turbulence levels for the streamwise, radial and spanwise components are presented in figures 7(iii)-(viii). Streamwise levels reach maxima of $0.08-0.09 V_b$ near the side-walls with the corresponding radial and spanwise levels being generally lower, rising to about $0.06 V_b$ near the walls. In the core flow region the levels do not exceed $0.02 V_b$. The distributions of all three components are similar and show maxima near the $r^*=1.0$ wall where there is considerable re-distribution of the streamwise isotachs.

Measurements of the streamwise components were also made at the symmetry plane at $Re=10,000$ and confirmed the similarity of the flow patterns throughout the turbulent regime: the inlet boundary layers were about 1-2% thicker with the lower Reynolds number and the mean components were within 3-4% of those measured at $Re=40,000$.

3.3 C-Diffuser: Laminar and Turbulent Flow Results

Measurements were made in the symmetry plane and the exit plane of the unidirectional 45 degree diffuser at $Re=790$ and $40,000$. The streamwise component isotachs and radial component profiles are presented in figure 8 and may be compared with figures 2(iii) and 3(iii) for laminar flow and 4(iii) and 5(iii) for turbulent flow for the corresponding measurements in the S-diffuser. The turbulence quantities measured show qualitative and quantitative similarities with those in the S-diffuser and are not presented. The streamwise isotachs (figure 8(i) and (iii)) indicate the migration of the high velocity core towards the outer wall of the diffuser, while significant deceleration of the flow is evident along the inner wall. The distortion of the isotachs near the convex wall is more pronounced than at the exit plane of the S-diffuser in both the laminar and turbulent flows, the velocities at $r^*=0.9$ on the symmetry plane are about half those measured in the doubly-curved duct indicating that detachment of the

flow is more likely in the unidirectional diffuser. Symmetry plane measurements showed that the development of the flow in the first 22.5° is very similar in both ducts and quantitative differences, although small, are evident in the second bend.

The cross-stream flow pattern (see figure 8(ii) and (iv)) is similar to that encountered in unidirectional bends with near-wall maxima of about $0.15 V_b$ which may be compared with maxima of about $0.25 V_b$ measured at the 45° plane of the constant area duct of Enayet et al (1982) of the same curvature. The reduction of the secondary flow magnitudes with the expansion in the cross-section is in agreement with the findings of McMillan (1982) in a 40° curved diffuser.

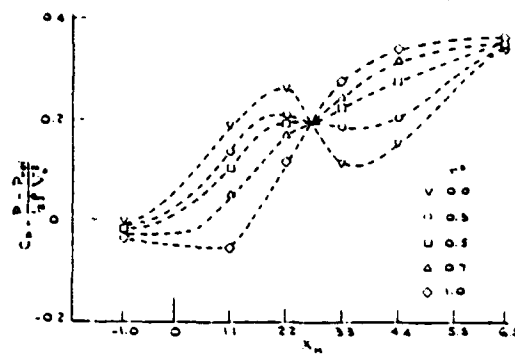
Measurements in the symmetry plane at $X_H=0.0, 2.5$ and 5.5 in both diffusers in laminar flow showed that the inlet profiles are identical (to within the accuracy of the measurement) but the velocity maximum is nearer the $r^*=1.0$ wall at $X_H=2.5$ and nearer the $r^*=0.0$ wall at $X_H=5.5$ in the unidirectional duct, indicating a very fast growth of the slow flow region near the convex wall. Comparison of the laminar and turbulent flow profiles in the C-diffuser shows that the high velocity core is located much nearer the concave wall at the exit in the laminar case, and the cross-stream velocities in the near-stagnant region in the vicinity of the convex wall are almost zero. The maxima of the radial velocities are similar with both Reynolds numbers.

The wall static pressure measurements for the turbulent flow case are shown in Figure 6(ii). The pressure recovery in both diffusers is similar, about one fifth of the velocity head.

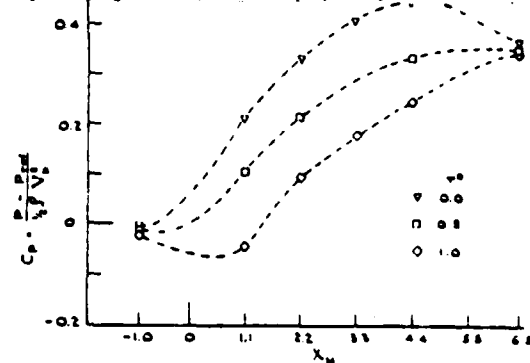
4. DISCUSSION

The principal interest of the present investigation lies in the determination of the influence of the expansion in area on the flows in S- and C-shaped passages. Cross-stream flows are produced in a sigmoid diffuser due to the curvatures of the constituent bends, and are influenced by the area increase. The cross-flows due to the area increase in a two-dimensional straight diffuser are directed away from the centre-line in radial planes and can readily be estimated, by considering the re-direction of the streamlines, to be no more than a few per cent of the bulk velocity, while the pressure-driven secondary flows measured previously in the constant area C-duct and S-duct were of the order of 0.25 and $0.15 V_b$ respectively. However, the flow behaviour in the diffusers cannot be explained simply on the basis of the cross-flows as the migration of the core flow, and the accumulation of low velocity fluid on the $r^*=1.0$ wall complicate the processes involved. The effects of curvature on the cross-stream flows dominate those due to the area expansion and the two flow mechanisms complement or counteract each other depending on the location in the duct. In the turbulent regime, helped by the thinner boundary layers, the flow behaviour is more akin to potential flow, with the core lying closer to the inner wall at the inlet of the diffusers and migrating in an almost straight line path through the ducts. Cross-stream velocities are in general larger in the laminar flow cases, mainly due to the thicker inlet boundary layers. The radial velocities are larger in the symmetry plane of the S-shaped diffuser than in a uniform area S-duct, due to the core migration; near the side-walls the cross-stream velocities are of similar magnitude in the first bend of both geometries, but are generally smaller in the second sector of the diffuser. This last observation is consistent with the patterns revealed by the flow visualization, in that the onset of the secondary flow due to the second curvature occurs further downstream in the diffusing duct.

The secondary flows measured in both the S-shaped and the unidirectional diffusers are larger than those in the 40° curved diffuser of McMillan (1982); this is likely to be a result of the 1.5 cross-sectional aspect ratio at the inlet of the latter geometry. The aspect ratio of the duct influences the generation and importance of the secondary flows since if the larger dimension is in the spanwise direction (as in McMillan's geometry) the vortices generated are located nearer the side-walls and

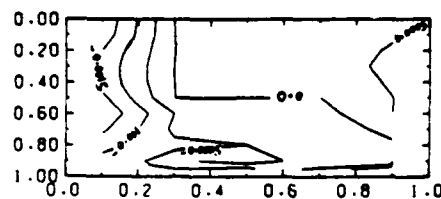


(i) S-diffuser

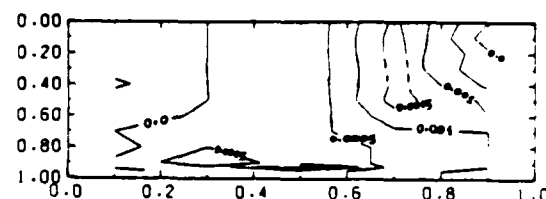


(ii) C-diffuser

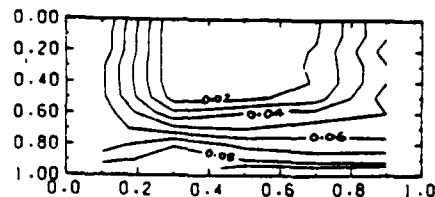
Figure 6 Turbulent flow: wall static pressure measurements



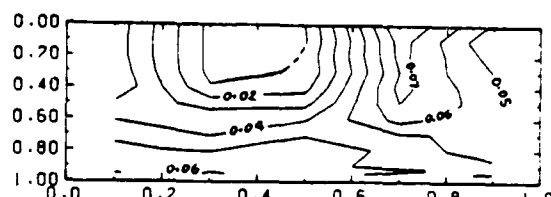
(i) \overline{uv}/v_b^2 ; $x_H = 1.65$



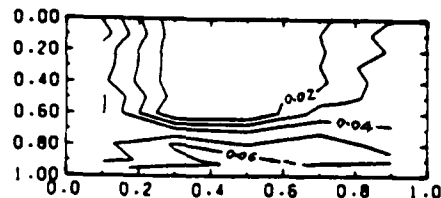
(ii) \overline{uv}/v_b^2 ; $x_H = 5.5$



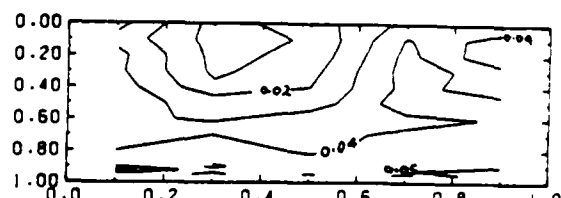
(iii) \bar{u}/v_b ; $x_H = 1.65$



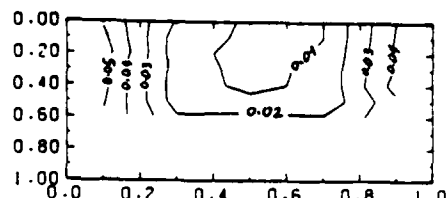
(iv) \bar{u}/v_b ; $x_H = 5.5$



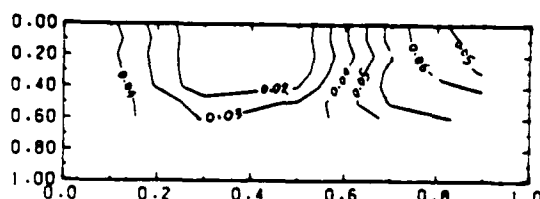
(v) \bar{v}/v_b ; $x_H = 1.65$



(vi) \bar{v}/v_b ; $x_H = 5.5$

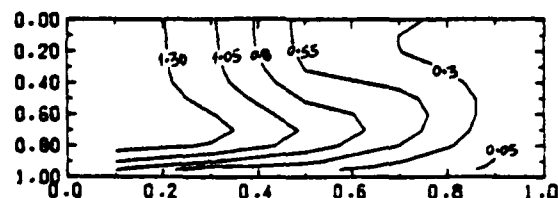


(vii) \bar{w}/v_b ; $x_H = 1.65$

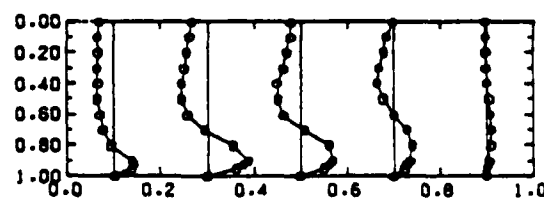


(viii) \bar{w}/v_b ; $x_H = 5.75$

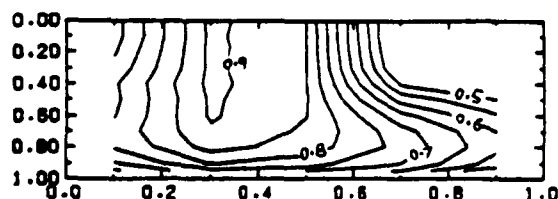
Figure 7 S-diffuser: contours of cross-correlations and turbulence levels



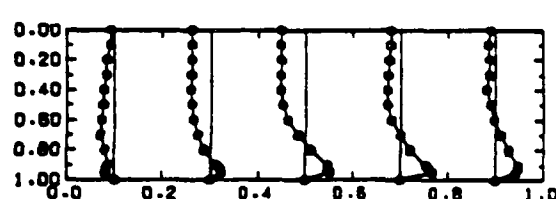
(i) Laminar flow: U/v_b



(ii) Laminar flow: V/v_b $\rightarrow 0.2v_b$



(iii) Turbulent flow: \bar{U}/v_b



(iv) Turbulent flow: \bar{V}/v_b

do not affect as much of the flow cross-section. The influence of cross-sectional shape on the flow is currently being investigated in a similar S-diffuser of circular cross-section.

Separation is more likely in the C-diffuser as a result of the dependence of the shape of the boundary layer velocity profile on the pressure gradient which, along the wall at $r^*=1.0$ in a C-diffuser is more adverse than in the S-diffuser (see Fig. 6(ii) and McMillan, (1982)). Before any significant accumulation of boundary layer fluid is made along the $r^*=1.0$ wall (up to, say, $X_H=1.65$), the boundary layer thickness on the concave wall increases (a potential flow effect due to the streamwise pressure gradient) while that on the convex wall decreases and thus the tendency to recirculate along the inner wall is suppressed. After $X_H=1.65$ this trend is, however, reversed. A 1-2mm wide region of transitory stall was observed at $r^*=1.0$, $X_H=4.4$ in the turbulent regime in the C-diffuser.

The efficiency of the pressure recovery in curved diffusers is affected by the inlet boundary layer thickness (see Schlichting, 1979): a typical value of the efficiency in unidirectional diffusers geometrically similar to the present ones but with thinner layers is 0.7, while both the S- and C-diffuser have an efficiency of 0.66. Surprisingly, the recovery in the 45° C-diffuser is greater (by 15%) than that in the 40 degree case of McMillan with smaller inlet boundary layers (0.05D_H). The pressure continues to recover one hydraulic diameter downstream of the exit, in accordance with observations in straight diffusers (Ward-Smith, 1980).

The turbulence structure is similar in both diffusers. Turbulence levels are in general lower in the diffusing ducts: the measured maxima of u are of the order of 0.09 V_b compared with e.g. 0.15 V_b in the S-duct, but the differences in the v and w levels are less pronounced. The maxima of the uv cross-correlations are approximately half those measured in constant area ducts (0.003 V_b^2). Small turbulence levels, of up to 0.02 V_b are present in the core region, and rise to maxima in the boundary layers. Increased turbulent mixing occurs along the concave ($r^*=0.0$) wall of both diffusers around the inlet where the boundary layer grows faster than on the convex side. After the inflexion plane of the S-diffuser, high values are to be found near the $r^*=1.0$ wall also, while the turbulence generated at the opposite wall in the first bend persists. The near-wall values of the fluctuations are similar to those measured in the 40° diffuser of McMillan (1982) and over a flat plate (Klebanoff, 1955), with maxima of about 0.08 V_b .

The generally small magnitudes of the turbulence quantities and the existence of an extensive 'core' region where potential flow effects are predominant, suggest that the use of a simple Prandtl-Kolmogorov relationship (see Levy et al. 1983) may be adequate and appropriate for the representation of turbulence effects in the calculation of the flow. Although the turbulence structure is important, it does not introduce any new features in comparison with the non-diffusing bend flows. More detailed consideration of the turbulence structure may be necessary, however, to represent the properties of the near-wall region.

5. CONCLUDING REMARKS

1. Detailed measurements are presented of the velocity characteristics of laminar and turbulent developing flows in rectangular diffusers, of 1.5 exit-to-inlet area ratio, with an S-shaped and with a C-shaped centre-line formed by two 22.5° sectors.

2. Cross-stream flows arise in the diffusers, as a result of the curvature-induced secondary motions and of the increase in area. In the S-diffuser, they reach maxima of 0.4 V_b and 0.15 V_b in the laminar and turbulent flows respectively. The secondary flow set up by the curvature of the first 22.5° sector is sustained near the outer wall of the second sector, while a secondary flow in the opposite direction is generated by the second curvature. In the C-diffuser secondary flows

with a single sense of rotation are present in both flow regimes, and they reach maxima of around 0.2 and 0.15 V_b in the laminar and turbulent cases. The existence of larger radial velocities in the laminar flow is attributed partly to the thicker inlet boundary layers.

3. The flow in the diffusers is qualitatively similar to that in constant area ducts. The cross-stream velocity magnitudes are generally higher near the symmetry plane in the diffusing S-duct due to the core flow migration, but the secondary flows near the side-wall are quantitatively similar in both configurations in the first bend but smaller in the second half of the diffuser. In the C-diffuser the cross-flows are nearly half of those measured in corresponding constant area ducts.

4. The pressure recovery across both diffusers is about a fifth of the velocity head.

5. The turbulence quantities measured in both diffusers are smaller than those encountered in constant area ducts.

6. This paper presents benchmark measurements against which the results of flow calculations may be compared. The results indicate that marching techniques employing a simple representation of turbulence may be adequate for the calculation of the flows.

ACKNOWLEDGEMENT

The authors are glad to acknowledge financial support from NASA, Lewis Research Center, and are grateful to B. Anderson, H. McDonald and A. M. K. P. Taylor, for many useful discussions.

REFERENCES

- Bansod, P. and Bradshaw, P. (1972) The Flow in S-Shaped Ducts. *Aeronautical Quarterly*, **23**, 131.
- Enayet, M. M., Gibson, M. M. and Yianneskis, M. (1982) Measurements of Turbulent Developing Flow in a Moderately Curved Square Duct. *Int. J. Heat & Fluid Flow*, **3**, 221.
- Humphrey, J. A. C., Taylor, A. M. K. P. and Whitelaw, J. H. (1977) Laminar Flow in a Duct of Strong Curvature. *J. Fluid Mech.*, **83**, 509.
- Humphrey, J. A. C., Whitelaw, J. H. and Yee, G. (1981) Turbulent Flow in a Square Duct with Strong Curvature. *J. Fluid Mech.*, **103**, 443.
- Klebanoff, P. S. (1955) Characteristics of Turbulence in a Boundary Layer with Zero Pressure Gradient. NACA TR 1247.
- Levy, R., Briley, W. R. and McDonald, H. (1983) Viscous Primary/Secondary Flow Analysis for Use with Non-Orthogonal Coordinate Systems. AIAA 21st Aerospace Sciences Meeting, Reno, Nevada, January 1983.
- McMillan, O. J. (1982) Mean-Flow Measurements of the Flow Field Diffusing Bend. NASA Contractor Report 3634.
- Schlichting, H. (1979) *Boundary Layer Theory*. McGraw-Hill, New York.
- Taylor, A. M. K. P., Whitelaw, J. H. and Yianneskis, M. (1982a) Developing Flow in S-shaped Ducts. Part I: Square Cross-Section Duct. NASA Contractor Report 3550.
- Taylor, A. M. K. P., Whitelaw, J. H. and Yianneskis, M. (1982b) Developing Flow in S-Shaped Ducts. Part II: Circular Cross-Section Duct. NASA Contractor Report.
- Taylor, A. M. K. P., Whitelaw, J. H. and Yianneskis (1982c) Curved Ducts with Strong Secondary Motion. Velocity Measurements of Developing Laminar and Turbulent Flow. *J. Fluids Engng.*, **104**, 350.
- Ward-Smith, A. J. (1980) *Internal Fluid Flow*. Clarendon Press, Oxford.

EFFECTS OF STREAMLINE CURVATURE ON LAMINAR AND TURBULENT WAKES

Hide S. Koyama

Department of Mechanical Engineering
Tokyo Denki University
Tokyo, Japan

ABSTRACT

To investigate the stabilizing, destabilizing and secondary flow effects of the streamline curvature on laminar and turbulent wakes, qualitative and quantitative experiments were performed by a smoke-wire visualization technique, a hot-wire anemometer and a signal analyser. From the experimental results, the development of the turbulent wake was found to be promoted due to the destabilizing effect and suppressed due to the secondary flow effect.

INTRODUCTION

The effects of Coriolis, buoyancy and centrifugal forces, wherein the last force is derived by the streamline curvature, on the shear flows are very interesting problems in physics, engineering and environmental sciences. The well known examples are turbulent boundary layer on a curved wall and a rotating wall, a curved mixing layer and a turbulent shear flow in thermally stratified field. The apparent analogy between the effects of those forces has been mentioned by Bradshaw[1]. From many experimental studies concerning these flows[2-16], the phenomena due to the effects may be summarized as follows.

- (1) Promotion and suppression of the development of two-dimensional laminar and turbulent boundary layers,
- (2) Generation of a Taylor-Goertler type longitudinal vortices in a turbulent boundary layer and a large-scale vortices in a channel.

The phenomena (1) and (2) are due to the stabilizing and destabilizing effects and due to the secondary flow effect respectively. For example, in a curved flow, if there is a velocity gradient in the transverse direction the motion of the fluid particles are stabilized in the shear flow with positive velocity gradient as compared with that of the curved potential flow, and is destabilized with negative velocity gradient. Therefore, these are defined as the stabilizing and destabilizing effects of the streamline curvature. If there is a velocity gradient in the spanwise direction, a secondary motion is arisen because of an imbalance between a centrifugal force due to the streamline curvature and a pressure gradient force towards the centre of curvature. Therefore, this is defined as the secondary flow effect of the streamline curvature.

The majority of the experimental results for the boundary layer development on a curved wall showed the coupled effects of stability and secondary flow, especially, in the turbulent boundary layer on a concave wall. Taylor-Goertler type vortices were generated in the turbulent boundary layer on a concave wall and will be broken up[16]. Consequently, the development of the turbulent boundary layer will be promoted considerably.

The objective of the present study is to make clear the stabilizing, destabilizing and secondary flow effects of the streamline curvature on turbulent shear flows.

Thus, qualitative and quantitative experiments were performed on laminar and turbulent wakes behind a circular cylinder which was spanned transversely and spanwisely a curved potential flow field.

Studies on a curved turbulent mixing layer by Margolis and Lumley[17], on a flow around a sphere placed in a rotating curved potential flow by Fette[18], on a turbulent wake behind a cascade of blades by Raj and Lakshminarayana [19] and on a Karman vortex street[20,21] were available for the present experimental study.

APPARATUS AND TECHNIQUES

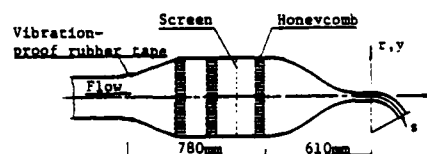


Fig. 1. Experimental apparatus

A streamwise cross section of a wind tunnel employed in the present study is shown in Fig. 1. Air is delivered to the wind tunnel by a fan blower, having a capacity of $0.5 \text{ m}^3/\text{s}$ at a delivery pressure of 980 Pa. The air flows through a rectification chamber to a test channel via a converging nozzle of 1 to 14.8. The chamber is made up of several layers of honeycomb flow-straighteners and screens. Straight and curved channels were employed as the test channel to produce two-dimensional straight and curved potential flow fields. The channels have a dimension of $280 \text{ mm} \times 50 \text{ mm}$ and its length is 210 mm. The radius of curvature of the curved channel is 200 mm. A circular cylinder was spanned transversely and spanwisely at 5 mm upstream of the test channel to generate laminar and turbulent wakes in potential flow field. Fixing condition of the cylinder is having a fine effect on the wake development at lower Reynolds numbers. Therefore, the present experiment was performed by changing the test channel as the cylinder was fixed. The author sought to clarify the effects of streamline curvature on the wake behind a circular cylinder by comparison between the experimental results for the cases of straight and curved channels.

Fig. 2 shows the schematic diagram of a measuring system employed in the present study. A constant temperature anemometer (KANAMAX, 7000) with a $5 \text{ }\mu\text{m}$ tungsten hot-wire was used for the time-mean and fluctuating velocity measurements. A hot-wire sensor can be moved continuously along the transverse, streamwise and spanwise directions by a controlled traversing mechanism. Output of a multiple turn potentiometer which indicates the hot-wire position, d.c. signal and a.c. signal (the root mean square of the fluctuations) of the hot-wire anemometer

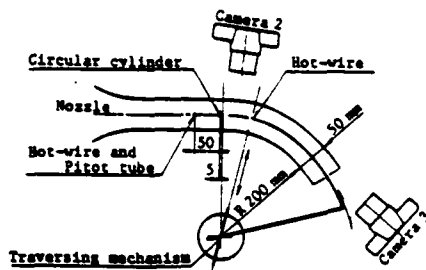


Fig. 2. Schematic diagram of measurements

are recorded on X-Y recorders (YEW, 3063). An a.c. signal was also fed to a 12 bit signal analyser (IWATSU, SM-2100A) by which frequency spectrum was obtained. The results were stored on the magnetic disk and recorded on an X-Y plotter (IWATSU, DPL-3321).

Mean velocity components and Reynolds shear stress measurements were carried out by a following method. Six different hot-wires having an angle with stream were introduced instead of a single rotatable hot-wire [22]. The wires were moved vertically by the traversing mechanism. Data reduction was performed utilizing the equations derived by Fujita and Kovaszny [22].

Flow visualization is one of effectual methods in experimental fluid mechanics. Using a smoke-wire method, one of the flow visualization techniques, the flow behind a circular cylinder was also studied. A Nichrome wire of 0.1 mm diameter is placed perpendicularly to the flow and the circular cylinder. The wire is painted with liquid paraffin. White color mist is produced by a strong electric current through the wire. Photographs of top, side and front views are taken by cameras shown in Fig. 2.

Reynolds number, $Re = U_1 d / \nu$, based on the diameter, d , of a circular cylinder and the free stream velocity, U_1 , upstream of the cylinder was chosen for the test conditions. The free stream velocity is measured by a hot-wire and a Pitot tube at 50 mm upstream of the cylinder, and is controlled by changing the rotational speed of the fan blower.

RESULTS AND CONSIDERATION

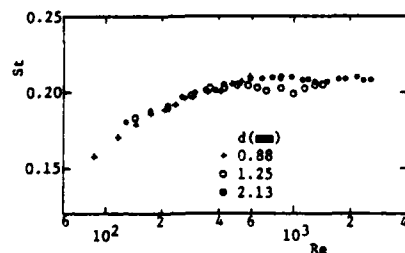


Fig. 3. Strouhal number in terms of Reynolds number

Fig. 3 shows the Strouhal number, St , based on the shedding frequency, f_k , of a Karman vortex street in the flow past a circular cylinder in terms of the Reynolds numbers, Re . The experimental points were obtained with circular cylinders of three different diameters and at different velocities in the range of Reynolds numbers from about 90 to 2570. The shedding frequency was measured by a signal analyser. The results obtained in the present experiment agree with that performed by Roshko [23]. The Reynolds numbers $Re = 150$ and 1500 were chosen for the experimental conditions of Karman vortex street in laminar flow and two-dimensional turbulent wake respectively.

Secondary flow effect

For inviscid, incompressible flow the equation of in the cylindrical coordinates is expressed as follows.

$$\frac{DV}{Dt} - \frac{u^2}{r} = \frac{uv}{r} t = -\frac{1}{\rho} \nabla p \quad (1)$$

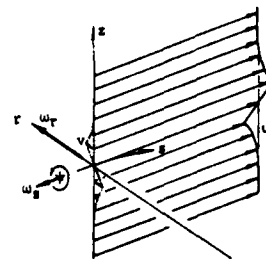


Fig. 4. Generation of secondary vorticity

where V denotes velocity vector with components u , v and w in the azimuthal, radial and axial coordinates, and (n, t, k) denote the unit vectors in the respective directions. The 2nd and 3rd terms of left side of equation (1) mean the centrifugal and Coriolis accelerations. These terms arise automatically on transformation from rectangular to cylindrical coordinates.

Taking the rotation of equation (1) we have the following vector equation for the vorticity, ω .

$$\frac{D\omega}{Dt} - \frac{\partial}{\partial z} \left(\frac{uv}{r} \right) n - \frac{\partial}{\partial z} \left(\frac{u^2}{r} \right) t + \left[\frac{\partial}{\partial r} \left(\frac{uv}{r} \right) + \frac{1}{r} \frac{\partial}{\partial \theta} \left(\frac{u^2}{r} \right) \right] k = 0 \quad (2)$$

It is considered from equation (2) that the components of the vorticity will be changed due to the velocity gradients in curved flow [24]. Assuming that there is a two-dimensional vortex in a curved potential flow field as shown in Fig. 4, vorticity vector which was directed across the stream initially will lie at angle to it and a streamwise component ω_s will be generated. In other words, secondary flow shown by a dotted line will be generated in the vortex. Therefore, this is defined as the secondary flow effect of the streamline curvature.

First of all, to investigate the secondary motion generated in a curved flow, qualitative experiment were performed by a smoke-wire visualization technique. Fig. 5 shows the photographs of the instantaneous smoke-streaklines pattern behind a circular cylinder, which was spanned transversely a straight and a curved potential flow at Reynolds number, $Re = 150$, based on the diameter, $d = 3.0$ mm, of the cylinder. Smoke-wire was placed at a distance of 10 mm behind the cylinder. In the photograph of side

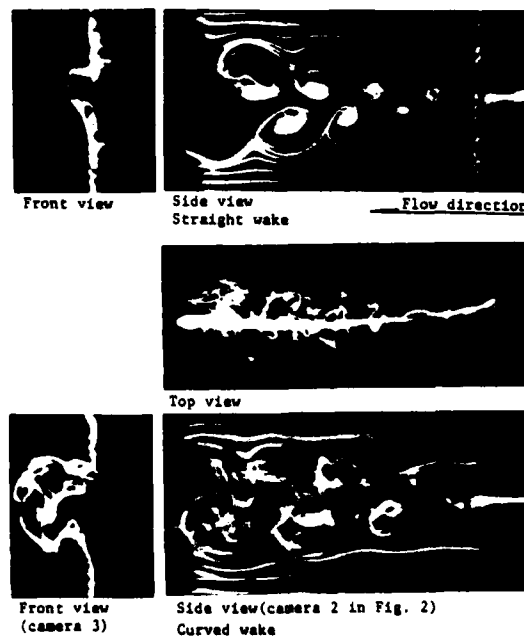


Fig. 5. Smoke-streaklines patterns behind a circular cylinder at Reynolds number, $Re = 150$. Delay time = 10 msec

view for the straight wake, a very regular asymmetric vortex pattern, known as the Karman's vortex street, is observed distinctly. It is also observed that the moving velocity of vortices is slower than the free stream velocity. The ratio of the spanwise to the longitudinal spacing of the vortices near wake of the cylinder was about 0.3 from many photographs. This ratio showed a tendency to increase downstream in the present experiment. For the case of curved wake, the formation of an asymmetric vortex street is not clear, in other words, the vortices are breaking down in comparison with the case of straight wake. Large-scale secondary flow towards centre of the curvature is observed in the photographs of the top and front views. Small-scale secondary flow in the vortices is also observed in the photograph of top view.

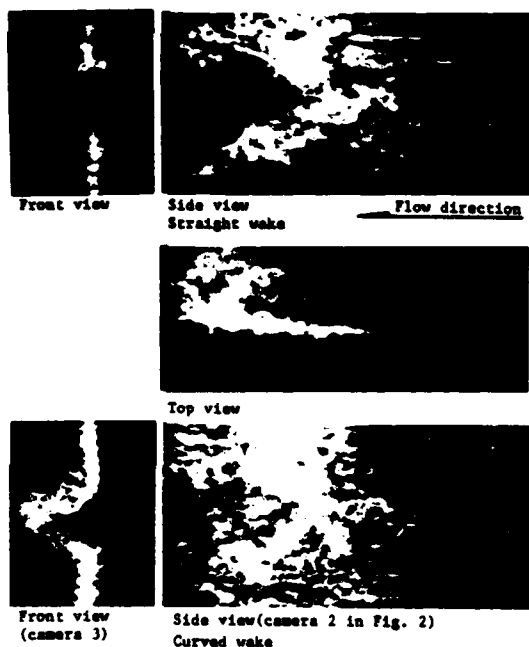


Fig. 6. Photographs of flow behind a circular cylinder at Reynolds number, $Re = 1500$. Delay time = 100 msec

In the wake behind a circular cylinder at higher Reynolds numbers, the regular asymmetric vortex pattern became turbulent and was not observed by the smoke-wire visualization technique. Photographs shown in Fig. 6 were taken at Reynolds number, $Re = 1500$. In the straight wake, the velocity defect region is observed, while in the curved wake that is not clear. The width of curved wake is narrower than that of straight wake. For the case of curved wake, secondary flow towards the centre of curvature is observed in the photographs of top and front views. The secondary flow has a maximum velocity at centre-line of the wake. Secondary motion confirmed by the visualization technique is predicted from the consideration of the generation of the secondary vorticity.

Fig. 7 shows the power spectra of signal from the hot-wire anemometer for the cases of the straight and curved wakes at Reynolds numbers, $Re = 150, 200, 300$ and 500 . A hot-wire was placed at x/d or $s/d = 2$ and $z/d = 1$ behind a circular cylinder. Output of 10 volt from the hot-wire anemometer is equivalent to the velocity of 10 m/s for the power spectrum analysis. The results obtained here were analysed in the range of frequencies, f , from 0 to 2 kHz. Principal, first and second harmonic peaks of a Karman vortex street are seen at frequencies f_k , $2f_k$ and $3f_k$ respectively. A small peak is also seen at lower frequency, f_s . The peak may be a disturbance, which propagate in the streamwise direction, due to the surface roughness of the cylinder and fixing situation of it in channel. It was not seen upstream of the cylinder. Many peaks with sidebands are seen at Reynolds numbers $Re = 150$ and 200 for the case of the curved wake. The full widths of half maximum of the principal and harmonic peaks

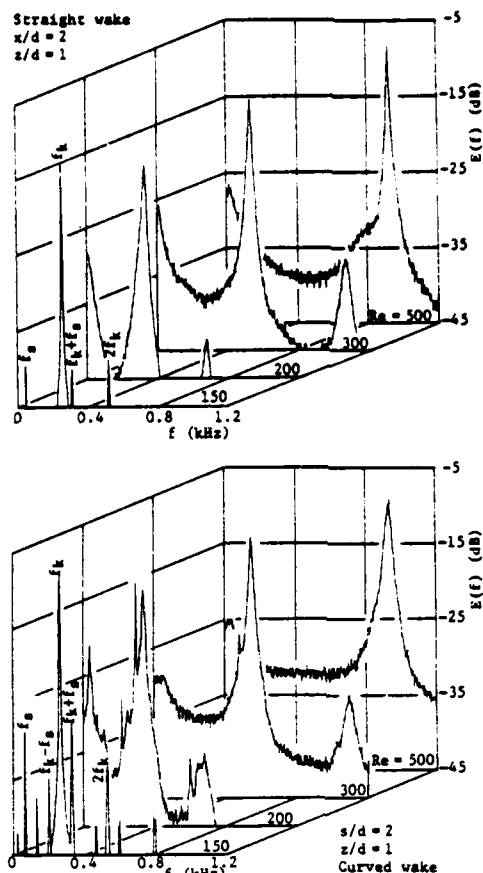


Fig. 7. Power spectra of fluctuating velocity behind a circular cylinder at $Re = 150, 200, 300$ and 500

for the case of the curved wake are wider than that of the case of the straight wake. The results obtained at Reynolds number $Re = 150$ are analogous to a frequency spectrum of an amplitude modulated signal, e_{out} , expressed by the following equation:

$$e_{out} = K[E_s(1 + m\cos(2\pi f_s t))] \cdot [E_c \cos(2\pi f_c t)] \\ = 1/2 \cdot KE_s E_c m [\cos 2\pi(f_c + f_s)t + \cos 2\pi(f_c - f_s)t] \\ + KE_s E_c \cos(2\pi f_c t) \dots \dots \dots (3)$$

Where K , E_s , E_c and m are a constant, the modulating sig-

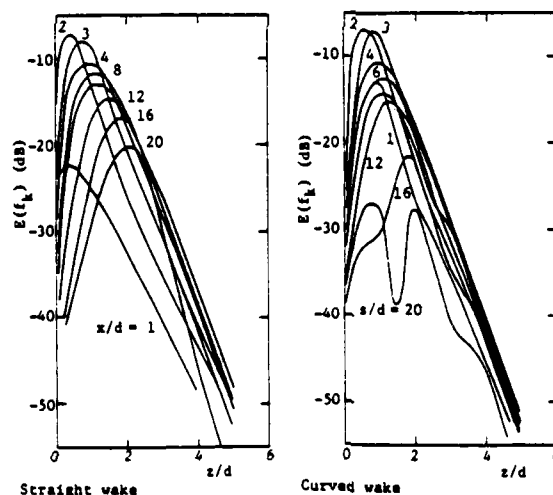


Fig. 8. Distributions of power $E(f_k)$ at shedding frequency of Karman vortex street at Reynolds number, $Re = 150$

nal amplitude, the carrier amplitude and the degree of modulation. Here we have the band of the carrier at f_s and the two sidebands at $(f_c + f_s)$ and $(f_c - f_s)$. Therefore, it is considered that the modulating and carrier frequencies correspond to those of the disturbance and the Karman vortex street in the present experiment.

In the curved wake, a breakdown of shedding vortices was observed by the smoke-wire visualization technique. It is very important to make clear the flow mechanism around and just behind the circular cylinder because the secondary flow is related to an integral value of the velocity gradient in the curved wake. Therefore, measurements of the power spectrum of fluctuating velocity were performed in detail in the wake just behind the circular cylinder.

Fig. 8 shows the distributions of power $E(f_k)$ at shedding frequency, f_k , of a Karman vortex street for the cases of the straight and curved wakes at Reynolds number $Re = 150$. Peak of the power profile means the centre of the vortex. In the wake just behind the cylinder, there is no difference in the maximum power between both cases. However, extension of the shedding vortices towards spanwise direction is suppressed slightly in the curved wake, and the vortices are seen to be broken down at distance of about $s/d = 16$.

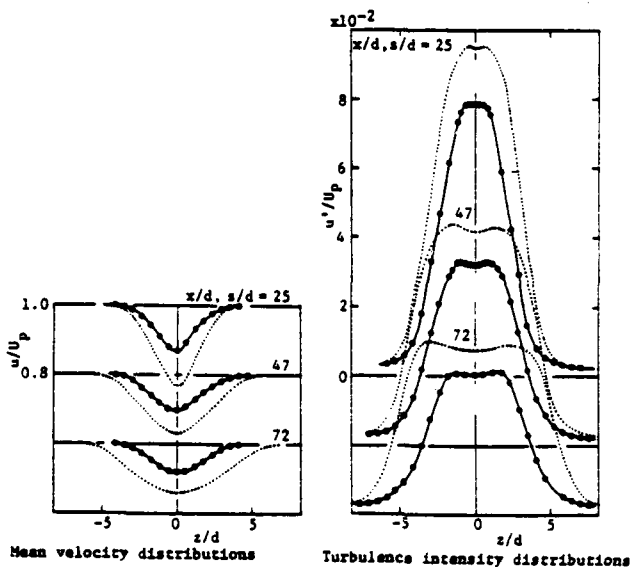


Fig. 9. Mean velocity and turbulence intensity distributions at Reynolds number $Re = 1500$

Fig. 9 shows the mean velocity and turbulence intensity distributions in straight and curved wakes behind a circular cylinder of 2.13 mm in diameter, which was spanned transversely upstream of the test channel. Measurements were performed at three different locations of x/d or $s/d = 25, 47$ and 72 for Reynolds number $Re = 1500$. In the following figures of mean velocity, turbulence intensity, Reynolds stress, etc., solid and dotted lines indicate the distributions for the cases of the curved and straight wakes respectively. The wake profiles are symmetric about the wake centre-line for the both cases of the straight and curved wakes. The width of the straight wake increases as the distance from the cylinder, while that of the curved wake remains constant. The velocity defect, which is the difference between the velocity and the imaginary potential velocity in the wake, and the turbulence intensity in the curved wake are smaller than those in the straight wake.

Fig. 10 shows the distributions of the transverse velocity component, v , and the Reynolds shear stresses in the wake at positions of x/d or $s/d = 72$ at Reynolds number $Re = 1500$. The preceding consideration concerning a secondary flow in a vortex is also valid for a curved turbulent wake. In the curved turbulent wake there exists a secondary flow, which is directed towards the centre of the curvature of the primary flow, because of the unbalance between a centrifugal force due to the

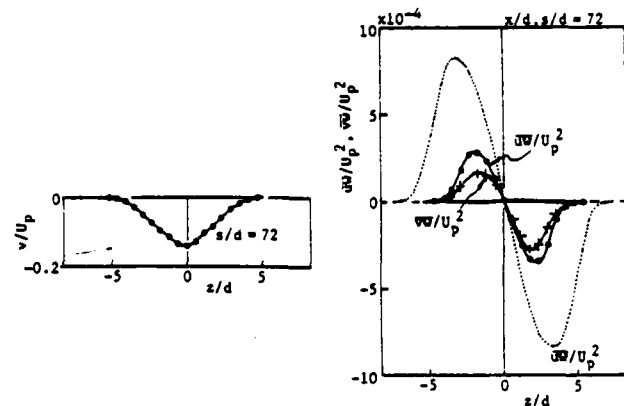


Fig. 10. Distributions of transverse velocity component and Reynolds shear stresses at Reynolds number $Re = 1500$

curvature of the particle pathline and a pressure gradient force towards the centre of the curvature of the primary flow. The maximum transverse velocity occurs at centre of the wake. The results obtained here is similar to that on a photograph of the front view (see Fig. 6.). Reynolds shear stresses change sign at centre of the wake, and maximum stresses on either side of centre-line of the wake are the same. Reynolds stress $\overline{w'u_p^2}$ in the curved wake is considerably small as compared with that in the straight wake. Shear stress $\overline{w'u_p^2}$ is generated in the curved wake due to the spanwise gradient of transverse velocity component.

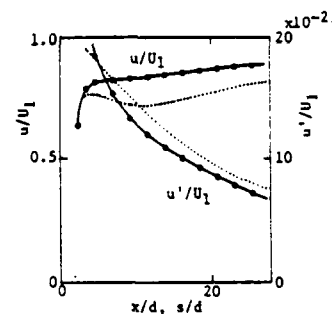


Fig. 11. Variation of mean velocity and turbulence intensity at wake centre-line. Reynolds number $Re = 1500$

Fig. 11 shows the variation of the mean velocity and turbulence intensity at wake centre-line at Reynolds number $Re = 1500$. It is found that the mean velocity increases rapidly just behind the circular cylinder.

Fig. 12 shows a power spectrum of a fluctuating velocity in a turbulent wake behind a circular cylinder at Reynolds number $Re = 1500$. Generally, it is consider-

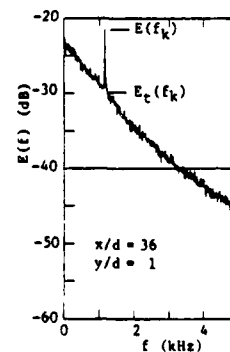


Fig. 12. Power spectrum of fluctuating velocity in a turbulent wake behind a circular cylinder

ed that in a two-dimensional wake behind a circular cylinder a two-dimensional, large wave of Karman vortex street and three-dimensional, small waves of disturbances propagate along the primary flow. A principal frequency at a Strouhal number $St = 0.22$ for a Karman vortex street is observed in the power spectrum of velocity fluctuations. The spectrum also contains a continuous power distribution due to the presence of turbulence superimposed to the Karman vortices.

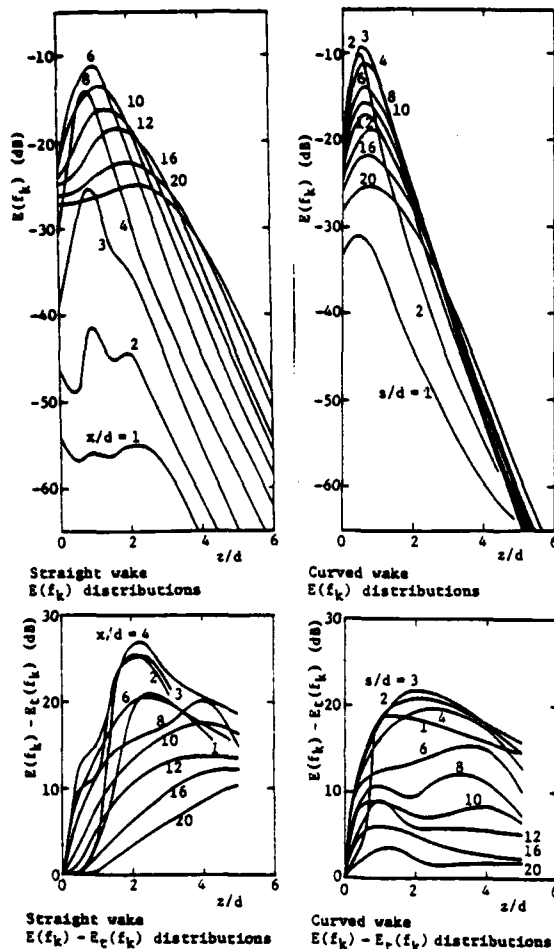


Fig. 13. Distributions of power $E(f_k)$ and power difference $E(f_k) - E_c(f_k)$ at shedding frequency of Karman vortex street. Reynolds number $Re = 1500$

Fig. 13 shows the distributions of the power $E(f_k)$ at a principal frequency, f_k , of a Karman vortex street and the power difference $E(f_k) - E_c(f_k)$, where $E_c(f_k)$ means an interpolated imaginary power at f_k . Measurements were performed at Reynolds number $Re = 1500$ for the cases of the straight and curved wakes. Spanwise spacing of the shedding vortices is smaller than that of the straight wake. Extension of the vortices towards spanwise direction is suppressed considerably as compared to the case of the straight wake. Breakdown of the vortices is also observed in the curved wake.

Stability

Two-dimensional wake along the spanwise direction in a curved potential flow becomes a stability problem. The motion of fluid particles are destabilized in the inside region of a two-dimensional, curved turbulent wake and stabilized in the outside region because of an imbalance between a centrifugal force due to the curvature of the particle path and a pressure gradient force towards the centre of curvature.

Fig. 14 shows the mean velocity and turbulence intensity distributions in straight and curved wakes behind a circular cylinder which was spanned along the spanwise di-

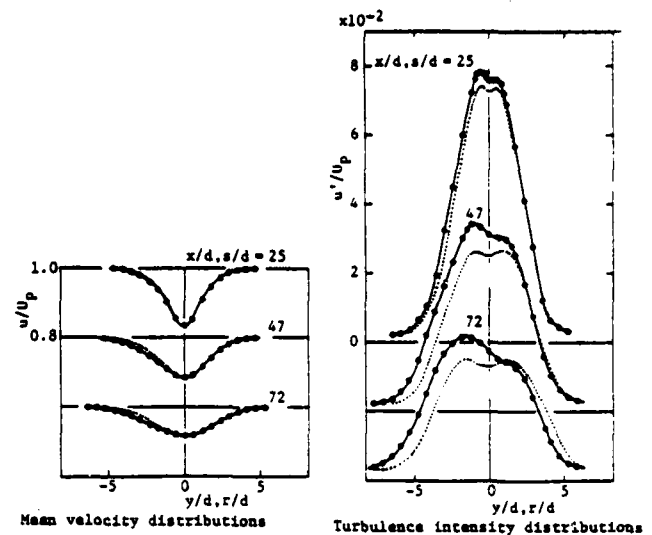


Fig. 14. Distributions of mean velocity and turbulence intensity at Reynolds number $Re = 1500$

rection at different locations of x/d or $s/d = 25, 47$ and 72 at $Re = 1500$. The wake profiles are asymmetric about the wake centre-line for the case of the curved wake. The asymmetry is due to the stabilizing and destabilizing effects of the curvature of primary flow. The destabilizing effect is observed in the mean velocity and turbulence intensity profiles. The stabilizing effect is observed only in the intensity profiles. Maximum turbulence intensity is observed in the unstable region of the curved wake. The turbulence intensity in the unstable region of the curved wake is higher than that in the straight wake. The opposite result is observed in the stable region of the curved wake. From the results, it seems that the destabilizing effect on the development of two-dimensional, turbulent wake is slightly stronger than the stabilizing effect on it.

Fig. 15 shows the distributions of the interpolated imaginary power $E_c(f_k)$ at a principal frequency, f_k , of Karman vortex street and power difference $E(f_k) - E_c(f_k)$. The profiles of the imaginary power $E_c(f_k)$ show asymmetry about the wake centre-line. This is similar to the turbulent intensity distributions shown in Fig. 14. Principal peaks at f_k were found to disappear at the downstream distance of about 60 diameters in the straight wake. The

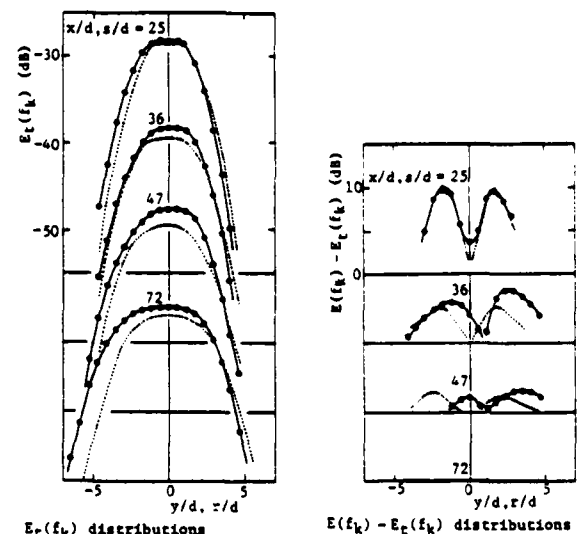


Fig. 15. Distributions of power $E_c(f_k)$ and power difference $E(f_k) - E_c(f_k)$ at shedding frequency of a Karman vortex street. Reynolds number $Re = 1500$

disappearance of peaks in the unstable region on the wake is faster than that in the stable region.

CONCLUSIONS

To clarify the stabilizing, destabilizing and secondary flow effects of the streamline curvature on the shear flow, experimental study on laminar and turbulent wakes behind a circular cylinder placed in a curved potential flow field. Conclusions based on the experimental results are summarized below.

(1) For a turbulent wake behind a circular cylinder spanned spanwisely, profiles of mean velocity, turbulence intensity and power spectrum of fluctuating velocity are not symmetric about the wake centre-line. However, two-dimensionality of the wake is preserved. Development of the inside wake region is promoted, while that of the outside region is suppressed. The destabilizing effect on a turbulent shear flow is slightly large than the stabilizing effect on it.

(2) For a turbulent wake behind a circular cylinder spanned transversely, profiles of mean velocity, turbulence intensity and power spectrum of fluctuating velocity are symmetric about the wake centre-line. Secondary flow, which has a maximum velocity at the wake centre-line, towards the centre of curvature is arisen because of an imbalance between a centrifugal force and a pressure gradient force.

(3) Breakdown of a shedding vortices is observed at lower Reynolds numbers because of the secondary flow effect of streamline curvature.

ACKNOWLEDGMENTS

This work was supported in part by grant-in-aid for scientific research of the Ministry of Education and also in part by the Center for Research, Tokyo Denki University. The author acknowledge Messrs. T. Endo and M. Ohuchi, Tokyo Denki University, for design and manufacture of an electrical equipment used in the present study.

REFERENCES

- Bradshaw, P., "The Analogy between streamline curvature and Buoyancy in Turbulent Shear Flow," Journal of Fluid Mechanics, vol. 36, Part 1, 1969, pp. 177-199.
- Hill, P. G., and Moon, I. M., "Effects of Coriolis Forces in the Turbulent Boundary Layer in Rotating Machines," Rep No. 69, 1962, Gas Turbine Laboratory, M.I.T.
- Moore, J., "A wake and an Eddy in a Rotating, Radial-Flow Passage (Parts 1 and 2)," ASME Journal of Engineering for Power, Vol. 95, Series A, 1973, pp. 205-219.
- Johnston, J. P., Halleen, R. M., and Lazius, D.K., "Effects of Spanwise rotation on Structure of Two-Dimensional Fully Developed, Turbulent Channel Flow," Journal of Fluid Mechanics, Vol. 56, 1972, pp. 533-588.
- Wagner, R. E., and Velkoff, B. R., "Measurements of Secondary Flows in a Rotation Duct," ASME Journal of Engineering for Power, Vol. 94, Series A, 1972, pp. 261-270.
- Murakami, M., and Kikuyama, K., "Effects of Rotation on Diffuser Flow," JSME, Vol. 42, NO. 355, 1976, pp. 828-836.
- Hart, J. E., "Instability and Secondary Motion in a Rotating Channel Flow," Journal of Fluid Mechanics, Vol. 45, Part 2, 1971, pp. 341-352.
- Rothe, P.H., and Johnston, J. P., "Effects of System Rotation on the Performance of Two-Dimensional Diffusers," ASME Journal of Fluid Engineering, Vol. 98, Series 1, 1976, pp. 422-430.
- Koyama, H., et al., "Stabilizing and destabilizing Effects of Coriolis Force on Two-Dimensional Laminar and Turbulent Boundary Layers," ASME Journal of Engineering for Power, Vol. 101, No. 1, 1979, pp. 23-31.
- Koyama, H., et al., "Turbulence Structure and Three-Dimensionality of a Rotating Two-Dimensional Turbulent Boundary Layer," Proceedings of the 2nd Symposium on Turbulent Shear Flows, 1979, pp. 4.22-4.27.
- Tani, I., "Production of Longitudinal Vortices in the Boundary Layer along a Concave Wall," Journal of Geophysical Research, Vol. 67, No. 8, 1962, pp. 3075-3080.
- Bradshaw, P., "Effects of streamline curvature on turbulent flow," AGARD-ograph 169, 1973.
- Honami, S., et al., "Investigation of Turbulent Flows in curved Channels," ASME Paper, No. 75-FE-32.
- Meroney, R. N., and Bradshaw, P., "Turbulent boundary layer growth over a longitudinal curved surface," AIAA Journal, Vol. 13, No. 11, 1975, pp. 1448-1453.
- Ramaprian, B. R., and Shivaprasad, B. G., "The structure of turbulent boundary layers along mildly curved surfaces," Journal of Fluid Mechanics, Vol. 85, Part 2, 1978, pp. 273-303.
- So, R. M. C., and Mellor, G. L., "Experiment on Turbulent Boundary Layers on a concave Wall," Aeronautical Quarterly, Vol. 26, 1975, pp. 25-40.
- Margolis, D. P., and Lumley, J. L., "Curved Turbulent Mixing Layer," The Physics of Fluids, Vol. 8, No. 10, pp. 1775-1784.
- Fette, Von Heimo, "Stroemungs versuche im rotierenden Laboratrium," Zeitscher. f. tech. Physik, Nr. 7, 1933, pp. 257-266.
- Raj, R., and Lakshminarayana, B., "Characteristics of the wake behind a cascade of airfoils," Journal of Fluid Mechanics, Vol. 61, Part 4, 1973, pp. 707-730.
- Sarpkaya, T., "Vortex-Induced Oscillations," Journal of Applied Mechanics, Vol. 46, 1979, pp. 241-258.
- Perry, A. E., Chong, M. S., and Lim, T. T., "The vortex-shedding process behind two-dimensional bluff bodies," Journal of Fluid Mechanics, Vol. 116, 1982, pp. 77-90.
- Fujita, H., and Kovaszny, L. S. G., "Measurement of Reynolds Stress by a single Rotated Hot Wire Anemometer," The Review of Scientific Instruments, Vol. 39, 1968, pp. 1351-1355.
- Roshko, A., "On the development of turbulent wakes from vortex streets," NACA Rep. 1191, 1954.
- Squire, W. B., and Winter, K. G., "The Secondary Flow in a Cascade of Airfoils in a Nonuniform Stream," Journal of the Aeronautical Sciences, 1951, pp. 271-277.

EXPERIMENT ON TURBULENT BOUNDARY LAYERS OVER A CONCAVE SURFACE - EFFECTS OF INTRODUCTION OF CURVATURE -

Takaaki Shizawa
Research Associate,
Department of Mechanical Engineering,
Science University of Tokyo.

and

Shinji Honami
Associate Professor,
Department of Mechanical Engineering,
Science University of Tokyo,
Shinjuku, Tokyo 162, Japan.

ABSTRACT

The response to the introduction of streamwise concave surface curvature without substantial pressure gradient is discussed to obtain an adequate flow model. The detailed mean velocity and turbulence measurements were performed near the onset of curvature. The behavior of the effective curvature is also reported. The effects of the step change in geometric curvature on the structure of mean flow and turbulence properties are examined.

NOMENCLATURE

$C_f/2$	Skin-friction coefficient
C_{pw}	Static pressure coefficient, $(P_{sw}-P_{swref})/(1/2)\rho U_{pw}^2$
H_1	Shape factor, δ_1/δ_2
K	Acceleration parameter, $(\nu/U_{pw}^2)(dU_{pw}/dx)$
k	Effective curvature
k_{geo}	Geometric curvature, -1.667 m
P_{sw}	Surface static pressure
R	Radius of curvature, 600 mm
U, V, W	Mean velocities
u, v, w	Fluctuating velocities
U_p	Potential flow velocity
U_{pw}	Potential flow velocity at surface
x, y, z	Curvilinear coordinate
δ	Thickness at which velocity is 99.5% of potential flow velocity
δ_1	Displacement thickness
δ_2	Momentum thickness
Π	Coles profile parameter
ζ	Vorticity around z -axis, $-(\partial U/\partial y)-kU/(1+ky)$

subscript

ref Reference, $x=-240 \text{ mm}$

INTRODUCTION

Turbulent shear flows over a concave surface are subjected to complicating influences by extra rates of strain like streamwise curvature. There is a possible influence of streamwise pressure increase at the onset of curvature, unless an effective control of deceleration is conducted. In addition to these effects, turbulent boundary layers become strongly three-dimensional in the mean flow because of the formation of the contra-rotating pairs of longitudinal vortices.

Among the previous researches concerning the concave surface curvature(1-7), So & Mellor(3) studied the response to step change in streamwise curvature by detailed turbulence measurements and concluded that the Reynolds stress $-\overline{uv}$ was increased by the influence of concave curvature. Nakano et al.(6) investigated the effects of stable and unstable free-streams on the flow over a concave surface, and showed that Reynolds

stresses were increased both in the boundary layer and free-stream in case of unstable free-stream condition. Prabhu & Rao(5) studied the effects of strong curvature for different inlet boundary layer thicknesses. The flow patterns did not change appreciably even when the inlet boundary layer thickness varied by a factor of two.

There was substantial deceleration at the onset of curvature in these works. Jeans & Johnston(7) minimized deceleration or acceleration effects and made visual surveys of the flow on the concave surface. The spanwise vortices did not exhibit the stationary pattern.

The flow with the step change in streamwise curvature, like flat to concave surface, is affected by both streamwise concave curvature and streamwise pressure increase at the onset of curvature. These flow situations are found on the pressure sides of turbine blades or wings and at the portions of ducts. There has been no quantitative investigation in which these effects are studied separately. And it is instructive to understand the effects of the introduction of curvature on the physics of the flow in order to establish a new flow model and to design and construct new flow facilities.

The objectives of the present paper are to clarify experimentally the effects of streamwise concave curvature on the turbulent boundary layer flows without substantial deceleration. The study is performed to understand the response of the structure of mean flow and turbulence properties to the step change in curvature by use of flow visualization, mean flow and turbulence measurements. The momentum thickness Reynolds number is 2900 and the ratio of boundary layer thickness to radius of curvature, δ/R , is 0.044 at the onset of curvature.

EXPERIMENTAL FACILITIES AND METHODS

Figure 1 shows the schematic of concave flow facility. The test section is a 150 degrees curved tunnel of rectangular cross-section, followed by a 2000 mm straight recovery tunnel. The curved tunnel is attached to the end of a 1500 mm long, straight development tunnel, in order to attain an equilibrium boundary layer at the reference station ($x=-240 \text{ mm}$). The tunnel is a closed-return type and the surfaces of the curved section are made of transparent Plexiglass plates to permit visual access. A large aspect-ratio of the tunnel, 6, is employed to eliminate the influence of the secondary flow at the mid-span ($z=200 \text{ mm}$) of the tunnel owing to the skewed boundary layer development on the end surfaces.

One of the objectives of the present study is to set up such a flow that the surface static pressure is constant not only over the development surface, but also over the concave surface. The opposite surface configuration (convex side) is adjusted to minimize deceleration and acceleration, like the streamwise pressure

gradient due to streamwise curvature and boundary layer blockage. A test surface has pressure taps 0.5 mm in diameter at 10 to 50 mm intervals. The accuracy of the pressure measurements is ± 0.04 Pa using an improved Chattock gauge.

Flow visualization in boundary layers was conducted by means of the smoke-wire method to check two-dimensionality on the convex surface and the existence of three-dimensional longitudinal vortices over the concave surface. Another object of flow visualization is to fill the gap in understanding of flow patterns and the physics of the flow by the introduction of the step change in curvature.

Eleven stations for measurements are used along the center line of the tunnel ($z = 0$ mm), as shown in Figure 1. At stations 3, 9 and 11 among these, the probe is continuously traversed both spanwise and normal to the surface.

Mean and turbulence velocity measurements were taken using a constant-temperature hot-wire anemometer and a linearizer with a temperature compensation circuit. A specially designed cobra type probe with a space resolution of 0.01 mm was used for the measurements in the vicinity of the surface. This probe has a sensor-wire 5 μ m in diameter and 1 mm in length as well as 20 mm long prongs with a fine copper lead 50 μ m in diameter and 3 mm in length at the tip. The probe location from the surface was determined by a touch of the sensor portion to the surface, resulting in a rapid voltage rise in the hot-wire signal. In each case the tentative origin of the y-coordinate was adjusted to give the actual origin fitting to the linear velocity distribution in the viscous sub-layer. The hot-wire output signals were averaged by an integral-voltmeter. The flow temperature was kept constant within 0.4 °C while a test run.

Reynolds stress tensor measurements were made also using the constant-temperature anemometer. The normal wire around the z-axis was rotated to provide $\overline{u^2}$, $\overline{v^2}$ and $-\overline{uv}$ in a similar method(10).

RESULTS AND DISCUSSIONS

Static Pressure Distribution

Figure 2 shows the distribution of static pressure coefficient C_{pw} over the flat to the concave surface. The pressure coefficient changes from 0.01 to -0.015 in the streamwise direction, and the spanwise variation is 0.006 over the development surface and 0.005 over the curved one, respectively. The acceleration parameter K , is also shown in Figure 2. The largest value of K is 2.6×10^{-7} and is about an order of magnitude lower than the value needed to significantly change the turbulence structure near the surface. Thus, the experimental results might not be affected by any pressure gradients.

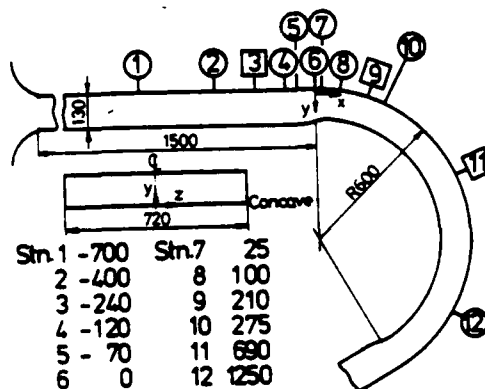


Figure 1 Schematic of experimental apparatus (all dimensions in mm's.)

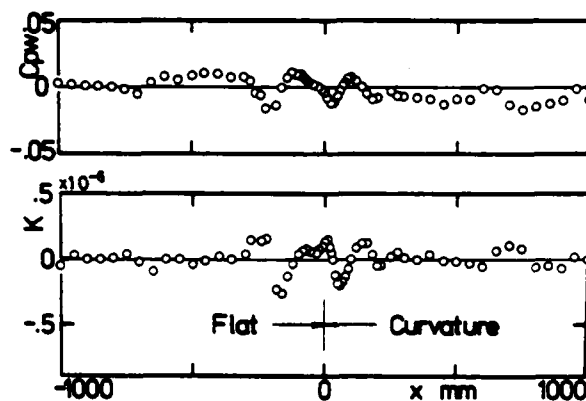


Figure 2 Static pressure coefficient and acceleration parameter

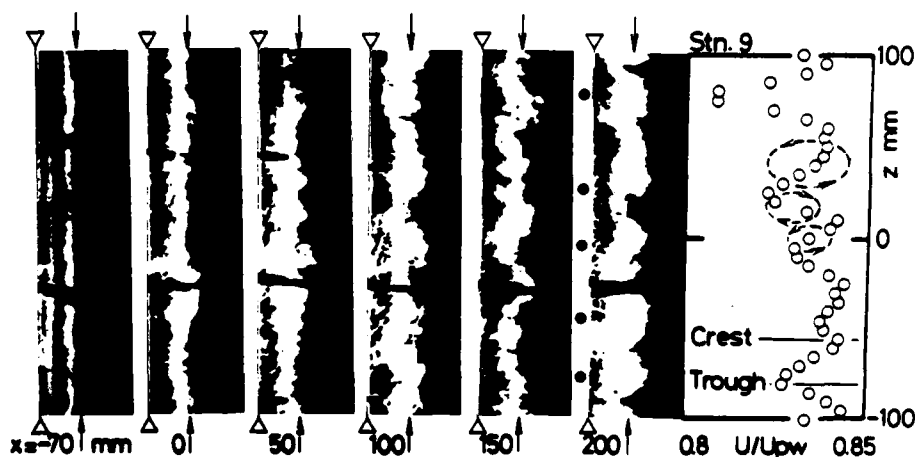


Figure 3 Smoke-wire visualization of longitudinal vortices, mean velocity distribution at $y/d=0.8$ at station 9 and schematic of longitudinal vortices (•; location of trough)

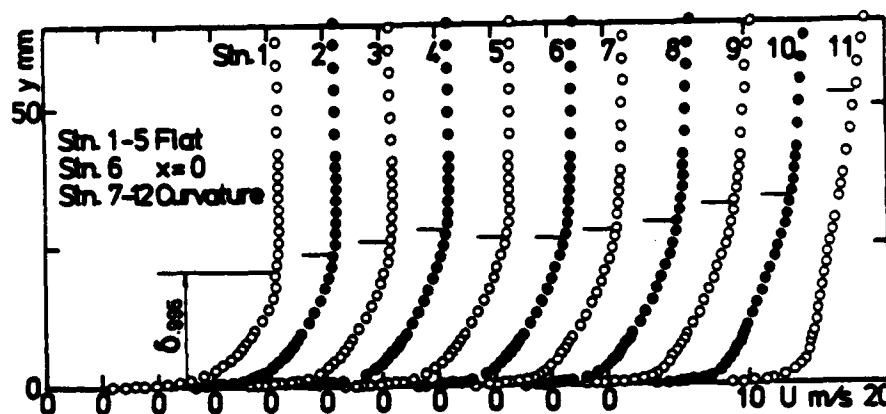


Figure 4 Streamwise distributions of mean velocity and boundary layer thickness

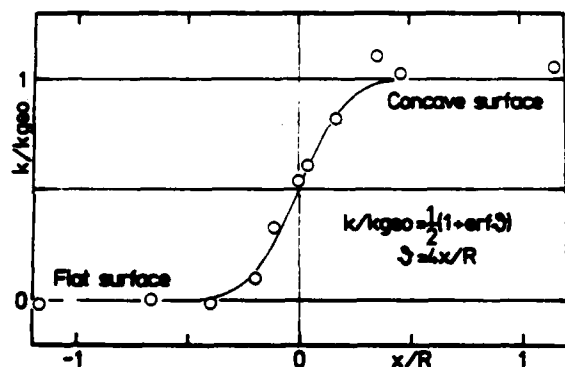


Figure 5 Effective curvature vs. streamwise distance

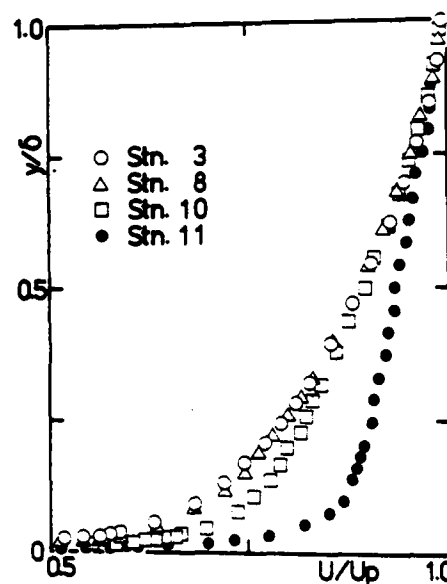


Figure 6 Mean velocity profiles in boundary layer

Flow Visualization

Figure 3 shows the typical results of flow visualization with the spanwise distribution of mean velocity at station 9. The photos indicate the change in flow patterns within the boundary layer over the flat to the concave surface, especially in the vicinity of the onset of curvature. The smoke wire location is set at $x=-150$ mm and $y/\delta=0.8$ away from the surface.

The discrete, stationary smoke lumps and the wavy profiles of the mean velocity indicate the existence of the three-dimensional longitudinal vortices. The contra-rotating pairs of vortices exist between wavelength of the mean velocity profile as illustrated in Figure 3. In the velocity profile, the locations of velocity maxima are called the crest and the minima are the trough, respectively. The smoke lumps locations correspond to the trough between vortices, as shown by the symbol (e) in Figure 3. The smoke uniformly distributes parallel to the development surface upstream of the onset of curvature. Then, the smoke shows spanwise non-uniformity with approaching the onset of curvature. Over the concave surface, the smoke clearly lumps at the trough.

The center section of the tunnel, where measuring stations are located, is found to be in the halfway of the trough and the crest of longitudinal vortices by flow visualization and spanwise measurement of the mean velocity.

Mean Velocity

Figure 4 indicates profiles of mean velocity and boundary layer thickness at the center section of the tunnel ($z=0$ mm). The boundary layer thickness is almost constant near the onset of curvature. The potential flow velocity U_p is given as,

$$U_p = U_{pw} / (1 + ky) \quad (1)$$

where effective curvature k and potential flow velocity at the surface U_{pw} are determined by a least square method using velocity data in the free stream region. The acceleration in free stream velocity occurs even at station 4 owing to the introduction of streamwise curvature.

Figure 5 shows effective curvature reduced by the above method. The results also show a transitional region from the flat to the concave surface; about 8 boundary layer thicknesses "up" and downstream of the onset of curvature. The solid line in Figure 5 is a Gaussian integral curve given by

$$k/kg_{00} = (1/2)(1 + \text{erf } \theta) \quad (2),$$

where

$$\theta = (\sqrt{2}\sigma/R)^{-1/2} (x/R),$$

$$(\sqrt{2}\sigma/R)^{-1/2} = 4$$

and the standard deviation is

$$\sigma = 0.177R$$

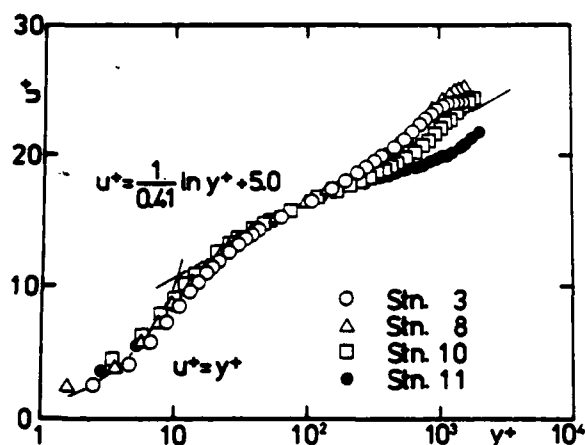


Figure 7 Mean velocity profile plotted in wall coordinates

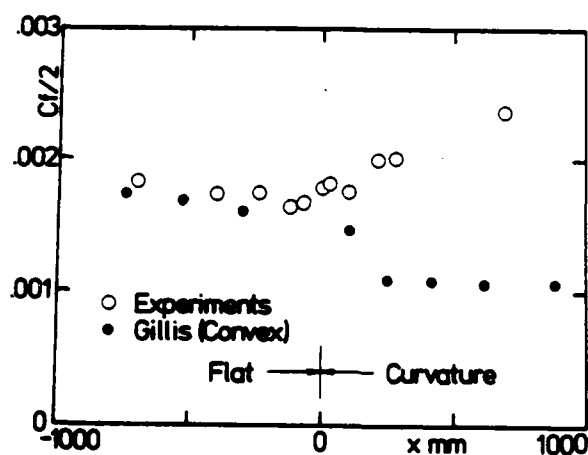


Figure 8 Skin friction coefficients vs. streamwise distance with convex data by Gillis'

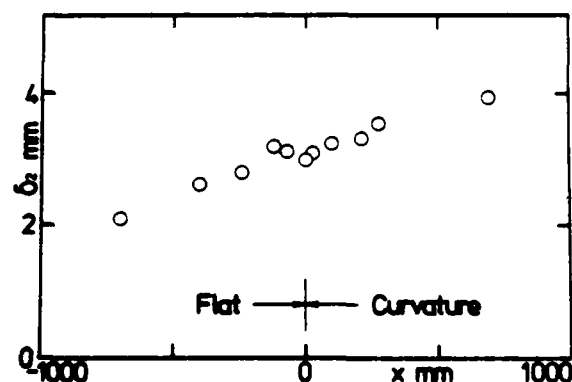


Figure 9 Momentum thickness vs. streamwise distance

Equation (2) closely represents the actual variation, the standard deviation being decided by the data obtained. Since an upstream flow is obviously affected by the step change of curvature in the downstream, a conventional model of effective curvature, like a first-order lag equation, should be modified by a different model.

Figure 6 shows the mean velocity profile in the boundary layer. The velocity profiles at stations 1 to 7 show the same trend as on the flat surface. The defect of the velocity near the surface becomes small as the flow moves downstream of station 8. The profile at station 11 shows quite small defects. The mean velocity profile in the boundary layer responds to concave curvature three boundary layer thicknesses downstream of the onset of curvature, since the effects of concave curvature are observed at station 8.

Figure 7 shows the mean velocity profile in wall coordinate. The profiles in the curved region follow the law of the wall. The inner layer shows the same tendency as on the flat surface even on the concave surface. The profiles of the outer layer indicate the distinct features, i.e., Coles profile parameter Π . The value of Π tends to decrease in the curved region and becomes almost zero or negative at stations 9 to 11 where effective curvature comes up to geometric curvature. Π is evaluated by

$$u^+ = \frac{1}{0.41} \ln(y^+) + 0.5 - \frac{\Pi}{0.41} 2 \sin^2(\pi y / 2\delta) \quad (3),$$

at $y = \delta$.

Figure 8 depicts the skin friction coefficient determined by assuming the logarithmic law. For comparison, the skin friction distributions over the convex surface obtained by Gillis et al. (10) are also included. The concave skin friction increases gradually upstream of the onset of curvature. The effects of curvature on the skin friction shows the same trends as the free stream velocity profile. Further downstream of station 10, the value of $Cf/2$ seems to include the effects of the longitudinal vortices together with curvature, since it shows a monotonous increase.

Figure 9 shows the momentum thickness plotted as a function of streamwise distance. Data shows that the momentum thickness develops slowly near the onset of curvature. In the region with finite effective curvature, the definition of the integral parameter is given as,

$$\int_0^{\delta_1} U dy = \int_0^{\delta} (U_p - U) dy \quad (4)$$

$$\int_0^{\delta_2} U^2 dy = \int_0^{\delta} U(U_p - U) dy \quad (5)$$

Effective curvature in Equation (1) is used to reduce the integral parameters in Equations (4) and (5). The differences in δ_1 , δ_2 , and H_{12} between the above mentioned definitions and the conventional ones at station 11 are -3%, -5.5%, and 3.5%, respectively.

A detailed list of boundary layer parameters is given in Table 1.

Table 1 Boundary layer parameters

x mm	δ mm	δ_2 mm	H_{12}	$Cf/2$ $\times 10^{-3}$	Π
-700	20.9	2.10	1.40	1.81	0.333
-400	24.0	2.62	1.38	1.71	0.387
-240	26.3	2.80	1.36	1.75	0.315
-120	28.2	3.18	1.38	1.64	0.492
-70	26.6	3.09	1.37	1.67	0.508
0	26.5	2.97	1.34	1.77	0.401
25	27.9	3.07	1.33	1.78	0.360
100	29.3	3.23	1.33	1.75	0.448
210	32.4	3.32	1.27	1.98	0.200
275	33.8	3.52	1.26	2.01	-0.079
690	52.2	3.94	1.15	2.33	-0.355

Turbulence Intensity and Reynolds Stress

Figure 10 shows turbulence intensity profiles with those for the flat surface by Klebanoff(11) as well as the convex case by Gillis(10). Turbulence intensity shows a higher level on the concave surface than on the flat and convex one. It is interesting that these profiles at stations 1 to 7 are very similar and the profile at station 8 starts to deviate from the upstream similar profiles. The effects of curvature affect clearly the profile shape downstream of station 8. The profiles at stations 8 to 10 show a higher level of turbulence intensity from $y/\delta = 0.05$ to 0.8, while bulging of increased turbulence in the outer boundary layer ($y/\delta > 0.5$) is observed at station 11. Figure 10 shows the rapid response of turbulent intensity to curvature. In all stations, the turbulence activity very close to the concave surface is remarkable.

Figure 11 shows the profiles of \bar{v}^2 with those obtained by Klebanoff(11) and Gillis(10). The profile at stations 1 to 7 are decreased monotonically but the data show a higher level of \bar{v}^2 near the surface. Downstream of station 8, the profile shows a maximum apart from the concave surface. The response of \bar{v}^2 profiles to the introduction of concave curvature is rapid.

Figure 12 shows the isometric plot of Reynolds stress $-\bar{uv}$. Reynolds stress shows a maximum away from the surface downstream of station 5. As to the shape of the $-\bar{uv}$ profile, the maximum is remarkable downstream of station 8, i.e., 36 downstream of the onset of

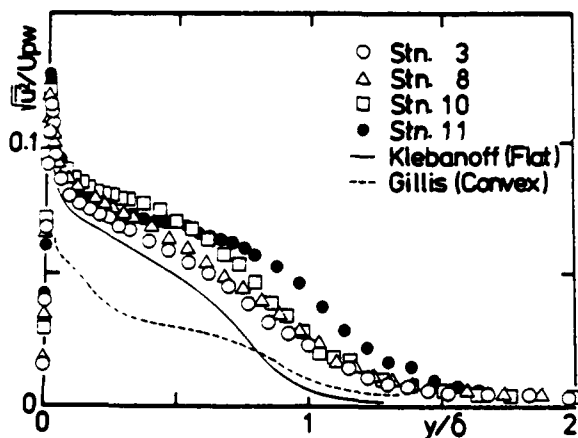


Figure 10 Turbulence intensity

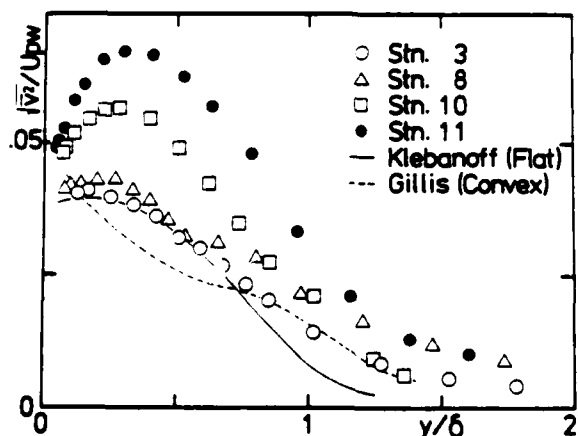


Figure 11 Distributions of \bar{v}^2

curvature. The response of the production of $-\bar{uv}$ to concave curvature is clearly associated with the behavior of effective curvature. The location of the maximum at station 11 is observed at $y/\delta = 0.35$. The values of maximum increase in the downstream region of the concave surface. The productions of $-\bar{uv}$ and \bar{v}^2 respond rapidly to the introduction of curvature.

Each production term in turbulent Reynolds stress transport equation is given by Equations (6) to (11).

Production of

$$1/2 \bar{u}^2 : \{ \bar{u}^2 (\frac{\partial U}{\partial x} - kV) - \bar{uv}(1+ky) (\frac{\partial U}{\partial y} - \frac{kU}{1+ky}) \},$$

$$(-\bar{uw}(1+ky) \frac{\partial U}{\partial z}) \quad (6)$$

$$1/2 \bar{v}^2 : \{ -\bar{v}^2(1+ky) \frac{\partial V}{\partial y} - \bar{uv} (\frac{\partial V}{\partial x} - 2kU) \},$$

$$(-\bar{vw}(1+ky) \frac{\partial V}{\partial z}) \quad (7)$$

$$1/2 \bar{w}^2 : \{ 0 \},$$

$$(-\bar{w}^2(1+ky) \frac{\partial W}{\partial z} - \bar{uw} \frac{\partial W}{\partial x} - \bar{vw}(1+ky) \frac{\partial W}{\partial y}) \quad (8)$$

$$-\bar{uv} : \{ \bar{u}^2 (\frac{\partial V}{\partial x} - 2kU) + \bar{v}^2(1+ky) (\frac{\partial U}{\partial y} - \frac{kU}{1+ky}) \},$$

$$((1+ky) (-\bar{uv} \frac{\partial W}{\partial z} + \bar{uw} \frac{\partial V}{\partial z} - \bar{vw} \frac{\partial U}{\partial z})) \quad (9)$$

$$-\bar{uw} : \{ -\bar{uw}(1+ky) \frac{\partial V}{\partial y} - \bar{vw}(1+ky) (\frac{\partial U}{\partial y} - \frac{kU}{1+ky}) \},$$

$$(\bar{u}^2 \frac{\partial W}{\partial x} + \bar{w}^2(1+ky) \frac{\partial U}{\partial z} + \bar{uv}(1+ky) \frac{\partial W}{\partial y}) \quad (10)$$

$$-\bar{vw} : \{ (\bar{uw} (\frac{\partial V}{\partial x} - 2kU) - \bar{vw} (\frac{\partial U}{\partial x} + kV)) \},$$

$$(\bar{v}^2(1+ky) \frac{\partial W}{\partial y} + \bar{w}^2(1+ky) \frac{\partial V}{\partial z} - \bar{uw} \frac{\partial W}{\partial x}) \quad (11)$$

The first term denotes the production in a two-dimensional curved flow. The second term corresponds to a three-dimensional flow.

Figure 13 illustrates the production mechanism of the six Reynolds stresses. Each production term for the stress in a circle is expressed by multiplying the stress in the next circle or itself by the mean rate of strain on an arrow line. The extra strain rates due to curvature are on the lines

- 1 ; $-\partial V/\partial x + 2kU$
- 4 ; h_z
- 7 ; $-\partial U/\partial x - kV$

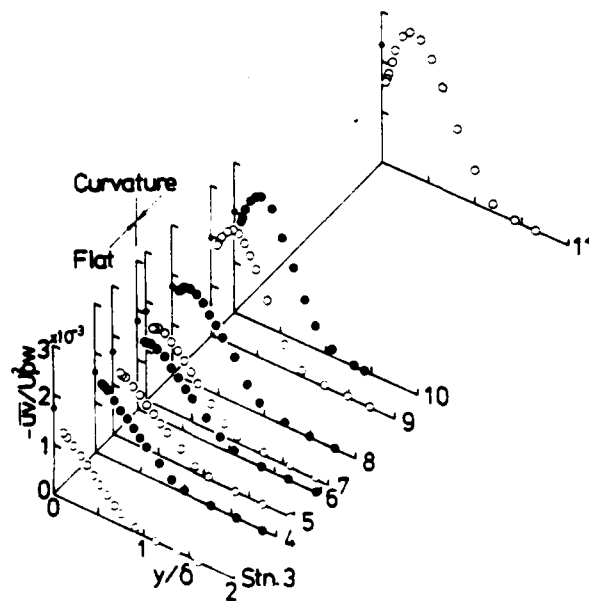


Figure 12 Isometric plot of Reynolds stress $-\bar{uv}$

The strain rate $2kU$ on the line 1 makes a positive contribution to $-\overline{uv}$ and $\overline{v^2}$ production, where a sign of uv in the circle is normally negative. And the vorticity component h_z on the line 4 makes a positive contribution to $-\overline{uv}$ and $\overline{u^2}$ production.

Figure 14 shows the ratio of $2kU$ to h_z to estimate the contribution to the production of each Reynolds stress. The plot shows that the effects of curvature are distinctively observed in the outer layer of the boundary layer downstream of station 8. The concave curvature affects the production of Reynolds stress $-\overline{uv}$ and $\overline{v^2}$ downstream of the onset of curvature. This result agrees well with the results shown in Figures 11 and 12. The production of the Reynolds stresses $-\overline{uv}$ and $\overline{v^2}$ are followed by the behavior of the extra strain rates. This gives another confirmation of rapid response of the production of Reynolds stress to curvature.

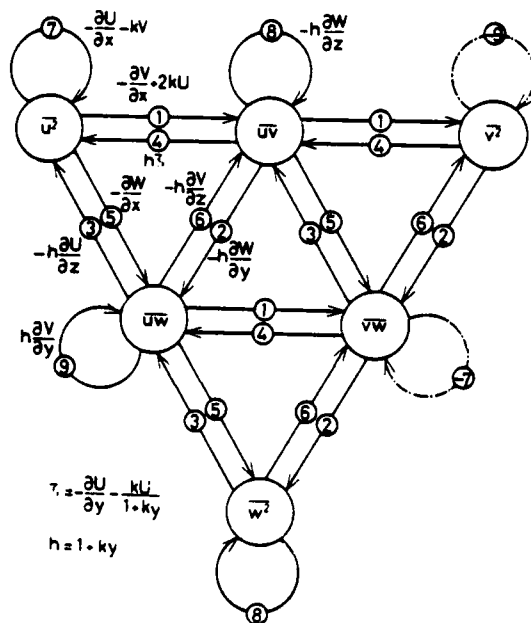


Figure 13 Reynolds stress production mechanism

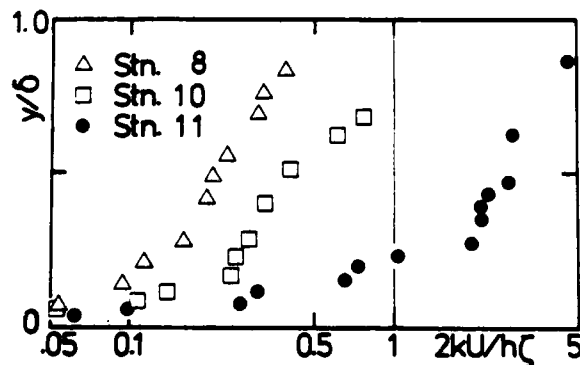


Figure 14 Distributions of $2kU/h_z$

CONCLUSIONS

The main conclusions are as follows.

- 1 The behavior of effective curvature derived from mean velocity distributions in the free stream is made clear. It tends to change upstream of the onset of geometric curvature. Concave curvature affects rapidly the free stream properties.
- 2 The response of the mean flow properties in the boundary layer to concave curvature appears rapidly three boundary layer thicknesses downstream of the onset of curvature.
- 3 Reynolds shear stresses $-\overline{uv}$ and $\overline{v^2}$ increase in rapid response to concave curvature. The extra strain rate due to curvature $2kU$ contributes the production of the stress $-\overline{uv}$ and $\overline{v^2}$. The effects of curvature on the production of $-\overline{uv}$ and $\overline{v^2}$ are remarkable downstream of the onset of curvature.
- 4 The response of the mean flow and turbulence properties to concave curvature is associated with the behavior of effective curvature.

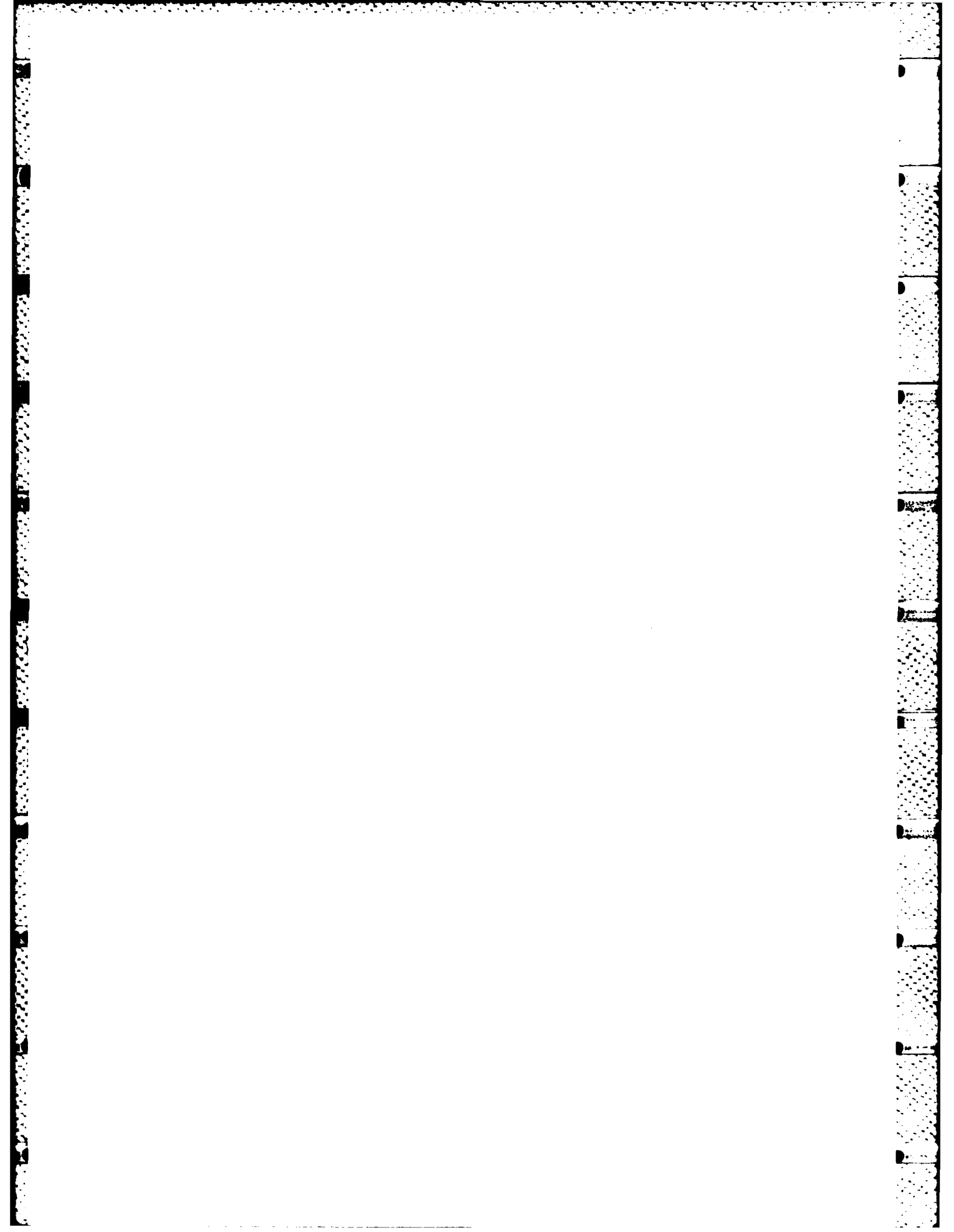
ACKNOWLEDGMENTS

The authors gratefully acknowledges to Professors I. Nakamura, and S. Yamashita in Nagoya University offered many suggestions for the new hot-wire prong design.

During the course of the work, Messrs M. Shirakawa, S. Yana, H. Inoue, M. Fukagawa, and T. Kishida assisted the experiments and reduction of data.

REFERENCES

- 1 Tani, I., 1962, "Production of Longitudinal Vortices in the Boundary Layer along a Concave Wall", J. Geophys. Res., 67-8, 3070.
- 2 Patel, V.C., 1968, "Measurements of Secondary Flow in the Boundary Layer of a 180 Channel", Aero. Res. Council Rep., 30428, 1.
- 3 So, R.M.C., & Mellor, G.L., 1975, "Experiment on Turbulent Boundary Layers on a Concave Wall", Aeronaut. Q., 26, 35.
- 4 Smits, A.J., et al., 1978, "The Effects of Short Regions of High Surface Curvature on Turbulent Boundary Layers", J. Fluid Mech., 94-2, 209.
- 5 Prabhu, A., & Rao, B.N.S., 1981, "Effect of Concave Streamline Curvature on Turbulent Boundary Layers", AIAA 14th Annual Fluid and Plasma Dynamics Conference, Rept. No. AIAA-81-1193.
- 6 Nakano, S., et al., 1981, "Effects of Stable and Unstable Flow over a Concave Surface", 3rd. Sympo. on Turbulent Shear Flows, 4-18.
- 7 Jeans, A.H., & Johnston, J.P., 1983, "The Effect of Concave Curvature on Turbulent Boundary Layer Structure", Structure of Complex Turbulent Shear Flow, Springer Verlag, 89.
- 8 Simon, T., & Honami, S., 1981, "Proc. 1980-81 AFOSR Stanford Conf. on Complex Turbulent Flows", 1, 94.
- 9 Fujita, H., & Kovasznay, L.S.G., 1968, "Measurement of Reynolds Stress by a Single Rotated Hot Wire Anemometer", Rev. Sci. Instrum., 39-9, 1351.
- 10 Gillis, J.C., et al., 1980, "Turbulent Boundary Layer on a Convex Curved Surface", Stanford Univ. Rep., HMT-31.
- 11 Klebanoff, P.S., 1955, "Characteristics of Turbulence in a Boundary Layer with Zero Pressure Gradient", NACA Rep. 1247.



SESSION 7 - JETS

W. Rodi - Chairman

MEASUREMENTS IN A TURBULENT RECTANGULAR FREE JET

W.R. Quinn
Graduate Student

A. Pollard
Associate Professor,
Supervisor

G.F. Marsters
Professor

Department of Mechanical Engineering
Queen's University
Kingston, Ontario
Canada K7L 3N6

ABSTRACT

Mean velocities and turbulence quantities have been measured using hot-wire anemometry in the two central planes of a turbulent free jet of air issuing into still air surroundings from a sharp-edged rectangular slot of aspect ratio 10. It is found that the mean streamwise velocity decay on the jet centreline consists of four regions: a core region, a typical decay region, a transition region and a final decay region; also the mean streamwise velocity profiles in the plane of the slot major axis are characterized by off-centre peaks within the typical decay region. The data imply that there may be some negative production of turbulence kinetic energy in the neighbourhood of the off-centre velocity peaks. The flow does not seem to be completely self-preserving in the region investigated.

INTRODUCTION

Turbulent jets issuing from rectangular slots are useful in a number of engineering areas such as upper surface blowing to increase the maximum lift coefficient, thrust augmentation in V/STOL aircraft, heating, ventilation and air-conditioning systems, fluidics and disposal of pollutant effluents. For low to moderate aspect ratios (i.e. 5 to about 30), these jets are three-dimensional.

Turbulent jet flows issuing from three-dimensional rectangular slots have been investigated experimentally by Krothapalli et al (1981), Marsters (1978, 1981), Trentacoste and Sforza (1967), Sfeir (1976, 1979) and Sforza et al (1966). McQuirk and Rodi (1977) investigated the flow from sharp-edged slots numerically. The experimental studies involved the use of slots of various aspect ratios, Reynolds numbers and exit conditions; but, Krothapalli et al (1981) were the first to extensively measure mean velocities and turbulent quantities in three-dimensions, although not for a sharp-edged slot. A unique characteristic of the flow from these slots is the appearance of off-centre velocity peaks in the plane of the major axis, and these peaks appear prominently only when the flow exits from a slot that is sharp-edged. As an alternative to some other explanations, such as three-dimensional vortex interactions, Marsters (1978), or turbulence driven secondary flows, McQuirk and Rodi (1977), a tentative physical explanation for the existence of these peaks has been put forward by the present authors (Quinn et al (1983)) who indicated that these peaks may be due to a non-uniform pressure

field. Indeed, it is because of the existence of this type of pressure field that McQuirk and Rodi (1977) probably did not detect these peaks, since their calculations assumed that the flow was parabolic. Although the jets issue from slots of various geometries, it is found that the changes in slope of the centreline mean velocity decay are coincident with the location of the merging of the shear layers emanating from the long and short sides of the jet. It is also noticed from the aforementioned investigations that a limited range of Reynolds numbers (12,000 - 88,000) have been used and that the results appear only weakly, if at all, Reynolds number dependent. A more substantial review of the previous work can be found in Quinn (1983).

The purpose of this paper is to provide data of the flow issuing from a sharp-edged rectangular slot at one Reynolds number. These data include all three mean velocities, turbulence kinetic energy, and Reynolds shear stresses.

EXPERIMENTAL DETAILS

The flow facility consisted of a small commercial fan supported on anti-vibration neoprene mounts. The fan drew air from the laboratory and supplied it to a settling chamber via a flexible duct. The settling chamber was a 0.76 m x 0.61 m x 0.61 m plywood box which contained a baffle at the upstream end, six mesh wire screens and a filter. The rectangular slot (designed in accordance with British Standard BS 1042 (1943)) was 12.7 mm x 127 mm and it was attached to the downstream face of the settling chamber. This downstream face was flush with a large plywood wall, so as to ensure that entrainment at the nozzle exit plane was normal to the jet centreline. The top and sides of the rig were covered with 1.59 mm mesh wire screen to prevent large-scale movement of air (room draughts) into the jet.

Single normal wire and X-wire probes were used to diagnose the flow. The wires were calibrated in situ in the core of the jet and were operated by linearized constant temperature anemometers. Temperature variations of about 4°C occurred within the jet. These were monitored with a thermocouple in the neighbourhood of the hot-wire probe and the data subsequently corrected using a modified version of the procedure given by Bearman (1971). The effect of tangential cooling on the wires of the X-wire probes was accounted for by utilizing the corrections of Champagne and Sleicher (1967).

The experiments were performed in a 9.02 m

x 7.39 m x 3.76 m room into which traffic was strictly controlled. Checks of ambient flow conditions verified the hypothesis that external disturbances and those produced by the jet itself were indeed very small.

The jet fluid had a velocity of about 55 m/s at the centre of the slot exit plane. This resulted in a Reynolds number of about 47,000 based on the height (tp) of the slot. The mean streamwise velocity profile at the slot exit plane was found to be flat. The streamwise turbulence intensity at the centre of the slot exit plane was about 0.7%.

The bilateral symmetry of the flow was utilized in acquiring the data and checks were made to ascertain that symmetry did in fact exist in the two planes containing the major and minor axes of the slot. The coordinate system used is as shown in Fig. 1.

The initial boundary layer was turbulent with a quasi-laminar core. This was substantiated by spectral measurements on the jet centreline and in the shear layer region in the near flow field.

PRESENTATION AND DISCUSSION OF RESULTS

Mean Flow

The decay of the mean streamwise velocity along the jet centreline is as shown in Fig 2. Shown also for comparison purposes are the results of Sforza et al (1966) and Sfeir (1979). Four regions can be identified. The first is a constant velocity region known as the potential core which ends at about $x/tp = 3$. Note that this curve begins at $x/tp = 1$ at which point the maximum velocity is found due to the existence of a vena contracta in the plane of the minor axis of the jet. At this location, the centreline mean velocity has increased by about 7% above the mean exit velocity. This is followed by a typical decay region (i.e. aspect ratio, upstream shaping, etc.; see, for example, Sfeir (1979)); this decay region ends at about $x/tp = 30$ at which point the shear layers, emanating from the minor axis sides, merge. The velocity in this region

decays approximately as $x^{-0.34}$. The third decay region can be regarded as a transition between the typical and final decay regions. It starts after $x/tp = 30$ and ends just before $x/tp = 60$, at which point the final decay region begins. The velocity in this final region decays more or less like that of a jet from a circular nozzle and has therefore been called "axisymmetric decay region" by Sforza et al (1966) and Trentacoste and Sforza (1967).

The axisymmetric decay region implies that the mean streamwise velocity should decay as x^{-1} . However, the decay in this region varies depending upon whether the initial boundary layer is laminar, turbulent or a mixture of these, Hussain and Clark (1977). As noted above, the initial boundary layer was a mixture and so we deduce mean streamwise velocity decay as $x^{-1.11}$. This value appears to be in accord with Sfeir (1979), since it can be deduced from his data that the mean streamwise velocity decays as $x^{-1.07}$.

Profiles of the mean streamwise velocity in the two planes of symmetry (X-Y, X-Z) are shown in Figs. 3 and 4. The profiles in the X-Y plane are flat in the core region (Fig. 3a, $x/tp = 2$). They are characterized by off-centre peaks in the typical decay region (Fig. 3a, b, $x/tp = 5, 10, 20$). Note the asymmetry of the profiles in the neighbourhood of the peaks at $x/tp = 5$ and 10 (Fig. 3a, b). The profiles are self-similar beyond $x/tp = 30$. The X-Z plane profiles have the usual bell shape (Fig. 4a) and are self-similar beyond $x/tp = 10$.

The growth (spread) of the jet in the two

planes of symmetry is shown in Fig. 5. The results of Sforza et al (1966) and Sfeir (1979) are again included for comparison. Both half-widths decrease initially but then start to increase monotonically when the shear layers growing in the respective planes reach the jet centreline. The initial decrease in both half-widths is attributable to vena contracta effects associated with the flow from a sharp-edged slot. It is interesting to note that at $x/tp = 150$, the jet half-widths cross again, implying that the flow is still developing. We believe that this is the first evidence of a second crossover. Even so, further measurements are needed to confirm this trend.

Mean spanwise velocity profiles are presented in Fig. 6. These profiles consist of negative spanwise velocities (i.e. mean spanwise velocities pointing toward the jet centreline) up to $x/tp = 30$ whereafter the profiles are made up of mostly positive spanwise velocities.

Mean lateral velocity profiles are presented in Fig. 7. Apart from the profile at $x/tp = 2$, all profiles indicate positive lateral velocities. The mean lateral velocities, it will be noticed, are larger than the mean spanwise velocities.

The mean lateral and transverse velocity profiles are similar to those obtained by Krothapalli et al (1981); but, it should be noted that they used a slot geometry very different from the present one.

TURBULENCE QUANTITIES

The variation of the centreline turbulence intensities with downstream distance is shown in Fig. 8. Initially, there is a steep increase in turbulence intensities as the shear layers from all four sides of the slot grow and interact. This increase peaks at about $x/tp = 15$, thereafter dropping as the shear layers from the shorter sides of the nozzle reach the jet centreline. The turbulence intensities increase again in a monotonic fashion after $x/tp = 30$. The behaviour of the turbulence intensities on the jet centreline seems to confirm that the initial condition is not fully turbulent, (see Hill et al (1976), and Bradshaw (1966)).

Turbulence kinetic energy profiles derived from turbulence intensity data are presented in Figs. 9 and 10. The turbulence kinetic energy increases with downstream distance on the jet centreline and peak values of this quantity are found in the shear layer regions in both planes of symmetry. The locations of the peaks do not coincide with those of the maximum mean streamwise velocity gradient at the corresponding measurement stations. This is most likely due to the lateral shift of the spanwise and lateral turbulence intensity peaks from the location of the maximum mean streamwise velocity gradient as observed both here and by Wygnanski and Fiedler (1970). One feature, however, deserves attention; namely, the decrease in turbulence kinetic energy in the neighbourhood of the peaks at $x/tp = 5$ and 10 (Fig. 9a,b). It should be recalled that the velocity profiles in the neighbourhood of the off-centre velocity peaks were asymmetrical at $x/tp = 5$ and 10. As has been noted by Hinze (1970) and Eskinazi and Erian (1969), asymmetry about a zero velocity gradient point in a flow leads to negative production of turbulence kinetic energy. This appears to account for the observed decrease in turbulence kinetic energy at $x/tp = 5$ and 10. The decrease is probably not due to stabilizing streamline curvature otherwise it should have been observed also at $x/tp = 20$.

Turbulent shear stress profiles are presented in Figs. 11 and 12. These profiles

are characterized by peaks in the shear layer region, as expected. The zero shear stress point at $x/tp = 5$ and 10 in the X-Y plane does not appear to coincide with the point of zero mean streamwise velocity gradient thus lending support to the argument made above of negative production of turbulence kinetic energy in the region of the mean velocity peaks. The turbulent shear stress in the X-Z plane is smaller than that in the X-Y plane at all but two of the measurement stations ($x/tp = 5, 150$, this latter station is not shown). This seems to be indicative of strong memory of the initial conditions. The flow seems to be close to a self-preserved state as far as the turbulent shear stresses are concerned. This may not be surprising since the turbulent shear stresses reach a self-preserved state before the normal stresses do in other free shear flows (see Boguslawski and Popiel (1979)).

CONCLUSIONS

Mean flow and turbulence quantities have been measured in a three-dimensional turbulent rectangular free jet of aspect ratio 10. The following conclusions are drawn:

- The mean streamwise velocity decay on the jet centreline consists of four regions, namely, a potential core, a typical decay region, a transition region and final decay region.
- The flow in the typical decay region in the X-Y plane is characterised by off-centre velocity peaks which apparently disappear just before the region ends. These peaks are not found in the potential core or in the X-Z plane of the typical decay region.
- The mean velocity profiles exhibit self-similarity in the X-Z plane. Self-similarity in the X-Y plane occurs only after about $x/tp = 30$.
- The turbulence kinetic energy and shear stress profiles do not show any signs of self-preservation, for $x/tp \leq 100$ at least.
- Memory effects of the initial conditions may be strong in the flow.

ACKNOWLEDGEMENTS

The authors acknowledge the financial support of the Natural Sciences and Engineering Research Council of Canada.

REFERENCES

- Bearman, P.W. (1971) "Corrections for the effect of ambient temperature drift on hot-wire measurements in incompressible flow", DISA Information, 11, 25.
- Boguslawski, L. and Popiel, Cz. O. (1979) "Flow structure of the free round turbulent jet in the initial region". Journal of Fluid Mechanics, Vol. 90, pp. 531-539.
- Bradshaw, P. (1966) "The effect of initial conditions on the development of a free shear layer", Journal of Fluid Mechanics, 26, 225.
- Champagne, F.H. and Sleicher, C.A. (1967) "Turbulence measurements with inclined hot-wires -- Part 2. Hot-wire response equations", Jn. of Fluid Mechanics, 28, 177.
- Eskinazi, S. and Brian, P.F. (1969) "Energy reversal in turbulent flows". The Physics of Fluids, Vol. 12, No. 10, pp. 1988-1998.
- Hill, W.G., Jenkins, R.C. and Gilbert, B.L. (1976) "Effects of the initial boundary layer state on turbulent jet mixing", AIAA Journal, 14, 1513.
- Hinze, J.O. (1970) "Turbulent flow regions with shear stress and mean velocity gradient of opposite sign". Applied Scientific Research, Vol. 22, pp. 163-175.
- Hussain, A.K.M.F., and Clark, A.R. (1977) "Upstream influence of the near field of a plane turbulent jet", Phys. Fluids, 20, 1416.
- Krothapalli, A., Baganoff, D. and Karamcheti, K. (1981) "On mixing of a rectangular jet", Journal Fluid Mechanics, 107, 201.
- Marsters, G.F. (1978/79) "The effects of upstream nozzle shaping on incompressible turbulent flows from rectangular nozzles", Transactions of CSME, 4, 197.
- Marsters, G.F. (1981) "Spanwise velocity distributions in jets from rectangular slots", AIAA Journal, 19, 148.
- McGuirk, J.J. and Rodi, W. (April 1977) "The calculation of three-dimensional turbulent free jets", Symposium on Turbulent Shear Flows, University Park, Pennsylvania, Vol.1, pp. 1.29.
- Quinn, W.R. (1983) "Three-dimensional turbulent free jet flow", Ph.D. Thesis, Queen's University, in preparation.
- Quinn, W.R., Pollard, A. and Marsters, G.F. (1983) "On saddle backed velocity distributions in a three-dimensional turbulent free jet", Paper 83-1677, AIAA Fluid and Plasma Dynamics Conference, Danvers, Mass. July.
- Sfeir, A.A. (1979) "Investigation of three-dimensional turbulent rectangular jets", AIAA Journal, 17, 1055.
- Sfeir, A.A. (1976) "The velocity and temperature fields of rectangular jets", International Journal of Heat and Mass Transfer, 19, 1289.
- Sforza, P.M., Steiger, M.H. and Trentacoste, N. (1966) "Studies on three-dimensional viscous jets", AIAA Journal, 4, 800.
- Trentacoste, N. and Sforza, P.M. (1967) "Further experimental results for three-dimensional free jets", AIAA Journal, 5, 885.
- Wynagnanski, I. and Fiedler, H.E. (1970) "The two-dimensional mixing region". Journal of fluid Mechanics, Vol. 41, pp. 327-361.

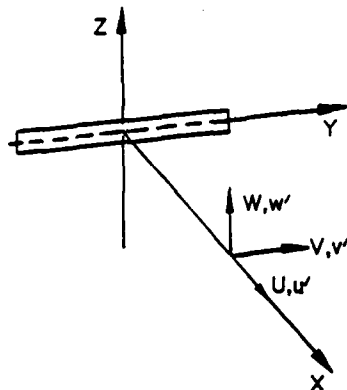


Fig. 1: Flow Coordinate System.

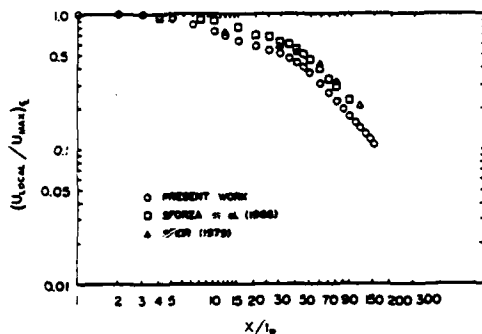


Fig. 2: Mean Streamwise Velocity Decay on the Jet Centreline.

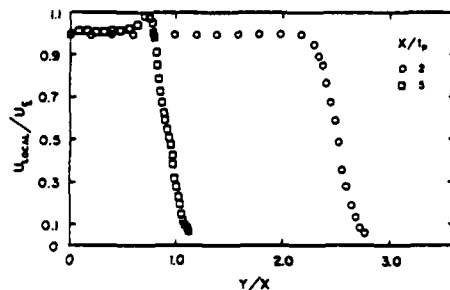


Fig. 3a: Mean Streamwise Velocity Profiles in the X-Y Plane.

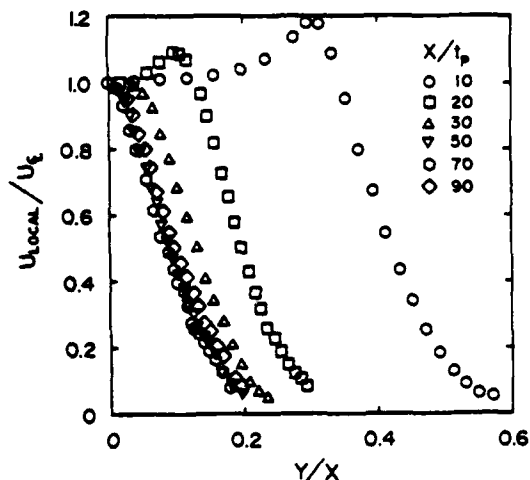


Fig. 3b: Mean Streamwise Velocity Profiles in the X-Y Plane.

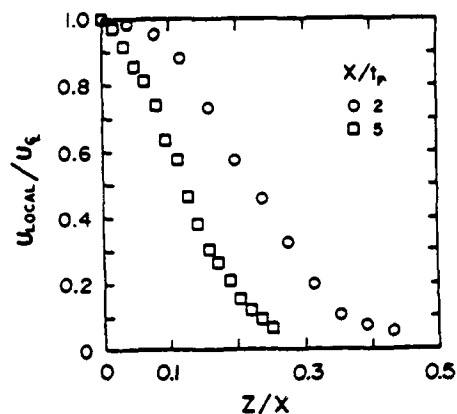


Fig. 4a: Mean Streamwise Velocity Profiles in the X-Z Plane.

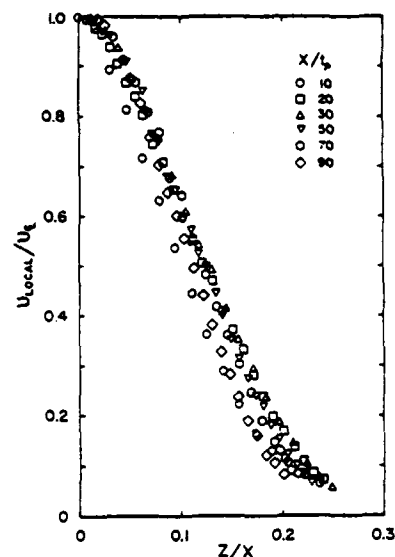


Fig. 4b: Mean Streamwise Velocity Profiles in the X-Z Plane.

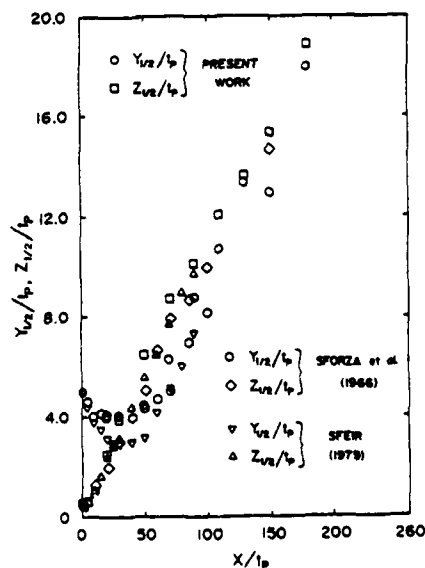


Fig. 5: Jet Growth (Spread) in the X-Y and X-Z Planes.

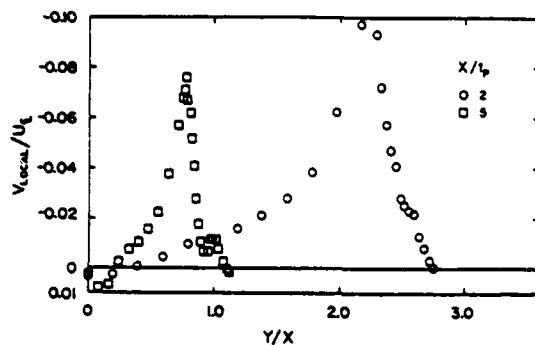


Fig. 6a: Mean Spanwise Velocity Profiles in the X-Y Plane.

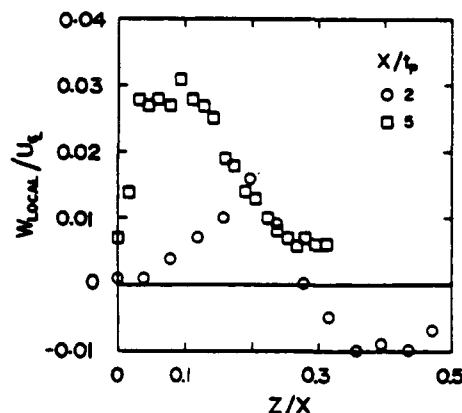


Fig. 7a: Mean Lateral Velocity Profiles in the X-Z Plane.

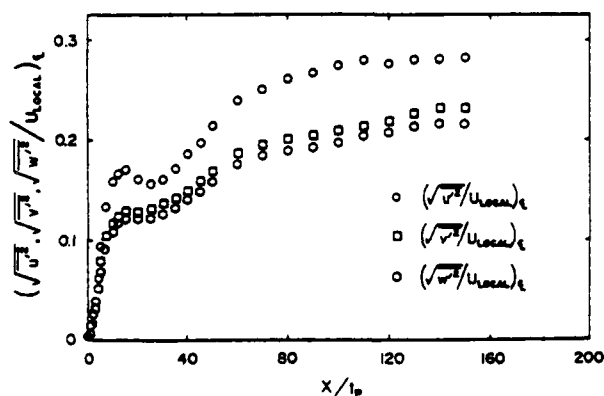


Fig. 8: Variation of the Turbulence Intensities on the Jet Centreline.

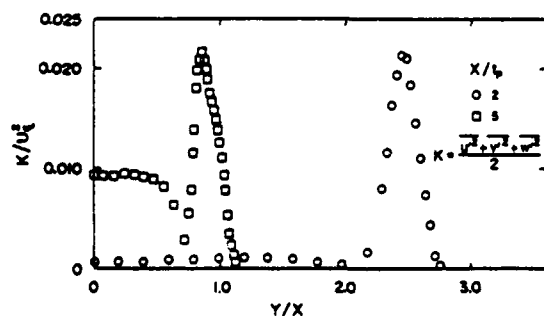


Fig. 9a: Turbulence Kinetic Energy Profiles in the X-Y Plane.

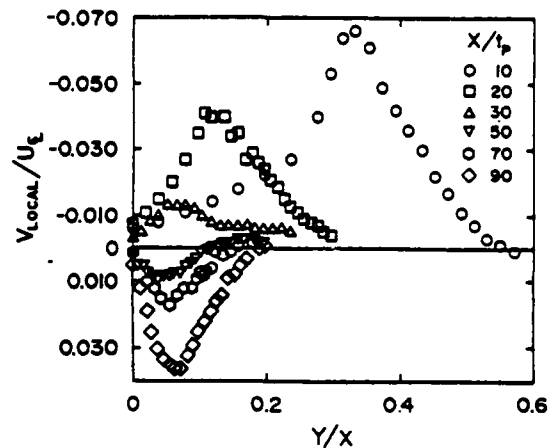


Fig. 6b: Mean Spanwise Velocity Profiles in the X-Y Plane.

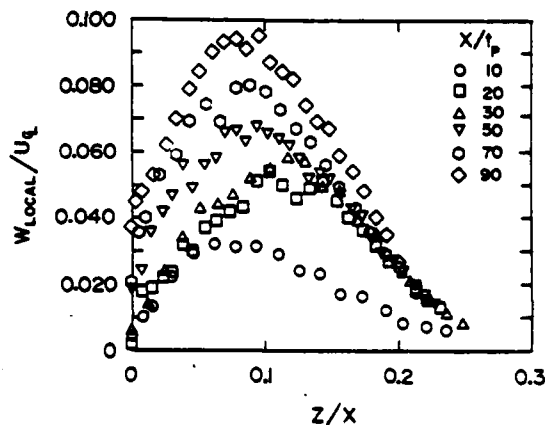


Fig. 7b: Mean Lateral Velocity Profiles in the X-Z Plane.

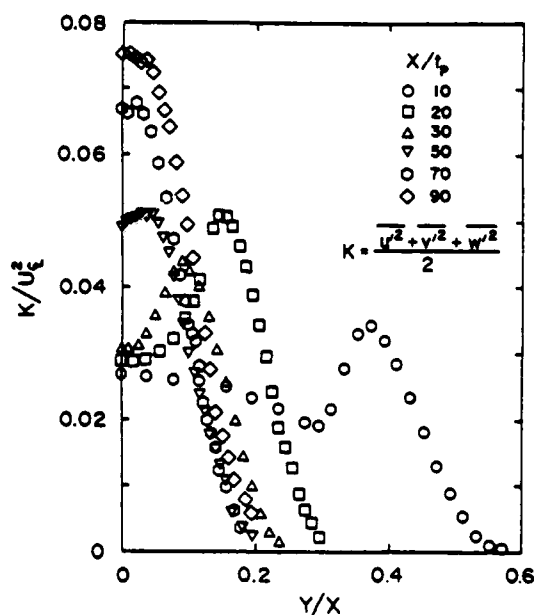


Fig. 9b: Turbulence Kinetic Energy Profiles in the X-Y Plane.

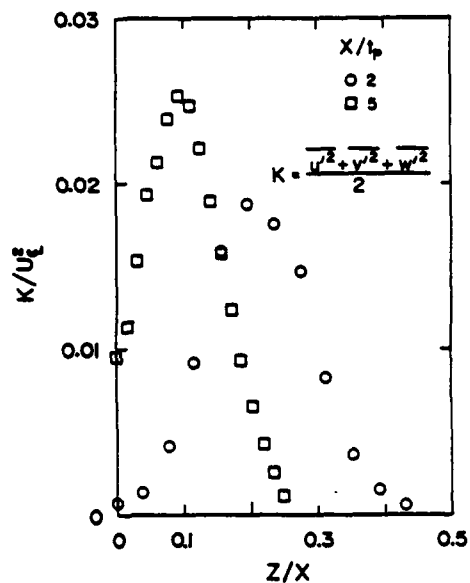


Fig. 10a: Turbulence Kinetic Energy Profiles in the X-Z Plane.

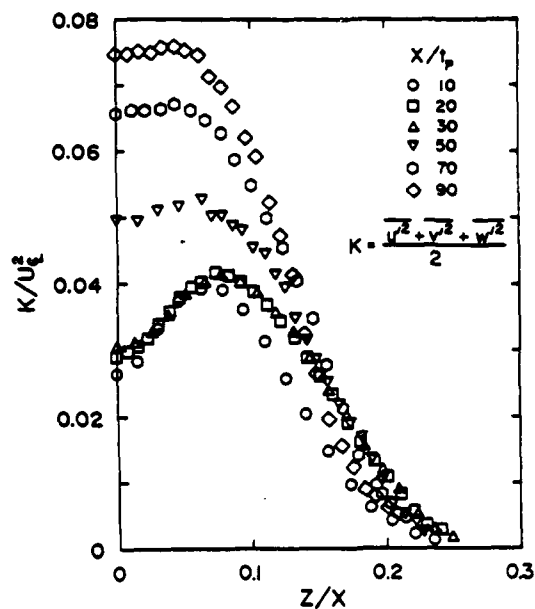


Fig. 10b: Turbulence Kinetic Energy Profiles in the X-Z Plane.

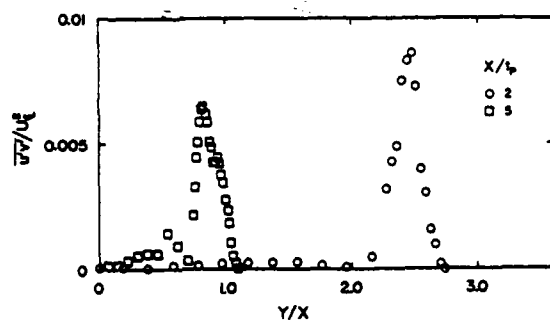


Fig. 11a: Turbulent Shear Stress Profiles in the X-Y Plane.

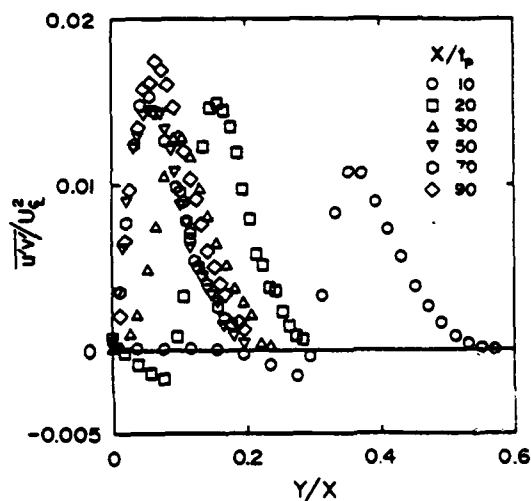


Fig. 11b: Turbulence Shear Stress Profiles in the X-Y Plane.

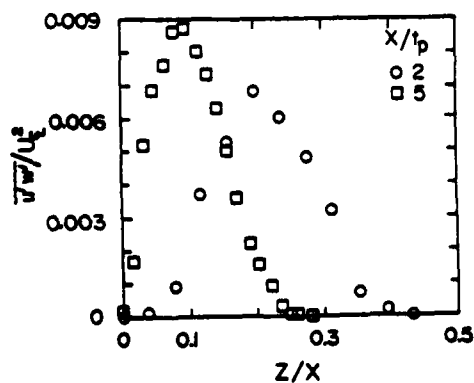


Fig. 12a: Turbulent Shear Stress Profiles in the X-Z Plane.

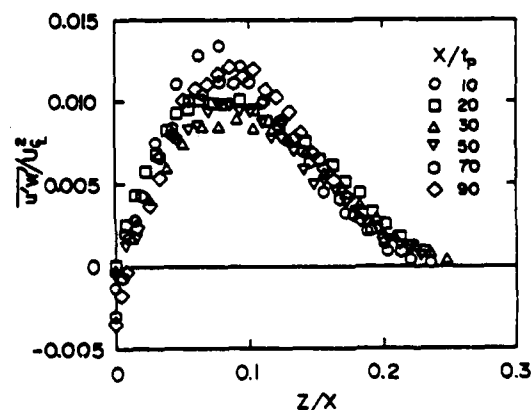


Fig. 12b: Turbulent Shear Stress Profiles in the X-Z Plane.

MEASUREMENTS IN TWO-DIMENSIONAL JETS AND PLUMES

M.S. Chandrasekhara and B.R. Ramaprian

Iowa Institute of Hydraulic Research
The University of Iowa
Iowa City, IA, USA

ABSTRACT

Experimental results on plane asymptotic nonbuoyant jets and buoyant plumes are presented. All the significant plume parameters have been measured—many of them for the first time—using two-component, frequency shifted Laser Doppler anemometry and resistance thermometry. These results show that buoyancy has significant effect on the turbulence structure. The plume data can be used as bench mark values in the development of turbulence models for these complex flows.

INTRODUCTION

Buoyancy-driven flows represent an interesting class of complex turbulent flows. Such flows are also of considerable practical interest because of many engineering applications. There is very little information available on the detailed turbulence structure of these flows. The lack of comprehensive set of data on these flows has been a major drawback in the development of calculation methods for their prediction. The available literature consists of single component velocity measurements only. [See Kotsovinos(1975) for plane plumes and George et al (1977), Nakagome & Hirata (1976) for axisymmetric plumes]. The purpose of the present study was to obtain these data in a basic buoyancy dominated flow situation, namely a two-dimensional asymptotic plume. For a comparative study, corresponding measurements were also obtained in two-dimensional nonbuoyant jets in the same apparatus using the same instrumentation.

EXPERIMENTAL PROCEDURE

Plumes were produced in the present experiments by discharging heated water vertically upwards from a two-dimensional slot located on the floor of a large reservoir containing cold water. The slot was 25 cm long and 0.5 cm wide (D). Two-dimensionality of the flow was improved by confining the flow between two vertical plexiglas sidewalls spaced 25 cm apart. Traverses were made for obtaining simultaneous velocity (U,V) and temperature (ΔT) across the flow (y-direction) using two-component frequency-shifted Laser Doppler Anemometry (LDA) and resistance thermometry. The LDA system was used in the 3-beam fringe mode with polarization being used to separate the two components. Frequency trackers were used to process the signals from the photodetectors. Instantaneous temperatures were measured using commercially available quartz fiber-coated hot film probes (DISA 55R11), as "cold film" probes in a Wheatstone bridge circuit. A temperature measuring system was developed for this purpose. This system uses two probes one of which is placed in the flow and the other in the "ambient", so

that the excess temperature (ΔT) in the flow can be measured directly. This system has a flat response upto about 65 Hz, which was adequate for the present study. The three channels of data (U,V from LDA and ΔT from the temperature system) were acquired, digitized and processed using the HP-1000 minicomputer at the Institute. Data sampling rates, sample sizes and record lengths were appropriately chosen to obtain acceptable accuracy in the measurement of the various mean and turbulent properties of the flow.

The nominal experimental conditions corresponding to the plume studies are the following:

- (i) exit velocity, $U_j = 10$ cm/s, exit excess temperature $\Delta T_j = 22^\circ$ C. This flow will be referred to as MSC3.
- (ii) exit velocity, $U_j = 5$ cm/s, exit excess temperature $\Delta T_j = 22^\circ$ C. This flow will be referred to as MSC4.

In addition, experiments were also conducted on a nonbuoyant jet (MSC2) with $U_j = 30$ cm/s, and $\Delta T_j = 5^\circ$ C and an isothermal jet (MSC1) with $U_j = 30$ cm/s and $\Delta T_j = 0^\circ$ C. These results will be used for comparison with those of the plumes.

Use of LDA in heated flows presents certain serious problems associated with the fluctuations of refractive index. These were largely overcome by using a simple but very effective technique. This consisted of passing each of the three beams through tubes (7.5 cm long x 3 mm dia) filled with water and closed at one end with Wratten gelatin filter. The beams were thus isolated from the heated fluid over a large part of their passage through the fluid over a large part of their passage through the fluid. The tubes ended about 5 cm away from the measurement point so as not to disturb the measurements. It was confirmed (from measurements made with and without tubes in nonbuoyant/isothermal jets) that there was no significant effect of the tubes on the measurements (see figure 5).

RESULTS AND DISCUSSION

In the following paragraphs, results from the measurements obtained in the region $20 < x/D < 60$ are presented. It was found that all the three flows had attained near-asymptotic behavior beyond $x/D = 30$. Extensive results including mean velocities, mean temperature, Reynolds shear stress, heat fluxes, turbulent diffusion, energy spectra and intermittency distributions have been obtained in this region and are discussed in detail in Ramaprian and Chandrasekhara (1983). Of these, only the major results, especially those that are of direct relevance to turbulence model development are presented here.

Richardson Number

An important parameter used to characterize the plane buoyant jet is the Richardson number R , defined as, (see Kotsovinos, 1975)

$$R(x) = [Q(x)/M(x)]^3 / \beta(x) \quad (1)$$

Here,

$$Q(x) = \int_{-\infty}^{\infty} U dy \quad (2)$$

$$M(x) = \int_{-\infty}^{\infty} U^2 dy \quad (3)$$

$$\text{and } \beta(x) = \int_{-\infty}^{\infty} \alpha g (\overline{U \Delta T} + \overline{U T}) dy \quad (4)$$

are the kinematic mass, momentum and buoyancy fluxes respectively. α is the thermal expansion coefficient of water. When a buoyant jet reaches the asymptotic state, namely the plume, it is completely characterized by its kinematic buoyancy flux, which is conserved when α is constant. (Rouse et al, 1952). It can be shown that the Richardson number for the plume is a universal constant and is approximately equal to 0.3. Figure 1 which shows the values of $R(x)$ at different axial locations for the two plumes MSC3 and MSC4 confirms this. The two flows despite their different initial conditions are seen to approach the same terminal value of R (In this and other figures, x_0 is a virtual origin obtained from plots of momentum variation with the streamwise distance x). Kotsovinos (1975) reported a value of 0.6 for this terminal Richardson number. It can be shown that this value is not consistent with his other measurements. (See Chandrasekhara, 1983).

Decay Rates of Maximum Velocity and Excess Temperature

It is well known that the centerline velocity U_m in a plane nonbuoyant jet varies as the inverse square root of the distance from the virtual origin. Dimensional analysis for the asymptotic plane plume shows that

$$U_m \sim \beta^{1/3} \quad (5)$$

or,

$$U_m / \beta^{1/3} = \sigma_u = \text{constant.}$$

Hence, U_m should be a constant along the plume. Figure 2a shows that this is indeed the case. Plotted in this figure are the centerline velocities for the two buoyant jets, normalized by $\beta^{1/3}$. The present experiments suggest that

$$\sigma_u = U_m / \beta^{1/3} = 2.15. \quad (6)$$

This value is different from the value of 1.66 quoted by Kotsovinos (1975). The value of 1.88 quoted by Rouse et al (1952) is also shown for comparison in the figure. Figure 2a also shows that both the buoyant jets have reached the plume state in the experimental range.

Dimensional analysis shows that in the plane plume, the centerline excess temperature decays according to the relation

$$\beta^{2/3} / (\alpha g \Delta T_m) = \sigma_t x. \quad (7)$$

Figure 2b shows that the centerline temperature excess decreases linearly with x , as per the plume similarity law, eq. (7). Both the plumes show the same decay rate within experimental scatter. The data indicate that $\sigma_t = 0.37$. There is better agreement among available results in the literature on temperature decay possibly because temperature can be measured more easily and reliably.

Mean Velocity

All available data show that the velocity profiles in jets and plumes are nearly Gaussian. This is supported by the present study (figure 3). Slight deviations can be seen near the edges. In fact, very slight negative velocities were also measured there. Since these were of the same order of magnitude as the measurement uncertainties, not much importance can be

given to this observation. The temperature profiles also exhibited self-similar, near-Gaussian shape at all the measurement stations. Hence, both can be described well by the expressions,

$$U/U_m = \exp(-Ay^2/b_u^2) \quad (8)$$

$$\text{and } \Delta T/\Delta T_m = \exp(-Ay^2/b_t^2) \quad (9)$$

where

$$A = -\ln(0.5)$$

$$b_u = \text{velocity half width}$$

$$\text{and } b_t = \text{temperature half width.}$$

Lateral Mean Velocity

Figure 4 shows the distributions of the transverse mean velocity, V , in the plume at different x/D . Even though there is some scatter, the trend is very clear and self-similarity of the profiles is perceivable. The velocity in the central region of the plume is nearly zero showing that the streamlines are nearly parallel there. This agrees with the fact that the axial mean velocity is constant in the plume and hence,

$$\frac{\partial U}{\partial x} \Big|_{y=0} = -\frac{\partial V}{\partial y} \Big|_{y=0} = 0$$

from the continuity equation. The theoretical distribution obtained by integrating the mass conservation equation as

$$\frac{V}{U_m} = \frac{db_u}{dx} [n \exp(-An^2) - \frac{1}{2} \sqrt{\frac{\pi}{A}} \text{erf}(n\sqrt{A})] \quad (10)$$

(with $n \equiv y/b_u$) has also been plotted in the figure. Some differences can be seen, especially near the edges. However, the agreement should be considered to be satisfactory particularly when it is noted that the velocities measured are of the order of a few (0-8) millimeters/second. Quantitative differences are primarily due to measurement uncertainties and possible non-Gaussian behavior of the axial velocity near the edges.

The distribution for the nonbuoyant jet MSC2 is also shown in the figure for comparison. The distributions of V across jets and plumes are quite different from each other as expected. Since, $\partial U/\partial x \neq 0$ at the centerline of a nonbuoyant jet, $\partial V/\partial y$ is also nonzero and the streamlines diverge near the centerline. The distribution of V , therefore, crosses zero on both sides of the jet. Also, of particular interest is the comparison of the entrainment coefficients for the jet and plume. The entrainment coefficient α_0 , is usually defined as

$$\alpha_0 = \frac{1}{U_m} \frac{dQ}{dx} = \frac{2|V_e|}{U_m} \quad (11)$$

From the asymptotic theory, one gets,

$$\alpha_0 = 0.122 \text{ for the nonbuoyant jet}$$

$$\text{and } \alpha_0 = 0.222 \text{ for the plume.}$$

Experimental data also show this relative increase, though the individual magnitudes are seen to be lower. This shows that a plume entrains nearly twice as much ambient fluid as the jet. Further, since U_m is constant in a plume, V_e is also constant everywhere along the plume, unlike in a jet in which it decreases continuously.

Reynolds Shear Stress

Figure 5 shows distributions of the Reynolds shear stress uv in the plume MSC3 at different x/D and also its typical distribution in the plume MSC4. To the best knowledge of the authors, these are the first shear stress data available on two-dimensional plumes. Also plotted are the theoretical distribution (obtained from the momentum equation) and the distributions measured in the isothermal (MSC1) and nonbuoyant (MSC2) jets. The comparison between the jets MSC1 and MSC2 validates the technique used for overcoming the refractive index problem. The measured values for the plume indicate that the normalized shear stress profiles are self-similar (within experimental scatter) and that the peak value of $\sigma = 0.03$ is about 45%

higher than the value of about 0.02 measured in the jets. The line shown in figure 5 is drawn by eye-ball judgement through the data at the last measurement station. The theoretical distribution of uv is obtainable from the momentum equation as

$$\frac{uv}{U_m^2} = \frac{db_u}{dx} \left[\frac{U}{U_m} \right]^2 - \left(\frac{U}{U_m} \right) \left(\frac{V}{U_m} \right) - \frac{1}{2} \frac{db_u}{dx} I_{2n} - \frac{I_2}{I_1} \frac{I_{1n}}{2} \frac{db_u}{dx} \quad (12)$$

where

$$I_{1n} = \int_{-n}^n \left(\frac{U}{U_m} \right) dn$$

$$I_{2n} = \int_{-n}^n \left(\frac{U}{U_m} \right)^2 dn$$

I_1 and I_2 are the integrals I_{1n} and I_{2n} evaluated between $-n$ to n . The theoretical result is also shown in figure 5. It indicates a higher maximum value = 0.034, compared to the measured value. But, the general agreement between theory and measurement is satisfactory over most of the plume. Quantitative differences are once again due to possible limitations of the theory as well as measurement uncertainties. The fact that uv_{max} is nearly 45% higher in plumes is significant and shows that the turbulence activity is enhanced by buoyancy.

Longitudinal Heat Flux

Plotted in figure 6 are the distributions of $uT/U_m \Delta T$ for the nonbuoyant jet MSC2, and plumes MSC3 and MSC4. It is evident from the figure that the values for the plumes are larger at all points in the flow. Of particular interest is the total area under the curve, or $\int uT dy$, which represents the longitudinal turbulent heat flux. This quantity is about 10% of the mean kinematic heat flux, $\int U \Delta T dy$. The value of 40% reported by Kotsovinos (1975) in this connection is thus contradicted by the present study. On the other hand, the present results are in qualitative agreement with those of George et al (1977) and Nakagome and Hirata (1976) for round plumes. These results confirm that the asymptotic plume is not drastically different from any other boundary layer-like flow.

Triple Correlations

Two triple correlation terms, namely u^2v and v^3 , relevant to the diffusion of the turbulent kinetic energy were measured. These compared in figures 7 and 8 for an isothermal jet and plume MSC3. It can be seen that the terms are generally larger for the plume. A point of interest is the fact that the u^2v distribution has a crossover on either side of the axis. This occurs at approximately the maximum intensity point in the u' profile. v^3 profiles for the plume have no crossovers, unlike that for the jet. It was found that the v' distribution was flat near the axis for the plume whereas in the case of the jet there was a valley near the centerline. These results thus seem to support the concept of a gradient transport model for turbulent kinetic energy (or its individual components). Many of the reported measurements on jets do not show these crossovers (See Everitt and Robins, 1978). But, it should be noted these were obtained with hotwires and the errors of measurement are maximum for the triple correlations.

Eddy Viscosity

The eddy viscosity ϵ_m is defined by

$$-uv = \epsilon_m \frac{\partial U}{\partial y} \quad (13)$$

or

$$\epsilon_m = \frac{(-uv/U_m^2)}{\partial(U/U_m)/\partial n} \quad (14)$$

Velocity derivatives obtained by differentiating the Gaussian fit to the velocity data, and a smoothed shear stress profile were used for the calculation. The resulting distributions of $(\epsilon_m/U_m b_u)$ are presented in

figure 9. An average constant value of 0.028 seems appropriate for the normalized eddy viscosity in the isothermal jet. The value for the plume is seen to be about 0.040. This represents an increase of nearly 45% in the plume, which is very significant. Also, the distribution of ϵ_m in the plume is flatter and shows that the overall turbulence activity is increased everywhere in the plume.

Mixing Length

The Prandtl mixing length l , as defined by

$$l^2 = -uv / \left[\left(\frac{\partial U}{\partial y} \right) \left| \frac{\partial U}{\partial y} \right| \right] \quad (15)$$

was calculated for both the flows. Figure 10 shows the distributions of the nondimensional mixing length. An increase of 15-20% in the mixing length can be seen for the plume. It is also not constant across the plume. This suggests that a constant mixing length model is not applicable to jets and plumes. A constant eddy viscosity model seems to describe the structure of these flows better.

CONCLUDING REMARKS

A simple but effective technique has been developed for the LDA measurements in nonisothermal flows. Using this technique, the first successful measurements of many turbulent properties, notably the Reynolds shear stress, of the asymptotic plume have been made. Comparison with measurements in nonbuoyant jets shows that buoyancy increases the Reynolds stresses significantly. All the quantities relevant to the development of turbulence models for buoyancy driven flows are presented. Complete details of the study and a full set of original data are available from Ramaprian and Chandrasekhara (1983).

ACKNOWLEDGEMENT

The study was supported by the National Science Foundation through Grants No. ENG77-22756 and No. CME-8006797. This support is gratefully acknowledged.

REFERENCES

1. Chandrasekhara, M.S., 1983, "Study of Vertical Plane Turbulent Jets and Plumes", Ph.D. thesis, Mechanical Engineering Program, The University of Iowa, Iowa City, Ia.
2. Chen, C.J., Rodi, W., 1978, "On Decay of Vertical Buoyant Jets in Uniform Environment", 6th Int. Heat Transfer Conference, Toronto, Canada.
3. Everitt, K.W., Robins, A.G., 1978, "The Development and Structure of Plane Jets", J. Fluid Mech., 88, 563.
4. George, W.K., Alpert, R.L., Tamanini, F., 1977, "Turbulence Measurements in an Axisymmetric Buoyant Plume", Int. J. Heat and Mass Transfer", 20, 1145.
5. Kotsovinos, N.E., 1975, "A Study of the Entrainment and Turbulence in a Plane Buoyant Jet", W.M. Keck Laboratory of Hydraulics and Water Resources, Rep. No. KH-R-32, California Inst. of Technology.
6. Nakagome, H., Hirata, M., 1976, "The Structure of Ambient Diffusion in an Axisymmetric Thermal Plume", Proc. ICHMT, Seminar on Turbulent Buoyant Convection, Dubrovnik, Yugoslavia.
7. Rouse, H., Yih, C.S., Humphreys, H.W., 1952, "Gravitational Convection from a Boundary Source", Tellus, 3, 201.
8. Ramaprian, B.R., and Chandrasekhara, M.S., 1983, "Study of Vertical Plane Turbulent Jets and Plumes", Inst. of Hydraulic Research Report 257, The University of Iowa, Iowa City, Ia., USA.

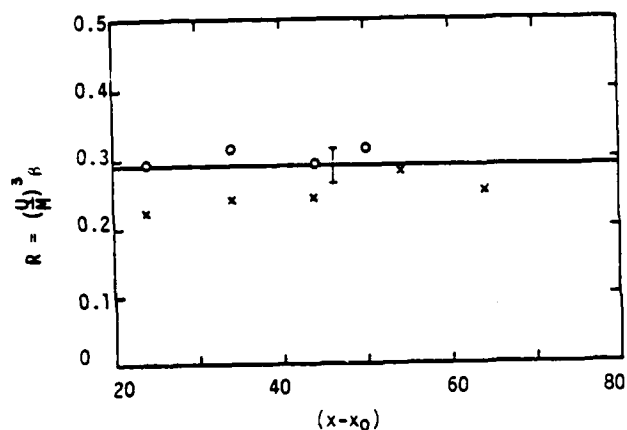


Figure 1. Local Richardson number in plumes. x, MSC3; o, MSC4; —, $R = 0.29$.

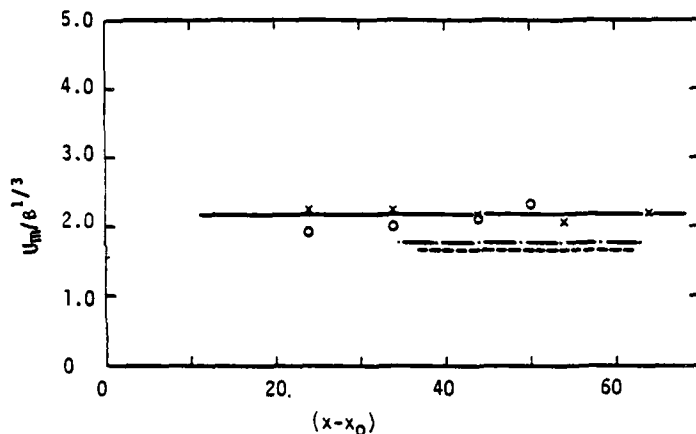


Figure 2a. Decay of centerline velocity in plumes. x, MSC3; o, MSC4; ---, Kotsovinos (1975); ----, Rouse et al (1952); —, line corresponding to $\sigma_u = 2.15$ (present recommendation).

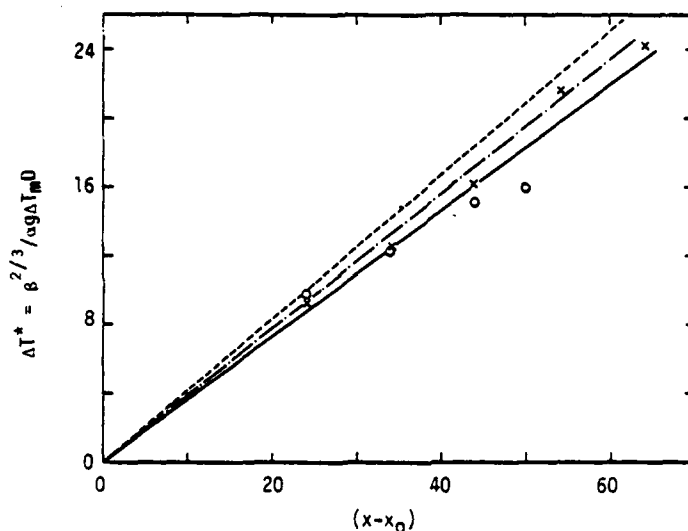


Figure 2b. Decay of centerline excess temperature (or density difference) in plume. ($\Delta T^* = C(x - x_0)$). Present experiments: $C = 0.37$; x, MSC3; o, MSC4. Kotsovinos (1975): ---, $C = 0.42$. Rouse et al (1952): ----, $C = 0.38$.

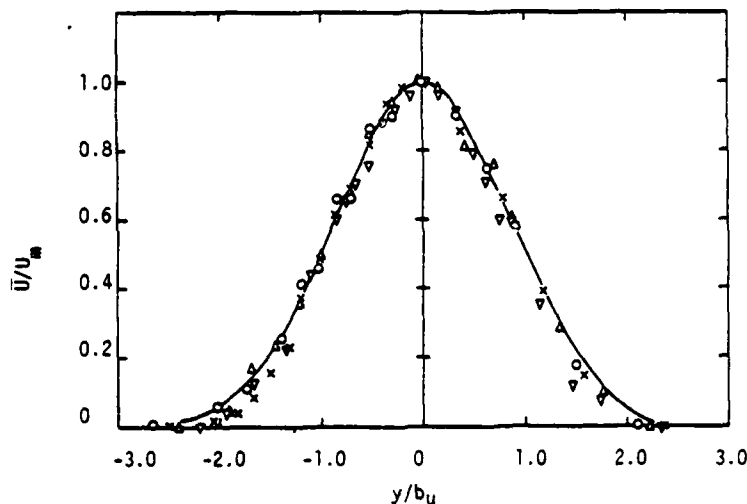


Figure 3. Longitudinal mean velocity distribution in plume MSC3. x, $x/D = 20$; o, $x/D = 30$; Δ , $x/D = 40$; ∇ , $x/D = 60$; —, Gaussian.

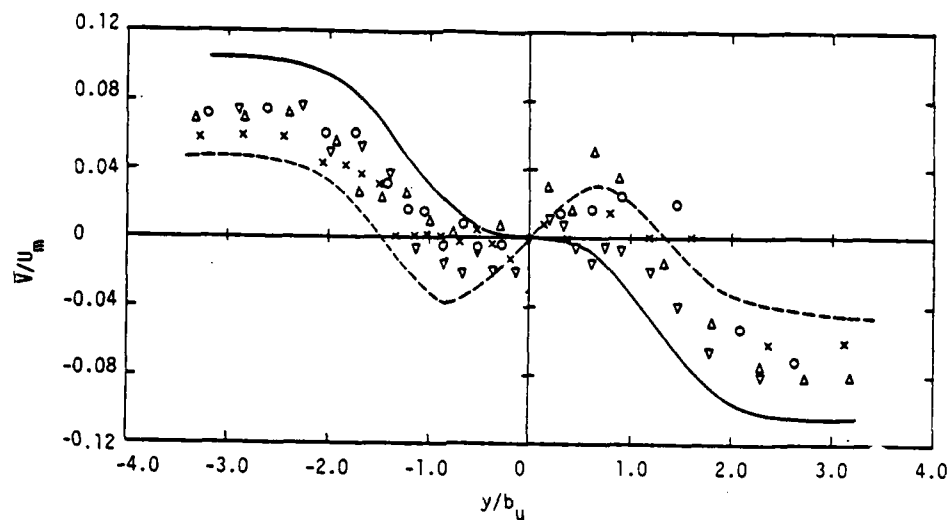


Figure 4. Lateral mean velocity distribution in plume MSC3. x, $x/D = 20$; o, $x/D = 30$; Δ , $x/D = 40$; ∇ , $x/D = 60$; —, from eq. 10; ---, Data for isothermal plane jet.

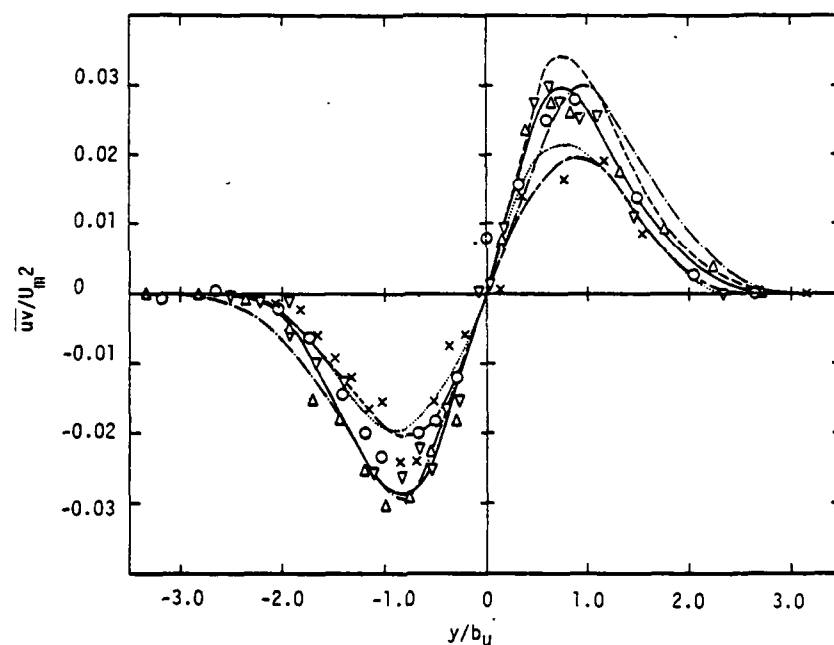


Figure 5. Reynolds shear stress distribution in plumes. Plume MSC3: x, $x/D = 20$; o, $x/D = 30$; Δ , $x/D = 40$; ∇ , $x/D = 60$; --- eq. 12, - · - · -, plume MSC4; - - - -, jet MSC1, jet MSC2.

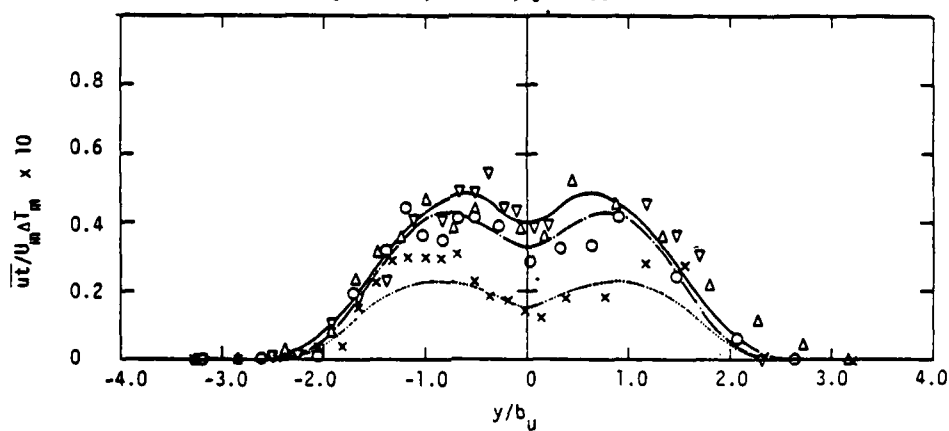


Figure 6. Distribution of longitudinal heat flux in plumes. (symbols same as in figure 5).

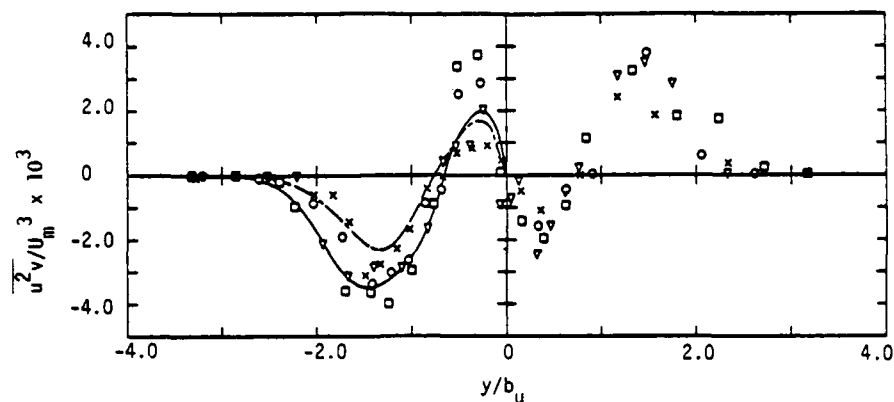


Figure 7. Distribution of $\overline{u^2 v} / U_m^3$. \times , $x/D = 20$; o , $x/D = 30$; Δ , $x/D = 40$; \square , $x/D = 60$; ---, jet MSC1.

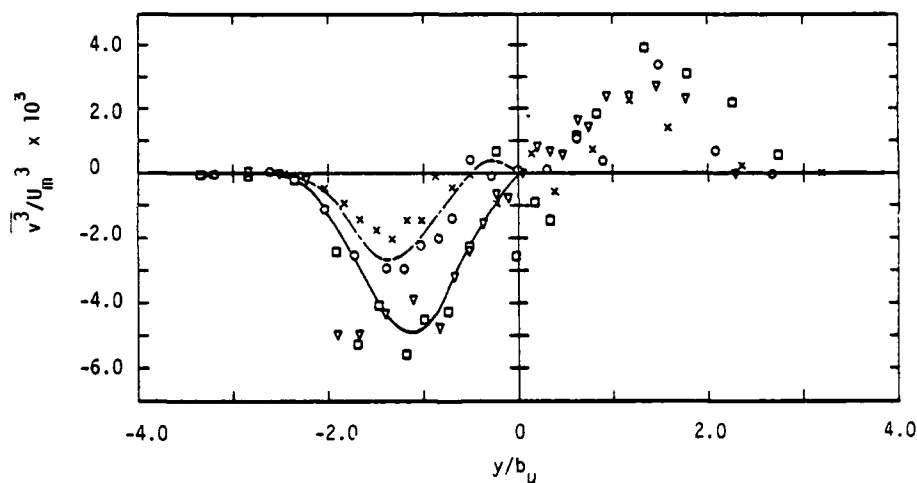


Figure 8. Distribution of $\overline{v^3} / U_m^3$. (symbols same as in figure 7)

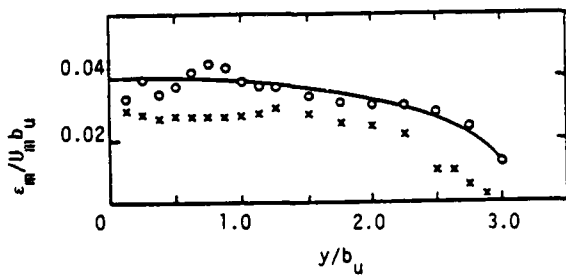


Figure 9. Distribution eddy momentum diffusivity. \times , jet MSC1; o , plume MSC3

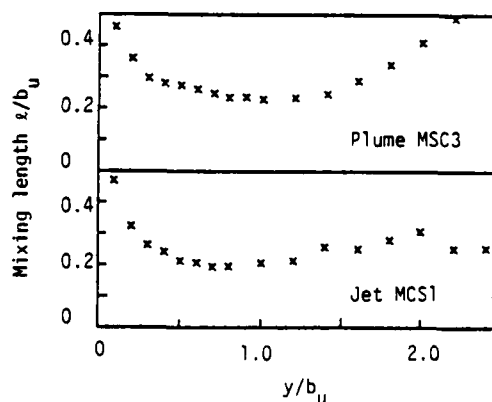


Figure 10. Distribution of mixing length in the jet and the plume.

ON A FORCED ELLIPTIC JET

E. Gutmark and C.M. Ho
Department of Aerospace Engineering
University of Southern California
Los Angeles, California 90089-1454

ABSTRACT

A forced elliptic jet of small aspect ratio (2:1) was studied experimentally. The measurements included flow visualization in a water jet and hot-wire measurements in an air jet. The flow visualization results show clearly the switching of the major and minor axes of the elliptic vortex rings convected downstream. At low forcing frequencies, the deformation of the vortex rings in the jet, agrees with the analysis of an isolated elliptic vortex. At high forcing frequencies, vortex merging occurred. The evolution of the vortices during merging was very complicated. The measured velocity field of the forced jet was similar to the unforced case. For example, the difference of the flow fields in the major and minor sides was evident. The large spreading rate of the minor axis side relative to the low rate of the major axis side resulted in a switching of the jet axes.

INTRODUCTION

In the analysis of an isolated elliptic vortex ring by Dhanak & DeBernardinis (1981), it was shown that the major and minor axes switched as the vortex moved in the downstream direction. At the same time, the side cross section of the vortices also deformed. The deformations were a strong function of the vortex aspect ratio. It was also observed in a two dimensional jet (Sforza & Trentacoste 1967) that there is a difference in the mean flow field between the two axes planes. It was the purpose of the present research to investigate the vortex evolution in a forced jet and the effect of forcing on the elliptical jet.

In the flow visualization experiment, the forcing frequency, f_p , was varied in a wide range with respect to the most amplified frequency, f_n , so that $1.6f_n < f_p < 1/6f_n$. In the hot wire measurements, the air jet was forced only at the preferred mode frequency.

FACILITY AND INSTRUMENTATION

The experiments were performed in two facilities. The flow visualization was carried out in an elliptic water jet, and the flow field was measured by a hot-wire in an air jet.

Both jets had an elliptic nozzle with a major and minor axes of 50.8 mm and 25.4 mm, respectively (Aspect ratio 2:1, Figure 1). The shape of the nozzles was circular at the side which was connected to the cylindrical stagnation chamber and elliptic at the exit. The contraction contours on both axes were fifth order polynomials.

The water jet had a 127 mm diameter pipe as a settling chamber. The area contraction ratio was 12.5:1. Honeycomb and screens were installed inside the settling chamber to reduce the turbulence level. The entire jet was submerged in a water tank (737 x 737 x 1219 mm³). The water jet was driven by a water pump at a Reynolds Number of 7000 (based on the nozzle's major radius and the exit velocity). The jet forcing was applied by a rotating butterfly valve which was installed in the hose that supplied the water. The forcing frequency varied between 1 Hz to 10 Hz. The natural most amplified frequency was 6 Hz. Food color injected into the flow at the nozzle lip, was used for flow visualization.

The air jet had a similar nozzle to that of the water jet, with an area contraction ratio of 18:1. An axial fan was used to blow air through the jet at a Reynolds number of 17000. The air jet stagnation chamber was a 212 mm diameter pipe. Honeycomb and screens were installed in this pipe to reduce the turbulence level to 0.1% at the exit. Forcing was applied to the jet by a loudspeaker installed at the side of the stagnation chamber. The loudspeaker was driven by a sinusoidal signal generated by a function generator and amplified by a power amplifier. The forcing level was 4% of the mean exit velocity. The forcing frequency was 60 Hz which was the preferred mode frequency of the jet at $U_j = 10$ m/sec and also the organ pipe resonance frequency of the jet.

The flow field was measured by a constant temperature hot-wire anemometer, which had a 30 kHz frequency response. The hot-wire signals were digitized and analyzed by a PDP 11/55 minicomputer.

EXPERIMENTAL RESULTS

Flow Visualization

The dye injector used in the flow visualization experiment enabled a uniform injection of dye around the nozzle lips so that the entire vortex rings could be visualized. Four sequences of the vortex evolution in the jet, for three different forcing frequencies, are given in figures 2-5. All the forcing frequencies were lower than the natural instability frequency (6Hz). The instability frequency was suppressed because of the high forcing level, and the vortices were formed in the forcing frequency. Riley and Metcalfe (1980) also showed that if the subharmonic frequency is introduced to the flow without the fundamental frequency, the pairing process is bypassed and vortex roll-up occurs in the subharmonic frequency. Figure 2 shows the case of $f_p = 1/4f_n = 1.4$ Hz. This is a view of

the minor axis side.

The vortex section of the Minor axis side moves faster than the other sections of the vortex, causing deformation of the vortex. This trend is changed when axes switching occurs, yielding a straightening of the vortex crosssection. At $f_F = 2.7\text{Hz} = 1/2 f_n$, (figures 3 and 4) the vortex structures are depicted in both the minor axis plane (figure 3) and major axis plane (figure 4). Two switchings of the major and minor axes can be observed in this case. The major and minor axes become equal first at $X/a = 1.75$, and a second time at $X/a = 3.4$. (a is the major axis radius.) The lag of the minor axis section behind the major axis section of the vortex, near the nozzle, is clearly demonstrated in figure 4. In the downstream direction, at $X/a = 4.3$, a vortex merging occurs. Prior to this merging azimuthal instability starts to develop around the vortices.

Using a set of pictures of the two planes at this forcing frequency, three sided views of the jet vortices evolution are reconstructed in figure 5. The vortex switching is evident especially from the top view. This data is used to compare with the evolution of isolated elliptic vortex rings as calculated by Dhanak and De Bernardinis 1981 (figures 6 and 7). The present case which has an elliptic nozzle with an aspect ratio of 0.5, is compared with two isolated vortex rings aspect ratios, discussed in this paper, of 0.4 and 0.6. Two geometrical aspects of the vortex structures are compared. In figure 6a the variation of the vortex crosssection width in the downstream direction is given in the two planes, as a function of its relative time in the switching period. Figure 6b describes the variation of the vortices deflection height (H). The forced elliptic jet vortices have a very similar evolution pattern as the isolated vortex rings, when the above geometric characteristics are compared. The jet behavior is somewhat closer to the isolated vortex ring with a 0.6 aspect ratio.

A very complicated vortex interaction pattern is demonstrated in the higher forcing frequency of $f_F = 3.9\text{Hz}$. The merging in this case is accompanied by a strong distortion of the participating vortices. The merging location moved upstream ($X/a = 2.5$), relative to its location at $X/a = 4.3$ for $f_F = 2.7\text{Hz}$ (Figure 3), as a result of the increase in the forcing frequency.

An oblique view of the vortices (figure 8) reveals the evolution of the elliptic vortex, through the switching process, as it moves downstream. Three consecutive switchings can be observed in this case.

The Velocity Field

The mean velocity profiles were measured on both major and minor axes planes from $x/a = 0.05$ (where a is the radius of the major axis) to $x/a = 15$. (figures 9, 10). The difference between the spreading patterns on both axes is striking. The jet spreads much more rapidly in the minor axis plane. Similar behavior was also observed in a unforced elliptic jet (Gutmark and Ho 1983A, Gutmark and Ho 1983B). This rapid spreading resulted in a substantially higher entrainment of this jet relative to an axisymmetric or plane jet. A more illustrative demonstration of the switching process and the different spreading rates of both axes is shown in figure 11, where the jet width at the major and minor axes planes are compared. The width is defined here as the distance from the jet axis to the location where the velocity drops to 50% of its maximum value ($Y_{0.5}, Z_{0.5}$) or to 30% ($Y_{0.3}, Z_{0.3}$). The jet width on the minor axis plane increases continuously from the nozzle exit and becomes equal to the major axis at $x/a = 4$. The jet width on the major axis plane ($Y_{0.5}$) decreases up to $x/a = 6$ and then increases again.

In an unforced elliptic jet, the narrowing of the major axis side was not observed and the major axis side remained constant up to $x/a = 12$.

The variation of the mean axial velocity and the axial fluctuating velocity component with the axial position is given in figure 12. The mean velocity remains constant up to $x/a = 4$, while the axial component of the intensity reaches maximum value at $x/a = 9$. This behavior is different from a axisymmetric jet, where both these locations are at the end of the jet potential cone, at a distance of about 4.5 diameters from the nozzle.

CONCLUSION

The visualization of an unforced elliptic jet did not show clear vortex ring structures. The reason for this is, probably, because the higher mode instability waves are more pronounced in this jet. In a jet with spatially coherent forcing, the elliptic rings are clearly observed. When the forcing frequency is about the preferred mode frequency, $f_F = 1/4 f_n$, the vortex rings behave according to the theoretical prediction (Dhanak and De Bernardinis 1981). At $f_F = 1/2 f_n$, vortex merging occurs. The vortices deform in a very complicated manner during their merging.

Hot wire measurements were done only in one forcing frequency, $f_F = 1/4 f_n$. The mean flow characteristics of the present forced elliptic jet are very similar to the unforced jet (Gutmark and Ho 1983), but they are very different from an axisymmetric jet. The large difference in the spreading rates of the major and minor axes results in a switching of the two axes.

ACKNOWLEDGEMENT

This work is supported by AFOSR under contract No. F49620-82-K-0019.

REFERENCES

1. Dhanak, M.R. and De Bernardinis, B., 1981, "The Evolution of an Elliptic Vortex Ring", J. Fluid Mech., 109, 189.
2. Gutmark E. and Ho, C.M., 1983A, "The Development of an Elliptic Jet", To be submitted to J. Fluid Mech.
3. Gutmark E. and Ho, C.M., 1983B, "Near Field Pressure Fluctuations of an Elliptic Jet", AIAA No. 83-0663. (Submitted to AIAA J.).
4. Riley, J.J. and Metcalfe, R.W., 1980, "Direct Numerical Simulation of a Perturbed Turbulent Mixing Layer", AIAA No. 80-0274.
5. Trentacoste, N. and Sforza, M.P., 1967, "Further Experimental Results for Three Dimensional Free Jets", AIAA J., 5, 5, 885.

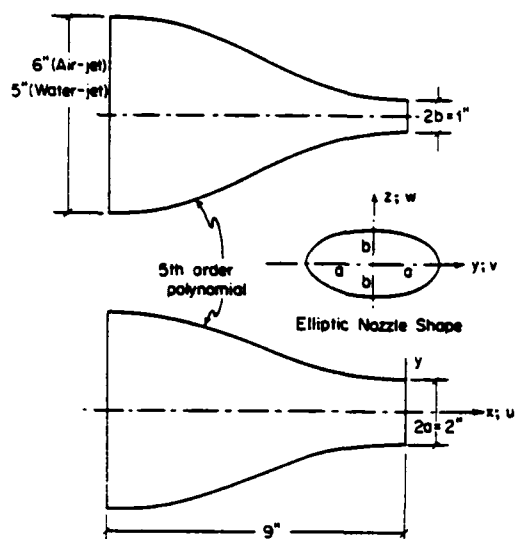


Figure 1: The Elliptic Nozzle

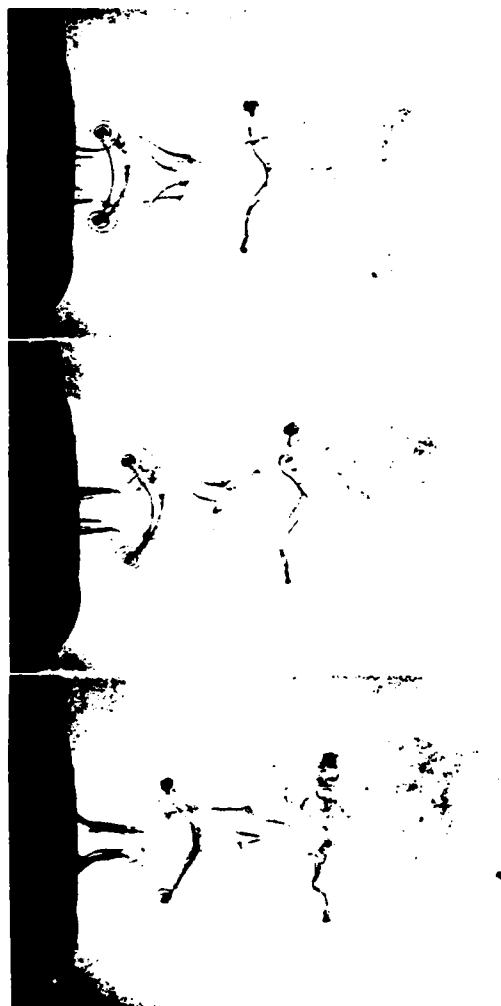


Figure 2: Side view of the jet vortices on the minor axis plane. ($f_p = 1.4\text{Hz}$).

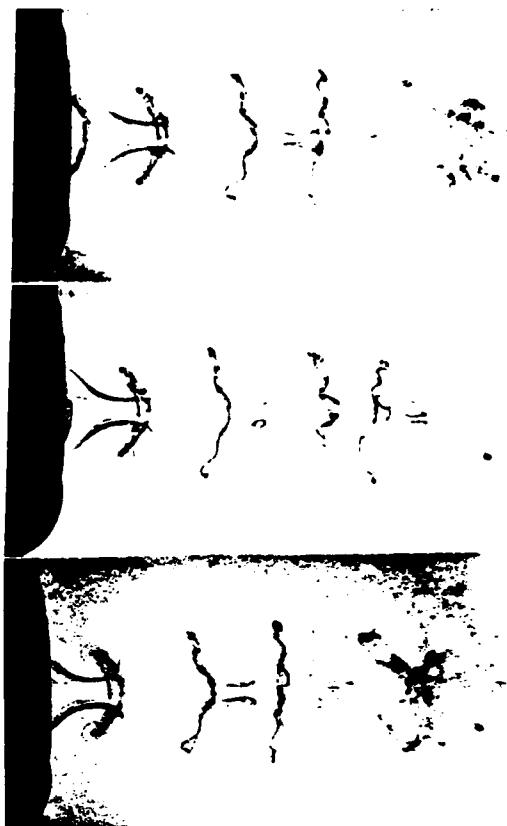


Figure 3: Side view of the jet vortices on the minor axis plane. ($f_p = 2.7\text{Hz}$).

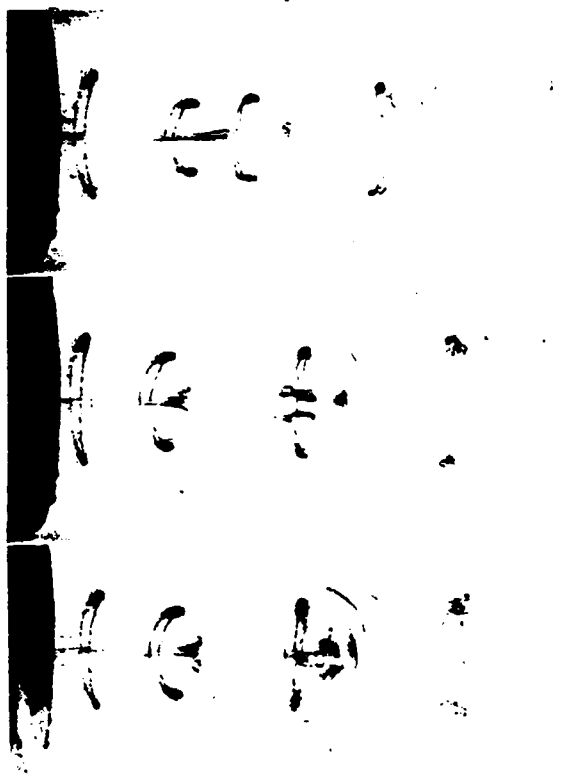


Figure 4: Side view of the jet vortices on the major axis plane. ($f_p = 2.7\text{Hz}$).

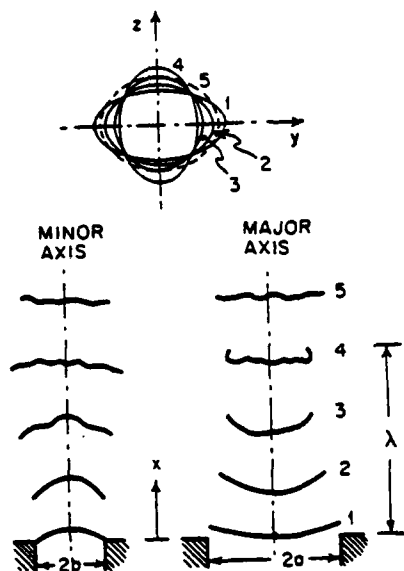


Figure 5: The jet vortex evolution at $f_p = 2.7\text{Hz}$.

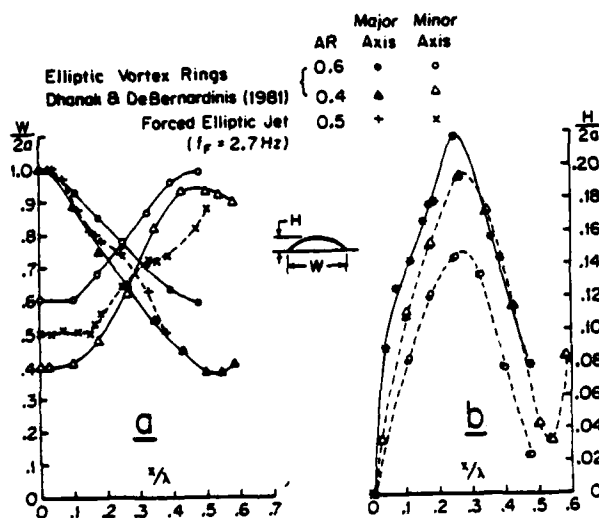


Figure 6: A comparison between the evolution of the elliptic jet vortices and isolated elliptic vortex rings.

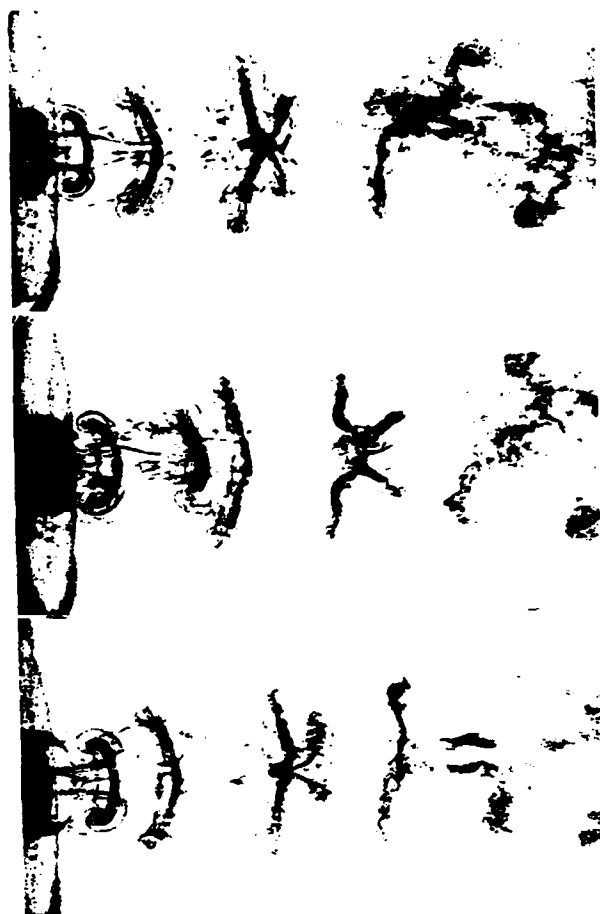


Figure 7: Side view of the jet vortex merging on the minor axis plane. ($f_p = 3.9\text{Hz}$).

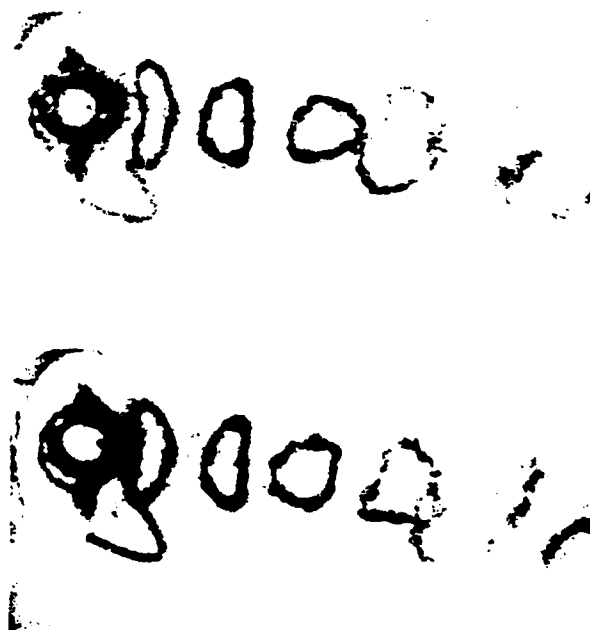


Figure 8: Oblique view of the elliptic jet vortices axes switching ($f_p = 2.7\text{Hz}$).

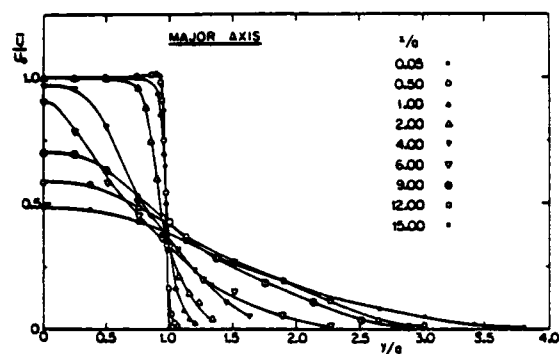


Figure 9: Mean Velocity Profiles on the Major Axis Plane.

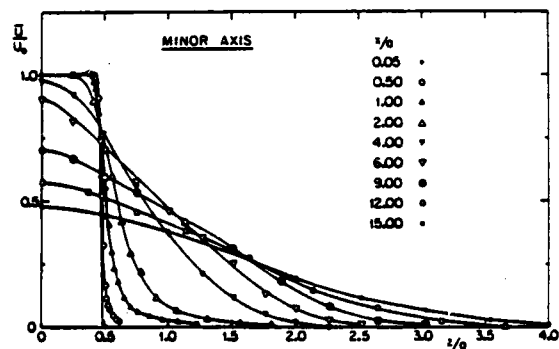


Figure 10: Mean Velocity Profiles on the Minor Axis Plane.

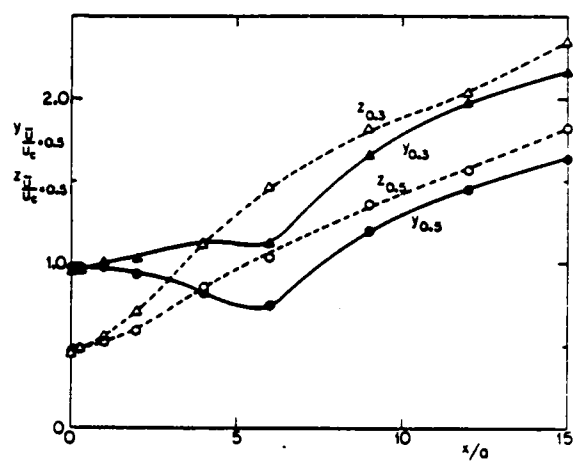


Figure 11: The Spreading of the Jet on the Major and Minor Axis Planes

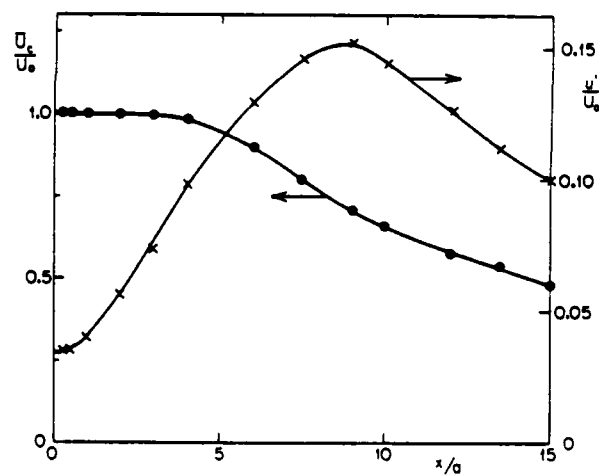


Figure 12: Mean Velocity and Axial Velocity Fluctuations Along the Jet Axis.

CONFINED JETS IN A DIVERGING DUCT

G. BINDER and K. KIAN

Institut de Mécanique de Grenoble
Laboratoire Associé au Centre National de la Recherche Scientifique
Université Scientifique et Médicale et Institut National Polytechnique
B.P. 68 - Saint Martin d'Hères Cédex - France

ABSTRACT

Axi-symmetric turbulent confined jets in a diverging duct have been investigated experimentally by means of pressure measurements, laser Doppler velocimetry and flow visualizations. It is shown that the 2.5° angle divergence of the duct has an important effect on the flow especially when the inlet conditions lead to recirculation: the recirculation eddies extend further upstream and have larger volume flow, the pressure rise is steeper and higher and the jet expands faster than in constant area ducts flows with identical inlet conditions. The turbulent characteristics depart significantly from those of the free jet. The overall flow pattern is highly unsteady in the presence of recirculation.

INTRODUCTION

Confined jets are of great practical importance since such flows occur in a variety of industrial apparatus, in particular, in combustors and in ejectors. From a more basic point of view they also present a number of interesting features such as approximate similarity, entrainment in an adverse pressure gradient and recirculation. Despite the apparent complexity of these flows a great deal of physical insight into their behaviour may be derived from the knowledge of simple turbulent shear flows.

The main distinguishing factor of confined jets is the presence of an adverse pressure gradient. Hence, the jet evolves in an ambient stream with decreasing velocity. In a constant area duct this pressure gradient is solely generated by the turbulent entrainment of the driving jet. Indeed, because of the entrainment the mass-flow-rate of the jet increases with downstream distance and since the total mass-flow-rate through the duct is constant that of the ambient stream must decrease and so must, therefore, the ambient velocity. The pressure gradient generated by the ducted jet influences, in turn, its evolution and entrainment as compared to those of the free jet. The knowledge of the relationship between total pressure rise in the mixing duct and ambient mass flow rate is essential for the design of ejectors.

Since the jet also spreads while it entrains two different types of flow occur depending upon whether the jet reaches the wall before it has entrained all the ambient fluid or whether the jet has entrained all the ambient fluid before it reaches the wall. In the latter eventuality the ambient velocity vanishes in the section where this occurs. Since the jet does not cease to entrain beyond this point the ambient velocity continues to decrease and reverse flow sets in. The jets entrains thus fluid coming from downstream. Such recirculation plays a crucial role in combustors since it brings hot gases back upstream thereby stabilizing the flame. Since the entrainment capacity of the jet is roughly proportional to the entrance excess velocity, it is seen that in a fixed geometry recirculation may be

produced by increasing the jet velocity while keeping the ambient flow constant.

Down to the end of the recirculation zone or to the point where the jet reaches the duct wall the jet excess momentum is the dominant physical parameter and the boundary layer on the duct wall plays only a minor role. Further downstream, however, once most of the jet excess momentum has been mixed across the duct the wall effects become important and the pressure gradient becomes negative. The flow in this region has little in common with jets and will not be discussed further herein.

CRAYA and CURTET (1,2) were the first ones to recognize that confined jets in constant area ducts may be described in terms of a single similarity parameter, namely the dimensionless total impulse or the related number C_t (for definition see Fig. 1), provided the entrance streams are clean, in particular that they have thin boundary layers and negligible turbulence, and that the jets remain approximately self-similar. This proviso, in particular, implies that the length of the initial region with the potential core is short compared to the total length of the jet development also that $d_0/D_0 \ll 1$. In the axisymmetric case it is sufficient to have $d_0/D_0 < 1/3$ (3). Usually the wall shear stress may be neglected compared to the change in momentum; C_t is then a constant in the flow direction. If $d_0 \ll D_0$ and $u_0 \ll w_0$, as is often the case then C_t may be approximated by: $C_t = u_0 D_0 / u_{\infty} d_0$. Large or small values of C_t correspond therefore, respectively to jets with either small or large excess momentum sometimes described as weak or strong. In cylindrical ducts recirculation occurs for $C_t < 0.9$ (4,5).

In variable area ducts the pressure gradient induced by the entrainment is evidently modified by the geometry. But the geometry may also have a more subtle effect on the turbulent entrainment itself so that the behaviour of the resulting flow may not simply be inferred from the knowledge of confined jets in constant area ducts. In particular, in a diverging duct the positive pressure gradient is enhanced by the divergence of the walls but it is, a priori, not possible to predict how it will modify the spread of the jet, the conditions of incipient recirculation or the magnitude of the recirculation. It is the purpose of the present research to try to answer some of these questions. Although some favorable effects due to changes in the duct shape have been observed and are included in some designs of furnaces or ejectors, there have been very few investigations carried out on the influence of the duct geometry on the flow (6-8) and there are virtually no results published in journals.

APPARATUS. INSTRUMENTATION.

A schematic view and the main characteristics of the test section are shown on Fig. 1. The flowing medium is water. The divergence angle $\theta = 2.5^\circ$ was chosen such as to produce a high pressure gradient without separation for an inlet velocity profile with thin boundary layers and no jet so as to induce measurable effects on the

confined jets without radically altering the flow. The geometry is axisymmetric.

The velocities were measured with a laser velocimeter operating in the fringe mode and the Doppler frequency was measured with a counter. The sign of the velocity was detected by using a double fringe pattern which was obtained by circular polarization of one of the interfering beams. The length and waist of the probe volume were respectively 14.7 and 0.75 mm. In order to minimize refraction effects on the conical surface of the duct it was immersed in a water-tank with plane lateral walls. Despite this precaution measurements were not possible in the outer third of a cross section when the plane of the incident laser beams was inclined at 45° to the duct axis.

The flow was visualized by injecting air bubbles into the jet through a hypodermic needle. The bubble diameter was approximately 0.2 - 0.3 mm and remained remarkably constant. The rise of the bubbles was quite small compared to the axial velocities.

The jet velocity was 6.5 m/s for the flow visualizations and the pressure measurements and 40 cm/s for the velocity measurements in order to have Doppler frequencies compatible with the frequency response of the photodiode circuit.

Although the CRAYA-CURTET number C_t is not constant in variable area ducts its value at the inlet may conveniently be used to characterize both the kinematical and the geometrical conditions of the entrance flow. It is, further more, very useful for the comparison with flows in constant area ducts since for a given value of C_t the differences observed between the flows in variable and constant area ducts are then solely due to the duct geometry.

THE CRITICAL CRAYA-CURTET NUMBER

Flow visualizations were performed first with the aim to determine the critical value of C_t for incipient recirculation and the extent of the recirculation region. These results provided useful guidance for the selection of the test cases in which detailed measurements were carried out as well as during these measurements for their interpretation. The mean positions of the beginning and of the end of the recirculating eddy, i.e. the points of separation S and reattachment R , were determined from several photographs for a given value of C_t . It was difficult to localize the point R with some accuracy because of the instability of the reattachment. Since this point was close to the exit of the duct which was feeding directly into the downstream-tank through a sudden expansion this instability may have been worse than usual here despite a set of stilling grids.

The results are presented on Fig. 2 together with those of the cylindrical duct (4,5). It is seen that S moves upstream with decreasing C_t while the position of R is independent of C_t in both geometries. As expected, however, separation occurs earlier and reattachment later in the diverging than in the cylindrical duct. The largest increase in the length of the recirculation region due to the duct divergence is about 1.2 D_0 and occurs for $C_t \approx 0.75$.

The intersection of the S -curve with the median line of the reattachment band determines the critical value of C_t of incipient recirculation. For the diverging duct $C_{t,cr} \approx 1.1$ where as its value is 0.9 for the cylindrical duct. Consequently in a conical duct with a 2.5° divergence recirculation may be produced with an ambient velocity about 20 % larger than in a constant area duct all other factors being the same. On the basis of these results it was decided to make measurements in the following three cases: $C_t = 1.23$ without recirculation, $C_t = 0.45$ with moderate recirculation and $C_t = 0.59$ with strong recirculation.

Still photographs (fig.3) and moving pictures show that the recirculating flow is highly unsteady when $C_t < 0.6$. The tail of the jet disintegrates into eddies which are swept downstream. For very small values of C_t , say $C_t < 0.3$, the jet oscillates from one wall to the other and the recirculating eddy alternatively swells and shrinks from a maximum size equal to the duct radius to almost zero. There are large negative velocities in the eddy when it is big and when it is small the fluid is

nearly stagnant. Since these visualizations were made with a single plane light-sheet they only give the intersection of a more complicated three-dimensional motion with this plane. It would be interesting to capture this motion by making simultaneous observations in two orthogonal planes. Behaviours similar to those described above have been observed in the cylindrical duct (4).

THE PRESSURE DISTRIBUTION

The measured pressure distributions for a range of CRAYA-CURTET numbers are shown on Fig. 4. The ideal pressure recovery in the diverging duct for a stream with a uniform velocity distribution, i.e. without a central jet ($C_t = 0$), is also drawn on the figure for reference. The estimated value (~ 0.58) of the total pressure recovery taking into account the growth of the boundary layers is shown too.

To understand these distributions of the pressure along the duct it is helpful to separate the effects of the three following mechanisms:

- a) the jet entrainment discussed earlier
- b) the contraction of the ambient flow and especially the expansion of the core flow due to the presence of the recirculation bubbles
- c) the divergence of the duct.

The pressure rise due to the first two-mechanisms is entirely due to the loss of momentum generated by the turbulent homogenization of the transverse velocity distribution. The maximum possible pressure rise due to the mixing of momentum $(\Delta p)_{max}^{mom}$ for uniform exit flow and a constant area duct is

$$\frac{(\Delta p)_{max}^{mom}}{\rho u_0^2/2} = \frac{1}{\rho u_0^2 S} \left[\left(\int_S u^2 dS \right)_{inlet} - \left(\int_S u^2 dS \right)_{exit} \right] \approx \frac{2}{C_t}$$

where the assumptions $d_0 \ll D_0$, $u_0 \ll W_m$ leading to

$C_t \approx u_0 D_0 / W_m d_0$ have been made. In the present experiments $d_0/D_0 = 1/10$ and $\frac{1}{20} \leq \frac{u_0}{W_m} \leq \frac{1}{7}$ so that the

above result is qualitatively correct. It clearly shows that the pressure rise scales with $\frac{1}{2} \rho u_0^2$ for C_t of the order one, that it is a decreasing function of C_t and that for $C_t < 1$ it can greatly exceed $\frac{1}{2} \rho u_0^2$.

The pressure gradient due to the geometry alone is approximately

$$\frac{(dp)_{geom}}{\rho u_0^2/2} \approx 4 dR/R$$

if $\ell^2 \ll R^2$, ℓ being the jet width (see Fig.1). Since in the present experiments $\ell/R < 1/2$, this result again is qualitatively correct. It means that the pressure gradient due to the duct divergence depends mainly on the local ambient velocity u and not on the velocity of the jet. However, since the jet entrainment produces a decrease in u the jet will steepen this gradient, an effect which again is a decreasing function of C_t .

The first set of curves (Fig.4) for $C_t \geq 1.14$ may be explained from the combined influence of mechanisms a) and c). Clearly in the absence of a core jet, the pressure distribution would lie below the ideal fluid curve due to the thickening of the boundary layers. The fact that all the distributions lie above this curve may solely be accounted for by the jet entrainment. The increase of the pressure rise with decreasing C_t underscored above is born out by the measurements.

This influence of C_t is even more marked for $C_t < 1.1$ on the second set of curves in the first part of the duct where the pressure rise is very steep for low values of C_t . It is seen that the pressure along the first half of the recirculation zone is nearly constant as had been postulated in some early furnace design methods (10, 11). In this region the effect of the contraction of the ambient flow is roughly offset by the entrainment and the geometry. After this region of relatively constant pressure, there is a very sharp pressure

rise which can neither be accounted for by the entrainment nor by the geometry and is due to the rapid divergence of the core flow on the downstream side of the recirculation bubble. For instance for a pressure rise of about $4 \text{ (} \frac{1}{2} \text{ atm)}$ as measured here for $C_t = 0.57$, it is sufficient to have a bubble width of $R/3$. This final pressure rise is steeper and larger for smaller values of C_t , a fact consistent with the increase in size of the recirculation bubble. It is noteworthy to observe that these successive trends of the pressure distribution are already observed for the critical CRAYA-CURTET number although the changes are less abrupt.

Similar behaviours have been observed by BARCHILON (4,5) in the cylindrical duct. As expected the pressure distribution in the divergent duct for nearly the same value of C_t is located above that of the cylinder. In this geometry a pressure decrease just upstream of the separation point S has actually been observed for $C_t = 0.51$ which can only be explained by the convergence of the streamlines of the ambient flow.

THE MEAN VELOCITY FIELD

Similarity of the mean velocity. Similarity of the mean velocity distribution of the jet is of practical interest since the profile may then be described by a single velocity and length scale. Such similarity has been assumed in all integral theories of confined jets (1,2 ; 12, 13). Strict similarity requires that w_m/μ_0 remains constant, a condition which generally is not satisfied and could only be so by tailoring the duct walls. For practical purposes, approximate similarity is sufficient. This may be realized if $u_0 \ll W$ which insures that the pressure gradient $u_0 \frac{\partial u}{\partial x}$ has a small effect on the jet and, of course, only so far downstream as the jet is well defined, also approximately as far as the middle of the recirculation region.

Fig. 5 shows that for $C_t = 0.77$ similarity is satisfactory. The scatter around a mean curve is rather worse for $C_t = 0.59$ and $C_t = 1.23$. It may be remarked that if the pressure gradient has a small effect on the central part of the jet, it must affect the edges where W is small and must, therefore, change the shape of the profile. Since approximate similarity is nevertheless maintained it is due to the vigorous mixing of the turbulence.

Jet flow rate. The down stream variations of excess flow rate of the jet q_j are strongly affected by the inlet - C_t (Fig.6). The initial differences in q_j/Q between the three cases are quickly overshadowed by the differences in growth rate also of the entrainment rate. The latter rate depends, of course, upon the velocity difference W_m which increases with decreasing C_t . But this alone cannot account for the large differences in the observed growth rate of q_j . Indeed, in the present experiments μ_{10} ($\mu_{10} = \mu_{10} + W_{m10}$) was kept constant so that $\Delta \mu_{10}/\mu_{10} \approx \Delta C_t/10$, and that between the test cases $C_t = 0.775$ and 0.59 the velocity scale in the initial region W_{m10} differs only by 2 % (but μ_{10} differs by about 30 %) while the differences in $dq_j/Q/dx/R_0$ are obviously much larger. Clearly the entrainment rate via the turbulence must be influenced by the pressure gradient.

This basic problem has so far received very little attention in the case of free shear flows. The only work known to the authors is that REBOLLO (14) who investigated a plane shear layer in a diverging channel. He also found an increase in entrainment caused by the positive pressure gradient. This effect could possibly be explained by the tendency of such a gradient to increase velocity differences also the mean shear and hence the turbulence production.

The values of q_j/Q larger than one are due to the entrainment of the recirculating flow. Based on a continuity argument, it is assumed that the jet extends to the point of minimum velocity in the recirculation zone. The decrease of q_j/Q beyond the maximum must, of course, not be interpreted as meaning negative entrainment ! It is only a consequence of the arbitrary definition of the

jet which is meaning less there as well as the distinction between jet and ambient flow.

Finally, the maximum recirculating flow $((q_j/Q)_{\max} - 1)$ is notably larger than in a straight duct. Recirculating flows of 0.2 and 0.6 respectively are obtained here for $C_t = 0.78$ and 0.59 . To produce such recirculation in a cylindrical duct would require values of C_t equal to approximately 0.5 and 0.3 (4,5). In other terms, this means that in the present diverging duct the same recirculation can be maintained with a secondary flow discharge $q_{10}/q_{j0} \approx 7$ and 6 corresponding to $C_t \approx 0.8$ and 0.6 respectively as compared with $q_{10}/q_{j0} \approx 4$ and 3 in the constant area duct, also with nearly twice the secondary flow discharge. This finding is particularly significant for the design of combustion chambers.

Center Line Velocity Decay. Contrary to the jet volume flow the centerline velocity decay, depends very little upon C_t (Fig.7) and consequently upon the positive pressure gradient. This is not surprising since the pressure gradient has a comparatively small effect on the parts of the flow where the inertia and hence the velocity is large.

Jet Spread. The jet width ℓ is determined from the relation $q_j = \pi \ell^2 w_m$. In the absence of self-similarity the rate of spread of the jet $d\ell/dx$ cannot be rigorously independent of the downstream position (Fig.8). But in order to compare the various flows with each other it is convenient to use a mean rate obtained from a best fit straight line as long as $d\ell/dx$ for a given flow does not vary too rapidly. This is actually the case even in the presence of recirculation approximately as far as the center of the eddy.

Fig. 9 demonstrates that the spreading rate of the jet is strongly affected both by C_t and by the duct divergence. Its decrease with C_t and the values below the one of the free jet in still surroundings are due to the inertia of the ambient stream (larger C_t implying larger μ_0/μ_{10} ratios). This is analogous to the progressive slow-down of the spread of a jet in an unconfined ambient stream.

The rates of spread higher than that of the free jet and the faster spread in the diverging duct as compared to that in the constant area duct for a set value of C_t may only be accounted for by the pressure gradient. It should be stressed that the jet width used here is based on the volume flow of the jet and not on the half-width of the mean velocity profile whose growth includes the turbulent spread as well as the divergence of the streamlines due to the pressure gradient when it is present. The growth rate of the half-width would, therefore, no longer be a true measure of the turbulent entrainment in this case.

REBOLLO (14) mentioned above found that a 2.7° half angle divergence of the channel produced a 60 % increase in the spread of the plane shear layer. This observation confirms also the present results.

It is rather remarkable that integral methods like that of CRAYA-CURTET (1,2) correctly predict this change in spread with C_t in constant area ducts. It remains however, to be tested for variable area ducts. The essential ingredient of the method leading to these successful predictions is the strong closure assumption of a self-similarity identical to that of the free jet with the same average value of $\overline{u'v'}/w_m$ although this is strictly speaking incompatible with the presence of either an ambient flow or a pressure gradient. It would no doubt be instructive to find out which combination of basic mechanisms could account for this result.

THE TURBULENCE

The longitudinal turbulent intensity remains roughly similar but the profile is notably different from the free jet profile as may be seen on Fig. 10 for $C_t = 0.59$. In particular, the intensity on the axis is about 20 % less than in the free jet whereas it is higher in the outer region. This is consistent with the effect of increased shear due to the effect of pressure

gradient in this region suggested above. But since the measurements of the turbulence there include the contributions from the velocity variations caused by the global instabilities of the jet this interpretation must be viewed with caution. This instability seen on the visualizations is also clearly visible on time recordings of the velocity on the edge of the jet which changes sign at time intervals much larger than the period of the slowest turbulent fluctuations. Apparent also is that these fluctuations are much more energetic when the velocity is positive also when the point is swept by jet as compared to their level when the point is in the reverse flow.

The influence of the CRAYA-CURTET number on the downstream evolution of the turbulent intensity is manifest on Fig. 11, especially the difference between flow with or without recirculation. In the latter case the intensity increases steadily and exceeds the asymptotic level of the free jet; the structure of the flow from jet-like becomes wake-like. In the former a constant level below that of the free jet is reached.

The turbulent shear stress was measured in the case $C_t = 0.59$. The profiles are shown on Fig. 12 and the downstream evolution of the maximum value on Fig. 13. Considering the measurement difficulties the accuracy of the data appears satisfactory. It is seen that the profiles evolve continually in the downstream direction and do not stabilize near the profile of the self-preserving free jet. In particular the maximum value does not remain constant once it reaches - and somewhat overshoots - the value of the fully developed free jet contrary to the behaviour of the turbulent intensity. But this immediate decrease of $(-\overline{u'v'})/\overline{w'^2}$ max is not really surprising if we observe that its beginning coincides with that of the recirculation. Comparison with the rare results in cylindrical ducts seems to indicate a faster initial increase of this parameter in the diverging duct consistent with the faster spread discussed earlier. Finally it is noteworthy to observe that the shear stress profiles are somewhat narrower than the equilibrium free jet profile again unlike the behaviour of the turbulent intensity.

Some integral length scales L have also been determined from auto-correlation measurements also for $C_t = 0.59$. Beyond 15 do the ratio L/ℓ is constant and approximately equal to 0.5 as in the free jet (15). It should be remembered that in this instance ℓ increases faster than in the free jet. The turbulent length scale keeps also up with the growth of the mean flow.

The turbulence data collected clearly does not confirm the similarity assumption made in integral theories. Not only does the downstream evolution of the longitudinal intensity depend upon C_t and differ from that of the free jet but the shear stress displays a complete lack of similarity.

Finally these measurements do not reveal a turbulent activity of much greater intensity than in the free jet which could simply account for the larger entrainment and faster spread observed in these confined jets.

CONCLUDING REMARKS.

The results of the present experimental investigation establish the beneficial effect of the duct divergence on various properties of confined jets, in particular the pressure rise and the intensity of the recirculation flow which are crucial for the performance of jet pumps and combustion chambers. It is also shown that the turbulent entrainment rate is enhanced in the presence of a positive pressure gradient. The turbulence data collected does unfortunately not hint any simple explanation of this basic observation.

The basic problem of the influence of a positive pressure gradient on the entrainment characteristics on free shear flows and the importance of the effects observed here would, no doubt, warrant further research. Because of the global instabilities of the confined jets at small values of C_t it would also be interesting to perform conditionally sampled measurements in order to obtain the effection turbulent Reynolds stresses. Such measurements could shed some light on the question of the entrainment.

Calculations with the turbulence $k-\epsilon$ model (16)

have been performed on jets in a constant area duct. The predictions for the recirculating flow, eddy location and size are in reasonable agreement with the experimental data.

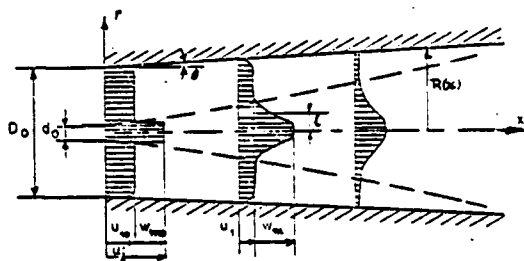
It would be interesting to repeat such computations for the flows in a diverging duct presented here and to make more extensive comparisons with the experiments especially with the pressure distributions, the jet expansion rate and the Reynolds stresses. If good agreement is obtained the turbulent model could then be used to gain a better understanding of the respective importance of the various mechanisms which influence the flow and of their interactions in terms of the parameter C_t . Some insight could then hopefully also be gained from these on the influence of the pressure gradient on the turbulent entrainment. In case of good agreement it would then be useful for practical purposes to investigate the influence of the divergence angle or of more complex shapes on the flow.

ACKNOWLEDGMENT

This research was initiated by R. CURTET before he died in 1979.

REFERENCES

1. CRAYA A. and CURTET R. : Sur l'évolution d'un jet en espace confiné. Comptes rendus Acad. Sci., Vol. 241 (1955) 621-622.
2. CURTET R. and RICOU F.P. : On the Tendency to Self-Preservation in Axisymmetric Ducted Jets. J. Basic Engr. vol. 86, Series D, n°4, 1964, 765-776.
3. RAZINSKY E et BRIGHTON J.A. : "Confined jet mixing for nonseparating conditions" Journal of Basic Engr. Septembre 1971, pp. 331 - 349.
4. BARCHILON M. and CURTET R. : Some details of the Structure of an Axisymmetric confined Jet with Backflow. J. Basic Engr. vol. 86, series D (1964), n° 4, 777-787.
5. BARCHILON M. : Contribution à l'étude des courants de retour engendrés par un jet confiné. Publications Scientifiques et Techniques du Ministère de l'Air, 1969, 94 p.
6. HELMBOLD, LEUSSEN et HEINRICH : "An experimental comparison of constant pressure and constant diameter jet pumps" Repor n° 147, Univ. of Wichita, Sci. Engrg. 1954.
7. SANGER : "Noncavitating and cavitating performance of two low-area-ratio water jet pumps with throat lengths of 5.66 diameters" N.A.S.A., T.N.D. -4759, 1968.
8. SHUE et STAUFFER : "Research on coaxial jet air mixing" Office of Naval Research, San Diego, 1960.
9. THRING et NEWBY : "Combustion length of enclosed turbulent jet flames" 4th Symposium on Combustion -1953 The Williams and Wilkins Company - Baltimore p. 789.
10. CURTET R. : "Sur l'écoulement d'un jet entre parois" P.S.T. Ministère de l'Air, Paris, 1960. pp. 23-30.
11. HILL P.G. : "Turbulent jets in ducted streams" Journal of Fluid Mechanics, Vol. 22, Part.1. 1965-pp.161-186
12. HILL P.G. : "Incompressible jet mixing in converging-diverging axisymmetrical ducts" Journal of basic engineering, vol.89, n°1, 1967 (ASME paper n°66-WA/FE)
13. RAZINSKY E et BRIGHTON J.A. : "A theoretical model for nonseparated mixing of a confined jet" Journal of basic engineering, 1972, pp. 551-557.
14. REBOLLO M.R. : "Analytical and experimental investigation of a turbulent mixing layer of different gases in a pressure gradient. Ph. D. Dissertation, Aeronautical Laboratories, California Institute of Technology (1973)
15. WYGNANSKI I. and FIELDER H. : "Some measurements in the self-preserving jet" J. Fluid Mech. vol 38 (1969) 577-612.
16. GOSMAN A.D., KHALIL E.E. and WHITELAW J.H. : "The Calculation of Two-Dimensional Turbulent Recirculating Flows" Turbulent Shear Flow I Durst F. et al ed., Springer Verlag 1979, pp. 237-255.



Definitions

$$u = u_1 + u_2$$

(1) : ambient flow

(2) : jet

$$\text{total discharge : } Q = q_1 + q_2$$

$$\text{jet width } l(x) : q_2 = \pi l^2 \bar{u} = 2\pi \int_0^R \bar{u} r dr$$

$$\text{CRAVA-CURTET number } C_t = 1/\sqrt{m}$$

$$\text{where } m = \frac{S}{Q^2} \int_S (\bar{u} + p/\rho) dS - \frac{1}{2}$$

$$\frac{u_1}{u_2} + p/\rho = 0$$

Experimental conditions

$$d_0 = 16 \text{ mm} \quad D_0 = 160 \text{ mm} \quad D_{\text{max}} = 218 \text{ mm}$$

$$L_0/D_0 = 4 \quad \theta = 2.5^\circ$$

$$u_{j0} = 40 \text{ cm/s} \quad u_{10} = 2 - 6 \text{ cm/s}$$

$$\text{for pressure measurements and visualizations : } u_{j0} = 6.5 \text{ m/s}$$

Fig. 1 Sketch of flow configuration and definitions

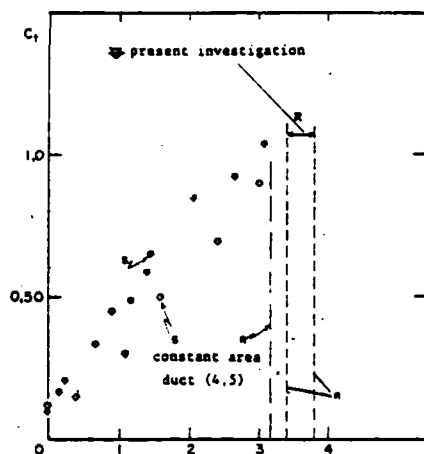


Fig. 2 Position of the recirculation region vs \$C_t\$



Fig. 3 Flow visualization \$C_t = 0.59\$

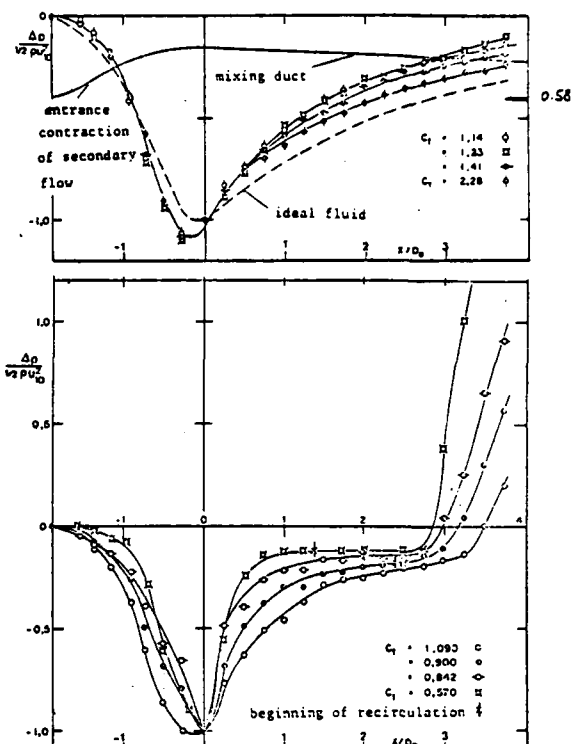


Fig. 4 Pressure distribution along the duct

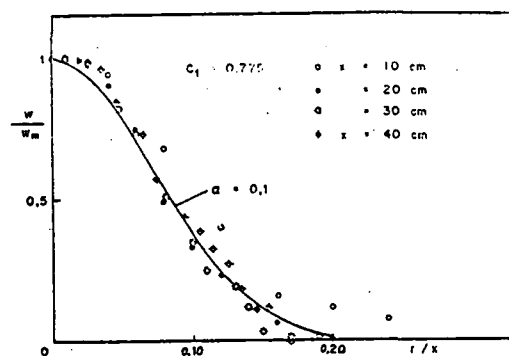


Fig. 5 Transverse velocity distribution (\$l = \alpha(x)\$)

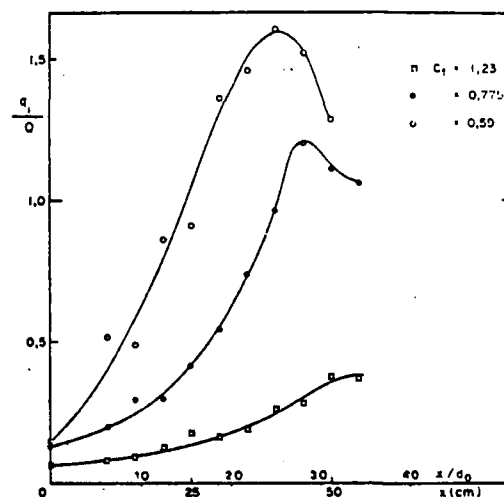


Fig. 6 Variations of jet flow rate with streamwise distance

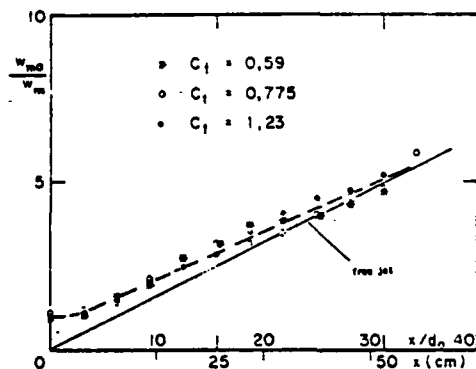


Fig.7 Jet centerline velocity decay

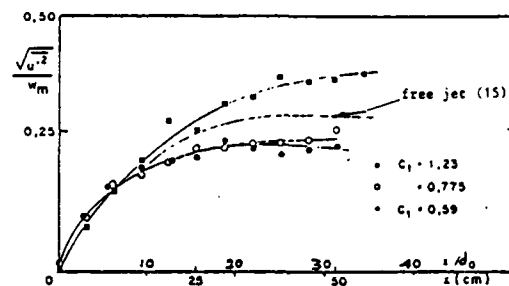


Fig.11 Streamwise evolution of centerline longitudinal turbulent intensity

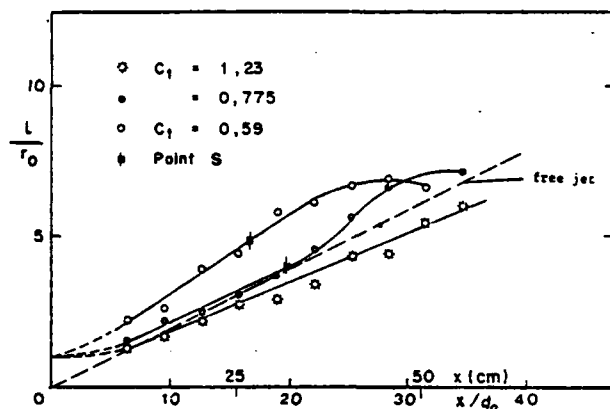


Fig.8 Axial evolution of the jet width

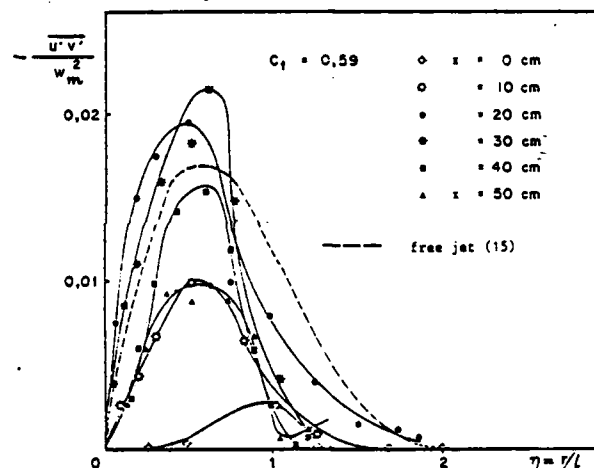


Fig.12 Radial distribution of turbulent shear stress

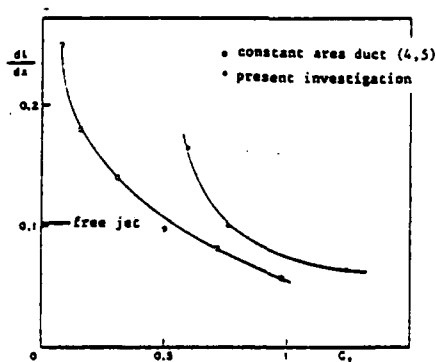


Fig.9 Jet rate of spread vs C_1

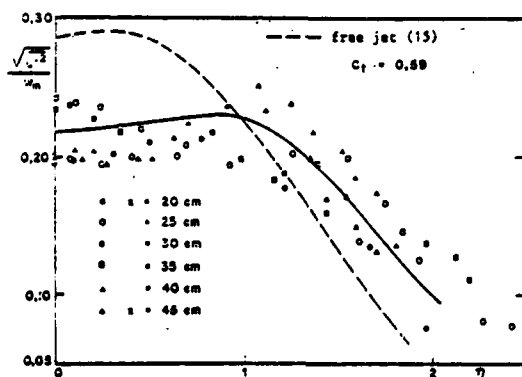


Fig.10 Radial distribution of longitudinal turbulent intensity

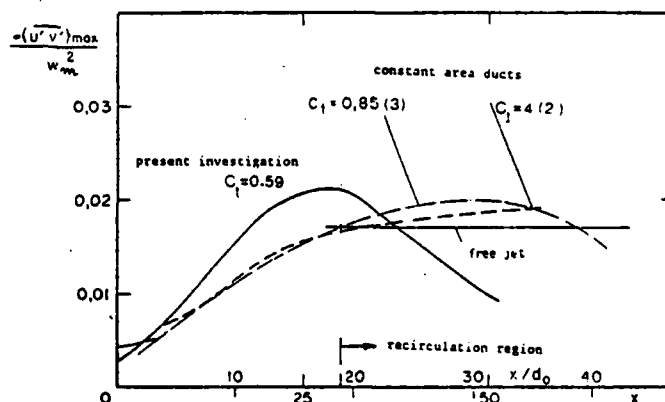


Fig.13 Streamwise evolution of maximum turbulent shear stress

AN EXPERIMENTAL STUDY OF THE MIXING OF A JET INTO A CROSS FLOW USING HEAT AS A PASSIVE SCALAR

by J. Andreopoulos
Sonderforschungsbereich 80,
University of Karlsruhe, FRG

ABSTRACT

Spectral analysis results and conditional averages of various turbulent quantities are presented for various velocity ratios and Reynolds numbers. A unique conditional sampling technique has been used which separates contributions from the turbulent-jet flow, the irrotational jet-flow, the turbulent cross-flow and the irrotational cross-flow. The intermittency factor profiles indicate that irrotational cross-flow intrudes the pipe but does not contribute to the average turbulent quantities while the jet-pipe irrotational flow contributes significantly to them in the region above the exit where the interaction between the boundary layer eddies and those of the pipe starts to take place. Further downstream the contributions of the oncoming boundary layer eddies to the statistical average reduce significantly. The downstream development depends mainly on the relative eddy size of the interacting turbulent fields.

NOMENCLATURE

I_θ	intermittency function based on hot/cold discrimination
I_{uv}	intermittency function based on turbulent/non-turbulent discrimination
D	pipe diameter
f	frequency
R	V_j/U_∞ jet to cross-flow velocity ratio
U, V, W	instantaneous velocity components in x, y, z directions respectively
$\bar{U}, \bar{V}, \bar{W}$	mean velocity components
u, v, w	fluctuating velocity components
x, y, z	coordinates: streamwise, normal and lateral respectively
St	fD/U_∞ Strouhal number
T	instantaneous temperature
\bar{T}	fluctuating temperature
Y	intermittency factor
Φ	one dimensional power spectrum

SUBSCRIPTS

∞	cross-flow at infinity
j	jet flow at infinity
HT	Hot and Turbulent fluid
HN	Hot and Non-turbulent fluid
CT	Cold and Turbulent fluid
CN	Cold and Non-turbulent fluid

1. INTRODUCTION

This paper is one of a series reporting on jet-in-a-cross-flow experiments carried out at this department. The experimental program included a flow visualisation study, wall static pressure measurement, and mean and fluctuating velocity measurements including the flow regions inside the paper. The results have been reported by Foss (1980), Andreopoulos (1982a) and Andreopoulos and Rodi (1982).

The present paper describes some structural characteristics of flow, additional to those observed by Foss, and tries to illuminate the way the cross flow boundary layer mixes and/or interacts with the jet-pipe flow (see figure 1). Although it is established that, at high velocity ratios, the near field of jets in a cross-flow is controlled largely by complex inviscid dynamics so that the influence of turbulence on the flow development is rather limited, the flow downstream is always influenced by turbulence and at small velocity ratios even the near field is turbulence dominated. The aim of the present investigation is to increase the physical understanding of the turbulence processes which are involved in the complex situation of a jet in a cross-flow, where the initial jet layer interacts with the oncoming cross-flow boundary layer and turbulence is subjected to extra rates of strain like those resulting from streamwise curvature, lateral divergence and longitudinal accelerations.

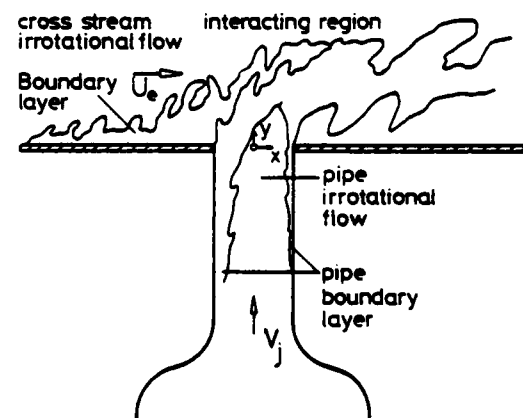


Fig. 1: Flow configuration with interacting shear layers.

2. EXPERIMENTAL TECHNIQUES

2.1 Experimental set-up. The measurements were made in the closed circuit wind tunnel at the Sonderforschungsbereich 80. The experimental set-up is fully described by Andreopoulos (1982a). Both interacting flow fields, i.e. the pipe flow and the

the cross flow, were found to be developing turbulent flows for all the investigated velocity ratios. At $x/D = -4$ upstream the jet exit, on the plate, where the jet interference on the cross stream was negligible a friction coefficient $C_f = 0.0037$ and a boundary layer thickness of $\delta = 0.278D$ were measured at a cross stream velocity of $U_\infty = 13.9$ m/s. Velocity signals were obtained with a DISA x-wire probe type P51 and fed the Hewlett-Packard Fourier Analyser 5154C which had four Analog to Digital Converters of 12 bits per word resolution. It was found that such a probe could give good results if the data analysis and techniques can account for the high pitch and yaw angle of the instantaneous velocity vector. As it has been mentioned in Andreopoulos and Rodi (1982), the present flow configuration includes regions with reasonably high turbulence levels and therefore the response of the hot wire at higher pitch or yaw angles should be known. For this reason the algorithm proposed by Andreopoulos (1981) has been adopted to reduce the data. The effect of the third velocity component W has not been taken into account in the hot wire response equation, on the ground that U and V are the main velocity components if some superposition arguments are applied (see Andreopoulos (1982a)). This assumption certainly causes some error on the results which has been estimated by Tutu and Chevray (1975). From their table II, an error due to combined effects of high turbulence intensity (i.e. rectification effects) and lack of sensitivity to the W -component is quoted, for 30 % turbulence intensity as follows: 6.3 % error on \bar{U} , 5.2 % on \bar{U}^2 , 11.9 % on \bar{U}^3 and 13.6 % on \bar{U}^4 .

For the spectral analysis each of the cross wire channels was feeding two ADC: one working on DC-mode to yield the mean value of the input voltage and the second to calculate fluctuating quantities. This allowed an exploitation of the whole dynamic range of the ADC since a resolution of 0.24 mv/word has been achieved. The cut off frequency of AC mode input was at about 0.3 Hz. All inputs were low pass filtered at 10 kHz and digitized at 25 kHz per channel.

2.2 Conditional-sampling techniques. Many investigations of turbulent shear flows have used the technique of conditional-sampling to provide more information about regions of interest in these flows. Antonia (1981) describes the various existing conditional-sampling techniques which have been applied to studies of turbulent flows and points out that probably the most plausible way to investigate the interaction of two, initially separate, turbulent fields is to use temperature as a passive marker of one of the interacting fields, idea which is due to Bradshaw (1974). This tagging of the flow allows a distinction to be made between hot-zone and cold-zone contributions. In the present case, it was decided to heat slightly the jet-pipe flow by means of heating elements at the exit of the 2 two stage compressor which supplied the secondary pipe flow and before the plenum chamber.

The part of the pipe which was inside the wind-tunnel and underneath the flat plate was carefully insulated to avoid additional heat transfer by convection. In this way the jet flow was heated by 4 to 5°C above the ambient cross stream temperature, and therefore any asymmetry in the temperature profiles can be attributed to the cross flow and not to cooling of the pipe by the wind-tunnel flow.

Turbulence measurements were made with DISA type 55M01-anemometers and DISA miniature cross-wire probes type 55P51 with 5 μ m platinum wires. Temperature measurements were measured with 1 μ m "cold wires" mounted on home-made probes clamped to the side of the cross-wire probe. The cold wire was operated by a constant-current home-made circuit with a heating current of 0.2 mA. The temperature-wire output was compensated in "real time" by a conventional operational-amplifier network. The compensation was adjusted to obtain the sharpest possible rise and fall of the temperature signal at the leading and trailing edges of bursts of hot fluid, while avoiding an "overshoot" of temperature below the free stream value. The techniques associated with the temperature fluctuations are similar to those described in the wake study of Andreopoulos and Bradshaw (1980).

The employed data reduction scheme is similar to that des-

cribed in section 2.1. The signals were digitized at 5 kHz per channel and stored on digital mag tapes for later data reduction. As will be seen later the agreement between the measurements of Andreopoulos and Rodi (1982) obtained with a triple wire sensor and those obtained with a cross-wire is rather satisfactory, i.e. within the limits mentioned earlier in chapter 2.1. To increase the accuracy of the measurements the probe was aligned parallel to the mean flow.

The conditional-sampling algorithm is similar in principle to that used by Andreopoulos and Bradshaw (1980) and is fully described by Weir, Vood and Bradshaw (1981). Fluid is labelled "hot", i.e. jet fluid, if its temperature exceeds a certain threshold value, usually around 0.1°C. To distinguish the end and the beginning of hot periods as sharply as possible, data points are also labelled "hot" if the time derivative of the temperature exceeds a certain small value. As it has been previously explained and also clearly shown in figure 1, the heated jet flow is a developing turbulent flow, i.e. significant regions of potential core are present in addition to the turbulent flow regions. Similar is the situation in the unheated boundary layer flow which entrains cross-stream potential flow. It is also expected that the irrotational fluid fluctuations of both flow fields will contribute to the conventional mean quantities. In the light of the unsteady character of the jet, these contributions might be significant. It is therefore necessary to further discriminate the flow to turbulent and non-turbulent fluid. In this case fluid labelled as "hot" and "turbulent" belongs to a jet flow eddy while "cold" and "turbulent" fluid is part of an eddy of the flat plate boundary layer flow. Fluid that is labelled as "hot" and "non-turbulent" or "cold" and "non-turbulent" comes from the jet irrotational flow or cross stream irrotational flow respectively.

The conditional-sampling algorithm discriminates firstly between the hot/cold fluid and subsequently the turbulent/non-turbulent fluid. The temperature serves as the "conditioning function" in the former discrimination and the uv -signal is used in the latter case of turbulent/non-turbulent discrimination, mainly because uv is directly involved in the production of turbulence.

The advantages of choosing the uv -signal for making the turbulent/non-turbulent decisions have extensively discussed by Murlis et al. (1982) and Muck (1980). If the time derivative of the instantaneous uv -signal is above a prescribed threshold value, the fluid is described as turbulent. The second derivative of the uv -signal is also used as back up criterion. According to the above discussion the following definitions have been made for the intermittency function I_θ and I_{uv} of the hot/cold and turbulent/non-turbulent respectively:

$$I_\theta = \begin{cases} 1 & \text{IF } T \geq \theta_1 \text{ and/or } dT/dt \geq \theta_2 \\ 0 & \text{else} \end{cases}$$

$$I_{uv} = \begin{cases} 1 & \text{IF } duv/dt \geq \theta_3 \text{ and/or } d^2uv/dt^2 \geq \theta_4 \\ 0 & \text{else} \end{cases}$$

Figure 2 shows highly idealized temperature and uv traces somewhere in the interaction region, above the exit plane of the jet. It is obvious that the beginning and the end of a "hot" burst may not correspond with the beginning and the end of turbulent activities shown in the uv -signal. This difference cannot be attributed to problems of the spatial resolution of the probe; displacement of the cold-wire in relation to the cross-wire is not the reason for that; even with the "cold"-wire 1 mm ahead of the cross-wire the difference in arrival time is not more than one digitization interval. It is also clear in this idealized figure that turbulence activities shown in uv -trace may not correspond to any temperature excursion. The output of the hot/cold discrimination part of the algorithm corresponding to the temperature trace of the figure is shown immediately below it. The output of the turbulent/non-turbulent discrimination part of the algorithm corresponding to the uv -trace is shown below it. Combination of both parts of the algorithm yields to the final discrimination shown at the most lower part of that figure. The suffix C is used to indicate Cold fluid, i.e. cross flow, the suffix H is used to indicate Hot fluid, pipe flow, the suffix T is

used to indicate Turbulent fluid and finally N is used to indicate irrotational fluid regardless if it is pipe-jet or cross stream flow. Two suffices are needed to describe fully the flow. HT indicate Hot and Turbulent fluid, i.e. turbulent pipe fluid, CT indicate Cold and Turbulent fluid, i.e. flat plate boundary layer fluid, HN indicate H and Non-turbulent fluid, i.e. irrotational pipe flow, and CN indicate Cold and Non-turbulent fluid, i.e. irrotational cross stream flow.

The results presented here measure all fluctuations with respect to the conventional-average velocity. The conditional-average products of velocity fluctuations can be presented as contribution of the above-mentioned zones to the conventional average. If Q is any velocity fluctuations product of the form $u^m v^n$, with m, n integers, then the contributions of the four zones can be summed to give the conventional average:

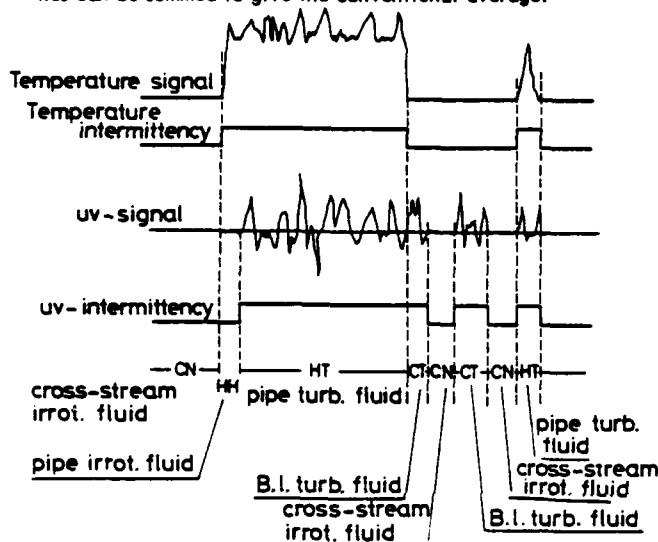


Fig. 2: Deduction of Cold and Non-turbulent (CN)-, Hot and Non-turbulent (HN)-, Cold and Turbulent (CT)- and Hot and Turbulent (HT) zones from uv- and temperature signals.

$$\bar{Q}_{HT} + \bar{Q}_{CT} + \bar{Q}_{HN} + \bar{Q}_{CN} = \bar{Q} \quad (1)$$

If γ is the mean value of the intermittency function I , hereafter simply called intermittency, then the zone average \bar{Q} is related to zone contributions as follows:

$$\bar{Q}_{HT} = \bar{Q}_{HT} / \gamma_{HT}$$

where γ_{HT} is the intermittency of the Hot and Turbulent zone. Similar are the definitions for γ_{HN} , γ_{CT} and γ_{CN} . In the present work the discrimination scheme of "retail" intermittency has been employed (see Murlis et al., 1982) without the explicit application of any "hold time" other than digital sampling time. This scheme is believed to follow more closely the highly re-entrant nature of the interface which is clearly shown in the smoke pictures. Although the intermittency measurement itself depends on the length and the number of the irrotational "drop-outs", the zone contributions to the fluctuations statistics are much less dependent on the drop-outs. The present intermittency scheme has been applied and tested in the case of a partially heated boundary layer flow with satisfactory results. Small differences between the two discrimination schemes were found, but the effect on the conditional averages was negligible. Therefore any significant difference in the zonal contributions to \bar{Q} in equation (1) are genuine and are not caused by relatively small errors in intermittency. Following the suggestions of Muck (1980) the thresholds Θ_3 and Θ_4 used in the turbulent/non-turbulent discrimination are directly connected to the derivatives of the uv signal in the turbulent zone averages $\partial uv / \partial t$ and $\partial^2 uv / \partial t^2$ respectively that is the thresholds were continually updated. Similarly the "cold fluid temperature level" T was continually updated in the temperature intermittency scheme.

It is emphasized here that the thresholds for the uv-derivative scheme are not necessarily the same for both turbulent zones. This allows the present scheme to handle cases where the length-scale of one turbulent zone differs from that of the other.

3. RESULTS

Figure 3 shows some typical u - and v -spectra obtained at three different points on the jet exit plane for $R = 0.25$. These points were properly selected to represent one of the three characteristic regions at the exit: The first point at $x/D = -0.35$ is inside the annular pipe-boundary layer which is developing near the upstream edge of the pipe under the influence of an adverse pressure gradient. The second measuring point lies very close to the pipe axis where the flow has a rather intermittent behaviour between turbulent and non-turbulent fluid with rather small turbulence intensity. The last point at $x/D = +0.40$ is close to the downstream edge of the pipe where the flow is developing under the influence of a favourable pressure gradient. The peak frequency at 108 Hz shown in the figures was also evident on the autocorrelation plots, but it was more clearly pronounced at $x/D = +0.4$ at less at $x/D = -0.35$. One more interesting point is that the u - and v -spectra at $x/D = .40$ consist of two widely different bands.

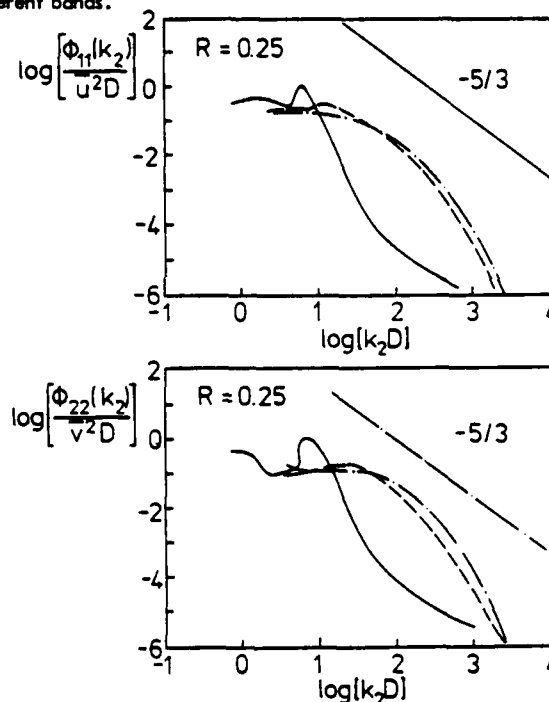


Fig. 3: (a) Power Spectrum of u -fluctuation. (b) Power Spectrum of v -fluctuation at the jet exit for $R = 0.25$. — $x/D = 0.40$, --- $x/D = -0.14$, - - - $x/D = -0.35$. Wave number $k_2 = \omega/\bar{V}$.

In this first band containing the peak around $\log_{10} k_2 D \approx 0.8$, the spectral density falls rapidly until around $\log_{10} k_2 D = 1.6$, where the slope changes to $-5/3$ indicating that turbulence of the pipe boundary layer at the downstream edge of the pipe is present with its long inertial subrange. At the other two positions closer to the upstream edge, the inertial subrange is shorter which is an indication of the developing turbulent flow under the adverse pressure gradient which exist at that part of the flow.

Figure 4 shows the Strouhal number $St = Df/U_e$ as a function of the Reynolds number $Re = V_j D/\nu$. St results are remarkably constant while the structure of the exiting pipe flow changes significantly with R . This suggests that St is associated with puffing or vortex ring roll up or some mechanism due largely to the change from pipe to jet flow. In fact these measurements agree quite well with the measurements of Yule (1978) in the turbulent

regime of a round jet issuing in "still" air.

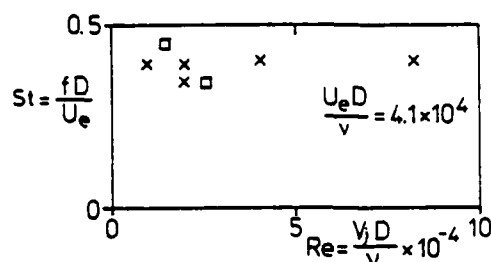


Fig. 4: Strouhal number versus $Re = V_j D / \nu = 4.1 \times 10^4$
x Present measurements; \square Yule (1978).

It has been documented in the past (Yule, 1978, Crow and Champagne, 1971) that the free jet flow is strongly Reynolds number and initial conditions dependent and can undergo various kinds of instabilities (see Yule, 1978), which cause the rolling up of the annular mixing layer and the formation of toroidal vortices. These vortices or vortical rings, as they travel downstream, can undergo successive interactions like pairing and tearing. However, there might be some other possible explanations of the appearance of this peak frequency in the spectra. Vortex shedding might be one since it has been reported previously (see McMahon et al., 1971) that such shedding takes place at very high velocity ratios. In these cases the jet penetrates very deeply inside the cross flow before starts to bend over and therefore behaves like a rigid cylinder. In the present case, however, the jet penetrates in the cross flow no more than 2 diameters. It seems therefore quite unlikely that vortex shedding, in the strict sense of shedding of Ω_y vorticity, takes place in the smaller velocity ratios. Apart from that, if shedding of Ω_y vorticity was happening, the frequency at the plane of symmetry should be double than that measured at a position far outside the plane of symmetry. In fact by moving the hot wire probe on a plane perpendicular to x-axis no variations in frequency were observed. There are two other possible explanations of the found frequency peak, namely "puffing" of the jet or some sort of "flapping". The first could be due to an unsteady operation of the two-stage blower which was supplying the jet flow. However, no frequency peaks were observed at a position of half a diameter upstream, inside the pipe where measurements have also obtained. It can be therefore concluded that puffing due to blower unsteadiness does not take place.

Flapping of jet is known to take place in the case of a plane jet (Goldsmid and Bradshaw, 1971) and nothing similar has been reported for the jet into a cross flow so far. It is therefore unlikely to take place in the present case. Some rough estimates of time correlations of the signals of two cross wires placed at opposite side of the jet in the z-direction show that the U-velocity-components were in phase while the W-velocity-components were in antiphase.

This indicates that the jet has a sort of a pulsating character, i.e. the frequency peaks are due to "puffing" of the jet. In addition a flow visualization study of the flow has been made by putting smoke in the plenum chamber of the jet. A fast camera has been used to take pictures of the flow at various Reynolds numbers and velocity ratios. This study revealed the existence of large eddy structures in the flow, sometimes well organized and sometimes not, depending on the flow parameters. These structures have a periodicity in their appearance and as they pass downstream induce free stream unsteadiness, i.e. fluctuations of the irrotational fluid. As the Reynolds number increases, the regularity of the appearance of the large eddies leaving the pipe decreases and these eddies now occupy a wide range of sizes. At downstream positions they grow in size and entrain irrotational cross stream fluid and the flow is quite intermittent. The early pictures of Ramsey and Galstein (1971) also indicate the intermittent character of the flow and the formation of large eddies at further downstream stations. As these eddies are coming out from the pipe, they interact with the on-

coming flat plate boundary layer eddies which carry opposite vorticity. Thus flat plate boundary layer eddies may significantly help the vorticity diffusion of the pipe eddies in the immediate downstream region.

In the formation of the large eddies described here entrainment by these eddies of potential core fluid of the pipe flow, outside the pipe may also be significant. Their role in the process of entrainment of irrotational fluid and the interaction with the boundary layer eddies is illustrated in the conditional-sampling analysis. These results which are presented below have been obtained at $R = 0.5$ and $Re = V_j D / \nu = 20500$ where these large eddies have an irregular character.

Measurements have been taken at seven different streamwise positions, $x/D = -0.25, 0, 0.25, 0.5, 2, 4, 6$. The first four positions are stations above the exit, in the immediate region of interaction, while the remaining three positions represent stations in the downstream region.

Figures 5(a) and 5(b) show the intermittency profiles for the four postulated flow zones at $x/D = -0.25$ and 6 respectively. Since any fluid particle must belong to one of the four mutually exclusive zones, that is CN, CT, HN, and HT the addition law of equation (1) reduces to

$$Y_{HT} + Y_{HN} + Y_{CT} + Y_{CN} = 1$$

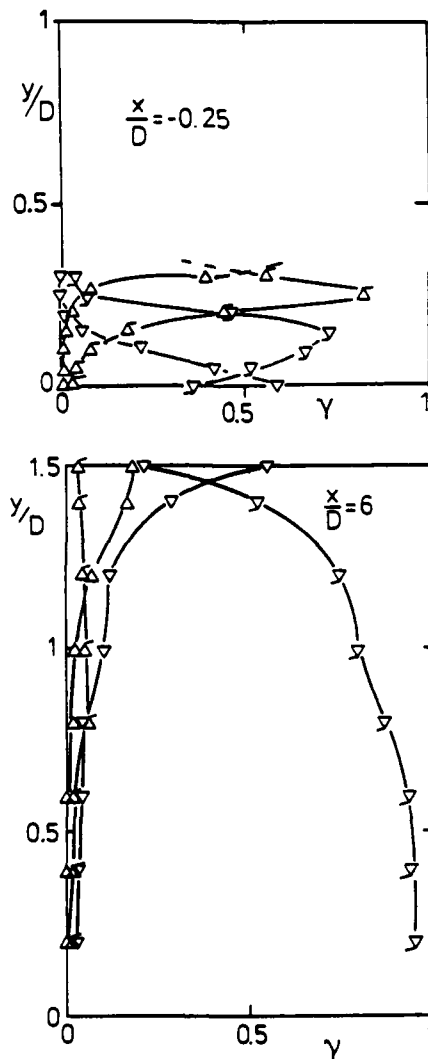


Fig. 5: Intermittency profiles: (a) $x/D = -0.25$, (b) $x/D = 6$: ∇ , HN; \circ , HT; \square , CN; \diamond , CT. Mnemonic: rising plum for Hot zone values, iceberg for Cold zone values, flagged symbols for Turbulent zone values, non-flagged symbols for Non-turbulent zone values.

The profiles at $x/D = -0.25$ in figure 5(a), show clearly that cold, turbulent fluid (CT) has penetrated the hot jet flow down to the exit plane $y/D = 0$. In other words, there is a significant ($\approx 3\%$) probability of finding boundary layer turbulent fluid on the exit plane, where the probability of finding turbulent pipe fluid (HT) is about 36.5%. However, as expected there is more the irrotational pipe fluid (HN) here, while the appearance of cross stream irrotational fluid (CN) has an extremely low probability of appearance here. At higher y/D distances above the exit, the intermittency factors of both HN and CN fluids vary monotonically with y/D : that of HN is reduced and practically vanishes at $y/D \geq 0.25$ and that of CN increases (particularly above $y/D = 0.25$), and must, by equation (1), reach values of 1 at some further y distances. Quite different is the behaviour of the pipe- and boundary layer-turbulent fluid intermittency factors: the probability of finding HT fluid is increased with y/D and at $y/D = 0.15$ reaches its highest value of 73.5%. Then, it reduces rapidly and at the last measuring point $y/D = 0.4$, has a value of 5% only. The probability of finding flat plate boundary layer eddies increases with y/D and its maximum takes place at about $0.30D$ away from the exit. All the intermittency profiles at positions above the exit show that there are quite large regions of the flow, which receive significant contributions from all of the four possible zones. There are of course regions where the flow "time shares" partially say, between two of the four postulated possible zones.

At the downstream stations (fig. 5b) the boundary layer eddies (CT fluid) become rare, i.e. the probability of finding any of them is of the order of 6%. According to Foss (1980) CT fluid travels downstream by passing over the exit or around the exit. It is also interesting to see that the probability of finding HN fluid at x/D is very high.

Figures 6 to 8 show conditional and conventional averages of the normal - and shear stresses. The former are plotted as contributions to the latter using equation (1).

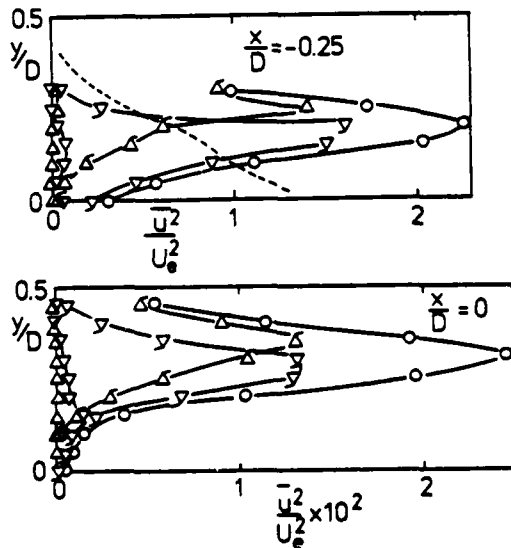


Fig. 6: $\overline{u^2}$ -profiles: (a) $x/D = -0.25$, (b) $x/D = 0$
o, conventional values; dotted line, profile at $x/D = -0.5$ taken from Andreopoulos and Rodi (1982); \square , triple wire sensor; rest symbols as in figure 5.

It is clearly shown that the two turbulent fields start to interact strongly, soon after they meet and both turbulent fields are the main contributors to the total average quantities. The irrotational fluctuations of the cross stream have practically a zero contribution while those of the pipe contribute sometimes significantly as it is particularly shown in the $\overline{v^2}$ -profiles at stations over the exit plane (figures 7a,b). There, hot fluid irrotational fluctuations can account for 25 to 30% of the conventional $\overline{v^2}$ -average which is 2 to 3 times greater than their contributions to the $\overline{u^2}$ -conventional average. Note that $\overline{v^2}_{HN}$

is appreciable only for $x/D < 0.5$ and it is likely to be puffing of the pipe flow which causes usual irrotational effects in all potential regions outside the shear layers.

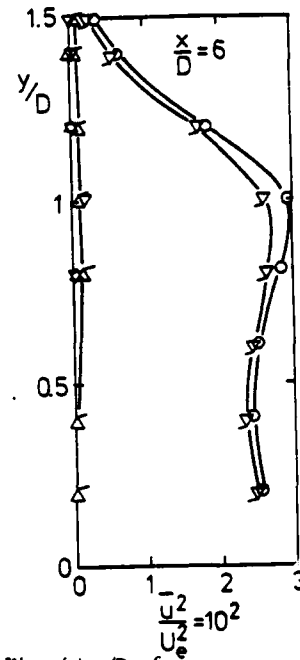


Fig. 6: $\overline{u^2}$ -profiles: (c) $x/D = 6$
o, conventional values; dotted line, profile at $x/D = -0.5$ taken from Andreopoulos and Rodi (1982); \square , triple wire sensor; rest symbols as in figure 5.

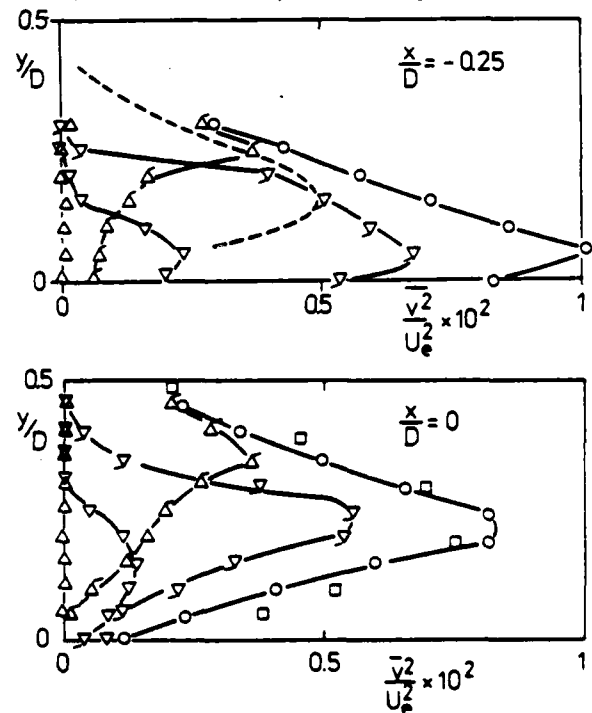


Fig. 7: $\overline{v^2}$ -profiles: Symbols as in figure 6.

In figures 6a, 7a and 8a, the corresponding profiles of $\overline{u^2}$, $\overline{v^2}$ and \overline{uv} at $x/D = -0.50$ are also plotted for direct comparison. Since mixing has not yet started at $x/D = -0.5$ the conventional averages in the measurements of Andreopoulos and Rodi represent quite closely conditional averages of quantities of boundary layer fluid, i.e. these quantities at $x/D = -0.5$ can be directly compared with the downstream profiles of conditional averages of "cold and turbulent" fluid. This can give us an indication of the

strength of the interaction in the near field region. It is remarkable to see how the downstream profiles have changed dramatically from those upstream.

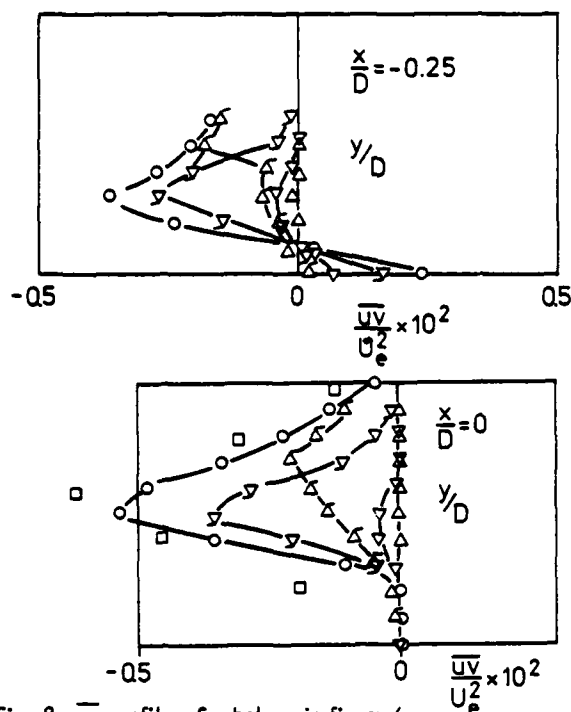


Fig. 8: \overline{uv} -profiles: Symbols as in figure 6.

Generally contributions from the boundary layer fluid to any of turbulence quantity are considerably decreased with downstream distance. Typically this is shown in figure 9 where the maximum values of the "cold and turbulent" zone of each downstream station are plotted against x . Among the three stresses, the normal stress u_{CT}^2 seems to be drastically affected by the interaction: within less than one diameter from the point where the interaction started roughly at the upstream edge of the pipes it has reduced by more than 50 % of its initial value, while it decays slowly further downstream.

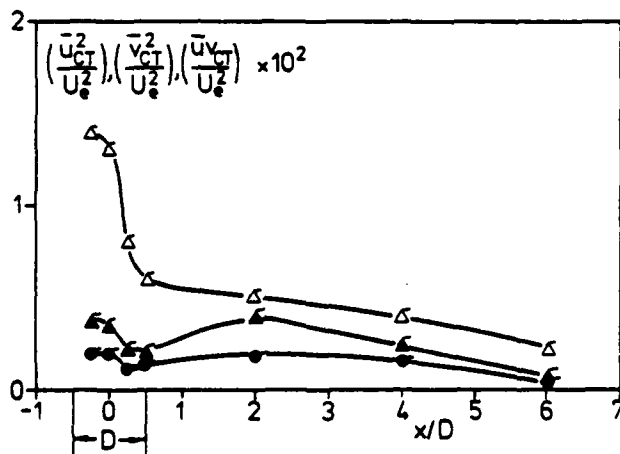


Fig. 9: Longitudinal decay of maximum stresses of the boundary layer fluid (CT-zone): Δ , u_{CT}^2 ; \square , v_{CT}^2 ; \circ , uv_{CT} .

However, the fact that the advection of u_{CT}^2 in the longitudinal direction $U \partial u_{CT}^2 / \partial x$ is high but negative does not imply that the mean life time of a turbulent-boundary layer-eddy is very short in the above of the exit region, because advection in the normal direction is positive.

The total picture of the flow would be incomplete without the zone-average velocity \bar{U} and \bar{V} profiles some of which are shown in figures 10 and 11. At $x/D = 6$ the pipe fluid has taken a boundary layer character: turbulent fluid moves slower and

irrotational fluid moves faster than the mean flow in the x -direction with exactly the opposite taking place in the normal direction (see Kovaszny et al. 1970, Murlis et al., 1982). The boundary layer-turbulent-fluid moves faster in the downstream direction and slower than the mean flow in the normal direction.

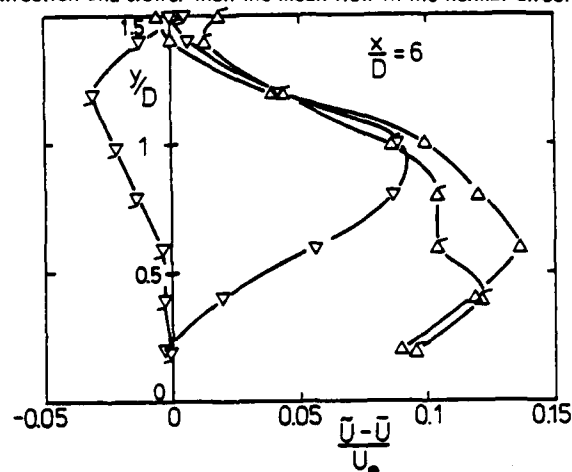


Fig. 10: Zone-average U-velocity component. $x/D = 6$. Symbols as in figure 6.

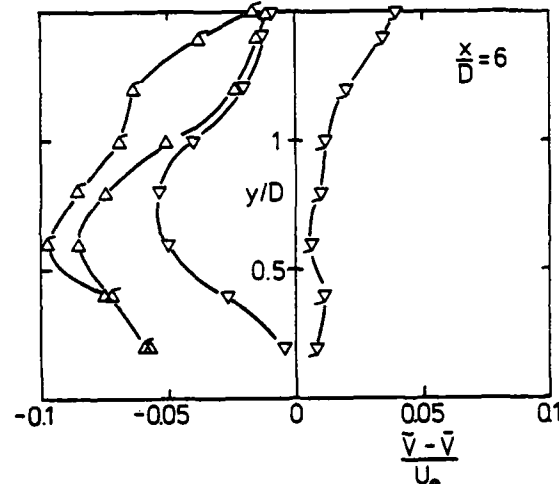


Fig. 11: Zone average V-velocity component. Symbols as in figure 6.

At these downstream stations CN fluid behaves similarly to that associated with an isolated "simple" boundary layer as does the HN fluid.

CONCLUSIONS

The present experiment has shown the existence of large eddies in the jet which are rather well organized at low Reynolds numbers. As these pipe eddies leave the pipe, they give a "pulsating" character to the jet flow and have a periodicity in their appearance which seems to scale with the cross-free stream velocity U_e and the pipe diameter D at all investigated velocity ratios and Reynolds numbers. These pipe eddies interact with upstream boundary layer eddies of opposite vorticity and at the end of the strong interaction region eddies with a boundary layer character are present.

The interaction region was explored by means of quite elaborate conditionally sampling techniques which indicated that the flow "time shares" between four possible zones, namely: irrotational cross stream flow, irrotational pipe flow, turbulent boundary layer flow which develops over the flat plate and turbulent pipe flow. This was made possible by heating the pipe flow and then further discriminating the turbulent/non-turbulent interface.

The conditionally sampled average quantities show that most of interaction takes place in the region above the exit at $R = 0.5$

where the contributions of the cross stream are very high. At downstream stations the jet-turbulent fluid contributions of all turbulent quantities approach closely the conventional averages while the boundary layer-turbulent fluid contributions tend to zero. The distance where this takes place depends mainly on the relative size of the length scales of the initial flows (for a given velocity ratio R). If the boundary layer length scale L_{BL} is much lower than that of the pipe flow L_p then this distance is short. If L_{BL} is of the same order of magnitude of L_p , the distance increases with increasing ratio L_{BL}/L_p . This tendency is not, however, true if $L_{BL} \gg L_p$. In this case the situation is different since boundary layer-fluid contributions approach the conventional total averages and the pipe flow contributions asymptote to zero values. A quantitative or even qualitative description of the interaction in this case, requires some further investigation of the jets into a cross flows at low velocity ratios.

ACKNOWLEDGEMENTS

The research reported here was sponsored by the Deutsche Forschungsgemeinschaft and benefited from stimulating discussions with Dr. D.H. Wood and Prof. J.F. Foss.

REFERENCES

- Andreopoulos, J. (1981): "Comparison Test of Various Hot Wire Data Analysis Methods with Respect Their Performance at Various Pitch Angles". *Rv. Scient. Instr.* 52 (9), 1376.
- Andreopoulos, J. (1982a): "Measurements in a Jet-Pipe Flow Issuing Perpendicularly into a Cross-Stream". *ASME, J. Fluid Engg.*, 104, 493-499.
- Andreopoulos, J. (1982b): "Statistical Errors Associated with Probe Geometry and Turbulence Intensity in Hot Wire Anemometry". Report SFB 80/E/204. To appear in *Physics E: Sci. Instr.*
- Andreopoulos, J. and Bradshaw, P. (1980): "Measurements of Interacting Turbulent Shear Layers in the Near Wake of a Flat Plate". *J. Fluid Mech.* 100, 639.
- Andreopoulos, J. and Rodi, W. (1982): "An Experimental Investigation of Jets in a Cross Flow". Rep. SFB 80/E/219, University of Karlsruhe.
- Antonia, R.A. (1981): "Conditional Sampling in Turbulence Measurements". *Ann. Rev. Fluid Mech.* 13, 131.
- Bradshaw, P. (1974): "Mixing in Complex Turbulent Flows". *Proceedings, Project Squid Workshop, Purdue University, May 1974*, Editor S.N.R. Murthy, Plenum Press, New York, 1975.
- Crow, S.C. and Champagne (1971): "Orderly Structure in Jet Turbulence". *J. Fluid Mech.* 48, 547.
- Foss, J.F. (1980): "Interaction Region Phenomena for the Jet in a Cross-Flow Problem", Rep. SFB 80/E/161, University of Karlsruhe.
- Goldmidt, V.W. and Bradshaw, P. (1973): "Flapping of a Plane Jet". *Physics of Fluids* 16 (3), 354.
- Kavaszny, L.S.G., Kibens, V., and Blackwelder, R.F. (1970): "Large Scale Motions in the Intermittent Region of a Turbulent Boundary Layer". *J. Fluid Mech.* 41, 283.
- McMahon, H.M., Hesten, D.D., and Palfery, J.G. (1971): "Vortex Shedding from a Turbulent Jet into a Cross-Wind". *J. Fluid Mech.* 48, 73.
- Muck, K.C. (1980): "Comparison of Various Schemes for the Generation of the Turbulent Intermittency Function". *Imperial College Aero Report* 80-03.
- Murlis, J., Tsai, H.M., and Bradshaw, P. (1982): "The Structure of Turbulent Boundary Layers at Low Reynolds Numbers". *J. Fluid Mech.* 122, 13.
- Ramsey, J.W. and Goldstein, R.J. (1971): "An Interaction of a Heated Jet with a Deflecting Stream". *J. Heat Transfer* 94 (4), 365.
- Tutu, N.K. and Cherray, R. (1975): "Cross Wire Anemometry in a High Intensity Turbulence". *J. Fluid Mech.* 71, 785.
- Yule, A.J. (1978): "Large-Scale Structure in the Mixing Region of a Round Jet". *J. Fluid Mech.* 89, 413.
- Weir, A.D., Wood, D.H., and Bradshaw, P. (1981): "Interacting Turbulent Shear Layers in a Plane Jet". *J. Fluid Mech.* 107, 237.

SESSION 8 - FREE SHEAR AND PERIODIC FLOWS

T.J. Hanratty - Chairman

INVESTIGATION OF A PLANE MIXING LAYER

S.V. Sherikar
Department of Mechanical Engineering
State University of New York
Stony Brook, NY 11794

and

R. Chevray
Department of Mechanical Engineering
Columbia University
New York, NY 10027

ABSTRACT

The results of a study of a plane mixing layer are presented in this paper, the objective being to understand better the role of coherent structures in the mechanisms of entrainment and mixing. The study involved chiefly flow-visualization with simultaneous velocity measurements, with a scheme to synchronize the two, that enables us to get a better picture of the coherent structures which strongly influence the flow. Initial conditions, which are of critical importance in the development of turbulent shear flows, are documented. Mean velocity profiles in the mixing layer and the corresponding spreading rate were found to be in general agreement with the range of results of other investigators.

INTRODUCTION

A plane mixing layer, formed when two separated streams moving at different velocities are brought together at the end of a splitter plate, represents one of the simplest free turbulent shear flows. It has attracted the interest of researchers in fluid mechanics for many years now because it is both simple and yet possesses several features that can not be adequately described. The understanding of the physics involved in such cases therefore becomes essential before more complicated schemes of practical interest, such as those involving combustion, can be handled with a full knowledge of the nature of processes involved.

One important feature in free turbulent shear flows is the existence of quasi-deterministic, large two-dimensional coherent structures. Crow and Champagne[1], Roshko[2], Brown[2,3], Dimotakis[3] and several other researchers have brought to light several important features of these coherent eddies (and also several controversies). Most of these studies indicate the importance of experimental conditions, especially the role played by the initial conditions in the development of the flow downstream[4-6]. Evolving from the Kelvin-Helmholtz instability at the splitter plate, coherent structures dominate the large scale motions in the mixing layer and strongly influence the gross features of the flow such as spreading rate, entrainment, mixing etc. It has also been suggested[7,8] that coherent structures have possible upstream influence as well and cause feedback. While the early conclusions regarding the nature of these coherent structures were based primarily on flow visualization experiments, subsequent quantitative measurements involved the difficulties associated with phase scrambling and jitter[9] which resulted in apparent loss of coherence and means had to be developed to avoid this problem.

In this study, a plane mixing layer is investigated with the idea of determining the local velocity field of coherent structures and their role in entrainment and mixing. The region studied is the early part of the mixing layer where there is no pairing of any of these

large structures (such as one pointed at in plate 1[10]). This region was selected firstly because the structures are well defined in this stage of analysis, and secondly because this region being characterized by much mixing is important for several practical applications.

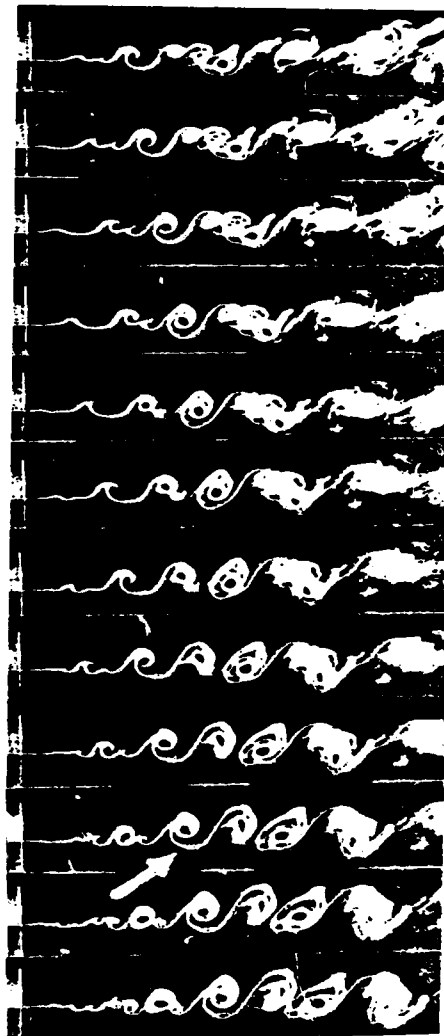


Plate 1: A sequence from flow-visualization cine film of plane mixing layer (from Sherikar and Chevray[10])

First, cine flow visualization alone was employed to observe the flow and later velocity measurements synchronized with cine flow visualization were made which allowed the determination of velocity field of coherent structures in the flow which were recorded on film. In this way the variation of phase of coherent structures is not allowed to smear the velocity data.

EXPERIMENTAL FACILITY

The investigation was carried out in the same wind tunnel facility used in earlier flow visualization studies [10]. The test-section 25 cm x 15 cm in cross-section and 100 cm long had glass sides to facilitate flow-visualization as well as LDV measurements. With the velocities employed (1-3 m/s) the Reynolds number for the flow in the test-section is of the order of 10^5 based on maximum distance downstream. Cloth resistances and perforated boards at the exit of the blowers helped achieve desired velocities and also were beneficial in reducing the effects of turbulence and non-uniformity of the velocity profile at the blower exit on the flow at the test-section.

For flow-visualization, the reaction of ammonia (NH_3) and hydrogen chloride (HCl) which spontaneously produces dense white fumes of ammonium chloride (NH_4Cl) was used. This reaction is fast and irreversible at room temperature; thus, when two flows are seeded only near the splitter plate with NH_3 and HCl respectively the reaction is complete immediately downstream of the splitter plate and aerosol is formed due to the condensation of NH_4Cl which marks the large organized structures evolved from the instability at the splitter plate and subsequent roll-up. Details of this technique are given by Sherikar and Chevray [10]. The lighting became of critical importance when velocity measurements were to be made simultaneously using laser Doppler velocimetry (LDV). This requires the LDV optics to be placed so that measurements at the desired location are possible without obstructing the view of the camera. In addition, the test-section is to have the required illumination while the background is to be dark enough for the camera to get good photographic record, while contributing minimum noise to the photomultiplier. After many trials, an arrangement with three 1500 W straight-line-filament quartz lamps illuminating the flow from behind was found satisfactory.

Velocity measurements were made using a DISA 55X modular LDV system. NH_4Cl aerosol is unsuitable as scatterer for LDV measurements, during simultaneous measurements because of its small size and non-uniform spatial distribution (it would result in poor signal characteristics as well as bias in the measurements). A TSI 9306 atomizer which generated silicone oil particles approximately 1 μm mean diameter proved to be an excellent choice for scattering particles for LDV. The photomultiplier signal was processed by a DISA 55L90 counter processor, the analog output of which was used. While making velocity measurements simultaneously with flow visualization, with proper choice of acceptance window levels for the incoming Doppler signals and with built-in validation schemes of the counter processor, the signals from NH_4Cl particles (which was essentially noise as far as velocity measurements were concerned) were virtually eliminated. The results thus are superior to the earlier results (Sherikar and Chevray [11]) when a tracker was used (where the advantage of continuous analog signal was somewhat offset by problems of noise, dropout and tracker going out of lock).

The data acquisition system consists of a PDP-11/23 micro-computer having 256 kB of RAM with extended memory support. The system is equipped with a real time clock, 16 channel A/D converter (with a DMA control), 4-channel D/A converter and a DMA data buffer (with DMA controller). Peripherals include a dual floppy disk drive, a 20MB Winchester hard disk drive, magnetic tape unit with 800/1600 bpi/45 ips capability, plotter and a line printer. Two timer-counter circuits were used - one with a seven segment LED display for cine flow visualization set-up and the other, driven by the same clock, for synchronization of the above with the data collected by the data acquisition system.

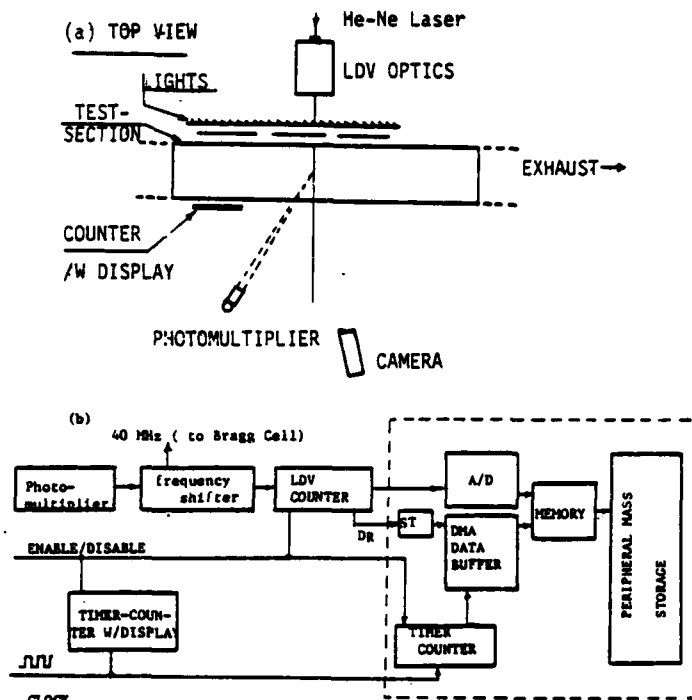


Fig. 1 (a), (b). Schematic of the measuring technique

Technique for Simultaneous Measurements.

A schematic of the technique of synchronizing the velocity information and the flow-visualization record on the film is shown in fig 1 (a) and (b) along with the experimental set-up. Initially, the data ready (DR) signal from the LDV counter processor is inhibited while both the timer-counters are held initialized (i.e. count zero). Flow is established and once the camera starts photographing, a DPST switch enables the LDV counter processor and the two timer-counters at the same time. At every DR signal from the counter-processor, one measurement for velocity and corresponding time count is recorded. Since the two timer counters are driven by the same clock and started to count simultaneously, it is insured that both the counters will always have exactly the same count. Consequently it is easy to relate every frame from the flow visualization film to the corresponding velocity measurements since the LED display of one timer-counter appears on the film while the count of the other is stored against the corresponding velocity reading.

This technique is superior to the one used earlier. Firstly, use of counter processor for LDV is more suitable here than a tracker. Also the scheme of using timer-counters and LED display to keep track of time allows the history of individual structures to be recorded very accurately and neatly.

The following analysis was then carried out. A particular set of coherent structures was selected from the film if they did not distort significantly while passing through the measuring location (i.e. LDV measuring volume). Then by projecting individual frames, the coherent structures with loci of corresponding points of velocity measurement in them were reproduced on paper. Finally, from the time information both on the film and velocity data, velocities corresponding to these points were overlaid on the picture of the coherent structure(s) being analyzed to get an overall picture.

RESULTS AND DISCUSSION

Velocity measurements were made in the boundary layer at the splitter plate at $x = -0.5$ cm using hot-wire (DISA 55M CTA system). This was important because initial conditions have been shown to be of great significance when data from different sources are to be com-

pared. The results of these measurements are given in Fig 2 (a) and (b).

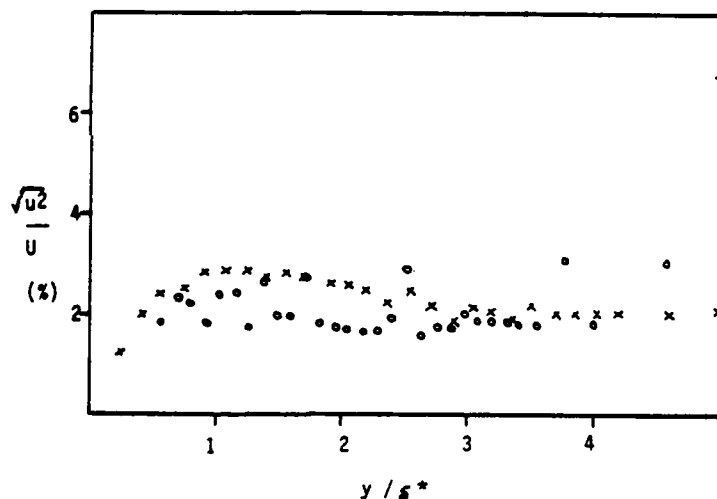
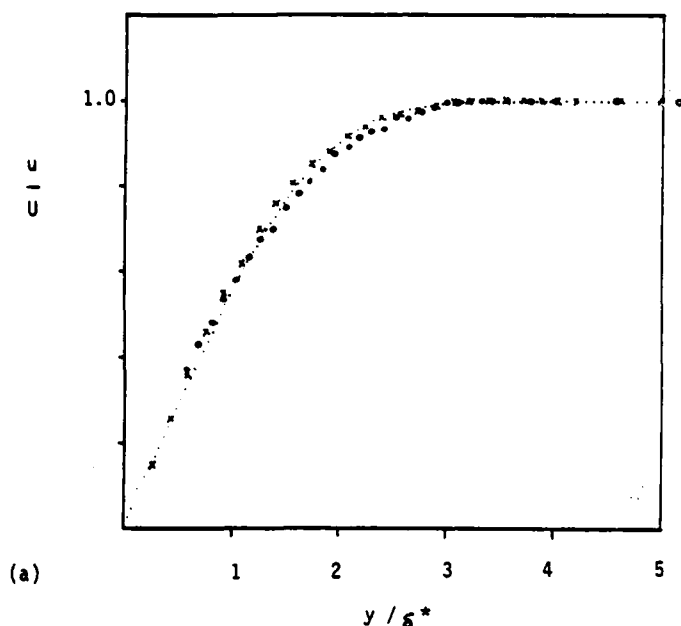


Fig. 2: Boundary layer at the splitter plate. (a) Mean velocity profile, (b) fluctuation intensities: x - lower stream, $U = 3.14$ m/s, $\delta = 4.83$ mm, $\delta_m = 0.6$ mm, $H (= \delta^* / \delta_m) = 2.537$; \circ - upper stream ($U = 1.13$ m/s), $\delta = 7.11$ mm, $\delta_m = 0.93$ mm, $H = 2.4$;-Blasius profile

The boundary layer was laminar in both upper (slow) as well as lower (fast) stream with shape factors of 2.54 and 2.4 respectively. The corresponding values of momentum thickness, δ_m , were 0.93 mm and 0.6 mm respectively. The fluctuation intensities in the boundary layer were fairly constant, about 2%, in both boundary layers and did not show any trend. Former analysis of the u-component fluctuations showed that the frequency content was confined to low frequencies (< 10 Hz) and to discrete frequencies. This leads one to believe that the origin of these may be in the vibrations of the splitter plate and of the structure as well. The boundary layer profiles almost collapse on the Blasius profile as shown in the figure.

Fig. 3 shows the development of the mean velocity profile across the mixing layer at three downstream locations. These measurements were made with LDV and one-dimensional weighting procedure (McLaughlin and Tieder-

man[12]) was used. The mean velocity profile seems to be close to self-preservation even at $x = 26.7$ cm.

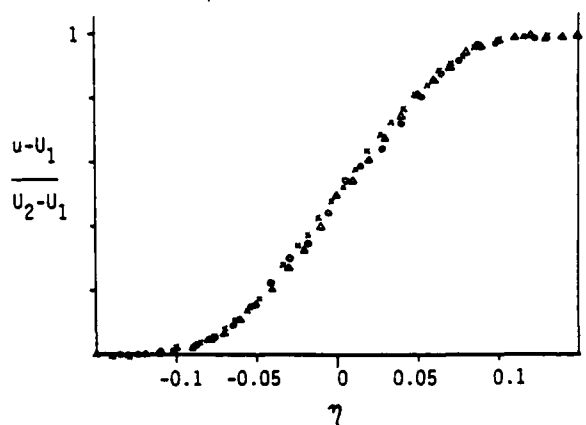


Fig. 3: Mean velocity profile in the mixing layer at $x = 26.7$ cm (\times), 35.6 cm (\circ) and 43.2 cm (Δ). $x_0 = -7.5$ cm.

Taking vorticity width,

$$\delta_w = \left[\frac{\partial \left(\frac{u - U_1}{U_2 - U_1} \right)}{\partial y} \right]_{\max}^{-1}$$

as a characteristic measure of the width of the mixing layer, the spread rate is given by

$$\frac{\delta_w}{(x - x_0)} = 0.153 \quad (x_0 = -7.5 \text{ cm})$$

This corresponds to the similarity parameter, σ_f , of 12.6. These values are in general agreement with the results of other researchers in this area. While more information could be obtained from further measurements, this has not been done yet.

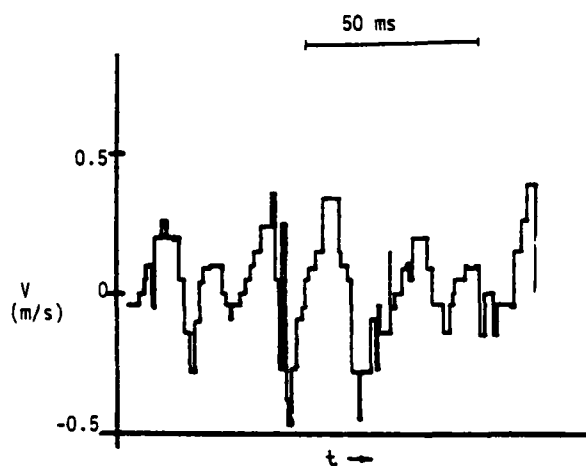


Fig. 4: Trace of v-component of velocity in the center of the mixing layer at $x = 22$ cm during simultaneous flow-visualization. Data Rate 500 Hz (for LDV)

Fig. 4 shows the trace of u-component of velocity in the mixing layer at $x = 22$ cm. There is ambiguity in that there is a periodicity in the flow (although it is turbulent) and it seems to be coming from the orderly coherent structures. This argument is supported by the fact that the periodicity seen in fig. 4 also corresponds roughly to the passage frequency of coherent structures in corresponding cine film record of flow-visualization. It is easy to see the jitter in the signal and hence the apparent loss of coherence that would appear in the cor-

relation measurements due to phase scrambling effects.

Fig. 5 (a) - (c) show typical variation of velocity (v-component) in the coherent structures obtained from simultaneous measurements. A word of caution here regarding the instantaneous flow field of these organized coherent structures - while it is expected that they will possess a deterministic flow pattern (or at least partly so), the possibility of variation in size, orientation etc. and therefore detailed nature is open and at this stage what is sought is the trend that could give more information regarding the general behavior of these structures. Besides the difficulties that may be involved in getting details of the small scale motion in the coherent structures with the present technique, it is doubtful whether this knowledge would be necessary in understanding phenomenon occurring on macro scale such as entrainment, growth and other interactions with the flow. It may be conjectured that the area of influence of the small scales would be in mixing at molecular level, in the development of three-dimensional instabilities in the large organized structures and others such as contribution to Reynolds stresses, viscous dissipation etc. For now, the investigation is aimed at getting a general picture of the velocity field in these orderly eddies and its implications.

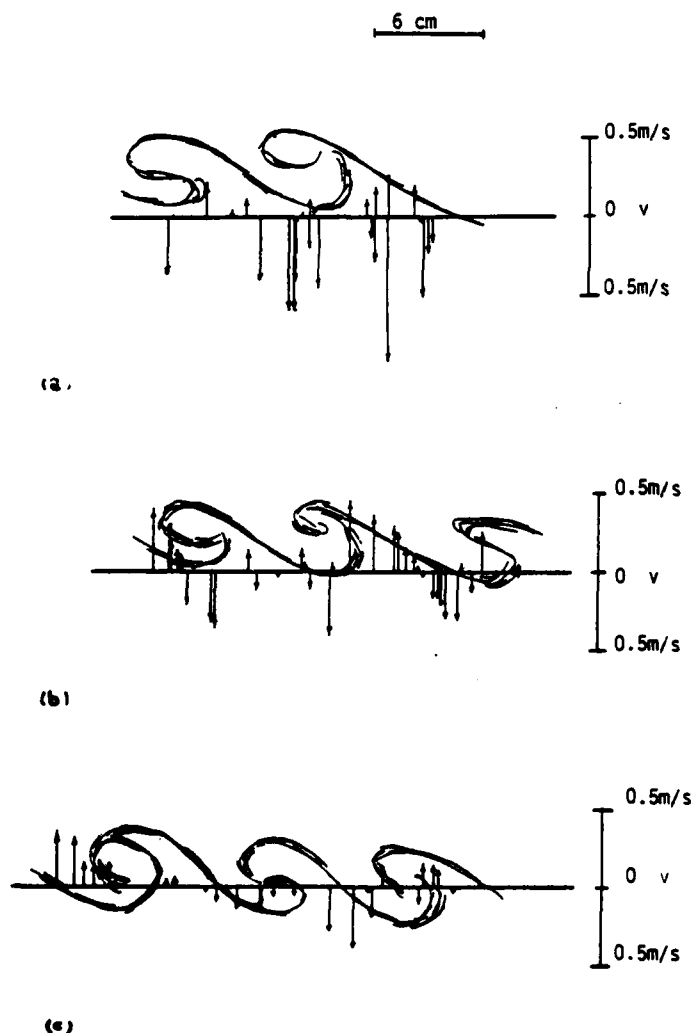


Fig. 5: (a), (b) and (c) Distribution of v-component of velocity in coherent structures at different cross-sections.

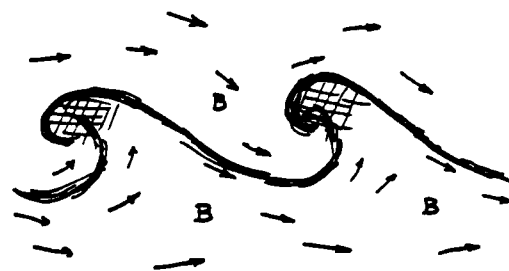


Fig. 6: Typical velocity pattern in a coherent structure.

Fig. 5 (a) - (c) show actual velocities (v-component) measured simultaneously with flow visualization, obtained with the technique described earlier. Each of these are separate sets of measurements. Minor variation seen in the appearance of these structures were ignored for reasons explained before. It can be concluded that the interface, marked by aerosol during flow-visualization (which also identifies the coherent structure), behaves much like a material surface. This is quite evident in fig. 5 (a). The entrainment of potential fluid into the coherent structures by an induced velocity component during the roll-up of the core is evident in fig. 5 (b) and (c). A train of these organized eddies appear like vortices spaced somewhat equidistant and joined by a thin interface as depicted in Fig. 6. This interface is important in that the fluid from the potential region that is entrained during roll up of these vortices is directed in a spiral towards the core where turbulent fluctuations are induced. The motion of this interface can also be seen to cause potential fluctuations much like a material surface. The vortices are convected by the flow and interact with each other (and the flow itself), periodically rolling around one another and finally coalescing into a larger one. Rarely, but definitely, tripling also takes place whereby three structures merge to form one downstream.

These are not the only mechanisms at work (which makes this problem interesting). There are also secondary instabilities along the interface connecting these structures^[13] which probably result in what many researchers have called "nibbling". This is best illustrated by the fact that this interface which is sharp initially, is less so as the flow develops further downstream.

CONCLUDING REMARKS

The mean velocity profiles measured in the mixing layer and its spreading rate are in agreement with the results of previous researchers, but they do not give any new information about the flow. In terms of determining the nature of velocity field of the coherent structures and in the estimation of entrainment due to these, it is expected that the technique of simultaneous velocity measurement with flow visualization would be helpful in isolating jitter and phase scrambling in the flow. From the measurements the pattern of velocity field appears to be as shown in Fig. 6. Much of the small-scale mixing appears to take place at the core (shaded region in fig 6), and regions indicated by 'B' are regions where the potential fluid is drawn into the mixing region. The instantaneous velocity patterns are a result of several different mechanisms at work in the flow, the main ones being the motion of the vortices, the material surface like behavior of the interface and secondary instabilities in the two-dimensional flow field that enhance mixing. This, together with the variation in size, orientation and geometry of coherent structures allows for their description only in terms of an "average" velocity field from observation of many similar coherent structures.

ACKNOWLEDGEMENT

The authors would like to thank the Department of Energy for its generous support under Contract No. DE-AC02-82ER13003.

REFERENCES

- 1) Crow, S.C. and Champagne, F.H., "Orderly Structures in Jet Turbulence", *Journal of Fluid Mechanics*, vol. 48, part 3, 1971, pp 547-594.
- 2) Brown, G.L. and Roshko A., "On Density Effects and Large Structures in Turbulent Mixing Layers", *Journal of Fluid Mechanics*, vol. 64, 1974, pp 775-816.
- 3) Dimotakis, P.E. and Brown, G.L., "Large Structure Dynamics and Entrainment in Mixing Layers at High Reynolds Numbers", *Journal of Fluid Mechanics*, vol. 78, 1976, pp 535-560.
- 4) Foss, J.F., "The Effects of Laminar/Turbulent Boundary Layer States on the Development of a Plane Mixing Layer," *Symposium on Turbulent Shear Flows*, The Penn State University, University Park, Pa., April 1977, pp 11.33-11.42.
- 5) Husain, Z.D. and Hussain, A.K.M.F., "Axisymmetric Mixing Layer: Influence of Initial and Boundary Conditions", *AIAA Journal*, vol. 17, No. 1, May 1979, pp. 48-55.
- 6) Batt, R.G., "Some Measurements on the Effect of Tripping the Two-Dimensional Shear Layer", *AIAA Journal*, vol. 13, pp 245-246.
- 7) Ho, C.M. and Nosseir, N.S., "Dynamics of an Impinging Jet, Part 1: The Feedback Phenomenon", *Journal of Fluid Mechanics*, vol. 105, April 1981, pp 119-142.
- 8) Laufer, J. and Monkewitz, P., "On Turbulent Jet Flows: A New Perspective", *AIAA Aerocoust Conf.*, 6th, Hartford, Conn., June 4-6 1980.
- 9) Yule, A.J., "Phase Scrambling Effects and Turbulence Data Analysis", *Proc. Second Symposium on Turbulent Shear Flows*, July 2-4, 1979, Imperial College, London.
- 10) Sherikar, S.V. and Chevray, R. "Aerosol Formation in a Mixing Layer", *Turbulent Shear Flows*, 3, Springer (1983), pp 124-131.
- 11) Sherikar, S.V. and Chevray, R., "Simultaneous Measurements and Flow Visualization in a Plane Mixing Layer," *Proceedings, International Symposium on Applications of Laser Doppler Anemometry to Fluid Mechanics*, Lisbon, July 5-7, 1982.
- 12) McLaughlin, D.K. and Tiederman, W.G., "Biasing Correcting for Individual Realization of Laser Anemometer Measurements in Turbulent Flows, *Physics of Fluids*, vol. 16, 1973, pp2082-2088.
- 13) Roshko, A., "The Plane Mixing Layer: Flow Visualization Results and Three-Dimensional Effects", *Proc. International Conference on the Role of Coherent Structures in Modelling Turbulence and Mixing*, Madrid, Spain, 1980.

NUMERICAL STUDY OF THE PHENOMENON OF TURBULENCE SUPPRESSION IN A PLANE SHEAR LAYER

M. Nallasamy and A. K. M. F. Hussain
Department of Mechanical Engineering
University of Houston
Houston, Texas 77004

ABSTRACT

The phenomenon of turbulence suppression in a free shear layer due to controlled excitation has been studied using vortex-in-cell method. When the amplitude of the sinusoidal excitation is low, the maximum suppression occurs for excitation at the maximally unstable frequency ($St_0 = 0.017$) of shear layer, consistent with experimental data. An interesting new result of the numerical simulation is that the above Strouhal number preference is lost at high amplitudes of excitation. Also, it is found that the level of random fluctuations superimposed on the initial sinusoidal disturbance affects the extent of suppression significantly.

INTRODUCTION

The phenomenon of turbulence suppression due to controlled excitation of free shear layers was experimentally investigated by Zaman & Hussain (1981) in a number of experimental facilities—circular jets, a plane jet and a single-stream plane mixing layer. They identified the conditions for the occurrence of maximum suppression in free shear flows. The main findings of their study are: (a) The turbulence suppression depends on the laminar exit shear layer characteristics (no suppression has been detected when the exit boundary layer is turbulent). (b) The suppression effect is maximum when the shear layer is forced at the maximally unstable frequency, i.e. $St_0 = 0.017$ (Michalke 1965). Here $St_0 = (f \theta_0 / U_0)$ is the excitation Strouhal number, f is the forcing frequency, θ_0 and U_0 are the exit boundary layer momentum thickness and free stream velocity, respectively. Since the phenomenon is associated with the initial shear layer instability, it occurs not only in circular jets but also in plane jets and plane mixing layers. (c) The suppression occurs over the entire thickness of the shear layer. Suppression is observed in longitudinal and transverse fluctuations as well as in the Reynolds stress. (d) The maximum suppression characterized by U'_{xx}/U'_{xx} (the ratio of longitudinal fluctuation intensities with and without excitation) occurs at an axial location of about $400\theta_0$ downstream from the separation point (i.e., $x=0$). The axial extent of suppression observed in jets was in the range of $0.75D < x < 8D$. In a single-stream plane mixing layer, they observed the suppression effect to persist as far downstream as $6000\theta_0$. From flow visualization and conditional sampling studies of excited and unexcited shear layers, they concluded that excitation at $St_0 = 0.017$ produces the fastest growth and roll up of the shear layer, resulting into early saturation and transition (breakdown) of the structures, and inhibits the formation of large energetic vortices. As a consequence, the large fluctuation intensity, otherwise caused by the passage and interaction of the energetic vortices is reduced. Thus, Zaman & Hussain established that the turbulence suppression occurs in a range of Strouhal numbers (0.009–0.021) due to the laminar instability characteristics of the shear layer. Note that

Vlasov & Ginevskiy (1974) and Petersen et al. (1974) independently reported turbulence suppression at jet excitation Strouhal numbers $St_0 = 2.75$ and 3.0 , respectively, even though they neither focused on this observation nor attempted to explain the phenomenon. In an effort to further investigate and understand the phenomenon of turbulence suppression in shear flows, a numerical study of turbulence suppression was undertaken. The attractiveness of the numerical simulation is that the amplitude and frequency of the sinusoidal excitation as well as the exit boundary layer momentum thickness can be varied at will. Furthermore, controlled initial turbulence can be introduced numerically. In an experiment these characterizing parameters cannot be independently varied, limiting the choices available.

This paper reports the results of numerical simulation of excitation of a plane two-dimensional mixing layer. First, a brief description of the numerical simulation technique is given. Then the results of the simulation are discussed in relation to experimentally observed suppression along with the limitations of the simulation.

NUMERICAL SIMULATION

Mixing layers are known to be dominated by quasi-two-dimensional structures which develop initially from the Kelvin-Helmholtz instability of a vortex sheet (Batchelor 1967). Controlled excitation studies of jets and mixing layers suggest that the sensitivity of the normally turbulent flows to external forcing is related to the rotational inviscid behavior of these flows. Then, an inviscid two-dimensional computation (with no vortex stretching and dissipation which are crucial to the energy cascade argument) may shed light on at least the dynamics of large structures. To this end, several shear layer simulations which essentially solve two-dimensional Euler equations have been reported (Acton 1976; Delcourt & Brown 1979; Ashurst 1979; Aref & Siggia 1980). In these simulations, the vorticity, originally confined in a thin layer, is concentrated further into a finite number of point vortices for simulation purposes. In other words, the piecewise continuous distribution of vorticity ω is replaced by a finite sum of N delta functions,

$$\omega(\underline{x}, t) = \sum_{n=1}^N \Gamma_n \delta(\underline{x} - \underline{x}_n(t)), \quad (1)$$

where δ is the Dirac delta function, $\underline{x}_n = (x_n, y_n)$ is the location of the N th vortex of circulation Γ_n . The motion is followed by integrating the system of ordinary differential equations,

$$\frac{d\underline{x}_n}{dt} = \underline{u}(\underline{x}_n, t). \quad (2)$$

The solution of the equations (1) and (2) presumably represents the solutions of the two-dimensional Euler equations:

$$\frac{\partial \omega}{\partial t} + (\mathbf{U} \cdot \nabla) \omega = 0, \quad (3)$$

$$\nabla^2 \psi = -\omega, \quad (4)$$

$$U_x = \frac{\partial \psi}{\partial y}; \quad U_y = -\frac{\partial \psi}{\partial x}. \quad (5)$$

No precise answer can be given for the question of the number N of vortices required for a simulation. For a given N and t , confidence in the method is based on comparison with experimental results. The selection of a reasonable N is based on the requirement of the simulation and is many a time limited by the computer time and memory requirements (Saffman & Baker 1979; Leonard 1980; Aref 1983).

The velocity field induced by the vorticity distribution may be calculated in two different ways. One way is the classical direct summation procedure in which one calculates the velocity field by directly summing the velocity fields of the individual point vortices. The other method is the vortex-in-cell method (Christiansen 1973) in which a grid is superimposed on an array of point vortices and the stream function at the grid points is computed by solving the Poisson equation for ψ (Eq. 4) after ω has been redistributed onto the mesh points. The velocity at \mathbf{x}_n is then found by interpolation. The inversion of Poisson equation (4) can be performed very efficiently by using the fast Fourier transform method. The advantage of the vortex-in-cell method is that the amount of computation is linear in N , whereas in direct summation it is quadratic in N . Also, the viscous effects can easily be incorporated in the vortex-in-cell method.

The mixing layer in a laboratory is a spatially developing flow. However, simulation of spatially developing mixing layer is computationally expensive. Only Ashurst's (1979) simulation is that of a space-developing mixing layer. All other simulations consider time-developing mixing layer. In the time-developing perturbed shear layer simulation, Riley and Metcalfe (1979) solve directly the fully nonlinear low pass-filtered equations of motion using pseudo-spectral methods. This is called direct numerical simulation (sometimes referred to as large eddy simulation when sub-grid scale modeling is employed).

We consider a time-developing two-dimensional shear layer and use the vortex-in-cell method. The method is briefly discussed below. The superimposed grid has mesh spacings Δx and Δy , assumed uniform in x and y directions, respectively. To obtain the stream function ψ , a finite difference (central difference) approximation is made to eqn. (3).

$$\frac{(\psi_{i+1,j} - 2\psi_{i,j} + \psi_{i-1,j})/(\Delta x)^2 + (\psi_{i,j+1} - 2\psi_{i,j} + \psi_{i,j-1})/(\Delta y)^2}{\Delta t} = -\omega_{i,j}. \quad (6)$$

The vorticity is represented at the points (x_n, y_n) and so a redistribution scheme is introduced to assign values at the grid points and the eqn. (6) is solved. Figure 1 shows the redistribution scheme,

$$\omega(k) = A_k \Gamma_n / \Delta x \Delta y, \quad (7)$$

where the A 's are the areas shown. Equation (6) is solved using a fast Poisson solver (Hockney 1970) using a fast Fourier transform method. To determine the velocity of a point vortex, the velocities at the nearest four grid points are calculated using a central difference formula,

$$U_{i,j} = (\psi_{i,j+1} - \psi_{i,j-1}) / 2\Delta y \quad (8)$$

$$V_{i,j} = -(\psi_{i+1,j} - \psi_{i-1,j}) / 2\Delta x, \quad (9)$$

and then interpolated,

$$U_n = \left(\sum_{k=1}^4 U(K) A_k \right) / \Delta x \Delta y. \quad (10)$$

The vortices are moved forward in time using a stable second order accurate method,

$$X_n(t + \Delta t) = X_n(t) + 0.5(U_n(X_n) + U_n(\bar{X}_n))\Delta t, \quad (11)$$

$$Y_n(t + \Delta t) = Y_n(t) + 0.5(V_n(Y_n) + V_n(\bar{Y}_n))\Delta t, \quad (12)$$

where

$$\bar{X}_n = X_n(t) + U_n(X_n)\Delta t, \quad (13)$$

and

$$\bar{Y}_n = Y_n(t) + V_n(Y_n)\Delta t. \quad (14)$$

In this way the vorticity distribution at $(t + \Delta t)$ is computed, and the procedure is repeated to study the evolution of the flow in time.

In the present simulation, we superimpose a 128×128 grid on the flow field of the shear layer represented by 4096 point vortices with periodic boundary conditions in the x -direction. 4096 point vortices have been found to be adequate in representing the shear layer in the present simulation. The computation was carried out on the AS 9000/N computer system. Preliminary calculations were done on a 64×64 grid with 2048 vortices. The adequacy of the time stepping accuracy has been verified on both the solution of a single shear layer with sinusoidal disturbance and the evolution of two shear layers with symmetric sinusoidal disturbance (simulating 'puffing' instability of a plane jet). Although smoothing procedures (Moore 1981) could be employed to extend the useful evolution time, no such procedure was attempted in the present simulation.

The shear layer in the present simulation is given an initial thickness by representing it by four rows of point vortices. The distance between the rows was arrived at by examining the velocity profile and momentum thickness in a number of configurations. It was found that a transverse distance between the rows of 0.2 times the mesh size results in a velocity profile which compares well with the tanhyperbolic velocity profile (Fig. 2). The particular configuration chosen yields a momentum thickness which enables the study of excitations at various St_θ on the chosen grid.

The excitation frequency St_θ in the numerical simulation is expressed as $St_\theta = 0.5\theta_e/\lambda$; θ_e is the initial momentum thickness of the undisturbed shear layer and λ is the wavelength of the perturbation. Thus, in the numerical simulation we choose the wavelength λ to obtain the desired frequency St_θ of excitation. This is equivalent to the experimental procedure adopted by Zaman & Hussain (1981) for a single-stream plane mixing layer, where they varied the frequency of excitation at constant values of the exit velocity U_e and the momentum thickness θ_e .

The excitation cases are studied by specifying a regular sinusoidal initial disturbance of the chosen frequency to the initial distribution of point vortices representing the shear layer. An extremely small random disturbance is superimposed on the sinusoidal disturbance for enabling different realizations for ensemble average. The unforced case is obtained by computing the roll up and evolution of the large-scale vortex structures without any sinusoidal initial perturbation. The number of frequencies investigated is limited by the grid size and the periodic boundary conditions. The amplitude of

excitation has been varied over a large range. The effect of superimposing random fluctuations (representing the high frequency random fluctuations that exist in a real flow) on the regular sinusoidal disturbance has also been studied with different levels σ of the random fluctuations.

RESULTS AND DISCUSSION

For any initial disturbance specified, the temporal evolution of the shear layer is computed. At any instant of time the position of vortices and the velocities on the grid points are known in the simulation. The mean velocity \bar{u} is obtained as x average,

$$\bar{u}(y, t) = \int u(x, y, t) dx. \quad (15)$$

The mean velocity \bar{u} goes to a constant value $\Delta U/2$ well above the shear layer and $-\Delta U/2$ well below the shear layer. We can compute the momentum thickness as,

$$\theta(t) = \int (0.25 - (\bar{u}/\Delta U)^2) dy \quad (16)$$

The momentum thickness and the width of the shear layer $B (= y_{0.95} - y_{0.05})$ are computed at every time step; $y_{0.95}$ and $y_{0.05}$ are the transverse locations where \bar{u} is 95% and 5% of the freestream velocity difference ΔU . At regular intervals the profiles of turbulence intensities and Reynolds stress are obtained. The typical interval for the time averages were such that the momentum thickness increases by about 5% during the interval. The ratio u'_{ex}/u'_{ux} of the peak longitudinal fluctuation with excitation u'_{ex} to the peak longitudinal fluctuation without excitation u'_{ux} is defined as the suppression factor. Preliminary investigations showed no noticeable change in the evolutions of the shear layer for amplitudes of excitation A/λ between 0.003 and 0.125. Figure 3 shows the width of the shear layer as a function of time for two Strouhal numbers, 0 and 0.017 for an excitation amplitude of 0.0125. We observe near linear variation of the width with time, with little difference between the forced and unforced cases. In this amplitude range of excitation, no recognizable suppression occurs. However, in the range of amplitude of excitation 0.025 to 0.2, significant changes in flow development occur, and we observe turbulence suppression as discussed below. A major part of the results of suppression reported below has been obtained for an excitation amplitude of 0.05. In the experiments of Zaman & Hussain, the excitation amplitude (u'_e/U_e) was in the range of 0.3 to 1%. The higher forcing levels required in the simulation compared to those used in the experiments may be an inherent constraint of the simulation. The inadequacy may partly stem from the grid size and number of vortices employed. Acton (1980) found similar requirements of high forcing levels in her numerical simulation compared to experimental levels. The suppression factor u'_{ex}/u'_{ux} as a function of time is shown in Fig. 4 for four Strouhal numbers for an excitation amplitude of 0.05. It is seen that the maximum suppression occurs for a Strouhal number of 0.017, the theoretical 'maximally' unstable frequency. The suppression for $St_\theta = 0.034$ and 0.008 is less pronounced. This is in qualitative agreement with the experimentally observed results. For a Strouhal number (0.067) much higher than the maximally unstable frequency, we observe turbulence augmentation rather than suppression. The maximum suppression observed at $St_\theta = 0.017$ is about 35%. It may be instructive to note that the maximum suppression observed by Zaman & Hussain was about 42% at $U_e = 20$ m/sec and about 58% at $U_e = 10$ m/sec for a plane mixing layer. The measurements were made at a constant transverse distance $y (= 1.27$ cm from the lip) whereas the suppression factor reported here is the ratio of peak longitudinal fluctuations which occur at a different y . Another aspect of the numerical simulation is that the results show oscillations which are not observed in acoustic excitation measurements. Crighton & Gaster's (1976) analyses showed that small differences in the mean velocity profile could result in significant changes in instability characteristics.

The observed oscillations in the numerical simulation could be due to the difference in the simulation initial velocity profile (Fig. 2). Also, a larger simulation and an ensemble average of large samples will reduce the oscillations.

Figure 5 shows the transverse peak velocity fluctuation ratio v'_{ex}/v'_{ux} against time. We notice that the observed Strouhal number preference ($St_\theta = 0.017$) for suppression in longitudinal fluctuations does not exist for transverse velocity fluctuations. Zaman & Hussain obtained the distribution of the longitudinal and transverse components of the turbulence intensities u' and v' over the entire width of the shear layer at $St_\theta = 0.017$ with and without excitation. They found that for the excitation case both longitudinal and transverse components of turbulence intensities are small, over the entire cross-section compared to the corresponding values in the unexcited case. But it is not clear if the Strouhal number preference for the maximum suppression will be true for the transverse component of the turbulence intensity too. The experiments show that \overline{uv}/U_e^2 also suffer suppression with excitation of 0.017. The ratio of $\overline{uv}_{ex}/\overline{uv}_{ux}$ obtained in the simulation is shown in Fig. 6. We see that the Reynolds stress shows large excursions due to the small number of rolled up vortices in the simulation. That is, the excursions are large statistical fluctuations in a small sample, and this can be demonstrated numerically (Aref and Siggia 1980). Because of cancellations due to fluctuations in the sign of uv , we need a larger simulation length of the shear layer and a larger ensemble size for this quantity than for the longitudinal or transverse velocity fluctuations which are positive definite quantities. To obtain a smooth average one needs a large system of vortices and an ensemble average of large samples. In the present case because of the small number of roll-up vortices considered an ensemble average of 3 realizations was found to result in only a marginal improvement of the results. The evolution of the momentum thickness [Eq. (16)] and width of the shear layer are shown in Figs. 7 and 8 respectively, for the Strouhal numbers, 0.008, 0.017 and 0.034. We see that the growth rate for Strouhal numbers 0.017 and 0.034 are not very much different.

We need to digress a little here and discuss the success of the numerical methods in predicting the velocity fluctuations. Ashurst's computations incorporated viscosity twice, using both the random walk and the viscous increase of size (aging of the discrete vortices) in an effort to match the simulation fluctuation velocity components to the experimental ones. Even after inclusion of viscous effects he could match the longitudinal and transverse fluctuation intensities of the simulation with those of experiments only for low Reynolds numbers. For high Reynolds numbers he could match only the longitudinal intensities. He conjectured that the pressure strain correlations ($\overline{p\partial u/\partial x}$), which are responsible for maintaining the transverse velocity fluctuations, may not be correctly simulated. Aref & Siggia found that the peak velocity fluctuations in their simulation (256×256 grid with 4096 vortices) were high compared to the experimental values. Also, the transverse velocity fluctuations were larger than the longitudinal ones though the reverse is true at high Reynolds numbers. Acton (1980) also found that the values of fluctuation components were much higher than the experiments, which is true with the present simulation too. Since we are considering only the ratios of the fluctuation intensities, it is believed that the results of suppression have been reasonably correctly predicted in the simulations. No attempt was made to include viscous effects in the present simulation.

Next, it is of interest to see if the Strouhal number dependence of turbulence suppression is true for any amplitude of excitation. We obtained the suppression factor u'_{ex}/u'_{ux} for three Strouhal numbers for an excitation amplitude of 0.2. The results are shown in Fig. 9. We see that at this amplitude of excitation the strong Strouhal number preference of the maximum suppression is lost. An experimental study of suppression at high amplitude ($u'_e/U_e = 4.5\%$) carried out by us in an axisymmetric mixing layer clearly showed that the Strouhal

number preference is lost at high amplitudes. The maximum suppression was found to occur at $St_0 = 0.022$ (maximum frequency studied in the experiment) and not at 0.017, the maximally unstable frequency. At high amplitudes of excitation nonlinear effects dominate the flow evolution. A high initial amplitude together with the fast transition (inferred from the longitudinal velocity spectra at $U/U_e = 0.7$ along x) for excitation frequencies larger than the maximally unstable frequency produces less energetic smaller structures earlier in x . The saturation amplitude at a high frequency is also less. The combined effect of these is to produce a higher suppression.

The dependence of the extent of suppression on the amplitude of excitation is shown in Fig. 10 for $St_0 = 0.017$. The maximum suppression is found to increase with increase in the amplitude of excitation. However, one would expect the suppression to saturate at some maximum amplitude of excitation. This does not occur in the present simulation since the disturbance is in the position of the point vortices. For amplitudes of excitation greater than 0.2, the shear layer becomes so thick that it does not evolve and grow. This is shown in Fig. 11 and 12, which show the variations of B and θ with time at different amplitudes of excitation. We see that as the excitation amplitude increases, the growth rate decreases. Such behavior at high amplitudes of excitation in point vortex simulation has been reported by Acton (1976). The initial velocity disturbance introduced corresponding to each amplitude of excitation is shown in the figure. We see that for amplitudes of excitation greater than 0.2, the disturbance velocity decreases, indicating the non-physical nature of the shear layer representation. Thus the simulation is meaningful only up to an amplitude of excitation of 0.2.

The disturbance introduced into intrinsically unstable shear layer, appears as high frequency random fluctuations superimposed on low ones, depending on the frequency of the disturbance (Ho & Nossier 1981, Oster & Wygnanski 1982). Also in a real flow situation there always exist random (incoherent) velocity fluctuations, whose effect on the flow depends on the level of these fluctuations. To incorporate these random fluctuations in the simulation, we superimposed random fluctuations (of positions of vortices) over the regular sinusoidal fluctuations of the specified frequency. The level (σ , standard deviation) of the random fluctuations was varied and its effect on the suppression of longitudinal turbulence intensity studied. The results are shown in Fig. 13. We see that the maximum suppression increases with increase in the level of random fluctuations. As with the amplitude of excitation, the maximum suppression increases with increase in the level of random fluctuation without attaining a saturation level. For values of σ beyond 0.037, the general shape of the curve (u_{ex}/u_{ix} against time) changes, and the suppression increases drastically which is not physically meaningful. The reason for this is the excessive initial thickening of the shear layer with such high levels of random fluctuation as shown in Figs. 14 and 15.

CONCLUSIONS

The present numerical simulation results may be summarized as follows:

1. No noticeable suppression occurs in the range of amplitude of excitation 0.003 - 0.0125. Turbulence suppression occurs in the range of amplitude of excitation 0.025 - 0.2.
2. At an amplitude of excitation of 0.05, the simulation shows that the maximum suppression occurs at the maximally unstable frequency of $St_0 = 0.017$, consistent with the experimental results.
3. At high amplitudes of excitation ($A/\lambda = 0.1$) this Strouhal number preference is lost. (This has been verified experimentally by us recently).

4. The level of random fluctuations superimposed on the sinusoidal fluctuations has significant effect on the extent of suppression.

The research is supported by the National Science Foundation under Grant MEA 81-11676.

REFERENCES

- Acton, E., 1976 *J. Fluid Mech.* **76**, 561.
- Acton, E., 1980 *J. Fluid Mech.* **98**, 1.
- Aref, H., 1983 *Ann. Rev. Fluid Mech.* **15**, 345.
- Aref, H. & Siggia, E. D., 1980 *J. Fluid Mech.* **100**, 705.
- Ashurst, W. T., 1979 in *Turbulent Shear Flows I*, 402, Springer-Verlag.
- Bachelor, G. K., (1967) *An Introduction to Fluid Mechanics*, Cambridge University Press.
- Christiansen, J. P., 1973 *J. Comput. Phys.* **13**, 423.
- Crighton, D. G. & Gaster, M., 1976 *J. Fluid Mech.* **77**, 397.
- Delcourt, B. A. G. & Brown, G. L., 1979 in *Turbulent Shear Flows*, London.
- Ho, C. M. & Nossier, N. S., 1981 *J. Fluid Mech.* **105**, 119.
- Hockney, R. W., 1970 in *Methods of Computational Physics*, 9, Academic Press.
- Leonard, A., 1980 *J. Comput. Phys.* **37**, 289.
- Michalke, A., 1965 *J. Fluid Mech.* **22**, 351.
- Moore, D. W., 1981 *SIAM J. Sci. Stat. Comput.* **2**, 65.
- Oster, D. & Wygnanski, I., 1982 *J. Fluid Mech.* **123**, 91.
- Riley, J. J. & Metcalfe, R. W., 1980 *AIAA Paper NO.* 80-0274.
- Saffman, P. G. & Baker, G. R., 1979 *Ann. Rev. Fluid Mech.* **11**, 95.
- Zaman, K. M. B. Q. & Hussain, A. K. M. F., 1981 *J. Fluid Mech.* **103**, 133.

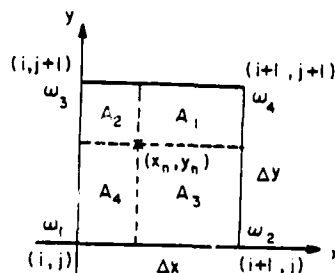


FIG 1 DEFINITION SKETCH OF THE VORTEX-IN-CELL REDISTRIBUTION PROCEDURE

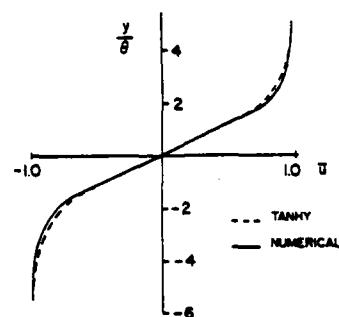


FIG. 2 INITIAL VELOCITY PROFILE

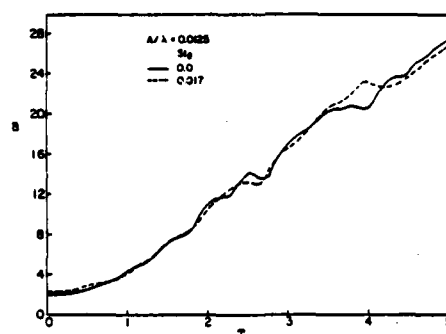


FIG. 3 LOW AMPLITUDE EXCITATION

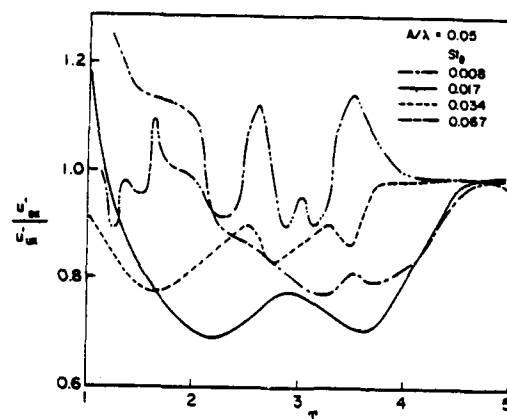


FIG. 4 EFFECT OF S_θ

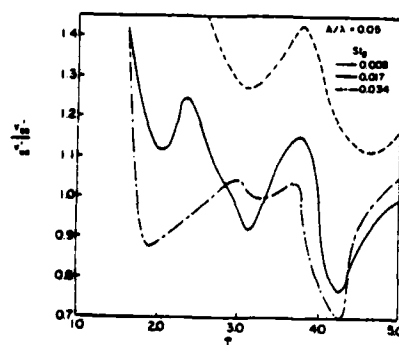


FIG. 5 SUPPRESSION IN TRANSVERSE COMPONENT

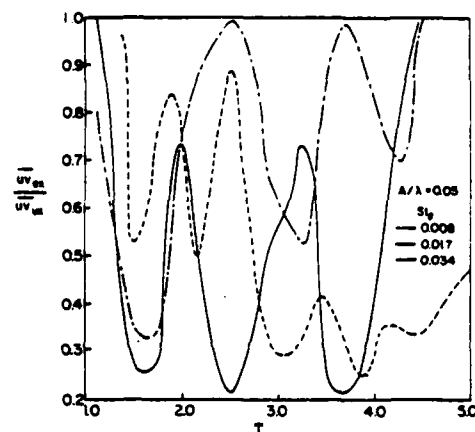


FIG. 6 SUPPRESSION IN REYNOLDS STRESS

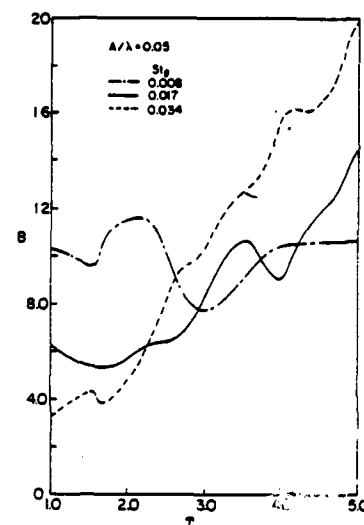


FIG. 7 VARIATION OF HALFWIDTH δ^* WITH S_θ

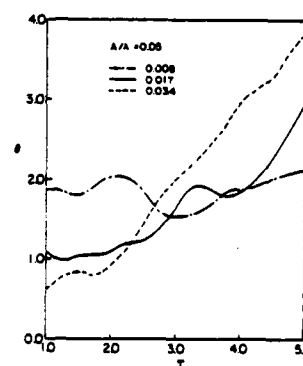


FIG. 8 VARIATION OF θ WITH S_θ

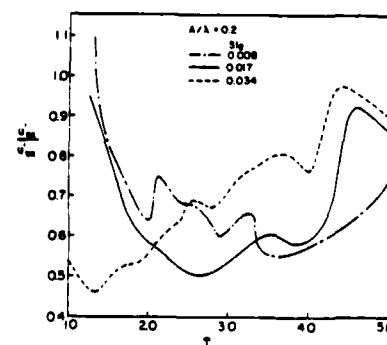


FIG. 9 HIGH AMPLITUDE EXCITATION ($A/\lambda = 0.2$)

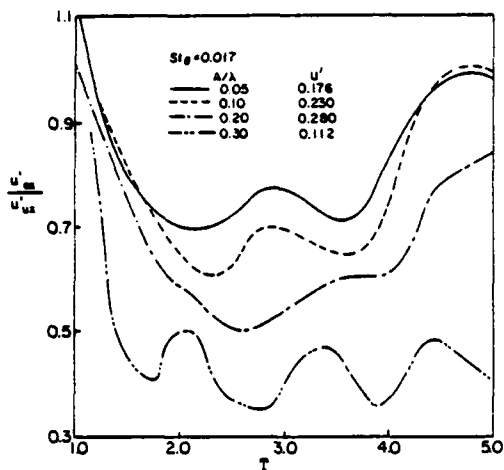


FIG. 10 EFFECT OF AMPLITUDE OF EXCITATION

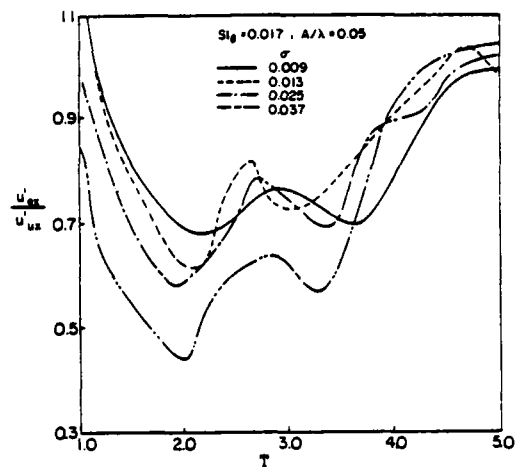


FIG. 13 EFFECT OF RANDOM FLUCTUATION

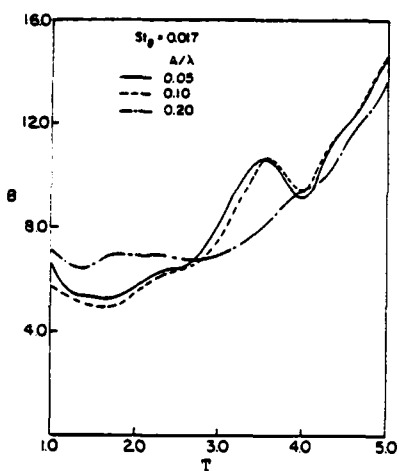


FIG. 11 VARIATION OF HALFWIDTH WITH AMPLITUDE

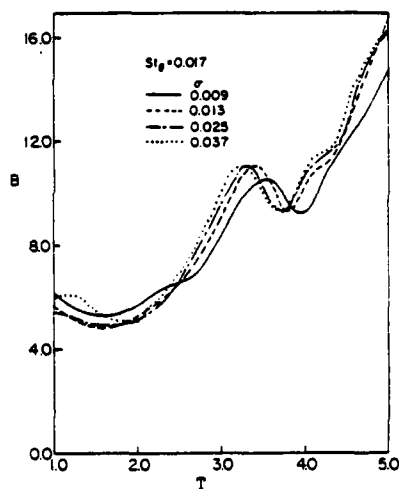


FIG. 14 VARIATION OF HALFWIDTH WITH RANDOM FLUCTUATION

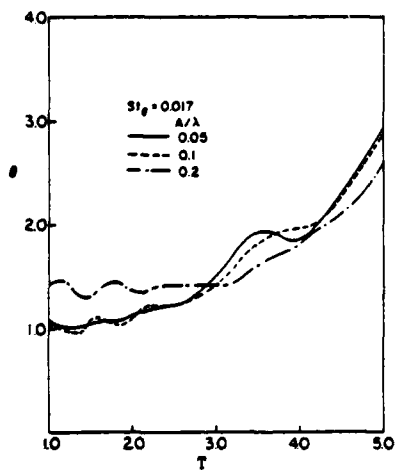


FIG. 12 VARIATION OF θ WITH AMPLITUDE

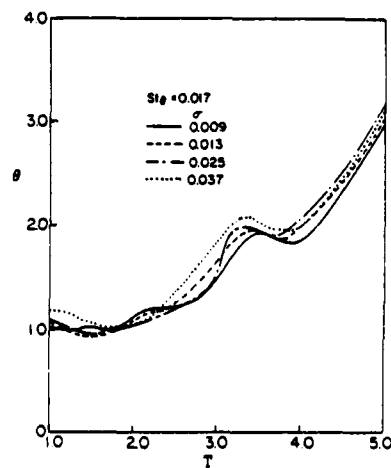


FIG. 15 VARIATION OF θ WITH RANDOM FLUCTUATION

HYSTERESIS OF TURBULENT STRESSES IN WALL FLOWS SUBJECTED TO PERIODIC DISTURBANCES

K. Hanjalić and N. Stošić
Mašinski fakultet, Sarajevo
Yugoslavia

ABSTRACT

The paper discusses some specific features of turbulent flows subjected to the periodic variation of external conditions. A particular emphasis is placed on the lagging response of turbulent structure and the hysteresis of turbulent stresses that were detected experimentally in a number of periodic flows. Several sets of experimental data were analysed in this light and attempts were made to obtain their prediction by means of single- and double-scale models of turbulence. Attention was focused on a case of simulated tidal flow where the above mentioned features are particularly pronounced. Some modifications of the standard stress-dissipation model of turbulence yielded a noticeable improvement of the prediction of major properties of this and some other periodic flows.

INTRODUCTION

If a turbulent flow is subjected to the space- or time variation of the external conditions, the turbulent interactions associated with different parts of the wave number spectrum will not generally respond in the same manner. Consequently, the turbulence and mean flow parameters are bound to exhibit different phase shifts and amplitude modulations. A number of recent publications on unsteady turbulent flows revealed the existence of a definite time-space lag between the response of turbulent structure and the mean flow parameters, but also a different variations of these shifts across the flow. This effect may become particularly pronounced if the external disturbances have a periodic character, the intensity of the lag depending upon the pulsation frequency and their amplitudes. Furthermore, because the response of the turbulence structure varies over the wave number spectrum, the time lags during the acceleration period are markedly different from those which occur during the deceleration phase, so that some of the turbulence parameters display a pronounced hysteresis (Anwar and Atkins, 1980). Yet, most authors report that both the mean flow and turbulence parameters, when normalized appropriately, yield the same quantitative behaviour as those in corresponding steady flows. These findings can hardly be justified in cases where the phase shifts of dependent variables and normalizing parameters do not remain constant across the flow.

The above mentioned features impose significant effects upon the transport processes in turbulent flows and they are, therefore, of substantial practical interest. Boundary layer development on rotating airfoils and turbomachinery blades, heat transfer and flow resistance in heat exchangers with pulsating flows such as the air intercoolers of two-stage compressors and dispersion of dissolved pollutants in coastal waters, are just some of the many such examples.

On the other hand, the inertial lag of the dynamics of turbulence structure behind the mean flow distortion in pulsating flows is a challenging feature that may serve as a severe test for the verification of modelling techniques.

It is generally recognized that the current prediction methods, verified in steady flows of varying complexity, give poorer performances when applied to the calculation of unsteady and periodic flows. This is in particular the case with eddy viscosity models, even if the transport coefficient is supplied by the differential equations, such as implied by k - ϵ model. Shemer and Wygnanski (1981) introduced separate eddy viscosity coefficients for the steady and time dependent parts of the phase averaged field. Cousteix et al. (1981) emphasised the importance of the inclusion of the normal stress production in the kinetic energy equation (usually neglected in calculation of boundary layers), and reported that a decisive improvement had been achieved by solving the equations for all turbulent stress components in comparison with k - ϵ model.

In fact, depending on frequency and amplitude, the pulsating flow may be expected to depart from both the spatial- and spectral equilibrium and any model that relies upon the equilibrium assumption is bound to be more or less unsatisfactory. This evidence was recognized earlier by the present and other authors (e.g. Hanjalić, Launder and Schiestel, 1979) when analysing some steady nonequilibrium flows including simple cases such as the development of turbulence when passing through a sudden contraction of the cross-sectional area, or boundary layers subjected to a sudden deceleration (or acceleration), followed by the relaxation of the imposed pressure gradient. The latter case bears some resemblance to a half cycle period of an unsteady periodic flow. In most of the mentioned cases the standard k - ϵ model, or even the full stress model did not yield the satisfactory reproduction of the experimental results.

The difference in the quality of predictions obtained by k - ϵ and stress models, as found by Cousteix et al. (1981) and the present authors suggests that the structural parameter $\overline{u_1 u_2}/k$ does not remain constant as found in steady equilibrium wall boundary layers, nor do their phase shifts exhibit the same behaviour. This in fact emphasises the importance of both the spatial- and spectral transports of individual stress components, particularly in flows with preferential straining direction. Hence an adequate account for this should be made in order to achieve a satisfactory simulation of turbulence dynamics.

Similar dissatisfaction was experienced in attempts to calculate the unsteady periodic flows discussed in the present work. However, contrary to the findings of Cousteix et al (1981), the application of full stress model as postulated by Launder Reece and Rodi (1975),

although performing better than simple k - ϵ model still did not yield the acceptable agreement with the experiments. One of the reasons for a different outcome may be attributed to a different treatment of the viscosity-affected near-wall region, which in the present work is bridged over by means of wall functions. It is believed, however, that the major reason lies in a general inadequacy of the single-point methods to represent the nonequilibrium situations.

In fact, if the difference in response of various turbulence parameters can be attributed to the spectral nonequilibrium, then, in order to achieve a closer simulation of the real processes, the mathematical model should account for the spectral dynamics, in addition to the modelling of processes in the physical space. This condition can not be fully satisfied by any of the present single point closure schemes.

Yet the simplicity and a wide verification of single point models seem to justify all efforts towards their further improvement and extension of their validity.

The present work describes our efforts in exploring the suitability of single- and two-scale second order closure models in standard and modified forms for predicting the earlier mentioned features of wall turbulent flows subjected to periodic disturbances of external flow conditions. In the first phase of the work the testing was carried out with the k - ϵ and the Reynolds stress-dissipation models, with several modifications, proved earlier to produce some improvement in predicting the nonequilibrium and recirculating turbulent flows. One of the modifications implies a different formulation of the source term in the dissipation equations (Manjalić et al., 1981, Launder et al., 1981), which ensures somewhat weaker coupling of the modelled dynamics of ϵ with the dynamics of turbulent kinetic energy. Other modifications concern different specification of wall functions of both mean and turbulence parameters. These employ $k^{1/2}$ instead of friction velocity U_* as the characteristic velocity scale and the relaxation of the constant stress-turbulent energy constraints in the near-wall region in sense of proposals given by Chieng and Launder 1980.

In the second part of the work the use was made of the two-scale model of turbulence (Manjalić, Launder and Schiestel, 1979), with some minor modifications concerning the division of the energy spectrum and the consequent redefinition of the empirical coefficients. The work is still in progress and the preliminary results of the application of the two-scale models are encouraging.

The models were used to calculate a number of the pulsating turbulent water and air flows having different frequencies and amplitudes of the external perturbations. Particular attention was paid to the results of experimental simulation of tidal flow of Anwar and Atkins (1980) with large period of oscillation, in which the responses of turbulent stresses during the acceleration and deceleration periods show distinctly different features and a visible hysteresis.

CONSIDERED MODELS AND THEIR MODIFICATIONS

Single-scale stress-dissipation model

It is generally recognized that the weakest point in the single-point closure models is the transport equation governing the turbulence scale. Most of the models employ at present the turbulence energy dissipation rate ϵ which, in combination with the kinetic energy, yields the characteristic time or length scale of turbulence. The source term in the equation for ϵ is usually modelled in form:

$$S_\epsilon = (C_{\epsilon 1} P - C_{\epsilon 2} \epsilon) \epsilon / k \quad (1)$$

where P is the production of turbulent kinetic energy.

Serious criticisms have been placed in the past on this formulation, the major one being that the source of ϵ is too closely linked with the source of kinetic energy itself. Bearing in mind that ϵ represents in fact the energy transfer rate across the wave number spectrum which equals the energy dissipation rate only under the conditions of spectral equilibrium, one may

expect that the production of ϵ will depend on mean rate of strain (not necessarily in the same manner as the production of kinetic energy itself), but also upon the mean vorticity, turbulence anisotropy (as advocated earlier by Lumley and coworkers) and other parameters that may influence the energy transfer. A functional combinations of variables at disposal, satisfying the invariance conditions, may be written in the form (retaining only the first order terms):

$$S_\epsilon = f(\overline{u_i u_j} \frac{\partial U_i}{\partial x_j}, k(\frac{\partial U_i}{\partial x_j})^2, k(\epsilon_{ijk} \frac{\partial U_i}{\partial x_j})^2, A \frac{\epsilon^2}{k}, \frac{\epsilon^2}{k}, \dots) \quad (2)$$

where A represents the first invariant of the stress anisotropy.

Extensive testings would be required to find a usable form of the expression (2) and to prove its superiority over the current simple practice which uses only the first and the last terms. However, equally simple alternative.*

$$S_\epsilon = C_{\epsilon 1} k(\frac{\partial U_i}{\partial x_j})^2 - C_{\epsilon 2} \frac{\epsilon^2}{k} \quad (3)$$

which yielded noticeable improvement of the calculation of both the simple nonequilibrium flows and more complex recirculating flows behind a step (Launder et al. 1981), helped also to improve the predictions of pulsating cases, considered in the present work.

It should be mentioned that the new term offers some potential advantages since it relaxes the linkage between the energy and ϵ equation as implied by standard models. The expression (3) implies also that the first term ("production") is now scaled by the time scale of the mean flow deformation $(\partial U_i / \partial x_j)^{-1}$. This seems plausible since the energy transfer rate through the spectrum is controlled primarily by the "large" eddies which are strained almost entirely by the mean rate of strain (Townsend, 1980). The second term ("destruction") remains to be scaled by turbulence scale (k/ϵ) , implying that the attenuation of the transfer process is controlled by turbulence itself.

Other modifications, considered earlier, concern the diffusive term in the ϵ equation but none of the remedies proved to be equally beneficial in different flow situations and have not been pursued further in this work.

Two-scale model

The idea of modelling separately the dynamics of low and high wave-number parts of the energy spectrum, as implied by the two-scale model of Manjalić, Launder and Schiestel (1979), seems particularly attractive for predicting the flows subjected to strong variation of external conditions. Indeed, the two-scale k - ϵ model produced a more adequate response of some steady homogeneous and wall flows that were exposed to sudden changes of pressure gradient. The improvements reported in the above-mentioned paper encouraged us to employ the same model to the periodic flows, considered here. The two-scale k - ϵ model produced, however, somewhat better predictions (e.g. Fig. 1), but they appear to be still inferior to those obtained by single-scale stress model.

As it was noted earlier, it is believed that the two-scale model failed to produce all the effects that were expected because the energy spectrum was divided at too high wave number with too much energy assigned to the low wave-number portion of the spectrum. Attempts have been made, therefore, to move the partitioning wave number into the production region as to include the mean rate-of-strain effect into the equations governing the high wave-number structure. Positive effects, achieved by considering all stress components in the single-scale model, discussed earlier, give some justification for exploring an all-stress variant of the two-scale model. This approach requires however an extensive testing of various steady flows to determine a number of new empirical coefficients, before the model is applied to an unsteady situation.

In the moment of writing this paper we had completed only the preliminary testing of the model in homoge-

* This remedy has an effect only in stress-models while in k - ϵ model it reduces to the standard form.

neous flows. The starting set of the equations can be written in the form:

$$\frac{D\overline{u_i u_j^p}}{Dt} = P_{ij}^p - \phi_{ij}^p - \frac{2}{3} \delta_{ij} \epsilon_p + 2 \overline{u_i u_j^p}^p \quad (4)$$

$$\frac{D\overline{u_i u_j^t}}{Dt} = P_{ij}^t - \phi_{ij}^t + \frac{2}{3} \delta_{ij} \epsilon_p - \frac{2}{3} \delta_{ij} \epsilon_t + 2 \overline{u_i u_j^t}^t \quad (5)$$

$$\frac{D\epsilon_p}{Dt} = C_{\epsilon p} C_\mu k_p \left(\frac{\partial u_i}{\partial x_j} \right)^2 - C_{\epsilon 2p} \frac{\epsilon_p^2}{k} + D\epsilon_p \quad (6)$$

$$\frac{D\epsilon_t}{Dt} = C_{\epsilon t} C_\mu k_t \left(\frac{\partial u_i}{\partial x_j} \right)^2 + C_{\epsilon 1t} \frac{\epsilon_p \epsilon_t}{k_t} - C_{\epsilon 2t} \frac{\epsilon_t^2}{k_t} + D\epsilon_t \quad (7)$$

where indices "p" and "t" refer to the production and transfer regions of the energy spectrum, respectively. P_{ij} is the stress production and ϕ_{ij} pressure redistribution. The latter term was modelled in the manner proposed by Launder et al. (1975).

For the beginning it was assumed that coefficients in all terms of stress equations for "p" and "t" region have the same values, equal to those in the single-scale model. The model, applied to a series of homogeneous flows, that were considered at the 1980-81 AFOSR-HTTM Stanford Conference, produced in the whole better reproduction of the experimental data than the single-scale model. This is illustrated in Fig. 1., where, comparison is given between the predictions of kinetic energy distribution, obtained by two models, in an axisymmetric contraction of Tan-atchat (1980).

The solution of the full set of equations (4) to (7) in a more complex flows does not seem rational at present and we turned to a simplified form which solves the contracted form of the equation (5) (for k_t), while the individual stress components in "t" region are calculated from algebraic expressions worked out on the basis of equation (5). In this way only two new differential equations are solved in addition to the single-scale stress model. This work is still in progress.

Treatment of the near-wall region

A common practice to avoid the need for incorporating the viscous and nearwall effects into the modelled transport equations and solving them within the viscous sublayer is to employ wall functions by which the viscosity-affected region is bridged over. The boundary condition for the mean velocity, specified in the first point of the numerical grid, placed usually just outside the viscous layer, is defined most often by means of the logarithmic velocity law, which is assumed to prevail even under a severe variation of the external flow conditions. A number of authors presume that the standard form of the law of the wall remains valid at every time instant in an unsteady situation. This assumption relies on condition that the phase shift of the mean velocity in the logarithmic region equals that of the wall shear stress. This argument was confirmed directly for a case of periodic boundary layer by Cousteix et al (1981) on the basis of their own experimental results and data of Patel (1977). However, one should bear in mind that in the cases considered the amplitude of the mean velocity oscillation was not very high (in fact less than 15% of the time averaged mean velocity) and the conclusion may not hold for higher amplitudes or different frequencies. If the amplitude of the periodic velocity component increases sufficiently to bring the phase-averaged (ensemble-averaged) velocity at a certain time instant close to zero or to have negative values, logarithmic law will fail. The argument can be extended to a case of oscillating turbulent flow with zero time mean velocity. Hence the question may be raised about the limiting amplitude ratio up to which the standard law of the wall may be regarded as valid. Bearing this in mind, the use of k as the velocity scale in the logarithmic law, as proposed by Launder and Spalding (1973) appears to be an attractive proposition for periodic flows. In this way the logarithmic law may be expected to extend its validity not only to cases of large amplitude of periodic velocity oscillations, but also to other situations in which the ratio $\overline{u_1 u_2}/k$ does not remain constant.

An attempt to confirm this assumption was made by replotting the velocity profiles of some reported cases of periodic flows, where the standard form of logarithmic law did not show a convincing universality, such as in the mentioned flow of Anwar and Atkins. However, because of the large experimental scatter of data it was not possible to draw a definite conclusion. Yet, the computations that used the wall function based on $k^{1/2}$ showed improvements and were used consistently in all cases presented here.

As far as the turbulence parameters are concerned, their modelling in the wall region requires a specific approach. Most of the numerical finite difference or finite volume schemes presume linear variation of all dependent variables between the grid nodes as computationally most economical. This practice seems to be satisfactory everywhere except in the vicinity of the rigid wall where turbulent parameters may exhibit a very steep variation. This is particularly important for the control cell closest to the wall which may encompass not only the viscous sublayer, but also a portion of fully turbulent regime. Chieng and Launder (1980) split the near-wall cell into two parts. The wall-adjacent part represents the viscous layer, the edge of which is defined by a prespecified value of turbulent Re-number. By assuming a quadratic variation of kinetic energy and zero shear stress in the inner zone and linear variations of both properties in the outer part, the mean values of the energy production and dissipation over the cell were evaluated.

The idea can be extended to presume the variation of each stress component over the first numerical cell and to calculate the average values of source terms in each transport equation of a full-stress turbulence model, but the uncertainties in formulating the source terms within the viscous region discourage any attempts in this direction.

In this work we adopted a simpler route and calculated only the averaged value of ϵ over the cell, but related the values of normal stresses in the first grid point to that of the shear stress, which was calculated from the mean momentum equation. Because the kinetic energy is used only to obtain the average ϵ , we adopted a parabolic expression $k=(ay+b)^{2/3}$ to define the variation of k in the outer part of the cell, while in the inner part we employed the quadratic distribution as Chieng and Launder (Fig.2).

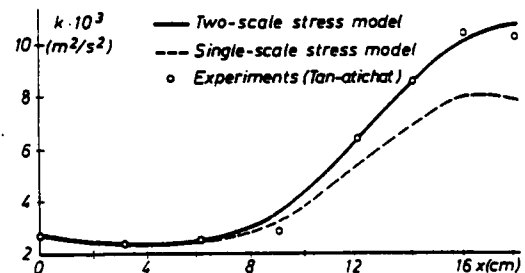


Fig.1.- Variation of kinetic energy in an axisymmetric contraction

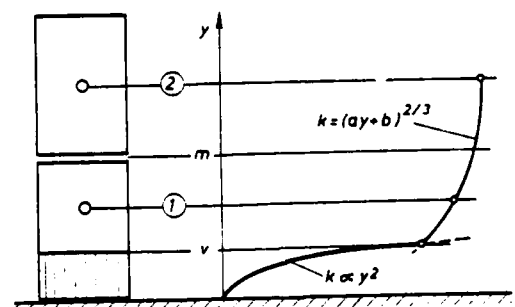


Fig.2.- Distribution of kinetic energy in the near-wall region

With the assumption that in the outer part the local ε may be approximated by $\varepsilon = k^{3/2}/(C_1 y)$, the adopted distribution of k yields a simple expression for the mean value of ε over the cell (notation is given in Fig.2):

$$\bar{\varepsilon} = \frac{k_v^{3/2}}{10 y_m} + \frac{1}{C_1 y_m} [a(y_2 - y_1)] \quad (8)$$

where:

$$k_v^{3/2} = 200 \frac{U}{k_v^{1/2}} + b; \quad a = \frac{k_2^{3/2} - k_1^{3/2}}{y_2 - y_1}; \quad b = k_1^{3/2} - a y_1 \quad (9)$$

PRESENTATION AND DISCUSSION OF RESULTS

Frequency and amplitude are the parameters that characterize the unsteady turbulent flows and these can be varied in a wide range. In his review lecture L.W. Carr (1981) attempted to classify the available experimental data on unsteady boundary layers according to these two variables and concluded that, although low amplitude or low frequency does not necessarily mean quasisteady behaviour, there is a small range of amplitude and frequency for which no unsteady effects have been reported. He concluded further that, provided the frequency remained lower than the critical value (related to turbulent bursts), the turbulent structure remains unaffected by oscillation of the flow field. This argument holds if one considers the properties averaged over a large number of cycles in periodic situations. However, there are flows of practical relevance, such as tidal currents, where a strong influence upon the turbulence mechanism was noticed due to the flow unsteadiness, although the frequency of oscillation was very low (Anwar and Atkins). The analysis of a detailed behaviour of turbulence properties and global parameters over a single cycle seems to be in such cases of a significant theoretical and practical importance.

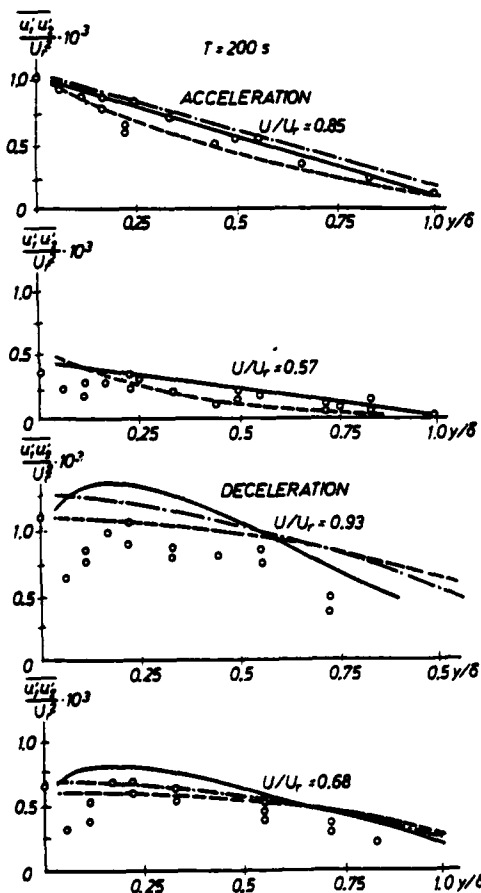


Fig.4 - Turbulent shear stress in simulated tidal flow; o-experiments, —single scale stress model, ---single scale $k-\varepsilon$ model, ---two-scale $k-\varepsilon$ model

We consider first the experiments of Anwar and Atkins (1980) that were obtained in a flume in which the water was first accelerated at a constant rate, and then decelerated for the same period of time. Three different cases were examined with acceleration/deceleration times of $T=200, 300$ and 550 seconds. The predictions of all three cases were carried out by means of single-scale stress-dissipation turbulence model with the modifications described earlier. Also the case with $T=200$ sec. was solved by the both, single-scale and double-scale $k-\varepsilon$ models. The solution of the equations was accomplished by use of Patankar-Spalding (1972) parabolic numerical scheme, which was modified as to be applicable to unsteady situations.

Fig.3. shows the mean velocity variation in time for $T=200$ sec. together with the normalised turbulent

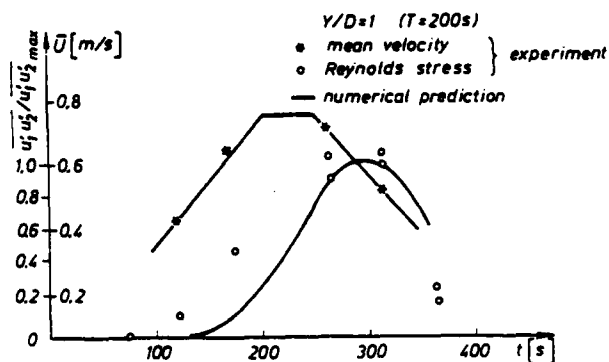


Fig.3 - Temporal variation of velocity and Reynolds shear stress

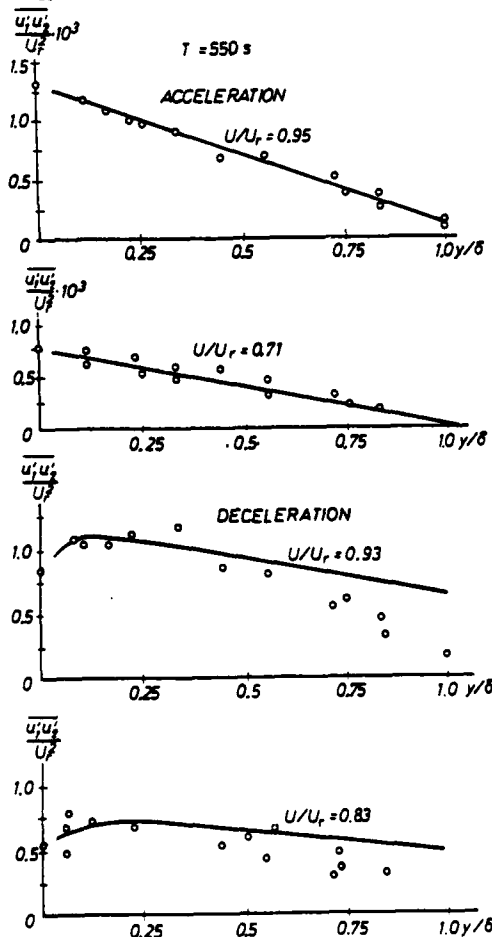


Fig.5 - Turbulent shear stress in simulated tidal flow; o-experiments, —predictions

shear stress close to the free surface (at the reference boundary layer edge, $y/\delta=1$). The predicted $\overline{u_1 u_2}$ curve shows a good qualitative behaviour, with a pronounced time lag behind the mean velocity. It should be pointed out that the absolute values of $\overline{u_1 u_2}$ are very small and a discrepancy between the predicted and experimental data should not be regarded as serious, as could be seen in Fig. 4, where detailed distribution of $\overline{u_1 u_2}$ is given at several points in the cycle.

Fig. 4 shows the predictions obtained by the three mentioned types of turbulence model. All three models yielded the results in acceptable agreements with experiments, though the single-scale stress model seems superior, in particular during the deceleration part of the cycle. Even better agreement was achieved in case with $T=550$ as shown in Fig. 5.

Fig. 6 shows the hysteresis of turbulent shear stress and kinetic energy as well as their ratio at three different flow depths. In all cases shown, the hysteresis is very pronounced what may have a significant practical consequences for example on transport of sediment or dispersion of pollutants in natural water bodies. The hysteresis of $\overline{u_1 u_2}/k$ ratio, on the other hand, is an indication of the departure of turbulence structure from the local equilibrium and is probably the cause of discrepancy between the predictions obtained with $k-\epsilon$ and stress models. Fig. 6 indicates also that the hysteresis, though qualitatively the same, has different intensity at different depths, the larger values occurring in the outer flow region closer to the water surface.

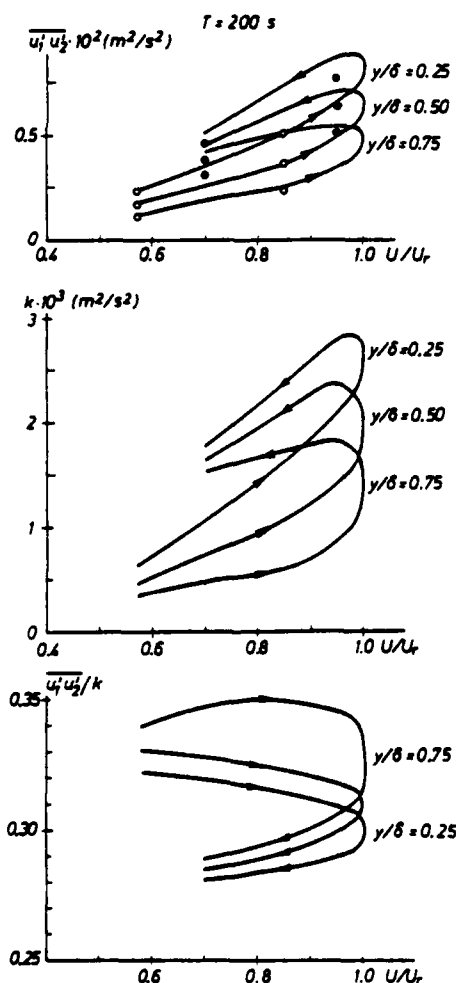


Fig. 6 - Hysteresis of turbulent shear stress and kinetic energy, — predictions, experiments: o acceleration, • deceleration (Anwar and Atkins)

We consider next the two flows markedly different from the previous one. These are the pulsating flow in a channel, investigated by Acharya and Reynolds (1975) with frequencies of 24 and 40 Hz, but small amplitude, and the oscillating boundary layer in zero pressure gradient, explored by Cousteix et al (1977) with large amplitude ($\sim 37\%$), and frequency of 43 Hz. A selection of predicted results, compared with experimental data is given in figures 7 to 12. Fig. 7 presents the prediction of the phase-averaged velocity profiles at several characteristic time instants with in a cycle of Cousteix et al. flow. The obtained results are in excellent agreement with measurements. The predicted phase shift of the velocity across the flow, shown in Fig. 8 may also be regarded as satisfactory. The same could be concluded for the boundary layer shape factor which is shown in Fig. 9, but in a specific way as to emphasize its hysteresis. In the same figure the maximum- and the wall values of the shear stress are presented, exhibiting also a visible hysteresis. The maximum values do not agree well with the experiments (the authors did not quote the wall values), what is surprising, considering an excellent reproduction of the mean velocity profiles.

Similar shapes of hysteresis were exhibited by both shear and normal stresses in the experiment of Acharya and Reynolds. In this case the predictions are in much closer agreement with experiments as shown in Fig. 10 for three different positions in the flow.

Interesting shapes and orientation of hysteresis curves require a careful analysis, but we have not been

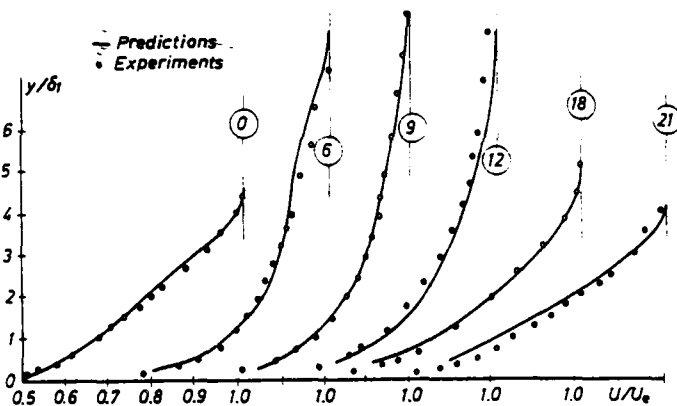


Fig. 7 - Phase-averaged velocity profiles at different time instants; o-experiments (Cousteix et al. (1977), — predictions

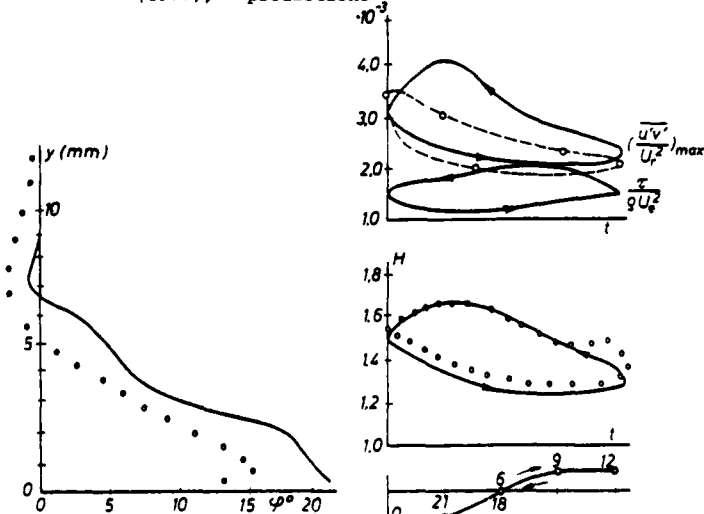


Fig. 8 - Velocity phase predictions o experiments

Fig. 9 - Shape factor and wall and maximum shear stress predictions o experiments

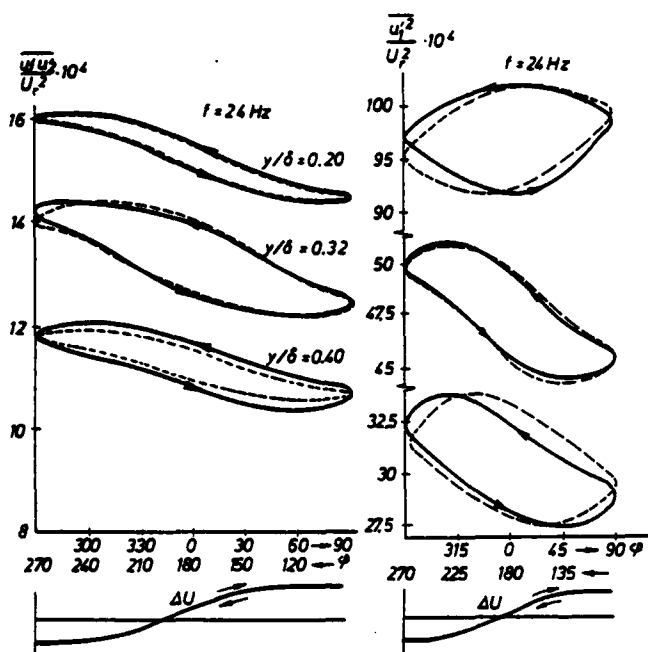


Fig.10 - Hysteresis of turbulent stresses at different flow depths in pulsating boundary layer: — predictions, --- experiments (Acharya and Reynolds).

able as yet to correlate any of the characteristic parameters.

Finally, in Fig.1 the variation across the flow of the amplitudes and phases of the mean velocity and some components of turbulent stresses is presented. The overall agreement with the experiments can be regarded as acceptable though some improvement would be desirable. At present we were not able to explain the excessive discrepancy of ΔU in the region close to the wall.

CONCLUSIONS

Three different types of periodic unsteady flows were analysed and predicted: The flow with a very low frequency and large amplitude, the second one with large frequency but small amplitude, and the third type with large values of both parameters. Attention was concentrated to the behaviour of ensemble-averaged turbulent stresses within a single cycle of the flow oscillation. All three cases showed clearly that the turbulence structure lags behind the mean flow field and that both mean-flow- and turbulence parameters show visible hysteresis. This feature may in some cases have a significant effects upon the global effects and transport processes within the flow.

In an attempt to predict all three considered cases, single-scale $k-\epsilon$ and stress model, as well as two-scale $k-\epsilon$ model were used. The closest agreement with experiments was achieved by means of the stress-dissipation model with some modifications that also helped earlier to improve the predictions of some steady nonequilibrium flows.

It is believed that still further improvements can be achieved with two scale model that is based on separate transport equations for each stress component. This model is still in the stage of testing, but its application to a family of homogeneous flows, as shown in Fig. 1, seems very encouraging.

ACKNOWLEDGEMENT

The authors acknowledge the financial support of Selfgoverning Community of Interest in Science of Bosnia

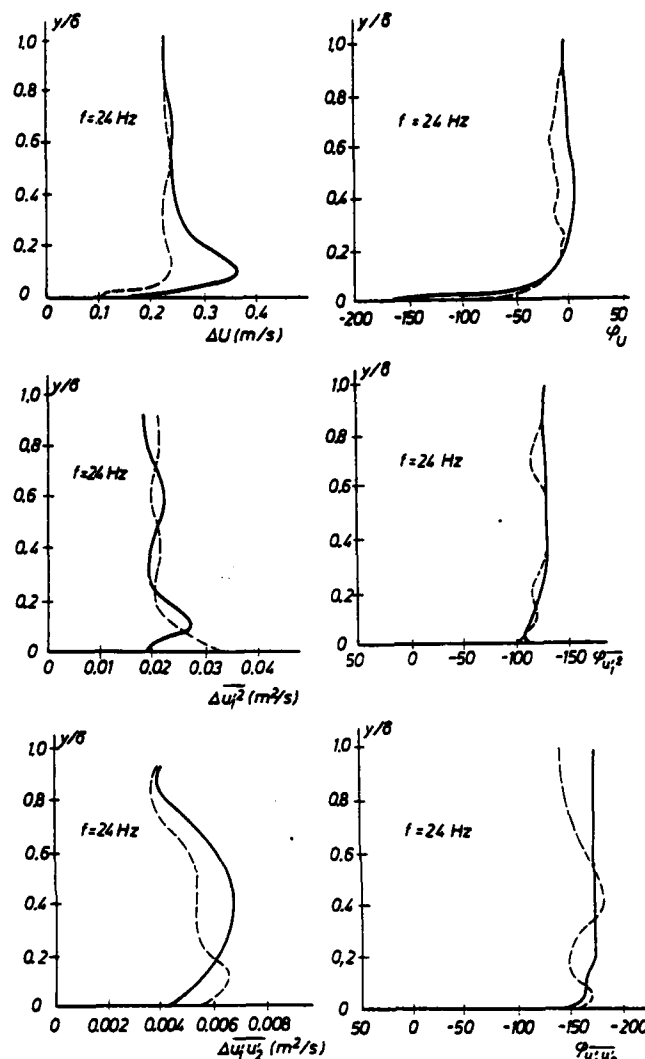


Fig.11 - Amplitudes and phase shifts of mean velocity and turbulent stresses: — predictions, --- experiments (Acharya and Reynolds, 1975)

and Hercegovina. A large part of computation was carried out in the Computer Centre of Energoinvest. Sincere thanks are due to our colleagues R. Selimović and S. Vasić for their valuable help in carrying out the numerical computations.

REFERENCES

- Acharya, M., Reynolds, W.C., 1975, Rept. TF-8, Mech. Eng. Dept., Stanford Univ.
- Anwar, H.O., Atkins, R., 1980, J. Hydr. Div., HY8, p1273
- Carr, L.W., 1981, Unsteady Turb. Shear Flows, IUTAM Symp., Springer
- Chiang, C.C., Launder, B.E., 1980, Numeric. Heat Transfer, 3, p 189.
- Cousteix, J., Houdeville, R., Javelle, J., 1981, IUTAM Symp., Unsteady Turb. Shear Flows, Springer.
- Cousteix, J., Desopper, A., Houdeville, R., 1977, Turb. Shear Flows 1, Springer
- Hanjalić, K., Launder, B.E., Schiestel, R., 1980, Turb. Shear Flows 2, Springer
- Hanjalić, K. et al, 1981 The 1980-81 AFOSR-HTTM Stanford Conf.
- Launder, B.E., Reece, G.J., Rodi, W., 1975, J. Fluid Mech., 68, p 537
- Launder, B.E. et al., 1981, The 1980-81 AFOSR-HTTM Stanford Conf.
- Launder, B.E., Spalding, D.B. 1973 Imp. Coll. Mech. Eng. Dept. Rept. HTS/73/2
- Patankar, S.V., Spalding, D.B., 1970 Heat and mass transfer in bound. layers, Intertext, London
- Shemer, L., Wygnanski, I., 1981, Turb. Shear Flows 3, Davis
- Townsend, A.A., J. Fluid Mech., 81, p 171

PERIODIC TURBULENT SHEAR FLOWS

by

B.R. RAMAPRIAN
Professor of Mechanical Engineering
Iowa Institute of Hydraulic Research
The University of Iowa
Iowa City, Iowa

S.W. TU
Engineer
Bechtel Civil and Mineral Inc.
San Francisco, California

A.N. MENENDEZ
Graduate Research Assistant
Iowa Institute of Hydraulic Research
The University of Iowa
Iowa City, Iowa

ABSTRACT

Experimental results for a fully developed periodic turbulent pipeflow and a time-mean zero pressure gradient periodic turbulent boundary layer are presented. Both of them are characterized by large amplitude and frequency of oscillation. Their similarities and differences are discussed.

INTRODUCTION

There has been considerable interest, in recent years, in the study of unsteady turbulent shear flows. This is because of their many practical applications such as helicopter rotor blade flows, turbomachinery blade flows, aircraft flutter, gusts on structures etc. Some fundamental experimental studies of the structure of turbulent shear flows which are subjected to an externally imposed deterministic unsteadiness have been reported in the past few years. These include studies of fully developed periodic turbulent flow [e.g., Mizushima, Maruyama and Shiozaki (1973), Mizushima, Maruyama and Hirasawa (1975), Kirmse (1979), Ramaprian and Tu (1980), etc.] and studies of periodic turbulent boundary layers [e.g., Cousteix, Houdeville and Javelle (1981), Parikh, Reynolds and Jayaraman (1982), etc.]. A comprehensive review of the state of the art in this field was made by Carr (1981) and hence will not be repeated here. While these studies have provided a significant amount of information on the effect of imposed periodicity on the behavior of turbulent shear flows, there are a large number of areas in which information is either not available or is controversial. This is particularly true for flows in which the imposed periodicity is at a frequency large enough to interact with a dominant frequency of the turbulent motions--such as the "bursting" frequency, and/or has a large amplitude. There is a general feeling that imposed periodicity has no effect on the time-mean properties of the flow. However, previous work by the present authors on pipeflow (referred earlier) showed that the time-mean velocity distribution in a pipe shows a small but measurable effect of imposed periodicity. There is no general consensus on the quantitative response of wall shear stress and near-wall flow to imposed periodicity. In fact, no data on shear stress at the wall or Reynolds shear stress distribution in the unsteady shear flows are available at high frequencies and large amplitudes of imposed oscillation.

An extensive program of study of periodic turbulent shear flows has been in progress at Iowa during the last several years. Under this program a comprehensive study of fully developed periodic turbulent pipeflow has been completed. This was followed by the study of a turbulent boundary layer in a periodically modulated freestream. This latter study

is being performed in an unsteady flow water tunnel recently built at Iowa and the study has already yielded a large volume of very useful data. Both the pipeflow and boundary layer studies have been/will be described in detail elsewhere. The present paper contains some of the major results from the two studies. The experimental results are used to study the similarity and differences in the response of pipeflow and boundary layer flow to imposed external periodicity. The main features that distinguish both the present studies from most other similar studies are the combination of high frequency and large amplitude oscillation, wall shear stress measurements in the pipeflow experiments and Reynolds shear stress measurements in the boundary layer experiments. The experiments are briefly described below.

PIPEFLOW EXPERIMENTS

Experimental Conditions

These experiments were performed in a long circular pipe of radius (R) 2.5 cm and length 10 meters through which water flow was maintained at a cross-sectional, time-average velocity (\bar{U}) of about 1 m/s, corresponding to a mean Reynolds number of about 50,000. This Reynolds number was modulated by varying the discharge through the pipe sinusoidally with time using a rotating sleeve valve at the pipe exit. The details of the apparatus and experiment are described in Ramaprian and Tu (1982). Detailed measurements including instantaneous longitudinal velocities, U (using frequency-shifted LDA) and instantaneous wall shear stress, τ_w (using a flush mounted hot film gage) were obtained.

The instantaneous velocities U were decomposed into time-mean component \bar{U} , periodic component U_p and random component u , by obtaining ensemble averages over 1000 cycles of oscillation. The first series of experiments included measurements of steady flow at five different Reynolds numbers ranging from 20,000 to 80,000. These experiments were used not only to test the experimental procedures but also as the basis for obtaining information on the quasi-steady flow (i.e., flow at infinitely low oscillation frequency). The quasi-steady behavior was then compared with the results of the second series of experiments, in which the flow was oscillated sinusoidally around a mean Reynolds number of 50,000. Two oscillation frequencies (f), namely 0.5 Hz and 3.6 Hz were studied. The higher frequency is of the order of the estimated mean bursting frequency in the flow. The lower frequency can be considered to be an intermediate frequency at which the flow still deviated significantly from quasi-steady behavior. In both experiments the amplitude of modulation γ of the velocity U_p was large enough (15% at 3.6 Hz and 64% at 0.5 Hz) to yield new and significant results. From the measurements made,

detailed information on various aspects such as velocity, turbulence intensity and Reynolds shear stress was obtained, the last quantity being determined from the momentum equation.

Results

As already mentioned, only the major results will be discussed in this paper.

Time-Mean Velocity Profile. The time mean velocity distribution across the pipe is shown for the two oscillation frequencies (Fig. 1). In each case the results are compared with those for a quasi-steady (zero-frequency) flow of the same amplitude y_m . It is seen that at the higher frequency, there is a small but perceptible decrease in the velocity near the wall ($n = y/R = 0$) which is more clearly seen as a corresponding increase in velocity near the centerline as required by global continuity. The effect on the mean velocity at the lower frequency is, however, much smaller. Unfortunately, the geometry of the tube did not allow measurements to be made at closer distances from the wall than shown in the figure. It was in fact observed that the time-mean velocity distribution does not follow the universal logarithmic law, especially at the higher frequency.

Amplitude and Phase Results. The phase averaged local velocity at any point y away from the wall and at a phase position θ in the oscillation cycle can be represented, to a good approximation, by

$$\langle U \rangle (y, \theta) = \bar{U} [1 + \gamma_U \cos (\theta + \phi_U)]$$

Figure 2 shows the amplitude ratio $[(\gamma_U \bar{U})/(\gamma_m U_m)]$ and the phase angle ϕ_U of the phase-averaged velocity, for the two oscillation frequencies. The results, in each case, are compared with the exact solution [from Uchida (1956)] for fully developed periodic laminar flow in the same pipe at the same frequency. It is seen that the turbulent and laminar flow results are very different from each other. The turbulent flow exhibits a larger overshoot in amplitude and a very much larger "Stokes layer" within which unsteady effects are present. More striking is the result that the phase angle ϕ_U does not seem to extrapolate to a value of more than about +10 degrees at the wall in the turbulent flow even at the higher frequency, while the laminar solution indicates the asymptotic value of +45 degrees.

The phase lead of the wall shear stress was also found to be less than 10 degrees even at the higher frequency as shown by the filled symbols at $n = 0$ in Figure 2, thereby corroborating the LDA results for the velocity.

Ensemble Averaged Turbulence Intensity. The ensemble averaged rms turbulence intensity u' is defined as $u'(y, \theta) = [\langle u'^2 \rangle]^{1/2}$. Figures 3 and 4 show distributions of u' across the pipe at a few typical phase positions in the oscillation cycle, for the two oscillation frequencies. It is seen that at the intermediate frequency, the ensemble averaged turbulent intensity profiles are affected across the entire pipe. Crossovers and distortions can be observed in these distributions. The Reynolds shear stress distributions (not shown here) were also found to exhibit qualitatively the same trend (except in the outer region during a part of the cycle) indicating an equilibrium state between these two turbulent properties. At high frequency (figure 4), the ensemble averaged turbulent intensity remains frozen in the outer region. The ensemble averaged Reynolds shear stress, however, was found, in this case, to vary slightly with U_m even in the outer region.

Structural Equilibrium It was observed that at both the intermediate and high frequency of oscillation studied, the mean flow, the turbulent kinetic energy and the Reynolds shear stress were mutually out of phase with one another. Thus, eddy viscosity type models either of the "gradient" or "bulk" type relating the

turbulent transport either to the local mean flow or turbulent structure at an instant (in a quasi-steady manner) cannot accurately describe such flows. This is seen in figure 2, where the predictions of the unsteady flow obtained by using a well-known eddy viscosity model are shown. Details of this calculation method are discussed in Ramaprian and Tu (1982). The departure of the flow from structural equilibrium is illustrated by Figure 5 which shows the behavior of a characteristic "structure parameter" $a_p = [-\langle uv \rangle / u'^2]$ during the oscillation cycle. This parameter should remain constant at a value of about 0.26 in an equilibrium flow. The variation of a_p in the periodic flow, therefore, demonstrates the breakdown of the structural equilibrium, partially during the cycle at intermediate frequency and completely at the high frequency.

BOUNDARY LAYER EXPERIMENTS

The pipe flow experiments, while being very extensive, had two limitations. These are (i) the uncertainty of the measurements very near the wall (caused by the wall curvature) and (ii) the lack of direct measurements of the ensemble-averaged Reynolds shear stress $\langle uv \rangle$. These limitations have been removed in the complimentary experiments on a periodic boundary layer on a flat plate currently under progress. A two-component LDA system is being used in these experiments so that u' , v' and $\langle uv \rangle$ can be measured directly. A large and unique unsteady flow water tunnel has been built for this study. The tunnel is designed such that the freestream velocity at the test section can be varied with time in a prescribed manner. Fig. 6 shows a layout of the tunnel. The tunnel works under a constant head of about 8 meters. The test section is 50 cm x 22.5 cm in cross section and 2.4 m in length. A smooth brass plate 50 cm wide x 2.4 m long forming the bottom wall of the test section is used as the test surface for the boundary layer studies. The tunnel has presently been set up for a freestream velocity variation given by

$$U_\infty = \bar{U}_\infty [1 + \gamma_U \cos (2\pi ft)]$$

with $\bar{U}_\infty = 0.90$ m/s, $\gamma_U = 0.4$ and $f = 2$ Hz. (The bursting frequency in the boundary layer is estimated to be about 4 Hz). The amplitude and frequency of oscillation can be varied. It may be noted that, because of the wide separation between the oscillation frequency and the acoustic frequency in this hydraulic system, the amplitude and phase of the freestream velocity variation is constant along the test section. The description of the tunnel and a complete documentation of the flow quality in the tunnel will be available from a forthcoming report. Instantaneous velocities have been measured at 5 longitudinal locations ranging from $(2\pi fx/\bar{U}_\infty) = 8 - 27$, with x measured from the contraction exit. The data have been processed to yield mean, periodic and turbulent properties of the flow including Reynolds shear stress and some triple correlations. All the raw as well as processed data are on digital tape. Experiments at a lower oscillation frequency of 0.5 Hz will soon begin.

Only, the data relevant for comparison with the "high-frequency" pipeflow results will be presented in this paper. Further, only data from the last measuring station, corresponding to $(2\pi fx/\bar{U}_\infty)$ will be used in these comparisons.

Results

Time-Mean Velocity Profile. Figure 7 shows the time-mean velocity distributions in the periodic boundary layer ($f = 2$ Hz), quasi-steady boundary layer ($f = 0$) at the same amplitude and steady boundary layer for a freestream velocity of \bar{U}_∞ . The quasi-steady and steady flow show negligible difference between each other suggesting that nonlinear (Reynolds number) effects are not important in this case. The unsteady flow results, however, indicate a definite, though small reduction in the time mean velocity near the wall, compared to the quasi-steady flow. This result, thus confirms the

pipeflow results. The apparent increase in the time-mean velocity in the outer part of pipeflow is simply a consequence of normalizing the velocities by the time-mean cross-sectional average velocity \bar{U}_m , rather than by the time-mean centerline velocity U_{max} .

Phase and Amplitude Results. The phase ϕ and amplitude (γ) distributions of the local ensemble averaged velocity $\langle U \rangle$ are shown in figure 8. The distributions are very similar, even quantitatively, to those for pipeflow. The maximum phase shift measured near the wall is still of the order of 10 degrees and the amplitude overshoot near the wall is less than 10%. The boundary layer thickness δ at this station was about 4 cm, corresponding to y/d (in figure 8) = 0.4. The nondimensional "Stokes layer" thickness (about 0.25 δ) in the boundary layer can be seen to be comparable to that in the pipeflow. The flow beyond the Stokes layer behaves slug-like in both cases.

Ensemble Averaged Turbulent Stresses u' and $\langle uv \rangle$. Figures 9 and 10 show the distributions of $\langle u'^2 \rangle$ (y, θ) and $\langle uv \rangle$ (y, θ) for a few typical phase positions in the oscillation cycle. The distributions $\langle u'^2 \rangle$ are in complete agreement with the pipeflow results at the higher oscillation frequency. The intensity remains frozen during the oscillation cycle in the outer 75 per cent of the boundary layer. A similar freeze in the outer layer is observed in the case of $\langle uv \rangle$ also. This last result is in some disagreement with the pipeflow results at 3.6 Hz which indicated a slight modulation in $\langle uv \rangle$ even in the outer region.

Structure parameter. Similar differences between the pipe and boundary layer results can be observed in the behavior of the structure parameter α , shown in figure 11. It is seen that very near the wall the two results are very similar. The turbulent structure shows departure from equilibrium. However, beyond about 0.2 δ , the turbulent structure in the boundary layer seems to be in a state of frozen equilibrium, in contrast with the pipeflow in which there is a complete breakdown of structural equilibrium in the outer flow. This difference in behavior might be ascribed to the difference between the structure of the outer flow in the boundary layer and that in fully developed pipeflow. The outer flow in the pipe is still controlled by the wall via global momentum and continuity constraints whereas the outer flow in the boundary layer is not. The boundary layer data are now being analyzed in greater detail to obtain a better understanding of the response of the different regions of the flow to imposed unsteadiness.

CONCLUSIONS

(1) The experimental data on both pipeflows and boundary layers indicate that externally imposed periodicity produces a small but detectable effect on the time-mean velocity at high frequency and large amplitude of oscillation.

(2) Stokes layer thickness, as well as phase and amplitude of the velocity variation are very similar in both the flows, with the phase angle near the wall being of the order of +10 degrees. Thus, the response of periodic turbulent shear flows is very different from that of periodic laminar shear flows.

(3) Turbulence structure very near the wall is disturbed from equilibrium in both the flows at high frequencies. The outer layer of the boundary layer flow is in a state of frozen equilibrium while that in the pipeflow appears to be still disturbed from equilibrium either partially (at moderate frequencies) or completely (at high frequencies) during the oscillation cycle.

ACKNOWLEDGEMENT

The work reported in this paper was supported by the U.S. Army Research Office, through their Grant/Contract No. DAAG-29-79-G-0017 and DAAG29-83-K-0004 with Dr. R.E. Singleton as Scientific Program Officer. The authors gratefully acknowledge this support.

REFERENCES

- Carr, L.W., "A Review of Unsteady Turbulent Boundary-Layer Experiments", IUTAM Symposium on Unsteady Turbulent Shear Flows, Toulouse, France, 1981.
- Cousteix, J., Houdeville, R., Javelle, J., "Response of a Turbulent Boundary Layer to a Pulsation of the External Flow with and without Adverse Pressure Gradient", IUTAM Symposium on Unsteady Turbulent Shear Flows, Toulouse, France, 1981.
- Kirmse, R.E., "Investigations of Pulsating Turbulent Pipe Flow", Transaction of ASME, 79-WA/FE-1.
- Mizushima, T., Maruyama, T., Shiozaki, Y., "Pulsating Turbulent Flow in a Tube", J. of Chemical Engineering of Japan, v.6, No. 6, 1973, pp. 487-494.
- Mizushima, T., Maruyama, T., Hirasawa, H., "Structure of the Turbulence in Pulsating Pipe Flows", J. of Chemical Engineering of Japan, v. 8, No. 3, 1975, pp. 210-216.
- Parikh, P.G., Reynolds W.C., Jayaramon, R., "Behavior of an Unsteady Turbulent Boundary Layer", AIAA Journal, v. 20, No. 6, 1982, pp. 769-775.
- Kamaprian, B.R., Tu, S.W., "An Experimental Study of Oscillatory Pipe Flow at Transitional Reynolds Numbers", J.F.M., v. 100, 1980, pp. 513-544.
- Uchida, S., "The Pulsating Viscous Flow Superposed on the Steady Motion of Incompressible Fluid in a Circular Pipe", Z.A.M.P., v.7, 1956, pp. 403-421.

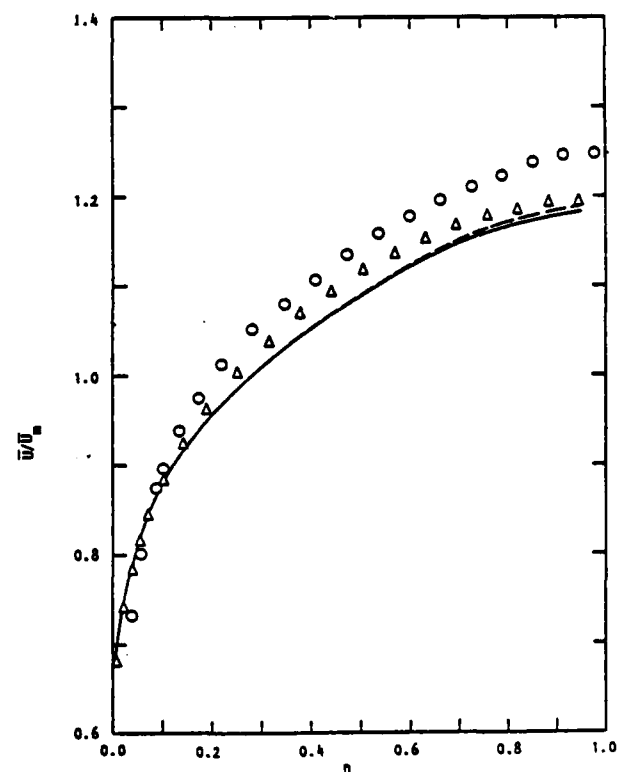


Figure 1. Time-mean velocity profiles in unsteady and quasi-steady pipeflow at $Re = 50,000$. O , $f = 3.6$ Hz, $\gamma_{um} = 15\%$; Δ , $f = 0.5$ Hz, $\gamma_{um} = 64\%$; ----, quasi-steady flow, $\gamma_{um} = 15\%$; —, quasi-steady flow, $\gamma_{um} = 64\%$. The velocity profile in steady flow at the same time-mean Reynolds number is indistinguishable from the dashed line.

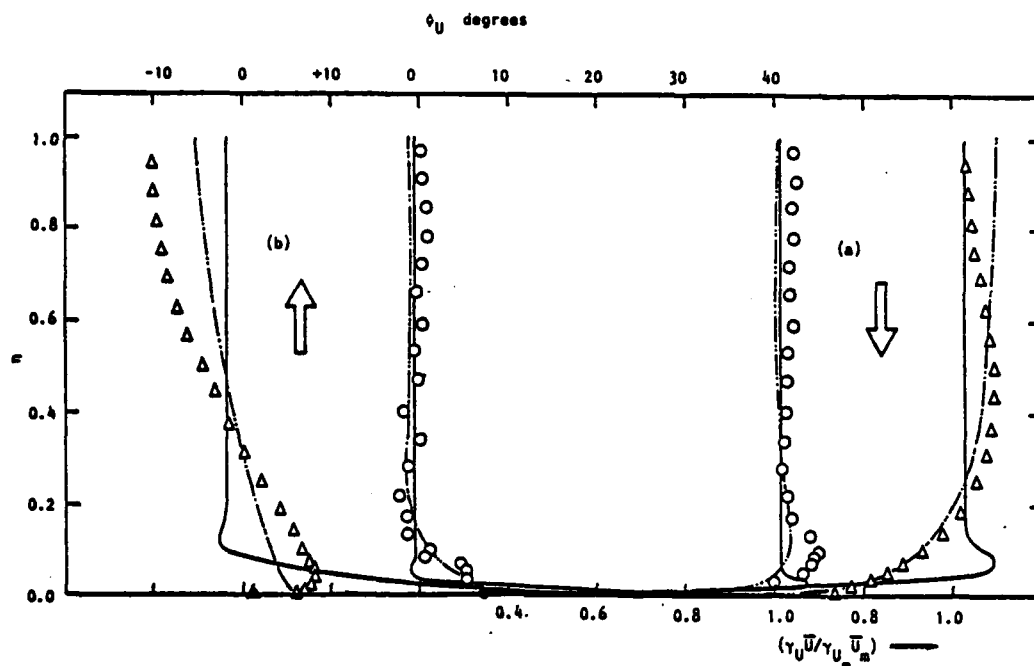


Figure 2. Amplitude and phase of the ensemble averaged velocity in pipeflow (a) amplitude (b) phase. 0, 3.6 Hz; Δ , 0.5 Hz; Filled symbols represent wall shear stress data: \bullet , 3.6 Hz; Δ , 0.5 Hz; —, laminar theory (Uchida 1956); - - -, numerical calculations using a typical eddy viscosity model (from Ramaprian and Tu, 1982).

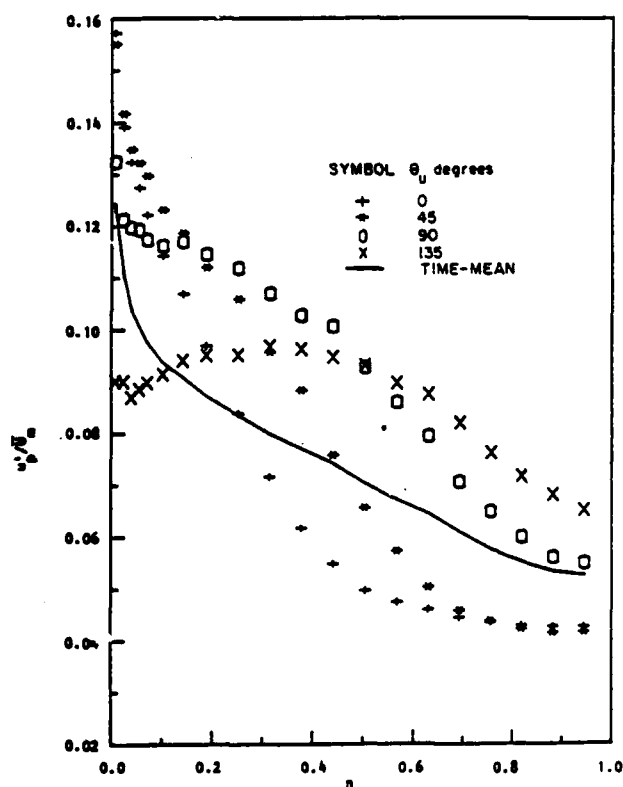


Figure 3. Ensemble averaged longitudinal turbulent intensity in pipeflow at $f = 0.5$ Hz. Decelerating period. —, time-mean distribution, u' .

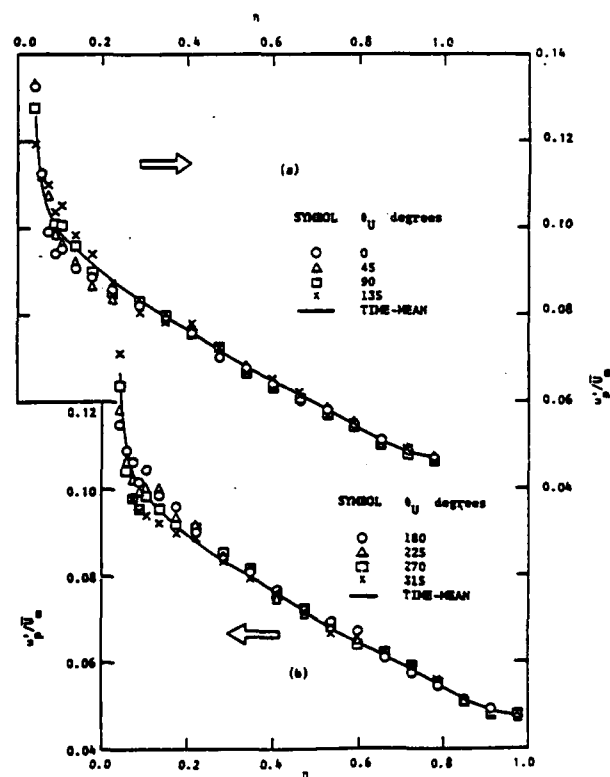


Figure 4. Ensemble averaged longitudinal turbulent intensity in pipeflow at $f = 3.6$ Hz. (a) decelerating period (b) accelerating period. —, time-mean distribution, u' .

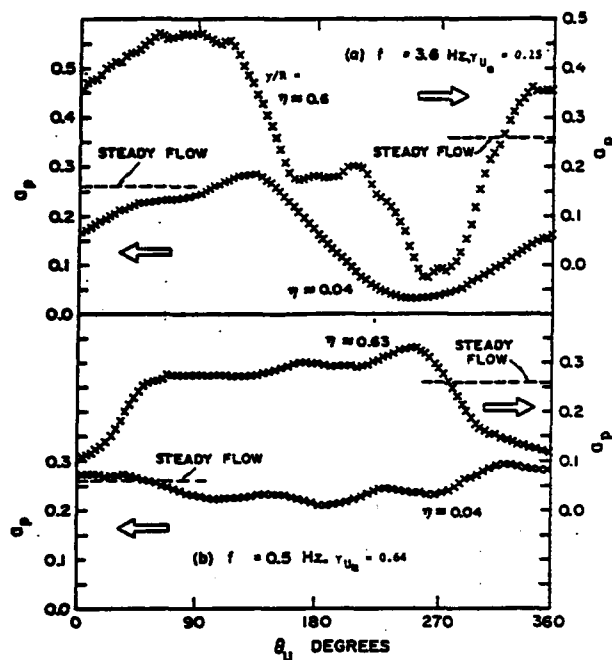


Figure 5. Phasewise distribution of the structure parameter a_p in pipeflow.

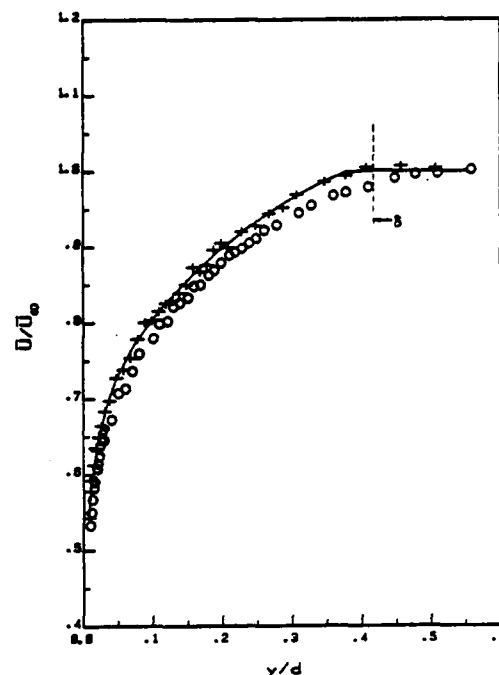


Figure 7. Time-mean velocity profiles in unsteady and quasi-steady boundary layer flow, U_0 , unsteady flow; —, quasi-steady flow; +, steady flow at the time-mean freestream velocity.

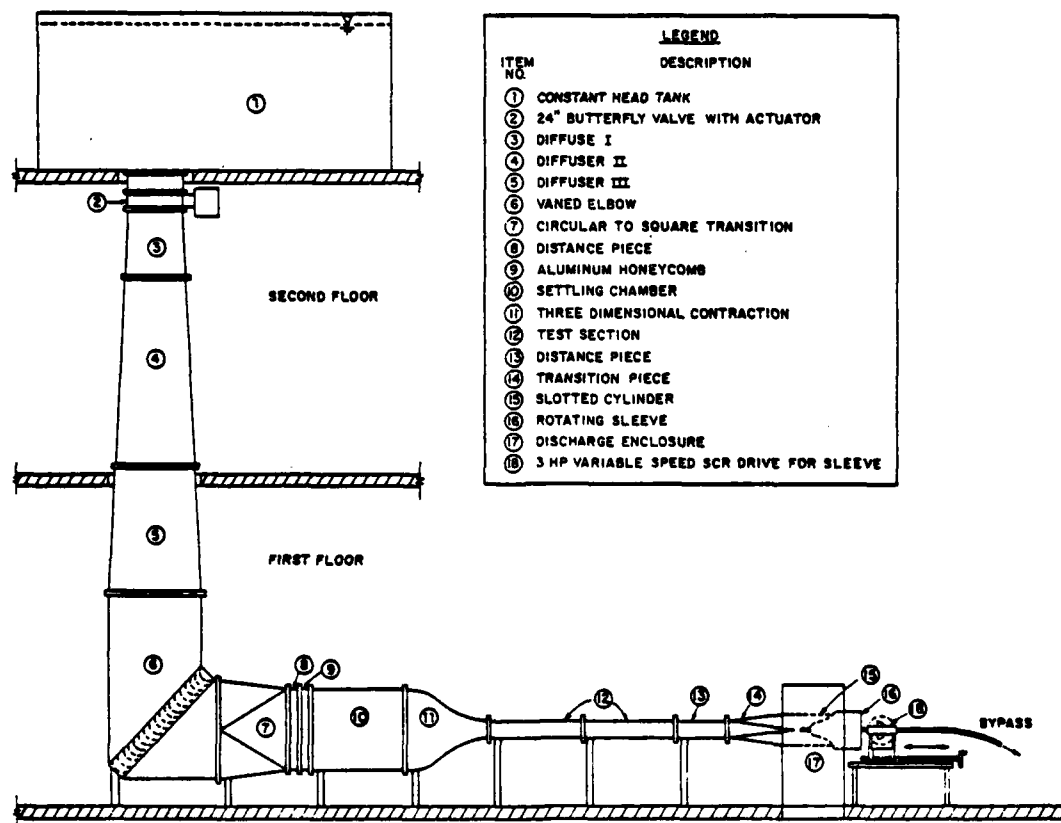


Figure 6. Lay-out of the periodic flow water tunnel.

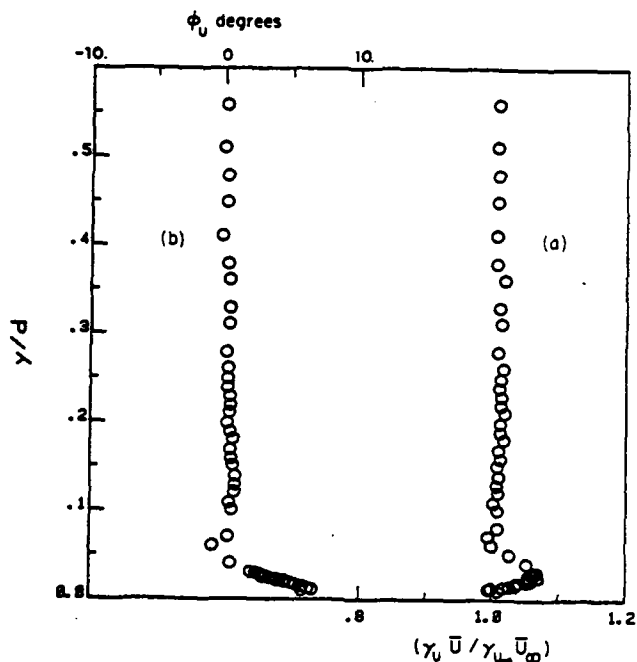


Figure 8. Amplitude and phase of the ensemble averaged velocity in boundary layer flow. (a) amplitude (b) phase.

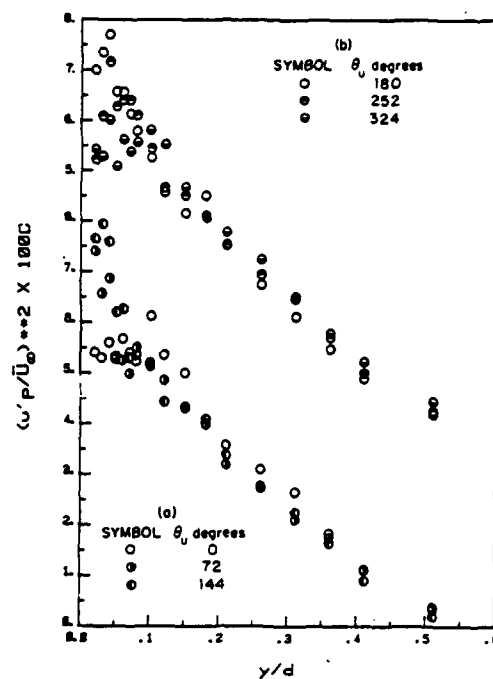


Figure 9. Ensemble averaged longitudinal turbulent intensity in boundary layer flow. (a) decelerating period (b) accelerating period.

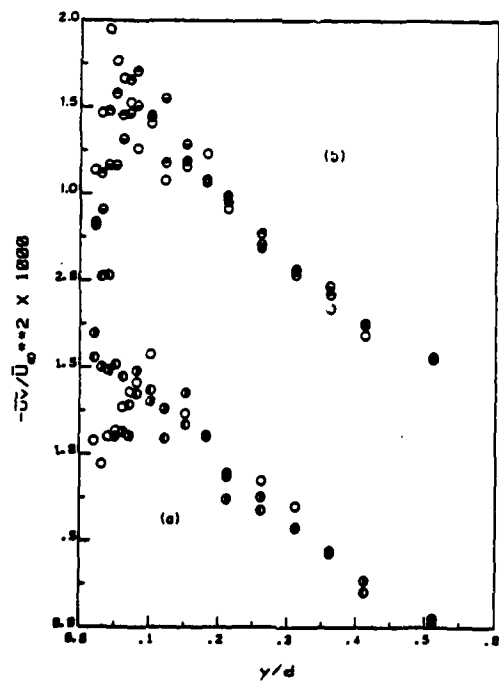


Figure 10. Ensemble averaged Reynolds shear stress in boundary layer flow. (a) decelerating period (b) accelerating period. Symbols as in Fig. 9.

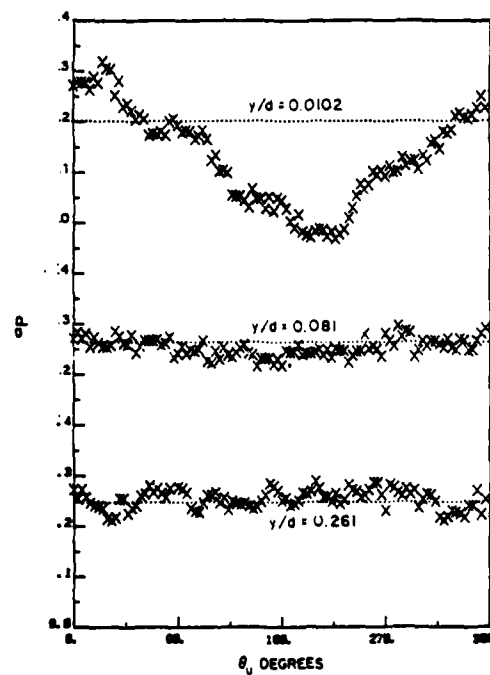


Figure 11. Phasewise distribution of the structure parameter a_p in boundary layer flow., steady flow value.

SESSION 9 - FUNDAMENTALS I

J. Mathieu - Chairman

Parameterization of Turbulent
Transport in Swirling Flows*
I - Theoretical Considerations

David Ettestad
John L. Lumley
Cornell University
Ithaca, New York 14853
U.S.A.

ABSTRACT

A second order closure scheme is proposed for turbulent transport in swirling flows. Specifically, a scheme is constructed according to the same principles that led to the successful description of buoyancy-driven turbulent flows (Zeman, 1975; Zeman & Lumley, 1976a, b, c; Lumley et al 1978). In the narrow gap approximation the scheme takes on a particularly simple form, which can be rationalized by a simple physical model.

INTRODUCTION

By swirling flows, we mean flows in which the mean streamlines are locally helical (which have a non-negligible component of azimuthal velocity). We consider here only flows which are axisymmetric, and we exclude from consideration here flows which are recirculating, that is, we consider only flows in which the mean axial velocity is everywhere positive.

Flows of this type occur frequently in nature and technology. The flow in a tornado is of this type, as is that in an aircraft trailing vortex. Flow in a gas turbine combustor is generally recirculating and not axisymmetric; hence, our considerations will not be directly applicable to this flow. We hope, however, that a successful parameterization of swirl under these simplified conditions will lead to an understanding of the more complex flow.

Swirling flows present a challenge to the modeler due to the influence on radial turbulent transport of the radial distribution of azimuthal velocity. This is weakly analogous to the effect of density stratification in a flow with gravity. That is, a small-disturbance stability analysis of a layer of fluid heated from below (Pellew & Southwell, 1940) and of isothermal circular Couette flow (Taylor, 1923) leads to the same equation, where the radial distribution of angular momentum in the Couette flow plays the role of the vertical distribution of density in the heated flow.

The analogy is not strict, however, since the mechanisms differ. In the heated flow, a parcel of fluid displaced upward (in the limit of no molecular transport) carries with it its (potential) temperature (Lumley & Panofsky, 1964), and hence experiences a density anomaly at its new height, if the local (potential) temperature is different. In the case of swirl, a parcel displaced radially approximately conserves its angular momentum; whether it will return or continue depends on the radial pressure gradient it needs for equilibrium compared to that at its new location. The essential difference is the necessary presence of an azimuthal

fluctuation in the case of swirl, so that a Reynolds stress is induced in the azimuthal plane. In the heated flow case, no horizontal fluctuation is necessarily associated with a vertical fluctuation, in the absence of wind shear. Hence, in the swirl case we will have strong coupling between the radial and azimuthal components of all fluxes.

We do anticipate that a radial distribution of angular momentum increasing outward will have a stabilizing influence, and will suppress radial transport and reduce the rate of spread of a scalar marker, while a radial distribution of angular momentum decreasing outward will have a destabilizing influence, and will augment radial transport, and increase the rate of spread of a scalar marker. This is borne out by experiment (Eskinazi & Yeh, 1956; Wyngaard, 1968). We can also construct a simple example to illustrate this. If we consider motion confined to planes perpendicular to the axis, and neglect viscosity and non-linear and unsteady terms, and assume that fluid displaced radially conserves angular momentum, we can write for the radial displacement ξ of a material point

$$\ddot{\xi} = -2(V/r)(V' + V/r)\xi \quad (1.1)$$

where $V(r)$ is the azimuthal velocity. Thus, if $V' + V/r \geq 0$ (radial gradient of angular momentum positive) the displacement is stable. The induced azimuthal velocity fluctuation is

$$v = -(V' + V/r)\xi \quad (1.2)$$

so that, if $V' + V/r \geq 0$, a point displaced outward will be moving slower than its surroundings. Following now the same procedure as was used in Lumley et al (1978), we imagine a velocity field u_0, v_0 which evolves from $t=0$ without the influence of rotation, so that we may write to first order

$$u = u_0 - 2(V/r)(V' + V/r) \int_0^t \int_0^t u_0(\tau') \quad (1.3)$$

Hence, to first order we have

$$\overline{u^2} = \overline{u_0^2} [1 - 4(V/r)(V' + V/r) \overline{t^2}] \quad (1.4)$$

(squaring and averaging (1.3)), where T is a Lagrangian integral time scale for the field undisturbed by rotation. We see that, if $V' + V/r > 0$, $\overline{u^2}$ is indeed reduced below the value for a field without rotation. We may also obtain another form which will be useful for later comparisons. Since, to first order

$$v = v_0 - (V' + V/r) \int_0^t u_0 \, d\tau \quad (1.5)$$

we may write

*Supported in part by the U.S. Office of Naval Research under the following programs: Physical Oceanography (Code 422PO), Fluid Dynamics (Code 438), Power (Code 473); in part by the U.S. National Science Foundation under grant no. ATM 79-22006 and CME 79-19817; and in part by the U. S. Air Force Office of Scientific Research.

$$\overline{uv} = -(v' + v/r) \alpha \overline{u^2} \quad (1.6)$$

if we take the u^0, v^0 field as having no Reynolds stress. Hence, we may write (1.4) as

$$\overline{u^2} = \overline{u^2} [1 + 4B(v/r) \overline{uv} / \alpha \overline{u^2}] \quad (1.7)$$

This form should be compared with a similar form from Lumley et al (1978) for the vertical velocity:

$$\overline{w^2} = \overline{w^2} [1 + 8g \theta_w T / \theta_0 w^2] \quad (1.8)$$

where g is the acceleration of gravity, and θ and θ_0 the fluctuating and mean potential temperature respectively. In the case of an atmospheric inversion θ_w becomes negative, effectively cutting off vertical transport; here we may expect uv to become negative in a region of positive $v' + v/r$, also cutting off radial transport.

While it is tempting to try to parameterize swirl directly in a $k-\epsilon$ model (Jones & Launder, 1973) using forms such as (1.4) and (1.6), we will give our attention here to the development of a more complete Reynolds stress model similar to that developed by Zeman (1975), Zeman & Lumley (1976a, b, c) and Lumley et al (1978). From the experience gained from this model, we may hope to be in a better position to develop a simple parameterization.

In modeling of swirling flows, there are more problems than the parameterization of turbulent transport. In particular, the equation for the dissipation, or equivalently for a length scale, has not been satisfactorily extended to axisymmetric non-swirling flows; a beginning has been made on its extension to swirling flows (Launder et al, 1977), but it is expected that bringing this effort to a satisfactory conclusion will be non-trivial. However, we will not treat this difficult problem here. Recent experimental evidence (Ramaprian & Shivaprasad, 1981) indicates that it is the differences in the turbulent transport that are largely responsible for the observed differences in structure in turbulent boundary layers; hence, by attacking the transport first we feel we are according appropriate priorities.

MATHEMATICAL PRELIMINARIES

We will work in cylindrical coordinates. If x^1, x^2, x^3 is a Cartesian system, we define the cylindrical system $\overline{x}^1, \overline{x}^2, \overline{x}^3$ by

$$\begin{aligned} x^1 &= \overline{x}^1 \cos \overline{x}^2 \\ x^2 &= \overline{x}^1 \sin \overline{x}^2 \\ x^3 &= \overline{x}^3 \end{aligned} \quad (2.1)$$

We use the notation of Lumley (1970), appendix 2. The transformation matrices are given by

$$\begin{aligned} \overline{x}_j^i &= \begin{vmatrix} \cos \overline{x}^2 & -\overline{x}^1 \sin \overline{x}^2 & 0 \\ \sin \overline{x}^2 & \overline{x}^1 \cos \overline{x}^2 & 0 \\ 0 & 0 & 1 \end{vmatrix} \quad \overline{x}_j^i = \begin{vmatrix} \cos \overline{x}^2 & \sin \overline{x}^2 & 0 \\ -\sin \overline{x}^2 / \overline{x}^1 & \cos \overline{x}^2 / \overline{x}^1 & 0 \\ 0 & 0 & 1 \end{vmatrix} \end{aligned} \quad (2.2)$$

The only non-zero Christoffel symbols are $\Gamma_{12}^2 = \Gamma_{21}^2 = 1/\overline{x}^1$, $\Gamma_{22}^1 = -\overline{x}^1$. The metric tensor is diagonal, with $g_{11} = g_{33} = 1$, $g_{22} = (\overline{x}^1)^2$. Rather than attempting to obtain equations for the fluctuating velocities, and to form from them equations for the Reynolds stress and higher moments, we will write the equations for the moments directly in general tensor form and specialize them for our particular case.

Note that we will use the co- and contravariant velocities obtained from the Cartesian velocities by

formal transformation, so that

$$\overline{u}_2 = \overline{x}_j^2 u_j = \overline{x}^1 v_\theta \quad (2.3)$$

$$\overline{u}^2 = \overline{x}_j^2 u_j = v_\theta \sqrt{\overline{x}^1} = \overline{g}^{22} \overline{u}_2$$

where v_θ is the physical azimuthal velocity. Hence, neither u^1 nor u_2 is physically a velocity; u^2 is an angular velocity, and u_2 an angular momentum. These are mathematically the most convenient coordinates; however, for comparison with experiment it is necessary to change to physical velocities. Only the azimuthal component need be changed (since $g_{11} = g_{33} = 1$); for the physical component we have

$$\overline{u}^2 (\overline{g}^{22})^{1/2} = \overline{u}^2 (\overline{g}^{22})^{1/2} = v_\theta \quad (2.4)$$

To simplify the notation, where no confusion can arise, we will omit the bars.

THE "RAPID" PRESSURE TERMS

Working in Cartesian coordinates for the moment, we may split the pressure into two components in a well-known way (Lumley, 1978):

$$-p_{,ii}^{(1)}/\rho = 2U_{i,j} u_{j,i}, \quad -p_{,ii}^{(2)}/\rho = u_{i,j} u_{j,i} \quad (3.1)$$

where $p^{(1)}$ is referred to as the linear or "rapid" part of the pressure, while $p^{(2)}$ is the return-to-isotropy part.

In Lumley (1978) it was shown that, in the equation for the third moment, the convection and production terms, and the "rapid" pressure correlation terms, were of smaller order than the other terms, and could be neglected. Here, however, we will have to retain these terms when they are multiplied by the swirl component, since we are presuming that to be the dominant effect. Thus, we will need a form for the "rapid" pressure correlations.

We can write (still in Cartesian coordinates)

$$-p_{,l}^{(1)} u_r u_s / \rho = 2U_{i,j} \int \psi_{jrs} \kappa_i \kappa_l / \kappa^2 d\kappa \quad (3.2)$$

where

$$\int \psi_{jrs} d\kappa = \overline{u_j u_r u_s} \quad (3.2)$$

If we write

$$I_{iljrs} = \int \psi_{jrs} \kappa_i \kappa_l / \kappa^2 d\kappa \quad (3.4)$$

then I_{iljrs} must satisfy the following conditions:

$$\begin{aligned} I_{iljrs} &= I_{lijrs}; \quad I_{iljrs} = \overline{u_j u_r u_s}; \\ I_{illrs} &= 0; \quad I_{iljrs} = I_{iljrs} \end{aligned} \quad (3.5)$$

If we take a general linear form for I_{iljrs} in terms of $\overline{u_j u_r u_s}$, we find that the conditions are sufficient to determine all the coefficients, giving

$$I_{iljrs} = (2/5) \delta_{il} \overline{u_j u_r u_s} - (1/10) (\delta_{ij} \overline{u_l u_r u_s} + \delta_{lj} \overline{u_i u_r u_s}) \quad (3.6)$$

This is the same form which produces the pressure trans-

port expression

$$-\overline{p^{(2)}u_k}/\rho = I_{ijkij} = \overline{q^2u_k}/5 \quad (3.7)$$

(Lumley, 1978) which has been so successful (Janicka & Lumley, 1981a, b; Taulbee & Lumley, 1981).

The full $p^{(1)}$ correlation in the equation for $\overline{u_i u_j u_k}$ consists of expression (3.2) plus the two permutations. On the left side of the equations we have the terms (still in Cartesian coordinates)

$$U_{i,l} \overline{u_l u_j u_k} + U_{j,l} \overline{u_l u_i u_k} + U_{k,l} \overline{u_l u_i u_j} \quad (3.8)$$

When these are combined with the rapid pressure terms obtained from (3.2) by use of (3.6), we find that they combine to give

$$(2/5)S_{il} \overline{u_l u_j u_k} + (2/5)S_{jl} \overline{u_l u_i u_k} + (2/5)S_{kl} \overline{u_l u_i u_j} \quad (3.9)$$

where S_{ij} is the strain rate, $(1/2)(U_{i,j} + U_{j,i})$.

Note that the expression resulting from the combination of (3.2) and (3.6) satisfies realizability in the sense that they vanish when the velocity components in question vanish.

Hence, the net effect of the "rapid" pressure is to remove the contribution of the vorticity to the production, and to reduce the contribution of the strain rate to the production.

THE VISCOUS TERMS

Appearing in each equation for a third moment, we have a viscous term. For example, in the equation for $\overline{u_i u_j u_k}$ (now in general coordinates) we have a term of the form

$$-(2/3)(\overline{\epsilon}/q^2)(g_{ik} \overline{q^2 u_j} + g_{ij} \overline{q^2 u_k} + g_{jk} \overline{q^2 u_i}) \quad (4.1)$$

(see Lumley, 1978). In a simple situation in which the equations are not cross-coupled (no buoyancy, no rotation) it is straight-forward to calculate $\overline{q^2 u_i}$ from the equation for $\overline{u_i u_j u_k}$ and substitute it.

Here, however, the equations are strongly cross-coupled, and the complexity introduced by these viscous terms is formidable. We propose a simplification which will retain some of the physics.

In the viscous terms only, in cylindrical coordinates, we propose to write

$$\overline{q^2 u_k}/3 = \overline{u^1 u_1 u_k} = \overline{u^2 u_2 u_k} = \overline{u^3 u_3 u_k} \quad (4.2)$$

so that, for example, the viscous terms in the equation for $\overline{u^2 u_1}$, can be replaced in the following way:

$$\begin{aligned} -(2/3)(\overline{\epsilon}/q^2)g_{33} \overline{q^2 u_1} &= -2(\overline{\epsilon}/q^2)g_{33} \overline{u^3 u_3 u_1} \\ &= -2(\overline{\epsilon}/q^2) \overline{u^2 u_1} \end{aligned} \quad (4.3)$$

The term is now of the same form as the return to isotropy term (Lumley, 1978), and can be combined with it, the net result being a change in the value of the time scale. We are saying, effectively, that

$$\overline{\epsilon}_{\alpha\alpha i} = (\overline{\epsilon}/q^2) \overline{u^2 u_i} \quad (4.4)$$

where $\epsilon_{\alpha\alpha}$ is the α -component of the dissipation. This is surely somewhat in error, because the dissipation should be more nearly isotropic than the velocity at large Reynolds numbers. The error, however, should be small relative to the errors introduced by our other approximations, and the simplification is considerable.

Equation (4.4) is not as serious an approximation as writing $\overline{\epsilon}_{ij} = \overline{u_i u_j}$ (see Corrsin, 1972), since we are dealing here only with the diagonal components.

THE EQUATIONS FOR THE MECHANICAL THIRD MOMENTS

We follow the approach outlined in Lumley (1978). There, however, we showed that the convection and production terms were of higher order relative to the term retained, and could be neglected. Here, we suppose that at least some of the mean velocities and their gradients are large enough to keep the convection and production terms; in particular, we expect the azimuthal (physical) velocity to be large, and the radius small, so that

$$(V_\theta/r)(l_c/u) = O(1) \quad (5.1)$$

even as $l_c/r \rightarrow 0$, where l_c is a turbulent length scale, defined, say, by $\epsilon = u^3/l_c$, $3u^2 = q^2$, and l is a scale characteristic of cross-stream gradients of axial velocity,

$$\partial V_z / \partial r = |\Delta V_z|_{\max} / l \quad (5.2)$$

(where $|\Delta V_z|_{\max}$ is the maximum difference in V_z , the axial velocity). Reasoning in this way, we will keep all convection and production terms involving the azimuthal velocities, and neglect the rest. The order of magnitude analysis of Lumley (1978) can be carried over exactly, otherwise, since we may work in Cartesian coordinates and transform to generalized coordinates afterward.

In general coordinates, then, the equation for $\overline{u_i u_j u_k}$ becomes (incorporating the results of section 3)

$$\begin{aligned} &(\overline{u_i u_j u_k})_{,p} U^p + (2/5)S_{ip} \overline{u_p u_j u_k} + (2/5)S_{jp} \overline{u_p u_i u_k} \\ &+ (2/5)S_{kp} \overline{u_p u_i u_j} + (\overline{u_i u_j})_{,p} \overline{u^p u_k} + (\overline{u_i u_k})_{,p} \overline{u^p u_j} \\ &+ (\overline{u_j u_k})_{,p} \overline{u^p u_i} = -3C_1(\overline{\epsilon}/q^2) \overline{u_i u_j u_k} \\ &+ (\overline{\epsilon}/q^2)(C_1 - 2)(g_{ij} \overline{q^2 u_k} + g_{ik} \overline{q^2 u_j} + g_{jk} \overline{q^2 u_i})/3 \end{aligned} \quad (5.3)$$

where, for simplicity of notation in this section and below we are suppressing the overbars which would otherwise indicate that these velocities are written in a general non-Cartesian coordinate system. We will, of course, apply also the results of section 4 to the last term when we write (5.3) in component form.

The only velocity we retain is the azimuthal, U^2 ; hence

$$\begin{aligned} (\overline{u_i u_j u_k})_{,p} U^p &= (\overline{u_i u_j u_k})_{,2} U^2 \\ &= (-\Gamma_{12}^p \overline{u_p u_j u_k}) - \Gamma_{j2}^p \overline{u_i u_p u_k} - \Gamma_{k2}^p \overline{u_i u_j u_p} U^2 \end{aligned} \quad (5.4)$$

since $\partial/\partial x^2$ of all quantities is taken to be zero by axisymmetry.

The mean velocity gradients we retain are

$$U_{1,2} = -U_2/\overline{x}^1 \quad U_{2,1} = \partial U_2 / \partial \overline{x}^1 - U_2/\overline{x}^1 \quad (5.5)$$

so that the non-zero components of the strain rate are

$$S_{12} = S_{21} = (1/2) \partial U_2 / \partial \overline{x}^1 - U_2/\overline{x}^1 \quad (5.6)$$

If for simplicity we write

$$3C_1\overline{E}/q^2 = 1/T, \quad A = \Gamma^2_{12}U^2 - (2/5)S^2_1$$

$$(\overline{E}/q^2)(C_1-2) = K/T, \quad B = (2/5)S^1_2 - \Gamma^1_{22}U^2 \quad (5.7)$$

$$(1-3K)/T = 1/T'', \quad (1-K)/T = 1/T'$$

then our equation can be written as

$$-3A\overline{u_2u_1}^2 + 3(\overline{u_2^2})_{,p}\overline{u_1}^p = -\overline{u_1^3}/T'' \quad (5.8)$$

$$-2A\overline{u_1u_2}^2 + B\overline{u_1^3} + (\overline{u_2^2})_{,p}\overline{u_1}^p\overline{u_2}^p$$

$$+ 2(\overline{u_1u_2})_{,p}\overline{u_1}^p\overline{u_2}^p = -\overline{u_1^2u_2}/T' \quad (5.9)$$

$$2B\overline{u_1u_2}^2 - A\overline{u_2^3} + (\overline{u_2^2})_{,p}\overline{u_1}^p\overline{u_2}^p$$

$$+ 2(\overline{u_1u_2})_{,p}\overline{u_1}^p\overline{u_2}^p = -\overline{u_1u_2^2}/T' \quad (5.10)$$

$$-A\overline{u_2u_3}^2 + 2(\overline{u_1u_3})_{,p}\overline{u_1}^p\overline{u_3}^p + (\overline{u_2^2})_{,p}\overline{u_1}^p\overline{u_3}^p = -\overline{u_1u_2^3}/T' \quad (5.11)$$

$$3B\overline{u_1u_2}^2 + 3(\overline{u_2^2})_{,p}\overline{u_1}^p\overline{u_2}^p = -\overline{u_1^3}/T'' \quad (5.12)$$

$$B\overline{u_1u_2}^2 + 2(\overline{u_2u_3})_{,p}\overline{u_1}^p\overline{u_3}^p + (\overline{u_2^2})_{,p}\overline{u_1}^p\overline{u_2}^p = -\overline{u_2u_3^2}/T' \quad (5.13)$$

$$-A\overline{u_2u_3}^2 + B\overline{u_1u_3}^2 + (\overline{u_1u_2})_{,p}\overline{u_1}^p\overline{u_3}^p + (\overline{u_1u_3})_{,p}\overline{u_1}^p\overline{u_2}^p$$

$$+ (\overline{u_2u_3})_{,p}\overline{u_1}^p\overline{u_1}^p = -\overline{u_1u_2u_3}/T \quad (5.14)$$

$$-2A\overline{u_1u_2u_3} + (\overline{u_2^2})_{,p}\overline{u_1}^p\overline{u_3}^p + 2(\overline{u_1u_3})_{,p}\overline{u_1}^p\overline{u_2}^p = -\overline{u_1^2u_3}/T' \quad (5.15)$$

$$2B\overline{u_1u_2u_3} + (\overline{u_2^2})_{,p}\overline{u_1}^p\overline{u_3}^p + 2(\overline{u_2u_3})_{,p}\overline{u_1}^p\overline{u_2}^p = -\overline{u_2^2u_3}/T' \quad (5.16)$$

These equations may be separated into non-interacting groups. For example, (5.11) and (5.13) are dependent only on each other; (5.14), (5.15) and (5.16) also form an autonomous group; and (5.8), (5.9), (5.10), (5.12) are also mutually dependent.

Let us take the largest group first. If we define

$$\Omega = 1 + 3ABT'T'', \quad \Omega' = 1 + 3ABT'T'' + 4ABT'^2 \quad (5.17)$$

then we may define a matrix

$$B_{ij} = \frac{-\Omega T'}{\Omega' + \Omega(\Omega-1)} \times \quad (5.18)$$

$\Omega'T''/\Omega T'$	$3AT''$	$6A^2T'T''/\Omega$	$6A^3T'T''^2/\Omega$
$-BT''$	1	$2AT'/\Omega$	$2A^2T'T''/\Omega$
$2B^2T'T''/\Omega$	$-2BT'/\Omega$	1	AT'
$2B^2T'T''/\Omega$	$-2BT'/\Omega$	1	AT'
$-6B^3T'T''^2/\Omega$	$6B^2T'T''/\Omega$	$-3BT''$	$\Omega'T''/\Omega T'$

and we may write the solution in terms of B_{ij} :

$$\begin{vmatrix} \overline{u_1^3} \\ \overline{u_1^2u_2} \\ \overline{u_1u_2^2} \\ \overline{u_2^3} \end{vmatrix} = \frac{B}{\Omega} \begin{vmatrix} 3(\overline{u_1^2})_{,p}\overline{u_1}^p\overline{u_2}^p \\ (\overline{u_1^2})_{,p}\overline{u_1}^p\overline{u_2}^p + 2(\overline{u_1u_2})_{,p}\overline{u_1}^p\overline{u_2}^p \\ 2(\overline{u_1u_2})_{,p}\overline{u_1}^p\overline{u_2}^p + (\overline{u_2^2})_{,p}\overline{u_1}^p\overline{u_2}^p \\ 3(\overline{u_2^2})_{,p}\overline{u_1}^p\overline{u_2}^p \end{vmatrix} \quad (5.19)$$

We may now collect the terms and write in matrix form

$$\begin{vmatrix} \overline{u_1^3} \\ \overline{u_1^2u_2} \\ \overline{u_2^2u_1} \end{vmatrix} = \begin{vmatrix} 3\beta_{11}\overline{u_1}^p\overline{u_1}^p + \beta_{12}\overline{u_1}^p\overline{u_2}^p & 2\beta_{12}\overline{u_1}^p\overline{u_1}^p + 2\beta_{13}\overline{u_1}^p\overline{u_2}^p & \beta_{13}\overline{u_1}^p\overline{u_1}^p + 3\beta_{14}\overline{u_1}^p\overline{u_2}^p \\ 3\beta_{21}\overline{u_1}^p\overline{u_1}^p + \beta_{22}\overline{u_1}^p\overline{u_2}^p & 2\beta_{22}\overline{u_1}^p\overline{u_1}^p + 2\beta_{23}\overline{u_1}^p\overline{u_2}^p & \beta_{23}\overline{u_1}^p\overline{u_1}^p + 3\beta_{24}\overline{u_1}^p\overline{u_2}^p \\ 3\beta_{31}\overline{u_1}^p\overline{u_1}^p + \beta_{32}\overline{u_1}^p\overline{u_2}^p & 2\beta_{32}\overline{u_1}^p\overline{u_1}^p + 2\beta_{33}\overline{u_1}^p\overline{u_2}^p & \beta_{33}\overline{u_1}^p\overline{u_1}^p + \beta_{34}\overline{u_1}^p\overline{u_2}^p \end{vmatrix} \times \begin{vmatrix} (\overline{u_1^2})_{,p} \\ (\overline{u_1u_2})_{,p} \\ (\overline{u_2^2})_{,p} \end{vmatrix} \quad (5.20)$$

The fourth component can also be written in this form:

$$\overline{u_2^3} = (\overline{u_2^2})_{,p} [3\beta_{41}\overline{u_1}^p\overline{u_1}^p + \beta_{42}\overline{u_1}^p\overline{u_2}^p]$$

$$+ (\overline{u_1u_2})_{,p} [2\beta_{42}\overline{u_1}^p\overline{u_1}^p + 2\beta_{43}\overline{u_1}^p\overline{u_2}^p]$$

$$+ (\overline{u_2^2})_{,p} [\beta_{43}\overline{u_1}^p\overline{u_1}^p + 3\beta_{44}\overline{u_1}^p\overline{u_2}^p] \quad (5.21)$$

We see the appearance here of the same matrix form found by Zeman (1975), Zeman & Lumley, 1976a, b, c; Lumley et al (1978), and the coefficients are of the general type (1.7).

The group of three equations may be attacked in a similar way. If we define a matrix

$$B_{ij}^1 = \frac{-T'}{1+4ABT''} \begin{vmatrix} 1+2ABT'' & 2AT & 2A^2T'T' \\ -BT & T/T' & AT \\ 2B^2T'T' & -2BT & 1+2ABT'' \end{vmatrix} \quad (5.22)$$

then the solution may be written as

$$\begin{pmatrix} \overline{u_1^2 u_3} \\ \overline{u_1 u_2 u_3} \\ \overline{u_2^2 u_3} \end{pmatrix} = \frac{\beta}{\alpha} \begin{pmatrix} (\overline{u_1^2})_{,p} \overline{u_3} + 2(\overline{u_1 u_3})_{,p} \overline{u_1} \\ (\overline{u_1 u_2})_{,p} \overline{u_3} + (\overline{u_1 u_3})_{,p} \overline{u_2} + (\overline{u_2 u_3})_{,p} \overline{u_1} \\ (\overline{u_2^2})_{,p} \overline{u_3} + 2(\overline{u_2 u_3})_{,p} \overline{u_2} \end{pmatrix} \quad (5.23)$$

Now, however, when we expand, we cannot directly write the result in the form (5.20) due to the presence of such terms as $\overline{u_1^2 u_3}$.

It is tempting to suppose that u_3 is produced from the mean 3-velocity gradient by the u_1 fluctuation, and that the u_2 fluctuations are principally due to angular momentum conservation under l-excursions. This is a kind of mixing length assumption, leading to $u_3 \sim u_1 u_2$. Then we can write

$$\overline{u_1 u_2 u_3} = \overline{u_1 u_2} \overline{u_3}$$

$$\overline{u_1 u_3 u_2} = \overline{u_1 u_3} \overline{u_2} \quad (5.24)$$

$$\overline{u_1 u_2 u_3} = (1/2) [\overline{u_1 u_3} \overline{u_2} + \overline{u_2 u_3} \overline{u_1}]$$

This, however, is not quite what we need. We need the derivatives $(\overline{u_1^2})_{,p} \overline{u_3}$ etc. If we attempt to write

$$(\overline{u_1^2})_{,p} \overline{u_3} = (\overline{u_1 u_3})_{,p} \overline{u_1} \quad (5.25)$$

even assuming that the coefficients of proportionality are not functions of position, we find that (5.25) fails due to the different groups of Christoffel symbols on the two sides.

The only way the issue can be simply resolved is to assume that $l/r \ll 1$, where l is the scale of the radial gradient of the Reynolds stress. This assumption amounts to either very thin shear layers relative to the radius, or to large radius; essentially this is the small gap approximation familiar in stability analyses of circular Couette flow.

This is not inconsistent with our previous assumptions, which were simply that V_0/r is of the same order as u/l . If $l/r \ll 1$ and $l_c/r \ll 1$, but $V_0/r \sim u/l_c$, then $V_0/u \sim (r/l)(l/l_c) \gg \gg 1$. Hence, we must have very large velocities relative to turbulent intensities.

If we make the narrow gap assumption, then for turbulent quantities the only important covariant derivative is radial, and that is essentially given by the ordinary radial derivative.

Now we can write

$$(\overline{u_1^2})_{,1} \overline{u_3} = (\overline{u_1 u_3})_{,1} \overline{u_1} \quad (5.26)$$

$$(\overline{u_2^2})_{,1} \overline{u_3} = (\overline{u_2 u_3})_{,1} \overline{u_2}$$

$$(\overline{u_1 u_2})_{,1} \overline{u_3} = (1/2) [(\overline{u_1 u_3})_{,1} \overline{u_2} + (\overline{u_2 u_3})_{,1} \overline{u_1}]$$

With the approximation (5.26), we can write

$$\begin{pmatrix} \overline{u_1^2 u_3} \\ \overline{u_1 u_2 u_3} \\ \overline{u_2^2 u_3} \end{pmatrix} = \begin{pmatrix} 3\beta'_{11} \overline{u_1^2 u_1} + (3/2) \beta'_{12} \overline{u_1^2 u_2} & (3/2) \beta'_{12} \overline{u_1^2 u_1} + 3\beta'_{13} \overline{u_1^2 u_2} \\ 3\beta'_{21} \overline{u_1^2 u_1} + (3/2) \beta'_{22} \overline{u_1^2 u_2} & (3/2) \beta'_{22} \overline{u_1^2 u_1} + 3\beta'_{23} \overline{u_1^2 u_2} \end{pmatrix} \times \begin{pmatrix} (\overline{u_1 u_3})_{,1} \\ (\overline{u_2 u_3})_{,1} \end{pmatrix} \quad (5.27)$$

and the third component also can be written in this form:

$$\begin{aligned} \overline{u_2^2 u_3} &= (\overline{u_1 u_3})_{,1} [3\beta'_{31} \overline{u_1^2 u_1} + (3/2) \beta'_{32} \overline{u_1^2 u_2}] \\ &+ (\overline{u_2 u_3})_{,1} [(3/2) \beta'_{32} \overline{u_1^2 u_1} + 3\beta'_{33} \overline{u_1^2 u_2}] \end{aligned} \quad (5.28)$$

Finally, we may solve the group of two, defining

$$\beta^2_{ij} = \frac{-T^i}{1+ABT^2} \begin{vmatrix} 1 & +AT^i \\ -BT^i & 1 \end{vmatrix} \quad (5.29)$$

and

$$\begin{pmatrix} \overline{u_1 u_3^2} \\ \overline{u_2 u_3^2} \end{pmatrix} = \frac{\beta^2}{\alpha} \begin{pmatrix} (\overline{u_3^2})_{,p} \overline{u_1} + 2(\overline{u_1 u_3})_{,p} \overline{u_3} \\ (\overline{u_3^2})_{,p} \overline{u_2} + 2(\overline{u_2 u_3})_{,p} \overline{u_3} \end{pmatrix} \quad (5.30)$$

To place this in the same form as (5.20) and (5.27), we must make the narrow gap assumption, discard (),₂, and assume

$$(\overline{u_1 u_3})_{,1} \overline{u_3} = (\overline{u_3^2})_{,1} \overline{u_1} \quad (5.31)$$

$$(\overline{u_2 u_3})_{,1} \overline{u_3} = (\overline{u_3^2})_{,1} \overline{u_2}$$

which can be justified in the same way. Then

$$\overline{u_1 u_3^2} = (\overline{u_3^2})_{,1} [3\beta^2_{11} \overline{u_1^2 u_1} + 3\beta^2_{12} \overline{u_1^2 u_2}] \quad (5.32)$$

$$\overline{u_2 u_3^2} = (\overline{u_3^2})_{,1} [3\beta^2_{21} \overline{u_1^2 u_1} + 3\beta^2_{22} \overline{u_1^2 u_2}]$$

DISCUSSION

Now, of course, this formalism must be applied to the calculation of well documented swirling flows. It is necessary first, of course, to model homogeneous swirling flows, like that of Traugott (1958) and of Wigeland & Nagib (1978), to calibrate the other aspects of the model (notably the dissipation equation) which we have ignored here.

We should then attempt modeling of such swirling flows as the swirling jet of Rose (1962), the curved channel flow of Eskinazi & Yeh (1956), the curved mixing layer of Wyngaard et al (1968) and perhaps even the rotating channel flow of Lezius & Johnston (1972) (see also Schetz, 1980). In all of these, (but particularly the spinning jet), new modeling of the dissipation equation will doubtless be necessary.

It is interesting that the primary effect of swirl is not through the pressure terms, as one might have expected. From section 3 we see that the effect of the pressure terms is to cancel the effect of rotation (at least as far as the mean velocity gradients are concerned) so that under solid body rotation ($S_{ij} = 0$) the terms in the mean velocity gradients contribute nothing. Rather, the effect of rotation comes about entirely through the rotation of the coordinate system, an essentially geometrical effect (felt through the convective derivative). Of course, it is felt indirectly through the modification of the value of u^2 , which will come about through the second moment equations, and which appears in the diffusion coefficient in the third moment equations due to the rotation of the frame.

References

- Corrsin, S. 1972. Comment on "Transport equations in turbulence". Physics of Fluids 16: 157-158.
- Eskinazi, S. & Yeh, H. 1956. An investigation on fully developed turbulent flows in a curved channel. J. Aersp. Sci. 23: 23-34.
- Janicka, J. & Lumley, J. L. 1981a. A note concerning the pressure transport terms in second order modeling. In preparation.
- Janicka, J. & Lumley, J. L. 1981b. Second order modeling in non-constant density flows. Sibley School of Mechanical and Aerospace Engineering Report No. FDA-81-01. Ithaca, New York: Cornell.
- Jones, W. P. & Launder, B. E. 1973. The calculation of low-Reynolds number phenomena with a two-equation model of turbulence. Int. J. Heat Mass Transf. 16: 1119-30.
- Launder, B. E., Priddin, C. H. & Sharma, B. I. 1977. The calculation of turbulent boundary layers on spinning and curved surfaces. J. Fluids Engineering 99:231-239.
- Lezius, D. & Johnston, J. P. 1972. The structure and stability of turbulent wall layers in rotating channel flow. J. Fluid Mech. 56:533-555.
- Lumley, J. L. 1970. Stochastic Tools in Turbulence. New York: Academic Press.
- Lumley, J. L. 1978. Computational modeling of turbulent flows. In Adv in Applied Mech 18, ed. C.-S. Yih, pp. 123-176. New York: Academic Press.
- Lumley, J. L. & Panofsky, H. A. 1964. The Structure of Atmospheric Turbulence. New York: Interscience.
- Lumley, J. L., Zeman, O., & Siess, J. 1978. The influence of buoyancy on turbulent transport. J. Fluid Mech. 84:581-597.
- Pellew, A. & Southwell, R. V. 1940. On maintained convective motion in a fluid heated from below. Proc. Roy. Soc. A 176, 966: 312-343.
- Ramaprian, B. R. & Shivaprasad, B. G. 1981. The instantaneous structure of mildly curved turbulent boundary layers. J. Fluid Mech. Submitted for publication.
- Rose, W. G. 1962. A swirling round turbulent jet. J. Applied Mech. 29, 12: 615-625.
- Schetz, J. A. 1980. Injection and Mixing in Turbulent Flow. Progress in Astronautics and Aeronautics, 68; ed. M. Summerfield. New York: American Institute of Aeronautics and Astronautics.
- Taulbee, D. B. & Lumley, J. L. 1981. Prediction of the turbulent wake with a second order closure model. Sibley School of Mechanical and Aerospace Engineering Report No. FDA-81-04. Ithaca, New York: Cornell.
- Taylor, G. I. 1923. Stability of a viscous fluid contained between rotating cylinders. Phil. Tr. 223: 289-343.
- Traugott, S. C. 1958. Influence of solid body rotation on screen-produced turbulence. NACA TN 4135.
- Wigeland, R. A. & Nagib, H. M. 1978. Grid generated Turbulence with and without rotation about the streamwise direction. Fluids and Heat Transfer Report R78-1. Chicago: Illinois Institute of Technology.
- Wyngaard, J. C., Tennekes, H., Lumley, J. L. & Margolis, D. P. 1968. Structure of turbulence in a curved mixing layer. Physics of Fluids 11: 1251-1253.
- Zeman, O. 1975. The dynamics of entrainment in the planetary boundary layer: a study in turbulence modeling and parameterization. Ph. D. Thesis, University Park: The Pennsylvania State University.
- Zeman, O. & Lumley, J. L. 1976a. Turbulence and diffusion modeling in buoyancy-driven mixed layers. In Proceedings of Third Symposium on Atmospheric Turbulence, Diffusion Air Quality, Raleigh, NC, pp. 38-45. Boston, MA: American Meteorological Society.
- Zeman, O. & Lumley, J. L. 1976b. Modeling buoyancy-driven mixed layers. J. Atmos. Sci. 33,10: 1974-88.
- Zeman, O. & Lumley, J. L. 1976c. A second order model for buoyancy-driven mixed layers. In Proceedings, 9th ICHMT International Seminar "Turbulent Buoyant Convection", Dubrovnik, pp. 65-76. Washington, DC: Hemisphere Publishing.
- Zeman, O. & Lumley, J. L. 1979. Buoyancy effects in entraining turbulent boundary layers: a second order closure study. In Turbulent Shear Flows, eds. F. Durst, B. E. Launder, F. W. Schmidt and J. H. Whitelaw, pp. 295-302. Berlin/Heidelberg: Springer-Verlag.

EFFECTS OF ROTATION ON ISOTROPIC TURBULENCE

B. AUPOIX, J. COUSTEIX and J. LIANDRAT

ONERA/CERT
TOULOUSE (FRANCE)

ABSTRACT

The reduction of the energy transfer in an initially isotropic turbulence, submitted to a solid-body rotation, is brought into evidence with the help of direct simulation. Direct simulations and large-eddy simulations are then used to validate an EDQNM model which describes the evolution of the energy transfer in presence of rotation. This EDQNM model is then used to develop new one-point closures, which account for rotation effects.

1 - INTRODUCTION

Both experiments and direct simulations on quasi-isotropic, homogeneous turbulence submitted to solid-body rotation have shown that rotation alters the rate of decay of turbulence.

However, no effect of rotation is taken into account in the standard one-point closures. This may be important not only in rotating cases (e.g. turbomachinery) but also for shear flows as shear can be decomposed as strain plus rotation.

A cascade of turbulence models will be developed to study the effects of rotation on turbulence: direct simulations and large eddy simulations will help us to validate an EDQNM closure. This EDQNM model will lead us to a new transport equation for the kinetic energy dissipation rate which will be checked by comparison with experiment for both rotation and shear cases.

2 - ANALYSIS OF ROTATION EFFECTS

FOURIER transforms are very suitable for studying homogeneous flows. The pressure term in the NAVIER equation is discarded by solving a POISSON equation. For incompressible homogeneous rotating turbulence, the equations then read:

$$\begin{aligned} k_i u_i(\underline{k}) &= 0 \\ \left(\frac{\partial}{\partial t} + \nu k^2\right) u_i(\underline{k}) + \frac{i}{2} \Delta_{ijl}(\underline{k}) \int u_j(\underline{p}) u_l(\underline{k} - \underline{p}) d^3 p \\ + 2 \epsilon_{jpk} \Delta_{ijl}(\underline{k}) \omega_p u_q(\underline{k}) &= 0 \\ \text{with } \Delta_{ij}(\underline{k}) &= \delta_{ij} - \frac{k_i k_j}{k^2} \quad \Delta_{ijl}(\underline{k}) = k_i \Delta_{jl}(\underline{k}) + k_j \Delta_{il}(\underline{k}) \end{aligned}$$

where \underline{k} , \underline{p} , \underline{q} are wave vectors, u_i the components of the FOURIER transformed velocity field and ϵ_{ijk} the alternating tensor.

Equations for the cumulants can be deduced from this set of equations.

The second, third and fourth-order cumulants are defined as:

$$\begin{aligned} S_{\alpha\beta}(\underline{k}) &= \langle u_\alpha(\underline{k}) u_\beta(-\underline{k}) \rangle \\ T_{\alpha\beta\gamma}(\underline{k}, \underline{p}) &= \langle u_\alpha(\underline{k}) u_\beta(\underline{p}) u_\gamma(-\underline{k} - \underline{p}) \rangle \\ Q_{\alpha\beta\gamma\delta}(\underline{k}, \underline{p}, \underline{q}) &= \langle u_\alpha(\underline{k}) u_\beta(\underline{p}) u_\gamma(\underline{q}) u_\delta(-\underline{k} - \underline{p} - \underline{q}) \rangle \end{aligned}$$

with $\underline{k} \neq -\underline{p}$, $\underline{k} \neq -\underline{q}$, $\underline{p} \neq -\underline{q}$.

The equations for the second and third-order cumulants read:

$$\begin{aligned} \left(\frac{\partial}{\partial t} + 2\nu k^2\right) S_{\alpha\beta}(\underline{k}) &= -\frac{i}{2} \int [\Delta_{\alpha\beta\sigma}(\underline{k}) T_{\beta\sigma\alpha}(-\underline{k}, \underline{p}) \\ + \Delta_{\beta\sigma\alpha}(-\underline{k}) T_{\alpha\sigma\beta}(\underline{k}, \underline{p})] d^3 p - 2 \epsilon_{jpk} \omega_p [\Delta_{\alpha j}(\underline{k}) S_{\beta q}(-\underline{k}) \\ + \Delta_{\beta j}(-\underline{k}) S_{\alpha q}(\underline{k})] \\ \left[\frac{\partial}{\partial t} + \nu(k^2 + p^2 + q^2)\right] T_{\alpha\beta\gamma}(\underline{k}, \underline{p}) &= \\ -\frac{i}{2} \int [\Delta_{\alpha\beta\sigma}(\underline{k}) Q_{\beta\gamma\sigma\alpha}(\underline{p}, \underline{q}, \underline{r}) + \Delta_{\beta\sigma\alpha}(\underline{p}) Q_{\alpha\gamma\sigma\beta}(\underline{k}, \underline{q}, \underline{r}) \\ + \Delta_{\gamma\sigma\alpha}(\underline{q}) Q_{\alpha\beta\sigma\gamma}(\underline{k}, \underline{p}, \underline{r})] d^3 r \\ - i [\Delta_{\alpha\beta\sigma}(\underline{k}) S_{\beta\sigma}(\underline{p}) S_{\gamma\sigma}(\underline{q}) + \Delta_{\beta\sigma\alpha}(\underline{p}) S_{\alpha\sigma}(\underline{k}) S_{\gamma\sigma}(\underline{q}) \\ + \Delta_{\gamma\sigma\alpha}(\underline{q}) S_{\alpha\sigma}(\underline{k}) S_{\beta\sigma}(\underline{p})] - 2 \epsilon_{jpk} \omega_p [\Delta_{\alpha j}(\underline{k}) T_{q\beta\gamma}(\underline{k}, \underline{p}) \\ + \Delta_{\beta j}(\underline{p}) T_{\alpha q\gamma}(\underline{k}, \underline{p}) + \Delta_{\gamma j}(\underline{q}) T_{\alpha\beta q}(\underline{k}, \underline{p})] \end{aligned}$$

with $\underline{q} = -(\underline{k} + \underline{p})$

For an isotropic turbulence, we have:

$S_{\alpha\beta}(\underline{k}) = \Delta_{\alpha\beta}(\underline{k}) \frac{E(\underline{k})}{4\pi k^2}$. Then, the CORIOLIS term vanishes in the second-order cumulant equation. Even for anisotropic turbulence, the CORIOLIS term does not appear in the equation for the energy spectrum:

$$E(k) = \frac{1}{2} \int_{|\underline{k}|=k} S_{\alpha\alpha}(\underline{k}) d^3 k$$

However, third-order cumulant are affected by rotation. The CORIOLIS term "orientates" the third-order cumulant. As the third-order cumulant appears in the equation for the second-order cumulant, the turbulence does not remain isotropic and evolves towards an axisymmetric state. The "orientation" of the third-order cumulants also modifies the energy transfer.

This analysis is not at variance with the results of BARDINA (1982): in direct simulations of initially isotropic turbulence submitted to rotation, he pointed out a different influence of rotation whether the rotation was applied at the beginning of the computation or after several time steps. At the beginning of his direct simulation, the velocity field is gaussian, i.e. third-order cumulants are zero, so the rotation cannot act immediately. After several time steps, third-order cumulants are built up and rotation acts.

3 - EDQNM MODEL FOR ROTATING TURBULENCE

The above set of equations for the cumulants is open and an infinite hierarchy can be so derived. For isotropic turbulence without rotation, this set of equations is solved with the EDQNM model (ORSZAG (1970)) (ANDRE - LESIEUR (1973)).

The velocity fluctuations exhibit a nearly gaussian behaviour. If they were strictly gaussian, third and fourth-order cumulants should be zero. Quasi Normal approximation consists of assuming that third-order cumulants, which are responsible for energy transfer, are non zero, but fourth-order cumulants are zero. The third-order cumulant equation can then be solved analytically. However, the damping of third-order cumulant is only due to viscous term $\nu(k^2 + p^2 + q^2) T_{\alpha\beta\gamma}(k, p)$ so that the third-order cumulants increase unrealistically. The damping term is modified by introducing an Eddy Damping which accounts for fourth-order cumulant, so that the damping becomes: $[\mu(k) + \mu(p) + \mu(q)] T_{\alpha\beta\gamma}(k, p)$ with $\mu(k) = \eta(k) + \nu k^2$

$$\eta(k) = \lambda \left(\int_0^k p^2 E(p) dp \right)^{1/2}$$

Markovianisation is used when solving the third-order cumulant equation to ensure realizability. Finally, for isotropic turbulence, the EDQNM model gives the evolution of the energy spectrum as:

$$\left(\frac{\partial}{\partial t} + 2\nu k^2 \right) E(k) = T(k) = \iint_{k=p+q} \frac{1}{\mu_k + \mu_p + \mu_q} b(k, p, q) (E(k)E(p) - E(p)E(q)) d^3p d^3q$$

where $b(k, p, q)$ is a function of the shape of the triangle made by the wave vectors k, p, q .

With rotation, the solution of the third-order cumulant equation is much more intricate (CAMBON (1982 b)) and out of purpose. The complete solution of an EDQNM model must deal with $S_{\alpha\beta}(k)$ as the rotation will promote favourite directions and the turbulence will not remain isotropic but will become axisymmetric. An approximate solution has been proposed by CAMBON (1982 a): the isotropic EDQNM model presented above is used as a model for the evolution of the energy spectrum while the damping term is modified to take into account the mean rotation as:

$$\eta(k) = \lambda \left[\int_0^k p^2 E(p) dp + 2 \omega^2 \right]^{1/2}$$

Such a model gives a reduction of energy transfer in the presence of rotation but gives no information about the anisotropisation of turbulence. In the following, EDQNM computations will stand for the resolution of the evolution equation for the energy spectrum using the EDQNM formulation for the energy transfer with the above modified damping.

4 - VALIDATION OF THE EDQNM MODEL

4.a - Direct simulations

One of the most reliable method to study the effects of rotation on an initially homogeneous isotropic turbulence is to solve directly the continuity and NAVIER equations, without modelling. Such a direct simulation is only feasible at very low Reynolds numbers. Direct simulations were performed with a $32 \times 32 \times 32$ points grid, the NAVIER equations being solved in terms of FOURIER components of the velocity field with periodic boundary conditions in all three space directions. Initial data were similar to the ones used by ORSZAG and PATTERSON in their numerical experiment, i.e. a $k^4 \exp(-k^2)$ initial energy spectrum corresponding to initial Reynolds number:

$$R_\epsilon = \frac{(q^2)^2}{9\nu\epsilon} = 80, R_\lambda = \frac{(1/2 q^2)^{1/2} \lambda}{\nu} = 35 \quad (\lambda \text{ is TAYLOR micro-scale}).$$

The computation was performed over seven eddy-turnover times for various rotation rates. The energy spectra at the final time are plotted on figure 1. As the rotation rate increases, the peak of the energy spectrum increases, i.e. the energy is "trapped" in the large scales as the energy transfer from the large eddies to the small ones decreases in the presence of rotation. The agreement between the direct simulations and the EDQNM computation is very good for all rotation rates; the EDQNM model is then assumed to give a good representation of the effect of rotation on energy transfer for small Reynolds numbers.

4.b - Large eddy simulations

Direct simulations are not feasible at large Reynolds numbers, due to computers limitations. So, in large eddy simulations, only the large eddies are computed by solving the NAVIER equations while the small eddies have to be modelled. The "large eddy" NAVIER equation reads, in physical space for the sake of clarity:

$$\frac{\partial}{\partial t} \overline{u_i}(\underline{x}) + \frac{\partial}{\partial x_k} \overline{u_i u_k}(\underline{x}) = -\frac{1}{\rho} \frac{\partial \overline{p}}{\partial x_i} + \nu \frac{\partial^2 \overline{u_i}}{\partial x_k^2} - 2 \epsilon_{ipq} \omega_p \overline{u_q}(\underline{x})$$

where $\overline{u_i}(\underline{x}) = \int f(\underline{x} - \underline{x}') u_i(\underline{x}') d^3x'$ is the filtered velocity field relative to the large eddy.

As $\overline{u_i}(\underline{x}) = \overline{u_i}(\underline{x}) + u_i'(\underline{x})$, the non-linear term reads:

$$\overline{u_i u_k}(\underline{x}) = \overline{u_i}(\underline{x}) \overline{u_k}(\underline{x}) + R_{ie}(\underline{x})$$

$$R_{ie}(\underline{x}) = \overline{u_i}(\underline{x}) u_e'(\underline{x}) + u_i'(\underline{x}) \overline{u_e}(\underline{x}) + u_i'(\underline{x}) u_e'(\underline{x})$$

A subgrid-scale model is needed to take into account the subgrid-scale stress R_{ie} which is responsible for the energy exchanges between small and large eddies.

Two kinds of subgrid-scale models were used. The simplest one (SGS1) consists of a constant eddy viscosity model derived from the EDQNM model. The model developed by AUPOIX and COUSTEIX (1982) for isotropic turbulence has been extended to the rotation case by using the CAMBON's EDQNM model. Let us remind that this model expresses the eddy viscosity in term of the small eddies:

$$R_{ij}(\underline{x}) = \frac{2}{3} \epsilon_{ij} R_{kk}(\underline{x}) = 2 \nu_t S_{ij}(\underline{x})$$

$$S_{ij}(\underline{x}) = \frac{1}{2} \left(\frac{\partial \overline{u_i}}{\partial x_j} + \frac{\partial \overline{u_j}}{\partial x_i} \right)$$

$$\nu_t = \frac{0.196}{K_0^3} \frac{(1/2 q^2)^2}{\epsilon} \frac{2}{1 + \left(1 + \frac{16}{(3K_0)^3} \left(\frac{\omega}{\epsilon} \right)^2 \right)^{1/2}}$$

where K_0 is the KOLMOGOROV constant ($K_0 \approx 1.4$), $1/2 q^2$ the kinetic energy of the subgrid scales and ϵ the kinetic energy dissipation rate.

A more elaborate subgrid-scale model (SGS2) is obtained by performing an EDQNM computation of the evolution of the small scale coupled with the large eddy simulation. The evaluation of the energy spectrum in the small scales enables us to calculate the detailed energy transfers between large and small eddies. This technique, presented by CHOLLET (1983) for isotropic turbulence has been extended to rotating turbulence by using the CAMBON's EDQNM model.

Computations were performed using the experimental COMTE-BELLOT and CORRISIN's spectrum as initial data. Reynolds numbers are $R_\epsilon \approx 3200$ and $R_\lambda \approx 75$. The decrease in turbulence was studied over the experimental time, i.e. roughly thirteen eddy turnover-times for various rotation rates. The energy spectra at the final time are plotted on figure 2. The agreement between the large eddy simulations and the EDQNM model is still very good. In the large eddy simulations, the energy transfer between large and small eddies is computed with a subgrid scale model consistent with the EDQNM model but the energy transfer among large eddies, which is at least of the same order of magnitude for the selected rotation rates, is directly computed by solving the NAVIER equations. So the EDQNM model seems to be still able to represent the reduction of energy transfer due to rotation for higher Reynolds numbers.

5 - APPLICATION TO ONE-POINT CLOSURES

Without rotation, isotropic turbulence decays at high Reynolds numbers in a self-similar way, i.e. the energy spectrum has always the same shape. This can be seen from EDQNM computations of decaying isotropic turbulence (LESIEUR - SCHERTZER (1978)).

With the following schematic shape for the energy spectrum (W.C. REYNOLDS (1975)):

$E(k) = A k^s$, $k < k_m$ $\frac{\partial A}{\partial t} = 0$, $1 \leq s \leq 4$ very large eddies

$E(k) = K_0 \epsilon^{2/3} k^{-5/3}$, $k > k_m$ inertial range

the decay law for the kinetic energy reads :

$$\frac{1}{2} q^2 = \tau^{-\frac{2(s+1)}{s+3}}$$

So the kinetic energy evolution is ruled by the following equations which form the simplest ($\sqrt{2} q^2, \epsilon$) model :

$$\frac{d}{dt} \frac{1}{2} q^2 = -\epsilon$$

$$\frac{d}{dt} \epsilon = -\frac{3s+5}{2(s+1)} \frac{\epsilon^2}{\sqrt{2} q^2} = -C_{\epsilon_2}(s) \frac{\epsilon^2}{\sqrt{2} q^2}$$

where the only adjustable coefficient only depends upon the exponent of the energy spectrum in the very large eddies.

With rotation, no experiment gives us any information about the evolution of the energy spectrum. EDQNM computations have been performed for various initial Reynolds numbers ranging up to $R_e \approx 18\,000$, $R_\lambda \approx 520$ and various exponents of the energy spectrum in the very large eddies. As the energy is "trapped" in the large eddies due to transfer reduction, no self-similar behaviour can be observed. The reduction of energy transfer due to the rotation leads to an increase in the rate of decay of the energy dissipation rate and, therefore, the rate of decay of energy decreases.

From the EDQNM computation, the normalized dissipation rate evolution : $C_\epsilon^* = \frac{\sqrt{2} q^2}{\epsilon^2} \frac{d\epsilon}{dt} - C_{\epsilon_2}(s)$ has been calculated. In figure 3, it is plotted versus the normalized rotation rate $\omega^* = \frac{\omega \sqrt{2} q^2}{\epsilon}$ which is the inverse of a ROSSBY number. When the turbulence is set into rotation with a small initial normalized rotation ($\omega^* < 1$ at the beginning of rotation), the equilibrium curve shown on figure 3 is rapidly reached for a large range of Reynolds numbers ($R_e > 500$, $R_\lambda > 75$).

The ($\sqrt{2} q^2, \epsilon$) model now reads, to take rotation effects into account :

$$\frac{d}{dt} \sqrt{2} q^2 = -\epsilon$$

$$\frac{d\epsilon}{dt} = -(C_{\epsilon_2} + C_\epsilon^*(\omega^*)) \frac{\epsilon^2}{\sqrt{2} q^2}$$

The coefficient $C_\epsilon^*(\omega^*)$, deduced from EDQNM simulations, is quite different from the models previously proposed by HANJALIC and LAUNDER (1980) and BARDINA (1982). BARDINA proposed a linear relation $C_\epsilon^*(\omega^*) = 0.15 \omega^*$ based upon a large eddy simulation of an experiment of WIGELAND and NAGIB while HANJALIC et al. proposed a quadratic form $C_\epsilon^*(\omega^*) = 0.27 \omega^{*2}$ fitted for round-jet calculations.

This new ϵ -equation has also been used for calculating homogeneous turbulence submitted to shear or strain. With energy production, the standard form of the ϵ -equation reads :

$$\frac{D\epsilon}{Dt} = + C_{\epsilon_1} \frac{P\epsilon}{\sqrt{2} q^2} - C_{\epsilon_2} \frac{\epsilon^2}{\sqrt{2} q^2}$$

where $P = -u_i u_j \frac{\partial u_i}{\partial x_j}$ is the turbulent kinetic energy production. C_{ϵ_2} has been modified to take rotation into account as $C_{\epsilon_2}(s) + C_\epsilon^*(\omega^*)$ and a standard value $s = 2$ has been selected. C_{ϵ_1} was chosen such as to verify the constraint :

$$C_{\epsilon_1} = -C_\epsilon \frac{\chi^2}{(2a_1)^2} + [C_{\epsilon_2}(s) + C_\epsilon^*(\omega^*)]$$

$$\chi = 0.41 \quad a_1 = 0.15 \quad C_\epsilon = 0.069$$

imposed in the logarithmic region of a boundary layer.

A variable C_{ϵ_1} , i.e. verifying this relation whatever ω^* ($\omega^* = 1/2a_1$ in ϵ_1 a logarithmic region), has been chosen to remain consistent for strain calculation. An optimized formulation $C_{\epsilon_1}(\omega^*)$ should be better.

The Reynolds stress transport equation model used was that of LAUNDER, REECE and RODI (1975). No modification of the pressure-strain term was introduced to take rotation effects into account, while the initial anisotropisation of isotropic turbulence submitted to rotation is due to third-order cumulant and will appear in the non-linear part of the pressure-strain term.

6 - COMPARISON WITH EXPERIMENTS

6.a - Rotation

The experiments of WIGELAND and NAGIB on rotating wind tunnel turbulence are the most extensive and documented at the present time. Several test cases have been selected from their figures, with particular interest for the higher total rotation ($\omega.t$) cases.

For each grid and mean velocity, the no-rotation case was used to adjust the exponent s of the spectrum shape for very large eddies. When rotation is imposed, the HANJALIC et al. model has been discarded as it gives a too strong decay of the energy dissipation rate leading to a negative dissipation rate. Figure 4 shows some comparisons between WIGELAND and NAGIB experiments and the ($\sqrt{2} q^2, \epsilon$) models. Both BARDINA's model and the present model improve the prediction of the decay of the kinetic energy by taking rotation into account. However, as the normalized rotation ω^* usually remains smaller than 4 in these test cases and only reaches 7.5 at the end of the PG2 case, the difference between the two laws for C_ϵ^* is small, so that the two models give similar results.

These results are extremely good when we look at the Reynolds number range of the experiments ($R_e \sim 10$, $R_\lambda \sim 10$). This can be explained as follows : the coefficient was fitted to the no-rotation case, taking into account a part of the low Reynolds number effects while figure 3 shows that the $C_\epsilon^*(\omega^*)$ law is fairly sensitive to Reynolds number.

6.b - Shear

Two test cases were used, i.e. the experiments of CHAMPAGNE et al. (1970) and HARRIS et al. (1977). The initial data are taken from the 1980-81 AFOSR-HTTM STANFORD Conference. Figure 5 shows the evolution of $\sqrt{2} q^2$ and $-\overline{uv}$. The present model improves the calculation for both low and high shears, while BARDINA's gets some trouble. However, these results are not definitive as the C_{ϵ_1} term has to be revised as the pressure-strain term to take rotation effects into account.

7 - CONCLUSION

Direct simulations and large eddy simulations have been used to validate an EDQNM model predicting the energy transfer diminution due to rotation. This EDQNM model gave a new transport equation for the energy dissipation rate. This new equation gives results in good agreement with experiment for rotating homogeneous turbulence and for shear homogeneous turbulence.

However, rotation does not directly act upon the dissipation, but upon the energy transfer. A new multi-scale model is now developed to take rotation effects into account at the energy transfer level. Attention has to be paid to the influence of rotation on the pressure-strain term.

REFERENCES

- ANDRE J.C., LESIEUR M., 1977, "Influence of helicity on the evolution of isotropic turbulence at high Reynolds number", J.F.M. Vol. 81, p. 187-207
- AUPOIX B., COUSTEIX J., 1982, "Simple subgrid scale stresses models for homogeneous isotropic turbulence", La Recherche Aérospatiale, English Edition n° 1982-4, p. 1-10
- BARDINA J., FERZIGER J.M., REYNOLDS W.C., 1982, "Effects of rotation on isotropic turbulence : computation and modelling", STANFORD University

CAMBON C., BERTOGLIO J.P., JEANDEL D., 1982-a, "Comparison of computation with experiment", The 1980-81 AFOSR-HTTM, STANFORD Conference on Complex Turbulent Flow, Vol. III, p. 1307-1311

CAMBON C., 1982-b, "Etude spectrale d'un champ turbulent incompressible soumis à des effets couplés de déformation et de rotation imposés extérieurement", Thèse d'Etat, Université C. Bernard, LYON

CHAMPAGNE F.M., HARRIS V.G., CORRSIN S., 1970, "Experiments on nearly homogeneous shear flow", J.F.M. Vol. 41, Part 1, p. 81-139

CHOLLET J.P., 1983, "Two-point closures as a subgrid scale modelling for large eddy simulations", Fourth Symposium on Turbulent Shear Flows

COMTE-BELLOT G., CORRSIN S., 1971, "Simple Eulerian time correlations of full- and narrow-band velocity signals in grid-generated, 'isotropic' turbulence", J.F.M. Vol. 48-2, p. 273-337

HARRIS V.G., GRAHAM J.A.M., CORRSIN S., 1977, "Further experiments on nearly homogeneous shear flow", J.F.M. Vol. 81, Part 4, p. 657-687

HANJALIC K., LAUNDER B.E., 1980, "Sensitizing the dissipation equations to irrotational strains", Journal of Fluids Engineering, Vol. 102

LAUNDER B.E., REECE G.J., RODI W., 1975, "Progress in the development of a Reynolds stress turbulent closure", J.F.M. Vol. 68, Part 3, p. 537-566

LESIEUR M., SCHERTZER D., 1978, "Amortissement auto-similaire d'une turbulence à grand nombre de Reynolds", Journal de Mécanique, Vol. 17-4, p. 609-646

ORSZAG S., 1970, "Analytical theories of turbulence", J.F.M., Vol. 41-2, p. 363-386

ORSZAG S., PATTERSON G.R., 1971, "Numerical simulation of turbulence", Lecture Notes in Physics, Vol. 12, p. 127-147

REYNOLDS W.C., 1975, "Computation of turbulent flows", Report n° TF4 Thermosciences Division, Department of Mechanical Engineering, STANFORD University

WIGELAND R.A., NAGIB H.M., 1978, "Grid-generated turbulence with and without rotation about the streamwise direction", IIT Fluids and Heat Transfer Report R78-1, ILLINOIS Institute of Technology, CHICAGO

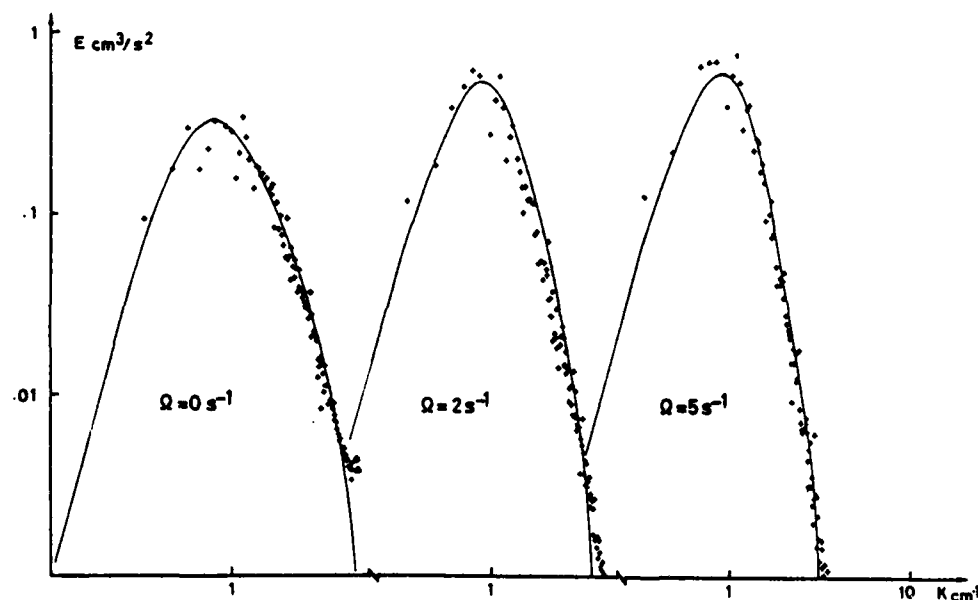


Figure 1

Comparison between direct simulations and EDQNM computations of low Reynolds number, rotating turbulence

+ direct simulations
- EDQNM computations

Figure 2

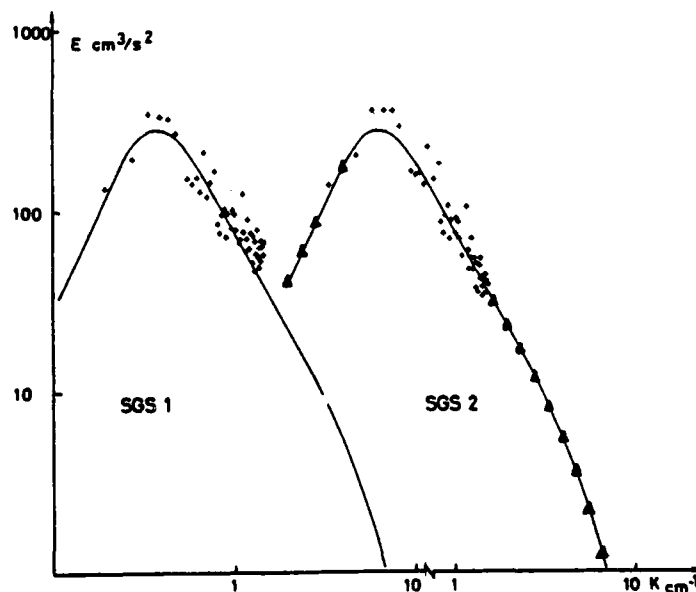
Figure 2

Comparison between large eddy simulations and EDQNM computation of rotating turbulence

+ large eddy simulation

Δ EDQNM evaluation of the small scales together with the large eddy simulation

- EDQNM computation



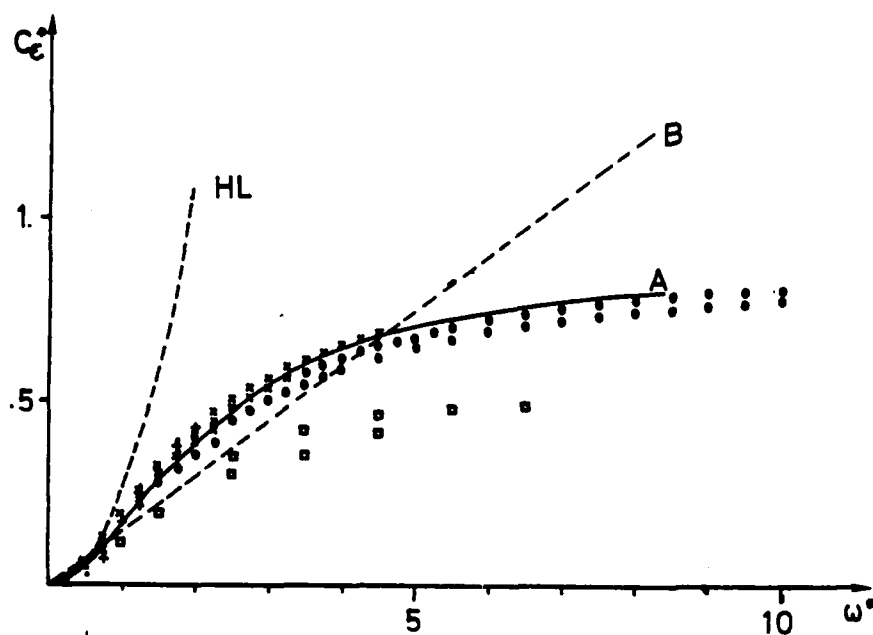


Figure 3

Modification of the ϵ transport equation

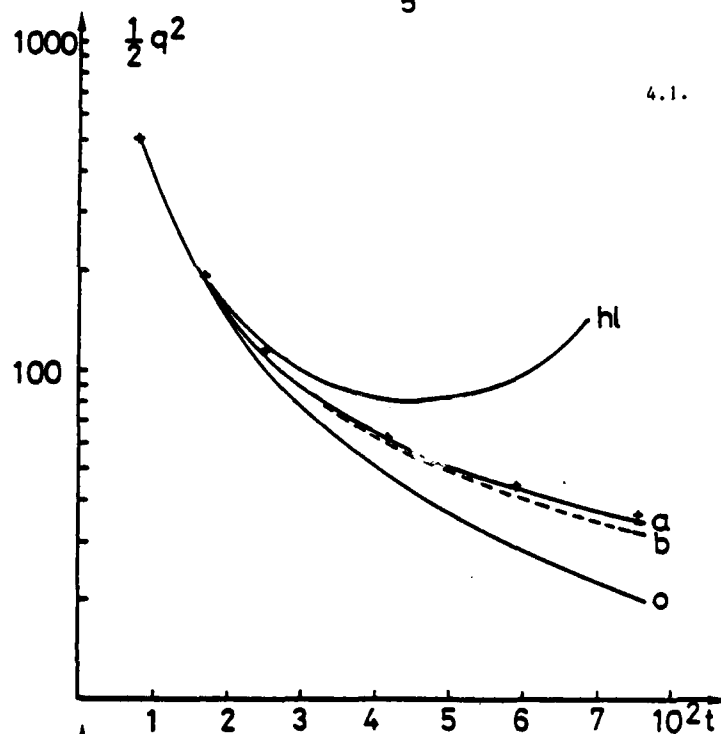
x o + EDQNM computations

□ very low Reynolds number EDQNM computations

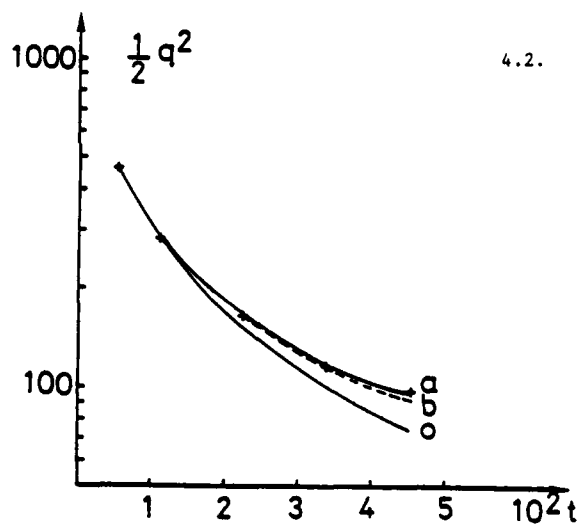
A present model

B BARDINA model

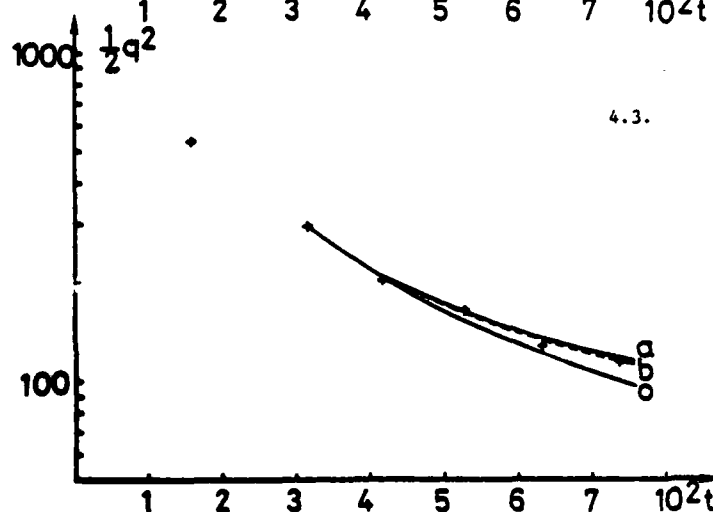
HL HANJALIC and LAUNDER model



4.1.



4.2.



4.3.

Figure 4

Comparison of the one-point closures - WIGELAND and NAGIB experiment

4.1. Screen 5 $U = 6$ m/s $\Omega = 80$ rad/s

4.2. Screen 5 $U = 9$ m/s $\Omega = 80$ rad/s

4.3. PG2 Screen $U = 6$ m/s $\Omega = 80$ rad/s

+ experiments

o standard ($1/2 q^2$, ϵ) model

a present model

b BARDINA model

hl HANJALIC and LAUNDER model

ERRATUM : Due to a bug in our code, the conclusions of § 6.b. have to be revised. Both BARDINA and present model improve the prediction for low and high shears.

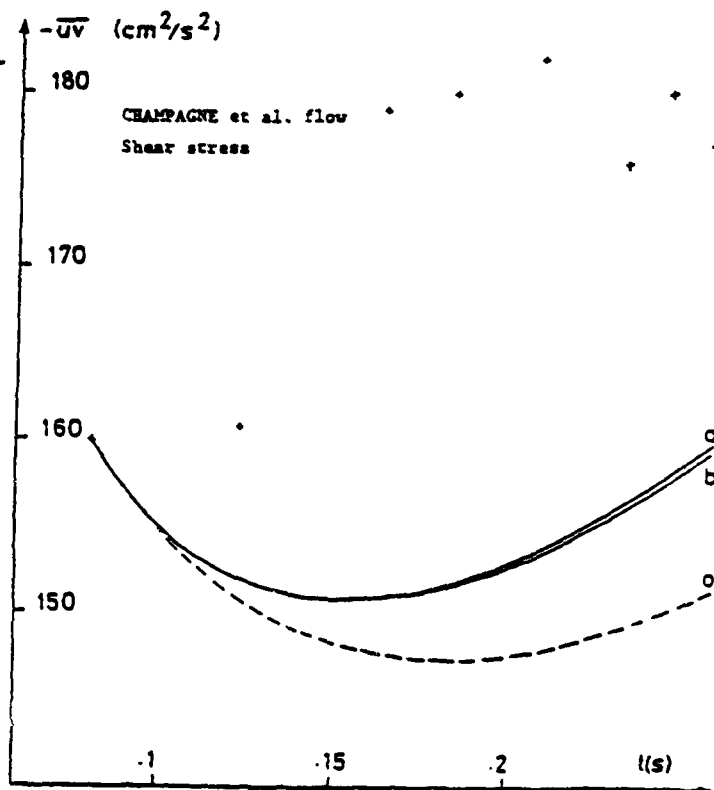
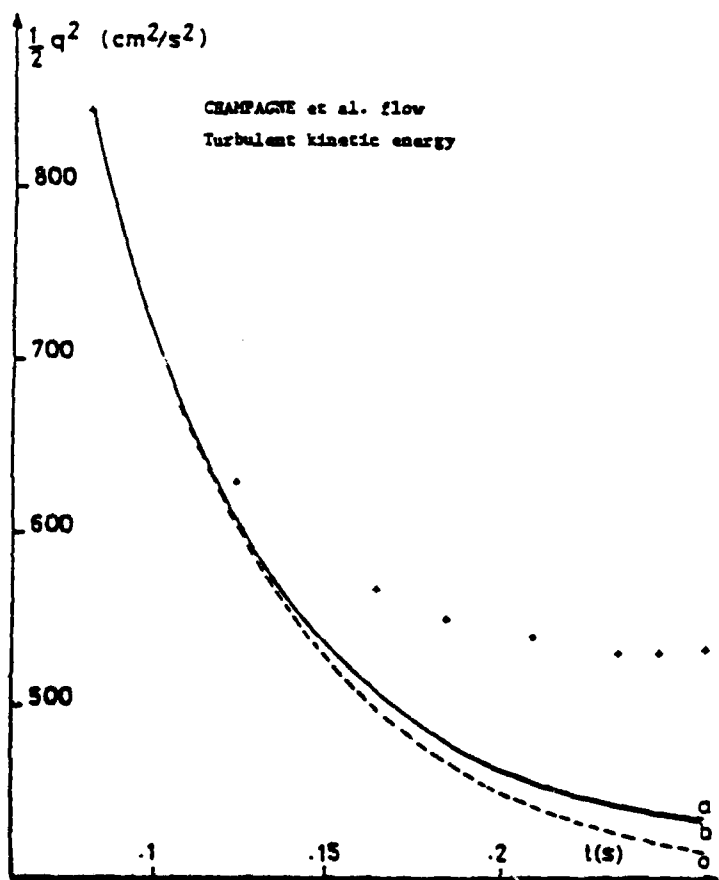
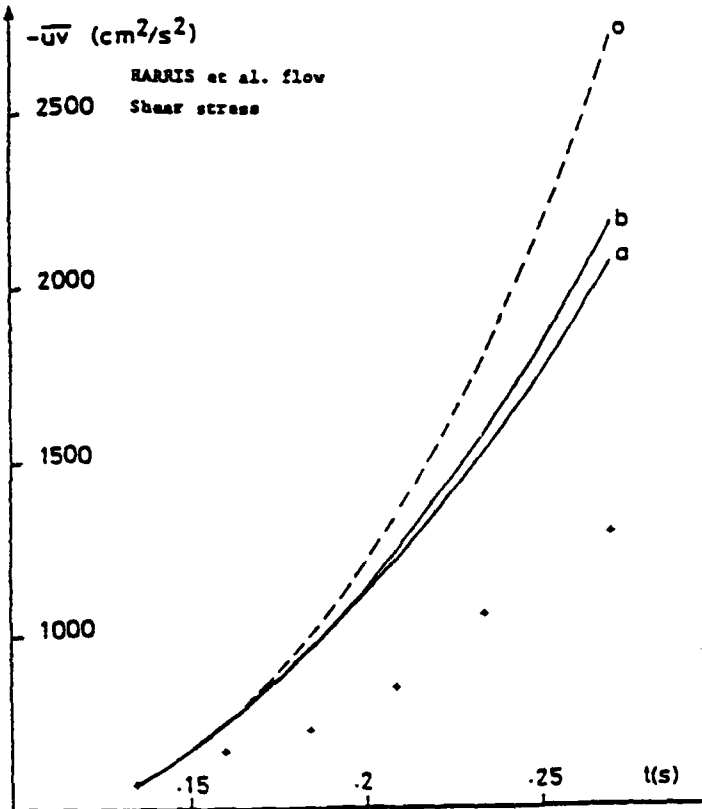
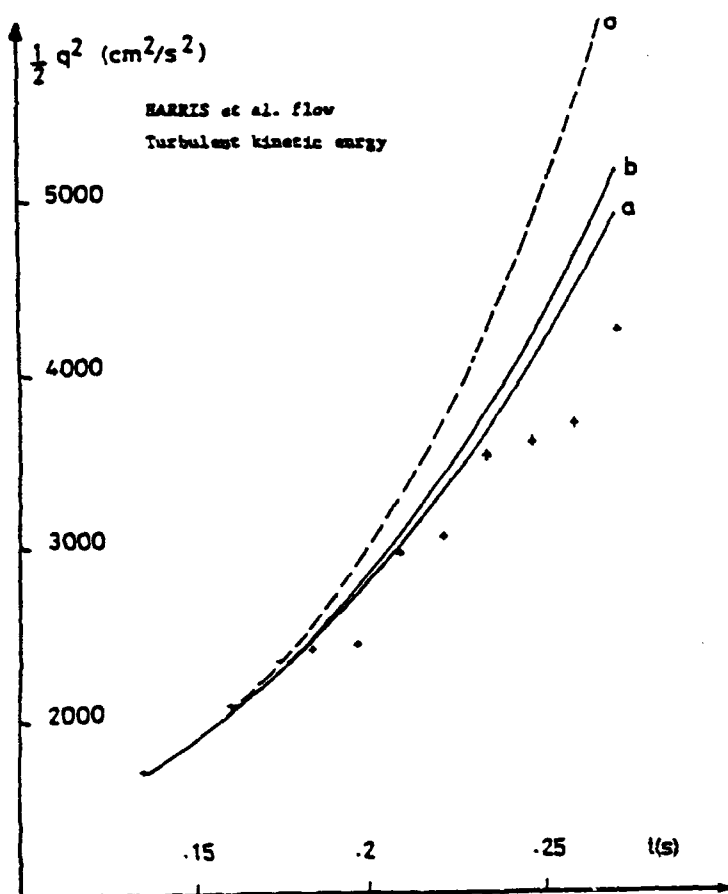


Figure 5

Shear flows experiments - Computation with the LAUNDER-REECI-RODI model for the Reynolds stresses transport equations.
 * experiments o standard ϵ equation
 a present model b BARDINA model

AD-A135 034

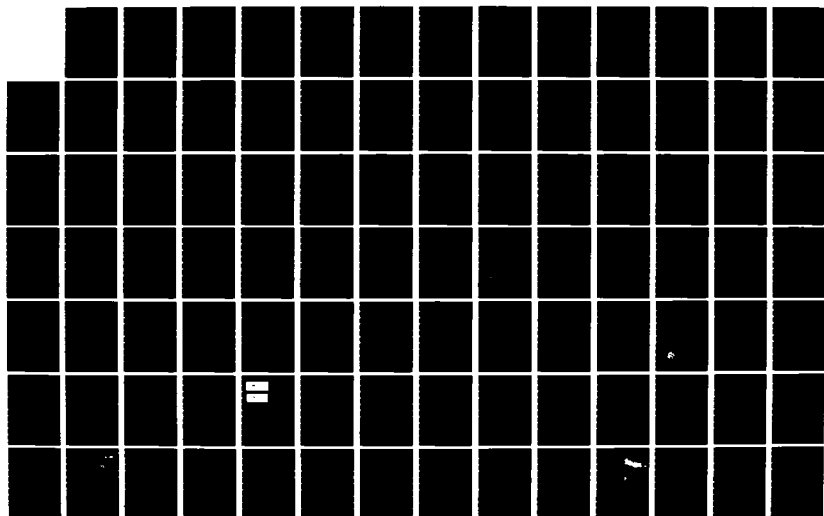
SYMPOSIUM ON TURBULENT SHEAR FLOWS (4TH) HELD AT
KARLSRUHE UNIVERSITY (GERMANY FR) 12-14 SEPTEMBER 1983
(U) KARLSRUHE UNIV (GERMANY F R) SEP 83

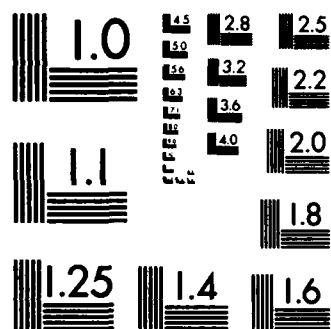
4/7

UNCLASSIFIED

F/G 28/4

NL





MICROCOPY RESOLUTION TEST CHART
NATIONAL BUREAU OF STANDARDS-1963-A

TWO-POINT CLOSURES AS A SUBGRID SCALE MODELING FOR LARGE EDDY SIMULATIONS

J.P. CHOLLET

Institut de Mécanique de Grenoble,
C.N.R.S. (L.A. 6), Université de Grenoble

and

National Center for Atmospheric Research
Boulder, Colorado 80307

ABSTRACT

A two-point statistical closure -the Eddy Damped Quasi Normal Markovianized (E.D.Q.N.M.)-approximation is used to model subgrid scales (SGS) in a large eddy simulation (L.E.S.) of three-dimensional homogeneous turbulence. First, eddy viscosity and diffusivity are derived from the hypothesis of a $k^{-5/3}$ energy spectrum to parameterize the small scale velocity and passive scalar fields. Then the distribution of energy among the small scales is taken into account completely. Finally the numerical simulation of large eddies is assessed from the standpoint of Predictability studies.

1. INTRODUCTION AND EQUATIONS

The velocity field of a three-dimensional high Reynolds number flow cannot be computed over the whole range of scales of interest, even when using the most powerful computers currently available. Therefore, the velocity field is computed explicitly in the large scales only, taking account of the small scales statistically, in order to at least ensure some dissipation of energy. We have to couple a large eddy simulation (L.E.S.) -numerical solution of the equations of the flow field- to a statistical model of small scales. The two-point closures are able to represent in a statistical sense the distribution of energy among the various scales and the interactions between the large scales (completely calculated through the L.E.S.) and the small scales (S.G.S., modeled statistically). We use the eddy damped quasi-normal Markovianized (E.D.Q.N.M.) approximation, extensively described with references to satisfactory comparisons with numerical results and experiments, in Larcheveque et al. (1980) and Herring et al. (1982). For the purpose of tractable EDQNM computations, we have to assume homogeneity and isotropy.

We focus our attention on the free-decay turbulence whose small-scale energy evolves in time; in stationary flows some empirical modeling can be adjusted (as illustrated by Siggia and Patterson, 1978), even if it takes some computing time and lacks strong theoretical justification. In most of our calculations, we consider initial velocity fields with zero energy in the small scales, in such a way that we can check upon a realistic evolution of the SGS transfers, whether or not an inertial subrange exists.

The equations to be considered for a numerical LES of the velocity field are:

$$\left[\frac{\partial}{\partial t} + \nu k^2 \right] u_i(\vec{k}, t) = -i k_m P_{ij} \int_{\vec{p} + \vec{q} = \vec{k}} u_j(\vec{p}, t) u_m(\vec{q}, t) d\vec{p} + T^> \quad (1.1)$$

$|\vec{p}|, |\vec{q}| < k_c$

with the usual notations and $P_{ij} = \delta_{ij} - k_i k_j / k^2$.
For small scales $|\vec{k}| > k_c$: the time-evolution of the energy spectrum $E(k, t)$

$$\left[\frac{\partial}{\partial t} + 2\nu k^2 \right] E(k, t) = \iint_{\substack{\vec{p} + \vec{q} = \vec{k} \\ p, q > k_c}} S(k, p, q) dp dq + T^<(k|k_c, t) \quad (1.2)$$

The formulation of $S(k, p, q)$ is not described in detail here; it is related to the values of the energy spectrum $E(k, t)$ over the whole range of wave-numbers in a way which depends on the particular closure used (here the EDQNM approximation).

The interactions between large and small scales are represented by $T^>$ and $T^<$. The large scales are affected by the small scales through $T^>$ (i.e., a global effect of energy dissipation).

$$T^> = -i k_m P_{ij} \int_{\substack{\vec{p} + \vec{q} = \vec{k} \\ |\vec{p}| \text{ or } |\vec{q}| > k_c, |\vec{k}| < k_c}} u_j(\vec{p}, t) u_m(\vec{q}, t) d\vec{p} \quad (1.3)$$

The subgrid-scale modeling we define is based upon the distribution of energy $E(k, t)$ and is necessarily isotropic. An eddy-viscosity formulation, suggested by Kraichnan (1976), is convenient and its spectral formulation used here can be related to the classical notions of eddy-viscosity and mixing length (Lesieur and Chollet, 1980).

$$T^> = -\nu(k|k_c, t) k^2 u_i(\vec{k}, t) \quad (1.4)$$

As we define $\nu(k|k_c, t)$ statistically, we derive it from a transfer of energy:

$$\nu(k|k_c, t) = -T^>(k|k_c, t) / 2k^2 E(k, t) \quad (1.5)$$

with

$$T^>(k|k_c, t) = \iint_{\substack{\vec{p} + \vec{q} = \vec{k} \\ p \text{ or } q > k_c, k < k_c}} S(k, p, q) dp dq \quad (1.6)$$

The large scales affect the small scales through $T^<$ (i.e., a global effect of energy production).

$$T^<(k|k_c, t) = \iint_{\substack{\vec{p} + \vec{q} = \vec{k} \\ p \text{ or } q < k_c, k > k_c}} S(k, p, q) dp dq \quad (1.7)$$

We notice that the coupling terms of the transfer $T^<$ and $T^>$ in (1.6) and (1.7) depend on the distribution of energy $E(k, t)$ over the whole range of wave numbers

We also consider the advection of a passive scalar, that is any fluctuation of temperature or any tracer concentration provided, that it does not react on the velocity field. We do not describe the equations of the scalar field evolution since they are very similar to (1.1) to (1.7) (see Chollet (1983), Chollet and Lesieur (1982)).

In section 2, we derive a simple SGS model which depends on the existence of an inertial subrange. In section 3, we present a more complete coupling of statistical modeling with large eddy computations. We consider high Reynolds number turbulence ; also, we cannot compute a "reference solution" including dissipative scales, and we only check the existence of inertial and inertio-convective spectra up to the cut-off wave-number.

Aupiais and Cousteix (1982) used the same method at lower Reynolds number and obtained results which compared satisfactorily with the experiments by Comte-Bellot and Corrsin.

2. SGS MODELING WITH EDDY-VISCOSITY AND DIFFUSIVITY

To a first approximation, the small scales equation (1.2) reduces to : $E(k,t) \sim k^{-5/3}$ for $k \in [k_c, \infty[$ which makes sense for high Reynolds number flows with $k_c \gg k_\eta$ (k_η is the Kolmogorov dissipation wave number).

As $E(k_c, t)$ is known for $k > k_c$, $t^>$ is the only coupling term to be computed. The large scales are still calculated with (1.1), but we consider a large-scale spectrum $E(k) \sim k^{-5/3}$ to compute $t^>$, which is realistic if k_c is not located at the very beginning of the inertial range. $\nu(k|k_c, t)$ is formulated in a non dimensionalized form :

$$\nu(k|k_c, t) = \nu_c^+(k/k_c) (E(k_c, t)/k_c)^{1/2}$$

as extensively described in Chollet and Lesieur (1981).

The eddy viscosity $\nu_c^+(k/k_c)$ is plotted in Fig. 1, along with the eddy diffusivity $D_c^+(k/k_c)$ and the eddy Prandtl number ν_c^+/D_c^+ ; D_c^+ is derived from the transfer of passive scalar variance T_θ in a way very similar to the derivation of ν_c^+ (Chollet, 1983 ; Chollet and Lesieur, 1982). The only constants are those adjusted for the relaxation times of the EDQNM two-point closure : $\lambda = 0.36$ for the kinetic energy (André and Lesieur, 1977) $\lambda = 0$, $\lambda' = 3.61 \lambda$ for the passive scalar (Herring et al., 1982).

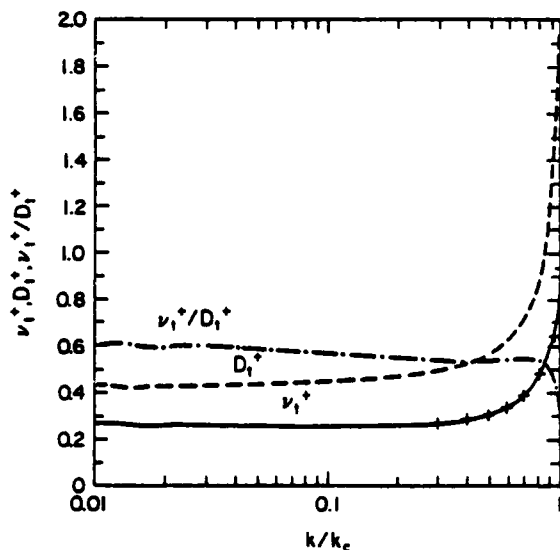


Fig. 1 - Non dimensionalized eddy-viscosity, eddy-diffusivity and eddy Prandtl number. (+ + eddy viscosity from Kraichnan (1976)).

The SGS modeling has been tested first in an EDQNM computation of the whole range of scales since it allows the calculation of a reference solution which includes dissipative scales. Results of such parametrized statistical computation are presented for energy and scalar spectra in Chollet and Lesieur (1982) ; they can be very useful to study long-term decays of energy.

The subgrid-scale modeling has been used in a spectral code of large eddy simulation whose resolution is 32^3 both for the velocity and a passive scalar field ; the eddy Prandtl number ν_c^+/D_c^+ was assumed to be constant and equal to 0.6 as suggested by Fig. 1. In Figs. 2 a) and b) we notice the decay of the spectra and their tendency to obey inertio-convective $k^{-5/3}$ laws.

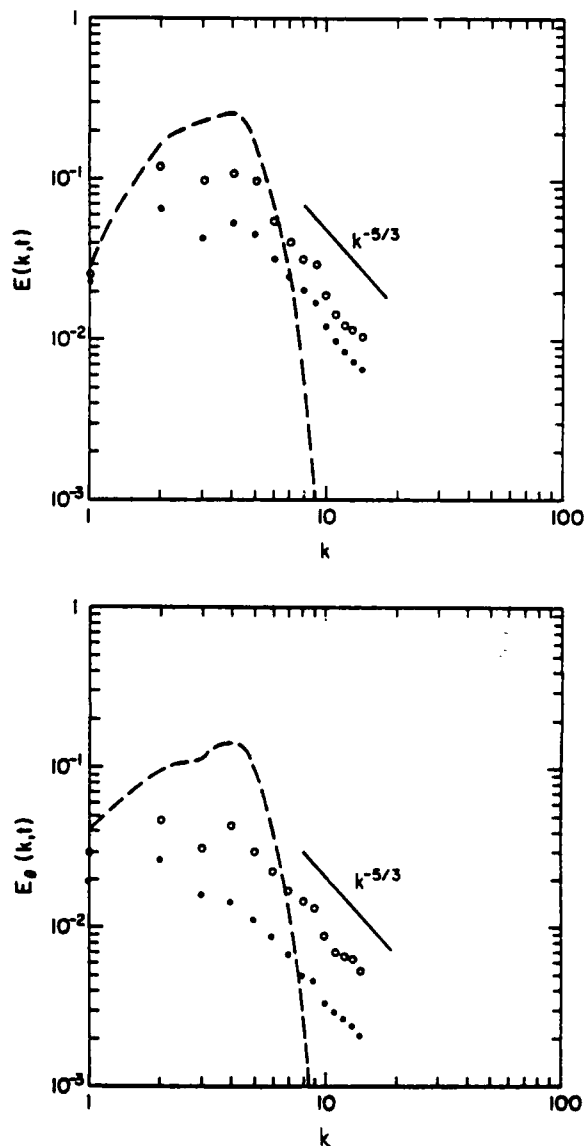


Fig. 2 - L.E.S. with subgrid scale modeling (ν_c^+ of Fig. 1 and $\nu_c^+/D_c^+ = 0.6$).

--- $t = 0.01$; $\circ \circ \circ t = 1.0$ s ;

$\bullet \bullet \bullet t = 2.0$ s

a) kinetic energy : $E(k,t)$; b) scalar variance $E_\theta(k,t)$.

Upon close examination of the cusp of ν_c^+ (Fig. 1), we notice (Chollet, 1983) that we can approximate it with a $(k/k_c)^4$ dependence which means that the eddy viscosity can be viewed as a sum of an eddy viscosity operator (∇^2) and a higher order dissipativity $(\nabla^2)^3$ which is effective for the interactions local to k_c . These dissipation operators can be compared to the very high dissipativity used by Basdevant et al. (1981) in two-dimensional large eddy simulations. This interpretation could be used to translate this spectral parametrization into physical space provided that some attention is paid to the filtering problems.

The way spectra exhibit quite satisfactory $k^{-5/3}$ ranges can be interpreted as an a-posteriori justification for the values of the closure constants, especially for the more debatable values of λ and λ' . (The cusp of

ν_t^+ and D_t^+ , and the influence of a dissipative range in the smallest scales, or non-inertial large scales close to k_c are analysed in Chollet, 1983.

3. FULL STATISTICAL MODELING OF SMALL SCALES

The assumption of a $k^{-5/3}$ spectrum used to derive a SGS modeling is not very realistic for :

- (1) free-decay spectra when the spectra are steeper than $k^{-5/3}$,
- (2) k_c close to k_η (where k_η is the Kolmogorov dissipation wave number),
- (3) k_c close to the very beginning of the inertial range.

To take full account of the distribution of energy over the whole range of wave numbers, we have to solve completely (1.1) and (1.2) and formulate the coupling terms $T^<$ and $T^>$.

The large scales are computed with the 32^3 spectral code mentioned in section 2 and the small scales are computed with the EDQNM code already used in statistical computations (Chollet and Lesieur, 1981).

The time evolutions of the large scales ($k < k_c$) and the small scales ($k > k_c$) are linked only by the coupling terms (1.4) and (1.7). At every time-step, the evolution of the energy spectrum of small scales is calculated with (1.2) and the evolution of the velocity field in large scales is calculated with (1.1). The coupling terms $T^>$ and $T^<$ are derived from an energy spectrum $E(k)$ whose :

- (1) small-scales contributions come from the EDQNM evolution (1.2)
- (2) large-scales contributions come from averaging spectra on the computed velocity field

The results pertaining to a time evolution of a realization of the velocity field are given in Fig. 3 (the initial energy is still zero for $k > k_c$). We observe the tendency toward the inertial range and the continuity of the energy spectrum when going across k_c .

This continuity is also observed on Fig. 4, which shows the total energy flux and the flux associated to the "coupling terms" of the energy transfer.

We have not attempted to study in detail the "coupling" procedure since it is much more expensive than the ν_t^+ procedure of section 2, especially with our numerical code whose EDQNM part could not be vectorized. We only aim at proving the feasibility of the procedure. From what we know about the EDQNM and LES computations of the scalar field, we can infer that such a coupling procedure is also valid for any numerical simulation of a scalar field.

4. PREDICTABILITY OF LARGE SCALES, FROM LES RESULTS

In a large eddy simulation, the subgrid scales are not calculated in detail ; by comparison with the large scales, they can be considered as computed with some unspecified (in nature and amount) inaccuracies and errors. These errors contaminate the large scales in a finite time, which impairs the relevance of the numerical simulation ; this is a problem of "predictability" of large scales.

The initial fields we consider correspond to evolved solutions of simulations with their energy distributed over a wide range of wave-numbers including scales beyond the cut-off k_c . The corresponding initial energy spectrum exhibits a $k^{-5/3}$ inertial range. We compare two realizations $u^{(1)}$ and $u^{(2)}$ of the velocity field beginning with the same initial field except in the smallest scales. We refer here to two methods to create the initial decorrelation in the small scales (characteristics are given in table 1) :

- (1) two different cut-off wave-numbers $k_c^{(1)} < k_c^{(2)}$ but the fields are identical for $k < k_c^{(2)}$; this straight forward method corresponds to a study of the dependance of results with the amount of small scales used by the numerical simulation.
- (2) $k_c^{(1)} = k_c^{(2)}$, a range of high wave numbers is altered in a proper way - a rotation of each velocity vector whose axis is in the direction of the wave vector -. Unfortunately the intensity of this alteration has to be quite strong

in order not to be swept out by the eddy viscosity.

In this section, all the computations use the SGS modeling described in section 2.

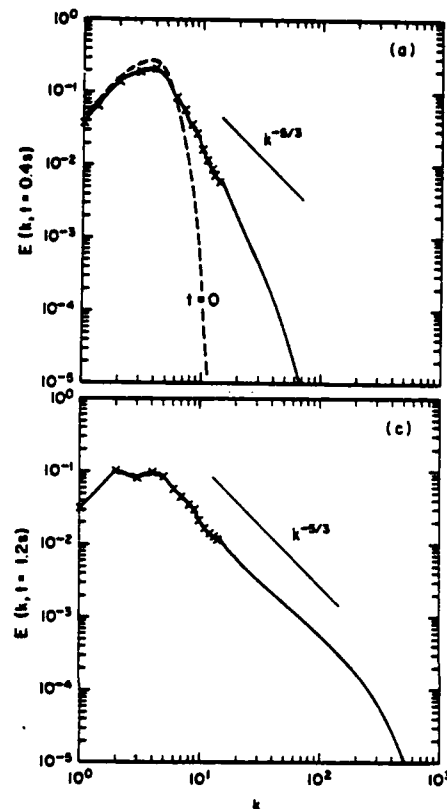


Fig. 3 - L.E.S. with full coupling in a decay experiment of velocity field (x x x LES).

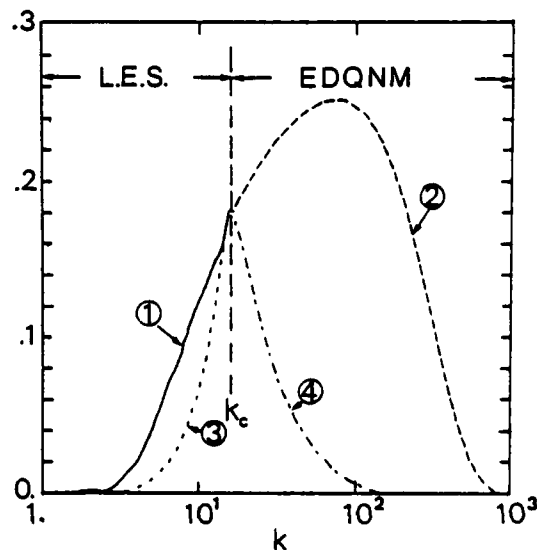


Fig. 4 - Energy flux in a LES with full coupling (at $t = 1.2$ sec)

- (1) total flux from LES : $-\int_{k_c}^k T(k) dk$
- (2) total flux from EDQNM : $\int_{k_c}^k T(k) dk$
- (3) from SGS modeling : $\int_{k_c}^k \tau(k) dk$
- (4) from large scales modeling : $\int_{k_c}^k \tau(k) dk$

Instead of the cross-spectrum $E_{\Delta}(k)$ previously used in Chollet and Lesieur (1981) for preliminary studies of decorrelation, we prefer the more significant "error spectrum" $E_{\Delta}(k) = E(k) - E_W(k)$. The initial distribution of error-energy $E_{\Delta}(k)$ is not controlled since it is just a consequence of the initial alteration of the field in the smallest scales; this is a difference between these computations and the predictability calculations done by Metais et al. (1983) with a statistical (EDQNM) approach in the same case of freely decaying turbulence. The schematic spectra of figure 5 show differences and similarities between a closure and a LES approach for predictability studies, especially because we simulate only a short range of wave-numbers in the explicitly computed scales of the LES.

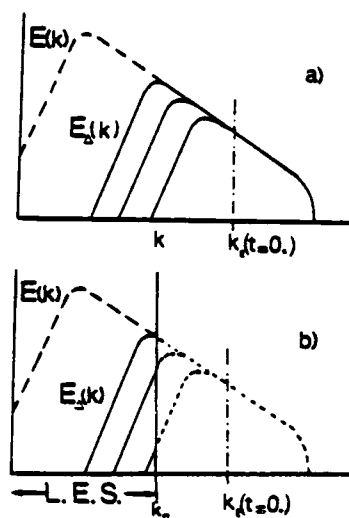


Fig. 5 - Contamination of energy spectra by small scale errors.

- a) in statistical computations.
- b) in LES computations.

A time-evolution of energy spectra and error spectra for LES calculations is shown in fig. 6. We note that in spite of the different methods used to create the initial decorrelation in small scales, the evolutions are quite similar. Moreover, the increasing range of the error-spectra seems to behave like k^4 , in agreement with the analysis by Metais et al. (1983), using properties of the EDQNM closure.

Run	$k_c^{(1)}$	$k_c^{(2)}$	alteration of u(2)	symbols in Fig. 7
3031	15.	14.	(1)	— — —
3047	15.	10.	(1)	■ ■ ■
3041	15.	15.	(2) at $k = 10$.	○ ○ ○
3046	15.	15.	(2) for $k \in [10, k_c^{(2)}]$	▲ ▲ ▲
1920	15.	13.	(1)	● ● ●

Table 1

To characterize the contamination of the scales by the error, we define a wave-number k_E :

$$F = E_{\Delta}(k_E, t) / E(k_E, t)$$

This "local" parameter is more suitable than the relative amount of the error:

$$r(t) = \int_0^{\infty} E_{\Delta}(k, t) / \int_0^{\infty} E(k, t)$$

in order to use quantities which do not depend explicitly on small scales ($> k_c^{(2)}$) or on large scales which cannot be calculated very accurately. The value of f can be chosen arbitrarily since the increasing part of the spectrum behaves like k^4 . In order to include k_E in

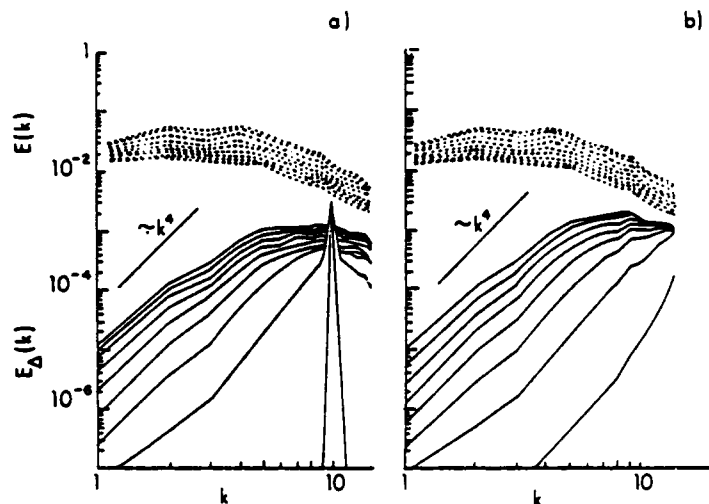


Fig. 6 - Energy spectra $E(k)$ and error-spectra $E_{\Delta}(k)$, every 0.4 sec (the initial large eddy turnover time is 0.18 sec).
a) run 3031 ; b) run 3041.

the range of calculated wave-numbers, we choose $f = 0.01$. The evolution of k_E is drawn in fig. 7, we note that it does not depend on the way the initial decorrelation is generated, at least after some time. The t^{-1} law is in agreement with the EDQNM results of Metais et al. (1983).

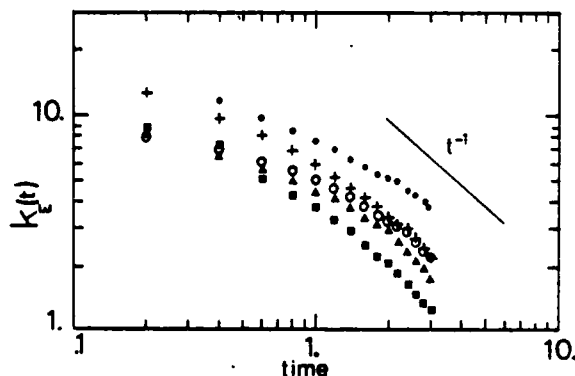


Fig. 7 - Evolution with time of the error wave number k_E (symbols in table 1).

From these results, it appears that the decorrelation evolves with time independently of the way it is generated. There is no major difference between dropping a range of small scales or keeping them after some alteration. The contamination of the large scales of a two-dimensional turbulence would be quite different (Metais et al. 1983) with an error spreading first over the whole range of scales; a paradoxical conclusion could be that three-dimensional LES are more accurate than two-dimensional LES, even with a lower resolution.

CONCLUSIONS

The statistical theories (here, the EDQNM approximation) provide a consistent model of subgrid scales in three-dimensional turbulence. Large Eddy Simulations of velocity and scalar fields exhibit good $k^{-5/3}$ inertio-convective spectra up to the cut-off wavenumber even when there is no energy in the initial field for $k > k_c$.

As the LES computation is independent of the EDQNM code except for the SGS model, these results can be

interpreted as a validation of the values attributed to the closure-constants ; on the other hand, it justifies the concepts of eddy-viscosity and diffusivity.

To drop any assumption of an inertial range, we have considered the coupling of a full statistical description of the small scales and the numerical computation of the velocity field for large scales. This method can be used to compute turbulence with any value of the Reynolds number and any shape of the energy spectrum, and with no constraints on the relative location of the cut-off with respect to integral scales. Even with this improvement, the SGS model is only statistically relevant and any information about phases correlation on either side of k_c is lost. Predictability concepts can be used to estimate the relevance of results from LES, giving rise to other tests for the validation of SGS modeling.

ACKNOWLEDGMENTS

We are grateful to M. Lesieur and J.R. Herring for comments and suggestions, to N. Dalfes for help in using efficiently the computer at NCAR, to D. Harvey for reviewing the english manuscript, to M. Meneguzzi for providing the numerical code used as a basis to develop the simulation. The simulations were performed on the CRAY 1 at NCAR. The National Center for Atmospheric Research is sponsored by the National Research Foundation.

REFERENCES

- André, J.C., and M. Lesieur, 1977, "Influence of helicity on the evolution of isotropic turbulence at high Reynolds number", *J. Fluid Mech.*, 81, 181.
- Aupoix, B., and J. Cousteix, 1982, "Modèles simples de tensions de sous-maille en turbulence homogène isotrope", *Rech. Aerosp.*, 1982-4, 273.
- Basdevant, C., B. Legras, R. Sadourny and M. Beland, 1981, "A study of barotropic model flows : Intermittency, waves and predictability", *J. Atmos. Sci.*, 38, 2305.
- Chollet, J.P., 1983, "Statistical closure to derive a subgrid-scale modeling for large eddy Simulations of three-dimensional turbulence", NCAR Technical Note, TN-206 + STR.
- Chollet, J.P., and M. Lesieur, 1981, "Parametrization of small scales of three-dimensional isotropic turbulence utilizing spectral closures", *J. Atmos. Sci.*, 38, 2747.
- Chollet, J.P., and M. Lesieur, 1982, "Modélisation sous-maille des flux de quantité de mouvement et de chaleur en turbulence tridimensionnelle isotrope", to be published in *La Météorologie*.
- Herring, J.R., D. Schertzer, M. Lesieur, G.R. Newman, J.P. Chollet and M. Larcheveque, 1982, "A comparative assessment of spectral closures as applied to passive scalar diffusion", *J. Fluid Mech.*, 124, 411.
- Kraichnan, R.H., 1976, "Eddy viscosity in two and three dimensions", *J. Atmos. Sci.*, 33, 1521.
- Larcheveque, M., J.P. Chollet, J.R. Herring, M. Lesieur, G.R. Newman and D. Schertzer, 1980, "Two-point closure applied to a passive scalar in decaying isotropic turbulence", in *Turbulent Shear Flow II*, Springer-Verlag, 50.
- Lesieur, M., and J.P. Chollet, 1980, "Introduction aux théories statistiques de la turbulence", in *Bifurcation and Nonlinear Eigenvalue Problems*, Springer-Verlag, Lecture Notes in Mathematics, 101.
- Métais, O., J.P. Chollet and M. Lesieur, 1983, "Predictability of the large scales of freely evolving three and two-dimensional turbulence", *Proceedings of the Workshop on "Predictability of Fluid Motions"*, La Jolla Institute, ed. by G. Holloway and S.J. West, (Springer-Verlag), to be published.
- Siggia, E.D., and G.S. Patterson, 1978, "Intermittency effects in a numerical simulation of stationary three-dimensional turbulence", *J. Fluid Mech.*, 86, 567.

STUDY OF SUBGRID MODELS FOR SHEARED TURBULENCE

J.P. BERTOGLIO and J. MATHIEU
Laboratoire de Mécanique des Fluides
Ecole Centrale de Lyon
36, Av. Guy de Collongue
F 69130 Ecully-France

ABSTRACT

The validity of the usual subgrid models for Large Eddy Simulations is discussed for anisotropic turbulence. We study the transfer between large eddies and subgrid scales in the framework of a two-point closure. An eddy-viscosity model is thereafter used to parameterize the small scales in a two-point closure computation. Comparisons are made with the results of the same two-point closure applied to the whole turbulent spectrum. The results presented in this paper have been obtained in the case of an homogeneous shear flow. They show the limits of eddy viscosity subgrid models for non isotropic turbulence.

NOMENCLATURE

- $G(\vec{K})$: filter in Fourier space
 $\bar{u}_i(\vec{K})$: large scale velocity field
 $= G(\vec{K}) u_i(\vec{K})$
 $\langle U_i \rangle$: mean velocity field
 $\Phi_{ij}(\vec{K})$: three-dimensional spectral tensor
 $\bar{\Phi}_{ij}(\vec{K})$: filtered three-dimensional spectral tensor
 $T_{ij}(\vec{K})$: three-dimensional spectral transfer
 $T_{ij}^>(\vec{K})$: contribution of the small scales to the three-dimensional spectral transfer
 $T_{ij}^{+>}(\vec{K})$: part of $T_{ij}^>$ called backscatter or input
 $T_{ij}^{->}(\vec{K})$: part of $T_{ij}^>$ called drain or output
 $\varphi_{ij}(K)$: integral of $\bar{\Phi}_{ij}$ over a spherical shell of radius K
 $t_{ij}(K)$: integral of $T_{ij}^>$ over a spherical shell of radius K
 $\nu_e(K)$: eddy viscosity

1 INTRODUCTION

Nowadays direct numerical simulation is certainly one of the major tools for the study and prediction of turbulence. At low Reynolds number, it is possible to make a Full Simulation over the whole range of scales of the turbulent spectrum. For large Reynolds number flows, this is not possible : only the large eddies of such flows can be captured on a computational mesh. The small scales, or subgrid scales, have to be modeled. The problem of parameterizing these small scales is of very large importance today since Large Eddy Simulation (L.E.S.) is becoming very popular.

Most of the subgrid scale models are based on the concept of eddy viscosity. This concept postulates that the motion of small scales is introducing a viscosity in the equation for the large scales, in the same way as molecular thermal agitation is responsible for the viscous term in the Navier Stokes equation. To be rigorously justified this assumption supposes a separation of scales between large and small eddies, which generally does not occur in turbulence. Nevertheless eddy viscosity is used for L.E.S., its main advantage being that it at least ensures a drain of energy from the explicit scales to the subgrid scales. In the particular case of isotropic homogeneous turbulence, this drain of energy being the very preponderant effect of small scales, eddy viscosity formulations have been shown to lead to good predictions of the turbulent kinetic energy decay.

In return, for anisotropic turbulence, the validity of eddy viscosity models seems to be more questionable. In particular, in the case of homogeneous turbulence submitted to a uniform shear, comparisons between Large Eddy Simulation on a coarse grid and Full Simulation on a refined mesh have shown important disagreements (see Mc Millan et al. (1980)).

Since Kraichnan (1976) first suggested that the Direct Interaction Approximation was providing an analytical framework in which to investigate eddy viscosity concepts, two point closures have been extensively used for this purpose. The Eddy Damped Quasi Normal Markovian closure has in particular been very helpful (see Leslie (1979) and Lesieur (1981)). Such studies resulted in a better understanding of the physical mechanisms operating, in a partial justification of eddy viscosity, and in subsequent improvements of the usual formulations. In particular the dependence of the eddy viscosity with the wavenumber has been investigated, and numerical values have been proposed. Very recently the dependence with the Reynolds number has been taken into account by proposing methods coupling E.D.Q.N.M. with L.E.S. (see Chollet (1983) in the present volume, and Aupoix (1983)).

At the present time, all these studies have essentially been confined to the field of isotropic turbulence*. This is very restrictive and seems to make their relevance to Large Eddy Simulation of any real industrial problem very doubtful. The aim of the present paper is to extend the investigation to anisotropic homogeneous turbulence. Our tool will be the EDQNM closure applied to homogeneous shear flows. It will be shown that if the eddy viscosity formulation remains acceptable for the part of the interaction accounting for the drain of energy from the large scales to the small scales, it is inadequate for the term traducing a return of energy from the subgrid (input term in Kraichnan (1976) or backscatter in Leslie (1979)).

* In Leslie (1979), an extension to non isotropic turbulence is proposed, but strong assumptions concerning anisotropy are made.

The second part of the paper is intended to determine whether the error introduced when using eddy viscosity in non isotropic turbulence is liable to alter the behaviour of large eddies. For this purpose, we shall compare the results of an EDQNM computation of the whole spectrum of a sheared turbulence with the results of the same EDQNM model in which the effects of the small scales are parameterized by an eddy viscosity. In both cases, the EDQNM closure will not be treated in a straightforward way. A modeled form, previously derived by Bertoglio (1981), will be used since the complete calculation would result in too cumbersome computations.

2 STUDY OF THE SPECTRAL TRANSFER BETWEEN LARGE AND SMALL SCALES OF AN HOMOGENEOUS TURBULENCE: EQUATIONS

We make the usual decomposition of the velocity field:

$$U = \bar{U} + U'$$

in which \bar{U} corresponds to the large scales or explicit scales, and U' denotes the subgrid scales. The explicit scales are defined by using a filtering process

$$\bar{U}(\vec{x}) = \int_{\mathbb{R}^3} G(\vec{x}-\vec{x}') U(\vec{x}') d\vec{x}' ,$$

which can easily be written in spectral space:

$$\bar{U}(\vec{k}) = G(\vec{k}) U(\vec{k}) ,$$

$G(\vec{k})$ being the Fourier transform of $G(\vec{x})$.

It must be pointed out that, even if the filtering operation often consists in an "average" over a small volume in X space, no statistical average is introduced by the filter.

We now make the Reynolds decomposition of both \bar{U} and U' :

$$\bar{U} = \langle \bar{U} \rangle + \bar{u}$$

$$U' = \langle U' \rangle + u'$$

by introducing a statistical average over an ensemble of realizations: $\langle \rangle$.

The average of the subgrid scale $\langle U' \rangle$ is very often equal to zero. This will in particular be true for homogeneous turbulence ($\langle U' \rangle$ will only have a non zero contribution in the case of strong inhomogeneities having scales comparable to the computing mesh). We shall then identify \bar{u} and u' .

Starting from the Navier Stokes equation written in spectral space, one can easily obtain the equation for the turbulent fluctuation

$$u = U - \langle U \rangle$$

By filtering, it is then straightforward to obtain the equation for the large scales in which the contributions of small scales can be isolated by writing

$$U(\vec{k}) = G(\vec{k}) U(\vec{k}) + (1-G(\vec{k})) U(\vec{k})$$

$$U(\vec{k}) = G(\vec{k}) U(\vec{k}) + (1-G(\vec{k})) U(\vec{k})$$

The resulting equation is:

$$\left\{ \frac{\partial}{\partial t} + \nu K^2 + i K_\ell \langle U_\ell \rangle \right\} \bar{u}_i(\vec{k}) = \frac{\partial \langle U_\ell \rangle}{\partial x_m} \left\{ K_\ell \left(\frac{\partial \bar{u}_i(\vec{k})}{\partial k_m} - \frac{K_i \bar{u}_m(\vec{k})}{K^2} \right) + P_{i\ell}(\vec{k}) \bar{u}_m(\vec{k}) \right\} - \frac{i}{2} P_{ijm}(\vec{k}) \int_{\vec{p}+\vec{q}=\vec{k}} \left\{ \underbrace{G(\vec{k}) G(\vec{p}) G(\vec{q})}_{\text{I}} + \underbrace{G(\vec{k}) [G(\vec{p})(1-G(\vec{q})) + G(\vec{q})(1-G(\vec{p}))]}_{\text{II}} + \underbrace{G(\vec{k}) (1-G(\vec{p})) (1-G(\vec{q}))}_{\text{III}} \right\} u_j(\vec{p}) u_m(\vec{q}) d\vec{p} d\vec{q} \quad (1)$$

in which

$$P_{ijm}(\vec{k}) = K_j P_{im}(\vec{k}) + K_m P_{ij}(\vec{k})$$

with

$$P_{ij}(\vec{k}) = \delta_{ij} - \frac{K_i K_j}{K^2}$$

The integral in (1) extends over all wavevectors and which can form a triad such as $\vec{k} = \vec{p} + \vec{q}$.

It is relevant to note at this point that:

- the first term of the left-hand-side of (1) is accounting for the effects of the mean velocity gradients and does not involve subgrid scale contributions. This term will therefore be exactly taken into account by L.E.S.
- term I corresponds to triadic interactions between large scales (and is therefore exactly taken into account by L.E.S.).
- term II corresponds to triadic interactions involving one subgrid mode.
- term III corresponds to triadic interactions involving two subgrid modes.

In physical space, term III corresponds to the term called true subgrid

$$\frac{\partial \bar{u}_i \bar{u}_j}{\partial x_j}$$

meanwhile term II corresponds to the cross term:

$$\frac{\partial \bar{u}_i u_j}{\partial x_j} + \frac{\partial u_i \bar{u}_j}{\partial x_j}$$

Multiplying (1) by $\bar{u}_i(-\vec{k})$ and averaging give the equation for $\langle \bar{u}_i(\vec{k}) \bar{u}_j(-\vec{k}) \rangle$. This equation leads to the equation for the filtered three-dimensional spectrum $\Phi_{ij}(\vec{k})$ by using the classical relation

$$\langle \bar{u}_i(\vec{k}) \bar{u}_j(-\vec{k}) \rangle = \Phi_{ij}(\vec{k}) \delta(\vec{k}+\vec{k})$$

We close this last equation in the frame of the Eddy Damped Quasi Normal Markovian approximation. This closure is appropriate to the present problem because of its good behaviour in the inertial range of the spectrum.

We can symbolically write the E.D.Q.N.M. assumption:

$$\langle uuuu \rangle = \sum \langle uu \rangle \langle uu \rangle - \mu \langle uuuu \rangle$$

which is used to close the equation for the third order correlation

$$\frac{\partial \langle uuuu \rangle}{\partial t} = \left\langle \frac{dU}{dx} \right\rangle \langle uuuu \rangle + \langle uuuu \rangle - \nu \langle uuuu \rangle$$

The term $\langle \frac{\partial u_i}{\partial x_j} \rangle \langle u_i u_j u_k \rangle$ explicitly accounting for the direct action of the mean velocity gradients on triple moments is furthermore neglected. This last assumption has been previously introduced by Cambon (1981) and Bertoglio (1981) and will not be discussed here.

We finally obtain :

$$\left\{ \frac{\partial}{\partial t} + 2\nu k^2 \right\} \bar{\Phi}_{ij}(\vec{k}) = \text{terms exactly taken into account by L.E.S.} + T_{ij}^{+>}(\vec{k}) + T_{ij}^{->}(\vec{k}) \quad (2)$$

in which

$$T_{ij}^{+>}(\vec{k}) = -\frac{1}{2} \int_{\vec{p}+\vec{q}=\vec{k}} \left\{ G(\vec{k}) G(\vec{p})(1-G(\vec{q})) + G(\vec{k}) G(\vec{q})(1-G(\vec{p})) + G(\vec{k})(1-G(\vec{p}))(1-G(\vec{q})) \right\} S_{ij}^{+}(\vec{k}|\vec{p}, \vec{q}) d\vec{p} d\vec{q} \quad (3)$$

and

$$T_{ij}^{->}(\vec{k}) = -\frac{1}{2} \int_{\vec{p}+\vec{q}=\vec{k}} \left\{ G(\vec{k}) G(\vec{p})(1-G(\vec{q})) + G(\vec{k}) G(\vec{q})(1-G(\vec{p})) + G(\vec{k})(1-G(\vec{p}))(1-G(\vec{q})) \right\} S_{ij}^{-}(\vec{k}|\vec{p}, \vec{q}) d\vec{p} d\vec{q} \quad (4)$$

with

$$S_{ij}^{+}(\vec{k}|\vec{p}, \vec{q}) = \left\{ \eta(k) + \eta(p) + \eta(q) \right\}^{-1} \left\{ P_{ikl}(\vec{k}) P_{jlm}(\vec{p}) \bar{\Phi}_{lm}(\vec{p}) \bar{\Phi}_{ln}(\vec{q}) + P_{jkl}(\vec{k}) P_{ilm}(\vec{q}) \bar{\Phi}_{lm}(\vec{p}) \bar{\Phi}_{ln}(\vec{q}) \right\}$$

$$S_{ij}^{-}(\vec{k}|\vec{p}, \vec{q}) = \left\{ \eta(k) + \eta(p) + \eta(q) \right\}^{-1} \left\{ P_{ikl}(\vec{k}) P_{jlm}(\vec{p}) \bar{\Phi}_{lm}(\vec{q}) + P_{jkl}(\vec{k}) P_{ilm}(\vec{q}) \bar{\Phi}_{lm}(\vec{p}) \right\}$$

with the notations :

$$E(k) = \frac{1}{2} \int_{\text{sphere of radius } K} \bar{\Phi}_{ii}(\vec{k}) dS$$

$$\eta(p) = \lambda \left[\int_0^p k^2 E(k) dk \right]^{1/2} + \nu p^2$$

$T_{ij}^{+>}(\vec{k})$ and $T_{ij}^{->}(\vec{k})$ are the terms accounting for the effect of subgrid scales on the explicit eddies. $T_{ij}^{+>}(\vec{k})$ contains only contributions involving $\bar{\Phi}_{ij}(\vec{p})$ and $\bar{\Phi}_{ij}(\vec{q})$ (two vectors different from \vec{k}). It is known that the effect of such a term is typically an input of energy at the wave vector \vec{k} . $T_{ij}^{+>}(\vec{k})$ is the contribution of subgrid scales to the input or backscatter term. In return, $T_{ij}^{->}(\vec{k})$ that involves $\bar{\Phi}_{ij}(\vec{k})$ is the contribution of subgrid scales to the output term or drain. It is worth noting that the distinction between backscatter and drain is not intrinsic to Quasi Normal closures but that it also exists in the case of the D.J.A. (see Kraichnan (1976)).

The term

$$T_{ij}^{>}(\vec{k}) = T_{ij}^{+>}(\vec{k}) + T_{ij}^{->}(\vec{k})$$

which is the subgrid contribution to the transfer, perfectly defines the exchange of energy between grid and subgrid scales for a closure computation. However it provides only a statistically averaged information that is not sufficient for a subgrid model in L.E.S. The subgrid model must furthermore account for the effects of small scales on one particular realization of the large scale field (Basdevant et al. (1978)). To "desaverage" the information, we have to make further hypothesis. The more common way to do so is to introduce the eddy viscosity concept.

In the present paper we do not propose new desaveraging models. We only intend to discuss the validity of the eddy viscosity formulation.

3 RESULTS CONCERNING THE SPECTRAL TRANSFER

In order to discuss the eddy viscosity formulation, we have to compute the terms $T_{ij}^{+>}(\vec{k})$ and $T_{ij}^{->}(\vec{k})$ appearing in equation (2). This is done at a fixed value of time : t_c .

The values for the spectrum $\bar{\Phi}_{ij}(\vec{k}, t_c)$ used here correspond to an initially isotropic turbulence distorted by a shear. They have been computed by using the E.D.Q.N.M. model presented in Bertoglio (1981). The value of the dimensionless parameter characterizing the distortion is $S t_c = 2$, in which S is the mean shear :

$$S = \frac{\partial \langle u_1 \rangle}{\partial x_3} = 4.5 s^{-1}$$

The initial isotropic spectrum was deduced from the measurements of Comte-Bellot (1971).

We have investigated the case of two different filters :

• a Gaussian filter :

$$G(\vec{k}) = \exp - \frac{\delta^2 k^2}{24}$$

• a sharp filter in wavespace

$$G(\vec{k}) = 1 \quad \text{if } k \leq K_c$$

$$G(\vec{k}) = 0 \quad \text{if } k > K_c$$

They are the most employed filters, the former being used for finite difference simulations, the latter for spectral simulations.

In figure 1, we have plotted the double correlation spectra $\bar{\Phi}_{ij}(k)$ and their filtered values $\bar{\Phi}_{ij}(k)$ in the particular case of a Gaussian filter whose width $\delta = 2.7$ cm corresponds to a simulation on a 16^3 grid of a "classical laboratory turbulence" (for example Comte-Bellot (1972)). $\bar{\Phi}_{ij}$ and $\bar{\Phi}_{ij}$ are quantities integrated over spherical shells of radius K , respectively the integrals of $\bar{\Phi}_{ij}(\vec{k})$ and $\bar{\Phi}_{ij}(\vec{k})$.

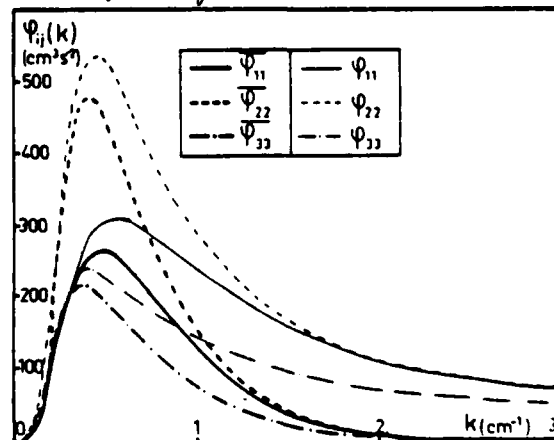


Fig. 1 : Double correlation spectra (unfiltered $\bar{\Phi}_{ij}$, and filtered $\bar{\Phi}_{ij}$) ($S t_c = 2$).

Figure 2 shows the contributions of small scales to the non linear transfer

$$t_{ij}^>(K) = \text{integral of } T_{ij}^>(K) \text{ over the spherical shell of radius } K.$$

It can be seen that $t_{ij}^>(K)$ is more isotropic than $\bar{\varphi}_{ij}(K)$. It is relevant to recall at this point that an eddy viscosity subgrid parameterization would model $t_{ij}^>$ as having the same anisotropy as $\bar{\varphi}_{ij}$. We can for example define the eddy viscosity as

$$\nu_e(K) = \frac{t_{ii}^>(K)}{2K^2 \bar{\varphi}_{ii}(K)} \quad (5) \text{ (summation over the repeated indices)}$$

This formulation is an extension of the form used by Chollet (1983) for isotropic turbulence

$$\nu_e(K) = \frac{T^>(K)}{2K^2 E(K)}$$

with the notation

$$T(K) = 1/2 t_{ii}(K)$$

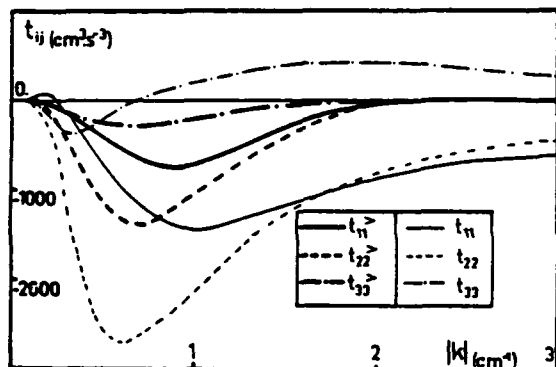


Fig. 2: Spectral transfer t_{ij} , and part of the spectral transfer relative to the exchange between explicit and subgrid scales $t_{ij}^>$ ($S_L = 2$).

In this case, the effects of the modeled subgrid scales would be equivalent to the term

$$t_{ij}^{>M}(K) = 2 \nu_e(K) \bar{\varphi}_{ij}(K)$$

which is plotted in figure 3. It can be seen, in particular, that this term would tend to overestimate the drain of energy from the $\bar{\varphi}_{33}$ component.

Results concerning the sharp filter confirm the same trends.

A separated study of $T_{ij}^>(K)$ and $T_{ij}^<(K)$ indicates that the eddy viscosity is less adequate for the backscatter $T_{ij}^<$, as suggested by Kraichnan (1976) and Leslie (1979). It can be shown by using visualizations over spherical shell of radius K : in figure 4 $T_{ij}^<$ is less connected to $\bar{\varphi}_{ij}$ than $T_{ij}^>$ is.

We have then pointed out a deficiency of the eddy viscosity subgrid model. Whether this deficiency may have important consequences will be examined in section 4.

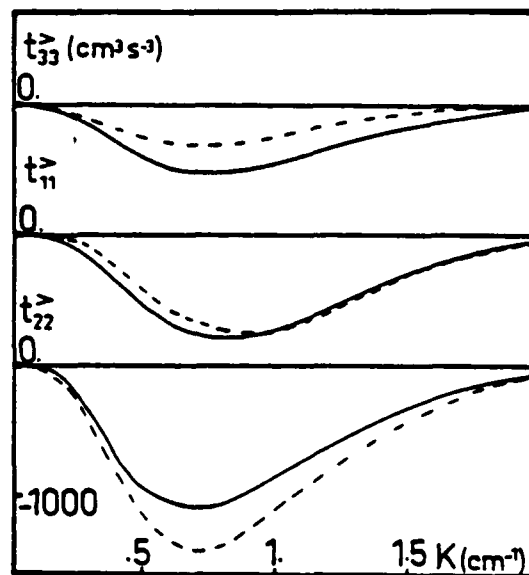


Fig. 3 Comparison between the spectral transfer due to small scales $t_{ij}^>$: ----, and the eddy viscosity modeled form : $\nu_e(K) \bar{\varphi}_{ij}(K)$: —.

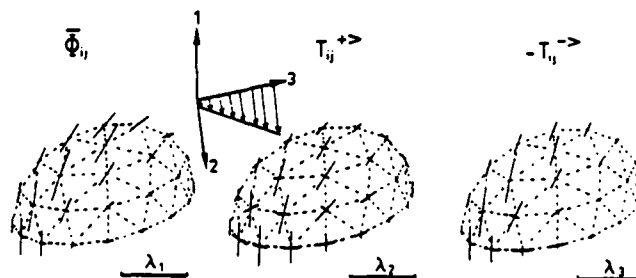


Fig. 4 Comparison between spectral tensor $\bar{\varphi}_{ij}$, subgrid backscatter $T_{ij}^<$, and subgrid drain $T_{ij}^>$ ($S_L = 2$). Over spherical shells of radius K , the principal axes of the tensors are visualized and segments proportional to the eigen values are plotted.

4 SUBGRID EDDY VISCOSITY IN A CLOSURE MODEL

A self consistent way to test a subgrid model is to introduce the subgrid model into a closure computation. Then only the large scales are taken into account by the closure, and the subgrid model is used to parameterize the small eddies. Comparisons with the closure applied to the whole range of the spectrum are thereafter very easily made. The advantage is that, in both cases, the interactions between large scales are treated with the same approximation. Obviously we have to be faithful in the behaviour of the closure near the cutoff of the filter.

Chollet and Lesieur (1981) have already used this technique to test a subgrid model in the case of isotropic turbulence. We now extend the comparison to sheared homogeneous turbulence. We have tested several eddy viscosity formulations. In order to point out the inaccuracy of eddy viscosity in the specific field of anisotropic turbulence, we present the results obtained with the formulation that gives the best results for isotropic turbulence. This formulation is obtained by evaluating, at each wavenumber and at each time step, the value of the eddy viscosity that would give the right amount of energy transferred to the small scales. This evaluation is performed by making, in parallel, a second closure computation, over the whole range of the spectrum.

Therefore two closure computations are simultaneous carried out : the first one to take into account the interactions between large eddies, the small scales being parameterized by $\nu_t(K)$, the second one to determine the values of $\nu_t(K)$ by computing the interactions involving subgrid scales.

The specific form for ν_t is given by eq. (5), and is the one used by Chollet (1983) and Aupoix (1983), to parameterize the small scales in a coupled method L.E.S./closure.

For sheared homogeneous turbulence, calculations resulting from the complete E.D.Q.N.M. equations are unfortunately so cumbersome and expensive that the evolution with time of the turbulent field has always been considered as impossible to compute without simplifying assumptions. Accordingly, the test of the subgrid model cannot be made in a straightforward way. We have however proposed a method (Bertoglio (1981)) which requires only a few computations of the 3D E.D.Q.N.M. transfer, this term being interpolated between the computed values.

In figure 5 the evolutions with time of the spectra are plotted. In this case the filter is sharp and $K_c = 1.27 \text{ cm}$. It can be seen that even for from the filter cutoff ($K/K_c = .35$) the error caused by the subgrid model is important.

The discrepancy between results obtained with an without subgrid model first appears on $\bar{\psi}_{33}$. As it could be expected from the results of section 3, the subgrid model tends to drain too much energy from $\bar{\psi}_{33}$. $\bar{\psi}_{33}$ is therefore underestimated. In a second stage this defect will contaminate the other components since the production of $\bar{\psi}_{23}$

$$= \bar{\psi}_{33} \frac{\partial \langle u_2 \rangle}{\partial x_3}$$

is affected. Lately the production of $\bar{\psi}_{22}$ is affected too.

The error caused by the subgrid model is about 10 per cent. It is relevant to note that in an isotropic case the subgrid model introduces only a relative error smaller than 1/1000, for a corresponding evolution time.

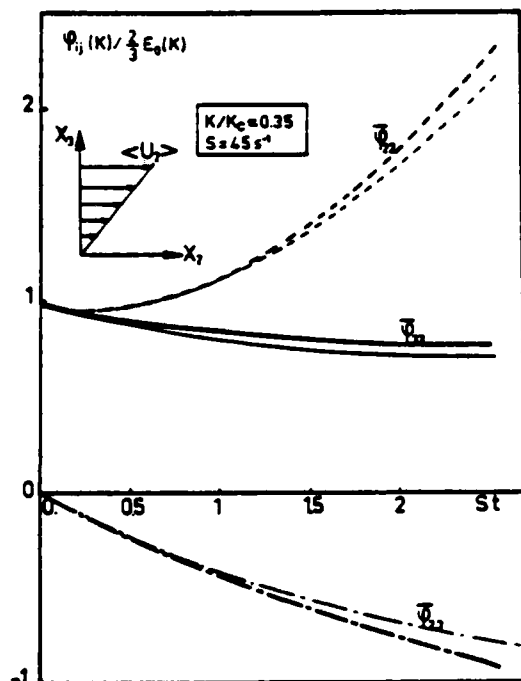


Fig. 5 : Evolution with time of the components of the double correlation spectrum. Comparison between E.D.Q.N.M. -----, -----, -----, and E.D.Q.N.M. with a subgrid model - - - - - (wave number cutoff $K_c = 1.27 \text{ cm}$).

5 CONCLUSIONS

We have pointed out the inadequacy of eddy viscosity subgrid model for anisotropic turbulence. The eddy viscosity parameterization seems in particular unjustified for the backscatter or input term, which takes into account the return of energy from the small eddies to the large eddies. In the case of a coupled method taking into account large eddies by a simulation and subgrid scales by a closed computation, new "desaveraging" models seems to be needed to model the backscatter before applying the method to sheared turbulence.

We have only considered here isotropic filters, but the effect of non isotropic filter could be investigated, as they corresponds to has spectral simulation of sheared turbulence, since Rogallo (1981) has introduced a distortion of the computational grid to preserve spatial periodicity.

REFERENCES :

- AUPOIX B., COUSTEIX J and LIANDRAT J., 1983, "Effects of Rotation on Isotropic Turbulence", Fourth Symposium on Turbulent Shear Flows.
- BASDEVANT C., LESIEUR M. and SADOURNY R., 1978, "Subgrid-Scale Modeling of Enstrophy Transfer in Two-Dimensional Turbulence", Journ. of Atm. Sc. Vol. 35, N° 6.
- BERTOGLIO J.P., 1981, "A Model of Three-Dimensional Transfer in Non-Isotropic Homogeneous Turbulence", Third Symp. on Turb. Shear Flows. Springer-Verlag.
- CAMBON C., JEANDEL D., and MATHIEU J., 1981, "Spectral Modeling of Homogeneous Non-isotropic Turbulence", J. Fluid Mech., 104.
- CHOLLET J.P. and LESIEUR M., 1981, "Parameterization of Small Scales of Three-Dimensional Isotropic Turbulence Utilizing Spectral Closures", J. Atm. Sc., 38;
- CHOLLET J.P., 1983, "Two-Point Closures as a Subgrid Scale Modeling for Large Eddy Simulations", Fourth Symposium on Turbulent Shear Flows.
- COMTE-BELLOT G. and CORRSIN S., 1971, "Simple Eulerian Time Correlation of Full and Narrow Band Velocity Signals in Grid-generated Isotropic Turbulence", J. Fluid Mech. 48.
- KRAICHNAN R., 1976, "Eddy Viscosity in Two and Three Dimensions", J. Atm. Sc., 33.
- LESLIE D.C., and QUARINI G.L., 1979, "The Application of Turbulence Theory to the Formulation of Subgrid Modelling Procedures", J. Fluid Mech., 91, part 1.
- Mc MILLAN O.J., FERZIGER J.M. and ROGALLO R.S., 1980, "Tests of New Subgrid-Scale Models in Strained Turbulence", AIAA 13 th Fluid and Plasma Dynamics Conference.
- ROGALLO R.S., 1981, "Numerical Experiments in Homogeneous Turbulence", NASA Report 81315.

A SPECTRAL MODEL FOR THE CALCULATION OF HOMOGENEOUS TURBULENT FLOWS

Y. Yassour and M. Wolfshtein

Department of Aeronautical Engineering
Technion - Israel Institute of Technology
Haifa, Israel

ABSTRACT

The paper deals with modelling of the energy equation for homogeneous flows in the wave numbers space, concentrating on the energy carrying wave number region. The energy transfer between wave numbers is studied, and two spectral transfer mechanisms are proposed, namely the similar transfer and the isotropizing transfer. It is shown that this proposal mechanism can describe homogeneous turbulent flows.

1. INTRODUCTION

1.1. Background

Most turbulence models are based on two equations representing the scale and amplitude of the turbulent fluctuations. Although predictions based on such models produce useful results, the universality of such models is limited, and the predictions are not always successful. Considering the reasons for such weaknesses, a distinction should be made between the turbulent energy equation, and the second equation (for the length scale, dissipation, or some other similar quantity). While the turbulent energy equation is usually considered fairly reliable, the second equation is somewhat questionable, due to its complexity, and the lack of experimental data on the balance between its terms.

The problem may, perhaps, be resolved by improvements and modifications of this equation. There is, however, another possibility, namely to formulate the energy equation for various eddy sizes, or wave numbers. When this is done, the energy contained at each wave number is calculated, and the scale of turbulence ceases to be a major dependent variable, but it is calculated from the energy spectrum. Thus, a two equation model reduces to a single equation but of a higher dimension, because now the wave number becomes an additional dependent variable, in addition to the spatial coordinates and the time.

In this paper we try to examine this idea, and to find out how to formulate such equation. It should be pointed out that the closure problem exists in this formulation as much as it does in the usual two equation models.

1.2 Literature Survey

A. The Usefulness of a Spectral Mode. Apart from relieving us from the need for a scale equation, the present approach appears to have another advantage over the usual two equations model. The conventional formulations are based on the assumption that the energy spectrum is self-similar. However, such an assumption is not correct, and the usual models can not cope with variations of the spectral distribution of the turbulent energy. This point has already been

recognised by Hanjalic and Launder [1] - proposed a two-scales model. However, they formulated their equations in terms of two scale equations rather than the approach of an additional coordinate which is utilised here. The idea of formulating equations in the wave numbers space is, of course, not new. A very well known example is the Rapid Distortion Analysis, as used by Hunt [2], Townsend [3], or Deissler [4]. However, these researchers tended to neglect the non-linear turbulent convection terms rather than model them. Yet they have solved problems of two-dimensional shear flows and obtained very interesting results for rapidly strained turbulence.

B. The Spectral Equation. The spectral equation for the energy tensor E_{ij} is obtained by a Fourier transform of the dynamic equation for the two point velocity correlation tensor Q_{ij} . Batchelor [5] considered the problem of homogeneous flows and suggested to average the correlation functions over all directions. Summation of the trace of the transformed tensors gives the dynamic equation for the energy spectrum:

$$\frac{\partial}{\partial t} E(k,t) = P(k,t) + F(k,t) - 2\nu k^2 E(k,t) \quad (1)$$

where:

- $E(k,t)$ - the energy spectrum
- $P(k,t)$ - the production term
- $F(k,t)$ - spectral energy transfer
- $2\nu k^2 E(k,t)$ - spectral distribution of the viscous dissipation.

The transfer function $F(k,t)$ is a product of the two point third order velocity correlation. The production P is obtained from the components of E_{ij} (also from the off diagonal terms, $i \neq j$) and therefore it requires an estimate if the scalar equation (1) is solved. Such estimates were suggested by Tchen [6] and will be described below.

Special cases of Eq. (1) are as follows:

- (i) Isotropic flow, with no production. (1a)
- (ii) Steady flow with $\partial/\partial t = 0$. (1b)
- (iii) Isotropic flow ($P=0$), in the energy carrying wave numbers range, where the local dissipation is relatively small. (1c)
- (iv) Steady flow in the energy carrying wave numbers range. (1d).

C. The Closure Problem. As mentioned above, the transformation to the wave numbers space does not resolve the closure problem. In the nomenclature of Eq. (1) it means that the transfer function $F(k,t)$ is not known and should be modelled. It is often more convenient to consider the energy flux - $G(k,t)$, defined by:

$$G(k, t) = \int_0^k F(k, t) dk \quad (2)$$

which represent the energy transfer from wave numbers smaller than k to wave numbers larger than k . This energy transfer may occur by stretching of small vortices by larger vortices and by vortex breakdown and merging.

Three possibilities for modelling of the flux exist:

- (i) Local algebraic modelling, relating the flux G to the local values of E and k :

$$G(k, t) = B(t) k^m E^n(k, t) \quad (2a)$$

where B can be a dimensional function of time. Such proposals were given by Kovasznay [7], Panchev [8], Pao [9] and Lin [10].

- (ii) Diffusional modelling, relating G to the energy spectrum gradient $\partial E / \partial k$, or in physical terms relating G to the energy spectrum in the adjacent wave numbers:

$$G(k, t) = B(t) k^{m_1} \frac{d}{dk} [k^{m_2} E^n(k, t)] \quad (2b)$$

Such proposals were given by Leith [11] and Kraichnan and Spiegel [12].

- (iii) Integral modelling, relating G to wide range of wave numbers using some integral properties. Such models are based on the assumption that energy transfer may be obtained between wave numbers which are remote from one another. The relation is integral and takes the form:

$$G(k, t) = B(t) \left[\int_0^k X(k, E) dk \right]^a \int_k^\infty Y(k, E) dk \quad (2c)$$

where X , Y denote various functions. Such proposals were given by Heisenberg [13], Obukhoff [14], Von Karman [15], Ellison [16] and Dagstad [17].

Physical intuition suggests that all these three proposals are possible. However, the solutions obtained by those models ([7]–[17]) are limited to the high wave numbers range – the inertial range and the dissipative range, and none of them can describe the energy flux in the low wave numbers range – the energy containing range. Usually most of the models predict the $-5/3$ Kolmogorov power law in the inertial range and differ from one another in the dissipative range.

In this context, it is worth while mentioning here Von Karman's [18] empirical interpolation proposal for the energy spectrum in the low wave numbers range (tending to Loitsianskii's fourth power spectrum at $k \rightarrow 0$ and to Kolmogorov $-5/3$ power law at the inertial range):

$$E(k, t) = B \left(\frac{k}{k_e} \right)^4 \left[1 + \left(\frac{k}{k_e} \right)^2 \right]^{-17/6} \quad (3)$$

where B and k_e are functions of time.

D. Experimental Results. The Von Karman empirical formula (3) for the energy spectrum appears to be satisfactory for the isotropic homogeneous flow. Other important quantities which have been studied are as follows:

- (i) The turbulent energy and the macroscale evolution during the decay of isotropic homogeneous field have been studied theoretically and experimentally. Comte-Bellot and Corrsin [19] performed a very careful study of this problem. In their experimental research they suggested an empirical power law for the decay of the turbulent energy:

$$e(t) \propto t^{-1.3} \quad (4a)$$

and growth of the macroscale:

$$L(t) \propto t^{+0.38} \quad (4b)$$

- (ii) The idea of relating the dissipation ϵ to similar quantities of the low wave numbers range is widely discussed by Batchelor [5]. By equalizing the time scale of the energy containing range and the time scale of the dissipation, Batchelor suggested the correlation:

$$\epsilon(t) = A e(t)^{3/2} / L(t) \quad (5)$$

where A is a constant ($A=0(1)$). This correlation was experimentally tested by Batchelor and Townsend [19].

1.3 Definition of the Problem

The purpose of this paper is to propose a model for the energy transfer term F in Eq. (1), which is also suitable for the low wave numbers range – the energy carrying wave number range. The present paper is confined to incompressible homogeneous flows, and to one dimensional spectral analysis, but we want to extend the model to non-homogeneous shear flow and tensorial analysis in the future.

The model should handle both isotropic and non-isotropic flows. Although we are interested in a model for F (or G), we shall have to consider a model for the production term P as well, for non-isotropic homogeneous shear flow. However, the model to be used for P will follow the proposal of Tchen [6] for low non-isotropy, and not developed here.

2. FORMULATION OF THE MODEL

2.1 Properties of the Model

When we consider the transfer functions G or F , we know that for homogeneous flows this is the only term which represents energy transfer between different wave numbers, rather than changes in the energy content at a given wave number. Two modes of such energy transfer are possible. The first one is concerned with energy transfer without changes in the shape of the energy spectrum as found, for instance, in the decay of homogeneous isotropic turbulence. We call this mode the self-similar energy transfer – $F_i(k, t)$, and associate it with the Townsend's energy cascade and the universality of the inertial range.

However, this mode alone can not represent all the processes occurring when turbulence is undergoing changes and developments. We therefore have to consider another mechanism by which the shape of the energy spectrum changes as well. Experimental evidence suggests that when the shear is removed from any turbulent flow, the spectrum tends towards a universal shape, which we call the isotropic energy spectrum – $E_i(k, t)$. Thus it appears that the second nonsimilar part of the spectral energy transfer is the term which forces it to reach its universal isotropic shape. We call this mode the isotropizing term – $R(k, t)$, and associate it with the interaction between the component of the turbulent velocity or to the non-isotropy of the flow. Such non-isotropy may depend in spectral space on a driving force which is related to the difference between the current value of E and the isotropic value – E_i . Thus, the difference ($E - E_i$) is an interpretation of the non-isotropy in spectral space. Thus the spectral energy transfer F (Eq. 1) can be described as follows:

$$F(k, t) = F_i(k, t) + R(k, t) \quad (6)$$

Models for the two terms which represent the energy transfer between wave numbers are presented in

the next paragraphs.

2.2 Self-Similar Energy Transfer

In homogeneous isotropic flow ($P = 0$, $R = 0$) Eq. (1a) represents the dynamics of the energy spectrum during its similar decay, and the closure problem is reduced to a proposal for one term, the transfer function F_i . In this similar field we evaluate the first mode - the self-similar energy transfer.

Heisenberg [13] already realized that this mode is related to the spectral distribution of the dissipation. Following his proposal we may write:

$$G(k, t) = -H(k, t) 2\nu \int_k^\infty k^2 E(k, t) dk \quad (7)$$

where $H(k, t)$ is a dimensionless spectral function which we call "the loading function".

If we limit ourselves to high Re_t , the flux in the inertial range equals the dissipation - $\epsilon(t)$:

$$\epsilon(t) = 2\nu \int_0^\infty k^2 E(k, t) dk = 2\nu \int_{k_1}^\infty k^2 E(k, t) dk \quad (8)$$

where k_1 is a typical wave number for the inertial range. Therefore, in the inertial range:

$$H(k_1, t) = 1 \quad (9a)$$

On the other hand, for very small k , $E \rightarrow 0$ as well as $\frac{\partial E(k, t)}{\partial t}$. Thus we may assume that also F_i and G vanish

for $k \rightarrow 0$. Since $k^2 E dk$ is finite we obtain:

$$H(k, t) = \frac{\partial H(k, t)}{\partial k} = 0 \quad \text{for } k \rightarrow 0 \quad (9b)$$

The actual form of the similar loading function may be obtained by studying the self-similar spectral equation for the homogeneous isotropic field as follows:

We define the following dimensionless parameters:

$$\phi(\beta) = E(k, t)/E_m(t) \quad (10a)$$

$$\beta(k, t) = k/k_m(t) \quad (10b)$$

where $E_m(t)$ and $k_m(t)$ are the maximal value of E and its location respectively. We also know that $\phi(\beta)$ is a given function for self-similar isotropic spectrum. Therefore:

$$\phi(\beta=1) = 1 \quad (11)$$

and the turbulent energy can be described by:

$$e(t) = E_m(t) k_m(t) I_e \quad (12)$$

where I_e is the energy constant:

$$I_e = \int_0^\infty \phi(\beta) d\beta \quad (12a)$$

In a similar way we calculate the macroscale:

$$L(t) = \frac{1}{e(t)} \int_0^\infty \frac{1}{k} E(k, t) dk = \frac{1}{I_e} \frac{1}{k_m(t)} \quad (13)$$

where:

$$I_L = \int_0^\infty \frac{1}{\beta} \phi(\beta) d\beta \quad (13a)$$

and the dissipation (from Eq. 5):

$$\epsilon(t) = I_e E_m(t)^{3/2} k_m(t)^{5/2} \quad (14)$$

where:

$$I_e = A I_e^{5/2} / I_L \quad (14a)$$

In the isotropic case, Eq.(1) reduces to Eq. (1a):

$$\frac{\partial E(k, t)}{\partial t} = F_i(k, t) - 2\nu k^2 E(k, t) \quad (1a)$$

By substitution of the relations (10-14) in Eq. (1a) and integration over all wave numbers, we obtain:

$$\frac{1}{E_m} \frac{dE_m}{dt} + \frac{1}{k_m} \frac{dk_m}{dt} = - \frac{I_e}{I_e} E_m^{1/2} k_m^{3/2} \quad (15)$$

This equation is analog to the total energy decaying equation:

$$\frac{de(t)}{dt} = - \epsilon(t) \quad (15a)$$

In this equation the transfer function does not appear as its integral vanishes. However, if we perform the integration from zero only to a finite wave number in the energy carrying wave number range, the dissipation is relatively small and the dynamic Eq. (1) reduces to Eq. (1c):

$$\frac{\partial E(k, t)}{\partial t} = F_i(k, t) \quad (1c)$$

This equation may be so arranged (using our proposal (7) for G) to get the following form:

$$\begin{aligned} \left[\frac{1}{E_m} \frac{dE_m}{dt} + \frac{1}{k_m} \frac{dk_m}{dt} \right] I_e^\beta(\beta) - \frac{1}{k_m} \frac{dk_m}{dt} \beta \phi(\beta) = \\ = - I_e E_m^{1/2} k_m^{3/2} H(\beta, t) \end{aligned} \quad (16)$$

where:

$$I_e^\beta(\beta) = \int_0^\beta \phi(\beta) d\beta \quad (16a)$$

Eqs. (15), (16) may be rearranged to give:

$$\frac{dE_m}{dt} = - I_e E_m^{3/2} k_m^{3/2} \left\{ \frac{1}{I_e} - \frac{1}{\beta \phi(\beta)} \left[\frac{I_e^\beta(\beta)}{I_e} - H(\beta, t) \right] \right\} \quad (17a)$$

$$\frac{dk_m}{dt} = - I_e E_m^{1/2} k_m^{5/2} \frac{1}{\beta \phi(\beta)} \left[\frac{I_e^\beta(\beta)}{I_e} - H(\beta, t) \right] \quad (17b)$$

Now if the term:

$$\frac{1}{\beta \phi(\beta)} \left[\frac{I_e^\beta(\beta)}{I_e} - H(\beta, t) \right] = \gamma \quad (18)$$

than γ must be a dimensionless constant for similar energy transfer, and therefore:

$$H(\beta, t) = H(\beta) = \frac{I_e^\beta(\beta)}{I_e} - \gamma \beta \phi(\beta) \quad (19)$$

Equation (19) is the representation of the self-similar loading function. Alternative representation of $H(\beta)$ is:

$$H(\phi) = \frac{1}{e(t)} \left[\int_0^k E(k,t) dk - \gamma I_e E(k,t) \right] \quad (19a)$$

By substitution of this loading function into Eq. (7), we may obtain:

$$G(k,t) = \frac{-2\nu}{e(t)} \left[\int_0^k E(k,t) dk - \gamma I_e E(k,t) \right] \int_k^\infty k^2 E(k,t) dk \quad (20)$$

This allows an expression for the similar energy transfer:

$$F_i(k,t) = \frac{-2\nu}{e(t)} \left[(1-\gamma I_e) E(k,t) - \gamma I_e k \frac{\partial E(k,t)}{\partial k} \right] k^2 E(k,t) dk \quad (21)$$

Notice that for the energy carrying wave numbers range $-(k < k_1)$, $H(k,t)$ is governing the spectral distribution of the energy transfer.

2.3. The Isotropizing Term - $R(k,t)$

This term represents additional energy transfer function in a mode which is not limited to self-similar spectral energy distribution. We have already suggested that this term depends on $(E-E_i)$ as a driving force. Dimension analysis gives the functional form which we propose:

$$R(k,t) = \frac{1}{\tau_r} [E_i(k,t) - E(k,t)] \quad (22)$$

where τ_r is a typical time scale for this process and E_i is the isotropic energy spectrum corresponding to E . This form may satisfy our first requirement that when other forces are not present this term drives E into its isotropic form in an asymptotic way.

We still have to evaluate E_i . We give E_i the Von Karman universal form (3), and choosing it's parameters by the following integral requirements:

(i) energy transfer between large eddies only:

$$\int_0^{k_1} E(k,t) dk = \int_0^{k_1} E_i(k,t) dk = e(t) \quad (23a)$$

(ii) some scale ratio:

$$\int_0^{k_1} \frac{1}{k} E(k,t) dk = q \int_0^{k_1} \frac{1}{k} E_i(k,t) dk \quad (23b)$$

where q is the scale ratio to be determined by comparison to experiments. Those integral relations are sufficient to determine $E_i(\phi, km, Em)$.

Another interesting feature is that by selection of the time scale τ_r we may decide how fast the action of the isotropization terms is, in comparison to the dissipation process.

2.4. The Final Equation

If we assume that the expressions for self-similar transfer (21) and for the isotropizing term (22) are valid also for non-isotropic flows, the final equation for E in the large eddies region is:

$$\begin{aligned} \frac{\partial E(k,t)}{\partial t} = & P(k,t) - \frac{e(t)}{e(t)} [(1-\gamma I_e) E(k,t) - \gamma I_e k \frac{\partial E(k,t)}{\partial k}] + \\ & + \frac{1}{\tau_r} [E_i(k,t) - E(k,t)] \end{aligned} \quad (24)$$

This equation could be written schematically:

$$\frac{\partial E(k,t)}{\partial t} = \begin{matrix} P(k,t) \\ \text{production} \end{matrix} + \begin{matrix} F_i(k,t) \\ \text{self similar} \\ \text{transfer} \end{matrix} + \begin{matrix} R(k,t) \\ \text{isotropizing} \\ \text{transfer} \end{matrix} \quad (24a)$$

3. THE ISOTROPIC HOMOGENEOUS CASE

3.1. The Decay Parameter γ

The decay parameter γ controls the rate of energy decay and the growth of the macroscale. By substituting (18) into Eq. (17b), we can see that $km(t)$ decreases with time for positive γ . According to relation (13), if km decreases the macroscale L increases as all the experimental data suggests and thus γ must be positive. On the other hand when $\gamma I_e > 1$ the maximal value of E , $Em(t)$ (Eq. 17a), is increased with time, which is not at all realistic. Thus, the decay parameter γ is bounded by:

$$0 \leq \gamma \leq 1/I_e \quad (25)$$

When $\gamma=0$ km (and the macroscale) is constant and when $\gamma=1/I_e$ Em is constant.

The self similar transfer has two subterms:

$$(i) - \frac{\epsilon}{e} [(1-\gamma I_e) E(k,t)] \quad (26a)$$

This term is a local transfer subterm associated with interaction between large and small eddies.

$$(ii) + \frac{\epsilon}{e} \gamma I_e k \frac{\partial E(k,t)}{\partial k} \quad (26b)$$

This term is a differential transfer subterm associated with interaction between adjacent large eddies. From these subterms we can see that if $\gamma=0$, the model is purely local and as γ increases the model becomes more diffusive and less local.

A better understanding of the influence of γ is obtained in the next paragraphs.

3.2 Self-Similar Decay

The isotropic homogeneous case is governed also by Eqs. (17a, 17b). If we substitute the model for $H(k,t)$ (Eq. 19a) in those equations we get:

$$\frac{1}{km} \frac{dkm}{dt} = -\gamma I_e Em(t)^{1/2} km(t)^{3/2} \quad (27a)$$

$$\frac{1}{Em} \frac{dEm}{dt} = -I_e (1/I_e - \gamma) Em(t)^{1/2} km(t)^{3/2} \quad (27b)$$

For convenience we replace Em and km by the energy $e(t)$ (Eq. 12) and the integral time scale τ_e , given by:

$$\tau_e(t) = \left[\frac{e(t)}{e(t)} \right]^{-1} = \frac{1}{\lambda(t)} \quad (28)$$

by substitution of (12) and (28) in (27), we obtain:

$$\frac{de(t)}{dt} = -\lambda(t) e(t) \quad (28a)$$

$$\frac{d\lambda(t)}{dt} = -(\gamma I_e + 0.5) \lambda^2(t) \quad (28b)$$

the solution of (28) is:

$$\lambda(t) = \lambda_0 [1 + \left(\frac{\lambda_0}{\lambda(t)}\right)(t-t_0)]^{-1} \quad (29a)$$

$$e(t) = e_0 [1 + \left(\frac{\lambda_0}{\lambda(t)}\right)(t-t_0)]^{-M} \quad (29b)$$

where e_0 and λ_0 are the values at time t_0 , and:

$$M = (\gamma I_e + 0.5)^{-1} \quad (30)$$

The constant γI_e should be determined by comparison to experiments. Using (25), we may write the following limitations:

$$0.67 \leq M \leq 2 \quad (31)$$

The macroscale ($L \approx 1/\text{km}$) is easily calculated as well:

$$L = L_0 [1 + (\lambda_0/M)(t-t_0)]^N \quad (32)$$

where:

$$N = 1 - M/2 \quad (33)$$

and from (31) we obtain:

$$0 \leq N \leq 0.67 \quad (34)$$

3.3 Comparison with Previous Results

Many investigators have referred to the time powers M and N of Eqs. 29b and 32 respectively. Most of the previous results are special cases of the present theory, as demonstrated by the following table:

Reference	M	N	γI_e
<u>Theoretical</u>			
Korneyev and Sedov [20] - ▲	1	0.5	0.5
Hinze [21] - ●	1.2	0.4	0.33
Kolmogorov [22] - ■	1.428	0.286	0.2
<u>Experimental</u>			
Batchelor [5] - ▲	1.0	0.5	0.5
Comte-Bellot and Corrsin [18] - ○	1.3	0.38	0.27
Tan and Ling (final decay) [23] - □	2.0	-	0.0

The dependence of M and N on the decay parameter is shown in Fig. 1 as well as some of the values given in the above table.

The most suitable value of γI_e for the isotropic decaying field appears to be $\gamma I_e = 0.27$ as carefully measured by Comte-Bellot and Corrsin [18].

3.4 The Decay of the Energy Spectrum

If we considered the energy carrying wave number range in the homogeneous isotropic case and substitute our model for F_i , we obtain from Eq. (24):

$$\frac{\partial E(k,t)}{\partial t} = - \frac{\varepsilon(t)}{e(t)} [(1-\gamma I_e)E(k,t) - \gamma I_e k \frac{\partial E(k,t)}{\partial k}] \quad (35)$$

Using the Von Karman spectrum (3) as an initial condition, the detailed evolution of the energy spectrum can be solved. Some modes of the spectral decay are shown in Figs. 2-4 for $\gamma I_e = 0, 0.27, 0.5$. From those figures we can see that the bigger eddies became more and more permanent as γ increases. In Fig. 5 we can see that the self similar transfer function - F_i , becomes more intensive in the higher wave numbers and less energy transfers from lower wave numbers as γ increases.

Comparison of the present results for $\gamma I_e = 0.27$ with Sato's [24] experimental results is shown in Fig. 6. The agreement is good.

4. THE HOMOGENEOUS CASE

The flows discussed here are not isotropic. However, we still consider the trace of the

correlation tensor E_{ij} . Therefore, we can distinguish between the isotropic case and non-isotropic case only by the shapes of the spectrum functions. Generally we shall assume that the isotropic energy spectrum is given by (3).

We consider two cases of homogeneous flows. The first one is such that the spectrum is different from the isotropic spectrum due to the previous history of the flow, but without production. In the second case we study the homogeneous full developed shear flow. In such steady flow, there is a constant strain:

$$\frac{d\bar{u}_1}{dx_2} = \text{const.}, \quad \bar{u}_2 = \bar{u}_3 = 0 \quad (36)$$

4.1 Isotropizing of Non-Isotropic Flow

In this case the production is zero, but all other terms of (24) is finite. Assuming that the isotropizing process is faster than the self-similar energy transfer, we obtain:

$$\tau_r \ll \tau_f \quad (37)$$

where $\tau_f = e(t)/\varepsilon(t) (= \tau_e)$ is the time scale of the self-similar transfer. In addition, for the first period of the isotropizing, $(E-E_i)$ is big enough to assume $R \gg F_i$. Concentrating in the energy carrying wave number range, Eq. (24) reduces to:

$$\frac{\partial E(k,t)}{\partial t} = \frac{1}{\tau_r} [E_i(k,t) - E(k,t)] \quad (38)$$

This interpretation assumes that the spectrum tends to its isotropic shape much faster than its lost energy.

Thus Eq. (38), with the integral conditions (23), can be solved numerically for any arbitrary initial energy spectrum. We perform to illustrate this process with double hump initial energy spectrum and for $q=1$ (L is constant during the isotropizing). The results are shown in Fig. 7 where various spectra for advancing time are plotted. The spectrum appears to tend to its isotropic form in a continuous way.

4.2 The Homogeneous Steady Shear Flow

This is a case where all terms in Eq. (24) are significant. Therefore the production $P(k)$ should be formulated. Basically the production is a tensorial term. For the case where the mean velocity is given by (36) the production is given by:

$$P_{i,i} = (k_1 \frac{\partial E_{i,i}}{\partial k_2} - 2E_{1,2}) \frac{d\bar{u}_1}{dx_2} \quad (39)$$

Tchen [6] has modelled this expression for the case of low production (one dimensional model):

$$P(k) = \delta \left(\frac{d\bar{u}_1}{dx_2} \right)^2 [E(k)/k^3]^{1/2} \quad (40)$$

where δ is a free parameter. This model is suitable only for low non-isotropy.

If we assume that F_i and R , which were introduced in the previous cases are the only terms which represent energy transfer between wave numbers and limit our attention to the fully developed steady case, Eq. (24) with Tchen model (40) gives a steady balance equation for the energy carrying wave numbers range:

$$\frac{1}{\tau_p} \left(\frac{d\bar{u}_1}{dx_2} \right) [E/k^3]^{1/2} - \frac{1}{\tau_f} [(1-\gamma I_e)E - \gamma I_e k \frac{dE}{dk}] - \frac{1}{\tau_r} [E_i - E] = 0 \quad (41)$$

where $\tau_p = \left(\frac{d\bar{u}_1}{dx_2}\right)^{-1}$ is a time scale for the production.

If we limit ourselves to the simple case $\gamma = 0$, Eq. (41) becomes algebraic:

$$\frac{1}{\tau_p} \left(\frac{d\bar{u}_1}{dx_2}\right) [E/k^3]^{1/2} - \frac{1}{\tau_f} E(k,t) + \frac{1}{\tau_r} (E_i - E) = 0 \quad (41a)$$

The solution of Eq. (41a) is:

$$E(k)^{1/2} = \frac{1}{2\psi} [\theta k^{-3/2} + [\theta^2 k^{-3} + 4\psi E_i(k)]^{1/2}] \quad (42)$$

where:

$$\theta = \tau_r / \tau_p \left(\frac{d\bar{u}_1}{dx_2}\right) \quad (42a)$$

$$\psi = \left(\frac{\tau_r}{\tau_f} + 1\right) \quad (42b)$$

This solution shows that the energy spectrum for homogeneous shear flow depends on the isotropic universal spectrum. Limitation of (42) to low non-isotropy case gives:

$$\frac{\tau_r}{\tau_p} \ll 1, \quad \frac{\tau_r}{\tau_f} \ll 1 \quad (43)$$

It is easy to find the asymptotic form of (42). Thus for vanishing small k , E depends on the production model (40):

$$E(k) = \left(\frac{\theta}{\psi}\right)^2 k^{-3} \quad (44)$$

Clearly, this solution is not valid for $k \rightarrow 0$, but otherwise it may be used. For very large k (below k_1) we obtain:

$$E(k) = \frac{1}{\psi} E_i(k) \quad (45)$$

This solution indicates that as E_i follows the $-5/3$ power law so does E , and the high wave numbers range is universal while for lower wave numbers, the influence of the production is increased.

Equation (42) is a balance equation between the three following terms: (i) The production, (ii) The isotropizing (diffusive), (iii) The self-similar transfer (diffusive). In Fig. 8 we give the spectral energy balance for the energy carrying wave numbers range, under the limitation (43). In this energy balance, the total production - p is equal to the dissipation - ϵ .

Physical interpretation of this balance is that the energy is generated at lower non-dissipative wave numbers. The isotropizing term transfers energy from the production region to higher wave-numbers (below k_1) and the self-similar term transfers energy to dissipative wave-numbers (above k_1).

5. CONCLUSIONS

The paper deals with the spectral energy equation. We propose two diffusive mechanisms, for a similar energy transfer and for isotropizing. The fundamental property of the self-similar energy transfer is to preserve the original shape of the energy spectrum and transfers energy to the dissipative range. The isotropizing transfer mechanism changes the spectral energy distribution and takes place only in the energy containing range. These mechanisms are formulated and used to describe three different cases. In steady homogeneous shear

flow turbulence an energy balance exists between the production, the isotropizing and self-similar energy transfer. When the production is stopped the isotropizing mechanism governs the spectrum and when the spectrum becomes isotropic, the energy spectrum decays in a similar way.

We believe that extension of the model to the tensorial equations does not pose any serious difficulties.

References

1. Hanjalic, K. and Louder, B.E.: 2nd Symp. on Turbulence Shear Flows, Imperial College London, (1979).
2. Hunt, J.C.R.: J. Fluid Mech., 61, 625, (1973).
3. Townsend, A.A.: J. Fluid Mech., 98, 171, (1980).
4. Deissler, R.G.: The Physics of Fluids, 4, 1187, (1961).
5. Batchelor, G.K.: "The Theory of Homogeneous Turbulence", Cambridge University Press, New-York (1953).
6. Tchen, C.M.: J. Research Natl. Bur. Standards, 50, 51, (1953).
7. Kovasznay, L.S.G.: J. Aeronaut. Sci., 15, 745, (1948).
8. Panchev, S.: "Random Functions and Turbulence", Pergamon Press, N.Y. (1971).
9. Pao, Y.A.: The Physics of Fluids, 11, 1371, (1968).
10. Lin, J.T.: The Physics of Fluids, 15, No. 1, (1971).
11. Leith, C.E.: The Physics of Fluids, 10, 1409, (1967).
12. Kraichnan and Spiegel: The Physics of Fluids, 5, 583, (1962).
13. Heisenberg, W.: Proc. Roy. Soc. London, A195, 402, (1948).
14. Obukhoff, A.M.: Compt. Acad. Sci. URSS, 32, 19, (1941).
15. Von-Karman, Th.: Proc. Natl. Acad. Sci. USA, 34, 530, (1948).
16. Ellison, T.H.: "Mecanique de la Turbulence", p. 113, Symposium, Marseille, France, (1961).
17. Dagstad, I.: Meteorologisk Annalr. Norske Meteor. Inst., 4, No. 17, 441, (1962).
18. Comte-Bellot, G. and Corrsin, S.: J. Fluid Mech., 25, 657, (1966).
19. Batchelor, G.K. and Townsend, A.A.: Proc. Roy. Soc., A193, 539, (1948).
20. Korneyev, A.J. and Sedov, L.I.: Fluid Mec., Soviet Res., 5, 37, (1976).
21. Hinze, J.D.: "Turbulence", 2nd Ed., McGraw-Hill, N.Y. (1975).
22. Kolmogorov, A.N.: Compt. Rand. Acad. Sci. USSR, 31, 538, (1941).
23. Tan, H.S. and Ling, S.C.: The Physics of Fluids, 6, 1693 (1963).
24. Sato, H.: J. Physics Soc. Japan, 6, 387; 7, 392 (1952).

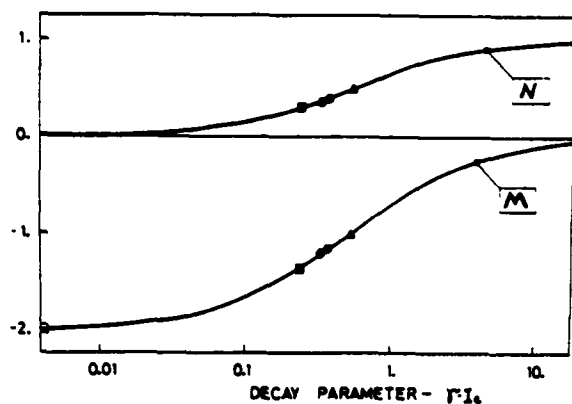


Fig. 1. The dependence of M and N on the decay parameter $-\gamma$.

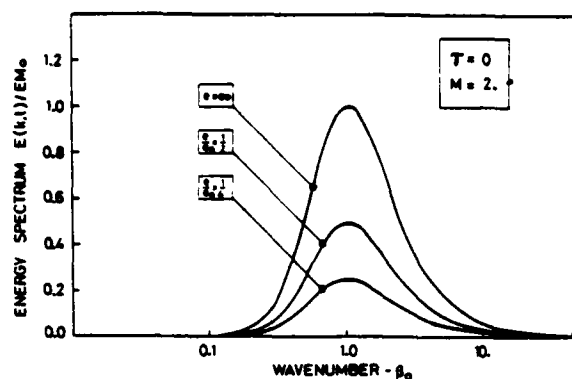


Fig. 2. The decay of the energy spectrum for $\gamma_{le}=0$.

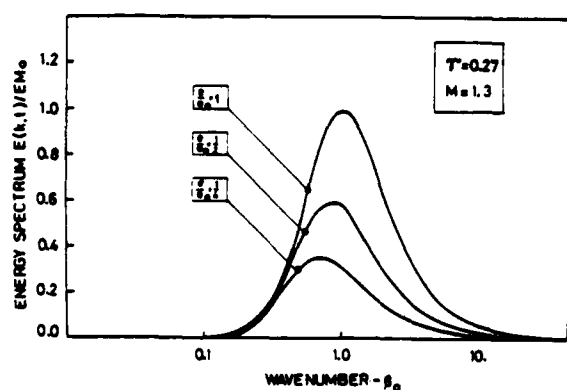


Fig. 3. The decay of the energy spectrum for $\gamma_{le}=0.27$.

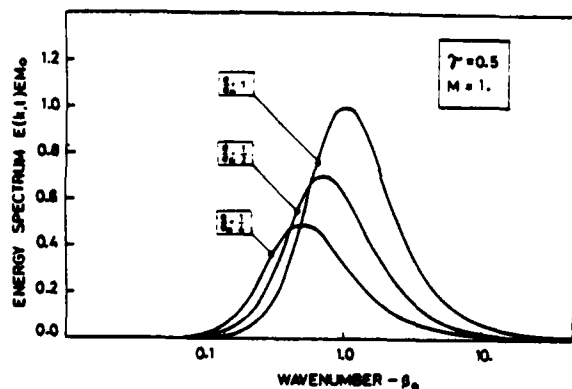


Fig. 4. The decay of the energy spectrum for $\gamma_{le}=0.5$.

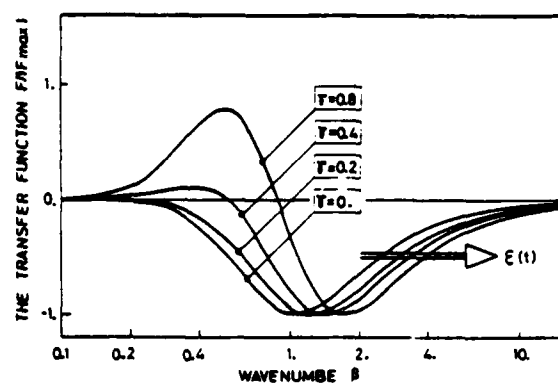


Fig. 5. The dependence of the transfer function $F(k)$ on the decay parameter $-\gamma$.

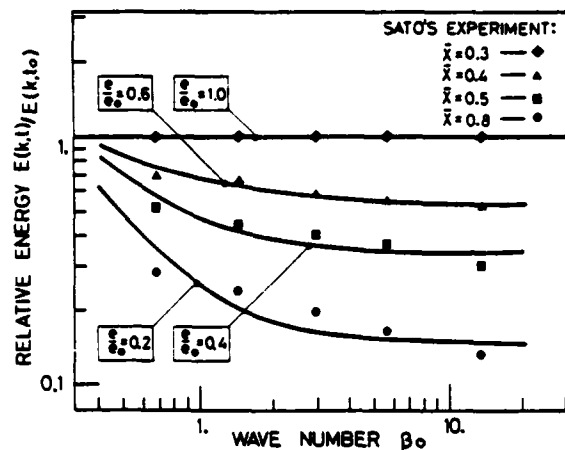


Fig. 6. Comparison of the decay of the spectral components with Sato's experiment.

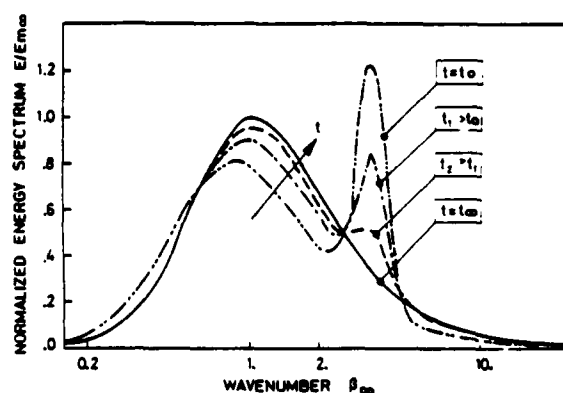


Fig. 7. The isotropizing process.

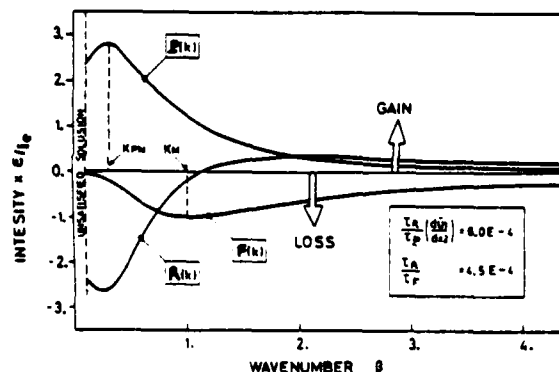


Fig. 8. Spectral energy balance in homogeneous shear flow turbulence.

SOME DEVELOPMENTS IN THE APPLICATION OF RENORMALISATION METHODS TO TURBULENCE THEORY

W.D. McComb and V. Sharmugasundaram
Department of Mechanical Engineering
University of Edinburgh
King's Buildings
EDINBURGH EH9 3JL
UK

ABSTRACT

The use of renormalisation methods in turbulence theory is discussed. A renormalised perturbation theory (McComb 1978) is used to calculate the statistical parameters of freely-decaying isotropic turbulence. Some preliminary results show that the theoretical spectra are in good agreement with experimental results. Also, some preliminary results are presented for the isotropic part of the effective viscosity calculated by a new technique of Iterative Averaging (McComb 1982).

INTRODUCTION

As is well known, the fundamental problem in the theory of well-developed turbulence is the need to close the infinite hierarchy of moment equations, which is generated when one averages the equation of motion. This closure problem stands in the way of engineering calculations and fundamental studies alike. In the first case, it is normally seen as the need to relate single-point quantities (e.g. the mean velocity, the Reynolds stress) to each other. In the second, it involves two-point quantities and is usually restricted to isotropic turbulence, where the mean rate of shear is zero and the moment hierarchy may be studied in isolation. In this paper we are concerned with the fundamental problem and, in particular, with reporting some new results obtained by using renormalisation methods.

Originally renormalisation was the procedure for removing the divergences that occur in the Feynman graph expansion of quantum electrodynamics. The term has now spread to other methods of handling perturbation expansions - mainly in statistical mechanics - and the general approach may be conveniently referred to as renormalised perturbation theory (RPT).

The application of renormalisation methods to turbulence began with Kraichnan (1959), who used RPT to obtain the Direct-Interaction Approximation (DIA). The main advance of this work was that the realisability of the theory was assured (i.e. spectra would always be positive). Its main success has been its ability to predict the decay of grid turbulence at low-to-moderate microscale Reynolds numbers, without recourse to adjustable constants or *ad hoc* assumptions. However, at high Reynolds numbers, DIA fails to yield the Kolmogoroff ($k^{-5/3}$) spectrum.

Of course nowadays there is some debate about whether compatibility with the Kolmogoroff spectrum is a crucial test for a turbulence theory. It is argued that when intermittency is taken into account, the exponent may not be exactly $5/3$. We shall make only two points about this here. First, the experimental

confirmation of $k^{-5/3}$ at large Reynolds numbers means that a failure to agree closely with Kolmogoroff implies a failure to agree with experiment. Second, there are some grounds for believing that $k^{-5/3}$ may be the rigorous solution for a second-order closure, in the limit of infinite Reynolds numbers.

Kraichnan's DIA had a dramatic effect on the subject and many papers followed during the 1960s and early 1970s. A general discussion may be found in the book by Leslie (1973). In all cases, these theories - mostly self-consistent methods - gave the same energy equation as DIA. But in some cases the equation for the renormalised response (or propagator) function differed from the DIA form. However, with only two exceptions, these theories also failed to give the Kolmogoroff spectrum.

The two exceptions are the Abridged Lagrangian-History form of DIA (ALHDI : Kraichnan 1965) and the Entropy Maximisation of Edwards and McComb (1969). Both these theories have their disadvantages; namely great complexity and the need for *ad hoc* simplifications. However ALHDI gave good results at large Reynolds numbers.

More recently, a new version of the Lagrangian-History approximation, Strain-Based ALHDI (or SBALHDI) has proved able to give accurate predictions of freely-decaying isotropic turbulence at both low and high Reynolds numbers (Kraichnan and Herring 1978; Herring and Kraichnan 1979).

In this paper we shall present some preliminary results for freely-decaying isotropic turbulence, as calculated using the Local Energy Transfer (LET) theory (McComb 1974, 1976, 1978). This theory is a purely Eulerian closure which differs from DIA by the presence of an additional term in the response equation. It is compatible with the Kolmogoroff spectrum in the infinite Reynolds number limit.

Finally, in recent years, the success of Renormalisation Group (RG) theory in critical phenomena (Wilson 1975) has led to a drift away from RPT approaches to RG methods. So far RG Theory has generally only been applied to some rather restricted problems (e.g. see the review by Kraichnan 1982) but more ambitious approaches have been the applications to sub-grid modelling for scalar transport (Rose 1977) and, by a new method of averaging (Iterative Averaging : McComb 1982), to shear flows. We shall also present some preliminary calculations of eddy viscosities from the latter theory.

THE STATISTICAL EQUATIONS

Let us consider an incompressible fluid occupying a cubical box of side L . At a later stage we shall take

the limit $L \rightarrow \infty$ (which is required for rigorous isotropy) and summation will then be replaced by integrals. If we let the velocity field be $U_\alpha(\underline{x}, t)$, then the Fourier components of this are defined by

$$U_\alpha(\underline{x}, t) = \sum_{\underline{k}} U_\alpha(\underline{k}, t) e^{i\mathbf{k} \cdot \underline{x}}. \quad (1)$$

The equation of motion may be written as

$$\left(\frac{\partial}{\partial t} + \nu_0 k^2\right) U_\alpha(\underline{k}, t) = \Pi_\alpha(\underline{k}) + \sum_{\underline{j}} M_{\alpha\beta\gamma}(\underline{k}) U_\beta(\underline{j}, t) U_\gamma(\underline{k}-\underline{j}, t), \quad (2)$$

where ν_0 is the molecular kinematic viscosity, $\Pi_\alpha(\underline{k})$ is an external pressure gradient, and the inertial transfer operator $M_{\alpha\beta\gamma}(\underline{k})$ is defined by

$$M_{\alpha\beta\gamma}(\underline{k}) = (2i)^{-1} \{k_\beta D_{\alpha\gamma}(\underline{k}) + k_\gamma D_{\alpha\beta}(\underline{k})\} \quad (3)$$

and

$$D_{\alpha\beta}(\underline{k}) = \delta_{\alpha\beta} - k_\alpha k_\beta / k^2. \quad (4)$$

The pair correlation of velocities may be defined, thus:

$$\left(\frac{1}{2\pi}\right)^3 \langle U_\alpha(\underline{k}, t) U_\beta(-\underline{k}, t') \rangle = Q_{\alpha\beta}(\underline{k}; t, t'), \quad (5)$$

where $\langle \rangle$ means average value. For isotropic turbulence, the correlation function $Q(\underline{k}; t, t')$ may be introduced through the relationship

$$Q_{\alpha\beta}(\underline{k}; t, t') = D_{\alpha\beta}(\underline{k}) Q(\underline{k}; t, t'). \quad (6)$$

In theoretical work it is normal to use the ensemble average. For reasons which will emerge, we shall discuss time-averages and we shall represent these by either overbars or Dirac brackets as convenient. For quasisteady flows, the average with respect to time, is defined as

$$\bar{U}_\alpha(\underline{k}, t) = \frac{1}{2T} \int_{-T}^T U_\alpha(\underline{k}, t+s) ds. \quad (7)$$

The averaging period $2T$ must be long enough to smooth out the fluctuations associated with the turbulent cascade but must also be shorter than the time-scale associated with any external time-dependence that we might wish to study.

The formulation of statistical equations is well known and proceeds as follows. Let us represent the instantaneous velocity field as the sum of a mean and a fluctuation from the mean, thus:

$$U_\alpha(\underline{k}, t) = \bar{U}_\alpha(\underline{k}, t) + u_\alpha(\underline{k}, t), \quad (8)$$

where $u_\alpha(\underline{k}, t)$ is the fluctuating field. Substitution of (8) into (2) and averaging using (7) yields

$$\left(\frac{\partial}{\partial t} + \nu_0 k^2\right) \bar{U}_\alpha(\underline{k}, t) = \Pi_\alpha(\underline{k}) + \sum_{\underline{j}} M_{\alpha\beta\gamma}(\underline{k}) \{ \bar{U}_\beta(\underline{j}, t) \bar{U}_\gamma(\underline{k}-\underline{j}, t) + \left(\frac{2\pi}{T}\right)^3 Q_{\beta\gamma}(\underline{k}, t) \}. \quad (9)$$

This is a form of Reynolds equation but is only valid away from solid boundaries, as we have neglected the surface integral terms when eliminating the internal pressure.

Also, subtracting (9) from (2), multiplying by $u_\alpha(\underline{k}, t')$ and averaging, yields the general equation for the fluctuating field

$$\left(\frac{\partial}{\partial t} + \nu_0 k^2\right) Q_{\alpha\alpha'}(\underline{k}, \underline{k}'; t, t') = \sum_{\underline{j}} M_{\alpha\beta\gamma}(\underline{k}) \{ 2\bar{U}_\gamma(\underline{j}, t) \}$$

$$+ Q_{\beta\gamma}(\underline{k}-\underline{j}, \underline{k}'; t, t') + Q_{\beta\gamma\alpha'}(\underline{j}, \underline{k}-\underline{j}, \underline{k}'; t, t, t') \}, \quad (10)$$

where $Q_{\alpha\beta\gamma}$ is a triple moment, defined by analogy with (5). If we attempt to obtain an equation for $Q_{\alpha\beta\gamma}$ then it will contain the fourth-order moment $Q_{\alpha\beta\gamma\delta}$; and so on. This is, of course, the closure problem.

Traditionally, engineering applications have focused on equation (9) and various hypotheses have been used to relate the Reynolds stresses $Q_{\alpha\beta}$ to the mean velocity \bar{U}_α . Generally the idea of an effective viscosity has been most valuable. In recent years, such hypotheses have been extended to single-point versions of (10), in order to develop relationships between the various components of $Q_{\alpha\beta}$, the dissipation rate, and the mean velocity.

In contrast, fundamental studies have concentrated on isotropic turbulence, where we may take $\bar{U} = 0$ (more strictly, its spatial gradient is zero and then we can transform to a co-ordinate system moving with the mean velocity). Under these circumstances equation (9) becomes irrelevant and equation (10) reduces to:

$$2\left(\frac{\partial}{\partial t} + \nu_0 k^2\right) Q(\underline{k}; t, t') = \sum_{\underline{j}} M_{\alpha\beta\gamma}(\underline{k}) \times Q_{\beta\gamma\alpha}(\underline{j}, \underline{k}-\underline{j}, -\underline{k}; t, t, t'), \quad (11)$$

with corresponding equations for the third and higher moments.

We shall touch on both approaches in this paper. In the next section we discuss the LET theory for isotropic turbulence.

THE LOCAL ENERGY TRANSFER (LET) THEORY

Theories of isotropic turbulence are generally formulated in the following way. At some time in the remote past, we assume that the nonlinear term is switched off and that the velocity field $U_\alpha^{(0)}(\underline{k}, t)$ results from the action of random stirring forces, which are taken to have a normal distribution. The assumption of normal (or Gaussian) statistics allows one to work out all the moments of the zero-order field in terms of $Q^{(0)}$. Under these circumstances, we can introduce the zero-order propagator $H^{(0)}$, such that

$$U_\alpha^{(0)}(\underline{k}, t) = H_{\alpha\sigma}^{(0)}(\underline{k}; t, s) U_\sigma^{(0)}(\underline{k}, s), \quad (12)$$

where $H^{(0)}$ satisfies

$$\left(\frac{\partial}{\partial t} + \nu_0 k^2\right) H_{\alpha\beta}^{(0)}(\underline{k}; t, t') = D_{\alpha\beta}(\underline{k}) \delta(t-t'), \quad (13)$$

and has the properties

$$H_{\alpha\sigma}^{(0)}(\underline{k}; t, s) H_{\sigma\beta}^{(0)}(\underline{k}; s, t') = H_{\alpha\beta}^{(0)}(\underline{k}; t, t') = D_{\alpha\beta}(\underline{k}) H^{(0)}(\underline{k}; t, t') \\ H^{(0)}(\underline{k}; t, t) = 1. \quad (14)$$

If we now switch on the nonlinear terms, then the modes of the zero-order field become coupled together in a systematic fashion. Thus the exact velocity field $U_\alpha(\underline{k}, t)$ is obtained from the sum of interactions of the zero-order field. And, as all the moments of the zero-order field can be evaluated, the exact correlation Q is given by the sum of a corresponding expansion in terms of $H^{(0)}$ and $Q^{(0)}$.

Formal analyses of the primitive perturbation series show that renormalisation is achieved (to second order) by replacing $H^{(0)}$ and $Q^{(0)}$ by their exact forms H and Q , and retaining terms quadratic in Q . In DLA a separate equation is derived for $H^{(0)}$ (strictly $G^{(0)}$, in Kraichnan's notation: $G^{(0)}$ relates infinitesimal changes in the velocity field to the corresponding infinitesimal changes in the stirring forces). Renormalisation of this second equation is achieved in the

same way ($Q^{(0)} \rightarrow Q$; $G^{(0)} \rightarrow G$) and terms quadratic in G are retained.

In LET, the equations for both Q and H are obtained directly from the primitive series. Renormalisation is anticipated by introducing the exact propagator formally. By analogy with equation (12), H is introduced by

$$U_a(\underline{k}, t) = H_{aG}(\underline{k}; t, s) U_G(\underline{k}, s) \\ = D_{aG}(\underline{k}) H(\underline{k}; t, s) U_G(\underline{k}, s), \quad (15)$$

with properties analogous to those given by equations (14) for $H^{(0)}$.

The derivation of the LET equations for H and Q may be found elsewhere (McComb 1978). Here we quote the result for isotropic, non-stationary turbulence as follows:

$$\left(\frac{\partial}{\partial t} + \nu_0 k^2\right) H(\underline{k}; t, t') = W(\underline{k}; t, t'), \quad t' \leq t \quad (16)$$

$$\left(\frac{\partial}{\partial t} + \nu_0 k^2\right) Q(\underline{k}; t, t') = P(\underline{k}; t, t'). \quad (17)$$

The inertial transfer terms W and P are given by

$$W(\underline{k}; t, t') = \int d^3 \underline{j} L_{kju} \\ \times \int_0^{t'} ds \frac{H(\underline{k}; t', s) Q(\underline{j}; t, s) Q(|\underline{k}-\underline{j}|; t, s)}{Q(\underline{k}; s, s)} \\ - \int_0^t ds H(\underline{k}; s, t') H(\underline{j}; t, s) Q(|\underline{k}-\underline{j}|; t, s) \quad (18)$$

and

$$P(\underline{k}; t, t') = \int d^3 \underline{j} L_{kju} \\ \times \int_0^{t'} ds H(\underline{k}; t', s) Q(\underline{j}; t, s) Q(|\underline{k}-\underline{j}|; t, s) \\ - \int_0^t ds Q(\underline{k}; s, t') H(\underline{j}; t, s) Q(|\underline{k}-\underline{j}|; t, s), \quad (19)$$

where

$$L_{kju} = \frac{[u(k^2 + j^2) - kj(1 + 2u^2)](1 - u^2)kj}{k^2 + j^2 - 2kju}, \quad (20)$$

and u is the cosine of the angle between the vectors \underline{k} and \underline{j} .

It should be noted that equations (17) and (19) are identical (notational differences aside) to the corresponding DIA equations, whereas (16) and (18) differ from their DIA equivalents by the presence of the first term (i.e. the one containing Q^{-1}) on the right-hand side of (18) for $W(\underline{k}; t, t')$.

Equations (16) and (17) were integrated forward in time, from a variety of initial conditions, using the methods previously used by Kraichnan (1964) for DIA. Full details will be given elsewhere so we shall just summarise some interesting features here. Four of the trial spectra were of the form

$$\text{Spectra I-IV: } E(k, 0) = C_1 k^{C_2} \exp(-C_3 k^{C_4}), \quad (21)$$

where $C_1 - C_4$ are constants. The fifth initial spectrum was given by:

$$\text{Spectrum V: } E(k, 0) = 2\pi k^{-5/3}. \quad (22)$$

Spectra I, II, and III were identical to spectra B, C and D of Kraichnan (1964). The LET equations were computed using each of these initial spectra to give evolved microscale Reynolds number $R_\lambda \sim 20$. In general LET was found to behave much like DIA, with evolved spectra becoming independent of initial spectrum shape and also showing self-preservation. However, LET gave higher values of energy transfer and of evolved skewness factor than DIA.

Spectrum IV was chosen in the light of comments by Van Atta and Chen (1969) to test the effect of a lower value of the peak wavenumber. In this case ($C_1 = 0.4$, $C_2 = 1$, $C_3 = 0.5$, $C_4 = 1$) calculations were made for an evolved $R_\lambda \sim 40$. The results for the one-dimensional dissipation spectrum $k^2 \phi_1(k, t)$ are shown in Fig. 1 where they are compared with the DIA value and with some representative experimental results. Here $u(t)$ is the RMS velocity and k_d is a characteristic wavenumber (Kraichnan 1964).

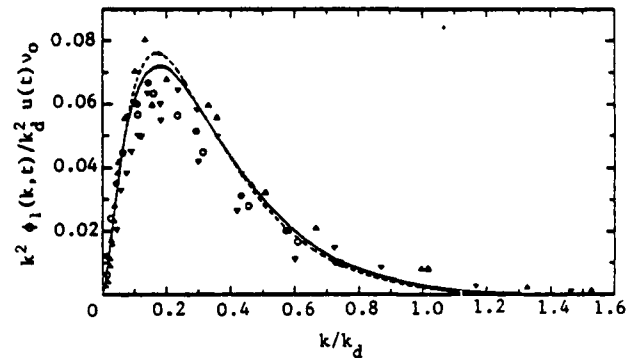


FIG. 1 Comparison of evolved one-dimensional dissipation spectra at moderate values of R_λ .

Computed results for Spectrum IV at $tu(0)/L(0) = 1.0$: —, LET, $R_\lambda = 38.2$; - - -, DIA, $R_\lambda = 40.5$.

Experimental results: ∇ , $R_\lambda = 39.4$, $x/M = 30$ (Stewart & Townsend 1951); \circ , $R_\lambda = 49.0$ and \oplus , $R_\lambda = 35.0$ at $x/M = 48$ (Chen 1968); Δ , $R_\lambda = 38.1$, $x/M = 240$ and \triangle , $R_\lambda = 36.6$, $x/M = 385$ (Comte-Bellot & Corrsin 1971); ∇ , $R_\lambda = 45.2$, $x/M = 174.4$ (Frenkiel & Klebanoff 1971).

The remaining results in this section are from the calculations at high Reynolds numbers. Spectrum V was computed for an evolved $R_\lambda \sim 533$. In Fig. 2 we show the evolution of the one-dimensional spectrum plotted as $(k/k_g)^{5/3} \phi_1(k, t) / (\epsilon \nu_0^2)^{1/2}$ against k/k_g , where ϵ is the dissipation rate and k_g is the Kolmogoroff wavenumber. In Fig. 3 we show the evolved one-dimensional spectrum compared with experimental results from four different investigations. Clearly the spectrum calculated from LET agrees quite well with the measured spectra.

Finally, in Fig. 4 we compare the evolved spectrum with the computed spectra using ALHDI and SBALHDI (Herring and Kraichnan 1979) and with some representative experimental results. By plotting $k^{5/3} \phi_1(k, t)$ we show up differences more clearly than on the plot of $\phi_1(k, t)$ against k . Even so, the three theories agree quite well with each other and with experiment within the scatter of the experimental data. It is noteworthy that LET agrees more closely with SBALHDI than with ALHDI. A comparison of all four theories (LET, DIA, ALHDI and SBALHDI) at low Reynolds numbers (Spectrum III: $R_\lambda = 19.0$) showed that the agreement between LET and SBALHDI was significantly closer than that between any other pair of theories.

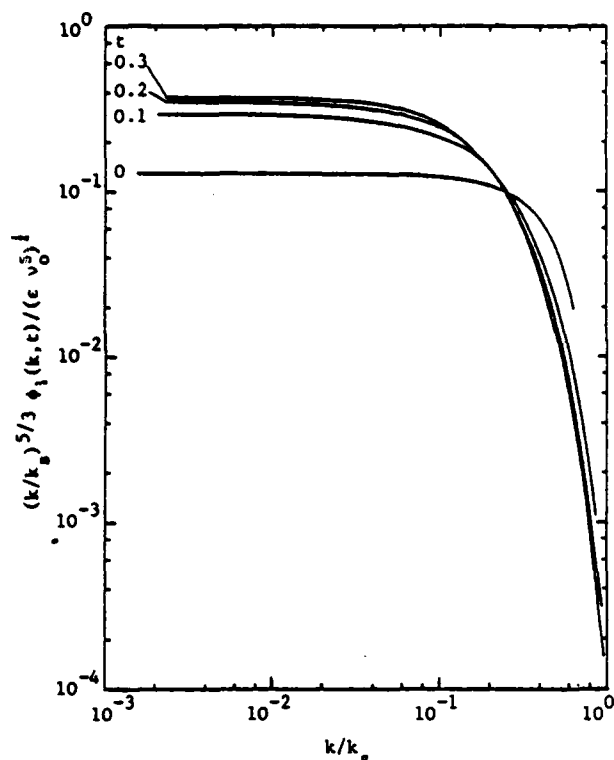


FIG. 2 Evolution of normalised one-dimensional energy spectrum : Spectrum V.

ITERATIVE AVERAGING AND RG

RG theory involves the progressive scaling away of the highest wavenumbers, whose effect on smaller wavenumbers can be retained in average form, as a contribution to a transport coefficient. When the system becomes invariant under such transformations it is said to have reached a fixed point. In general this fixed point corresponds to a critical point.

Rose (1977) has applied RG theory to the sub-grid modelling of passive scalar convection. However the method can readily be generalised to the mathematically similar problem of obtaining an equation for the mean velocity from equation (2). The procedure consists of three stages as follows:

- (1) Divide up the velocity field into $u^<(k, t)$ and $u^>(k, t)$ where $u^>$ are the modes such that $k > k_0$ (say). Eliminate the high- k modes by solving equation (2) for $u^>$ and substituting into the equation for $u^<$.
- (2) Average over the high- k modes.
- (3) Re-scale k , t , and $u^<$ so that the new equation looks like equation (2). This step involves the introduction of renormalised transport coefficients.

We shall return to Rose's formulation later in order to compare it with our own (McComb 1982).

Let us now reconsider the problem of solving equation (2) for the mean velocity. We replace the Reynolds averaging (equations (7) - (9)) by the following procedure. We introduce the iterative averaging technique by defining

$$\langle U(t) \rangle_n = \tau_n^{-1} \int_0^{\tau_n} U(t+s) \text{sinc}(\pi s/\tau_n) ds, \quad (23)$$

where $\text{sinc} x = x^{-1} \sin x$ and τ_n is a member of the set $\{\tau_0, \tau_1, \dots, \tau_n, \dots\}$ such that $\tau_0 < \tau_1 < \dots < \tau_n$. Then

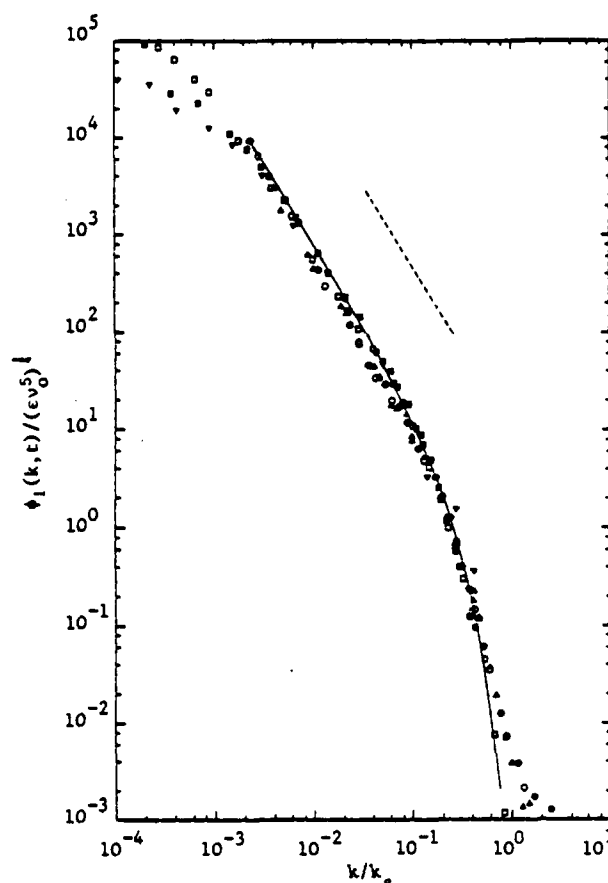


FIG. 3 Comparison of evolved one-dimensional energy spectrum with experimental results.

Theory: —, LET, $R_\lambda \sim 533$.
Experiments: $\circ, \bullet, \Delta, \triangle, R_\lambda \sim 2000$ (2/2/60, Grant et al. 1962); $\blacksquare, R_\lambda \sim 538$ (Kistler & Vrebalovich 1966); $\nabla, R_\lambda \sim 308$ (Uberoi & Freymuth 1969); $\square, R_\lambda \sim 850$ (Coantic & Favre 1974). ---, $k^{-5/3}$.

averaging over τ_0 smooths out frequencies greater than $\omega_0 = \pi/\tau_0$. And so on, for $\tau_1 \dots \tau_n \dots$

We now wish to develop an iterative solution for the mean velocity. We divide up the velocity field as follows:

$$U(t) = U^-(t) + U^+(t) \quad (24)$$

where

$$\langle U(t) \rangle_n = U^-(t) \quad (25)$$

and

$$\langle U^+(t) \rangle_n = 0. \quad (26)$$

Let us begin with $n = 0$ and take τ_0 to be small. If we Fourier-transform (23) into the frequency domain we obtain

$$\langle U(\omega) \rangle_0 = A_0(\omega) U(\omega) \quad (27)$$

where $A_0(\omega)$ is the Fourier Transform of $a_0(t)$ and we have used the convolution theorem. Then

$$U^+(\omega) = \{1 - A_0(\omega)\} U(\omega) \quad (28)$$

and hence taking positive ω ,

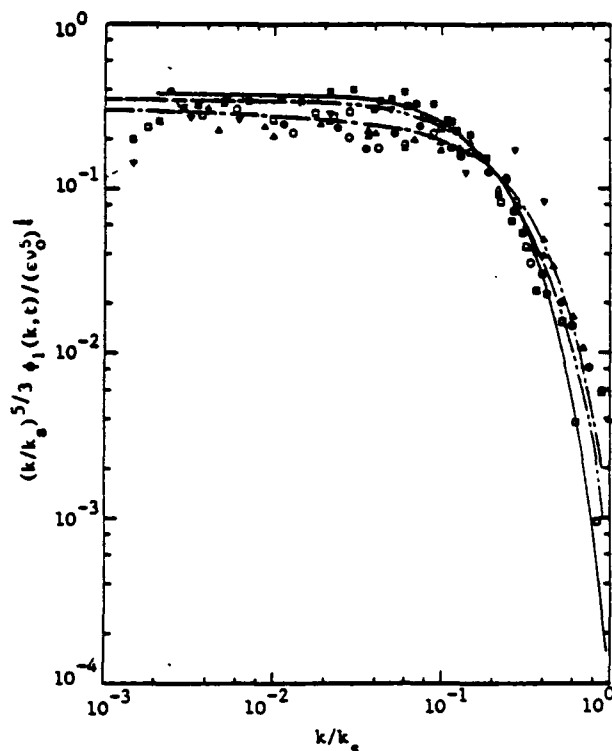


FIG. 4 Comparison of evolved $k^{5/3} \phi_1(k, t)$ with other theoretical and experimental results.

Theory: —, LET; — — —, ALHDI and — — — —, SBALHDI (Herring & Kraichnan 1979).

Experiment: O, Δ , \square , ∇ (Grant et al. 1962); \bullet (Kistler & Vrebalovich 1966); \circ (Uberoi & Freymuth 1969); \square (Coantic & Favre 1974).

$$U^+(\omega) = 0 \text{ for } 0 \leq \omega \leq \pi/\tau_0 \\ = U(\omega) \text{ for } \pi/\tau_0 < \omega < \infty. \quad (29)$$

Noting that: (a) U^+ is small compared to U^- ; and (b) the decay of U^+ is controlled by v_0 (together, these conditions are our criterion for the choice of τ_0), we substitute (24) into (2) and average each term using (23) with $n = 0$. The resulting equation for U^- is then subtracted from (2) to give an equation for U^+ . The solution for U^+ (which contains only frequencies $\geq \pi/\tau_0$) may be obtained using the zero-order (viscous) Green function. Then substitute for U^+ back into the equation for U^- - the result being an incremental change to the viscosity $v_0 \rightarrow v_0 + \delta v_0$ - rename $U^- \rightarrow U$ and repeat for $\tau_1 > \tau_0$.

After the first iteration, equation (2) becomes (McComb 1982),

$$\left(\frac{\partial}{\partial t} + v_0 k^2 \right) \int d^3 j L_{kju} (v_0 j^2)^{-1} Q_0^*(|k-j|, t) U_a^-(k, t) \\ = \Pi_a(k) + \int j M_{a\beta\gamma}(k) U_\beta^-(j, t) U_\gamma^-(|k-j|, t), \quad (30)$$

where Q_0^* is defined by analogy with Q as given by equation (5) and L_{kju} is given by equation (20). Using the same notation, Rose's (1977) method gives equation (2) in the form

$$\left(\frac{\partial}{\partial t} + v_0 k^2 \right) \int d^3 j L_{kju} (v_0 j^2)^{-1} Q_0^*(|k-j|, t) U_a^-(k, t) \\ = \Pi_a(k) + \int j M_{a\beta\gamma}(k) U_\beta^-(j, t) U_\gamma^-(|k-j|, t)$$

$$= \Pi_a(k) + \int j M_{a\beta\gamma}(k) U_\beta^-(j, t) U_\gamma^-(|k-j|, t) \\ + 2 \int j M_{a\beta\gamma}(k) M_{\beta\delta\gamma}^*(j) (v_0 j^2)^{-1} \\ \times U_\gamma^-(k-j, t) U_\delta^-(j, t) U_\gamma^-(j, t), \quad (31)$$

where a plus superscript on a quantity indicates that the corresponding wavenumber argument is greater than k_0 . The connection between the two may be made using the well known Taylor hypothesis of frozen convection, thus: $kU = \omega$, where U is the local mean velocity. Evidently equation (31) mainly differs from the preceding equation in that it contains the low- k triple product $U^- U^- U^-$ on the righthand side.

This difference assumes greater importance as the iteration proceeds. We choose the averaging times to be

$$\tau_n = h^{-n} \tau_0, \quad (32)$$

where h satisfies $0 \leq h \leq 1$ and $\tau_0 = (v_0/\epsilon)^{1/2}$, ϵ being the energy dissipation rate. The recursion relation for the effective viscosity is found to be:

$$v_{n+1}(k, t) = v_n(k, t) + \delta v_n(k, t), \quad (33)$$

$$\delta v_n(k, t) = \frac{\int d^3 j L_{kju} Q_n^*(|k-j|, t)}{v_n(j) k^2 j^2}. \quad (34)$$

This can be obtained inductively from equation (30). Clearly the corresponding result from (31) will be more complicated as it will receive a contribution from the $U^- U^- U^-$ term. We shall not give further details here and reference should be made to Rose (1977) for the equation which corresponds to (34) in the present work.

Our formulation is completed by the transformations:

$$t \rightarrow h^{-n} \tau_0 t', \\ k \rightarrow (\pi \tau_0^{-1} h^n U^{-1}) k' = k_n k', \quad (35)$$

Using the procedures of McComb (1982), calculations were carried out for the stationary case on the assumption that the fluctuations are isotropic with spectrum $E(k) = \alpha \epsilon^{2/3} k^{-5/3}$ where α is a constant. Under these circumstances, (33) and (34) imply:

$$v_n(k_n k') = \alpha^{1/2} \epsilon^{1/3} k_n^{-4/3} v_n^*(k'), \quad (36)$$

$$\delta v_n^*(k') = \frac{1}{4\pi} \int d^3 j L_{k'j} |k'-j|^{-11/3} \\ v_n^*(j) k'^2 j'^2 \quad (37)$$

for $1 < |k'-j| < h^{-1}$ and $1 < k', j' < \infty$. The recursion relationship then becomes:

$$v_{n+1}^*(k') = h^{4/3} \{ v_n^*(hk') + \delta v_n^*(hk') \}. \quad (38)$$

Equations (37) and (38) were computed numerically. Various trial values were assumed for the arbitrary parameters v_0 (which fixes τ_0) and h . Fig. 5 shows v_n^* plotted against n for $h = 0.6$, $k' = 5.0$ and for a range of values of the (scaled) initial viscosity, v_0^* . The recursion relation was found to reach a fixed point, such that $\text{Lt } v_n^*(k') \rightarrow v^*(k')$ as $n \rightarrow \infty$. Clearly this result is independent of the initial viscosity for a wide range of v_0^* .

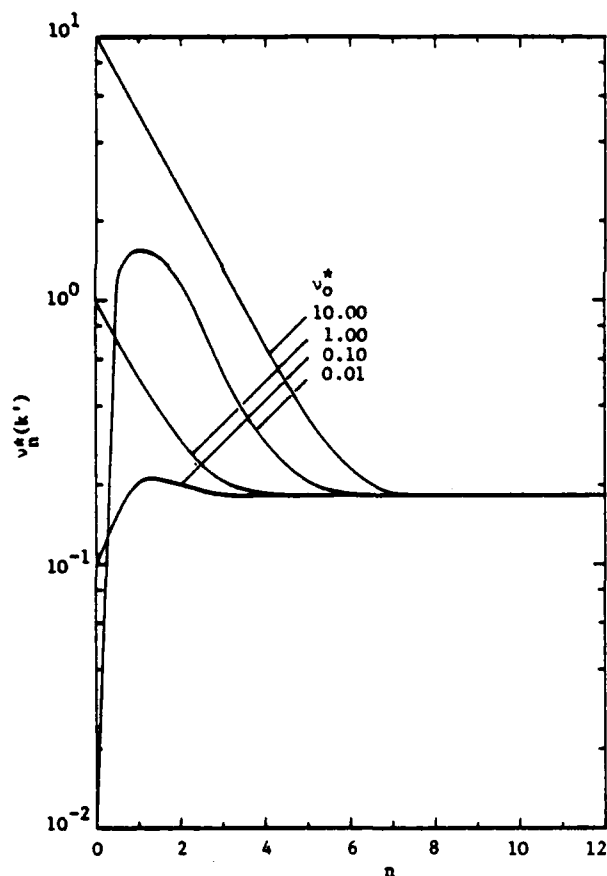


FIG. 5 Effect of choice of v_0^* on $v_n^*(k')$ for $h = 0.6$ and $k' = 5.0$

A particularly interesting result is the evolution of $v_n^*(k')$ to the fixed functional form $v_n^*(k') = 2.5 (k/k_N)^{-4/3}$, as seen in Fig. 6. From equation (36) we find that the eddy viscosity becomes

$$v_N(k) = \alpha^{1/2} \epsilon^{1/3} k_N^{-4/3} v_n^*(k') = 2.5 \alpha^{1/2} \epsilon^{1/3} k^{-4/3}. \quad (39)$$

This is only the isotropic part of the eddy viscosity so it cannot be compared to the eddy viscosities measured in shear flows. However on comparison with the effective viscosity for eddy decay rates in closures like LET, equation (39) does at least seem to be of the correct order of magnitude.

CONCLUSION

The results given above for LET, and for the Iterative Averaging technique, may be seen as encouraging. But they are not going to produce an overnight transformation in the way turbulent shear flows are calculated. It is quite well known that closures like DIA (e.g. Leslie 1973) or LET (let alone the Lagrangian History forms) are much too complicated to allow the computation of even the simplest shear flow using present-day computers.

However, if we may be permitted a mildly optimistic speculation, then we would suggest that the two theories could be used to considerable effect in Large-Eddy Simulations. The Iterative Averaging method can be employed to formulate the equations for LES, with the sub-grid drain modelled in terms of $v^*(k')$. In turn, this requires the energy spectrum at large wavenumbers, which could be calculated using the LET theory.

In principle, this looks like an attractive strategy. In practice, there are, of course many problems

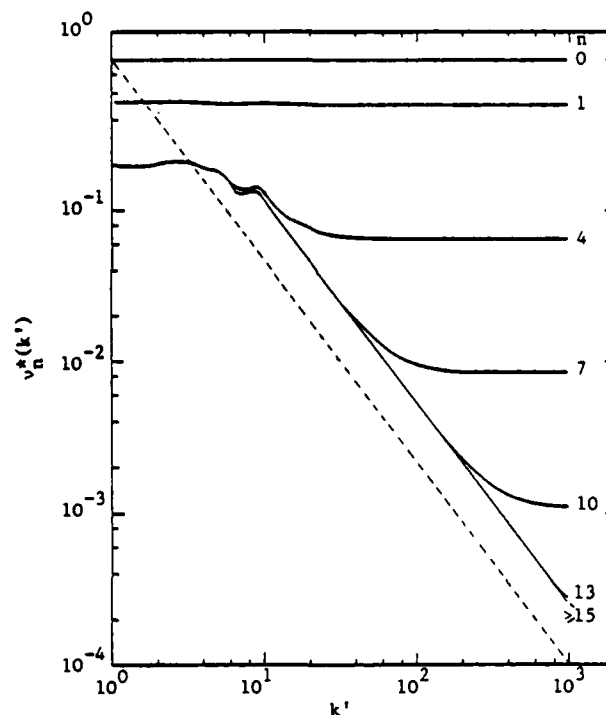


FIG. 6 Evolution of $v_n^*(k')$ for $h = 0.6$

to be overcome. At present we are in the preliminary stages of tackling plane channel flow by this method and time alone will tell whether mild optimism is justified.

REFERENCES

1. Chen, W.Y., 1968, "Spectral energy transfer and higher-order correlations in grid turbulence", Ph.D. Thesis, University of California, San Diego.
2. Coantic, M. and Favre, A., 1974, "Activities in, and preliminary results of, air-sea interaction research at I.M.S.T.", Adv. Geophys., 18A, 391.
3. Comte-Bellot, G. and Corrsin, S., 1971, "Simple Eulerian time correlation of full- and narrow-band velocity signals in grid-generated, 'isotropic' turbulence", J. Fluid Mech., 48, 273.
4. Edwards, S.F. and McComb, W.D., 1969, "Statistical mechanics far from equilibrium", J. Phys., A2, 157.
5. Frenkiel, N.F. and Klebanoff, P.S., 1971, "Statistical properties of velocity derivatives in a turbulent field", J. Fluid Mech., 48, 183.
6. Grant, H.L., Stewart, R.W. and Moilliet, A., 1962, "Turbulence spectra from a tidal channel", J. Fluid Mech., 12, 241.
7. Herring, J.R. and Kraichnan, R.H., 1979, "A numerical comparison of velocity-based and strain-based Lagrangian-history turbulence approximations", J. Fluid Mech., 91, 581.
8. Kistler, A.L. and Vrebalovich, T., 1966, "Grid turbulence at large Reynolds numbers", J. Fluid Mech., 26, 37.
9. Kraichnan, R.H., 1959, "The structure of isotropic turbulence at very high Reynolds numbers", J. Fluid Mech., 5, 497.
10. Kraichnan, R.H., 1964, "Decay of isotropic turbulence in the direct-interaction approximation", Phys. Fluids, 7, 1030.

11. Kraichnan, R.H., 1965, "Lagrangian-history closure approximation for turbulence", *Phys. Fluids*, 8, 575.
12. Kraichnan, R.H., 1982, "Hydrodynamic turbulence and renormalisation group", *Phys. Rev. A*, 25, 3281.
13. Kraichnan, R.H. and Herring, J.R., 1978, "A Strain-based Lagrangian-history turbulence theory", *J. Fluid Mech.*, 88, 355.
14. Leslie, D.C., 1973, "Developments in the Theory of Turbulence", Oxford University Press.
15. McComb, W.D., 1974, "A local energy-transfer theory of isotropic turbulence", *J. Phys. A: Math., Nucl. Gen.*, 7, 632.
16. McComb, W.D., 1976, "The inertial-range spectrum from a local energy-transfer theory of isotropic turbulence", *J. Phys. A: Math. Gen.*, 9, 179.
17. McComb, W.D., 1978, "A theory of time-dependent, isotropic turbulence", *J. Phys. A: Math. Gen.*, 11, 613.
18. McComb, W.D., 1982, "Reformulation of the statistical equations for turbulent shear flows", *Phys. Rev. A*, 26, 1078.
19. Rose, H.A., 1977, "Eddy diffusivity, eddy noise and subgrid-scale modelling", *J. Fluid Mech.*, 81, 719.
20. Stewart, R.W. and Townsend, A.A., 1951, "Similarity and self-preservation in isotropic turbulence", *Phil. Trans. Roy. Soc.*, A 243, 359.
21. Uberoi, M.S. and Freymuth, P., 1969, "Spectra of turbulence in wakes behind circular cylinders", *Phys. Fluids*, 12, 1359.
22. Van Atta, C.W. and Chen, W.Y., 1969, "Measurements of spectral energy transfer in grid turbulence", *J. Fluid Mech.*, 38, 743.
23. Wilson, K.G., 1975, "The renormalisation group: Critical phenomena and the Kondo problem", *Rev. Mod. Phys.*, 47, 773.

A NEW LOOK ON TURBULENT SHEAR FLOW

by

Sin-I. Cheng
Princeton University
Princeton, NJ 08544 U.S.A.

ABSTRACT

Recent mathematical theory suggests that fluid turbulence is deterministically represented by the discrete, chaotic solutions of the N-S equations. This is constructively demonstrated with a computational simulation of the development of large disturbances into turbulent spots at $Re = 3000$. The propagating turbulent front appears to be the only universal feature of the intermittent, turbulent shear flows with "organized" structures. In this light, the premises of the statistical theory of turbulence and the secondary instability theory of transition are examined. The physical nature of such turbulent fronts is then explained as the coalesced wave fronts of the propagating pressure disturbance pairs generated to restore the solenoidal velocity field of an incompressible fluid. Such turbulent fronts mark the local solution bifurcations on the way to ultimate chaos. Implications of the physical model are briefly explored.

INTRODUCTION

Transitional and turbulent shear flows either as free layers or wall layers away from solid surface are "intermittently turbulent" and exhibit some global, "coherent" large scale structures although sufficiently varied in details under different configurations^[1,2]. There have been frequent conjectures with artistic rendering of the various structures as to their "quasi-deterministic" nature. The development of statistical theory of turbulence has focused on the closure difficulty without paying much attention to these observations. The closure process has led to much speculation of new physics, either as some property(ies) of turbulence statistics, or as some conservation relations of some global turbulent property(ies) such as stresses, length scales, etc.

Recent mathematical developments^[3] suggest that turbulence results naturally (as a "generic property") from repeated solution bifurcations of nonlinear systems at sufficiently large parametric values. The details of such a chaotic solution is sensitive to data perturbations, so that the problem is not well set in Hadamard sense. It is however, deterministic for each data set. The "Route to Turbulence" or its path of development to some ultimate chaotic state is well defined without any "New Physics". This ultimate or fully developed state of turbulence, defined by a given nonlinear operator is not unique but varies with initial-boundary data. The nonlinear equations systems may be algebraic (difference), differential or integro-differential, etc., for different physical systems or for different approximations to a given physical system. Fluid turbulence is the one defined by the Navier-Stokes system at sufficiently large Reynolds numbers. While computational studies with simple nonlinear model equations have provided

ample support of the theorem, computational simulation of fluid turbulence with the N-S system has been disappointing. Chaotic results are promptly obtained at Reynolds numbers substantially below the transition range without displaying any features that the mathematical theory implies and the physical experiments suggest. Thus, for fluid turbulence, either the mathematical theory or the computational simulation can be suspect.

The statistical and the deterministic views of turbulence point to different faults in the computational simulation. Statistical theory emphasizes energy cascading down to dissipation scale eddies, and calls for very refined computational resolution or suitable sub-grid model(s) to be incorporated in the N-S system. Alternatively the N-S system is simplified either through linearization with stochastic functions or through postulating vorticity transport as the dominant mechanism. The deterministic view suggests, on the other hand, that the N-S system should not be tampered with while high resolution is not necessarily a prerequisite for satisfactory computational simulation of the global features of turbulent shear flows, if N-S system is presumed to be adequate for defining fluid turbulence^[4].

Studies of "strange attractors" as the abstract mathematical image of turbulence^[3] can doubtfully resolve the above practical questions. Bifurcations are varied for different nonlinear systems. Even for a given system bifurcations can become increasingly complex at later stages. We note that such complex phenomena take place in the immediate vicinity of a bifurcation point, too small to be experimented with either physically or computationally^[5]. We are not that much interested in such details, but only in the bifurcated solution(s) that determines the successive stages of later bifurcations on its route to turbulence. Thus we would be satisfied with computational methods of generating transitional states valid merely globally to provide tests against well known large scale features of shear flow turbulence.

For this stated purpose, the results of Feigenbaum^[6] on the "Metric Universal Properties" of period doubling bifurcations is of special interest. It is proved for the one-parameter family mapping of a sufficiently smooth function, having a unique extreme within the interval of the map. This mapping represents the process of functional iterations for the solution of the nonlinear equation $x = F(x, R)$ computationally, where the n -th iterate x_n is calculated from the n th iterate as $x_{n+1} = F(x_n, R)$. If the function $x = x^*$ remains unchanged by the mapping, i.e. $x^* = F(x^*, R)$ then x^* is a solution or a fixed point. The universal properties are: 1) The convergence toward the ultimate turbulent state as is measured by the departure of some parametric value Λ_n of the n th bifurcation from the limiting value Λ_∞ when $n \rightarrow \infty$

is geometric and with some universal rate of $\Lambda_\infty - \Lambda_n \sim \delta^{-n}$ with $\delta = 4.6992$ at sufficiently large n .

2) The functions in the immediate vicinity of every and all bifurcating points are similar and can be reduced to some universal form after some universal scaling of the characteristic length or physical dimension of the bifurcation, i.e. $dn \sim |\alpha|^{-n}$ with $\alpha = 2.5029...$, at sufficiently large n .

3) The universal values are essentially reached in a few bifurcations.

The bifurcation processes of the N-S system and of its discrete approximations are likely more complicated than the period doubling type, but such detailed events of bifurcation processes are hardly significant outside a small region around the bifurcation point. As such, adequate computational simulation of global phenomena may require only modest discrete resolution for a reasonable representation of the first few bifurcations (not the first few harmonics of spectral resolutions). With proper discrete formulations, currently available computers should generate simulated results that compare favorably with experimental observations. This is in sharp contrast with what the statistical theory of turbulence suggests as to the need of very refined mesh resolution and/or sub-grid modeling under the presumption of eventual "convergence" of such discrete approximations to the "solution".

With chaotic solution of the N-S system sensitive to the data, we cannot expect convergent approximations but only asymptotic approximations in some sense. Consistent and stable discrete approximations of some simple, steady, nonlinear equation in one space dimension (Burger's Equation) have indeed been demonstrated to diverge at vanishingly small meshes, but can give adequate asymptotic approximations at coarse meshes. The universality relations provide some basis for expecting such reasonable asymptotic approximations for the time-dependent N-S equations in three space dimensions. In view of the inherent uncertainties of asymptotic approximations, constructive comparison with experimental data is much needed. Therefore we choose to carry out the computational simulation of the development of some large disturbances into a turbulent spot in a Couette Flow of an incompressible fluid over a flat plate to facilitate experimental comparison.

COMPUTATIONAL FORMULATION

The computational solution of nonlinear problems has long been plagued by spurious oscillations generated by the presence of large gradient(s) in the field. They are visualized as "error waves" or "Numerical Turbulence", and often smeared over by various computational artifices. We now wish to compute a turbulent field, with many large gradients. How can we distinguish "numerical" from "physical" turbulent fluctuations? How can we suppress or smooth the numerical instability while permitting the physical instability to develop into turbulence?

The deterministic view of turbulence provides a simple answer. If the N-S operator, F_N is to develop chaotic fields, $\partial F_N / \partial x$ will contain unstable eigenvalues ($\lambda_{b1}, \lambda_{b2}, \dots$) arranged in sequential order of their associated bifurcations leading toward chaos. If an iterative computational algorithm with mesh size h , i.e.

$$x^{n+1} = F_{Nh}^n(x, R)$$

will not give any bifurcating unstable eigenvalues of $\partial F_{Nh} / \partial x$ that enter into the sequence prior to λ_{b2} , then the first two bifurcations is unlikely to be affected by the "unstable" algorithm. This requirement on the computational algorithms, adequate for computing the global features of turbulent or transitional fields, appears to be more lenient than that for computing the steady state problems where no unstable eigenvalues are allowed. Why then should numerical turbulence plague the computational simulation of fluid turbulence more than that of steady state flow problems? The origin of excessive "numerical turbulence" may be "physical" in its formulation rather "numerical" in its execution.

Consider first the integration of the time dependent N-S system of an incompressible fluid in terms of the primitive variables, i.e. velocity and static pressure (\bar{q}, p).

$$\text{Momentum} \quad \frac{\partial \bar{q}}{\partial t} + \bar{q} \cdot \nabla \bar{q} = -\nabla p + \frac{1}{Re} \nabla^2 \bar{q} \quad (1)$$

$$\text{Continuity} \quad \nabla \bar{q} = 0 \quad (2)$$

where the density ρ of the incompressible fluid is taken as unity and the Reynolds number Re is expressed in terms of some convenient reference variables. The fundamental difficulty of integrating (1) and (2) with a given set of initial-boundary data is the absence of $\frac{\partial p}{\partial t}$. The correct pressure $p(\bar{x}, t)$ should advance $\bar{q}(\bar{x}, t)$ from (1) such that $\bar{q}(\bar{x}, t)$ will remain solenoidal, $\nabla \bar{q} = 0$, at all times. We do not know of any direct method of finding such a $p(\bar{x}, t)$, nor any apparent converging iterative procedure to fulfill this condition. The divergence of the momentum equation (1) gives

$$\nabla^2 p = -\left(\frac{\partial}{\partial t} - \frac{1}{Re} \nabla^2\right)(\nabla \bar{q}) + \nabla(\bar{q} \cdot \nabla \bar{q}) \quad (3)$$

which may be solved with the source terms evaluated in many different ways for iteratively predicting the advanced pressure field. These had been tried extensively [8], but failed to restore satisfactorily any solenoidal velocity field despite various smoothing computational artifices.

The system (1) and (2) is a singular limit of the N-S for compressible fluid where the continuity relation $\nabla \bar{q} = -\frac{1}{\rho} \frac{d\rho}{dt} = -\frac{\epsilon}{\rho} \frac{dp}{dt}$ is replaced by (2) with the term $\epsilon < 1$ dropped. To restore an initial value problem, the continuity relation is modified as

$$\epsilon \frac{\partial p}{\partial t} + \nabla \bar{q} = 0 \quad (4)$$

where ϵ is some sufficiently small quantity as an approximation. The difficulty remains because any residual $\text{div } \bar{q}$ will lead to very large changes of pressure. The diverging situation as $\epsilon \rightarrow 0$ renders any approximate calculations at small ϵ meaningless. To render a "converging" approximation sequence as $\epsilon \rightarrow 0$, the method of artificial compressibility [9,10] alters the momentum equations as:

$$\frac{\partial \bar{q}}{\partial t} + \bar{q} \cdot \nabla \bar{q} = -\nabla p + \bar{F}(\bar{q}, \epsilon) + \frac{1}{Re} \nabla^2 \bar{q} \quad (5)$$

with an artificial force field $\bar{F}(\bar{q}, \epsilon)$, chosen to satisfy $\lim_{\epsilon \rightarrow 0} \bar{F}(\bar{q}, \epsilon) = 0$ and to guarantee a convergent sequence so that computational solutions of (4) and (5) at some sufficiently small ϵ promises some approximation to the solution of the incompressible problem (1) and (2). For periodic or otherwise trivial boundary formulation, $\bar{F} = \frac{1}{\epsilon} \bar{q} \text{ div } \bar{q}$ is an appropriate choice. For nontrivial boundary value problems, our analysis showed that \bar{F} depends intricately on a nontrivial boundary integral. Explicit determination of \bar{F} for a given nontrivial boundary formulation is difficult. Since we wish to study different initial boundary value problems of practical interest this approach is not suitable.

To avoid the direct solution of pressure, we take the curl of equation (1) to obtain the vorticity transport equation

$$\frac{\partial \bar{\omega}}{\partial t} = \nabla \times (\bar{q} \times \bar{\omega}) + \frac{1}{Re} \nabla^2 \bar{\omega} \quad (6)$$

with

$$\bar{\omega} = \nabla \times \bar{q} \quad (6a)$$

It looks as if $\bar{\omega}$ could be solved from (6) iteratively with (6a) without referring to the pressure field. It appears even more so when the iterative procedure is simplified to merely correcting the induced velocity field for changes in vorticity due to convective displacement and vorticity stretching [11]. This presumption is not true. The boundary condition of vorticity on a stationary solid surface is $7 \times \bar{\omega} = -Re \nabla p$. As will be discussed later an ad hoc boundary formulation without any reference to

perturbed pressure field, will lead to nonsolenoidal \bar{q} and $\bar{\omega}$. Equation (6) is then no longer the curl of (1), and its chaotic solution is not fluid turbulence but numerical noise. The role of pressure disturbances is essential.

The residual divergences of \bar{q} and $\bar{\omega}$ at any point in the field represent physically impulsive forces or moments^[12]. Such impulses generate pressure waves, propagating at "infinitely" large speed to relax to a physical, solenoidal state of \bar{q} and $\bar{\omega}$ with an altered smooth pressure field. The correction to \bar{q} (or $\bar{\omega}$) due to the relaxation of these impulsive forces is derivable from a potential function $\phi(x,t)$, or $\psi(x,t)$, since the equilibration process is too fast for viscosity or any other dissipative processes to be effective. Therefore, if the nonphysical state with residual divergences $\bar{\xi}$ and \bar{q}_T respectively, the physical vorticity and velocity are:

$$\bar{\omega} = \bar{\xi} + \nabla\psi \quad (7)$$

$$\bar{q} = \bar{q}_T + \nabla\phi \quad (8)$$

so that

$$\nabla^2\psi = -\text{div } \bar{\xi} \quad (9)$$

$$\nabla^2\phi = -\text{div } \bar{q}_T \quad (10)$$

Neumann condition is prescribed on the boundary so as to avoid disturbing physical conditions normal to the boundary. To facilitate computation, we replace (6a) by

$$\nabla^2\bar{q} = -\nabla \times \bar{\omega} \quad (11)$$

So that (9)-(11) represent five Poisson equations with source terms to be evaluated with the latest available data. Thus we set up three iterative loops in calculating the grid values at an advanced time step: (a) vorticity loop with equations (6), (7) and (9) for obtaining a solenoidal $\bar{\omega}$ with a given solenoidal \bar{q} , (b) velocity loop with equations (8), (10) and (11) for obtaining a solenoidal \bar{q} with the latest available solenoidal $\bar{\omega}$ (c) Quasi-linearization loop with nested loops a and b and some prescribed format of estimating the average convective velocity $\bar{q}^{n+1/2}$ in the interval form $n\Delta t$ to $(n+1)\Delta t$.

The solenoidal \bar{q} and $\bar{\omega}$ that minimizes satisfactorily the residue in loop (c) are taken as their values at the advanced time step. Then the pressure field p at the advanced time step is solved from (3) with greatly simplified source terms. The iterative processes proved to be rapidly converging even with a simple discretization algorithm.

The correction $\nabla\psi$ is determined in Loop (a) with $\frac{\partial\psi}{\partial n} = 0$ on a non-slip solid boundary where the vorticity component normal to the surface must vanish. The correction $\nabla\phi$ tangent to the solid boundary does not vanish, and there are no physical requirements why they should.

The correction $\nabla\phi$ is determined in loop (b) with $\frac{\partial\phi}{\partial n} = 0$ on an impermeable non-slip solid surface. The relaxation of the residual divergences in the field, will introduce, however, nonzero tangential component $\frac{\partial\phi}{\partial s}$ next to the surface, creating a large vorticity parallel to the surface.

For flow problems in two space dimensions (x_1, x_2) there is no residual divergences of vorticity by definition; and loop (a) is not needed. The introduction of a harmonic stream function eliminates further any residual divergences of the velocity field. Then the two-dimensional problem is simply computed; but it excludes three dimensional disturbances and the pressure mechanism of vorticity production at a solid boundary. Loops (a) and (b) evaluate the effect of the pressure disturbances accompanying vorticity transport in three space dimensions or caused by computational errors, in the interior and on the boundary. The only physical state is the "equilibrium state" at the end of loop (c) when both $\bar{\omega}$ and \bar{q} are solenoidal and the quasi-linear relations have been relaxed to sufficient accuracy. This is why the pressure field is determined only at the end of loop (c) through the Poisson equation

(3), with the boundary condition on a non-slip surface derived from the solenoidal vorticity field as:

$$\frac{\partial p}{\partial n} = \bar{n} \cdot \nabla p = -\frac{1}{Re} (\nabla \times \bar{\omega}) \cdot \bar{n} \quad (12)$$

where \bar{n} is the unit normal to the solid boundary.

DEVELOPMENT OF LARGE DISTURBANCES IN A COUETTE FLOW

We discretize equations (6)-(11) with the simple forward time and centered space algorithm using the latest available values during each sweep. $\bar{q}^{n+1/2} = \frac{1}{2}(\bar{q}^n + \bar{q}^{n+1})$ is used as the average convective velocity in loop (c). The discretized Poisson equations are solved with ADI process, each with a constant acceleration parameter. The acceleration parameters and the number of iterations in each loop were determined from model studies. The development of "large" disturbances in a uniform shear flow between a stationary plate at $y = 0$ and a plate moving in the plane $y = 1$ with velocity (1, 0, 0) at $Re = 3000$ was then computed with a coarse grid $15 \times 15 \times 15$ at $\Delta t = 0.2$.

Impulsive disturbances were applied at $t = 0$ at a group of grid points in the lower middle of the computational region. Unit impulses of the streamwise component of vorticity ω_x never grow. The uniform shear flow was reestablished at $50 \Delta t$. There was no numerical turbulence and the flow regains the laminar condition.

Unit impulses of v-component velocity normal to the stationary plate at $y = 0$ generates a horse-shoe vortex, lifting rapidly away from $y = 0$ while being stretched and convected downstream. By $60 \Delta t$, an apparently laminar shear flow is again established with a decaying and diffuse horse-shoe vortex in the middle. There was no chaotic vortical flows like turbulence in the field.

Unit impulses of u-component velocity generates a complicated three-dimensional vortical flow hugging onto the wall $y = 0$, bounded by a high vorticity front propagating slowly in all directions into the neighboring laminar flow. By $50 \Delta t$, this highly vortical region assumes the well known shape of a turbulent spot over a flat plate as was observed in experiments. Within the vortical region, the flow is somewhat chaotic or "turbulent". Outside of the region, the flow is orderly but severely distorted from the undisturbed uniform shear state.

The following is a summary of some observations of the developing spot. (i) the turbulent spot is marked by an irregular high vorticity front advanced into the neighboring distorted laminar region. A vorticity plateau is present in the center of the spot. Figure 1 illustrates the horizontal sections at $y^* = 11$ parallel to the plate at $56 \Delta t$ to $66 \Delta t$ and $86 \Delta t$. The grid points marked by "+" possess local vorticity magnitudes larger than 5. (ii) Within the growing "turbulent spot" there is a dominant but somewhat diffuse horse-shoe vortex anchored at the lower plate $y = 0$. The whole structure grows in size and convects downstream at a velocity slightly larger than half the moving plate velocity. Figure 2 illustrates the u, v, velocity components in the plane of symmetry of the initial disturbance at $50 \Delta t$. (iii) In the plane of symmetry of the initial disturbance, there is a concentrated "sheet" of vertical jet stream directed away from the plate. Figure 3 illustrates the v-w velocity components in a transverse section across the spot at $50 \Delta t$. It lies in a low pressure valley which extends well below the visible jet stream. (iv) The velocity fluctuation w' in the lateral direction is significantly larger than v' except in the plane of symmetry; and in many place comparable to u' or even u within the spot. Figure 4 illustrates the u-w velocity component field in the horizontal section at $y^* = 11$. The w' suddenly reaches very large values at the trailing edge of the spot, generating significant trailing wave packets that decay gradually further upstream outside of the spot. (v) The static pressure variation normal to the plate $p(y)$ in a transverse section across the spot at $56 \Delta t$ is illustrated in Figure 5. Here $K = 8$ is the symmetry plane in the midst of the pressure valley where the

"jet stream" in (iii) is located. The temporal developments of the dynamic pressure $p(y)$ and the velocity $u(y)$ are illustrated in Figure 6. Both the pressure and the mean flow velocity are significantly depleted in this region.

The restoration of laminar flow conditions for the first two cases provides considerable confidence that "numerical turbulence" is not a significant component in our computed results of spot development. We are further encouraged that the calculated results are in general agreement with experimental observations. The feasibility of asymptotic computational simulation of the discrete nature of transition and turbulence is demonstrated.

TURBULENT SHEAR FLOW - DETERMINISTIC vs. STATISTICAL VIEWS

Successful computational simulation with the N-S, provides a constructive demonstration, if not a proof, of the basic thesis of the deterministic view of turbulent shear flows. It strengthens and extends the significance of the theorem of Ruelle and Takens. We shall now review and explain the various experimental and computational observations in turbulent shear flows and examine their implications with regard to the classical theory(ies) of turbulence.

The propagating turbulent spot, as a localized turbulent region in a shear flow over a solid surface was first reported by Emmons^[13]. Many other forms of such more or less "organized" or "coherent" large scale structures have been identified in different types of shear flows, given different names, and studied extensively through experimentation, analysis and artistic rendering^[1,2]. They appear to be "permanent" structures in the sense of its persistence to very large flow Reynolds numbers. Once the structure is formed, the global kinematic features are reminiscent of vortical motions in inviscid fluids, and encourage the presumption that convection and stretching of vortex lines may constitute fluid turbulence, especially the free turbulence. Questions related to the dynamics as to their creation, propagation and decay are rarely addressed.

The deterministic solutions of different initial-boundary value problems of the time dependent N-S equations are generally different. An ensemble of such solutions having some common macroscopic boundary data (i.e. with different initial data and/or small perturbations of the boundary data) must have some global features with dimensions comparable to the common boundary specifications. After all, the eigenvalues are characterized by where the boundaries lie and what the nature of the boundary constraints are. The large scale structures of all the solutions in the ensemble should therefore appear "coherent", regardless of the details, but can vary somewhat for different sub-set ensemble averages. The situation is quite similar to those average data from different wind tunnels. For distinctly different boundary configurations defining different ensembles, the "coherent" structures will naturally be different. Thus we expect to see various types of organized large scale structures in various standard classes of free or wall turbulence. The variations of their topographies will display prominently different kinematic features of the ensembles although not the underlying dynamics common to all such structures.

The only dynamic feature common to all these large scale structures is the propagating turbulent front that produces the "on-off" or "intermittent" signals temporally and spatially. "Intermittency" was reported by Townsend^[14] quite early for the turbulent wake behind a cylinder where the large scale eddies enhances mixing or entrainment of the outer "laminar" fluid by a "turbulent" core. It was later identified in all free turbulent flows (such as jets, wakes and mixing layers) and the outer edges of turbulent boundary layers over solid surfaces^[1,2]. The suggestion of double layer structure was explicit although the laminar-turbulent boundary as a propagating front was not emphasized. Experimental determination of intermittency factor is more qualitative

than quantitative. Little is known about the nature and structure of this turbulent front. Neither are they important for the present purposes.

Shortly after their discovery of intermittency through indirect measurements, Batchelor and Townsend^[15] speculated on theoretical grounds that such phenomenon of intermittency should be present at higher wave numbers and with finer structures. With increasing sophistication of experimental techniques in recent years, evidences of intermittency at fine scales and high wave numbers begin to emerge especially in the proximity of the wall^[1,2]. Mathematically speaking^[5] the high wave number components are not very space-filling and their distributions in space should indeed be sparse. No matter how and where we turn, intermittency appears to be present at all scales everywhere in turbulent shear flows. The deterministic view collaborates these experimental observations and the theoretical speculation of the persistence of "intermittency" into ever more refined scales through repeating solution bifurcations. The associated fronts of discrete changes at successive bifurcations from laminar to some turbulent state or from some turbulent state to another are of varied scales and distributed over the field (x,t) . Such is the complex, patchy state of affairs of turbulent shear flows at large but finite Reynolds numbers as is predicted by the deterministic mathematical theory and as is observed in experiments. What do all these mean to the classical theory(ies) of turbulence?

It is difficult to reconcile "abrupt" transition, both temporally and spatially with Landau and Lifschitz mechanism of transition^[16] from secondary instability to turbulence through periodic, organized solution states. The Hopf bifurcation of a limit cycle is of period doubling type^[3]. In the deterministic view, transition is discrete and proceeds in steps to a succession of "chaotic" or turbulent states, not organized states. The computed results also suggest that they are clearly not smooth transitions through successive oscillatory states, no matter what scale we mean by "abrupt" transition.

The present discrete view can be brought into harmony with the notion of distribution function in the statistical theory of turbulence so long as it is not claimed to be universal and as it is useful in the evaluation of the statistical averages of physical quantities in a turbulent field. We are not particularly concerned if a distribution function is discrete or continuous, universal or not, but we do hope to identify the specific properties of each entity. The energy distribution function $E(k)$ defined as the Fourier transform of some correlation function is often interpreted as representative of the amplitudes of sinusoidal eddies of different wave numbers visualized in experimental results. There are, however, notable exceptions even in isotropic turbulence, such as $\lim_{k \rightarrow 0} E(k)$ does not represent the energy of the largest scale eddy but some integral scale over all wave numbers. Hence such energy distribution function is merely convenient mathematics in terms of a set of basis functions without physical identity. We note further that intermittency and discrete states need not imply a discrete distribution function, since each step function has its continuous Fourier representation.

From a physical point of view, the step changes of turbulent states at bifurcation can be looked upon as delta-functions of local turbulent states. The situation reminds us of Planck's quantization in describing the black body radiation distribution curve in wave number space through the discrete quantized energy states. Each such turbulence source and discrete state is indeed associated with an eigenvalue characterizing the secondary instability and bifurcation of the solution of the N-S under the specified boundary formulation, in the same manner how an energy quantum is derived from the Schrödinger equation. The eigenvalues are numerous, if not so refined, within the context of repeated bifurcation ad infinitum on the route to ultimate turbulence. The analogy might appear awkward if we look at turbulence with an exclusive interest in the continuum description of fluid flows, but not so with a broader view. Since there

are uncertainties in turbulence measurements even in the fluid flows, we really should not alarm at the apparent "wave-particle dualism" at hand. There is ample room for wondering about "quantizing" the turbulence or "turbulizing" the quanta. Such speculations on the formalism are not meaningful, however, without appropriate physical content of the "turbulence quanta". Our primary task is therefore to identify the physical entity of the discrete turbulent jumps, (or discrete turbulent states) and to provide the distribution function with specific physical meaning such as the probabilistic interpretation of the quantum-mechanical wave function in modern physics. To this end, an attempt will be made in the next section to identify the mathematical and physical entity of a turbulent front, across which an apparently discrete finite jump in turbulent states takes place.

CONTINUUM DYNAMIC MODEL OF DETERMINISTIC TURBULENT SHEAR FLOW

While both experimental and mathematical evidences suggest propagating fronts of solution bifurcation or laminar-turbulent transition, we are not aware of any proposal of wave mechanism for turbulence in incompressible fluids. Indeed, turbulence has traditionally been recognized as a diffusive and/or convective phenomenon, described by the vorticity transport equation (6). Recent successes in mimicking the chaotic, turbulent motions of vortical flows with the vorticity transport equation [2] tend to perpetuate this conviction. The circumstances, nevertheless, cast more mystery over the origin and mechanism of intermittency, the various organized structures, and other dynamic turbulent phenomena in shear flows [2].

We propose that the wave nature of fluid turbulence results from the pressure disturbances needed to maintain a solenoidal velocity field of an incompressible fluid, interpreted here to mean sufficiently small fluid compressibility $\epsilon = \frac{1}{\rho} \frac{dp}{dc} \ll 1$ and large speed of sound. When a velocity perturbation \bar{q}_{12} is introduced somehow into a physical flow field (\bar{q}_1, p_1) with $\text{div } \bar{q}_1 = 0$, it has to be accompanied by a corresponding pressure disturbance p_{12} that creates the \bar{q}_{12} according to Newton's Law

$$\left(\frac{d}{dt} - \frac{1}{Re} \nabla^2 \right) \bar{q} = - \frac{1}{\rho} \nabla p. \quad (1)$$

If the disturbed velocity field $\bar{q}_2 = \bar{q}_1 + \bar{q}_{12}$ is solenoidal, i.e. $\text{div } \bar{q}_{12} = 0$, as is required by the continuity equation (2), the pair of velocity and pressure disturbances, \bar{q}_{12} and p_{12} is compatible with physical laws, both kinematically and dynamically. This disturbed field (\bar{q}_2, p_2) is physically realistic.

A general velocity disturbance, as may be created by vorticity transport or by some external agents, need not be solenoidal. Then the disturbed state (\bar{q}_2, p_2) will fail to satisfy the physical requirements somewhere. The physical system must eliminate the residual divergence, by modifying both \bar{q}_2 and p_2 further. The simplest recourse of such needed dynamic adjustment is to introduce impulsive force-pairs [12] to annihilate the residual divergences everywhere as was indicated in Section 2. The elimination of the residual divergences thus leads to the opposite impulsive force-pairs superposed on p_{12} that will propagate into the neighboring field as "waves" to secure dynamic equilibrium.

These pressure waves will propagate and interact throughout the flow field and reflect from the boundaries to change the velocity and the pressure field everywhere. It is possible that after a few passes of the waves over the field, a smooth, continuous (\bar{q}_3, p_3) will be established without any further, apparent wave processes. In view of the very large signal speed, such a process of relaxation can be accomplished in a very short period of time compared with the characteristic times of vorticity transport and/or diffusion. This relaxed state of (\bar{q}_3, p_3) can thus be conveniently determined through the use of a potential function ϕ

as was done in Section 2 without the detailed solution of the wave propagation problem. This asymptotic "steady" state (\bar{q}_3, p_3) is a physical state with $\text{div } \bar{q}_3 = 0$ and a smooth and dynamically compatible p_3 . The change in velocity represents the velocity "induced" by the vorticity displacement, and may be evaluated through the Biot-Savart Law directly without any reference to the pressure changes and the wave propagation phenomena. The dynamic nature of this velocity change at a distance brought about by an elementary local change in vorticity can be implemented only through pressure waves within the framework of classical fluid dynamics.

At sufficiently large Reynolds numbers, the N-S equations will not be able to generate such a smooth, asymptotic "steady" solution everywhere [3]. It will generate in some locality(ies) non-smooth or discontinuous fronts propagating with a velocity compatible with dynamics as a result of local solution bifurcation. Physically, such finite amplitude fronts are formed through the coalescence of waves in (\bar{x}, t) generated at different positions at earlier times. Such a coalesced wave front will propagate with a group velocity that can be much different from the signal speed, i.e. the speed of sound. It may propagate into a field that has been modulated by waves from other parts of the field already settled into its quasi-asymptotic state. Thus the induced velocity generated in the smooth part of the dynamic field might appear as a precursor of the finite amplitude waves, although it is not produced by the direct dynamic action within the finite amplitude wave itself and does not forecast the pending arrival of some finite amplitude wave.

The coalesced front may mean discontinuous jumps of rms vorticity and/or turbulent pressure across it, but p_3 must be continuous across the front since pressure discontinuities have been relaxed. In this sense, the front is more like a contact discontinuity than a shock wave. On the other hand, since it propagates relative to mass motion, it is more like a shock wave than a contact discontinuity. We are not clear about the physical nature and the structure of such coalesced wave fronts just as we are not clear on the mathematical events of solution bifurcation. We do not know how and if the propagation speed is related to the jump(s) across the front, both being dependent on the source distribution in (\bar{x}, t) and on the field geometry through which the waves propagate, interact, and reflect. It might have some universal structure, but as yet unknown. Despite our ignorance on such details we are pleasantly surprised with the few sample results computed according to the global principle given above, where both the smooth solution and the bifurcated solution with propagating turbulent fronts are obtained. We are particularly encouraged that the calculated solutions with bifurcating fronts display many features in agreement with experimental observations in turbulent shear flows.

We shall now explain that vorticity transport leads to residual divergences of the velocity field so that the wave phenomena discussed above is general rather than special. We claim first that equation (3), as the divergence of the evolution equation (1) for velocity \bar{q} , should be recognized as an evolution equation for $\text{div } \bar{q}$, i.e.

$$\left(\frac{d}{dt} - \frac{1}{Re} \nabla^2 \right) (\nabla \cdot \bar{q}) = - [\nabla^2 p + \frac{\partial u_j}{\partial x_i} \frac{\partial u_i}{\partial x_j}] \quad (13)$$

It is only when the continuity equation (2) $\nabla \cdot \bar{q} = 0$ is satisfied at all times and everywhere that this evolution equation is reduced to the subsidiary relation:

$$\nabla^2 p = - \frac{\partial u_j}{\partial x_i} \frac{\partial u_i}{\partial x_j} = - (\omega_k \omega_k + \frac{\partial u_j}{\partial x_i} \frac{\partial u_i}{\partial x_j}) \quad (14)$$

i.e. a Poisson equation relating pressure p to the solenoidal velocity field. The solution of p from this equation can, however, include eigen solutions of the homogeneous equation $\nabla^2 p = 0$, i.e. any harmonic function satisfying the particular trivial mixed boundary conditions. Such eigen solutions of p do not change $\nabla^2 p$ in equation (13); but will alter \bar{q} development according to equation (1)

These changes in \bar{q} produces changes in $\bar{\omega}$ and

$\frac{\partial u_i}{\partial x_j}$ non-trivially in equation (13) to bring about

non-zero $\text{div } \bar{q}$. It is the $\text{div } \bar{q} = 0$ that determines the correct content of the harmonic eigen solution of pressure that represents the wave system (pressure waves or disturbances) generated by vorticity transport. Equations (13) and (14) show clearly that the transport of a large vorticity (ω_k) will generate correspondingly large pressure disturbances or waves. Thus a turbulent front, once formed, tends to perpetuate itself.

The impulsive force pairs introduced as delta functions in our computational simulation to eliminate the residual divergence can also arise from errors in approximate procedures. The discontinuous pressure fronts created by the computed residual divergences include the often dominant numerical errors in computational simulation. If not suppressed, this numerically generated pressure waves would inevitably lead to numerical turbulence. The elimination of these residual divergences through the potential function ϕ (loop b) prior to the quasi-linear iteration (loop c) as is described in Section 2 is to prevent the nonlinear interaction of the nonphysical waves to form numerical turbulence. The appropriate content of the harmonic pressure waves is then allowed to interact "nonlinearly" to develop into physical turbulence. The quasi-linear form of nonlinear interactions is crude but proved adequate. The successful demonstration in the computational simulation of both the smooth and non-smooth solutions therefore lends considerable credibility to the proposed wave mechanism of turbulent shear flow. It also substantiates our suppositions that: (i) Numerical turbulence can be largely eliminated by preventing the numerical errors from participating in the nonlinear interaction. (ii) The correct content of the harmonic pressure-waves due to vorticity convection can be preserved by enforcing the solenoidal velocity field with large numerical errors suppressed. (iii) Quasi-linearization can be adequate for computational simulation of nonlinear interaction to permit the physical pressure-waves to develop into fluid turbulence.

The propagation, interaction and coalescence of all of these pressure-waves are much dependent on the location, configuration and nature of the boundary. Thus, the ensemble average of the many realizations with the same boundary will appear "coherent" although displaying great variability in details.

The reflection of an obliquely incident pressure wave at a solid surface generates mass motion parallel to the surface, thereby creating vorticity components tangent to a non-slip boundary. This is an effective mechanism of generating rms vorticity on the boundary although it is highly transient and oscillatory. If rms vorticity is taken as some measure of turbulence, this wave reflection process is an effective mechanism of turbulence production, independent of the magnitude of viscosity or Reynolds number if the non-slip condition is enforced on the boundary as $u \cdot \nabla \times \omega = -\nabla p$. This wave mechanism of turbulence production is distinct from the conventional production term

$-\frac{\partial u_i}{\partial x_j} \frac{\partial u_j}{\partial x_i}$, and is likely related to $u_i \frac{\partial p}{\partial x_i}$ in the

averaged turbulence kinetic energy equation. The importance of this wall production mechanism is indicated by the previous results that the turbulent spot hugs onto the wall while propagating downstream. There are other evidences. With this wave mechanism of turbulence production dominating, we expect spots, and other forms of organized, large scale structures of wall turbulence to persist to very large Reynolds numbers, or even to the inviscid limit.

The incidence and reflection of a pair of steep compression-expansion waves (or a somewhat modulated N-wave) next to a solid surface generates very large vorticity. While it could be suppressed by the viscous effects in the proximity of the wall, some intense, transient, local vortical activity will result away from

it. The situation reminds us of "Bursts"^[1,2]. It is likely a local, higher order solution bifurcation triggered by some steep incident wave pair. A steep incident wave pair may be generated directly by the transport of large vorticity at some point on the turbulent front of the large scale structure. It may also result from the "focusing" of such waves. In this manner, the highly localized and transient violent activity of "burst" will naturally be related to the scale of the large organized structure(s) comparable to the global thickness of the turbulence boundary layer. The incidence of the pair of strong impulses of opposite sign can also produce unusual mass motion of the fluid, with oppositely faced jet streams parallel to an impermeable wall eventually jetting away from the wall.

The physical model proposed above is compatible with the mathematical theorem as to the deterministic and discrete nature of turbulence. The model provides rational dynamic explanations to many perplexing experimental observations. It should remain valid for compressible fluid with necessary modifications for finite signal speeds. It also suggests various approaches to the solution of practical problems quite different from what may have been perceived according to the statistical theory of turbulence.

SUMMARY AND CONCLUSIONS

A constructive demonstration of the deterministic, discrete view of turbulence was given through computational solution of the N-S equations in three space dimensions. The abrupt or discrete, local transition is not reconcilable with the quasi-periodic view of Landau-Lifshitz. The present discrete view can, however, be brought into harmony with the statistical theory of Taylor, if the distribution function is no longer conceived as universal.

A physical basis of the deterministic model of turbulence is proposed as a complex wave phenomenon induced by vorticity transport. Wave coalescence like repeated solution bifurcation ad infinitum leads to "ultimate turbulence". This model provides rational explanations to various experimental observations in turbulent shear flows of incompressible fluids. This model is equally applicable to turbulent shear flows of compressible fluids.

REFERENCES

1. Hinze, J. O., *Turbulence*, Second Edition, McGraw-Hill (1975). General Reference.
2. Cantwell, B. J., "Organized Motion in Turbulent Flow", *Ann. Review Fluid Mech.* **13**, pp. 457-515 (1981). General Reference.
3. Ruelle D. and Takens, F., "On the Nature of Turbulence", *Comm. Math. Phys.* **20**, pp. 167-192 (1971).
4. Leray, J., "Sur le mouvement d'un liquide visqueux emplissant l'espace", *Acta Math.* **63**, pp. 193-248 (1934).
5. Iooss, G. and Langford, W. F., "Conjectures on the Routes to Turbulence via Bifurcations", *Annals of the New York Academy of Sciences*, Vol. 357, pp. 489-505 (1980).
6. Feigenbaum, M. J., "The Metric Universal Properties of Period Doubling Bifurcations and the Spectrum for a Route to Turbulence", *Annals of New York Academy of Sciences*, Vol. 330, pp. 330-336 (1980).
7. Cheng, S. I., "Asymptotic Behavior and Best Approximation in Computational Fluid Dynamics", *Math. in Comp. in Simulation*, **24**, pp. 37-48 (1982).
8. Nichols, B. and Hirt, C., "Calculation 3D Free Surface Flows in the Vicinity of Submerged and Exposed Structures", *Jour. Comp. Phys.* **12**, pp. 234-246 (1973), also reports of Los Alamos Lab.
9. Teman, R., "Navier-Stokes Equations", North Holland Elsevier (1978).
10. Chorin, A. J., "Numerical Solution of the Navier-Stokes Equations", *Math. Comp.* pp. 745-762 (1968).
11. Leonard, A., "Vortex Simulation of 3D Spot-Like Disturbances in a Laminar Boundary Layer", Second Symposium of Turbulent Shear Flows. Proceedings, London, (1979) or NASA TM78579.

12. Lamb, H., "Hydrodynamics", Sixth Edition, Dover Publications, Art. 1, p. 10, Art. 119, pp. 161-162, Art. 152, pp. 214-216 (1932).
13. Emmons, H. W., "The Laminar-Turbulent Transition in a Boundary Layer", Jour. Aero. Sci. 18, pp. 490-498 (1951).
14. Townsend, A. A., "Measurements in the Turbulent Wake of a Cylinder", Proc. Roy. Soc. London Ser. A. 190, pp. 551-561 (1947).
15. Batchelor, G. K. and Townsend, A. A., "The Nature of Turbulent Motion at Large Wave Numbers", Proc. Roy. Soc. London. Ser. A. 199, p.238 (1949).
16. Landau, L. D. and Lifshitz, E.M., "Fluid Mechanics", Oxford, Pergamon (1959).

ACKNOWLEDGEMENT

This work was performed under the grant NSF MEA 80-10876. The author wishes to express his appreciation of the interest and support of the National Science Foundation.

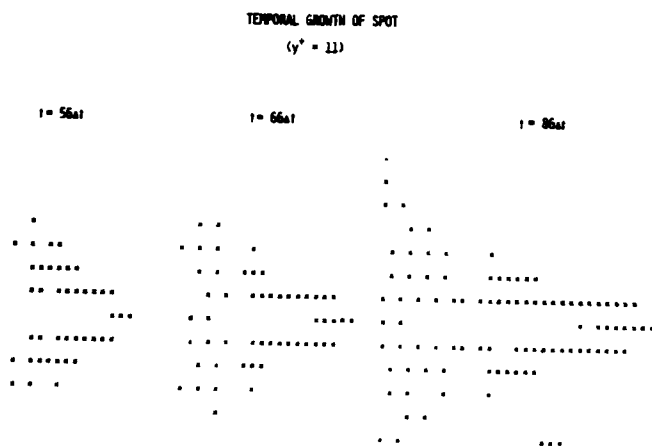


Fig. 1

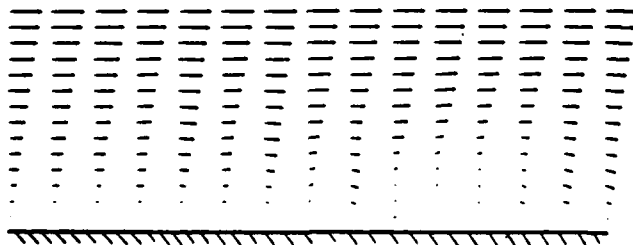


Fig. 2. u-v velocity components in plane of symmetry $k = 8$ at $50 \Delta t$.

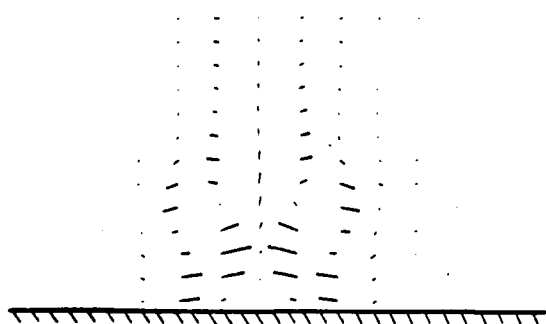


Fig. 3. v-w velocity components in a transverse section across the spot at $50 \Delta t$.

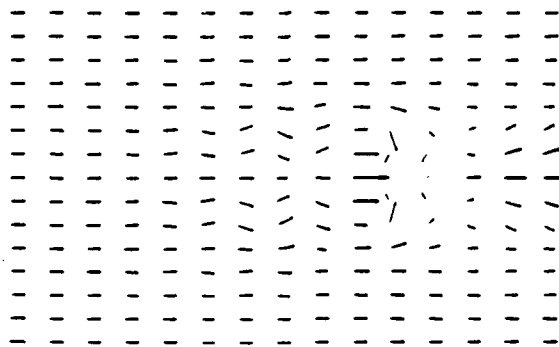


Fig. 4. u-w velocity components in horizontal section at $y^* = 11$ at $50 \Delta t$.

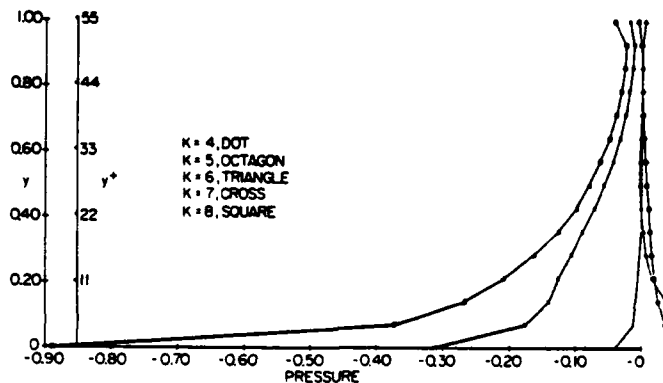


Fig. 5. pressure profile p in a transverse section across the spot at $50 \Delta t$.

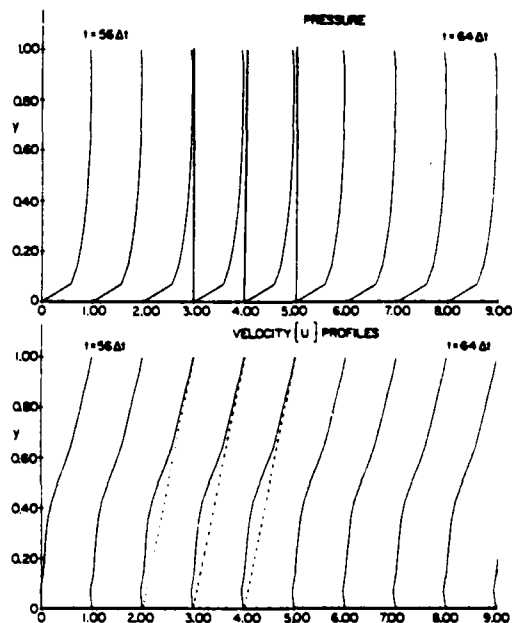


Fig. 6. temporal development of p and u at a point within the spot from $56 \Delta t$ to $64 \Delta t$.

SESSION 10 - REACTING FLOWS

W. Leuckel - Chairman

TURBULENT PREMIXED COMBUSTION IN A BOUNDARY LAYER

M. Champion

L.A. 193 - E.N.S.M.A. - 86034 Poitiers (FRANCE)

and

P.A. Libby

University of California San Diego, La Jolla 92093 CA

ABSTRACT

A theoretical study is made of the structure of the fully turbulent boundary layer which is obtained by injecting a fresh reactant mixture through a porous flat plate into an incoming flow of hot products. The aerothermochemistry is described by a joint probability density function of the velocity field and the product mass fraction. The flow is described by means of similar solutions of the complete set of equations for mean quantities and second order correlations. The model is validated through a comparison with available experimental data, in the case of small heat release and moderate injection rate.

NOMENCLATURE

c product mass fraction
f similar part of the stream function
F injection rate
l length scale of turbulence
L similar part of l
P pressure
P probability density function
 \bar{Q} mass weighted kinetic energy of turbulence
Q similar part of \bar{Q}
T temperature
 $\vec{V}(u,v,w)$ velocity field
x,y,z cartesian coordinates
 α, β, γ parameters of P
 δ boundary layer thickness
 ϵ_{ab} dissipation rate of a"b"
n similarity variable
 ρ density
 τ heat release parameter
 \bar{w} chemical production rate
 Ω similar part of \bar{w}

SUBSCRIPTS

e external
p product (c = 1)
r reactant (c = 0)
w wall

OVERSCRIPTS

\bar{a} , a' mean and fluctuating part of a, conventional average
 \bar{a} , a" mean and fluctuating part of a, mass weighted average.

INTRODUCTION

In a series of paper Bray, Libby and coworkers (Bray, Moss, 1977 ; Libby, Bray, 1981 ; Bray et al, 1981) show that within turbulent premixed flames an interaction between the density fluctuations due to heat release and force fields due to gradients of either the mean pressure or Reynolds stresses results in new processes of turbulent transport and turbulent produc-

tion. In such flames the mean pressure gradients can be self-induced but more generally depend along with the Reynolds stress gradients on the hydrodynamics of the flow in which the turbulent flame is embedded. It is clearly of interest to determine the importance of these processes in other turbulent flows involving density inhomogeneities. To that end the present work is a theoretical study of the structure of a turbulent layer which results from injection through a porous plate of a fresh reactant mixture into an external potential flow of the fully burned products of that mixture. Such a configuration has been already studied in the case of non premixed combustion. The work of Rosner (1975) deals with the cooling of a plate by injecting H_2 and gives a numerical calculation of the energy and mass transfer rates at the wall. An experimental study of the turbulent velocity field is made by Wooldridge and Muzzy (1966). More recently Senda et al (1976, 1979) have presented measurements of the turbulent velocity and temperature fields in both cases of reactive and non-reactive flows. Concerning the case studied in the present paper, i.e. injection of premixed air and reactant, the laminar problem has been treated by Libby and Economos (1963) who assumed similarity to solve the system of balance equations for velocity and mass fraction fields.

Our objective is to describe the flow field by means of similar solutions of the complete set of equations for mean velocity, mean product mass fraction and all second order correlation and using the Bray-Moss-Libby model for the aerothermochemistry of premixed turbulent combustion. Accordingly, no restrictive closure assumption, such as the introduction of a positive eddy viscosity, are made. This allows the existence and validity of gradient laws for the fluxes $\bar{u}''v''$ and $\bar{v}''c''$ to be investigated.

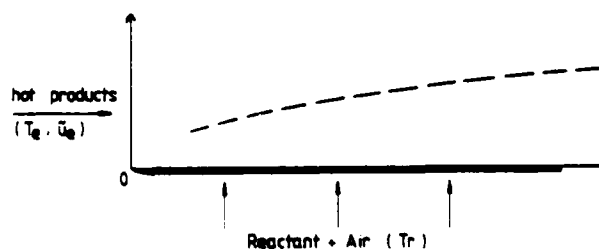


Fig. 1 - Schematic representation of the reactive boundary layer.

ANALYSIS

Figure 1 indicates schematically the physical configuration of the flow investigated. The fresh reactant mixture is injected through a porous plate at a rate defined by :

$$F = \frac{\bar{\rho}_w \bar{v}_w}{\bar{\rho}_e \bar{u}_e} \quad (1)$$

The usual approximations made in studies of premixed turbulent combustion are retained, namely the Lewis number is assumed to be unity; the Mach number is everywhere small so that the pressure is negligible; and the flow is adiabatic. Under these circumstances and with the assumptions of fast chemistry and intense turbulence the Bray-Moss thermochemistry applies so we have:

$$\rho^* = \frac{\bar{\rho}}{\bar{\rho}_e} = \frac{1 + \tau}{1 + \tau \bar{c}} = \frac{T_e}{T} \quad (2)$$

where τ is a heat release parameter clearly defined as:

$$\tau = \frac{T_e}{T_r} - 1 \quad (3)$$

A further consequence of these approximations is that the multivariate p.d.f. of velocity and progress variable is:

$$P(\underline{v}, c; \underline{x}) = \alpha \delta(c) P(\underline{v}, 0; \underline{x}) + \beta \delta(1-c) P(\underline{v}, 1; \underline{x}) + O(\gamma) \quad (4)$$

with $\gamma \ll 1$

where on the right side are conditional p.d.f.'s for reactant and products.

The following balance equations for the boundary layer involving Favre averages are now needed in a second moment formulation:

- mass

$$\frac{\partial \bar{\rho} \bar{u}}{\partial x} + \frac{\partial \bar{\rho} \bar{v}}{\partial y} = 0 \quad (5)$$

- x momentum

$$\bar{\rho} \frac{D \bar{u}}{Dt} + \frac{\partial}{\partial y} (\bar{\rho} \bar{u} \bar{v}^{\prime\prime}) = - \frac{\partial \bar{P}}{\partial x} \quad (6)$$

- y momentum

$$\frac{\partial}{\partial y} (\bar{\rho} \bar{v}^{\prime\prime 2}) = - \frac{\partial \bar{P}}{\partial y} \quad (7)$$

- product mass fraction

$$\bar{\rho} \frac{D \bar{c}}{Dt} + \frac{\partial}{\partial y} (\bar{\rho} \bar{c} \bar{v}^{\prime\prime}) = \bar{\omega} \quad (8)$$

- Reynolds shear stress

$$\begin{aligned} \bar{\rho} \frac{D \bar{u} \bar{v}^{\prime\prime}}{Dt} + \frac{\partial}{\partial y} (\bar{\rho} \bar{u} \bar{v}^{\prime\prime 2}) = \\ - \bar{\rho} \bar{v}^{\prime\prime 2} \frac{\partial \bar{u}}{\partial y} - \bar{u} \frac{\partial \bar{P}}{\partial y} - \bar{v} \frac{\partial \bar{P}}{\partial x} - \bar{\rho} \bar{\epsilon}_{uv} \end{aligned} \quad (9)$$

$$\begin{aligned} \bar{\rho} \frac{D \bar{u}^{\prime\prime 2}}{Dt} + \frac{\partial}{\partial y} (\bar{\rho} \bar{u}^{\prime\prime 2} \bar{v}^{\prime\prime}) = \\ - 2 \bar{\rho} \bar{u}^{\prime\prime} \bar{v}^{\prime\prime} \frac{\partial \bar{u}}{\partial y} - 2 \bar{u} \frac{\partial \bar{P}}{\partial x} - \bar{\rho} \bar{\epsilon}_{uu} \end{aligned} \quad (10)$$

$$\bar{\rho} \frac{D \bar{v}^{\prime\prime 2}}{Dt} + \frac{\partial}{\partial y} (\bar{\rho} \bar{v}^{\prime\prime 3}) = - 2 \bar{v} \frac{\partial \bar{P}}{\partial y} - \bar{\rho} \bar{\epsilon}_{vv} \quad (11)$$

$$\bar{\rho} \frac{D \bar{w}^{\prime\prime 2}}{Dt} + \frac{\partial}{\partial y} (\bar{\rho} \bar{w}^{\prime\prime 2} \bar{v}^{\prime\prime}) = - 2 \bar{w} \frac{\partial \bar{P}}{\partial z} - \bar{\rho} \bar{\epsilon}_{ww} \quad (12)$$

- transverse species flux

$$\begin{aligned} \bar{\rho} \frac{D \bar{v}^{\prime\prime} \bar{c}^{\prime\prime}}{Dt} + \frac{\partial}{\partial y} (\bar{\rho} \bar{v}^{\prime\prime 2} \bar{c}^{\prime\prime}) = \\ - \bar{\rho} \bar{v}^{\prime\prime} \frac{\partial \bar{c}}{\partial y} - \bar{c} \frac{\partial \bar{P}}{\partial y} - \bar{v} \bar{\omega} - \bar{\rho} \bar{\epsilon}_{cv} \end{aligned} \quad (13)$$

where D/Dt is the mean convective operator.

Similar solutions of equations (5)-(13) are sought by defining a boundary layer thickness $\delta(x)$ and an external velocity profile $u_e(x)$ such that:

$$\begin{aligned} \delta &= c_\delta x^p \\ u_e &= c_u x^m \end{aligned}$$

and a stream function ψ is introduced such that:

$$\psi = u_e \delta f(\eta) \quad (14)$$

where η is the similarity variable defined by:

$$\eta = \frac{1}{\delta} \int_0^y \frac{\bar{\rho}}{\bar{\rho}_e}(\eta) d\eta \quad (15)$$

so that:

$$\frac{\bar{u}}{u_e} = \frac{df}{d\eta}$$

The introduction of equations (14)-(15) into eqs (6) and (8) shows that, taking $d\delta/dx$ as a small parameter, the existence of a similar solution, at first order in $d\delta/dx$, requires:

$$\frac{\bar{u} \bar{v}^{\prime\prime}}{u_e^2} = \frac{d\delta}{dx} G_{uv}(\eta) + \dots \quad (16)$$

$$\frac{\bar{c} \bar{v}^{\prime\prime}}{c_e} = \frac{d\delta}{dx} G_{cv}(\eta) + \dots \quad (17)$$

and the chemical production term must be such that:

$$\frac{\bar{\omega}}{\bar{\rho}} = \frac{u_e}{\delta} \frac{d\delta}{dx} \Omega(\eta) \quad (18)$$

where Ω is given by Libby and Bray (1980)

$$\Omega = k \left(\frac{u_1}{u_e} \right)^{1/2} \frac{1}{L} \frac{\bar{c}(1-\bar{c})}{L} \quad (19)$$

Similar considerations applied to the balance equations for the second order correlations, Eqs (9)-(13) are more complex and details are not given here. Result of the analysis indicates that a consistent formulation imposes restriction on the terms describing the effects of dissipation and pressure fluctuations and leads to the well known approximation associated with balancing the two dominant terms in each equation, those describing production and dissipation. Thus introducing new dimensionless variables:

$$\bar{\epsilon}_{ab} = \frac{u_e^3}{\delta} \frac{d\delta}{dx} E_{ab}(\eta) \quad a, b = u, v, w \quad (20)$$

$$2 \frac{\bar{u} \bar{v}^{\prime\prime 2}}{\bar{\rho} \frac{d\delta}{dx}} = \frac{u_e^3}{\delta} \frac{d\delta}{dx} P_{aa}(\eta) \quad a, b = u, v, w \quad (21)$$

eqs (9) - (13) reduce to:

$$E_{uv} + P_{uv} + \rho^* G_{vv} \frac{d^2 f}{d\eta^2} = O\left(\frac{d\delta}{dx}\right) \quad (22)$$

$$E_{uu} + P_{uu} + 2\rho^* G_{uv} \frac{d^2 f}{d\eta^2} = O\left(\frac{d\delta}{dx}\right) \quad (23)$$

$$E_{vv} + P_{vv} = E_{ww} + P_{ww} = O\left(\frac{d\delta}{dx}\right) \quad (24)$$

$$\begin{aligned} E_{cv} + P_{cv} + \rho^* G_{vv} \frac{d\bar{c}}{d\eta} - \rho^* \frac{\tau}{1+\tau} \bar{c}(1-\bar{c}) \frac{d}{d\eta} (\rho^* G_{vv}) = \\ O\left(\frac{d\delta}{dx}\right) \end{aligned} \quad (25)$$

Equations for \bar{u} and \bar{c} become in due course the principal equations. The closing of these two equations requires expressions for G_{uv} and G_{cv} (cf. eqs (16)-(17)), which are obtained through eqs (22)-(26). The modelling of the various E_{ab} and P_{ab} quantities is made after noticing that the boundary layer we consider involve region of uniform composition $\bar{c} = 1$ and region of uniform composition $\bar{c} = 0$. Since in these regions the distributions of the statistical properties of the velocity components are not uniform, it is necessary to supplement the model used in studies of the premixed

turbulent flames reflecting variable density effects (Bray, Libby, 1980) with conventional models for constant density turbulence. Within the context of Bray-Moss thermochemistry, we deal with the three regions associated with $\beta = 1$, $\alpha = 1$ and $\gamma \ll 1$ and introduce closure approximations which describe the effects in all three. Accordingly in eqs (20)-(25) the dissipation $\tilde{\epsilon}_g$ of a quantity g is written as :

$$\tilde{\epsilon}_g = \frac{1}{\rho} (\alpha \rho_r \tilde{\epsilon}_{g,r} + \beta \rho_p \tilde{\epsilon}_{g,p}) + \tilde{\phi}_g \quad (26)$$

where $\tilde{\epsilon}_{g,r}$ and $\tilde{\epsilon}_{g,p}$ are conditioned dissipation terms within reactant and products respectively $\tilde{\phi}_g$ is the dissipation due to chemical reaction (Libby, Bray, 1980) Eq (26) has the virtue of having the proper behaviour in the limiting cases of $\tilde{\epsilon} = 0, 1$ and may be expected to describe satisfactorily dissipation for general values of $\tilde{\epsilon}$. Derivation of new balance equations for these conditioned dissipation rates is an uneasy task which leads to new closure problems. To avoid this difficulty we choose to use the well known algebraic model :

$$\tilde{\epsilon}_{g,a} = c_\mu \tilde{q}_a^{3/2} / l \quad a = r, p \quad (27)$$

where l is the length scale for dissipation in both reactants and products and c_μ is an empirical constant with the value 0.09. Now aerothermochemical considerations related to the effect of temperature on the kinematic viscosity and to the rates of strain in reactants and products lead to the relation :

$$\tilde{\epsilon}_{g,r} = \tilde{\epsilon}_{g,p} / (1 + \tau)^*$$

when combined with the values of α and β this leads to :

$$\tilde{\epsilon}_g = \tilde{q}^{3/2} h(\tilde{\epsilon}) / l + \tilde{\phi} \quad (28)$$

with $h(\tilde{\epsilon}) = c_\mu (\tilde{\epsilon} + (1-\tilde{\epsilon})/(1+\tau)^*) / (\tilde{\epsilon} + (1-\tilde{\epsilon})/(1+\tau)^*)^{8/3} / 3/2$

In a similar fashion the additional dissipation terms are modeled with the contributions in the constant density regions determined after Launder et al (1975), and with those within the reaction region after Libby et al (1981) ; we have :

$$\tilde{\epsilon}_{ab} = \frac{\tilde{a}^* \tilde{b}^*}{\tilde{q}} (\tilde{\epsilon}_q - \tilde{\phi}) + \tilde{\phi}_{ab} \quad a, b = u, v, w \quad (29)$$

$$\tilde{\epsilon}_{cv} = \tilde{\phi}_{cv} \quad (30)$$

where

$$\tilde{\phi}_{ab} = k_{ab} \frac{\tilde{a}^* \tilde{c}^* \tilde{b}^* \tilde{c}^*}{(\tilde{c}^* (1 - \tilde{c}^*))^2} \frac{\tilde{w}}{\rho} \quad a, b = u, v, w \quad (31)$$

If Eqs. (29) and (30) are put into similarity form, they yield

$$E_{ab} = G_{ab} \frac{E}{Q} + O\left(\frac{d\delta}{dx}\right)^2 \quad a, b = u, v, w \quad (32)$$

$$E_{cv} = O\left(\frac{d\delta}{dx}\right) \quad (33)$$

with $E_q = h Q^{3/2} / L$

$$\text{and} \quad Q = \frac{1}{2} \int_a G_{aa}$$

where L is a dimensionless length scale defined by :

$$1 = \delta \left(\frac{d\delta}{dx}\right)^{1/2} L(\eta)$$

and is to be a specified function of η .

Since the $\tilde{\phi}$ and $\tilde{\phi}_{ab}$ terms are absent to lowest order,

we conclude from Eqs (32) - (33) that in a turbulent boundary layer described by a similarity solution the dissipation due to chemical reaction, found to be important within turbulent flames, is unimportant and that on the contrary the operative dissipation is associated with the regions of constant density.

The various effects due to pressure fluctuations are a special problem in reacting flows since heat release provides a distinct source of such fluctuations. At present we must ignore this source and assume that the conventional models for these effects are adequate. Accordingly we use the expressions given by Launder et al (1975) and Hanjalic and Launder (1972) as transcribed for Favre-averaging and have :

$$\begin{aligned} \frac{P_{ij}}{\rho} \left(\frac{\partial u_i^*}{\partial x_j} + \frac{\partial u_j^*}{\partial x_i} \right) &= -c_1 \frac{\tilde{\epsilon}_q}{\tilde{q}} (u_i^* u_j^*) - \frac{2}{3} \delta_{ij} \tilde{q} \\ &- c_3 (P_{ij} - \frac{2}{3} \delta_{ij} P) - c_4 \tilde{q} \left(\frac{\partial u_i^*}{\partial x_j} + \frac{\partial u_j^*}{\partial x_i} \right) - c_5 (D_{ij} - \frac{2}{3} \delta_{ij} P) \end{aligned} \quad (34)$$

$$\text{with} \quad P_{ij} = - \frac{\tilde{u}_i^* \tilde{u}_j^*}{\tilde{u}_i^* \tilde{u}_k^*} \frac{\partial \tilde{u}_j^*}{\partial x_k} + \frac{\tilde{u}_j^* \tilde{u}_k^*}{\tilde{u}_j^* \tilde{u}_k^*} \frac{\partial \tilde{u}_i^*}{\partial x_k}$$

$$\text{and} \quad D_{ij} = - \frac{\tilde{u}_i^* \tilde{u}_k^*}{\tilde{u}_i^* \tilde{u}_k^*} \frac{\partial \tilde{u}_j^*}{\partial x_k} + \frac{\tilde{u}_j^* \tilde{u}_k^*}{\tilde{u}_j^* \tilde{u}_k^*} \frac{\partial \tilde{u}_i^*}{\partial x_k}$$

$$P = \frac{1}{2} P_{kk}$$

where c_3, c_5 depend explicitly on c_1 and c_2 , empirical constants with widely accepted values :

$$c_3 = (c_2 + 8)/11, \quad c_4 = (30 c_2 - 2)/55, \quad c_5 = (8c_2 - 2)/11$$

$$c_1 = 1.5 \quad c_2 = 0.4$$

It is easy to verify that these pressure-velocity correlations have the form required by Eqs. (20)-(21). After using the boundary layer assumptions and introducing similarity forms of the mean flow field, the P_{ab} defined by Eqs. (21)-(25) are :

$$\begin{aligned} P_{uv} &= c_1 G_{uv} \frac{E}{Q} - (c_3 G_{vv} + c_5 G_{uu} - c_4 Q) \rho^* \frac{d^2 f}{dn^2} + O\left(\frac{d\delta}{dx}\right) \\ P_{vv} &= c_1 \frac{E}{Q} (G_{vv} - \frac{2}{3} Q) + \frac{(2c_3 - 4c_5)}{3} G_{uv} \rho^* \frac{d^2 f}{dn^2} + O\left(\frac{d\delta}{dx}\right) \\ P_{uu} &= c_1 \frac{E}{Q} (G_{uu} - \frac{2}{3} Q) - \frac{(4c_3 - 2c_5)}{3} G_{uv} \rho^* \frac{d^2 f}{dn^2} + O\left(\frac{d\delta}{dx}\right) \\ P_{ww} &= c_1 \frac{E}{Q} (G_{ww} - \frac{2}{3} Q) + \frac{2}{3} (c_3 + c_5) G_{uv} \rho^* \frac{d^2 f}{dn^2} + O\left(\frac{d\delta}{dx}\right) \end{aligned} \quad (35)$$

The pressure-scalar correlation is taken from Hanjalic and Launder (1972) and transcribed into Favre-averaged quantities. In terms of similarity variables we find :

$$P_{cv} = c_{1c} \frac{E}{Q} G_{vc} \quad (36)$$

where c_{1c} is an empirical constant with the widely accepted value of 3.2.

We are now able to assemble the expressions for E_{ab} and P_{ab} in Eqs. (22)-(25) and to express the second-moment correlations in terms of $d^2 f / dn^2$. The following results :

$$\begin{aligned} G_{uu} &= A_u Q \\ G_{vv} &= A_v Q \\ G_{uv} &= A_{uv} Q \end{aligned} \quad (37)$$

where the kinetic energy of turbulence Q is :

$$Q = (A_{uv} \frac{1}{h} \rho^* d^2 f / dn^2)^2 \quad (38)$$

$$\text{with } A_u = \frac{2}{33(1+c_1)} (15 + 11 c_1 + 6 c_2) > 0$$

$$A_v = \frac{2}{33(1+c_1)} (12 + 11 c_1 - 15 c_2) > 0$$

$$A_{uv} = - ((-c_3 + 1) A_v - c_5 A_u + c_4)^{1/2} / (1+c_1)^{1/2} < 0.$$

It is finally shown that fluxes G_{uv} and G_{cv} are expressed as follows :

$$G_{uv} = - K_1 \rho^{*2} L^2 \left(\frac{d^2 f}{dn^2} \right)^2 \quad (39')$$

$$G_{vc} = - K_2 \rho^{*2} L^2 \frac{df}{dn} \frac{dc}{dn} + K_2 \frac{\tau}{1+\tau} \tilde{c} (1 - \tilde{c}) \frac{d(\rho^* Q)}{dn} / \frac{d^2 f}{dn^2} \quad (40)$$

where K_1 and K_2 are two constants related to A_u , A_v , A_{uv} , whose numerical values are 3.33, 6.37 respectively.

Thus the usual gradient approximation is proved to be still valid for the Reynolds stress but a new term appears in the expression of $\tilde{v}^2 \tilde{c}^n$ (G_{vc}) which is non zero when $\tau \neq 0$.

Final similar solutions of (5)-(8) can be written:

$$(1+S) f \frac{d^2 f}{dn^2} - \frac{d G_{uv}}{dn} + S \left(\frac{1}{\rho^*} - \left(\frac{df}{dn} \right)^2 \right) = 0 \quad (41)$$

$$(1+S) f \frac{dc}{dn} - \frac{d G_{cv}}{dn} + Q = 0 \quad (42)$$

$$\text{with } S = \frac{m}{p} \quad (43)$$

RESULTS AND DISCUSSION

Equations (41)-(42) for f and \tilde{c} are integrated using the quasi-linearization technique with 5 boundary conditions including the wall law ($n=0$) for f , df/dn , \tilde{c} and external flow conditions ($n \rightarrow +\infty$) for \tilde{c} and f . In particular F and $f(0)$ must be related through :

$$F = - (1+S) \frac{d\delta}{dx} f(0) \quad (44)$$

Numerical solutions are obtained for a range of values of the heat parameter τ , the injection rate $f(0)$ and the external pressure parameter S . The numerical solution of the equations, for any values of τ and S , is found to be increasingly difficult as $f(0)$ increases. Thus practical considerations limit our results to $f(0) = 0.2$, which correspond to a moderate but not uninteresting injection rate.

Before presenting and discussing general results from numerical integration of eqs. (41)-(42) it is of interest to compare the numerical predictions with available experimental data. As we have already pointed out, the experiment of Meunier et al. (1982) corresponds to injection rates which are out of the range permitted by the numerical analysis performed in this paper. We have selected the experiment of Senda et al. (1979) whose

geometry and parameters are in the best agreement with the assumptions made in the present study. Then, mean velocity and turbulent kinetic energy profiles are compared with measurements by Senda et al. in the limiting case : $\tau \approx 0.1$, $S \approx 0$ and no chemical production. This experiment is characterized by a Reynolds number at the measurement location x which is about 10^4 . The numerical value of $d\delta/dx$ is evaluated to be 0.04. Thus according to eq. (44) the lower value of the injection rate F used by Senda et al. (1979) corresponds to $f(0) = 0.05$ in our study.

Comparisons are given in figures 2a and 2b and show a relatively good agreement. The small discrepancies observed at both edges of the boundary layer for \tilde{q} are due to the fact that $u^{1/2}$, $v^{1/2}$, $w^{1/2}$ depart slightly from similar profiles.

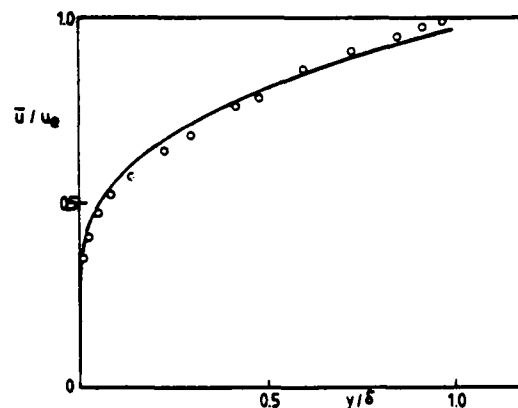


Fig. 2a - Velocity profile.
o Senda et al. (1979)
— present work.

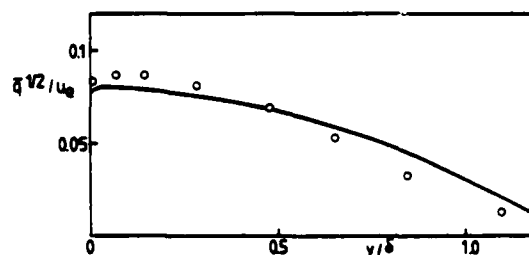


Fig. 2b - Kinetic energy of turbulence.
o Senda et al. (1979)
— present work.

In the general case, figures 3 and 4 show the mean velocity and product mass fraction profiles through the boundary layer for different values of the heat release parameter and the injection rate.

The effect of the transverse mean pressure gradient on the turbulent diffusion, through the flux term $\tilde{v}^2 \tilde{c}^n$ is illustrated in figure 5 where a comparison is drawn between results obtained from those same equations (39)-(42) where the transverse pressure term is numerically dropped. It appears that this effect is relatively small except in the vicinity of the outer edge of the boundary layer ; this difference increasing when dP/dx increases.

* Experimental results are directly compared with Favre mass weighted averages. This is justified when the heat release parameter is small.

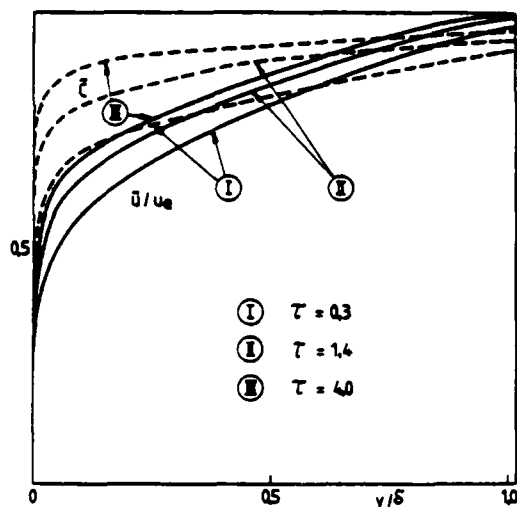


Fig. 3 - Mean velocity and mass fraction profiles
 $f(0) = -0.05$, $S = 0.17$.

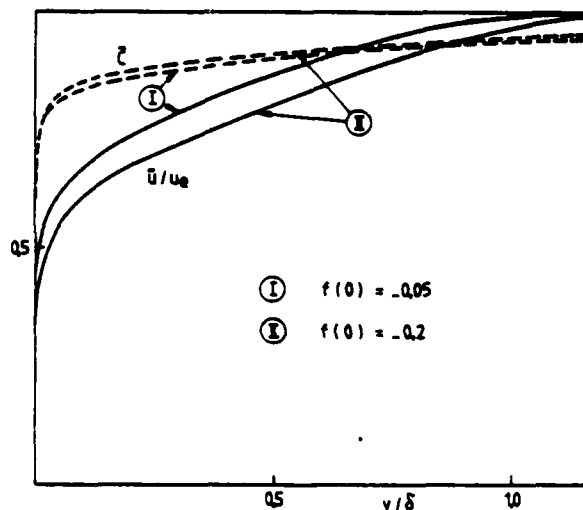


Fig. 4 - Mean velocity and mass fraction profiles
 $\tau = 2.4$, $S = 0.17$.

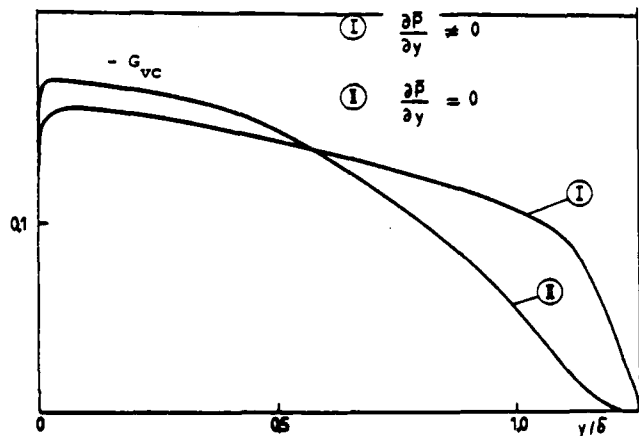


Fig. 5 - Effect of transverse pressure gradient on \tilde{c} equation
 $f(0) = -0.2$, $\tau = 2.4$, $S = 0.5$.

Thus the usual gradient law is found to overpredict the actual value of the flux $\tilde{v}''c$ close to the wall and underpredict it close to the outer edge of the boundary layer.

The distribution of turbulent kinetic energy through the boundary layer is shown in figures 6, 7, 8 for different values of τ , S and $f(0)$. In figure 6 we present the Q profiles for three different values of the heat release parameter. The decrease of the maximum value of Q for increasing τ is due to the dilatation of the fluid. The displacement of the maximum of Q towards the outer edge of the boundary layer which occurs when the injection rate is increased is clearly indicated in figure 7. This mechanism has been observed experimentally by Meunier et al. (1983) in flows with higher injection rates.

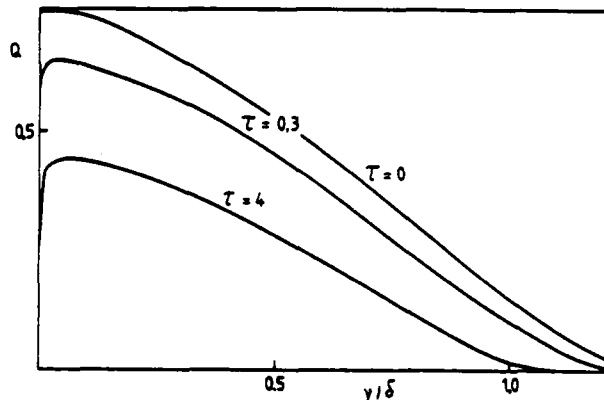


Fig. 6 - Variation of the kinetic energy of turbulence profile with the heat release.
 $f(0) = -0.05$, $S = 0.17$.

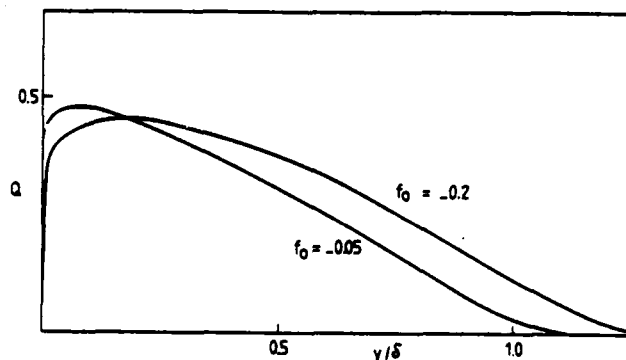


Fig. 7 - Variation of the kinetic energy of turbulence profile with injection.
 $\tau = 2.4$, $S = 0.17$.

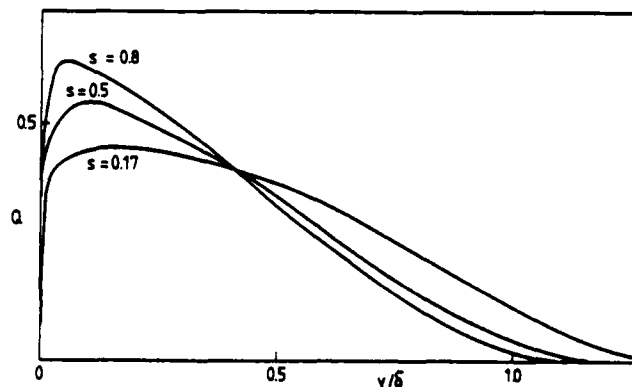


Fig. 8 - Effect of $(d\tilde{P}/dx)_e$ on the Q profile.
 $f(0) = -0.2$, $\tau = 2.4$.

CONCLUSION

The structure of a reactive turbulent boundary layer obtained by injecting a fresh mixture of reactant and air into a stream of hot product has been investigated theoretically. It has been assumed that this combustion is mixing limited and a bi-modal probability density function of velocity and product mass fraction fields has been introduced, according to the Bray-Moss-Libby theory of turbulent combustion. Then we have shown that, when the derivative $d\delta/dx$ is taken as a small parameter, similar solutions of the reactive boundary layer equations can be derived in this case. The following results are obtained from the analysis of the problem and numerical calculations.

(i) at first order in $d\delta/dx$ balance equations for \tilde{u}^{**} , \tilde{v}^{**} , \tilde{w}^{**} , $\tilde{v}^{**}C^{**}$ reduce to four "super-equilibria". Moreover, as no third order correlation appear in these equilibria, no further closure assumption is required to solve the system at this stage.

(ii) in the case of the flux \tilde{u}^{**} , the usual gradient is shown to be valid.

(iii) in the case of the scalar $\tilde{v}^{**}C^{**}$, the gradient law is modified by an additional term proportional to the heat release and to the mean transverse pressure gradient. This term, in the numerical cases investigated here, is always smaller than the gradient term, except in the vicinity of the outer edge of the boundary layer.

(iv) dissipation through the flamelets as defined by Libby and Bray (1980) appears in the equations at a lower order than the usual small scale model. Then the dissipation rate of turbulence in the reactive boundary layer is directly related to dissipation rates in fresh mixture and burnt gas.

REFERENCES

- Bray, K.N.C., Moss, J.B., (1977), A unified statistical model of the premixed turbulent flame, *Acta Astronautica*, 4, 291.
- Bray, K.N.C., Libby P.A., Masuya, G. and Moss, J.B., (1981), Turbulence production in premixed turbulent flames, *Comb. Sci. and Tech.*, 25, 127.
- Hanjalic, K., Launder, B.E., (1972), A Reynolds stress model of turbulence and its application to thin shear flows, *J.F.M.*, 52, 609.
- Launder, B.E., Reece, G.J. and Rodi, W., (1975), Progress in the development of a Reynolds stress turbulence closure, *J.F.M.*, 68, 538.
- Libby, P.A., Bray, K.N.C., (1980), Implications of the laminar flamelet model in premixed turbulent combustion, *Comb. and Flame*, 39, 33.
- Libby, P.A., Bray, K.N.C., (1981), Counter gradient diffusion in premixed turbulent flames, *A.I.A.A. Journal*, 19, 205.
- Libby, P.A., Economos, C., (1963), A flame zone model for chemical reaction in a laminar boundary layer with application to the injection of hydrogen-oxygen mixture, *Int. J. of Heat and Mass Tr.*, 6, 113.
- Meunier, S., Champion, M., Bellet, J.C., (1983), Premixed combustion in a turbulent boundary layer with injection, *Comb. and Flame*, 50, 231.
- Rosner, D.E., (1975), Correlation and prediction of boundary layer energy transfer rates in the presence of chemical reactions and mass injection, *Comb. Sci. and Tech.*, 10, 97.
- Senda, M., Suzuki, K. and Sato, T., (1976), *Memoirs Fac. Engng.*, Kyoto University, 38, 21.
- Senda, M., Suzuki, K. and Sato, T., (1979), Turbulence structure related to the heat transfer in a turbulent boundary layer with injection, 2nd Symposium on Turbulent Shear Flows, 9-17.
- Wooldridge, C.E., Muzzy, R.J., (1966), Boundary layer turbulence measurements with mass addition and combustion, *A.I.A.A. J.*, 4, 2009.

ACKNOWLEDGEMENTS

The research reported here is supported by a grant NSF-CNRS. It was carried out when M. Champion was a visitor to U.C.S.D..

LAGRANGIAN MODELS FOR TURBULENT COMBUSTION

by R. BORGHINI* and E. POURBAIX

Office National d'Etudes et de Recherches Aéronautiques (ONERA)
BP 72 92322 CHATILLON CEDEX

ABSTRACT

Turbulent combustion is discussed with a Lagrangian point of view. It is shown that simple models can be derived, or already known models can be very well explained. In the case of non homogeneous turbulent flow field, a model is proposed that is able to handle multispecies, non infinitely fast chemistry in a turbulent medium.

INTRODUCTION

During the five or ten past years, the prediction of turbulent flows with combustion has been classically led by numerical means, giving fairly detailed results. But these results are only approximate, because they are obtained from equations where many physical phenomena are "modelled" or, even, simplified, and the accuracy of each approximation is difficult to assess.

Two types of methods have mainly been used : the first one is based on the calculation of the probability density function of species and temperature, (p.d.f.) by means of a balance equation, as introduced first in the field of combustion by Dopazo and O'Brien (1974).

The second one is a method where the p.d.f. is approximately calculated from the moments, which are themselves given by the solution of their balance equations, Lockwood and Naguib (1975), Bray and Moss (1977), Borghi and Moreau (1977) and Donaldson and Varma (1976).

These two methods suffer from deficiencies of two types : the right modelling of physical phenomena is difficult, and the computation time, especially for the first method, can be prohibitive if a multidimensional p.d.f. is needed. One way to remedy to these facts could be the use of Lagrangian models, which are able to improve the physical significance of modelling assumptions and to simplify numerical integration. The first advantage of Lagrangian models has been emphasized by D.B. Spalding (1977) and led him to propose his ESCIMO. The second one has been noted by S. Pope (1979), who established a correspondence between p.d.f. balance equations and Lagrangian models (or "particle models", as called by S. Pope (1979)). Anyway, Lagrangian model have been used previously in the field of chemical engineering Yamazaki, and Ichigawa (1970) or, even, turbulent combustion (Frost (1975)).

This paper will first discuss in details the perspective of Lagrangian models for turbulent combustion with respect to their ability to use more physical closure assumptions. However, for practical use (and for the moment), it will be proposed to adopt an Eulerian-Lagrangian calculation method in order to compute non homogeneous turbulent flows with combustion; a particular example will be solved and, in addition, an Eulerian-Lagrangian version of ESCIMO will be given.

The Lagrangian models, as they are discussed here, are able to bring new lights on the prediction of turbulent combustion influenced by the velocity fluctuations, and not, on the contrary, on the velocity fluctuations modified by the combustion ; this part of the general problem is to be attacked by classical Eulerian equations.

II. LAGRANGIAN MODELS FOR TURBULENT HOMOGENEOUS REACTING FLOWS

We consider in this section only statistically homogeneous turbulent flows.

II.1. The I.E.M. Lagrangian Model

For many years, chemical engineers have been using a Lagrangian model called Interaction by exchange with the mean (I.E.M.), in which the mass fraction of a fluid particle satisfies the Lagrangian balance equation

$$\frac{dY}{dt} = \frac{\bar{Y} - Y}{\tau_{ex}} + \dot{w}(Y)$$

The fluid particle is small enough for the reaction rate \dot{w} (which is assumed here for simplicity to depend on one variable Y only) to be given by chemical kinetics only ; the mass fraction Y is randomly fluctuating, due to the turbulent exchanges between this fluid particle and the others. The term $(\bar{Y} - Y)/\tau_{ex}$ models these exchanges, and is the core of the equation. It assumes that there is an exchange frequency $1/\tau_{ex}$, which is known, depending only on the turbulence itself, and that all the exchanges with any other particle are well represented by an exchange with a "mean particle", that is having a mass fraction \bar{Y} , the mean value for all the particles.

The previous equation for Y is not a random equation, there is no random term in it ; but Y is random due to two things : first, the initial conditions can be random, second, the residence time within the homogeneous flow field is random.

In a steady homogeneous turbulent medium (an ideal configuration more or less realized in the "well stirred reactor" of chemical engineers), we can write

$$\bar{Y} = \int_0^\infty Y \tilde{P}(Y) dY$$

where, $\tilde{P}(Y)$ is the p.d.f. of Y , as well as :

$$\tilde{P}(Y) = \int_0^\infty \int_0^\infty Y(t) \cdot S(t) f(t) P_0(Y_0) dt dY_0$$

where $f(t)$ is the residence time distribution, and $P_0(Y_0)$ the p.d.f. at the inlet ($t = 0$) ; and similarly for all other moments of Y .

This Lagrangian model has been used by Aubry and Villermaux (1975), Yamazaki and Ichigawa (1970) in particular. S. Pope (1979), recently, demonstrated that, in the same homogeneous turbulent flow field, the p.d.f. balance equation found by Dopazo and O'Brien (1974), namely :

* Also Lab. de Thermodynamique, Université de Rouen, 76130 Mt St Aignan

$\frac{\partial}{\partial t} P(Y) = \frac{\partial}{\partial Y} (\dot{W}(Y) P(Y)) + \frac{\partial}{\partial Y} \left(\frac{6d}{\lambda_Y^2} (Y - \bar{Y}) P(Y) \right)$
 was exactly equivalent to the I.E.M. model with $1/\tau_{ex} = 6d/\lambda_Y^2$.

And, in general, any p.d.f. equation, where the mixing term is $g(Y)$, is equivalent to a Lagrangian model where the exchange is modelled as: $\dot{Y} = g(Y)/P(Y)$

The study of V.A. Frost (1979) takes as starting point a Lagrangian model of about the same type:

$$\rho \frac{dY}{dt} = -\bar{P} \frac{Y - \bar{Y}}{\tau_Y} + \rho \dot{W}(Y)$$

In addition, he uses a Lagrangian model for the velocity fluctuations, in the form of a Langevin equation:

$$\rho \frac{d\vec{u}}{dt} = -\bar{P} \frac{\vec{u} - \bar{\vec{u}}}{\tau_u} + (\bar{\rho} \rho) \vec{f}$$

where \vec{f} is random force, of Markovian type, related to the turbulence kinetic energy. He was able to derive the joint probability density function $\mathcal{P}(Y, \vec{u})$ as:

$$\rho \frac{\partial \mathcal{P}}{\partial t} + \rho u_i \frac{\partial \mathcal{P}}{\partial x_i} = \frac{\partial}{\partial u_i} \left\{ \bar{P} \frac{u_i - \bar{u}_i}{\tau_u} \mathcal{P} \right\} + \bar{P}^2 \frac{\partial^2}{\partial u_i \partial u_i} (\bar{\rho} \mathcal{P}) + \frac{\partial}{\partial Y} \left\{ \bar{P} \frac{Y - \bar{Y}}{\tau_Y} \rho \dot{W}(Y) \mathcal{P} \right\}$$

which is exactly similar, concerning Y , to the one of Dopazo and O'Brien.

In the I.E.M. model, τ_{ex} , as well as τ_Y and τ_u in the Frost model, or $6d/\lambda_Y^2$ in the Dopazo-O'Brien equation, has to be prescribed, related to the turbulence. Indeed, a turbulence model need to be joint with the turbulent combustion model in order to compute the time scale τ_{ex} . A classical assumption is to simply relate τ_{ex} proportionally to τ_u , τ_u being defined as a time scale of the velocity fluctuations, for instance k/ϵ , if a $k-\epsilon$ model is used.

II.2. The I.E.M. Model Applied to Multireactive Mixture

It is easy to generalize the I.E.M. model to multireactive mixtures, and this will allow us to compute very simply the multidimensional p.d.f., knowing only the p.d.f. for one particular species, for instance an inert tracer.

In a multireactive mixture, the I.E.M. model reads:

$$\frac{dY_i}{dt} = \frac{Y_i - \bar{Y}_i}{\tau_{ex}} + \dot{W}(Y_i, j=1 \dots n)$$

Assuming for the moment that the \bar{Y}_i are known, the previous equations can be simultaneously integrated to give $Y_i = Y_i(t, Y_{i0})$, $\forall i$; if we consider now the phase plane where Y_1 , one inert tracer, and one Y_i are on the two axes, both relations $Y_1 = Y_1(t, Y_{10})$ and $Y_i = Y_i(t, Y_{i0})$ represent a single trajectory beginning at (Y_{10}, Y_{i0}) and finishing, for $t = \infty$, at the same point where $\dot{W} = (Y_i - \bar{Y}_i)/\tau_{ex}$ and $Y_1 = \bar{Y}_1$.

In the particular case where $P_0(Y_0)$ is concentrated at the two points (Y_{10}, Y_{i0}) and $(0,0)$, the figure 1 shows an example of the two trajectories obtained.

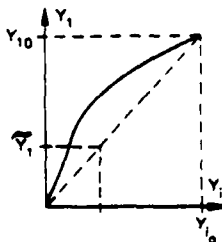


Fig. 1

Of course, we do not know for the moment neither \bar{Y}_1 , nor \bar{Y}_i , but it is easy to see that, if we know $P_0(Y_{10}, Y_{i0})$ and $\mathcal{L}(t)$, or equivalently $P_1(Y_1)$, it is possible to find $P_1(Y_i)$ and consequently \bar{Y}_i ; indeed

$$\bar{P}_i(Y_i) = \iint P_0 \cdot \bar{P}_1(Y_1(Y_i, Y_{10}, Y_{i0})) \frac{dY_1}{dY_i} dY_{10} dY_{i0}$$

or simply, in the case of fig. 1:

$$\bar{P}_i(Y_i) = \bar{P}_1(Y^*(Y_i)) Y_1^*$$

where $Y_1^*(Y_i)$ is the equation of the two trajectories and $Y_1^* = dY_1^*/dY_i$. Whatever $\bar{P}_1(Y_1)$ can be, the I.E.M. model leads to the result that the multidimensional p.d.f. occupies, in the multidimensional phase plane, only the trajectories determined by the Lagrangian balance equation and the known inlet conditions. In the simple case where the homogeneous flow field is seeded by two different jets of known composition, the multidimensional p.d.f. is then only one dimensional: it occupies only a segment of a curved line. More details on these trajectories can be found by Borghi and Fourbaix (1981).

This very simple conclusion will allow us to attempt very easily the computation of multireactive turbulent flows. Previously, more than two-dimensional p.d.f. was clearly improper to numerical computation, either with the p.d.f. equation or with the moments equations (may be the monte carlo method of Flagan and Appleton (1974) or Pope (1981) remained the only hope). In addition, we can see that simplifications like the one used by Janicka and Kollman (1978), which assumes that a reactive species Y_i and an inert one Y_1 are fluctuating independently: $P(Y_i, Y_1) = \bar{P}_i(Y_i) \cdot \bar{P}_1(Y_1)$ are clearly in contradiction with the simple I.E.M. model: here Y_i and Y_1 are so strongly related that $Y_1 = Y_1^*(Y_i)$.

II.3. Possible Improvements of the I.E.M. Model

a) Of course, the I.E.M. model is just a model, and we have for the moment no direct proof that it is realistic. In fact, we already know that the Dopazo O'Brien closure assumption is in some aspect unrealistic, and it follows that the I.E.M. model possesses the same discrepancy. The Curl model, or the one proposed by Janicka et al. (1978), seem more satisfactory; they have been proposed as closure assumption for the p.d.f. equation, and can be incorporated into a Lagrangian model; the differential equation would be more complicated than the one with the I.E.M. model, and the mixing term would involve $\bar{P}_1(Y_1)$ itself and not only Y_1 .

It is easy to see that the important property found in II.2, that is $P(Y_1, Y_i)$ occupies only known lines in the (Y_1, Y_i) plane, holds also with these new models; in fact any mixing term of the type $1/\tau_{ex} \cdot g(P_1(Y_i))$ will give the same result. The crucial point is the knowledge of the exchange frequency: if τ_{ex} is a non random quantity, the previous property holds.

b) A better model would be probably one involving a random exchange frequency. Indeed k/ϵ represents only a mean turbulent time scale, and a full spectrum of τ_k exists, ranging from a few times k/ϵ to τ_k , the Kolmogorov time scale ($\tau_k = (\epsilon/\nu)^{-1/2}$). In order to incorporate this in the I.E.M. model, or the others extracted from the Curl or Janicka assumptions, we need only to consider the same differential equation, but with $1/\tau$, random parameter, instead of $1/\tau_{ex}$.

The joint p.d.f. $\bar{P}(Y_1, Y_i)$ in the (Y_1, Y_i) plane is then thickened as shown by the trajectories of fig. 1 bis.

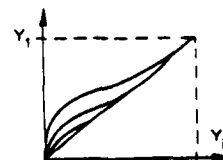


Fig. 1 bis - Each trajectory corresponds to a value of $1/\tau$.

Of course, the p.d.f. of $1/\tau$ is now to be given, or calculated, in order to get the complete $\tilde{P}(Y_1, Y_i)$. In an homogeneous turbulent medium, this new p.d.f. is to be related to the autocorrelation curve for the velocity fluctuations.

It is to be noticed that, if Y_i was an inert species like Y_1 , with the same molecular diffusion, the joint p.d.f. of $\tilde{P}(Y_1, Y_i)$ would not be thickened by the fluctuations of τ . Indeed, if we consider the simple case of fig. 1, the joint p.d.f. would always be the straight line $Y_1 = Y_i Y_0 / Y_{01}$ following from the similarity of the exact balance equation for Y_1 and Y_i (see Borghi (1979)). Then, the effect of the random nature of τ is amplified by the reaction, and because combustion is a non linear reaction (that is a reaction with a strongly varying time scale) the mean line of the joint p.d.f. of fig. 1 bis is not a curve corresponding to the mean $1/\tau$; it corresponds to another trajectory given by a Lagrangian model where $1/\tau$ is not constant but depending on the \dot{w} .

c) In the limiting case where the combustion is very fast with respect to the mixing (and the Reynolds and Peclet numbers are very large), the previous trajectories are easier to find. Let us consider first the case of a premixed combustion in a ideally homogeneous burner feeded by fresh mixture and perfectly burnt gases (for stabilization). If the combustion is very fast, the p.d.f. of the fuel, for instance, is composed only by two peaks, corresponding to the fresh mixture or to perfectly burnt gases; on the other hand the p.d.f. for the tracer involves intermediate states. We obtain therefore fig. 2.

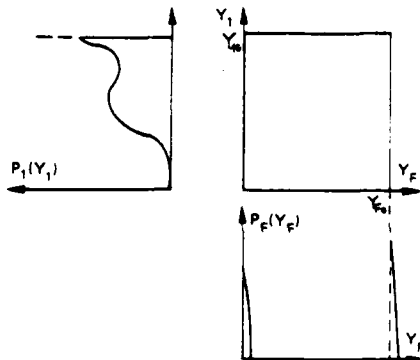


Fig. 2 - Joint p.d.f. for Y_1, Y_F in a fuel lean premixed flame with very fast combustion (Y_F is the fuel mass fraction).

Let us consider now the case of a diffusion flame when the chemical reactions are very fast. Fig. 2 bis shows the trajectories obtained, and $\tilde{P}_F(Y_F)$ related.

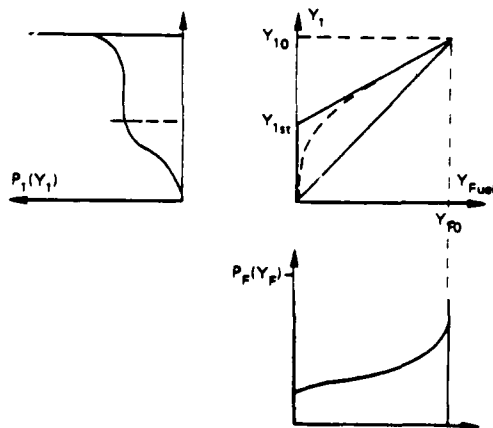


Fig. 2 bis - Joint p.d.f. Y_1, Y_F for a diffusion flame with very fast reaction.

The heavy lines, on the Y_1, Y_F plane correspond to the case where a single reaction occurs between fuel

and oxidizer, for instance $F + O \rightarrow P$, and where Y_0 and Y_F have the same diffusion coefficient; in this case the very fast reaction assumption implies that either Y_F or Y_0 are zero, and that $\phi = rY_F - Y_0$ is a conserved species; the trajectories are then composed of $Y_F = 0$ when $Y_1 < Y_{1st} = Y_{01} / (rY_{F0} + Y_{01})$ and a straight segment joining $(Y_{1st}, 0)$ to (Y_{10}, Y_{F0}) when $Y_1 > Y_{1st}$. In the case where the combustion cannot be represented by a single reaction, and if the Lewis numbers of all involved species are unity, the two straight lines become one curve, corresponding to the chemical equilibrium to the mixture, which is shown as the broken heavy line on the diagram.

All Lagrangian models must exhibit such a behaviour in these limiting cases. The IEM model with infinitely small chemical time does give the right answer in both cases.

The differential equation $dY_i/dt = (Y_i - Y_i)/\tau_{ex} + w_i(Y_F)$ with very large \dot{w} leads in a very short time to the quasi steady state for reactive species, where $w_i = (Y_i - Y_i)/\tau_{ex}$ while the inert tracer behaves gently.

In the case of a premixed lean flame, the trajectory issued from Y_{10}, Y_{F0} is then a straight time parallel to the Y_F axis, followed by a line very close to the Y_1 axis, corresponding to the quasi steady state, which is, for $Y_F, Y_F \approx 0$. The quasi steady state leads to

$$\dot{w}_F(Y_F) = -\frac{\tilde{Y}_F}{\tau_{ex}}$$

If we integrate this relation in order to obtain the mean reaction rate \bar{w}_F , one gets easily that $\bar{w}_F = \bar{S}(Y_F = 0) \cdot (-\tilde{Y}_F/\tau_{ex})$, where $\bar{S}(Y_F = 0)$ is the area of the peak situated in $Y_F = 0$ on the Y_F p.d.f.; but $\bar{S}(Y_F = 0) = 1 - \bar{S}(Y_F = Y_{F0}) = 1 - \tilde{Y}_F/Y_{F0}$, and that gives finally :

$$\tilde{W}(\tilde{Y}_F) = -\frac{1}{\tau_{ex}} \tilde{Y}_F \left(1 - \frac{\tilde{Y}_F}{Y_{F0}}\right)$$

This formula is exactly the one derived from the Bray and Moss model (1977), and very similar to Eddy break up model of D.B. Spalding.

In the case of the diffusion flame, the trajectory issued from (Y_{10}, Y_{F0}) attain instantaneously the quasi steady state too, but it corresponds here to $Y_{01} \approx 0$ and Y_F varies according to $\frac{Y_1 + Y_{F0}}{Y_{F0} + Y_{01}} = Y_1$ with $\phi = rY_F$ until ϕ becomes zero (and $Y_1 = Y_{1st}$); at this point we cross the stoichiometric line and, after that, Y_F remains close to zero. The instantaneous reaction rate \dot{w}_F can also be deduced from the I.E.M. model; when $Y_1 > Y_{1st}$, $\dot{w}_F = r\dot{w}_F = -\dot{w}/\tau_{ex}$ and when $Y_1 < Y_{1st}$, $\dot{w}_F = -\tilde{Y}_F/\tau_{ex}$; we obtain finally

$$\tilde{W}_F = -\frac{1}{\tau_{ex}} \left[\frac{\tilde{Y}_0}{r} \int_{Y_{1st}}^{Y_{10}} \tilde{P}(Y_1) dY_1 + \tilde{Y}_F \int_0^{Y_{1st}} \tilde{P}(Y_1) dY_1 \right]$$

This formula is the diffusional version of the Eddy Break up model; of course it is fully possible to avoid the use of such a formula in order to compute \tilde{Y}_F , as we can have it simply by:

$$\tilde{Y}_F = \int_{Y_{1st}}^{Y_{10}} Y_F^*(Y_1) \tilde{P}(Y_1) dY_1$$

where $Y_F^*(Y_1)$ is the equation of the straight segment joining $(Y_{1st}, 0)$ to (Y_{10}, Y_{F0}) . This later formula is evidently the same one that derived following the ideas originated by Toor (see for instance Lin and O'Brien (1974)).

b) The real Lagrangian equation is, in any case :

$$\rho \frac{d}{dt} Y_i = \frac{\partial}{\partial x_j} \left(\rho D_{ij} \frac{\partial Y_i}{\partial x_j} \right) + \rho \dot{w}_i$$

The role of Lagrangian models is to approximate the first term on the right hand side, because it is impossible to compute for turbulent flows.

When we suspect that the turbulent motion acts only to randomly displace flame fronts or diffusion fronts

(that is any length scale and time scale of the turbulence are large enough with respect to the ones related to the laminar flame), we can replace this equation by its known solution (by experimental or theoretical means) for purely laminar flame. Then the trajectories in any plane Y_1, Y_i are given by the deterministic relation $Y_i(Y_1)$ existing in the corresponding laminar flame.

We join here the "flamelet model" use recently by Bray, Moss (1981) in order to compute CO production in a turbulent diffusion flame.

When the time scales of the turbulence are small enough to interact with the ones of the laminar flame, these laminar flamelets are stretched by the turbulence. There are many trajectories : $Y_i(Y_1, \chi)$, each one corresponding to a laminar flame with a particular stretching rate χ . If we can know, theoretically or experimentally, the relation $Y_i(Y_1, \chi)$, we can use it, jointly with the probability density function of Y_1 and χ (which, perhaps, may be separated in two independent p.d.f.'s), to compute all Y_i etc... We join here the recent discussion of N. Peters (1983), and similarly the ideas of D.B. Spalding for ESCIMO (1977), and of Broadwell and Marble for their "Coherent flame model" (1977). But when the length scales of the turbulence are small enough compared to the laminar flame length scales, the flamelets do not exist anyway; instead of flamelets, the turbulent reacting medium is occupied by interactions of flamelets, and the solution of the lagrangian equation cannot be performed for each individual flamelet. Physical modelling is then needed in this case, and, in particular, the model I.E.M. intend to address these phenomena.

III. EULERIAN-LAGRANGIAN METHODS FOR NON HOMOGENEOUS TURBULENT REACTING FLOWS

III.1. Extension to Non Homogeneous Turbulent Reacting Flows

We consider now a non homogeneous turbulent flow, and, more precisely, the case of a turbulent flame within the mixing zone of two parallel streams A and B, as schematized fig. 3.

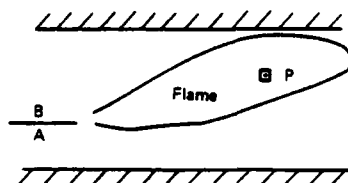


Fig. 3 -

The problem that we intend now to discuss is the use of Lagrangian models for non homogeneous flows. The model of Frost (1975) is a way to solve this problem ; but Frost, in fact, did not solve directly the Lagrangian equations ; he solves the p.d.f. equation to what the model led.

In the case of very fast reactions and when the Lewis numbers of all involved species are unity, the generalization to non homogeneous flows is straightforward. Neither for premixed flames, nor for diffusion flames, the trajectories of fig. 2 and 2 b. have to be influenced by the non homogeneity. It suffices, then, to get a right calculation of $P_i(Y_1, \chi)$, at each point of the flow field, to solve the problem.

We shall now propose two Lagrangian non homogeneous models, which will leads to Eulerian-Lagrangian calculation methods. One is the extension of the I.E.M. model, the other one appears almost equivalent to the ESCIMO model of D.B. Spalding. (1977)

III.2. The Eulerian-Lagrangian Extension of I.E.M. Model

A Lagrangian model as discussed previously cannot be applied directly, because neither Y_i or $P_i(Y_i)$, nor τ_{ex} are constants along the physical trajectories between A, or B, the inlet streams, and the point P. But we can continue to use the homogeneous model, in the vicinity of any particular point P, provided, that

we consider that the initial points Y_{i0} of the differential equations do not correspond to the streams A and B, but constitute a set of parameters, to be chosen conveniently. With this principle in mind, we can propose the following Eulerian-Lagrangian method.

i) We know that the turbulent flow field can be calculated with Eulerian balance equations for mean velocity, turbulent kinetic energy k , dissipation rate ϵ ; with equations for the mean concentration Y_1 of an inert species (assumed injected with B only) and the variance $Y_1'^2$, we can compute at each point of the flow, the p.d.f. of Y_1 , assuming a particular shape (for instance a β -function) ; it is possible also to compute $\tilde{P}_1(Y_1)$ more exactly, but less easily, with a balance equation conveniently closed.

ii) Then, considering all the reactive species Y_i , we can compute the two trajectories issued from A and B, with the homogeneous Lagrangian model applied to each point of the flow, and with the balance equation for Y_i :

$$\frac{\partial}{\partial x} (\rho \tilde{u}_i \tilde{Y}_i) = \frac{\partial}{\partial x} \left(\rho D_{ik} \frac{\partial \tilde{Y}_i}{\partial x} \right) + \tilde{P} \int_{Y_{i0}}^{\tilde{Y}_i} \tilde{\omega}_i(Y_1) \tilde{P}_1(Y_1) dY_1$$

We need for that to rely D_{ik} and τ_{ex} to k and ϵ , and we use classical relations :

$$\tau_{ex} = k/\epsilon, \quad D_{ik} = k^2/\epsilon$$

The chemical source term is closed owing the knowledge of the trajectories in the phase space and $\tilde{P}_1(Y_1)$.

iii) We can also compute all the $P_i(Y_i)$, and recalculate Y_i by

$$\tilde{Y}_i = \int_{Y_{i0}}^{\tilde{Y}_i} Y_i \tilde{P}(Y_i) dY_i \quad (\equiv \tilde{Y}_i^L)$$

This new \tilde{Y}_i^L will not coincide with the one computed with the Eulerian balance equation, because the p.d.f.'s are wrong : only two trajectories have been considered, as in the case of homogeneous flows. But we can correct all the $P_i(Y_i)$ with other trajectories, one for each Y_i , in order to get coincidence in the two values of Y_i . This implies only a linear set of equations to be solved if the initial points Y_{i0} are chosen ; if these initial points are chosen on the limits of the domain allowed for $P(Y_1, Y_i)$, as shown in fig. 3bis, the linear set of equation will have always a physical solution.

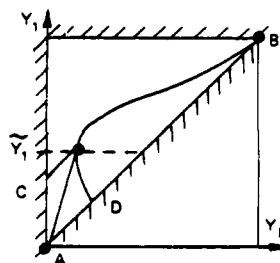


Fig. 3bis - Allowed domain and trajectories for $P(Y_1, Y_F)$ where Y_F is the fuel consumed by reaction, at the point P of the flame of Fig. 4.

iv) It is possible again to refine the shape of $\tilde{P}(Y_1, Y_i)$ adding new trajectories, in order to verify the Eulerian balance equations for the $Y_i'^2$; after that, we can consider the $Y_i' Y_i$ and so on ...

If the heat release is low, the steps ii), iii), iv).... would not modify the step i) ; but this is generally not the case for combustions, and iterations have to be performed ; there is no guaranty that they will converge, but our experience has shown that they do.

We remark that the way to compute the turbulence in this method is fully classical ; of course, we can improve that, when it is necessary, following the results of new researches on the influence of combustion on turbulence.

The Eulerian-Lagrangian method explained previously has been successfully applied to the case of a premixed turbulent flame in a parabolic mixing

layer, where the combustion has been modeled as a single reaction, and using the simple I.E.M. model. The steps i), ii), iii), have been operated with satisfactory convergence in Borghi and Pourbaix (1983). A first attempt to compute a more complicated chemistry has also been made, but only with the step i) and ii) (see Borghi and Pourbaix (1981)).

III.3. The Eulerian-Lagrangian Version of ESCIMO

a) ESCIMO is a Lagrangian model too ; but the fluid particle that is considered is not as small as the previous one : there is a structure inside, which consists in a laminar flame (or quasi laminar) propagating ; the turbulence itself acts at the scale of the fluid particle (called here a "fold"), stretching it without any exchanges of mass . These particular types of fluid particles have to be produced in the mixing and reaction zone ; consequently, in addition a birth rate and a $P_b(Y_1)$ of these folds have to be prescribed.

This is, strongly summarized, the essence of ESCIMO.

One can represent, in the plane (Y_1, Y_F) , the $\tilde{P}(Y_1, Y_F)$ that is implied by the model ; here Y_1 and Y_F are the mass fraction of one inert and the fuel, respectively, within the fold : they are mean values at the scales smaller than the fold itself. The fig. 4 shows the trajectories obtained.

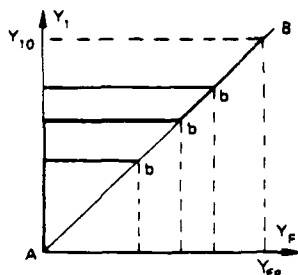


Fig. 4 - Trajectories in the case of a model of the type of ESCIMO, with very sudden combustion.

Before the birth points, nothing can occur, except, perhaps, small scale mixing ; then all birth points are on the straight line AB. After, each fold evolution is such that the inert matter inside is constant and the fuel is decreasing. Of course, this stops when there is no more fuel.

The ESCIMO model appears as a Lagrangian model with very sudden combustion, but not very fast combustion. In the first calculation, D.B. Spalding chose only one birth point : this can be, at first sight, justified by the fact that the "folds" are not fluid particles, but "coherent structures", and their p.d.f. are consequently thinner than $\tilde{P}_1(Y_1)$ itself. As a first approximation, we can assume that $P_b(Y_1) = \delta(Y_1 - Y_b)$, and, in an homogeneous medium, it follows that $Y_b = Y_1$.

The Lagrangian equations of ESCIMO are :
 $\frac{dY_F}{dt} = +\tilde{\omega}_F = -\frac{Y_F}{\lambda_0}$, μ_F is the laminar flame speed (inside the fold) and $d\lambda/dt = -\lambda/\tau$; by elimination of t and λ , it comes:

$$\tilde{\omega}_F = dY_F/dt = -(\tilde{Y}_1 - Y_F)/\tau - \mu_F/\lambda_0$$

where τ is the turbulent stretching time (again k/ϵ), and λ_0 the size of the folds at their birth, that is a turbulence length scale for the inert species Y_1 . By averaging $\tilde{\omega}_F$, we simply obtain :

$$\tilde{\omega}_F = -\frac{\tilde{Y}_1 - Y_F}{\tau} - \frac{\mu_F}{\lambda_0}$$

This formula constitutes the mean reaction rate of ESCIMO, in the case we are interested only in Y_F and not in other species, and neglecting the influence of the stretching on ω_F . It avoids any computation of residence time distributions, at the contrary of the original ESCIMO, of purely Lagrangian type ; instead of that, a simple calculation of \tilde{Y}_1 , an inert species diffusing like the fuel, is needed.

The physical meaning of τ is such that it can be identified with k/ϵ , but the one of λ_0 is not too

precise; in particular, is λ_0 to be proportional to the integral scale $l = k^{3/2}/\epsilon$ or the Taylor microscale λ_t for the species Y_1 ? The question is of importance : in the first case $\tilde{\omega}_F$ would be influenced by the molecular diffusivity and a chemical time, both appearing through ω_F ; in the second one the molecular diffusivity would disappear, as $\omega_F \propto d^{1/2}$ as well as λ_t^2 .

b) Taking into account only one birth point ($Y_b = Y_1$) is probably a shortcoming of the ESCIMO model. It is possible to avoid that, taking advantage of $\tilde{P}_1(Y_1)$.

We will now identify the folds with fluid particles, and the birth points will be defined as points where a turbulence time is equal to a given chemical time. Suppose we know an ignition delay, as a function of temperature and concentrations, for a given reaction ; nonburning fluid particles corresponding to a point on the diagonal in the plane (Y_1, Y_F) have, each one, an ignition delay $\tau_c(Y_1)$; if, for the same particle, there is a range of turbulence times around the mean value k/ϵ , the probability that the particle will be ignited is the probability that $\tau > \tau_c$.

We propose then a model where $P_b(Y_1)$ is a curve depending on two parameters : the first one, the mean value \tilde{Y}_b , is to be related to the ignition chemistry and k/ϵ ; the second one, characterizing Y_b , is to be related, in addition, to Y_F . In terms of $P_b(Y_1)$, referring to Fig. 4, one can easily show that \tilde{Y}_F^L as defined in sec. III.2) is given by :

$$\tilde{Y}_F^L = \int_0^{Y_{F0}} \frac{Y_F}{\lambda_0} Y_1 X_b(Y_1) \tilde{P}_1(Y_1) dY_1$$

$$\text{where } X_b(Y_1) = \int_0^{Y_F} Y_b P_b(Y_b) dY_b$$

$$\text{one obtain also : } \tilde{\omega}_F = -\tilde{Y}_F \int_0^{Y_{F0}} \frac{(1 - X_b(Y_1)) \tilde{P}_1(Y_1) dY_1}{\tau_c(Y_1)}$$

$\tilde{\tau}_c$ can be prescribed such that $k/\epsilon = \tau_c(\tilde{Y}_b)$, $\tilde{\tau}_c$ being an appropriate chemical model for the ignition delay. After that \tilde{Y}_b has to be adjusted to identify \tilde{Y}_F and \tilde{Y}_F calculated from the Eulerian balance equation with the previous $\tilde{\omega}_F$; simple shapes for P_b , depending on three parameters, can be used, as the clipped gaussian one, or one with peaks and rectangles...

IV CONCLUDING REMARKS

The use of a Lagrangian view is useful to study turbulent combustion. The main results of the discussions presented here can be summarized as follows :

- i) A Lagrangian view in the "phases plane" for a reactive (consumed) species and an inert one give us simple, or less simple, turbulent combustion models.
- ii) The problem of multispecies, non infinitely fast turbulent combustion can be attacked also with some chances of success, contrary to the previous p.d.f. approaches.
- iii) A coupling between Lagrangian calculations in the phases planes, and Eulerian calculations in the physical plane is very suitable for non homogeneous flow fields. First practical calculations have been successfully performed by Borghi and Pourbaix (1981).

REFERENCES

- Aubry, C., Villiermaux, J., (1975), "Representation du mélange imparfait de deux courants de réactifs dans un réacteur agité continu" J. Chem., Eng. Sci., vol. 30, p. 457.
- Borghi, R., and Moreau, P., (1977), "Turbulent combustion in a premixed flow" Acta Astronautica, n° 3-4, p. 321.
- Borghi, R., and Pourbaix, E., (1981), "On the coupling of complex chemistry with a turbulent combustion model" Physico chemical hydrodynamics, vol. 2 n° 1, p. 65.

- Borghi, R., Pourbaix, E., "Une modélisation eulérienne-lagrangienne pour la combustion turbulente" La Recherche Aéronautique, To be published.
- Borghi, R., (1979) "Reactions chimiques en milieu turbulent" ONERA Pub. 1979/2.
- Borghi, R., Pourbaix, E., "Numerical investigation of a model of turbulent combustion of hydrocarbons", AIAA 19th Aerospace Sciences Meeting St Louis 12-15 January, 1981.
- Bray, K.N.C., and Moss, B., (1977) "A unified statistical model of premixed turbulent flame" Acta Astronautica, vol. 4, n° 3-4, p. 291.
- Donaldson, C.D., and Varma, A.K., (1976), "Remarks on the construction of a second order closure description of turbulent reacting flows" - comb. Sci. Tech. Vol. 13, p. 1-6.
- Dopazo, C., and O'Brien E.E., 1974, "An approach to the auto ignition of a turbulent mixture" Acta Astronautica, vol. 1, p. 1239.
- Flagan, R.C., and Appleton, J.P., (1974), A stochastic model of turbulent mixing Frost, V.A., (1975), "Model of a turbulent, diffusion-controlled flame jet" Fluid Mechanics, Soviet Research, Vol. 4, n° 2, p. 124.
- Janicka, J., Kollmann, W., (1978), "A two variable formalism for the treatment of chemical reactions in turbulent H₂-Air flames" 17th Symp. (Int.) on combustion p. 421.
- Janicka, J., Kolbe, W., Kollmann, W., (1978) "The solution of a P.D.F. transport equation for turbulent diffusion flames" Proc. Heat Transfer and Fluid Mech. Inst., Stanford U. Press, p. 296.
- Liew, S.K., Bray, K.N.C., Moss, J.B. (1981), "A Flamelet model of turbulent non premixed combustion", Comb. Sci. Tech., vol. 27, p. 69-73.
- Lin, O'Brien, E.E., (1974) "Turbulent shear flow mixing and rapid reactions : an analogy" J.F.M., vol. 64, part 1, p. 195-206.
- Lockwood, F.C., and Naguib, A.S., 1975, "The prediction of the fluctuations in the properties of Free, Round jet, turbulent, diffusion flames" Combustion and Flame, vol. 24 n° 1, p. 109.
- Marble, F.E., Broadwell, J.E., (1977), "The coherent flame model for turbulent chemical reactions", Project Squid Tech. Rep. TRW-9-Pu.
- Peters, N., Flamelets models for non premixed turbulent combustion, Conference INRIA, Paris Déc. (1982).
- Pope, S.V. (1979), "The relationship between the probability approach and particle models for reaction in homogeneous turbulence" Combustion and Flame, vol. 35, p. 41.
- Pope, S.V., (1981), "A Monte Carlo method for the P.D.F. Equations of turbulent reactive Flow", comb. Sci. Tech. vol. 25, pp. 159-174.
- Spalding, D.B., (1977), "A general theory of turbulent combustion" J. Energy vol. 2, n° 1, p. 16.
- Yamazaki, H., Ichigawa, A., (1970), Int. Chem. Eng. Vol. 10, p. 471.
- with chemical reaction..." Comb. Flame, 23, pp. 249-267.

SIMULTANEOUS MEASUREMENT OF VELOCITY AND SCALARS IN A TURBULENT NONPREMIXED FLAME BY COMBINED LASER DOPPLER VELOCIMETRY AND LASER RAMAN SCATTERING

R. W. DIBBLE

R. W. SCHEFER

Sandia National Laboratories,
Livermore, CA 94550

ABSTRACT

This paper describes a new combined laser Doppler velocimeter-laser Raman scattering apparatus which simultaneously measures velocity and scalars. Measurements in a ducted nonpremixed turbulent flame using this apparatus are presented. Results include an analysis of the turbulent momentum transport and both conventional and Favre averages of variables.

INTRODUCTION

Analytical and numerical solutions of the time-dependent Navier-Stokes equations for turbulent fluid flow are not in general possible with existing methods, and such solutions are improbable for the foreseeable future. In lieu of direct solution of the Navier-Stokes equations, the most common approach is numerical solution of the time-averaged Navier-Stokes equations. It is not possible to solve the time-averaged equations without relying on empiricism to model the new correlation terms that emerge as a consequence of time-averaging the nonlinear terms. This empirical approach has been most successful for constant-density, nonreacting flows for which the largest set of experimental observations exists. The extension of these submodels to turbulent combustion presents two additional problems: 1) how to incorporate the variable density aspect of the flow into the model and 2) how to model the chemical reactions (which have an exponential temperature dependence) when the temporal and spatial fluctuations of temperature are comparable to the mean temperature. Progress in the modeling of turbulent combustion will be accelerated by obtaining measurements which address these two problems.

Measurements in turbulent reacting flows have been fewer and of greater uncertainty than measurements in nonreacting

flows, largely due to the hostile environments associated with turbulent combustion which make conventional measurements difficult, if not impossible. The emergence of laser-based diagnostics in the last decade has improved the prospects of making the necessary measurements in turbulent reactive flows. This paper presents a combined laser Doppler velocimeter (LDV)-laser Raman scattering system which simultaneously measures velocity, temperature, and species concentration. The paper also presents recent measurements obtained in a turbulent nonpremixed flame. These new simultaneous measurements allow direct comparison of aforementioned correlation terms for which an empirical model must be postulated. The data reduction scheme presented here emphasizes obtaining velocity and density measurements in an adiabatic, chemical equilibrium flow with large variation in the density. From the simultaneous measurements of density with velocity, the turbulent momentum transport as well as the density-weighted (Favre) velocity are deduced. A closing comment is made on the possibility of using the apparatus in nonadiabatic and nonequilibrium flows.

EXPERIMENTAL

All measurements were made in the Sandia Turbulent Diffusion Flame Facility, an induced-draft, horizontal wind tunnel with an axisymmetric fuel jet located at the upstream end of a test section. A fully windowed test section has a 30-cm-square cross section and is 200 cm long. The fuel nozzle inside diameter D is 0.53 cm. The bulk velocity of the fuel mixture (22 mole percent argon in hydrogen) is 154 m/s, and the velocity of the coflowing air stream is 8.5 m/s. The jet Reynolds number, based on the pipe inside diameter and bulk fuel velocity, is 24,000. The use of this fuel mixture allows direct comparison to earlier LDV-Rayleigh measurements in the same facility (Driscoll, *et al.* 1983).

Velocity-scalar correlations are obtained from simultaneous measurements of the velocity and the associated scalar. In this work, the simultaneous measurements are made with a combined LDV-laser Raman scattering apparatus. Because this apparatus (Fig.1) has recently been discussed by Dibble, *et al.* (1983), only the salient features will be addressed here. An LDV event triggers the pulsed dye laser. Species concentration and temperature are determined from measurements of laser Raman scattering from gases in the probe volume.

The LDV was a commercially available forward-scattering system. Velocimeter laser beams (488nm, 4 Watt) were focused in an optical volume having a diameter of 0.5mm and a length of 2.0mm. Through this optical probe volume we focused light from a flashlamp-pumped dye laser (1 J/pulse, 1 pulse/s, 2- μ s pulsewidth, $\lambda=514.5$ nm, $\Delta\lambda=0.1$ nm), which was located 20 m from the test facility in an adjacent room. Raman-scattered light was collected at right angles by a 30-cm-focal-length, $f/2$ collection lens and was relayed at X3 magnification to the entrance slit of a 3/4-m grating spectrometer. The entrance slit width determined the length of the Raman probe volume (1mm) while the height of the probe volume was determined by the laser beam diameter (less than 1mm). Since the slit height was 6mm, the measured Raman signal was not sensitive to small movement of the laser beam, which could result from beam steering by the turbulent flame (Starner and Bilger, 1980). Five photomultiplier tubes were positioned at the exit plane of the spectrometer to receive the Stokes-shifted vibrational Raman scattered light from N_2 , O_2 , H_2 , H_2O , and the anti-Stokes vibrational Raman scattering from N_2 . In addition, elastically scattered (Rayleigh and Mie) laser light was measured. Laser pulse energy was measured with a vacuum photodiode which received the attenuated laser light after it had passed through the test section. Electrical outputs from the phototubes were connected to a twelve-channel charge integrator (CAMAC), which was gated open for the duration of the laser pulse. As an indication of the overall efficiency of the Raman collection system, 3000 photoelectrons per Joule of laser light were collected from vibrational Raman scattering of N_2 in room air.

DATA REDUCTION

The use of laser Raman scattering for thermometry and concentration measurement has been reviewed by several authors (Lapp and Penney, 1973; Lederman, 1977; Eckbreth, 1981; and Rahn, *et al.*, 1981). In brief, the integrated charge

Q_i from a given photomultiplier tube is linearly related to laser energy Q_{laser} and species concentration $[N_i]$ as follows:

$$Q_i = k_i Q_{laser} [N_i] f_i(T). \quad Eq.(1)$$

The proportionality constant k_i is dependent on the vibrational Raman cross section and optical collection efficiency. System calibration to determine k_i was accomplished using vibrational Raman scattering from gas samples at room temperature and pressure. The bandwidth factor $f_i(T)$ accounts for the temperature-dependent distribution of molecules in their allowed quantum states. Also convolved into the bandwidth factor $f_i(T)$ are the spectral location, shape, and bandwidth of the spectrometer and the bandwidth of the laser. The bandwidth factor can be calculated for N_2 , O_2 , and H_2 ; however, the calculation is less reliable for triatomic species such as H_2O (e.g. Stephenson, 1981). After calibration, a measurement of species concentration requires that laser pulse energy, Raman signal, and temperature be measured. The need for a temperature measurement can be eliminated by careful attention to the parameters that affect the bandwidth factor as was done by Eckbreth (1979) and Smith (1980). Under these circumstances, Smith (1980) showed that the bandwidth factor could be made equal to unity with an uncertainty of $\pm 3\%$ over the entire temperature range of interest here. The 3% uncertainty may be further reduced by relating the temperature to another measured quantity such as the nitrogen concentration; i.e., $f_{N_2}(T) = f_{N_2}(T([N_2]))$. Such a specification is possible when local chemical equilibrium and adiabaticity are assumed. These assumptions were previously examined by Dibble, *et al.* (1983) and found to be acceptable for this flame. With these assumptions, there exists a unique relationship between the nitrogen concentration and the density, as illustrated in Fig. 2a for the present fuel mixture and as illustrated in Fig. 2b for the case of pure hydrogen fuel. Figure 2b will be discussed below.

RESULTS AND DISCUSSION

A typical experiment yields a data matrix with 160 rows (laser shots) and 8 columns: axial velocity (u), Q_{N_2} , Q_{O_2} , Q_{H_2} , Q_{H_2O} , Q_{N_2} -anti-Stokes, $Q_{Rayleigh}$, and Q_{laser} . For the purpose of measuring temperature and density in this flow, it suffices to measure Q_{N_2} and Q_{laser} and then to infer the density and temperature through Eq. 1 and Fig. 2a.

Figure 3 shows scatter plots of velocity and density fluctuations u' and ρ' . This data was collected in the middle of the shear layer at radial location $y/D=4$ and at axial location $x/D=50$ which is near the mean location of the flame

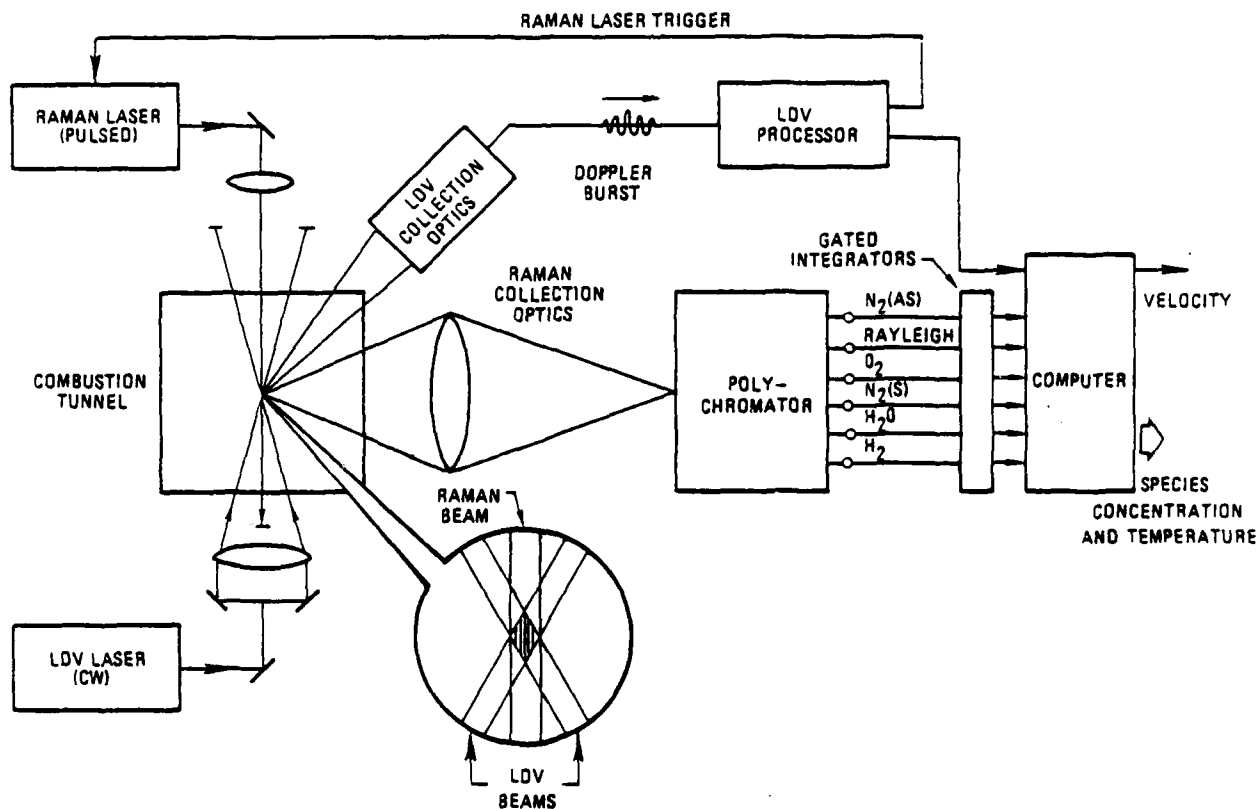


Fig. 1. Schematic diagram of combined laser Doppler velocimeter-laser Raman scattering apparatus.

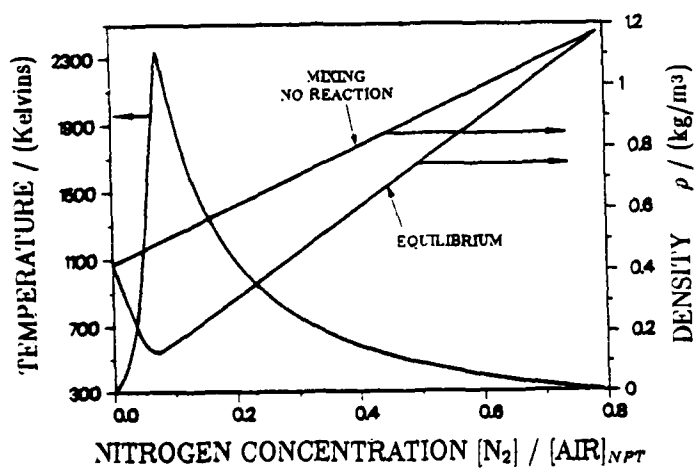


Fig. 2(a) Relationship between density or temperature and nitrogen concentration of fuel-air mixtures. The fuel is 22 mole percent argon in hydrogen. The concentration of nitrogen has been normalized by the concentration of air at normal pressure and temperature.

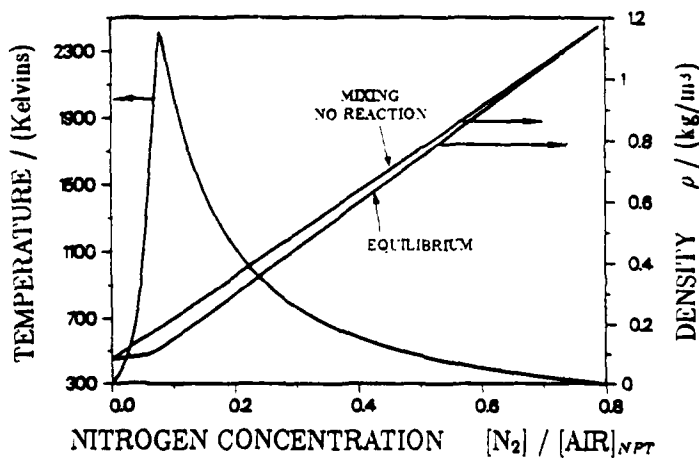


Fig. 2(b) Same as Fig. 2(a) except fuel is pure hydrogen

tip. The fluctuations were determined by subtracting the mean velocity \bar{u} and mean density $\bar{\rho}$ from each simultaneously measured velocity-density pair $\rho - u$. Each point represents a single LDV-Raman event. Scatter in the data is due to the fluctuations, which are fundamental to turbulence. The correlation of these points $\overline{\rho' u'}$ is directly related to turbulent transport. Data presented in Figs. 3a, b, and c were collected in the same manner except that the time delay Δt between the LDV event and the Raman laser pulse was increased from $\Delta t = 40 \mu s$ in Fig 3a to $\Delta t = 2000 \mu s$ in Fig 3b to $\Delta t > 1 s$ in Fig 3c. In comparison to Fig 3a, the data points in Fig. 3b are more randomly distributed, and, correspondingly, the correlation $\overline{\rho' u'}$ is reduced. In Fig. 3c, the time delay is sufficiently large so that the correlation is, within statistical error, zero. By systematically varying the time delay, an integral time scale τ_p is determined (Tennekes and Lumley, 1972). The product $\tau_p \bar{u}$ is an integral length scale $\lambda_p = 2 \text{ cm}$. Since the integral length scale is large compared to the largest dimension of the probe volume (1mm), the spatial resolution of the LDV-Raman probe is adequate for the integral scale. However, the probe dimension is six times larger than the Kolmogoroff microscale (0.15mm) calculated for the measurement location and conditions of Fig. 3 (Goulard, *et al.* 1976). The spatial averaging is not expected to be significant since the amplitude of the microscale fluctuations is expected to be small.

It has been suggested that notions gained from modeling constant density flows can be extended to the analogous variable density flows through the use of density-weighted (Favre) variables (Libby and Williams, 1980; Jones and Whitelaw, 1982). In addition to providing direct measurement of the turbulent momentum transport, the correlation $\overline{\rho' u'}$ can be used to generate the Favre mean velocity \bar{u} via the identity

$$\bar{u} = \bar{u} \left(1 + \frac{\overline{\rho' u'}}{\bar{\rho} \bar{u}} \right). \quad \text{Eq. (2)}$$

Radial profiles of the mean velocity and the Favre mean velocity are presented in Fig. 4a. The close agreement between the two velocities is a consequence of the small value of the correlation $\overline{\rho' u'}$ relative to the product of the mean density and the mean velocity $\bar{\rho} \bar{u}$. Correspondingly, the turbulent transport of axial momentum, which is equal to the density-velocity correlation $\overline{\rho' u'}$, is negligible when compared to the convective transport $\bar{\rho} \bar{u}$. Hence, overall model predictions for this flow system are insensitive to the modeling of this term. In particular, this explains why a model which incorporates a gradient diffusion for the axial turbulence transport does not produce unreasonable agreement with observations,

in spite of measurements which show that the axial turbulent transport is often counter to the gradient (Driscoll, *et al.* 1983). The Favre average of other scalars can be generated using equations analogous to Eq. (2). The radial profiles of mean and Favre mean temperature are presented in Fig. 4b. The difference between the two means implies a negative value for the density-temperature correlation $\overline{\rho' T'}$, which might have been anticipated *a priori* by noting the inverse relationship between temperature and density in Fig. 2a.

The difference between the mean and the Favre mean is relatively insensitive to the position inside the shear layer (see Fig. 4a and b). Plotted in Fig. 4c are the radial profiles of mean density $\bar{\rho}$ and rms of density fluctuation ρ'_{rms} . When density fluctuations are zero the mean and the Favre mean should be the same, as they are outside the shear layer (i.e. $y/D > 8$ or $y/D < -8$). Therefore, one might expect that since the rms of the density fluctuations go through a minimum at the centerline, the difference between the mean and Favre mean (Fig. 4a and b) should do so as well. Such expectations overlook the corresponding minimum at the centerline of the mean density which has a compensating effect.

Comments on the Potential Application to Heat Transfer Research. In both turbulent combustion and turbulent heat transfer, variable density flows are accompanied by heat transfer without mass transfer and, possibly large departures from chemical equilibrium. In order to investigate this class of flows with the LDV-Raman apparatus (Fig. 1) it will be necessary to relax the assumptions of adiabaticity and chemical equilibrium. A limiting case of chemical nonequilibrium occurs when there is mixing without chemical reaction. In this case, the relationship between density and nitrogen concentration is represented by a straight line which (see above Fig. 2a) connects fuel density with air density. This pure-mixing line is coincident with the line which results from the assumption of any amount of chemical reaction, assuming nitrogen to be inert, but neglects chemical heat release. Between the mixing line and the adiabatic equilibrium line is the set of allowed states obtainable by the inclusion or removal of chemical energy, i.e., the relationship between density and nitrogen concentration is bounded by the pure mixing line and by the adiabatic chemical equilibrium line. Thus, there is an uncertainty in assigning a density to a given measurement of nitrogen concentration. The uncertainty is largest when the nitrogen concentration is equal to 0.08; at this concentration the density may be between

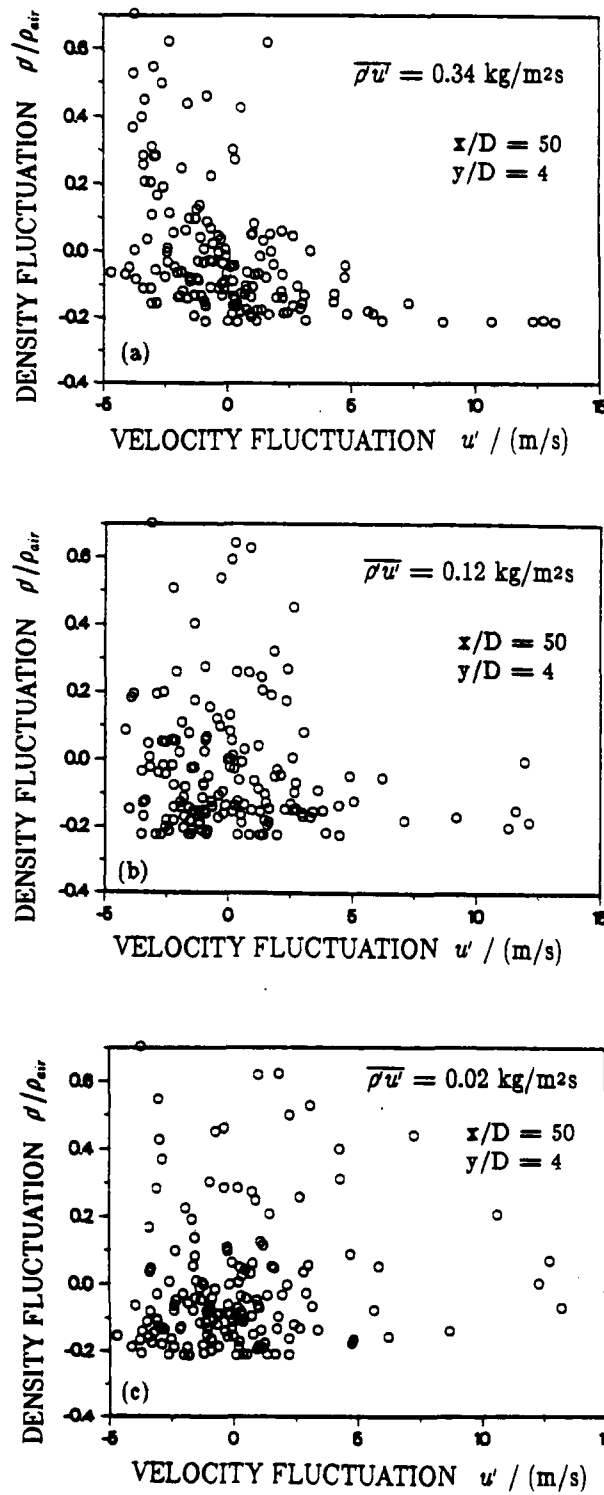


Fig. 3. Scatter plot of fluctuating density ρ' and velocity u' pairs. In Fig. 3.(a), (b), and (c), the time delay Δt between the LDV event and the laser Raman pulse has been varied as follows: (a) $\Delta t = 40 \mu\text{s}$ (b) $\Delta t = 2000 \mu\text{s}$ and (c) $\Delta t > 1 \text{ s}$. As the time delay Δt increases, the correlation $\overline{\rho u'}$ decreases.

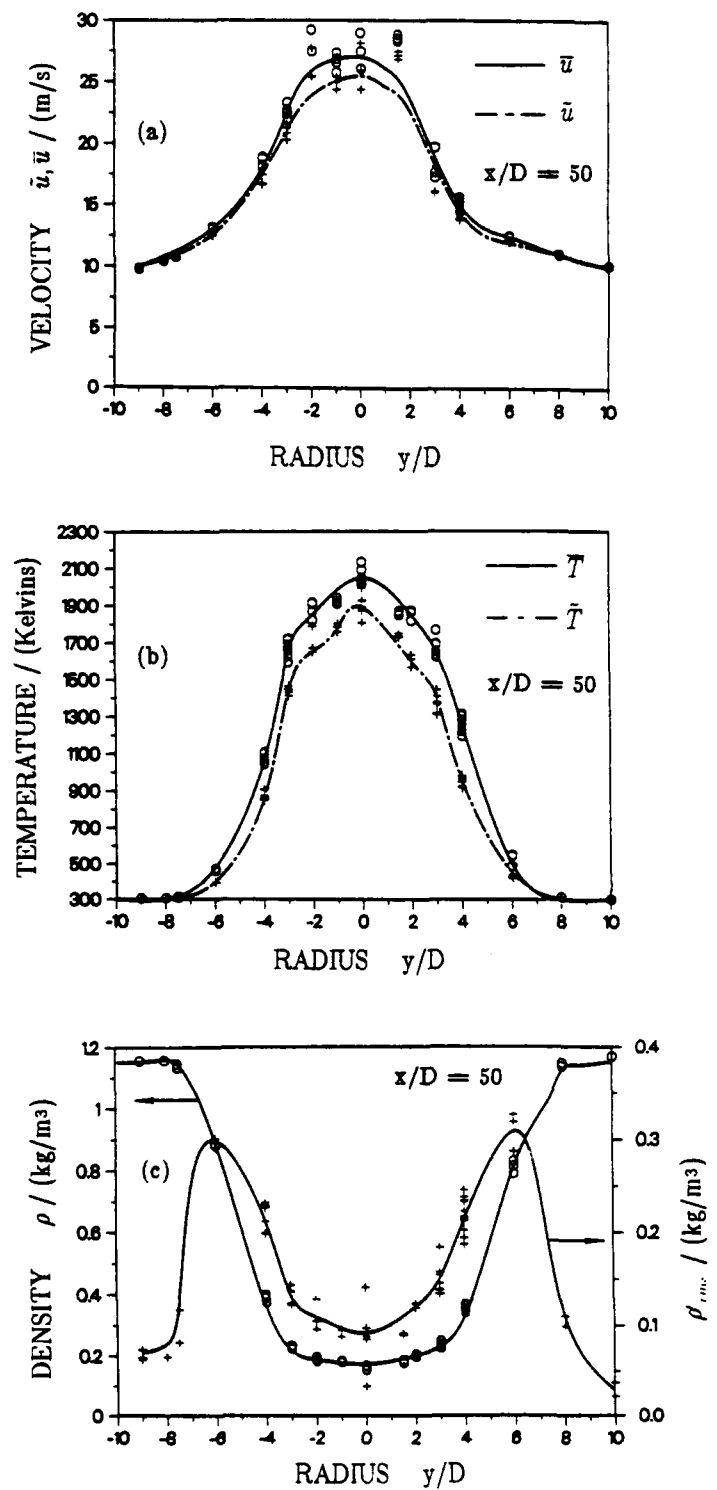


Fig. 4. (a) Radial profile of mean velocity \bar{u} and density-weighted mean velocity \tilde{u} . (b) Radial profiles of mean temperature \bar{T} and density-weighted mean temperature \tilde{T} . (c) Radial profiles of mean density $\bar{\rho}$ and density fluctuation rms ρ_{rms} .

0.16 kg/m³ and 0.51 kg/m³. The use of hydrocarbon fuels, which have molecular weights greater than present argon-in-hydrogen fuel, would exacerbate the uncertainty problem. Since relationship between the nitrogen concentration and the density no longer exists, it becomes necessary to simultaneously measure the temperature and the density of all of the major species. Such an undertaking is, at best, difficult, particularly if the more advanced laser diagnostics such as CARS or inverse Raman (Rahn, et al. 1981) are to be used. However, an alternative does exist. One can note that the uncertainty in the relationship between density and nitrogen concentration would not exist if the fuel had zero mass. As Fig. 2b illustrates, the ideal of a massless fuel is reasonably approximated when pure hydrogen is used as fuel. When the fuel is hydrogen, the conclusion is that the measurement of the nitrogen concentration will allow the density to be inferred with small uncertainty; in particular, the LDV-Raman apparatus presented in Fig. 1 could be used to investigate variable density flows which have both heat transfer and departures from chemical equilibrium.

SUMMARY

This paper describes a new LDV-laser Raman system with which one can simultaneously measure velocity, density, and species concentration. Simultaneous measurements in a turbulent nonpremixed flame are reported. From the simultaneous measurements, one can compute the density-velocity correlation which is the turbulent momentum transport. In addition, this correlation and the density-temperature correlation are used to compute the density weighted (Favre) mean of the axial velocity \bar{u} and temperature \bar{T} . Comparison between the unweighted means and density-weighted means show the density-weighted mean to be smaller than the mean by no more than 10%. The potential application of this LDV-laser Raman system to investigations into turbulent heat transfer has been discussed.

ACKNOWLEDGEMENTS

This work was supported by the Department of Energy, Office of Basic Energy Sciences, Division of Chemical Sciences.

REFERENCES

- Dibble, R. W., Kollmann, W., and Schefer, R. W. (1983), Conserved Scalar Fluxes Measured in a Turbulent Nonpremixed Flame, *Comb. and Flame*, (to appear)
- Driscoll, J. F., Schefer, R. W., and Dibble, R. W. (1983), Mass Fluxes $\overline{\rho u'}$ and $\overline{\rho v'}$ Measured in a Turbulent Nonpremixed Flame, *Nineteenth Symposium (International) on Combustion*, The Combustion Institute, 447.
- Eckbreth, A. C., Bonczyk, P. A., and Verdick, J. F. (1979), Combustion Diagnostics by Laser Raman and Fluorescence Techniques, *Prog. Energy Combust. Sci.*, 5, 253.
- Eckbreth, A. C. (1981), Recent Advances in Laser Diagnostics for Temperature and Species Concentration in Combustion, *Eighteenth Symposium (International) on Combustion*, The Combustion Institute, 1471.
- Goulard, R., Mellor, A. M., and Bilger, R. W. (1976), Combustion Measurements in Air Breathing Propulsion Engines. Survey and Research Needs, *Comb. Sci. and Tech.* 14, 195.
- Jones, W. P. and Whitelaw, J. H. (1982), Calculation Methods for Reacting Turbulent Flows: A Review, *Comb. and Flame*, 48,1.
- Lapp, M. and Penney, C. M., eds. (1973), *Laser Raman Gas Diagnostics*, Plenum Press, New York.
- Lederman, S. (1977), The Use of Laser Raman Diagnostics in Flow Fields and Combustion, *Prog. Energy Combust. Sci.*, 3, 1.
- Libby, P. A. and Williams, F. A. (1980), *Turbulent Reacting Flows*, (P. A. Libby and F. A. Williams, Eds.) Springer-Verlag, New York, 65.
- Rahn, L. A., Mattern, P. L., and Farrow, R. L. (1981), A Comparison of Coherent and Spontaneous Raman Combustion Diagnostics, *Eighteenth Symposium (International) on Combustion*, The Combustion Institute, 1533.
- Smith, J. R. (1980), Temperature and Density Measurements in an Engine by Pulsed Raman Spectroscopy, *Transactions of the SAE*, 89, Paper No. 800137, 808.
- Stephenson, D. A. (1981), High Temperature Raman Spectra of CO₂ and H₂O for Combustion Diagnostics, *Applied Spectrosc.* 35(6), 582
- Tennekes, H. and Lumley, J. L. (1974), *A First Course in Turbulence*, Third Printing, MIT press, Cambridge, Mass.

NONEQUILIBRIUM CHEMISTRY IN AN ISOTHERMAL TURBULENT FLOW

N.R. Mudford
and
R.W. Bilger
University of Sydney
N.S.W. 2006
Australia

ABSTRACT

The mixing of two air streams doped respectively with NO and O₃ in an isothermal turbulent flow and the resulting nonequilibrium chemical reaction have been studied using a recently developed Turbulent Smog Chamber and relatively fast chemiluminescent analysers. Joint probability density functions of reactant concentration, mixture fraction, reaction progress variable, reaction time and mean reaction rates are presented and interpreted in the light of preliminary flow characterisation results.

INTRODUCTION

Progress in the theory of turbulent reacting flow (see e.g. Libby & Williams (1980)) has been hampered by the lack of experimental data with sufficient time and space resolution to elucidate the effects of turbulence and chemical kinetic time scales on the instantaneous concentrations of reactive species. While some data using laser-Raman spectroscopy (Drake et al, 1981) and fibre optic absorption probes (Batt (1977) and Sherikar and Chevray (1981)) have become available the concentration requirements of these techniques are so high that the results have only been obtained where kinetic effects are small and the reaction and species concentrations are essentially mixing limited.

One chemically reacting system of particular interest is that in the atmosphere during the formation of photochemical smog. The reaction between ozone (O₃) and nitric oxide (NO) is known (Bilger (1980)) to be affected by turbulent mixing and it is also probable that the rates of chemical reaction and of turbulent mixing are of the same order so that coupling between these phenomena should be evident in the instantaneous concentrations of the reacting species.

In the experiments reported here a laboratory simulation of the atmospheric reaction between ozone and nitric oxide is attempted. Large scale, slowly moving turbulence is produced in a Turbulent Smog Chamber so that the time scales of sampled species concentration fluctuations are sufficiently low (< 1 second) that adequate information can be obtained using chemiluminescent analysers with 12 Hz frequency response. Concentrations of the reactants can be varied so that a range of ratios of chemical time scale to turbulence time scales can be produced over the range of interest, i.e. where they are of the same order.

APPARATUS

A detailed description of the Turbulent Smog Chamber (TSC) and associated instrumentation appears in Mudford and Bilger (1983). Briefly the component parts of the apparatus are as follows.

Turbulent Smog Chamber

The TSC consists of 0.15 mm thick polyethylene film formed into a roughly cylindrical bag of diameter 2.8 m, length 9 m and total volume 50 m³. Two 1 m diameter, 1 m s⁻¹ opposed air jets enter the chamber close to one end as shown in Fig. 1. The co-ordinate system used here is also shown in this figure. Turbulence and swirl in

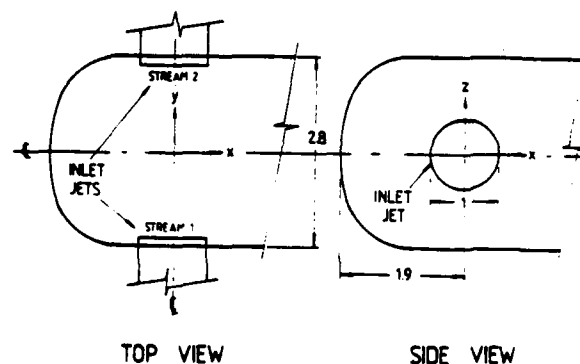


Figure 1. Geometry and dimensions (m) of the inlet end of the Turbulent Smog Chamber with cartesian co-ordinate system shown. Inlet nozzle separation = 2m.

the inlet jets are minimised through the use of a perforated plate, an anti-swirl honeycomb and a woven wire screen. The flow leaves the chamber via a 0.7 m diameter butterfly valve at the far end of the chamber.

The slight reactivity of polyethylene with ozone is not considered a problem in the present experiments (Mudford and Bilger (1983)). Polyethylene has the advantages of being easy to fabricate and being resistant to tearing and damage by folding. Also, it is transparent to ultra-violet radiation, a property required in experiments to be conducted later.

Chemiluminescent Analysers

NO and O₃ concentrations are measured by two fast (12Hz) high sensitivity (~0.4 Hz ppt⁻¹) chemiluminescent analysers which employ the chemiluminescent properties of the NO + O₃ reaction. Sample withdrawal from the TSC flow is accomplished through a 2.4 m long, 4.5 mm i.d. teflon tube with a critical metering orifice at the intake end. The presence of the sample tube in this configuration leads to negligible degradation of the frequency response which is limited by the ~10 msec residence time in the reaction cell. Sample withdrawal rate is 150 cm³s⁻¹ at TSC conditions implying a sample volume in the TSC per cell changeover of ~1.5 cm³.

Swinging Hot Wire

The high turbulence intensities and the occurrence of back flow in most regions of the TSC flow preclude the use of a fixed hot wire anemometer which requires the presence of a large mean velocity for the successful interpretation of the output signals (Bradshaw (1971)). In order to overcome this problem, a "swinging" hot wire has been developed. This apparatus intermittently sweeps the hot wire through a small portion of the flow thus artificially inducing a large mean velocity over the wire. The instantaneous components of velocity being measured are then yielded by subtraction of the wire velocity from the effective cooling velocity, recorded by the anemometer, in a manner appropriate to the type of probe being used.

Twin Resistance Thermometers

Integral length scales of the turbulence, based here on the fluctuations of a conserved scalar, were estimated by heating one of the inlet streams and correlating the temperature fluctuations recorded by two resistance thermometers at various separation distances, r , along the desired direction. The integral length scale measure used is that given by Bradshaw (1971),

$$L \equiv \int_0^\infty R \, dr$$

where R = correlation coefficient.

Data Collection

Signals from the above instruments were recorded on a Honeywell 5600C FM tape recorder and later played back via an A/D converter into a VAX 11/80 computer for analysis.

VELOCITY FIELD

Experiments and Results

Preliminary measurements of the variation of the x component of velocity, u_x , across the horizontal mid-plane ($z = 0$) have been made at two downstream stations using the swinging hot wire fitted with a 'u' probe. The means and standard deviations of u_x are shown in Fig. 2 as a function of cross-stream distance, y .

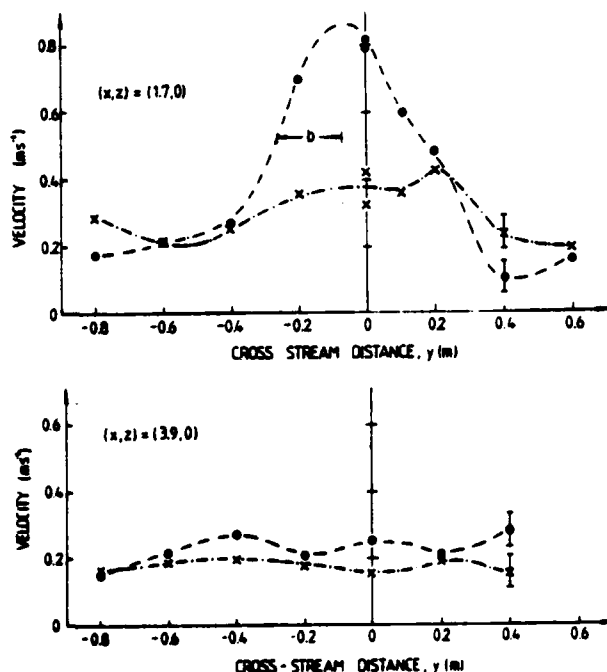


Figure 2. Mean (O) and standard deviation (x) of the x -component of velocity, u_x , vs. cross-stream distance y

on the horizontal mid-plane ($z = 0$). Jet half width b shown for $x = 1.7$ m station. Experimental error bars as shown.

At $x = 1.7$ m, the flow consists of a jet with peak $u_x = 0.86 \text{ ms}^{-1}$ at $y = -0.07$ m flanked by slower moving fluid with $u_x = 0.2 \text{ ms}^{-1}$. We shall define the jet half-width, b , as the distance from the jet peak location to the point where $u_x = (\text{peak } u_x + \text{flanking } u_x)/2$ as illustrated in Fig. 2. For $x = 1.7$ m, then, $b = 0.2$ m.

By $x = 3.9$ m, the jet observed upstream has been dissipated. Mean velocity is then $u_x = 0.25 \text{ ms}^{-1}$ across the range of y surveyed. At both stations the turbulence intensity based on u_x is very high, varying from ~ 0.5 at the jet peak to ~ 1.0 elsewhere.

Integral length scales have been measured for a small number of locations and directions. The results are shown in Table 1. The scales in the cross-stream (y) direction show linear growth with x and their magnitude at $(x, y, z) = (1.7, 0, 0)$ accords with the 0.2 m jet half width found there. On the basis of these velocities and length scales the Reynolds Number and the turbulent Reynolds Number are both $\sim 1 \times 10^4$ in the body of the flow.

FIXED PROBE LOCATION			MEASURE- MENT DIRECTION	INTEGRAL LENGTH SCALE L (m)
x (m)	y (m)	z (m)		
1.7	-0.06	0	+ y	0.14
2.45	-0.06	0	+ y	0.18
3.7	-0.06	0	+ y	0.26
1.7	-0.7	0	+ y	0.14
2.45	0	0	- z	0.24

Table 1. Integral length scale measurements

The observation of a narrow ($2b = 20\%$ of inlet duct separation), rapidly decaying, high turbulence intensity jet agrees qualitatively with the work of Witze and Dwyer (1976) on impinging axisymmetric jets. Quantitative agreement appears to be precluded by the significant differences in geometry and operating conditions between their apparatus and that of the present study.

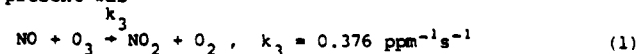
The flowfield in the chamber appears to be stable and repeatable. The velocity results presented in Fig. 2 were obtained over several days with the flow turned off between most runs. Deployment of an aerodynamic tuft showed that the impingement region between the jets lies within 0.1 m of the vertical centre plane ($y = 0$). This position is unaffected by start-up procedure, temporary blocking of one jet etc. A small increase in the inlet duct separation, of the order of 20% , does, however, have a marked effect on the impingement region moving it away from its central location. This is in agreement with Luna (1965) who reports that the impingement region location is indeterminate for opposed jets with separation distances between 2 and 8 jet diameters.

Extension of these preliminary flow field experiments is in progress and a more complete picture of the chamber flow should be available in the near future.

SCALAR FIELDS

Experiments

In the scalar field experiments reported here, the inlet jet denoted STREAM 1 in Fig. 1 was doped uniformly and steadily with NO to produce $[\text{NO}]_1 = 1$ ppm in that jet. STREAM 2 was similarly doped with O_3 to produce $[\text{O}_3]_2 = 1$ ppm. The inlet jets thus formed the two streams of a two stream mixing problem. All experiments were performed in the UV dark so that the only reaction present was



A survey was carried out in which simultaneous measurements of [NO] and [O₃] were made at a large number of points in the $x > 0$ region. The sampling locations are given in Table 2 and those lying on the horizontal mid-plane are shown in Fig. 3.

EXPT.	SAMPLING POINT			MIXTURE FRACTION, ξ_c				[NO] (pphm)		[O ₃] (pphm)		[NO][O ₃] (pphm) ²		[NO][O ₃]	
	x(m)	y(m)	z(m)	MEAN	STD.DEV.	SKEWNESS	KURTOSIS	MEAN	STD.DEV.	MEAN	STD.DEV.				
T	0.3	-0.2	-0.4	1	0	-	-	94.6	0	0	0	0	-	-	-
b	0.36	-0.35	-0.45	0.956	0.082	-1.43	4.24	53.0	13.1	1.1	2.0	37.7	0.65	-	-
a	0.36	-0.35	-0.40	0.806	0.104	0.32	2.24	54.2	16.6	4.8	3.0	220.6	0.85	-	-
U	0.40	-0.28	-0.63	1	0	-	-	94.6	0	0	0	0	-	-	-
A	0.41	-0.07	0	0.344	0.366	0.68	1.95	29.2	34.5	60.1	33.6	605.0	0.34	-	-
Q	0.42	-0.31	0.45	1	0	-	-	94.6	0	0	0	0	-	-	-
c	0.44	-0.26	-0.45	0.960	0.089	-1.75	10.31	81.5	14.6	1.4	3.3	89.7	0.79	-	-
M	0.50	-0.38	-0.91	0.689	0.089	1.03	4.37	41.4	13.5	8.8	3.6	324.4	0.89	-	-
N	0.50	-0.38	-0.74	0.782	0.122	0.33	2.16	56.2	19.3	6.0	4.1	267.6	0.79	-	-
O	0.50	-0.38	-0.57	0.938	0.103	-1.21	3.23	80.4	16.5	1.7	2.6	96.9	0.71	-	-
P	0.50	-0.38	0.58	0.865	0.127	-0.38	2.70	68.8	19.8	4.9	5.1	264.8	0.79	-	-
d	0.63	-0.33	-0.40	0.781	0.069	0.61	3.45	50.8	11.5	4.8	2.4	228.3	0.94	-	-
e	0.63	-0.33	0	0.789	0.058	0.63	3.67	47.8	9.2	6.7	2.9	307.4	0.96	-	-
f	0.80	-0.32	0	0.744	0.043	0.44	4.55	44.9	6.6	6.9	2.7	301.9	0.97	-	-
D	0.90	-0.20	0	0.819	0.081	-0.63	8.51	65.7	12.8	4.9	4.4	306.1	0.95	-	-
C	0.90	0	0	0.184	0.268	1.91	5.66	12.5	25.5	69.9	26.9	291.4	0.33	-	-
S	0.90	0.08	-0.45	0.186	0.122	1.53	10.78	4.8	8.5	66.3	17.9	298.4	0.94	-	-
R	0.90	0.08	0.45	0.260	0.074	-0.41	7.17	4.4	3.3	51.9	12.3	218.2	0.96	-	-
B	0.90	0.20	0	0.267	0.094	-0.65	2.88	6.4	2.3	50.1	15.4	295.6	0.92	-	-
F	1.10	-0.22	0	0.774	0.086	-2.63	2.01	56.1	10.4	7.7	9.2	424.7	0.98	-	-
i	1.10	-0.17	0	0.754	0.087	-2.85	18.83	41.6	17.3	3.5	10.2	130.2	0.89	-	-
h	1.10	-0.08	0	0.772	0.157	-2.45	10.61	52.0	14.9	8.7	18.5	358.7	0.79	-	-
g	1.10	0	0	0.555	0.330	-0.19	1.46	40.0	30.7	38.5	34.9	583.2	0.38	-	-
E	1.10	0	0	0.481	0.304	0.11	1.47	40.0	33.5	42.6	31.0	803.6	0.47	-	-
G	1.10	0.22	0	0.367	0.070	0.74	18.08	9.7	6.8	36.3	10.1	348.4	0.99	-	-
K	1.70	-0.40	0	0.783	0.055	-3.37	27.91	55.8	6.4	5.7	5.0	310.4	0.98	-	-
J	1.70	-0.20	0	0.737	0.110	-2.10	8.33	53.0	11.3	11.5	11.0	545.4	0.89	-	-
I	1.70	0	0	0.585	0.169	-0.24	1.85	40.6	19.2	23.3	14.6	732.7	0.77	-	-
H	1.70	0.20	0	0.447	0.119	1.39	4.60	21.5	15.2	32.7	9.6	617.0	0.88	-	-
j	2.40	0.24	0	0.564	0.110	0.16	1.96	22.8	12.4	20.2	9.9	336.9	0.73	-	-
k	2.50	-0.03	0	0.620	0.103	-0.60	2.51	28.0	10.3	13.9	10.3	295.7	0.76	-	-

Table 2. Sampling locations for the scalar field survey together with fundamental statistical measures for the mixture fraction measure, ξ_c , and the reacting scalars [NO] and [O₃]. Also shown are parameters associated with mean reaction rates for the locations.

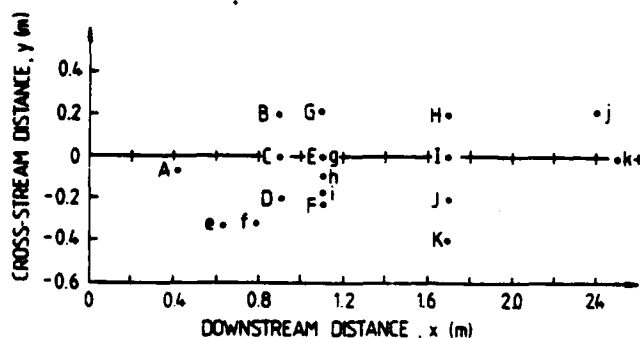


Figure 3. Horizontal mid-plane ($z = 0$) sampling locations for the [NO], [O₃] survey. Letters refer to list in Table 2.

Results

Species Concentrations. Insight into the mixing and chemical reaction processes occurring in the TSC can be most readily gained by consideration of the spatial variation of the joint probability density function of the raw data variables [NO] and [O₃], denoted $p([NO], [O_3])$ for sampling locations A, g, I and k, which lie along or close to the TSC centreline, (y, z) = (0, 0), are shown in Fig. 4 in normalised form, the normalisation factors being the respective inlet jet concentrations $[NO]_1$ and $[O_3]_2$.

The lines marked FR and EQ on these plots are the frozen and equilibrium chemistry limits, respectively, for samples formed by the mixing of the inlet jet material. The majority of samples can be seen to lie far from both these limits indicating a high degree of chemical nonequilibrium. The experiment is thus well-designed with chemical kinetic and turbulent mixing time scales of the same order.

The simultaneous progress of mixing and reaction with increasing downstream distance, x , can be seen clearly in Fig. 4. $p([NO], [O_3])$ at location A consists of two peaks at $([NO]/[NO]_1, [O_3]/[O_3]_2) = (1, 0)$ and $(0, 1)$ representing pure inlet jet material and a plateau, containing ~ 40% of the data, lying between the peaks, representing material which has mixed but has not yet reacted significantly. At location k, $p([NO], [O_3])$ is confined to the lower left hand corner of the region between the frozen and equilibrium limits indicating that both mixing and chemical reaction are well-advanced although the system is still some distance from the end-point for this experiment at $([NO], [O_3]) = (0, 0)$.

$p([NO], [O_3])$ for locations F and G, lying -0.22m and +0.22m, respectively, in the cross-stream direction (y) from location g, are shown together in Fig. 5. The well-reacted nature of the material at these locations is to be expected from the lower velocities, and thus higher mean residence times, pertaining there. Comparison of Figs. 4 and 5 shows that the two well-reacted lobes appearing in $p([NO], [O_3])$ at g arise from incursions onto the chamber centreline of material from either side of

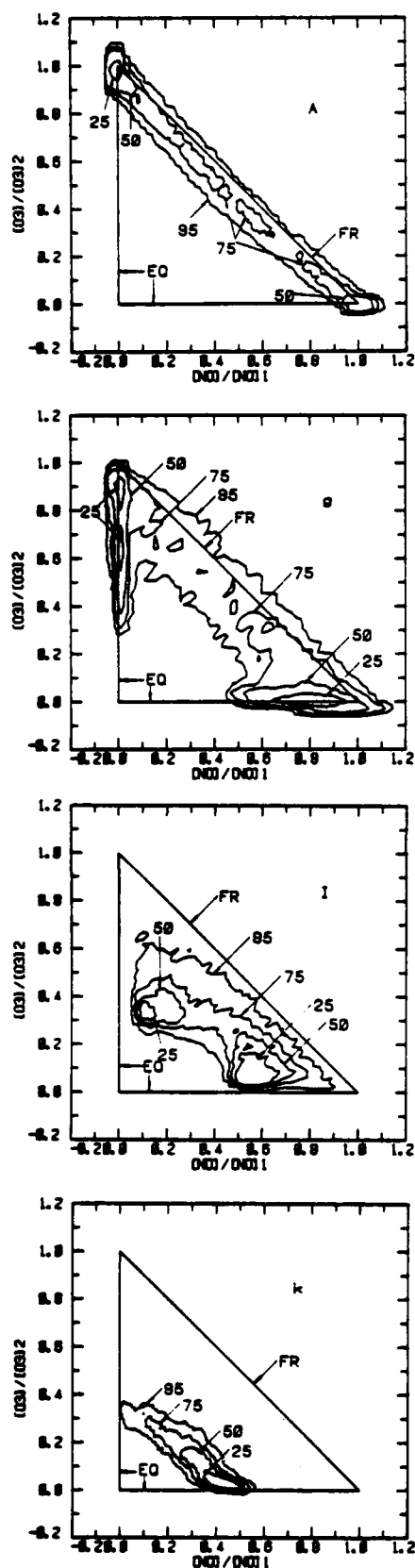


Figure 4. Joint probability density functions, $p([NO], [O_3])$, for sampling locations A, g, I and k on or close to TSC centreline. Numbers associated with contours show the percentage of data enclosed by them summing from the highest probability density regions, e.g. contour denoted

25 encloses that 25% of data having the highest probability density. FR, EQ denote the frozen and equilibrium chemistry lines.

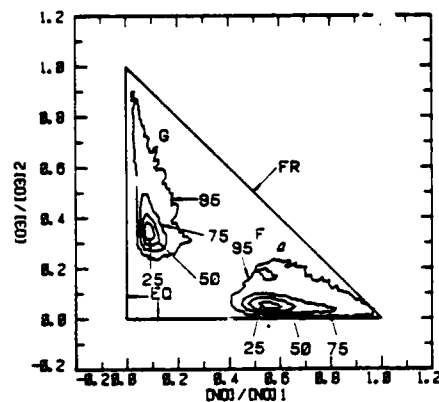


Figure 5. Joint probability density function $p([NO], [O_3])$ for off-centreline sampling locations F and G. See Fig. 4 for key to numbers etc.

the centreline (the z -dependence of $p(\cdot)$ is weak in the survey region). The nearly frozen material occurring at g has doubtless been advected from the region between the inlet jets by the centreline jet discussed above.

Mixture Fraction. A quantitative measure of the degree of mixing in a sample can be obtained by defining a mixture fraction, ξ , as the mass fraction, in the sample, of material originating in stream 1. A measure of ξ can be formulated from the $[NO]$ and $[O_3]$ measurements as

$$\xi_c \equiv \frac{[NO] - [O_3] + [O_3]_2}{[NO]_1 + [O_3]_2} \quad (2)$$

due to the conserved nature of the scalar $[NO] - [O_3]$. Lines of $\xi_c = \text{constant}$ are, parallel straight lines of positive slope on the $([NO], [O_3])$ plane.

The means ($\bar{\xi}_c$), standard deviations ($\bar{\xi}_c'^2$) and the moment coefficients of skewness and kurtosis of the probability density functions $p(\xi_c)$ are given in Table 2 for each sampling location together with the means and standard deviations of the reacting scalars $[NO]$ and $[O_3]$.

In Fig. 6 the contours of $\bar{\xi}_c$ and $\bar{\xi}_c'^2$ are shown on the $z = 0$ plane. $p(\xi_c)$ for the chamber centreline sampling locations A, g, I and k and those for the off-centreline locations F and G appear in Figs. 7 and 8 respectively. The rapid progress of mixing, noted above,

is seen again here with $\partial \bar{\xi}_c / \partial y$ and $\bar{\xi}_c'^2$ decreasing markedly, with increasing x , over only two jet diameters. The decrease of $\bar{\xi}_c$ with increasing y and the $p(\xi_c)$ for F and G show that the contributions to the material on each side of the chamber originate predominantly, although not exclusively, from the jet on that side of the chamber.

An interesting feature of the development of $p(\xi_c)$ on the centreline, clearly linked to the latter phenomena, is the persistence of the bimodal nature of the distribution with the simultaneous rapid decrease in $\bar{\xi}_c'^2$.

Reaction Progress and Reaction Time. In order to measure the degree of chemical reaction which has taken place in a sample we define a reaction progress variable as

$$r \equiv \frac{[O_3] - [O_3]_f}{[O_3]_e - [O_3]_f}, \quad 0 < r < 1 \quad (3)$$

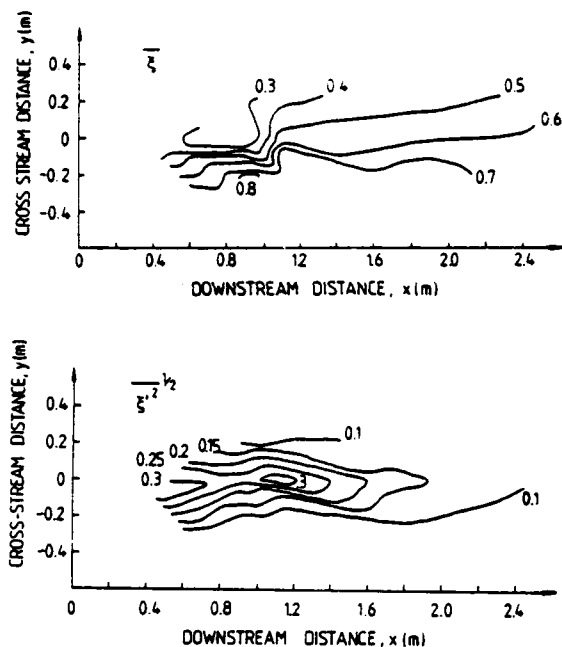


Figure 6. Contours of mixture fraction mean ($\bar{\xi}_c$) and standard deviation ($\bar{\xi}_c^{1/2}$) on the horizontal mid-plane ($z = 0$).

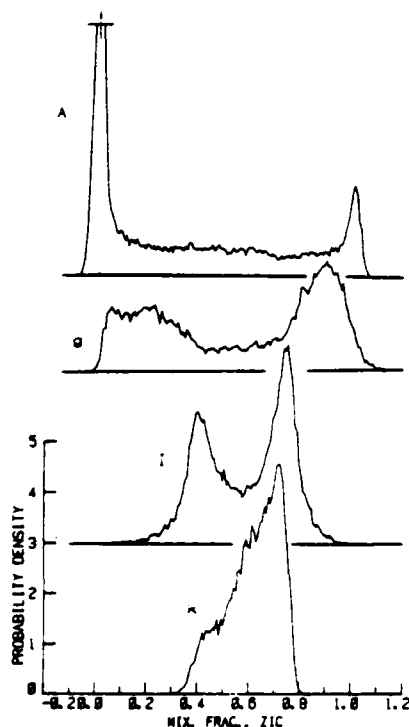


Figure 7. Probability density function, $p(\xi_c)$, for sampling locations A, g, I and k on or close to TSC centreline.

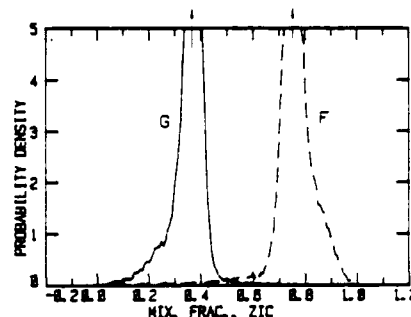


Figure 8. Probability density function, $p(\xi_c)$, for off-centreline sampling locations F (---) and G (—).

where subscripts f and e refer to the frozen and equilibrium concentrations at the sample mixture fraction.

The interpretation of r in terms of the 'age' of a sample is complicated by the rate of change of r at constant ξ , say, being dependent on ξ . Additionally, $r \rightarrow 1$ only as time allowed for reaction $\rightarrow \infty$. In order to provide a more direct measure of sample age, we define the parameter t_c as the time for reaction to produce the measured ($[NO]$, $[O_3]$) from the frozen reactant concentrations at the sample mixture fraction, viz

$$t_c \equiv \begin{cases} \frac{1}{k_3([NO]_f - [O_3]_f)} \ln \left(\frac{[O_3]_f}{[NO]_f} \left(1 - \frac{[O_3]_f - [NO]_f}{[O_3]_f} \right) \right), & \xi \neq \xi_s \\ \frac{1}{k_3[O_3]_f} \left(\frac{[O_3]_f}{[O_3]_f} - 1 \right), & \xi = \xi_s \end{cases} \quad (4)$$

where ξ_s is the stoichiometric mixture fraction. An equivalent expression for t_c may be formulated as a function of $[NO]$. The significance of t_c as a flow parameter is that it is the minimum time required to produce a sample with a given ($[NO]$, $[O_3]$) from inlet jet material via mixing and chemical reaction processes i.e. $t_c \leq \bar{t}_s \equiv$ mean residence time of the sample constituents, where $t_s = 0$ is defined for each sample portion to be the time at which it underwent its first mixing operation.

A simple proof of this assertion may be formulated as follows. Initially, $t_c = \bar{t}_s = 0$ by definition for all material entering the chamber. By definition, also, chemical reaction processes, in the absence of further mixing will maintain the inequality as $\Delta t_c = \Delta t_s$. Now the surface $t_c([NO], [O_3])$ in ($[NO]$, $[O_3]$, t_c) space is concave from above (i.e. from t_c large). This can be shown by plotting eqn. (4) on the ($[NO]$, $[O_3]$) plane. Suppose that $t_c \leq \bar{t}_s$ for two samples A and B represented by two points on this surface. Mixing these samples in proportion β then yields a mixture with

$$[\]_m = \beta [\]_A + (1 - \beta) [\]_B$$

$$\text{and } \bar{t}_{s,m} = \beta \bar{t}_{s,A} + (1 - \beta) \bar{t}_{s,B}$$

$$\text{but with } t_{c,m} \leq \beta t_{c,A} + (1 - \beta) t_{c,B} \leq \bar{t}_{s,m}$$

Because both chemical reaction and mixing preserve the initial inequality we can conclude that $t_c \leq \bar{t}_s$.

The joint probability density functions $p(\xi_c, r)$ and $p(\xi_c, t_c)$ are shown for sampling locations g and k in Figs. 9 and 10 respectively. These plots contain conditionally sampled data in that 35% of the data at g and 1% of that at k has been excluded on the grounds that, ξ_c was outside the range (0.05, 0.95), thereby producing indeterminate values of r and t_c , or $[O_3]$ was outside the range ($[O_3]_e$, $[O_3]_f$) due to instrument noise etc.

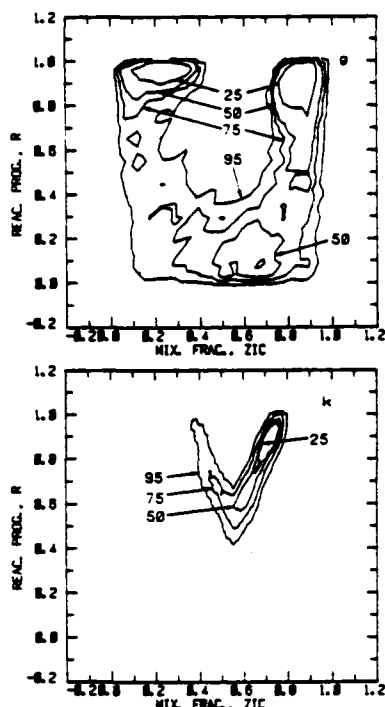


Figure 9. Joint probability density function, $p(\xi_c, r)$, for sampling locations g and k on TSC centreline. See Fig. 4 for key to numbers etc.

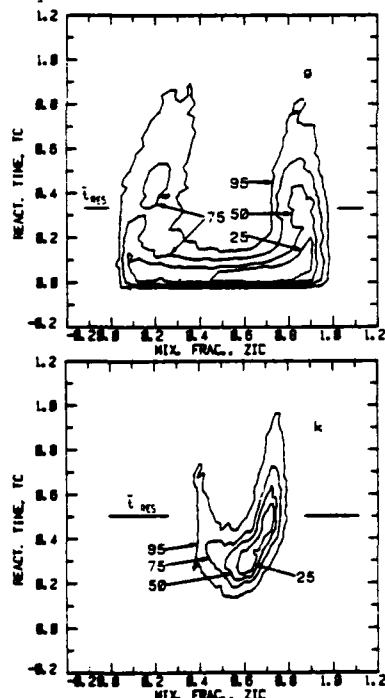


Figure 10. Joint probability density function, $p(\xi_c, t_c)$, for sampling locations g and k on TSC centreline. t_{RES} indicated is mean residence time in TSC at sampling location. See Fig. 4 for key to numbers etc.

In Fig. 10, t_c is normalised by the mean residence time (25 sec) in the TSC and the mean residence times up to each sampling location, t_{RES} , are also shown on the figure. Both forms of the data indicate, as expected from the foregoing, that the material having high or low ξ_c is more fully reacted and 'older' than material having intermediate ξ_c .

Reaction Rates. By writing each reacting species concentration as the sum of a mean ($\bar{[]}$) and a fluctuating component ($[]'$), the mean rate of reaction (1) can be expressed as

$$\frac{d[NO]}{dt} = -k_3 \overline{[NO][O_3]} = -k_3 (\overline{[NO][O_3]} + \overline{[NO]'[O_3]'})$$

i.e. as the sum of a product of means and a covariance. The values of $\overline{[NO][O_3]}$ and $\overline{[NO]'[O_3]'}/(\overline{[NO][O_3]})$ are given in Table 2 for the survey sampling locations. In some regions of the flow the latter parameter is as low as 0.33 indicating that for this flow the use of $-k_3 \overline{[NO][O_3]}$ as a mean reaction rate could lead to significant errors.

CONCLUSION

Measurements with good spatial and temporal resolution have been made of the concentrations of the two reactants, NO and O_3 , in an isothermal turbulent flow in which the turbulent mixing and chemical kinetic rates are of the same order. Joint probability density functions of reactant concentrations and other parameters of interest obtained from the measurements showed in detail the development of the flow under the influence of these two competing processes.

Results of preliminary flowfield characterisation experiments showed a number of features, such as a jet on the chamber centreline, which could be simply related to the scalar field results.

Data such as that presented here should provide a good test of models of nonequilibrium chemistry in turbulent flows.

ACKNOWLEDGEMENTS

This work is supported by the Australian Research Grants Scheme. A number of the velocity and integral length scale measurements were made by Mr. R. Romanous.

REFERENCES

- Batt, R.G., 1977, "Turbulent Mixing of Passive and Chemically Reacting Species in a Low-speed Shear Layer", *J. Fluid Mech.*, 82, 60.
- Bilger, R.W., 1980, "Perturbation Analysis of Turbulent Nonpremixed Combustion", *Comb. Sci. Techn.*, 22, 251.
- Bradshaw, P., 1971, *An Introduction to Turbulence and its Measurement*, Pergamon Press.
- Drake, M.C., Lapp, M., Penney, C.M., Warshaw, S. and Gerhold, B.W., 1981, "Measurements of Temperature and Concentration Fluctuations in Turbulent Diffusion Flames Using Pulsed Raman Spectroscopy", Eighteenth Symposium (International) on Combustion, The Combustion Institute, 1521.
- Libby, P.A. and Williams, F.A., ed, 1980, *Turbulent Reacting Flows*, Springer.
- Luna, R.E., 1965, "A Study of Impinging Axisymmetric Jets and Their Application to Size Classification of Small Particles", Ph.D thesis, Princeton University.
- Mudford, N.R. and Bilger, R.W., 1983, "A Facility for the Study of Nonequilibrium Chemistry in an Isothermal Turbulent Flow", to be presented at Eighth Australasian Fluid Mechanics Conference, Newcastle, N.S.W., Australia, Nov. 1983.
- Sherikar, S.V. and Chevray, R., 1981, "A Chemically Reacting Plane Mixing Layer", Third Symposium on Turbulent Shear Flows, Univ. of Calif., Davis.
- Witze, P.O. and Dwyer, H.A., 1976, "The Turbulent Radial Jet", *J. Fluid Mech.*, 75, 401.

ASSESSMENT OF TWO TURBULENCE MODELS FOR TURBULENT ROUND DIFFUSION JETS WITH COMBUSTION

F.C. Lockwood
and
P. Stolakis

Imperial College of Science and Technology,
London, England. SW7

ABSTRACT

The k-ε model of turbulence and an algebraic stress model have been tested and the implications of their use are discussed. Both of them were tested for axisymmetric gaseous jet diffusion flames and a direct comparison of the performance of these models shows the k-ε model to be superior.

The effect of radiation losses is examined and it is proven to be significant. The implications of neglecting these losses - which was the general practice up to the present day - in combustion calculations are explored and discussed.

NOMENCLATURE

a_g	acceleration of gravity
$a_{g,n}$	grey gas weighting coefficient
$b_{1,n}, b_{2,n}$	constants in grey gas expressions
c	soot concentration (kg/m^3)
\bar{c}_p	mean specific heat
E	activation energy
f	mixture fraction
g	mean square mixture fraction fluctuations
h	enthalpy
H	calorific value of the fuel
k	turbulence energy/gas absorption coefficient
L	geometric path length
m	mass fraction
n	grey gas index for gas/soot
P	production of turbulence energy
P	partial pressure/probability density function
q_{rad}''	radiated energy per unit volume
R	perfect gas constant
r_s	stoichiometric oxygen requirement to burn 1 kg of soot
S	source term
S_{fu}	stoichiometric air requirement to burn 1 kg of fuel
T	instantaneous temperature
U	instantaneous streamwise velocity
u	fluctuating part of U
V	instantaneous cross-stream velocity
v	fluctuating part of V
w	fluctuating part of the velocity normal to the x,y plane
x	streamwise direction
y	cross-stream direction
β	volumetric expansion coefficient
δ	width of the jet
ΔU_m	maximum velocity difference across the jet
ϵ	turbulence energy dissipation
ϵ_g	emissivity of the gas/soot mixture
μ_t	effective viscosity
$\xi = \left[\frac{\delta}{\Delta U_m} \left(\frac{\partial U}{\partial x} - \left[\frac{\partial U}{\partial x} \right] \right) \right]^{0.2} \quad (\text{Rodi (15)})$	

ρ	density
σ	Prandtl or Schmidt number, or Stefan Boltzman constant
ϕ	a scalar quantity

Subscripts

c	CO_2
co	CO
ϵ	centre-line
d	destruction
f	formation
fu	fuel
g	gas
ox	oxygen
s	soot
w	water

Superscripts

'	fluctuating part
---	------------------

INTRODUCTION

There have been relatively few attempts to predict the turbulent round jet diffusion flame using modern computational procedures. In part this has been due to a scarcity of suitable data for validation purposes although this problem has now largely been eliminated due to the perseverance of a handful of experimentalists working in the field, see for example (1 to 5). It is also partly because there is no possibility of succeeding in the task in the absence of a good turbulence model and turbulence modellers have been hard enough pressed to devise reliable simulations of non-reacting jet flows.

The available turbulence models range from zero- to multi-equation ones, an orderly description of them is presented by Launder and Spalding (6). The two-equation k-ε model was originally applied in flow computations by Jones and Launder (7) and Launder and Spalding (8) and has since become widely used in engineering calculations. It appears to combine an optimal mix of computer economy and predictive precision. It is least satisfactory in the presence of body forces such as those due to swirl or buoyancy both of which are often significant in practical combustors. In the former case the isotropic effective viscosity implied by the k-ε model is less than satisfactory, while in the latter case the striking discrepancies between horizontal and vertical buoyant shear layers are for example not well simulated by the simple k-ε model.

Some workers, for example Launder et al (9) and Gibson and Launder (10) have examined multi-equation Reynolds stress turbulence models with some small advantage. However, the extra computational burden is very significant and has not so far been superimposed on the already heavily charged background of combustion

calculations. In an effort to enhance significantly the validity of turbulence models researchers have explored diverse avenues such as the formulation of multiple time scale equations (e.g. (11)). The reader is referred to a 'state of the art' review by Gibson et al (12).

In sum no new turbulence model has emerged which affords more than a marginal improvement in predictive ability and this is always at the expense of greatly increased computational costs. There is no doubt that industry would pay dearly for absolutely trustworthy and precise predictions but they cannot as yet be so satisfied. Fortunately combustor predictions of useful engineering accuracy are often procurable at a correspondingly acceptable expense with the simple k-ε model. To some extent this is because other processes such as the thermal radiation often exercise a dominating influence and an accurate representation of the turbulence is not essential.

THE TURBULENCE MODELS

The k-ε Model

The parabolic and axisymmetric forms of the equations for the turbulence energy, k, and turbulence energy dissipation, ε, are:

$$\rho U \frac{\partial k}{\partial x} + \rho V \frac{\partial k}{\partial y} = \frac{1}{y} \frac{\partial}{\partial y} \left(y \frac{\mu_t}{\sigma_k} \frac{\partial k}{\partial y} \right) + P - \rho \epsilon + \beta \rho a_g \overline{uT'} \quad (1)$$

$$\rho U \frac{\partial \epsilon}{\partial x} + \rho V \frac{\partial \epsilon}{\partial y} = \frac{1}{y} \frac{\partial}{\partial y} \left(y \frac{\mu_t}{\sigma_\epsilon} \frac{\partial \epsilon}{\partial y} \right) + \frac{\epsilon}{k} (C_{\epsilon 1} P - C_{\epsilon 2} \rho \epsilon) + C_{\epsilon 3} \frac{\epsilon}{k} \beta \rho a_g \overline{uT'} \quad (2)$$

where the production term is given by:

$$P = -\rho (\overline{uv} \frac{\partial U}{\partial y} + \overline{u^2} \frac{\partial U}{\partial x} + \overline{v^2} \frac{\partial V}{\partial y} + \overline{w^2} \frac{\partial V}{\partial x})$$

From dimensional considerations the turbulence viscosity is:

$$\mu_t = \rho C_\mu \frac{k^2}{\epsilon} \quad (3)$$

Assuming laminar flow analogy the turbulence stresses may be expressed as (13):

$$-\overline{uv} = \mu_t \frac{\partial U}{\partial y} \quad (4)$$

$$-\overline{u^2} = -\frac{2}{3} \rho k + 2\mu_t \frac{\partial U}{\partial x} \quad (5)$$

$$-\overline{v^2} = -\frac{2}{3} \rho k + 2\mu_t \frac{\partial V}{\partial y} \quad (6)$$

$$-\overline{w^2} = -\frac{2}{3} \rho k + 2\mu_t \frac{\partial V}{\partial x} \quad (7)$$

When the flow is reacting an additional turbulence equation for the mean square of the mixture fraction fluctuations, $g \equiv (\overline{f-f})^2$, is required:

$$\rho U \frac{\partial g}{\partial x} + \rho V \frac{\partial g}{\partial y} = \frac{1}{y} \frac{\partial}{\partial y} \left(y \frac{\mu_t}{C_g} \frac{\partial g}{\partial y} \right) + c_{g1} \mu_t \left(\frac{\partial f}{\partial y} \right)^2 - c_{g2} \rho \frac{\epsilon}{k} g \quad (8)$$

The preceding equations constitute the usual k-ε model, or more properly the k-ε-g model for reacting parabolic flows. They are solved along with those for continuity, U-momentum conservation, energy conservation and mixture fraction, f, conservation. The last buoyancy production term in eq. (1) is exact for small temperature variations and can be modelled by a simple gradient approximation. The corresponding term of eq. (2) is a modelled one proposed by Bessain and Rodi (14). We have found that these terms do not improve the predictions in a straightforward application of the k-ε-g model and they are omitted for the predictions shown. All correlations involving density fluctuations are ignored so the system is equivalent to a Favre-averaged one. The values of the model constants are given in Table I.

Table I Values of Constants for k-ε Model

C ₁	C _{ε1}	C _{ε2}	C _{g1}	C _{g2}	σ _k	σ _ε	σ _g	σ _g
0.09-0.045	1.44	1.92-0.0667	2.8	2.0	1.0	1.3	0.7	0.7

The Algebraic Stress Model

The algebraic relations for the Reynolds stresses are extracted by assuming local equilibrium of turbulence production and dissipation (16). The relations which have been derived for non-reacting flows are (14,16):

$$-\overline{uv} = \frac{1-C_2}{C_1} \frac{\overline{v^2}}{k} \left[1 + \frac{\beta a_g k}{C_{1T} \epsilon} \frac{\partial T}{\partial y} \right] \frac{k^2}{\epsilon} \frac{\partial U}{\partial y} \quad (9)$$

$$\frac{\overline{u^2}}{k} = 0.94 \quad (10)$$

$$\frac{\overline{v^2}}{k} = \frac{2}{3} \left[\frac{1-C_2}{C_1} \right] = 0.53 \quad (11)$$

$$\frac{\overline{w^2}}{k} = 0.53 \quad (12)$$

$$-\overline{vT'} = \frac{1}{C_{1T}} \frac{\overline{v^2}}{k} \frac{k^2}{\epsilon} \frac{\partial T}{\partial y} \quad (13)$$

$$\overline{uT'} = \frac{1}{C_{1T}} \frac{k}{\epsilon} \left[\overline{uv} \frac{\partial T}{\partial y} + (1-C_{2T}) \overline{vT'} \frac{\partial U}{\partial y} - \beta a_g (1-C_{2T}) \overline{vT'} \right] \quad (14)$$

The constants in eqs. (10) to (12) for the normal stresses are empirical and, strictly, pertain only to non-combusting flows (16). The equation for the temperature fluctuations is solved in its full form since to do so makes no additional modelling demands. It is (12):

$$\rho U \frac{\partial \overline{T'^2}}{\partial x} + \rho V \frac{\partial \overline{T'^2}}{\partial y} = \frac{1}{y} \frac{\partial}{\partial y} \left[y C_g \rho \frac{k}{\epsilon} \left(\overline{v^2} \frac{\partial \overline{T'^2}}{\partial y} + \overline{uv} \frac{\partial \overline{T'^2}}{\partial x} \right) \right] - 2 \rho \overline{vT'} \frac{\partial T}{\partial y} - \frac{2}{C_T} \rho \frac{\epsilon}{k} \overline{T'^2} \quad (15)$$

The values of additional constants needed for the algebraic stress model are given in Table II (14).

Table II Values of Additional Constants Pertaining to Algebraic Stress Model

C ₁	C ₂	C _{1T}	C _{2T}	C _T	C _{ε3}	C _g
2.2	0.55	3.2	0.5	1.0	1.1	0.11

The Combustion Model

The formulation embodied by the 'simple chemically reacting system' concept, as originally used by Pun and Spalding (17), was adopted. This model has formed the basis of all the attempts to predict the turbulent diffusion flame by modern computational methods. The underlying assumptions are: a single step global reaction which excludes intermediate species, a chemical kinetic rate which is fast compared to the turbulence mixing rate, equality of the turbulent mass diffusion coefficients, and low Mach number.

The statistical description of non-linear functions of the mean flow parameters is assisted by the use of a probability density function (pdf) the shape of which may be calculated (e.g. (18, 19)) or assumed. Since the pdf equation is little explored and its computation is as yet too expensive for engineering purposes we adopt the latter course. Two assumed forms for the pdf of mixture fraction are commonly used, the clipped Gaussian function (20) and the Beta function (21). We have explored both and found that there is little to choose between them with the latter exhibiting perhaps some marginal predictive superiority.

Mean values of all properties φ, such as T, which are non-linear functions of f are determined from:

$$\bar{\phi} = \int_0^1 \phi(f) p(f) df \quad (16)$$

where p(f) is the assumed (Favre-averaged) pdf. In the case of the Beta function assumption:

$$p(f) = \frac{f^{a-1} (1-f)^{b-1}}{\int_0^1 f^{a-1} (1-f)^{b-1} df}, \quad 0 < f < 1 \quad (17)$$

with

$$a = f \left[\frac{\bar{\phi} - \phi}{\phi} - 1 \right], \quad b = \frac{(1-\bar{\phi})}{\bar{\phi}} a \quad (18)$$

The temperature is calculated from:

$$T = \frac{h - \overline{w_{fu}} H}{\bar{c}_p} \quad (19)$$

where \bar{c}_p is calculated according to Tribus (22).

Since a fast reaction is presumed it might be thought more appropriate to compute \bar{T} from equilibrium chemistry. Experience reveals (23) that this is not satisfactory in the fuel-rich region where, for example, CO is significantly overpredicted. It seems likely that this fault can probably be eliminated by the imposition of flammability limits but this remedy is insufficiently explored.

Previous workers have always assumed that the flame is adiabatic in which case the enthalpy is, for the above specified reaction model, a linear function of f . In the present work we allow radiation losses to the surroundings. The appropriate functional relation between h and f is then not evident, and this too in an underexplored subject. We presume that $h_{rad} = h_{ad}$ at $f = 0$ and $f = 1$, $h_{rad} = h_{ad}$ - radiation source at $f = f$, and that the relations between these three points are linear. This prescription cannot be greatly in error.

The Radiation Model

The radiation loss from the flame to the surroundings has been ignored in most previous attempts to predict laboratory turbulent diffusion flames. Although it has been argued that the radiation loss is probably rather small its neglect is none the less, as we shall see, to the detriment of model validation studies especially since the available data are mainly for temperature.

Since the experimental flames have all been situated in cool, open laboratories the transfer of radiative energy from the surroundings to the flame may be ignored. And since these laboratory flames are optically rather thin we should also without too much error be able to neglect self-absorption. The flame is then a simple emitter and the rate of heat emission per unit volume is:

$$\dot{q}_{rad}^m = 4k_g \sigma T^4 \quad (20)$$

where σ is the Stefan Boltzman constant and k_g is the grey gas absorption coefficient. Strictly the emission behaviour of the emitting gases and the soot is non-grey but this complication can be circumvented by imagining the real gas and soot to be replaced by a mixture of grey gases plus one clear gas (24). This formulation has been adopted by Truelove (25) who presumes a mixture of two grey gases, a clear gas, and soot, and provides a correlation for the total emittance of the form:

$$\epsilon_g = \sum_n a_{g,n}(T) [1 - \exp(-k_{g,n}(P_w + P_c + P_{co}) - k_{s,n} - k_{CH4,n} P_{CH4})] \quad (21)$$

$$\text{where } a_{g,n}(T) = b_{1,n} + b_{2,n} T \quad (22)$$

The absorption coefficient may be deduced from a pseudo grey relation:

$$\epsilon_g = (1 - e^{-k_g L}) \quad (23)$$

The Soot Model

The luminosity of laboratory flames is usually rather small, all the same soot is highly emitting and some account of its presence must be given if radiation transfer is not neglected. We solve a balance equation for the soot mass fraction:

$$\rho U \frac{\partial s}{\partial x} + \rho V \frac{\partial s}{\partial y} = \frac{1}{y} \frac{\partial}{\partial y} (y \frac{\mu_c}{\sigma_s} \frac{\partial s}{\partial y}) + S_s \quad (24)$$

where $S_s = S_s - S_d$, S_s = soot formation rate and S_d = its destruction rate. The Schmidt number σ_s is set equal to 0.7.

The chemical kinetics of soot formation is a tremendously complex subject and for this reason it is little developed. We choose a very simple expression which exhibits the right behavioural features. It has its origins in diesel engine studies and has been used with some success in steady flow combustors by Abbas et

al (26):

$$S_f = C_f P_{fu}^n \exp(-E/RT) \quad (25)$$

where P_{fu} is the fuel partial pressure, ϕ is the equivalence ratio = $S_{fu}/(F/(1-f))$, S_{fu} = the fuel stoichiometric air requirement, the parameters E/R , n and C_f are respectively assigned the values 20140, 3, and 0.01 as a result of validation studies.

The soot particles are so small (typical size is $1 \mu m$ in spray flames (27) and in gaseous ones, as in the present study, much smaller) that their consumption rate will be determined by laws applicable to gas species. We adopt the simple expression of Magnussen et al (28) who, by adopting the conventional assumption to the effect that the reaction rates controlled by turbulence decay, link the soot burn out rate to the product of its mean concentration and the turbulence time scale ϵ/k :

$$S_d = \min \left[A m_s \frac{\epsilon}{k}, \frac{A m_{ox} \epsilon}{r_s k} \frac{m_s r_s}{m_s r_s + m_{fu} S_{fu}} \right] \quad (26)$$

where A is an adjustable constant assigned (28) the value of 4. The second term restricts the soot consumption in the absence of sufficient oxygen.

THE NUMERICAL SOLUTION PROCEDURE

The governing differential equations were solved using a parabolic version (29) of the Imperial College TEACH code (30). The code features a grid which is caused to expand with the flow. The expansion is accommodated by appropriate alterations of the cell face convection and diffusion coefficients. The non-orthogonality of the grid is small and the orthogonal forms of the governing differential equations are retained with little error (31). Because substantial changes in density and temperature may occur between adjacent streamwise stations iteration is employed. For the first iteration the V -velocities at the downstream station are set equal to the corresponding upstream ones. Subsequently: (i) the downstream U -velocities are determined, (ii) new downstream V 's are obtained from the continuity equation, (iii) the remaining downstream dependent variables are solved for along with the density and other ancillary information, and (iv) the sequence returns to (i) until a convergence criterion is satisfied. Note that a pressure correction equation is not solved, it is expedient and sufficiently precise to ignore the small cross-stream pressure variations.

COMPARISON OF PREDICTIONS WITH DATA

There now exist a good number of data sets for turbulent diffusion flames. The scope of this study is arbitrarily restricted to four experimental hydrocarbon flames. We have considered two flames of Lockwood and Moneib (1), both for methane fuel but one with the fuel stream mass diluted by 42 per cent by volume of nitrogen. We have included the German natural gas flame of Wittmer and Günther (4) and Lenz and Günther (3). And we have considered the town gas flame of Lockwood and Odidi (5). All of these flames had Reynolds numbers in excess of 15,000. The various flames studied are summarized in Table III.

Mean Velocities

Mean velocity data for the Lockwood and Moneib methane flames are reported in (2). Velocity data are also reported by Wittmer and Günther (4). Predictions are compared with these data in panels (a) to (d) of Fig. 1. The predicted jet spread of the algebraic stress model is excessive. Tamanini (32) mentions a similar discrepancy although he shows no predictions. The $k-\epsilon$ predictions are superior, and the effect of radiation on the velocity is evidently small.

The marked superiority of the $k-\epsilon$ model is surprising. In common with other workers (e.g. (32)) we find only marginal difference between them, in favour of the algebraic stress model for inert flows. We might expect the algebraic stress formulation to exhibit again marginal superiority for flames since the buoyancy influences should be better modelled. That it does not

Table III Experimental Flame Conditions

Flame	Fuel volumetric composition	Burner diameter (mm)	Re
Methane flame (1)	93.63% CH ₄ 5.54% hydrocarbons 0.83% inerts	7.74	15,000
Nitrogen diluted methane flame (1)	As above but diluted with 42% by volume N ₂	7.74	15,000
Methane flame of (3,4)	81.1% CH ₄ 15.3% N ₂ 0.7% CO ₂ 2.9% hydrocarbons	8.00	37,000
Town gas flame (5)	55% H ₂ 27% CH ₄ 4% CO 2% C ₂ H ₆ 8% CO ₂ 4% N ₂	5.00	24,000

is presumably due to inconsistencies in the derivation of the present algebraic stress model when substantial density fluctuations occur. We are currently rederiving the model for this variable density case. It is of interest to note that when the last (buoyancy generation) terms are dropped from eqns. (1) and (2) the discrepancies in the algebraic stress predictions are made only slightly worse.

The last term of the k equation is an example of one for which the effect of the large density variations are incorrectly simulated since the use of $\bar{\rho}$ in the term implies small temperature fluctuations. The unapproximated term is $g u \rho'$. It would be of interest to retain the correct term and solve a modelled equation for the correlation $u \rho'$. We have so far simply expressed it as $-\rho u \rho' = (\rho/\rho_0) \partial \rho / \partial x$. The predictions are little affected by this 'improvement'. We also note that the dissipation of the $u T'$ equation assumes a uniform fluid specific heat and thermal conductivity but in view of the preceding observation we would expect this to be of small consequence. We conclude that the possible inconsistencies associated with the fluctuating density and the fluctuating pressure (see Bilger (33) and Jones (34)) arise in the simplifications used to procure the algebraic stress relations.

Mean Temperature

Mean temperature data are available for all five flames; they are compared with the predictions in the several panels of Figs. 2 to 5. The influence of the thermal radiation loss is significant, rather less so for the cleaner burning nitrogen diluted (Fig. 3) and town gas (Fig. 5) flames. The poor performance of the algebraic stress model, in particular its over prediction of the spreading rate, is again seen here.

It has mainly been assumed in previous studies that the radiation loss from these laboratory flames is small, and this caused us to believe that the present crude model would be more than sufficient. It is clear that a more elaborate radiation simulation is called for. Better simple models exist which are quite easy to incorporate (35). We may expect the inclusion of self-absorption will raise the predicted temperatures and so enhance the already rather satisfactory performance of the k - ϵ model.

Godoy (36) has presented k - ϵ predictions for the undiluted flame of (1) based on the presumption of full chemical equilibrium chemistry (Figures 2(a), (b) and 4(a), (b)). Although radiation was neglected it is clear that the on-axis temperature peak would be somewhat too far downstream were the results to be corrected for the radiation loss. The reason is that in the fuel rich regions the chemical equilibrium supposition substantially

overpredicts the CO concentration levels, delaying burn out. Combustion models based on equilibrium chemistry would appear to require the introduction of an extinction component based on the flammability limits. At this point it should be noted that Liew et al (23) appear to obtain satisfactory concentration predictions by straightforwardly applying the concentration versus mixture fraction functions determined from laminar flame experiments.

Fluctuating Velocity

A few data for the fluctuating velocity components exist and these are shown in Figs. 6 and 7 along with the corresponding predictions of the algebraic stress formulation. On the whole the agreement is surprisingly good. In general the level of turbulence is somewhat overpredicted, with the values of $(u^2)^{1/2}$ being least in error. The algebraic stress model overpredicts the jet spread with significant adverse consequences for the temperature predictions. The predicted uv correlation which has higher values than the measured ones, for the Wittmer and Günther flame (4) as shown in Fig. 6(c), is responsible for this discrepancy.

Some k - ϵ predictions of uv are shown in the same Fig. 6(c) and it is obvious that they are in much better agreement with the data. Radiation losses have only a small effect on the fluctuating velocity calculations.

Fluctuating Temperature

Somewhat more fluctuating temperature data are available than for fluctuating velocities (Figs. 8,9,10). The on-axis r.m.s. temperature is generally underpredicted in the upstream region. The poorer performance pattern of the present algebraic stress predictions re-emerges here. Allowing for the thermal radiation both increases and decreases the magnitude of $(T'^2)^{1/2}$ but, on the whole its effect is smaller than for mean temperatures and the predictions are here not generally improved by its inclusion. The peak r.m.s. temperatures of the methane flames of (1) tend to be overpredicted by both methods (Figs. 8(b),(c) and 9(b),(c)) and this may possibly indicate insufficient compensation of the thermocouple data. The best predictions are for the nitrogen plumes. In a sense the natural gas flames of (3) may also be considered as nitrogen diluted because of the high nitrogen content of the fuel.

CONCLUDING REMARKS

The most striking outcome of these straightforward validation studies has been that the role of the thermal radiation transfer is much greater than had previously been suspected. Satisfactory model validation studies, especially, can therefore not be performed for the typical laboratory turbulent jet flame if the radiation transfer is neglected.

The k - ϵ turbulence model, combined with a standard fast reaction combustion model, is able to simulate these flames fairly satisfactorily. The effect of the additional buoyancy source terms on these equations is small. These results should give heart to the mathematical modellers of combustion equipment who would prefer for reasons of economy the simple k - ϵ model.

The algebraic stress model performs poorly. This is not the case for inert flows of the present kind where it is marginally superior. This may be due to two main reasons. The first one is that the large density fluctuations that occur in reacting flows are not properly modelled. The assumptions made which are based on non-reacting flows are precarious in this case. The second one is that pressure variation correlations that appear in the Reynolds stress and turbulent flux equations (see (34)) may be significantly big to influence the calculations. Bigler (33) discusses the possible effects of a similar term appearing in the turbulence energy equation. We have not worked out a consistent formulation of the algebraic stress expressions, but we suspect that it may well prove more expedient to solve the stress equations in their full forms. Finally, we might note that the time scale of the temperature fluctuations decay rate appears not to be equal to the turbulence time scale, and

varies considerably (37). The conventional assumption in modelling the dissipation term in the T'^2 equation is that the ratio of these two time scales is unity, or at most a constant value close to unity. We have assumed a unity ratio.

REFERENCES

1. Lockwood, F.C. and Moneib, H.A. (1982) Fluctuating temperature measurements in turbulent jet diffusion flames. *Comb. and Flame*, **47**, 291-314.
2. El-Banhawy, Y., Hassan, M.A., Lockwood, F.C. and Moneib, H.A. (1983) Velocity and unburned hydrocarbon measurements in a vertical turbulent free jet diffusion flame. To appear in *Comb. and Flame*.
3. Lenz, W. and Günther, R. (1980) Measurements of fluctuating temperature in a free-jet diffusion flame. *Comb. and Flame*, **37**, 63-70.
4. Wittmer, V. and Günther, R. (1980) Correlation measurements of velocity and temperature fluctuations in a free jet diffusion flame. AGARD Conference, Proceedings No. 28, 10.
5. Lockwood, F.C. and Odidi, A.O.O. (1974) Measurement of mean and fluctuating temperature and of ion concentration in round free-jet turbulent diffusion and premixed flames. 15th Symp. (Int.) on Combustion, 561-571.
6. Launder, B.E. and Spalding, D.B. (1972) Mathematical models of turbulence. Academic Press.
7. Jones, W.P. and Launder, B.E. (1972) The prediction of laminarization with a two-equation model of turbulence. *Int. Journal of Heat and Mass Transfer*, **15**, 301.
8. Launder, B.E. and Spalding, D.B. (1974) The numerical computations of turbulent flows. *Computer Methods in Applied Mechanics and Engineering*, **3**, 269-289.
9. Launder, B.E., Reece, G.J. and Rodi, W. (1975) Progress in the development of a Reynolds-stress turbulence closure. *J. Fluid Mech.*, **68**, 537-566.
10. Gibson, M.M. and Launder, B.E. (1978) Ground effects on pressure fluctuations in the atmospheric boundary layer. *J. Fluid Mech.*, **86**, 491-511.
11. Hanjalic, K., Launder, B.E. and Schiestel, R. (1979) Multiple-time-scale concepts in turbulent transport modelling. 2nd Symp. on Turbulent Shear Flows. Imperial College, London.
12. Gibson, M.M., Jones, W.P., McGuirk, J.J. and Whitelaw, J.H. (1980) Outline lecture notes on fundamentals of turbulence and their application to calculation methods. Dept. of Mech. and Chem. Eng., Imperial College.
13. Pope, S.B. and Whitelaw, J.H. (1976) The calculation of near wake flows. *J. Fluid Mech.*, **73**, 9-32.
14. Hossain, M.S. and Rodi, W. (1976) Influence of buoyancy on the turbulence intensities in horizontal and vertical jets. In: *Turbulent Buoyant Convection*, editor D.B. Spalding, Hemisphere Publishing Corp.
15. Rodi, W. (1978) Turbulence models and their application in hydraulics. A state of the art review. Report SFB 80/T/127, Universität Karlsruhe.
16. Launder, B.E. (1975) On the effects of a gravitational field on the turbulent transport of heat and momentum. *J. Fluid Mech.*, **67**, 569-581.
17. Pun, W.M. and Spalding, D.B. (1967) A procedure for predicting the velocity and temperature distributions in a confined, steady, turbulent, gaseous diffusion flame. Proc. Int. Astronautical Federation Meeting, Belgrade.
18. Janicka, J., Kolbe, W. and Kollmann, W. (1978) The solution of a p.d.f.-transport equation for turbulent diffusion flames. Proc. of the Heat Transfer and Fluid Mechanics Institute, Stanford University Press.
19. Pope, S.B. (1979) A Monte Carlo method for the p.d.f. equations of turbulent flow. Dept. of Mech. Eng., Massachusetts Institute of Technology.
20. Lockwood, F.C. and Naguib, A.S. (1975) The prediction of the fluctuations in the properties of free round jet turbulent diffusion flames. *Comb. and Flame*, **24**, 109-124.
21. Richardson, J.N., Howard, H.C. and Smith, R.W. (1953) The relation between sampling-tube measurements and concentration fluctuations in turbulent gas jets. Proc. 4th Symp. (Int.) on Combustion, The Combustion Institute, p. 814.
22. Tribus, M. (1961) *Thermostatistics and thermodynamics*. Van Nostrand, London.
23. Liew, S.K., Bray, K.N.C. and Moss, J.B. (1981) A flamelet model of turbulent non-premixed combustion. *Comb. Sci. and Tech.*, **27**, 69-73.
24. Hottel, H.C. and Sarofim, A.F. (1967) *Radiative transfer*. McGraw-Hill Book Co.
25. Truelove, J.S. (1976) A mixed grey gas model for flame radiation. AERE, Harwell, R8494.
26. Abbas, A.S., Koussa, S.S. and Lockwood, F.C. (1980) The prediction of particle laden flows. 18th Symp. (Int.) on Combustion, The Combustion Institute.
27. Chigier, N.A. (1977) Instrumentation techniques for studying heterogeneous combustion. *Prog. Energy Comb. Sci.*, **3**, 175-189.
28. Magnussen, B.F. and Hjertager, B.H. (1976) On mathematical modelling of turbulent combustion with special emphasis on soot formation and combustion. 16th Symp. (Int.) on Combustion, Combustion Institute.
29. Patankar, S.V. and Spalding, D.B. (1970) *Heat and mass transfer in boundary layers*. Intertext Books.
30. Gosman, A.D. and Ideriah, F.J.K. (1976) TEACH-T: a general computer program for two-dimensional, turbulent, recirculating flows. Mech. Eng. Dept. Report, Imperial College.
31. Bergeles, G. (1976) Three-dimensional discrete-hole cooling processes; an experimental and theoretical study. Ph.D. Thesis, Imperial College, University of London.
32. Tamanini, F. (1977) Reaction rates, air entrainment and radiation in turbulent fire plumes. *Comb. and Flame*, **30**, 85-101.
33. Bilger, R.W. (1976) Turbulent jet diffusion flames. *Prog. Energy Combust. Sci.*, **1**, 87-109.
34. Jones, W.P. (1979) Models for turbulent flows with variable density and combustion. Von Karman Inst. for Fluid Dynamics, Lecture Series 1979-2 Prediction Methods for Turbulent Flows. January 1979.
35. Gibb, J. (1982) Central Electricity Generating Board, Marchwood, England. Private Communication.
36. Godoy, S. (1982) Turbulent diffusion flames. Ph.D. Thesis, Imperial College, University of London.
37. Warhaft, Z. and Lumley, J.L. (1978) An experimental study of the decay of temperature fluctuations in grid generated turbulence. *J. Fluid Mech.*, **88**, 659-684.

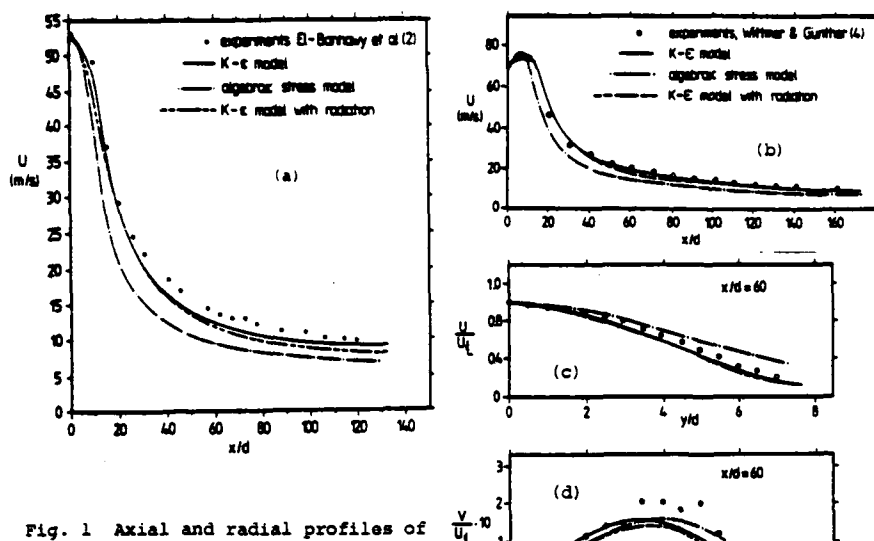


Fig. 1 Axial and radial profiles of mean velocities
(a) Methane flame (2)
(b,c,d) Flame of (4)

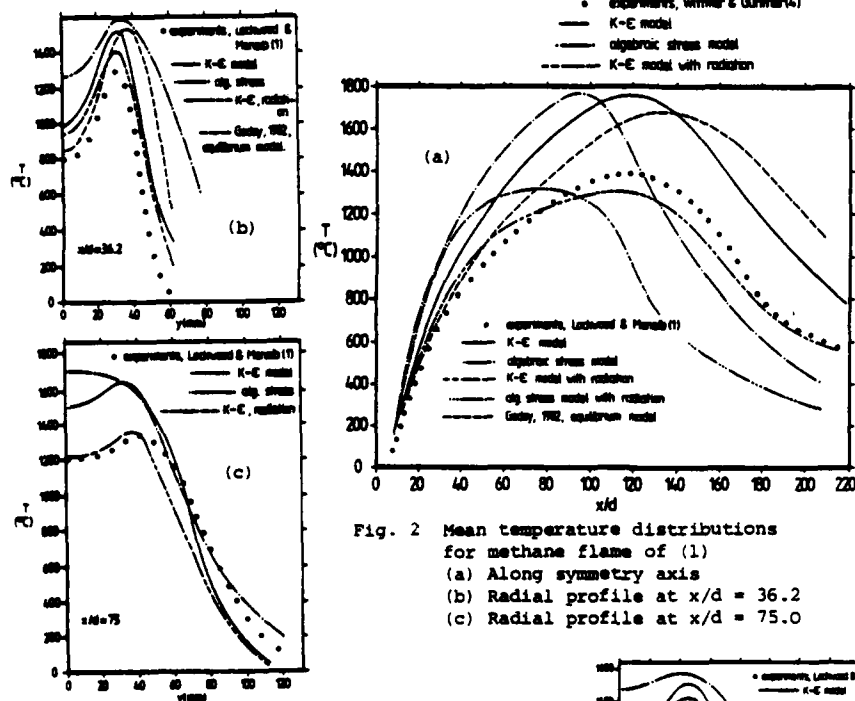


Fig. 2 Mean temperature distributions for methane flame of (1)
(a) Along symmetry axis
(b) Radial profile at $x/d = 36.2$
(c) Radial profile at $x/d = 75.0$

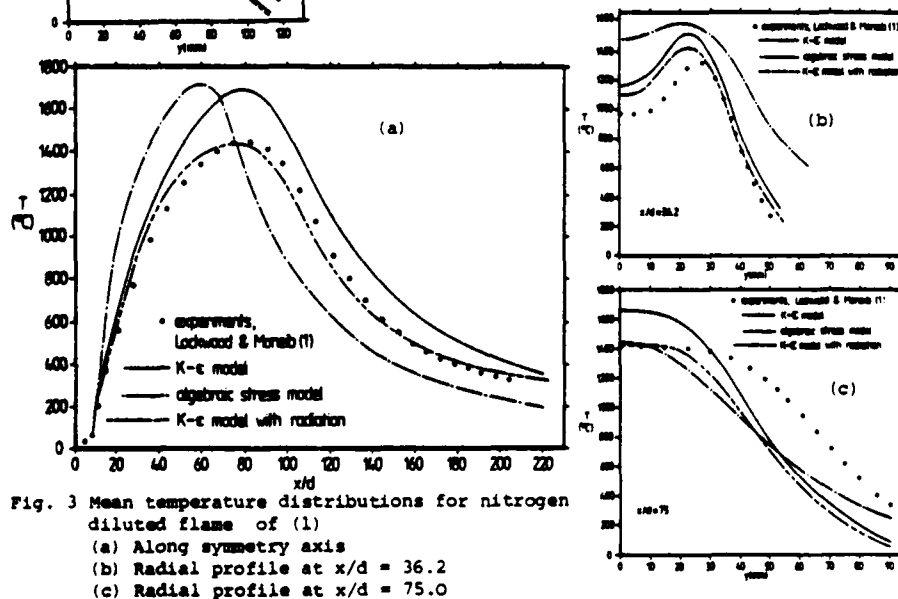


Fig. 3 Mean temperature distributions for nitrogen diluted flame of (1)
(a) Along symmetry axis
(b) Radial profile at $x/d = 36.2$
(c) Radial profile at $x/d = 75.0$

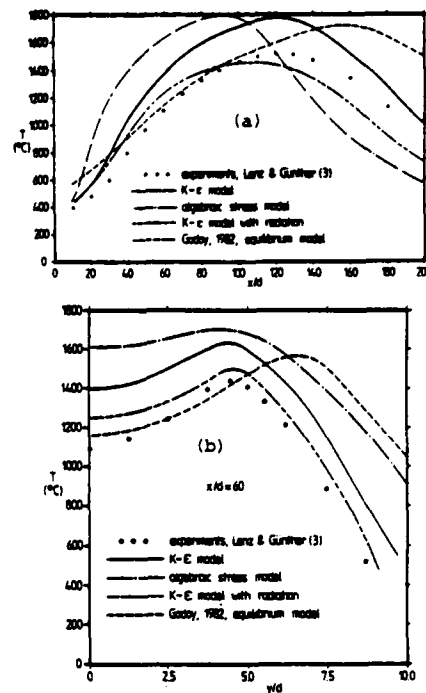


Fig. 4 Mean temperature distributions for flame of (3)
(a) Along symmetry axis
(b) Radial profile at $x/d = 60$

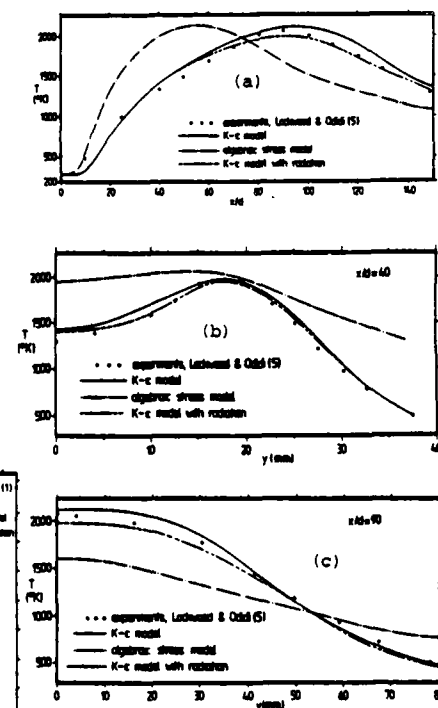


Fig. 5 Mean temperature distributions for flame of (5)
(a) Along symmetry axis
(b) Radial profile at $x/d = 40$
(c) Radial profile at $x/d = 90$

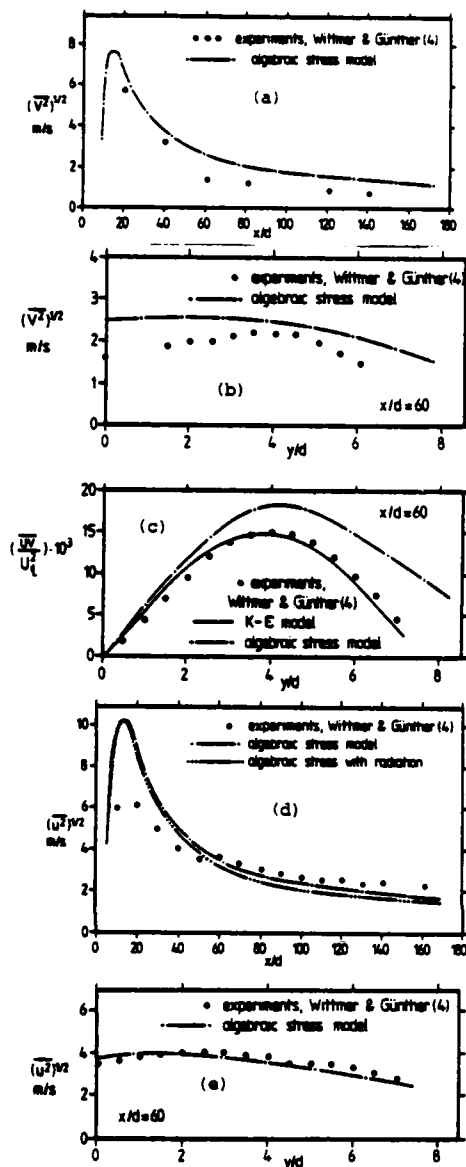


Fig. 6 Axial and radial distributions of normal and shear stresses for flame of (4)
 (a) Axial distribution of $(v^2)^{1/2}$
 (b) Radial distribution of $(v^2)^{1/2}$ at $x/d = 60$
 (c) Radial distribution of $(uv)^{1/2}$ at $x/d = 60$
 (d) Axial distribution of $(u^2)^{1/2}$
 (e) Radial distribution of $(u^2)^{1/2}$ at $x/d = 60$

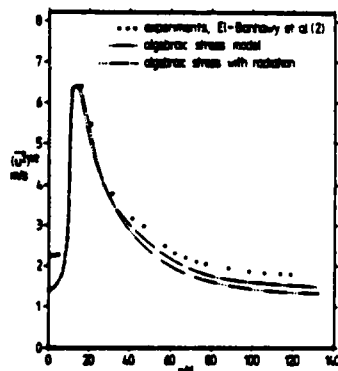


Fig. 7 Distribution of streamwise normal stress along symmetry axis for methane flame of (2)

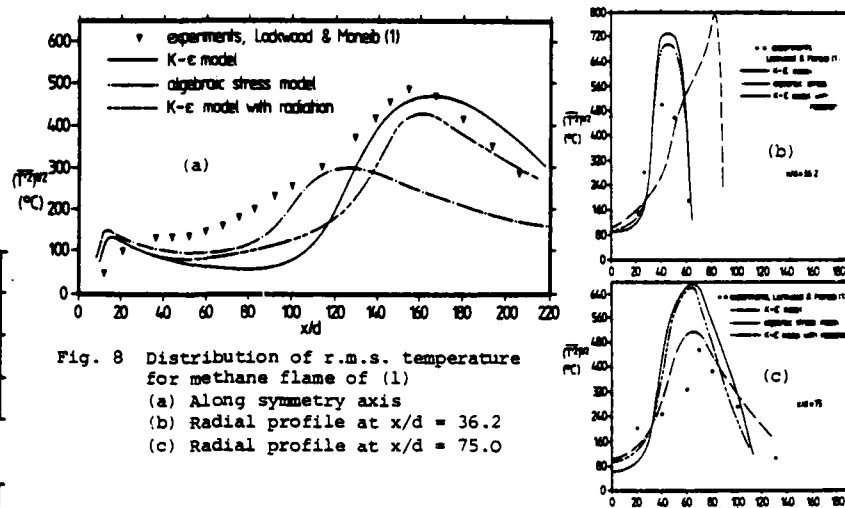


Fig. 8 Distribution of r.m.s. temperature for methane flame of (1)
 (a) Along symmetry axis
 (b) Radial profile at $x/d = 36.2$
 (c) Radial profile at $x/d = 75.0$

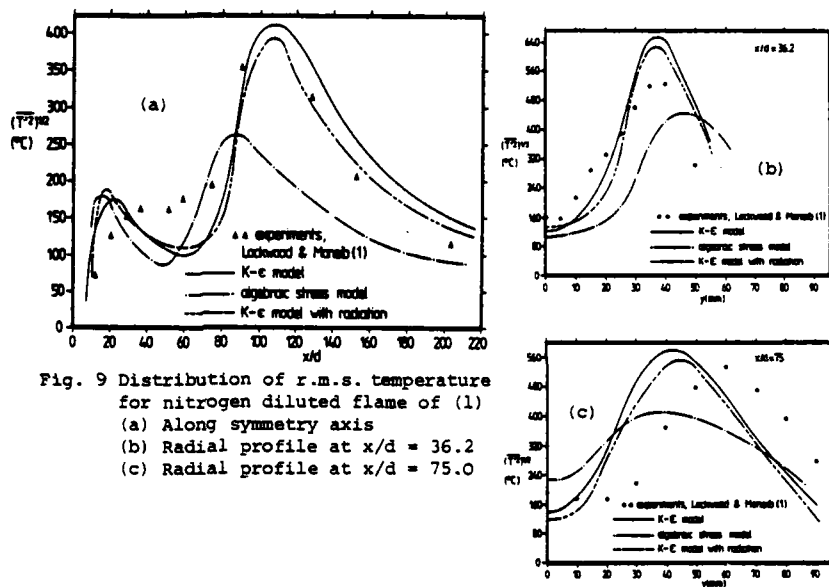


Fig. 9 Distribution of r.m.s. temperature for nitrogen diluted flame of (1)
 (a) Along symmetry axis
 (b) Radial profile at $x/d = 36.2$
 (c) Radial profile at $x/d = 75.0$

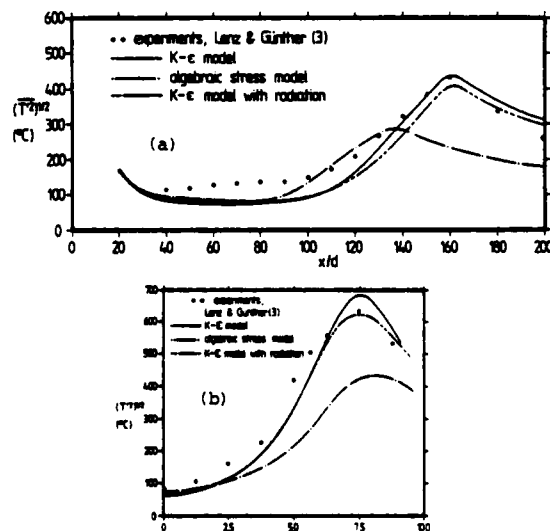


Fig. 10 Distribution of r.m.s. temperature for flame of (3)
 (a) Along symmetry axis
 (b) Radial profile at $x/d = 60.0$

A MODEL FOR FLAME EXTINCTION IN TURBULENT FLOW

S. Byggstøyl
Researcher, SINTEF Avd. 15
and
B.F. Magnussen
Professor, Engineering Thermodynamics
The Norwegian Institute of Technology
Division of Thermodynamics
N-7034 Trondheim-NTH, Norway

ABSTRACT

In this paper a model for local extinction in turbulent flow is developed. The model is based on the Eddy Dissipation Concept (EDC) for chemical reaction in turbulent flow developed by Magnussen (1981)¹. A review of this concept is included in the paper. The (EDC) is a reactor concept which is unique in that it takes into account the intermittent behaviour of the smallscale structures of turbulence, as well as the effect of the fine structures on the chemical reactions. Both fast and slow chemical reactions can be treated simultaneously and consequently the extinction process. In this paper the extinction is assumed to take place in the fine structure. The lift-off and blow-out conditions for turbulent diffusion flames are calculated and compared with experimental data. The turbulent flame propagation velocity is also discussed with regards to the same concept.

NOMENCLATURE

c_i	concentration (kg/m^3)
C_p	specific heat
D	nozzle diameter
F	flatness factor
F	characteristic fine structure flatness factor
ΔH_R	reaction enthalpy difference
k	turbulence kinetic energy
L^*	characteristic length scale of fine structures
L'	characteristic turbulence length scale mixing length
L'', L'''	characteristic turbulence length at different structure level
\dot{m}	exchange rate of mass with fine structures
Re_λ	turbulence Reynolds number
r	stoichiometric oxygen requirement to burn 1 kg fuel
T	temperature (K)
ΔT	excess temperature of reacting fine structures
U_B	turbulent flame velocity
U	mean flow velocity
u^*	characteristic velocity of fine structures
u'	turbulence velocity
u'', u'''	characteristic turbulence velocity at different structure level
x	axial coordinate
Y	fractional conversion parameter
y	lateral coordinate
ρ	density
ϵ	rate of dissipation of turbulence kinetic energy
μ_t	effective turbulent viscosity
ν	kinematic viscosity
γ^*	intermittency factor
γ_λ	mass fraction occupied by fine structures
γ_λ	mass fraction occupied by fine structures regions

τ^*	time scale for the fine structure
τ_{ch}	chemical time scale
τ_λ	time scale for the fine structure regions
τ_M	bulk mixing timescale

INTRODUCTION

Local extinction in a practical turbulent combustion situation can influence important combustion characteristics like stability, noise generation, flame propagation, fuel consumption and heat transfer. These characteristics are of main importance for the performance and operation of combustion engines, combustion chambers, flare burners and fire fighting equipment.

From a fundamental point of view the extinction characteristics of chemical reactions in turbulent flow can give some new information about the geometry and the dynamics of the small scale turbulent structure and the interaction between the structure and chemical reactions which is some of the main problems in turbulence. The classical way to treat extinction phenomena is to apply Karlovitz-Kovasznays criterion recently used in a turbulent combustion situation by Chomiak (1982)². Turbulent structure models have been developed and used by Lockwood and Megahed (1978)³ and Tabaczynski (1981)⁴. Common for these models is that the chemical kinetic properties of the fluid is expressed through the laminar flame speed.

Recently Peters (1982)⁵ treated the extinction process in turbulent flow by considering the quenching of diffusive flamelets where both the intermittent behaviour of turbulence and chemical kinetics were taken into account.

REVIEW OF EDC

Chemical reactions take place when reactants are mixed at molecular scale at sufficiently high temperature¹. In turbulent flow the reactant consumption is strongly dependent on the molecular mixing. It is known that the microscale processes which are decisive for the molecular mixing as well as dissipation of turbulence energy into heat are severely intermittent i.e. concentrated in isolated regions whose entire volume is a small fraction of the volume of the fluid.

These regions are occupied by fine structures whose dimensions are small in one or two directions, however not in the third. These fine structures are believed to be vortex tubes, sheets or slabs whose characteristic dimensions are of the same magnitude as the Kolmogorov microscale. 6,7,8,9,10

The fine structures are responsible for the dissipation of turbulence into heat. Within these structures one can therefore assume that reactants will be mixed at molecular scale. These structures thus create the reaction space for non-uniformly distributed reactants.

In a modelling context one can assume that the reactants are homogeneously mixed within the fine structures. Thus, in order to be able to treat the reactions within this space, it is necessary to know the reaction volume and the mass transfer rate between the structures and the surrounding fluid.

The following describes a concept for treating chemical reactions in turbulent flow which include basic features of the preceding.

Turbulence energy dissipation

In turbulent flow energy from the mean flow is transferred through the bigger eddies to the fine structures where mechanical energy is dissipated into heat. This process is schematically described in Fig. 1.

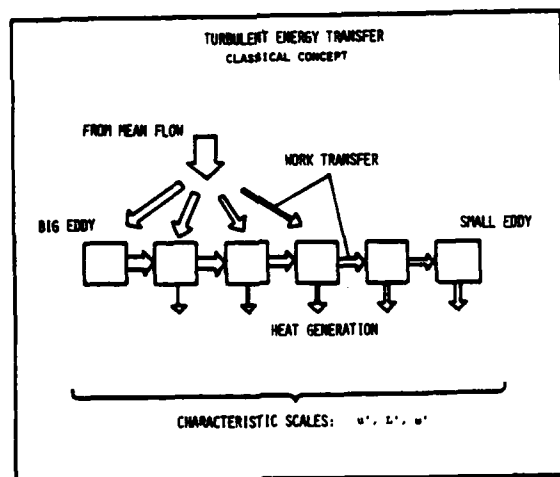


Fig. 1. Turbulent energy transfer

In general, high Reynolds number turbulent flow will consist of a spectrum of eddies of different sizes. Mechanical energy is mainly transferred between neighbouring eddy structures as indicated in Fig. 1. For the same reason the main production of turbulence kinetic energy will be performed by the interactions between bigger eddies and the mean flow.

The dissipation of kinetic energy into heat, which is due to work done by molecular forces on the turbulence eddies, on the other hand mainly takes place in the smallest eddies.

Important turbulent flow characteristics can for nearly isotropic turbulence be related to a turbulence velocity, u' , and a turbulent length, L' . These quantities are linked to each other through the turbulent eddy velocity:

$$v_{\epsilon} = u' \cdot L' \quad (1)$$

Modelling interstructural energy transfer

Figure 2 schematically illustrates a model for the transfer of mechanical energy from bigger to smaller turbulent structures¹¹.

The first structure level represents the whole spectrum of turbulence which in an ordinary way is characterized by a turbulence velocity, u' , a length scale, L' , and vorticity, or characteristic strain rate

$$\omega' = u'/L' \quad (2)$$

The rate of dissipation can for this level be expressed by

$$\epsilon' = \zeta^2 \left(12 \frac{u'}{L'} \cdot u'^2 + 15 \cdot v \left(\frac{u'}{L'} \right)^2 \right) \quad (3)$$

where ζ is a numerical constant.

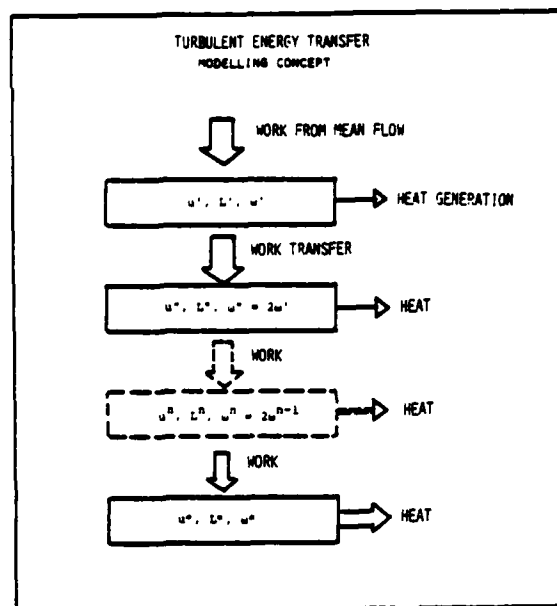


Fig. 2. A modelling concept for transfer of energy from bigger to smaller turbulent structures

The next structures level represent part of the turbulence spectrum characterized by a vorticity

$$\omega'' = 2\omega' \quad (4)$$

velocity, u'' , and length scale, L'' . The transfer of energy from the first level to the second level is expressed by

$$w' = \zeta^2 12 \frac{u'}{L'} u'^2 \quad (5)$$

Similarly the transfer of energy from the second to the third level where

$$\omega''' = \omega'' \quad (6)$$

is expressed

$$w'' = \zeta^2 12 \frac{u''}{L''} \cdot u''^2 \quad (7)$$

The part which is directly dissipated into heat is expressed

$$q'' = \zeta^2 \cdot 15 v \left(\frac{u''}{L''} \right)^2 \quad (8)$$

The turbulence energy ballance for the second structure level is consequently given by

$$\zeta^2 12 \frac{u'}{L'} u'^2 = \zeta^2 \left(12 \frac{u''}{L''} \cdot u''^2 + 15 \cdot v \left(\frac{u''}{L''} \right)^2 \right) \quad (9)$$

This sequence of turbulence structure levels can be continued down to a level where all the produced turbulence kinetic energy is dissipated into heat. This is the fine structure level characterized by, u^* , L^* , and ω^* .

The turbulence energy transferred to the fine structure is expressed by

$$w^* = \zeta^2 \cdot 6 \frac{u^*}{L^*} \cdot u^{*2} \quad (10)$$

and the dissipation by

$$q^* = \zeta^2 \cdot 15 v \left(\frac{u^*}{L^*} \right)^2 \quad (11)$$

According to this model nearly no dissipation of energy into heat takes place at the highest structure

level. Similarly it can be shown that 3/4 of the dissipation takes place at the fine structure level.

Taking this into account and by introducing $\zeta = 0.18$ the following three equations are obtained for the dissipation of turbulence kinetic energy for nearly isotropic turbulence:

$$\epsilon = 0.2 \frac{u'^3}{L} \quad (12)$$

$$\epsilon = 0.267 \frac{u'^3}{L^*} \quad (13)$$

$$\epsilon = 0.67 \nu \left(\frac{u'}{L^*} \right)^2 \quad (14)$$

Introducing the Taylor microscale a fourth equation is obtained

$$\epsilon = 15 \nu \left(\frac{u'}{\lambda} \right)^2 \quad (15)$$

By combination of equations (13) and (14) the following characteristics (scales) for the fine structures are obtained

$$u^* = 1.74 (\epsilon \cdot \nu)^{1/4} \quad (16)$$

and

$$L^* = 1.43 \nu^{3/4} / \epsilon^{1/4} \quad (17)$$

where u^* is the mass average fine structure velocity. The scales are closely related to the Kolmogorov scales.

The fine structures

The tendency towards strong dissipation intermittency in high Reynolds number turbulence was discovered by Batchelor and Townsend¹¹, and then studied from two points of view; different statistical models for the cascade of energy starting from a hypothesis of local invariance or selfsimilarities between motions of different scales, and then by consideration of hydrodynamic vorticity production due to stretching of vortex lines.

It can be concluded that the smallscale structures who are responsible for the main part of the dissipation are generated in a very localized fashion. It is assumed that these structures consist typically of large thin vortex sheets, ribbons of vorticity of vortex tubes of random extension folded or tangled throughout the flow (Fig. 3).

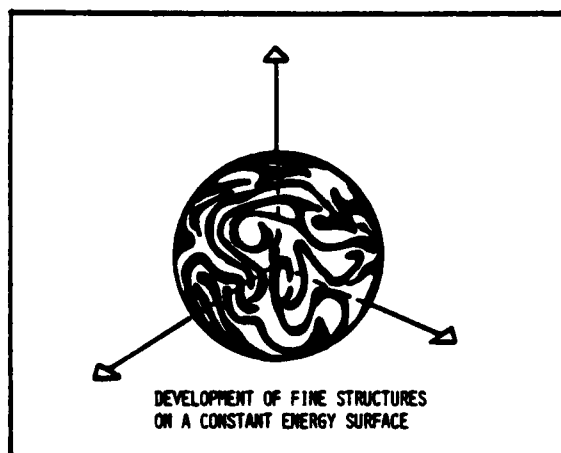


Fig. 3. Schematic illustration of fine structures developed on a constant energy surface

The fine structures are localized in certain fine structure regions whose linear dimensions are considerably larger than the fine structures therein¹⁰. These regions appear in the highly stained regions between the bigger eddies.

Modelling characteristics of the fine structures

It is assumed that the mass fraction occupied by the fine structures, on the basis of consideration of the energy transfer to these structures (eqs. 12 and 13) can be expressed by

$$\gamma^* = \left(\frac{u^*}{u'} \right)^3 \quad (18)$$

If it is assumed that the fine structures are localized in nearly constant energy regions, then the mass fraction occupied by the fine structure regions can be expressed by

$$\gamma^* = \gamma_\lambda \left(\frac{u^*}{u'} \right)^2 \quad (19)$$

giving the following expression

$$\gamma_\lambda = \frac{u^*}{u'} \quad (20)$$

Assuming nearly isotropic turbulence and introducing the turbulence kinetic energy and its rate of dissipation the following expressions are obtained:

$$\gamma^* = 9.7 \cdot \left(\frac{\nu \cdot \epsilon}{k^2} \right)^{3/4} \quad (21)$$

and

$$\gamma_\lambda = 2.13 \cdot \left(\frac{\nu \cdot \epsilon}{k^2} \right)^{1/4} \quad (22)$$

Similarly by introducing the turbulence Reynolds number

$$\gamma^* = 40.2 \cdot Re_\lambda^{-3/2} \quad (23)$$

and

$$\gamma_\lambda = 3.42 \cdot Re_\lambda^{-1/2} \quad (24)$$

Kuo and Corrsin⁸ have given some results for the flatness factor of $\partial u / \partial t$ as a function of Re_λ (Fig. 5). In order to compare the above results with these results an empirical expression has been developed for the relationship between the flatness factor and the intermittency factor:

$$F_M = 1.5 \cdot (1 + 1/\gamma) \quad (25)$$

Figure 4 shows a comparison between some experimental results¹⁰ and the given empirical expression.

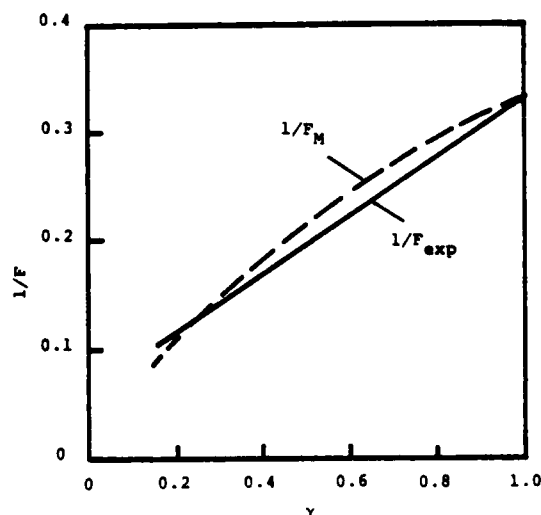


Fig. 4. Comparison between experimental results and empirical expression for the flatness factor as a function of the intermittency factor.

When eq. (25) is applied the following expression for the flatness factor for the fine structures is obtained.

$$F_{\lambda} = 1.5 + 0.44 \cdot Re_{\lambda}^{0.5} \quad (26)$$

Equation (26) is compared with the experimental results of Kuo and Corrsin⁹ in Fig. 5.

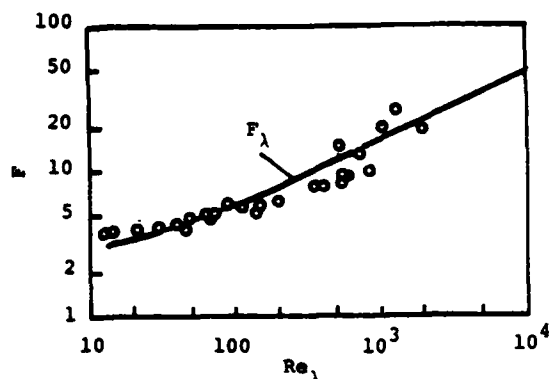


Fig. 5. Flatness factor of $\partial u/\partial t$ as a function of Re_{λ} compared with theoretical flatness factor for the fine structures.

From this comparison it can be concluded that the overall features of the physics seem to have been taken care of by the suggested expressions.

On the basis of simple geometrical considerations the transfer of mass per unit of fluid and unit of time between the fine structures and the surrounding can be expressed as follows

$$\dot{m} = 2 \cdot \frac{u^*}{L^*} \cdot \gamma^* \quad (1/s) \quad (27)$$

Expressed by k and ϵ for nearly isotropic turbulence eq. (27) turns into

$$\dot{m} = 23.6 \cdot \left(\frac{v^* \epsilon}{k} \right)^{1/4} \cdot \frac{\epsilon}{k} \quad (1/s) \quad (28)$$

Molecular mixing and reaction processes

The rate of molecular mixing is determined by the rate of mixing between the fine structures and the surrounding fluid.

The mean mass transfer rate between a certain fraction, χ , of the fine structures and the rest of the fluid, R_i , can for a certain specie, i , be expressed as follows:

$$R_i = \dot{m} \cdot \chi \cdot \left(\frac{c_i^0}{\rho} - \frac{c_i^*}{\rho^*} \right) \quad (29)$$

where $*$ and 0 refer to conditions in the fine structures and the surrounding.

The mass transfer rate can also be expressed per unit volume in the fine structure fraction, χ , as

$$R_i^* = \frac{\dot{m} \cdot \rho^*}{\gamma^*} \cdot \left(\frac{c_i^0}{\rho} - \frac{c_i^*}{\rho^*} \right) \quad (30)$$

Finally, the concentration of a specie, i , in the fraction, χ , of the fine structures and in the surrounding is related to the mean concentration by:

$$\bar{c}_i = \frac{c_i^*}{\rho^*} \cdot \gamma^* \cdot \chi + \frac{c_i^0}{\rho} \cdot (1 - \gamma^* \cdot \chi) \quad (31)$$

It is now possible to put up balance equations for reacting fine structures and the surrounding fluid including chemical kinetic rate expressions.

Combustion rates

If the rate of reaction between fuel and oxygen is considered infinitely fast, the rate of reaction will be limited by the mass transfer between the bulk and the fine structures. In this case the concentration of fuel or oxygen will be very small within the reacting fine structures. If the reaction took place in all the fine structures, the rate of combustion would be expressed by:

$$R_{fu} = \dot{m} \cdot \frac{\bar{c}_{min}}{1 - \gamma^*} \quad (32)$$

where \bar{c}_{min} is the smallest of \bar{c}_{fu} and \bar{c}_{O_2}/r_{fu} , where \bar{c}_{fu} and \bar{c}_{O_2} are the local mean concentrations of fuel and oxygen, and r_{fu} the stoichiometric oxygen requirement.

Not all the fine structures will be sufficiently heated to react. This is obviously the case in combustion of premixed gases where both fuel and oxygen are present in the fine structures.

The fraction of the fine structures which reacts can be assumed proportional to the ratio between the local concentration of reacted fuel and the total fuel concentration:

$$\chi = \frac{\bar{c}_{pr}/((1+r_{fu}) \cdot \gamma_{\lambda})}{\bar{c}_{pr}/((1+r_{fu}) \cdot \gamma_{\lambda}) + \bar{c}_{fu}} \quad (33)$$

where \bar{c}_{pr} is the local mean concentration of reaction products. Equation (33) implies the assumption that the reaction products are kept within the fine structure region until a concentration is reached which yields χ equal to unity.

By combination of equations (32) and (33) the following general equation is obtained for the rate of combustion at infinite reaction rate between fuel and oxygen:

$$R_{fu} = \dot{m} \cdot \frac{\chi}{1 - \gamma^* \chi} \cdot \bar{c}_{min} \quad (34)$$

The reacting fine structures under these conditions will have a temperature, ΔT , in excess of the local mean temperature:

$$\Delta T = \frac{\Delta H_R \cdot \bar{c}_{min}}{\bar{\rho} \cdot c_p} \quad (35)$$

where ΔH_R is the heat of reaction and c_p the local specific heat capacity. The temperature, T^* , of the reacting fine structures is consequently:

$$T^* = \bar{T} + \Delta T \quad (36)$$

and the surrounding temperature:

$$T^0 = \bar{T} - \Delta T \cdot \frac{\gamma^* \cdot \chi}{1 - \gamma^* \chi} \quad (37)$$

where \bar{T} is the local time mean temperature.

Chemical controlled reaction rate

On the basis of the previous there can be defined characteristic mixing time scales:

The bulk mixing time scale

$$\tau_M = 1/\dot{m} \quad (38)$$

The fine structure time scales

$$\tau^* = \gamma^*/\dot{m} \quad (39)$$

$$\tau_{\lambda} = \gamma_{\lambda}/\dot{m} \quad (40)$$

These time scales can be compared with chemical kinetic time scales in order to establish whether the reaction is mixing or chemical controlled, and even established criteria for extinction of flames.

MODELING FLAME EXTINCTION AND TURBULENT FLAME PROPAGATION ACCORDING TO THE EDC

Extinction

According to the previous concept heat and mass balance including chemical kinetics can easily be set up for the fine structures and the surrounding fluid. Consequently, knowing the chemical kinetics, a criterium for the extinction of the fine structures can be obtained. When a typical timescale for the combustion reaction is small compared to τ^* the fuel consumption is independent of chemical kinetics and is a purely hydrodynamic problem. However when the residence time becomes smaller than a typical chemical time scale the reaction will not be completed in the fine structure and the fuel consumption is strongly influenced by chemical kinetics. As the residence time decreases extinction will finally occur.

The chemical time scale, however, is not a uniquely defined quantity. Many different expressions can be found in the literature describing the various steps in the reaction process. In addition it is very difficult to find relevant data for different fuels.

When studying turbulent extinction a common substitute for the lacking chemical kinetic data has been time scales based on the laminar flame propagation behaviour of the mixture^{3,4}. These time scales are, however, more dependent on the diffusive properties of the fluid than the chemical kinetics. Another time scale that has been used is the chemical induction time or ignition delay time. This time scale is usually measured in shock tube experiments where the reaction starts from the very low radical concentration level of the unheated gases. This is not the case in flames and other reacting systems where there exists a source of free radicals somewhere in the system. Here the induction time is much shorter. In a typical turbulent combustion situation it is believed that radicals are already present in the regions where the fine structures are located. When it is further assumed that the internal mixing inside the fine structures are fast then the fine structures can be considered as a well stirred reactor.

On the basis of the previous the fractional conversion parameter for the reactor is defined as (cfr. Fig. 6)

$$Y = \frac{c_{fu}^o - c_{fu}^* \frac{\rho}{\rho^*}}{c_{fu}^o} \quad (41)$$

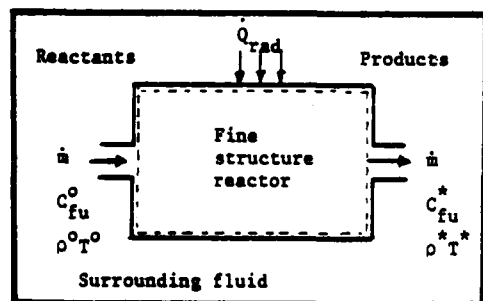


Fig. 6. Schematic illustration of a reacting fine structure

For a one step irreversible reaction the mass and heat balance for the fine structure can be expressed as

$$Y = \frac{R_{fu}^* \cdot \tau^*}{c_{fu}^o} \frac{\rho}{\rho^*} \quad (42)$$

$$Y = \frac{c_p (T^* - T^o) \rho^o}{\Delta H_R c_{fu}^o} \quad (43)$$

where the fine structure is considered to be adiabatic and the specific heat of the fluid is assumed to be constant. The extinction time scale can then be found from eq. (42) and (43) according to Fig. 7, where the extinction time scale τ_{ext}^* is indicated.

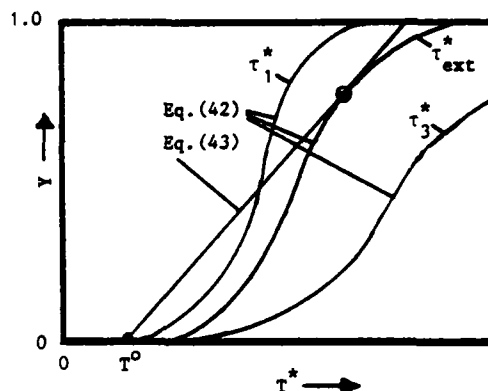


Fig. 7. Schematic illustration of Extinction in the fine structure $\tau_1^* > \tau_{ext}^* > \tau_3^*$

Turbulent flame propagation

The propagation of a plane flame in turbulent flow can be expressed by

$$U_B \frac{\partial c_{fu}}{\partial x} = \frac{\nu_T}{\sigma} \frac{\partial^2 c_{fu}}{\partial x^2} + R_{fu} \quad (44)$$

where U_B is the turbulent flame propagation velocity, ν_T is the turbulent viscosity and σ is the turbulent Schmidt number. With R_{fu} expressed according to Eq. (34), the only physical meaningful solution to Eq. (44) reads

$$U_B = 2 \left(\frac{\dot{m} \nu_T}{\gamma \lambda \sigma} \right)^{1/2} \quad (45)$$

By introducing the turbulent viscosity from the k- ϵ model this transforms into

$$U_B = 2 \sqrt{\frac{k}{\sigma}} \quad (46)$$

In a typical shear flow situation $k \approx u'^2$ and $\sigma \approx 1$. This gives a turbulent flame propagation velocity

$$U_B \approx 2u' \quad (47)$$

This is generally in relatively close agreement with the experimental data collected by Bradley et al. (1981)¹⁴

When the fine structure-time scale τ^* is reduced to the same magnitude as the chemical time scale, the turbulent flame speed is reduced due to local extinction in the fine structures. At a critical value of the fine structure-time scale the flame will be quenched by the turbulence. This leads to the following general qualitative relation for the turbulent flame speed:

$$\frac{U_B}{u'} = f(\tau_{ch}^*/\tau^*) \quad (48)$$

Due to the strong interaction between T^* and τ_{ch}^*/τ^* , the flame quenching appears like a catastrophe as indicated in fig. 8.

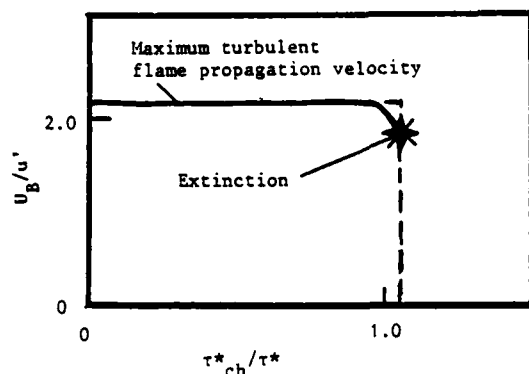


Fig. 8. Schematic illustration of the turbulent flame propagation velocity variation.

The abrupt extinction has been shown experimentally by Chomiak et al. (1982)³. In these experiments extinction for a methane mixture occurred at a fine structure time scale of approximately $\tau^* \approx 10^{-4}$ s. This is in close agreement with the chemical time scale deduced from the global reaction rate used by Bradley et al. (1976)^{15,16} and is also in reasonable agreement with the multistep kinetic calculations for methane-air mixture reported by Martenay (1970)¹⁷.

Lift-off and blow-off of turbulent diffusion flames

According to the extinction model and the result for the turbulent flame speed a lifted diffusion flame will be stabilized near the position on the stoichiometric contour where the fine structure time scale equals the chemical time scale. The reason why the stabilization point is located at or near the stoichiometric contour is that the reaction rate has its maximum near this contour. This is shown in Fig. 9, where also some calculated fine structure time scales at the stabilization points are indicated. By gradually increasing the exit velocity the stabilization point moves further downstreams. This continues until the stabilization point is at a position where the mean flow velocity is nearly equal to the maximum flame propagation velocity, then the flame is blown-off. This is shown in Fig. 9 where also some calculated fine structure timescales at the stabilization points are indicated.

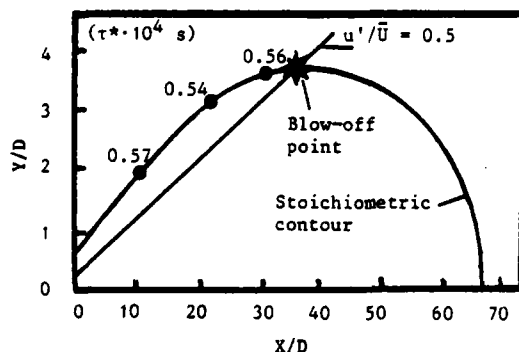


Fig. 9. Localisation of lift-off and blow-off points for a round free jet. Experimental data from Horch (18) for $D = 0.01$ m.

The extinction model has been tested by performing numerical calculations of the jet flow based on the $k-\epsilon$ model of turbulence and then extracting the quenching time scales by comparison with the experimental data of Horch (1978)¹⁸.

Figure 10 shows a comparison between experimental and predicted lift-off heights. The predictions have been based on a constant fine structure timescale, $\tau^* = 0.56 \cdot 10^{-4}$ s.

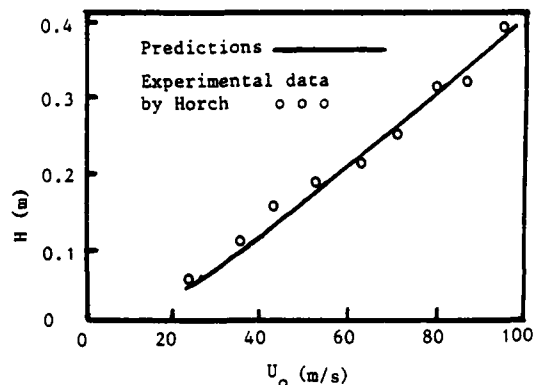


Fig. 10. Comparison between experimental and predicted lift-off heights.

For a constant nozzle diameter the fine structure timescale at the stabilization points was nearly constant as shown both in Figs. 9 and 10, indicating that the fine structures are of main importance in the extinction process. The time scale did, however, decrease with increasing diameter, as indicated in Table 1.

Table 1. Mean structure time scale at the stabilisation point for different nozzle diameters.

D (mm)	4	6	8	10
$\tau^* \cdot 10^4$ (s)	1.18	0.80	0.67	0.56

We assume that this diameter effect is due to radiative heat transfer between the fine structures at the flame stabilization point and its surroundings. This effect will tend to increase the fine structure temperatures and consequently reduce the extinction time scales for increased nozzle diameter. As such this effect can readily be handled by the described concept. At the blow-off point the ratio of a typical turbulence velocity to the mean flow velocity was nearly equal to $u'/\bar{U} \approx 0.5$. This is shown in Fig. 9 and table 2.

Table 2. Turbulence intensity at blow-off point for different nozzle diameters.

D (mm)	4	6	8	10
u'/\bar{U}	0.51	0.47	0.49	0.48

According to the previous, the mean velocity is nearly equal to the maximum turbulent flame propagation velocity at the blow-off point.

CONCLUSIONS

The previous have shown that extinction processes in turbulent combustion can be treated by the eddy dissipation concept (EDC) of Magnussen. Predictions deduced from the proposed extinction model compares well with experimental data.

The flame stabilization point for lifted diffusion flames is located at the stoichiometric contour and at positions where the fine structure mixing time scale τ^* is approximately equal to the chemical time scale τ_c .

An expression for the turbulent flame propagation velocity is deduced from the EDC. This expression gives results which are in close agreement with experimental data. It is shown that blow-off for turbulent diffusion flames occurs at a point where the maximum turbulent flame propagation velocity is equal to the mean flow velocity.

ACKNOWLEDGEMENTS

This work has been financially supported by STATOIL. The authors would like to thank Mrs. I. Eidissen and Miss P. Magnussen for assistance in typing the paper.

REFERENCES

- 1 Magnussen, B.F., "On the Structure of Turbulence and a Generalized Eddy Dissipation Concept for Chemical Reactions in Turbulent Flow", 19th AIAA Sc. meeting, St. Louis, USA, 1981
- 2 Chomiak, J., and Jarosinski, J., "Flame Quenching by Turbulence", Comb. and Flame, 1982, 48, 241
- 3 Lockwood, F.C., and Megahed, I.E.A., "Extinction in Turbulent Reacting Flows", Comb. Sci. Techn., 1978, 19, 77
- 4 Tabaczynski, R.J., "Premixed Turbulent Flame Blowoff Velocity Correlations Based on Coherent Structures in Turbulent Flows", Comb. and Flame, 1982, 42, 19
- 5 Peters, N., "Local Quenching Due to Flame Stretch and Non-Premixed Turbulent Combustion", Comb. Sci. Tech., 1982, 30, 1
- 6 Kolmogorov, A.N., "A Refinement of previous Hypotheses concerning the Local Structure of Turbulence in a viscous incompressible fluid at high Reynolds number", J. Fluid Mech., 1962, 13, 82
- 7 Corrsin, S., "Turbulent Dissipation Correlations", Phys. Fluids, 1962, 5, 1301
- 8 Tennekes, H., "Simple Model for Small-Scale Structure of Turbulence", Phys. Fluids, 1968, 11, 3
- 9 Kuo, A.Y., and Corrsin, S., "Experiments on Internal Intermittancy and Fine-Structure Distribution Function in Fully Turbulent Fluid", J. Fluid Mech., 1971, 50, 285
- 10 Kuo, A.Y., and Corrsin, S., "Experiments on the Geometry of the Fine-Structure Regions in fully Turbulent Fluid", J. Fluid Mech., 1972, 56, 477
- 11 Magnussen, B.F., "Some Features of the Structure of a Mathematical Model of Turbulence, Report, NTH, 1975
- 12 Batchelor, G.K., and Townsend, A.A., "The Nature of Turbulent Motion at large Wave-Numbers", Proc. Roy. Soc., 1949, A 199, 238
- 13 Wygnanski, I. and Piedler, H.J., "Some Measurements in the Self-Preserving Jet", J. Fluid Mech., 1969, 38, 577
- 14 Bradley, D., and Abdel-Gayed, R.G., "A two Eddy Theory of Premixed Turbulent Flame Propagation", Proc. Roy. Soc., 1981, A 1457, 1
- 15 Bradley, D., Chin, S.B., Draper, M.S., and Hankinson, G., 16 Int. Symp. on Comb., 1976, 1571
- 16 Byggstøl, S., and Magnussen, B.F., "Flame Extinction in Turbulent Structure", Task Leaders Conf., IEA, Italy, 1982
- 17 Martenay, P., "Analytical Study of the formation of Nitrogen Oxides in hydrogen air combustion", Comb. Sci. Tech., 1970, 1, 461
- 18 Horch, K., "Zur Stabilität von Freistrahldiffusionsflammen", Ph.D. Thesis, Universität Karlsruhe, FRG, 1978

SESSION 11 - GEOPHYSICAL FLOWS

J.C. André - Chairman

TRANSITION FROM A HORIZONTAL TURBULENT BUOYANT JET TO A MIXING LAYER: AN ENTRAINMENT MODEL

Gerhard H. Jirka
School of Civil and Environmental Engineering
Cornell University
Ithaca, NY 14853

ABSTRACT

An entrainment model for the transition from a horizontal turbulent buoyant jet to a mixing layer is developed using the mean energy equation for closure. The model predicts the reduced entrainment and the mean profile distortion that occur in such motions.

INTRODUCTION

Many geophysical flow situations and engineering applications involve the horizontal inflow of a buoyant fluid into a larger basin at, and parallel to a horizontal boundary. This may be in the form of a light fluid at the surface of water body (e.g. river flows into the ocean) or of heavy fluid at the bottom (e.g. cold air flows or sediment currents). Frequently the initial flow condition is jet-like with intense shearing and turbulence generation. The influence of buoyancy makes itself felt, however, by a gradual damping of the turbulent structure and, in second consequence, an overall modification of the flow geometry. Ultimately, the flow approaches a buoyant mixing layer structure in which the turbulence generation is limited to a thin and continuously contracting shear layer zone while the remainder of the flow approaches shear flow conditions.

This structure is illustrated in Fig. 1 for a two-dimensional flow situation with the upper boundary of the unlimited fluid being slip-like, such as a free water surface. The flow is generated by the steady-state injection of a horizontal momentum flux per unit width m_0 and a buoyancy flux per unit width p_0 adjacent to the bounding surface. Two photographs from laboratory experiments by Rajaratnam and Subramanyan (1983) are

shown in Fig. 2 with a variable initial bulk Richardson number $Ri_0 = 0.037$ and 0.105 , respectively, in which $Ri_0 = p_0 h_0^{3/2} / m_0^{3/2}$ and h_0 is the height of the discharge slot.

A special comment is in order as to the type of equations and boundary conditions governing this two-dimensional flow situation. For small x , the flow is clearly of jet-type and purely upstream controlled. It is supercritical as defined by a bulk densimetric Froude number $F > 1$, in which $F = u (g^* h)^{-1/2}$, u = characteristic velocity, g^* = characteristic buoyancy and h = layer depth and hence can be described by a parabolic equation system in the bulk integrated form. For larger x , however, the finite jet momentum is increasingly opposed by the buoyant pressure force as the layer increases in thickness. Ultimately, therefore, the flow will reach a subcritical regime, $F < 1$. In the sense of classical long wave dynamics - wave length of the order of layer depth h - the flow will then be influenced by the downstream boundary condition as well and is, in fact, of the elliptic type. Several consequences arise at this point: If the domain is unlimited, $x \rightarrow \infty$, there exists no steady-state solution and the downstream flow will increase in thickness due to the effect of interfacial shear. This will lead to jump-like transitions to the upstream regime, until the jet becomes full submerged ("flooded"). Similar conditions may arise for finite, but large, x or if some blocking exists at the downstream boundary. Several devices can be used in practice (see Jirka, 1982) to generate flows that are jump-free and predominantly upstream controlled - although never purely upstream controlled in the sense of the definition diagram, Fig. 1. These are a slight co-flow in the lower layer, a slight slope of the bounding sur-

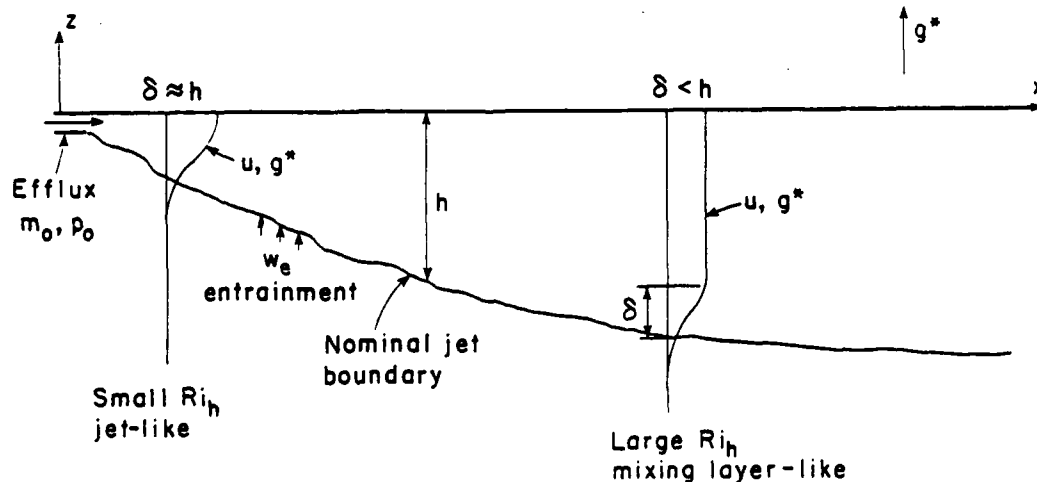
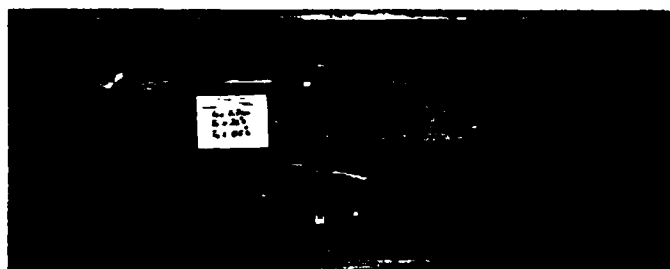


Fig. 1: Definition Diagram.



a) $Ri_0 = 0.037$



b) $Ri_0 = 0.102$

Fig. 2: Horizontal buoyant jet experiments. Jet flow (left to right) is confined to top portion of flume. From Rajaratnam and Subramanyan (1983).

face, a slightly non-conservative buoyancy flux (e.g. heat loss), a gradual expansion or the vicinity of a control section (with suction or release into a wide reservoir).

The entrainment model development given below is directed at an ideal, jump-free and upstream controlled transition from a jet to a mixing layer regime. Its primary purpose is to study the effects of the small wave dynamics - of order of the shear layer depth δ , $\delta \leq h$, see Fig. 1 - on jet entrainment. Although not given here, some of the "non-ideal", second-order effects (e.g. boundary slope) can be incorporated into the model.

MODEL FORMULATION

A turbulent entrainment model for this transition flow is developed using the integral approach for free turbulent motions. An entrainment coefficient α is defined as $\alpha = \frac{1}{u_c} \frac{dq}{dx}$ in which q is the volume flux, u_c the jet or mixing layer centerline velocity and x the horizontal distance. The functional dependence on bulk Richardson number, $\alpha = \alpha(Ri_h)$, is the object of the analysis in which $Ri_h = \frac{g_c^* h}{u_c^2}$ where h is the total jet or layer thickness and g_c^* its centerline buoyancy.

Using the four conservation equations for jet discharge, horizontal momentum, mean kinetic energy and buoyancy flux it is possible to derive the following expression for the entrainment coefficient by the requirement of internal consistency (Jirka, 1982)

$$\alpha = - \frac{2 I_1}{I_3} \frac{\int_0^1 \bar{f}_B df}{(1 + \frac{2 I_2}{I_3} Ri_h)} \quad (1)$$

in which $f(\eta)$ is the non-dimensional velocity profile, varying between zero and unity, $\bar{f}_B(\eta)$ the associated shear stress profile under the influence of buoyancy, η the transverse normalized coordinate and I_1 , I_2 , and I_3 different integral constants. The integral $\int_0^1 \bar{f}_B df$ in Eq. 1 is different from that for the non-buoyant jet ($Ri_h = 0$) because of two simultaneous effects: first, the reduction of the turbulent stress intensity due to the stable buoyancy gradient, and second, the distortion of the jet profile to a uniform profile with an attached

mixing layer (Fig. 1). The first mechanism is a stabilizing one, while the second destabilizes by increasing the value of the gradient Richardson number. The model describes this interplay with the result that for large Ri_h the jet tends to a stable non-entrainment condition without ever completely attaining it.

Reduction of Shear Stress by Buoyancy: Reference is made to the structural kinship between non-buoyant jets and mixing layers, as regards the shape of f (mean velocity) and \bar{f} (turbulent shear stress) profiles for the shear zones, denoted in general by a width δ (see Fig. 1). The numerical value of f , and hence of the resulting integral, is smaller by about 2 for the non-buoyant mixing layer (data of Bradshaw et al., 1964) but this variation is neglected relative to further approximations. Considering then a slightly buoyant jet or mixing layer, it is assumed that the shape of the mean flow profile f is unaffected by buoyancy while the shear stress profile \bar{f}_B is similar in shape to, but differs in magnitude from, the non-buoyant case. Both of these assumptions are well supported by Gartrell's (1979) data. Using the transverse momentum equation and subtracting its non-buoyant counterpart, it can be shown that the transverse Reynolds stress profile may be expressed

$$\bar{f}_B = \bar{f} \left(1 - \frac{Ri_\delta}{Ri_*} \right) \quad (2)$$

where $Ri_\delta = \frac{g_c^* \delta}{u_c^2}$ is the bulk Richardson number of the shear zone alone and $Ri = 1/4$ its theoretical (and experimental) limit value for turbulence damping. The assumptions leading to Eq. 2 are similar to those for rapid-distortion theory (e.g. Townsend, 1976), namely - in the present case - the buoyancy-turbulence interaction is instantaneous while the effect on the mean flow field is delayed. A result similar to Eq. 2 is also inherent in Launder's (1975) algebraic stress equation for buoyancy-turbulence interaction.

Gradual Distortion of Flow Profiles: The ratio Ri_δ/Ri_* in Eq. 2 can also be seen as a ratio δ/δ_* where δ_* is the critical shear layer thickness that, for a given g_c^* and u_c , insures stability. As long as the flow is turbulent the actual shear layer thickness δ is smaller the δ_* , but tends toward it, $\delta \rightarrow \delta_*$. This approach is considered in two asymptotic stages: (i) Initial stage, $\delta_* \geq h > \delta$, i.e. the deviation from the pure jet profile. (ii) Final stage, $h > \delta_* \geq \delta$, i.e. the approach to uniform profile with a thin attached shear layer. In each of these stages an argument similar to the Monin-Obukhov theory in atmospheric boundary layer analysis is used to predict an intensification of the rate of strain of the motion. Algebraic matching between these two limiting cases results in

$$\frac{Ri_\delta}{Ri_*} = \frac{\delta}{\delta_*} = \frac{Ri_h}{(Ri_h^2 + Ri_*^2)^{1/2}} \quad (3)$$

Combining Eqs. 1, 2, and 3 yields the complete entrainment law

$$\alpha = \alpha_0 \left(1 - \frac{Ri_h}{(Ri_h^2 + Ri_*^2)^{1/2}} \right) (1 + Ri_h)^{-1} \quad (4)$$

consisting of three major contributions: (1) $\alpha_0 = (-2I_1/I_3) \int_0^1 f df$ is the entrainment constant for the turbulent non-buoyant jet motion ($\alpha_0 = 0.06$ based on direct volume flux measurements or on the above integration of measured Reynolds stress profiles). (2) The first parenthesis represents the modification by buoyancy of the turbulent structure, i.e. intensity reduction and profile distortion. (3) The second parenthesis represents the additional work against the longitudinal pressure gradient that must be done by the flow and therefore is not available for turbulent entrainment. The overall derivation of Eq. 4 from the mean energy equation is in line with Townsend's (1970) conclusion that the entrainment rate "depends on overall properties of flow, in particular, on those that control the energy balance".

AGREEMENT WITH DATA

Different data sources have been analyzed. Fig. 3 gives a comparison of Eq. 4 with Ellison and Turner's (1959) data, the only detailed experiments on horizontal buoyant jets that include measurement of the mean entrainment rate. Also included in Fig. 3 are related experiments on inclined plumes or horizontal motions in crossflow. The agreement is satisfactory both in trend and magnitude.

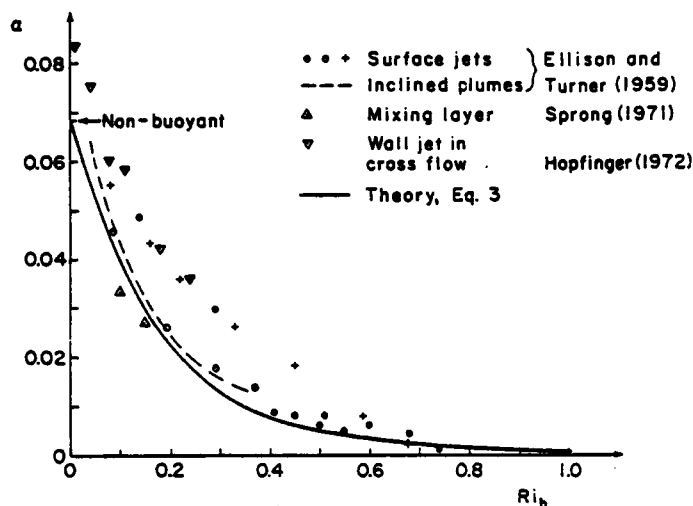


Fig. 3: Entrainment as a function of Richardson number. Comparison of theory and experiments.

The behavior of Eq. 4 in the limiting stages is also of interest: In the initial stage, $Ri_h \ll Ri_* < 1$, one obtains

$$\alpha/\alpha_o = 1 - Ri_h/Ri_* = (1 + 8Ri_h)^{-1/2} \quad (5)$$

with $Ri_* = 1/4$. This is almost identical to Munk and Anderson's (1948) expression for the vertical momentum transfer coefficient in weakly stratified flow if we note the similarity between α and the eddy viscosity. In the final stage, $Ri_h \gg Ri_*$, one obtains

$$\alpha/\alpha_o = \frac{1}{2} \frac{Ri_*^2}{(1 + Ri_h) Ri_h^2} = Ri_h^{-3} \quad (6)$$

On the basis of mean velocity scaling - which is, of course, also implied in Eq. 4 - Price (1979) showed that in the large Ri_h range different types of stress-driven entrainment experiments followed a $Ri_h^{-3/2}$ dependence, obtained as an empirical best-fit. In fact, inspection of Price's (1979; his Fig. 4) summary plot shows that the minus third power dependence, Eq. 6 is in equally good agreement with the data. The latter limit also agrees with recent measurements (Sargent and Jirka, 1982) on entrainment into saline estuary wedges.

Finally, it can be noted that Eq. 3 implies a profile distortion

$$\frac{\delta}{h} = \left(1 + \frac{Ri_h^2}{Ri_*^2}\right)^{-1/2} \quad (7)$$

i.e. the shear layer δ becomes a limited fraction of the total layer depth h . This distortion feature is documented by the measurements of Rajaratnam and Subramanyan (1983) who used the hydrogen bubble method to obtain mean velocity profiles at various jet distances. Their data for $Ri_o = 0.19$ ($F_o = 2.3$) are shown in Fig. 3 and clearly demonstrate the transition from a jet-like profile for short normalized distance $x/(h_o F_o^{4/3})$ to a

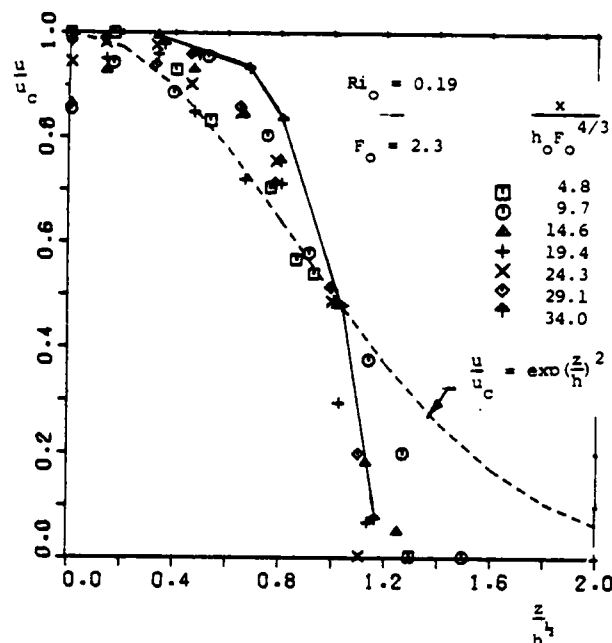


Fig. 4: Observed distortion in velocity profile as a function of distance. After Rajaratnam and Subramanyan (1983).

uniform flow with an attached shear layer for large distances. In particular, the solid line indicates a ratio $\delta/h = 1/4$ which is in agreement with Eq. 7 since at this position the local bulk Richardson number $Ri_h = 1$, i.e. the transition to the mixing layer is largely completed. Similar agreement is found with the limited observations by Wilkinson and Wood (1971) and Stefan (1972).

In summary, an entrainment model is presented that predicts both the reduced entrainment and the mean profile changes that occur as a horizontal jet flow collapses into a buoyant mixing layer. Such transitions are a feature of a wide class of buoyant shear flows and the model appears applicable in these cases. Further extensions of the model, to incorporate such effects as boundary slope and shear into the governing equations, and hence into the entrainment formulation, are under investigation.

ACKNOWLEDGMENTS

Research supported by the U. S. National Science Foundation, Grant No. CME-8012682.

BIBLIOGRAPHY

- Bradshaw, P., Ferriss, D. H. and Johnson, R. F., 1964, "Turbulence in the noise-producing region of a circular jet", *J. Fluid Mech.*, 27, 231-252.
- Gartrell, G. Jr., 1979, "Studies on the Mixing in a Density - Stratified Shear Flow", W. M. Keck Laboratory of Hydraulic and Water Resources, California Institute of Technology, Tech. Rep. No. KH-R-39.
- Jirka, G. H., 1982, "Turbulent Buoyant Jets in Shallow Fluid Layers", in *Turbulent Buoyant Jets and Plumes*, W. Rodi, Ed., Pergamon Press.
- Laundier, B. E., 1975, "On the Effects of a Gravitational Field on the Turbulent Transport of Heat and Momentum", *J. Fluid Mech.*, 67, 569-581.
- Munk, W. H. and Anderson, E. R., 1948, "Notes of a Theory of the Thermocline", *J. Marine Res.*, 7.
- Price, J. F., 1979, "On the Scaling of Stress - Driven Entrainment Experiments", *J. Fluid Mech.*, 90, 509-529.
- Rajaratnam, N. and Subramanyan, S., 1983, "An Experimental Study of Plane Turbulent Buoyant Surface Jets and Jumps", Tech. Report 83-3, Water Resources Engineering, University of Alberta, Edmonton, Alberta.

8. Sargent, F. E. and Jirka, G. H., 1982, "A Comparative Study of Density, Currents and Density Wedges", Tech. Report, School of Civil and Environmental Engineering, Cornell University, Ithaca, New York.
9. Townsend, A. A., 1970, "Entrainment and the Structure of Turbulent Flow", J. Fluid Mech., 41, 13-46.
10. Townsend, A. A., 1976, The Structure of Turbulent Shear Flow, 2nd. Ed., Cambridge University Press.
11. Stefan, H., 1972, "Dilution of Buoyant Two-Dimensional Surface Discharges", J. Hydraulic Div., Proc. ASCE, 98, HY 1.
12. Wilkinson, D. L. and Wood, I. R., 1971, "A rapidly varied flow phenomenon in a two-layer flow", J. Fluid Mech., 47, 241-256.

KATABATIC WIND IN OPPOSING FLOW

David R. Fitzjarrald
National Center for Atmospheric Research*
Boulder, Colorado 80307

*The National Center for Atmospheric Research is sponsored by the National Science Foundation.

ABSTRACT

This paper introduces a one-dimensional model of katabatic winds in opposing flow that includes advection effects and examines the consequences of using empirical laboratory relations to parameterize entrainment.

INTRODUCTION

Two components of mountain-valley wind systems are slope winds driven by radiative cooling on the valley walls at night and a larger-scale outflow down the valley floor. This paper deals only with slope winds, defined here to be local winds that occur on large, homogeneous slopes, along which channelling of the flow by topography is not a dominant influence. In particular, the aim is to examine the derivation of existing one-dimensional models from the shallow fluid equations of motion and to extend them to include cases in which the retarding effect of an opposing ambient wind is strong.

This work resulted from questions raised during a field project conducted by the author in the mountains along the coast of the Gulf of Mexico in Veracruz state, Mexico. A regular katabatic wind occurs in this region in the summer months, but its onset time is in the morning hours, sometimes even after sunrise. The sequence of profiles in Fig. 1 shows that downslope motion begins just after 0533 LST and subsequently thickens until the surface layer becomes unstable by 0800. This is extremely late in comparison with onset times reported at many other places in the world (Atkinson, 1982). Understanding this phenomenon has immediate application in the formulation of schemes to predict the ventilation of and consequent abatement of nocturnal pollutant concentrations in cities located on slopes. Two qualitative explanations come to mind for the late development of the katabatic wind. First, the downslope wind in Veracruz in summer is opposed by regular easterly trade winds; second, one might expect that radiative cooling rates in the humid environment of coastal Mexico to be less than those in midlatitude mountainous areas. Each of these influences would delay the growth of the katabatic wind; the model presented here was made to study their relative importance.

Manins and Sawford (1979a,b) argued that shear-induced entrainment of air into the top of a katabatic layer dominates its mass, momentum, and thermodynamic budgets. In prototype, the flow is one-dimensional with Archimedean accelerations downhill being opposed by entrainment and frictional effects in the uphill direction. It appears that the uncomplicated nature of this prototype makes it especially suitable for comparison with laboratory fluid dynamics experiments.

BULK MODELS OF KATABATIC WINDS

Model Presentation

In this section I generalize the bulk (integrated in the vertical) theory of gravity winds in the boundary layer by adding the effect of an ambient wind.

Ball (1957) found katabatic wind equations through analogy with open channel hydraulics. Ellison and Turner (1959, referred to as ET) showed how the growth of a dense layer flowing down a slope could be understood as an entrainment problem. Their laboratory observations led to an empirical relationship between the entrainment rate and a bulk Richardson number defined by the flow. Their theoretical formulation of the entraining gravity current formed the basis for the subsequent work by Smith (1975) on deep boundary currents in the ocean. Manins and Sawford (1979a, referred to as MS) extended this approach to the atmosphere by including effects of ambient stratification and cooling along the slope. MS created their bulk model by integrating the equations of motion up to a constant reference height. This contrasts in a subtle way from the second method in which the equations are integrated up to a variable height.

Coordinate directions are down a slope inclined at angle α to the horizontal (s direction) and normal to that slope (n direction). Assume that a turbulent boundary layer exists below an inviscid ambient flow, which serves as a reference state. Since observations of Manins and Sawford (1979b) show the gradient Richardson number to be small near the top of the katabatic layer, it is reasonable to concentrate on turbulence generated within the katabatic layer. Additional model assumptions are:

- (a) The incompressible continuity equation holds.
- (b) Flow normal to the slope in an approximate hydrostatic balance. Mahrt (1982) shows that this requires that the aspect ratio of the flow and/or the slope angle be small.
- (c) Coriolis terms are negligible and there is no flow parallel to the slope. Coriolis effects play a role in flows of large horizontal extent at relatively high latitudes if they last long enough (Mahrt, 1982), but here the emphasis is on diurnal development along tropical slopes. Neglecting cross-slope winds eliminates the possibility of modeling terrain channeling effects that sometimes influence katabatic winds (e.g., Manins and Sawford, 1979b).
- (d) Turbulent entrainment into the flow is a function only of bulk Richardson numbers characteristic of the flow.

I write wind components in the boundary layer as $u + u_a$ (down the slope) and $w + w_a$ (normal to the slope), where u and w are relative winds and subscript a denotes an ambient value, and subtract a steady ambient momentum equation from the boundary-layer shallow slope flow solution given by Mahrt (1982).

Bulk models of katabatic winds result from integrating the basic equations from the surface to the top of the boundary layer $h(s,t)$ (as in Zeman, 1982, referred to as Z82), or to a constant height at which the effects of the flow are negligible, H (as in MS). In the former case, I define h to be the level at which the wind speed and temperature are effectively the same as ambient conditions, and turbulent heat and momentum fluxes are negligible. In practice, one can set criteria to define h based on the percentage deviation of a quantity from its ambient value.

One-dimensional models derived by vertical integration of the basic equations described the evolution of average boundary layer properties. The distinction between the two integration methods occurs both in the definition of average properties and in the presence of terms that result from applying Leibnitz' rule. Definitions of these averages (Table 1) are different for the two integration techniques. The pressure gradient force appears in the integrated model as the twice-integrated form (MS, Mahrt, 1982):

$$\int_0^h \text{or } H \int_0^n \left(\frac{g}{\theta_r} d \cos \alpha \right) dn'$$

and related to the bulk scales by definition f), Table 1. Variable d is the deviation of the potential temperature in the katabatic layer from its ambient value. Note that the definition of h in the constant- H integration method results from simultaneous solution of definition a) for U_h and definition b) for U^2h , equivalent to setting momentum and displacement thicknesses equal. In the Leibnitz model, definitions of average quantities are more conventional. With the exception of S_U , the shape factors in Table 1 are normally < 1 in realistic situations, equalling one in well-mixed flow. Here $S_d = 0.8$ and $S_U = 1.4$, values appropriate to the vertical structure given by Prandtl's (1952) solution and let $S_1 = 0.5$ as in MS. The magnitude of these parameters in real atmospheric flows is not yet well established. Additional observations must be made to improve these estimates.

The integrated continuity equation illustrates an important distinction between the two methods. A definition for the growth of the boundary layer top height is (Z82):

$$h_t + u_a h_s = w_a + w_e \quad (2.1)$$

where w_a is the ambient vertical velocity at h and w_e describes the growth of the boundary layer through turbulent entrainment. If the model is made by integrating equation to the constant height H ,

$$w_a = -w_e \quad (2.2)$$

The incompressible flow continuity equation is integrated:

$$\int_0^h (u + u_a)_s dn + \int_0^h (w + w_a)_n dn = 0 \quad (2.3)$$

For integration to variable h , (2.6) and (2.8) sum to produce:

$$h_t + [(U + u_a)h]_s = w_e \quad (2.4)$$

Integration to constant H leads to:

$$(Uh)_t = w_e \quad (2.5)$$

When $u_a = 0$ and at steady state, the continuity equations are identical, but (2.5) is not correct when

u_a is not zero. In the following equations, setting $S_d = S_U = 1$ and omitting underlined terms recovers the formulation of MS. Setting $S_2 = 1$ gives the formulation using the variable height integration. In the well-mixed limit, the left sides of these equations are equivalent to those of Z82. Underlined terms result from use of the Leibnitz rule.

$$(hA)_t + [hA(S_d U + u_a)]_s + U h^2 (\sin \alpha - S_3 E \cos \alpha) - \underline{w_e} \delta_a = \frac{g}{\rho_r c_p \theta_r} [R_H - R_0 - \dot{Q}_0] \equiv B \quad (2.6a)$$

$$(Uh)_t + [Uh(S_U U + u_a)]_s - \underline{w_e} u_a = -\frac{1}{2} (S_1 h \Delta \cos \alpha)_s + S_2 h \Delta \sin \alpha + (\tau_h - \tau_0)/\rho_r \quad (2.6b)$$

where R_H and R_0 are the contribution to the buoyancy deficit hA due to radiative fluxes at h and at the surface; \dot{Q}_0 is the surface layer temperature flux, τ_0 is the surface layer stress, c_p is the specific heat of air at constant pressure and $\delta_a \equiv g/\theta_r$ evaluated at h . The temperature and momentum fluxes and the buoyancy deficit at the upper level are assumed zero. Except in Section 4(a), the definitions of h and H imply that the turbulent stress at boundary layer top, τ_h , is zero. Formally and intuitively, the Leibnitz approach is preferable to the constant H approach, especially when ambient wind effects are being considered. The net effect of cooling along the slope is included in a parameter B , defined in (2.6a), and held constant here.

To close the equations, the boundary fluxes of heat and momentum must be related to the state variables. For steady solutions the model employs a quadratic drag formulation with a constant drag coefficient for the surface stress:

$$\frac{\tau_0}{\rho_r} = u_*^2 = C_D (U + u_a)^2 \text{sign}(U + u_a) \quad (2.7)$$

Manins and Sawford (1979b) suggested that surface stress is not a critical control on katabatic flows.

Entrainment of air with ambient momentum leads to an effective stress in the katabatic layer. Moving the second term on the left in (2.6b) to the right leads to several terms, one of which is $-U[(S_U U + u_a)h]_s$. Using (2.5) and writing $w_e = EU$, this leads to a term $-w_e U = -EU^2$, an effective retarding stress. If one uses the constant- H result (2.5) this stress term is $-E(U + u_a)U$, leading to zero effective stress when $U = -u_a$, a time at which the stress should be large. Thus, rigorous application of the constant H integration leads to a model that is wrong when there is opposing flow. It is interesting to note that ET stated the correct, steady form of (2.4) in their paper, though they gave no derivation.

Bulk models require specification of the entrainment rate of ambient air into the gravity current. Deardorff and Willis (1982) review work that demonstrates that the entrainment rate depends on the velocity jump at the top of the layer and also on the shear stress at a nearby surface. Z82 noted that entrainment formulas presented thus far apply to specific situations and geometries only. He presented an interpolation formula that applies both to convective and stable situations. Deardorff (1983) has made an entrainment formulation that has the correct behavior in certain asymptotic situations. Tennekes and Lumley (1972) indicate that the neutral value of the entrainment rate should be near 0.3 u_* , a limit approached by the Z82 and Deardorff (1983) entrainment relations. Zeman's formula was based on analysis of the mean kinetic energy equation, and entrainment due to shear in the outer of two layers was modeled using an eddy viscosity. This eddy viscosity depends directly on u_* , a feature that makes the Z82 formula inapplicable here. When a wind initially moving uphill reverses as a slope wind develops, u_* passes through zero but shear-induced entrainment may be large at this time. Deardorff's (1983) entrainment

parameterization is based on the density fluctuation and turbulent kinetic energy budgets. This scheme relates the entrainment rate to Richardson numbers based on the convective, stress, and shear velocity scales, respectively. Here, convective effects are ignored and only $R_t = h\Delta/u_*^2$ and $R_i = h\Delta/U^2$ are considered. This parameterization was tuned with the surface jet measurements of ET in the limit where entrainment is dominated by shear-induced turbulence. It provides a smooth way to move from the regime where mixing is dominated by stress effects and to the regime (R_t large, R_i small) where mixing is done primarily by shear-induced effects. Deardorff's relations for entrainment as a function of R_t and R_i are shown in Fig. 2. When R_t is large, as would be the case in the developed katabatic flow, this relation indicates that there is negligible entrainment when $R_i > 0.8$. MS used the form:

$$w_e = EU \quad (2.8a)$$

$$E = \frac{A}{S_1 R_i + K} \quad (2.8b)$$

with A , K , and S_1 chosen to agree with the laboratory data given in ET for inclined plumes. Deardorff's fit was done so that the entrainment at $R_i = 0$ would agree with wall jet values. In this application, the entrainment when $\Delta = 0$ is due to surface stress effects and not to shear effects. When R_t is large, either the MS relation or the Deardorff one agrees satisfactorily with the laboratory results of ET. Since there is a good deal of scatter, new measurements would improve the entrainment estimate. However, only the Deardorff scheme was designed to be in accordance with data at the small R_i, R_t limit. For steady flows R_t will be large, and I present results using the MS method. The MS scheme has the advantage of being analytic. The iterative scheme in Deardorff's method is cumbersome when implemented in the model. Sample comparisons between the two methods are presented later.

It is useful to present the equations in nondimensional form based on a base scaling distance s_r and using the ambient wind to scale velocities. The model equations in nondimensional form are:

$$h_c + [(U + u_a)h]_s = w_e \quad (2.9a)$$

$$(h\Delta)_c + [(S_1 U + \frac{1}{2})h\Delta]_s + C_2(1 - C_3 E)Uh = B \quad (2.9b)$$

$$(Uh)_c + [Uh(S_1 U + \frac{1}{2})]_s - w_e u_a = -\frac{1}{2} C (h^2 \Delta)_s + h\Delta - \tau_0 \quad (2.9c)$$

δ_a in (2.6a) is assumed zero for convenience. Subsequently, dimensional variables will be denoted by the superscript asterisk. This nondimensional form removes the explicit appearance of the slope angle though such dependence is contained in C . One can interpret solutions using either MS scaling or the one based on slope distance and the ambient wind speed. Sample values illustrate the ambient wind scaling: If $|u_a| = 10 \text{ m s}^{-1}$ (uphill), $\alpha = 5^\circ$, and $s_r = 10 \text{ km}$, then the height scale is 200 m, the entrainment scale is 0.02, and a nondimensional cooling rate $B = 0.25$ corresponds to cooling of 2 K h^{-1} over 100 m. The size of the scaling for cooling depends strongly on the ambient wind. If $u_a = 5 \text{ m s}^{-1}$, the nondimensional cooling rate equal to one corresponds to cooling of 1 K h^{-1} over 100 m.

In this paper I set $C_2 = 0$, restricting to neutral stability, or to the situation in which the advective time scale (τ_m) is much shorter than the Brunt-Väisälä period ($\tau_m/\tau_N \ll 1$), and assume that the ambient wind speed is constant. In the scaled equations this means that $u_a = -1, 0, +1$ refers to ambient flow downhill, zero, and uphill, respectively.

STEADY SOLUTIONS

Description of the ultimate steady state the system (2.4) and (2.6) approaches is preliminary to studying

the development time of the katabatic wind. When this time is short, steady solutions are important in their own right. Typically, authors (MS; Mahrt, 1982) classify types of steady solutions based on bulk Richardson or Froude number criteria. With an ambient wind, the shear-based Richardson number is not identical to the Froude number, and the criteria are changed. In this section I discuss general types of steady solutions of (2.11) and show how previous solutions by ET and MS are special cases.

Solutions presented in this section apply only if entrainment is a function of R_i alone, requiring in the Deardorff formulation that R_t be large. Using the steady form of the model equations and the definition of R_i , one can generate an expression for the change of R_i along the slope.

Solutions of the steady equations are degenerate along the line where $\partial R_i / \partial s$ is undeterminate. The degeneracy is often related to a Froude number (Mahrt, 1982), here defined as:

$$Fr = (1 + \frac{u_a^2}{U^2}) R_i^{-1} \quad (3.1)$$

The inverse of this Froude number is the same as the shear-based bulk Richardson number when there is no ambient wind. Recall that Fr compares the interfacial wave speed to the flow speed; R_i determines the amount of entrainment occurring. The degenerate condition forms the boundary between two types of steady flow regimes, called "shooting" and "tranquil" respectively, in analogy with the hydraulic jump Froude number conditions (Ball, 1957; ET). When there is an ambient wind, this condition is:

$$CRI = \frac{2(U/u_a + 2) S_U + u_a/U}{S_\Delta (U/u_a) (S_\Delta U/u_a + 1) + U/u_a} \quad (3.2)$$

When the flow is well-mixed ($S_U = S_\Delta = 1$) and the scaled $u_a = -1$, the critical criterion is:

$$CRI = (1 - \frac{1}{U})^2$$

Steady shooting flows moving downhill ($U > 1$) can occur only for relatively small values of CRI . Shooting flows moving uphill occur only for relatively small values of U .

The quantity in square brackets on the left side of (2.11b) is the buoyancy deficit flux in the katabatic layer. Calling this flux F , and integrating the relation results in:

$$F = [(S_\Delta U + u_a)h\Delta] = B_s + F_0 \quad (3.3)$$

where F_0 is the value of F at the beginning of the slope. When $B = 0$, the flux is constant, and the modeled situation is akin to that in laboratory experiments, where a constant source of heavy salt solution is injected into a fresh-water flow at a point. Because the source of negative buoyancy driving the flow is external to processes on the slope, one may call the $B = 0$ limit, drainage flow. When $F = 0$ and $B \neq 0$, the katabatic wind is produced along the slope and one may call this limit, slope flow. Since the steady equations are three ordinary differential equations, their solutions may be presented in a phase space of three variables. It is convenient here to choose CRI as one axis, constructing a phase space with axes CRI , U , and Uh , the latter known as "discharge" in ordinary hydraulics. Subsequent discussion features the phase plane CRI vs U . For the remainder of this paper I set C to 0.11, corresponding to a 5° slope. The boundary between shooting and tranquil flow (3.2) is shown on the phase plane in Fig. 3. When $u_a = 0$, this boundary is $CRI = S_U$, corresponding to the limit $U/u_a \rightarrow \infty$. Note that the form of the boundary when $u_a \neq 0$ depends on the shape factors. When $S_\Delta < 1$, there are two branches of shooting flow. Shooting flows that move downhill are

restricted for the most part to small values of CRI. An important feature of the solution type boundary when $S_A < 1$ is that steady shooting flows are not allowed near the stagnation point ($U = |u_a|$), reflecting the fact that the flow speed cannot exceed the wave speed if the flow is nearly stagnating. Because the flow speed is smaller than the gravity wave speed, tranquil flows are subject to downstream control. Tranquil flows in an ambient wind are not characterized necessarily by small entrainment and large h , as Mahrt (1982) noted when $u_a = 0$. When the flow stagnates, the Froude number goes to zero, but Ri may still be small enough to allow appreciable entrainment. Lines of constant buoyancy deficit flux (3.3) are also shown on the phase plane. Drainage flows occur along a given isoline; slope flows cross isolines as cooling causes the buoyancy deficit to increase.

Steady Slope Flow with Local Cooling ($B \neq 0$, $u_a \neq 0$).

MS presented analytic solutions of (2.14) for $u_a = C_2 = 0$. Solutions with constant Richardson number along the slope are possible. For $CRI > 1$ ("tranquil flow") they found the steady solutions to be unstable to spatial inhomogeneities. The flow stagnates as the pressure gradient force due to the increasing thickness of the boundary layer balances the downslope Archimedeian force. Entrainment effects are small for tranquil flow situations when $u_a = 0$, shown by MS to refer to flows on slopes of small angles. For $CRI < 1$ ("shooting flow") the solutions are stable. Trajectories of their solutions approach horizontal lines on the phase plane.

When $u_a \neq 0$, constant Ri solutions are not possible. However, if U increases along the slope, (3.2) indicates that in an ambient wind the solution approaches the slope Ri found by MS when $u_a = 0$, but this limit may occur very far down the slope. Pure slope flow ($F = 0$) is only possible if $Ri \rightarrow 0$ as $s \rightarrow 0$. Trajectories of steady solutions for constant ambient wind uphill (scaled $u_a = -1$) are shown in Fig. 4 for given initial conditions and several values of the bulk cooling rate, B . Examples A and E in Fig. 4 refer to flows in motion at the top of a slope. At some distance along a slope, cooling causes deceleration that makes all uphill-moving solutions critical (Example A). Example E describes a downhill-moving flow for which entrainment effects cause deceleration going down the slope. The flow has too much momentum initially, but it approaches the equilibrium solution for flow with no initial momentum in one distance scale. This is an example of combined drainage and slope flow. One easily can integrate the steady equations given an initial buoyancy deficit flux at some part of the slope, but these examples describe layers that have momentum as they enter or leave the slope. I discuss types of steady solutions the flow approaches starting from a neutral state when one specifies only the slope and a cooling rate (Examples B, C, and D) below.

TRANSIENT SOLUTIONS

Now I consider transient solutions to address the questions:

- (1) How long does it take for the katabatic wind to develop in opposing flow?
- (2) Under what circumstances do advective effects dominate the solutions?
- (3) What type of steady solutions evolve from an initially neutral upslope flow subjected to cooling?

It is convenient to rewrite (2.13) in advective form:

$$h_t + (U + u_a)h_s = w_e - hU_s \quad (4.1a)$$

$$\Delta_t + \frac{(S_A U + u_a) \Delta_s}{\{B + w_e(\delta_a - \Delta) + \Delta[(1 - S_A)Uh]_s\}/h} \quad (4.1b)$$

$$U_t + \frac{(S_A U + u_a) U_s}{\Delta + \tau_h/h - (C_D/E_M)(U + u_a)^2/h - \frac{1}{2} Ch \delta_a - c h \delta_s + \{w_e(u_a - U) + U[(1 - S_A)Uh]_s\}/h} \quad (4.1c)$$

where underlined terms contain derivatives.

Constant Thickness Transient Solutions Along a Homogeneous Slope

If h is constant, (4.1a) indicates that there is no entrainment. To model the stress effect of ambient winds on the momentum balance in the katabatic layer, we must consider the tangential stress at h , τ_h . This stress is zero according to the definition of h used in all other sections of this paper. However, if h cannot vary, one can expect some turbulence at that level, and hence, a nonzero τ_h . Mahrt (1982) has also suggested that not all stress effects in the katabatic layer need be associated with mass entrainment. I write $\tau_h = \epsilon U^2$, with ϵ being a general momentum exchange coefficient, and also replace the surface drag coefficient C_D/E_M in (4.1) with ϵ , a simplification introduced to facilitate an analytical solution of a simple model that has basic properties of opposed katabatic flow. Underlined terms in (4.1) drop out by the homogeneity assumption and (4.1a) becomes $\Delta = (B/h)t$, assuming that $\Delta = 0$ at the initial moment. The momentum equation (4.1c) reduces to:

$$U_t = (B/h)t - (\epsilon/h)(U + u_a)^2 \text{sign}(U + u_a) - (\epsilon/h)U^2 \quad (4.2)$$

This simplified model now resembles the layer model of A (Defant 1933, in F. Defant, 1949). Consider a situation with ambient wind uphill ($u_a < 0$) with $U(t=0) = u_a/2$ corresponding to an initial steady state. Define t_f to be the time required for the flow to stagnate ($U + u_a = 0$), a lower estimate for the onset time for the katabatic wind. If $\epsilon = 0$,

$$t_f = (-u_a h/B)^{1/2}$$

For a 5 degree slope (see Table 2) with $u_a = -10 \text{ ms}^{-1}$, $h = 100 \text{ m}$, and $B = 2.5 \times 10^{-3} \text{ m}^2 \text{ s}^{-3}$, t_f^* is about 20 minutes, consistent with the observation that the onset occurs shortly after sunset if ambient wind stress effects are small. If $\epsilon \neq 0$, t_f is determined by the solution of

$$t_f - \exp[2u_a(\epsilon/h)t] + [2u_a(\epsilon/h)]^{-1} - u_a^2(\epsilon/h)(B/h)^{-1} = 0 \quad (4.3)$$

When $t_f \gg [2u_a(\epsilon/h)]^{-1}$, the asymptotic solution is

$$t_f = u_a^2(\epsilon/h)(B/h)^{-1} - [2u_a(\epsilon/h)]^{-1} \quad (4.4)$$

Solutions of (4.3) and (4.4) plotted on the B/h versus ϵ/h plane in Fig. 4 indicate that if $\epsilon/h > 0.5$, (4.4) is a good approximation. Only small relative cooling rates combined with a large stress coefficient can result in large values of t_f .

If $h^* = 50 \text{ m}$, $u_a^* = -5 \text{ m}$, and $B^* = 5 \times 10^{-4} \text{ m}^2 \text{ s}^{-3}$ (0.5 K h^{-1} over 100 m), the stagnation time t_f^* can reach 5.5 hours with stress coefficient $\epsilon^* = 3.6 \times 10^{-2}$, more than a hundred times larger than the value (3×10^{-4}) assumed for the surface bulk drag coefficient.

Transient Solutions with Entrainment Along a Homogeneous Slope

When h is constant, Fig. 4 gives the conditions needed to produce large values to t_f , but gives no indication how to choose the stress coefficient ϵ . Can such large stress effects at h result from the entrainment described in the laboratory experiments of ET? Return to the previous definition for h , i.e., the level at which $\sigma = 0$ and temperature fluxes vanish, allow entrainment, and retain the assumption of homogeneity along the slope. I solved the model, now (4.1a,b,c), omitting the underlined terms, as a standard set of ordinary differential equations, assuming $\Delta(0) = 0$, $h(0) = 0.3$, and $U(0)$ to be the small value determined by requiring the initial momentum balance to be steady.

Note that shape factors are irrelevant in this case and that information about the slope angle enters only through the entrainment scaling parameter, E_M . Solutions for t_f as a function of B (Fig. 9) indicate: (1) that the Deardorff entrainment method gives only slightly larger values than the MS method, and (2) that for $B < 0.2$, t_f can be quite large. The reciprocal relation between t_f and B found for the constant h case (4.4) continues to hold.

In dimensional terms, $t^* = s_r/u_a$ and $B^* = u_a^3$. Thus, increasing u_a at constant cooling rate makes nondimensional B small, making t_f potentially large. For the 5 degree slope case in Table 2, $B = 0.8$, corresponding to a cooling rate of 2 K h^{-1} over 100 m when $u_a^* = -5 \text{ m s}^{-1}$, leads to $t_f^* = 1.1$ hours, but if $u_a^* = -10 \text{ m s}^{-1}$, the same cooling rate leads to $B = 0.1$ with $t_f^* = 2.8$ hours.

Transient Solutions with Entrainment and Advection

Advection of lower momentum from uphill establishes the balance that determines the steady solutions discussed earlier, indicating that conditions at the top of the slope are important to the final steady solution all along the slope. Transient solutions with no advective effects do not approach a steady state. Solutions that include both effects presented in this section allow one to determine when and where each effect is most important. The model used is now (4.1a,b,c) including all terms.

The system of model equations is hyperbolic, and in principle may be solved by the method of characteristics. Because of the presence of the pressure gradient term due to the changing depth of the flow, the characteristics are not simply described by the respective advection velocities for each variable. (Note that when the shape factors are different from one, the advection velocities are different for U , h , and Δ). I solved (4.1) in finite-difference form, using the positive-definite advection scheme with small implicit diffusion described by Smolarkiewicz (1983).

The initial conditions for all model calculations presented below are $h = 0.3$, $U = 0.05$, and $\Delta = 0$. This value of U makes the flow steady initially with a balance between the pressure gradient force that drives the uniform ambient velocity and surface stress that results from assuming that the drag coefficient C_D is 3×10^{-4} . Although this initial value of h is necessarily arbitrary, it is small compared to solutions that develop after several time units. Since $\Delta = 0$ at the start, the time referred to may be compared to the time after sunset in the actual situation.

Results found using the two alternative entrainment parameterizations discussed earlier indicate that the main difference between the solutions is that the total effect of entrainment using the Deardorff form is larger than when using the MS form. This must occur through enhanced entrainment in the early stages of the integration, since R_T is quite large near the end. Subsequent results presented use the MS entrainment form. Development times for the katabatic wind would be slightly larger if the Deardorff method were used.

As the cooling rate B is increased, the modeled wind reverses direction more quickly. Contours of the variable magnitudes on time-slope distance diagrams illustrate the dependence of the solutions on B . For $U + u_a$ (Fig. 7) trajectories of the flow in time are analogous, but not identical, to familiar plots of solution characteristics for hyperbolic equations. Plots of h and Δ are shown in Fig. 8. The trajectory of the mean wind in all of these plots is a straight line whose slope is -1 .

Along the slope, contours of a variable are horizontal if local effects determine the solution and vertical if advective effects dominate, as in the steady state. Models of homogeneous slopes are limited to the

period in which the contours are approximately horizontal. The speed with which information about the top of the slope progresses down the slope, defined here arbitrarily as the time at which the contours of $U + u_a$ are at 45° , is approximately 3.5, 3, and 2 units of u_a for B equal to 0.5, 1, and 2, respectively. The solutions after ten time units are plotted on the phase plane in Fig. 5 (Cases B, C, and D). Note that the equilibrium being approached in each case is tranquil, and that solutions fall nearly along the same line.

Three time characteristics of the katabatic wind may be defined using the model solutions: (1) the time t_1 required for the flow to reverse and begin to move downhill (identified by the zero contour of $U + u_a$), (2) the time t_2 required for the flow to reach approximate equilibrium (when all variable contours are approximately vertical), and (3) the time t_3 required for a parcel originally moving uphill to return to its original starting point (when the trajectory crosses the original s). The time t_3 is relevant to the problem of predicting pollutant concentration on the slope. The same air returns to pass over a source some hours later when motions parallel to the slope are not important, though concentrations might be reduced because of boundary layer growth in the interim. For example, with $B = 0.5$, a parcel initially at $s = 1.9$ returns there about ten time units later and the flow speed is very small along the slope above the point. On a 5° slope 20 km long with an opposing ambient wind of 5 m s^{-1} , a dimensionless cooling rate 0.5 corresponds to cooling of 1 K h^{-1} over 100 m , a reasonable estimate for the situation in Veracruz mentioned in Section 1. Since the time unit is about 1.1 hours, a delay in the onset of downslope motion of 4 to 8 hours caused by the retarding effect of the ambient wind is predicted by the model, in rough agreement with observations. Presumably, the variation of onset time could be related to variation in ambient wind strength. As the cooling rate is increased, as might be expected in midlatitudes, the reversal would occur very quickly.

Reversal time t_1 is a strong function of the cooling rate. With the large cooling rate $B = 2$, reversal occurs at points along the slope for $s > 0.5$ is less than one time period. For $B = 0.5$, the flow does not reverse for $s < 0.5$ even after ten time units, and for $s > 0.5$ reversal occurs after three to ten time units.

The equilibrium adjustment time t_2 , from 4 to 8 time units (see Fig. 8), is smaller for h and U than for Δ . As the cooling rate increases, the adjustment toward the advectively determined steady solution occurs more rapidly, and the Δ gradient becomes concentrated near the top of the slope.

CONCLUSIONS

The katabatic wind model presented here is consistent with previous work in the limits of opposing ambient flow with no cooling along the slope (Ellison and Turner, 1959), no ambient wind with cooling along a slope (Manin and Sawford, 1979a), and homogeneously mixed heavy layers on a horizontal plane (Zeman, 1982). The development of a more general one-dimensional model of katabatic winds in opposing flow indicates that it is preferable to integrate equations of shallow fluid flow on a slope to a variable height, where terms from application of Leibnitz' rule enter, than to integrate to a fixed height.

Steady solutions in opposing flow divide naturally into shooting (supercritical) and tranquil (subcritical) flows depending on a Froude number (or bulk Richardson number) condition, as is the case when there is no ambient flow, but tranquil flows can be characterized by appreciable entrainment. Katabatic winds resulting from cooling along the slope, defined here as slope flows, are tranquil.

If entrainment into katabatic winds behaves as it does in inclined laboratory gravity currents, model results indicate that the katabatic wind onset time is

very sensitive to the retarding effect of opposing flow as well as to the cooling rate on the slope. The thickness of the katabatic layer that grows against opposing flow should be seen to increase steadily even though boundary-layer wind speeds do not change appreciably. Another qualitative feature predicted here is that temperatures along the slope should go to a minimum and increase toward a somewhat warmer value later (see Fig. 8), as initial local cooling is overcome by entrainment and advective effects, and ultimately approaches a cooler steady value.

ACKNOWLEDGEMENTS

This work was done during an Advanced Study Program Fellowship at the National Center for Atmospheric Research. Many people offered valuable suggestions; those of James Drake and Dale Durran were particularly useful. Special thanks go to Piotr Smolarkiewicz, who offered patient explanations of numerical methods and help in implementing his advection scheme. Ursula Rosner did an excellent job typing several early drafts and the final version. Jo Ann Fankhauser also helped in preparing early drafts.

REFERENCES

- Atkinson, B. W., 1981: Meso-scale Atmospheric Circulations, Academic Press, 495 p.
- Ball, F. K., 1956: The theory of strong katabatic winds. Aust. J. Phys., 9, 373-386.
- Barry, R. G., 1981: Mountain Weather and Climate, Methuen, 313 p.
- Deardorff, J. W., 1983: A multi-limit mixed-layer entrainment formulation. Submitted to J. Phys. Oceanogr.
- and G. E. Willis, 1982: Dependence of mixed-layer entrainment on shear stress and velocity jump, J. Fluid Mech., 155, 123-149.
- Defant, F., 1949: Zur Theorie der Hangwinde, nebst Bemerkungen zur Theorie der Berg- und Talwinde, Arch. Meteor. Geophys. Bioklim., A1, 421-450.
- , 1951: Local winds, Compendium of Meteorology, T. F. Malone, Ed., Amer. Meteor. Soc., 665-672.
- Ellison, T. H., and J. S. Turner, 1959: Turbulent entrainment in stratified flows. J. Fluid Mech., 6, 423-448.
- Henderson, F. M., 1966: Open Channel Flow, Macmillan, 522 p.
- Mahrt, L., 1982: Momentum balance of gravity flows, J. Atmos. Sci., 39, 2701-2711.
- Manins, P. C., and B. L. Sawford, 1979a: A model of katabatic winds, J. Atmos. Sci., 36, 619-630.
- and —, 1979b: Katabatic winds: a field case study, Quart. J. R. Met. Soc., 105, 1011-1025.
- Prandtl, L., 1952: Essentials of Fluid Dynamics, Hafner, 452 p.
- Smith, P. C., 1975: A streamtube model for bottom boundary currents in the ocean, Deep-Sea Res., 22, 853-873.
- Smolarkiewicz, P. K., 1983: A simple positive definite advection scheme with small implicit diffusion. Accepted for publication in Mo. Wea. Rev., March 1983.
- Tennekes, H., 1973: A model for the dynamics of the inversion above a convective boundary, J. Atmos. Sci., 30, 558-567.
- and J. L. Lumley, 1972: A First Course in Turbulence, The MIT Press, Cambridge, MA.
- Zeman, O., 1979: Parameterization of the dynamics of stable boundary layers and nocturnal jets, J. Atmos. Sci., 36, 1974-1988.
- , 1982: The dynamics and modeling of heavier-than-air cold gas releases, Atmos. Env., 16, 741-751.
- Fig. 2 Entrainment rate as function of Ri for values of R_τ . (A) $R_\tau = 10^{-2}$, (B) $R_\tau = 1$, (C) $R_\tau = 10^2$. (D) $R_\tau = 10^2$.
- Fig. 3 Phase plane Cri vs. relative speed U . Note that $U > 1$ refers to downhill motion. Solid lines divide tranquil flows (above and to the right) from shooting flows. Lines of constant buoyancy deficit flux are dashed: (A) -0.0625, (B) -0.0833, (C) -0.125, (D) -0.25, (E) 1, (F) 1.33, (G) 2, (H) 4.
- Fig. 4 Solutions plotted on the phase plane. Letters indicate conditions at the top of the slope: (A) Uphill-moving shooting flow (dotted), B = 0.10; transient solutions at $t = 10$ (Section 4); (B) B = 0.5; (C) B = 1.0; (D) B = 2.0. (E) Steady shooting flow moving downhill, B = 1.0 (dotted).
- Fig. 5 Contours of the time t_f required for flow initially neutral and moving uphill to reverse as a function of the stress coefficient c and the cooling rate B. Boundary-layer thickness h is constant for this model. Dashed lines give solutions of approximation (4.4). All values are dimensionless.
- Fig. 6 The relation between t_f , the time for flow initially neutral and moving uphill at equilibrium to reverse, and B, the boundary-layer cooling rate. The solid curve was found using (2.12); the dashed line was found using the Deardorff entrainment parameterization.
- Fig. 7 Contours of $U + u_z$ plotted on the time-slope distance plane. Dashed contours indicate negative values. Solid lines with arrows indicate sample trajectories. Cooling rates are (a) B = 0.5, (b) B = 1.0, (c) B = 2.0.
- Fig. 8 Contours of h and Δ plotted on the time-slope distance plane: (a) h , B = 0.5; (b) Δ , B = 0.5; (c) h , B = 1.0; (d) Δ , B = 1.0; (e) h , B = 2.0; (f) Δ , B = 2.0.

Table 1
Definitions of Average Quantities and Shape Factors

Concept & Method	Leibnitz Method (h Variable)
(a) $U_h = \frac{1}{h} \int_0^h u(s, n, t) dn$	(g) $U_h = \frac{1}{h} \int_0^h u(s, n, t) dn$
(b) $U^2_h = \frac{1}{h} \int_0^h u^2(s, n, t) dn$	(h) $S_U U^2_h = \frac{1}{h} \int_0^h u^2(s, n, t) dn$
(c) $U_h \Delta_h = \frac{1}{h} \int_0^h u \delta dn$	(i) $S_U U_h \Delta_h = \frac{1}{h} \int_0^h u \delta dn$
where $\delta = \frac{1}{U_h} (\theta(s, n, t) - \theta_{v0})$	(j) $h \Delta_h = \frac{1}{h} \int_0^h \delta dn$
(d) $S_{U_h} = \frac{1}{h} \int_0^h \delta dn$	
(e) $u(h) h - S_{U_h} = \frac{1}{h} \int_0^h u dn$	
(f) $\frac{1}{2} S_U h^2 \Delta_h = \frac{1}{h} \int_0^h \int_0^h \delta dn \int_0^h \delta dn$	

Note all $S_i \leq 1$ except $S_U \geq 1$.

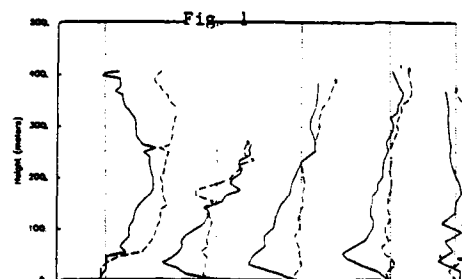


FIGURE CAPTIONS

Fig. 1 Wind profiles on 23 July 1980 at times (LST). Ticks on the ordinate represent units of 100 m altitude. (1) 0533; (2) 0621; (3) 0643; (4) 0707; (5) 0805. The components parallel to and normal to the fall lines are shown by solid and dashed lines respectively. A thin dashed line indicates zero speed.

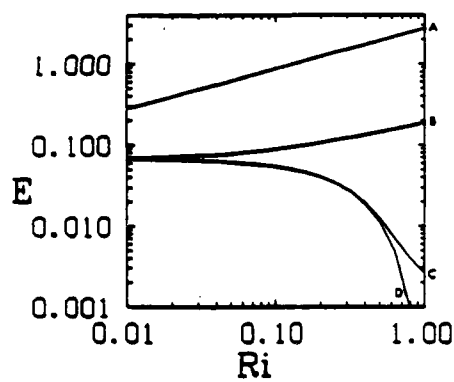


Fig. 2

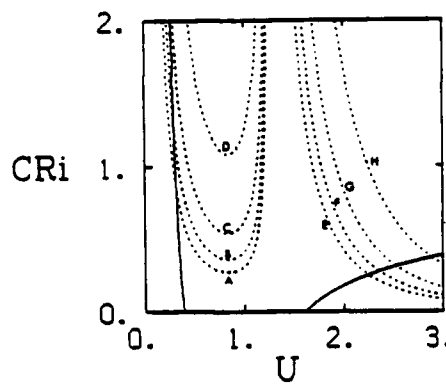


Fig. 3

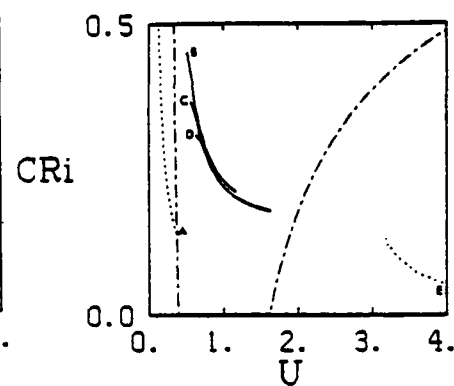


Fig. 4

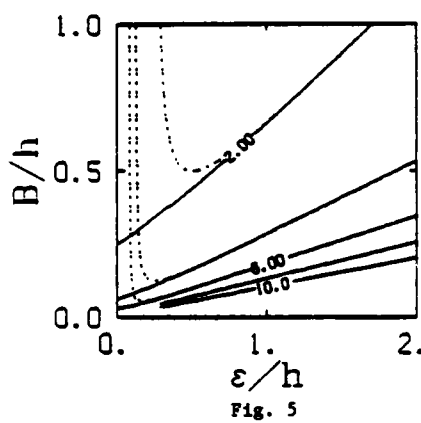


Fig. 5

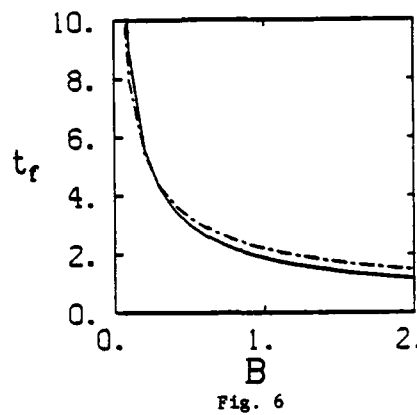


Fig. 6

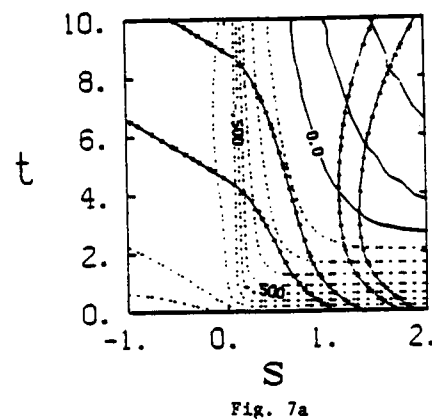


Fig. 7a

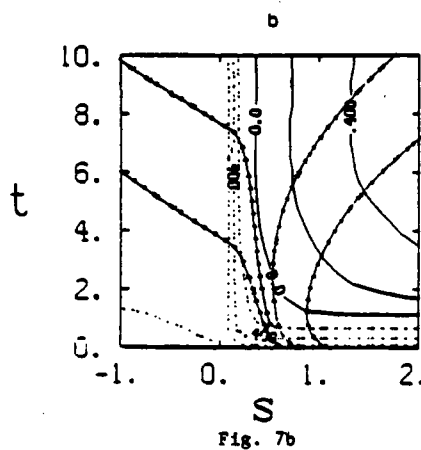


Fig. 7b

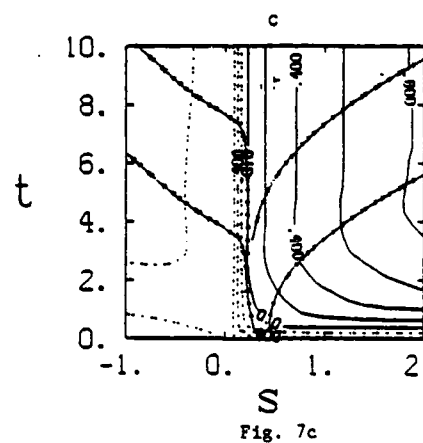


Fig. 7c

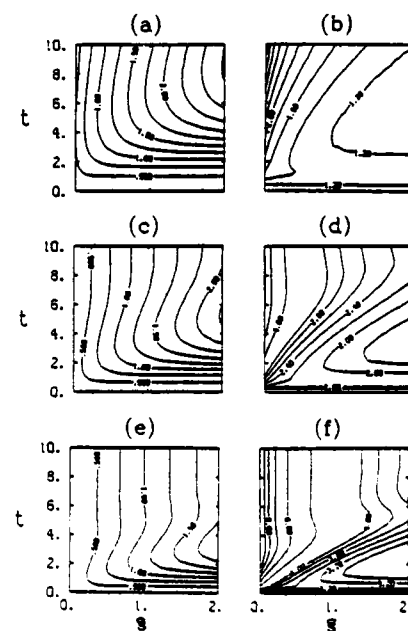


Fig. 8

TURBULENCE STRUCTURE IN STRATIFIED TURBULENT SHEAR FLOW HORIZONTALLY DISCHARGED AT WATER SURFACE

A. Murota and K. Nakatsuji

Department of Civil Engineering
Osaka University, Suita City
Osaka 565, Japan.

ABSTRACT

Characteristics and hydraulic roles of the large scale quasi-ordered structure observed in the initial development of the buoyant surface discharge were investigated by means of detailed measurements of density and streamwise and vertical velocity fluctuations. The cross sectional averages of turbulent energy and volume flux are evaluated by integrating the mean kinetic energy equation and the continuity equation respectively, and then, streamwise variations of turbulent energy balance and an entrainment velocity are examined. It becomes clear that the quasi-ordered structures evolution and their active coalescence process is the essential mechanism of the energy production and entrainment, by which the shear layer grows. The stratification due to the density difference controls the development of the quasi-ordered structure and reduces the vertical movement of fluid and the Reynolds stress production. The shear layer width is dependent of a characteristic length scale determined by the buoyancy force.

NOMENCLATURE

B	mean buoyancy = $(\rho_a - \rho)/\rho_a g$
b	buoyancy fluctuation
$-\overline{bv}$	buoyancy flux in vertical direction
f	frequency
f_v	frequency of vortex passing
g	gravitational acceleration
H	local jet width
h	maximum slope thickness
L_b	local buoyancy length scale = U^2/B
P_y	power spectra of vertical velocity fluctuation
q^2	turbulent kinetic energy = $(u^2 + v^2)/2$
Ri	overall Richardson number
Ruv	cross correlation coefficients = $-\overline{uv}/\sqrt{u^2 v^2}$
U	mean flow velocity in streamwise direction
U_c	convection velocity in streamwise direction
u	velocity fluctuation in streamwise direction
$-\overline{uv}$	mean Reynolds stress
V_e	entrainment velocity across stratified interface
v	velocity fluctuation in vertical direction
x	streamwise coordinate
z	vertical coordinate
$\sqrt{\quad}$	root mean square value
δ	turbulent shear layer length scale
ϵ	dissipation rate of turbulent kinetic energy
θ	momentum thickness
ν	kinematic viscosity of fluid
ρ	density
τ	time parameter

Subscripts

a	ambient fluid
o	outlet
s	water surface
j	jet width

INTRODUCTION

Shearing flow in a stratified fluid is commonly observed in oceans and atmosphere, of which typical examples in engineering are disposal of waste water, thermal discharge from power plants, etc. Therefore, substantial works have been done on the behaviors of the discharging water, the entrainment reduction, and development of schemes predicting the concentration and temperature fields caused by such discharges into environment. The works, however, have been less fruitful in making clear the dynamics of entrainment and the mechanism of turbulent transport under the influence of stratification. Very scant reliable data have been accumulated on the turbulence structure.

If a stable stratification is introduced into a turbulent field, the vertical motion of fluid is suppressed due to the buoyancy force. This results in the reduction of the Reynolds stress and may cause the decay of turbulence and the diminution of the vertical exchange of momentum, heat or substances. Therefore, the fluid motion in the stratified shear flow is supposed to remarkably differ from the motion in a homogeneous shear flow even under the same boundary conditions.

When the energy production rate by shear is larger than the removal rate of the energy by the buoyancy force, the entrainment and intense mixing take place across the stratified interface. On the contrary, when the buoyancy force is dominant, the gravitational stability is superior to the turbulent production, resulting in the more stable stratification. Holmboe (1962) and Hazel (1972) have theoretically analyzed the temporal instability in such a system, and Browand and Winant (1972), Thorpe (1973) and Koop and Browand (1979) experimentally investigated the spatial growth characteristics of disturbances. They concluded that (1) the turbulence in the shear flow can not be maintained in the presence of even very slight amount of stratification, and (2) the critical initial Richardson number is 0.08 - 0.125 and the turbulence structure is expected to change drastically at this critical value. There exist two distinct modes of instability depending on the degree of stratification; (a) an active turbulent Rayleigh mode that is characterized by the presence of the large scale quasi-ordered vortical structures very familiar in homogeneous flows and (b) a small scale Holmboe mode in which no roll-up occurs and breaking is less violent because of the strong stratification.

According to many recent researches on various turbulent shear flows since Brown and Roshko (1974), the coalescence of adjacent vortical structures is believed to be the fundamental mechanism governing the shear-layer growth. The entrainment of fluid into the turbulent shear layer is, of course, controlled by the quasi-ordered vortical structures. Quantitative information about the structure in the stratified shear flow has been obtained by some researchers such as Perry and Hoffman (1976), and Rajagopalan and Antonia (1981) mainly by means of conditional sampling and averaging

techniques. In spite of significant previous studies, questions still remain, i.e. how this quasi-ordered structure is affected by the stratification and how it correlates with the turbulent transport process.

Recently, the authors (1983) presented flow-visualization of the large scale quasi-ordered vortical structure behaviors, and provided quantitative information on their evolution and interactions in the initial developing region of the two-dimensional buoyant surface jet.

The main purpose of this paper is to present more comprehensive results relating to the vortical structure evolution under the stratification and to specify its hydraulic roles on the shear-layer growth and decay process by means of measurements of density and stream-wise and vertical velocity fluctuations.

EXPERIMENTAL ARRANGEMENT AND DATA PROCESSING

The experiments were carried out in a rectangular straight flume of 600 cm long, 15 cm wide and 50 cm deep made of lucid acrylic plate. The flume was equipped with a horizontally located guide plate to supply smoothly fresh water at an outlet and a valve to supply salt water into the lower layer. Fresh water was discharged horizontally at the water surface into the flume initially filled up with salt water. Through all the experiments, salt water was fed into the lower layer in proportion to an entrained volume and a weir height at the downstream end of the flume was skillfully adjusted in order to keep a steady state of the buoyant surface jet.

All measurements were made at a free-stream velocity U_0 of 10 cm/s and the outlet depth H_0 was about 2 cm at the outlet. The density difference between the discharging and the ambient fluid is varied in four steps; 0.0, 0.0013, 0.0050 and 0.0100 g/cm³. Therefore, the initial Richardson number, Ri_0 , based on the maximum slope thickness is in the range from 0.004 to 0.059 depending on the density difference.

Measurements of fluctuating velocities and density were made with a X-type film probe operated at a constant temperature anemometer (KANOMAX 21-1312) and a platinum black coated platinum wire operated with a hand-made salino-meter, respectively. The spanwise separation of two probes was 1.2 cm. The output signals from both instruments were stored in a data recorder (TEAC R-210) and were converted to digital signals (TEAC DR-2100A) of 3000 samples with a frequency of 100 Hz. The digitized data were processed with a computer ACOS-S1000 at Data Processing Center of Osaka University. The Cl⁻-concentration-density calibration curve was then used for calculation of the actual fluctuating density ρ and the buoyancy fluctuations $b = (\rho_a - \rho)/\rho_a g$, in which ρ_a is the ambient fluid density.

Data were collected at 14 x-stations in the range of 110 cm downstream from the outlet, and at various vertical depths from 12 to 16 inside the buoyant discharges in each station.

The flow was also made visible by fluorescent dye-cloud injected on the lower side of the shear layer near the outlet through a needle of an injector. Brilliant dye-cloud was recorded photographically with a high-speed 16 mm cine camera (PHOTO-SONIC).

FLOW-VISUALIZATION

The evolution of the large scale quasi-ordered structure is roughly divided into four stages: (1) the shear layer instability, (2) the initial nonlinear rolling-up, (3) the mutual interaction of neighbouring vortices, and (4) the breakdown. The shear layer growth in the very early stage (1) is predicted theoretically and experimentally by the linear instability theory. The mechanism of nonlinear-predominating stages (2) and (3) cannot but lean on the help of experiments because of difficulties containing in analysis. Besides, these stages are of great importance to the shear-layer growth.

Photos 1 and 2 show the characteristic vortical motion observed in the shear layer of the buoyant surface jet of $Ri_0 = 0.017$, in which typical, but infrequently occurring events of organization are recognized. Partial fractions slightly tinged with black represent the fluorescent dye-cloud illuminated by the thin slot light.

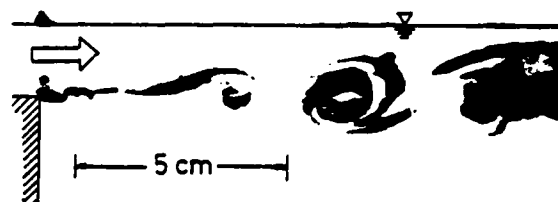


Photo 1. Rolling-up of quasi-ordered structure.

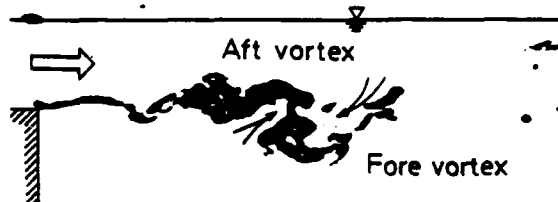


Photo 2. Coalescence of neighbouring structures.

Small disturbances, which characterize the linear instability stage, are evident on the left-hand side of Photo 1. After two or three wavelengths, the dye marking the fluid with vorticity becomes concentrated into a periodic train in discrete vortical structures and it rolls the low-speed heavier fluid up in the high-speed lighter fluid accompanied with its growing. These large scale structures are observed to be two-dimensional. In the breakdown of these rolling-up structures, the intense mixing between both fluids takes place. The similar phenomenon is observed in homogeneous shear flows. In the stratified case, an additional vorticity is generated by the buoyancy force, which opposes the growth of such structures. As a result, although there is also an initial growth stage, vortical lumps soon collapse. Both types of the structures are easily distinguished visually.

Photo 2 demonstrates that the large scale structures are continually rotating around one another in pairs and merge into a single larger structure. During this coalescence process, the low-speed heavier fluid is entrained or digested by the engulfment of the fluid entrapped between the fore and aft structures. This process is observed to occur repeatedly, controlling the growth and overall characteristics of the shear layer.

VORTEX EVOLUTION UNDER THE INFLUENCE OF STRATIFICATION

There are two analyses in clarifying quantitatively evolution of the quasi-ordered vortical structure. One is a Lagrangian method to trace the identifiable vortex paths on a space-time diagram from aligned displays of cine-film frame sequences. The other is an Eulerian point measuring of velocities and density fluctuations.

Experimental results on the basis of the former method was reported in the latest authors' paper (1983). An example is presented in Fig. 1. It shows the variation

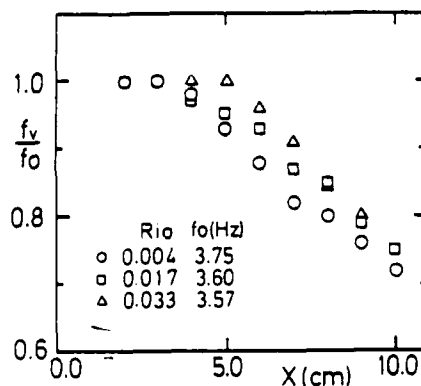


Fig. 1. Frequency of individual vortical structure passages as a function of downstream position.

of an individual vortex passage frequency, f_v/f_0 with distance, in which f_0 represents the occurring frequency of the vortical structure. The passage frequency was calculated as a reciprocal of an average period at each selected downstream position with the distance 1 cm, which was obtained from the trajectories of about two hundred structures. The value of f_v/f_0 has an inclination to decrease with distance. Since the decrease of f_v/f_0 might be caused by the above-mentioned coalescence of neighbouring structures, its degree can be roughly considered as an occurrence rate of the coalescence. It is evident that about twenty five percents of the occurring structures disappear even in the range of $x < 10$ cm. It requires that half the structures should be participated in the coalescence process; so that the movements of fluid is conjectured to be under the influence of strong nonlinear interactions. In the case of the larger Richardson number, its rate is slightly small. This means that the stratification suppresses the evolution and the coalescence of the vortical structures.

Figures 2 and 3 show the variations of power spectra and cross-correlation coefficients of velocity fluctuations in order to elucidate the dynamic features of the vortex evolution. The measuring points are the depth in which the value of the Reynolds stress is maximum at each downstream position. The vertical velocity fluctuations were adopted in evaluating the power spectra. This is due to the reason that movements of the vortical structure are well reflected in them, and this fact appears evidently in the vertical convection velocity variation of the adjacent structures undergoing coalescence as pointed out by the authors (1983) and Acton's simulation (1976) of the vortex evolution.

In Fig. 2, the spectra of $Ri_0 = 0.004$ and 0.033 are included for comparison. The structure originated near the point of $x = 1.5$ cm begin to be affected by nonlinear interactions with distance. The spectra at $x = 4$ cm indicates predominant double peaks in both cases. Further-downstream, double peaks are absorbed into a lower frequency peak at $x = 8$ cm. It is worthy to note that its frequency agrees precisely with half the occurrence frequency. This means that the first round of coalescence would take place in the range of $x < 8$ cm. In the region downstream, the coalescence occurs so repeatedly that the peak frequency shifts gradually to the lower frequency range and that the ratio of energy containing in the lower frequency range to the total energy becomes increasing. Its tendency is quite inconsistent with the cascade of energy from the largest, energy extracting scales to the smallest, dissipating scales.

Judging from the variations of power spectra, the coalescence comes to an end at the range of $x < 50$ cm for $Ri_0 = 0.004$, and $x < 35$ cm for $Ri_0 = 0.033$. When normalized by an initial momentum thickness at the outlet, the value of x/δ_0 is less than almost 280 for both cases. This range is shorter than the value of $x/\delta_0 \approx 1000$, obtained at the homogeneous mixing layer by Bradshaw (1966). It is obvious from this fact that the quasi-ordered structures would soon break down by the influence of stratification. After breakdown, peaks observed in the power spectra disappears, shifting to a perfect turbulent state followed by the $-5/3$ power laws.

This tendency is also recognized in the nondimensional cross-correlation coefficients between streamwise and vertical velocity fluctuations, Ruv . Figure 3 is a case of $Ri_0 = 0.004$. In the range of $x = 4 \sim 10$ cm, the value of Ruv changes little with downstream distance, i.e., $Ruv(0) = -0.58$, thus indicating highly correlated u - and v -fluctuations. In addition, respective auto-correlation coefficients are significantly similar in this range. It indicates the fluid motion to be fairly quasi-ordered. The coefficients Ruv , however, decreases with increase of the distance from the outlet.

Next, in order to clarify the influence of stratification on the shear-layer development, characteristic length scales are examined. They are a local buoyancy length scale, $L_b = U^2/B$, and a turbulent shear layer length, δ . In this case, five times of the characteristic integral length scale determined by a buoyancy profile is adopted as the turbulent shear layer length, $\delta = 5\delta_b$, because it agrees well with the observed shear layer thickness. Figure 4 shows the ratio of these length

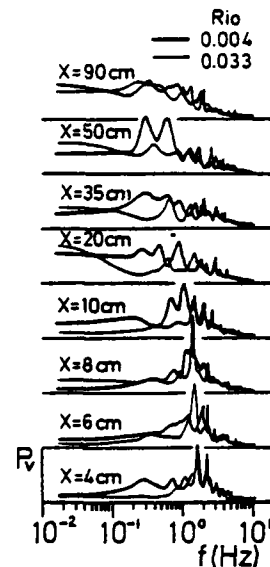


Fig. 2. Variation of power spectra of vertical velocity fluctuations ($Ri_0 = 0.004$ and 0.033).

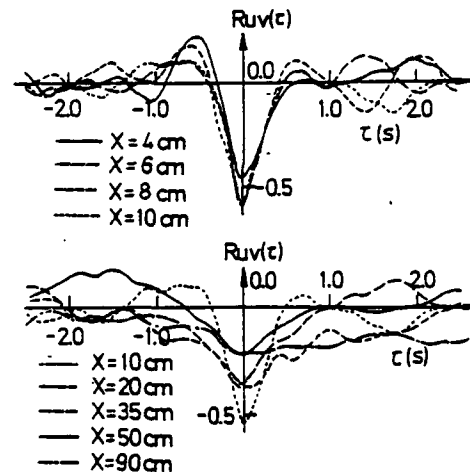


Fig. 3. Cross-correlation coefficients between streamwise and vertical velocities as a function of downstream position ($Ri_0 = 0.004$).

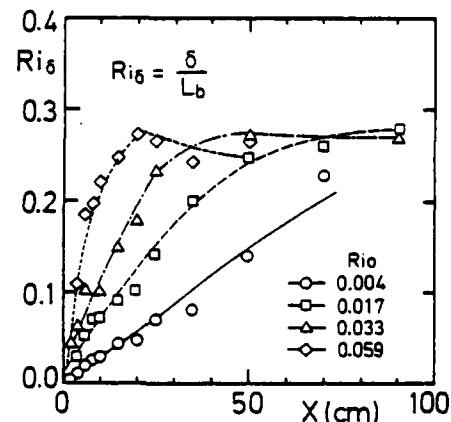


Fig. 4. Variation of shear layer Richardson number with downstream distance.

scales, δ/L_b . It can be put in the following form;

$$\delta/L_b = B\delta/U^2 = Ri_\delta \quad (1)$$

Then, it also represents the local shear layer Richardson number.

The value of Ri_δ is monotonously increasing with downstream distance from an initial value of Ri_0 to the final maximum value of 0.28. This means that the turbulent shear layer length scale finally approaches to the equilibrium value against the local buoyancy length scale; that is, the former is dependent of the latter. The maximum shear layer Richardson number is comparatively consistent with the data of Koop and Browand or Thorpe considering different definition of δ . Their result is 0.32 ± 0.02 for $Ri_0 < 0.1$. Since an increase in Ri_δ indicates that the stratification due to the buoyancy force is predominant to the inertia force, the shear layer spreading $d\delta/dx$ decreases gradually associated with a distance from the outlet and with increase in Ri_δ . Therefore, the higher the initial Richardson number, the shorter is the distance. The buoyant surface jet clearly lacks self-similarity as the value of Ri_δ approaches to the maximum.

TURBULENT INTENSITIES AND REYNOLDS STRESS

Figure 5 shows the maximum values of the rms velocity and buoyancy fluctuations at each downstream position for several values of the initial Richardson number, which are normalized by the time-mean streamwise velocity and buoyancy at the outlet. The effect of the vortex evolution on the turbulent intensities is clearly produced in the initial development region, and in the far downstream region of $x > 8 \sim 10$ cm there is no longer a definite effect of vortical structures. In general, the turbulent intensities reach their maximums at nearly $x = 8$ cm and then sharply fall off downstream. The variation curve for $\sqrt{b^2}/B_0$ is larger than the corresponding curves for $\sqrt{u^2}/U_0$ and $\sqrt{v^2}/U_0$, but these variations resemble each other quantitatively and qualitatively. The data of Koop and Browand (1979) differ from the present data for $\sqrt{b^2}/B_0$ and $\sqrt{u^2}/U_0$ in the far downstream region, whose data collapse to a single curve provided for $Ri_0 < 0.125$.

If examined in detail, the maximum values for each intensity increase with decrease of the initial Richardson number. This means that the variation of turbulent fluctuations would be systematically influenced by the stratification even in the region where the quasi-ordered structures are predominant. Furthermore, beyond the point of maximum shear layer Richardson number, the buoyancy fluctuations intensities show a decay of proportional to $x^{-3/4}$. This rate of decay coincides with that of scalar quantities in the isotropic grid turbulence as measured by Lin and Pao (1979) and in the stratified shear flow by Koop and Browand (1979).

The similar tendency is not seen for the velocity fluctuations. In particular, the magnitude of $\sqrt{v^2}$ changes depending on the initial Richardson number. Then, the ratio of the intensities of vertical and streamwise velocity fluctuations in the form ($\sqrt{v^2}/\sqrt{u^2}$) is presented in Fig. 6. The measuring point is a depth of maximum Reynolds stress for each downstream position. In general, $\sqrt{v^2}/\sqrt{u^2}$ increases sharply at around $x = 8$ cm. After once decreasing, it reaches a maximum near at $x = 50 \sim 90$ cm. The first peak is intensely connected with the vortex evolution in the initial development. It confirms the authors' flow-visualization results that the mutual interactions and coalescence of the quasi-ordered structures give rise to the vertical motion of fluid. And, the second peak corresponds to the region where the stratification due to the buoyancy force begins predominating. In that region the production of u' is reduced, and then, the value of $\sqrt{v^2}/\sqrt{u^2}$ becomes larger, since the vertical gradients of streamwise velocity profiles become smaller and the behavior of Reynolds stress fluctuations is suppressed by the stratification.

The distributions of Reynolds stress at each downstream position is shown in Fig. 7 for two different initial Richardson numbers. As the quasi-ordered structures are brought up in the initial development region, the Reynolds stress are also seen to increase rapidly

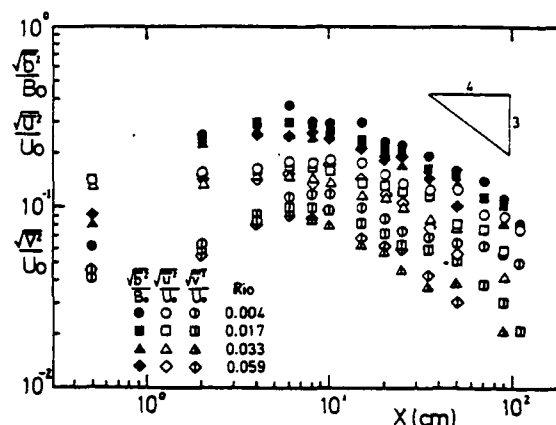


Fig. 5. Variation of turbulent intensities of buoyancy and velocity fluctuations, $\sqrt{b^2}/B_0$, $\sqrt{u^2}/U_0$ and $\sqrt{v^2}/U_0$.

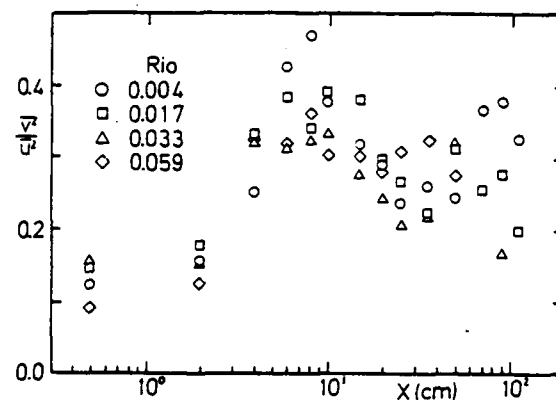


Fig. 6. Variation of anisotropy between streamwise and vertical velocity fluctuations, $\sqrt{v^2}/\sqrt{u^2}$.

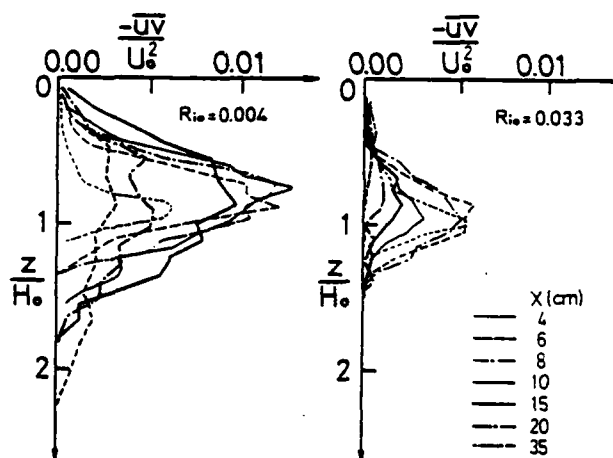


Fig. 7. Distributions of Reynolds stress $-\overline{uv}$ as a function of downstream position.

and to spread over the shear layer width. However, in the far downstream region of $x > 15$ cm, the Reynolds stress gradually decreases, although it continues to spread within the layer. The depth, in which the Reynolds stress is maximum, is about $x/H_0 = 0.8 \sim 0.9$, which changes little in streamwise direction. It can be seen that the magnitude of $-\overline{uv}$ for $Ri_0 = 0.004$ is about half the value for $Ri_0 = 0.033$. This comparison reveals that the Reynolds stress reduction would be directly caused by the stratification due to the buoyancy force.

ROLES OF QUASI-ORDERED STRUCTURES

Conditional sampling and averaging methods have been used by many researchers for obtaining the quantitative properties of the quasi-ordered structures in various shear flows. Although the distributions of the Reynolds stress, turbulent buoyancy fluxes, etc. can be resolved within the educed structure in detail by applying this methods, it is difficult to evaluate quantitatively the effect of the quasi-ordered structure upon the shear layer development or the relationship between the quasi-ordered structure's evolution and the stratification. Therefore, in this section the flow properties integrated across the cross section for each downstream position will be discussed.

TURBULENT ENERGY BALANCE

If integrated the turbulent energy equation across the jet width considering two boundary conditions ($V = 0$ and $v = 0$ at $z = 0$, $V = -Ve$, $q^2 = 0$ and $p = 0$ at $z = H_j$), the diffusion and the pressure terms integrated are canceled, and then, cross-sectional averages of turbulent energy are computed from the following equation;

$$\begin{aligned} \frac{\partial}{\partial x} \int_0^{H_j} U \bar{q}^2 dz & - \int_0^{H_j} [-\overline{uv} \frac{\partial U}{\partial z}] dz - \int_0^{H_j} [-\overline{bv}] dz \\ \text{Convection} \quad \text{Shear-production} \quad \text{Buoyancy-production} \\ + \int_0^{H_j} \epsilon dz & = 0 \quad (2) \\ \text{Dissipation} \end{aligned}$$

where $\bar{q}^2/2 = \bar{u}^2 + 2\bar{v}^2$ and $\epsilon = \nu (\partial u_i / \partial x_j \partial u_i / \partial x_j)$. The convection term is approximately represented by

$$U_c \partial \left[\int_0^{H_j} \bar{q}^2 dz \right] / \partial x, \quad (3)$$

making use of the flow visualization result that the turbulent energy \bar{q}^2 could be transported by the quasi-ordered structure with a convection velocity of $U_c = 0.56 U_0$. Then, the convection term and the production terms due to both shear and buoyancy can be directly computed from the measured profiles. The remaining dissipation term could be estimated as the residual of the turbulent energy equation.

In Fig. 8 the variation of the integrated turbulent energy balance is presented, normalized by U_0^3 . The energy production due to the buoyancy force is not included in this figure, since three order smaller compared with another terms. It is apparent that the energy production due to the shear force rapidly increases accompanied with increasing the Reynolds stress in a range of $x < 6-8$ cm, and that almost all of them are transformed to the kinetic energy. In the far downstream region, the production gradually decreases with downstream distance, which bears proportion to the dissipation. That is to say, since the produced energy is almost digested by the viscosity dissipation, the turbulent energy balance is estimated to be well proportioned. The energy production comes to an end at $x \approx 70$ cm for $Ri_0 = 0.004$ and at $x \approx 35$ cm for $Ri_0 = 0.033$. It is interesting to note that these positions correspond to the terminal position in which the active coalescence of the quasi-ordered structures is over, from a judgement of the power spectra changes as shown in Fig. 2. These facts clarify that the energy production is closely related to the vitalities of the large scale quasi-ordered structures. This result is also supported by the fact that the amount of energy production becomes larger in the case of smaller initial Richardson numbers. It can be seen from Fig. 1 that the coalescence frequently occurs in such cases.

From the facts described above, we may conclude that the buoyancy effect contributes to the reduction of the Reynolds stress or the diminution of energy production due to the shear force in the manner that the stratification due to the buoyancy force controls the evolution and coalescence process of the large scale quasi-ordered structures.

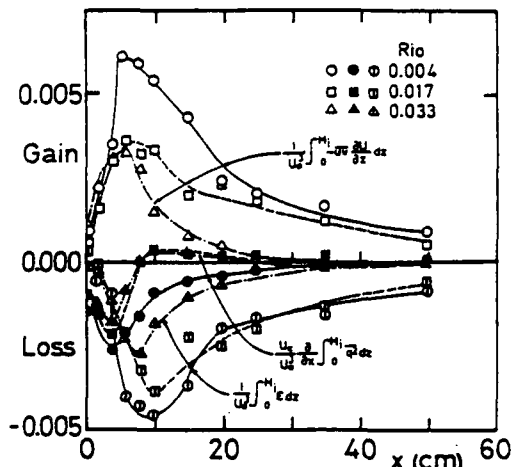


Fig. 8. Variation of energy balance cross-sectionally integrated at each downstream position.

ENTRAINMENT VELOCITY

Entrainment is commonly understood as the process of mass transport across an interface between two adjacent flowing fluids with different densities. The entrainment volume transport is named the entrainment velocity, because it has the same dimension as velocity, the volume passing across unit area in unit time. Therefore, the degree of mixture is determined by the magnitude of the entrainment velocity. The entrainment is estimated by integrating the continuity equation across the jet width in the following form;

$$Ve(x) = \frac{\partial}{\partial x} \int_0^{H_j} U(x, z) dz \quad (4)$$

in which $V = 0$ at $z = 0$, and $V = -Ve$ at $z = H_j$. That is to say, it represents the rate of volume flux integrated across the cross section in streamwise direction and can be easily evaluated by use of the measured profiles of $U(x, z)$.

Figure 9 shows the variation of the entrainment velocity normalized by U_0 . In the initial development region ($x < 10$ cm), the value of Ve/U_0 is to be larger than 0.02 for $Ri_0 = 0.004$ and 0.017, and larger than 0.01 for $Ri_0 = 0.033$. This means that the intense mass transport from a heavier and lower velocity fluid to the turbulent higher velocity one would take place in this region. Moreover, the position in which Ve/U_0 approaches to zero is about 70 cm and 35 cm respectively. This distance from the outlet is equivalent to the disappearance point of the quasi-ordered structures' coalescence mentioned above. Then, the entrainment of ambient fluid, in other words, the spread of turbulent fluid is conjectured to be closely related to movements of the quasi-ordered structure.

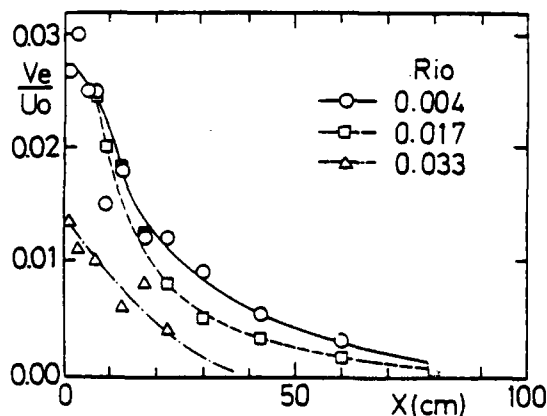


Fig. 9. Variation of entrainment velocity.

The effect of stratification on the entrainment phenomena at the interface can be estimated by evaluating the Richardson number based on the local structure of the turbulence, such as the intensity and scales of velocity and buoyancy distributions. The detailed experiments on buoyant surface jets have been attempted by many researchers. Among of them are well known Ellison and Turner (1959) and Chu and Vanvari (1976), who used differently defined characteristic scales in estimating the Richardson number. There is considerably discrepancy between their data, even though the different definitions are taken account. The results of the present study agree very well with those of Ellison and Turner, when compared with three data in respective formulation. Since Chu and Vanvari's definition is based on the self-preserving hypothesis, their data show considerably smaller entrainment rates. Their definition is not suitable for a larger initial Richardson number in which the motion of fluid changes from a jet-like flow to a stratified flow.

Then, the relationship between the entrainment velocity Ve/U_s and the local shear layer Richardson number Ri_h is presented in Fig. 10, in which U_s and B_s are the surface velocity and buoyancy respectively at each downstream position, and $Ri_h = B_s h / U_s^2$ based on the maximum slope thickness $h = U_s / (\partial U / \partial z)_{max}$. The data in this figure are a little scattered compared with Ellison and Turner's data. It is also clear that the slope of an approximate curve changes distinctly at $Ri_h = 0.12$; that is, while Ve/U_s rapidly decreases with increasing Ri_h in the range of $Ri_h < 0.12$, the decreasing rate of Ve/U_s is very small in the range of $Ri_h > 0.12$. Although opinions are so varied, the value of $Ri_h = 0.08 \sim 0.15$ is critical bounds whether the coalescence of the large quasi-ordered structures could take place or not. It is reported that the dispersive internal waves are predominant in the range of $Ri_h > 0.15$. In the former the coalescence between the quasi-ordered structures causes intense engulfing and digesting of the ambient fluid into the turbulent one. On the other hand, in the latter the breaking of internal waves is substantial in the mixing process. Therefore, both regions could be named the shear layer type and the internal wave type, respectively, because of their turbulence origin.

CONCLUSION

The following conclusions can be drawn from this study;

- (1) The coalescence of the adjacent quasi-ordered structures results in not only enlargement of their sizes but also amalgamation of energy.
- (2) Although turbulent intensities rapidly increase through the coalescence, the growth of turbulence is soon suppressed as the stratification due to density difference proves fruitful. The maximum shear layer thickness is dependent on the characteristic length scale determined by the buoyancy.
- (3) As the magnitude of the Reynolds stress is remarkably influenced by the stratification, the variation of the cross-sectionally integrated turbulent energy balance was evaluated. This result makes clear that the overall shear layer characteristics such as energy production, entrainment and spread of turbulent region are closely related to the evolution and coalescence of the large scale quasi-ordered structures.
- (4) The relationship between the entrainment velocity and the shear layer Richardson number reveals that the Ri_h is very important factor to define the shear layer type and the internal wave type and that its critical value is $Ri_h = 0.12$.

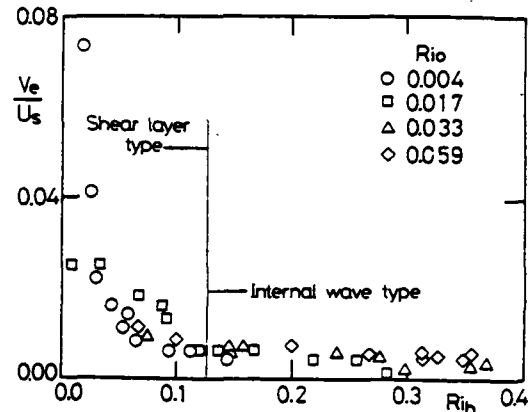


Fig. 10. Nondimensionalized entrainment velocity plotted against shear layer Richardson number.

ACKNOWLEDGEMENT

The authors are grateful to Mr. T. Togami (a graduate student) for his assistance in this work.

REFERENCES

- Acton, E. 1976 The modelling of large eddies in a two-dimensional shear layer. *J. Fluid Mech.* 76, 561.
- Bradshaw, P. 1966 The effect of initial conditions on the development of a free shear layer. *J. Fluid Mech.* 26, 225.
- Browand, F.K. and Winant, C.D. 1973 Laboratory observations of shear-layer instability in a stratified fluid. *Boundary Layer Met.* 5, 67.
- Brown, G.L. and Rosko, A. 1974 On density effects and large structure in turbulent mixing layer. *J. Fluid Mech.* 64, 775.
- Chu, V.H. and Vanvari, M.R. 1976 Experimental study of turbulent stratified shearing flow. *J. ASCE.* 102, HY6, 691.
- Ellison, T.H. and Turner, J.S. 1959 Turbulent entrainment in stratified flows. *J. Fluid Mech.* 6, 423.
- Hazel, P.G. 1972 Numerical studies of the stability of inviscid stratified shear flows. *J. Fluid Mech.* 51, 39.
- Holmboe, J. 1962 On the behaviors of symmetric waves in stratified shear layers. *Geophys. Publ.* 24, 67.
- Koop, C.G. and Browand, F.K. 1979 Instability and turbulence in a stratified fluid with shear. *J. Fluid Mech.* 93, 135.
- Lin, J.T. and Pao, Y.H. 1979 Wakes in stratified fluids. *Ann. Rev. Fluid Mech.* 11, 317.
- Murota, A. and Nakatsuji, K. 1983 A flow-visualization study on vortex evolution in the initial development of two-dimensional buoyant surface jet. XX Congress of IAHR Cal4.
- Perry, A.E. and Hoffman, P.H. 1976 An experimental study of turbulent convective heat transfer. *J. Fluid Mech.* 77, 355.
- Rajagopalan, S. and Antonia, R.A. 1981 Properties of the large structure in a slightly heated turbulent mixing layer of a plane jet. *J. Fluid Mech.* 105, 261.
- Thorpe, S.A. 1966 Experiments on instability and turbulence in a stratified shear flow. *J. Fluid Mech.* 61, 731.

ELLIPTICAL TURBULENCE IN THE ATMOSPHERE

D. Schertzer, S. Lovejoy

Météorologie Nationale

EERM/CRMD

2 Ave. Rapp,

Paris, 75007,

FRANCE

ABSTRACT

We present a new scheme of atmospheric turbulence: small scales structures are continuously flattened at larger and larger scales. This continuous deformation may be characterised by defining an "elliptical dimension" D_{el} . We show both theoretically and empirically that $D_{el} = 23/9 \approx 2.56$. Atmospheric motions are therefore never "flat" ($D_{el}=2$), nor isotropic ($D_{el}=3$).

Intermittency, in the context of this "elliptical turbulence" is discussed: dimension of the support of turbulence and divergence of higher statistical moments of the different fields.

INTRODUCTION

The classical scheme of atmospheric motions (e.g. Monin (1972)), considers the large scale as two-dimensional, and the small scale as three-dimensional, a transition named, for obvious reasons, a "dimensional transition" by Schertzer and Lovejoy (1983), is expected to occur in the meso-scale, possibly in association with a "meso-scale gap" (Van der Hoven (1957)).

This scheme favours the simplistic idea that at planetary scales the atmosphere look like a thin envelope, whereas at human scales, it looks more like an isotropic volume.

A dimensional transition, if it were to occur, would be likely to have fairly drastic consequences because of the significant qualitative difference of turbulence in two and three dimensions (Fjortoft (1953), Kraichnan (1967), Batchelor (1969)): the all important stretching and folding of vortex tubes, in three dimensions, cannot occurs in two dimension.

Since the 50's, there has been a wide debate over the effective dimension of atmospheric turbulence, due in particular to the extension of two-dimensional results to the case of quasi-geostrophy (Charney (1971), Herring (1980)).

Although, a dimensional transition should be readily observable, experiments over the last 15 years have failed to detect it (Pinus (1968), Vinnechenko (1969), Morel and Larchevêque (1974), Macpherson and Issac (1977), Gage (1979), Gilet et Al. (1980), Lovejoy (1982), Larsen et Al. (1982), Lilly and Peterson (1983), Nostrum and Gage (1983)). There is a large body of evidence consistent with a uniform scaling on the horizontal up to, at least 1500 km.

Schertzer and Lovejoy (1983) have examined the different theoretical ideas underlying these experimental results. They pointed out that the prevalence of this uniform scaling should be connected with the fact that many non-linear equations do not introduce a characteristic length, and thus admit scaling solu-

tions.

In principle, this scaling could be broken either by non-scaling boundary conditions or a non-scaling forcing. However, Mandelbrot (1982) has found evidence that the topography is scaling up to planetary scales, and different analyses (Gautier (1982-personnal communication), Lovejoy (1982), Schertzer and Simonin (1982), and Simonin (1982)) of the sources and sinks of diabatic heating indicate also a scaling behaviour.

Because of the non-linear coupling between the different meteorological fields, the existence of a characteristic length scale in one, is likely to manifest itself in the others. It is therefore likely that over a given range all fields are scaling.

We may add that our current understanding of intermittency (e.g. Batchelor (1969) or Curry et Al. (1982)) as the frequent transitions between quiescence and chaos lead us to doubt the existence of a well-defined transition (such as the "meso-scale gap").

THE VERTICAL STRUCTURE

Perhaps the most serious objection to the hypothesis of a scaling behaviour of atmospheric motions arises from the special role of the vertical axis. Indeed, there has been a deluge of papers based on non-scaling techniques which reject implicitly a priori any possibility of vertical scaling (e.g. "one point closures"). In what follows, it will be apparent that this rejection has had unfortunate consequences.

The vertical direction plays a key role for the following reasons:

- i) The gravity field defines a direction at every point.
- ii) The atmosphere is globally stratified.
- iii) It has a well defined thickness (exponential decrease of the mean pressure).
- iv) The fundamental sources of disturbances are the vertical shear and the buoyancy force (e.g. the Kelvin-Helmoltz instability).

In the following, we examine the possibility that the atmosphere is in fact scaling in the vertical as well as in the horizontal direction. To do so, we examine the wind and temperature fields, attempting to capture two basic and conceptually distinct properties of these fields:

Scaling: The scaling relation relates the fluctuations ΔX of a field X for large scales $\lambda \Delta z$ ($\lambda \gg 1$) to the small scales Δz by:

$$X(\lambda \Delta z) \stackrel{d}{=} \lambda^H \Delta X(\Delta z)$$

where H is the scaling parameter and " $\stackrel{d}{=}$ " means equality in probability distributions. Note that the exponent of the corresponding power spectrum ($-\beta$) is related to H by $\beta = 2H + 1$, in the case of finite variance.

Intermittency: This is directly connected with the probability law. One is particularly interested in the tail of this law, since it controls the relative frequency of the extreme (intermittent) behaviour. For instance, if the distribution has an algebraic fall-off at large fluctuations, then the degree of intermittency can be characterised by the exponent α (the hyperbolicity):

$$\Pr(\Delta X' > \Delta X) \sim \Delta X^{-\alpha}; \quad \Delta X \gg 1$$

where "Pr" denotes "probability".

This kind of distributions have been invoked in other fields of physics (e.g. "Holtmark distribution", Feller (1971), see Mandelbrot (1982) for other examples), and are usually called "hyperbolic distributions". Behaviour of this sort was predicted for the non-linear flux of energy in turbulence according to a phenomenological model of intermittency (Mandelbrot (1974)).

Note that, in the case of hyperbolic distributions, all moments of order α or higher diverge, a fact that has important consequences. Levy (1937) and Feller (1971) are standard texts, in the case $\alpha < 2$, (cf. the Levy-stable laws which form a convolution semi-group).

We shall primarily be interested in the vertical fluctuations of the horizontal velocity field (dv) and in the buoyancy force per unit mass acting across a layer of thickness dz : $df = g d \ln \Theta$, where Θ is the potential temperature, and g the acceleration of gravity. These quantities are related to two fundamental frequencies: that of the vertical shear (s) and the Brunt-Vaisala frequency (n):

$$s = dv/dz \text{ and } n^2 = g d \ln \Theta / dz = df/dz$$

The ratio of the squares of these frequencies defines the dimensionless Richardson number:

$$Ri = n^2 / s^2$$

The shear frequency characterises the dynamical processes, and the Brunt-Vaisala frequency, the stability (and gravity waves). The dominant process has the highest frequency. To determine their scaling regime, Fourier analysis could be used. Here, we analyse directly the scaling of the probability law by measuring quantities across atmospheric layers of thickness Δz . This has the advantage that it enables the scaling parameters (H 's) and the hyperbolicities (α 's) to be obtained simultaneously. We therefore define:

$$s^2(\Delta z) = v^2(\Delta z) / \Delta z^2; \quad n^2(\Delta z) = g \Delta \ln \Theta(\Delta z) / \Delta z$$

$$Ri(\Delta z) = n^2(\Delta z) / s^2(\Delta z)$$

DATA ANALYSIS

S , n , Ri were evaluated from the high resolution radiosonde data obtained in the 1975 experiment in Landes, France. Θ , v and the humidity were obtained every second ($\sim 3m$ in the vertical) and processed to yield low noise data every 5s (15-20m, see Tardieu (1979) for more details). All estimates of n , s , Ri were made over layers at least 50m thick, and from the ground up to the arbitrary height of 6km. The data examined are from 80 soundings taken at 3 hour intervals at Landes.

From the Log-Log plots shown in Fig. 1, 2, 3 it can easily be verified that the probability distributions of Δv , Δf and Ri exhibit both scaling and hyperbolic behaviour. The easiest way to see this, is to recall that for hyperbolic distributions:

$$\Pr(\Delta X' > \Delta X) \sim (\Delta X / \Delta X^*)^{-\alpha_X}$$

ΔX^* is the "width" of the distribution, or the amplitude of the fluctuations. Scaling implies then that the width grows with the separation as:

$$\Delta X^*(\Delta z) \sim \Delta z^H$$

this is observed by the constant shift $H \log 2$ for each

doubling of the separation Δz . The value ($- \alpha$) is the slope of the straight line asymptote.

We obtain:

$$\begin{array}{ll} H_v \approx 3/5 & \alpha_v \approx 5 \\ H_{\ln \Theta} \approx 9/10 & \alpha_{\ln \Theta} \approx 10/3 \\ H_{Ri} \approx 1 & \alpha_{Ri} \approx 1 \end{array}$$

The H 's and α 's are given rational expressions, since, as explained below, they can often be deduced by dimensional considerations.

Another quantity of interest is the flux of non-linear transfer of energy (ϵ). This is the fundamental dynamical quantity in a turbulent cascade of energy from large to small scales. We obtained a probability distribution by reploting Merceret's aircraft data. The result, see Fig. 4, leads to:

$$\Pr(\bar{\epsilon}' > \bar{\epsilon}) \sim \bar{\epsilon}^{-5/3} \quad \alpha_{\bar{\epsilon}} \approx 5/3$$

Merceret (1976) obtained his value of $\bar{\epsilon}$ by calculating averaged spectrum of horizontal wind fluctuations every second ($\sim 100m$).

We assume this average to have been taken over an horizontal straight line (the bar notation indicates a one dimensional spatial average).

THE TURBULENT RICHARDSON NUMBER

The fluctuations of the Richardson number are very large, since $\alpha_{Ri} \approx 1$, even its mean may not converge (if $\alpha_{Ri} < 1$). This fact seems to have been recognised since a long time if one considers the series of "modified" Richardson numbers (based on the ratio of two statistics and not the ratio of the random variables s and n), for instance the Richardson of flux R_f .

The erratic nature of Ri is directly related to the phenomenon of intermittency, since it controls the onset of turbulence. Its law can be easily understood since s and n are weakly correlated ($\rho = .048 - .018$) and have a non-zero probability density at the origin (e.g.

Student's distribution) and thus lead to a Cauchy-type law.

ELLIPTICAL TURBULENCE

Considering the velocity-field, we find an exponent of the vertical scaling: $H_v = 3/5$. This exponent is confirmed by Adelfang (1977) up to 14 km, and Endlich et Al. (1969) found $\beta = 5/2$ (thus, $H = 3/4$) up to 16 km. The slight discrepancy of the latter result seems due to considerable interpolation of the data. In any case, no evidence of characteristic vertical length scales is found.

A similar result was predicted almost 25 years ago for the directionally averaged spectrum in the so-called "buoyancy subrange", by Obukhov (1959), and independently by Bogliano (1959). The vertical scaling can be thus deduced by the same derivation or by considering directly the physically meaningful quantity ϕ the flux of buoyancy force variance. The latter derivation has the advantage that it does not depend on the Boussinesq approximation:

$$\bar{\phi}(\Delta z) = \tau^{-1}(\Delta z) \Delta f^2(\Delta z)$$

where $\tau(\Delta z)$ is a characteristic time for the transfer process. Dimensional analysis yields:

$$\Delta v(\Delta z) \propto \bar{\phi}(\Delta z)^{1/5} \Delta z^{3/5} \quad (1)$$

While the quite different Kolmogorov scaling is supposed to hold in the horizontal:

$$\Delta v(\Delta x) \propto \bar{\epsilon}(\Delta x)^{1/3} \Delta x^{1/3} \quad (2)$$

Objects which scale in the same way in all directions are called self-similar fractals because the large scale can be simply viewed as a magnification of the small scale. In the atmosphere, we have argued that scaling, although present in all directions, and over a wide range of lengths, is quite different in the vertical and horizontal. Large scale structures can no longer be

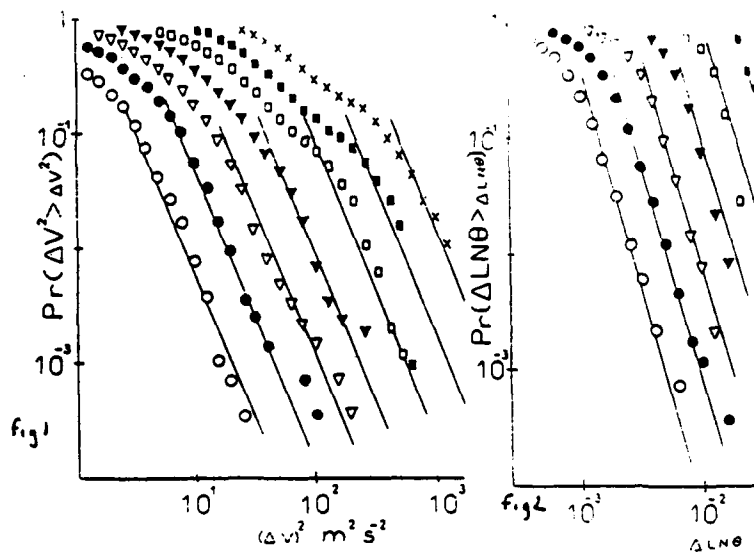


Fig.1: The probability distribution of fluctuations in the quantity $\Delta v^2(\Delta z)$ where v is the horizontal velocity, for different vertical layers, as follows: \circ : $\Delta z = 50m$, \bullet : $\Delta z = 100m$, ∇ : $\Delta z = 200m$, \blacktriangledown : $\Delta z = 400m$, \square : $\Delta z = 800m$, \blacksquare : $\Delta z = 1600m$, \times : $\Delta z = 3200m$.

Fig.2: The probability distribution of fluctuations of the buoyancy force. Same symbols as in Fig.1.

simply regarded as large-scale copies of smaller ones. In addition to magnification, we must also stretch. This can be expressed as follows:

$$\Delta \underline{v}(\underline{G}, \underline{\lambda}, \underline{\Delta x}) \stackrel{H}{\sim} \lambda^H \Delta \underline{v}(\underline{\Delta x}) \quad (3)$$

($\underline{x} = (x, y, z)$), the group $(\underline{G}, \lambda^H)$ is a kind of renormalization group, and behaves as:

$$\underline{G} \lambda^H \sim \begin{bmatrix} \lambda & 0 & 0 \\ 0 & \lambda & 0 \\ 0 & 0 & \lambda H_z \end{bmatrix} \quad \text{with } H_z = H/H_v$$

It introduces an elliptical geometry, further exploited in Schertzer et Al. (1983) with more general expression of \underline{G} . Here, $H = 1/3/3/5 = 5/9 \Rightarrow D = 23/9$.

Fig. 5 shows how a small vertically oriented cross-section of an eddy is transformed at larger scales. The magnification and stretching process transforms the vertically oriented "convective" type eddy into a large horizontally oriented "Hadley" type eddy. Note that \underline{G} transforms the statistical properties of the eddies.

This transformation increases the volume of an eddy by the factor:

$$\lambda \cdot \lambda \cdot \lambda^{H_z} = \lambda^{D_{el}}; D_{el} = 2 + H_z$$

In an isotropic three dimensional turbulence, $H_z = 1$, $D_{el} = 3$, and in the isotropic two-dimensional case, $H_z = 0$ and $D_{el} = 2$. Writing the above relationship in the form:

$$\text{Det } \underline{G} = \lambda^{D_{el}}$$

we are lead to the more general definition of D_{el} :

$$D_{el} = \text{Tr} \left(\frac{d\underline{G}}{d\lambda} \right)_{\lambda=1}$$

The number $N(\ell)$ of eddies of horizontal scale ℓ may now be written:

$$N(\ell) \sim \ell^{-D_{el}}$$

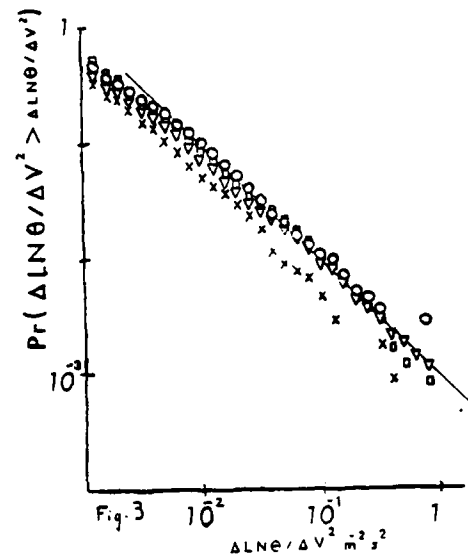


Fig.3: The probability distribution of fluctuations in the quantity $\Delta \ln \theta(\Delta z) / \Delta v^2 = Ri \Delta z$, Ri being the Richardson number. Same symbols as in the previous figures. The curves for 100, 400, 1600m have been suppressed for clarity of presentation.

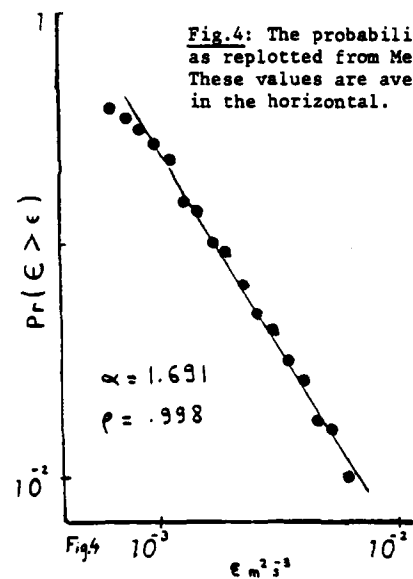


Fig.4: The probability distribution of $\bar{\epsilon}$ as replotted from Merceret (1976) Fig.14. These values are averages over $\sim 100m$ in the horizontal.

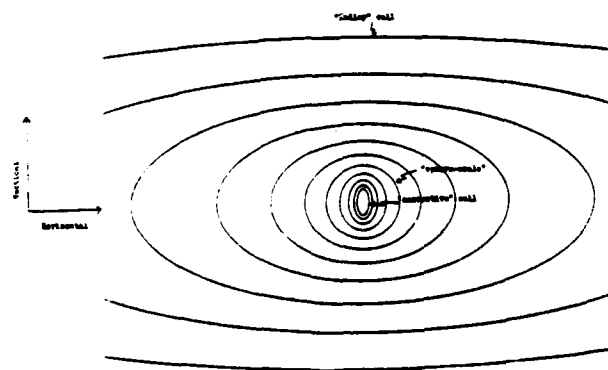


Fig.5: Isocontours of \underline{G} , which may be interpreted as the shapes of the vertical cross-sections of averaged eddies at different scales. "Hadley cell" and "convective cell" are suggestive labels for very large, and respectively very small structures.

THE SPHERO-SCALE

The distinction between isotropy and anisotropy is profound. An horizontal cross-section will have an area proportional to l^2 whereas a vertical cross-section will have an area proportional to l^{1-H} . Their ratio gives a quantitative measure of the verticalness of the vortex.

There therefore exists a scale at which this ratio is 1, the turbulence appears then as isotropic three-dimensional: the horizontal and vertical fluctuations have the same amplitude. This scale, that we call "sphero-scale" for obvious reasons, will depend on the relative fluctuations of $\bar{\epsilon}$ and $\bar{\phi}$ (due to equations 1 and 2) both of which show large fluctuations. The size of this scale may vary in an extremely erratic manner, unless $\bar{\epsilon}$ and $\bar{\phi}$ are totally dependent.

STOCHASTIC STRATIFICATION

By the action of G_p , stratification may be seen rather as the result of a stochastic process, hence a "stochastic stratification". Fig. 6a shows an isotropic gaussian field with $H = 1/2$ and $D_{el} = 2$. Fig. 6b shows the corresponding field for $D_{el} = 3/2$ (the same white noise field was used in both cases to generate via Fourier transforms, the random fields).

Investigations of this process for the logarithm of the pressure and the temperature will be pursued elsewhere. Note that the hydrostatic relation is recovered by assuming that the vertical scaling of $\log p$ has the parameter: $H_V(\log p) = 1$.

INTERMITTENCY

Intermittency expresses the fact, that, roughly speaking, the turbulence doesn't fill all the volume of the space available to it, the "spottiness" of turbulence (Batchelor and Townsend (1949), Batchelor (1953)). This is related to Leray's (1933) conjecture on the existence of a set of singularities of the Euler equations.

Kolmogorov (1962) and Yaglom (1966) presented a corrected spectrum to take into account intermittency, by assuming a log-normal distribution of $\bar{\epsilon}$. Orszag (1970), Mandelbrot (1974) have pointed out several theoretical difficulties with this hypothesis.

In particular, Mandelbrot, building upon an earlier, explicit model for "spottiness" (Novikov and Steward (1964)) showed that log-normality may only be expected under rather special conditions, whereas hyperbolic behaviour was likely. This latter possibility was unfortunately dropped in Kraichnan (1974) and Frisch et Al (1978), and subsequent works which retained only the notion of the fractal dimension of the support of turbulence, D_s .

Mandelbrot's model is in fact quite general and can be divided in two cases. The first is "curdling", it generates eddies strictly into either completely "dead" or uniformly "active" regions at each stage of the cascade. It is often referred as the " β -model". This is the only case where no divergence of moments occurs whatever the dimension of the spatial average. The second case is "weighted curdling" where active regions no longer have uniform intensity. Schertzer and Lovejoy (1983), who extended this model to the case of "elliptical turbulence", stressed the fact that in this case divergence occurs for any spatial average of dimension D_A such as: $D_{el} - D_s < D_A < D_{el} - D_\infty$

where D_∞ characterises the dimension of the "very active regions". They proposed that this latter case could be called " α -model", because of the hyperbolic exponent it introduces.

Note that the various dimensions intervening in the case of the " α -model" may be interpreted in terms of a "multi-fractal" (Parisi, private communication, (1983)) composed of different fractals, on each of them the velocity field has a certain scaling (i.e. a certain singularity type, described by its scaling parameter).

The experimental results obtained indicate:

$$23/9 = D_{el} > D_s > D_{el} - 1; D_s > D_\infty$$

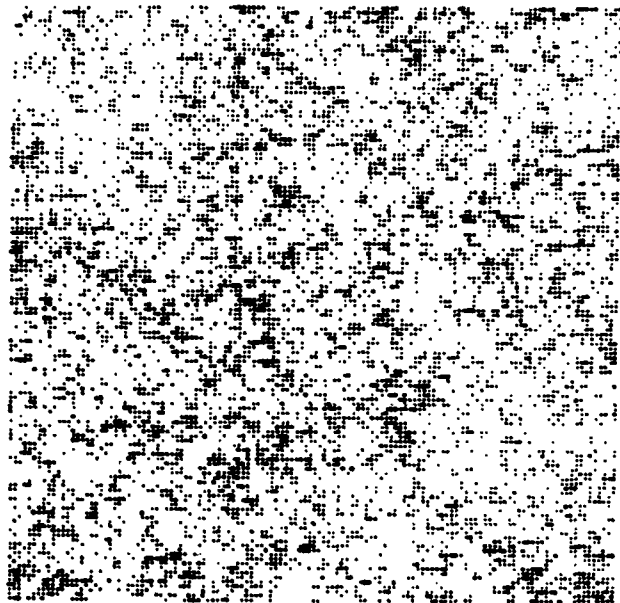


Fig. 6a : A random isotropic field with $H = 1/2$, the intensity of the field is proportional to the shade of the grey.

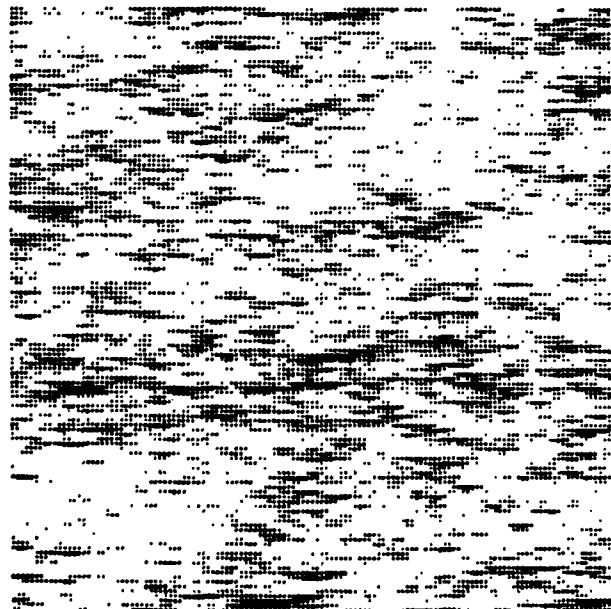


Fig. 6b : An example of stochastic stratification. This figure is the same as Fig. 6a, except that $D_{el} = 1.5$, instead of 2 (both figures are obtained by taking the same gaussian white noise). In one direction, $H = 1$ and in the direction perpendicular, $H = 1/2$, the "sphero-scale" has a value of $\sim 1\%$ of the length of one side of the figure.

DIVERGENCE OF THE FIFTH MOMENT OF THE VELOCITY

Since we may assume, either on physical arguments or only dimensional arguments (see equation 2):

$$\bar{\epsilon}(\Delta x) \propto \Delta v^3 (\Delta x) / \Delta x$$

hence: $\alpha_{\bar{\epsilon}} = \alpha_v / 3$

thus our present results based on radiosonde data and Mercier's ones confirm: $\alpha_v \approx 5$; $\alpha_{\bar{\epsilon}} \approx 5/3$; $\alpha_{\bar{\phi}} = 1$

This shows also that various fields may be not only related by simple algebraic equations satisfied by their scaling exponents, the same should be true for their hyperbolic exponents.

For, instance relation between dynamics and rain-field is urgently needed, because it is a case where numerical modeling is notoriously difficult. Indeed, Lovejoy (1981) shows that changes of the rate of rain in isolated storms have a hyperbolic law, ($\alpha = 5/3$, but this quantity is a 2-D lagrangian statistic, and $\bar{\epsilon}$ is a 1-D eulerian one in our study).

An interesting feature of hyperbolic distributions is that they are presumably related to the classical phenomenology of meteorological fields: Mandelbrot and Wallis (1969) pointed out that they have the effect of causing that the largest fluctuations have an overwhelming effect, which they called "Noah effect". This is investigated in detail for the horizontal rain areas by Lovejoy (1981), Lovejoy and Mandelbrot (1983).

Fig. 7 shows an "hyperbolic fractal animal" obtained by stochastic simulation in an anisotropic space: one main "animal" dominates the smaller ones. It could correspond to a vertical section of a rain-field.

HYPERBOLIC RENORMALIZATION AND ELLIPTICAL TURBULENCE

The results obtained here *throw into doubt* the renormalization procedures used in turbulence. Usually called "spectral closures" (e.g. Herring et Al (1982)), they have been developed in a quasi-gaussian framework which is no longer tenable if the hyperbolic behaviour of the different fields is confirmed.

Conversely, placing renormalization procedures in an hyperbolic context should be particularly rewarding, since renormalization has encountered, in the quasi-gaussian context, three closely linked fundamental difficulties: random galilean invariance, renormalization of the vertex, intermittency. Until now, the two former have been overcome only by more or less ad-hoc procedures. By stating the problem of intermittency as the problem of renormalizing in a hyperbolic context, it suggests to develop what one might call "hyperbolic renormalization".

On the other hand, the "fractally anisotropic" framework of the "elliptical turbulence" (i.e. a scaling anisotropy) may also be essential to overcome difficulties encountered in anisotropic cases where so far only formal manipulation of renormalization schemes have succeeded (e.g. Kraichnan (1964)).

CONCLUSION AND COMMENTS

We have investigated the scaling and the hyperbolic behaviour of the vertical shear, the buoyancy force and the Richardson number.

We think that the hypothesis of a dimensional transition (2D/3D) between large scales and small scales is no longer tenable either theoretically or empirically.

The observed structure of the atmosphere can be explained by a simpler hypothesis; it is anisotropic and scaling throughout, a fact that can be characterised by the "elliptical dimension": $D_{el} = 23/9 = 2.56$, (i.e. "two plus the scaling of Kolmogorov over the one of Bogliano and Obukhov").

On the other hand, intermittency plays a key role at the different scales, due to the low hyperbolic exponents observed. In particular as $\alpha \sim 5$, the fifth statistical moment of the velocity field may diverge, and as $\alpha \sim 1$, even the statistical mean of the Richardson number may diverge. This points out that use of theory based on limited expansions in Ri (e.g. Lilly (1983)) are to be understood in a widely intermittent context: there is no uniform separation between waves and turbulent regimes.

This new scheme of atmospheric turbulence introduces some new notions which have been briefly discussed (e.g. the sphero-scale, which is not a characteristic scale; the "stochastic stratification").

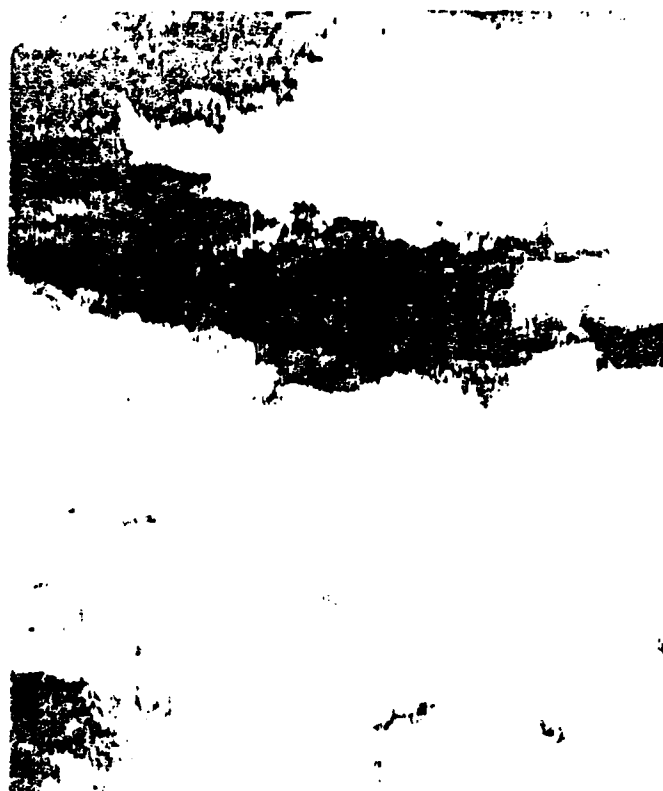


Fig. 7: An example of a hyperbolic fractal animal on an anisotropic space, with dimension $D_{el} = 1.80$. The log intensities are indicated by the intensities of grey. This model is on an 800X800 point grid, and the sphero-scale has the value of 30 pixels. The fine structure is therefore oriented perpendicularly to the overall shape.

On the other hand, intermittency plays a key role at the different scales, due to the low hyperbolic exponents observed. In particular as $\alpha \sim 5$, the fifth statistical moment of the velocity field may diverge, and as $\alpha \sim 1$, even the statistical mean of the Richardson number may diverge. This points out that use of theory based on limited expansions in Ri (e.g. Lilly (1983)) are to be understood in a widely intermittent context: there is no uniform separation between waves and turbulent regimes.

This new scheme of atmospheric turbulence introduces some new notions which have been briefly discussed (the "sphero-scale", "stochastic stratification"...). We questioned the relevance of certain of the usual assumptions of existing renormalisation methods in the case of strongly intermittent and anisotropic flows. It is hoped that the phenomenology of the different animals crowding the meteorological zoo (e.g. fronts, bands, dust devils, blocks etc.) may be understood as the result of scaling in an anisotropic hyperbolically intermittent context (in particular, the "Noah effect").

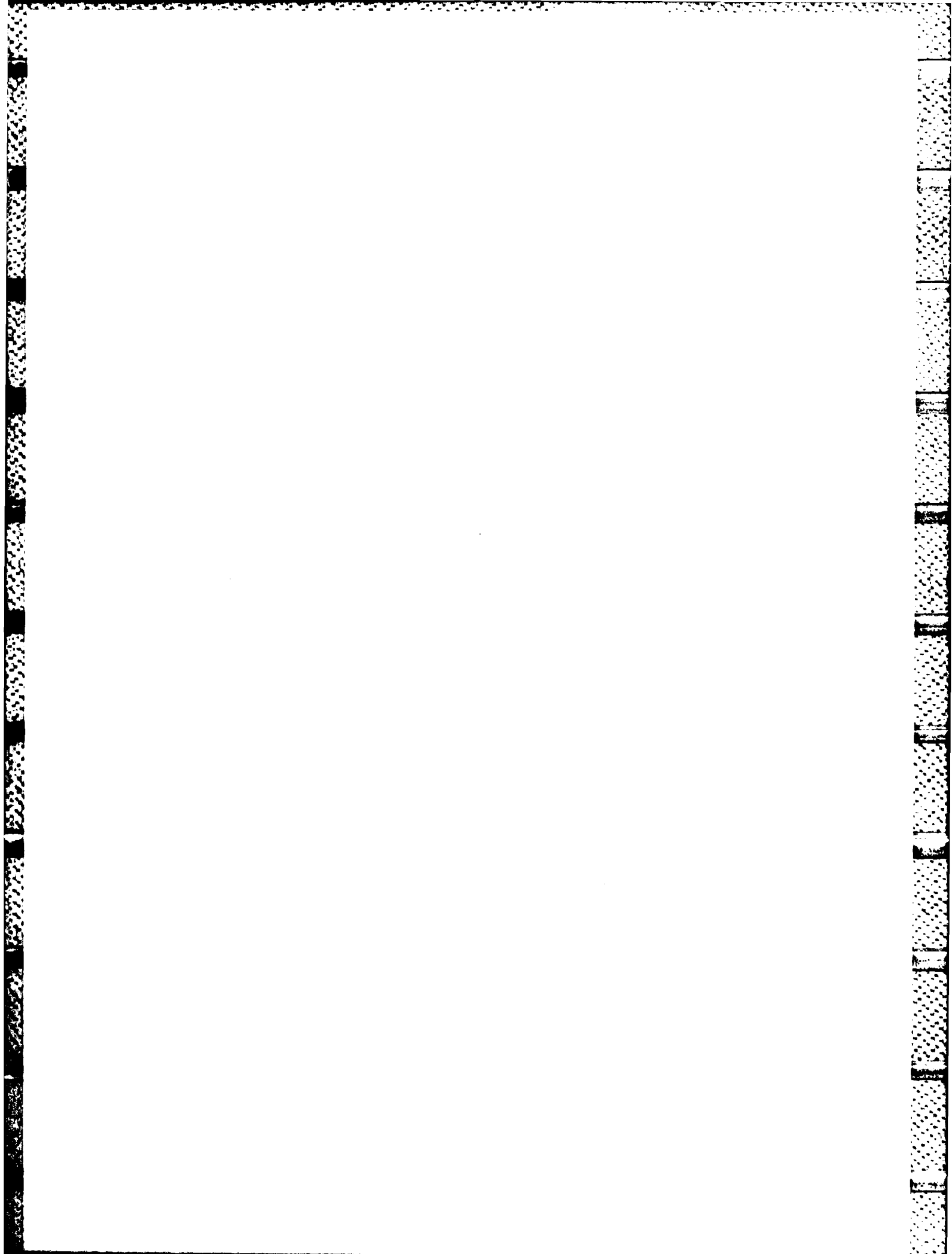
Although far more work is needed to provide definite answers to different questions, we may safely conclude that atmospheric turbulence is fractally homogeneous (highly intermittent), and fractally anisotropic (anisotropic scaling).

ACKNOWLEDGEMENTS:

We would like to thank the following for helpful discussions, comments, and criticism: G.L. Austin, K. Gage, J.J. Goutorbe, J. Herring, J.P. Kahane, D.K. Lilly, B. Mandelbrot, J. Puyrière, J. Tardieu, G. Therry, T.E. Van Zandt, T. Warn.

REFERENCES

- Adelfang, S.I., 1971, "On the relation between wind shears over various intervals", *J. Atmos. Sci.*, 10, 138.
- Batchelor, G.K., 1953, "The Theory of Homogeneous Turbulence". University Press, Cambridge, 198pp.
- Batchelor, G.K., and Townsend, A.A., 1949, "The nature of turbulent motion at large wave numbers", *Proc. Roy. Soc. A*, 199, 238.
- Bogliano, R., 1959, "Turbulent spectra in a stratified atmosphere", *J. Geophys. Res.*, 64, 2226.
- Charney, J., "Geostrophic turbulence", *J. Atmos. Sci.*, 38, 2747.
- Curry, J.H., Herring, J.R., Longcaric, J. and Orszag, S.A., 1982, "Order and disorder in two and three dimensional Benard convection", NCAR preprint, Boulder.
- Endlich, R.M., Singleton, R.C. and Kaufman, J.W., 1969, "Spectral analysis of detailed vertical wind speed profiles", *J. Atmos. Sci.*, 26, 1030.
- Feller, W., 1971, "An Introduction to Probability Theory and its Applications", vol. II, John Wiley and sons, New York, 567pp.
- Fjortoft, R., 1953, "On the changes in the spectral distribution of kinetic energy for two-dimensional, non divergent flow. *Tellus*, 5, 225.
- Frisch, U., Sulem, P.L. and Nelkin, M., 1978, "A simple dynamical model of intermittent fully-developed turbulence", *J. Fluid Mech.*, 87, 719.
- Gage, K.S., 1979, "Evidence for a $k^{-5/3}$ law inertial range in the meso-scale two-dimensional turbulence", *J. Atmos. Sci.*, 36, 1950.
- Gilet, M., Nicoloff, S. and Klaus, V., 1980, "Dual doppler radar measurements of winds and turbulence ahead of a cold front", 19th conf. on radar Met., AMS, Boston, 30.
- Herring, J.R., 1980, "On the statistical theory of quasi-geostrophic turbulence", *J. Atmos. Sci.*, 37, 969.
- Herring, J.R., Schertzer, D., Lesieur, M., Newman, G.R., Chollet, J.P. and Larcheveque, M., 1982, "A comparative assessment of spectral closures as applied to passive scalar diffusion", *J. Fluid Mech.*, 124, 411.
- Kolmogorov, A.N., 1962, "A refinement of previous hypothesis concerning the local structure of turbulence in a viscous incompressible fluid at high Reynolds number", *J. Fluid Mech.*, 13, 82.
- Kraichnan, R.H., 1964, "Direct-interaction approximation for shear and thermally driven turbulence", *Phys. Fluids* 7, 1048.
- Kraichnan, R.H., 1967, "Inertial ranges in two-dimensional turbulence", *Phys. Fluids*, 10, 1417.
- Kraichnan, R.H., 1974, "On Kolmogorov's inertial-range theories", *J. Fluids Mech.*, 62, 305.
- Leray, J., 1933, "Etudes de diverses équations intégrales non linéaires et de quelques problèmes que pose l'hydrodynamique", *J. Math. Pures et Appl.*, 12, 1.
- Lévy, P., 1937, "Théorie de l'Addition des Variables Aléatoires", Gautmiers Villars, Paris, 384pp.
- Lilly, D.K., 1983, "Stratified turbulence and the meso-scale of the atmosphere", in press *J. Atmos. Sci.*
- Lovejoy, S., 1981, "A statistical analysis of rain areas in terms of fractals", 20th conf. on Radar Met., AMS, Boston.
- Lovejoy, S., 1982, "The area-perimeter relation for rain and clouds areas", *Science*, 216, 185.
- Lovejoy, S., B. Mandelbrot 1983: A fractal model of rain. Preprint, CRM/EERM, Mét. Nat., Paris.
- Macpherson, J.I., and Isaac, G.A., 1977, "Turbulent characteristic of some cumulus clouds", *J. Appl. Met.*, 16, 81.
- Mandelbrot, B., 1974, "Intermittent turbulence in self-similar cascades: divergence of high moments and dimension of the carrier", *J. Fluid Mech.*, 62, 331.
- Mandelbrot, B., 1982, "The Fractal Geometry of Nature", Freeman and co., San Francisco, 461pp.
- Mandelbrot, B., and Wallis, J.R., 1968, "Noah, Joseph and operational hydrology", *Wat. Resources Res.*, 4, 909.
- Merceret, F.J., 1976, "The turbulent microstructure of hurricane Caroline (1975)", *Mon. Wea. Rev.*, 104, 1297.
- Monin, A.S., 1972, "Weather Forecasting as a Problem in Physics", Cambridge, Mass.
- Monin, A.S., and Yaglom, A.M., 1975, "Statistical Fluid Mechanics", vol II, MIT Press, Cambridge, Mass., 566pp.
- Morel, P., and Larcheveque, M., 1974, "Relative dispersion of constant level balloons in the 200mb general circulation", *J. Atmos. Sci.*, 31, 2189.
- Nastrom, G.D., and Gage, K.S., 1983, "A first look at wave-number spectra from GASP data", in press, *Tellus*, 35.
- Novikov, E.A., and Stewart, R.W., 1964, "Intermittency of turbulence and spectrum of fluctuations of energy dissipation", *Izv. Akad. Nauk., SSSR, Seria Geofiz.* 3, 408.
- Obukhov, A.N., 1959, "Effect of archimedean forces on the structures of the temperature field in a turbulent flow", *Dokl. Akad. Nauk., SSSR*, 125, 1246.
- Orszag, S.A., 1970, "Indeterminacy of the moment problem for intermittent turbulence", *Phys. Fluids*, 13, 2210.
- Pinus, N.Z., 1968, "The energy of atmospheric macro-turbulence", *Izv. Atmos. and Oceanic Phys.*, 4, 461.
- Schertzer, D. and Simonin, O., 1982, "A theoretical study of radiative cooling in homogeneous and isotropic turbulence", *Selected Papers from the 3rd Int. Symp. on Turb. Shear Flows*, Springer-Verlag, Berlin-Heidelberg.
- Schertzer, D., and Lovejoy, S., 1983, "The dimension of atmospheric motions", submitted to *J. Atmos. Sci.*
- Schertzer, D., Lovejoy, S., and Peyriere, J., 1983, "Fractales elliptiques", preprint, CRM n°11, EERM, Mét., Nat., Paris.
- Simonin, O., 1982, "Interaction turbulence, rayonnement", Thèse, IMST, Marseille.
- Tardieu, J.J., 1979, Tech. Note 23 EERM, Mét. Nat., Paris.
- Van der Hoven, J., 1957, "Power spectrum of horizontal wind speed in the frequency range from 0.0007 to 900 cycles per hour", *J. Meteor.*, 14, 160.
- Vinnichenko, N.K., 1969, "The kinetic energy spectrum in the free atmosphere from 1 second to 5 years", *Tellus*, 22, 158.
- Yaglom, A.M., 1966, "The influence of the fluctuation in energy dissipation on the shape of turbulent characteristics in the inertial range", *Sov. Phys. Dokl.*, 2, 26.



SESSION 12 - TWO PHASE FLOWS

P. Humphrey - Chairman

AD-A135 034

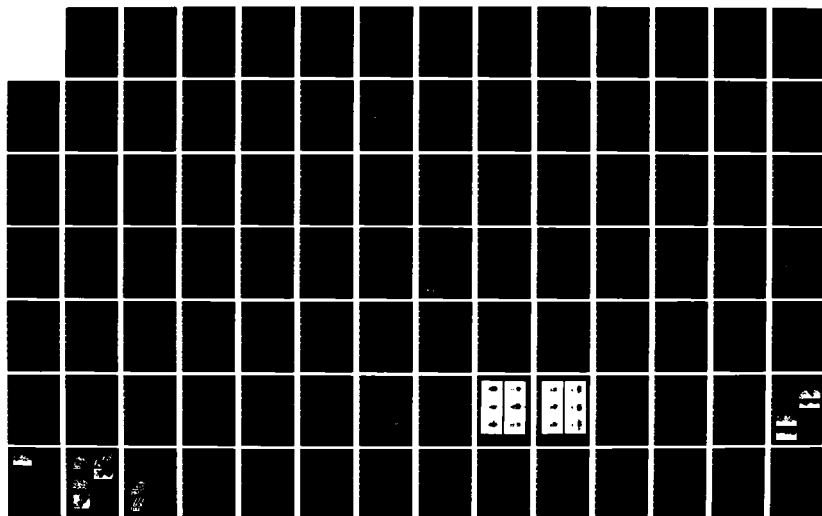
SYMPOSIUM ON TURBULENT SHEAR FLOWS (4TH) HELD AT
KARLSRUHE UNIVERSITY (GERMANY FR) 12-14 SEPTEMBER 1983
(U) KARLSRUHE UNIV (GERMANY F R) SEP 83

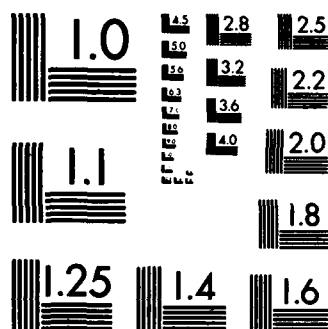
5/7

UNCLASSIFIED

F/G 20/4

NL





MICROCOPY RESOLUTION TEST CHART
NATIONAL BUREAU OF STANDARDS-1963-A

TURBULENT FLOW OF INCOMPRESSIBLE MIXTURES

M.C. Roco
Department of Mechanical Engineering
University of Kentucky, KY 40506

C.A. Shook
Department of Chemical Engineering
University of Saskatchewan, SASK. S7N 0W0

ABSTRACT

The spatial nonuniformities and the interactions between the components determine the flow behavior of multicomponent systems. A space/time averaging approach of the governing equations modelling these factors is presented in this paper. It is defined for a weighted averaging volume which is related to the local scale of turbulence. Numerical solutions for concentration and velocity distributions are obtained using integral finite volume techniques. The predictions are compared with good results to multi-species particle slurry flows in pipelines.

INTRODUCTION

The hydraulic handling of bulk materials of broad size distribution (coal, limestone, etc.) is widely applied in mining, chemical and other industrial processes. Despite the large area of application, the known models do not completely satisfy the scientific rigor and engineering needs for numerical predictions. Increased research activities have been oriented in this domain in the last few years.

This paper presents a model for the turbulent flow of multi-species particle suspensions, in which a new set of equations is derived using a space/time averaging approach.

The temporal nonuniformities in single fluid turbulent flows are shown in the mean flow equations using time averaging. The Reynolds stresses appear in this way in momentum equations and have predominant values compared to the viscous stresses. To express the spatial nonuniformities in multicomponent flows it is also necessary to average the governing equations by volume. As the time averaging yields terms showing new qualitative effects, so the space averaging is expected to reveal not only quantitative changes of the nonlinear terms but also some new qualitative aspects of the component interactions.

The formulation of the governing equations for heterogeneous flows has been done either by considering each phase separately with corresponding interaction terms, by assuming a continuum medium with averaged field quantities, or by using volume averaging (see Soo, 1967; Whitaker, 1973; Hestroni, 1982). The local volume averaging procedure for multiphase systems may be performed in various ways related to the specific flow conditions (for porous media Slattery, 1967; for fluidized beds, Anderson and Jackson, 1967; for boiling, Vernier and Delhaye, 1968, etc.). In this paper we discuss an averaging approach specifically for multicomponent turbulent flow.

The spatial nonuniformities in multi-species particle flow are reflected in the random distributions of the flow components, as well as in particle cluster formation in shear suspension flows. The spatial nonuniformities

strongly affect the non-linear terms in the equations of motion. To analyze the multicomponent flows, we suggest a weighted averaging by a local volume whose dimensions are related to the length scale of turbulence. The weighted averaging is appropriate since it is known that the spatial cross-correlations in turbulent flow decrease with the space interval. The computation of the component velocities and concentrations is performed using an appropriate integral finite volume technique. The results are compared with a large set of experimental results considering one to five species of particles (of size up to $d \leq 13 \text{ mm}$) flowing with water in various pipes (rectangular, circular $D = 40-495 \text{ mm}$).

In the space allowed by this paper we detail aspects related to the momentum equation and concentration calculation.

COMPOSED AVERAGED EQUATIONS

The local volume averaging of the differential equations has to be performed in agreement with the averaging of the quantities used in equations. A typical situation is when the temporal averaged measurement of the considered quantities is taken over a prescribed volume or surface. This is the case for our velocity measurements reported later in the paper. Another situation occurs when the time dependent flow is analyzed using the instantaneous spatial averages in the equations. In this case the averaging space is related to the flow conditions. Sometimes, the volume averaging may be also considered to improve the continuity and derivability of the variables. The spatial averaging has a supplementary meaning and computational significance when finite volume techniques are employed. All these situations are covered by the weighted average by volume proposed in the following paragraph.

Alternatively, to calculate the instantaneous point variables one must use the time dependent equations with a very fine grid compared to the length scale of turbulence and a small timestep. This approach was tested only for single fluid flow in small domains and proved to be very expensive and thus without immediate practical interest.

Space/Time Averaging Approach

Let us consider a flowing mixture of N solid components in an incompressible fluid. The space/time average of a function f for the K -th component at a position \underline{r} and time t , in steady-state mean flow, is:

$$\bar{f}^K = \frac{1}{\Delta T} \int_{t-\Delta T/2}^{t+\Delta T/2} \langle \alpha(\underline{r}, t) \rangle_K \cdot \langle f(\underline{r}, t) \rangle^K \cdot dt \quad (1)$$

where:

$\langle \alpha(\underline{r}, t) \rangle_K$ - bulk space averaged concentration for the K -th component

$\langle f(\underline{r}, t) \rangle^K$ - intrinsic space average of f for the K -th component

ΔT - averaging time interval

The volume averaging for the K -th component is weighted by the Eulerian cross-correlation for velocities $R_K(\underline{\xi} - \underline{r})$, which gives a measure of the influence of flow parameters at $\underline{\xi}$ on the flow parameters at \underline{r} (Figure 1):

$$R_K(\underline{\xi} - \underline{r}) = \frac{V'_K(\underline{r}) \cdot V'_K(\underline{\xi})}{\sqrt{V'_K(\underline{r})^2 \cdot V'_K(\underline{\xi})^2}} \quad (2)$$

where:

$V'_K(\underline{r})$, $V'_K(\underline{\xi})$ - instantaneous fluctuating velocities of the K -th component at \underline{r} and $\underline{\xi}$, respectively.

If the same lump of fluid, or the same turbulent eddy, involves both points \underline{r} and $\underline{\xi}$, the $R_K(\underline{\xi} - \underline{r}) = 1$. If $R_K(\underline{\xi} - \underline{r}) = 0$ no interaction between the turbulence parameters at $\underline{\xi}$ and \underline{r} occurs. It is well known that in turbulent flows the largest eddies may have dimensions close to the characteristic length of the flow domain. A global measure of the cross-correlations $R_K(\underline{\xi} - \underline{r})$ is the mixing length Λ_K .

The intrinsic volume averaging about \underline{r} is:

$$\langle f(\underline{r}, t) \rangle^K = \frac{\int_{\Delta v} f(\underline{\xi}, t) \cdot K(\underline{\xi}, t) \cdot R_K(\underline{\xi} - \underline{r}) \cdot dv}{\int_{\Delta v} K(\underline{\xi}, t) \cdot R_K(\underline{\xi} - \underline{r}) \cdot dv} \quad (3)$$

where:

$f(\underline{\xi}, t)$ - instantaneous local value of f

Δv - averaging volume, about \underline{r} (Figure 1)

$\underline{\xi}$ - interior point in Δv

$K(\underline{\xi}, t) = \begin{cases} 1 & \text{if component } K \text{ resides at } (\underline{\xi}, t) \\ 0 & \text{otherwise} \end{cases}$

$R_K(\underline{\xi} - \underline{r})$ - spatial cross-correlation, defined in (2)

The averaging volume should be taken as a domain large enough to contain large scale turbulent eddies. In usual situations only an ellipsoid with the main axes equal to the mixing lengths around \underline{r} may be sufficient (at its boundaries R_K is very small or approaches zero).

The bulk space average of concentration is:

$$\langle \alpha(\underline{r}, t) \rangle_K = \frac{\int_{\Delta v} K(\underline{\xi}, t) \cdot R_K(\underline{\xi} - \underline{r}) \cdot dv}{\int_{\Delta v} R_K(\underline{\xi} - \underline{r}) \cdot dv} \quad (4)$$

The first integral is the weighted averaging volume over the K -th component, the second - over all the components.

By using this averaging approach (1) one can take into account the spatial non-uniformities which affect the flow behavior at a point, including cluster formations and macroturbulent structure. The volume averages (3) and (4) can be used if data on the spatial cross-correlation $R_K(\underline{\xi} - \underline{r})$ and particle distributions $K(\underline{\xi}, t)$ are available. The data can be obtained using various experimental techniques (three dimensional camera, Graham et al., 1982; laser apparatus, Lee and Durst, 1982) or from analytical considerations. Since there are fewer data on volume integrals we present here a conversion from the weighted space integrals to weighted time integrals.

From Volume Averaging to Time Averaging

There are two reasons to replace the space with time integrals: (1) it is easier to measure the time variations at a point (Eulerian description), (2) the mathematical schemes already used for time averaging are available.

In an isotropic turbulent flow about a position \underline{r} the surface of equal $R_K(\underline{\xi} - \underline{r})$ are spherical, and the averaging volume Δv may be taken as a sphere. When the turbulence has an anisotropic character the averaging volume should be an ellipsoid, bounded by a surface of constant cross-correlation (2). The presence of solid walls may produce an asymmetrical surface of constant $R_K(\underline{\xi} - \underline{r})$. When the sheared flow has a predominant direction, so has the averaging volume. A simplified approach is to employ a volume defined by Λ_K , without weighting function R_K (Roco, 1983).

Let us consider the stream tube passing through \underline{r} , which should be along the largest semiaxis of the averaging ellipsoid. The initial integrals on Δv from (3) and (4) are replaced by integrals on stream tubes $\Delta v' = \Delta A \cdot \Delta s$ (Figure 1, b), assuming the same spatial nonuniformity occurs on both averaging volumes. Changing the variable at $\Delta t = \Delta s / V_K$ we obtain from (3):

$$\langle f(\underline{r}, t) \rangle^K = \frac{\int_{t-\Delta t/2}^{t+\Delta t/2} f(\underline{r}, \tau) \cdot K(\underline{r}, \tau) \cdot R_K(\tau - t) \cdot d\tau}{\int_{t-\Delta t/2}^{t+\Delta t/2} K(\underline{r}, \tau) \cdot R_K(\tau - t) \cdot d\tau} \quad (5)$$

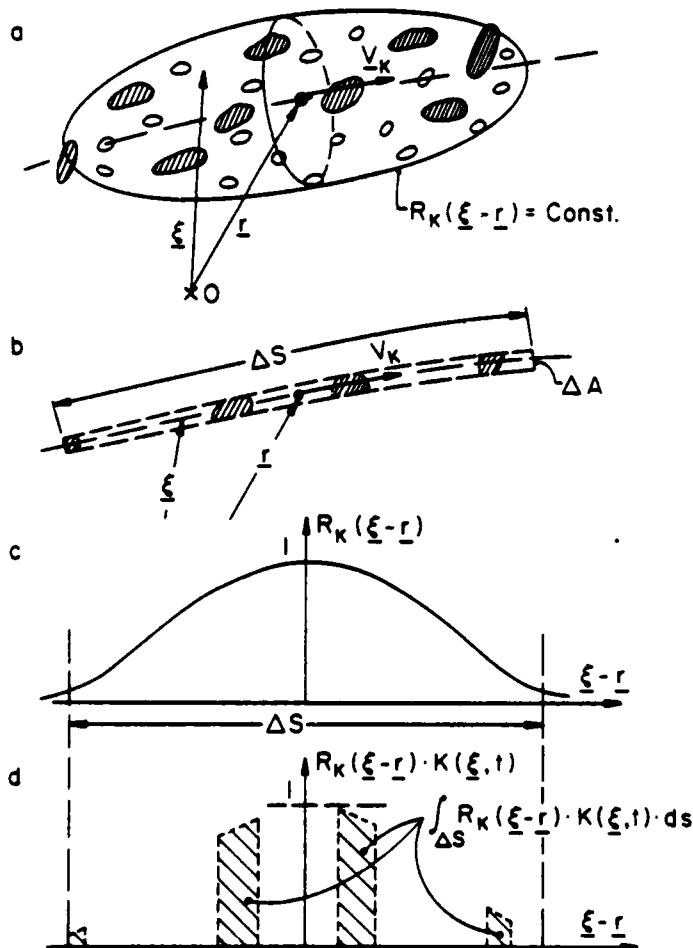


Figure 1. Averaging volume (Δv).

where: $\tau = |\underline{x} - \underline{x}'|/V_K$

in which \underline{x} and \underline{x}' are on the same stream tube, and V_K is the mean velocity of the K-th component.

$$R_K(\tau-t) = \frac{V'_K(t) \cdot V'_K(\tau-t)}{V'_K(t)^2} \quad (6)$$

$R_K(\tau-t)$ is the Eulerian time correlation

$$\int_{t-\Delta t/2}^{t+\Delta t/2} K(\underline{x}, \tau) \cdot R_K(\tau-t) \cdot d\tau = Z_K \cdot \langle \alpha(\underline{x}, t) \rangle_K \quad (7)$$

in which Z_K is the Eulerian time scale for the K-th component.

The time-space averaging operator (1) becomes a double time averaging operator:

$$\bar{f}^K = \frac{1}{\Delta T} \int_{t-\Delta T/2}^{t+\Delta T/2} \left[\frac{1}{Z_K} \int_{t-\Delta t/2}^{t+\Delta t/2} f(\underline{x}, \tau) \cdot K(\underline{x}, \tau) \cdot R_K(\tau-t) \cdot d\tau \right] \cdot dt \quad (8)$$

A local instantaneous value differs from the main value \bar{f}^K by two fluctuating components: one reflecting the spatial nonuniformities $(f'_K)_t$, the second the time nonuniformities of the spatial average $(f'_K)_T$:

$$f'_K = f_K - \bar{f}^K = (f'_K)_t + (f'_K)_T \quad (9)$$

where: $(f'_K)_t = f_K - \langle f_K \rangle^K$

$$(f'_K)_T = \langle f_K \rangle^K - \bar{f}^K$$

Averaged Conservation Equations

The local instantaneous conservation equation can be written for each component K, as well as for the entire mixture, in a general form:

$$\frac{\partial}{\partial t} (\rho \psi) + \nabla \cdot (\rho \psi \underline{U}) + \nabla \underline{J} - S = 0 \quad (10)$$

where: ρ - density

\underline{U} - velocity vector

ψ - specific quantity attached to mass

\underline{J} - flux term

S - source term

By averaging for each component $K = 1, N$ the conservation equations of mass, momentum and energy dissipation one obtains a new system of equations to determine mean velocity, concentration and turbulence index distributions. We rearranged the equations in such a way for solutions to be conveniently obtained by an iterative explicit scheme.

Let us consider the momentum equation in the i direction: ψ_K corresponds to the projection of the velocity vector, \underline{J}_K to the projection of the shear stress tensor and S_K to the projection of the body force vector.

The space/time averaging process of the local instantaneous momentum equation in the i direction yields for the K-th component in steady-state regime without component generation (no attrition) is:

$$\rho_K \frac{\partial}{\partial x_j} (\bar{\alpha}_K \bar{U}_{K1} \bar{U}_{Kj}) = \rho_K \bar{\alpha}_K \bar{b}_i - \frac{\partial}{\partial x_j} (\bar{\alpha}_K \bar{p}_K + \bar{\alpha}_K \bar{p}_K^r) + \frac{\partial}{\partial x_j} (\bar{\alpha}_K \bar{\tau}_{K1j1} + \bar{\alpha}_K \bar{\tau}_{K1j1}^r) -$$

$$\rho_K \frac{\partial}{\partial x_j} (\bar{\alpha}_K^r (\bar{U}_{K1} \bar{U}_{Kj})^r) + \bar{\alpha}_K \bar{U}_{K1} \bar{U}_{Kj}^r + \sum_{-K} \left[\frac{e_i}{\Delta T} \right] \int_{t-\Delta T/2}^{t+\Delta T/2} \frac{1}{Z_K} \cdot \sum_m \frac{\bar{T}_{KK'} \cdot \bar{n}_K}{\bar{U}_{KK'} \cdot \bar{n}_K} \cdot R_K(\tau-t) \quad (11)$$

where: $i, j = x, y, z$

\bar{f} is a simplified notation of \bar{f}^K

f' - fluctuating part of f given in (9)

$\bar{U}_{K1}, \bar{U}_{Kj}$ - projections of the fluctuating velocity, in the i and j directions, respectively.

$\sum_{-K} [\dots]$ - projection in the i direction of the interactions due to other flow components $K' = 1, N_K$, including viscous friction, collisions and Coulombic contacts between components.

m - denotes the number of an interface between K and other component K' passing through \underline{x} during the interval Δt .

$\bar{U}_{KK'}$ - velocity vector of the interface point crossing \underline{x}

$\bar{T}_{KK'}$ - stress tensor between the K-th and K' -th components

\bar{n}_K - unit normal vector to component K

\bar{e}_i - unit vector in the i direction

Assuming low correlations between α_K^r and p_K^r (i.e. $\alpha_K^r p_K^r$ neglected) the following terms in equations (11) have to be modeled:

$$\bar{\tau}_{K1j1}, \bar{\alpha}_K^r \bar{\tau}_{K1j1}^r, \bar{\alpha}_K^r (\bar{U}_{K1} \bar{U}_{Kj})^r, \bar{U}_{K1} \bar{U}_{Kj}^r \text{ and}$$

interaction terms $\sum_{-K} [\dots]$

To obtain engineering models for these terms we follow the steps: (1) find the physical interpretation, (2) identify the local parameters (dimensionless numbers, ratio particle size/turbulence scale, etc.) affecting the terms, and (3) propose constitutive equations based on comparison of the mean flow predictions with a large set of experiments.

We observe that the tensor $\bar{T}_{KK'}$ in the interaction term $\sum_{-K} [\dots]$ has components corresponding to $\bar{\tau}_{K1j1}$, $\bar{\alpha}_K^r \bar{\tau}_{K1j1}^r$, $\bar{\alpha}_K^r (\bar{U}_{K1} \bar{U}_{Kj})^r$, and $\bar{U}_{K1} \bar{U}_{Kj}^r$. It means that the same types of interactions occur between particles of the same species and particles of different species, i.e. similar models for both groups of terms may be employed. The physical interpretation of these terms is:

(1) $\bar{\tau}_{K1j1}$ - stress transmitted by Coulombic contacts between solid particles or by viscous effects when the flow component is a fluid. The Coulombic shear stress depends on the normal stress transmitted by particle contacts ($\bar{\tau}_{K1jj}$) and a friction coefficient ($\tan \delta$) independent of the rate of strain (Roco and Shook, 1982):

$$\bar{\tau}_{K1jj} = \bar{\tau}_{K1j1} / \tan \delta \quad (12)$$

where $\bar{\tau}_{K1jj}$ can be estimated as a supported load.

(2) $\rho_K \bar{\alpha}_K^r (\bar{U}_{K1} \bar{U}_{Kj})^r$ and $\bar{\alpha}_K^r \bar{\tau}_{K1j1}^r$ - stresses caused by elastic and plastic particle collisions, respectively. The global value of the repulsive normal stress (α_{DS}) acting between

sheared layers of suspensions due to collisions depends on the shear stress τ_{Sij} and a coefficient of dynamic friction ($\tan\theta$):

$$\sigma_{DSj} = \rho_K \frac{\overline{u_{Kj} u_{Kj}}}{\overline{u_{Kj} u_{Kj}}} + \frac{\tau_{Sji}}{\tan\theta} \quad (13)$$

where: $\tan\theta$ may be related to the local Froude number, taking values about $\tan\theta = .5$ (Roco and Shook, 1983).

- (3) $\rho_K \overline{u_{Kj} u_{Kj}}$ - turbulent inertial stress due to the random exchange of particles between neighboring layers. In our study two models for this term were used in parallel:

- eddy viscosity ϵ_{Kji} model (Boussinesq)

$$-\overline{u_{Kj} u_{Kj}} = \epsilon_{Kji} \frac{\partial u_{Kj}}{\partial x_j} \quad (14)$$

- streamtube diffusion coefficient λ_{Kji} model (Roco, 1980)

$$-\overline{u_{Kj} u_{Kj}} = \frac{\partial}{\partial x_j} (\lambda_{Kji} \overline{u_{Kj}^2}) \quad (15)$$

The Boussinesq model was used in conjunction with the transport equation for the dissipation rate (Roco and Balakrishnan, 1982). The second model was applied for two-phase liquid solid particle flow using a specific distance from the pipe wall (Roco and Shook, 1981). In both approaches the mixture turbulence parameter is obtained by taking the sum of the contributions of all the flow components.

The new set of equations resulting from the space/time averaging (8) of the conservation equations was rearranged for an iterative explicit scheme to calculate successively concentrations, velocities and turbulence parameter. The concentration equation is detailed further in this paper.

Concentration Equation

The equation for the K-th component is derived by subtracting from the momentum equation for the K-th component the equivalent momentum equation for a virtual mixture (-K) composed from all other components except K. The last equation is obtained by summing momentum equations for solid compounds $K' = 1, \dots, K-1, K+1, \dots, N$ and for the carrying liquid, multiplying the intermediate results by $\bar{\alpha}_K / \bar{\alpha}_{-K}$ and space/time averaging (where $\bar{\alpha}_{-K} = 1 - \bar{\alpha}_K$). Neglecting $\bar{\alpha}_K \bar{p}_{Kj}$, the equation is:

$$\frac{\partial}{\partial x_j} \bar{\alpha}_K [\rho_K \overline{u_{Kj} u_{Kj}} - \sum_{-K} \rho_{K'} \bar{\alpha}_{K'} \overline{u_{K'j} u_{K'j}} / \bar{\alpha}_{-K}] +$$

(A)

$$\sum_{-K} \left[\frac{\bar{\epsilon}_{Kj}}{\Delta T} \int_{t-\Delta T/2}^{t+\Delta T/2} \frac{1}{Z_K} \cdot \sum_{K'} \frac{\overline{u_{K'j} u_{K'j}}}{\overline{u_{K'j} u_{K'j}}} \cdot R_K(\tau-t) / \bar{\alpha}_{-K} + \right.$$

(B)

$$\frac{d}{dt} [\rho_K \overline{u_{Kj}^2} - \sum_{-K} \rho_{K'} \overline{u_{K'j}^2} / \bar{\alpha}_{-K}] +$$

(C1)

(C2)

$$\frac{\partial}{\partial x_j} [\rho_K \overline{u_{Kj} u_{Kj}} - \sum_{-K} \rho_{K'} \overline{u_{K'j} u_{K'j}} \cdot \bar{\alpha}_K / \bar{\alpha}_{-K}] +$$

(D1)

(D2)

$$\frac{1 - \delta_{it}}{\tan\theta} \cdot \frac{\partial}{\partial x_i} (\tau_{K_{it}} - \sum_{-K} \tau_{K'_{it}} \cdot \bar{\alpha}_K / \bar{\alpha}_{-K}) +$$

(E1)

(E2)

$$\frac{\partial}{\partial x_i} (\tau_{K_{ii}} - \sum_{-K} \tau_{K'_{ii}} \cdot \bar{\alpha}_K / \bar{\alpha}_{-K}) -$$

(F1)

(F2)

$$\bar{\alpha}_K \cdot (\rho_K - \rho_{-K}) \cdot g = 0 \quad (16)$$

(G)

where: \sum denotes the sum over all components except K. -K

The "concentration equation" for a component K (16) can be interpreted as an equilibrium between elemental forces acting on the ensemble of particles K, under the influence of gravitation (G), relative acceleration (A), relative mean flow compared to other flow components (B), mixing effects due to turbulent fluctuating velocities of component K (C1) and of the virtual mixture -K (C2), dispersive stress from particle collisions in flowing suspensions (D1, D2 - plastic collisions; E1, E2 - elastic collisions) and Coulombic contacts between particles (F1, F2).

Let us consider the equation (16) for the vertical direction y in a pipe. In the absence of the secondary currents the term (A) vanishes. The contributions of the interaction term between different species (B) may be combined with the interaction terms between particles of the same species (C2), (D2), (E2) and (F2). The models for the characteristic terms (12) - (15) are affected by the spatial nonuniformities in the averaging volume and by the ratio particle dimension/length scale of turbulence. Specific aspects resulting from the model application will be discussed later here.

Algorithm for Velocities and Turbulence Parameter

The following calculation approaches were adopted in previous work:

- (1) By summing the corresponding equation (11) in the same direction i for all flow components one obtains the mixture momentum equation where the interactions terms between components are reciprocally eliminated (similar to Roco and Shook, 1982). Together with the equations written for the relative velocity between each component and the mixture, the system of equations for mean velocities V_K can be solved. Compared to Soo's (1980), the equation has two additional terms due to the dispersive stress and Coulombic contacts between particles. Also, the mixture density in the convective term is weighted by the momentum flux and the space/time averaging for turbulent flow is applied in our approach.
- (2) The transport equation for mixture eddy viscosity contains terms due to diffusion, generation, decay and acceleration (ϵ model, Roco and Balakrishnan, 1982). A coherent calculation approach is used for both eddy viscosity (used in the velocity calculation) and eddy-diffusivity (employed in the concentration equation).
- (3) For the streamtube diffusion coefficient λ_{Kij} (15) a computational scheme was proposed which superposes the effects of various flow components (λ model, Roco and Shook, 1981).

EXPERIMENTAL

The model has been tested with data obtained in closed loop laboratory systems, using circular or rectangular conduits. In addition to the conventional determinations of frictional headloss as a function of mean velocity (magnetic flux flowmeters) and slurry

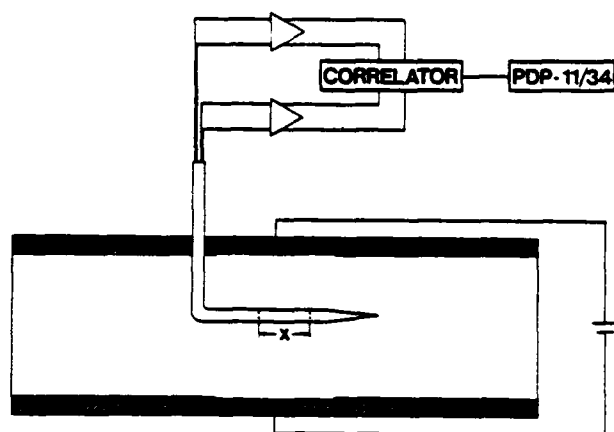


Figure 2. Scheme for solid particle velocity probe.

concentration, the particle concentration distribution was obtained experimentally in all the tests. These employed either gamma ray absorption (chord-average concentrations) or a photographic technique (Scarlett and Grumley, 1974). In some of the studies, particle velocities were determined using the probe shown in Figure 2. The amplitude of the cross-correlation, normalized with the autocorrelations, was determined a function of position (Brown and Shook, 1982).

For this last device, resistivity changes resulting from concentration fluctuations (α') produce voltage fluctuations at sensor electrodes displaced in the applied potential field normal to the direction of mean flow. The transit time for the distance x is determined by cross correlation of the signals from the sensor electrode pairs. From this, a mean velocity for the region defined by the sensor electrodes can be determined. For turbulent slurry flow, calibration studies showed particle retardation by the probe to be of the order of 3% of the local velocity provided conditions near deposition of particles at the bottom of the pipe were avoided. For a properly aligned probe, mean velocities varied little with the location or spacing x , provided a suitable displacement from the nose of the probe was maintained.

In addition to mean velocities, the probe has provided at least a qualitative indication of the structure of the flow through comparison of autocorrelations and cross correlations of electrode signals. With a sands of $d = 0.17$ mm and sensor electrode displacements of the order of 1 mm, autocorrelations in pipelines of 50 and 500 mm I.D. indicate mixing lengths approximately proportional to pipe diameter.

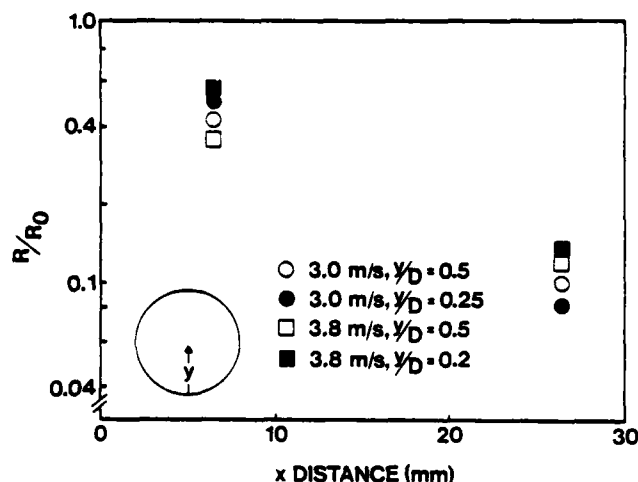


Figure 3. Concentration fluctuation Cross-correlation (R/R_0) vs. distance between electrodes (x).

With larger particles, of diameter greater than the sensor electrode displacement, the autocorrelations suggest that the electrodes respond to the passage of individual particles. For the finer particles, it is apparently clusters which produce the resistivity fluctuations to which the device responds. Such concentration fluctuations are always visually apparent at the pipe wall for slurries which display a concentration gradient within the pipe.

With increasing electrode pair separation distances (x values) the amplitude of the cross-correlation decays, presumably as a consequence of diffusion processes. Recent measurements of these amplitudes (R), normalized with the autocorrelations (R_0), are shown in Figure 3 for a 0.165 mm sand in a 50 mm I.D. pipeline, at a mean concentration of 10% by volume. For a sand of similar size in a 500 mm pipeline the decay process was correspondingly slower, requiring 100 mm to produce the same relative decrease as that produced at $x = 10$ mm in a 50 mm pipeline.

APPLICATION FOR TWO- AND MULTICOMPONENT FLOWS

The general approach was applied for uniform particle slurry flow in pipes, as well as for multispecies particle mixtures. The main set of experiments used for tests is given in Table I, for various materials sand ($S = 2.65$), glass ($S = 2.7$), coal ($S = 1.3 - 1.7$). The tests were performed at various flow conditions: pipe diameter between 50 mm and 500 mm, concentrations up to 40% by volume, particle diameters up to 13 mm and velocities up to three times the critical speed. Samples of experiments with sand and other solids in rectangular pipes (Roco and Shook, 1983) were tested also with positive results.

Table I. Experimental Data in Circular Pipes Used for Model Development

Run No:	Material	Specific Density	Pipe Diameter	Particle Diameter	Average Velocity	Average Concentration
-	-	S(-)	D(mm)	d(mm)	V_M (m/s)	α (% by vol.)
A1-A20	sand	2.65	51.5, 263, 495	.165	1.66-4.33	8.4-34.1
B1-B6		2.65	51.5	.48	1.66-3.44	6.3-29.6
C1-C5		2.65	50.7	.52	1.9 -4.0	11.4-24.7
D1-D2		2.65	263	13.0	3.2 -4.0	9.5-10.2
G1-G6	glass	2.7	40	.58	1.05-2.88	7.0-12.0
M1-M8	coal (multispecies particles)	1.31-1.73	158, 495	0-6.5	1.68-3.16	≤ 45.4

The system of equations for concentrations, velocities and eddy-viscosity (or streamtube diffusion coefficient respectively) was solved numerically using Integral Finite Volume techniques. The calculation domain is discretized and the variables are chosen at interior nodes. The integrals of the differential equations over a finite volume are transformed to a surface integral. The computation is performed using the interfaces between volumes to store and count the data. The interpolation law is suitable for large convective terms. The algorithm can be applied in 2-D and 3-D problems (Roco and Balakrishnan, 1982).

The calculation model is applied for uniform flow in linear sections of horizontal pipes. The volume averaging is reflected in the supplementary terms resulted from averaging and in their models. For modeling one can consider either the statistical analysis of the mixture flow characteristics using local instantaneous measurements, or dimensional analysis of the main local parameters in the averaging volume. For the first approach there is not yet available a complete set of data. Adopting the second approach, we found the main local parameters to be the ratio between the gravitation and inertial forces (F_g/F_i) and the relative dimension of solid particles compared to the averaging volume, i.e. the local scale of turbulence (d/λ) (Roco and Shook, 1982 and 1983; Roco, 1983). The dispersive and supported loads are determined by the first local dimensionless parameter. At the same time, the ratio d/λ determines the predominant terms in equation (11), the relative values of the fluctuating components $(f_k)_T$ and $(f_k)_C$, the ratio between eddy-viscosity and eddy-diffusivity.

The comparisons with experimental data show the ability of the calculation model to predict the velocity and concentration distributions in the pipe cross-section, as well as headlosses along the pipe. In Figure 4 it is illustrated the computed concentration distribution α_s in single species glass sphere ($d = .58$ mm)/water mixture flow compared to photography measurements (Scarlett and Grimley, 1974). In this first test a model and Integral Finite volume were used. Numerical predictions of concentration for multispecies coal/water

slurry flowing in 495 mm pipe employing λ model are given in Figure 5. Five species of coal particles of dimensions $d_1 = 4.8$ mm, $d_2 = 1.2$ mm, $d_3 = .51$ mm, $d_4 = .22$ mm, $d_5 = .01$ mm and specific densities $S_1 = 1.7$, $S_2 = 1.43$, $S_3 = 1.23$, $S_4 = 1.23$, $S_5 = 1.23$ were considered. The total coal concentration at an elevation Y over the pipe bottom α_6 is compared to gamma-ray measurements. Experimental and computed distributions of concentration α_s and velocity for sand .165 mm/water mixture flow in 51.5 mm pipe are presented in Figures 6 and 7. Measured and predicted headlosses in a 50.7 mm pipe with flowing suspension of sand .52 mm are plotted versus averaged velocity in Figure 8. The comparisons (Fig. 4-7) show the numerical simulations predict with good approximation considered sets of experimental data.

The suggested general approach may be applied to steady and unsteady flows, and can be extended to other two- or multicomponent flow patterns.

CONCLUSIONS

1. The suggested space/time averaging of differential equations maintains a good amount of information about the turbulence phenomenon, and reveals the significance (order of magnitude) of some terms in the equations of motion related to the ratio particle dimension/length scale of turbulence.
2. The computational approach for multi-species particle turbulent flow contains some new components, that are specific for turbulent flow of incompressible mixtures. Integral Finite Volume techniques are employed to numerically solve the system of differential equations derived from the conservation laws. The terms due to particle interactions are predominant at high concentrations and large particles.
3. The tests performed with different solid materials for various flow parameters in pipes show a satisfactory agreement of the predictions to experimental results. Design calculations can be made for any

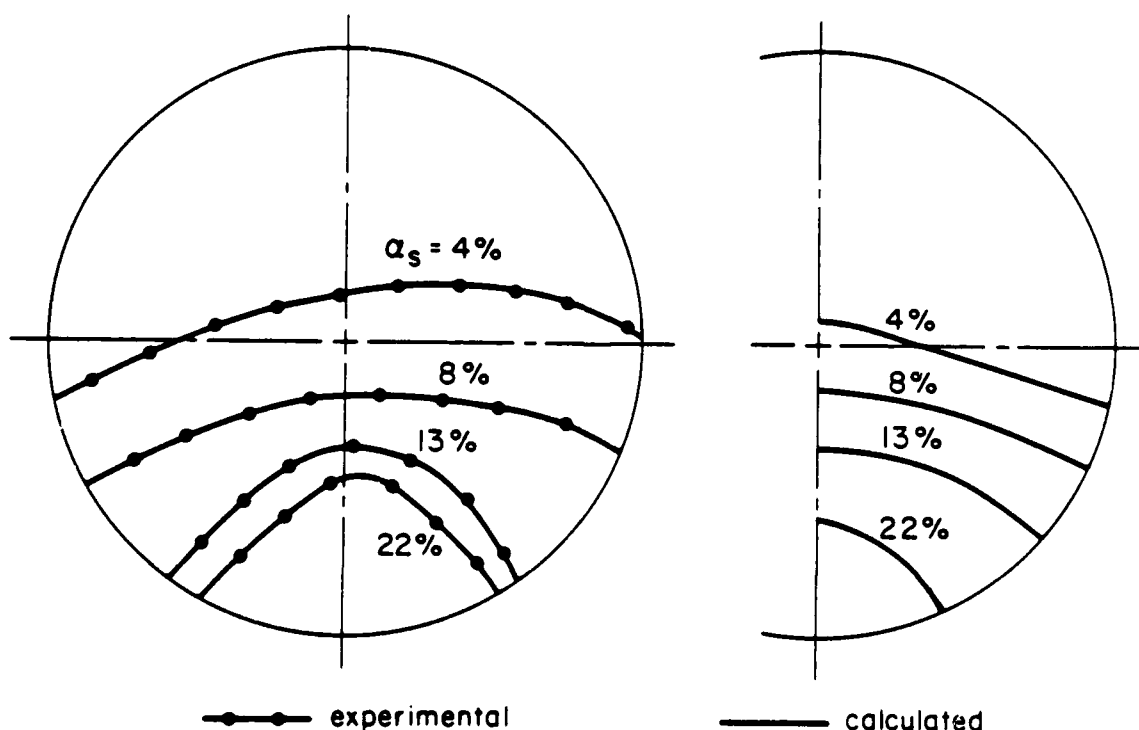


Figure 4. Experimental (Scarlett and Grimley, 1974) and calculated concentration distribution of glass sphere .58 mm/water mixture flow (Run G2).

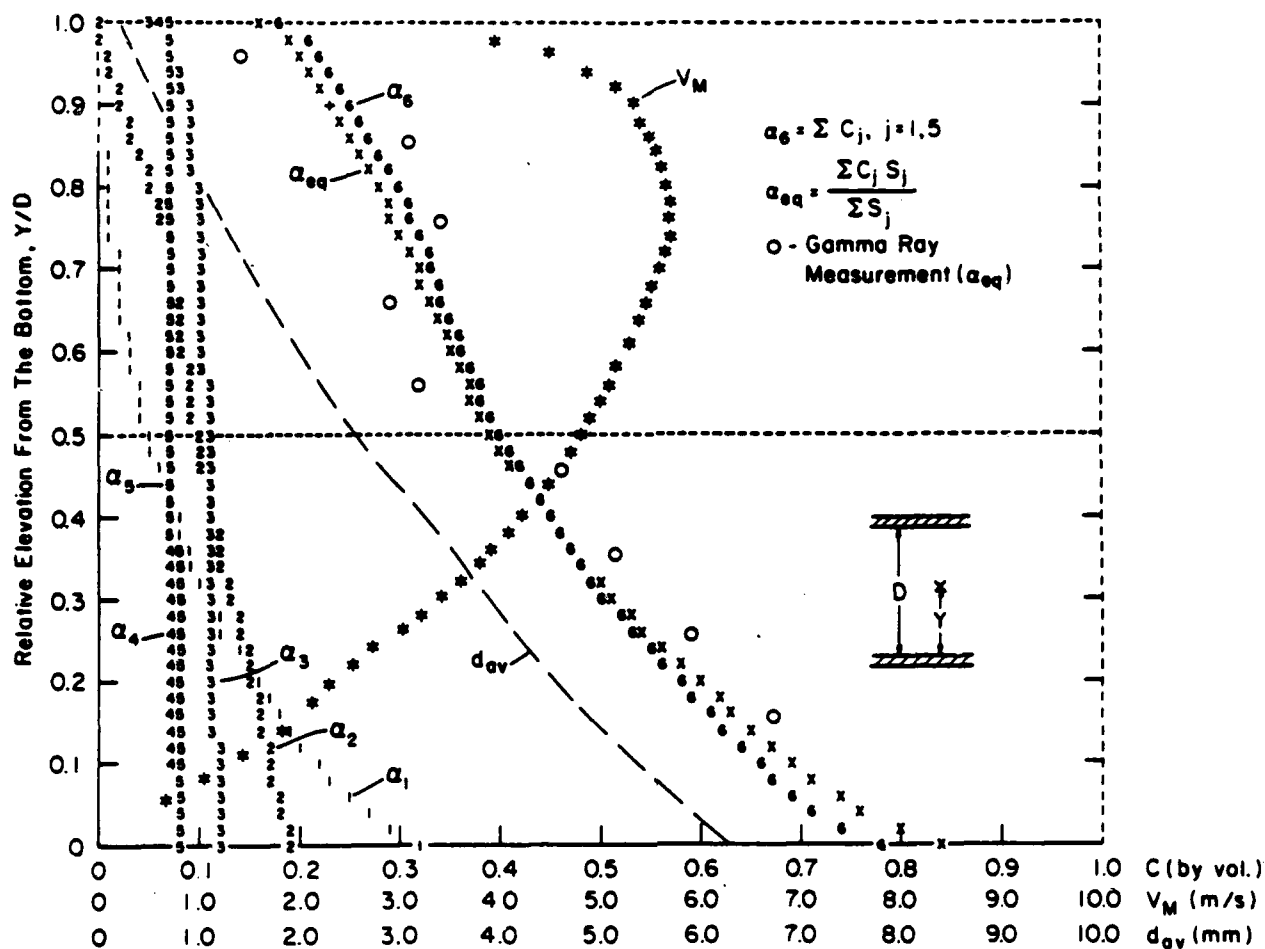


Figure 5. Concentrations ($\alpha_1, \alpha_2, \dots, \alpha_5$), velocity (V_M) and averaged particle size (d_{av}) distributions of Kaiser coal/water mixture flow in the vertical mid-plane of a circular pipe (Run M6).

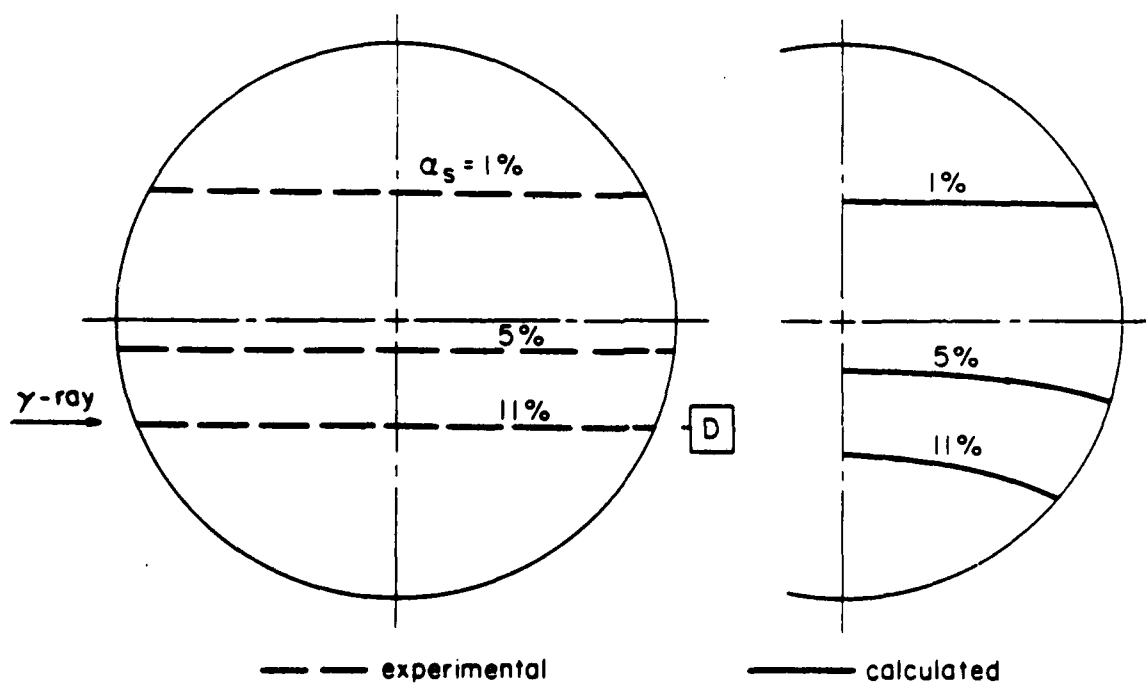


Figure 6. Experimental and calculated concentration (α_5) distribution of sand .165 mm/water mixture flow (Run A1)

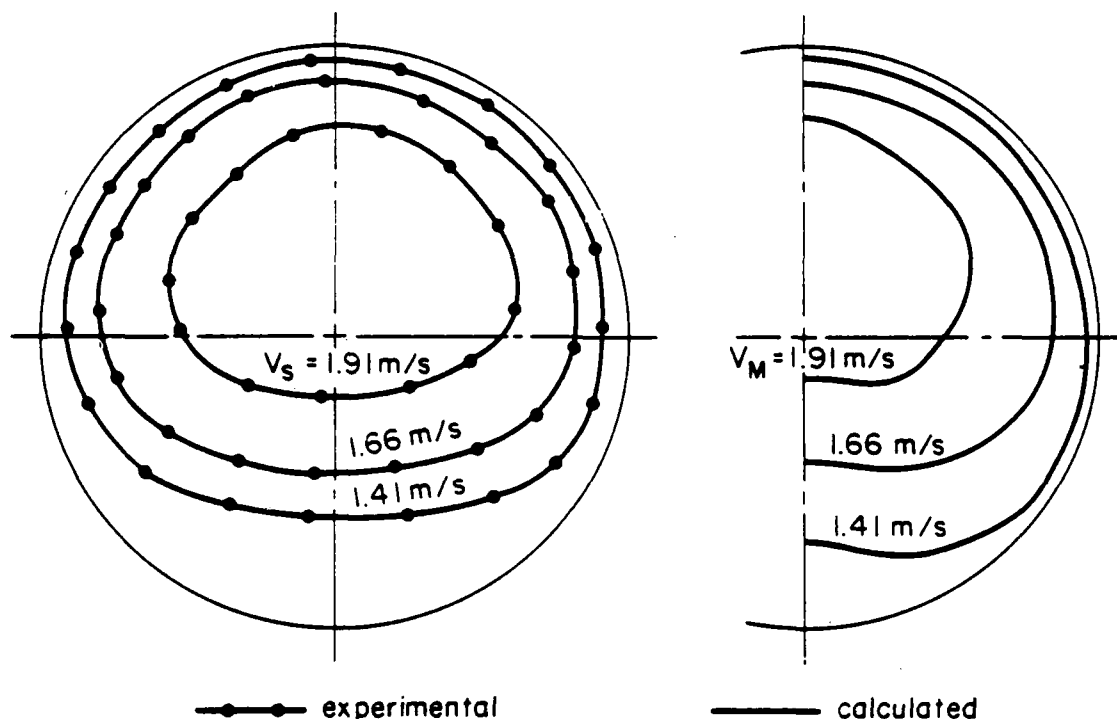


Figure 7. Experimental and calculated velocity distribution of sand .165 mm/water mixture flow (Run A1).

set of given parameters. The approach can be used to extrapolate experimental data from laboratory to industrial situations.

ACKNOWLEDGEMENTS

The studies reported here were supported by the National Science Foundation Grant CPE 8205217 and Canadian NSERC A1037.

BIBLIOGRAPHY

Anderson, T. B. and Jackson, R. A., 1967, "A Fluid-Mechanical Theory of Fluidized Beds", *Ind. Eng. Chem. Fund.*, **6**, 527.

Brown, N. P. and Shook, C. A., "A Probe for Particle Velocity", *Proc. Hydrotransport 8*, BHRA-Fluid Engineering, Cranfield, U.K., **8**, G1,339.

Graham, A. L., Steele, R. D. and Bird, R. B., Oct. 1982, "Particle Clusters in Concentrated Suspensions", 54th Annual Meeting of the Society of Theology, Evanson. Hestroni, G., 1982, "Handbook of Multiphase Flow", McGraw-Hill.

Lee, S. L. and Durst, F., 1982, "On the Motion of Particles in Turbulent Duct Flows", *Int. J. Multiphase Flow*, **8**, 125.

Roco, M. C., 1980, "Ein Neues Rechenmodell zur Untersuchung der Turbulenzströmung", *3 Rohre-Int'l*, **19**, Heft 6, 347.

Roco, M. C., June 1983, "Space/Time Averaged Equations for Multicomponent Turbulent Flow", Cavitation and Multiphase Forum, Spring ASME Fluid Mechanics Meeting, Houston.

Roco, M. C. and Balakrishnan, N., 1982, "Multi-dimensional Liquid-Solid Flow Analysis by Using an Integral Volume Approach", 54th Annual Meeting Soc. Rheology, Evanson, paper D30.

Roco, M. C. and Shook, C. A., 1981, "Calculation Model for Turbulent Slurry Flow", ASME/ASCE Mechanics Conference, Boulder, also *J. of Pipelines*, **4**.

Roco, M. C. and Shook, C. A., 1982, "Modeling Slurry Flow: The Effect of Particle Size", 13th Ann. Meeting FPS, also *Can. J. Chem. Eng.* (in press).

Roco, M. C. and Shook, C. A., 1983, "Dispersive Stress in Shear Slurry Flow", 3rd Multi-Phase Flow and Heat Transfer Symp., Miami (Ed. Veziroglu), Hemisphere.

Scarlett, B. and Grimley, A., 1974, "Particle Velocity and Concentration Profiles during Hydraulic Transport in a Circular Pipe", *Proc. Hydrotransport 3*, BHRA-Fluid Engineering, Cranfield, U.K., D3,23.

Shook, C. A., Gillies, R., Haas, D. B., Husband, H. W. and Small, H., 1982, "Flow of Coarse and Fine Sand Slurries in Pipelines", *J. of Pipelines*, **3**.

Soo, S. L., 1967, "Fluid Dynamics of Multiphase Systems", Blaisdell, Mass.

Soo, S. L., 1980, "Equations of Multiphase Multi-domain Mechanics", *Multiphase Transport* (Ed. Veziroglu), Hemisphere, **1**, 291.

Whitaker, S., 1973, "The Transport Equations for Multiphase Systems", *Chem. Eng. Sci.*, **28**, 139.

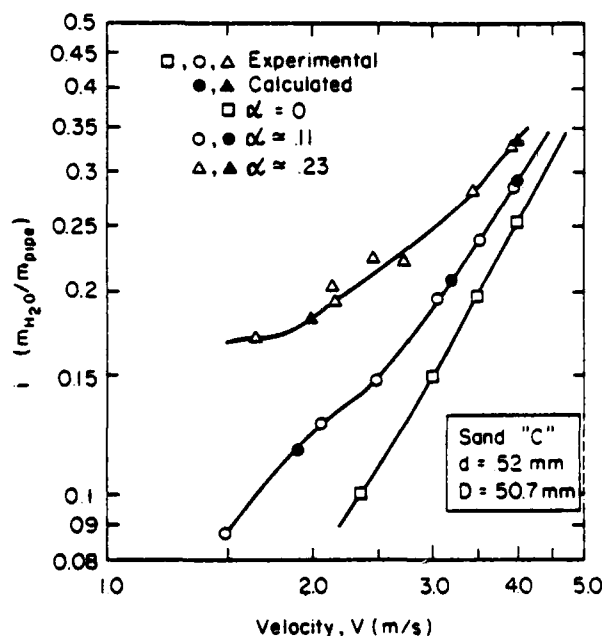


Figure 8. Headlosses vs. sand .52/mm water mixture velocity (Runs C1 - C5).

A TWO-EQUATION TURBULENCE MODEL FOR TWO-PHASE JETS

S. Elghobashi, T. Abou-Arab, M. Rizk and A. Mostafa
Mechanical Engineering Department
University of California
Irvine, California 92717

ABSTRACT

A recently-developed two-equation turbulence model for two-phase flows [6] is tested for the flow of a turbulent axisymmetric gaseous jet laden with spherical solid particles of uniform size. The agreement between the predictions and experimental data is good.

INTRODUCTION

Particle-laden turbulent jets occur in many engineering applications. Pulverised-coal combustors, diesel-engine sprays, aerosols and rocket plumes are some examples. In order to enhance the understanding of the interaction between the dispersed phase and the carrier fluid in these jets parallel experimental and theoretical studies are needed. The need for this coordinated effort stems from the fact that until very recently it was impossible to find in the literature a well-documented experimental study of a two-phase turbulent jet. In fact until a year ago the only two available experimental studies of two-phase turbulent jets [1,2] did not report the radial profiles of the main dependent variables at the nozzle exit. This information is essential for accurately predicting such flow as it is known that the dependence of the downstream flow upon the nozzle conditions persists for at least 50 nozzle diameters [3]. The recent experiment of Modarress et al [4,5], which was performed in parallel with the present work, provided a much needed data to help understand the behavior of two-phase turbulent jets and validate their theoretical models. Elghobashi and Abou-Arab [6] reviewed existing turbulence models for two-phase flows and indicated that these models are based on ad hoc modifications of single-phase turbulence models. They developed [6] a two-equation turbulence model for incompressible dilute two-phase flows which undergo no phase changes. The new model was based on rigorously derived transport equations for the two phases. The purpose of this paper is to apply this model to the flow of a turbulent axisymmetric gaseous jet laden with solid, uniform-size particles and compare the predictions with the data of Modarress et al [4,5].

THE FLOW CONSIDERED

Figure 1 shows a sketch of the two-phase turbulent jet considered in this work. Air carrying uniform size glass beads issues vertically downwards from a cylindrical pipe of diameter D (≈ 0.02 m). The jet is enclosed in a cylindrical container of diameter equal to $30 D$ to avoid ambient disturbances. Low velocity air stream surrounds the nozzle and extends to the container wall to provide well-defined boundary conditions. Table 1 lists the experimental conditions at $0.1 D$ downstream of the pipe exit.

MATHEMATICAL MODEL

Equations of the Mean Motion

The mean motion of each phase is governed by its momentum equations in the axial and radial directions and the conservation of its volume fraction. These equations were written in Cartesian tensor notations by Elghobashi and Abou-Arab [6]; they will be cast here in cylindrical coordinates for the axis-symmetric jet flow.

The modeled form [6] of the mean momentum equation of the carrier fluid in the axial (x) direction is:

$$\begin{aligned} \rho_1 \phi_1 U_{x,x} + \rho_1 \phi_1 U_{r,r} = & - \phi_1 p_{,x} - F \phi_2 (U_x - V_x) \\ & + \frac{1}{r} (\rho_1 \phi_1 r v_{t,x,r})_{,r} + c_{m1} \rho_1 U_{x,r} \left(\frac{v}{\sigma_\phi} \phi_{1,r} \right) \\ & + C_{\phi 5} \frac{1}{r} \left(\frac{k}{\epsilon} r u_{t,x,r} \right)_{,r} \left(\frac{v}{\sigma_\phi} \phi_{1,r} \right)_{,r} \\ & + C_{\phi 5} \frac{k}{\epsilon} \mu_{t,x,r} \left(\frac{v}{\sigma_\phi} \phi_{1,r} \right)_{,rr} \end{aligned} \quad (1)$$

The momentum equation of the solid phase in the axial (x) direction is

$$\begin{aligned} \rho_2 \phi_2 V_{x,x} + \rho_2 \phi_2 V_{r,r} = & - \phi_2 p_{,x} + F \phi_2 (U_x - V_x) + \frac{1}{r} (\rho_2 \phi_2 v_{p,x,r})_{,r} \\ & + (\rho_2 - \rho_1) g \phi_2 \end{aligned} \quad (2)$$

where $c_{m1} = 0.4$ and $c_{\phi 5} = 0.1$.

In the above equations the comma-suffix notation indicates differentiation with respect to the spatial coordinates x and r . U and V are respectively the mean velocities of the carrier fluid and dispersed phase. The subscripts 1 and 2 denote respectively the carrier fluid and the dispersed phase. ρ is the material density, ϕ the mean volume fraction, p the mean pressure, μ the eddy viscosity of the fluid, ν the kinematic eddy viscosity of the dispersed phase, σ_ϕ the kinematic eddy viscosity of the fluid, σ_ϕ the turbulent Schmidt number of the volume fraction and g is the gravitational acceleration.

We assumed in the above equations that the diffusional fluxes in the radial direction are much larger than those in the axial direction for the jet flow considered. The momentum equations of both phases in the radial direction can be written in a similar

manner and will not be presented here due to space limitation.

The quantities F and v_p are evaluated in the following section.

The Interphase Friction Factor F

The interphase friction factor F is given by

$$F = Z(18 \mu_f / d^2) \quad (3)$$

where d is the particle diameter, μ_f is the dynamic viscosity of the fluid, and Z is a correction factor of the Stokes' drag law which depends on the particle Reynolds number and can be obtained from the standard drag curve of steady flow around a sphere [7] as follows

$$Z = 1 + 0.1315 R_{pe} (0.82 - 0.05 \log_{10} R_{pe}), \quad 0.01 < R_{pe} < 20;$$

$$\text{and } Z = 1 + 0.1935 R_{pe}^{0.6305}, \quad 20 < R_{pe} < 260 \quad (4)$$

The particle Reynolds number R_{pe} is calculated from

$$R_{pe} = d |\vec{u} - \vec{v}| / \nu_f \quad (5)$$

where $|\vec{u} - \vec{v}|$ is the magnitude of the total relative velocity vector between the two phases, and ν_f is the kinematic viscosity of the fluid.

Turbulent Diffusivity of Solid Particles

The turbulent diffusivity of solid particles is evaluated by introducing the particle Schmidt number σ_p defined as:

$$\sigma_p = \frac{\nu_t}{\nu_p} \quad (6)$$

Since solid particles do not in general follow the motion of the surrounding fluid from one point to another it is expected that σ_p will be different from unity and vary with the particle relaxation time and local turbulence quantities. Alonso [8] reviewed the recent developments in evaluating σ_p and recommended the use of Peskin's [9] formula

$$\frac{\nu_p}{\nu_t} = (1/\sigma_p) = 1 - (3/2)(L_L/\lambda)^2 [Q^2/(Q+2)] \quad (7)$$

where

$$Q = (2\rho_p/2FT_L) \quad (8)$$

The local Lagrangian integral time scale, T_L , is evaluated assuming isotropic turbulence [10]; thus

$$\epsilon = 15\nu_f^2/\lambda^2 \text{ and } \lambda^2 = 24\nu_f T_L \text{ which give}$$

$$T_L = (5/12)k/\epsilon \quad (9)$$

The local Lagrangian length scale, L_L , appearing in (7), and the Eulerian microscale λ are calculated from

$$L_L = \sqrt{\frac{2}{3}} k T_L \quad (10)$$

$$\lambda = \sqrt{10} \nu_f k / \epsilon \quad (11)$$

When (L_L/λ) is much less than unity the fluid elements in the neighborhood of the solid particle will have similar velocities (i.e. homogeneous flow). Consequently, the correlation of fluid velocities encountered by the particle will be similar to the Lagrangian fluid correlation and σ_p , from (7), will approach unity. On the other hand as L_L becomes larger than λ the particle will be surrounded by random fluid velocities and its diffusivity will decrease relative to that of the fluid.

The Turbulence Model

The modeled form of the turbulence kinetic equation (k) of the carrier fluid; according to Elghobashi and Abou-Arab [6] is

$$\begin{aligned} \rho_1 \phi_1 U_{x,x} k + \rho_1 \phi_1 U_{r,r} k &= \rho_1 \phi_1 \nu_t U_{x,r} U_{x,r} \\ &+ \frac{4}{3} \rho_1 c_{\phi 5} \frac{\nu_t}{c_\mu} \left(\frac{\nu_t}{\sigma_\phi} \phi_{1,r} \right)_{,r} U_{r,r} \\ &- \rho_1 c_{\phi 5} \left(\frac{k}{\epsilon} \right) \nu_t \left(\frac{\nu_t}{\sigma_\phi} \phi_{1,r} \right) U_{x,r} U_{x,r} \\ &- F \phi_2 k \left[1 - \int_0^\infty \left(\frac{\Omega_1 - \Omega_R}{\Omega_2} \right) f(\omega) d\omega \right] - F(U_r - V_r) \left(\frac{\nu_t}{\sigma_\phi} \phi_{1,r} \right) \\ &+ c_{\phi 5} \left(\frac{\nu_t}{c_\mu} \right) F \left[1 - \int_0^\infty \left(\frac{\Omega_1 - \Omega_R}{\Omega_2} \right) f(\omega) d\omega \right] \left(\frac{\nu_t}{\sigma_\phi} \phi_{1,r} \right)_{,r} \\ &+ \rho_1 \phi_1 \frac{1}{\tau} \left(\frac{\nu_t}{\sigma_k} k_{,r} \right)_{,r} - \rho_1 \phi_1 \epsilon \end{aligned} \quad (12)$$

The turbulence energy dissipation rate equation (ϵ) is

$$\begin{aligned} \rho_1 \phi_1 U_{x,x} \epsilon + \rho_1 \phi_1 U_{r,r} \epsilon &= c_{\epsilon 1} \frac{\epsilon}{k} [\rho_1 \phi_1 \nu_t U_{x,r} U_{x,r} \\ &+ \frac{4}{3} \rho_1 c_{\phi 5} \left(\frac{\nu_t}{c_\mu} \right) \left(\frac{\nu_t}{\sigma_\phi} \phi_{1,r} \right) U_{r,r} \\ &- \rho_1 c_{\phi 5} \left(\frac{k}{\epsilon} \right) \nu_t \left(\frac{\nu_t}{\sigma_\phi} \phi_{1,r} \right)_{,r} U_{x,r} U_{x,r}] \\ &- c_{\epsilon 3} \frac{\epsilon}{k} [F \phi_2 k \left(1 - \int_0^\infty \left(\frac{\Omega_1 - \Omega_R}{\Omega_2} \right) f(\omega) d\omega \right) \\ &+ F(U_r - V_r) \left(\frac{\nu_t}{\sigma_\phi} \phi_{1,r} \right) \\ &- c_{\phi 5} \left(\frac{\nu_t}{c_\mu} \right) F \left(1 - \int_0^\infty \left(\frac{\Omega_1 - \Omega_R}{\Omega_2} \right) f(\omega) d\omega \right) \left(\frac{\nu_t}{\sigma_\phi} \phi_{1,r} \right)_{,r}] \\ &+ \rho_1 \phi_1 \frac{1}{\tau} \left(\frac{\nu_t}{\sigma_\epsilon} \epsilon_{,r} \right)_{,r} - c_{\epsilon 2} \frac{\epsilon}{k} (\rho_1 \phi_1 \epsilon) \end{aligned} \quad (13)$$

The terms, in (12) and (13), involving integration in the frequency domain (ω) represent additional dissipation of k or ϵ due to the slip between the particles and the fluid and depend on the magnitude of correlation between their respective instantaneous velocities. Details of the derivation of these terms are given in reference [6].

The Lagrangian frequency function, $f(\omega)$ is in general affected by the presence of the dispersed phase. In the low frequency range (inertial subrange), the modulation of the Lagrangian frequency function of the carrier fluid by the dispersed phase can be neglected [11]. Thus in the present work the Lagrangian frequency function is given by [12],

$$f(\omega) = \left(\frac{2}{\pi} \right) \left(\frac{T_L}{1 + \omega^2 T_L^2} \right) \quad (15)$$

where ω ranges from 1 to 10^4 (sec^{-1}) and T_L is calculated from (9). The functions Ω_1 , Ω_2 , Ω_R , α and β are evaluated according to [6] from

$$\begin{aligned} \alpha_1 &= \left(\frac{u}{u_0}\right)^2 + \sqrt{6} \left(\frac{u}{u_0}\right)^{3/2} + 3\left(\frac{u}{u_0}\right) + \sqrt{6} \left(\frac{u}{u_0}\right)^{1/2} + 1 ; \\ \alpha_2 &= \beta^{-2} \left(\frac{u}{u_0}\right)^2 + \sqrt{6} \beta^{-1} \left(\frac{u}{u_0}\right)^{3/2} + 3\left(\frac{u}{u_0}\right) + \sqrt{6} \left(\frac{u}{u_0}\right)^{1/2} + 1 ; \\ \alpha_R &= [(1-\beta)\omega/(\alpha\beta)]^2 ; \\ \alpha &= 12v_1 z/d^2 , \\ \beta &= 3\rho_1/(2\rho_2 + \rho_1) . \end{aligned} \quad (16)$$

The values of the coefficients appearing in equations (12) and (13) are listed in Table (2) below.

Table 2 Coefficients of the Turbulence Model

σ_ϕ	σ_k	c_u	σ_ϵ	$c_{\phi 5}$	$c_{\epsilon 1}$	$c_{\epsilon 2}$	$c_{\epsilon 3}$
1	1	$k-\epsilon_1$ [13]	1.3	0.1	1.44	$k-\epsilon_1$ [13]	1.2

It is seen that three new coefficients ($\sigma_\phi, c_{\phi 5}, c_{\epsilon 3}$) are now added to the well-established $k-\epsilon$ coefficients for single-phase flows, namely $\sigma_k, \sigma_\epsilon, c_u, c_{\epsilon 1}$ and $c_{\epsilon 2}$. The values of the new coefficients have been optimized to produce good agreement with the data of ref. [4,5] for one particle size (200 microns) and then used to predict the data of the other size (50 microns). It should be emphasized that more validation testing is required to establish the universality of these coefficients.

Boundary Conditions

The parabolic flow considered here requires the prescription of three boundary conditions for each dependent variable. Table (1) provides these conditions at the pipe exit plane and at the jet boundary. At the axis of symmetry ($r=0$) all the radial gradients are set to zero, in addition to the vanishing radial velocity of each phase.

NUMERICAL SOLUTION PROCEDURE

The marching finite-difference procedure employed in this work is a modified version of that developed and described by Spalding [14] for laminar two-phase flows and thus only a brief outline is given here.

The coordinates of the expanding finite-difference grid are x and ϕ , the stream function based on the mean gas-phase properties, i.e.

$$\phi = \int_0^x \rho_1 \phi_1 U_x r dr . \quad (17)$$

The steps followed to obtain the solution at a given axial location are:

- 1 - Guess the downstream ϕ_1^* distribution.
- 2 - Solve for U_x downstream.
- 3 - Solve for k and ϵ ; obtain r 's and solve for U_r 's.
- 4 - Obtain $p(r)$ from U_r equation.
- 5 - Solve for downstream V_x, V_r, ϕ_2 and get ϕ_1 .
- 6 - Compare the new ϕ_1 with the guessed ϕ_1^* and repeat steps 1 through 5 until the solution converges before marching to the next station.

It was found that 3 iterations are needed at each station to achieve convergence.

RESULTS AND DISCUSSIONS

The results presented here were obtained using 40 lateral nodes to span the flow domain between the centerline of the jet and its outer edge. Grid-dependence tests were conducted with 30, 40 and 50 lateral nodes and different axial step sizes and concluded that the 40 node grid results are virtually grid-independent.

In what follows we compare the predicted with the measured distributions of the mean velocities, volume fractions of the two phases, turbulence intensity and shear stress of the gaseous phase and the jet spreading rate.

Figure 2 shows the radial profiles of the mean axial velocities of the two phases at $x/D = 20$, normalized by the centerline velocity of the single-phase jet, $U_{c,s.ph.}$. The flow conditions are those of Case 3 in Table 1. Also shown is the mean velocity profile of the turbulent single-phase jet having the same Reynolds number (14100) at the pipe exit.

It is seen that the centerline velocity of the dispersed phase is about 1.8 times that of the carrier fluid although the latter is 1.3 times the former at the pipe exit. This can be explained by the fact that large-diameter ($> 10 \mu$) particles do not respond to the fluid turbulent fluctuations (Eqs. (7) & (8) indicate that for a fixed ρ_2 and T_1 we get $v_c < v_f$ for small F , i.e. large d) thus the main force that accelerates a particle in the radial direction is the viscous drag exerted on the particle by the fluid velocity, U_r . Now this drag force is proportional to $(U_r - V_r)$ and since U_r is negative in the outer region of the jet (and $V_r < U_r$) the resulting force will be inwards thus limiting the radial spread of the particles. This is evident in Figure 3 where the concentration of the solid particles vanish at a radial distance of $r/x = 0.12$ while the fluid spreads to at least three times this distance. Conservation of momentum of each phase then results in the solid-phase axial velocity being much higher than that of the fluid, and in turn the particles continue to be a source of momentum for the fluid. It is also clear from Figure 3 that the single-phase jet is wider than the particle-laden jet; this will be discussed later in this section. Both figures 2 and 3 display in general good agreement between the measured and predicted velocity and concentration profiles.

The measured and predicted mean velocity profiles for Case 2 ($d = 50 \mu$, $\phi_0 = 0.85$, $Re = 13300$) are shown in Figure 4. Similar qualitative behavior to that of Case 3 is exhibited here except that now the ratio between the experimental velocities of the solid and the fluid is only about 1.15 instead of 1.8 in Case 3 ($d = 200 \mu$, $\phi_0 = 0.8$, $Re = 14100$). The main difference between the two cases is the particle diameter, and thus any quantitative change in the mean velocity profiles is attributed to the interphase surface area acted on by the viscous drag. This surface area in Case 2 is four times that in Case 3, since, for nearly the same loading ratio, the number of the 50 μ particles is 64 times that of the 200 μ particles. This increase in the number of particles and interphase area results in augmenting the momentum sources of the carrier fluid thus reducing the rate of decay of its centerline velocity.

The agreement is very good between the measured and predicted fluid velocity while the solid-phase velocity is underestimated by 8% in the inner region, a discrepancy well within the bounds of experimental error. Figure 5 shows the mean velocity profiles at $x/D = 20$ for Case 1 (50μ , $Re = 13300$, $\phi_0 = 0.32$) which has a lower loading ratio, ϕ_0 , than Case 2, otherwise the two cases are identical. Again the behavior of the two phases is similar to that observed in the other two cases except that now the experimental ratio between the centerline velocities of the solid and the fluid is 1.2 instead of 1.15 in the higher-loading case (Case 2). This indicates that, other conditions being the same, higher loading reduces the rate of decay of the fluid centerline velocity. This is a result of the increase in the number of particles and hence their contribution to the fluid momentum as discussed earlier.

In order to distinguish between the dispersed phase effects on the mean motion (inertia and drag) and on turbulence (diffusion) we show (Fig. 5) the mean velocity profiles obtained by solving the complete two-

phase momentum equations (1), (2) together with the single-phase k and ϵ equations (i.e. Eqs. (3), (4) without the additional production and dissipation terms due to the dispersed phase). We see that the resulting increase in the fluid centerline velocity, as compared to that of the single-phase jet, is only half that measured and predicted by the new k - ϵ model. Stated differently, the modulation of the fluid mean-velocity profile by the dispersed phase is not only due to the particles inertia and drag but equally important due to the additional turbulence dissipation. This in turn reduces the fluid momentum diffusivity with the result of a peaked velocity profile near the jet centerline. The additional turbulence dissipation is caused mainly by the fluctuating particle slip velocity and its correlation with the fluid velocity fluctuation [6]. The consequent reduction in the fluid turbulence intensity and shear stress is displayed in figures 6 and 7 where the agreement between the measurement and prediction is good.

Figure 8 shows the effect of the dispersed phase on the spreading rate of the jet by comparing the different $Y_{1/2} \sim x$ distributions of the three cases, where $Y_{1/2}$ is the radius at which the fluid mean axial velocity is half that at the centerline. While for a turbulent single-phase jet the value of the slope ($dY_{1/2}/dx$) is constant (≈ 0.08), that for a two-phase jet is a function of the dispersed phase properties such as particle diameter and density and loading ratio. This dependence is displayed in the figure. For Case 3 ($d = 200\mu$, $\phi = 0.8$) the predicted slope value is 0.053, for Case 2 ($d = 50\mu$, $\phi = 0.85$) it is 0.046, and for Case 1 ($d = 50\mu$, $\phi = 0.32$) it is 0.064. Cases 3 and 2 have nearly the same loading ratio but the particle diameter in the latter is one quarter that of the former; the result being a reduction of the spreading rate by more than 13%.

Cases 1 and 2 are identical except that the loading ratio in the latter is 2.66 times that of the former; the result being a reduction of the spreading rate by 28%.

The figure also shows the discrepancy that results in predicting the spreading rate if the single-phase k - ϵ model is used instead of the proposed model. The former predicts for Case 1 a slope of 0.072 while the latter agrees with the experimental value of 0.064. As explained earlier this is due to the fact that the additional dissipation of turbulence energy due to the dispersed phase is accounted for in the proposed model.

CONCLUDING REMARKS

It has been shown that the turbulence model, introduced in ref [6], allows the correct simulation of the two-phase turbulent jet.

The additional dissipation produced by the slip velocity fluctuations has a significant effect on the jet development. Further testing is needed to check the universality of the coefficients in the model.

REFERENCES

- [1] Betseroni, G., and Sokolov, M., 1971, "Distribution of Mass, Velocity, and Intensity of Turbulence in a Two-Phase Turbulent Jet," J. Appl. Mech., 33, 735.
- [2] Popper, J., Abuaf, N. and Hetroni, G., 1974, "Velocity Measurements in a Two-Phase Turbulent Jet," Int. J. Multiphase Flow, 1, 715.
- [3] Barker, S., 1973, "Laser-Doppler Measurements on a Round Turbulent Jet in Dilute Polymer Solutions," J. Fluid Mech., 60, 721.
- [4] Modarress, D., Wuerer, J. and Elghobashi, S., 1982, "An Experimental Study of a Turbulent Round Two-Phase Jet," AIAA/ASME 3rd Joint Thermophysics, Fluids, Plasma and Heat Transfer Conference, St. Louis, Missouri.

- [5] Modarress, D., Tan, H. and Elghobashi, S., 1983, "Two-Component LDA Measurement in a Two-Phase Turbulent Jet," AIAA 21st Aerospace Sciences Meeting, Reno, Nevada.
- [6] Elghobashi, S. and Abou-Arab, T.W., 1983, "A Two-Equation Turbulence Model for Two-Phase Flows," Phys. Fluids, 26, 931.
- [7] Clift, R., Grace, J.R. and Weber, M.E., 1978, "Bubbles, Drops and Particles," Academic Press, New York.
- [8] Alonso, C.V., 1981, "Stochastic Models of Suspended Sediment Dispersion," A.S.C.E., 107, 733.
- [9] Peskin, R.L., 1971, "Stochastic Estimation Applications to Turbulent Diffusion," Int. Symposium on Stochastic Diffusion, C.L. Chiu, ed., Univ. of Pittsburgh, Pittsburgh, Pa., 251.
- [10] Calabrese, R.V. and Middleman, S., 1979, "The Dispersion of Discrete Particles in a Turbulent Fluid Field," A.I.Ch.E., 25, 1025.
- [11] AL Taweel, A.M. and Landau, J., 1977, "Turbulence Modulation in Two-Phase Jets," Int. J. Multiphase Flow, 3, 341.
- [12] Hinze, J.O., 1975, "Turbulence," McGraw-Hill, N.Y.
- [13] Launder, B.E., Morse, A., Rodi, W. & Spalding, D.B., 1972, "The Prediction of Free Shear Flows—a Comparison of the Performance of Six Turbulence Models," Imperial College, TM/TN/19.
- [14] Spalding, D.B., 1979, "Numerical Computation of Multiphase Flows," Lecture Notes, Thermal Sciences and Propulsion Centre, Purdue University, Indiana.

ACKNOWLEDGEMENTS

This work has been supported by a U.S. Department of Energy grant No. DE-FG22-80PPC-30303 and NASA grant No. NAG3-176. The authors express their thanks to Mrs. Verna Bruce for her expert typing of the manuscript.

Table 1
EXPERIMENTAL FLOW CONDITIONS AT
0.10 DOWNSTREAM OF PIPE EXIT

Gas-Phase (Air):	Case 1	Case 2	Case 3
Centerline velocity, $U_{x,c}$ (m/s)	12.6	12.6	13.4
Exponent, n , of power law velocity profile $U_x/U_{x,c} = (1-(2r/D))^{1/n}$	6.6		
Turbulence intensity ($u_x/U_{x,c}$)	$(0.04 + 0.1 r/D)$		
Density, ρ_1 (Kg/m ³)	1.178		
Mass flow rate \dot{m}_1 (Kg/s)	3.76×10^{-3}	3.76×10^{-3}	4×10^{-3}
Reynolds number $Re = (4\dot{m}_1/\pi\mu_1 D)$	13300	13300	14100
Uniform mean velocity of surrounding stream, $U_{x,s}$ (m/s)	0.05		
Intensity of turbulence in surrounding ($u_{x,s}/U_{x,s}$)	0.1		
Solid-Phase (Glass Beads):	Case 1	Case 2	Case 3
Particle diameter (microns)	50	50	200
Particle density, ρ_2 (Kg/m ³)	2990		
Centerline velocity, $V_{x,c}$ (m/s)	12.4	12.4	10.2
Exponent, n , of power law velocity profile	27.6		
Mass flow rate \dot{m}_2 (Kg/s)	1.2×10^{-3}	3.2×10^{-3}	3.2×10^{-3}
Ratio of mass flow rates \dot{m}_2/\dot{m}_1	0.32	0.85	0.8
Ratio of volumetric fractions $\phi_2/\phi_1 = (\dot{m}_2/\dot{m}_1)(\rho_1/\rho_2)(U_{x,c}/U_{x,s})$	1.1×10^{-4}	2.9×10^{-4}	3.52×10^{-4}

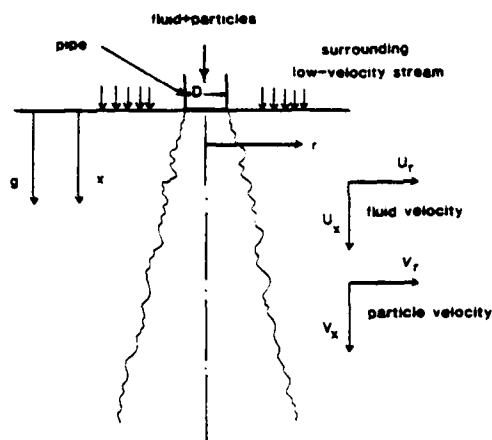


Figure 1 Flow schematic

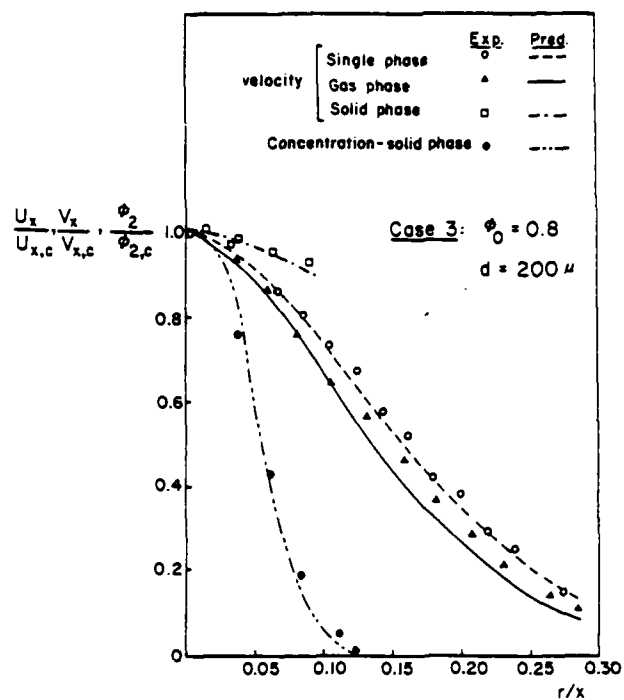


Figure 3 Normalized mean velocity and volume fraction profiles at $x/D = 20$ for Case 3

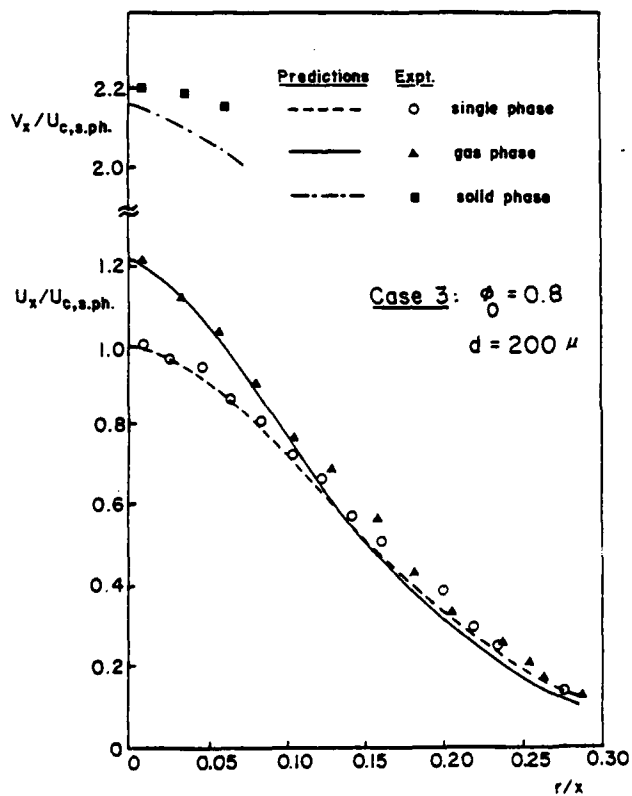


Figure 2 Mean velocity profiles at $x/D = 20$ for Case 3

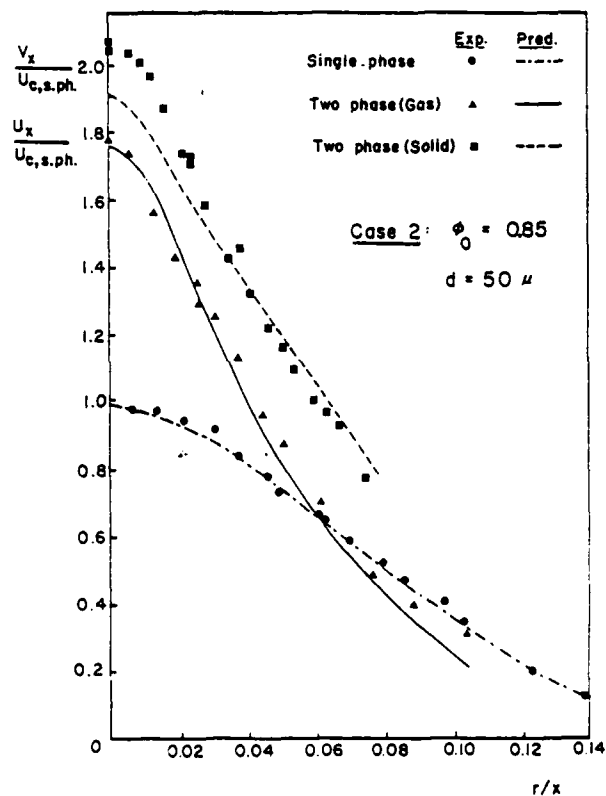


Figure 4 Mean velocity profiles at $x/D = 20$ for Case 2

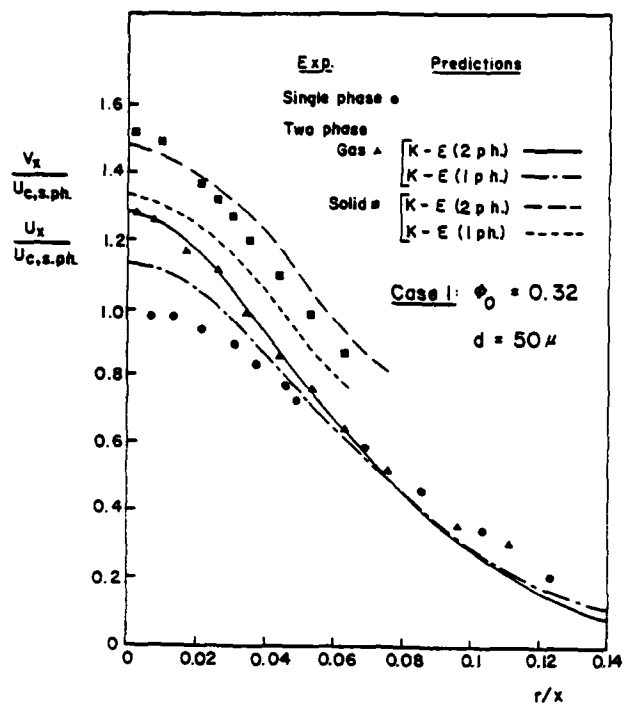


Figure 5 Mean velocity profiles at $x/D = 20$ for Case 1

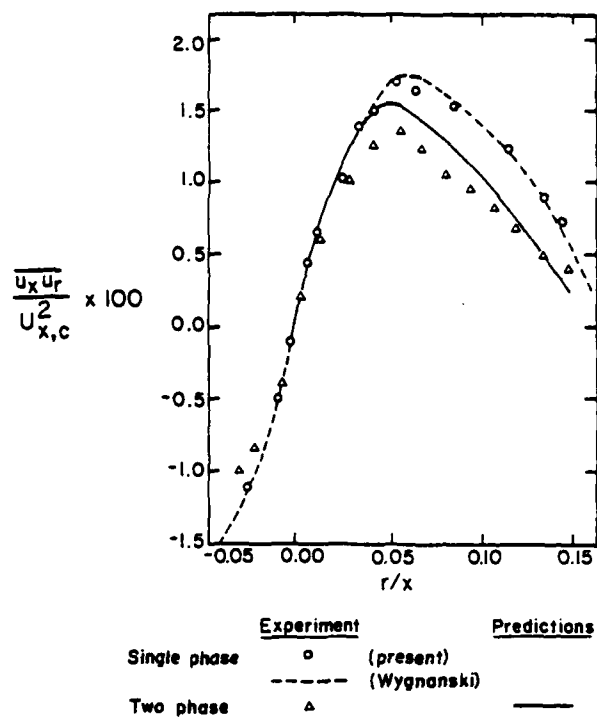


Figure 7 Turbulence shear stress profile at $x/D = 20$ for Case 3

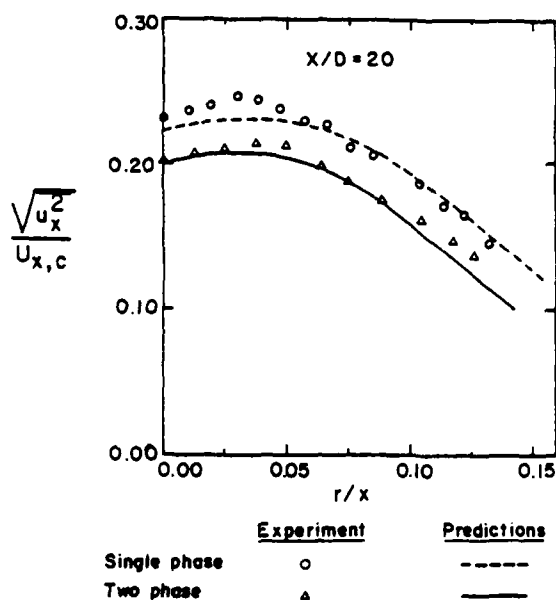


Figure 6 Turbulence intensity profile at $x/D = 20$ for Case 3

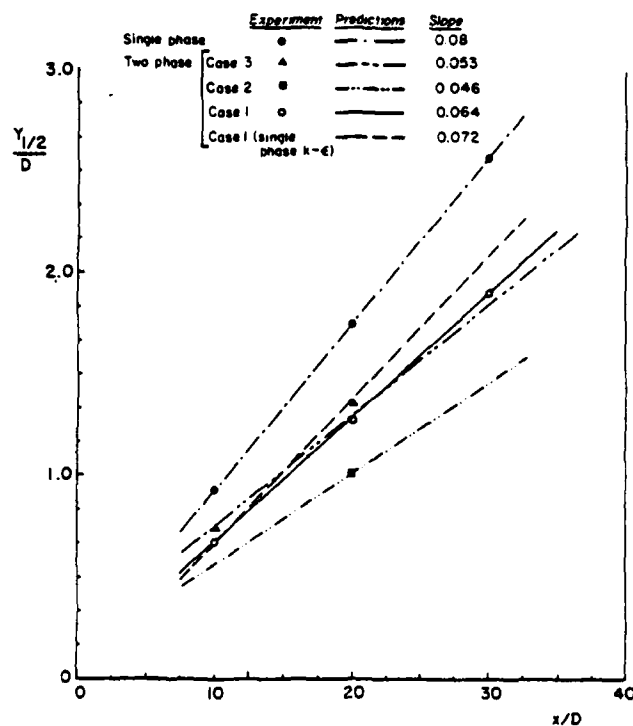


Figure 8 Jet spread rates for the three cases

EXPERIMENTAL RESULTS CONCERNING
SEPARATED TWO-PHASE FLOW AROUND A CIRCULAR CYLINDER

F. Hara
Science University of Tokyo
Tokyo 162, Japan

and

Y. Kawamoto
Toyo Engineering Co., Ltd.
Funabashi 273, Japan

ABSTRACT

This paper deals with experimental results concerning pressure fluctuations on the surface of a circular cylinder immersed perpendicular to a two-phase air-water bubble flow, and velocity fluctuations in the cylinder's separated flow region with respect to void fraction. A critical two-phase flow void fraction value exists to markedly classify flow characteristics: When the void fraction is less than the critical value, the flow structure resembles that of a single-phase fluid flow and, for a void fraction more than that value, this flow becomes very distinctive.

INTRODUCTION

Two-phase gas-liquid flows inevitably occur in energy-generation facilities such as large condensers, steam generators, or civil engineering structures like pilings submerged in a wave flow containing bubbles. Vibrations induced by the two-phase flow aggravate troubles in such facilities.

Investigation centering, first, on a single cylinder is the most important way to clarify the nature of flow-induced, unsteady forces acting on a cylinder and to further the understanding and prevention of two-phase flow induced vibrations in cylindrical structures involved in the construction of tube banks or offshore pilings.

Hara(1982) reported interesting results concerning the unsteady lift force acting on a stationary circular cylinder in a two-phase air-water cross flow: The force is rather periodic and less dependent on the two-phase flow void fraction when it is volumetrically less than 10%. For a void fraction exceeding 10%, however, the fluid force becomes less periodic and increases rapidly with the void fraction.

To understand this characteristic of the two-phase flow induced lift force, it is necessary to study flow characteristics around a circular cylinder, paying particular attention to vortices shed in the cylinder's separated flow region.

This paper deals with experimental results concerning pressure fluctuations on the surface of a circular cylinder immersed perpendicular to a two-phase air-water bubble flow and velocity fluctuations in a separated flow region of the cylinder with respect to air bubble concentration in the flow. Statistical values such as root mean square, power spectral density, and coherency are evaluated for both fluctuations and compared with those for a single-phase water flow. The major results are as follows:

- (1) The correlation between the pressure fluctuation at a point on the cylinder's surface at a 90° angle to the flow and velocity fluctuation near that point for a

void fraction less than 10% is very high, but they show less of a correlation when the void fraction exceeds 10%.

- (1) The separation point of the cylinder's boundary layer moves downward along the cylinder's surface when the void fraction exceeds 10%.
- (3) The turbulent structure of the separated two-phase flow around the cylinder resembles that of single-phase water flow when the void fraction is less than 10%, but seems to differ from that for a higher void fraction, implying that the wake becomes narrower, shear flow becomes thicker, and no vortex shedding occurs.

EXPERIMENTAL APPARATUS AND PROCEDURES

Experimental Test Loop

The experimental test loop in this study consisted mainly of a diffuser, a settling chamber, a nozzle, a rectangular test section, upper and lower tanks, a pump, and an air compressor. The loop was vertically installed. The test section, at the center of which a circular cylinder was set, had a 30 x 100 mm cross section and was 200 mm long. The nozzle connected to the test section had an area contraction ratio of 9:1. Two layers of honeycomb net installed 80 mm apart in the middle of the chamber produced a uniform velocity profile at the test section's entrance. The approach velocity profile was examined using an OEL laser doppler anemometer (LDA) and found to be uniform within 1% outside boundary layers. The intensity of the main flow's turbulence was approximately 10% at a flow velocity of 0.6 m/s in the test section.

Air was injected into the water flow at the exit of the settling chamber through 11 one-mm-diameter circular holes located at a 15 mm pitch in a 10-mm brass tube with a wall 1 mm thick. The average air bubble was 5 mm in the test section.

The circular test cylinder was 15 mm in diameter and 30 mm long. Two 1 mm holes for measuring pressure fluctuations were made in the middle section of the cylinder, one located at the cylinder's base and the other at a 90° angle point of the cylinder. The cylinder was installed at the center of the test section, perpendicular to the flow.

Instrumentation

Pressure. Pressure fluctuations of the cylinder surface and a test section wall were measured using two strain gage pressure transducers, and were amplified by dynamic strain amplifiers. Electric signals from these fluctuations were transmitted to a microcomputer, which calculated differential pressure fluctuations.

Velocity. Average flow velocity and fluctuation were measured using an OEL 5 mW LDA system around the

test cylinder and transmitted to the microcomputer for further data processing.

Bubble Motion. Air bubble size and rise velocity were measured by a bubble detector consisting of two light-emitting diodes driven by an electric pulse time series with different frequencies, two photodiodes for detecting light passing through the test section, and an electronic logic circuit to measure the duration when no light was detected.

Data Processing. Pressure and velocity fluctuations transduced to electric signals were digitized by an AD converter with a sampling period of 0.01 s. 1024 data for each fluctuation were used to evaluate average value, RMS, PSD, and coherency. From data obtained by the bubble detector, bubble size in the flow direction and speed of rising bubbles were calculated by the microcomputer using 1024 data sampled at 0.01 s.

Experimental Conditions

The approach velocity in the test section was 0.60 m/s with a turbulence within 10% and uniformly distributed across the test section within 1%. The Reynolds number based on the cylinder's diameter was 0.9×10^4 . The Strouhal number was 0.22 for a single-phase water flow.

The void fraction defined as air volume flow rate Q_a divided by total air and water flow rate $Q_a + Q_w$ was 0.0, 0.024, 0.048, 0.070, 0.091, 0.12, 0.15, and 0.20 for measuring pressure fluctuations and circumferential flow fluctuations near the cylinder surface (Figure 1). For flow fluctuation measurement in the separated region, a void fraction less than 10% was used.

Figure 1 gives measurement points of flow velocity fluctuations, where points along the cylinder surface are only for measuring the circumferential component of velocity fluctuations, points on the $X = 8$ line for in-line components, and points on the $Y = 9$ line for in-line and cross-flow components. Pressure fluctuations were measured at a point at a 90° angle to the flow and at the cylinder's base.

Uncertainty in RMS values of velocity fluctuations due to bubbles passing the LDA measurement area was evaluated and found to be less than about 10%.

Bubble size in the flow direction measured by the bubble detector was 5 to 6 mm, depending on the two-phase flow void fraction. Thus, the ratio of bubble size to cylinder diameter was about 0.33:0.4.

EXPERIMENTAL RESULTS

Correlation between Pressure and Velocity Fluctuations

The intensity of pressure fluctuation at a point 90° from the stagnation point in the mid section of the cylinder's surface is given in Figure 2 in terms of RMS value against void fraction. Pressure fluctuation increased slightly with a void fraction less than 9%. It increased rapidly, however, for void fractions more than 10%. Cylinder surface pressure fluctuation thus showed two different trends for low and high void fractions, also reported by Hara (1982).

Figure 2 also indicates velocity fluctuation in the main flow direction at point $X/D = 8/15$ and $Y/D = 0.0$, showing a trend very similar to that of pressure fluctuations.

Note that the dominant frequency component in pressure and velocity fluctuations was 9.0 Hz for void fractions less than 9%, equal to that of vortex shedding from the cylinder.

Figure 3 gives coherency between pressure and velocity fluctuations measured at the same points as in Figure 2. For void fractions less than 9%, both had good coherency at 9.0 Hz, meaning a high correlation due to an identical vortex-shedding cause. However, for $\alpha = 9.1\%$, coherency at 9.0 Hz was comparatively small.

Circumferential Velocity Fluctuation Around a Cylinder

Average and fluctuating circumferential velocity at points from the stagnation point to the base and 0.5 mm away from the cylinder surface (Figure 1) were measured by an LDA system. Figure 4 shows the average

velocity component distribution against the cylinder's circumferential coordinate, in degrees. The two-phase flow void fraction ranged from 0.0--a single-phase water flow--to 20%.

This indicates that the point where average circumferential velocity was zero remained at the same position ($\theta = 110^\circ$, corresponding to the separation point of a circular cylinder) as that of water flow for a two-phase flow with a void fraction less than or equal to 7%. However, when the void fraction rose above that value, the zero velocity point moved downward with void fraction increase, reaching $\theta = 122^\circ$.

Figure 5 shows the distribution of turbulence intensity of the circumferential velocity around the cylinder for void fractions from 0.0 to 20%. At $\theta = 110^\circ$, the intensity of water flow did not show a clear peak, but point $\theta = 110^\circ$ was concluded to be the separation point for the cylinder according to Schlichting (1965). For a two-phase flow with a void fraction less than or equal to 7%, the intensity had a sharp peak at point $\theta = 110^\circ$, meaning the two-phase flow separation point for the cylinder remained at the same position as that for a water flow. This finding is also supported by Figure 4. The peak in turbulence intensity distribution moved downward with a void fraction increase up to 20%.

This and the downward shift of the zero circumferential velocity point in Figure 4 indicate that the two-phase flow separation point moved toward the cylinder's base with void fraction increase when the void fraction exceeded a certain value--9% in our case, for example.

Velocity Fluctuation in a Separated Flow Region

In-line Axis Distribution. Along an in-line axis at $X/D = 8/15$, the in-line flow-velocity component was measured using the LDA system. Figure 6 gives the average velocity against Y/D for a void fraction from 0.0 to 9.1%. The shape of the distribution is roughly similar for each void fraction. The minimum point of the average velocity corresponded to the position in the shear flow region closest to the cylinder's separation point.

Due to air bubbles flowing upward with a slip velocity to water flow, the average velocity in the in-line direction became larger than that of the water flow.

Figure 7 illustrates turbulence intensity in the in-line flow component against Y/D for water and two-phase flows, showing a similar distribution for each case. The dominant peak in the distribution corresponded to the minimum average velocity point in Figure 6. For a two-phase flow with a small void fraction--e.g., $\alpha \leq 9.1\%$ --turbulence intensity was markedly reduced in the region of Y/D being 0.2 and 0.6, which belongs to the cylinder's shear flow region, because the average velocity was almost twice that of water flow, while the RMS value of flow velocity fluctuation was slightly smaller than that for water flow.

Cross Axis Distribution. In-line and cross-flow components of velocity fluctuation along the axis at $Y/D = 3/5$ were measured using the LDA system, and their average and RMS values evaluated. Figure 8 gives average values of flow velocity fluctuation in the in-line direction for void fractions from 0.0 to 9.1%. The distribution shape with respect to coordinate X/D was very similar for each void fraction. There was, however, a very significant trend in distributions: When the void fraction increased, the zero cross point of the average velocity moved slightly inward, meaning that the shear layer, defined as the average velocity derivative dU/dX being positive, became widened slightly as void fraction increased.

Figure 9 gives the cross-flow component of the average velocity against coordinate X/D . This component was rather small compared with the in-line component, but the distribution shape was complicated.

In the region where X/D was larger than about $3/5$, the distribution shape was very similar for each case. In the region from minimum to maximum points of distribution, however, a recognizable difference was found, meaning that, when void fraction increased,

distribution shifted inward.

Figure 10 gives the vector diagram of average flow velocity along line $Y/D = 3/5$, where solid arrows indicate water flow and empty ones two-phase flow with a void fraction of 9.1%.

This diagram indicates the following:

- (1) Flow in the wake directed toward the cylinder and wake region narrowed more for a two-phase flow with a void fraction of 9.1% than for water flow.
- (2) Corresponding to this, the shear flow region widened more for the two-phase flow than for water flow.
- (3) Inside and outside the shear flow region, \bar{U} became slightly larger for the two-phase flow than for water flow and, in the wake, both components (\bar{U} , \bar{V}) of the average two-phase flow velocity were larger than for a single-phase water flow. This indicates bubble motion mainly influenced the in-line component of average velocity in and outside the shear flow, but, owing to the very small flow-velocity value in the wake, bubble motion in the wake region affected both velocity components.

Figure 11 gives RMS values of flow velocity fluctuations in both directions for X/D at $Y/D = 3/5$, where empty symbols correspond to water flow and half-solid symbols to a two-phase flow with a void fraction of 9.1%. Triangles correspond to fluctuations in the in-line direction and circles for the cross-flow direction component. The RMS of the in-line velocity fluctuation had a large peak at $X/D = 8/15$ for water and two-phase flows and, in the wake region, the magnitude was almost the same.

There was a large difference in RMS value between water and two-phase flows in the main flow region: The RMS was almost twice for a two-phase flow with $\alpha = 9.1\%$ to that of water flow. The cross-flow component of velocity fluctuation had a local peak in its RMS distribution against coordinate X/D for both flow situations, and the peak position shifted inward for the two-phase flow compared with water flow. In the wake, the cross-flow component of two-phase flow velocity fluctuation was slightly smaller than that of water flow but, in main and shear flow regions, both components of two-phase flow velocity fluctuation became somewhat larger than those of water flow.

Figure 12 gives turbulence intensity σ_u/\bar{U} of the in-line component of velocity fluctuation against coordinate X/D at $Y/D = 3/5$. The distribution shape was very similar for each case, and the dominant peak located at $X/D = 2/5$ ($= 0.4$) for both water flow and the two-phase flow with a void fraction less than or equal to 7%. However, for a void fraction of 9.1%, the peak moved slightly inward. Turbulence intensity in the wake was somewhat smaller for two-phase flow than that of single-phase water flow. However, in the main flow region, the intensity for two-phase flow was larger than that of water flow.

Figure 13 gives the turbulence intensity for the cross-flow component, where the vertical axis expresses turbulence intensity σ_v/\bar{V} and the horizontal axis coordinate X/D at $Y/D = 8/15$. The void fraction ranged from 0.0 to 9.1%. Peak location at $X/D = 2/3$ was not influenced by adding air bubbles to the flow. This peak position coincided with the point $\bar{V} = 0$ at $X/D = 2/3$ in Figure 9, or the outer edge of the shear flow region (Figure 8). The inner peak shifted slightly inward for the two-phase flow due to bubble motion because of a very small flow velocity in that direction.

DISCUSSION

Vortex Shedding in a Two-phase Flow

The cylinder's Strouhal number was 0.22 in single-phase water flow. When dominant frequency f of pressure fluctuations at the 90° point on the cylinder's surface is employed for nondimensional number fD/U , this number equals Strouhal number 0.22 even in two-phase flow with a void fraction less than or equal to 9.1%. Figure 3 indicates that coherency between pressure and velocity fluctuations was almost

1.0 at 9.0 Hz for void fractions ($\alpha = 0.0$ to 7%), meaning pressure fluctuation may be said to be mainly produced by velocity fluctuation even for two-phase flow with a low void fraction. Considering the water flow situation, velocity fluctuations near a separation point are generated by vortex shedding from the cylinder.

Figures 4 and 5, then, indicate that the two-phase flow separation point of the cylinder remained at the same location as that in water flow for low void fractions.

Thus, two-phase flow velocity fluctuations at a point close to the separation point may most probably be generated by vortex shedding for low void fractions. We thus conclude that, when a two-phase flow void fraction is less than or equal to about 10%, a circular cylinder sheds vortices in a way similar to those in a single-phase fluid flow.

Two-phase Flow Separation Point

Figures 4 and 5 indicate that the two-phase flow separation point of a circular cylinder remained at the same position as that of water flow when the void fraction was less than or equal to 7%. When the void fraction was more than about 10%, however, the separation point moved downward and reached the 122° point of the cylinder for $\alpha = 20\%$. This is a marked influence of air bubbles on the flow structure around a circular cylinder.

Figure 14 aids in understanding this air bubble effect, and indicates bubble arrival frequency, measured by the bubble detector, against the void fraction, where solid circles indicate the average and the broken lines indicate average-standard deviation. When the void fraction was about 9%, the average-minus-standard-deviation frequency crossed the line of vortex shedding frequency $St = 0.22$.

Rising air bubbles are known to produce turbulence around them. Thus, bubbles flowing upward with a slip velocity near a cylinder's surface may disturb the flow in the boundary layer. The more frequently air bubbles pass near the boundary layer, the more intensely the flow is disturbed.

This indicates that the two-phase flow boundary layer of a cylinder may become very turbulent when the void fraction becomes larger than about 10%, leading to the analogy that the turbulent boundary layer of a two-phase flow forces the cylinder's separation point to move downward.

Turbulence Structure in a Separated Flow

In-line Axis Turbulence Structure. As Figure 7 indicates, two-phase flow turbulence intensity was almost half that of water flow in the shear flow region. This reduction in intensity is mostly due to the large increase in average velocity in the shear flow region owing to the relatively large velocity of air bubble rise. The structure of two-phase flow turbulence intensity distribution was very similar to that of water flow, as indicated in Figure 7, but the dominant peak in intensity distributions, apparently generated by vortex shedding from the cylinder, decreased markedly in magnitude for a two-phase bubbly flow.

This may indicate that vortex shedding contributes less to turbulence in the two-phase flow: Bubble-motion-generated disturbance may contribute more to flow turbulence than vortex shedding.

Cross-axis Turbulence Structure

Figures 11, 12, and 13 summarize the peak location of turbulence intensities σ_u/\bar{U} and σ_v/\bar{V} , and of RMS value σ_u , with respect to coordinate X/D and void fraction α in Figure 15, where symbols with parentheses () indicate uncertainties in experimental data not being small due to high air-bubble concentration in the flow. The σ_u/\bar{U} peak in Figure 12 indicates the inner edge of the shear flow region because of $\bar{U} = 0$ at the position of this peak. The outer peak of σ_v/\bar{V} indicates the outer boundary, because \bar{V} was almost zero at $X/D = 2/3$ (Figure 9). It may thus be said that air bubbles in the flow did not influence the width of the shear flow region when the void fraction was less than or equal to 7%. For a void fraction over 9%, however, the inner

and outer edges of the two-phase flow shear layer generated by the circular cylinder were refracted inward and outward.

The position of the σ_u peak coincides with the trajectory of the vortex center flowing downstream because at the position on the vortex center trajectory, flow fluctuation in both directions may be maximum for single-phase flow. This is supported by the fact that peaks in σ_u and σ_v for water flow were located at almost the same position, $X/D = 0.57$, as indicated in Figure 11.

The peak magnitude of σ_u for $\alpha = 9.1\%$ two-phase flow was slightly larger than that for water flow, and the difference between them seems to have been caused by air bubble motion in the flow. Thus, the peak of σ_u for both water and two-phase flows ($\alpha = 9.1\%$) may be produced by vortices shed from the cylinder.

The discussion above indicates that the vortex center's trajectory is bent inward with an increase in the two-phase flow void fraction.

CONCLUSIONS

This paper dealt with experimental results on turbulence characteristics of a separated two-phase bubbly flow around a circular cylinder, and showed the following major conclusions:

- (1) Vortex shedding from a circular cylinder still occurred in a two-phase bubble flow when the void fraction was less than about 9% and the bubble/cylinder diameter ratio was about 0.4.

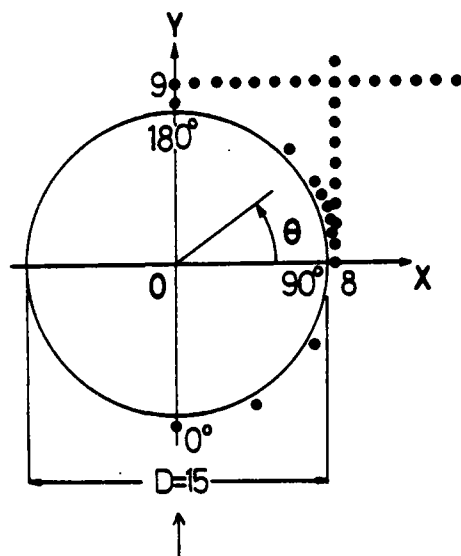


Fig. 1 Circular test cylinder dimension and points of velocity fluctuation measurement

- (2) The two-phase flow separation point of the circular cylinder stayed at the same position as that of water flow when the void fraction was less than about 9%. It moved downstream, however, to the cylinder for a high void fraction two-phase flow ($\alpha > 10\%$).
- (3) The shear flow region generated by a circular cylinder immersed perpendicular to a two-phase bubble flow had almost the same flow structure as that of water flow when the void fraction was less than 9%. For a void fraction higher than 10%, the shear flow region was widened inwardly and outwardly.
- (4) Corresponding to (3), above, the wake narrowed compared with that of water flow when the void fraction was higher than 9%.
- (5) The vortex center trajectory was not greatly influenced by disturbance generated through bubble motion in the two-phase flow.
- (6) Critical void fraction α_c was about 10%, which classified flow characteristics into two—one similar to that of a single phase fluid flow and the other peculiar to a two-phase bubble flow.

BIBLIOGRAPHY

- Hara, F., 1982, "Two-Phase Flow-Induced Forces Acting on a Circular Cylinder", ASME PVP-Vol.63, 9.
Schlichting, H., 1965, "Grenzschicht-Theorie", Verlag G. Braun, 736

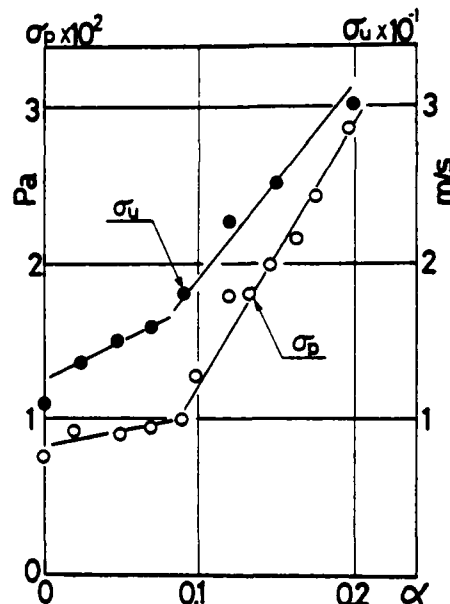


Fig. 2 Pressure and velocity fluctuations σ_p and σ_u against two-phase flow void fraction

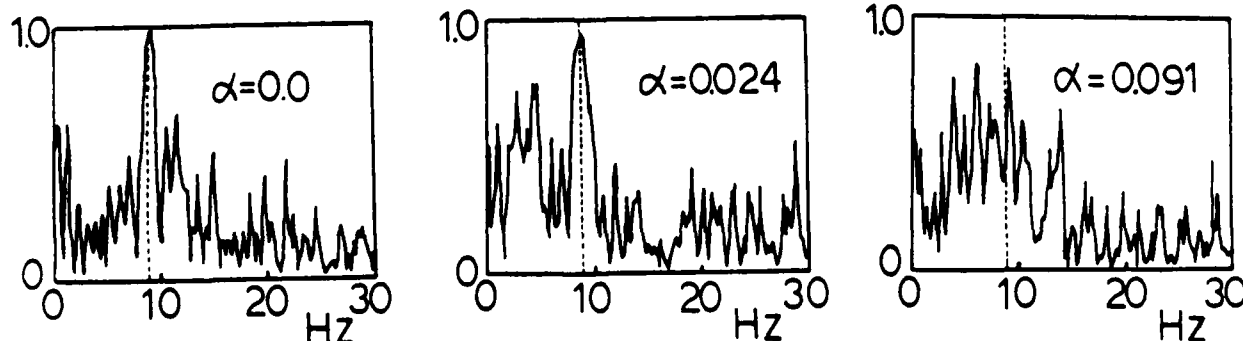


Fig. 3 Coherency between pressure and velocity fluctuations

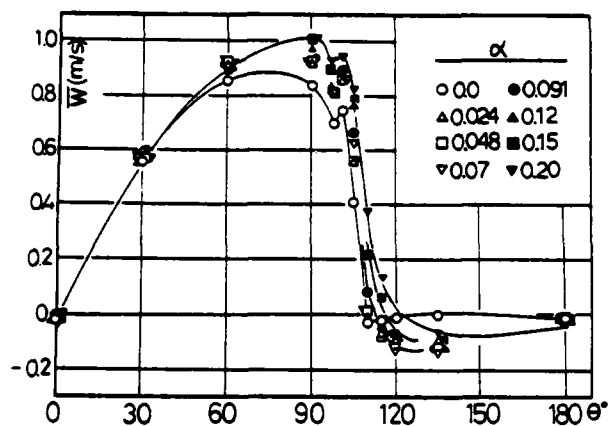


Fig. 4 Average circumferential flow velocity against circumferential position θ

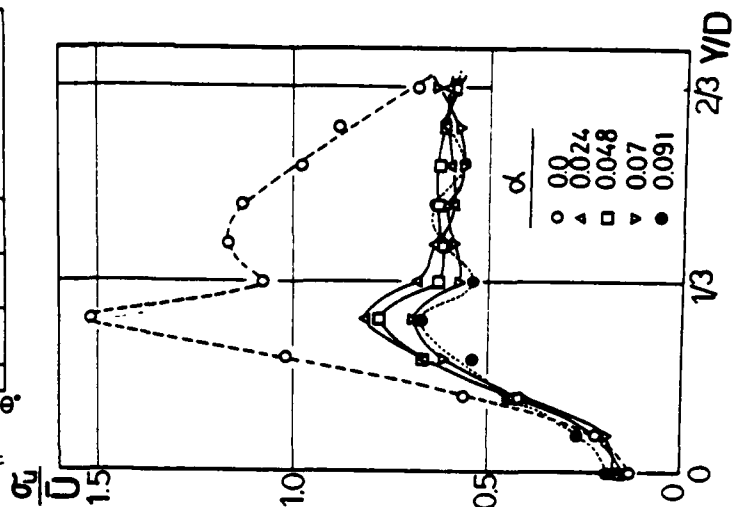


Fig. 7 Turbulence intensity of in-line velocity fluctuation on axis $X/D = 8/15$ against Y/D

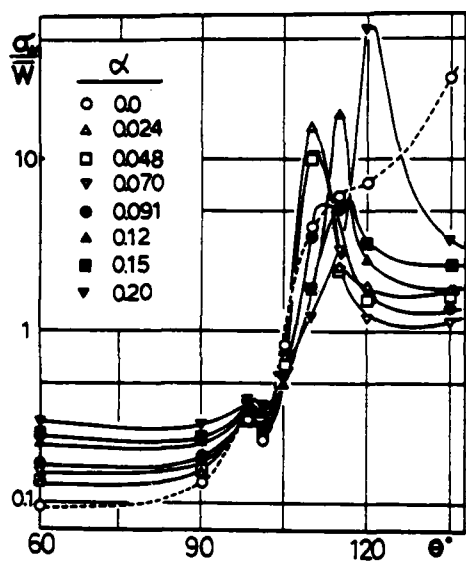


Fig. 5 Turbulence intensity of circumferential velocity fluctuation against θ

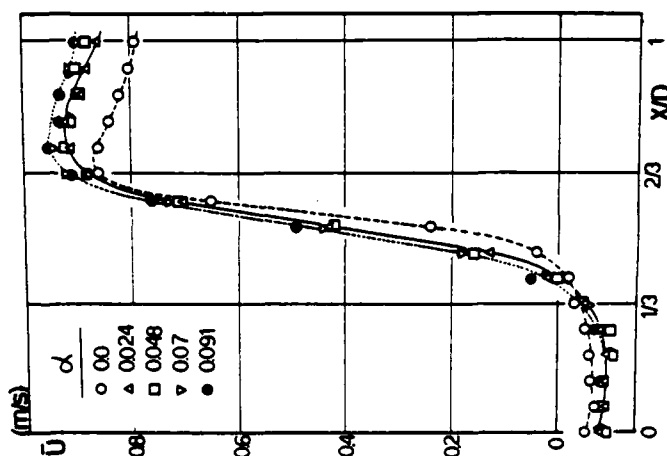


Fig. 8 In-line component of average flow velocity \bar{U} against coordinate X/D at $Y/D = 3/5$

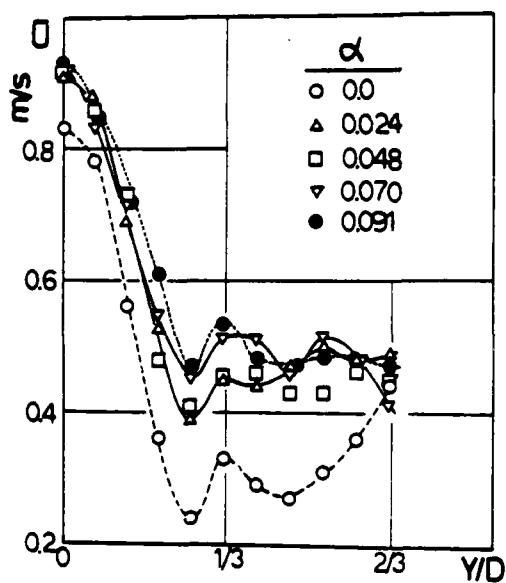


Fig. 6 Average in-line velocity \bar{U} on an in-line axis $X/D = 8/15$ against coordinate Y/D

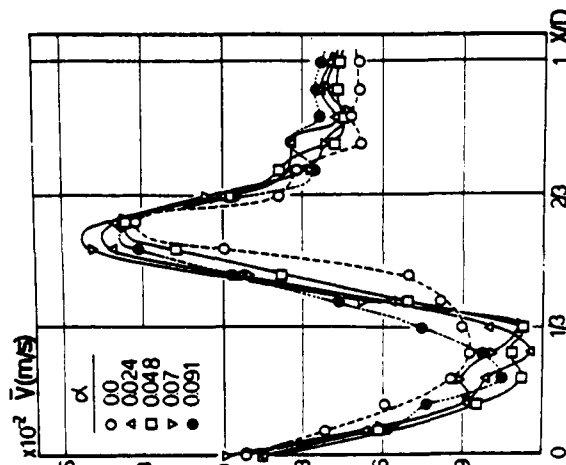


Fig. 9 Cross-flow component of average flow velocity \bar{V} against coordinate X/D at $Y/D = 3/5$

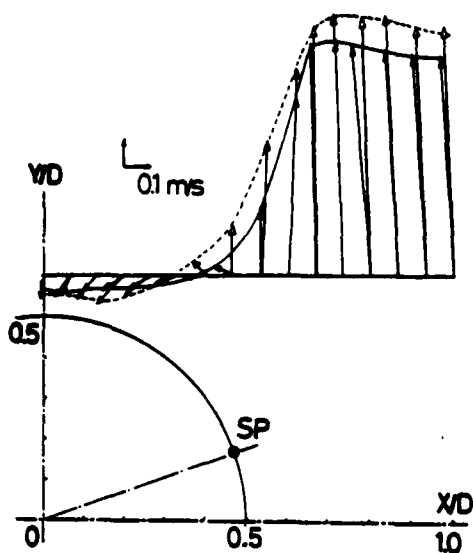


Fig. 10 Vector diagram of average flow velocity against coordinate X/D

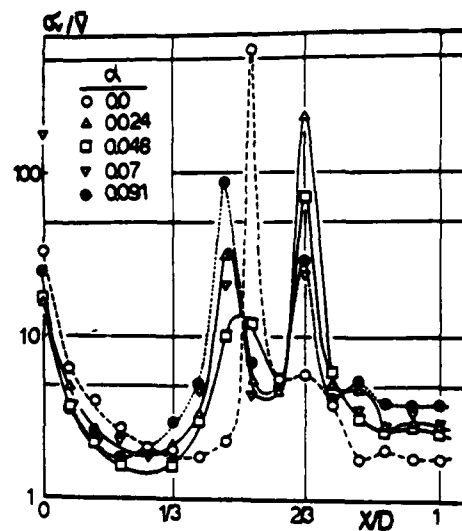


Fig. 13 Turbulence intensity of cross-flow velocity fluctuation σ_v/\bar{v} against X/D at $Y/D = 3/5$

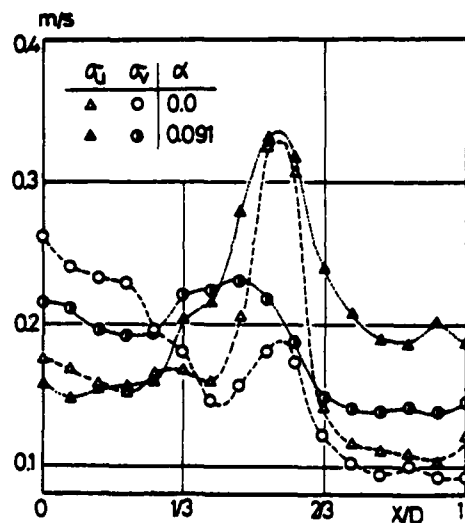


Fig. 11 σ_u and σ_v distribution against coordinate X/D

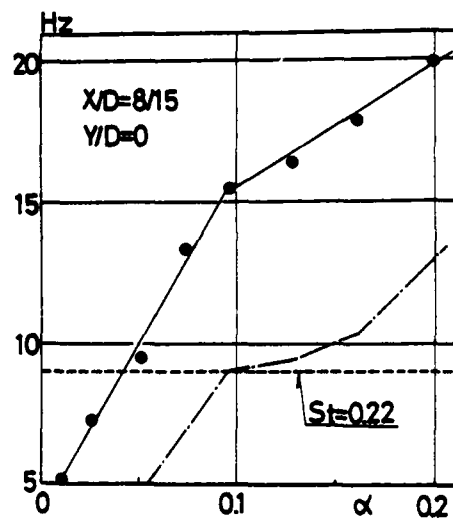


Fig. 14 Bubble arrival frequency against void fraction

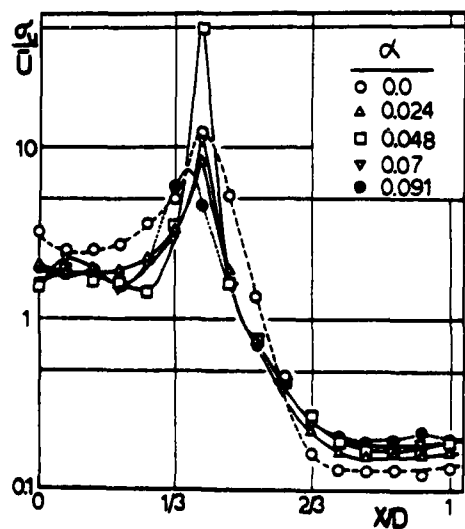


Fig. 12 Turbulence intensity of in-line velocity fluctuation σ_u/\bar{u} against X/D at $Y/D = 3/5$

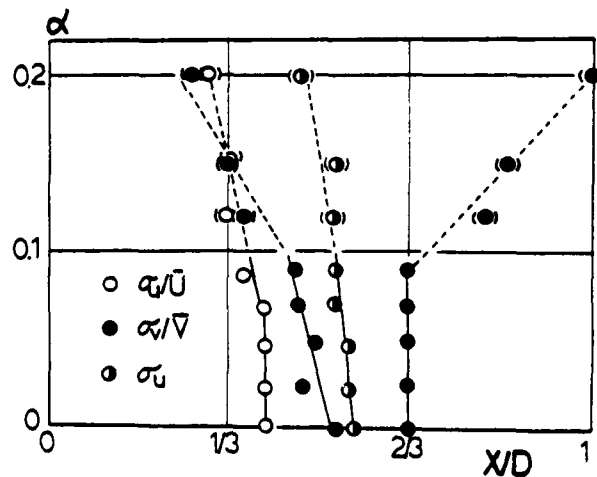


Fig. 15 Peak location of σ_u/\bar{u} , σ_v/\bar{v} , and σ_u

SESSION 13 - OPEN FORUM

B.E. Launder and J.H. Whitelaw - Chairmen

SESSION 14 - FUNDAMENTALS II

J. Lumley - Chairman

A COMPARISON OF TRIPLE-MOMENT TEMPERATURE-VELOCITY CORRELATIONS
IN THE ASYMMETRIC HEATED JET WITH ALTERNATIVE CLOSURE MODELS

by

I. Dekeyser,
IMST, Marseille,
France.

B.E. Launder,
UMIST, Manchester,
England.

ABSTRACT

Measurements are reported of all triple moments of velocity and temperature in a heated asymmetric two-dimensional turbulent jet involving velocity fluctuations in the x_1 - x_2 plane. The data thus obtained have been compared with those given by alternative algebraic models of the triple moments using, in the model formulae, experimental values of the second-moment quantities and the dissipation rate of kinetic energy. The study supports the view that in strongly asymmetric flows the contribution of mean temperature gradients to the triple moments can be appreciable. The comparison also provides some support for the use of the generalized gradient transport hypothesis in approximating dissipation of the triple moments.

1. INTRODUCTION

Most current efforts in second-moment closure adopt highly simplistic representations of the triple correlations appearing as unknowns in the transport equations for the second-moments. This practice may be regarded as both an invocation of the principle of receding influence and an appreciation that, since the non-zero triple moments are more numerous than those of second-rank, to adopt other than a rudimentary approximation may let the computer budget get out of hand. While undoubtedly a cruder approximation suffices for third than for second-moments it is not by any means established that the currently popular algebraic models give sufficient accuracy or width of applicability. Indeed, Lumley, Zeman & Siess (1978) have argued persuasively that the diurnal growth of the mixed layer in the atmospheric boundary layer is crucially dependent on the triple-moment approximations and that an explicit account of gravitational contributions to the triple-moment balances must be included[†].

The present paper has arisen from an examination of another flow - one with more direct connection with engineering flow problems - in which diffusive transport is more than usually important. This is the heated asymmetric jet shown in figure 1. A heated plane jet mixes on one side with stagnant surroundings and on the other with a moving stream. The shear flow has two features of particular interest: firstly the scale and the intensity of turbulent motions on the side of the jet mixing with stagnant fluid is markedly higher than on the other; secondly the unequal entrainment rates that result produce, after some development distance, a flow in which the maximum temperature is shifted laterally with respect to that for velocity. Thus, unlike the symmetric jet or wake, the regions where the generation rates of turbulence energy k and mean-square

[†]This point of view is implicitly supported by the earlier third-moment closure study of the same problem reported by André et al.

temperature variance, $\overline{\theta^2}$ occur are not coincident. In these circumstances there is liable to be departure from the commonly prescribed simple connections between the scalar and dynamic fields - such as a uniform turbulent Prandtl number or time-scale ratio R (Launder, 1976). The experiment, which is one of several on asymmetric turbulent flows to have been performed at the IMST in recent years (for earlier studies see Beguier et al (1978), Keffer et al (1979)) has given special attention to the measurement of the triple products of velocity and temperature which appear as the diffusive transport terms in the conservation equations for the second-moments. These measurements are directly compared with various simple models that express the triple-moments in terms of second-moments and their gradients. In addition to forms already in the literature the present work considers the addition of two further elements that extrapolate to the triple products ideas that have in the past been widely used in closing the second-moment equations.

2. THE EXPERIMENTAL PROGRAMME

Apparatus

A full account of the complete experimental programme is provided by Dekeyser (1982, 1983). Accordingly we here provide only a brief summary with emphasis on the measurement of the triple-moments.

The shear flow is formed by a heated high-velocity air jet (≈ 30 m/s) discharged through a slot 10 mm high and 200 wide. The air is heated in passage through a low-velocity settling chamber upstream of the jet contraction. The chamber consists of a dozen grills, each comprising 8 cylindrical electrical heaters. In the experiments reported here the air at discharge from the slot is warmed to approximately 32°C above ambient temperature. Buoyancy effects are entirely negligible. On its lower side the heated jet mixes with what, for the purposes of the present study, may be considered an infinite uniform-density stream. It is in fact a low velocity (8 m/s) unheated air stream discharged through a square opening 200 mm high. The low-velocity stream is bounded on its lower side by a smooth wall. The hot jet is free to entrain stagnant ambient air on its upper edge. Side walls are provided to constrain the shear flow to an essentially two-dimensional development; measurements showed that the streamwise enthalpy flux was conserved within 5% over a development from 40-100 slot heights downstream.

Instrumentation

The mean velocity and temperature fields were mapped respectively by a pitot tube and chromel-constantan thermocouple, the sensitivity of the latter offering a precision of about 0.2K. To improve stability the cold junction was in fact placed in the unheated uniform stream.

Temperature fluctuations were measured by a "cold"

platinum wire 1u in diameter and 0.4mm long with a resistance of about 100Ω. The wire is placed on a Wheatstone bridge circuit and heated by a constant current of about 150uA. There is a 3000:1 signal amplification and an electronic compensation circuit for thermal inertia. The overall sensitivity is approximately 50uV/K. For the majority of the measurements the cold wire, which was aligned normal to the flow, formed part of a 3-wire probe. The other two wires, of 5u diameter platinum were arranged as cross-wires (the angle between the wires being approximately 90°); the planes formed by each of the three wires with the mean flow vector were mutually parallel. It was operated with an overheat coefficient of 0.8 giving a wire temperature of approximately 200K above ambient. The sensitivities of the wires to velocity and temperature fluctuations were determined by constricting calibration curves for wire emf as a function of velocity for a series of different mean temperatures spanning the range encountered in the experiment. The cold wire sensibly responded only to temperature fluctuations; the hot wires were significantly sensitive to both velocity and temperature fluctuations though, as we see in figure 2, the rate of change of E^2 with voltage was independent of velocity. This encouraged the decision that the hot wires should be employed without linearizers. The separation of the instantaneous fluctuating velocity components and temperatures was achieved by means of an analogue circuit consisting of operational amplifiers similar to those used by Schon and Baille (1972). To obtain the triple correlations the separated velocity and temperature signals were passed through two successive amplifiers (the second a quadratic amplifier), a multiplier and a high-pass filter with a low-frequency cut-off set at 1Hz to remove the continuous part of the quadratic signal. The same circuit allowed simultaneous measurement of the double and triple correlations with the help of a DISA correlator.

The Measurements

All the measurements reported hereunder were obtained 50 jet slot heights downstream of discharge. The mean velocity and temperature profiles in figure 3 indicate that the temperature maximum is displaced relative to the velocity maximum in the direction of the stagnant surroundings. Figures 4 and 5 show the profiles of rms velocity and temperature fluctuations. The data of figure 4 were taken without heating the jet. The different sets were taken with the wires in the x_1 - x_2 plane (Δ , 0, Δ , Δ , 0) or the x_1 - x_3 plane (Δ , Δ , ∇); as noted above, unlinearized signals were used except for one case (Δ). There is an encouraging uniformity obtained from the various runs. As would be expected, the peak turbulence intensities occur on the upper side of the jet mixing with stagnant surroundings. The temperature variance is more symmetric than the turbulence intensities, reflecting the fact that the mean temperature profile is also fairly symmetric. The three sets of data included in figure 5 were obtained from a single 'cold' wire alone (O), a cold wire incorporated in the 3-wire probe but with the two hot wires turned off (Θ), and from the 3-wire probe in which the hot wires were functioning. There is close agreement between the first two profiles but some contamination of the cold probe signal by the hot wires is evident on the side of the jet mixing with stagnant surroundings though this only becomes serious for values of u greater than unity. It is, of course, necessary to use this last operating mode for finding θ when forming correlations with the velocity field.

The experimental data for the triple-moments are compared with the various model proposals in section 4.

3. THE MODELS CONSIDERED

The present section outlines the models of the triple moments to be compared with data of the asymmetric jet in the next section; approximations are provided for $u_i u_j u_k$, $u_i \theta u_k$ and $\theta^2 u_k$ which appear in the second-moment equations for the Reynolds stress ($\overline{u_i u_j}$), scalar flux ($\overline{u_i \theta}$) and scalar variance ($\overline{\theta^2}$). It is convenient to present the various models as closures, albeit very

crude ones, of the exact third-moment equations. It is reasonable to regard the formula resulting from any closure as a "package" whose usefulness does not necessarily reflect the correctness (or otherwise) of the individual closure assumptions made along the way. For example, all models considered here explicitly neglect convective transport of the triple-moments and it is likely that the more successful schemes are implicitly making some accounting for this in the choices made for the various empirical constants. Our attention is confined to relatively simple schemes that can be adopted without greatly adding to the computational labour involved in numerical simulations of turbulent shear flows with second-moment closures.

The exact equation for the transport of triple velocity products for a uniform density shear flow unaffected by external force fields may be written:

$$\frac{D \overline{u_i u_j u_k}}{Dt} = \underbrace{P_{ijk1} + P_{ijk2}}_{\text{'Generation'}} + \underbrace{d_{ijk2}}_{\text{Diffusion}} + \underbrace{\phi_{ijk}}_{\text{Pressure interactions}} - \underbrace{\epsilon_{ijk}}_{\text{Dissipation}} \quad (1)$$

where

$$\begin{aligned} P_{ijk1} &\equiv +(\overline{u_i u_j} \overline{u_k u_{m,m}} + \overline{u_k u_i} \overline{u_j u_{m,m}} + \overline{u_j u_k} \overline{u_i u_{m,m}}) \\ P_{ijk2} &\equiv -(\overline{u_i u_j u_m} \overline{u_{k,m}} + \overline{u_k u_i u_m} \overline{u_{j,m}} + \overline{u_j u_k u_m} \overline{u_{i,m}}) \\ d_{ijk} &\equiv -(\overline{u_i u_j u_k u_m} + \frac{P}{\rho} \overline{u_j u_k} \delta_{im} + \frac{P}{\rho} \overline{u_k u_i} \delta_{jm} \\ &\quad + \frac{P}{\rho} \overline{u_i u_j} \delta_{km} - \overline{u_i u_j u_k u_m}) \\ \phi_{ijk} &\equiv (p/\rho)(\overline{u_i u_j u_k} + \overline{u_k u_i u_j} + \overline{u_j u_k u_i}) \\ \epsilon_{ijk} &\equiv 2\nu(\overline{u_k u_i u_j u_m} + \overline{u_j u_k u_i u_m} + \overline{u_i u_j u_k u_m}) \end{aligned}$$

The notation is given under Nomenclature but is, in any case, what is standardly adopted. The pressure-containing correlation ϕ_{ijk} may be decomposed into a non-linear part ϕ_{ijk1} composed purely of fluctuating quantities and a linear part ϕ_{ijk2} comprising products of triple-moments and mean velocity gradients. Cormack et al (1978) in drawing comparisons with several simple triple-velocity closure proposals concluded that the scheme of Hanjalic and Launder (1972) performed the best. This model emerged from:

- neglecting convection and diffusive transport by pressure and molecular action
- approximating the pressure interactions by $\phi_{ijk1} = -\overline{u_i u_j u_k}/T$ and neglecting ϕ_{ijk2}
- making the Gaussian approximation for the quadruple velocity moment in d_{ijk} : $\overline{u_i u_j u_k u_m} = \overline{u_i u_j} \overline{u_k u_m} + \overline{u_j u_k} \overline{u_i u_m} + \overline{u_k u_i} \overline{u_j u_m}$
- retaining P_{ijk1} exactly but neglecting P_{ijk2} and ϵ_{ijk}

The resultant algebraic equation may be reorganized to give: $\overline{u_i u_j u_k} = c_s T (\overline{u_k u_i} \overline{u_j u_l} + \overline{u_j u_l} \overline{u_k u_i} + \overline{u_i u_l} \overline{u_j u_k})$ or, for brevity, $-\overline{u_i u_j u_k} = c_s T G_{ijk}$ (4)

The time-scale T in equations (2) and (4) is taken (k/ϵ) and the recommended value of the empirical coefficient c_s is 0.11. A similar, though simpler, version of the above form was earlier proposed by Daly

and Harlow (1970):

$$-\overline{u_i u_j u_k} = c'_s T \overline{u_k u_l} \overline{u_l u_j}, l \quad (5)$$

Eq. (5) may be thought of either as a simplification of (4) (in which just the first term is retained) or, more directly, as invoking the general gradient transport hypothesis

$$-\overline{u_k \phi} = T \overline{u_k u_l} \phi, l \quad (6)$$

a proposition extensively employed by the Los Alamos group in the late '60's and early '70's. In fact the value for c' of 2.0 suggested by Daly and Harlow (1970) has not been found to be usable by other groups. Wyngaard and Coté (1974) employed the same model but with $c' = 0.3$ while Launder et al (1975) adopted 0.22.

Besides the established simple proposals represented by equations (4) and (6), certain elaborations of them have been here examined. The first is purely the inclusion of mean-strain generation, P_{ijk2} . No approximations are needed and the triple moment model that results may be expressed:

$$-\overline{u_i u_j u_k} = c'_s T (G_{ijk} - P_{ijk2}) \quad (7)$$

This form has been compared with the present measurements of Dekeyser (1982) with some overall improvement on eq. (6). However, a weakness (at least in concept) of eq. (7) is that if one decides to include P_{ijk2} , one should also introduce a model for the mean-strain contribution to ϕ_{ijk} (the part referred to as ϕ_{ijk2}). At second-moment level a simple yet useful and very widely-used approximation for the effects of pressure fluctuations on mean-strain generation is that known as the 'isotropization of production' model:

$$\phi_{ij2} = -c_2 (P_{ij} - \frac{1}{3} \delta_{ij} P_{kk}) \quad (8)$$

where ϕ_{ij2} and P_{ij} are respectively the non-dispersive pressure interaction and stress-generation rates in the $u_i u_j$ transport equations associated with mean strain j (for further details see, for example, Launder et al, 1975). This same idea has been applied to model pressure effects on stress generation rates by buoyant forces and to the corresponding non-dispersive pressure effects on scalar flux generation rates, Launder (1975). The coefficient c_2 and the corresponding constants that arise in approximating the other processes mentioned by this isotropization-of-production idea are usually chosen in the range 0.5 ± 0.1 . The model has never been applied, so far as we know, to the triple-moments but it would seem an obvious extension to suppose:

$$\phi_{ijk2} = -0.5 P_{ijk2} \quad (9)$$

Here, as in corresponding approximations later, we set the coefficient equal to 0.5 on the grounds that that value is roughly what has been used in models involving the double moments and that, in view of other uncertainties, it is unlikely that any more refined tuning of the individual coefficients can be contemplated at present in view of the relative imprecision of the experimental data. In fact, if we are to apply the isotropization-of-production idea consistently we should assume that pressure fluctuations remove 50% of P_{ijk1} too. Launder (1982) points out that the exact P_{ijk1} (but unclosed) expression for ϕ_{ijk1} obtained by eliminating the pressure (via solution of its Poisson equation) in favour of velocity fluctuations does indeed suggest the need for such a process. Accordingly we would take

$$\phi_{ijk1} = -c^{-1} \frac{\overline{u_i u_j u_k}}{T} \quad (10)$$

The neglect of the dissipative terms in equation (1) is usually justified on the grounds of local isotropy. Wyngaard and Sumanarajan (1979) among others have shown

from considering the θ^3 budget in the atmospheric boundary layer that the usual assumption of local isotropy cannot be too freely applied to the triple moments. The viscous destruction terms in (1) consist of products of velocities and velocity gradients. Local isotropy would lead us to discard these terms because fine-scale motions (wherein the velocity gradients are dominant) are generally held to be uninfluenced by large-scale activities. It is now accepted, however, that there is some measure of linkage between the two: the most energetic large eddies are also the ones carrying the most intense fine-scale activity. In view of the foregoing it might appear reasonable to apply the general gradient transport hypothesis to model ϵ_{ijk} . From eq. (6) and the definition of ϵ_{ijk} (following eq. (1)) we obtain:

$$\epsilon_{ijk} = -T (\overline{u_k u_l} \epsilon_{ij,l} + \overline{u_j u_l} \epsilon_{ik,l} + \overline{u_i u_l} \epsilon_{jk,l}) \quad (11)$$

where $\epsilon_{ij} \equiv 2\nu \overline{u_i u_j}, m$. Moreover, if we now apply to the second-moment dissipation term the usual assumption of local isotropy $\epsilon_{ij} = \frac{2}{3} \delta_{ij} \epsilon$ we finally obtain:

$$\epsilon_{ijk} = -c_\epsilon T \epsilon, l (\overline{u_k u_l} \delta_{ij} + \overline{u_j u_l} \delta_{ki} + \overline{u_i u_l} \delta_{jk}) \quad (12)$$

Three models of $\overline{u_i u_j u_k}$ are compared with the measurements in the following section: These are: eq. (4) (the Hanjalic-Launder model); eq. (7) with the further addition of dissipation, eq. (12); and eq. (7) with the addition of dissipation (eq. (12)) and non-dispersive pressure interactions (eqs. (9) and (10)). The very simple gradient diffusion version given by eq. (5) did somewhat less well overall than eq. (4) (Dekeyser, 1982) and to avoid unnecessary clutter its variation is not shown on the curves in question.

Precisely parallel treatments to those discussed above at some length have been applied to the correlations giving rise to scalar flux diffusion $\overline{u_i u_j \theta}$ and to diffusion of the scalar variance $\overline{u_i \theta^2}$. For the former case, omitting molecular transport k effects, the exact equation may be written

$$\frac{D \overline{u_i u_j \theta}}{Dt} = P_{ki\theta1} + P_{ki\theta2} + d_{ki\theta1} + \phi_{ki\theta1} + \phi_{ki\theta2} - \epsilon_{ki\theta} \quad (13)$$

where the symbols on the right side of (13) have an analogous significance to those in eq. (1).

The most widely applied algebraic approximations to (13) neglect convective transport, molecular dissipation, generation due to mean field gradients $P_{ki\theta2}$ and the contribution of pressure transport in $d_{ki\theta}$.

Closure is effected by approximating the pressure interaction as:

$$\phi_{ki\theta1} = -c_\theta^{-1} \frac{\overline{u_i u_j \theta}}{T} \quad (14a)$$

$$\phi_{ki\theta2} = 0 \quad (14b)$$

assuming a normal distribution for the quadruple correlation in $d_{ki\theta}$:

$$d_{ki\theta} \equiv -\overline{u_k u_l \theta u_m} g_m = (\overline{u_k u_l} \overline{u_m \theta} + \overline{u_k u_m} \overline{u_l \theta} + \overline{u_l u_m} \overline{u_k \theta}), m \quad (15)$$

and by retaining $P_{ki\theta1}$ without the need for approximation:

$$P_{ki\theta1} \equiv (\overline{u_i u_k} \overline{\theta u_m}, m + \overline{\theta u_i} \overline{u_k u_m}, m + \overline{u_k \theta} \overline{u_i u_m}, m) \quad (16)$$

Introduction of eq. (14) - (16) into (13) produces:

$$-\overline{u_i u_k \theta} = c_\theta (\overline{u_k u_m} \overline{u_i \theta}, m + \overline{u_i u_m} \overline{u_k \theta}, m + \overline{\theta u_m} \overline{u_i u_k}, m) \quad (17)$$

a form essentially the same as that proposed by Deardorff

(1973). This is equivalent in its modelling concept to eq. (4). Simpler derivatives have been used in which the last term on the right is discarded (Owen, 1973) or the last two terms (Wyngaard and Coté, 1974). These simpler versions are less successful than (17) in reproducing the distribution of $u_i u_j \theta$ across the asymmetric jet, Dekeyser (1982), and will therefore not be included in the present comparisons.

The dissipative term $\epsilon_{ik\theta}$ denotes the following group of terms:

$$\epsilon_{ij\theta} = (\lambda + \nu) (\overline{u_k u_i \theta_{,m}} + \overline{u_i u_k \theta_{,m}}) + 2\nu \overline{u_i u_k \theta_{,m}} \quad (18)$$

Application of the gradient transport idea to the first pair of terms on the right of (18) produces a quantity proportional to

$$T (\overline{u_k u_i \theta_{,l}} + \overline{u_i u_k \theta_{,l}}).$$

However, the molecular dissipation of heat flux $\epsilon_{i\theta}$ is zero if, as before, we assume local isotropy to apply to all the fine-scale, second-moment correlations; the terms are thus discarded. The third term, while strictly not in a form appropriate to the gradient transport idea may nevertheless be treated in this way if we regard the instantaneous temperature as simply a "marker" of velocity fluctuations. With that assumption the model for $\epsilon_{ik\theta}$ emerges as:

$$\epsilon_{ik\theta} = -c_{\theta\theta} T \overline{u_i u_k \theta_{,l}} \epsilon_{l\theta} \quad (19)$$

Finally, if one adopts the 'isotropization-of-production' (IP) concept eq. (14a) is replaced by

$$\phi_{ki\theta} = -\hat{c}_{\theta}^{-1} \frac{\overline{u_k u_i \theta}}{T} - 0.5 P_{ki\theta} \quad (20)$$

The mean-field generation rate $P_{ki\theta}$ arises from both velocity and temperature gradients:

$$P_{ki\theta} = -(\overline{u_i u_k \theta_{,l}} U_{k,l} + \overline{u_k u_i \theta_{,l}} U_{i,l} + \overline{u_i u_k \theta_{,l}} \theta_{,l}) \quad (21)$$

Dekeyser (1982) concludes, however, that the contribution of mean velocity gradients is barely significant compared with that due to temperature gradients. Moreover, $\phi_{ki\theta}$ is associated only with velocity gradients (not temperature gradients) and according to the IP model its effect will be to halve an already marginal contribution to $P_{ki\theta}$. Accordingly, $\phi_{ki\theta}$ and the first two terms on the right of eq. (21) are omitted.

In section 4 we compare the distributions of $u_i u_j \theta$ resulting from eq. (17); from eq. (13) used in conjunction with eqs. (14), (15), (16) and (19); and eq. (13) closed by means of eqs. (15), (16), (19) and (20).

The exact equation for the transport of $u_k \theta^2$ may be written:

$$\frac{D \overline{u_k \theta^2}}{Dt} = P_{k\theta^2} + P_{k\theta^2} + d_{k\theta^2} + \phi_{k\theta^2} + \phi_{k\theta^2} - \epsilon_{k\theta^2} \quad (22)$$

Again the symbols retain a physical significance consistent with eqs. (1) and (13). The specific correlations denoted by the production and dissipation terms in (22) are

$$P_{k\theta^2} = \overline{\theta^2 u_k u_{l,l}} + 2 \overline{u_k \theta} \overline{u_l \theta_{,l}}$$

$$P_{k\theta^2} = -(\overline{u_l \theta^2} U_{k,l} + 2 \overline{u_k u_l \theta} \theta_{,l})$$

$$\epsilon_{k\theta^2} = 2(\nu + \lambda) \overline{\theta \theta_{,j} u_k \theta_{,j}} + 2\lambda \overline{u_k \theta_{,j} \theta_{,j}}$$

The counterpart of equations (4) and (17) is obtained from (22) by neglecting convective transport, molecular and pressure contributions to $d_{k\theta^2}$, and mean field gradients. On introducing the Gaussian approximation of quadruple moments and the usual return-to-isotropy representation for $\phi_{ki\theta}$, the following form, due to Deardorff (1973) emerges:

$$- \overline{u_k \theta^2} = c_{\theta}^* T (\overline{u_k u_l} \overline{\theta^2_{,l}} + 2 \overline{u_k \theta} \overline{u_l \theta_{,l}}) \quad (23)$$

Some workers (e.g. Launder and Samaraweera, 1979) have retained just the first term in parentheses to facilitate numerical solution. However, this truncation is less successful than (23) in describing the measured distribution of $u_i \theta^2$, Dekeyser (1982).

Two elaborations of eq. (23) are considered here. One is the form which results from retaining the constituents of (23) but now adding mean temperature gradients from $P_{k\theta^2}$ and approximating $\epsilon_{k\theta^2}$ by the generalized gradient transport hypothesis. Assuming, as in approximating $\epsilon_{ki\theta}$, that $\epsilon_{k\theta} = 0$ leads to

$$\epsilon_{k\theta^2} = -\hat{c}_{\theta} T \overline{u_k u_l} \epsilon_{\theta,l} \quad (24)$$

where ϵ_{θ} is the dissipation rate of θ^2 . The other form considered includes, in addition, the IP model for $\phi_{k\theta^2}$:

$$\phi_{k\theta^2} = -\hat{c}_{\theta}^{-1} \frac{\overline{u_k \theta^2}}{T} - 0.5 P_{k\theta^2} \quad (25)$$

The two forms precisely parallel the models considered above for $\overline{u_i u_j u_k}$ and $\overline{u_i u_k \theta}$.

4. COMPARISON BETWEEN MODELS AND EXPERIMENTS

The previous section has presented models for velocity and scalar triple moments in terms of second-moment quantities and their gradients. Here we compare the predicted distributions of the triple moments with directly measured values. In doing so we take from experiment the values of the second-moment quantities appearing in the various models. This goes equally for the dissipation rates ϵ and ϵ_{θ} though in this case the values used were those deduced as the closing term in the kinetic energy and θ^2 budgets (in the former case with pressure diffusion neglected).

In the comparisons the three coefficients of (4), (17) and (23) (i.e. c_{θ} , c_{θ} and c_{θ}^*) are, for uniformity, all set equal to 0.11 (no significant improvement would result from optimizing them separately). The corresponding coefficients in the more elaborate models (i.e. c_{θ} , \hat{c}_{θ} and \hat{c}_{θ}) are taken as 0.075 irrespective of whether or not the IP model is included. The dissipation coefficients c_{θ} , c_{θ} and c_{θ} take the values 0.2, 0.1 and 0.3 which amounts to choosing the value of the coefficients in eq. (6) to be 0.15, the value adopted by several workers in approximating the same correlations in the dissipation rate transport equations (wherein they appear as diffusion terms).

Comparisons between experiment and model prediction are provided in figures 6, 7 and 8 for respectively the triple velocities, the scalar flux transport and the scalar variance transport. The usual thin shear flow approximation has been made with only cross-stream gradients of mean or turbulence quantities being retained. Let us consider first the measurements of the triple-velocity correlation. In all figures the stagnant stream is on the right. The large scale mixing on this side is reflected in the large values of u_1^3 , $u_1^2 u_2$, $u_1 u_2^2$ compared with corresponding levels on the side of the shear flow entraining moving fluid. In contrast the u_2^3 profile is almost antisymmetric with the peak magnitudes on each side being nearly the same. This probably reflects the fact that this is the only one of the triple velocities presented in which mean-strain generation is negligible. The two profiles involving odd powers of u_1 are fairly similar in shape with positive values on the edges and negative values near the centre. The most complicated behaviour is displayed by $u_1^2 u_2$ with two minima and two maxima. The three models

for $\overline{u_i u_j u_k}$ all succeed in mimicking the basic features of the $\overline{u_i u_j u_k}$ profile shape; for example, they unerringly provide the correct number of maxima and minima for each component. The simplest of the three schemes, eq. (5), performs less well, however, than the others. Of the two new models tested, for all except for u_2^3 , the version that includes the IP model for non-dispersive pressure effects does slightly better; it gives a particularly impressive account of the undulations in $\overline{u_1 u_2}$ for $(x_2 - x_{2m})$ less than 3cm. For the exceptional

case, however, it produces an abrupt change of sign of the correlation on the moving-stream side which is not present in the data. This turns out to be provoked by a term proportional to $u' u' u'_{2m}$, which does not appear in either of the other models. All schemes produce markedly lower values than measured on the stagnant stream side. Hot-wire errors associated with intermittent, high-intensity turbulence will almost certainly produce measured values that are too high for $(x_2 - x_{2m}) > 5$. Nevertheless, it seems unlikely that experimental error in $u' u' u'_{2m}$ is the principal cause of the difference. The poor agreement could point to a fundamental weakness in the models and/or it might reflect an estimate of ϵ (obtained as noted as the closing term in the kinetic energy equation) that was also too high near the low velocity boundary[†].

The scalar flux diffusion shown in figure 7 exhibits (like the temperature and scalar variance profiles) a closer degree of symmetry about the two sides of the jet. Interestingly, slightly higher peak values now occur on the moving-stream side. While $u' \theta$ displays an uncomplicated variation that for $u' \theta$ shows inflectional behaviour near x_{2m} . The three models also show quite different distributions for $u' \theta$ and $u' \theta$ in the central region broadly in line with measurements. In the case of $u' \theta$ the measured levels near the shear flow edges are markedly higher than given by any of the models. It would have to be said that though the two models introduced in the present study give somewhat different distributions than eq. (17) they cannot really be said to be in any better overall accord.

The scalar variance diffusion in figure 8 exhibits a complex variation across the jet. The most striking feature is that $u' \theta^2$ takes on large negative values over the interior of the shear flow. This reflects the fact that negative values of u' (brought by newly-entrained fluid) are associated with larger fluctuations about the mean temperature than those of positive u' . The same feature of the flow is responsible for the large, negative readings of $u' \theta^2$ for $(x_2 - x_{2m})$ in the range 2-5 cm. None of the models succeeds in reproducing these features. Apart from this (serious) weakness, however, all three models capture broadly the trend of the distributions including, for example, the fact that the $u' \theta^2$ profile should display three maxima and two minima. The two models here introduced give rather different peak levels in different regions, but as with the scalar flux, it is not possible on the basis of the two sets of data shown here to declare one form conclusively superior to another.

5. CONCLUDING REMARKS

The paper has presented some of the data of the triple moments of velocity and temperature fluctuations recently obtained in an asymmetric heated jet. The flow is one where production of these triple products due to mean velocity and temperature gradients is comparable with that due to inhomogeneities in the second-moment distributions. Because of the structural asymmetry, the triple moment data display in many cases a complicated pattern.

The three models considered here all achieve a better than qualitative agreement with the third moment data but none can be said to be distinctly successful. For the triple velocity data the models based on a gradient approximation of the 'dissipative' term ϵ_{ijk} with or without the isotropization of production model of the non-dispersive pressure correlations are more successful than the earlier Hanjalic-Launder (1972) formulation which neglected both agencies. The discrepancies between experiment and prediction near the stagnant boundary are still very serious however. This behaviour is also present for $u' \theta$ but not, to any extent, for any of the other temperature-velocity triple products.

For the temperature-containing correlations we have been unable to conclude that any of the models performed distinctly better than the other two.

[†] Since ϵ appears in the denominator of the time scale too large values depress all the triple moments.

The study does not necessarily weaken the case for the two modelling ideas considered herein but it does suggest that on their own they are insufficient. Various further explorations are prompted that may lead to more definitive improvements; among these the question of adopting a single turbulent time scale (k/ϵ) as characterizing the rates of progress of all the pressure interactions is one of the more serious. In the case of $u' \theta^2$, the thermal time scale ϵ/ϵ_θ would certainly have been preferable. Alternative modelling suggestions by Lumley (1978) also merit testing.

A major concern must be the use of the Gaussian approximation for the quadruple moments in intermittent regions. The only reason for retaining it is that there is no alternative available that seems convincingly better. Lumley (1978) has correctly commented that conceptually the most satisfactory treatment of intermittent regions is to model them as precisely that. One might envisage either adopting a transport equation for the intermittency itself (Libby, 1975) or developing a scheme based on probability density functions. Before such approaches would attract interest amongst those making practical calculations, however, they need to be shown to be necessary. Whether this is so can be most effectively determined by incorporating the third moment models considered into a second-moment closure study of the present and other asymmetric flows.

ACKNOWLEDGEMENTS

The experimental work was undertaken at IMST, Marseille, and is published with the permission of the Director. Especial thanks go to Dr. C. Béguier for his material help and suggestions on all aspects of the experimental programme. Miss L. Towers at UMIST has prepared the camera-ready version of the paper. Authors' names appear alphabetically.

REFERENCES

- André, J.C., de Moor, P., Lacarrère, P., Therry, G. and du Vachat, R. 1979. 'The clipping approximation and inhomogeneous turbulence simulations. Turbulent Shear Flows - 1, 307. Springer Verlag, Heidelberg.
- Béguier, C., Fulachier, L. and Keffer, J.F. 1976. 'The turbulent mixing layer with an asymmetrical distribution of temperature'. J.Fluid Mech. 89, 561.
- Cormack, D.E., Leal, L.G. and Seinfeld, J.H. 1978. 'An evaluation of mean Reynolds stress turbulence models: the triple velocity correlation' ASME, J.Fluids Eng. 100, 47.
- Daly, B.J. and Harlow, F.H. 1970. 'Transport equations in turbulence'. Phys.Fluids 13, 2634.
- Deardorff, J.W. 1973. 'Three-dimensional numerical modelling of the planetary boundary layer'. Proc. Workshop on Micrometeorology, 271, Am.Met.Soc.
- Dekeyser, I. 1982. 'Etude d'un jet plan dissymétrique chauffé en régime turbulent incompressible'. Thèse Docteur-es-Sciences, Université d'Aix-Marseille II.
- Dekeyser, I. 1983. To appear in J.de Mécanique
- Hanjalic, K. and Launder, B.E. 1972. 'A Reynolds stress model of turbulence and its application to thin shear flows'. J.Fluid Mech. 52, 609.
- Keffer, J.F., Kwall, J.G., Giral, F. and Béguier, C. 1979. 'Analysis of turbulence structure in complex shear flows'. Proc. 2nd Symposium on Turbulent Shear Flows. London. 2-24.
- Launder, B.E. 1975. 'On the effects of a gravitational field on the transport of heat and momentum'. J. Fluid Mech. 67, 569.
- Launder, B.E., Reece, G.J. and Rodi, W. 1975. 'Progress in the development of a Reynolds stress turbulent model'. J.Fluid Mech. 68, 537.

- Launder, B.E. 1976. Chapter 6: Heat and Mass Transport in 'Turbulence'. Topics in Appl. Phys. Vol. 12. Ed. P. Bradshaw. Springer Verlag, Heidelberg.
- Launder, B.E. and Samaraweera, D.S.A. 1979. 'Application of a second-moment closure to heat and mass transport in thin shear flows' Int. J. Heat Mass Trans. 22, 1631.
- Launder, B.E. 1982. 'Second moment closure: methodology and practice'. EDF Summer School on Modélisation Numérique, Le Bréau, France.
- Libby, P.A. 1975. 'On the prediction of intermittent turbulent flows'. J. Fluid Mech. 68, 272.
- Lumley, J.L. 1978. 'Computational modeling of turbulent flows'. Adv. in Appl. Mech. 18, 123.
- Lumley, J.L., Zeman, O. and Siess, J. 1978. 'The influence of buoyancy on turbulent transport'. J. Fluid Mech. 84, 581.
- Owen, R.G. 1973. 'An analytical turbulent transport model applied to non-isothermal fully-developed duct flows'. Ph.D. thesis. Penn. State Univ.
- Schon, J.-P. and Baille, A. 1972. 'Méthode d'isolement des fluctuations turbulentes cinématiques et thermiques au moyen d'une sonde anémométrique à trois fils'. C.R.A.S. Paris A 274, 116.
- Wyngaard, J.C. and Coté, O. 1974. 'The evolution of a convective planetary boundary layer. A higher order closure model study'. Boundary Layer Met. 7, 289.
- Wyngaard, J.C. and Sundararajan, A. 1979. 'The temperature skewness budget in the lower atmosphere and its implications for turbulence modelling'. Turbulent Shear Flows - 1, 319, Springer Verlag, Heidelberg.

NOMENCLATURE

- d width of exit slot
- d_{ijk} diffusion of $\overline{u_i u_j u_k}$ (likewise for velocity-temperature $\overline{u_i u_j u_k}$ 3rd moments; subscript identifies quantity)
- k turbulence kinetic energy
- p fluctuating pressure
- P_{ij} generation rate of Reynolds stress
- P_{ijk} generation rate of $\overline{u_i u_j u_k}$ due to Reynolds stress gradients (1) and $\overline{u_i u_j u_k}$ strain (2)
- q' $\sqrt{2k}$
- T turbulent time scale (k/ϵ)
- u_i fluctuating velocity
- U_i mean velocity
- U mean streamwise velocity (in x_1 direction)
- u', v', w' rms velocity fluctuations in x_1, x_2 and x_3 directions
- x_1 streamwise coordinate
- x_2 cross stream Cartesian coordinate with origin at velocity maximum
- $x_{2\theta}$ x_2 position of temperature maximum
- $x_{2\frac{1}{2}}$ distance from $x_{2\theta}$ to position on stagnant stream-side where U is $\frac{1}{2}$ half maximum value
- $x_{2\theta\frac{1}{2}}$ distance from position of maximum temperature difference to position on stagnant stream side where $\Delta\theta$ is half maximum value
- γ_u intermittency of turbulent velocity sequal
- ϵ dissipation rate of turbulence energy
- ϵ_{ijk} 'dissipation' rate of $\overline{u_i u_j u_k}$
- η_u $x_2/x_{2\frac{1}{2}}$

- η_θ $(x_2 - x_{2\theta})/x_{2\theta\frac{1}{2}}$
- ν kinematic viscosity
- ρ density of fluid
- θ fluctuating temperature
- θ' $\sqrt{\overline{\theta^2}}$
- $\bar{\theta}$ mean temperature
- $\Delta\theta$ temperature above ambient
- $\Delta\theta_m$ maximum temperature difference across jet
- ϕ_{ijk} non-dispersive pressure correlation in $\overline{u_i u_j u_k}$

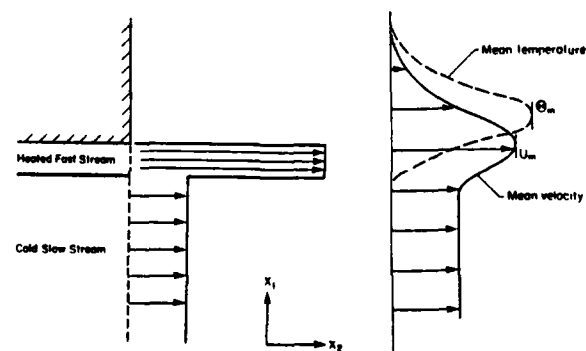


Figure 1 The flow configuration

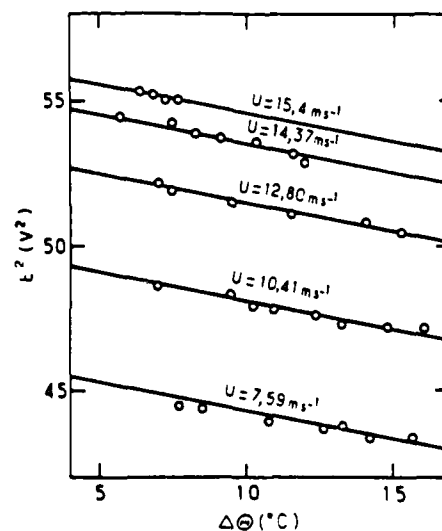


Figure 2 Hot wire sensitivity to velocity and temperature

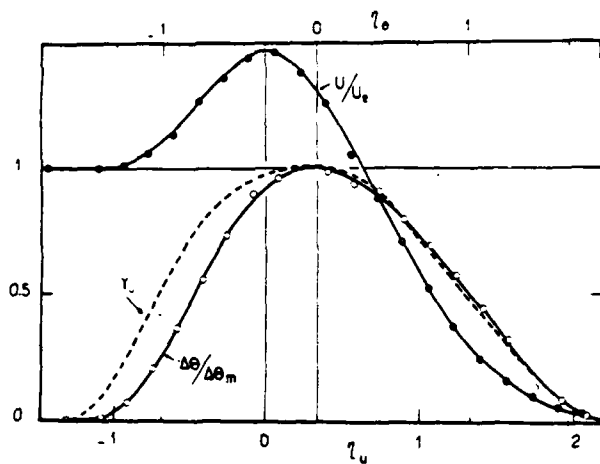


Figure 3 Mean velocity and temperature profiles at $x/d = 60$

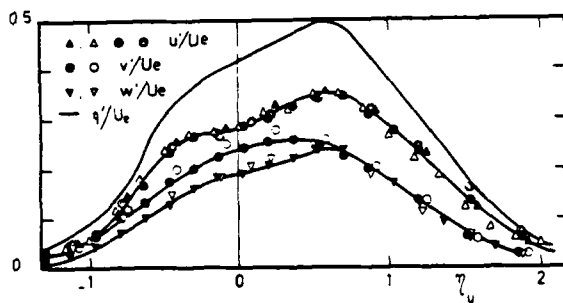


Figure 4 Turbulence intensity profiles across jet

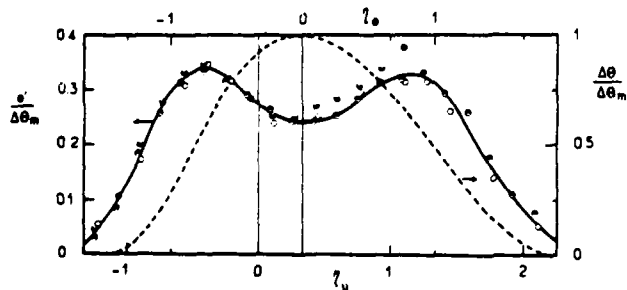


Figure 5 Intensity of temperature fluctuations across jet

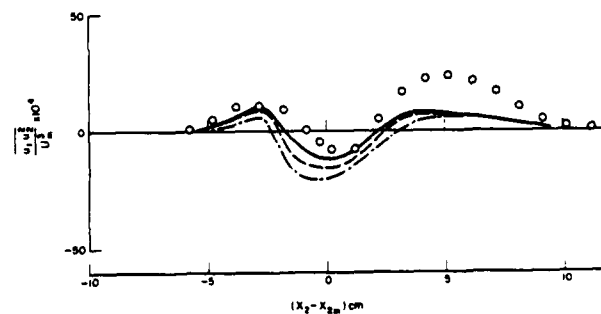
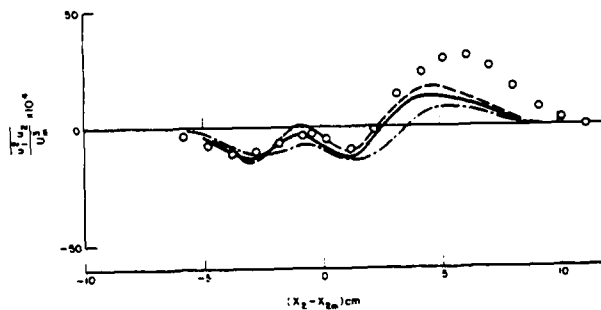
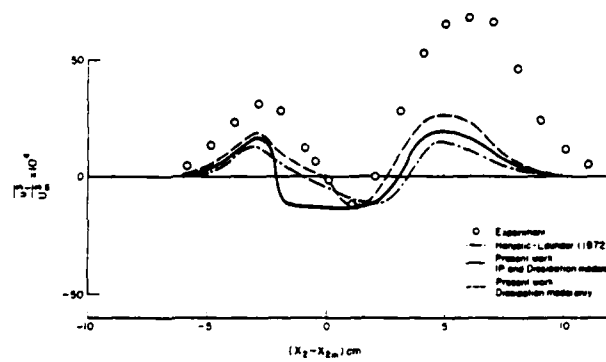


Figure 6 Profiles of $\overline{u_k u_j u_k}$: comparison between experiment and models

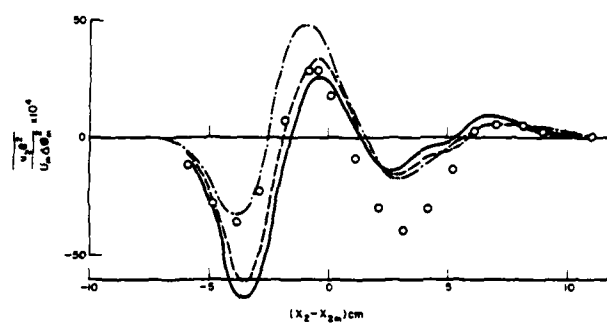
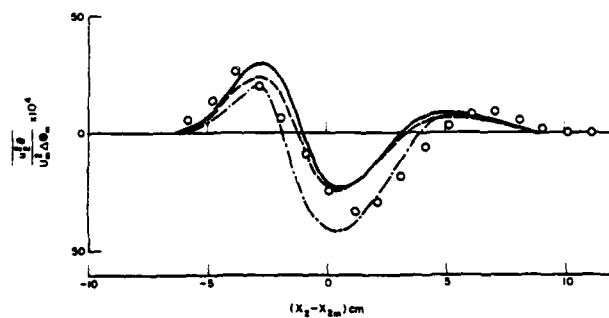
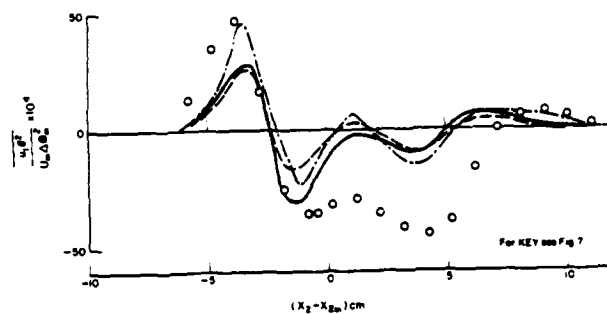
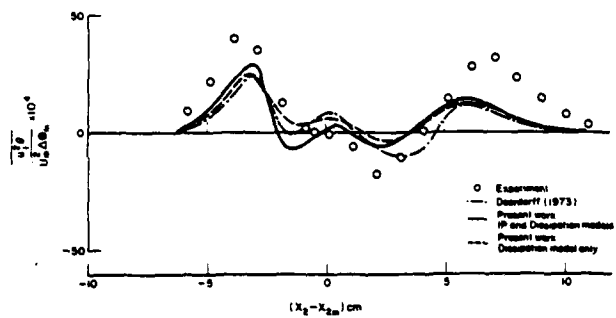


Figure 7 Profiles of $\overline{u_k u_{k+1} \theta}$: comparison between experiment and models

Figure 8 Profiles of $\overline{u_k \theta^2}$: comparison between experiment and models

Higher Order Derivative Correlations of Velocity and Temperature in Isotropic and Sheared Numerical Turbulence

ROBERT M. KERR

NASA Ames Research Center
M.S. 202A-1, Moffett Field, CA 94035
September 1983

Abstract

Through a combination of small scale statistics and flow visualization we will show that the small scales of a numerically generated turbulent flow are strongly aligned around vortex tubes. Movies of the time developing flow will be used to illustrate the nature of these structures. An inertial subrange is found with a Kolmogorov constant, α , equal to 2.45. This is consistent with simulated and measured values for the skewness, but disagrees with experimental values for the Kolmogorov constant, which usually range between 1.4 to 1.7.

Introduction

One approach to investigating the small scales of turbulence is through the higher order derivative correlations such as skewness and flatness factors. Experimentally (Antonia et al, 1982), this has been done for the velocity and temperature, which is a passive scalar when buoyancy is negligible. Our approach will be to use direct numerical simulation of the incompressible Navier-Stokes equation and several passive scalars to calculate a variety of third and fourth order derivative correlations between the velocity and passive scalars. We will then show how these correlations are related to turbulent structures seen in three dimensional graphics.

The advantage of direct numerical simulation is that more detail can be obtained than experiment and the conditions can be more closely controlled. The only higher order correlations accessible to a single probe (hot wire) experiment are the simple derivative skewness and flatness. But because all components of the velocity are known in a simulation, one is able to study many other correlations. We have studied a forced isotropic flow extensively and begun work on an infinite shear flow with a temperature gradient. The code uses up to 128 cubed mesh points and Taylor microscale Reynolds numbers up to 85. Details may be found in Kerr (1981) and Rogallo (1980).

Spectra and skewnesses

The most distinctive feature of fully developed turbulence is the $\frac{2}{3}$ Kolmogorov inertial subrange. Because we force the large scales in our code we are able to "drop" into the middle of the inertial range and do not need to waste computing power simulating large scale eddies. In figure 1 we plot several three dimensional velocity spectra for different Reynolds numbers. These have been normal-

ized by the Kolmogorov velocity and microscales and multiplied by the $-5/3$ Kolmogorov power law. The theoretical prediction of Pao (1965) for a Kolmogorov constant of 2.45 is plotted by the dashed line. While experimental values for the Kolmogorov constant as high as 2.1 have been reported, this value is much higher than the usual experimental value of 1.4 to 1.7 (see Monin and Yaglom, 1975, p.483-485). To understand the apparent differences between the calculated and experimental Kolmogorov constant we must consider the velocity derivative skewness. From this we will conclude that fitting the calculated spectra to Pao's theoretical form leads to anomalously high values for the Kolmogorov constant.

We examine three derivative skewnesses, defined as follows: the velocity derivative skewness

$$S_u = \frac{\langle (\frac{\partial u_1}{\partial x_1})^3 \rangle}{\langle (\frac{\partial u_1}{\partial x_1})^2 \rangle^{3/2}}, \quad (1)$$

the mixed derivative skewness

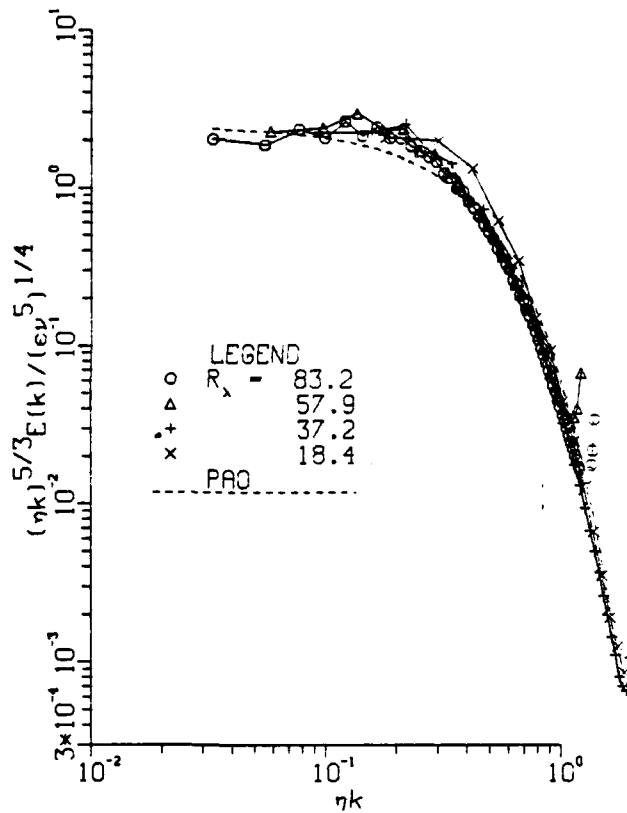
$$S_{u\theta} = \frac{\langle \frac{\partial u_1}{\partial x_1} (\frac{\partial \theta}{\partial x_1})^2 \rangle}{\langle (\frac{\partial u_1}{\partial x_1})^2 \rangle^{1/2} \langle (\frac{\partial \theta}{\partial x_1})^2 \rangle}, \quad (2)$$

and the scalar derivative skewness

$$S_\theta = \frac{\langle (\frac{\partial \theta}{\partial x_1})^3 \rangle}{\langle (\frac{\partial \theta}{\partial x_1})^2 \rangle^{3/2}}, \quad (3)$$

In our simulation the velocity and mixed derivative skewnesses are negative and reach a maximum amplitude of 0.5, independent of Prandtl number, and do not increase further with Reynolds number (figure 2). This contradicts predictions made by phenomenological models (Kolmogorov, 1962 and Frisch et al, 1979) and experiments at very high Reynolds numbers (Tavoularis, 1978), which all say that there should be a slight increase with Reynolds number. Theories by Saffman (1968) and Tennekes (1968) support our conclusion and experiments by Klebanoff (private communication) find S_u constant and equal to -0.43 for R_λ between 40 and 200 in a boundary layer. In isotropic flow the scalar

FIGURE 1
NORMALIZED KINETIC ENERGY SPECTRA



derivative skewness will be zero. But experiments in shear flow with a temperature gradient (Sreenivasan and Tavoularis, 1980) show it to be the order of one. Initial anisotropic simulations of ours support this result.

In isotropic flow it can be shown that the velocity derivative skewness is related to the fourth-order moment of the spectrum. To do this we use the following equation.

$$\frac{1}{2\nu} \frac{d}{dt} \epsilon = \int k^2 T_u(k) - 2\nu \int k^4 E_u(k) dk. \quad (4)$$

If $\frac{d}{dt} \epsilon \rightarrow 0$, we find that

$$-S_u = \frac{2 \int k^2 T_u(k) dk}{35 \left(\frac{15\nu}{15\nu} \right)^{1/2}} = \frac{2}{35} \frac{2\nu \int k^4 E(k)}{\left(\frac{15\nu}{15\nu} \right)^{1/2}} \quad (5)$$

When we integrate our spectra by this formula we find $S_u \sim -0.5$. If we integrate the spectral form of Pao (1965),

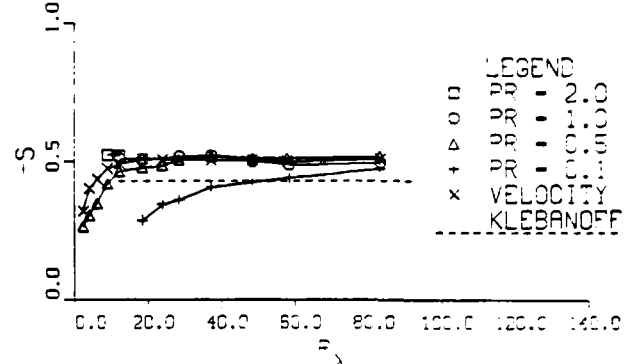
$$E(k) = \alpha \epsilon^{2/3} k^{-5/3} \exp(-1.5 \alpha \nu \epsilon^{-1/3} k^{4/3}) \quad (6)$$

we find

$$S_u = -2.40 \alpha^{-3/2}. \quad (7)$$

For $S_u = -0.5$, $\alpha = 2.85$. For a typical experimental Kolmogorov constant, $\alpha = 1.7$, (7) gives $S_u = -1.08$, which disagrees with the experimental measurements of the skewness. If the experimental values for the Kolmogorov constant and the skewness are correct, then Pao's spectral form is clearly a poor approximation to the experimental spectra. There are also significant differences between the calculated spectra of figure 1 and Pao's form near

FIGURE 2
VELOCITY AND MIXED SKEWNESSES



$(\eta k) \sim 0.2$. If the calculated Kolmogorov constant is to be consistent with the experiments (that is $\alpha \sim 1.7$), then at wavenumbers less than those simulated the correct spectrum must be below Pao's form for $\alpha = 2.45$. The skewness would not change in this case because the major contribution to it comes from the wavenumber regime already simulated. Experimental spectra by Champagne et al (1977) show an ultraviolet bump which is similar to the spectral shape we have proposed. Additional experiments which determine both the Kolmogorov constant and the skewness and make detailed comparisons with Pao's spectral form would help answer these questions.

§Fourth-order correlations

Four fourth order rotationally invariant velocity derivative correlations identified by Siggia (1981) are

$$I_1 = \langle e^4 \rangle \quad (8)$$

$$I_2 = \omega^2 e^2 \quad (9)$$

$$I_3 = \langle \omega_i e_{ij} e_{jk} \omega_k \rangle \quad (10)$$

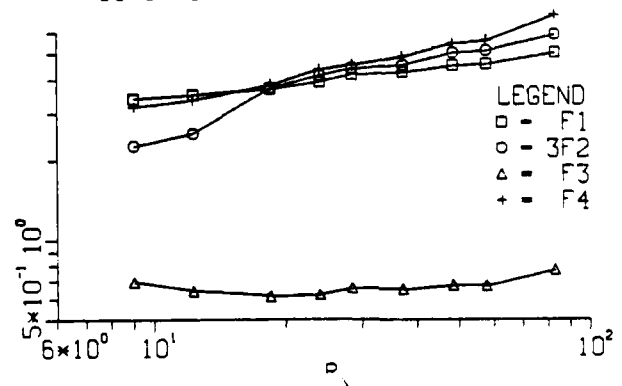
and

$$I_4 = \langle \omega^4 \rangle, \quad (11)$$

where e is the rate of strain and ω is the vorticity. Experimentally only one fourth order velocity derivative correlation has been measured,

$$F_u = \frac{\langle \left(\frac{\partial u_i}{\partial x_1} \right)^4 \rangle}{\langle \left(\frac{\partial u_i}{\partial x_1} \right)^2 \rangle^2} = F_1 = \frac{15}{7} \frac{I_1}{\langle e^2 \rangle^2}. \quad (12)$$

FIGURE 3
FOURTH-ORDER VELOCITY CORRELATIONS



It increases with Reynolds number (Antonia et al, 1982), with an exponent between 0.25 and 0.32. When normalized by the rate of strain, I_1 , I_2 , and I_4 increase with Reynolds numbers in our simulation in a similar manner, but each has a different exponent (figure 3). If power laws are applied to F_1 , F_2 , and F_4 in figure 3 for R_λ greater than 28 we find exponents of 0.18 ± 0.03 , 0.29 ± 0.03 , and 0.37 ± 0.03 , respectively. The lack of a single scaling exponent seems to contradict a major assumption of the phenomenological models. Using crossed wire probes experimentalists should be able to measure some of the correlations we have studied and test our results.

The scalar derivative flatness

$$F_\theta = \frac{\langle (\frac{\partial \theta}{\partial x_1})^4 \rangle}{\langle (\frac{\partial \theta}{\partial x_1})^2 \rangle^2} \quad (13)$$

is observed to increase with Reynolds number in a manner similar to the velocity flatness both in experiments (Antonia et al, 1982) and our simulation, but with a larger exponent (figure 4). This implies that the temperature field is in some sense more intermittent. The scaling exponent depends on the Prandtl number. If $F_\theta \sim 3R_\lambda^{\alpha_\theta}$, for Prandtl numbers 0.1, 0.5, and 1.0 we found $\alpha_\theta = 0.45$, 0.40, and 0.36, respectively.

There are four rotationally invariant correlations between the velocity and scalar derivatives which are discussed in detail by Kerr (1981) and Kerr (1983). These are

$$F_{\nabla\theta e1} = \frac{\langle \nabla\theta^2 e^2 \rangle}{\langle \nabla\theta^2 \rangle \langle e^2 \rangle} \quad (14)$$

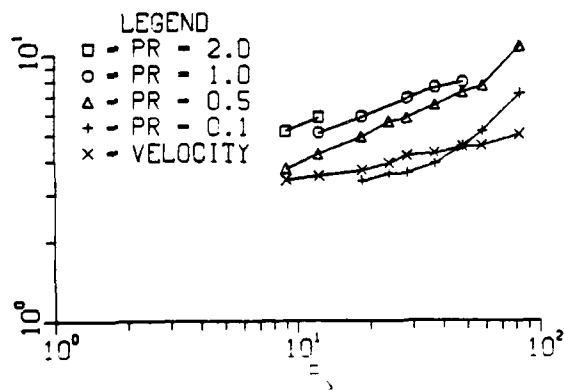
$$F_{\nabla\theta e2} = \frac{3 \langle \partial\theta/\partial x_i e_{ij} e_{jk} \partial\theta/\partial x_k \rangle}{\langle \nabla\theta^2 \rangle \langle e^2 \rangle} \quad (15)$$

$$F_{\nabla\theta\omega1} = \frac{\langle \nabla\theta^2 \omega^2 \rangle}{\langle \nabla\theta^2 \rangle \langle \omega^2 \rangle} \quad (16)$$

$$F_{\nabla\theta\omega2} = 3 \frac{\langle (\nabla\theta \cdot \omega)^2 \rangle}{\langle \nabla\theta^2 \rangle \langle \omega^2 \rangle} \quad (17)$$

Both correlations between the strain and the scalar derivative show a tendency to increase with Reynolds number, suggesting that the scalar gradients align themselves with the rate-of-strain. The first vorticity-scalar gradient correlation, $F_{\nabla\theta\omega1}$, is barely different than its uncorrelated value, showing that there is little correlation between the magnitudes of the vorticity and scalar derivative. But the

FIGURE 4
VELOCITY AND SCALAR FLATNESSES



second correlation, $F_{\nabla\theta\omega2}$, shows a strong anti-correlation between the direction of vorticity and the direction of the scalar gradient.

§Graphics

While the assortment of statistics presented might seem bewildering, each one predicts a different aspect of how the small scales are aligned. To demonstrate the alignment we have plotted short lines which represent the vorticity, scalar gradient, and rate of strain fields in figures 5 to 7. These are poor black and white, two dimensional projections of what our color movies will show. The fields have been conditionally sampled and only those grid points where the field is above a threshold are shown. The vorticity and scalar gradient are vectors and their direction can be represented by short lines easily. The most striking feature of the vorticity is its tendency to align in tubes, with the vorticity along the tubes. The scalar gradient is also found in structures, with the gradient perpendicular to the structures. Our movies will show that these structures are sheets wrapped around the vortex tubes. The low value for the second vorticity-scalar correlation (17) predicts that the scalar gradient and the vorticity should be aligned in this manner.

The rate of strain is a tensor and cannot be represented by single lines. Instead we plot only one of the principal rates of strain at a time. In figure 7 we plot the largest principal rate of strain at the conditionally sampled grid points. In all cases this is the compressive component. It can be shown that the velocity derivative skewness is related to the trace of the rate of strain cubed, and that because the skewness is negative, we expect the compressive component of the rate of strain to dominate at the conditionally sampled points. One should notice that the rate of strain structures are not as concentrated as the vortex structures of figure 5. This is expected because the vorticity flatness (11) is larger than the strain flatness (8). The rate of strain structures are found near, but outside the vortex tubes and are strongly aligned with the scalar gradient structures. We expect them to be near the vortex tubes because F_2 is large, but because F_3 is small we expect the largest component of the rate of strain (the compression) to be aligned perpendicular to the tubes. Comparison between figures 6 and 7 shows that the compressive component of the rate of strain is strongly aligned with the scalar gradient. We expect the rate of strain to be aligned with the scalar gradient because the correlations between them (14,15) are large. We expect the compressive component of the strain to be aligned with the scalar gradient because the mixed skewness is negative.

Our movies will rotate flow fields similar to those in figures 5 to 7 to give one a better perspective of the three dimensional character of the structures. Then we will show the fields evolving in time. Additional graphics planned include pictures of the stretching terms in the rate of strain and their correlation to the vortex tubes. Figures 5 to 7 come from a 64 cubed simulation at $R_\lambda = 58$. Graphics for a 128 cubed simulation at $R_\lambda = 83$ continue to show strong alignment on the small scales, but more random orientation with respect to the large scales. Very large numerical simulations are necessary if one wants to study detail as fine as we have considered. We have made two suggestions to experimentalists. First, that they check the consistency of the velocity derivative skewness and the Kolmogorov con-

FIGURE 5

VORTICITY



FIGURE 6

SCALAR GRADIENT

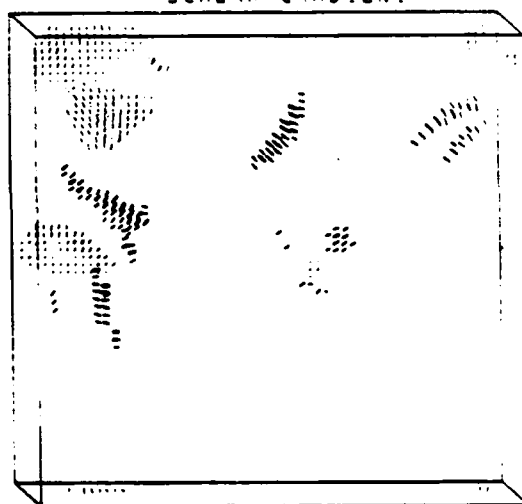
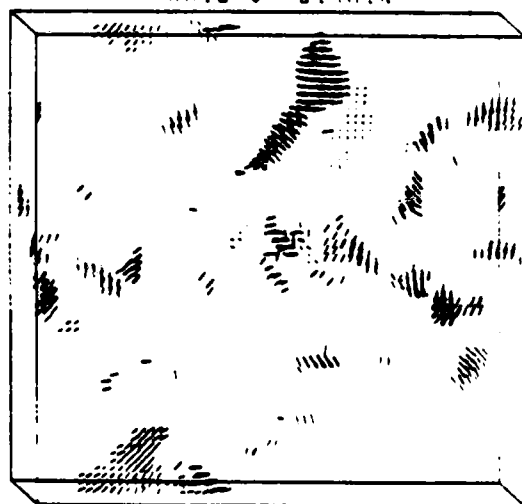


FIGURE 7

RATE OF STRAIN



stant. Second, that they use cross wired probes to measure more of the fourth order velocity derivative correlations. With this new understanding of the small scales, we hope that more progress can be made in finding effective means of modeling the small scales.

References

- Antonia, R.A., Satyaprakash, B.R., & Hussain, A.K.M.F. 1982 Statistics of fine-scale velocity in turbulent plane and circular jets. *J. Fluid. Mech.* 119, 55-89.
- Champagne, F.H., Friehe, C.A., LaRue, J.C., & Wyngaard, J.C. 1977 Flux measurements, flux estimation techniques and fine-scale turbulence measurements in the unstable surface layer over land. *J. Atmos. Sci.* 34, 515.
- Frisch, U., Sulem, P.L. & Nelkin, M. 1979 A simple model of intermittent fully-developed turbulence. *J. Fluid Mech.* 87, 719-736.
- Kerr, R.M. 1981 Theoretical investigation of a passive scalar such as temperature in isotropic turbulence. Ph.D. thesis; Cooperative Thesis no. 64, Cornell University and National Center for Atmospheric Research.
- Kerr, R.M. 1983 Higher order derivative correlations and small scale structures in isotropic numerical turbulence. NASA Technical Memo.
- Kolmogorov, A.N. 1962 A refinement of previous hypotheses concerning the local structure of turbulence in a viscous incompressible fluid at high Reynolds number. *J. Fluid Mech.* 13, 82-85.
- Monin, A.S. & Yaglom, A.M. 1975 *Statistical Fluid Mechanics*, vol. 2. Massachusetts Institute of Technology Press.
- Pao, Y-H. 1965 Structure of turbulent velocity and scalar fields at large wavenumbers. *Phys. Fluids* 8, 1063-1075.
- Rogallo, R.S. 1980 Numerical experiments in homogeneous turbulence. NASA TM 81315.
- Saffman, P.G. 1968 Lectures in homogeneous turbulence. in *Topics in Nonlinear Physics* (ed. N. Zabusky), 485-614. Springer.
- Siggia, E.D. 1981b Invariants for the one-point vorticity and strain rate correlation functions. *Phys. Fluids* 24, 1934-1936.
- Sreenivasan, K.R. & Tavoularis, S. 1980 On the skewness of the temperature derivative in turbulent flows. *J. Fluid Mech.* 101, 783-795.
- Tavoularis, S., Bennett, J.C. & Corrsin, S. 1978 Velocity-derivative skewness in nearly isotropic turbulence. *J. Fluid Mech.* 88, 63-69.
- Tennekes, H. 1968 Simple model for the small-scale structure of turbulence. *Phys. Fluids* 11, 669-671.

Reynolds stress closure model for conditional variables

J. Janicka
Lehrstuhl für Techn. Thermodynamik
RWTH Aachen
West Germany

W. Kollmann
Department of Mechanical Engineering
University of California
Davis, California 95616

INTRODUCTION

Free boundaries of turbulent shear flows show an intermittent character with a sharp interface separating instantaneously turbulent and non-turbulent zones shown by Corrsin and Kistler (1954). Prediction models for turbulent shear flows did not take this intermittent character into account so far. In this paper a second order closure model for turbulent shear flows based on conditional variables (Dopazo (1977)) is presented, that allows prediction of intermittency factor, zone-conditioned mean velocities and Reynolds-stresses. It is based on an earlier closure for intermittency factor, mean velocities and kinetic energy and dissipation rate (Byggstoyl and Kollmann (1981)) which used the concept of turbulent pseudo-viscosity for the turbulent zone. The equations for conditional moments contain explicitly terms accounting for the relative motion of turbulent and non-turbulent zones and the transport of various quantities through it. Some of those terms are non-closed on the second-order level and their closure will be discussed. The resulting conditional Reynolds-stress model will be evaluated by comparison of calculated properties of various thin shear flows with experimental results.

CLOSURE MODEL

The definition of conditional moments requires the notion of a non-negative discriminator variable $\phi(\underline{x}, t)$ such that $\phi \geq \epsilon > 0$ corresponds to turbulent flow at the point (\underline{x}, t) considered and $\phi < \epsilon$ to nonturbulent. If randomness and nonzero vorticity are accepted as properties defining the turbulent state of the flow, the scalar ϕ is given by

$$\phi(\underline{x}, t) = \omega'_k \omega'_k$$

where ω'_k is the vorticity fluctuation. The threshold ϵ for discrimination must be larger than zero for finite Reynolds numbers, because of the elliptic nature of the differential equations governing the motion. Then the indicator function $I(\underline{x}, t)$ can be defined

$$I(\underline{x}, t) = \begin{cases} 0 & \text{for } \phi(\underline{x}, t) < \epsilon \\ 1 & \text{for } \phi(\underline{x}, t) \geq \epsilon \end{cases}$$

The equation

$$S(\underline{x}, t) \equiv \phi(\underline{x}, t) - \epsilon = 0$$

defines implicitly a surface within the instantaneous interface separating turbulent and non-turbulent zones. If the interface velocity is denoted by \underline{v}^s , the speed V with which the interface progresses in its normal \underline{n}_s (positive into turbulent zone) relative to the fluid is given by

$$\underline{n}_s \cdot \underline{V} = \underline{v}_s^s - \underline{v}_s^f$$

Then follows that the indicator function is transported with points on the interface, which are not material point. Thus

$$\frac{\partial I}{\partial t} + \underline{v}_s^s \frac{\partial I}{\partial x_s} = 0 \quad (1)$$

and the derivatives of the indicator function can be expressed in terms of the interface properties

$$\frac{\partial I}{\partial t} = - \underline{v}_s^s n_s \delta(s) \quad (2)$$

and

$$\frac{\partial I}{\partial x_s} = n_s \delta(s) \quad (3)$$

Turbulent-zone moments are defined by

$$\bar{\phi} = \frac{\langle I \phi \rangle}{\langle I \rangle}, \quad \phi^* = \phi - \bar{\phi}$$

where $\bar{\phi} = \langle I \phi \rangle$ is the intermittency factor and non-turbulent zone moments by

$$\bar{\tilde{\phi}} = \frac{\langle (1-I) \phi \rangle}{1 - \langle I \rangle}, \quad \phi^0 = \phi - \bar{\tilde{\phi}}$$

The equations for intermittency factor $\bar{\phi}$ and zone-conditioned moments follow then using standard methods (see Dopazo (1977) and Byggstoyl and Kollmann (1981) appendix). The equations for first and second order conditional moments contain correlations analogous to the unconditional case and new correlations representing the interface movement and transport of mass and momentum through it. The closure of these new correlations will be discussed subsequently in some detail.

Intermittency factor

The exact transport equation for $\bar{\phi}$ follows from (1) by averaging

$$\frac{\partial \bar{\phi}}{\partial t} + \bar{\underline{v}}_s^s \frac{\partial \bar{\phi}}{\partial x_s} = - \frac{\partial}{\partial x_s} [\bar{\phi} (1 - \bar{\phi}) (\bar{\underline{v}}_s^s - \bar{\underline{v}}_s^f)] + \langle V \delta(s) \rangle \quad (4)$$

The intermittency source $\langle V \delta(s) \rangle$ which is the rate of entrainment of non-turbulent fluid per unit volume requires closure. The model of Byggstoyl and Kollmann (1981) can be applied in the form

$$\langle V \delta(S) \rangle \approx -C_{g1} \gamma (1-\gamma) \frac{\bar{v}_x \bar{v}_x'}{k} \left(\frac{\partial \bar{v}_x}{\partial x_3} + \frac{\partial \bar{v}_x'}{\partial x_3} \right) + C_{g2} \frac{k^2}{\epsilon} \frac{\partial \gamma}{\partial x_3} \frac{\partial \gamma}{\partial x_3} - C_{g3} \gamma (1-\gamma) \frac{\bar{\epsilon}}{k} \quad (5)$$

with $C_{g1} = 1.875$, $C_{g2} = 0.06$, $C_{g3} = 0.1$. The first term on the right hand side represents the growth of the turbulent zone due to the mean strain, the second the enhanced transport due to spatial inhomogeneity and the last term the shrinking of the turbulent zone due to viscous effects. The last term in (5) reflects the fact that a finite threshold level for the variable ϕ discriminating between turbulent and nonturbulent zones is used. Consequently should C_{g3} be a function of this level such that C_{g3} vanishes if the threshold value for ϕ vanishes. For the present calculations however C_{g3} was simply kept at the given value.

The difference of the conditional mean velocities, which acts as turbulent flux for the intermittency factor, is included in the closure model. For parabolic flows however only the longitudinal components are calculated and it is advantageous to model the difference of the cross-flow components. Thus

$$\bar{v}_x - \bar{v}_x' \approx C_8 \frac{k}{\epsilon} \bar{v}_x \bar{v}_x' \frac{1}{\gamma} (1-\gamma)^{\beta-1} \frac{\partial \gamma}{\partial x_3} \quad (6)$$

is applied for $\beta = 2$ only ($C_8 = 0.15$, $z_1 = 1.5$).

Conditional Momentum Sources

Conditional averaging of the momentum equations leads to new correlations representing momentum sources. The turbulent zone mean velocity satisfies

$$\frac{D}{Dt} \bar{v}_x = -\frac{1}{\gamma} \frac{\partial}{\partial x_3} (\gamma \bar{v}_x \bar{v}_x') - \frac{1}{\rho} \frac{\partial \bar{p}}{\partial x_3} + \nu \Delta \bar{v}_x + \bar{S}_x + (1-\gamma) (\bar{v}_x - \bar{v}_x') \frac{\partial \bar{v}_x}{\partial x_3} \quad (7)$$

where

$$\frac{D}{Dt} = \frac{\partial}{\partial t} + \bar{v}_x \frac{\partial}{\partial x_3}$$

The source term \bar{S}_x can be cast in the form

$$\bar{S}_x = \frac{1}{\gamma} \bar{F}_x'$$

$$\bar{F}_x' = \langle (v_x' v_x + p' n_x - \nu n_x \frac{\partial v_x'}{\partial x_3}) \delta(S) \rangle - \nu \frac{\partial}{\partial x_3} \langle v_x' n_x \delta(S) \rangle \quad ; \quad i = x, y, z$$

The non-turbulent zone mean velocity \bar{v}_x' is governed by

$$\frac{D}{Dt} \bar{v}_x' = -\frac{1}{1-\gamma} \frac{\partial}{\partial x_3} [(1-\gamma) \bar{v}_x \bar{v}_x'] - \frac{1}{\rho} \frac{\partial \bar{p}}{\partial x_3} + \nu \Delta \bar{v}_x' + \bar{S}_x' - \gamma (\bar{v}_x - \bar{v}_x') \frac{\partial \bar{v}_x'}{\partial x_3} \quad (8)$$

with source term

$$\bar{S}_x' = -\frac{1}{1-\gamma} \bar{F}_x''$$

Since the equations for \bar{v}_x and \bar{v}_x' can be combined according to (Byggstoyl and Kollmann (1981), appendix)

$$\bar{v}_x = \gamma \bar{v}_x + (1-\gamma) \bar{v}_x'$$

and

$$\bar{v}_x \bar{v}_x' = \gamma \bar{v}_x \bar{v}_x' + (1-\gamma) \bar{v}_x \bar{v}_x' + \gamma (1-\gamma) (\bar{v}_x - \bar{v}_x') (\bar{v}_x - \bar{v}_x')$$

to the equation for the unconditional mean \bar{v}_x , the following relation for the conditional momentum sources is obtained

$$\gamma \bar{S}_x' + (1-\gamma) \bar{S}_x = (\bar{v}_x - \bar{v}_x') S_x + \frac{1}{\rho} (\bar{p} - \bar{p}') \frac{\partial \gamma}{\partial x_3} \quad (9)$$

where $S_x = \langle V \delta(S) \rangle$ is the source term of the intermittency equation (4). An order of magnitude analysis shows that both terms on the right hand side of (9) are of the same order for the longitudinal component in thin shear layers. For the cross-flow component the pressure-difference term is dominant and balances the left hand side of (9). Relation (9) is important for the closure of equation (8) for the non-turbulent zone mean velocity.

Non-Turbulent Zone Stress Tensor

If the discriminating scalar ϕ is defined as enstrophy $\omega_i \omega_i'$, then follows that the vorticity fluctuations in the non-turbulent zone are below the threshold and therefore negligible. This condition can be expressed analytically in the Corrsin-Kistler (1954) equation (see Dopazo (1977)) for the non-turbulent zone stress tensor

$$\frac{\partial}{\partial x_3} [(1-\gamma) \bar{v}_x \bar{v}_x'] = \frac{\partial}{\partial x_3} [(1-\gamma) \bar{k}] - \langle (v_x' v_x' n_x - k' n_x) \delta(S) \rangle \quad (10)$$

where $k' = \frac{1}{2} v_x' v_x'$ and $\bar{k} = \bar{k}'$ denote kinetic energy in the non-turbulent zone. This relation has interesting properties: The diffusive term

$$\frac{\partial}{\partial x_3} [(1-\gamma) \bar{v}_x \bar{v}_x']$$

which appears in (8), can be split into diffusion due to normal stresses analogous to the mean pressure and diffusion due to shear and normal stresses which are created at the interface. Furthermore follows that the interface term can be represented as divergence of a flux

$$- \langle (v_x' v_x' n_x - k' n_x) \delta(S) \rangle = \frac{\partial}{\partial x_3} [(1-\gamma) \bar{F}_x''] \quad (11)$$

The equation for the non-turbulent zone mean velocity appears now in a form consistent with (9) and (11) as

$$\frac{D}{Dt} \bar{v}_x' = -\frac{1}{1-\gamma} \frac{\partial}{\partial x_3} [(1-\gamma) \bar{F}_x''] - \frac{1}{\rho} \frac{\partial \bar{p}}{\partial x_3} + \nu \Delta \bar{v}_x' - \frac{1}{1-\gamma} \frac{\partial}{\partial x_3} [(1-\gamma) \bar{k}] + (\bar{v}_x - \bar{v}_x') \frac{S_x}{1-\gamma} - \frac{1}{1-\gamma} \bar{S}_x' + \frac{1}{\rho} (\bar{p} - \bar{p}') \frac{1}{1-\gamma} \frac{\partial \gamma}{\partial x_3} - \gamma (\bar{v}_x - \bar{v}_x') \frac{\partial \bar{v}_x'}{\partial x_3} \quad (12)$$

It should be noted that in the derivation of (12) only the fluctuations of velocity in the non-turbulent zone are assumed irrotational. The mean vorticity may be non-zero.

Turbulent-zone mean velocity

All conditional moment equations can be cast in a form analogous to the equation for the unconditional moment plus a collection of interface terms (denoted by A with the appropriate indices). For \bar{v}_x these terms follow from (7) as

$$\bar{A}_x = \bar{S}_x + (1-\gamma)(\bar{v}_x - \bar{v}_x) \frac{\partial \bar{v}_x}{\partial x} \quad (13)$$

From the closure of the intermittency factor equation follows the expression for the second part without new assumptions as

$$(1-\gamma)(\bar{v}_x - \bar{v}_x) \frac{\partial \bar{v}_x}{\partial x} \approx C_5 \frac{k}{\epsilon} \bar{v}_x \bar{v}_x \frac{1}{\gamma} (1-\gamma) \frac{\partial \gamma}{\partial x} \frac{\partial \bar{v}_x}{\partial x} \quad (14)$$

For the closure of the first part the exchange of momentum between the turbulent and nonturbulent zones is considered. If the turbulent zone is faster it will lose momentum to the non-turbulent zone proportional to the velocity difference of the zones and vice versa. The amount of momentum transferred depends on the turbulent time scale and the crossing frequency of the interface which is given by S_γ . Then the following expression emerges

$$\bar{S}_x \approx -(\bar{v}_x - \bar{v}_x) \left[C_4 (1-\gamma) \frac{\partial \gamma}{\partial x} + \frac{1}{\gamma} \langle v \delta(s) \rangle \right] \quad (15)$$

where the model for the intermittency source is given by (5) and $C_4 = 5.0$, $z_2 = 2.0$

Non-turbulent zone mean velocity

For the closure of equation (12) two assumptions are required. First the flux \bar{F}_{x1} must be expressed in terms of known moments and second the pressure difference must be dealt with. For the flux the model

$$\bar{F}_{x1} \approx C_0 \gamma \frac{k}{\epsilon} \left(\frac{\partial \bar{v}_x}{\partial x} + \frac{\partial \bar{v}_x}{\partial x} \right) \quad (16)$$

which is a turbulent viscosity model with $C_0 = 0.2$ C_0 reduced constant. The pressure difference terms is assumed to balance with the following group

$$\frac{1}{\rho} (\bar{p} - \bar{p}) \frac{\partial \gamma}{\partial x} \approx \frac{1}{1-\gamma} \frac{\partial \gamma}{\partial x} [(1-\gamma) k] - \frac{\bar{F}_{x1}}{1-\gamma} \frac{\partial \gamma}{\partial x} \quad (17)$$

Thus the closed equation for \bar{v}_x is obtained using (15). It is given in the appendix where the complete model equations are assembled.

Turbulent-zone stress tensor

The terms analogous to the unconditional forms are modelled by carrying over the closure assumptions of the unconditional case (Lumley (1978) and Launder, Reece, and Rodi (1975)) to the turbulent zone variables. Closure assumptions like quasi-Gaussianity of the fourth moment for velocity fluctuations have certainly more justification for the conditional case than the unconditional because

the center spike corresponding to the small fluctuations in the non-turbulent zone is removed in the conditional case, thus bringing the flatness factors closer to the Gaussian value. The interface group (exact forms see Byggstoyl and Kollmann (1981)) requires new considerations. The turbulent zone propagates into the non-turbulent by increasing the vorticity of irrotational parcels of fluid. This propagation is only possible if the net effect on the turbulent zone stress is gain at the expense of non-turbulent-zone fluctuations. Thus

$$\bar{S}_{x1} \approx C_5 \gamma (1-\gamma) \frac{k}{\epsilon} \bar{v}_x \bar{v}_x \quad (18)$$

The contribution due to relative motion follows from model assumptions on entrainment and momentum transport introduced above. Then the interface group is given by

$$\begin{aligned} \bar{A}_{x1} \approx & C_5 (1-\gamma) \frac{k}{\epsilon} \bar{v}_x \bar{v}_x \frac{\partial \gamma}{\partial x} \frac{\partial \bar{v}_x}{\partial x} \frac{1}{\gamma} \frac{\partial \gamma}{\partial x} \\ & + (2\nu \frac{\partial \bar{v}_x}{\partial x} - \bar{v}_x \bar{v}_x) \frac{1}{\gamma} \frac{\partial \gamma}{\partial x} \\ & + \frac{1}{\gamma} (\nu \Delta \gamma - \langle v \delta(s) \rangle) \bar{v}_x \bar{v}_x + \bar{S}_{x1} \quad (19) \end{aligned}$$

where $C_5 = 0.5$.

Non-turbulent zone stress tensor

The principal axis of turbulent-zone and non-turbulent zone stress tensors are not aligned. Experimental evidence (Byggstoyl and Kollmann (1981)) suggests that the gradient of the intermittency factor is close to a principal axis of the non-turbulent stress tensor. In the present closure model these considerations were taken into account simply by setting $\bar{v}_x \bar{v}_x$ proportional to $\gamma \bar{v}_x \bar{v}_x$ with a factor $C_{11} = 0.5$ for normal stresses and $C_{12} = 0.2$ for the shear stress. These ad hoc relations do not enter the calculations directly and are applied to determine unconditional stress components only.

Dissipation rate

The dissipation rate in the non-turbulent zone is negligible, thus provides the propagation of the interface a gain of dissipation rate. The model for \bar{S}_ϵ is then

$$\bar{S}_\epsilon \approx C_6 \gamma (1-\gamma) \frac{k}{\epsilon} \quad (20)$$

where $C_6 = 1.0$. The complete interface group is given by

$$\begin{aligned} \bar{A}_\epsilon \approx & C_6 \frac{k}{\epsilon} \bar{v}_x \bar{v}_x (1-\gamma) \frac{1}{\gamma} \frac{\partial \gamma}{\partial x} \frac{\partial \bar{v}_x}{\partial x} \\ & + (2\nu \frac{\partial \bar{v}_x}{\partial x} - \bar{v}_x \bar{v}_x) \frac{1}{\gamma} \frac{\partial \gamma}{\partial x} \\ & + \frac{1}{\gamma} (\nu \Delta \gamma - \langle v \delta(s) \rangle) \bar{v}_x \bar{v}_x + \bar{S}_\epsilon \quad (21) \end{aligned}$$

APPLICATIONS

The conditional Reynolds-stress model was applied to several (parabolic) shear flows. For the plane jet the intermittency factor in fig. 1 shows the

expected distribution in agreement with the measurements of Gutmark and Wygnanski (1976). The turbulent zone and unconditional mean velocities \bar{U} , \bar{U} , in fig. 2 agree well with the experiments of Gutmark and Wygnanski (1976). The two normal stress components for the turbulent zone in fig. 3 show reasonable agreement with the measurements of Gutmark and Wygnanski (1976). In the core region the predictions are determined by the same modelling assumptions as the unconditional model whereas in the outer part the interface terms became significant. In the outer part of the turbulent zone stresses decrease slower than the experimental values. This leads to the smooth mean velocity profiles in fig. 2 agreeing well with measurements in the outer part of the flow field. The round jet calculation requires a change of the return to isotropy constant c_1 (see appendix) with the present closure to obtain the correct spreading rate. Then good agreement with experiments of Wygnanski and Fiedler (1969) is found for intermittency factor fig. 4 mean velocities (not shown) and normal stresses fig. 5 and fig. 6.

CONCLUSIONS

The closure of conditional moment equations leads to detailed information on the properties of the flow in turbulent and non-turbulent zones. The interaction of the zones requires some new model assumptions, which are however guided by the condition that conditional sources must combine appropriately to zero for the unconditional moment. This approach has further applications such as combustor flow, where the instantaneous flame front can be considered as interface.

ACKNOWLEDGEMENT

The second author (WK) was supported by DOE Grant AS03-76SF00034. Part of the work was done at the Combustion Research Facility of Sandia Livermore.

REFERENCES

- [1] Corrsin, S., Kistler, A. L., 1954, NACA TN-3133.
- [2] Dopazo, C., 1977, JFM, 81, 433.
- [3] Byggstoyl S., Kollmann, W., 1981, Int. J. Heat Mass Transfer, 24, 1181.
- [4] Lumley, J. L., 1978, Adv. Appl. Mech. 18.
- [5] Launder, B. E., Reece, G. J., and Rodi W., 1975, JFM, 68, 537.
- [6] Gutmark E., Wygnanski, I., 1976, JFM 73, 465.
- [7] Wygnanski, I. and Fiedler, H., 1969, JFM 38, 577.

APPENDIX

The complete set of model equations for Cartesian coordinates is given here in the form such that convection along unconditional mean streamlines is balanced by diffusion and sources. Intermittency factor γ :

$$\begin{aligned} \frac{D\gamma}{Dt} = & \frac{\partial}{\partial x_k} \left[c_3 \frac{k}{\epsilon} \overline{v_k^* v_k^*} (1-\gamma)^2 \frac{\partial \gamma}{\partial x_k} \right] \\ & - c_1 \gamma (1-\gamma) \frac{\overline{v_k^* v_k^*}}{k} \left(\frac{\partial \bar{U}}{\partial x_k} + \frac{\partial \bar{U}}{\partial x_k} \right) \\ & - c_2 \frac{k^2}{\epsilon} \frac{\partial \gamma}{\partial x_k} \frac{\partial \gamma}{\partial x_k} - c_3 \gamma (1-\gamma) \frac{\overline{v_k^* v_k^*}}{k} \end{aligned} \quad (A1)$$

Turbulent zone mean velocity \bar{v}_k :

$$\begin{aligned} \frac{D}{Dt} \bar{v}_k = & - \frac{1}{\rho} \frac{\partial}{\partial x_k} (\gamma \overline{v_k^* v_k^*}) - \frac{1}{\rho} \frac{\partial \bar{p}}{\partial x_k} \\ & + \nu \Delta \bar{v}_k + (\bar{v}_k - \bar{v}_k) \left[c_4 (1-\gamma)^2 \frac{\bar{U}}{k} + \frac{S_\gamma}{\gamma} \right] \\ & + c_5 \frac{k}{\epsilon} \overline{v_k^* v_k^*} \frac{1}{\gamma} (1-\gamma)^2 \frac{\partial \gamma}{\partial x_k} \frac{\partial \bar{v}_k}{\partial x_k} \end{aligned} \quad (A2)$$

The intermittency source S_γ is given by (5).

Non-turbulent zone mean velocity \bar{v}_k :

$$\begin{aligned} \frac{D}{Dt} \bar{v}_k = & \frac{\partial}{\partial x_k} \left[c_5 \frac{k}{\epsilon} \bar{v}_k^2 \left(\frac{\partial \bar{v}_k}{\partial x_k} + \frac{\partial \bar{v}_k}{\partial x_k} \right) \right] - \frac{1}{\rho} \frac{\partial \bar{p}}{\partial x_k} \\ & + \nu \Delta \bar{v}_k - (\bar{v}_k - \bar{v}_k) c_4 \gamma (1-\gamma)^2 \frac{\bar{U}}{k} \\ & + c_5 \frac{k}{\epsilon} \bar{v}_k^2 \gamma (1-\gamma)^2 \frac{\partial \gamma}{\partial x_k} \frac{\partial \bar{v}_k}{\partial x_k} \end{aligned} \quad (A3)$$

Turbulent zone stress tensor $\overline{v_k^* v_l^*}$:

$$\begin{aligned} \frac{D}{Dt} \overline{v_k^* v_l^*} = & \frac{\partial}{\partial x_j} \left(c_5 \frac{k}{\epsilon} \overline{v_k^* v_l^*} \frac{\partial}{\partial x_j} \overline{v_k^* v_l^*} \right) \\ & - \overline{v_k^* v_l^*} \frac{\partial \bar{U}}{\partial x_j} - \overline{v_l^* v_k^*} \frac{\partial \bar{U}}{\partial x_j} - \frac{2}{3} \delta_{kl} \bar{U} \\ & - c_1 \frac{\bar{U}}{k} (\overline{v_k^* v_l^*} - \frac{2}{3} \delta_{kl} \bar{U}) + \bar{\Phi}_{kl} + \bar{A}_{kl} \end{aligned} \quad (A4)$$

\bar{A}_{kl} is given by (19) and the fast response part of the pressure-strain correlation by Launder, Reece, and Rodi (1975)

$$\begin{aligned} \bar{\Phi}_{kl} = & - \frac{c_2 + 8}{11} (P_{kl} - \frac{2}{3} \delta_{kl} P) \\ & - \frac{30c_2 - 2}{55} k \left(\frac{\partial \bar{U}}{\partial x_k} + \frac{\partial \bar{U}}{\partial x_k} \right) \\ & - \frac{8c_2 - 2}{11} (D_{kl} - \frac{2}{3} \delta_{kl} P) \end{aligned} \quad (A5)$$

where

$$P_{kl} = - \overline{v_k^* v_l^*} \frac{\partial \bar{U}}{\partial x_j} - \overline{v_l^* v_k^*} \frac{\partial \bar{U}}{\partial x_j}$$

$$P = \frac{1}{2} P_{kk}$$

$$D_{kl} = - \overline{v_k^* v_l^*} \frac{\partial \bar{U}}{\partial x_k} - \overline{v_l^* v_k^*} \frac{\partial \bar{U}}{\partial x_k}$$

The constants are $c_1 = 1.5$ ($c_1 = 2.5$ for round jets) and $c_2 = 0.4$ of Launder, Reece, and Rodi (1975).

Dissipation rate $\bar{\epsilon}$:

$$\frac{D\bar{\epsilon}}{Dt} = \frac{2}{\partial x_n} \left(c_e \frac{\bar{k}}{\bar{\epsilon}} \overline{v_n^* v_n^*} \frac{\partial \bar{\epsilon}}{\partial x_n} \right) - c_1 \frac{\bar{\epsilon}}{\bar{k}} \overline{v_n^* v_n^*} \frac{\partial \bar{k}}{\partial x_n} - c_2 \frac{\bar{\epsilon}^2}{\bar{k}} + \bar{A}_\epsilon \quad (A6)$$

\bar{A}_ϵ is given by (21) and the constants are $c_e = 0.15$, $c_1 = 1.44$, $c_2 = 1.92$ of Launder, Reece, and Rodi (1975).

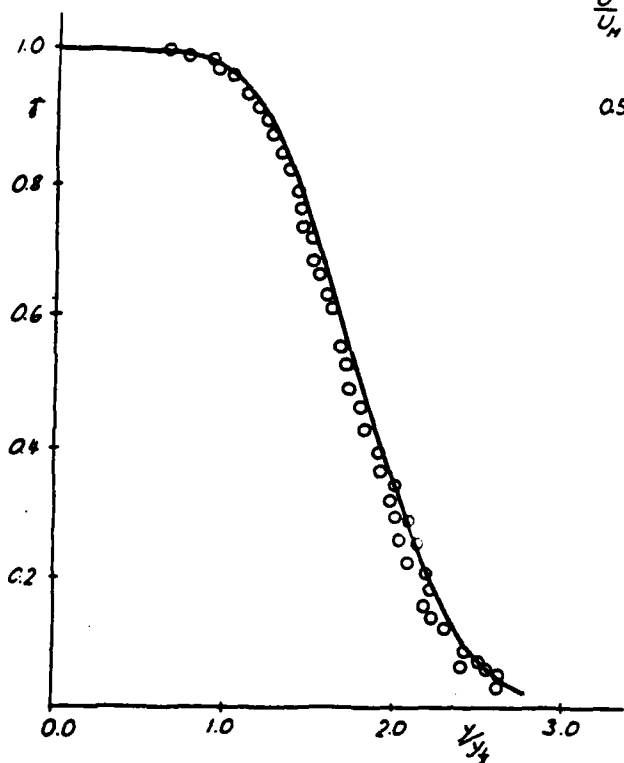


Fig. 1 Intermittency factor for plane jet. Symbols: [6]

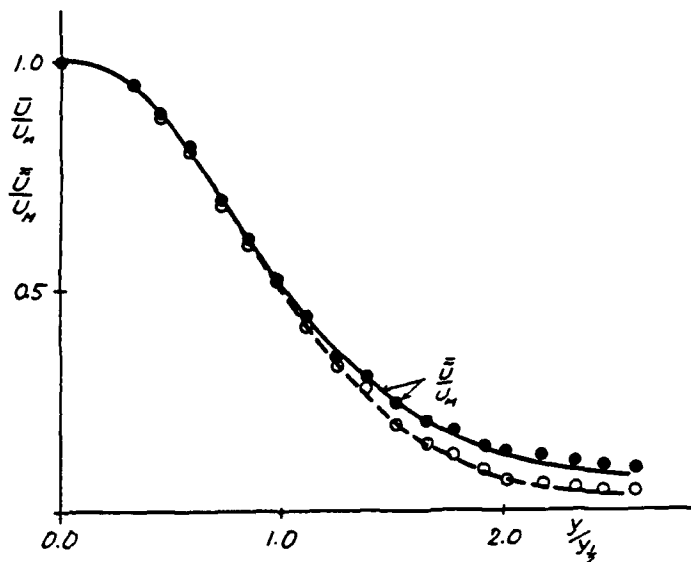


Fig. 2 Unconditional mean velocity \bar{U} and turbulent zone mean velocity \bar{U} for plane jet. Symbols: [6]

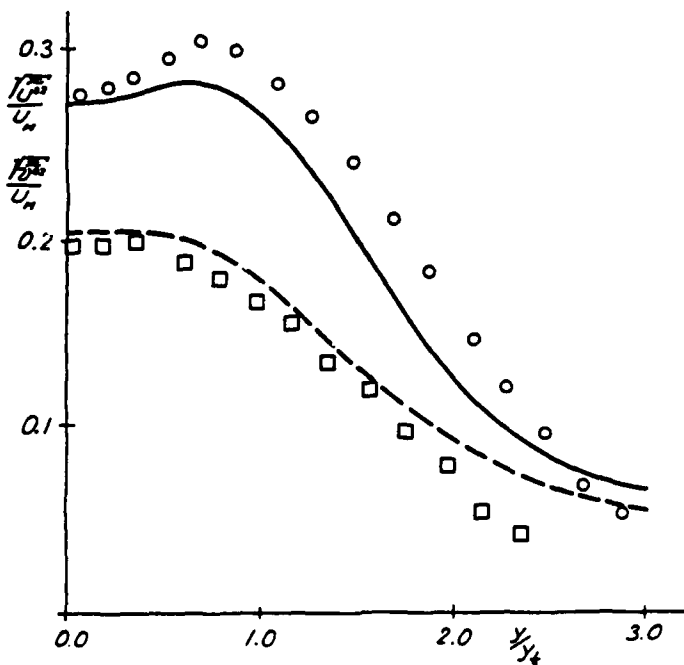


Fig. 3 Normal stresses $\overline{u^{*2}}$, $\overline{v^{*2}}$ for the turbulent zone in plane jet. Symbols: [6]

THE ASYMPTOTIC DEVELOPMENT OF NEARLY HOMOGENEOUS TURBULENT SHEAR FLOW

U. Karnik and S. Tavoularis
Department of Mechanical Engineering, University of Ottawa, Canada K1N 6N5

ABSTRACT

Turbulent flows with uniform mean velocity gradients and transversely homogeneous statistical features have been generated in a specially designed wind-tunnel. Values of the mean shear in the range 13.4 to 84 s^{-1} were achieved by adjusting the centreline speed and by inserting grids of different mesh sizes. In all cases, the components of the dimensionless Reynolds stress tensor attained quasi-universal asymptotic values, while the Reynolds stresses and the turbulent kinetic energy grew exponentially downstream. The present data as well as previous ones are utilized in a search for universal asymptotic features of uniformly sheared turbulence.

NOMENCLATURE

h	height of test section
K_{ij}	normalized Reynolds stress tensor
L_{11}	streamwise velocity integral length scale
ℓ	characteristic length
M	grid mesh size
P	turbulent kinetic energy production rate
q^2	turbulent kinetic energy ($= \overline{u_i u_i}$)
u_b	"barrier velocity"
u_i	velocity fluctuation in i direction
\overline{U}_1	streamwise mean velocity
\overline{U}_c	centreline mean velocity
x_g	downstream position of grid
x_i	co-ordinate axes; x_1 is parallel to the flow, x_2 is parallel to the mean shear and x_3 is perpendicular to the above

Greek Symbols

ϵ	turbulent kinetic energy dissipation rate
ν	kinematic viscosity

Suffixes

$()'$	root-mean-square value
$()_{\overline{}}$	time averaged quantity
$()_r$	reference value

INTRODUCTION

Nearly homogeneous turbulent shear flows have been generated and studied by several investigators, most notably by Rose (1966, 1970), Champagne et al. (1970), Mulhearn and Luxton (1970), Harris et al. (1977) and Tavoularis and Corrsin (1981). These experiments can be divided into two distinct groups: the former three correspond to mean shears $d\overline{U}_1/dx_2$ much lower than that in the latter two. Although the high shear experiments demonstrate a monotonic downstream increase of turbulent kinetic energy, $q^2 = \overline{u_i u_i}$, in the low-shear experiments, q^2 appears to level down to a roughly constant value. Harris et al. (1977) have attributed this discrepancy to insufficient flow development time for the low-shear experiments. Since there is little overlap between the ranges of parameters of the two groups of experiments, the existing information is insufficient for a conclusive study of uniformly sheared turbulence.

Most recently, Tavoularis (1983) has presented a semi-analytical prediction of the asymptotic features of such flows, which concluded that q^2 (as well as all individual Reynolds stresses) and L_{11} (the integral length scale) would grow exponentially as

$$q^2(x_1) = q_r^2 e^{2(x_1 - x_{1r})/\ell} \quad (1)$$

and

$$L_{11} = L_{11r} e^{(x_1 - x_{1r})/\ell} \quad (2)$$

where the characteristic length ℓ , defined as

$$\ell = \frac{U q^2}{P} \left(1 - \frac{\epsilon}{P}\right)^{-1} \quad (3)$$

is a constant for a given flow; in expression (3), P is the turbulent kinetic energy production rate $= \overline{u_1 u_2} d\overline{U}_1/dx_2$ and ϵ is the turbulent kinetic energy dissipation rate. Expressions (1) and (2) have been verified by the data of Tavoularis and Corrsin (1981).

The purpose of the present study is to generate flows with a wide range of mean shear and initial conditions, which will provide sufficient basis for a universal description of uniformly sheared turbulence.

FLOW FACILITY AND MEASUREMENT TECHNIQUES

All experiments were conducted in a specially designed open-circuit wind-tunnel at the University of Ottawa. The air-flow was produced by two centrifugal blowers and after passing through a filter, a honeycomb, a settling chamber with several turbulence-reducing screens and a 16:1 rectangular contraction, it entered the final section (shown in Figure 1) which was 30.5 cm high, nominally 45.7 cm wide, and 518 cm long. The vertical walls of the downstream end (about 304 cm long) of the wind-tunnel had adjustable distance for boundary layer compensation. The free-stream turbulent intensity at all examined speeds was below 0.3 %.

The desired mean velocity profile was produced with the use of a shear generator, inserted in the flow immediately following the contraction. The shear generator consisted of a set of 12 parallel aluminum plates, 15 cm wide and 2.54 cm apart, which separated the flow into 12 channels, and a system of interchangeable screens stretched across each channel which provided the desired channel pressure drop. A flow separator, consisting of 12 parallel aluminum plates 61 cm long and aligned with those in the shear generator, was inserted in the flow in order to produce transverse uniformity of the turbulent length scales.

As shown in Figure 1, the test section was 442 cm long and was equipped with four frames for the insertion of grids and other flow obstructions. All grids used in the present experiments consisted of parallel cylindrical rods and had a solidity of 0.35. Results using two grids with mesh sizes, M , respectively 2.54 cm and 5.08 cm are reported here, while measurements using other grids are still in progress.

The fluctuating velocity was measured with conventional, linearized, single- and cross-wire anemometers; data acquisition and processing was done using analog instrumentation as well as an LSI 11/23 digital micro-computer.

THE MEASUREMENTS

(a) The Mean Shear

The shear generator was designed and, later, further adjusted by trial and error, in order to produce the highest possible shear within the wind-tunnel limitations. The maximum shear measured exceeded 100 s^{-1} but corresponded to unstable fan operation. Typical stable values of the mean shear attained included 43, 60 and 84 s^{-1} , corresponding to centreline speeds \bar{U}_c equal to 6, 9 and 13 m/s. In all cases, the mean shear remained constant in the entire test section, excluding the boundary layers near the four walls (Figure 2(a)).

As expected, insertion of a grid resulted in significant reduction of the mean shear, although the resulting flow also had uniform mean velocity gradient (Figure 2(b)) and nearly homogeneous velocity fluctuations. Interestingly, each of the two grids reduced the mean shear by a

fixed factor (2.2 for the M 2.54 cm grid and 3.0 for the M 5.08 cm grid) for the entire range of variation of the centreline speed. The shear reduction factor was also independent of the downstream position of insertion of the grid.

(b) The Reynolds Stresses

The degree of transverse homogeneity of the Reynolds stresses was generally comparable to these in earlier realizations of uniformly shear flows (Figure 3), so only velocity fluctuation measurements along the wind-tunnel central axis will be presented here. To facilitate comparisons with the predictions of Tavoularis (1983), the data are plotted in semi-logarithmic coordinates.

Typical measurements of the centreline development of the turbulent kinetic energy q^2 , the three mean-squared velocity components u_1^2 , u_2^2 , u_3^2 and the shear stress $\overline{u_1 u_2}$ are shown in Figure 4, which contains one unobstructed flow case (Figure 4 a) and two cases of interaction with the two grids (Figures 4b and c). In all cases, the data followed the exponential law (1). Asymptotic self-similarity of the turbulence structure within a major part of the test-section is demonstrated by the parallel growth of all Reynolds stresses. As in previous experiments, the order of magnitudes was

$$\overline{u_1^2} > \overline{u_3^2} > \overline{u_2^2} > -\overline{u_1 u_2}$$

In general, the turbulent intensities presented a nearly stepwise increase across the grid plane. However, grid-generated turbulence decayed rapidly downstream, so that the asymptotic flow development was dominated by turbulent energy production due to shear.

(c) The Turbulent Kinetic Energy

Several measurements of the centreline turbulent kinetic energy are plotted together in Figure 5. All data are compatible with the exponential asymptotic law (1); the unobstructed flow and the M 2.54 cm grid flow correspond to positive exponent coefficients while the M 5.08 cm grid flow seems to have a nearly zero exponent. Another interesting observation is that, for each of the three presented cases, q^2 shows almost universal values at any given downstream position, when normalized with the centreline mean velocity \bar{U}_c . Although the value of \bar{U}_c should not be a factor for determining the asymptotic turbulence structure, it seems to act as a scale for determining turbulent intensity level.

(d) The Dimensionless Reynolds Stress Tensor

In all examined cases, all components of the dimensionless Reynolds stress tensor, K_{ij} , retained constant asymptotic values within significant regions of the test section, as shown typically in Figure 6. Characteristically, in all cases the initial values of K_{11} , K_{22} , K_{33} were closer to each other than the asymptotic ones; furthermore, a reversal of the relative magnitude of K_{22} and K_{33} occurred for the two grid cases. These observations confirm the predictions that the asymptotic tur-

bulence structure depends on the shearing mechanism alone and that all initial condition effects disappear downstream.

(e) The Integral Length Scales

Preliminary measurements of the streamwise velocity fluctuation integral length scale L_M are presented in Figure 7; these scales were determined by integrating the corresponding autocorrelation function up to its first zero. Considering the crudeness of the measurements, it appears that for each type of flow, L_{11} develops independently of the values of the mean shear $d\bar{U}_1/dx_2$ and the centreline velocity \bar{U}_c . The development law of L_{11} depends strongly on the grid mesh size. The available data on L_{11} are compatible with exponential development laws but with exponent coefficients different from those of the corresponding turbulent kinetic energy.

ANALYSIS AND DISCUSSION OF THE RESULTS

The present and earlier experiments span sufficiently wide ranges of mean shear, Reynolds number, dimensionless strain and length scales for a quantitative parametrization of possible universal features of uniformly sheared flow to be attempted. First, we search for a criterion for the attainment of an asymptotic turbulence structure, where self-similarity is exhibited by the constancy of properly normalized quantities. Figure 6 shows that the dimensionless Reynolds stresses remain constant away from flow disturbances in all present experiments; similarly, a careful examination of previous high- and low-shear experiments shows that, in the downstream part of the measuring volumes, these stresses were also constant and always in the order

$$K_{11} > K_{33} > K_{22} > -K_{12}.$$

Any imposed change of the asymptotic values of K_{ij} and/or reversal of the above order (e.g. by the insertion of grids) was eventually overcome by the shearing mechanism and the quasi-universal values of K_{ij} were restored. Average values for all existing experiments, summarized in Table 1, were

$$K_{ij} = \begin{bmatrix} 0.55 & -0.16 & 0 \\ 0.16 & 0.20 & 0 \\ 0 & 0 & 0.25 \end{bmatrix} \quad (4)$$

Our second concern was to establish experimental stability criteria for uniformly sheared flows. The exponential law (1) permits three possibilities for the downstream evolution of the turbulent kinetic energy q^2 , depending on the value of the ratio ϵ/P : exponential growth for $P > \epsilon$, constant value for $P \approx \epsilon$ and exponential decay for $P < \epsilon$; these three cases correspond to positive, zero and negative values of the inverse characteristic length $1/l$. As Table 1 shows, only the first two cases have been observed experimentally, the third one possibly corresponding to extremely weakly-sheared turbulence. An attempt to correlate the values of ϵ/P and $1/l$ with the value of mean shear failed because experiments with the same $d\bar{U}_1/dx_2$ (but differing initial condi-

tions) had widely different values of the above parameters; the same happened when the dimensionless total strain $(x_1/\bar{U}_c) d\bar{U}_1/dx_2$ was used as the independent variable.

At this point we recall that Hasen's (1967) stability analysis predicts a "stability barrier" for the initial disturbance of turbulent kinetic energy that can be expressed as

$$u_b = \frac{L d\bar{U}_1/dx_2}{R^{2/3}} \quad (6)$$

Substituting for the Reynolds number $R = (d\bar{U}_1/dx_2) L^2/\nu$, one gets

$$u_b = \left(\frac{1}{L} \frac{d\bar{U}_1}{dx_2} \right)^{1/3} \nu^{2/3} \quad (7)$$

Figure 8 shows an excellent correlation of the exponential coefficient $1/l$ with u_b . From this figure, it appears that, in flows with $u_b > 4.5$, q^2 grows exponentially, while in flows with $3 < u_b < 4.5$, q^2 reaches a constant asymptotic state. Ongoing research is expected to resolve remaining questions.

ACKNOWLEDGEMENT

Financial support for this project has been provided by the Natural Sciences and Engineering Research Council of Canada, through Operating and Equipment Grants, and by the University of Ottawa Rector's Fund.

REFERENCES

1. Champagne, F.H., Harris, V.G., and Corrsin, S., 1970, "Experiments in Nearly Homogeneous Shear Flow", *J. Fluid Mech.*, **41**, 81.
2. Harris, V.G., Graham, J.A.H., and Corrsin, S., 1977, "Further Experiments in Nearly Homogeneous Turbulent Shear Flow", *J. Fluid Mech.*, **81**, 657.
3. Hasen, E.M., 1966 "A Non-Linear Theory of Turbulence Onset in a Shear Flow", *J. Fluid Mech.*, **29**, 721.
4. Mulhearn, P.J., and Luxton, R.E., 1975, "The Development of Turbulence Structure in a Uniform Shear Flow", *J. Fluid Mech.*, **68**, 577.
5. Rose, W.G., 1966, "Results of an Attempt to Generate a Homogeneous Turbulent Shear Flow", *J. Fluid Mech.*, **25**, 97.
6. Rose, W.G., 1970, "Interaction of Grid Turbulence with a Uniform Mean Shear", *J. Fluid Mech.*, **44**, 767.
7. Tavoularis, S. and Corrsin, S., 1981, "Experiments in Nearly Homogeneous Turbulent Shear Flow with a Uniform Mean Temperature Gradient", *J. Fluid Mech.*, **104**, 311.
8. Tavoularis, S., 1983, "Asymptotic Laws for Transversely Homogeneous Turbulent Shear Flows", submitted for publication.

TABLE 1

	Unobstructed flow			M 2.54 cm grid at $x/h = 4.5$			M 5.08 cm grid at $x/h = 1.04$			Tavoularis & Corrsin	Champagne et al.	Rose	Mulhearn & Luxton	Units
\bar{U}_c	6	9	13	6	9	13	6	9	13	12.4	22.21	15.15	4.5	m s^{-1}
$d\bar{U}_1/dx_2$	43.5	60	84	18.4	28	38.4	13.4	20	29	48	12.9	13.7	5.45	s^{-1}
K_{11}	0.59	0.56	0.55	0.58	0.55	0.53	0.57	0.55	0.52	0.53	0.47	0.50	0.47	—
K_{22}	0.19	0.20	0.20	0.19	0.20	0.20	0.19	0.21	0.22	0.19	0.25	0.22	0.22	—
K_{33}	0.22	0.24	0.25	0.23	0.25	0.27	0.24	0.24	0.26	0.28	0.28	0.28	0.31	—
$-K_{12}$	0.165	0.165	0.165	0.17	0.17	0.17	0.155	0.155	0.155	0.14	0.165	0.16	0.165	—
ϵ	3.02	3.32	3.18	5.75	4.54	4.44	∞	∞	∞	4.36	∞	∞	∞	m
ϵ/P	0.72	0.72	0.71	0.66	0.58	0.55	1	1	1	0.57	1	1	1	—
L_{11} ($x_1/h=11$)	0.044	0.044	0.044	0.046	0.046	0.046	0.10	0.10	0.10	0.053	0.051	0.037	0.0254	m
u_b	6.06	6.74	7.55	4.48	5.16	5.73	3.11	3.56	4.03	5.89	3.85	4.36	3.64	m s^{-1} $\times 10^3$

16:1 contraction

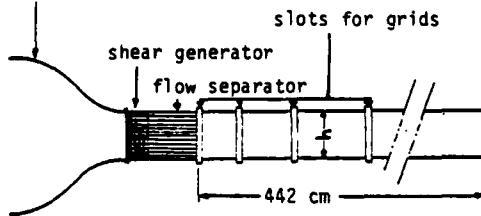


Figure 1. Schematic diagram of the wind tunnel.

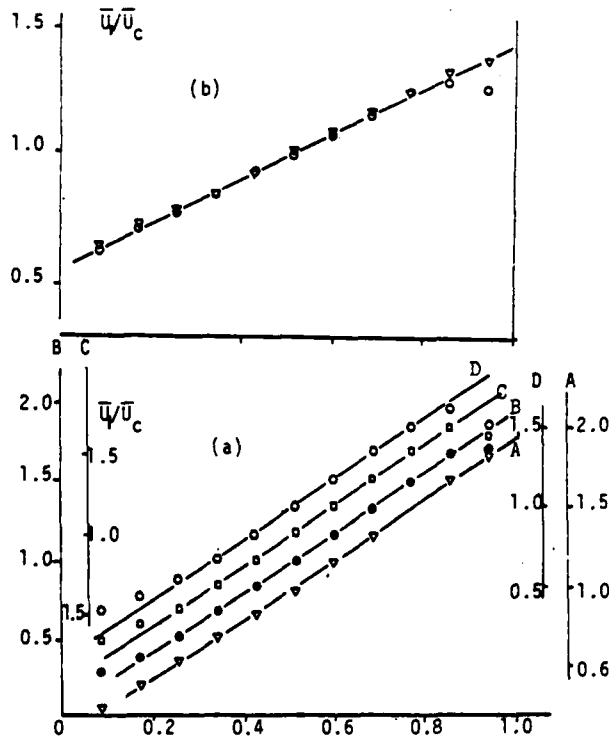


Figure 2. Typical transverse mean velocity profiles.

- (a) $\bar{U}_c = 13 \text{ m/s}$, $d\bar{U}_1/dx_2 = 84 \text{ s}^{-1}$; $x_1/h = 2.0$,
 $\bullet x_1/h = 7.5$, $\square x_1/h = 10.0$, $\diamond x_1/h = 13.0$.
 (b) with M 2.54 cm grid; $\bar{U}_c = 13 \text{ m/s}$,
 $d\bar{U}_1/dx_2 = 38.4 \text{ s}^{-1}$; grid position:
 $\nabla x_g/h = 1.04$, $\circ x_g/h = 4.5$.

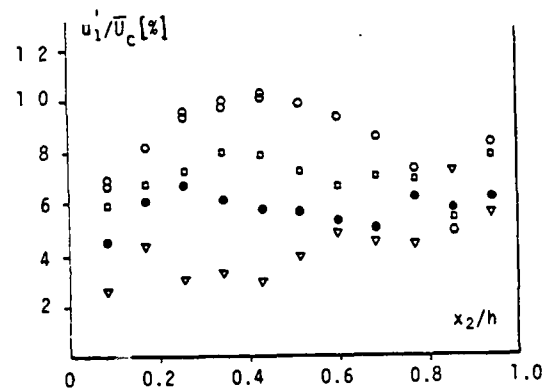


Figure 3. Typical transverse distribution of rms turbulent velocity; flow conditions and symbols as in Figure 2(a).

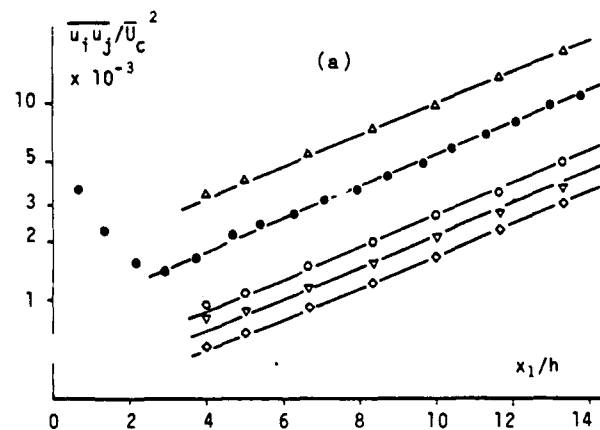


Figure 4. Downstream development of Reynolds stress tensor components; $\Delta q^2/\bar{U}_c^2$, $\bullet \bar{u}_1^2/\bar{U}_c^2$, $\nabla \bar{u}_2^2/\bar{U}_c^2$, $\diamond \bar{u}_3^2/\bar{U}_c^2$, $\square -\bar{u}_1 \bar{u}_2/\bar{U}_c^2$; $\bar{U}_c = 13 \text{ m/s}$,
 (a) $d\bar{U}_1/dx_2 = 84 \text{ s}^{-1}$, (b) $d\bar{U}_1/dx_2 = 38.4 \text{ s}^{-1}$,
 (c) $d\bar{U}_1/dx_2 = 29 \text{ s}^{-1}$.

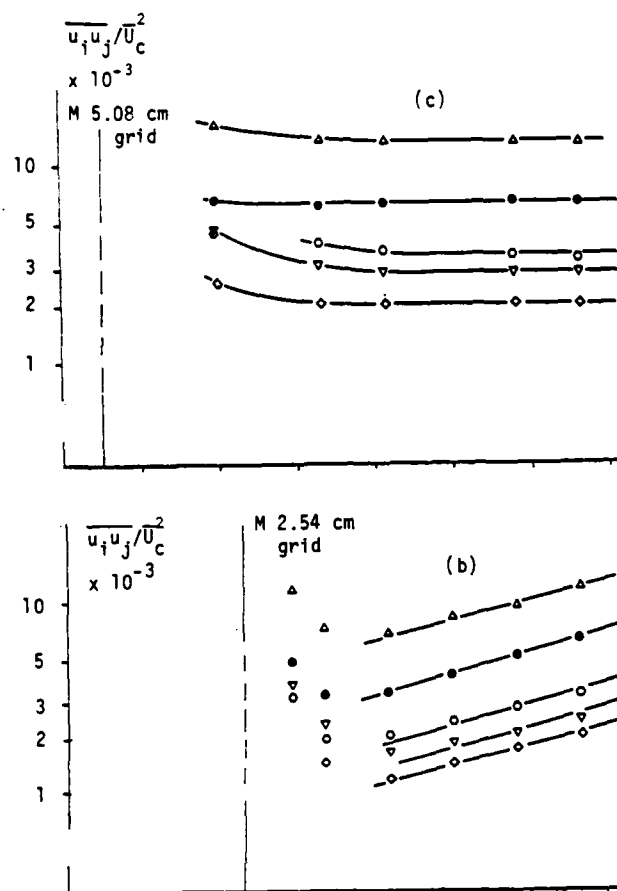


Figure 4. (Continued)

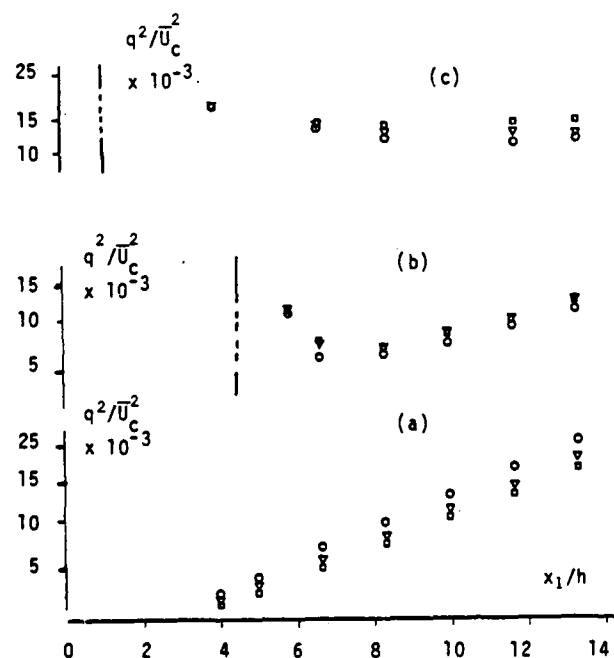


Figure 5. Downstream development of turbulent kinetic energy; $\circ \bar{U}_c = 6$ m/s, $\nabla \bar{U}_c = 9$ m/s, $\square \bar{U}_c = 13$ m/s
(a) unobstructed flow, (b) with M 2.54 cm grid
(c) with M 5.08 cm grid.

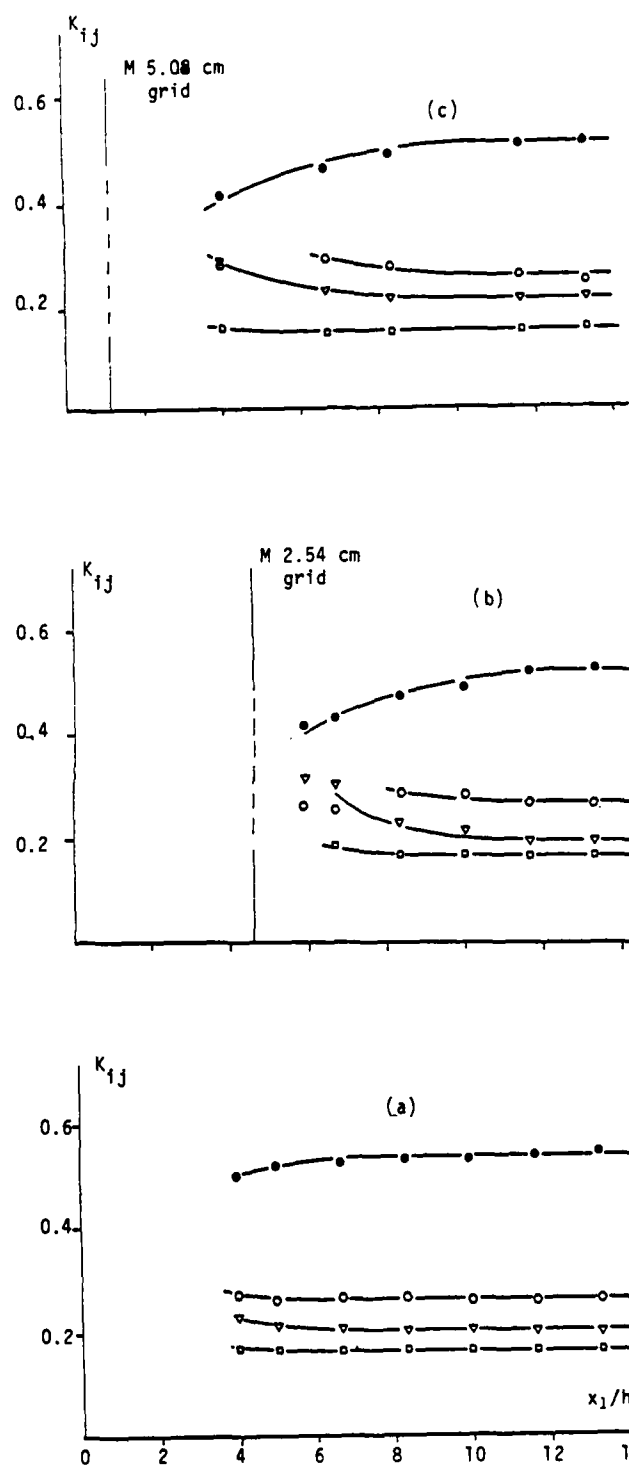


Figure 6. Typical asymptotic development of the dimensionless Reynolds stress tensor components;
 $\bullet K_{11}$, ∇K_{22} , $\diamond K_{33}$, $\square -K_{12}$; $\bar{U}_c = 13$ m/s;
(a) $d\bar{U}_1/dx_2 = 84 \text{ s}^{-1}$; (b) $d\bar{U}_1/dx_2 = 38.4 \text{ s}^{-1}$;
(c) $d\bar{U}_1/dx_2 = 2.9 \text{ s}^{-1}$.

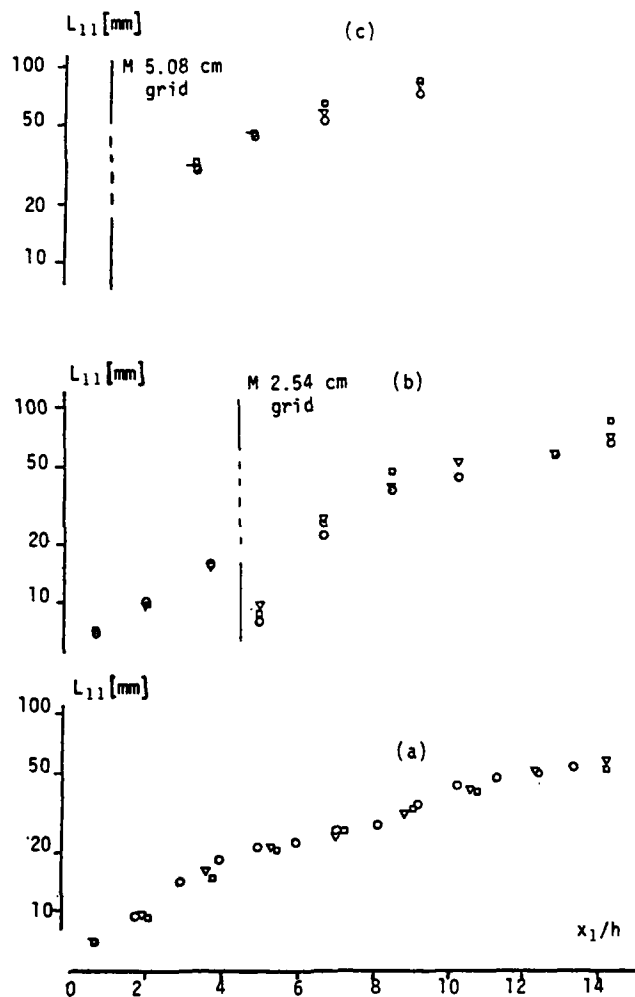


Figure 7. Development of integral length scales;
 $\circ \bar{U}_c = 6$ m/s, $\nabla \bar{U}_c = 9$ m/s, $\square \bar{U}_c = 13$ m/s;
 (a) unobstructed flow, (b) with M 2.54 cm grid,
 (c) with M 5.08 cm grid.

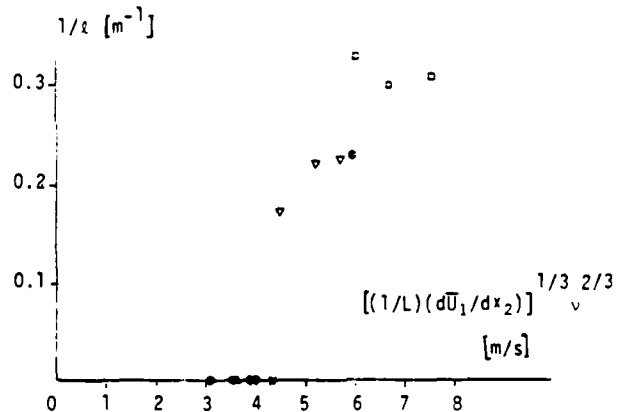


Figure 8. "Barrier velocity" v & exponent for turbulent energy growth; \circ M 5.08 cm grid, ∇ M 2.54 cm grid, \square unobstructed flow, \times Rose, \diamond Champagne et al., \triangle Mulhearn & Luxton, \bullet Tavoularis & Corrsin.

SESSION 15 - EXPERIMENTAL TECHNIQUES

L. Bradbury - Chairman

A COMPUTATIONAL PRESTON TUBE METHOD

W. NITSCHKE, R. THÜNKER, C. HABERLAND
INSTITUT FÜR LUFT- UND RAUMFAHRT, TU-BERLIN (FRG)

ABSTRACT

A computational Preston tube method to determine local wall friction forces is presented, which unlike the conventional Preston tube method offers a greater scope of application. The method is based on measuring the dynamic pressures of two wall-Pitot tubes of different diameters and determining the local wall shear stress by applying a mathematical boundary-layer law to the flow velocities corresponding to the measured dynamic pressures. The method is verified experimentally in a laminar-turbulent transition flow of a flat plate, in a pipe entrance flow, in a turbulent pipe flow with sudden enlargement, in strongly non-adiabatic turbulent boundary-layer flows and in turbulent boundary-layer flows with adverse pressure gradient.

NOMENCLATURE

A^+	Van Driest constant
a	Speed of sound
$c_f = \tau_w / \rho \cdot u_\infty^2$	Skin friction coefficient
c_p	Specific heat
$D, D_{1,2}$	Pipe diameters
$d, d_{1,2}$	Preston tube diameters
$d^+ = u_\tau \cdot d / \nu$	Non-dimens. Preston tube diameter
K	Displacement factor
$K_{1,2,\dots,i}$	Iteration parameters
$M_\tau = u_\tau / a_w$	Friction Mach number
p	Static pressure
$p^+ = (u / \rho \cdot u_\tau^2) \frac{dp}{dx}$	B.-l. pressure parameter
q	Dynamic pressure, $p_{total} - p_{static}$
$q^+ = q d^2 / 4 \rho \cdot \nu^2$	Non-dimens. dynamic pressure
\dot{q}	Heat flux rate
Re	Reynolds number
T	Temperature
u	Mean flow velocity
$u^+ = u / u_\tau$	Non-dimens. mean velocity
$u_\tau = \sqrt{\tau_w / \rho_w}$	Shear stress velocity
x	Longitudinal coordinate
y	Distance from wall
$y^+ = u_\tau \cdot y / \nu$	Non-dimens. distance from wall
$B_q = \dot{q}_w / (\rho \cdot c_p \cdot T) \cdot u_\tau$	B.-l. heat flux parameter
κ	v. Kármán constant
$\lambda = 8 \cdot \tau_w / \rho \cdot u_\infty^2$	Friction factor
λ_w	Thermal conductivity
ρ	Density
τ_w	Wall shear stress
$\tau^+ = \tau_w \cdot d^2 / 4 \cdot \rho \cdot \nu^2$	Non-dimens. wall shear stress
ν	Kinematic viscosity

Subscripts:

D	Diameter
e	Boundary-layer edge
f	Fluid
m	Mean value
w	Wall condition
x	Longitudinal direction
∞	Free stream condition

INTRODUCTION AND PRELIMINARY REMARKS

Local wall friction forces are one of the main quantities of interest in experimental boundary-layer investigations, as the local wall shear stress represents one of the boundary conditions of wall shear layers. Considerable effort has been made to develop dependable methods to measure these wall friction forces. A survey is given by WINTER (1977).

The Preston tube method (PRESTON, 1954) is one of the most widely used shear stress measuring techniques due to its simple construction and practicability. It is based on the similarity law of turbulent boundary-layers

$$u^+ = f(y^+); u^+ = \frac{u}{u_\tau}, y^+ = \frac{u_\tau y}{\nu} \quad (1)$$

This law of the wall is used to the effect that a measured quantity proportional to the velocity (in this case the dynamic pressure of a wall-Pitot tube) can be correlated to the local shear stress at known distance of the measuring point from the wall (y_{eff}). The correlation between the dynamic pressure and the corresponding wall shear stress is usually represented by a calibration curve of the type:

$$q^+ = F(\tau^+); q^+ = \frac{q d^2}{4 \rho \nu^2}, \tau^+ = \frac{\tau_w d^2}{4 \rho \nu^2} \quad (2)$$

The calibration parameters q^+ and τ^+ can be obtained directly from the variables of the law of the wall Eq.(1), when half the diameter of the Preston tube is taken as the characteristic wall distance:

$$q^+ = \frac{1}{2} \left(\frac{u}{u_\tau} \frac{u_\tau d/2}{\nu} \right)^2, \tau^+ = \left(\frac{u_\tau d/2}{\nu} \right)^2 \quad (3)$$

This direct relationship between the calibration parameters and the boundary-layer variables permits the calibration curve according to Eq. (2) to be calculated directly from the wall law (NITSCHKE, 1980), Fig. 1.

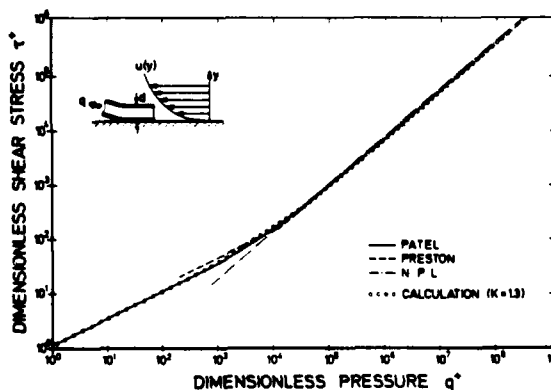


FIG. 1: CONVENTIONAL PRESTON TUBE CALIBRATION CURVE

This calculation was carried out using the appropriate law of the wall of turbulent flat plate flow and fully developed turbulent pipe flow respectively according to VAN DRIEST (1956)

$$u^+ = \int_0^{y^+} \frac{2 dy^+}{1 + [1 + 4(\kappa y^+)^2 (1 - \exp(-y^+/A^*))^2]^{0.5}} \quad (4)$$

$\kappa = 0.4 ; A^+ = 26$

and the simplified relationship for the effective wall distance

$$y_{eff.} = (d/2)K ; K = 1.3. \quad (5)$$

The results compare well with the empirical calibration curves according to PRESTON (1954), PATEL (1965) and the N.P.L. (1961), and hence, this calculation illustrates some essentials of the Preston tube method:

- (1) The Preston tube calibration curve is mainly about the transformation of a boundary-layer similarity law into directly measurable quantities of a wall-Pitot tube. The term 'calibration curve' is justified in so far as the correlation of the dynamic pressure to the effective wall distance of the corresponding velocity is an implicit part of the calibration, whereas the calculation assumes y_{eff} to be known.
- (2) For boundary-layer flows whose law of the wall deviate from the classical case, the calibration curve shown in Fig. 1 no longer holds true and unrestricted use leads to principle measuring errors.
- (3) To determine wall friction forces correctly in such cases (due to the direct relationship between boundary-layer law and the calibration curve), we have to take into account calibration curves that have been modified accordingly. Investigations for some boundary-layer parameters (dimensionless pressure gradient, heat flux, friction Mach number, wall roughness) have been carried out by NITSCH (1980) and HABERLAND/NITSCH (1982).
- (4) Calibration curves cannot be formulated for boundary-layer flows whose similarity law is unknown, and the classical Preston tube method as well as the extensions based on the use of the similarity laws fail.

The correlation of the dynamic pressure to the effective wall distance mentioned in (1) has been simplified according to Eq. (5) in the calculation of Fig. 1. As shown in Fig. 2, a more accurate function of the displacement factor K can be obtained by means of an approximation of the calculated calibration curve to empirical formulas. For the following calculations we use a K -function close to the curve obtained from the PATEL formulas but for $d^+ > 100$ fitted to the experimental results of Mc MILLAN (1956).

The principle measuring errors mentioned in (2) using the classical calibration curve in boundary-layer

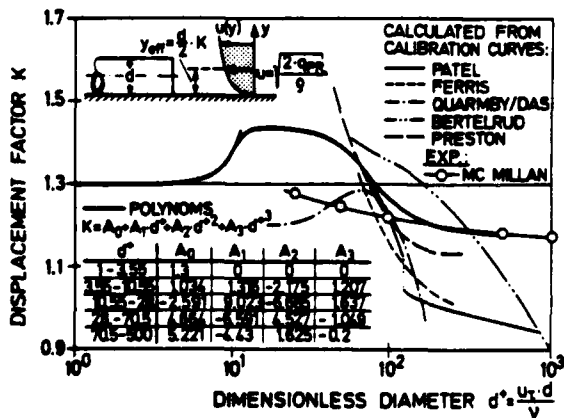


FIG. 2: DISPLACEMENT FACTOR DEPENDENT ON NON-DIMENSIONAL DIAMETER

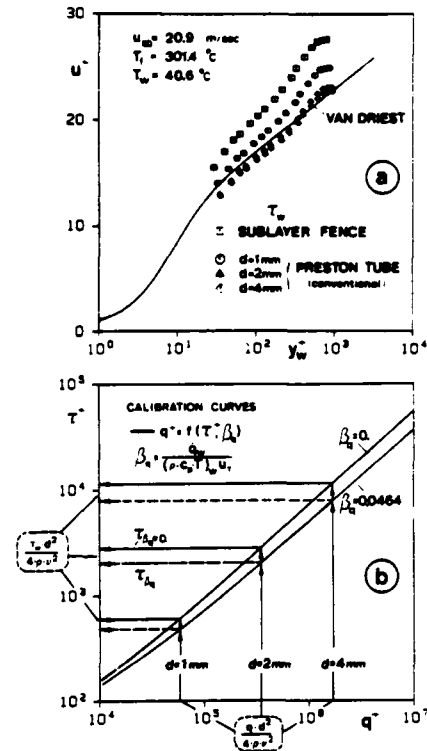


FIG. 3: MEASURING ERRORS IN NON-ADIABATIC FLOWS
(a): LAW OF THE WALL (b): CALIBRATION CURVES

flows, whose law of the wall deviate significantly from Eq. (4), is exemplified in Fig. 3. To represent the measured boundary-layer profile of a strongly non-adiabatic turbulent flow (heat flux rate $q_w \approx 2000 \text{ W/m}^2$) in law of the wall coordinates, the wall shear stresses resulting from the classical calibration curve for three Preston tubes of different diameters were used. As shown in Fig. 3a, increasing probe diameter causes growing deviation in the measurement as compared to that obtained from a sublayer fence. This effect is explicable from Fig. 3b, which shows the calibration curve for this flow type, calculated from the law of the wall of non-adiabatic turbulent flows given by NITSCH, THÜNKER, HABERLAND (1983), compared to the classical calibration curve. Increases in dimensionless pressure due to larger probe diameters lead to increasing measuring errors when using the classical calibration curve and to considerable deviations when the boundary-layer is represented in law of wall coordinates, Fig. 3a.

The need to consider modified calibration curves for changed wall laws, as mentioned in (3), is evident from Fig. 3. A further example is depicted in Fig. 4, which shows the calculated calibration curves for compressible flows given by HABERLAND/NITSCH (1982) as compared with the experimental results of ALLEN (1973) and the empirical set of calibration curves according to BRADSHAW/UNSWORTH (1973) based on these measurements.

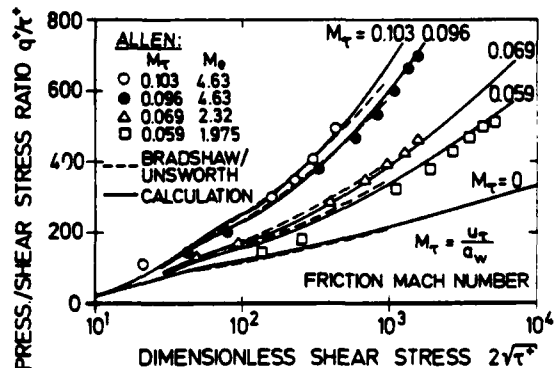


FIG. 4: CALIBRATION CURVES FOR COMPRESSIBLE FLOWS

This extended Preston tube method based on physical boundary-layer similarity laws, offers additional possibilities in terms of applications. However, since we cannot assume the boundary-layer laws to be known as a matter of principle for all flow types, general validity has to be ruled out. In addition, there are hardly any promising formulations available which describe the boundary-layer for many flows by means of similarity laws. Thus, the demand for a more generally valid Preston tube method necessarily requires the separation of the method from physical boundary-layer laws in order to overcome the restrictions they always involve.

COMPUTATIONAL PRESTON TUBE METHOD

As has been mentioned in the introduction, the conventional Preston tube method as well as its extensions are based on the unambiguous correlation of a velocity, corresponding to the measured dynamic pressure, to a characteristic wall distance and the wall shear stress determination via a boundary-layer similarity law. The unambiguity of this correlation is expressed by the fact that the diameter of the probe can be chosen freely within the range of validity of the assumed boundary-layer law, i.e. identical wall shear stresses are measured using probes of different diameters. The unambiguity of the measured shear stress has naturally to play a very important part in extending the Preston tube method to boundary-layer flows with unknown wall law: The former method fails due to the assumption of a non-appropriate law of the wall, as can be recognized by different wall shear stresses obtained from probes of different diameters. To a certain extent, the reversal of this fact allows correct measuring values to be expected for an unknown wall law, if we succeed in formulating a boundary-layer law which yields identical wall shear stresses when applied to dynamic pressures of Preston tubes of different diameters.

Basic Method

As shown in Fig. 1, the conventional Preston tube calibration curve can be computed by numerical integration of the wall law, Eq. (4), taking into account a relationship for the effective wall distance. In practical application of this calibration curve, the paired values q^+ and t^+ can be interpolated, however, it is more convenient to apply the numerical calculation method by an iteration process to the measured dynamic Preston tube pressure. Fig. 5 illustrates this procedure: In the first step, ($i=1$) the boundary-layer profile for a given initial wall shear stress value is calculated with the aid of the wall law up to the effective wall distance (obtained from the Preston tube diameter and the displacement function in Fig. 2).

Since the velocity u_1 calculated at y_{eff} does not satisfy the velocity corresponding to the measured dynamic pressure, the wall shear stress in the boundary-layer computation is varied iteratively, until the calculation matches the measured velocity. The local wall friction thus determined is equivalent to the τ_w -value obtained from the conventional calibration curve, Fig. 1, and this computer aided measuring technique can thus completely

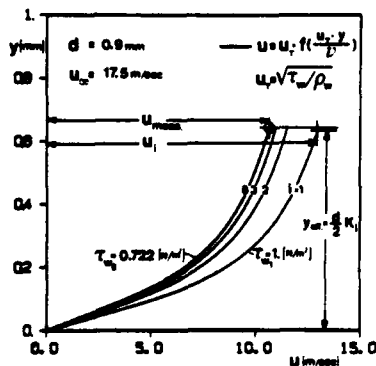


FIG. 5: BOUNDARY-LAYER ITERATION IN THE BASIC METHOD

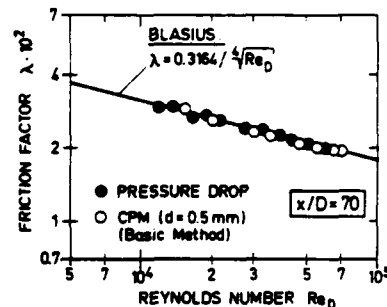


FIG. 6: FRICTION FACTORS OF FULLY DEVELOPED TURBULENT PIPE FLOW. CPM AND PRESSURE DROP DATA

replace the classical Preston tube method. Fig. 6 illustrates this with a comparison between the measured friction factors of a fully developed turbulent pipe flow, which were determined with the aid of this computational method and by means of pressure drop measurements respectively.

Extension To Boundary-Layers With Unknown Law Of The Wall

As a consequence of the assumed wall law, the computational Preston tube method in its basic version is certainly subjected to the same restrictions as the conventional method. However, it may be used in boundary-layers with known parameters of influence, for example in the case of non-adiabatic turbulent flows as shown in Fig. 3, through analogous application of appropriate wall laws.

However, even this method has to fail in measuring the wall friction for unknown wall law, as the necessary unambiguous correlation of measured dynamic pressures to the wall law can no longer be formulated. The intended extension thus requires the introduction of the unambiguity of the resulting measured value of τ_w as an additional criteria. The basic method described above can remain the starting point, it is, however, applied to the measured dynamic pressures of two Preston tubes of different diameters unlike the simple method based on the measured dynamic pressure of a single Preston tube. In case the resulting wall shear stresses do not coincide, the need for a wall law arises which - even when only mathematically formulated - will yield identical wall shear stresses for both measured dynamic pressures.

In order to achieve a great scope of application, the law of the wall used here necessarily has to permit extensive variations without yet violating fundamental principles of the boundary-layer theory, especially the boundary condition at the wall. Hence, it is convenient to base this formal law on that of turbulent boundary-layer flows, Eq. (4). By including the extension for near-separation boundary-layer flows, as proposed by SZABLEWSKI (1969), Eq. (4) can be formulated as a wall law with three free parameters

$$u^+ = \int_0^{y^+} \frac{2(1 + K_3 y^+)}{1 + [1 + 4(K_1 y^+)^2 (1 + K_3 y^+) (1 - \exp(-y^+ \sqrt{1 + K_3 y^+ / K_2}))^2]^{0.5}} dy^+ \quad (6)$$

with K_1 formally corresponding to the v .Kármán constant, K_2 to the Van Driest constant A^+ and K_3 to the dimensionless pressure parameter p^+ . For $K_1=0.4$, $K_2=26$, and $K_3=0$, this wall law is identical to Eq. (4).

Fig. 7 shows a parametric representation of Eq. (6) and illustrates the influence of the free parameters as well as the range of application of this wall law.

The flow chart shown in Fig. 8 illustrates the practical application of the computational Preston tube method based on this mathematical wall law. Initially, both wall shear stresses resulting from the classical law of the wall ($K_1=0.4$, $K_2=26$, $K_3=0$) are calculated from the measured dynamic pressures of the two probes. This first step is identical to the basic method, Fig. 5. In case the two resulting wall shear stresses do not coincide, the parameters K_i in the mathematical wall law are gradually varied by means of an trial-and-error iteration so that the difference between τ_{w1} and τ_{w2} decreases and

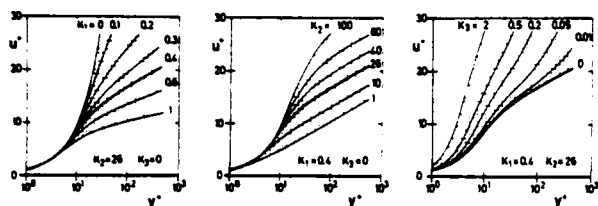


FIG. 7: BOUNDARY-LAYER MODEL USED IN THE CPM

vanishes in the last iteration step. Figs. 9a and 9b are examples illustrating this iteration using a K_1 -variation for measuring the skin friction in a laminar-turbulent transition flow of a flat plate. The basic method ($K_1=0.4$) yields a lower shear stress for the smaller Preston tube than for the larger one ($\tau_{w1}=0.238$, $\tau_{w2}=0.287$ N/m²), Fig. 9b. This becomes likewise clear from the first boundary-layer calculations, Fig. 9a, which show a larger velocity gradient at the wall for the measuring point 2.

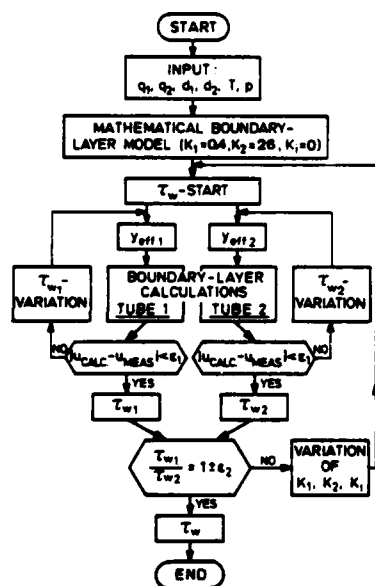


FIG. 8: CPM FLOW CHART

The first step of the main iteration loop ($i=1$, $K_1=0.45$) is used to determine the potential direction of the iteration procedure by comparing the resulting wall shear stresses with the basic values ($i=0$). In the following iteration steps the value of K_1 which yields identical wall shear stresses for both probes is determined iteratively ($K_1=0.156$, $\tau_{w1,2}=0.171 \text{ N/m}^2$), Fig. 9b. The convergence of the two wall shear stresses through the iteration process can as well be recognized from the respective boundary-layer profiles, Fig. 9a, which converge progressively and collapse on one another for $K_1=0.156$.

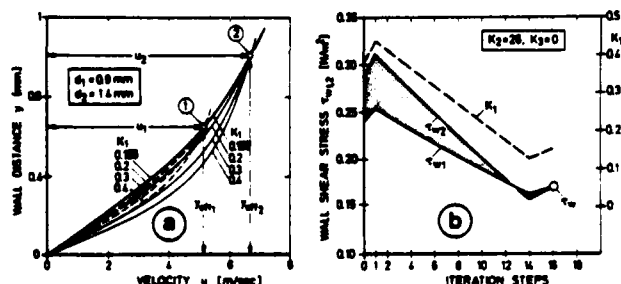


FIG. 9: BOUNDARY-LAYER ITERATION IN THE CPM

EXPERIMENTAL FACILITIES

In order to verify the computational Preston tube method, experimental set-ups were planned which could be expected to show considerable deviations in the boundary-layer laws from the classical cases of a turbulent flat plate and fully developed turbulent pipe flow. The first facility, the ILR-Thermo Wind Tunnel, is shown in Fig. 10. This tunnel consists of two separate circuits for hot and cold air with infinitely variable flow velocity and temperature, Fig. 10a. The upper test section wall, Fig. 10b, could be inclined with respect to the tunnel axis to achieve a positive pressure gradient, as well as heated or cooled with water to produce a positive or negative heat flux in the boundary-layer. Furthermore, the trip wire in the inlet nozzle could be removed, to obtain a laminar-turbulent transition flow. The probe arrangements at the test section wall are shown in the details of A_1 and A_2 : Skin friction measuring probes to be used as reference measuring devices were mounted in the wall close to the tip of the Preston tubes (A_1 : Surface hot film probe and thermocouples to control wall and probe support temperatures in order to avoid measuring errors caused by temperature effects (NITSCHKE, HABERLAND, 1983), A_2 : Sub-layer fence and thermocouples in the tunnel wall to determine the heat flux rate and the reference temperature to calculate the velocity from the dynamic pressure). The static pressure distribution was measured by pressure taps along the tunnel axis, the dynamic pressure of the Preston tubes determined by the total pressure of the probe and the static pressure obtained from a pressure tap at least ten probe diameters across the probe tip.

The test pipe shown in Fig. 11 was used as the second experimental set-up, whose probe arrangement was basically the same used in the Thermo Wind Tunnel.

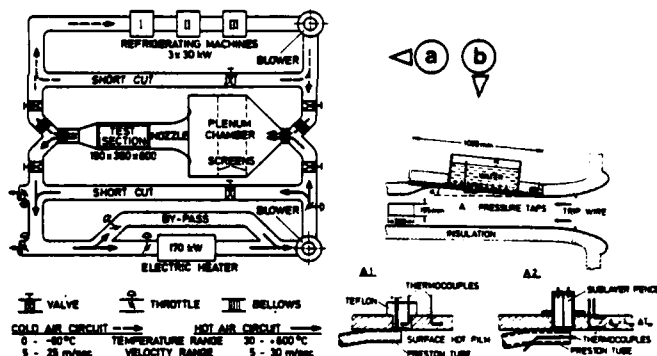


FIG. 10: THERMO WIND TUNNEL AND EXPERIMENTAL ARRANGEMENTS

The measuring station of the 50 mm test pipe, detail A₁, could be shifted towards the inlet nozzle up to $x/D=5$ for experiments in the inlet region. In addition, a measuring station in a 80 mm pipe could be coupled at the outlet side of the 50 mm pipe, detail A₂, enabling tests in a pipe flow with sudden enlargement.

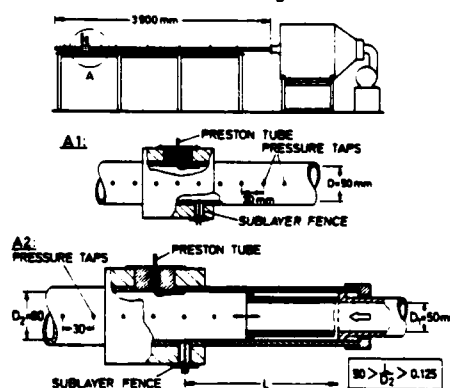


FIG. 11: TEST PIPE AND EXPERIMENTAL ARRANGEMENTS

ILR: Institut für Luft- und Raumfahrt (Department of Aero-
nautics and Astronautics) at Berlin Technical Univers.

RESULTS

Preliminary tests were first conducted on both the test facilities, in order to calibrate the reference measuring devices. Fig. 12a shows the skin friction coefficients measured in the Thermo Wind Tunnel (adiabatic turbulent flow, constant pressure) and Fig. 12a^{*} the measured friction factors in the 50 mm pipe at $x/D=70$. Independent of the measuring technique and of the used Preston tube diameters, good agreement between the data and the respective theoretical friction laws can be stated.

The results of the skin friction measurements conducted for varied test conditions are also summarized in Fig. 12. The Figs. 12b and c show the results obtained in the test pipe (b: Entrance flow, c: Sudden enlargement), the Figs. 12d-f the measurements carried out in the Thermo Wind Tunnel (d: Laminar-turbulent transition, removed trip wire, e: Adverse pressure gradient, inclined plate, f: Strong heating and cooling, $-46^{\circ}\text{C} < T_{\text{fluid}} < +300^{\circ}\text{C}$, $+20^{\circ}\text{C} < T_{\text{wall}} < +40^{\circ}\text{C}$). The respective upper diagrams include the data obtained from the reference measuring devices and from the conventional Preston tube method and indicate the breakdown of this method, illustrated by deviating

data obtained with different probe diameters. In contrast, the results of the computational Preston tube method in the respective lower diagrams are in good agreement with the sublayer fence and surface hot film data and give an impression of the wide range of application of this measuring technique.

In these investigations, the sublayer fence readings were corrected with respect to the local pressure gradient (if necessary) according to PATEL (1965), and the influence of changed temperatures (Fig. 12f) on the sublayer fence calibration curve was compensated by treating the fence formally like a very small Preston tube, i.e. all the properties in the calibration formula were taken at wall temperature, except for the density in the dimensionless pressure, which was taken at a reference temperature at half the height of the fence.

The measurements of negative shear stresses close to the backward facing step of the pipe ($x/D_2 < 2$), Fig. 12c, became possible by calibrating the fence in the forward and backward mode (turning of the pipe).

The CPM-results shown in Figs. 12b^{*}-d^{*} were obtained with a twin-probe, Fig. 13, the results in Figs. 12e^{*} and f^{*} with two single probes of different diameter.

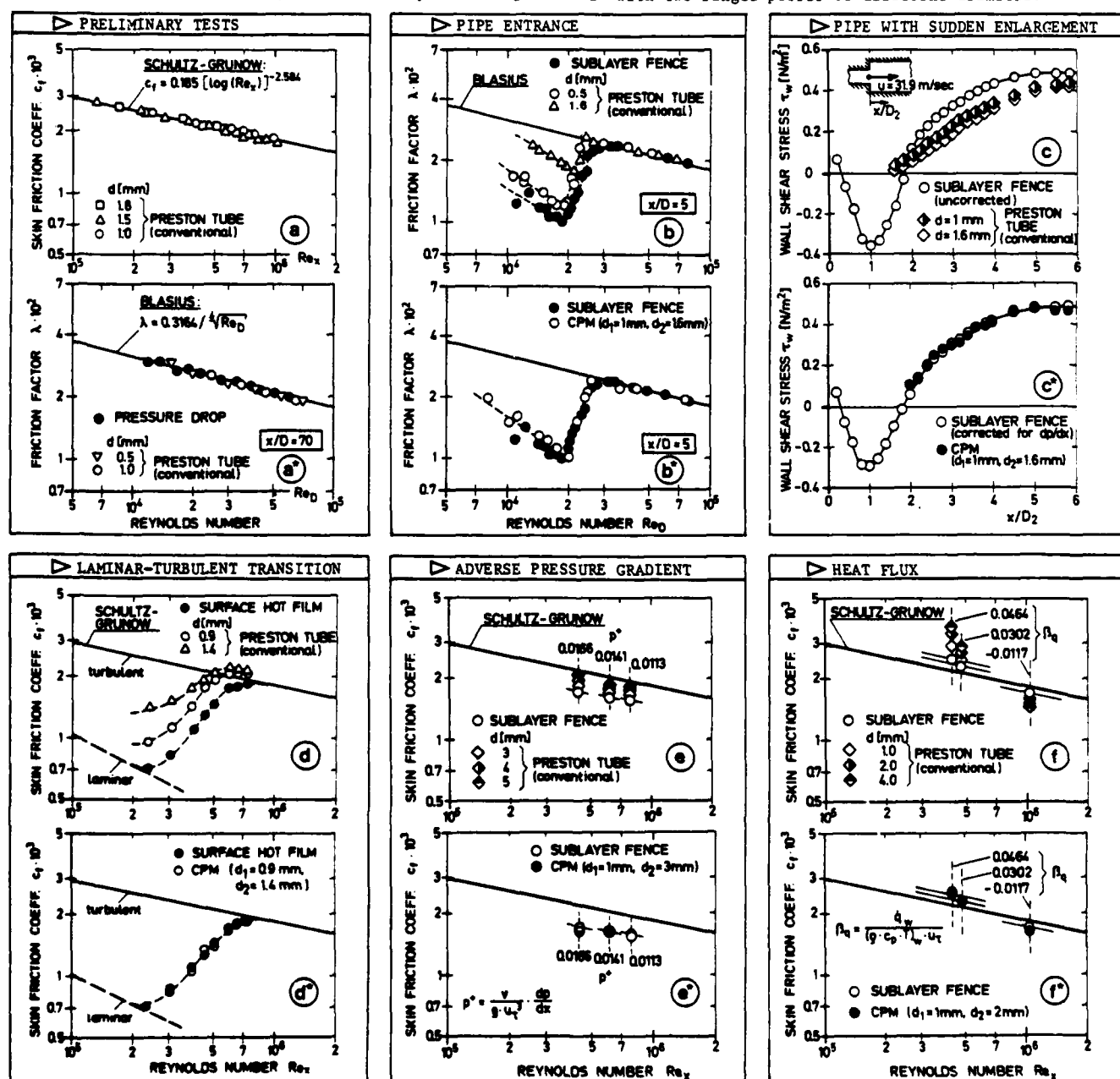
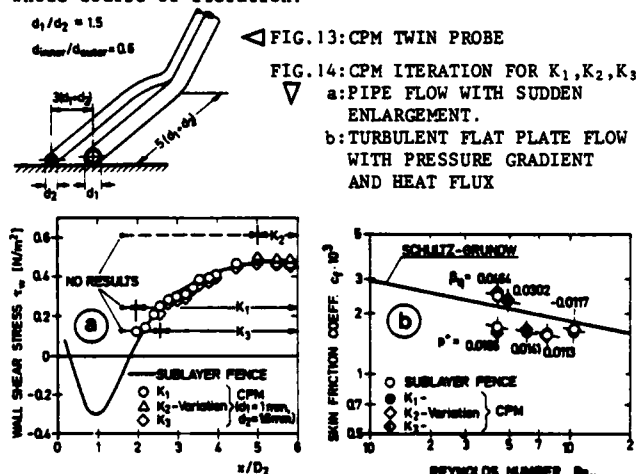


FIG. 12: SKIN FRICTION MEASUREMENTS AT VARIOUS TEST CONDITIONS. a and a^{*}: PRELIMINARY TEST RESULTS FOR TURBULENT FLAT PLATE AND FULLY DEVELOPED TURBULENT PIPE FLOW. b - f: CONVENTIONAL PRESTON TUBE METHOD COMPARED WITH REFERENCE MEASURING TECHNIQUES. b^{*}-f^{*}: COMPUTATIONAL PRESTON TUBE METHOD COMPARED WITH REFERENCE MEASURING TECHNIQUES

DISCUSSION AND CONCLUDING REMARKS

All the results of the computational Preston tube method shown in Fig. 12 were obtained by means of an K_1 -iteration without any exception. Certainly the question arises about the results we would obtain using the parameters K_2 and K_3 . Particularly, the unambiguousness of the measured wall shear stress had to be investigated. For that purpose, comparative computations using the K_1 , K_2 and K_3 parameters have been carried out. The results of the pipe flow with sudden enlargement, Fig. 14a, clearly indicate that for this flow type, the K_1 parameter is the most useful one and renders possible shear stress determinations up to the reattachment point. Closer than $x/D_2=2$ to the step, we obtain no results, since the mathematical wall law, Eq. (6), does not include recirculating effects. The variation parameters K_2 and K_3 are not as useful as K_1 , particularly the K_2 -variation yields only results for $x/D_2 > 5$. However, the main conclusion of these comparative computations is the fact that an unsuitable iteration parameter does not yield irregular wall shear stresses but no results at all. This is obvious from an K_1 and K_2 iteration for the measured dynamic pressures at $x/D_2=2.6$, shown in Fig. 15. Whereas the K_1 iteration yields coinciding wall shear stresses in the course of the computations, the K_2 iteration leads to no result, indicated by the convergence of the resulting wall shear stresses in the beginning of the iteration process but divergence for $K_2 < 20$ without matching in the whole course of iteration.



In case of successful iterations, the resulting shear stresses obtained with the particular iteration parameters do not agree exactly, but the differences are acceptable for wall shear stress measurements, Fig. 14a and b.

The error sensitivity of this method due to measuring errors in dynamic pressures is shown in Fig. 16. Errors of $\pm 1\%$, especially when occurring with change in sign, cause deviations in the resulting wall shear stress of 5% ($< 2\%$ when occurring in the same direction, detail of Fig. 16). To avoid these measuring errors to a large extent, the use of the twin probe shown in Fig. 13 is recommended, which allows both dynamic pressures to be measured simultaneously. Furthermore, the probe diameters should be small and not thicker than 20% of the boundary-layer, as the mathematical wall laws used in the CPM are valid only in the near wall region. In addition, the

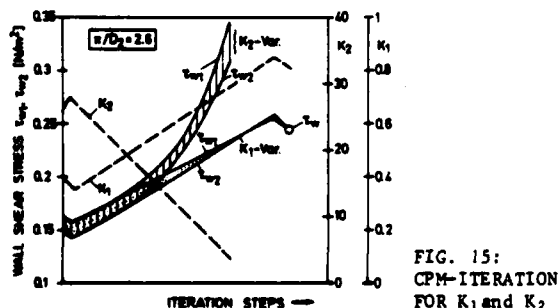


FIG. 15:
CPM-ITERATION
FOR K_1 and K_2

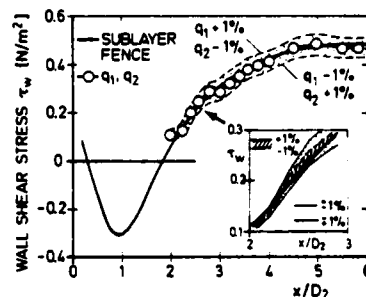


FIG. 16:
ERROR SENSITIVITY
DUE TO MEASURING
ERRORS IN DYNAMIC
PRESSURES

probe diameter ratio should be $d_1/d_2 \approx 1.5$, in order to get significant differences in the basic shear stresses.

Concluded, the results obtained from the computational Preston tube method are very encouraging and offer hope for skin friction measurements in arbitrary boundary-layer flows. Future efforts will concentrate on further extensions, for example the introduction of additional iteration parameters, which might be necessary for other flow types than the ones investigated here. Furthermore, a third Preston tube could be added to the iteration procedure in order to improve the measuring accuracy, especially to decrease the sensitivity due to measuring errors in dynamic pressures by considering the least mean squares between the computed and measured velocities.

ACKNOWLEDGEMENT

The authors are grateful to W. Pflingst, A. Schmiderer and N. Weiser for their assistance in carrying out the tests, to R. Suprayan and M. Prochnow for their help in preparing this paper. The research is supported by the German Science Foundation (DFG).

BIBLIOGRAPHY

- Allen, J.M., 1973, "Evaluation of Compressible Flow Preston Tube Calibration", NASA TN D-7190
- Bradshaw, P., Unsworth, K., 1973, "A Note on Preston Tube Calibrations in Compressible Flow", I.C. Aero Report 73-07
- Haberland, C., Nitsche, W., 1982, "Wall Shear Stress Determination in Boundary-Layers with Unknown Law of the Wall by a Modified Preston Tube Method", ICAS Paper 82-6.4.2 Proc. of the 13th ICAS/AIAA Conf., Vol. 1, 769.
- McMillan, F.A., 1956, "Experiments on Pitot Tubes in Shear Flow", ARC R&M 3028
- Nitsche, W., 1980, "Wandschubspannungsmessung mit Prestonrohren in Grenzschichtströmungen mit zusätzlichen Einflußparametern", Z. Flugwiss. Weltraumforsch. 4, Heft 3, 142. Transl.: "Measuring Skin Friction with Preston Tubes in Boundary-Layer Flows with Additional Parameters", Nat. Res. Coun. Canada, NRC/CNR TT-1989
- Nitsche, W., Thünker, R., Haberland, C., 1983, "Heat Transfer and Boundary-Layer Laws in Strongly Non-Adiabatic Turbulent Flows", 3rd Intern. Conf. on Numerical Methods in Thermal Problems, Seattle, USA
- Nitsche, W., Haberland, C., 1983, "Wall Shear Stress Measurements by Means of Surface Hot Film Probes with Respect to Temperature Effects", Transducer Technology: Development and Application (Sensor 83), Vol. 1, 42.
- Staff of Aerodynamics Division N.P.L., 1961, "On the Measurement of Local Surface Friction on a Flat Plate by Means of Preston Tubes", ARC R&M 3185
- Patel, V.C., 1965, "Calibration of the Preston Tube and Limitations on its Use in Pressure Gradients", J. Fluid Mech., 23, 185.
- Preston, J.H., 1954, "The Determination of Turbulent Skin Friction by Means of Pitot Tubes", J. Roy. Aeron. Soc., 58, 109.
- Szablewski, W., 1969, "Turbulente Grenzschichten in Ablösungen", Z. Angew. Math. Mech., 49, 215.
- Van Driest, E.R., 1956, "On Turbulent Flow Near a Wall", J. Aerospace Sci., 23, 1007.
- Winter, K.G., 1977, "An Outline of the Techniques Available for the Measurement of Skin Friction in Turbulent Boundary-Layers", Prog. Aerospace Sci., 18, 1.

MEASUREMENTS OF THE WALL SHEAR STRESS IN BOUNDARY-LAYER FLOWS

M. Acharya and M.P. Escudier
Brown Boveri Research Center
CH-5405 Baden, Switzerland

ABSTRACT

It is argued that a direct measurement of the wall shear stress is important in all but the simplest of boundary-layer flow situations. Wall shear stress data obtained with a floating element device are presented for a fully developed turbulent boundary layer on a rough (cast) surface, and for boundary layer transition on a smooth wall. Comparisons of the data with estimates of the wall shear stress obtained from indirect techniques in common use show considerable differences.

INTRODUCTION

An accurate measure of the wall shear stress τ is essential to the proper understanding of the behaviour of any boundary-layer flow. The techniques generally used to determine τ may be classified into three categories: momentum methods, wall similarity techniques and direct measurements. A description of these different approaches and their limitations so far as turbulent boundary layers are concerned is contained in articles by Brown and Joubert (1969) and Winter (1977).

The present paper underlines the importance of a means for the direct determination of the wall shear stress in all but the simplest of boundary-layer flow situations. Similarity techniques are all based on the existence of a region adjacent to the surface where a universal law of the wall $u/u_* = f(y/v)$ is assumed to exist, and are practically limited to turbulent boundary layers on smooth surfaces. The limitations of momentum integral methods to obtain the wall shear stress are well known, especially in rapidly developing flows and in the presence of pressure gradients. Even for nominally two-dimensional zero-pressure-gradient boundary layers, an extremely small change in flow cross-section suffices to introduce significant errors into the deduced skin friction.

In view of these limitations, questions are frequently raised about the validity and accuracy of skin friction data obtained using such techniques in 'non-standard' boundary layers such as those undergoing transition, or flows with wall roughness, pressure gradients, or three-dimensional effects. Efforts are being made to use laser anemometry for the measurement of the mean velocity gradient close to the wall (Mazumder et al. (1981), Reynolds (1983)) which could provide a useful alternative to obtain the wall shear stress for flow over smooth surfaces. However, at present, the direct measurement of wall shear stress using a floating element device is the only viable possibility in most instances, even though the use of such devices in the presence of pressure gradients is beset with difficulties.

In the following, measurements of the wall shear stress made using a floating element device are presented for two different situations: a fully developed turbulent boundary layer on a rough (cast) surface, and a boundary layer undergoing laminar-to-turbulent transition on a smooth wall. In both cases the flow is incompressible, with a low external turbulence level and zero pressure gradient. The data are examined and discussed in the context of currently accepted ideas about such flows.

FACILITY AND INSTRUMENTATION

Wind Tunnel

The experiments were conducted in an open-circuit low-speed boundary-layer tunnel of a design similar to that of Bradshaw (1972). An aerofoil-type centrifugal blower is followed by a straight-sided wide-angle diffuser leading to a settling chamber with nominal dimensions of 800x800 mm. A honeycomb and screens are installed in the settling chamber which is followed by an 8:1 two-dimensional contraction leading into the working section. This entire flow-conditioning section is mounted on a frame so as to be moveable as a unit. The 3 m-long test section has an entry cross-section of 800x100 mm and is mounted on an independent frame. The upper wall of the test section is the working wall on which the boundary layer of interest develops; the lower flexible wall may be adjusted to generate the desired streamwise pressure gradient. The test section and contraction may be bolted together directly or, for transition experiments, a boundary-layer bleed device may be inserted in between to obtain a laminar boundary layer with a well defined origin. Maximum airspeed for zero pressure gradient is about 45 m/s. A feedback control circuit regulates the blower speed to maintain the static pressure difference across the contraction (i.e., essentially the dynamic pressure at the contraction outlet) at a desired value. Different test plates with the desired surface characteristics may be installed. Each plate carries a series of 90 mm access ports with interchangeable plugs, so as to enable access to the boundary layer with a floating element device or probe traverse.

Instrumentation

With the exception of the floating element device, all instrumentation used is standard and will not be described here. Data acquisition is accomplished through a custom-built interface to a PDP 11/04 minicomputer. The system enables simultaneous acquisition of 8 channels of data, with a maximum data rate of 500 kHz for single-channel operation. Up to four channels of data can be pre-conditioned (biased and amplified) to make

best use of the ± 10 V (10 bit resolution) dynamic range of the ADC. Boundary layer profiles are measured under computer control and the data either processed on-line or stored for subsequent processing. Floating element data are individually recorded, with the element being checked for proper operation at each measurement.

Floating Element

The floating element, shown schematically in Figure 1, is of the nulling type, with a range of 1000 μ N, and a resolution of 1 μ N. The central component, which acts as a balance, is the movement of a precision galvanometer which supports the element itself, a disc of 20 mm diameter. The movement is carried on an assembly of five aluminium slabs. Nine differential screws, each with a movement of 50 μ m/turn, permit accurate positioning of the element in the surrounding baseplate. The position of the black-white interface on a target mounted on the back of the element is detected by a fibre-optic scanner with a spatial definition of 0.25 μ m.

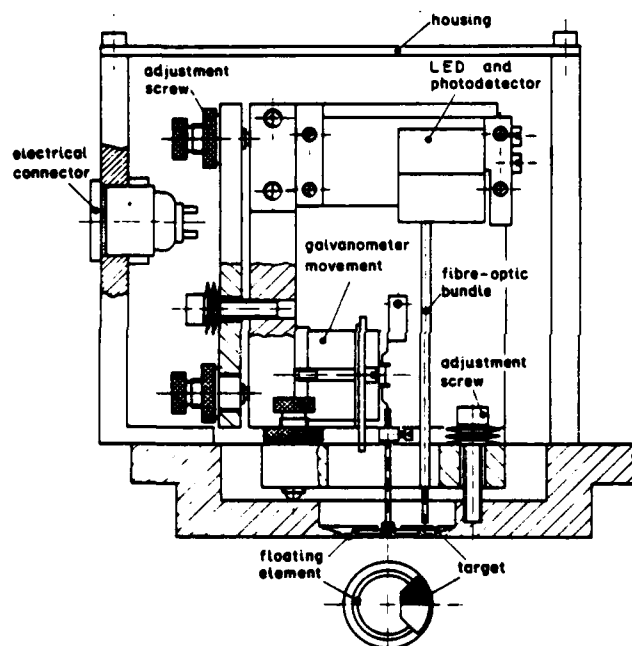


FIGURE 1 SCHEMATIC DRAWING OF FLOATING ELEMENT.

The galvanometer coil system and optical position detector operate in a feedback control loop. A force applied to the element moves it away from its null position. The resulting output of the position detector is amplified and integrated to produce a current through the coil which imposes a counteracting torque to drive the element back towards its null position. A proportional-integral-differential (PID) controller is used to ensure high accuracy and good transient behaviour. The coil current is directly proportional to the imposed force. A digital readout indicates the value of this force directly in micronewtons. The basic calibration of the instrument is against a precision (0.1 %) 100 mg weight hung from the face of the element with the coil axis and the arm supporting the element in a horizontal plane.

The entire floating-element mechanism is enclosed in a sealed housing and, during operation, the pressure difference across the element maintained close to zero.

Extensive tests were conducted to establish the limits of accuracy and reliability of the device in flows with and without pressure gradients. A detailed description of these tests, especially the behaviour of the element in the presence of pressure gradients will be presented elsewhere. For present purposes it suffices to say that in both laminar and fully developed turbulent boundary layers on smooth walls with zero pressure gradient, measurements with the floating element were in agreement with expected values to better than 5 % (see Figure 7).

THE ROUGH SURFACE BOUNDARY LAYER

There have been many investigations of the influence of surface roughness on the turbulent boundary layer. A large number of these have dealt with regular roughness geometries which, while giving some insight into the problem of roughness characterisation, are not of direct practical interest.

The measurements on a cast aluminium surface described here are part of a project aimed at examining rough surfaces with microgeometries similar to those encountered in engineering practice, as produced by various manufacturing and finishing processes. The microgeometry of such a surface may be characterised by a set of statistical quantities including, for example, the arithmetic average roughness, the distribution and autocorrelation of the surface height and the surface slope angle distribution. One of the aims is to establish which quantities are the most relevant and the minimum number which yield an acceptable description. Another aim is to determine if a correlation can be found between the skin friction developed on a rough surface and such statistical descriptors for the surface.

The zero-pressure-gradient boundary layer over the cast surface has been documented in detail, including measurements of the mean velocity, turbulence intensity and Reynolds shear stress profiles. The wall shear stress was measured using a floating element. The data were examined to investigate the feasibility of deriving the wall shear stress from a fit to the measured mean velocity distribution within the boundary layer.

In most investigations of turbulent boundary layers over rough walls that have been reported in the literature, the mean velocity profile has been represented following Perry and Joubert (1963) as a combination of the profile forms proposed by Clauser (1954) and Coles (1956):

$$\frac{u}{u_\tau} = \frac{1}{\kappa} \ln\left(\frac{yu_\tau}{\nu}\right) + B - \frac{\Delta u}{u_\tau} + \frac{\Pi}{\kappa} [y/\delta] \quad (1)$$

Here u is the mean velocity, y the normal distance from the aerodynamic origin (i.e., where u effectively goes to zero), ν is the kinematic viscosity of the fluid, κ and B are universal constants with values of 0.41 and 5.0 respectively, and u_τ is the friction velocity ($\equiv \tau_w/\rho$), τ_w being the wall shear stress and ρ the fluid density. $\Delta u/u_\tau$ is a measure of the influence of the roughness on the velocity profile (zero by definition for an aerodynamically smooth surface) known as the roughness function. The last term in equation (1) models the wake-like behaviour of the outer region of the boundary layer. Since it is in general the case that the aerodynamic origin does not coincide with either the mean surface location or the origin chosen for the measurements, y is replaced by $y + \epsilon$, where y is the distance measured from some arbitrary origin and ϵ is the incremental distance to the aerodynamic origin (again zero for a smooth surface). It has been usual in the past to use some procedure to fit measured mean velocity profiles to a representation of this kind, thereby obtaining a value for the wall shear stress together with the three other independent parameters: δ , ϵ , and $\Delta u/u_\tau$.

An indirect method of the kind just described to determine the wall shear stress is a direct extension of the procedure used for flow over smooth surfaces, where ϵ and $\Delta u/u_\tau$ are identically zero, and there are no essential difficulties in determining τ_w and δ by matching equation (1) to measured data. In fact, since the contribution of the wake component is usually negligible for $y/\delta < 0.5$, τ_w may easily be determined graphically using the method first suggested by Clauser (1954): the mean velocity data are plotted in semilogarithmic coordinates u/u_τ versus $\ln(u_\tau y/\nu)$, and compared with a fan of straight lines representing the velocity variation in the fully turbulent core, with c_f ($\approx 2\tau_w/\rho u_\tau^2$) as the only parameter. The line which best matches a measured velocity profile plotted on such a chart then yields a value for the corresponding skin friction coefficient c_f .

Figure 2 shows a typical Clauser chart for data taken in a zero pressure gradient fully developed smooth

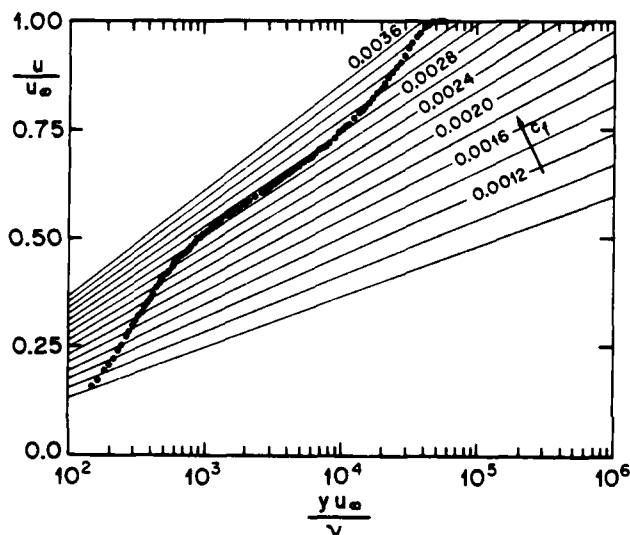


FIGURE 2 CLAUSER CHART FOR A MEAN VELOCITY PROFILE IN A SMOOTH-WALL BOUNDARY LAYER.

wall boundary layer. The values of c_f obtained from a Clauser chart and by fitting equation (1) (with ϵ and $\Delta u/u_\tau$ set equal to zero) to measurements according to a linear regression algorithm are generally within 2 or 3 per cent of each other, and are in good agreement with both Preston tube and direct floating element measurements of the wall shear stress.

For a rough surface, there is in principle again no difficulty in determining values for c_f and the two additional parameters ϵ and $\Delta u/u_\tau$, such that there is a minimum rms deviation, say, between equation (1) and an experimental profile. In practice, however, the process yields highly inaccurate values of c_f because of a crucial difference between the rough and smooth situations. This difference stems from the small deviations from linearity that are commonly found in the mean velocity profile in these coordinates (see Coles (1968)). For smooth surfaces these deviations are not of major significance. When a fitting procedure with only the two free parameters c_f and δ is used, these deviations from a semilogarithmic behaviour merely result in an increased rms scatter. For rough surfaces, on the other hand, the situation is quite different: the inclusion of the additional parameters ϵ and $\Delta u/u_\tau$ forces the measured profile to be as linear as possible in semilogarithmic coordinates, i.e., deviations, which may well be inherent to the data set, e.g., due to the influence of an individual roughness element, are reduced to a minimum. The additional degrees of freedom allowed by the simultaneous choice of slope (c_f) and

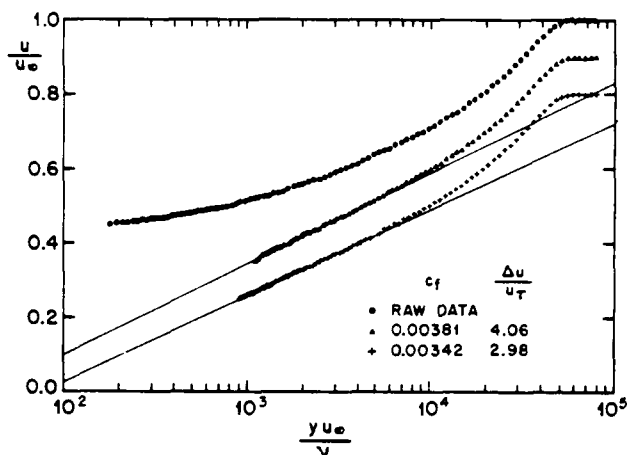


FIGURE 3 MEAN VELOCITY PROFILE IN A CAST SURFACE BOUNDARY LAYER (THE SECOND AND THIRD CURVES HAVE BEEN SHIFTED DOWN RELATIVE TO THE FIRST FOR THE SAKE OF CLARITY).

intercept ($\Delta u/u_\tau$) generally result in a much "better" fit in a statistical sense, but can produce erroneous values for these quantities. In fact, it is possible to obtain more than one set of values for the different parameters which yield essentially the same "goodness" of fit. Figure 3 shows the result of such a fitting procedure applied to a mean velocity profile measured in the cast surface boundary layer. The first curve represents the raw data; the second the results of a "best" fit. Also shown is the result obtained when the value of τ_w , independently measured using the floating element, was used as an input, thus eliminating one degree of freedom from the fitting procedure. The difference in values of c_f in this case is seen to be about 12%. Differences as large as 30% have been found in other cases. The results from a fitting procedure with all parameters to be determined were often found to be physically unrealistic: e.g. τ_w was found to increase with Reynolds number in some cases, and negative values of $\Delta u/u_\tau$ were obtained in other instances. On the other hand, when the values of τ_w , obtained from a direct floating element measurement, were used as an input to the fitting procedure, the resultant $\Delta u/u_\tau$ exhibited a consistent trend with Reynolds number. The skin friction data obtained with the floating element for the cast surface are plotted in Figure 4 against the momentum thickness Reynolds number. The corresponding values of the roughness function $\Delta u/u_\tau$ are plotted against a roughness Reynolds number in Figure 5.

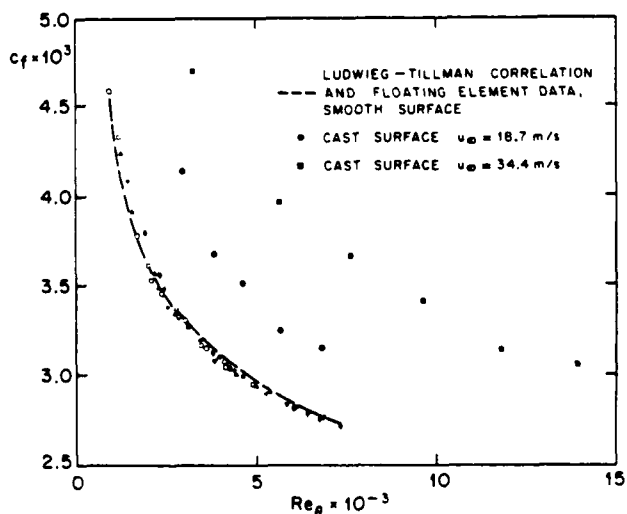


FIGURE 4 VARIATION OF SKIN FRICTION COEFFICIENT WITH MOMENTUM THICKNESS REYNOLDS NUMBER FOR THE CAST SURFACE.

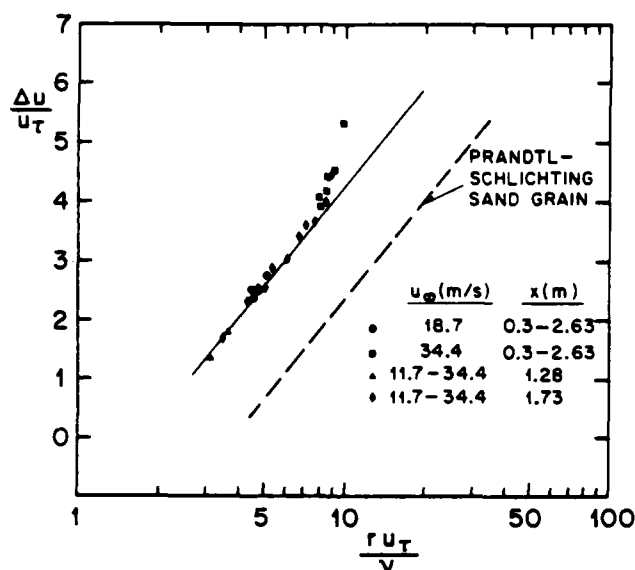


FIGURE 5 VARIATION OF ROUGHNESS FUNCTION WITH ROUGHNESS REYNOLDS NUMBER FOR THE CAST SURFACE. A LINE PARALLEL TO THE PRANDTL-SCHLICHTING SAND GRAIN LINE HAS BEEN DRAWN THROUGH THE DATA TO AID IN COMPARISON.

The difficulties associated with an extended Clauser plot approach of this sort have also been noted by Perry, Schofield and Joubert (1969). The effect is illustrated most vividly if the fitting procedure for a rough surface is applied to smooth surface data, i.e. ϵ and $\Delta u/u_\tau$ are not set identically equal to zero. The results of such an exercise for the data of Figure 2 are shown in Figure 6. The upper curve shows a comparison

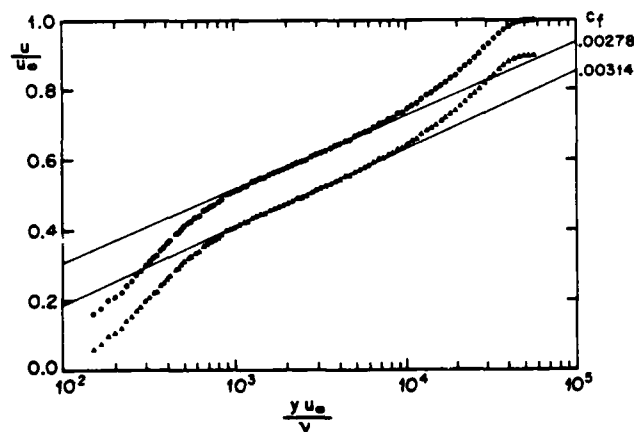


FIGURE 6 ROUGH SURFACE FITTING PROCEDURE APPLIED TO SMOOTH SURFACE DATA (THE SECOND CURVE HAS BEEN SHIFTED DOWNWARD FOR THE SAKE OF CLARITY).

with a "log-law" line corresponding to the value $c_f = 0.00278$ obtained from the floating element. The second curve shows the results of the fit: a value of 1.11 is obtained for $\Delta u/u_\tau$ and the value of 0.00314 obtained for c_f is 13% higher than the floating-element value. However, the match between the measured points and the logarithmic velocity distribution is excellent. About 20 smooth wall profiles were processed in this fashion. The average error in c_f was 12%, with a maximum deviation of 20%, and values for $\Delta u/u_\tau$ were in the range 0.3 to 2.0.

It is thus seen that significant errors can be made in the estimation of the wall shear stress using indirect techniques which apparently lead to excellent agreement with a standard representation of the mean velocity profile.

BOUNDARY-LAYER TRANSITION

The second type of flow examined is the low free stream turbulence, zero-pressure gradient boundary layer undergoing natural transition on a smooth wall. In such a situation it is important to consider the response of the floating element, which was designed to measure forces with steady time mean values, to sudden changes in the wall shear force that occur in the transition region due to the passage of a turbulent spot. As described in an earlier section, a PID controller is used to integrate the error signal and provide the necessary restoring coil current. Since the time constant of this system to a step input is about 0.5 seconds, the instrument cannot follow rapid changes in the imposed shear force. Nevertheless, it will register a true mean value of this force, as long as the changes in the force are not so large as to drive the instrument out of the operating range of the position detector. The output of the controller was monitored during the measurements, and it was established that the element remained within this operating range and yielded consistent and repeatable values for the wall shear force, except for small values of wall intermittency ($\gamma < 0.1$). At the start of the transition region the element was occasionally driven out of balance, presumably by the passage of a turbulent spot, and it took some time for equilibrium to be reestablished. For the transition measurements reported here, upper and lower bounds of the force registered by the element were recorded in addition to the mean value.

Experiments were conducted in which the wall shear stress was measured with a floating element and profiles of the mean velocity and streamwise turbulent intensity through the boundary layer were determined for a number of streamwise locations covering the laminar, transition and turbulent regions, and for a number of different free stream velocities. For each case, a zero pressure gradient was maintained and the free stream turbulence level was nominally the same (about 0.4%). The mean velocity measurements upstream of transition showed excellent agreement with the Blasius profile for all cases. From Figure 7, which shows the variation of skin friction coefficient with momentum thickness Reynolds number, Re_θ , it can be seen that the value of Re_θ at which transition begins decreases with increasing free stream velocity. This result is different from the

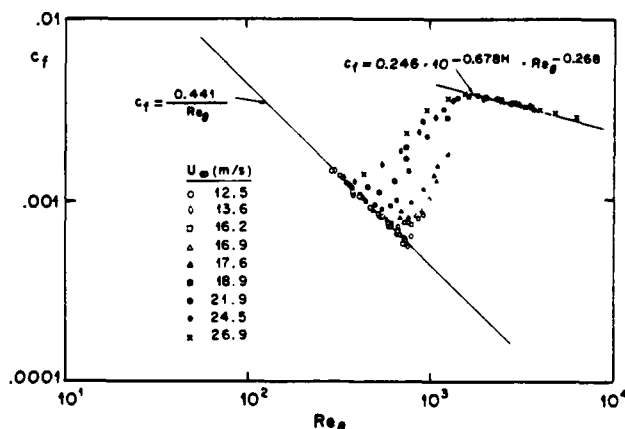


FIGURE 7 VARIATION OF SKIN FRICTION COEFFICIENT WITH MOMENTUM THICKNESS REYNOLDS NUMBER THROUGH THE TRANSITION REGION.

generally accepted view that for a given pressure gradient and free stream turbulence level, the value of Re_θ at the start of transition is unique. The variation of Re_θ with Re_θ for the different cases, shown plotted in Figure 8, is consistent with the floating element data of Figure 7.

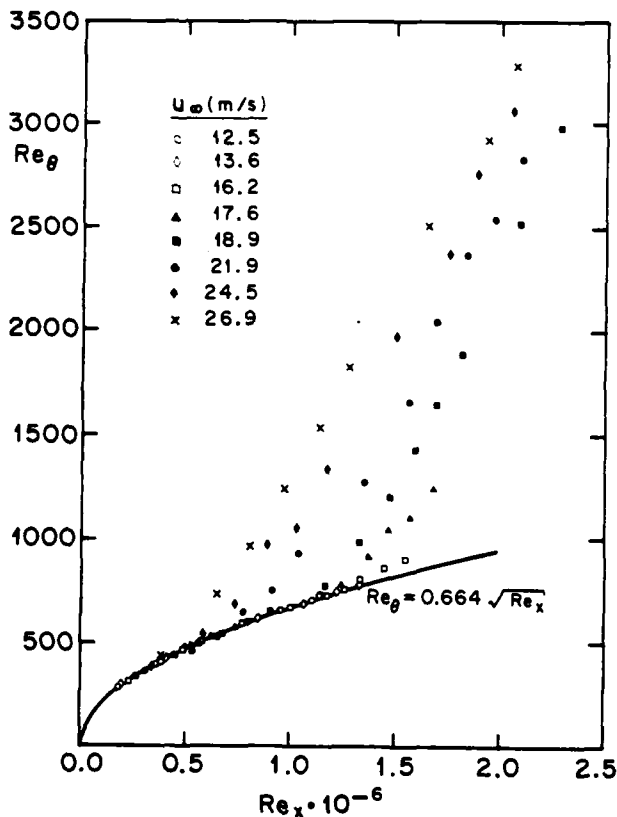


FIGURE 8 VARIATION OF MOMENTUM THICKNESS REYNOLDS NUMBER WITH THE X-REYNOLDS NUMBER FOR THE DATA OF FIGURE 7.

In the transition region, assumptions regarding the behaviour of the flow near the wall, such as those for the fully developed turbulent boundary layer that lead to the law of the wall, are invalid. In order to determine the wall shear stress in the transition region, it is the usual practice either to make use of the momentum integral equation and integral quantities from measured mean velocity profiles, or to obtain the wall shear stress as the intermittency weighted sum of the corresponding laminar and turbulent boundary-layer shear stress values at that Reynolds number:

$$c_f = (1 - \gamma_s) c_{fL} + \gamma_s c_{fT} \quad (2)$$

where γ_s is the value of the intermittency at the surface, c_{fL} is the laminar-flow value at the appropriate Reynolds number and value of the pressure-gradient parameter, and c_{fT} is obtained from any standard correlation in terms of Re_x for turbulent boundary layers with a proper choice for the origin of the turbulent boundary layer. Figure 9 shows one of the sets of skin friction data from Figure 7, plotted against the distance from the leading edge of the plate, with bands to indicate the upper and lower bounds on the shear force as recorded by the floating element. It is seen that the excursions are largest in the transition region. Also shown are the values for c_f computed from equation (2) using measured values of the wall intermittency γ_s . The origin of the turbulent boundary layer was chosen as $x = 550$ mm, a value determined from measurements of the wall intermittency and extrapolation of the measured boundary layer thickness in the turbulent region. The agreement between measurements and the computed values is seen to be good both upstream and downstream of the transition region, but the values obtained in the transition region from equation (2) are seen to under-predict the wall shear stress even when the uncertainties in both the floating element and the intermittency data are accounted for.

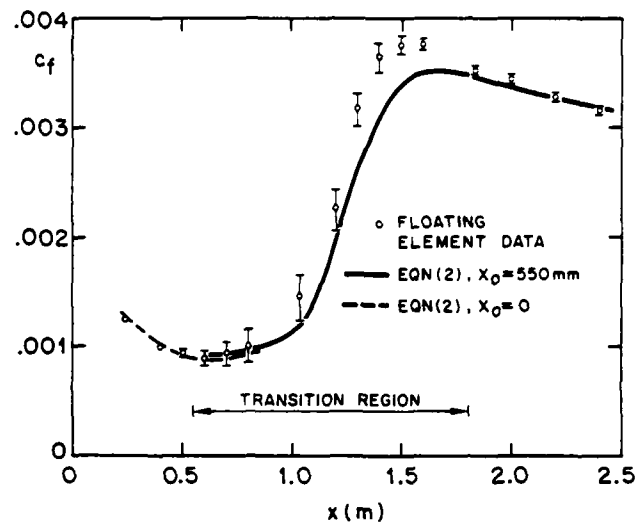


FIGURE 9 COMPARISON OF MEASURED AND COMPUTED SKIN FRICTION COEFFICIENTS FOR $U = 18.9$ M/S.

CONCLUSIONS

It has been shown that indirect techniques for the determination of wall shear stress for boundary layers developing on rough surfaces and those undergoing transition lead to considerable errors. A direct measurement of the wall shear stress is seen to be essential for these and other 'non-standard' situations.

REFERENCES

- Bradshaw, P., 1972, "Two more wind tunnels driven by aerofoil-type centrifugal blowers", Imperial College Aero. Rep. 71-10.
- Brown, K.C. and Joubert, P.N., 1969, "The measurement of skin friction in turbulent boundary layers with adverse pressure gradients", J. Fluid Mech. 35, 737.
- Clauser, F.H., 1954, "Turbulent boundary layers in adverse pressure gradients", J. Aero. Sci. 21, 91.
- Coles, D.E., 1956, "The law of the wake in the turbulent boundary layer", J. Fluid Mech. 1, 191.
- Coles, D.E., 1968, "The young persons guide to the data", Proc. Computation of turbulent boundary layers - 1968 AFOSR-IFP Stanford Conference, v II.
- Mazumder M.K., Wanchoo S., McLeod P.C., Ballard, G.S., Mozumdar S. and Caraballo, N., 1981, "Skin friction drag measurements by LDV", Applied Optics, 20, no. 16, 2832.
- Perry, A.E. and Joubert, P.N., 1963, "Rough-wall boundary layers in adverse pressure gradients", J. Fluid Mech. 17, 193.
- Perry, A.E., Schofield W.H. and Joubert P.N., 1969, "Rough wall turbulent boundary layers", J. Fluid Mech. 37, 383.
- Reynolds W.C., 1983, private communication.
- Winter, K.G., 1977, "An outline of the techniques available for the measurement of skin friction in turbulent boundary layers", Prog. Aerospace Sci. 18, 1.

A COMPARISON BETWEEN HOT-WIRE AND PULSED-WIRE MEASUREMENTS IN TURBULENT FLOWS

P. Dengel and J.-D. Vagt

Technische Universität Berlin

ABSTRACT

Comparative hot-wire and pulsed-wire measurements were performed in a free jet and a boundary layer. Because the pulsed-wire system is independent of turbulent intensities and structures, it is an instrument especially well suited to check hot-wire response equations in highly turbulent flows. The use of different corrections and their limitations (with and without rectification effects) for normal hot-wires are discussed.

INTRODUCTION

There are many reasons for taking measurements in highly turbulent flows. Hot-wire probes, single or multi sensor probes, are often not accurate enough at turbulent intensities higher than 20 %. So the following question arises: How high must the turbulent intensity be before errors caused by inadequate or ill-defined yaw-response characteristic of the sensor are no longer negligible (Castro 1975)? Of course, for different types of probes we find different answers. For example a single-wire probe can be used (apparently) at higher turbulent intensities than an x-wire probe because the range of the yaw response of an x-wire - a cone with an angle of about 20° - is much smaller. This is also true for three-wire probes which theoretically measure the instantaneous velocity, but only if this vector lies within the well defined region of yaw response.

There are many attempts to correct hot-wire measurements in highly turbulent flows or to give an error estimate for them. This was mainly done by considering higher order terms of series expansions like that of Champagne et al. (1967), for example. Among others corrections were developed by Heskestad (1965), Guitton (1968) and Vagt (1969). It is astonishing that the difference between various results evaluated from complex or more simpler considerations are small (see Vagt 1971). But in all these calculations the structure of the turbulence in terms of probability density distributions or statistical quantities was hardly ever taken into account. Furthermore the problem of reverse flow was first convincingly discussed by Tutu and Chevray (1975). They developed corrections for hot-wire measurements in highly turbulent flows with and without rectification effects based on probability density assumptions.

There was one attempt to overcome the problem of series expansion using squared response equations (Rodi 1975) at least for some Reynolds stress terms and for the mean velocity. Based on that analysis Acrivelliis (1977/78) tried to extend these considerations to flow fields of any turbulence. No rectification effects are discussed, however, in his paper and so the range of applicability of his theory must necessarily exclude all those turbulent flows which have reverse flow. Furthermore, as Gessner (1982) mentioned, not only response models have to be developed, a validation must follow in order to test how well posed or how ill conditioned the coefficient matrix may be.

More recently Bartenwerfer (1981) tested numerically some response equations, evaluated from series expansions and squared equations, using simple functions. But it is not clear whether these results can be used for real measurements because the functions used for the calculations are step-functions.

Nevertheless some of these results are very interesting. He finds that

- (1) the error expected in hot-wire measurements using squared signals is often larger than using non-squared signals and that
- (2) higher order response equations like those of Vagt (1969) do not necessarily give better results.

Thus, a standard for hot-wire measurements in highly turbulent flow can only be established by other measuring techniques which are independent of turbulent intensities and structures. Apart from Laser-techniques - error discussions start to appear - the only other technique which is applicable in highly turbulent flows is the pulsed-wire one according to Bradbury and Castro (1971). Finally another system should be mentioned which has a different physical background, that is the flying-hot-wire according to Coles and Wadcock (1979), but here we expect considerable interference problems.

Because the pulsed wire is much cheaper than a Laser velocimeter and can be handled more easily as far as data processing is concerned it is a very suitable instrument to check hot-wire response equations in highly turbulent flows.

PULSED-WIRE ANEMOMETER

Since the pulsed-wire anemometer has not been sponsored so heavily as the LV-system and is therefore less well known, some introductory remarks seem to be indicated.

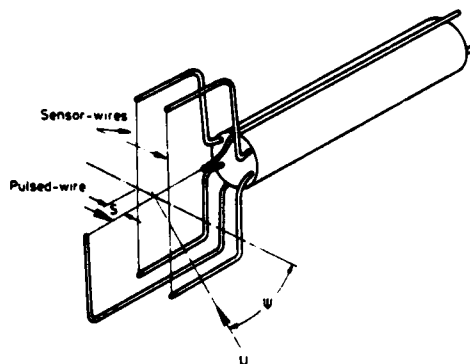


Fig. 1 Sketch of a pulsed-wire probe.

The pulsed-wire probe consists of three wires supported by prongs and a stem (Fig. 1). The central wire is the pulsed-wire. Because of a voltage pulse of about 5 μ sec. duration the wire temperature rises nearly instantaneously to about 300°C. A heat tracer is formed and convected away with the velocity u of the flow. The time taken for the tracer to reach a sensor wire ideally is

$$t = \frac{s}{|u| \cos \psi}$$

where s is the distance between the pulsed wire and the sensor wires and ψ the angle between the instantaneous direction of the velocity vector and the normal to the sensor wires. The largest angular deviation of the flow direction detected by the sensor is given by

$$\psi_{\max} = \tan^{-1} \frac{l}{2s}$$

where l is the length of the pick-up sensor wires. To obtain both the mean velocity and the rms-values of the fluctuations it is necessary to record a number of samples and average them.

$$\bar{u} = \frac{1}{N} \sum_{i=1}^N u_i \quad \text{and} \quad (\overline{u'^2})^{1/2} = \left(\frac{1}{N} \sum_{i=1}^N (u_i - \bar{u})^2 \right)^{1/2}$$

where N is the total number of samples and u_i is the velocity of the i th heat-tracer.

Because of diffusion and electronic processing it is necessary to calibrate the pulsed-wire probe.

EXPERIMENTS

Comparative measurements were performed in a free jet and in a boundary layer. Both flows were nominally isothermal and incompressible. For the free jet experiment we used a DISA-calibration tunnel. The diameter of the nozzle was $d = 3.9$ mm. Free jet profiles have been obtained at $x/d = 56$ where x is the distance between the nozzle and the measuring station along the jet axis. The velocity at the nozzle exit was about 40 m/s.

The boundary layer experiment was performed in an axisymmetric turbulent boundary layer with a severe adverse pressure gradient on the verge of separation (Dengel, Fernholz and Vagt 1981).

Mean and fluctuating velocities were measured by means of single normal hot-wire probes. These probes were developed in the laboratory (Dahm and Vagt 1977) and operated by means of a DFVLR (HDA III) constant temperature anemometer unit (Froebel 1972). For the measurements of velocity fluctuations a DFVLR (TGM III) turbulence-intensity measuring device was used (Froebel and Vagt 1977). The averaging time constant was about 15 sec.

For pulsed-wire measurements a Bradbury made pulsed-wire unit was used (Bradbury and Castro 1971) in conjunction with a PET 3032 and Bradbury/Castro made software. The number of samples for each point was 4000.

FREE JET MEASUREMENTS

The calibrations were performed on the centre line in the core of the free jet. The flow velocity was measured by means of an automatic micro-manometer (Froebel and Vagt 1974) using the pressure in the settling chamber. The contraction of the nozzle was about 25 : 1. The hot-wire probes were calibrated between 0 - 10 m/s, the pulsed-wire probe between - 9 m/s to + 9 m/s (positive and negative sensors). The hot wire calibration curves were linearized by a poly nominal linearizer (Froebel 1969). Though the calibration procedure was only "accurate" down to 1 m/s, the linearized output agrees well with the results from a small carriage type calibration device built for the velocity range 0 - 1 m/s (Vagt and Dengel 1980). Using this type of calibration device one can approximate hot-wire calibration curves very accurately in the range down to 0.1 m/s if the max. velocity is not higher than 7 m/s.

Because of the sensor-wire length pulsed-wire measurements have been performed in two different positions of the stem to find influences which may have been caused by different spatial integration. There appears to be

no such influence see Fig. 2.

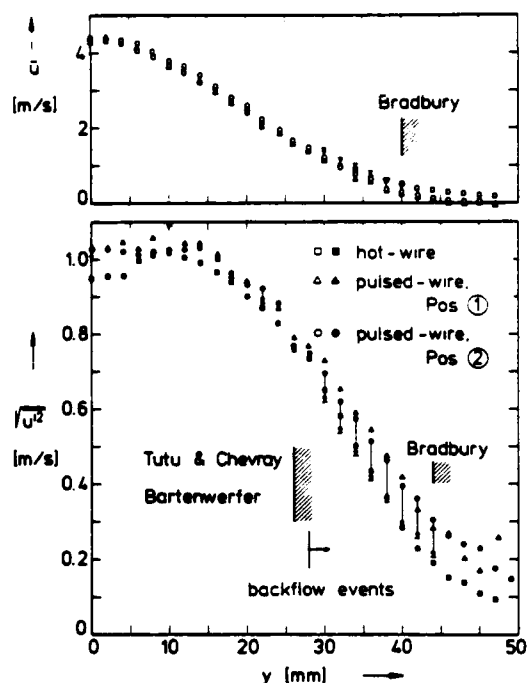


Fig. 2 A comparison between pulsed-wire and hot-wire measurements in a free jet.

Fig. 2 shows measurements performed by a hot wire and by a pulsed wire in a free jet at the same downstream position. Two things may be noted: (1) Repeatability between two subsequent measurements is good, (2) the mean values of the velocity \bar{u} measured by the two different techniques show good agreement (differences up to 5% at most) up to radial distances $Y_F/d = 8$ where Y_F is measured

from the jet axis and d is the nozzle diameter. At position further out in the jet the pulsed-wire has a distinct advantage over the hot wire in that it gives a velocity distribution which tends to zero at the edge of the free jet. Since the hot wire "adds up" its signal, the mean value of the velocity is necessarily larger than zero at the jet edge.

As far as the rms-values of the fluctuation velocity in x-direction are concerned (Fig. 2) the hot wire results are approximately 8 % smaller than the pulsed-wire data for Y_F smaller than 32 mm. This difference is however rather small if one takes into account that the local turbulence level is about 60 %. Even at $Y_F = 36$ mm where the turbulence level is approximately 80 % the rms-values agree fairly well.

Since the mean velocity in this range is so small that differences given in percent are not very useful, one should discuss absolute differences only. At $Y_F = 36$ mm this difference is about 0.2 m/sec.

BOUNDARY LAYER

The second part of this investigation was performed in a boundary layer with incipient separation (Dengel, Fernholz and Vagt 1981). In Fig. 3 pulsed-wire and hot-wire measurements are compared at an x-station without reverse flow events. The agreement between both measuring techniques is good, both for the mean and the fluctuating velocities which are plotted against the distance y normal to the wall. Differences do occur, however, when the turbulence level is small. This is due to specific properties of the pulsed-wire technique, like electronic noise, heat-tracer diffusion, tunnel vibration and perhaps sensor and pulsed-wire vibration which must be improved by further development work. A typical distribution of mean and fluctuating velocities at a position with nearly zero skin friction is shown in Fig. 4. The mean

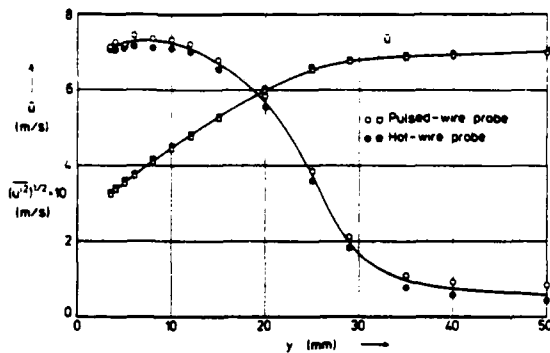


Fig. 3 A comparison between pulsed-wire and hot-wire measurements in a boundary layer without backflow events.

velocity, measured with both pulsed-wire and hot-wire, agrees fairly well in the outer region of the boundary layer ($y > 13$ mm). Closer to the wall ($y < 13$ mm) the pulsed-wire technique gives the correct results. The hot-wire data are too large here since the hot-wire cannot distinguish upstream and downstream flow velocities and adds up the signals. For the rms-distribution of the fluctuation velocity (x-component) the results of the two measuring techniques differ largely from each other in the range $y < 40$ mm. At $y = 40$ mm the local turbulence level is 21% measured with the hot-wire whereas the pulsed-wire gives 22.6%. This is a difference of about 7% based on the pulsed-wire measurements. At $y = 20$ mm the respective values are 50% measured by the hot-wire and 64% by the pulsed-wire, which is a difference of 28%. It is interesting to note that correction procedures (dealt with below) for hot-wire measurements at high turbulence levels improve agreement between hot-wire and pulsed-wire measurements considerably.

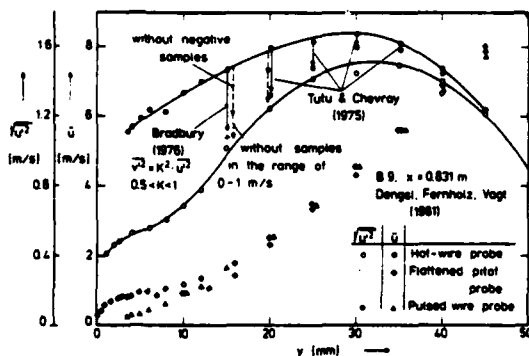


Fig. 4 A comparison between pulsed and hot-wire measurements in a boundary layer. Effect of hot-wire corrections.

DISCUSSION OF RESULTS

The hot-wire and pulsed-wire intensity measurements obtained so far show that the two measuring techniques agree well in the free jet up to local turbulence levels of 80% and disagree in the boundary layer from turbulence levels of about 20% upward. It is obvious therefore that the magnitude of the turbulence level cannot serve as a sufficient criterion for the applicability of the hot-wire technique but that the type of flow or some other property of the turbulence field must play a rôle. An explanation for the behaviour of the hot-wire in different flows can be given by looking at probability

density distributions obtained by means of the pulsed-wire technique. The following distinctions should be made:

- High local turbulence level at low mean velocities without any backflow.
- High local turbulence level at somewhat larger mean velocities without any backflow.
- High local turbulence level at low and high mean velocity range with backflow.

The probability density distributions in the free jet (Fig. 5) at the position $y_F/d = 5$ and $x_F/d = 56$

show no negative flow events. The mean velocity is small (< 3 m/s) but the local turbulence level $(u'^2)^{1/2}/\bar{u}$ is large (36%). If one remembers that the hot-wire "feels" only positive flow events agreement between the two techniques should perhaps be expected. (This is to be seen independently of nonlinearities in the hot-wire response equation). At this high level of turbulence differences of about 5% - 10% may be considered as small, because the mean velocity is small and its accurate measurement rather difficult.

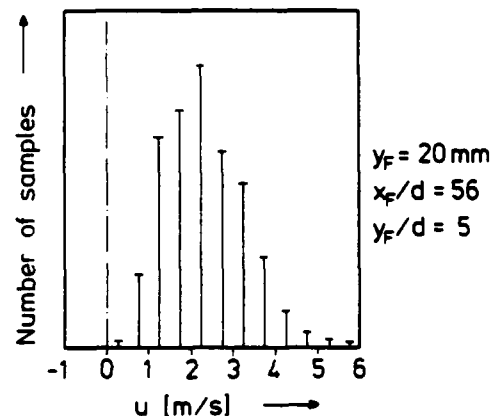


Fig. 5 Histogram (free jet).

The histogram presented in Fig. 6 shows a few negative samples in a free jet at $y_F = 34$ mm ($y_F/d = 9$ mm) and agreement between the two techniques should still be good. If one could measure the same histogram by means of a hot wire it would nevertheless look slightly different. The "negative" samples would be found added up on the right hand side and the width of the histogram would consequently be smaller. This means that the hot wire is seeing a slightly larger mean velocity and a slightly smaller turbulence intensity. The latter is directly proportional to the "width" of the histogram.

At $y_F = 46$ mm ($y_F/d = 12$) the number of positive and negative samples is of the same order, and the distribution is very narrow. Assuming again the negative samples added to the corresponding positive samples - that is what the hot-wire really "feels" - the indicated mean velocity will be larger, but the turbulence intensity becomes smaller.

We now turn to probability density distribution taken in an adverse pressure gradient turbulent boundary layer (Dengel et al. 1981).

Fig. 7 shows a histogram at a distance from the wall ($y = 45$ mm) where no "negative" flow events have occurred. The form of the histogram is quite different from any of these which we have observed in the free jet (Fig. 5 to 7) in that it is skewed. Since there are no "negative events" agreement between the two measuring techniques should be good. The mean velocity is 7.8 and 7.7 m/s measured by the pulsed wire and the hot wire respectively and the intensities given by the two techniques are almost identical.

Moving the probe further towards the wall the first negative events occur at $y = 30$ mm (Fig. 8). Their number increases with decreasing wall distance.

If we apply the reasoning presented above to the behaviour of a hot wire applied under the conditions

shown in Fig. 8, we can deduce that the value of the mean velocity would be relatively unaffected as long as the integral over the negative velocities remains small but that the intensity would be seriously erroneous. This latter effect is augmented by the fact that the square of the difference $\bar{u} - u_i$ enters into the calculation of the intensity. This effect becomes even stronger in the vicinity of the wall. In the range $y < 10$ mm the "folding-procedure" influences the mean velocity as well, since the distribution is now extremely changed. To confirm this model another test was made.

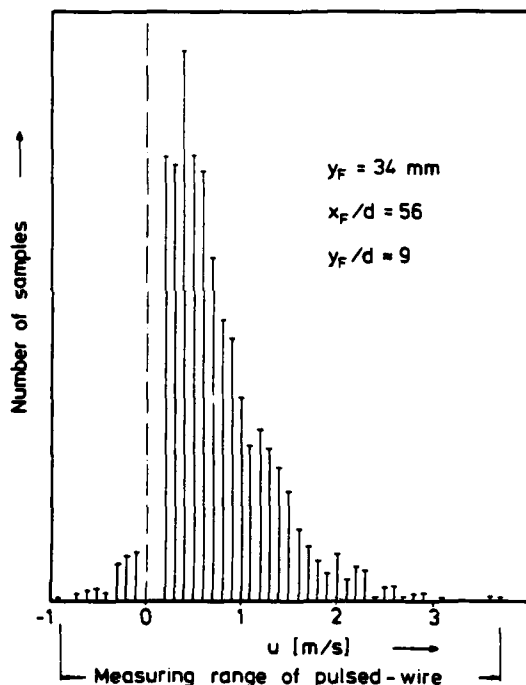


Fig. 6 Histogram (free jet).

It is possible to change the pulsed-wire program so that only positive events will be counted. This means that the pulsed-wire works almost in the same way as a hot wire with the important exception that the negative samples are not added to the positive samples as in the case of the hot wire. The result is shown in Fig. 4 as the long dashed-line "arrow". The intensities, measured by the pulsed wire are smaller when the negative samples are not counted and this brings the results closer to the (erroneous) hot-wire results. In addition we now neglect signals indicating velocities smaller than 1 m/s

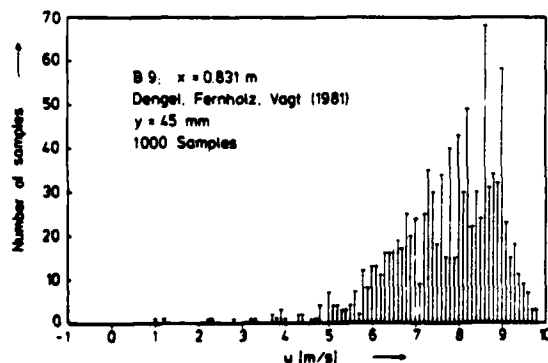


Fig. 7 Histogram (boundary layer).

(we know that the hot wire does not work very satisfactorily at velocities near zero because of insufficient approximation by a polynomial linearizer) the values are still closer to the hot-wire results short dashed-line "arrow". The remaining difference is due to not being able to simulate completely the "adding up" process performed by the hot wire.

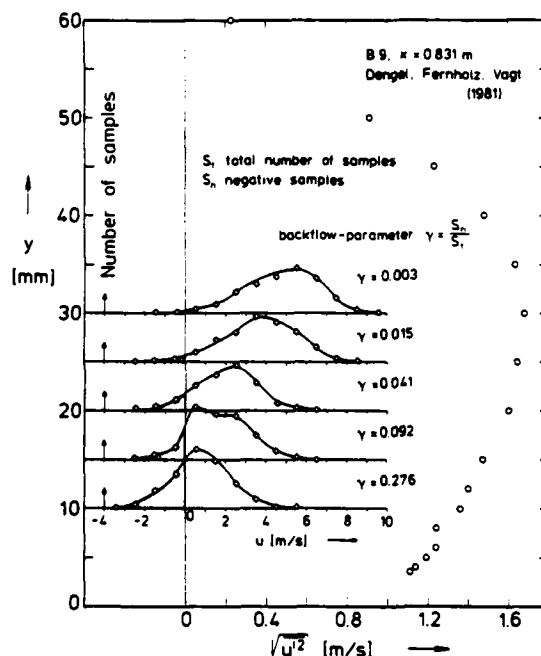


Fig. 8 Pulsed-wire measurements in a boundary layer.

Tutu & Chevray (1975) and Bradbury (1976) have developed error estimates for the mean and fluctuating velocity signals of normal hot wires.

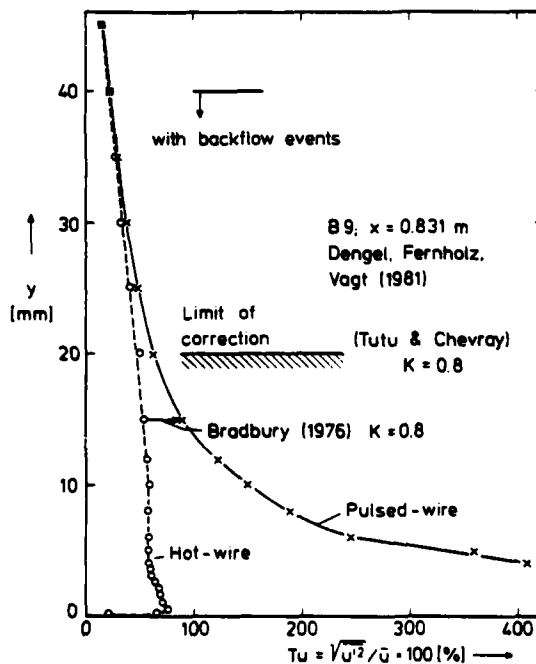


Fig. 9 A comparison between pulsed-wire and hot-wire in a boundary layer.

These error estimates or corrections can now be checked by comparing the hot-wire data with the pulsed-wire measurements under the assumption that the pulsed-wire signals are correct. Such a comparison has been performed for the intensity and the mean value in Fig. 2 (free jet), for the intensity in Fig. 4 (boundary layer close to separation) and for the turbulence level $Tu = (u'^2)^{1/2} / \bar{u}$ in Fig. 9 (boundary layer). Discussing Fig. 4 first, one may notice that the mean velocities measured by the two techniques differ only slightly (differences up to 10% occur at turbulence level of 50%) from each other whereas differences between the intensities are large. Using the error estimate given by the above authors which start from the true value the hot-wire signal can be predicted. This prediction is given by the full-line arrows. The agreement between prediction and measurement is surprisingly good. The same is true for the free jet experiment which is shown in Fig. 2. In Fig. 9 corrections for hot wires are given using again error estimates from Tutu and Chevray and Bradbury.

Fig. 10 shows examples for correction functions developed for normal-wire probes. In addition we present a curve developed from the free jet measurements, where it is again assumed that the pulsed-wire gives the true answer. This curve is very flat for $(u'^2)^{1/2} / \bar{u} < 0.5$ and rises steeply beyond $Tu = 60\%$. Two limits for the corrections may be noted. The lower limit is given by Bradbury (1976) or Tutu and Chevray (1975), and the upper limit is given by a direct comparison between hot-wire and pulsed-wire measurements, here performed in a free jet. In the mid range and further to the left similar correction curves for x-wires can be drawn like that of Bartenwerfer (1981), Tutu and Chevray (1975) and Vagt (1969).

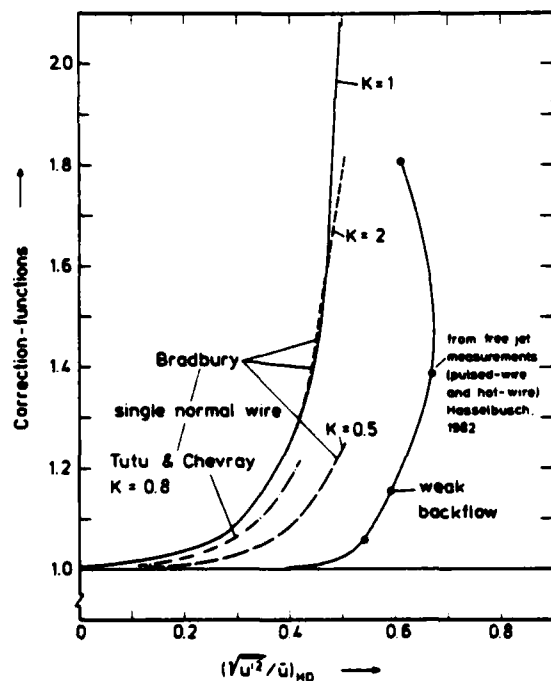


Fig. 10 Correction functions for hot-wires.

With the correction curves shown in Fig. 10, it would now be possible to correct hot-wire signals if the turbulence level of the shear flow investigated is below, say 50%, and if the probability density distribution of the flow is similar to the ones which the correction procedures of Tutu & Chevray and Bradbury are based on. This means that if the p.d.f. assumed for the correction procedure and that of the actual flow approximately agree, then the correction procedure works (of Figs. 2, 4 and 9). If the two p.d.f.s. disagree as in a shear flow with even weak reverse flow, then the "theoretical" correction underestimates the error and "experimental" correction curves are necessary which may be obtained by means of measuring techniques independent of p.d.f. such as the pulsed wire.

BIBLIOGRAPHY

- Acrivelllis, M., 1977, "Hot-wire measurements in flows of low and high turbulence intensity", DISA Inform. 23, 15-20.
- Acrivelllis, M., 1978, "An improved method for determining the flow field of multidimensional flows of any turbulence intensity", DISA Inform. 23, 11-16.
- Bartenwerfer, M., 1981, "Zur Analyse von Hitzdrahtsignalen turbulenter Strömungen", Diss. im FB 9 der TU Berlin.
- Bradbury, L.J.S. and Castro, I.P., 1971, "A pulsed-wire technique for velocity measurements in highly turbulent flows", J. Fluid Mech., Vol. 49, pp. 657-691.
- Bradbury, L.J.S., 1976, "Measurements with a pulsed-wire and a hot-wire anemometer in the highly turbulent wake of a normal flat plate", J. Fluid Mech., Vol. 77, part 3, pp. 473-497.
- Castro, I.P., 1975, "Statistics of the instantaneous velocity vector and the consequent errors in anemometer measurements", presented at Euromech 63, Technical University of Denmark.
- Champagne, F.H., Sleicher, C.A. and Wehrmann, C.H., 1967, "Turbulence measurements with inclined hot-wires, Part II", J. Fluid Mech., Vol. 28, pp. 153-176.
- Coles, D. and Wadcock, A.J., 1979, "Flying hot-wire study of two-dimensional turbulent separation on a NACA 4412 airfoil at maximum lift", AIAA J., Vol. 17, pp. 321-329.
- Dahm, A. and Vagt, J.D., 1977, "Entwicklung und Herstellung interferenzarmer Hitzdrahtsonden", Institutsbericht 01/77 Hermann-Föttinger-Institut für Thermodynamik, TU Berlin.
- Dengel, P., Fernholz, H.H. and Vagt, J.-D., 1981, "Turbulence and mean flow measurements in an incompressible axisymmetric boundary layer with incipient separation", Third Symposium on Turbulent Shear Flows, Davis, USA.
- Fröbel, E., 1969, "A new linearizer unit for hot-wire anemometry", DFVLR Institut für Turbulenzforschung, Int. Rep.
- Fröbel, E., 1972, "Beschreibung und Betriebsanleitung zum Hitzdrahtanemometer HDA III", Int. Bericht, DFVLR.
- Fröbel, E. and Vagt, J.D., 1974, "Ein automatisch abgleichendes Flüssigkeitsmanometer mit digitaler Anzeige", DLR-FB, 74-40.
- Fröbel, E. and Vagt, J.-D., 1977, "Meß- und Auswertverfahren von Hitzdrahtsignalen mit dem Turbulenzgradmesser TGM III der DFVLR", DLR-FB 77-61.
- Gessner, F.B., 1982, "Comments in: Three-dimensional turbulent boundary layers", IUTAM Symposium Berlin, p. 387 ff, Springer-Verlag Berlin, Heidelberg, New York.
- Guittou, D.E., 1968, "Correction of hot-wire data for high intensity turbulence. Longitudinal cooling and probe interference", Mech. Eng. Res. Laboratories, McGill University, Rep. No. 68-6.
- Hasselbusch, H., 1981, "Messung der mittleren Geschwindigkeit und der Schwankungsgeschwindigkeit (Effektivwert) in einem runden Freistrahle mittels Hitzdraht- und Pulsdrahttechnik", Studienarbeit, HFI, TU Berlin.
- Heskestad, G., 1965, "Hot-wire measurements in a plane turbulent jet", J. of Appl. Mech. 32, 721-734.
- Rodi, W., 1975, "A new method of analysing hot-wire signals in highly turbulent flow, and its evaluation in a round jet", DISA Inform. 17, 9-18.
- Tutu, N.K. and Chevray, R., 1975, "Cross-wire anemometry in high intensity turbulence", J. Fluid Mech. Vol. 71, 785-800.
- Vagt, J.D., 1969, "Hot-wire measurement technique in a highly turbulent flow and the calculation of intensities", Inf. Seminar on Heat and Mass Transfer, Herceg-Nov, Yugoslavia.
- Vagt, J.-D., 1971, "Hot-wire measurement technique - some basic problems", von Karman Institut, Lecture Series 36 Turbulent Jet Flows.

A MULTIPOINT DETECTION METHOD TO IDENTIFY COHERENT TEMPERATURE FRONTS IN A TURBULENT BOUNDARY LAYER OVER A ROUGH SURFACE

A. J. Chambers, R. A. Antonia, L. W. B. Browne
Department of Mechanical Engineering
University of Newcastle, N.S.W., 2308, Australia

and

M. R. Raupach
Division of Environmental Mechanics
C.S.I.R.O., Canberra, A.C.T., 2600, Australia

ABSTRACT

A conditional technique, based on the detection of temperature fronts at several points in the spanwise direction in a turbulent boundary layer, is developed and compared with a one point technique (VITA) and a method based on the visual detection of fronts. The multipoint approach represents an improvement over the one point technique. Conditional averages of temperature obtained with both techniques, are presented.

INTRODUCTION

The technique of conditional sampling and averaging (e.g. Kaplan, 1973; Antonia, 1980, 1981) has contributed in closing the gap between measurements often made in a Eulerian frame with information in a Lagrangian frame, inferred from flow visualisation experiments. The study of the organised large scale motion in different turbulent shear flows has benefited from the use of an array of sensors to simultaneously measure velocity or scalar field fluctuations at a number of points in the flow field (e.g. Blackwelder, 1979; Wignanski, 1979; Van Atta, 1979). Such an array can, at least in principle, help with the identification of the large scale motion and perhaps also shed some light on its generation, evolution with respect to space and time and obliteration or destruction.

A common approach in experimental turbulence research has been to apply the conditional sampling technique on information obtained at only one point of space. Such an approach has obvious limitations in the study of the large scale motion since the existence of a large structure implies that there should be some correlation and definite phase relationships between the motion at points throughout a region of space occupied by the structure. It should be made clear however that conditional averaging can be usefully applied to information obtained at one point of space provided the detection of the structure is based on a significant region of space. One example is the relatively happy marriage of simultaneous flow visualisation and one point hot wire or film anemometry (e.g. Falco, 1977). The possibility exists for one point conditional sampling technique such as VITA (variable interval time averaging) to be tested against the detection based on a multi-point scheme. Such a test was carried out by Subramanian *et al* (1982), hereinafter referred to as I, who compared VITA and other one point techniques with a method based on the visual detection of the temperature fronts (e.g. Chen and Blackwelder, 1978) sensed by a one-dimensional array of cold wires, deployed in the direction of main shear of a turbulent boundary layer. The comparison indicated that qualitative, but not quantitative, agreement could be obtained. Reliable estimates of the contribution of the large structure to the momentum and heat fluxes, required that a relatively high level of confidence is achieved for conditional averages of the appropriate turbulent quantities.

In the present paper, an attempt is made to extend the one point method to one where the detection is based

on information obtained at several points in space. The method is applied to temperature fronts obtained in a slightly heated rough wall boundary layer. The fronts were identified using one-dimensional arrays of cold wires deployed in either the spanwise (y) or main shear (z) directions. In view of the likely three-dimensionality of the structure, it was considered important to incorporate information simultaneously obtained in both these directions. For this purpose, a cross-like arrangement of cold wires, deployed in both y and z directions, was also used.

EXPERIMENTAL ARRANGEMENT

Figure 1 shows the co-ordinate system and (schematically) the experimental set-up in the environmental wind tunnel of the C.S.I.R.O., Division of Environmental Mechanics. The K-type rough surface consisted of densely packed gravel (average height ≈ 7 mm) glued to baseboards located on the floor of the working section (11 m long, 1.8 m wide and 0.65 m high). With the aid of an upstream trip (a 50 mm high fence), this surface generated a thick turbulent boundary layer in which the maximum wind speed U_p was 11 ms^{-1} . The artificial thickening was intended to simulate the flow within a neutral atmospheric surface layer. The height z_p (≈ 540 mm) corresponding to U_p at $x = 6.48$ m represents an approximation to the boundary layer thickness. In view of the lack of a free stream at this location, z_p and U_p cannot strictly be identified with δ and U_∞ . The roughness length $z_0 = 0.15$ mm and the zero plane displacement of the rough surface was 6 mm.

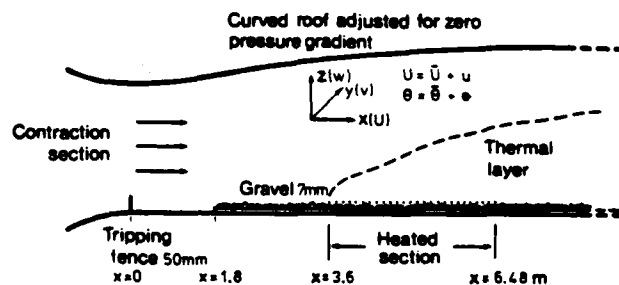


FIGURE 1 EXPERIMENTAL ARRANGEMENT IN THE WIND TUNNEL AND DEFINITION OF CO-ORDINATE AXES

Part of the rough surface was made into a planar heat source by running heated Nichrome wires laterally over the gravel, with a spacing of 2 cm between wires. The wires rested on the gravel and provided an effective heat source which spanned the tunnel width and had a streamwise extent of 2.88 m. Measurements were made at the downstream end of the heated section, 6.48 m from the fence. The "inter-

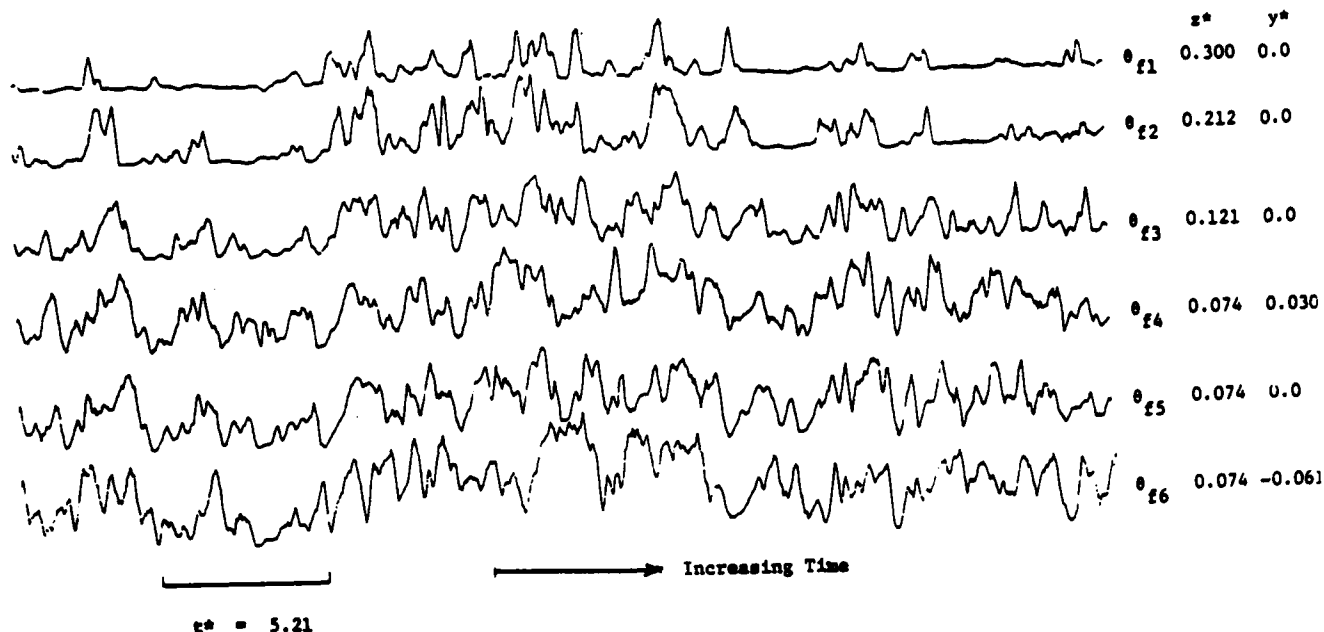


FIGURE 2 TEMPERATURE TRACES θ_{f1} USING AN ARRAY OF SENSORS DEPLOYED IN BOTH y AND z DIRECTIONS

nal" thermal layer (Figure 1) had a thickness, estimated from the mean temperature profile, of about $0.37 z_p$ at the measurement station.

In all experiments, an X-probe/cold wire arrangement was traversed in the z direction to measure velocity fluctuation components u and w and the temperature fluctuation θ . This arrangement was always at the same x and y locations as the cold wire array deployed in the z direction.

All cold wires were made of $0.63 \mu\text{m}$ Pt-10% Rh Wollaston wires and operated with circuits supplying a constant current of 0.1 mA . The X-wires were made of $5 \mu\text{m}$, Pt-10% Rh and were operated with TSI 1050-1 CTA's at a resistance ratio of 1.8. Signals from the array of cold wires and X-wire/cold wire combination were first recorded on an 8-channel FM tape recorder (HP3968A) at a speed of 19 cm s^{-1} and later digitised into a PDP 11/34 computer at a sampling frequency of 1 kHz . The duration of the digital records was about 60 s .

SOME EXPERIMENTAL RESULTS

The measured kinematic Reynolds shear stress $\tau/\rho = -uw$ was approximately constant up to $z^* = 0.2$ ($z^* = z/z_p$, where z is measured from the zero plane displacement surface), yielding a friction velocity $u_* = 0.50 \text{ ms}^{-1}$.

Displayed in Figure 2 are simultaneous temperature traces from an array of cold wires deployed in both y and z directions. Digital lump-sum filtering, equivalent to low-pass filtering with a cut-off frequency $f_c^* = 9.8$ (the asterisk denotes normalisation with respect to either z_p , U_p or both) was applied to these signals. The filtering was applied to allow easier visual focusing on signatures associated with the large scale motion, at the expense of some degradation in the sharpness of the front. The traces of θ_{f1} (the subscript f refers to filtered signals while 1 denotes a particular sensor in the array) reveal the characteristic slow increase in θ followed by a relatively sudden decrease at the temperature front and indicate good coherence over confined three-dimensional regions of space. The front is detected at approximately the same instant of time by wires at the same height z but at different spanwise location (the lower three traces in Figure 2) but occurs at increasingly earlier times as z increases. Whenever a temperature front is detected on all sensors of the z array, the spanwise sensors also detect the front. In view of the relatively small separation between the spanwise sensors (Figure 2), temperature fronts detected by these sensors are not always detected by all the vertical sensors.

Correlation coefficients have been obtained between temperature fluctuations obtained at the same z location

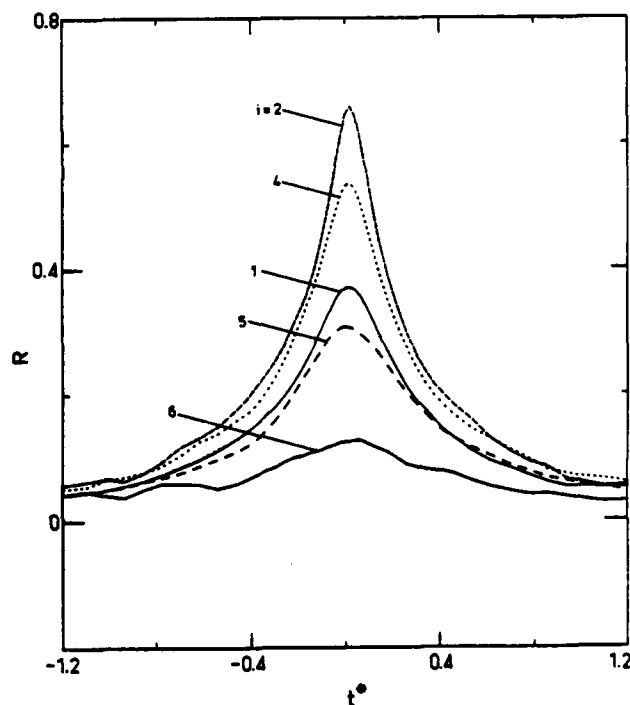


FIGURE 3 SPACE-TIME SPANWISE CORRELATIONS OF SPANWISE TEMPERATURE AT $z^* = 0.16$

The values of y^* for the six wires used are -0.18 (wire 6), -0.11 (5), -0.06 (4), 0 (3), $+0.04$ (2), $+0.10$ (1)

but different y values. The correlation coefficient $R(\Delta y, \tau) = \theta_3(y, t-\tau)\theta_1(y+\Delta y, t)/\theta_3\theta_1$ (τ is the time delay; the prime denotes the standard deviation) is determined between θ measured at wire 3 (located beside the X-probe at $y = 0$) and the temperature at any other spanwise location. $R(\Delta y, \tau)$ always exhibited a single maximum at $\tau \approx 0$ (Figure 3) lending some support to the two-dimensionality of the front, given the limited range of spanwise separations considered here.

Distributions of $R(\Delta y, 0)$ in Figure 4 compare well

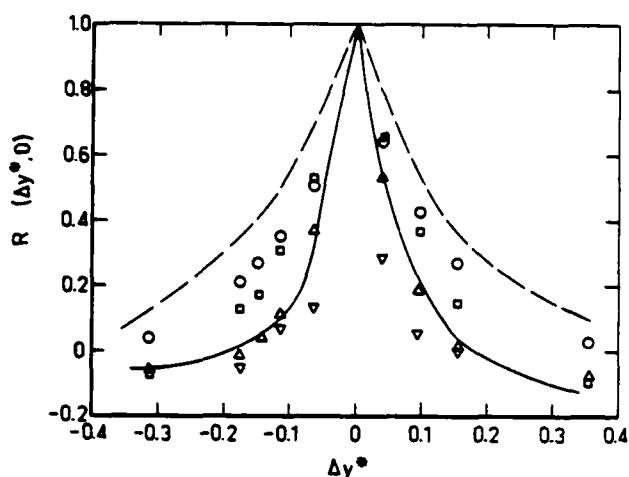


FIGURE 4 SPANWISE CORRELATION AT ZERO TIME DELAY
 O, $z^* = 0.33$; \square , 0.16; Δ , 0.06; ∇ , 0.02; —, Fulachier
et al (1974), $z/\delta = 0.03$; ---, Rajagopalan *et al* (1982),
 $z/\delta = 0.5$

with the smooth wall results of Fulachier *et al* (1974) and Rajagopalan *et al* (1982). Although the internal thermal layer is smaller than z_p , the similarity between the present correlations and those obtained in a smooth wall boundary layer suggest that, in the present experiment, the temperature marking of the large structure effectively extends to the edge of the thermal layer in the z direction. (This limitation is not serious since, for the technique developed here, use is made of the spanwise information only).

DESCRIPTION OF CONDITIONING METHODS

As in the study I, a detection criterion is applied to one or more signals (in this case θ_i) with the aim of identifying the signature of the temperature front. From a complete time history, the detection algorithm selects n time points τ_1, \dots, τ_n , at each of which the signature is detected. The output D of this algorithm is equal to unity at these time points and is zero otherwise. The conditional average of a variable g is then defined by

$$\langle g(t) \rangle = \frac{1}{n} \sum_{i=1}^n g(\tau_i + t)$$

so that $\langle g(t) \rangle$ represents the average behaviour of g in the neighbourhood of a detection point τ_i . The time $t = 0$ arbitrarily corresponds to the position where all points τ_i are made to coincide.

The three conditional techniques used here are RAKE, VITA (at one point) and MPVITA (multipoint VITA). RAKE is used, as in I, as the reference technique; the fronts are recognised visually on simultaneous temperature traces obtained with the cold wire array spanning a sufficiently large range of either z^* ($0.02 < z^* < 0.35$) or y^* ($|y^*| \leq 0.1$) or both. It is clear that there will be some arbitrariness, apart from that associated with the visual selection, as a result of the magnitude of the z^* and y^* ranges, covered by the sensors.

In VITA, D is set equal to 1 when the conditions

$$\ddot{\theta}_f^2 - \ddot{\theta}_f^2 > k \ddot{\theta}_f^2 \quad \text{and} \quad \ddot{\theta}_f < 0 \quad (1)$$

are first satisfied. The dot denotes a time derivative, k is a threshold parameter and the tilde represents the moving average

$$\tilde{\theta}_f = \frac{1}{T} \int_{t-\frac{1}{2}T}^{t+\frac{1}{2}T} \theta_f(t) dt$$

which is essentially a low-pass filtering operation with

cut-off at $\frac{1}{2}T$.

In MPVITA, advantage was taken of the fact that fronts were observed to occur (Figure 2) at essentially the same time, at least over a limited spanwise extent. VITA was first applied to each of a selected number N of points in the spanwise direction. The maximum value of N used here was 3 with the spacing between adjacent points approximately equal. At each point j , the VITA algorithm yielded a pulse train D_j equal to one or zero depending on whether or not conditions (1) were satisfied. The output D of the detection algorithm for MPVITA was set equal to one every time the product of all the D_j 's changed from zero to one, viz.

$$\prod_{j=1}^N D_j = 1 \quad (2)$$

D was set to zero otherwise. Conditions (2) obviously represent a more restrictive set of conditions than (1). From an experimental viewpoint, one would expect the use of (2), instead of (1), to lead to an improvement in the quality of detection, perhaps at the expense of statistical accuracy due to a reduction in the detected number of fronts for a time series of a given duration. Kovaszny (1979) has already pointed out that the penalty incurred with multipoint conditional sampling is a reduction in the number of samples with a concomitant increase in the total averaging time to achieve stable averages. We believe that this penalty is more than offset by the improved quality of detection.

COMPARISONS BETWEEN DETECTION SYSTEMS

The sensitivity of the frequency f^* of temperature fronts, using MPVITA, to the threshold k , the number N of points used and the maximum separation covered by these points was investigated, using as reference the number of fronts detected with RAKE. For $N = 3$ and equal spacing between sensors, values of k equal to 0.15 and 0.3 seemed optimum for separations $|\Delta y^*|_{\max}$ equal to 0.21 and 0.10 respectively.

The Table shows a comparison between fronts detected by RAKE (using two different observers), VITA and MPVITA. The total number of fronts detected by both observers was about the same (120) but the agreement between observers was only about 74%. For VITA and MPVITA, k and T^* were adjusted so that the detected frequency of fronts corresponded roughly to the visual estimate of RAKE. The important message in the Table is the relatively high correspondence of fronts achieved between MPVITA and RAKE. This correspondence, averaged between the two observers, is

Correspondence Between Fronts Detected by RAKE, VITA and MPVITA ($z^* = 0.18$)

Method	f^*	No. of Fronts	Correspondence Between Fronts	
			Visual	
			Observer A	Observer B
RAKE	Observer A	0.24 125	125 (100%)	91 (73%)
	Observer B	0.23 122	91 (75%)	122 (100%)
VITA ($k = 0.75$, $T^* = 0.34$)	0.24	130	76 (58%)	66 (51%)
MPVITA ($N = 3$, $T^* = 0.34$, $ \Delta y^* _{\max} = 0.21$)	$k = 0.135$	0.23 111	65 (59%)	77 (69%)
	$k = 0.20$	0.16 85	53 (62%)	67 (79%)
	$k = 0.30$	0.09 50	39 (78%)	44 (88%)

† Values in brackets denote the percentage correspondence

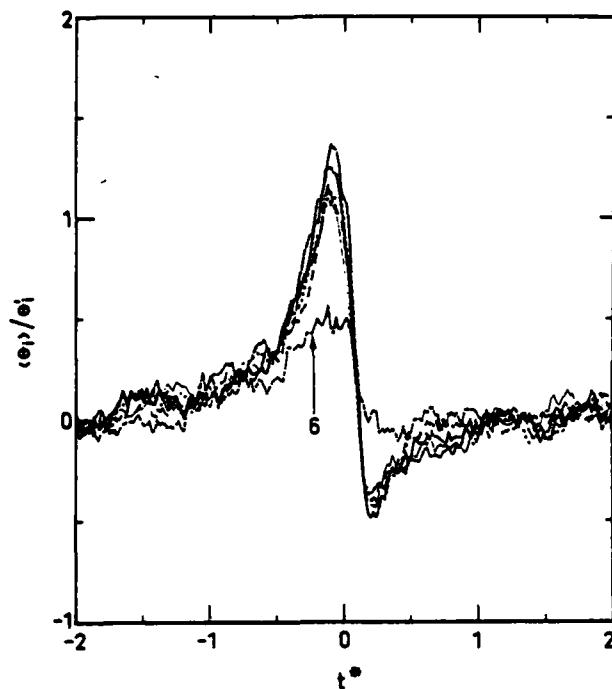


FIGURE 5 DISTRIBUTIONS OF SPANWISE $\langle \theta_1 \rangle$ AT $z^* = 0.18$
USING MPVITA ($|\Delta y^*|_{\max} = 0.21$, $N = 3$)
Spanwise positions for θ_1 are the same as for Figure 4.
MPVITA, $|\Delta y^*|_{\max} = 0.214$, $N = 3$ (sensors 1, 3, 5)

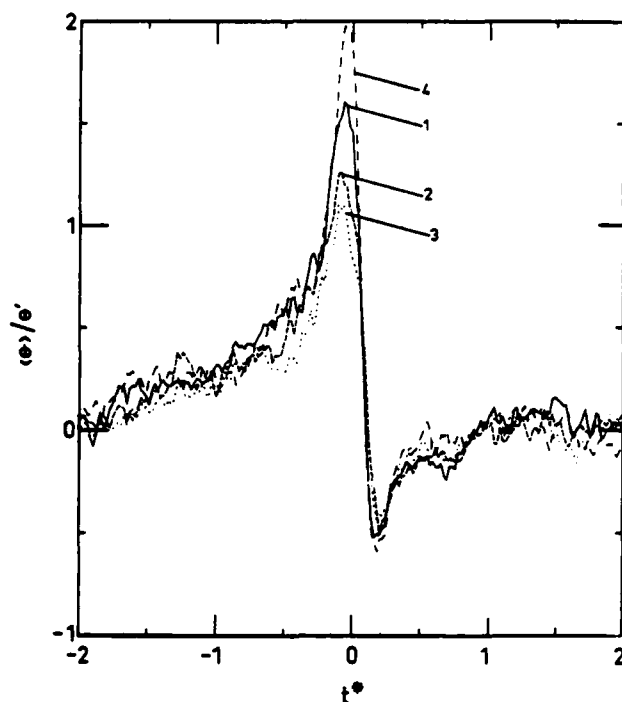


FIGURE 6 DISTRIBUTIONS OF $\langle \theta \rangle$ AT $z^* = 0.181$

Method	Identfn.	k	T*	y*	Sensors	f*
MPVITA	1	0.30	0.34	0.10	2, 3, 4	0.21
MPVITA	2	0.15	0.34	0.21	1, 3, 5	0.21
MPVITA	3	0.13	0.34	0.28	1, 3, 6	0.22
VITA	4	0.75	0.34	---	3	0.24

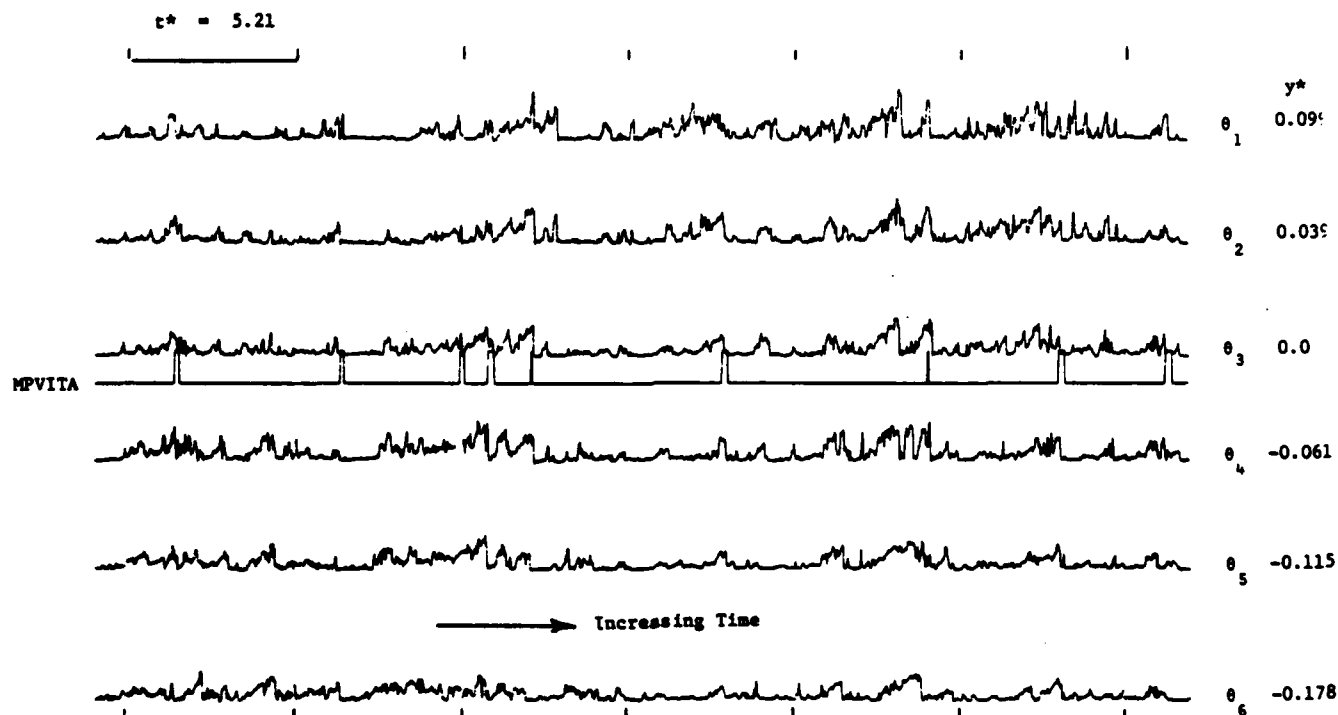


FIGURE 7 TIME SERIES θ_1 IN WHICH THE SENSORS ARE AT THE SAME $z^* = 0.18$ BUT DIFFERENT LATERAL POSITIONS
The pulse is generated using MPVITA (Identification 3, Figure 6)

about 65% and is larger than that achieved by VITA, 55%. Increasing k for MPVITA (keeping other parameters constant) will reduce the total number of events detected but increase the proportion of events that are in common with RAKE. In the Table, increasing k from 0.2 to 0.3 increases this correspondence from 70 to 84%. The correspondence between RAKE and VITA in the Table represents an improvement over that given in 1, possibly because of the low-pass filtering of θ before applying VITA. When VITA is applied to the unfiltered temperature signal and with T^* ($= 0.10$) and k ($= 1.55$) chosen to give $f^* = 0.23$, the correspondence with RAKE is only about 40%.

Distributions of conditional averages $\langle \theta_i \rangle$ at different spanwise locations in the boundary layer are shown in Figure 5. These were obtained using MPVITA with $N = 3$, $k = 0.2$ and $|\Delta y^*|_{\max} = 0.214$. Specifically, sensors 1, 3 and 5 (y^* values are given in caption of Figure 3) were used. For sensors 2 and 4, whose outputs were not used in the formation of D , $\langle \theta_i \rangle$ is the same as for sensors 1, 3, 5. In particular, there is remarkably little variation for $i = 1$ to 5 in the maximum amplitude of $\langle \theta_i \rangle$ near the origin. This behaviour was verified at other values of z^* greater than about 0.05 and suggests that it is not necessary to include extra sensors in the detection procedure when their locations fall within the span already covered by the (sensors used in the) algorithm. The conditional signature at sensor 6 differs appreciably from that which is common to all other sensors. When VITA is used to detect fronts at a particular location i of the array, averages at any other location j ($\neq i$), conditioned using the pulses generated at point i , are found to differ significantly from $\langle \theta_i \rangle$. In particular, the maximum value of $\langle \theta_i \rangle$ decreases quickly as the distance between points j and i increases.

Figure 6 compares $\langle \theta \rangle$ obtained with VITA and MPVITA for $N = 3$ but three different maximum values of $|\Delta y^*|_{\max}$ at $z^* = 0.18$. Temperature sensor 3, next to the X-wire, was used with VITA and MPVITA. The conditional distributions in Figure 6, obtained for approximately 200 fronts, are in qualitative agreement. However, the maximum value of $\langle \theta \rangle$ at or near $t^* = 0$ is largest when VITA is used. There may well be some degradation in the sharpness of the signature associated with MPVITA as a result of the inevitable, although small, uncertainty in precisely locating the position of the front when several points are involved in forming D . A possible palliative would be to use MPVITA for detection and then calculate averages using VITA after including in VITA only those events which are common with MPVITA.

A portion of the temperature time series for the array of cold wires used with MPVITA to obtain $\langle \theta \rangle$ in Figure 6 is shown in Figure 7. The output D , for MPVITA (method 3, Figure 7) shown below trace θ_3 , indicates good correspondence with the fronts. The pulse, labelled 1, is the only questionable occurrence while pulse marked 2 would strictly not qualify as a front as the ambient temperature is not reached in the upper trace at the location marked with an arrow.

CONCLUSION

The one point VITA technique has been extended to include detection of temperature fronts at several spanwise points. This extension represents an improvement in terms of correspondence of detection with the visual recognition of the fronts and should lead to more reliable conditional averages of velocity or temperature.

ACKNOWLEDGEMENTS

The first three authors gratefully acknowledge the support of the Australian Research Grants Scheme and the generous co-operation of the C.S.I.R.O., Division of Environmental Mechanics.

REFERENCES

- Antonia, R. A. : 1980. The Organised Motion in a Turbulent Boundary Layer, *Proc. 7th Australasian Hydraulics & Fluid Mechanics Conference*, Brisbane, 155-162.
- Antonia, R. A. : 1981. Conditional Sampling in Turbulence Measurement, *Ann. Rev. Fluid Mech.*, **13**, 131-156.
- Blackwelder, R. F. : 1979. Pattern Recognition of Coherent Eddies, *Proc. Dynamic Flow Conference - Dynamic Measurements in Unsteady Flows 1978*, Marseille/Baltimore, 173-190.
- Chen, C-H. P. and Blackwelder, R. F. : 1978. Large-Scale Motion in a Turbulent Boundary Layer : A Study Using Temperature Contamination, *J. Fluid Mech.*, **89**, 1-31.
- Falco, R. E. : 1977. Coherent Motions in the Outer Region of Turbulent Boundary Layers, *Phys. Fluids*, **20**, S124-S132.
- Fulachier, L., Giovanangeli, J., Dumas, R., Kovaszny, L. S. G. and Favre, A. : 1974. Structures des Perturbations dans une Couche Limite Turbulente : Zone Interne, *C.R. Acad. Sci. Paris, Series B*, **278**, 683-687.
- Kaplan, R. E. : 1973. Conditional Sampling Techniques, in G. K. Patterson and J. L. Zakin (eds.) *Turbulence in Liquids*, University of Missouri-Rolla, 274-283.
- Kovaszny, L. S. G. : 1979. Measurement in Intermittent and Periodic Flow, *Proc. Dynamic Flow Conference - Dynamic Measurements in Unsteady Flows 1978*, Marseille/Baltimore, 133-159.
- Rajagopalan, S., Subramanian, C. S., Antonia, R. A. and Chambers, A. J. : 1982. Spanwise Correlation of Temperature in a Turbulent Boundary Layer, *Phys. Fluids*, **25**, 1144-1145.
- Subramanian, C. S., Rajagopalan, S., Antonia, R. A. and Chambers, A. J. : 1982. Comparison of Conditional Sampling and Averaging Techniques in a Turbulent Boundary Layer, *J. Fluid Mech.*, **123**, 335-362.
- Van Atta, C. W. : 1979. Multi-Channel Measurements and High Order Statistics, *Proc. Dynamic Flow Conference - Dynamic Measurements in Unsteady Flows 1978*, Marseille/Baltimore, 919-941.
- Wynanski, I. : 1979. The Recognition of an Evoked Large Scale Structure, *Proc. Dynamic Flow Conference - Dynamic Measurements in Unsteady Flows 1978*, Marseille/Baltimore, 191-211.

A NEW DIAGNOSTIC TECHNIQUE FOR SIMULTANEOUS, TIME-RESOLVED MEASUREMENTS OF
CONCENTRATION AND VELOCITY IN SIMPLE TURBULENT FLOW SYSTEMS

William M. Pitts, B. J. McCaffrey, and Takashi Kashiwagi
Center for Fire Research
National Bureau of Standards
Washington, DC 20234

ABSTRACT

A new experimental method is described which allows the simultaneous real-time measurement of concentration and velocity in simple flow fields of binary gas mixtures. This method combines the use of Rayleigh light scattering for concentration measurements and hot-wire (or hot-film) anemometry. Calibration methods and representative results are discussed.

INTRODUCTION

As the first stage in a long range investigation of the complex coupling of aerodynamics and chemical heat release which occurs in chemically reacting turbulent flows, we have initiated an investigation of the effects on turbulent mixing of density differences between a simple gas jet and the surrounding gas. We have recently shown (Pitts and Kashiwagi 1983, 1983a) that laser-induced Rayleigh light scattering can be used as a simple diagnostic for absolute measurements of concentration in simple flow systems of two different gases. This technique is capable of high spatial and temporal resolution.

In order to more completely characterize the turbulent behavior in these flows it is also necessary to measure the velocity behavior. Ideally, it should be possible to measure concentration and velocity behavior simultaneously. Such measurements allow correlations to be calculated for the scalar value (concentration) and the vector quantity (velocity). Correlations of this type appear when the momentum equations describing turbulent flow are Reynolds- or Favre-averaged. A large portion of turbulence modelers' effort is required to estimate and justify values for these correlations. Despite the importance of these terms in turbulence theory and a great deal of effort to develop diagnostic techniques capable of simultaneous measurements of scalars and velocity, very few reliable results are available. In this work we will describe a new method based on the combination of Rayleigh light scattering and hot-wire or film techniques which will allow simultaneous velocity and concentration measurements in simple flow systems consisting of two gases.

BACKGROUND

The hot-wire and hot-film are velocity sensitive devices which have been widely used for velocity measurements in flows of single gases. For constant temperature operation, the electrical input to the device

* Certain commercial equipment, instruments, or materials are identified in this paper in order to adequately specify the experimental procedure. Such identification does not imply recommendation or endorsement by the National Bureau of Standards, nor does it imply that the materials or equipment are necessarily the best available for the purpose.

which is required to balance convective heat losses is often analyzed in terms of King's law, (King 1915):

$$E^2 = A + B\sqrt{V} \quad (1)$$

E is the voltage drop across the wire, and V is the projected velocity normal to the wire. A and B are parameters which depend on the wire dimensions and the composition of the surrounding gas.

Since E depends on both the composition and velocity of the gas, a single hot-wire or film cannot yield concentration and velocity in a flow where both properties are fluctuating. Way and Libby (1970) and McQuaid and Wright (1973) have attempted to overcome this limitation by using two different hot-wires (or a hot-wire and a hot-film) chosen so that the A and B values of each differed widely. For this case two independent equations are available, and in principle both concentration and velocity can be measured. However, the variations in voltage outputs for most gas pairs are not large enough to ensure accurate measurements. Some results have been reported by using a suitable choice of gas pairs (McQuaid and Wright 1974) or by letting the wires interact (Way and Libby 1971, Sirivat and Warhaft 1982). Unfortunately, this method is difficult to apply and has not come into widespread use.

It is clear that a much better means of obtaining reliable velocity values in a binary gas mixture using hot-wires is to measure concentration with an independent technique and then use this concentration value to derive values of A and B for substitution in Eq. (1). We have previously shown (Pitts and Kashiwagi 1983, 1983a) that the laser-induced Rayleigh scattering intensity from a binary gas mixture can be used to accurately determine the concentrations of the two gases. If hot-wire or film measurements could be made simultaneously within the same spatial volume, both concentration and velocity measurements could be obtained. In practice, this is not possible since scattering from the hot-wire or film will overwhelm the Rayleigh scattering intensity. However, when the scattering volume of the laser beam and the hot-wire can be located close enough together to ensure that their separation is small compared to the spatial scales of the concentration and velocity fluctuations, Eq. (1) can be used to obtain "simultaneous measurements" of concentration and velocity.

EXPERIMENTAL

Both hot-wires ($d = 4 \mu\text{m}$, $l/d = 330$) and hot-films ($d = 51 \mu\text{m}$, $l/d = 20$) have been used in this study. The probes as well as the anemometer electronics (model 1050) are from TSI, Inc.* All measurements have been made in the constant temperature mode. Standard velocities for anemometer calibrations were provided by a TSI calibrator (model 1125). Calibrations were performed for pure gases (air, CH_4 , C_2H_2 , and CO_2) and binary gas mixtures which were premixed in a holding tank.

Figure 1 shows the experimental apparatus used to perform simultaneous concentration and velocity measurements. It consists of the Rayleigh light scattering equipment which has been described in detail elsewhere (Pitts and Kashiwagi 1983, 1983a) and the anemometry set-up.

The flow system consists of an axisymmetric jet generated by a 6.35 mm i.d. nozzle and a 10.2 cm square glass enclosure through which a slow flow of the secondary gas is passed. The enclosure is necessary to prevent dust from entering the observation volume of the laser. The coflow volume flow rate is high enough to ensure that recirculation effects are absent. Both gas flows are filtered to remove particles. The entire flow system is mounted on a lathe bed which allows the fixed observation volume to be moved throughout the flow field.

Results will be reported for jet flows of CH_4 and C_3H_8 into air. Table 1 summarizes the flow conditions. V_0 is the average velocity for the jet, V_s is the surrounding coflow velocity, and Re is the Reynolds number defined as $\rho DV_0/\mu$, where ρ is the jet gas density, D is the jet diameter, and μ is the dynamic viscosity. Flow volumes are measured using calibrated rotameters.

Rayleigh scattering is induced by a CW argon ion laser with an output power of 7 W at 488 nm. The laser is focused to a diameter of 40 μm , and the observation volume is 400 μm in length. After collection at 90° the scattered light is detected by a photomultiplier. A frequency cutoff filter attenuates the high frequency components in the photomultiplier output before the time-resolved signal is digitized and stored in a Nicolet 1180 signal averaging computer.

The hot-wire or film is placed 1-2 mm above the center of the observation volume of the laser beam and is aligned along the propagation direction of the beam. This detector geometry makes the hot-film or wire sensitive to the axial component (U) of the flow velocity.

The anemometer output is digitized and stored simultaneously with the photomultiplier output. Up to 16,384 channels of each signal can be stored. For the experiments reported here, the digitization rate was 10 kHz. By performing calibrations for scattering from the pure gases, the Rayleigh signal can be converted directly into a time record of the concentration behavior. These concentrations are then used to generate values of A and B which are substituted into Eq. (1). Velocity values are then computed using the recorded voltages. The concentration and voltage time records can be offset by a fixed number of channels to allow for the time required for the fluid to flow from the observation volume of the laser beam to that of the velocity probe. Software has been written to calculate the average (\bar{U}) and rms (\bar{U}') of the time-resolved velocity data record. In addition, the correlation coefficient (R_{ux}) for the velocity and concentration can be calculated. This correlation coefficient is equal to $(\bar{u}-\bar{u})(\bar{u}-\bar{u})/\bar{u}^2$.

RESULTS

Hot-Wire and Film Calibrations in Gas Mixtures

As already noted, both hot-wires and films have been employed in this study. Hot-films have the advantage of being more sturdy and less likely to be broken. This advantage is offset somewhat by the smaller length to diameter ratio of the film compared to the wire. This smaller ratio complicates the application of heat transfer laws for infinite cylinders to the prediction of changes in hot-film response to variations in molecular properties and velocity. Additionally, earlier work (see Comte-Bellot (1977) for a discussion) indicates that a flow transition, which changes the heat transfer properties of the film or wire, occurs for $Re \approx 44$. This effect is only important for the hot-film at the flow velocities used in this study.

State-of-the-art calibrations of hot-wires or films generally avoid using heat transfer relations and instead fit polynomials directly to plots of voltage drop as a function of velocity. Despite this, we have chosen to fit our data using Eq. (1). In this way we are able to correlate the large amount of calibration data required, and the calculation of corrected velocities from recorded anemometer outputs is simplified. Our results indicate the use of this equation introduces errors in the results

which are less than 5% for the velocity ranges investigated.

Figure 2 shows changes in the voltage drop across a hot-wire as a function of velocity for several different methane/air mixtures. The solid curves drawn through the experimental points are least squares curve fits of Eq. (1). The insert within the figure shows the behavior of the parameters A and B as a function of methane mole fraction. These parameters have a linear dependence on concentration as indicated by the straight lines obtained from linear least squares curve fits.

The simple empirical heat transfer law of Kramers (1946) can be used to predict the behavior of the Nusselt number (Nu) for heat transfer from a cylinder.

$$Nu = 0.42(Pr)^{0.2} + 0.57(Pr)^{0.33}(Re)^{0.5} \quad (2)$$

where $Nu = hD/k$, $Pr = \mu C_p/k$, and the Reynolds number is that appropriate for flow past a cylinder. h is the heat transfer coefficient for the wire or film, k is the thermal conductivity of the gas, C_p is the specific heat of the gas, and the other molecular properties are as previously defined. The molecular properties are evaluated at the average of the heated wire or film and ambient gas temperatures. Using this law, it can be shown (Perry 1982) that the parameters A and B should have the following dependencies on molecular properties:

$$A \sim k(Pr)^{0.2} \quad (3)$$

$$B \sim k(Pr)^{0.33}(1/\nu)^{0.5} \quad (4)$$

The kinetic theory of gases shows that the transport properties of CH_4 /air mixtures should be linearly dependent on methane mole fraction. Since both Pr and ν (kinematic viscosity) are found to differ very little for CH_4 and air, A and B are predicted to be linearly dependent on CH_4 mole fraction, which is in good agreement with experimental observation.

A plot of E^2 versus $(V)^{0.5}$ for a hot-film in different C_3H_8 /air mixtures is shown in Fig. 3. A slight curvature can be seen in the plots, but linear least squares curve fits provide good representations of the experimental data. A and B values derived from these fits are shown as a function of C_3H_8 mole fraction in Fig. 4. The dependence of the parameters on mole fraction is highly nonlinear. Attempts to fit the dependencies of A and B to Eqs. 3 and 4 were unsuccessful. However, Fig. 5 shows that the C_3H_8 /air mixture results as well as other pure gas and mixture data can be well represented by

$$A \sim k(Ra)^{0.18} \quad (5)$$

where Ra is the Rayleigh number, which is equal to $Pr \cdot Gr$. Gr is the Grashof number and is expressed as $Gr = g\beta\Delta\theta D^3/\nu^2$, where g is the gravitational constant, $\Delta\theta$ is the temperature difference of the wire and surrounding gas, and β is the thermal coefficient of expansion of the gas. The dependence of A on Ra is somewhat surprising since most heat transfer laws for cylinders do not indicate a dependence on Gr , but an analysis of the physical dimensions of the hot-film and molecular gas properties indicates that mixed natural and forced convection effects should be important (Perry 1982). Figure 6 shows that the B values have a dependence on molecular properties which can be written as

$$B \sim k(Pr)^{0.21}/(\nu)^{0.71} \quad (6)$$

The fit of this equation is rather poor, and there are systematic variations in the data which indicate that B may have a more complicated dependence on molecular properties.

Using the results shown in Figs. 5 and 6, it would be possible to calculate values of A and B for any gas mixture involving C_3H_8 , CO_2 , air, or CH_4 . However, it would be necessary to generate the molecular properties for each different mixture. For this reason, we have chosen to model the dependencies of A and B on mole fraction for each gas pair using polynomial least squares curve fits. Such fits using second degree polynomials are shown in Fig. 4 for C_3H_8 /air mixtures. The calculated curves give a good representation of the experimental

data. Similar curves were found for C_3H_8/CO_2 mixtures, while linear dependencies were found for CH_4 /air mixtures for both the hot-film and hot-wire. Using these analytical expressions, it is possible to rapidly calculate accurate A and B values for any mixture of the gases we have studied. Once the A and B values are available, Eq. (1) can be used to convert a measured voltage drop across the hot-film or wire into a calculated velocity.

Measurements in Turbulent Flows

Figure 7 shows Rayleigh scattering intensity (converted to concentration values), voltage behavior of the hot-wire, and calculated velocity plotted as a function of time for a CH_4 jet flowing into air. This plot represents only a small portion of the entire real-time data record. These measurements were recorded at a downstream distance of z/r_0 (r_0 is the pipe radius) of 35 and an off-axis distance (r/r_0) of 6.9. This location is in the intermittent region of the jet, and both probes will spend part of the time in the coflow and part in the jet. This effect can be clearly seen in the concentration data where distinct "bursts" of CH_4 /air mixtures appear as spikes. The Rayleigh scattering intensity is noisy due to Poisson statistics which govern the detection of photons. Some of this noise is transferred to the velocity results when Eq. (1) is used to calculate U. However, it is clear that this noise is considerably less than the velocity fluctuations and will have a small effect on the statistical properties calculated for the time profile.

Examination of these plots shows that there is a partial correlation of the concentration and velocity. For instance, many of the large "bursts" of CH_4 are accompanied by sharp increases in flow velocity. This is expected since the presence of CH_4 indicates that the observation volume is within the boundary of the jet flow. The jet is turbulent and will have a higher velocity. Note that the velocities measured outside of the jet boundary (as indicated by the absence of CH_4) are close to the air coflow velocity of 0.27 m/s.

The average velocity at this point in the flow field is 0.38 m/s. A measurement on the jet centerline at the same downstream distance gives 2.76 m/s. Such a velocity falloff as a function of radial distance is expected for an axisymmetric jet.

Similar measurements have been made for a propane jet flowing into air. In this case a hot-film was used. Figure 8 shows time history plots of C_3H_8 concentration, anemometer voltage output, and calculated velocity on the centerline of the jet at $z/r_0 = 31.5$. Note that the concentration data are less noisy than those for CH_4 (Fig. 7). Propane scattering is much stronger than that of CH_4 , and the Poisson noise is substantially reduced. Like the CH_4 jet, the velocity and concentration fluctuations are partially correlated, but the correlation is clearly not total.

Measurements have been made for the C_3H_8 /air flow at several axial downstream positions. By varying the time delay between the concentration data and anemometer voltage data we find that the calculated average velocity (\bar{U}) is relatively insensitive to time delay, whereas the rms (\bar{U}) and, in particular, the cross correlation coefficient (R_{UX}) are extremely sensitive to the choice of this parameter. Calculations show that \bar{U} minimizes and R_{UX} maximizes at equivalent time delays, which we denote τ_D . τ_D was chosen as the appropriate time delay to use for the calculations. Table 2 lists values of τ_D , \bar{U} , \bar{U} , and R_{UX} for several downstream positions. In addition, \bar{U} and τ_D have been used to calculate the effective separation of the laser and hot-film. This separation is denoted z_s , and values are included in Table 2.

Pitot tube measurements of average velocity (\bar{U}_{pitot}) have been made for the same downstream positions as the hot-film measurements. These results have been corrected for gas density (from the Rayleigh scattering results) and velocity fluctuations (from the hot-film results) using this relation,

$$\bar{U}_{pitot} = (2\Delta P/\rho) \left(1 + \frac{\bar{U}^2}{\bar{U}^2 + 2(\rho/\bar{\rho})(\bar{U}-\bar{U})/\bar{\rho}\bar{U}} \right) \quad (7)$$

ΔP is the pressure drop across the pitot tube, and the other symbols are as already defined. Results of these

measurements are also included in Table 2.

DISCUSSION

The goal of this work has been to demonstrate the feasibility of performing simultaneous real-time measurements of concentration and velocity in binary gas mixtures. A validation of the technique requires answers to two questions: 1) Can suitable relationships be found to describe the behaviors of hot-wires and films in flows of variable gas composition?, and 2) Is the time response sufficiently high and the noise level sufficiently low to allow accurate measurements of \bar{U} and R_{UX} ? We will show that the answer to the first question is "yes" and to the second a qualified "yes".

Our calculations have shown that the determination of \bar{U} for C_3H_8 /air flows is strongly dependent on the average voltage drop across the sensor and the calibration parameters used in Eq. (1). The intensity of the concentration or velocity fluctuations has very little effect on the calculated value of \bar{U} . These measurements thus provide an answer to the first question. In Table 2 we list a comparison of \bar{U} recorded using both a hot-film and a pitot tube at varying positions along the centerline of the jet. On the average the hot-film gives results for \bar{U} which are 4.6% less than those obtained from the pitot tube. Given the widely different responses of these devices to concentration changes and the approximate nature of the hot-film calibrations, this agreement is considered excellent.

A second test of the \bar{U} measurements can be made by comparison of these results with those found in other studies. In general, it has been shown that plots of \bar{U}_0/\bar{U}_c versus z/r_0 are linear. Figure 9 shows the results of Table 2 plotted in this way. A very good straight line is found which can be represented as

$$\bar{U}_0/\bar{U}_c = C_1^{U'}(z-z_0^{1U})/r_0 \quad (8)$$

$C_1^{U'}$ is the slope of the line, and z_0^{1U} is a virtual origin for the plot. The data shown in the plot give $C_1^{U'} = 0.065$ and $z_0^{1U} = -7.0r_0$. Thriving and Newby (1953) have argued that plots of this type for different density jets can be collapsed to a single curve by using the concept of an effective radius (r_e) where

$$r_e = r_0(\rho_{propane}/\rho_{air})^{1/2} \quad (9)$$

When \bar{U}_0/\bar{U}_c is plotted against r_e , the slope (C_1^U) is found to be 0.082. List (1982) has compared many studies in the literature and recommends a value equivalent to $(C_1^U)_{air} = 0.081$ for air/air jets. The agreement of this value with our result is outstanding.

Due to the large differences in the molecular properties of C_3H_8 and air, velocity measurements in mixtures of these gases are extremely sensitive to changes in molecular composition. These mixtures are thus an excellent test of the ability of this technique to measure velocities in variable composition flows. The results discussed above indicate that this new technique is capable of measuring accurate average velocities and that our hot-film calibrations and calculational methods are adequate.

It is very difficult to show that our calculated velocity time profiles accurately reflect the actual behavior of the fluid velocity. There are many reports of problems associated with the use of hot-wires and films (eg. Comte-Bellot 1977, Perry 1982) in the absence of the complications introduced by concentration fluctuations and the separation of the observational volumes for the Rayleigh scattering and the heated cylinder. Furthermore, there are very few reliable studies with which to compare our results for \bar{U} and R_{UX} . In this context, perhaps the best we can hope to show is that our results are reasonable and are consistent with similar measurements which can be found in the literature.

Two important points which must be addressed are the time response of the technique and the effect of the spatial separation of the concentration and velocity probes. The time response of the Rayleigh scattering measurements has been analyzed (Pitts and Kashiwagi 1983, 1983a) and for this study was 5 kHz. The time response behavior of the hot-wire or film to combined velocity and

concentration fluctuations is very difficult to predict. However, visual comparisons of the light scattering and voltage time profiles shown in Figs. 7 and 8 indicate that the response of each is fast enough to follow changes which occur in the flows investigated here. This conclusion is supported by calculated power spectra for the Rayleigh scattering and voltage data which are nearly identical.

The results for z_s in Table 2 show that the laser beam and hot-film are separated by ≈ 1.5 mm. This separation is only slightly larger than the length of the hot-film (1 mm) and thus is not inconsistent with the smallest scales which can be measured in the flow. Measurements show that this separation may affect values of \bar{U} and/or R_{UX} at small values of z (where spatial scales are smaller), but that the effect decreases as z is increased.

Since the velocity decreases as a function of z , a frequency limit on the measurement of velocity would be expected to affect \bar{U} recorded at smaller downstream distances more than measurements made further downstream. Figure 10 shows a plot of \bar{U}_0/\bar{U}_c as a function of z/r_0 . It is well known that plots of this type are usually linear. The results of Table 2 do give a linear plot which can be fit by an equation of the form

$$\bar{U}_0/\bar{U}_c = C_2^U(z - z_0^{2U})/r_0 \quad (10)$$

where $C_2^U = 0.32$ and $z_0^{2U} = -10.4r_0$.

An asymptotic value for the fluctuation intensity can be found by dividing C_V^U by C_2^U to give $(\bar{U}_c/\bar{U}_c)_{as} = 0.20$. McQuaid and Wright (1974) have reported values of $(\bar{U}_c/\bar{U}_c)_{as}$ for a CO_2/air ($\rho_{\text{carbon dioxide}} = \rho_{\text{propane}}$) jet which indicate an asymptotic value > 0.25 . However, Wagnanski and Fiedler (1969) have made measurements on air/air jets which indicate $(\bar{U}_c/\bar{U}_c)_{as} \approx 0.28$. We have shown (unpublished results) that the negatively buoyant $\text{C}_3\text{H}_8/\text{air}$ jet has a smaller unmixedness $(\bar{X}_c/\bar{X}_c)_{as}$ than air/air jets. It seems reasonable to assume that $(\bar{U}_c/\bar{U}_c)_{as}$ would also be smaller. If so, our measured value of 0.20 would be consistent with the results of Wagnanski and Fiedler (1969). Until more reliable comparisons can be made, we can only state that our measurements may be somewhat low, but are consistent with past results.

Table 2 lists measured values of R_{UX} as a function of z/r_0 . The measurements are erratic, but appear to indicate values of $\approx +0.45$ for downstream values of R_{UX} . It is worth noting that when random voltage data or an assumed constant voltage output is combined with concentration data to give a calculated velocity profile, a strongly negative correlation is calculated.

For an argon/air jet, which is nearly as negatively buoyant as a $\text{C}_3\text{H}_8/\text{air}$ jet, McQuaid and Wright (1974) measured R_{UX} values which rose to a maximum of ≈ 0.7 at $z/r_0 \approx 16$ and then fell to ≈ 0.53 at $z/r_0 \approx 40$. The validity of a comparison of these results with our measurements is in doubt since these authors measured an unmixedness of ≈ 0.35 for the Ar/air jet, while our result for the $\text{C}_3\text{H}_8/\text{air}$ jet is $(\bar{X}_c/\bar{X}_c)_{as} \approx 0.27$ (unpublished data).

A few measurements of R_{UX} for air/air jets are available for various downstream distances. These results were obtained using marked (either heat or particles) jets and are summarized in Table 3. These values of R_{UX} are in good agreement with our results. Since these measurements were obtained using different experimental techniques, they provide a strong indication that our measurements of R_{UX} fall in the proper range.

It is clear that our calculated time profiles for velocity are consistent with the limited literature results available. Since our measurements are extremely sensitive to calibration constants, concentrations, and τ_D values, we conclude that Rayleigh scattering measurements of concentration do provide a suitable and straightforward means of correcting hot-wire or film results in order to obtain real time velocity profiles in binary mixtures where concentration is fluctuating.

FINAL REMARKS

This work has demonstrated that the combination of Rayleigh light scattering and hot-probe techniques

provides a powerful new diagnostic for simultaneous concentration and velocity measurement. Further work is required to assess possible sources of errors and limitations on such measurements. We hope that this work will stimulate other workers to adopt the use of heated probes in velocity fields having varying composition.

ACKNOWLEDGMENT

This work has been partially supported by the Air Force Office of Scientific Research (contract #MIPR 83-00012).

BIBLIOGRAPHY

- [1] Antonia, R.A., Prabhu, A., and Stephenson, S.E., 1975, "Conditionally Sampled Measurements in a Heated Turbulent Jet", *J. Fluid Mech.*, 72, 455.
- [2] Catalano, G.D., Morton, J.B., and Humphris, R.R., 1976, "Experimental Investigation of an Axisymmetric Jet in a Coflowing Airstream", *AIAA J.*, 14, 1157.
- [3] Chevray, R., and Tutu, N.K., 1978, "Intermittency and Preferential Transport of Heat in a Round Jet", *J. Fluid Mech.*, 88, 133.
- [4] Comet-Bellot, G., 1977, "Hot-Wire and Hot-Film Anemometers", in *Measurements of Unsteady Fluid Dynamic Phenomena* (ed. B.E. Richards), Hemisphere Publishing Corp.
- [5] King, L.V., 1915, "On the Precision Measurement of Air Velocity by Means of the Linear Hot-Wire Anemometer", *Phil. Mag.*, 29, 556.
- [6] Kramers, H., 1946, "Heat Transfer from Spheres to Flowing Media", *Physica*, 12, 61.
- [7] List, E.J., 1982, "Mechanics of Turbulent Buoyant Jets and Plumes", in *Turbulent Buoyant Jets and Plumes* (ed. W. Rodi), Pergamon Press.
- [8] McQuaid, J., and Wright, W., 1973, "The Response of a Hot-Wire Anemometer in Flows of Gas Mixtures", *Int. J. Heat Mass Trans.*, 16, 819.
- [9] McQuaid J., and Wright, W., 1974, "Turbulence Measurements with Hot-Wire Anemometry in Non-Homogeneous Jets", *Int. J. Heat Mass Trans.*, 17, 341.
- [10] Perry, A.E., 1982, *Hot-Wire Anemometry*, Oxford University Press.
- [11] Pitts, W.M., and Kashiwagi, T., 1983, "The Application of Laser-Induced Rayleigh Light Scattering to the Study of Turbulent Mixing", NBSIR 83-2644, National Bureau of Standards Internal Report.
- [12] Pitts, W.M., and Kashiwagi, T., 1983a, "The Application of Laser-Induced Rayleigh Light Scattering to the Study of Turbulent Mixing", submitted for publication in *J. Fluid Mech.*
- [13] Srivast, A., and Warhaft, Z., 1982, "The Mixing of Passive Helium and Temperature Fluctuations in Grid Turbulence", *J. Fluid Mech.*, 120, 475.
- [14] Thring, M.W., and Newby, M.P., 1953, "Combustion Length of Enclosed Turbulent Jet Flames", in the Fourth Symposium (International) on Combustion, The Standing Committee on Combustion, 789.
- [15] Way, J., and Libby, P.A., 1970, "Hot-Wire Probes for Measuring Velocity and Concentration in Helium-air Mixtures", *AIAA J.*, 8, 976.
- [16] Way, J., and Libby, P.A., 1971, "Application of Hot-Wire Anemometry and Digital Techniques to Measurement in a Turbulent Helium Jet", *AIAA J.*, 9, 1567.
- [17] Wagnanski, I., and Fiedler, H., 1969, "Some Measurements in the Self-Preserving Jet", *J. Fluid Mech.*, 38, 577.

Table 1			
Flow Conditions			
Gas Pair	V_0 (m/s)	V_s (m/s)	Re
CH_4/air	10.2	0.27	4130
$\text{C}_3\text{H}_8/\text{air}$	5.4	0.28	8260

Table 2

Results for C ₃ H ₈ /Air Jet						
z/r_0	τ_D (ms)	z_s (mm)	\bar{U} (m/s)	\bar{U}_{pitot} (m/s)	\bar{U} (m/s)	R_{UX}
15.7	0.34	1.4	4.06	4.39	0.73	0.26
23.6	0.45	1.5	3.19	3.30	0.59	0.25
31.5	0.6	1.5	2.57	2.61	0.47	0.40
39.4	0.7	1.4	2.02	2.15	0.38	0.38
47.2	0.9	1.6	1.74	1.81	0.34	0.39
55.1	1.1	1.7	1.55	1.59	0.30	0.46

Table 3

Selected Values of R_{UX} for Air/Air Jets			
z/r_0	R_{UX}	Marker	Reference
30	0.39	heat	Antonia et al. (1975)
118	0.48	heat	Chevray and Tutu (1978)
16	0.40	particles	Catalano et al. (1976)

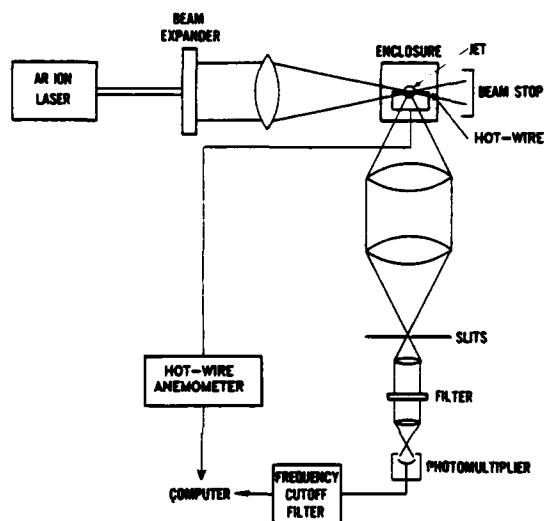


Figure 1. Experimental apparatus for simultaneous concentration and velocity measurements.

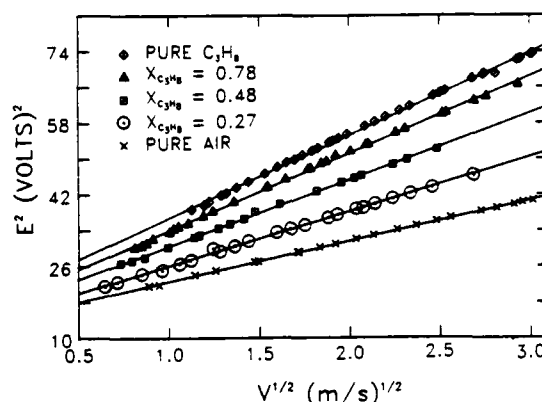


Figure 3. Plot of hot-film voltages squared versus the square root of velocity for the propane concentrations listed. Solid lines are linear least squares fits of the data.

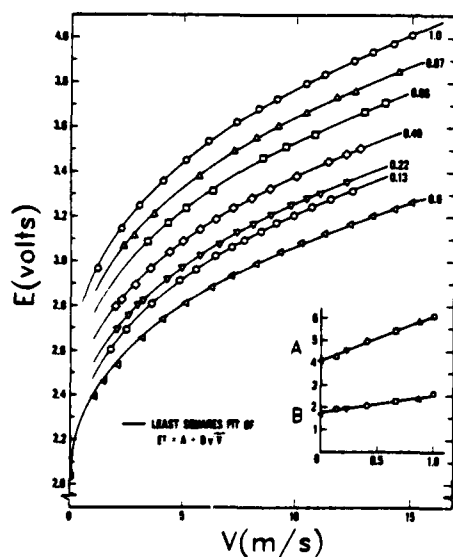
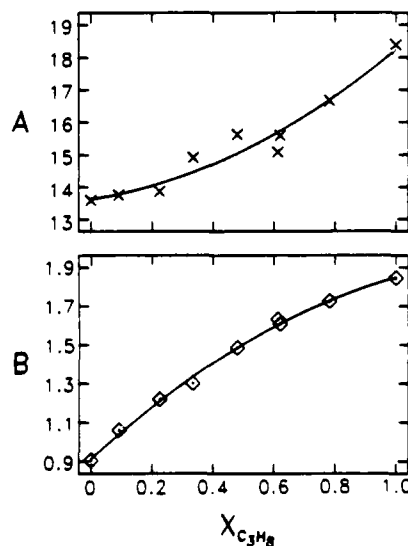
Figure 2. Voltage drop across a hot-wire as a function of flow velocity for several different methane-air mixtures (values of CH₄ mole fraction listed beside curves). Solid lines are least squares curve fits of Eq. 1. Insert shows corresponding A and B values fit to linear least squares curve fits.

Figure 4. Values of A and B (from Eq. 1) for a hot-film as a function of propane concentration. Solid lines are least squares curve fits of data to second degree polynomials.

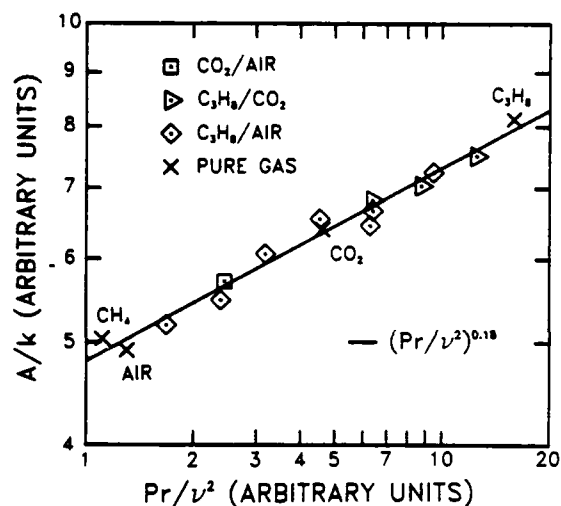


Figure 5. Log-log plot of A/k versus Pr/ν^2 , in arbitrary units, for the pure gases and mixtures listed. The solid line is a linear least squares curve fit of the data. For constant hot-film temperature $Gr \sim 1/\nu^2$, and the line is proportional to $(Pr \cdot Gr)^{0.18} = (Ra)^{0.18}$.

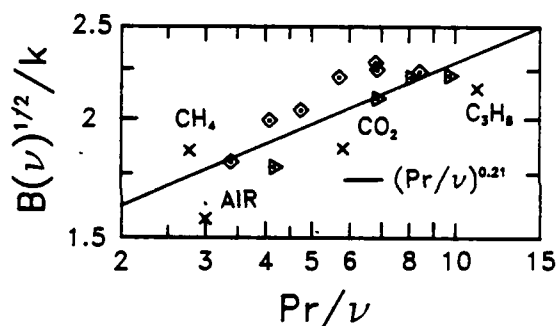


Figure 6. Log-log plot of arbitrary values for $B(\nu)^{0.5}/k$ versus Pr/ν for pure gases and mixtures. Symbols are the same as in Fig. 5. The solid line is a least squares fit of the results and indicates $B \sim kPr/(\nu)^{0.71}$.

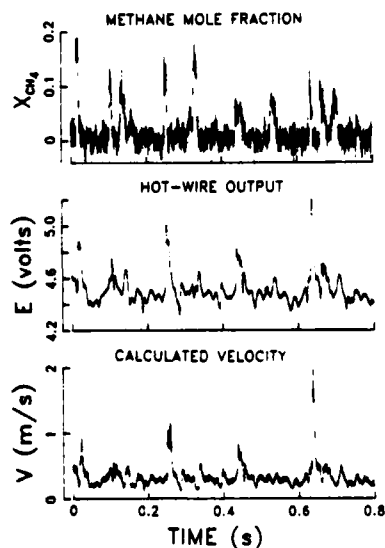


Figure 7. Time histories of concentration, hot-wire output, and calculated velocity for a methane-air jet. The probes are located at $z/r_0=35$, $r/r_0=6.9$.

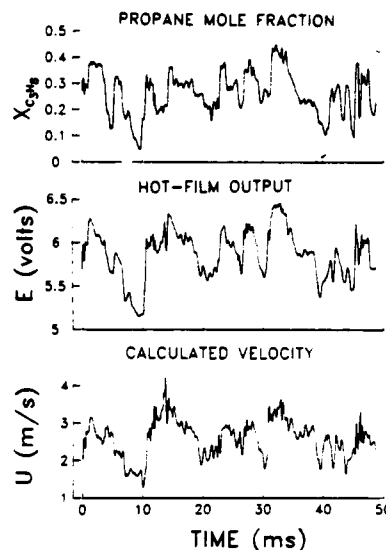


Figure 8. Time histories of concentration, hot-film output, and calculated velocity for a propane-air jet. The probes are located at $z/r_0=31.5$, $r/r_0=0$.

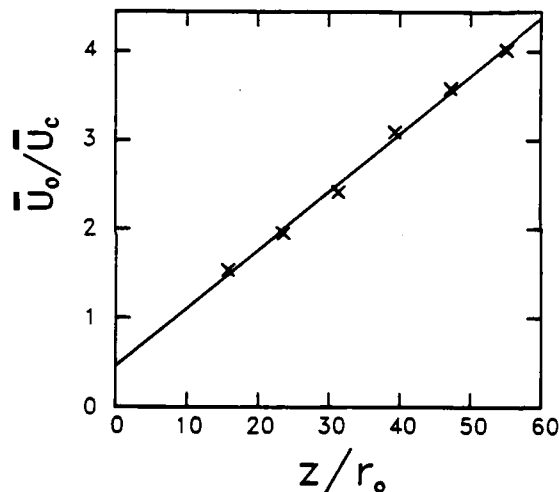


Figure 9. Inverse centerline velocity (normalized by exit velocity) of a propane jet is plotted as a function of nondimensionalized downstream distance. The solid line is a linear least squares fit of the data.

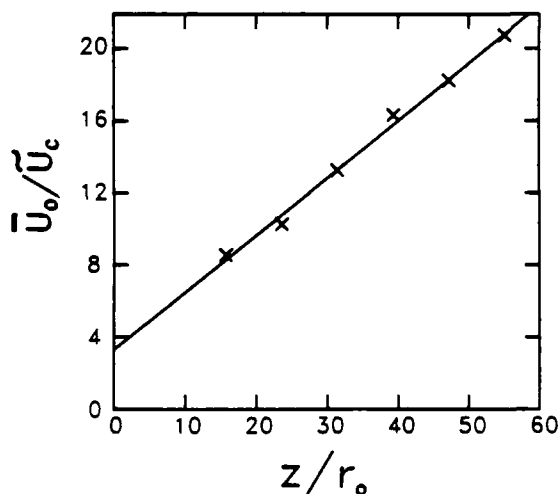


Figure 10. Inverse centerline rms velocity (normalized by exit velocity) of a propane jet is plotted as a function of nondimensionalized downstream distance. The solid line is a linear least squares fit of the data.

SESSION 16 - COHERENT STRUCTURES

A.K.M.F. Hussain - Chairman

TRANSITION TO TURBULENCE IN A SPHERICAL GAP

K. Bühler and J. Zierep

Universität (TH) Karlsruhe
Institut für Strömungslehre und Strömungsmaschinen
Kaiserstrasse 12, D-7500 Karlsruhe 1
Federal Republic of Germany

ABSTRACT

The present investigation deals with the transition to turbulence and the behaviour of turbulent flow in spherical gaps. Different initial and boundary conditions result in different routes of the transition from laminar to turbulent flows. The observed bifurcations are visualized and described. An analysis of the onset of turbulence is given for the case of a "sudden-acceleration" of the inner sphere.

INTRODUCTION

Basic aspects of the transition to turbulence are discussed for the gap flow between two concentric rotating spheres. Such aspects of these transitions are described in the book of SWINNEY and GOLLUB (1981) and in the paper of GOLLUB and BENSON (1980). Several authors try to describe the transition to turbulent flow with simplified mathematical models. The present situation may be summarized by MARSDEN's (1977) remark, that no solution of the Navier-Stokes equation is known that described a turbulent flow. In view of the exceptional mathematical difficulties connected with bifurcation processes, flows are of interest, which exhibit a sudden transition to turbulence, SCHULTZ-GRUNOW (1980). Such a process without discrete bifurcations can be realized in the spherical gap flow with a "sudden-acceleration" of the inner sphere.

SPHERICAL-GAP GEOMETRY

The experimental arrangement is principally shown in figure 1. The inner rotating sphere is surrounded by a transparent outer sphere at rest. The gap is filled with silicone oil with a kinematic viscosity of $\nu = 8 \cdot 10^{-6} \text{ m}^2/\text{s}$. Small aluminium flakes makes the flow visible. The dynamical behaviour of the flow is recorded by pressure measurements through holes in the equatorial plane of the outer sphere.

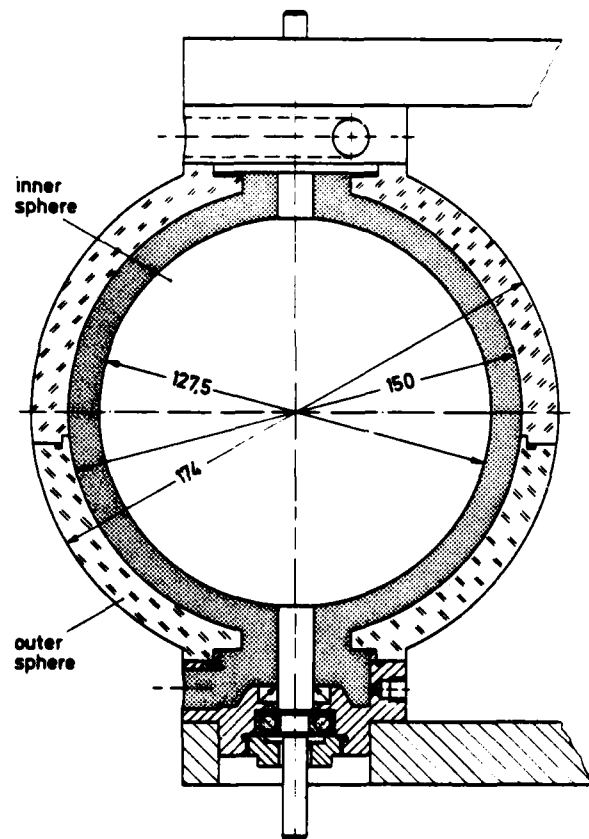


Fig. 1: Gap geometry of the experimental arrangements
 $R_2 = 75 \text{ mm}$, $R_1 = 63.75 \text{ mm}$, $\eta = R_1/R_2 = 0.85$,
 $\sigma = s/R_1 = 0.177$

SPHERICAL-GAP FLOW

The non-uniqueness of the solutions in the case of spherical gap flows at the same Reynolds number were first shown by SAWATZKI and ZIEREP (1970). The three different steady modes are shown schematically in figure 2. Mode I represents the rotationally symmetric three-dimensional basic flow without vortices. Mode III contains two vortices near the equator. Due to the basic flow the vor-

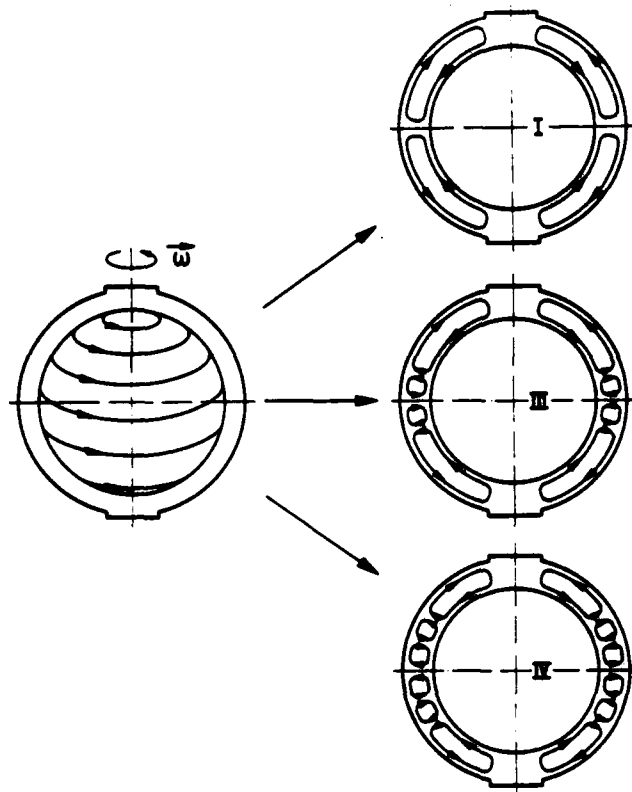


Fig. 2: Different steady and rotational symmetric modes of flow at supercritical Reynolds number

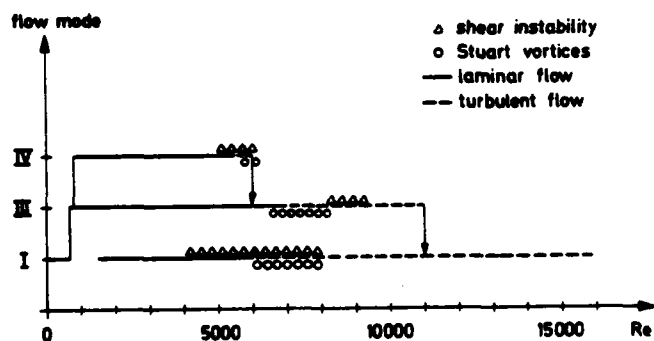


Fig. 3: Existence regions of the flow modes and different kind of instabilities

tices are directed inwards in the equatorial plane. Mode IV consists of four vortices near the equator. These modes can be realized by different accelerations of the inner sphere as shown by WIMMER (1976). Other aspects of these flows are also investigated by YAVORSKAYA et al. (1980) theoretically and experimentally. Based on these modes the transition to turbulence is now investigated for increasing Reynolds number.

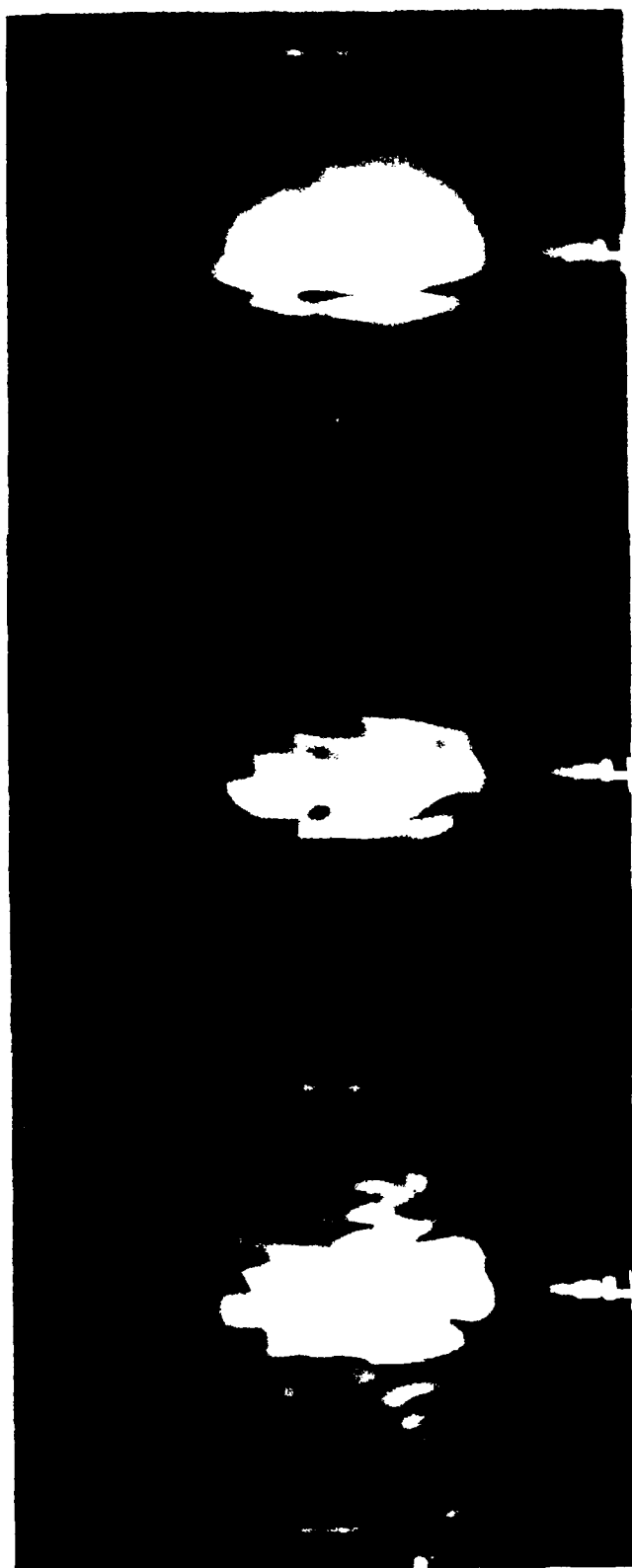
QUASISTATIC INCREASE OF REYNOLDS NUMBER

The flow regions for the different modes are plotted as a function of the Reynolds number in figure 3. The solid line represents laminar flow whereas dashed line shows partial or full turbulent flow regions. Characteristic instabilities are marked separately in figure 3.

Mode I: Figure 4 shows flow patterns for different Reynolds numbers. Shear instabilities directed from the poles toward the equator as shown in figure 4a occur for Reynolds numbers $Re > 4000$. Due to these shear instabilities the flow in the equatorial plane becomes wavy. For Reynolds numbers $Re > 6000$ Stuart vortices formed near the poles. The interaction between Stuart vortices and shear instabilities leads to a stochastic motion as shown in figure 4b. With increasing Reynolds number the turbulent flow region increases from the poles toward the equator and results in a large scale structure of the turbulent flow as shown in figure 4c. The characteristic length scale of the turbulent motion is of the order of the gap width, as marked by the distance of the two arrows. The waviness in the equatorial plane exists up to a Reynolds number $Re = 10\,000$. With increasing Reynolds number the influence of the secondary motion must be considered. Then, the length scale of the turbulence structure shrinks since with increasing Reynolds number the boundary-layer thickness decreases.

Mode III: Typical flow states are shown in figure 5 for different Reynolds numbers. These modes become unstable near the poles with respect to Stuart vortices for Reynolds numbers $Re > 6500$. These vortices with spiral axes are seen in figure 5a. Near $Re = 7000$ a sudden onset of stochastic motion occurs in the two vortices. The structure of these turbulent vortices can be seen clearly in figure 5b. For Reynolds numbers $Re > 8200$ shear instability becomes important, resulting in a waviness of the vortex boundaries and in a turbulent motion as shown in figure 5c. For Reynolds numbers $Re > 11\,000$ the vortices disappear in the basic flow so that mode I is established, but in a turbulent state.

Mode IV: This flow state with four vortices near the equator is shown in figure 6a. For Reynolds numbers $Re > 5000$ shear instability is found in spiral form from the poles toward the vortices. This leads to a waviness of the vortex boundaries as shown in figure 6b. For Reynolds numbers $Re > 5900$ Stuart vortices occur. The interaction between these Stuart vortices and shear instability leads to a stochastic motion as shown in figure 6c. If the turbulent region reaches the vortices near $Re > 6000$, a transition takes place to mode III. At this Reynolds number then the flow is completely laminar.



a) $Re = 4850$ b) $Re = 5750$ c) $Re = 6200$

Fig. 4: Mode I at different Reynolds numbers
 $Re = P_0 \cdot \omega / \nu$, the large arrow marks the equatorial plane



a) $Re = 6630$ b) $Re = 7700$ c) $Re = 8500$

Fig. 5: Mode III at different Reynolds numbers



a) $Re = 2450$ b) $Re = 5900$ c) $Re = 6260$

Fig. 6: Mode IV at different Reynolds numbers



a) t_0 b) t_0, t_1 c) t_0, t_2

Fig. 7: Growth of the turbulent region with time after a sudden acceleration to a final Reynolds number $Re_f = 2.1 \cdot 10^4$

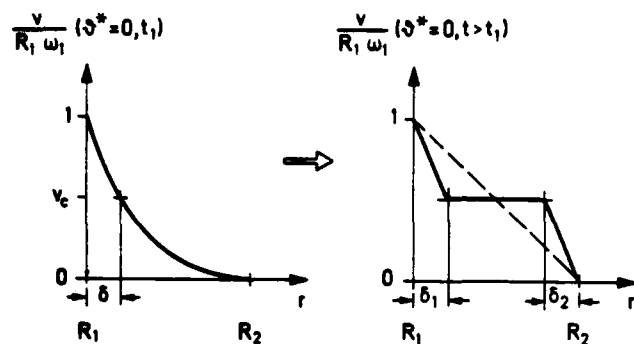


Fig. 8: Characteristic circumferential velocity distribution at the equator, on the left just before and on the right after the onset of turbulent motion

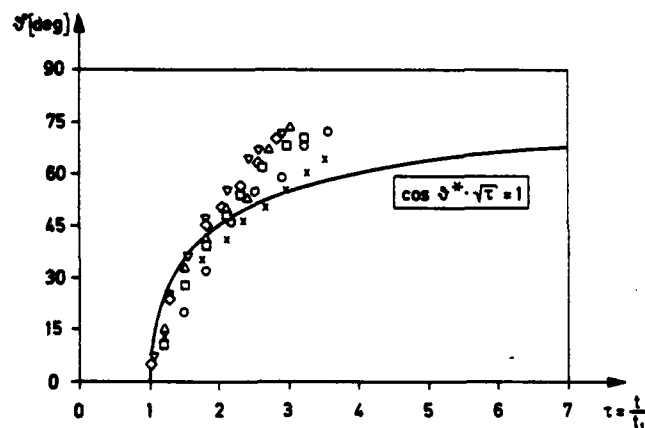


Fig. 9: Comparison of theoretical and experimental results

SUDDEN INCREASE OF REYNOLDS NUMBER

In the case of a "sudden-start" of the inner sphere to a final Reynolds number $Re_E \geq 8000$ the secondary motion starts suddenly in a turbulent form. The visualization of such an experiment is shown in figure 7. The turbulent motion starts in the equatorial region after a dead time since the sudden-start of the inner sphere. With increasing time, the turbulent region grows towards the poles. The turbulence structure is a function of the meridional coordinate ϑ^* . The time dependence of this event is typical and influenced by the final Reynolds number. The circumferential velocity profiles before and after the onset of the turbulent motion are shown schematically in figure 8. A time-dependent boundary layer is formed by the moving inner sphere similar to the plate-plate problem of Rayleigh-Stokes. After a characteristic deadtime t_1 this boundary layer profile becomes unstable and changes into

two boundary layers near the inner and outer sphere. Between these boundary layers the angular momentum is transferred by turbulent fluctuations. This transition from the laminar to the turbulent circumferential velocity distribution depends on the meridional coordinate while the circumferential velocity decreases with increasing ϑ^* . This fact is given by formula (1).

$$v(R_1, \vartheta^*) = R_1 \omega_1 \cdot \cos \vartheta^* \quad (1)$$

The development of the boundary layer in radial direction is given by relation (2).

$$v(r, \vartheta^*, t) = v(R_1, \vartheta^*) \cdot \operatorname{erfc} \frac{r^*}{2\sqrt{\nu t}} \quad (2)$$

r^* is the gap coordinate and erfc the complementary error function.

For $t \ll 1$ the asymptotic solution is

$$\cos \vartheta^* \cdot \sqrt{\tau} = 1 \quad \text{with} \quad \tau = \frac{t}{t_1} \quad (3)$$

This relation describes for a short time the onset of turbulent motion independent of the final Reynolds number. Experimental results are shown in figure 9 for final Reynolds numbers of $8 \cdot 10^3 < Re_E < 4 \cdot 10^4$. Figure 9 includes also the analytical solution. Within the experimental error a good agreement between theory and experiment is found.

CONCLUSION

The experimental results show different routes for the laminar-turbulent transition of spherical gap flows. Starting from different initial conditions one obtains over discrete bifurcations various transitions to turbulence. By means of the "sudden-start" experiment a direct transition turbulence without bifurcations is achieved. The time- and space-dependent onset of turbulent motion can be described by a universal relation derived from the Rayleigh-Stokes problem for the flat plate.

REFERENCES

- Swinney, H.L., and Gollub, J.P., 1981, "Hydrodynamic Instabilities and the Transition to Turbulence". Topics in Applied Physics, Vol. 45, Springer Berlin
- Gollub, J.P., and Benson, S.V., 1980, "Many routes to turbulent convection". J. Fluid Mech., vol. 100, 3, pp. 449-470
- Marsden, I.E., 1977, "Attempts to relate the Navier-Stokes Equations to Turbulence". Turbulence Seminar Berkeley 1976/77, Lecture Notes in Mathematics, No. 615, Springer Berlin

Schultz-Grunow, F., 1980, "Sudden transition to turbulence". IUTAM Symposium on Laminar-Turbulent Transition, pp. 388-395, Springer Berlin

Sawatzki, O., and Zierep, J., 1970, "Das Stromfeld im Spalt zwischen zwei konzentrischen Kugelflächen, von denen die innere rotiert". Acta Mechanica 9, S. 13-35

Zierep, J., and Sawatzki, O., 1970, "Three dimensional instabilities and vortices between two rotating spheres". Proceedings Eighth Symposium on Naval Hydrodynamics, Pasadena, pp. 275-283

Wimmer, M., 1976, "Experiments on a viscous fluid flow between concentric rotating spheres". J. Fluid Mech. 78, pp. 317-335

Yavorskaya, M.I., Belyaev, Yu.N., Monakhov, A.A., Astaf'eva, N.M., Scherbakov, S.A., and Vvedenskaya, N.D., 1980, "Stability non-uniqueness and transition to turbulence in the flow between two rotating spheres". Proceedings XVth Int. Congr. of Theoretical and Appl. Mechanics Toronto, pp. 431-443

A PERSPECTIVE VIEW OF THE PLANE MIXING LAYER

Javier Jimenez
IBM Scientific Center
Paseo Castellana 4, Madrid-1, Spain

Marta Cogollos
School of Aeronautics
Univ. Politecnica Madrid, Madrid-3, Spain

Luis P. Bernal (*)
California Institute of Technology
Pasadena, Ca. 91125

ABSTRACT

A three-dimensional model of the plane mixing layer is constructed by applying digital image processing and computer graphic techniques to laser fluorescent motion pictures of its transversal sections. A system of streamwise vortex pairs is shown to exist on top of the classical spanwise eddies. Its influence on mixing is examined.

INTRODUCTION

Some evidence has appeared lately implying that the nominally plane turbulent mixing layer contains secondary structures involving the deformation of the primary large scale eddies along their span (Konrad, 1976, Browand and Troutt, 1980, Roshko, 1980, Jimenez, 1983). That structure has been interpreted in some cases as being produced by an array of longitudinal (streamwise) vortex pairs sitting approximately on the braids connecting consecutive primary (spanwise) eddies (see Figure 1). Such an arrangement had been predicted theoretically on the grounds that any streamwise vorticity injected accidentally into the braids would be stretched by the straining field produced by the primary eddies into long longitudinal vortices (Corcos, 1979). Some measurements of the strength of these proposed vortices are given in Jimenez (1983), where their circulation is shown to be of the same order as that contained in each wavelength of the primary Kelvin-Helmholtz instability responsible for the formation of the primary eddies. This suggests that the longitudinal structures form as a result of the deformation of those initial two-dimensional eddies due to a three-dimensional instability.

Such instabilities have been studied theoretically by Pierrehumbert and Widnall (1982) and take the form of a wavelike deformation along the span of the two-dimensional vortices. Such a wavelike structure is strongly implied by pictures of the transition region published by Breidenthal (1981). The idea is that those waves will be stretched by the Corcos (1979) mechanism to give the elongated structures observed later in the flow. The motion pictures published in (Roshko, 1980, Bernal, 1981b) offer a direct visualisation of spanwise sections of the concentration field and clearly show longitudinal structures compatible with

the vortex pair model. We analyse here those pictures using image processing and computer graphic techniques with the purpose of reconstructing the three-dimensional topology of the flow and of determining the influence of the longitudinal structure on mixing.

EXPERIMENT AND DATA PROCESSING

The experimental arrangement and the original motion pictures are described in Bernal (1981b). The apparatus itself is the same one used by Breidenthal (1981). A mixing layer is established between two water streams in a tunnel with a 7x11 cm. cross section. One of the streams - the low speed one - contains a dye that fluoresces when illuminated with a sheet of laser light of the proper wavelength, and which is arranged perpendicular to the stream direction. Since the dye is transparent to the fluorescent radiation, the illuminated section can be observed through the body of the dyed stream (Dimotakis, unpublished). For our analysis we have used motion pictures of the time evolution of one such section. A frame from one of the films is shown in Figure 2.a; the flow comes towards the observer with the dye being contained in the light region on top. That section corresponds to a braid separating two large eddies, and the "curly" structures visible in the interface are the ones due to the longitudinal vortices.

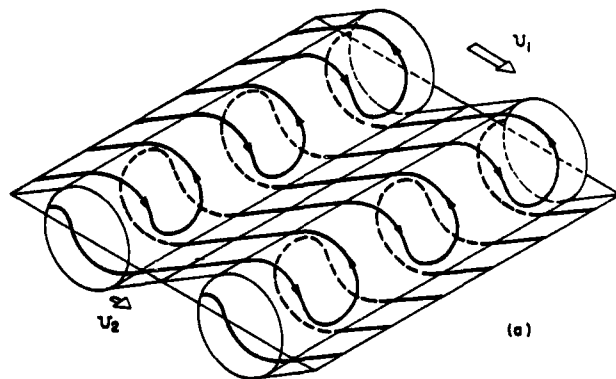


FIG. 1.- MODEL FOR STREAMWISE VORTICITY DISTRIBUTION. AFTER BERNAL (1981).

* Present address, Jet Propulsion Laboratories, Pasadena, Ca. 91109

Another section, taken at a higher Reynolds number, is shown in Figure 2.b. All the images were taken at a distance of 17 cm. from the splitter plate, and the Reynolds number was controlled by changing the free stream velocities. The momentum thickness of the boundary layers at the high speed side of the splitter plate were not measured directly in this experiment, but can be inferred from the values given by Breidenthal (1981) for the same apparatus. A summary of the relevant flow parameters for the two films used in this paper is given in Table 1. The downstream position of the illuminated section, expressed as a multiple of the initial boundary layer thickness, θ , is seen to be about 300 for the low Reynolds number case and 600 for the high Reynolds number case. According to the values given for the three-dimensional transition by Breidenthal (1981) and Jimenez (1983), the first film corresponds to the growth region of the three-dimensional instability, while the second one is already in the well developed region.

From these films we have extracted three sequences, two corresponding to the low, and one to the high Reynolds number case. Each sequence is formed by approximately 200 consecutive frames. Each frame was digitised and treated as the transverse section of a three-dimensional solid in which the third dimension, time, can be converted to space (x) by using a fixed convection velocity equal to the average between the two free stream speeds; the adequacy of this hypothesis will be discussed later. Digitisation converts each frame into a large numerical matrix in which each value represents the optical transmissivity at one point of the photographic negative. When all the consecutive frames are stacked together, they form a three-dimensional array which is a digital model of fluorescent intensity in the flow. Any section of this array, not just the original transversal ones, can now be displayed on a computer terminal. Figure 3 shows



FIG. 2.- TWO FRAMES FROM THE FILMS ANALYSED IN THIS PAPER. TOP: FILM 1, BOTTOM: 2.

Film	U1 cm/s	U2 cm/s	$(U1-U2)x/v$	θ cm	x/θ
I	15	6.4	14,600	.052	330
II	52	20	54,400	.028	613

TABLE 1.- FLOW PARAMETERS IN THE FILMS USED



FIG. 3.- STREAMWISE SECTIONS OF TWO OF THE SEQUENCES USED IN THE RECONSTRUCTION.

longitudinal sections of two of the sequences. These sections correspond to the classical two-dimensional ones shown, for example, in Brown and Roshko (1974) but, because in this case the coordinates are $y-t$ instead of $y-x$, the eddies are all at the same stage of their development and do not appear to grow.

The next step is to relate the optical density in the negatives to dye concentration in the fluid. In principle this density is proportional to the amount of light emitted by one point in the fluid which, in turn, is proportional to the product of the laser beam intensity and the concentration of dye. In practice the beam intensity is unknown and changes within the picture, mainly due to absorption by the dye and, although calibration is possible, it was not done when the present films were obtained. In the absence of that information we have taken the concentration to be proportional to the gray level, normalised by the initial light intensity estimated for each incoming (vertical) ray. There is no guarantee that the resulting images are adequate for more than a qualitative analysis of the concentration field.

Each frame was filtered using a local sliding average over a 5×5 pixel neighbourhood, and classified into three homogeneous regions on the basis of the resulting concentration. These regions are intended to represent each of the free streams and an intermediate "mixed" region; the choice of the thresholds separating them is somewhat arbitrary. In general it is quite easy to define thresholds giving the approximate "outer" limits of the mixing layer since, particularly in the low Reynolds number case, there is a visually sharp interface outside which the fluid is unmixed. Isolevel lines outside these thresholds have a very convoluted shape, typical of photographic noise



FIG. 4.- SEGMENTED VERSION OF THE FIGURE 2.A, AFTER CLASSIFICATION AND FILTERING.

while, inside them, they are much smoother. In the high Reynolds case the distinction is not so clear but an outer limit can still be defined.

Note that, because of the beam absorption problem, it is not possible to assign a single brightness level to each stream and to compute the thresholds as fractions of those levels.

The classified frames have to be smoothed further to eliminate the "salt and pepper" noise. This is done by using a three-dimensional majority voting scheme. Each element in the three-dimensional classified array is considered as the centre of a $3 \times 3 \times 3$ cube; the number of elements in the cube belonging to each class is counted, and the centre pixel is assigned to the class of the majority. The result of classification and filtering on Figure 2.a is shown in Figure 4.

The amount of storage needed for each sequence, when stored in this fashion, is relatively large. Each numerical array is approximately $200 \times 350 \times 450$ and, therefore, contains over 30 million elements. As a result, the arrays have to be kept in magnetic tape and can not be accessed fast enough for interactive display. To compact the information, the contours of the class corresponding to the "mixed" fluid are extracted, approximated by polygons and stored in a suitable designed data base. Each sequence can then be stored in approximately 400 Kbytes of disk space and accessed easily. The software used in this step is described in Jimenez and Navaion (1982).

THREE DIMENSIONAL RECONSTRUCTION

The polygons stored in the data bases generated above represent sections of a three-dimensional model of the mixing layer. Several methods are available for the display of complex three-dimensional objects, many of which are surveyed in the book by Foley and Van Dam (1982). We generate our solid model by con-

structing, for each section, a short cylinder (actually a prism) based on its contour and extending in the direction of the flow with a depth equal to the convection distance between frames. These prisms are then stacked together to form a polyhedral body (see Figure 5).

The resulting solid is displayed in a black and white monitor and photographed directly from the screen. The method used for hidden surface elimination is a slightly modified depth buffer (see Foley and Van Dam, 1982, ch. 15). Shading of the surfaces is done assuming that the object is matte and illuminated by a single point source, with a small amount of extra isotropic illumination (Phong, 1975). No shadows are computed, but the resulting unnatural aspect of the representations is controlled by keeping the light source relatively close to the observer. Both the orientation of the model and the position of the source can be controlled interactively, as is the clipping of the model by an arbitrary plane. The computer time needed for a complete display is between one and three minutes.

The model for sequence number 1, extracted from the low Reynolds number film, is shown in Figure 6. The flow runs from the top right to the bottom left corners of the picture and the two large horizontal eddies are the classical Brown-Roshko structures. The mixing layer is seen from its low speed side and a remarkably regular array of streamwise structures is seen superimposed on the primary eddies. The high speed side of the second eddy of the sequence is shown in Figure 7. The same streamwise structure is present, and a section by a horizontal plane shows that the interior of at least the central streamer contains two hollow (unmixed) tubes strongly suggestive of a vortex pair.

The thresholds used to isolate the mixed fluid for these two figures were the outer ones described above and, therefore, the model shown should contain most of the fluid actually mixed. It is somewhat surprising that a fairly large amount of mixed fluid is apparently present in the thick streamers of the braid region, where mixing would normally not be expected. Figure 8 shows this not to be the case; in the top part, a streamer has been isolated by clipping the same sequence used in Figure 6 with a pair of vertical streamwise planes; the bottom part shows the same clipped portion turned upside down. In the braid region the streamers, although apparently thick, are seen to be only a thin deformed shell containing a relatively small amount of mixed fluid. Interestingly, the densest concentration of mixed fluid is not found at the core of the large eddies; Figure 8 shows quite a lot of empty (unmixed) space in that region. Most of the mixing seems to happen above and below the eddy, and this impression is generally supported by other sections of the low Reynolds number film.

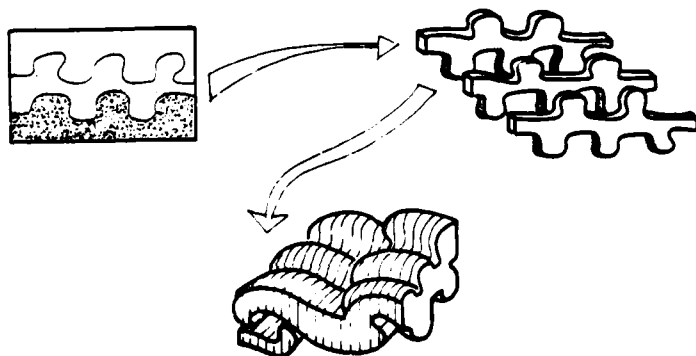


FIG. 5.- RECONSTRUCTION OF A THREE DIMENSIONAL SOLID FROM THE TRANSVERSAL SECTIONS.



FIG. 6.- THE LOW REYNOLDS NUMBER MIXING LAYER. FLOW IS FROM TOP RIGHT TO BOTTOM LEFT. VIEW IS FROM LOW SPEED SIDE.



FIG. 7.- SAME LAYER AS FIG. 6. HIGH SPEED SIDE. NOTE HORIZONTAL CUT SHOWING INTERIOR OF STREAMER.



FIG. 10.- THE HIGH REYNOLDS NUMBER MIXING LAYER.



FIG. 8.- SINGLE STREAMER ISOLATED FROM FIG. 6. TOP VIEW IS FROM LOW SPEED SIDE. BOTTOM, HIGH.

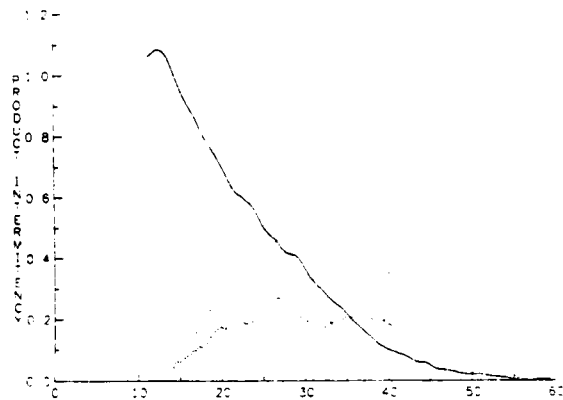


FIG. 9.- PRODUCT INTERMITTENCY IN THE LOW (TOP) AND HIGH (BOTTOM) REYNOLDS CASE. AVERAGE CONCENTRATION PROFILE INCLUDED FOR REFERENCE.

To check that this is indeed the case, a product intermittency was defined as the fraction of the time that mixed fluid was present at a given y position in the layer (integrated along the span). The result for sequence I is shown on the top part of Figure 9. The two curves in this plot correspond to the use of two different thresholds in the definition of mixed versus unmixed fluid, and they show that the character of the result does not depend on that choice. Although the result refers only to two eddies and is subject to all the inaccuracies noted above in the measurement of the concentration, it is interesting that the plot is bimodal with most of the mixed fluid above and below the centre line, consistent with the impression derived from the three-dimensional model.

The bottom part of Figure 9 shows the same quantity for the high Reynolds number film. No trace of bimodality is found in this case, and the presence of mixed fluid is generally much higher than in the previous one. A similar increase in the amount of mixing across the three-dimensional transition was first documented by Konrad (1976) and later by other investigators, but no bimodal profiles have been reported. It is possible that, over longer periods, the distribution is smeared by the different transverse position of the eddies and by the effect of amalgamations. In fact, when a profile is computed for a sequence containing a pairing, the distribution obtained is very flat but not bimodal.



FIG. 11.- LOW REYNOLDS NUMBER, INCLUDING A PAIRING. TOP IS HIGH SPEED SIDE, BOTTOM, LOW.

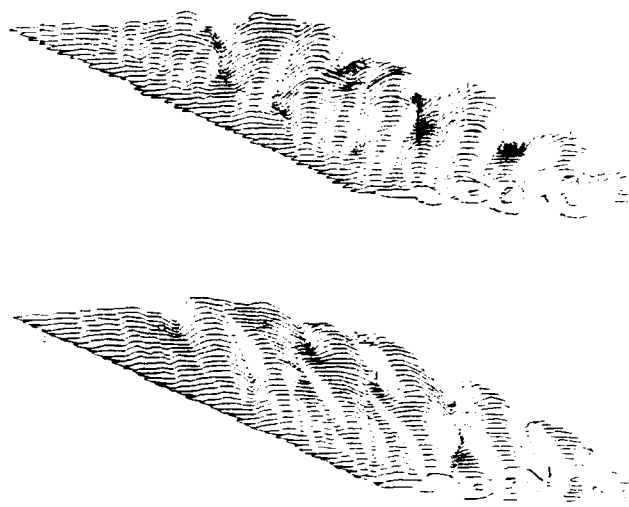


FIG. 12.- TOP AND BOTTOM VIEW OF SPATIALLY GROWING LAYER SHOWING CONVECTION VELOCITY. TOP, HIGH SPEED SIDE. BOTTOM, LOW.

A simple explanation is possible. At low Reynolds numbers the vorticity field is two dimensional, concentrated in the spanwise cores, and the mixing is low. During the transition, the streamwise vortices appear in the braids, but the vorticity is still largely two-dimensional both in the cores (spanwise) and in the braids (streamwise). The only real three-dimensionality is at those places where both systems intersect, above and below the classical cores. It is only there that mixing is enhanced. Further downstream, small scale turbulence is either produced or convected throughout the layer and mixing is more uniformly distributed.

A picture of the high Reynolds number sequence is shown in Figure 10. The lack of any interior voids containing unmixed fluid is apparent, but the longitudinal structures are still present. However, since in this case they are immersed in a sea of uniform mixing, it is difficult to say whether they correspond to active structures or to passive regions remaining from earlier stages in the development of the layer.

Figure 11 is a view of a sequence containing a pairing from the low Reynolds number film. In the top part of the picture the layer is seen from its high speed side. The pairing appears as a long "hook" extending from below the second eddy into the third. The low speed side of the same sequence is shown in the bottom part of the picture; the pairing is now a single continuous structure embracing the two eddies. The difference between the two views is striking but, most probably, is due to a failure of the convection hypothesis. As a pairing occurs, the downstream eddy is carried far into the low speed stream and is decelerated, at the same time that the other eddy is accelerated by the fast stream. As a consequence, and since we are observing the layer at a fixed downstream station, the former eddy stays longer in our field of view and looks elongated, while the latter is accelerated past the observation section and looks shorter. In fact, what we are seeing in Figure 11 is not the same object seen from two different points of view but an earlier and a later version of the same phenomenon. It is fascinating nevertheless to observe that, in the low speed paired view, only three longitudinal streamers

other side. Apparently the flow is able to sense the change in scale of the primary structure and to adapt itself so as to maintain geometric similarity.

The two different views in Figure 11 raise the question of the validity of the convection hypothesis: more precisely, whether the same convection velocity can be used throughout the layer. Figure 12 shows data extracted from a different film; in this case a spanwise averaged view of a mixing layer between gases of similar density (Bernal, 1981a). This is the same film used by Hernan and Jimenez (1982). The outlines of the mixing region have been extracted by a process very similar to the one used for the spanwise sections. There is no attempt of perspective in those pictures. Each section has been displaced upwards by a fixed amount and backwards by a distance corresponding to the average convection velocity. The top picture shows the view from the fast stream, and the bottom one has been reflected on a horizontal plane to show the low speed side. If everything moved with a single convection velocity the traces of all the eddies would be vertical in the page; the fact that they are not, proves that each side of the layer moves at a different speed. In fact, this figure suggests a view of the mixing layer which is slightly different from the normal one.

In the average convection frame an eddy grows and is deformed by the mean shear in such a way that the high speed part moves forward while the low speed part lags behind. These two parts follow fairly straight trajectories but the growth is enough to prevent them from splitting apart. In the process, the eddy just upstream, which is usually smaller because it is at an earlier stage of development, is occasionally engulfed and disappears; the large eddy is not specially perturbed by this process. Since the smaller eddy is normally the one that is carried into the fast stream, this creates an asymmetry between the two sides of the layer which is evident in Figure 12; the high speed side contains only one set of velocities, those of the tops of the large eddies which are not changed during pairings; the low speed side contains the velocities of the lower part of these eddies, but these velocities change occasionally when a pairing is involved. This asymmetry is interesting in view of the reports by various investigators of different amounts of entrainment on both sides of the mixing layer.

In our case the ratio of the two convection velocities (approx. 1.3) is not large enough to invalidate the approximate use of the convection hypothesis in the construction of the models. The only exception is probably during pairings. Figure 12, while suggesting a different behaviour of the pairing on both sides of the layer, is not consistent with the large differences shown in Figure 11 while, on the other hand, shows that convection velocities can vary enough during amalgamation to explain the discrepancy.

CONCLUSIONS

We have presented three-dimensional reconstructions of the concentration field of a nominally plane mixing layer. In the section corresponding to the developing region of the three-dimensional transition, the reconstruction shows longitudinal structures which

are, not only very marked, but strikingly well organised. Those structures give strong support to the interpretation that they are due to longitudinal vortex pairs topologically unconnected to the main spanwise vortices, in general agreement with the model in Figure 1. At that Reynolds number the intersection of the two orthogonal systems of vortices seems to control the location of small scale mixing. Further downstream, the longitudinal structure persists but it is now submerged in a broader region of generalised mixing and its dynamical significance is harder to decide.

We want to acknowledge the help of Dr. M.A.Hernan in digitising some of the film sequences used in this paper. J.L.Navalon is responsible for much of the contour extraction software. Dr. A.Roshko contributed with many helpful discussions in the interpretation of the pictures. M.Cogollos was partially supported by an IBM study fellowship.

REFERENCES

- BERNAL, L.P. 1981a The coherent structure in turbulent mixing layers, I: Similarity of the primary vortex structure. PhD. Thesis, Caltech.
- BERNAL, L.P. 1981b The coherent structure in turbulent mixing layers, II: Secondary streamwise vortex structure PhD. Thesis, Caltech.
- BREIDENTHAL, R.E. 1981 Structure in turbulent mixing layers and wakes using a chemical reaction. J.Fluid Mech. 116, 1-24
- BROWAND, F.K. & TROUTT, T.R. 1980 A note on spanwise structure in the two dimensional mixing layer. J.Fluid Mech. 97, 771-781
- BROWN, G.L. & ROSHKO, A. 1974 On density effects and large structure in turbulent mixing layers. J.Fluid Mech. 64, 775-816
- CORCOS, G.M. 1979 The mixing layer: Deterministic models of a turbulent flow. Report FM-79-2 Univ. California, Berkeley.
- FOLEY, J.D. & VAN DAM, A. 1982 Fundamentals of interactive computer graphics. Addison-Wesley, Reading, Mass.
- HERNAN, M.A. & JIMENEZ, J. 1982 Computer analysis of a high-speed film of the plane turbulent mixing layer. J.Fluid Mech. 119 323-345
- JIMENEZ, J. 1983 A spanwise structure in the plane mixing layer. J.Fluid Mech. 122, 319-336.
- JIMENEZ, J. & NAVALON, J.L. 1982 Some experiments in image vectorisation, IBM J. Res. and Development, 26, 724-734.
- KONRAD, J.H. 1976 An experimental investigation of mixing in two-dimensional turbulent shear flows with applications to diffusion-limited chemical reactions. PhD. Thesis, Caltech.
- PHONG, B.T. 1975 Illumination for computer generated pictures. Comm.ACM, 18, 311-317
- PIERREHUMBERT, R.T. & WIDNALL, S.E. 1982 The two and three-dimensional instabilities of a spatially periodic shear layer. J.Fluid Mech., 114, 59-82
- ROSHKO, A. 1980 The plane mixing layer, flow visualisation results and three dimensional effects. In The Role of Coherent Structures in Modelling Turbulence and Mixing, (ed. J.Jimenez) Lecture Notes in Physics, vol 126. 208-217, Springer.

AXIAL COHERENCE FUNCTIONS OF CIRCULAR TURBULENT JETS BASED ON AN INVISCID
CALCULATION OF DAMPED MODES

Peter Plaschko*
Hermann-Föttinger-Institut für Thermo-und Fluidodynamik
Technische Universität Berlin; 1000 Berlin
Federal Republic of Germany

*Present Address: Department of Mechanical Engineering
University of Houston
Houston, Texas 77004

ABSTRACT

It is often assumed that damped instability modes may exist even in the absence of viscosity, if during the downstream evolution of the waves velocity gradients become too small to support amplified disturbances. A modified inviscid calculation of damped modes is done and the inviscid results are used in a slow divergence stability theory and in a linear turbulence model. This yields theoretical predictions for amplitudes, phases and coherence functions that are in reasonable agreement with experimental trends.

INTRODUCTION

Such experimentalists as Fuchs (1972,1973), Armstrong (1981), Chan (1977) and Moore (1977) have been strongly interested in the problems of jet turbulence during the last decade. Artificial excitation has been used to raise more or less regular patterns above the random background and it has been demonstrated that there is a large-scale structure of considerable coherence volume. The influence of the Mach number has also been found to be small, and it was shown that only the lower order helical modes are important.

Crighton and Gaster (1976) and Plaschko (1979) first treated inviscid instability of slowly divergent jets which can only predict growing disturbances. The parallel-flow problem reappears in the leading order approximation. The influence of the divergence is incorporated in the higher order corrections, and is contained in a set of amplitude functions that vary slowly in the downstream direction. The growth of the disturbance is arrested by the influence of the flow divergence and the amplitudes grow exponentially only in the first downstream positions. Farther downstream the amplitudes tend toward maximal values and it was supposed that they decrease under the action of viscosity. Since the calculation of damped modes is beyond the scope of an elementary inviscid theory, the study of the downstream evolution was terminated at axial positions close to neutrality.

The main reason for the limitation to the inviscid case is the large computing time needed to handle slow flow divergence approximation to the viscous modes. This is because the calculation of an eigenvalue by means of solving the Orr-Sommerfeld equations requires a computing time two orders of magnitude higher than the corresponding computing time for an inviscid eigenvalue. Since the slow flow divergence theory deals with a great number of manipulations of the parallel flow quantities, the problem of computing time may render the development of such an Orr-Sommerfeld stability theory impractical.

Meanwhile, Tam and Morris (1980) proposed another method for calculating the eigenvalues inviscidly. They solved the inviscid disturbance equation in the complex plane. This equation is satisfied on the real axis except in a narrow region where pole branch cuts at certain

lines cross the real axis. Circumventing the branch cut by means of a proper deformation of integration contours, however, facilitates the calculation eigenvalues and eigenfunctions and it was speculated by Tam and Morris that this method may give the analytic continuation of the Orr-Sommerfeld solutions in the limit of infinite Reynolds number.

In the present paper we use the contour integral method to calculate the eigenfunctions and eigenvalues of damped modes in circular jets. Furthermore, these quantities are used to establish a slow flow divergence theory covering axial locations outside the potential core.

We also use these results to extend a linear model for the calculation of large coherent structures [Plaschko (1981)]. Let us now review the salient assumptions of this model: First of all, the analysis is restricted to the calculation of second order moments of the fluctuating pressure in inviscid incompressible jet flows. The jet turbulence is assumed to be stationary and homogeneous with respect to the azimuthal angle. The latter condition implies the statistical independence of the different helical modes. This assumption restricts the application of the model to circular jet turbulence.

Next we assume that the large coherent structures are created exclusively at the jet orifice and other possible excitation mechanisms are ignored. Furthermore, we assume that the amplitudes and phases of large coherent structures can be described by superposing linear instability waves for a slowly divergent jet flow. The fictitious turbulent velocity profile is assumed to be suitable modelled by the Michalke-Crighton-Gaster profile. The parabolic structure of the stability equations requires that their solutions contain unknown constants of the integration. These quantities are regarded as random functions of the frequency and they are determined by the application of a stochastic initial condition. This initial condition describes, in an overall manner, the excitation of the large scale structures at the position of the jet orifice. In the case of jet turbulence, however, a white-noise type excitation certainly does not take place. Hence, the spectral variation of the excitation has to be established by using an additional hypothesis. In the absence of reliable data on spectra close to the orifice we refrained from formulating such an hypothesis and resorted to fitting to experimental data.

Spectral quantities are considered exclusively and only the lowest helical modes are taken into account to describe the fluctuating pressure (experiments of Fuchs (1973) indicate that the decomposition of fluctuating velocities may need a greater number of helical constituents). In a previous paper we have shown that this model can predict the experimental trends of radial as well as circumferential coherence functions fairly well. Difficulties arise, however, when we consider axial coherence functions. This is because higher order helical modes are already damped, at a given location, while the lower ones continue to grow. Since the calculation of

damped modes is beyond the scope of an elementary inviscid stability theory, an attempt was undertaken to alleviate these complications by means of either a cut off approximation or continuation of inviscid quantities beyond the locations of neutrality. Such procedures lead to such unsatisfying results as discontinuities of the axial coherence at the position of the cut off.

The central goal of this paper is therefore to extend this linear inviscid turbulence model by means of the contour integral method of calculating damped modes.

This method offers a simple, and computing time saving, tool to enlarge the regime where the linear turbulence model can be applied. Since inviscid modes are the most unstable and the least damped, we believe that the inviscidly calculated amplitudes represent an upper limit to the crests of large coherent structures. However, as a result of neglecting viscous effects, there exists a certain region of forbidden radial locations within which the model fails to give predictions.

ANALYSIS

We shall survey the analysis only briefly.

The study is restricted to the investigation of the fluctuating pressure p' . This quantity is analyzed in cylindrical coordinates and it is represented by a superposition of partial instability waves as given by slow flow divergence theory. Hence we put

$$p' = \sum_{m=-\infty}^{\infty} \exp(im\phi) \int_{-\infty}^{\infty} \exp(-i\beta t) A_m(x, \beta) F_p^0(x, r, \beta) d\beta, \quad (1)$$

where β is the frequency and m is the helicity index.

The radial mode shape function F_p^0 , is defined as the regular solution of the second order inviscid disturbance equation ($c = \beta/\alpha$; α is the wavenumber)

$$\left[\frac{\partial^2}{\partial r^2} + \left(\frac{1}{r} - \frac{2\partial U_x/\partial r}{U_x - c} \right) \frac{\partial}{\partial r} - \left(\frac{m^2}{r^2} + \alpha^2 \right) \right] F_p^0 = 0, \quad (2)$$

where $U_x(x, r)$ is the velocity profile to be introduced later. In the slow flow divergence approximation, the amplitudes A_m are given by

$$A_m = \exp \left[\int_0^x (i\alpha - \frac{1}{k_m}) dx \right], \quad (3)$$

and the term $1/k_m$ represents the first order WKB-correction to the parallel flow amplitudes. The quantities $1/k_m$ and k_m are functionals of F_p^0 and its adjoint \bar{F}_p^0 of the type

$$\int_0^{\infty} G(F_p^0, \bar{F}_p^0, U_x, \dots) dr. \quad (4)$$

The velocity profile U_x is a fictitious quantity in the framework of linear stability theory. A reasonable approximation for fully turbulent jet flow seems to be the Michalke-Crighton-Gaster model. It is given by

$$U_x(x, r) = 0.5U_1(x) \{1 + \tanh \left[\frac{25}{3x+4} \left(\frac{1}{r} - r \right) \right]\} \quad (5)$$

$U_1(x)$ is the centerline velocity being modelled by two alternative forms (a_1 and a_2 are empirical constants)

$$U_1(x) = \begin{cases} 1 \\ \exp[-a_1 x^4 / (1 + a_2 x^3)] \end{cases} \quad (6)$$

A singularity at $U_x = c$ arises in (2). It is easy to show that the pole lies in the upper half plane for damped modes ($\alpha_1 > 0$; $\alpha_1 = \text{Im}(\alpha)$) and in the lower half plane ($\alpha_1 < 0$) for amplified modes, respectively. These poles are connected with branch cuts extending from the position of the pole downward to minus infinity. Hence for damped modes, we elude the pole and its branch cut with integration paths in the complex radial plane.

The regular solution of (2) contains a constant of the integration. It is assumed to be a random function of the frequency and is determined by a stochastic

initial condition reflecting the excitation of the large coherent structures at the jet orifice. Hence, we put (R is the jet radius)

$$p'(x=0, r=R, \phi, t) = \sum_{m=-\infty}^{\infty} \exp(im\phi) F_m(t). \quad (7)$$

Though the stochastic excitation functions $F_m(t)$ are unknown, we may demand that

$$\langle F_m(t) \rangle = 0 \text{ and } \langle F_m(t) F_n(t+\tau) \rangle = \delta_{n+m,0} g_m(\tau), \quad (8)$$

where $\delta_{n,m}$ is Kronecker's delta and $\langle a \rangle$ is the ensemble average of a . Equation (8) warrants the stationarity and azimuthal homogeneity of the jet turbulence.

Note that because of linearity, there would be no fluctuations ($p' \equiv 0$) if there is no excitation at the orifice ($F_m = 0$ for all m 's).

Equations (1) to (8) are now sufficient to calculate the second order moments. As a result of linearity the helical modes do not interact and because of (8) each mode makes its individual contribution to the second order moments.

When we calculate spectral quantities, $S_m(\beta)$ the Fourier transformation of the unknown autocorrelation functions of the excitation $g_m(\tau)$ will appear. The spectra S_m are determined by fitting to experimental data at each value of the frequency. The theoretically predicted coherence functions, however, are remarkably insensitive to this fitting procedure. It was shown that fitting to different experimental data (radial or circumferential coherence function at distinct spatial locations) yields to ignorable small deviations of the theoretically predicted quantities.

DISCUSSION OF NUMERICAL RESULTS AND COMPARISON WITH EXPERIMENTS

At the beginning of the iteration routines to determine the wave numbers, an initial estimate of the pole location was made and the corresponding branch cut was distantly circumvented. After the eigenvalue was located, however, the contour was contracted and at the same time the path-independence of the wave numbers was investigated. Claiming a six digit accuracy, the contraction was terminated whenever this accuracy limit was violated. Carefully performed numerical studies show that the contour may be drawn fairly close to the location of the branch cut. Because of the possibility of closely circumventing the branch cut in a rectangular manner, we may conclude that the branch cut exhibits the shape of a straight line.

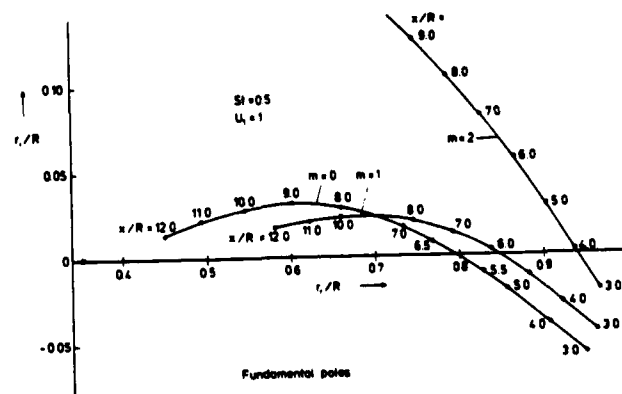


Figure 1: Location of the fundamental poles in the complex radial plane.

Figure 1 gives a survey of locations of the fundamental poles. For parallel flow, each of these curves coincides into a single point. The tendency of these locations is to move with increasing values of x toward the centerline of the jet. Hence we may conclude that there exists a regime of forbidden radial locations extending from positions close to the center of the boundary layer inward to the centerline.

Accordingly, in Figures 2 and 3 the pressure gains and phase speeds are plotted for a position outside of this forbidden region but fairly close to the center of the boundary layer. The quantities were calculated by deforming the contour of the functionals (4) in the usual manner and by testing the path-independence of the corresponding results. The waves grow in an initial stage exponentially, reach a peak, and decay slowly, farther downstream. Chan's observations of pressure gains reveal lower peaks at positions somewhat further upstream, and a markedly higher rate decay. These deviations might partially be the result of the non-linear forcing levels used in this experiments. However, it seems to be obvious, that an inviscid theory predicts a comparatively small rate of decay. We can therefore conclude that inviscid calculated amplitudes represent an upper limit to the downstream evolution of the crests of large structures.

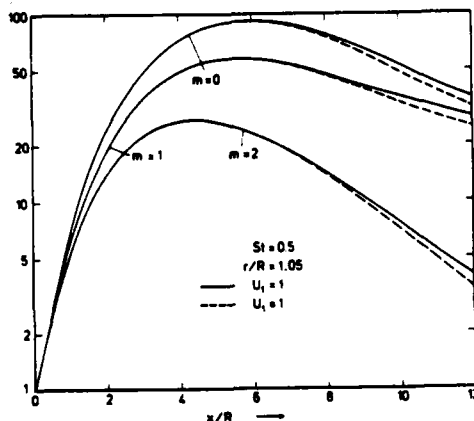


Figure 2: Pressure gains at radial positions close to the center of the boundary layer.

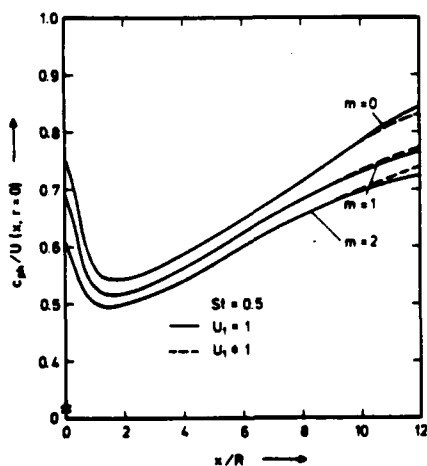


Figure 3: Phase speeds of pressure waves ($x/R = 1.05$).

In agreement with Chan's experiments we find that the higher the index of helicity m is, the lower the phase velocity will be. Furthermore, the tendency of c_{ph} to reach a minimum and increase farther downstream is confirmed by the experiments of Moore. Moore found the minimum of c_{ph} for $St = 0.48$ and $r = 0$ to be close to $x_{min}/R = 3$. The deviation of our theoretical results ($m = 0$: $x_{min}/R \approx 2$, for $St = 0.5$ and $r/R = 1.05$) might be caused by the different radial locations.

Looking on Figs. 2 and 3 we may conclude that the influence of the centerline velocity decay is fairly small within the range of axial positions that was considered.

Some numerical results pertaining the linear turbulence model are represented in the last two figures. For the sake of comparison with measurements done by Fuchs, in Figs. 4 and 5 the quantity

$$R_{p_1 p_2} = \frac{W_{p_1 p_2}}{W_{p_1 p_1} W_{p_2 p_2}}^{-1/2} \quad (9)$$

is depicted. $W_{p_1 p_2}$ is the real part of the pressure cross-spectral density and the power densities are denoted by $W_{p_1 p_1}$ and $W_{p_2 p_2}$, respectively. One pressure probe is kept at a fixed position ($x_1 = 6R$ and $r_1 = 0$) and the other probe varies in the axial direction. It is important to note that the fitting constants [the normalized excitation spectra $S_m(\beta)/S_0(\beta)$] are determined from Fuchs' experimental data for the circumferential coherence function at $x = 3R$.

The axial coherence function plotted in Fig. 5 corresponds to two radial locations where the axisymmetric mode is dominant. Hence the corresponding coherence function is somewhat lower than is the case represented in Fig. 4 with the moving probe located where the influence of the higher helical modes is greater. These figures show that the wave lengths of the axial coherence functions are fairly well predicted. Some deviation occurs, however, in the case of the coherence function - the envelope of these curves. This is certainly because the rate of amplitude decay is underpredicted. The comparatively greater deviations of experimental and theoretical values of $R_{p_1 p_2}$ in Fig. 5, however, might be attributed to the different radial positions of the moving probe within a regime of high gradients of the radial mode shape function.

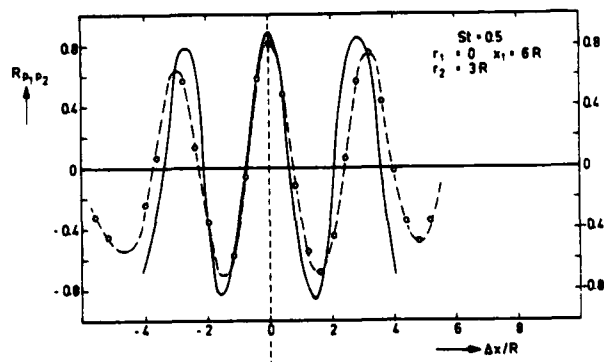


Figure 4: Axial coherence functions (— theory; ---- experiments of Fuchs (1972)).

CONCLUSIONS

A previously established linear turbulence model is extended with the aid of inviscid computation of damped modes. This method allows for the calculation of eigenvalues, eigenfunctions, gains and coherence functions outside a definite region of radial locations. Since the damping is caused merely by the attenuation of velocity gradients, the amplitudes and gains thus calculated represent an upper limit to the crests of the large coherent structures. However, the model is capable of predicting the experimental trends of phases, gains, and coherence functions of pressure waves. Hence, the conclusion emerges that a turbulence model based on a superposition of linear waves excited randomly at the orifice

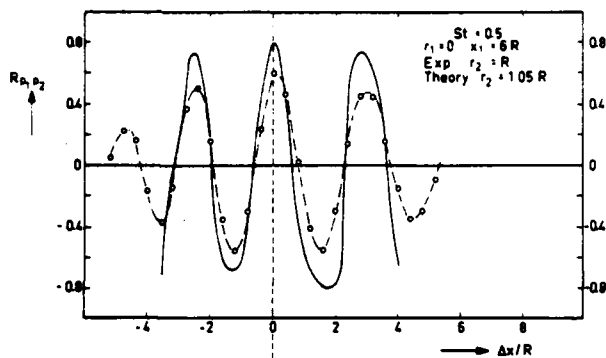


Figure 5: Axial coherence functions (for legend see Fig. 4).

represents a reasonable method of predicting the evolution of large coherent structures in jet turbulence.

REFERENCES

- R. R. Armstrong, AIAA J. 19, 677, (1981).
- Y. Y. Chan, AIAA J. 15, 992 (1977).
- D. G. Crighton and M. Gaster, J. Fluid Mech. 77, 397 (1976).
- H. V. Fuchs, AGARD-CP-131 (1973).
- H. V. Fuchs, J. Sound Vib. 23, 77 (1972).
- C. J. Moore, J. Fluid Mech. 80, 321 (1977).
- P. Plaschko, J. Fluid Mech. 92, 209 (1979).
- P. Plaschko, Phys. Fluids, 24, 187 (1981).
- C. J. W. Tam and P. J. Morris, J. Fluid Mech. 98, 349 (1980).

A MODEL OF THE EXCITATION OF ORDERLY STRUCTURES IN A SHEAR LAYER

D.W. Bechert
DFVLR, Abt. Turbulenzforschung
Mueller-Breslau-Str. 8
1000 Berlin (West) 12

ABSTRACT

The artificial excitation of shear layers is investigated theoretically and experimentally. The present paper describes quantitatively the coupling between exciting sound field and shear layer fluctuations. The mathematical model is restricted to low Strouhal numbers at which large scale structures are occurring. The theory does not contain any empirical constants and is confirmed by the experiments in the expected validity range.

1. INTRODUCTION

In previous investigations it has been shown that the occurrence of orderly structures and the spreading rate of shear layers depend strongly on the perturbation of the flow¹⁻⁴. The excitation of the shear layer can be produced either by sound or by vorticity convected with the flow. The jet shear layer is excited even in such situations where, inadvertently, sound is generated by the apparatus to produce the flow itself. The present paper deals with the mechanism of the introduction of such perturbations into the shear layer. In the mathematical model a thin semi-infinite shear layer is considered, which is shed from a semi-infinite plate. The shear layer is exposed to acoustical excitation. This simple configuration is well tractable mathematically and the analysis provides some insight into the interaction process, which would be less readily obtained by a purely numerical approach. The present research has been motivated by a number of observations with technological relevance:

- (i) The excitation of large scale structures in a jet can enhance the radiated broad band jet noise significantly^{5,6}. This effect has drawn considerable attention from aircraft and aero-engine producers⁷.
- (ii) The production of instability waves in the jet shear layer can extract energy from the exciting sound field. This latter effect is quite dramatic at low frequencies and it can be considered as a genuine sound absorption effect, different from the conventional dissipative absorption mechanisms^{8,9}.
- (iii) Shear layer excitation plays an important rôle also in the flow around bluff bodies. It has been shown recently^{10,11}, that these separated shear layers in such a flow are sensitive to exterior perturbations by sound and convected vorticity. By this mechanism the drag of bluff bodies can be both increased or decreased, depending on the actual configuration.

The present paper is a condensed version of a fairly elaborate DFVLR report¹² and of a AIAA-paper¹³. Thus, only basic ideas will be outlined and results will be discussed without providing all details of the calculations.

2. ONE STREAM MODEL

The objective of this paper is to investigate quantitatively the coupling between a forcing sound field and the generation of instability waves in shear layers. Fig. 1 shows the simplified configuration which will be modelled mathematically. We assume that there is no flow above the shear layer. There is no basic difficulty, however, to extend the calculations to two streams on both sides of the shear layer, having different velocities and densities^{12,13}. The acoustic field is assumed to be produced by a two-dimensional pulsating source outside the shear layer in the fluid at rest. The following simplifying assumptions are introduced:

1. two-dimensional problem
2. parallel mean flow
3. all fluctuating quantities harmonic in time, i.e., $\propto e^{-i\omega t}$
4. inviscid flow
5. linearized problem
6. incompressible flow
7. infinitesimally thin shear layer

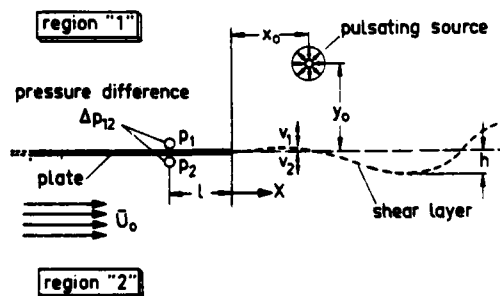


Fig. 1 Configuration of the analytic model.

The first five simplifications are common in the stability theory of free jets. The assumption of an inviscid flow works quite well at sufficiently high Reynolds number^{14,15}. The linearization is valid for relatively low fluctuation velocities which are found in the interaction region near the end of the splitter plate^{15,16}. The assumption of incompressibility is equivalent to the restriction to small Mach numbers and small Helmholtz numbers, where the Helmholtz number is defined as the ratio of the typical length of the problem to the wavelength of the sound waves. For our problem, the latter condition means, that the interaction region close to the lip should be small compared to the acoustic wavelength. It will turn out, that this region has a dimension of the order U_0/f (where U_0 is the mean flow velocity and f the sound frequency). Consequently, we should have

$\bar{U}_0/f \ll a_0/f$, where a_0/f is the acoustic wavelength. This is equivalent to $M = \bar{U}_0/a_0 \ll 1$, i.e., again the condition of small Mach number. The seventh assumption, the restriction to an infinitesimally thin shear layer will limit the validity range of the theory to the case where the shear layer thickness is small compared to the wavelength of the instability waves. In other words, the Strouhal number $f\delta/\bar{U}_0$ should be small. δ is the momentum thickness of the shear layer.

The classical approach would be to fulfill the boundary conditions at both sides of the shear layer. This means that both the displacement h and the pressure p should be equal there. The displacement h and the velocity v are connected in the following way

$$v = \frac{\partial h}{\partial t} + \bar{U} \frac{\partial h}{\partial x} \quad (1)$$

For a harmonic motion we find therefore (see also Fig. 1)

$$v_2 = v_1 + i \frac{\bar{U}_0}{\omega} \frac{\partial v_1}{\partial x} \quad (2)$$

This is an equation connecting the v -components of the fluctuation velocities at both sides of the shear layer.

A second equation for v_1 and v_2 will be derived subsequently from a consideration of the pressure field and its gradients at the shear layer. We start out by taking the x -derivative of the first Euler equation and the y -derivative of the second Euler equation. Both derivatives are added and some terms are eliminated using the continuity equation. We end up with

$$\nabla^2 p = -2\rho \frac{\partial v}{\partial x} \cdot \frac{\partial \bar{U}}{\partial y} \quad (3)$$

In our model (see Fig. 1), the mean velocity profile jumps from $\bar{U} = 0$ for positive y to $\bar{U} = \bar{U}_0$ for negative y . Thus, the right hand side of eq. (3) exists only in the shear layer. Eq. (3) can be considered as a non-homogeneous, Laplacean equation with a source distribution of varying strength in the shear layer. It should be stressed here, that these sources in the shear layer are pressure sources. A discussion on the nature of these sources is given in our report¹², but for the further progress of our calculation, a detailed knowledge of the pressure sources is not necessary. At the surface of the semi-infinite plate we have v and $\partial v/\partial x$ equal to zero. Consequently, the pressure source strength is zero on the plate surface. The only other location where $\nabla^2 p$ is non-zero is at the location of the exterior pulsating source (see Fig. 1).

The basic idea of the present approach is, that the pressure distribution in the whole field can be split into two contributions:

- (1) a pressure field which is symmetric with respect to the shear layer and which is caused by the pressure source distribution in the shear layer itself.
- (2) a pressure field which is produced by the exterior forcing, e.g., a pulsating source. The pressure fluctuations of this contribution are transmitted through the shear layer. The pressure gradient of this contribution is continuous through the shear layer and therefore it is antisymmetric close to the shear layer.

As a result of this splitting process we have

$$\begin{aligned} p_1 &= p_{1s} + p_{1f}; \quad p_2 = p_{2s} + p_{2f} \\ v_1 &= v_{1s} + v_{1f}; \quad v_2 = v_{2s} + v_{2f} \end{aligned} \quad (4)$$

The index s stands for shear layer and the index f labels the exterior forcing. The boundary conditions at both sides of the shear layer have to be fulfilled by the summations of the individual constituents, i.e., by v_1 and v_2 , as before. On the other hand, we have some new information: Since the induced field of the pressure sources in the shear layer is symmetrical (it is produced by sources of symmetrical directivity in a field with symmetrical boundary conditions) we obtain:

$$\frac{\partial p_{1s}}{\partial y} = - \frac{\partial p_{2s}}{\partial y} \quad \text{at } y = \pm 0 \quad (5)$$

and for the continuous pressure of the exterior forcing

$$\frac{\partial p_{1f}}{\partial y} = \frac{\partial p_{2f}}{\partial y} \quad \text{at } y = \pm 0 \quad (6)$$

These conditions for the pressure gradients in y -direction can be inserted into the 2nd Euler equation which gives

$$v_{2s} + i \frac{\bar{U}_0}{\omega} \frac{\partial v_{2s}}{\partial x} = -v_{1s} \quad (7)$$

$$v_{2f} + i \frac{\bar{U}_0}{\omega} \frac{\partial v_{2f}}{\partial x} = v_{1f} \quad (8)$$

Equations (7) and (8) can be added using eq. (4)

$$v_2 + i \frac{\bar{U}_0}{\omega} \frac{\partial v_2}{\partial x} + v_1 = 2v_{1f} \quad (9)$$

This is the desired second equation for v_1 and v_2 . The velocity v_{1f} is not an unknown quantity, it is the velocity which is generated by the exterior forcing without the mean flow being present, but in the presence of the semi-infinite plate. Equation (2) can be inserted into eq. (9) to obtain the non-homogeneous differential equation

$$2v_1 + 2i \frac{\bar{U}_0}{\omega} \frac{dv_1}{dx} - \left(\frac{\bar{U}_0}{\omega}\right)^2 \frac{d^2 v_1}{dx^2} = 2v_{1f} \quad (10)$$

The complete solution of this type of differential equation can be found in textbooks of mathematics¹⁷. We find

$$\begin{aligned} v_1 &= C_1 e^{\lambda_1 x} + C_2 e^{\lambda_2 x} + \\ &+ \frac{\omega}{\bar{U}_0} \int_0^x e^{-\lambda_2 x} v_{1f} dx - \frac{\omega}{\bar{U}_0} \int_0^x e^{-\lambda_1 x} v_{1f} dx \end{aligned} \quad (11)$$

with the abbreviation

$$\lambda_{1,2} = \frac{\omega}{\bar{U}_0} (i \pm 1) \quad (12)$$

The first two terms of eq. (11) are the solutions of the homogeneous differential equation. They are identical to the well-known spatial instability waves for an infinitesimally thin shear layer, extended from $x = -\infty$ to $x = +\infty$, which we will call the Helmholtz solutions. The constants C_1 and C_2 have the dimension of a velocity and will be determined with the boundary conditions. Equation (11) is a general solution and it has to be evaluated for different excitation velocity distributions v_{1f} . Before doing this, however, we will discuss briefly the question of the Kutta condition in conjunction with the determination of the constants C_1 and C_2 . In the full paper¹² the complete solution is evaluated for a fairly general case, where a sound source of any kind is located farther away from the trailing edge of the semi-infinite plate. It is shown there¹², that the forcing induced velocity close to the trailing edge is then

$$v_{1f} = C_3/\sqrt{x} \quad (13)$$

where the coefficient C_3 depends on strength, location and type of the source¹⁸. Equation (11) can be evaluated with this distribution

$$\begin{aligned} v_1 &= C_1 e^{\lambda_1 x} + C_2 e^{\lambda_2 x} + \\ &+ C_3 \frac{\omega\sqrt{\pi}}{\bar{U}_0} \left(\frac{e^{\lambda_2 x}}{\sqrt{\lambda_2}} \operatorname{erf}\sqrt{\lambda_2 x} - \frac{e^{\lambda_1 x}}{\sqrt{\lambda_1}} \operatorname{erf}\sqrt{\lambda_1 x} \right) \end{aligned} \quad (14)$$

valid for $x \geq 0$ and $y = \pm 0$. For $x < 0$ we have $v_1 = 0$. Using the condition of equal displacement on both sides of the shear layer (eq. (2)) we can determine also v_2 . By using eq. (2) we fulfill the condition of equal displacement on both sides of the shear layer. The condition of equal pressures on both sides of the shear layer leads after some intermediate calculations^{12,13}, to the finding that both C_1 and C_2 must be zero. This finding has important consequences:

- (1) Within the framework of the present linearized theory with symmetrical boundary conditions only forced shear layer motions are possible.

- (2) The flow leaves the trailing edge tangentially since $v_1 \approx x^{1.5}$ for small x . This is equivalent to a Kutta condition.

These conclusions have been drawn earlier¹⁸, but without detailed proof. Due to the confusion about the Kutta condition still caused by Orszag & Crow's paper¹⁹, this issue must be revisited. Of course our conclusions are only valid for low Strouhal numbers $f\delta/\bar{U}$, where the theory with an infinitesimally thin shear layer applies.

3. THE u -VELOCITY FIELD

By a procedure very similar to the preceding one we can also derive analytic solutions for u_1 and u_2 . The details are given in our report¹². We find

$$\begin{aligned} u_1 &= iC_3 \frac{\omega\sqrt{\pi}}{\bar{U}_0} \left(\frac{e^{\lambda_1 x}}{\sqrt{\lambda_1}} - \frac{e^{\lambda_2 x}}{\sqrt{\lambda_2}} \right) \\ u_2 &= C_3 \frac{\omega\sqrt{\pi}}{\bar{U}_0} \left(\frac{e^{\lambda_2 x}}{\sqrt{\lambda_2}} + \frac{e^{\lambda_1 x}}{\sqrt{\lambda_1}} \right) \end{aligned} \quad (15)$$

valid only for $x \geq 0$. These are the u -distributions just above and below the shear layer ($y=0$). For a comparison with experiments, it is also interesting to know the velocity field in the flow region ($y < 0$, see Fig. 1). A source distribution approach is used to compute u_2 from v_1 at $y = -0$. v_1 is given analytically for all x . In Fig. 2 the computed curves of the modulus of u_2 are plotted in nondimensionalized form versus $y = y_0/\bar{U}_0$ for different downstream distances $\tilde{x} = x_0/\bar{U}_0$ from the plate edge. The vertical scaling in Fig. 2 is logarithmical. Therefore, an exponential curve appears as a straight line. Such straight lines are found for locations farther downstream of the edge. At $x = 2$, e.g., which corresponds to $1/3$ wavelength of the instability waves the induced field is already dominated by the amplified instability wave. On the other hand, upstream of the edge at $x = -2$, the u -fluctuation is governed by the acoustic excitation field alone. For these two regions we find also fairly simple asymptotic equations¹².

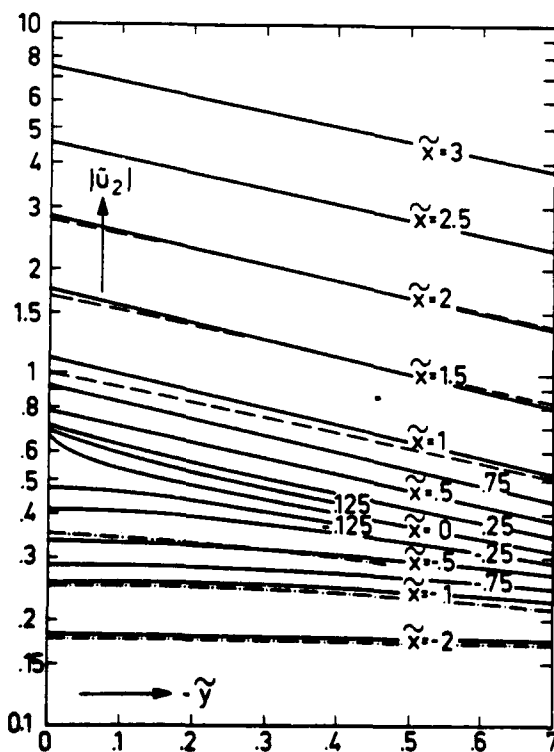


Fig. 2 Computed distribution of $|u_2|$ for various \tilde{x} and \tilde{y} .
--- downstream amplified instability wave alone.
-.-.- acoustic excitation alone.

4. A REFERENCE QUANTITY

It is of general concern in shear layer experiments to have a reference quantity for the acoustical excitation. In our above derivation, we have divided the pressure field into two constituents: (1) The pressure field radiated by the shear layer, which is symmetrical and (2) the pressure field of the excitation which is continuously transmitted through the shear layer and which is antisymmetrical close to the shear layer.

Two microphones upstream of the trailing edge and arranged as in Fig. 1 can be used to isolate the excitation field only. If we take the difference of the pressures $p_1 - p_2 = \Delta p_{12}$ we eliminate the symmetrical shear layer signal completely. By a fairly simple calculation¹² we can also relate the excitation velocity distribution v_{1f} to the pressure difference Δp_{12} :

$$v_{1f} = -\frac{1}{i\tilde{x}} \cdot \frac{i\Delta p_{12}}{4\sqrt{\pi}\bar{U}_0} \quad (16)$$

In this equation l is the distance between microphones and plate edge (see Fig. 1). The coefficient i is equivalent to a 90° phase shift. Also the coefficient C_3 in eq. (15) is determined by eq. (16). We have, e.g., for u_2

$$u_2 = -i \cdot \frac{\Delta p_{12}}{2\sqrt{\pi}\bar{U}_0} \cdot \frac{\sqrt{\pi}}{4} \left(\frac{e^{\lambda_2 x}}{\sqrt{\lambda_2-1}} + \frac{e^{\lambda_1 x}}{\sqrt{\lambda_1+1}} \right) \quad (17)$$

If we are mainly interested in the modulus of u_2 for distances slightly downstream of the plate edge where the decaying wave has vanished, we find

$$|u_2| = \frac{\Delta p_{12}}{2\sqrt{\pi}\bar{U}_0} \cdot \frac{\sqrt{\pi}}{4\sqrt{2}} \cdot e^{x\sqrt{\tilde{x}}/\bar{U}_0} \quad \text{for } x > \bar{U}_0/f \quad (18)$$

We will verify this equation experimentally in order to test the present theory. In the experiments we may use $\Delta p_{12}/\sqrt{T}$ as a reference quantity because it does not depend on the mean flow conditions, or we nondimensionalize the fluctuating velocity in the following way

$$\tilde{u}_2 = u_2 \cdot \frac{2\sqrt{\pi}\bar{U}_0}{\Delta p_{12}} \quad (19)$$

It is also convenient to nondimensionalize the downstream distance x

$$\tilde{x} = x_0/\bar{U}_0 \quad (20)$$

5. THE RELATIVE IMPORTANCE OF THE EDGE REGION

First, we should mention, that in this and the following sections we confine our considerations again to the one stream case with no flow above the shear layer. There is no particular difficulty, however, to extend all following considerations to the case of having two different streams on both sides of the shear layer. In section 2 it had been assumed that under almost all conceivable circumstances, a parabolic pressure field is created close to the plate edge. The relevance of this region to the shear layer excitation will be shown with a simple model (see Fig. 3).

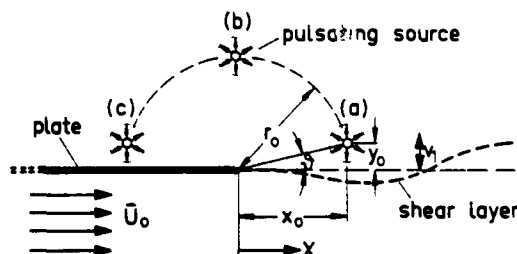


Fig. 3 Shear layer excitation by a monopole source.

The shear layer velocity v_1 far downstream of the edge will be determined, if a pulsating (two-dimensional) monopole source is located at different positions (a) close to the shear layer, (b) above the edge or (c) upstream of the edge (see Fig. 3). In the following calcu-

lation we will only consider the amplified instability wave constituent and not the decaying one, because this is irrelevant at great distances $x \gg \frac{U_0}{\omega}$. We have from eq. (11) with $C_1 = C_2 = 0$:

$$v_1 = -\frac{Q}{U_0} e^{\lambda_1 x} \int_0^\infty e^{-\lambda_1 x} v_{1f} dx \quad (2.)$$

for $x \gg U_0/\omega$ with $\lambda_1 = \frac{\omega}{U_0} (i+1)$.

If the upper boundary of the integral in eq. (11) is set equal to infinity, like in eq. (21), the total influence of the excitation is included. This expansion will provide the magnitude of the instability wave downstream of the interaction region with the monopole field. In a previous paper¹⁸ we had already given the induced field of a monopole above a semi-infinite plate. We have for v_{1f}

$$v_{1f} = -\frac{Q}{4\pi} \sqrt{2(r_0^2 - x_0^2)} \cdot \frac{1}{\sqrt{x}} \cdot \frac{x+r_0}{(x-x_0)^2 + y_0^2} \quad (22)$$

with $r_0^2 = x_0^2 + y_0^2$ and Q being the source strength $Q = Q_0 e^{-i\omega t}$.

After carrying out the integration of eq. (21) we end up with the following analytic solution

$$v_1 = +\frac{Q\omega\sqrt{2(r_0^2 - x_0^2)}}{8U_0} e^{\lambda_1 x} \left[\frac{\bar{T}}{\sqrt{-z_0}} e^{-z_0 \lambda_1} \operatorname{erfc} \sqrt{-z_0 \lambda_1} + \frac{T}{\sqrt{-z_0}} e^{-z_0 \lambda_1} \operatorname{erfc} \sqrt{-z_0 \lambda_1} \right] \quad (23)$$

with $z_0 = x_0 + iy_0$; $\bar{z}_0 = x_0 - iy_0$;

$$T = 1 + \frac{i(r_0 + x_0)}{y_0}; \quad \bar{T} = 1 - \frac{i(r_0 + x_0)}{y_0}$$

The solution contains x only in the instability wave term $e^{\lambda_1 x}$, but the coefficient governing the magnitude of these waves is fairly complex. We will, therefore, expand the solution for two typical cases, i.e., an excitation by a monopole source farther away from the lip ($r_0\omega/U_0 \gg 1$) and an excitation directly at the lip of the semi-infinite plate.

For the excitation at large distances, we have to expand the complex error functions for large arguments. If we take only the first term of the series expansion, we find after some intermediate calculations for the modulus of v_1 :

$$|v_1| = \frac{Q_0}{2\pi\sqrt{r_0}} \sin \frac{\vartheta}{2} \cdot \sqrt{\frac{\omega}{U_0}} \cdot \frac{\sqrt{\pi}}{\sqrt{2}} e^{\frac{\omega x}{U_0}} \times \left[1 + \frac{U_0}{2\omega r_0} (\cos \vartheta + \frac{1}{2} \cos 2\vartheta) \right] \quad (24)$$

for $\omega r_0/U_0 \gg 1$ and $x \gg r_0$.

The first part of this equation resembles very much the excitation velocity in the neighbourhood of the plate edge

$$v_{1f} = -\frac{Q}{2\pi\sqrt{r_0}} \sin \frac{\vartheta}{2} \cdot \frac{1}{\sqrt{x}} \quad (25)$$

for $x \ll r_0$.

One would obtain the following expression

$$|v_1| = \frac{Q_0}{2\pi\sqrt{r_0}} \sin \frac{\vartheta}{2} \cdot \sqrt{\frac{\omega}{U_0}} \cdot \frac{\sqrt{\pi}}{\sqrt{2}} e^{\frac{\omega x}{U_0}} \quad (26)$$

for $\omega x/U_0 \gg 1$

if one calculated the excitation by the parabolic field at the plate edge (eq. (25)) alone. Therefore, the expression in brackets in eq. (24) reflects the additional interaction with the source field farther downstream of the plate edge. The deviations from the pure interaction at the plate edge become small if $\omega r_0/U_0 > 1$. The conclu-

sion from this is, that the parabolic field at the plate edge dominates if the source is farther away from the edge. Consider the situation shown in Fig. 3. In which location (a), (b) or (c) of the source will the interaction be the strongest? Equation (24) will give a clear answer: at (c), upstream of the shear layer.

In that context an interesting question is, how far an "exterior excitation" can come from the turbulent shear layer itself downstream of the plate edge in a real flow situation. In our model, the pressure sources of the shear layer motion lie in the $y = 0$ plane. Therefore, in this model, no feedback from the downstream perturbations is possible ($\sin \vartheta/2 = 0$). However, in a real situation $\Gamma p = 0$ is still valid outside the shear layer. The pressure sources are in a region of small ϑ . Therefore, a very weak feedback of the downstream turbulent flow is possible. This consideration is not that naïve as it seems at the first glance, because the equation $\nabla^2 p = -2\partial U/\partial y \cdot \partial v/\partial x$ is also valid in three dimensions. The source term on the right hand side might look slightly different in a nonlinear flow situation, but the concept of having linearly superposable pressure sources in the shear layer will not break down, because the pressure is a linear quantity in all our equations, and deviations of this linearity will occur only if the pressure perturbation is of the same order as the ambient gas pressure. Anyway, eq. (24) shows clearly, why shear layers are highly sensitive to perturbations (such as sound) coming from upstream and not very sensitive to perturbations having their origin downstream of the edge in the shear layer.

6. THE EDGE EXCITATION

Those who know recent experiments on excited jets know that an excitation close to the lip is very efficient. The preceding calculations did not consider this case, because it was assumed, that $\omega r_0/U_0 \gg 1$. On the other hand, eq. (23) can be also expanded for $\omega r_0/U_0 \ll 1$, which would include the lip excitation case. After some intermediate calculations we find

$$v_1 = \frac{Q_0}{2U_0} e^{\lambda_1 x} [e^{-x_0 \lambda_1} \cos(y_0 \lambda_1) - 2\sqrt{\frac{r_0 \lambda_1}{\pi}} \sin \frac{\vartheta}{2}] \quad (27)$$

with $\lambda_1 = \frac{\omega}{U_0} (i+1)$ and valid for

$$\omega r_0/U_0 \ll 1 \text{ and } \omega x/U_0 \gg 1$$

There is some interesting physics hidden in eq. (27). Assume that $y_0 \lambda_1 \rightarrow +0$ and $\sqrt{r_0 \lambda_1} \sin \vartheta/2 \rightarrow 0$. Then we have a source just above the shear layer at small, say, positive x_0 . The source acts then as a δ -function with the strength $Q/2$ on the shear layer. $Q/2$ is just the flux which penetrates through the shear layer plane. With this in mind we reconsider the general solution for the shear layer motion, eq. (11)*. For v_{1f} we have

$$v_{1f} = -\frac{Q}{2} \delta(x-x_0) \text{ at } y = +0. \quad (28)$$

With eq. (11) we find the complete solution at once:

$$v_1 = \frac{Q_0}{2U_0} [e^{\lambda_1 x} \cdot e^{-\lambda_1 x_0} - e^{\lambda_2 x} \cdot e^{-\lambda_2 x_0}] \quad (29)$$

For the pure lip excitation with $\lambda_1 x_0 \rightarrow 0$ we have a simple analytic solution which might be utilized if the free shear layer is excited just at the plate edge

$$v_1 = \frac{Q_0}{2U_0} (e^{\lambda_1 x} - e^{\lambda_2 x}) \quad (30)$$

Also the u -distribution in the whole ambient field can be written in closed form. It contains exponential integrals of complex argument for the induced field of the instability waves truncated at $x = 0$ ($v_1 = 0$ for $x < 0$) and of the induced field of the source^{12,20}. For distances farther downstream, we have a ultra-simple equation for

*) with $C_1 = C_2 = 0$

the magnitude of the instability waves, where $|v_1| = |v_2| = |u_1| = |u_2|$. We find

$$|u_2| = \frac{Q\omega}{2\bar{U}_0} e^{\frac{\omega x}{\bar{U}_0}} \quad \text{at } y = -0 \quad (31)$$

and with the introduction of the decay in y direction

$$|u_{1,2}| = \frac{Q\omega}{2\bar{U}_0} e^{\frac{\omega(x-|y|)}{\bar{U}_0}} \quad (32)$$

for $x > U_0/\omega$ and $y \neq 0$.

Q is the volume flux (say, in m^2/s) of the excitation source. In a real situation with an arrangement like the one shown below (see Fig. 4) we suspect, that more than half of the volume flux Q penetrates through the $y = 0$ plane. Therefore, the efficiency might be even slightly higher than suggested by eq. (32).

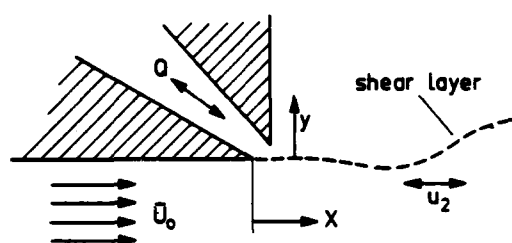


Fig. 4 Real edge excitation configuration.

7. FURTHER EXTENSIONS OF THE THEORY

The theory has been extended to the case of two streams of different velocity and density on both sides of the shear layer¹². Also the influence of additional walls for the case of a shear layer in a channel has been considered¹². The influence of a finite shear layer thickness has been also discussed^{12,13}. If one compares the present approach (with an infinitesimally thin shear layer) to the case of instability waves in a shear layer of finite momentum thickness θ , one finds that deviations from the theory are to be expected at Strouhal numbers above about $S_0 \approx 0.005-0.01$. The regime of amplified waves lies in the range of S_0 between 0 and 0.04. Therefore, the theory covers about the lower fourth of the amplified instability waves. This is also the regime of "large scale structures" in a shear layer.

8. EXPERIMENTS

Before we show the experimental data we have to outline the way in which the data are taken and processed. Fig. 5 shows the experimental setup. The splitter plate in the center of a rectangular channel separates a region of very slow entrainment flow ($\bar{U} < 0.1 \bar{U}_0$ at $y > 0$) from the mean flow region ($\bar{U} = \bar{U}_0$ at $y < 0$). The initial shear layer thickness can be controlled by boundary layer suction through a slit in the splitter plate near the plate edge.

The excitation is provided by two vibrating plates driven electromagnetically and operating in antiphase so that a surging motion around the edge of the splitter plate is produced. The magnitude of the excitation field

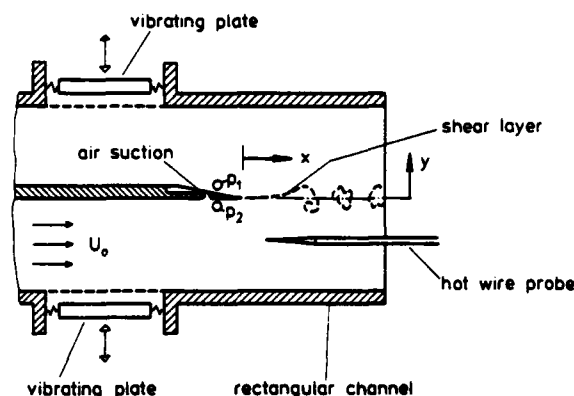


Fig. 5 Experimental arrangement.

is measured by two microphones on both sides of the splitter plate. The pressure difference $p_1 - p_2 = \Delta p_{12}$ is taken electronically and is a direct measure for the acoustic excitation.

In order to prevent effects of the suction slit on the sound field, the oscillating flow through the slit is compensated acoustically by a piston speaker in the suction duct. This piston speaker is adjusted in magnitude and phase so that zero oscillating flow condition through the slit is achieved. This is checked by a second hot wire probe (not shown in Fig. 5) inserted into the slit.

Fig. 6 shows a typical measurement taken by a hot wire probe. The mean velocity \bar{U} and the fluctuating velocity u_2 are taken at a constant downstream location x . The probe is moved perpendicularly (in y -direction) to the shear layer. For each data set the linearity between excitation pressure and velocity u_2 is tested by varying the excitation level. Only such data were chosen where linearity holds.

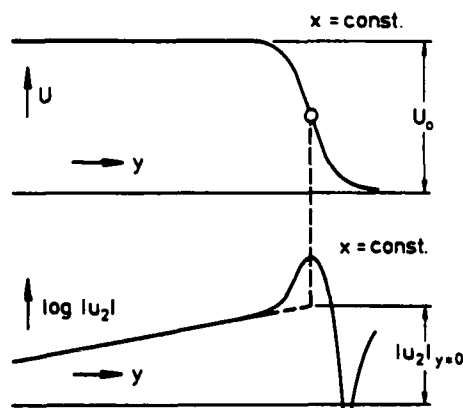


Fig. 6 Mean velocity \bar{U} and modulus of fluctuation u_2 plotted versus y at constant downstream location x

The modulus of u_2 is plotted versus y on semilogarithmic paper. Thus, an exponential decay of $|u_2|$ in the (minus) y -direction yields a straight line. If this straight line is extrapolated to the center of the shear layer, we find $|u_2|$ at $y = 0$, which is also predicted by our theory. As we see from the computations in Fig. 2, this extrapolation scheme will fail only for values very close to the plate edge.

In Fig. 7 our present data of $|u_2|$ at $y = 0$ are plotted versus x at different Strouhal numbers S_0 . $|u_2|$ and x are nondimensionalized as suggested by the theory (eqs (19) and (20)). The data compare well with our prediction, eq. (18). At increasing Strouhal numbers we

find the expected deviations.

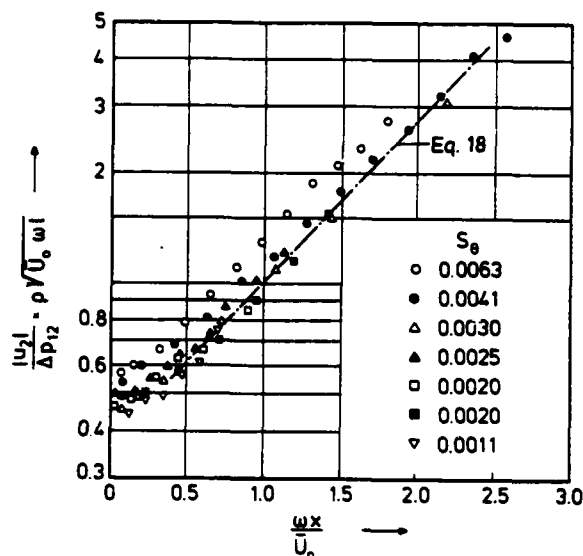


Fig. 7 Magnitude of instability waves as a function of downstream distance.

ACKNOWLEDGEMENT

The present work has been sponsored partly by NASA Lewis and by the Deutsche Forschungsgemeinschaft. The field calculations in section 3 are a repetition of earlier computations done by Dr. M. Nallasamy (University of Houston). He was also responsible for the elimination of some numerical convergence problems in this section. The author was encouraged by Professor A.K.M. F. Hussain (University of Houston) to carry out this research. He arranged also for the author's visit to Houston in this joint U.H.-DFVLR project.

9. BIBLIOGRAPHY

- [1] Y.V. Vlasov, A.S. Ginevski: "Generation and suppression of turbulence in an axisymmetric turbulent jet in the presence of an acoustic influence". NASA TT F-15721. Transl. from Russian: Izvestiya Akademiyi Nauk USSR, Mekhanika Zhidk., Gaza 6 Nov.-Dec. 1973, pp. 37-43.
- [2] K.B.M.Q. Zaman, A.K.M.F. Hussain: "Turbulence suppression in free shear flows by controlled excitation". J. Fluid Mech. 103 (1981), pp. 133-159.
- [3] P. Mensing: "Einfluß kontrollierter Störungen auf eine ebene turbulente Scherschicht". Dissertation: Techn. Univ. Berlin, Fachbereich 9, 1981.
- [4] B. Dziomba: "Experimentelle Untersuchung zum Einfluß von Anfangs- und Randbedingungen auf die Ausbreitung einer freien zweidimensionalen Scherschicht". Dissertation: Techn. Univ. Berlin, Fachbereich 9, 1981.
- [5] D.W. Bechert, E. Pfizenmaier: "On the amplification of broad band jet noise by a pure tone excitation". J. Sound & Vibr. 43 (1975), pp. 581-587.
- [6] C.J. Moore: "The role of shear layer instability waves in jet exhaust noise". J. Fluid Mech. 80 (1977), pp. 321-367.
- [7] C.G. Hodge, C.K.W. Tam: "Aeroacoustics" in: Aerospace highlights 1981. Astronautics & Aeronautics, Dec. 1981, pp. 28-29.
- [8] D.W. Bechert: "Sound absorption caused by vorticity shedding, demonstrated with a jet flow". J. Sound & Vibr. 70 (1980), pp. 389-405.
- [9] M.S. Howe: "The dissipation of sound at an edge". J. Sound & Vibr. 70 (1980), pp. 407-411.
- [10] I.S. Gartshore, A.M. Savill: "Some effects of free stream turbulence on the flow around bluff bodies". Euromech 160, Berlin, Sept. 1982.
- [11] R. Parker, M.C. Welsh: "The effect of sound on flow over bluff bodies". Euromech 160, Berlin, Sept. 1982.
- [12] D.W. Bechert: "Excited waves in shear layers". DFVLR-FB 82-23 (1982).
- [13] D.W. Bechert: "A model of the excitation of large scale fluctuations in a shear layer". AIAA paper 83-0724 (1983).
- [14] A. Michalke: "On spatially growing disturbances in an inviscid shear layer". J. Fluid Mech. 23 (1965), pp. 521-544.
- [15] P. Freymuth: "On transition in a separated laminar boundary layer". J. Fluid Mech. 25 (1966), pp. 683-703.
- [16] D.W. Bechert, E. Pfizenmaier: "Optical compensation measurements on the unsteady exit condition at a nozzle discharge edge". J. Fluid Mech. 71 (1975), pp. 123-144.
- [17] I.N. Bronstein, K.A. Semendjajew: "Taschenbuch der Mathematik", 19. Aufl. Frankfurt/M.: Verlag Harri Deutsch, 1980. (Translation from Russian, also available in English).
- [18] D.W. Bechert, U. Michel: "The control of a thin free shear layer with and without a semi-finite plate by a pulsating flow field". ACUSTICA 33 (1975), pp. 287-307.
- [19] S.A. Orszag, S.C. Crow: "Instability of a vortex sheet, leaving a semi-infinite plate". Studies Appl. Math. 49 (1970), pp. 167-181.
- [20] D.W. Bechert, U. Michel: "The control of a thin free shear layer with and without a semi-infinite plate with a pulsating monopole or dipole. Some new closed form solutions". DLR-FB 74-22, (1974).

AD-A135 034

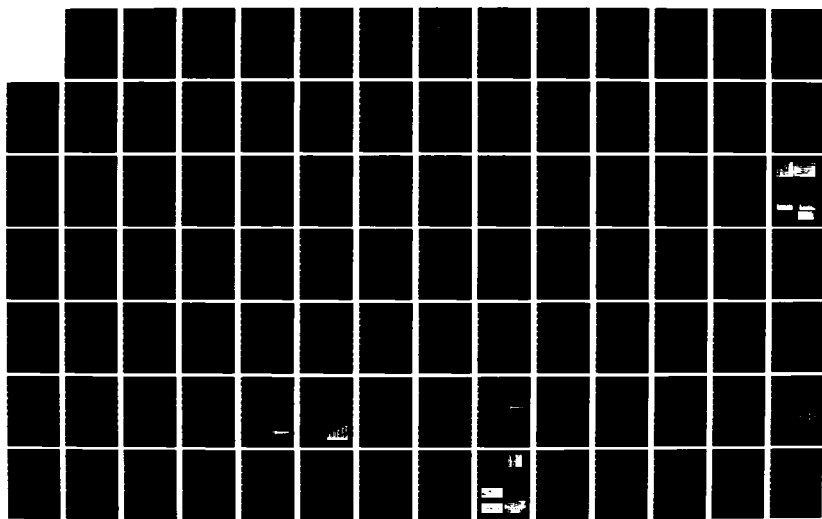
SYMPOSIUM ON TURBULENT SHEAR FLOWS (4TH) HELD AT
KARLSRUHE UNIVERSITY (GERMANY FR) 12-14 SEPTEMBER 1983
(U) KARLSRUHE UNIV (GERMANY F R) SEP 83

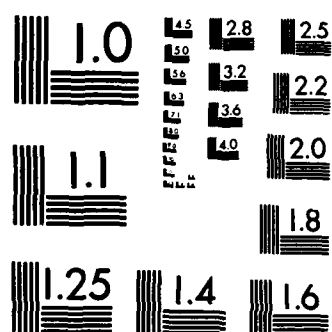
677

UNCLASSIFIED

F/G 20/4

NL





MICROCOPY RESOLUTION TEST CHART
NATIONAL BUREAU OF STANDARDS-1963-A

Large-scale Coherent Structure and Far-field Jet Noise

by

K. B. M. Q. Zaman
NASA Langley Research Center
Hampton, VA 23665, USA

Abstract

The phenomenon of broadband noise amplification/suppression under controlled excitation is investigated. The suppression is found to occur only at low jet speeds when the exit boundary layer is laminar; excitation at $St_0 = 0.017$ results in optimum suppression of the far-field broadband noise as well as of the near-flow-field turbulence. The noise amplification is found to be a function of the Mach number, the amplification is higher at higher Mach number for a given excitation Strouhal number and level. The amplification also depends on the Strouhal number (St_D), the maximum occurring in the range 0.65-0.85. Vortex pairing induced by the excitation appears to be at the heart of the noise amplification phenomenon under excitation.

Introduction

Recent experimental evidences make it abundantly clear that the noise-producing near-flow-field of an axisymmetric jet is dominated by large-scale, coherent, vortical structures (see, e.g., [1-4]). Several experimental investigations have also made it quite clear that these coherent structures can be significantly altered or manipulated under controlled, artificial excitation [2-8]. However, relatively little is known about the details of the effect of controlled excitation on the radiated noise and about the link between observed modification of the noise and the altered states of the coherent structures. An experimental investigation is currently in progress with the objective of achieving a better grasp on this link, obtaining a clearer understanding of the jet noise production mechanism being the ultimate goal. Some preliminary results of this study are presented here. Attention is focused in this paper on the conditions of excitation which result in an amplification or suppression of the broadband components of the far-field noise. The question of a 'Reynolds number barrier', in this regard [9], is also addressed.

Experimental Procedures

The experiments were carried out in a 9.1 m x 6.1 m x 7.6 m anechoic chamber. The jet flow was obtained by passing compressed air through an upright, 20 cm diameter, cylindrical settling chamber. The flow finally passed through a convergent nozzle which ended in a short straight section. A 2.54 cm diameter nozzle was used for most data reported here. Top-hat mean velocity

profiles with thin boundary layers were obtained at all speeds, the turbulence intensity at the exit center was less than 0.2 percent. The far-field noise was measured by one-half inch (B&K) microphones held fixed on an arc of a circle having the nozzle exit at the center; the microphones were at a distance $R/D = 120$ with the nozzle exit diameter D being 2.54 cm. Standard constant temperature anemometry was used for the flow measurements. The excitation was provided by means of two loudspeakers attached to the settling chamber, the cavity resonances were utilized to obtain the plane wave excitation. The excitation level at the jet exit was monitored by measurement of the filtered rms component of the velocity (u'_{fe}) at the driving frequency. The corresponding excitation level in terms of the SPL (L_e) was monitored by a one-eighth inch microphone fitted with a nose-cone and placed such that the jet exit plane bisected the opening in the nose-cone. All spectra, as well as u'_{fe} and L_e , were obtained by 1000-line narrow-band analysis using a Spectral Dynamics (SD360) analyzer. All data acquisition, probe traverses, etc were done under remote computer (PDP 1170) control from an adjacent room which housed all the instrumentation.

Results and Discussion

In order to evaluate the changes in the jet noise brought about by the excitation, a knowledge of the unexcited jet noise was necessary. The scaling of the power spectral density (PSD) of the far-field noise of subsonic, unheated, axisymmetric jets had been addressed in a prior study [10], based on a collection of data from the literature as well as data taken in the preliminary phase of the present experiment. A principal result of this previous study that concerns the results to be presented here is briefly described below.

The non-dimensionalized PSD of the far-field noise at $\theta = 90^\circ$ obtained in the present jet facility is shown in figure 1; θ is the angle of the measurement from the downstream jet axis. P^* equals $(p/(\rho U^2))^2 (R/D)^2 (U/(\Delta f D))$, where p is the rms pressure fluctuation, ρ is the density of the ambient air, U the jet exit velocity, R the distance of the measurement point from the jet exit center, and Δf the bandwidth of analysis. Note that $P^* M^{-3.5}$ is plotted versus the Strouhal number St_D ; here $M (=U/a_0)$ is the Mach number, a_0 being the sound speed in the ambient medium. It was shown in [10] that these are the coordinates which best collapsed the PSD data at 90° . (See [10] for further details and scaling of the PSD at other angles). These data should provide a basis for comparison of the far-field noise modification

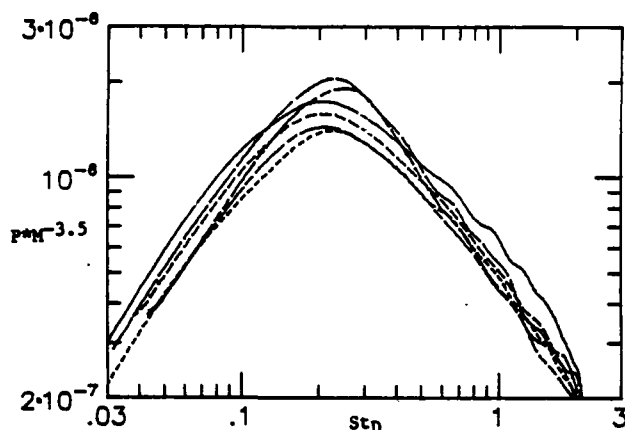


Fig. 1 PSD of far-field noise at $\theta=90^\circ$.

—, $M=0.84$; —, $M=0.78$;
 —, $M=0.68$; —, $M=0.57$;
 —, $M=0.52$; —, $M=0.59$.
 $D=1.27$ cm for $M=0.59$ case, all others taken
 in $D=2.54$ cm jet.

under excitation and in detection of any peculiarities in the unexcited jet noise PSD. However, in order to assess the precise effect of the excitation, the excited case data are always compared with the corresponding unexcited case data taken successively.

The peaks of the PSD curves in figure 1 do not show any sharp variation with the Reynolds number, over the measurement range 1.7×10^5 - 5.0×10^5 . Based on their own data at low Re_D and data at high Re_D from the literature, Long et al [11] had observed a 10 dB variation in the SPL above and below $Re_D = 3 \times 10^5$. The present data as well as several sets of data taken from the literature did not bear out such a ' Re_D -barrier' for the far-field noise amplitude [10].

Based on jet excitation data from the literature, Crighton [9] had, at first, observed a similar 'Reynolds number barrier' in connection with the phenomenon of broadband noise amplification/suppression. He observed that artificial excitation resulted in an amplification of the broadband spectral components (of turbulence and/or far-field noise) if the jet Reynolds number was above about 10^5 , but a suppression occurred when the Re_D was below 10^5 . Data taken in the present experiment show that the broadband noise suppression phenomenon is rather a function of the jet initial condition

(i.e., exit boundary layer state) and also of the excitation Strouhal number. The Reynolds number dependence enters the picture simply because for a given (untripped) jet, the initial boundary layer becomes transitional above a certain Re_D . It appears that this transitional Re_D in the investigations reporting suppression, as summarized by Crighton, happened to be about 10^5 in all cases. Indeed, the transitional Re_D in the present jet is also found to be about 10^5 . But this author believes from past experience that the transitional Re_D can be practically any number depending on the size of the jet and the care with which it is built. The following points are pertinent in connection with the broadband noise suppression:

(a) A reduction in the broadband turbulence at some point in the flow does not necessarily result in a broadband noise suppression. This is illustrated in figures 2(a) and (b). Figure 2(a) shows that the excitation inducing stable vortex pairing (i.e., periodic pairing of the vortex rings yielding the subharmonic spike; [4,5]) results in a large suppression of the broadband turbulence at locations nearer to the jet exit; S_u is u-spectrum shown with arbitrary vertical scale. The corresponding far-field noise at 90° (figure 2b), however, shows a consistent increase in the broadband components all over the frequency range.

(b) The suppression phenomenon is dependent upon the Strouhal number of excitation. Significant suppression of the far-field noise occurred only in the 'shear layer mode' of excitation, i.e., at Strouhal numbers falling close to the most unstable mode of the exit shear layer. Optimum suppression occurred at the most unstable Strouhal number $St_\theta = 0.017$ [12], where $St_\theta (=f_p \theta/U)$ is the Strouhal number based on the exit shear layer momentum thickness θ . Thus, the same flow which shows a broadband noise amplification at $St_D = 0.88$ in figure 2(b), shows a suppression when excited at $St_\theta = 0.017$ as shown in figure 3(b). In the latter case, there is broadband suppression in both near-field turbulence (figure 3a) and far-field noise. Note that excitation at $St_\theta = 0.017$ had been shown in a previous study [13] to be the condition resulting in maximum turbulence suppression for different free shear flows with initially laminar boundary layers. It is noteworthy, and perhaps, disappointing, that while the near-field turbulence suffers suppression of the total intensity (resultant of broadband, excitation tone and (sub)harmonics), the suppression in the far-field noise is only in the broadband components. The total fluctuation intensity u' in

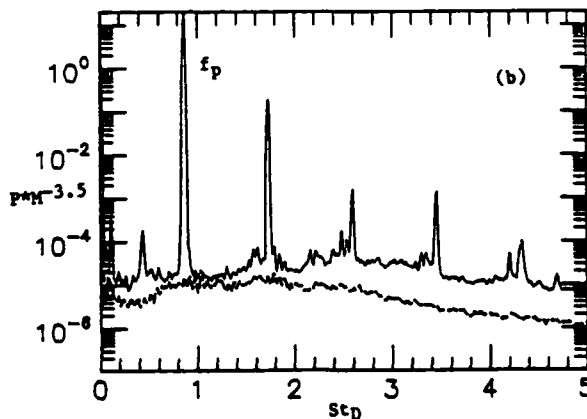
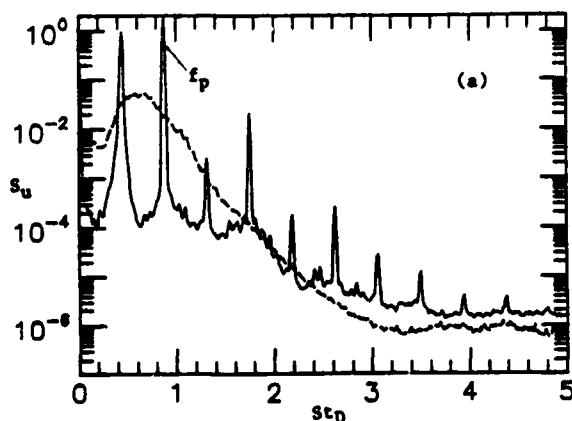


Fig. 2 Excitation inducing stable vortex pairing. $St_D=0.88$, $u'_{f_e}/U=1\%$, $M=0.12$, $Re_D=60000$. Dotted traces for unexcited case. (a) u-spectrum at $x/D=1.5$ on the jet axis. (b) PSD at $\theta=90^\circ$.

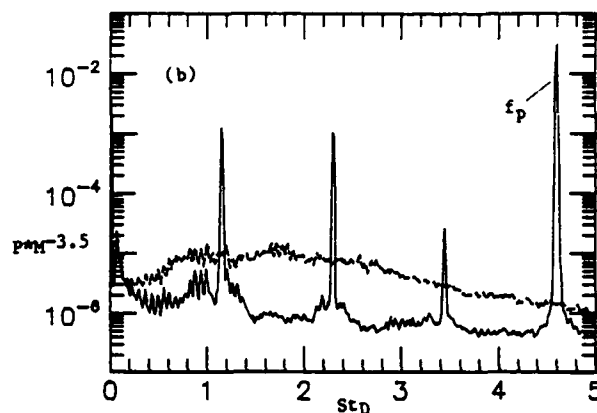
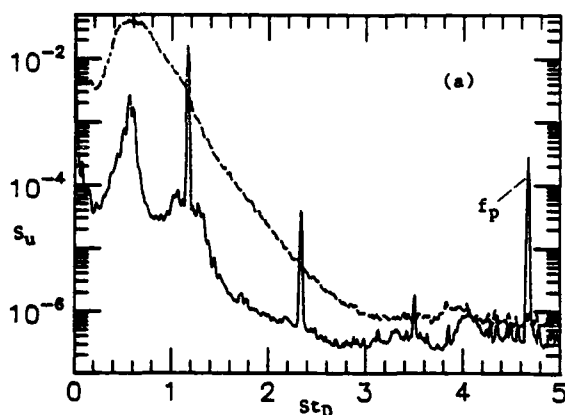


Fig. 3 Excitation inducing turbulence and broadband noise suppression. Dotted curves for unexcited case. $St_0=0.017$, $u'_{f_0}/U=0.03\%$, $M=0.12$, $Re_D=60000$.
(a) u -spectrum at $x/D=1.5$ on jet axis. (b) PSD at $\theta=90^\circ$.

figure 3(a) for the excited case is only 24 percent of the corresponding u' in the unexcited case; but the total SPL at 90° for excitation (figure 3b) far exceeded the corresponding unexcited value.

(c) Significant broadband noise suppression (like in figure 3b) could not be observed under any excitation condition for initially tripped jet or for the untripped jet operated at high M (or Re_D) when the initial boundary layer became transitional. For the untripped 2.54 cm jet in the present experiment, the exit boundary layer was found to be undisturbed laminar for $U < 60$ m/s but became 'nominally laminar' above this velocity. (A 'nominally laminar' boundary layer can be defined as one which has a U -profile agreeing fairly with the Blasius profile but which suffers significant fluctuation intensity, say above 1 percent of U ; see [14] for a discussion on this). Measurements up to $U = 173$ m/s showed that, the boundary layer still remained 'nominally laminar' or 'disturbed laminar' and did not become 'fully turbulent'. The exit boundary layer characteristics in the present jet are shown in figure 4 for two speeds below and above the onset of transition.

(d) The unexcited jet noise at low M (and Re_D) with initially laminar boundary layer is relatively higher—as should be evident by comparison of figure

3(b) and figure 1. The suppression phenomenon brings this level down to the asymptotic lower level found for the higher M cases. The turbulence suppression under excitation also behaves in a similar fashion. For the unexcited case, the near-field turbulence intensity is higher, and excitation at $St_0 = 0.017$ can only bring this level down to levels encountered in high M or initially turbulent boundary layer cases. As a matter of fact, the centerline u' variation for excitation at $St_0 = 0.017$ for $Re_D = 21000$ reported in [13], agree excellently with corresponding data in the present jet at $M = 0.44$ (see figure 10 later).

In the above context, the far-field broadband noise suppression phenomenon appears to be a special case, as far as practical jet noise suppression is concerned, and is observed only when the jet exhibits higher relative levels to start with.

Broadband Noise Amplification

When the unexcited jet noise is at the lower asymptotic level as in figure 1, excitation can only

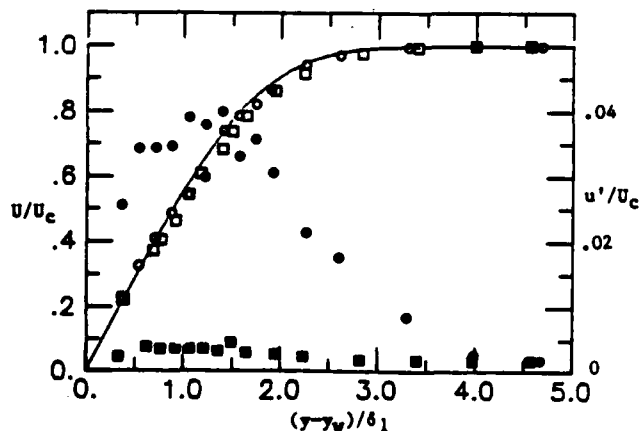


Fig. 4 Exit boundary layer characteristics. \square , $U=60$ m/s; \circ , $U=95$ m/s. Open data for mean velocity (U) profiles, solid data for rms fluctuation intensity (u') profiles. Solid line represents Blasius profile.

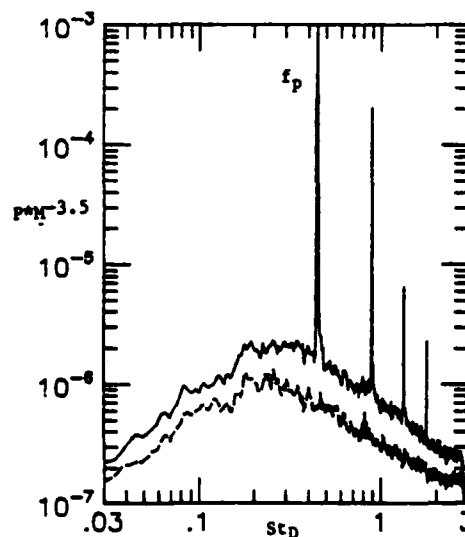


Fig. 5 PSD at $\theta=90^\circ$. $M=0.44$, $St_D=0.44$, $u'_{f_0}/U=0.46\%$ ($L_e=138$ dB). Dotted curve for unexcited case.

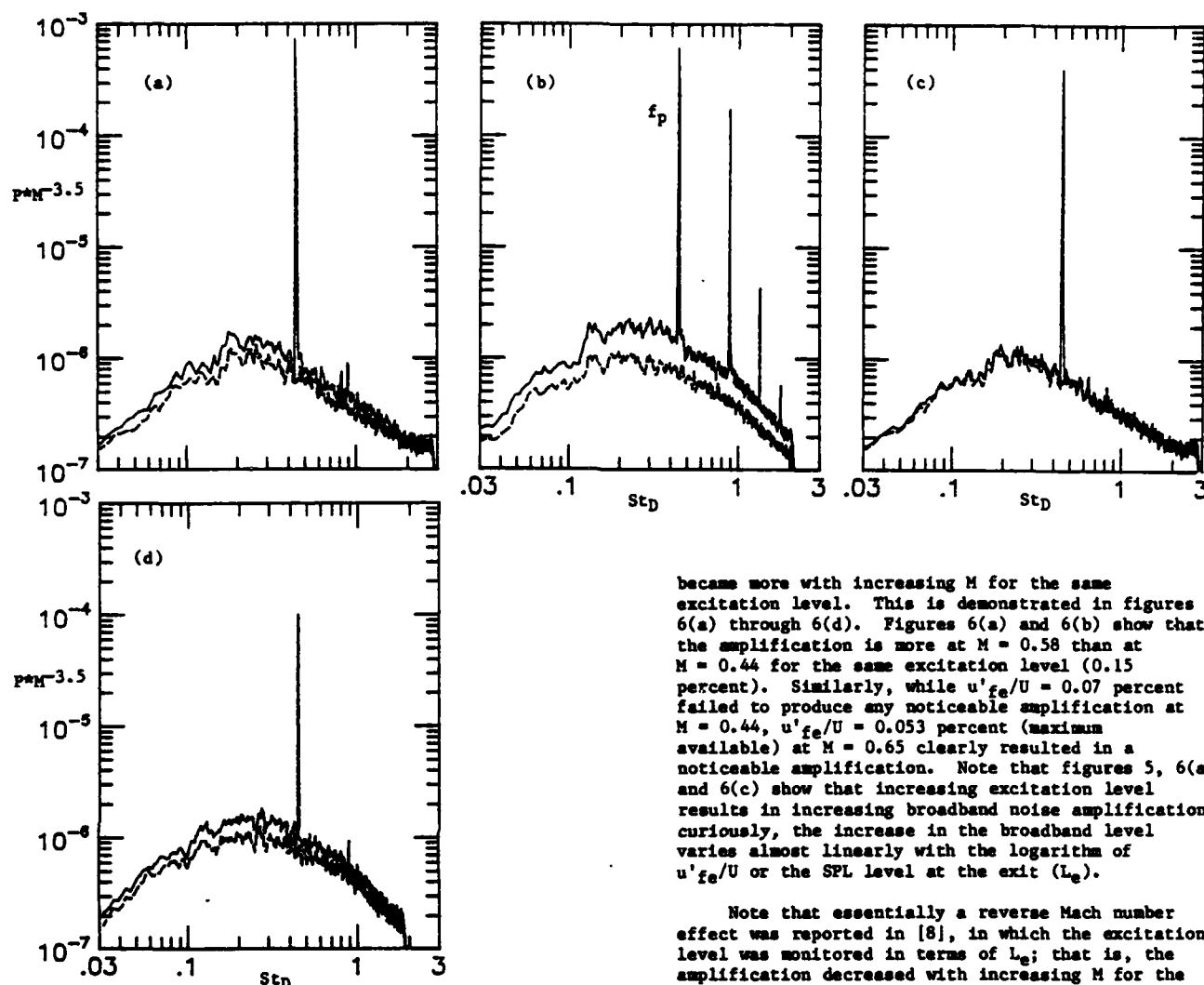


Fig. 6 PSD at $\theta=90^\circ$. Mach number effect. Dotted curves for unexcited cases.
 (a) $M=0.44$, $St_D=0.44$, $u'_{fe}/U=0.15\%$ ($L_e=131$ dB).
 (b) $M=0.58$, $St_D=0.44$, $u'_{fe}/U=0.15\%$ ($L_e=136$ dB).
 (c) $M=0.44$, $St_D=0.44$, $u'_{fe}/U=0.07\%$ ($L_e=125$ dB).
 (d) $M=0.65$, $St_D=0.44$, $u'_{fe}/U=0.053\%$ ($L_e=130$ dB).

result in an amplification. The broadband jet noise amplification phenomenon has been observed by many previous researchers [3,8,15,16]. Typical broadband noise amplification is shown in figure 5. The excitation in this case results in a uniform lift of the broadband level. The phenomenon is also essentially independent of the angle θ ; this is why data for $\theta = 90^\circ$ only are presented here, the inferences drawn from which are general and independent of the angle of observation.

In this study, it has been established that for a given level of excitation, the broadband noise amplification is a function of the Mach number and a strong function of the excitation Strouhal number.

Mach Number Effect: The Mach number effect became apparent while attempting to reproduce the results reported in [15]. Bechert and Pfizenmaier observed about 7 dB increase in the SPL for excitation at $St_D = 0.48$ for $M = 0.6$ with excitation level $u'_{fe} = 0.39$ percent. Initially, excitation at the same level but at lower M in the present experiment failed to produce as much increase in the SPL. Subsequently, it became clear that the amplification

became more with increasing M for the same excitation level. This is demonstrated in figures 6(a) through 6(d). Figures 6(a) and 6(b) show that the amplification is more at $M = 0.58$ than at $M = 0.44$ for the same excitation level (0.15 percent). Similarly, while $u'_{fe}/U = 0.07$ percent failed to produce any noticeable amplification at $M = 0.44$, $u'_{fe}/U = 0.053$ percent (maximum available) at $M = 0.65$ clearly resulted in a noticeable amplification. Note that figures 5, 6(a) and 6(c) show that increasing excitation level results in increasing broadband noise amplification; curiously, the increase in the broadband level varies almost linearly with the logarithm of u'_{fe}/U or the SPL level at the exit (L_e).

Note that essentially a reverse Mach number effect was reported in [8], in which the excitation level was monitored in terms of L_e ; that is, the amplification decreased with increasing M for the same St_D and L_e . Preliminary data in the present facility show that keeping a constant L_e rather results in a constant broadband noise amplification for different M . This apparent conflict will be addressed later but one has to remember that several factors come into play in this connection. For example, at higher M , a higher f_p (required to achieve the same St_D) may be approaching the cut-on frequency for higher order modes. In such case, the global excitation characteristics at the exit plane can become different. (The cut-on frequency for the first azimuthal mode through the nozzle was 5 kHz while $f_p = 3880$ Hz for figure 6d).

Strouhal Number Effect: The Strouhal number effect on the broadband noise amplification is demonstrated in figure 7(a) through 7(d)—all for $M = 0.44$ and $u'_{fe}/U = 0.15$ percent. Comparison of these four figures and figure 6(a) shows that maximum broadband noise amplification occurs at $St_D = 0.68$. Based on similar sets of data at other M and for different D , the optimum amplification was found to occur in the St_D range of 0.65–0.85. Figures 8(a) and 8(b) are further included for a lower M , to support this observation. Note that the unexcited jet noise at $M = 0.28$ in figure 8 shows deviations from the characteristic PSD's of figure 1—and indicate the presence of other competing noise sources. However, it is clear that excitation at $St_D = 0.67$ dramatically increases the broadband noise compared to the $St_D = 0.39$ case.

It had been shown in [4], with detailed measurements in [5], that excitation at $St_D = 0.85$

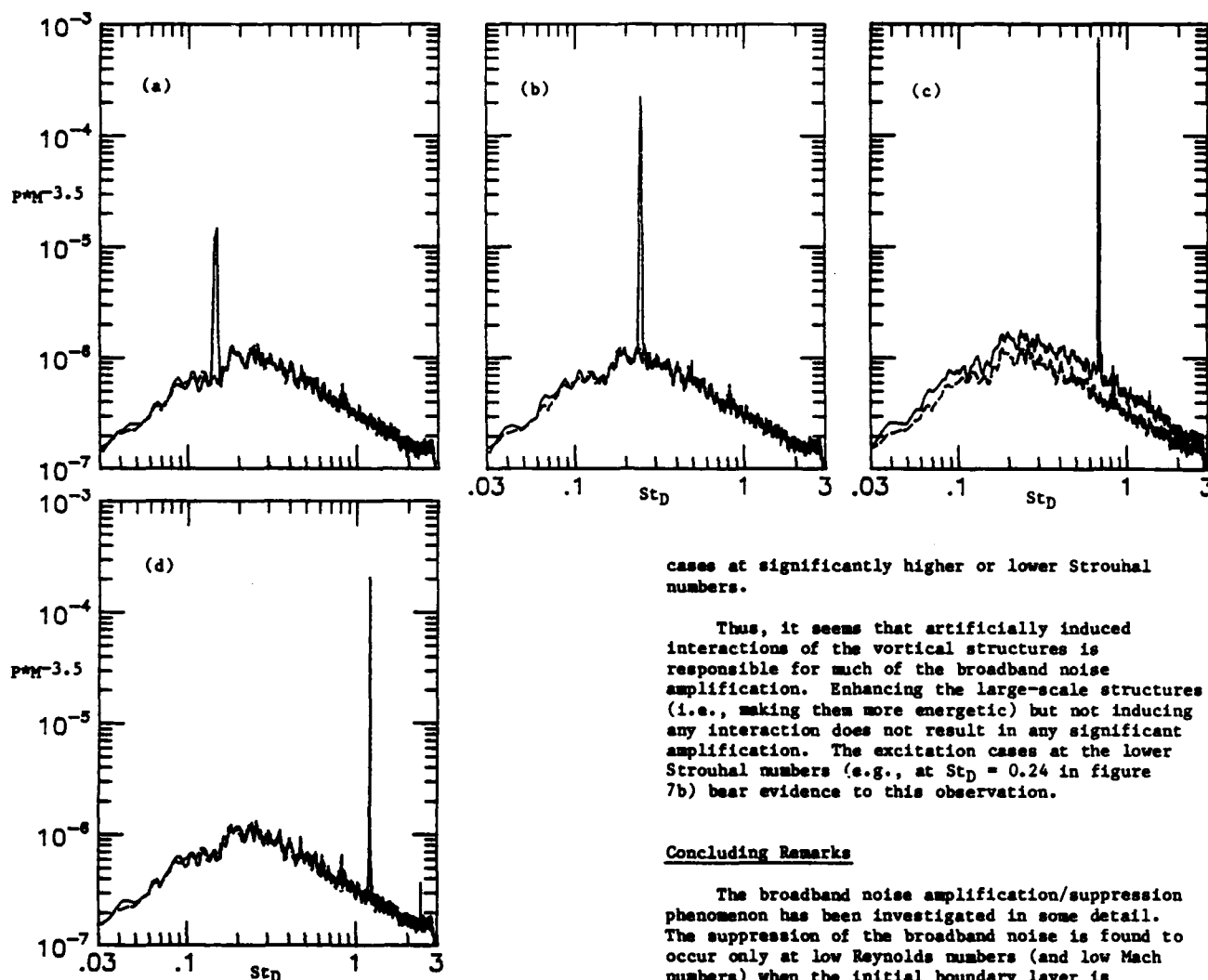


Fig. 7 PSD at $\theta=90^\circ$. Strouhal number effect. Dotted curves for unexcited case.
 (a) $M=0.44$, $St_D=0.14$, $u'_{fe}/U=0.15\%$ ($L_e=120$ dB).
 (b) $M=0.44$, $St_D=0.24$, $u'_{fe}/U=0.15\%$ ($L_e=121$ dB).
 (c) $M=0.44$, $St_D=0.68$, $u'_{fe}/U=0.15\%$ ($L_e=134$ dB).
 (d) $M=0.44$, $St_D=1.19$, $u'_{fe}/U=0.15\%$ ($L_e=125$ dB).

results in the 'jet column mode' of vortex pairing. With initially laminar boundary layer, the excitation at $St_D = 0.85$ results in 'stable' pairing of the vortices. Initially turbulent (or transitional) boundary layer cannot support stable pairing, but the strongest pairing activity is still induced at $St_D = 0.85$. Such pairing results in a broadband, but distinct, hump at the subharmonic frequency (instead of a spike). The pairing activity and the resulting hump at the subharmonic frequency, for excitation at $St_D = 0.68$ (figure 7c), is demonstrated in figure 9. It is also noteworthy that both unstable pairing (figures 7c, 9) and stable pairing (figures 2(a) and 2(b)) result in significant increase in the broadband noise. The variation of the longitudinal turbulence intensity along the jet axis for $St_D = 0.68$ is compared with the unexcited case and the case of excitation at $St_D = 0.44$ in figure 10. These variations agree well with the data in [4] where the pairing phenomenon was studied at much lower Mach number. Excitation results in an upstream shift of the $u'(x)$ curves associated with a faster spreading of the jet. The $St_D = 0.67$, inducing pairing, yields the fastest spread of the jet compared to excitation

cases at significantly higher or lower Strouhal numbers.

Thus, it seems that artificially induced interactions of the vortical structures is responsible for much of the broadband noise amplification. Enhancing the large-scale structures (i.e., making them more energetic) but not inducing any interaction does not result in any significant amplification. The excitation cases at the lower Strouhal numbers (e.g., at $St_D = 0.24$ in figure 7b) bear evidence to this observation.

Concluding Remarks

The broadband noise amplification/suppression phenomenon has been investigated in some detail. The suppression of the broadband noise is found to occur only at low Reynolds numbers (and low Mach numbers) when the initial boundary layer is laminar. The suppression is found to occur when the excitation is provided at the unstable frequency range of the exit shear layer, $St_D = 0.017$ resulting in maximum suppression. In this excitation condition there is also a remarkable suppression of the near-field turbulence. However, while the total turbulence intensity drops well below the corresponding unexcited level, the suppression in the far-field noise occurs only in the broadband components. The broadband noise suppression occurs in situations where the unexcited jet noise is 'unclean' to begin with, having a higher (nondimensional) PSD level compared to the asymptotically lower PSD level found at higher Mach numbers.

When the unexcited jet noise is at the asymptotically lower level, which is the case at higher M (and Re_p), the excitation can only result in an amplification of the broadband noise. The broadband noise amplification is found to be a function of the Mach number; with increasing M , the amplification is more for excitation at the same St_D and level. As previously found by others, the amplification is also observed to be a function of the excitation Strouhal number. It is shown in this work that the maximum amplification occurs at a St_D of 0.65 to 0.85. Excitation in this Strouhal number range had been found to induce strongest vortex pairing activity in the near-flow-field. Thus, the broadband amplification under excitation appears to be linked with the induced interactions of the large-scale structures. This result should bring up renewed/reinforced emphasis on the role of vortex pairing in jet noise production.

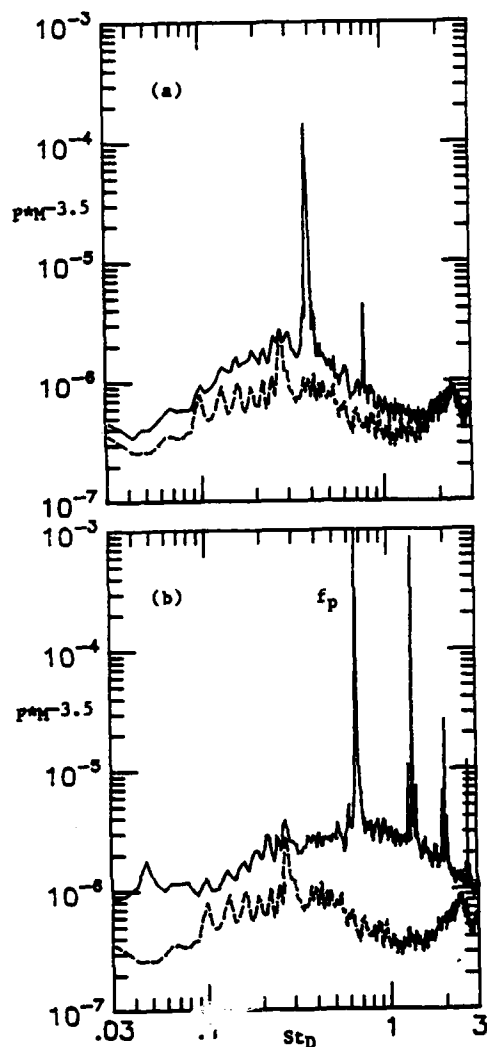


Fig. 8 PSD at $\theta=90^\circ$. Dotted curves for unexcited case.
(a) $M=0.28$, $St_D=0.39$, $u'_{fe}/U=1\%$ ($L_e=135$ dB).
(b) $M=0.28$, $St_D=0.67$, $u'_{fe}/U=1\%$ ($L_e=138$ dB).

A large set of data has been obtained for typical cases of broadband noise amplification under excitation. These cases include excitation at $St_D = 0.44$ and 0.68 at $M = 0.44$ and the corresponding unexcited case. Detailed time-average and spectral evolution data for the flow-field as well as the near-pressure field, have been acquired on a cross-sectional plane. Conditional sampling measurements are also being carried out for the eduction of the large-scale structures in these flows. These results are expected to shed further light on the mechanics of broadband noise amplification under excitation and on jet noise production mechanism in general, and will be summarized in a publication in the near future.

Acknowledgement: This research has been carried out while the author held a National Research Council fellowship.

References

1. Broward, F. K. and Laufer, J. 1975, *Turb. in Liquids* 5, 333, U. of Missouri-Rolla.
2. Crow, S. C. and Champagne, F. H. 1971, *J. Fluid Mech.* 48, 547-591.

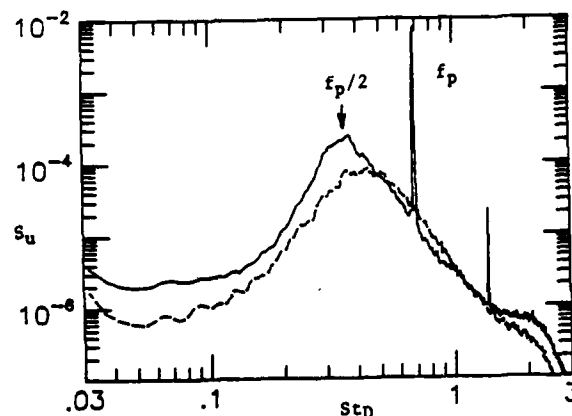


Fig. 9 u-spectrum at $x/D=1.5$ on the jet axis.
 $M=0.44$, $St_D=0.68$, $u'_{fe}/U=0.15\%$. Dotted curve for unexcited case.

3. Moore, C. J. 1977, *J. Fluid Mech.* 80, 321-367.
4. Zaman, K. B. M. Q. and Hussain, A. K. M. F. 1980, *J. Fluid Mech.* 101, 449-491.
5. Hussain, A. K. M. F. and Zaman, K. B. M. Q. 1980, *J. Fluid Mech.* 101, 493-544.
6. Kibens, V. 1979, *AIAA Paper No. 79-0592*.
7. Richarz, W. G. 1983, *AIAA J.* 21, 148-149.
8. Ahuja, K. K., Lepicovsky, J., Tan, C. K. W., Morris, P. J. and Burrin, R. H. (Lockheed-Georgia Co.), 1982, NASA CR-3538.
9. Crighton, D. 1981, *J. Fluid Mech.* 106, 261-298.
10. Zaman, K. B. M. Q. and Yu, J. C. 1983, "Power Spectral Density of Subsonic Jet Noise" (Submitted to *J. Sound and Vib.*).
11. Long, D., VanLent, T. and Arndt, R. E. A. 1981, *AIAA Paper No. 81-1962*.
12. Michalke, A. 1965, *J. Fluid Mech.* 22, 351.
13. Zaman, K. B. M. Q. and Hussain, A. K. M. F. 1981, *J. Fluid Mech.* 103, 133-159.
14. Hussain, A. K. M. F. 1980, *Lecture Notes in Physics* 136 (ed. J. Jimenez), 252-291.
15. Bechert, D. and Pfizenmaier, E. 1975, *J. Sound and Vib.* 43, 581-587.
16. Daneville, P. and Jacques, J. 1977, *AIAA Paper No. 77-1368*.

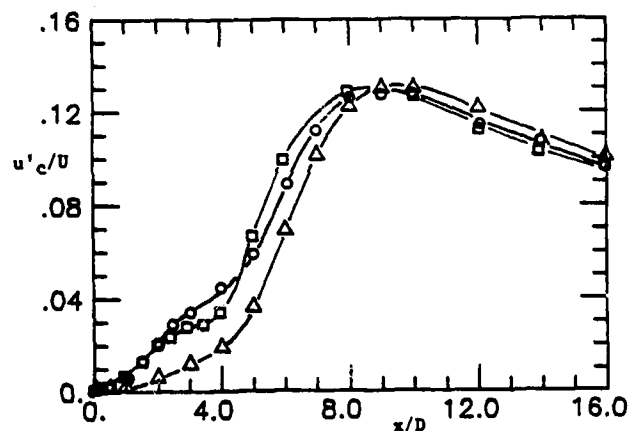


Fig. 10 Variation of longitudinal turbulence intensity along the jet axis for $M=0.44$ jet.
 \circ , $St_D=0.44$, $u'_{fe}/U=0.15\%$;
 \square , $St_D=0.68$, $u'_{fe}/U=0.15\%$;
 \triangle , unexcited jet.

SESSION 17 - HEAT TRANSFER

L. Back - Chairman

VERIFICATION OF THE EXTENDED GRADIENT DIFFUSION MODEL BY MEASUREMENTS OF THE MEAN AND FLUCTUATING TEMPERATURE FIELDS IN SODIUM FLOW DOWNSTREAM OF A MULTI-BORE JET BLOCK

L. Krebs

Kernforschungszentrum Karlsruhe
Institut für Reaktorbauelemente
Postfach 3640, 7500 Karlsruhe 1
Federal Republic of Germany

and

K. Bremhorst

Department of Mechanical Engineering
University of Queensland, St. Lucia
Queensland 4067, Australia

ABSTRACT

A diffusivity based model previously developed by the authors for the prediction of mean and fluctuating temperatures in water flow downstream of a multi-bore jet block in which one jet is heated, has been applied to flow of sodium in apparatus of identical geometry to that used for the water flow. Since the dynamic properties of water and sodium are very similar, the effect of the grossly different Prandtl numbers can be examined independent of the velocity field. Molecular conductivity terms are neglected relative to turbulent diffusion ones for water but are included for the sodium flow. In other respects the model is the same for both flows. Calculated and measured mean temperatures in sodium show a small difference when using model parameters determined in the water flow but show excellent agreement at different Reynolds numbers when an adjustment is made to the constant of proportionality in the diffusivity model. Measurements of the turbulence intensity downstream of the jet block in sodium using a miniature electromagnetic probe indicate that this adjustment is necessary due to a difference in the velocity field of water and sodium rather than oversimplification of the model.

INTRODUCTION

Coolant flow monitoring in fuel rod subassemblies of sodium cooled nuclear power reactors is important for safety as well as performance purposes. Reliable instrumentation for velocity measurements is not yet available, particularly, if turbulence quantities are required. It is necessary, therefore, to be able to interpret temperature measurements by means of mathematical models which will give some insight into the velocity field from temperature data. Such mathematical models are generally extensively tested by use of geometrically similar models in water since water and liquid sodium have similar kinematic viscosities - within a factor of two or three under normally used laboratory conditions - and nearly identical densities thus giving dynamic similarity. In the absence of a suitable velocity transducer for use in sodium the velocity field can, therefore, be obtained in water. If these velocity data can then be used in a model relating the velocity field to the temperature field when a part of the flow is heated, much can be deduced from just temperature measurements in the sodium flow.

In this work, an eddy diffusivity and gradient diffusion approach has been used to solve the mean and fluctuating temperature equations. Details of the model for the case of negligible molecular conductivity as in water have already been presented by Krebs et al. (1981). Simulation of the flow through tube bundles is by means of a multi-bore jet block set in a containment pipe. While the geometry of the flow cross-section is the inverse to that in the rod bundle, the downstream flow can

be expected to be affected only marginally. In both cases, the downstream flow will be similar to a grid generated flow. Turbulence decay laws are, therefore, similar to the present ones have been discussed by Brodkey (1975) and Gal-el-Hak and Morton (1979), but in both cases the blockage ratios are significantly different as also are the geometric details. Mathematical models suitable for present purposes are also absent.

MATHEMATICAL MODEL

The basic flow variables and the coordinate system are shown in Fig. 1. For steady incompressible flow with negligible heating by dissipation and no internal heat sources, the energy equation reduces to

$$U_i \frac{\partial \bar{T}}{\partial x_i} = \frac{\partial}{\partial x_i} \left[\alpha \frac{\partial \bar{T}}{\partial x_i} - \overline{u_i \delta} \right] \quad (1)$$

where the usual Reynolds decomposition has been used and the Einstein summation applies to repeated indices.

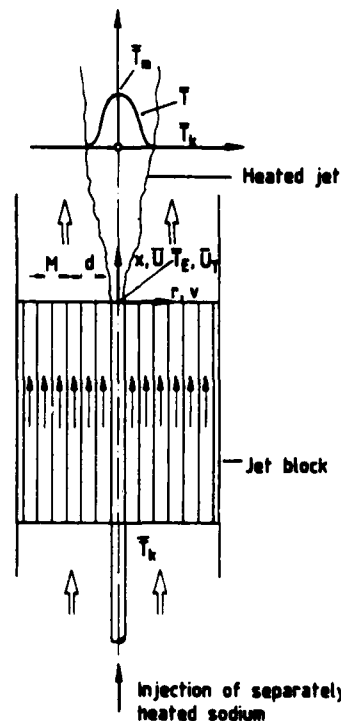


FIG. 1 COORDINATE SYSTEM AND FLOW VARIABLES.

Closure of Eq. (1) is obtained by use of the Boussinesq assumption

$$\overline{u_i \delta} = -\alpha_E \frac{\partial \overline{T}}{\partial x_i} \quad (2)$$

Except in the immediate vicinity of the exit, the flow is uniform in the radial and azimuthal directions, and rapid changes in \overline{T} are restricted to the radial direction. α_E , the eddy diffusivity, is therefore a function only of x , the streamwise coordinate. Unlike for water, Krebs et al. (1981), the molecular diffusivity is not negligible so that the simplified energy equation becomes in cylindrical coordinates

$$\overline{U} \frac{\partial \overline{T}}{\partial x} = \left[\alpha + \alpha_E(x) \right] \left[\frac{1}{r} \frac{\partial \overline{T}}{\partial r} + \frac{\partial^2 \overline{T}}{\partial r^2} \right] \quad (3)$$

where \overline{U} is the local mean streamwise velocity. The Lagrangian description of diffusion

$$\alpha_E(x) = v^1 L_L \quad (4)$$

is used to relate the eddy diffusivity to the velocity field. The particle velocity v^1 is assumed to be proportional to the streamwise velocity fluctuation, u , and the Lagrangian length scale, L_L , is assumed to be proportional to the Eulerian one, L_f . Introduction of the power law relationships found in water by Krebs et al. (1981)

$$\frac{\sqrt{u^2}}{\overline{U}} = 0.73 \left(\frac{x}{d} \right)^{-0.833} \quad (5a)$$

$$\frac{L_f}{d} = 0.14 \left(\frac{x}{d} \right)^{-0.44} \quad (5b)$$

permits $\alpha_E(x)$ to be expressed in the power law form

$$\alpha_E(x) = \frac{A}{d} \left(\frac{x}{d} \right)^{n-1} \quad (6)$$

where $A = 0.102 d^2 \overline{U}^3 s^{-1}$, d is in mm, \overline{U} in $mm s^{-1}$ and $n = 0.61$ if the proportionality factors in the change of v^1 and L_L to measurable quantities are assumed to be unity. For $x/d > 5$ (approximately) and the boundary condition that for large r , $\overline{T} = \overline{T}_k$, the solution of Eq. (3) becomes

$$\frac{\overline{T} - \overline{T}_k}{\overline{T}_E - \overline{T}_k} = \frac{S}{4\pi \left[\alpha + \frac{1}{n} \alpha_E(x) \right] x} \exp \left[- \frac{\overline{U}}{4 \left[\alpha + \frac{1}{n} \alpha_E(x) \right] x} r^2 \right] \quad (7)$$

where $\alpha_E(x)$ is given by Eq. (6), $S = \overline{U} \pi d^2 / 4$ = volume flow of heated jet, \overline{T}_k is the temperature of the fluid surrounding the heated jet and \overline{T}_E is the mean temperature of the heated jet at the jet block exit plane. At Reynolds number 308 000 in water, $A = 3020 mm^3 s^{-1}$. In that case, an experiment conducted at $Re = 154 000$ gave excellent agreement between measured and predicted temperature data for $A = 1510 mm^3 s^{-1}$ thus confirming the velocity dependence of A . This is, of course, a necessary condition if $\sqrt{u^2}/\overline{U}$ and L_f/d are approximately independent of Reynolds number.

The steady state balance for temperature fluctuations is, Launder (1976),

$$\overline{u_i \delta} \frac{\partial \overline{\delta^2}}{\partial x_i} = -2 \overline{u_i \delta} \frac{\partial \overline{T}}{\partial x_i} - \frac{\partial \overline{u_i \delta^2}}{\partial x_i} + \frac{\partial}{\partial x_i} \left(\alpha \frac{\partial \overline{\delta^2}}{\partial x_i} \right) - 2\alpha \frac{\partial \overline{\delta}}{\partial x_i} \frac{\partial \overline{\delta}}{\partial x_i} \quad (8)$$

$\overline{u_i \delta}$ is given by the Boussinesq approximation, Eq. (2), $\overline{u_i \delta^2}$ is modelled by the gradient approximation

$$\overline{u_i \delta^2} = -a \frac{\partial \overline{\delta^2}}{\partial x_i} \quad (9)$$

with $a = \alpha_E(x)$ as used by Krebs et al. (1981). The dissipation term in Eq. (8) can be expressed in terms of the temperature microscale.

$$2\alpha \frac{\partial \overline{\delta}}{\partial x_i} \frac{\partial \overline{\delta}}{\partial x_i} = 12\alpha \frac{\overline{\delta^2}}{\lambda_\delta^2} \quad (10)$$

For isotropic turbulence, λ_δ is related to the corresponding velocity microscale by

$$\lambda_\delta^2 = \frac{5}{3} \frac{m}{n_1} \lambda_\delta^2 Pr \quad (11)$$

if power laws are valid for the decay of the square of turbulence $\overline{u^2}$ and of the square of temperature fluctuation intensity $\overline{\delta^2}$ with power n_1 and m respectively and if turbulence Reynolds number, $\sqrt{u^2} \lambda_\delta / \nu$, and the turbulence Peclet number, $\sqrt{u^2} \lambda_\delta / \alpha$, are small, Hinze (1975). This was the case for water and will therefore also be the case for sodium. As will be seen later from the measurements the decay exponent of turbulence n_1 is independent of the Reynolds number whereas the decay exponent of temperature fluctuation intensity depends on Reynolds and Prandtl number. Combining Eqs. (10) and (11) yields

$$2\alpha \frac{\partial \overline{\delta}}{\partial x_i} \frac{\partial \overline{\delta}}{\partial x_i} = \frac{m}{n_1} \frac{20\nu}{\lambda_\delta^2} \overline{\delta^2} = \frac{m}{n_1} \frac{B_c}{x} \overline{\delta^2} \quad (12a)$$

where it has been assumed that $\lambda_\delta^2 \propto \nu x / \overline{U}$ which was verified experimentally for the water case. Thus B_c / \overline{U} will be constant and independent of the fluid.

Further simplification is possible since

$$(a) \quad \overline{U} \frac{\partial \overline{\delta^2}}{\partial x} \gg \frac{\partial \alpha}{\partial x_i} \frac{\partial \overline{\delta^2}}{\partial x_i} \quad \text{and}$$

(b) $\partial^2 \overline{\delta^2} / \partial x^2$ is negligible compared with the corresponding derivatives in the other two coordinate directions. Molecular diffusion must, however, be retained in this case due to the high conductivity of sodium. In cylindrical coordinates, Eq. (8) reduces to

$$\overline{U} \frac{\partial \overline{\delta^2}}{\partial x} = \alpha_E(x) \left[2 \left(\frac{\partial \overline{T}}{\partial x} \right)^2 + 2 \left(\frac{\partial \overline{T}}{\partial r} \right)^2 \right] + \left[\alpha + \alpha_E(x) \right] \left[\frac{\partial^2 \overline{\delta^2}}{\partial r^2} + \frac{1}{r} \frac{\partial \overline{\delta^2}}{\partial r} \right] - \frac{m}{n_1} \frac{B_c}{x} \overline{\delta^2} \quad (13)$$

for which the following boundary conditions apply

$$\overline{\delta^2}(x, D/2) = 0 \quad \text{and} \quad \frac{\partial}{\partial r} [\overline{\delta^2}(x, D/2)] = 0$$

for $D \gg$ width of temperature field, in this case D being the diameter of the containment pipe.

APPARATUS AND INSTRUMENTATION

Experimental data were obtained in the sodium test section of Fig. 2 which has the same jet block geometry and containment pipe diameter as the water test section used for earlier experiments. The test section consists of a containment pipe of 110 mm diameter, a multi-bore jet block which could be moved inside the test section relative to two fixed radial traversing stations, screens for smoothing the velocity profile upstream of the jet block and provision for injection of heated sodium into the central channel of the jet block. The latter has 158 bores of 7.2 mm diameter, placed on a triangular pitch of 8.2 mm with a length-to-diameter ratio of 16.7:1 for the individual bores. In order to minimize heat loss from the heated sodium in the injection pipe to the central jet, a double pipe construction was used with the space between the pipes being evacuated. The mass flow rate to the central jet was controlled independently of the main flow to ensure that the flow left the jet block with the same velocity as surrounding jets.

Mean temperatures and temperature fluctuations were measured with a 0.25 mm outside diameter, sheathed thermocouple. The insulating material was boron nitride with a thermal conductivity equal to that of the stainless steel sheath. This ensures a small time constant. Cut-off frequencies are in excess of 40 Hz which ensures that the energy containing part of the spectrum is captured with minimal attenuation. A thermocouple was also placed at the outlet of the central jet to permit measurement of the temperature of the separately heated sodium. The in-

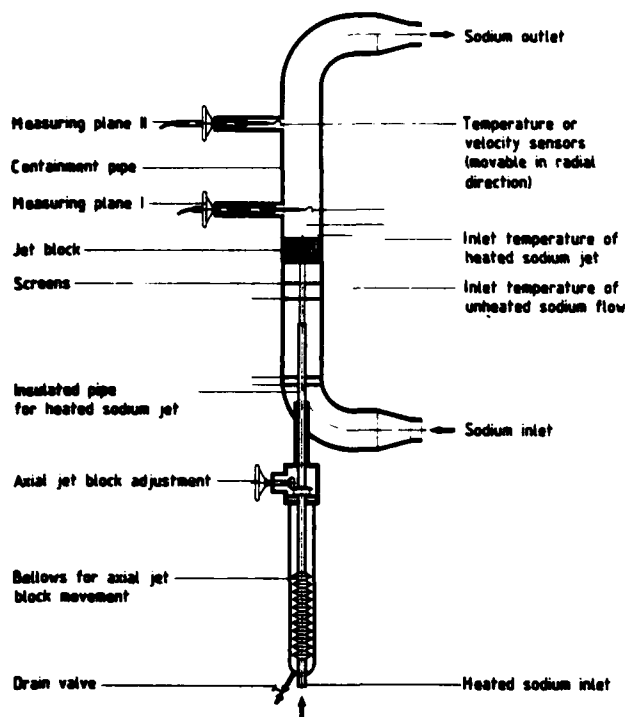


FIG. 2 SCHEME OF TEST SECTION.

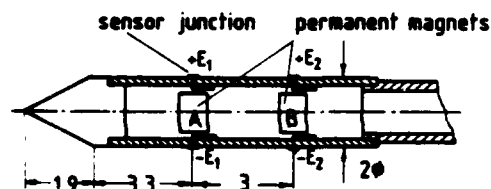


FIG. 3 MINIATURE ELECTROMAGNETIC FLOWMETER PROBE - DIMENSIONS IN mm.

let temperature of the sodium flow into the remaining jet block was also measured.

Velocity measurements were performed with a miniature permanent magnet flowmeter probe, Fig. 3, Müller et al. (1982). Two disc shaped magnets A and B with diametral magnetization are contained in a cladding tube which also carries the +E and -E electrodes. As the conducting liquid sodium moves normal to the magnetic field of the two magnets, voltages are induced in the flow and are sensed by the electrodes. Although the magnetic field which permeates the surrounding flow, is not homogeneous, the voltage induced was found to be proportional to the flow velocity over a wide range of velocities. Typical sensitivities are of the order of 20 μV per ms^{-1} . The purpose of the two sets of magnets and electrodes is to permit measurements of transit times. Unfortunately, the dimensions of the probe are still somewhat large in relation to the length scale of the flow which is set by the hole diameters of the jet block. It must, therefore, be expected that the mean velocity will be measured accurately but turbulence measurements will probably be affected by the lack of adequate spatial resolution.

MEASUREMENTS AND COMPARISON WITH CALCULATIONS

The measured mean velocity field in sodium flow is illustrated in Fig. 4 for various downstream stations. Minor deviations from a flat profile in the core region are observed. This is typical for such a device where there are many nearly identical flow paths in parallel.

Measured mean temperature profiles at two axial stations are shown in Fig. 5 together with Eq. (7) fitted for sodium flow with $A = 825 \text{ mm}^3 \text{ s}^{-1}$. $\Delta T = T_E - T_K = 24.8 \text{ K}$, S is given by the mean exit flow velocity and hole area and $n = 0.61$ as obtained in the experiments with water by Krebs et al. (1981). The corresponding measurement and

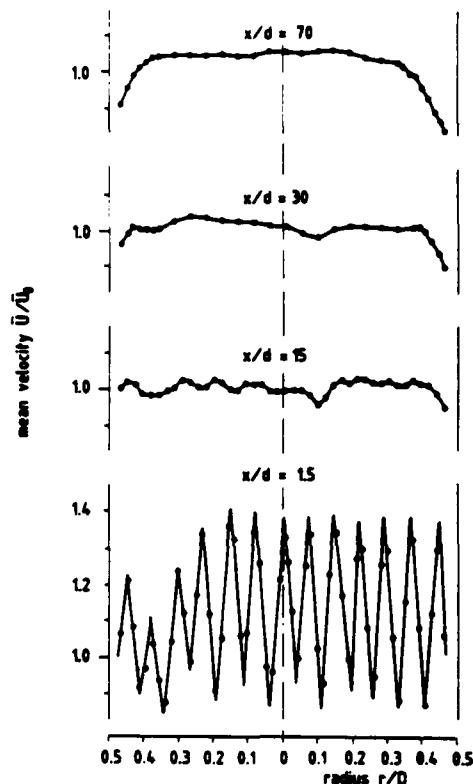


FIG. 4 MEAN VELOCITY PROFILES OF THE JET BLOCK - $Re = 308\,000$, $U_0 = 1.13 \text{ ms}^{-1}$.

calculation for water ($A = 3020 \text{ mm}^3 \text{ s}^{-1}$, $T_E - T_K = 9.9 \text{ K}$) are also shown from which the significant contribution to the spread of heat in sodium by its high molecular diffusivity can be seen.

Axial decay of the maximum mean temperature with downstream distance for two Reynolds numbers is given in Fig. 6. If the model were strictly correct, the transfer of the value of A required for solution of Eq. (7) should be possible from the water experiments to those in sodium. Simple considerations lead to the relation $A_{Na} = A_{H_2O} v_{Na} / v_{H_2O}$ with $v_{Na}(T = 300^\circ\text{C}) = 0.4 v_{H_2O}(T = 20^\circ\text{C})$. Using water, A amounts to $3020 \text{ mm}^3 \text{ s}^{-1}$ at $Re = 308\,000$. The corresponding value for sodium should be $1208 \text{ mm}^3 \text{ s}^{-1}$ but at the higher Reynolds number, Eq. (7) with $A = 825 \text{ mm}^3 \text{ s}^{-1}$ is seen to give a good fit. Since $A \propto U$, halving the Reynolds number requires halving the value of A . The results of Fig. 6 confirm this proportionality for sodium which was also obtained for water in the previous measurements. However, in contrast to water, the decay of maximum mean temperature in sodium is dependent on the Reynolds number due to the influence of the molecular diffusivity which can be derived also from Eq. (7).

On the left hand side of Fig. 7 the measured temperature fluctuation intensity profiles are shown at the distance $x/d = 28$ for sodium and water. These profiles are used as initial conditions for Eq. (13). On the right hand side of the figure the measured and calculated profiles are compared at the distance $x/d = 97$. The radial spread of the profiles for sodium is seen to be larger than for water.

The measured and calculated axial decay of temperature fluctuations is shown in Fig. 8. The axial decay exponents of the maximum of the square of temperature fluctuation intensities δ_m^2 are evaluated from the measurements shown in this figure. For $Re = 308\,000$ a decay exponent $m = -1.7$ and for $Re = 154\,000$ a decay exponent $m = -2.0$ are obtained in sodium flow compared to $m = -1.0$ for both Reynolds numbers in water. The power laws $\delta_m^2 = x^m$ are valid for axial distances of about $x/d > 20$ from the jet block. The axial decay of the temperature fluctuations in sodium is consequently much more rapid and unlike for water, is Reynolds number dependent too.

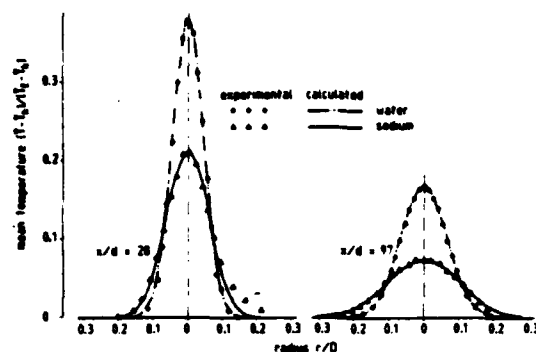


FIG. 5 COMPARISON OF MEASURED AND CALCULATED MEAN TEMPERATURE PROFILES - $Re = 308\ 000$, FOR WATER $\alpha = 0$, $A = 3020\ mm^3 s^{-1}$; $T_E - T_K = 9.9\ K$, FOR SODIUM $\alpha = 70\ mm^3 s^{-1}$, $A = 825\ mm^3 s^{-1}$; $T_E - T_K = 24.8\ K$, Eq. (7).

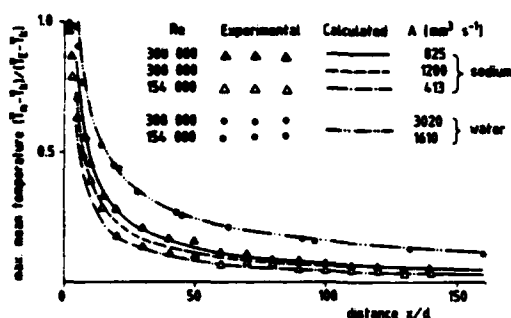


FIG. 6 AXIAL DECAY OF THE MAXIMUM MEAN TEMPERATURE - IN SODIUM AND WATER - COMPARISON OF MEASURED AND CALCULATED DATA.

In order to obtain some check on the quality of the temperature fluctuation measurements, a spectral analysis was performed of the signals. The spectrum of Fig. 9 is typical and indicates that the thermocouples with a cut-off frequency of above 40 Hz are only just adequate. Very little change in the spectrum was noted with changing downstream distance.

Since a key aspect of the model used is the adoption of parameters determined in a water flow some check on the velocity parameters should be attempted. Fig. 10 shows the decay of streamwise turbulence in water and sodium. Ideally these two results should have been identical. At this stage, the sodium results must be treated with caution as they would most likely have been affected by lack of spatial resolution of the miniature electromagnetic probe. In fact, near the jet block, turbulence scales will be smaller than further downstream. This could be the reason for the smaller slope of the intensity curve as well as its generally lower overall level.

DISCUSSION OF RESULTS

A general discussion and comparison of the model developed relative to existing turbulence models has already been presented by Krebs et al. (1981). Additional comments with the aid of the results in sodium are now warranted. The factor A in Eq. (6) is proportional to velocity if it is assumed that the turbulence intensity, Eq. (5a), and the integral length scale, Eq. (5b), are independent of Reynolds number. For isotropic turbulence, Hinze (1975) shows from theoretical considerations that both have a Reynolds number dependence. For the small range of Reynolds numbers used in the present work, this dependence could not be detected which is consistent with other experimental evidence behind grids as cited by Hinze (1975).

Available experimental data for the flow downstream of the jet block are consistent with the model derived except that the value of A required for solution of Eq. (7) can only roughly be transferred from the water

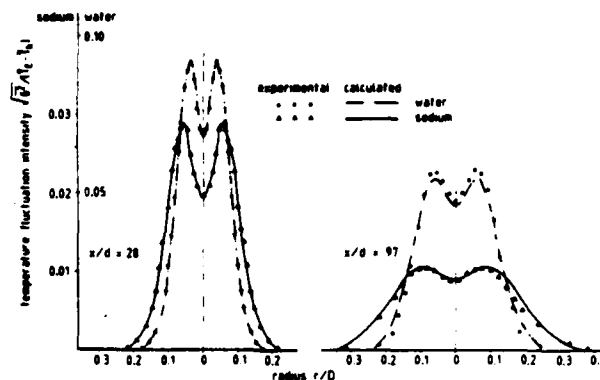


FIG. 7 COMPARISON OF MEASURED AND CALCULATED TEMPERATURE FLUCTUATION INTENSITY AT DIFFERENT DOWNSTREAM DISTANCES - Re , α and A as for FIG. 5, $m = -1.7$, $U_0/U = 3.7$ IN EQ. (13).

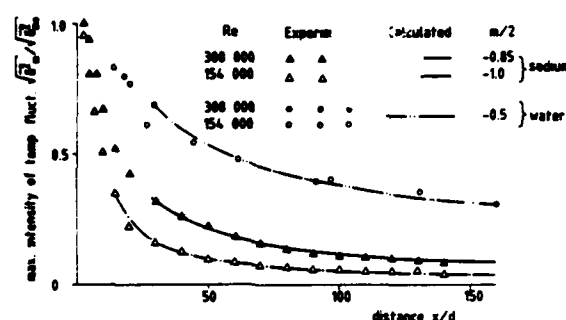


FIG. 8 AXIAL DECAY OF TEMPERATURE FLUCTUATIONS - IN SODIUM AND WATER - COMPARISON OF MEASURED AND CALCULATED DATA.

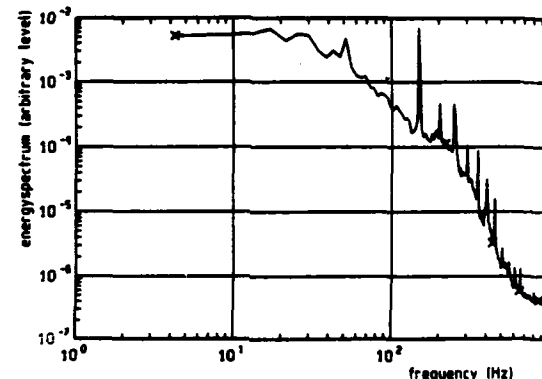


FIG. 9 TYPICAL TEMPERATURE SPECTRUM - $x/d = 40$.

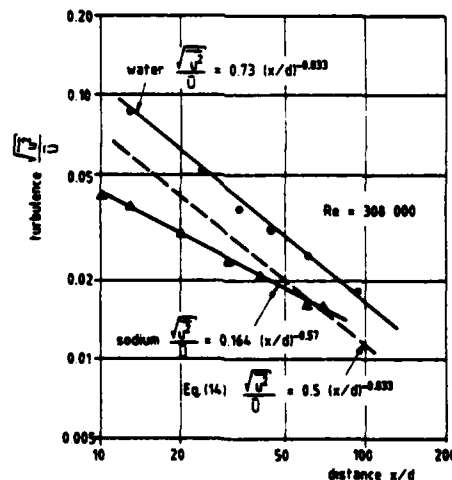


FIG. 10 AXIAL DECAY OF STREAMWISE TURBULENCE IN WATER AND SODIUM DOWNSTREAM OF THE JET BLOCK.

experiments to those in sodium. In view of the turbulence intensity measurements of Fig. 10 which show that the turbulence levels in sodium could be lower at a given x/d than in water, it is preferred to doubt this aspect rather than the basic model and its various assumptions. The dashed line in Fig. 10 representing the equation

$$\frac{\sqrt{u'^2}}{U} = 0.5 \left(\frac{x}{d}\right)^{-0.833} \quad (14)$$

shows how little change from the measured intensities would be required in order to remove this discrepancy. Unfortunately, clarification of this aspect will have to await the development of a velocity sensor with better spatial resolution or the repeat of the whole experimental program with a much larger geometry. If the integral scale, L_f , is also affected by the change from water to sodium, then the validity of the present model could be further enhanced.

The assumption that the eddy diffusivity of heat, α_T , and the eddy diffusivity of the temperature fluctuations, α , are equal was introduced with more formal than physical arguments. The present results do not permit further insight to be gained but it is noteworthy that except for a constant, this is in agreement with Launder (1976).

Other assumptions contained in the development of the temperature fluctuation equation, Eq. (13), are the relation between the velocity and temperature microscales, Eq. (11), and that $\lambda_T^2 = \nu x/U$. These are in agreement with theoretical predictions for isotropic turbulence, Hinze (1975). Assuming the same decay exponent $n_1 = -5/3$ for the turbulence square u'^2 in water and in sodium, the dissipation of the temperature fluctuations changes with the decay exponent m of δ_T^2 . Different values of m were obtained for water and sodium and in the case of sodium for different Reynolds numbers too. Up to now the decay exponent m can not be predicted as a function of Prandtl and Reynolds numbers. Further investigations are necessary to define this correlation. Calculating the dissipation of temperature fluctuations with the measured values of m and the constant $B_c/\bar{U} = 3.7$ which was derived from the water experiments, a remarkable fit was achieved for measured and calculated profiles of temperature fluctuation intensities. Consequently, the factor B_c in Eq. (12b) will be proportional to the stream velocity, or B_c/\bar{U} takes on the form of a universal constant. Present results appear to confirm this conclusion.

REFERENCES

1. Krebs, L., Bremhorst, K., and Müller, U., 1981, "Measurement and Prediction of the Mean and Fluctuating Temperature Field Downstream of a Multi-Bore Jet Block in Which One Jet is Heated", *Int. J. Heat Mass Transfer* **24**, 8, 1305-1312.
2. Brodkey, R.S., 1975, "Turbulence in Mixing Operations", Chapters 2 and 3, Academic Press, New York.
3. Gal-el-Hak, M. and Morton, J.B., 1979, "Experiments on the Diffusion of Smoke in Isotropic Turbulent Flow", *AIAA* **17**, 558-562.
4. Hinze, J.O., 1975, "Turbulence", McGraw Hill, New York.
5. Müller, St., Krebs, L., and Thun, G., 1982, "Permanent Magnet Flowmeter Probes, Sensors for Instrumentation in LMFRs", International Topical Meeting on Liquid Metal Fast Breeder Reactor Safety and Related Design, Lyon, July 19-23.
6. Launder, B.E., 1976, "Turbulence", Ch. 6 in *Topics in Applied Physics* **12**, 231-287 (ed. P. Bradshaw), Springer, Berlin.

THE INTERFERENCE OF MULTIPLE LINE SOURCES IN GRID TURBULENCE

Z. Warhaft

Sibley School of Mechanical and Aerospace Engineering
Cornell University, Ithaca, NY 14853 USA

ABSTRACT

The interference of two (and more) thermal line sources in decaying grid turbulence is studied by using the inference method described by Warhaft (1981) to determine the cross-correlation coefficient ρ between two sources. The evolution of ρ as a function of downstream distance, for $0.075 < d/l < 10$, where d is the wire spacing and l is the length scale of the turbulence, is determined for a pair of sources located at various downstream distances from the grid (x_0/M varying from 5 to 60 where x_0 is the distance of the sources from the grid and M is the grid mesh length). It is shown that a mandoline (Warhaft and Lumley, 1978) may be thought of, in a more fundamental way, as the interference of a number of line sources. Thus new light is shed on the rate of decay of scalar dissipation. New data for the thermal field very close to a line source is also presented. Full details of the work described here will appear in Warhaft 1983.

INTRODUCTION

The mixing of passive scalar contaminants in turbulence continues to be an active area of research both because of its practical importance in such areas as pollution dispersion and chemical reactions and because it is a fundamental, clearly defined, yet unsolved problem (even for a completely determined velocity field). One of the simplest ways of injecting a scalar into a turbulent field is by means of placing a fine heated wire in the flow. If the wire is fine enough and if the wire over-heat is small enough neither the wire's physical presence nor the resultant thermal wake will change the background velocity field, i.e., the resultant scalar field will be a passive contaminant. Important experiments concerning the spreading rate of both the mean and fluctuating thermal field for such a line source have been previously carried out by Uberoi and Corrsin (1953) and by Townsend (1954) although these workers have not concerned themselves with the thermal field in the immediate vicinity of the source.

The interference of two or more passive thermal wakes downstream of parallel line sources is an important and non-trivial extension of the case of a single source. The way these line sources mix will be a function of their spacing and the length scale and intensity of the turbulence. Experimental knowledge of this mixing is important in testing two particle dispersion theories such as that recently developed by Durbin (1980) (see also Sawford 1983). Furthermore, a study of the interaction of multiple line sources should provide deeper insight into the problem of scalar variance dissipation: the mandoline used by Warhaft and Lumley (1978) consists of an array of parallel wires and the non-unique value of the scalar dissipation rate observed in that study was due to

variations in the spacing (and downstream location from the grid) of the mandoline wires.

If we consider two line sources located in a turbulent flow (decaying grid turbulence for the situation to be studied here) the resultant temperature variance will be

$$\overline{\theta_B^2} = \overline{(\theta_1 + \theta_2)^2} = \overline{\theta_1^2} + \overline{\theta_2^2} + 2\rho\overline{\theta_1^2}\overline{\theta_2^2} \quad (1)$$

where θ_1 and θ_2 are the thermal fluctuations produced by each wire and ρ is the cross-correlation coefficient between the fluctuations produced by each wire. Warhaft (1981) has shown (for two distributed line sources) that ρ may be inferred by operating each

thermal source separately (thus determining $\overline{\theta_1^2}$ and $\overline{\theta_2^2}$) and then both together (determining $\overline{\theta_B^2}$). Equation 1 may then be solved for ρ . Here this inference method is used to study the interference of two parallel line sources placed in a plane, parallel to and downstream from, the grid (fig. 1).

Equation 1 can also be extended to examine the interference of multiple line sources. Here the relation for the temperature variance is

$$\overline{\theta_T^2} = \overline{\theta_1^2} + \overline{\theta_2^2} + \dots + 2\rho_{12}\overline{\theta_1^2}\overline{\theta_2^2} + \rho_{13}\overline{\theta_1^2}\overline{\theta_3^2} + \dots \quad (2)$$

Equation 2 shows that for a mandoline (a parallel array of evenly spaced, heated wires) the evolution of the temperature variance is solely a function of the temperature variance of each wire and ρ . The interference of multiple line sources is also described here.

APPARATUS

The experiment was carried out in a vertically oriented wind tunnel (Warhaft 1981) with a test section of 170 mesh lengths ($M=0.025m$) and cross section of 16 X 16 mesh lengths. The grid was a biplanar arrangement of 0.476 cm square section brass rods; the solidity was 0.34. The thermal line sources were nichrome wire of 0.127mm diameter (and for some experiments 0.203mm). Thus the (cold) wire Re was 57 (and sometimes 91). However for the study of the thermal field very close to the heated wire, $< 8M$, 0.025mm diameter platinum wire was used. For this case, the cold wire Re was 11. Care was taken to align the wire of the probe parallel to the heated line source in order to avoid resolution problems. For x'/M greater than about 10, where x' is the distance from the thermal source (placed at x_0) (fig. 1) experiments show (Warhaft 1983) that the spreading rate of the mean and variance of the thermal field is independent of wire diameter for (at least) the Reynolds number range 39 to 280.

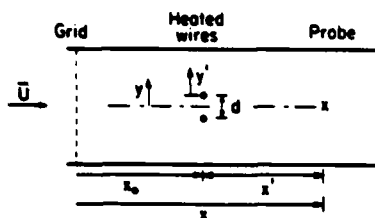


Fig. 1. Sketch of wind tunnel showing two heated wires. When two or more heated wires are used the transverse direction y (through which the probe is moved) is measured from the midpoint between the two central wires. For experiments with one wire only (figs. 2, 3 and 4) the transverse direction y' is measured from the wire itself.

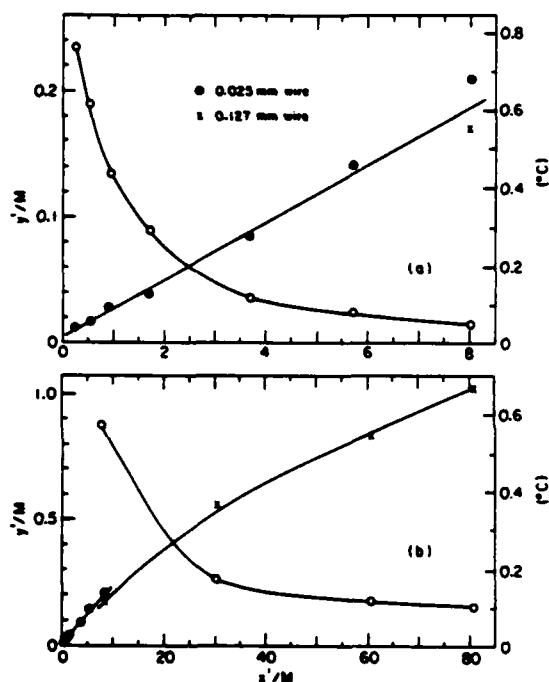


Fig. 2. Half width of the mean temperature wake behind a single wire (left hand axis) and center-line (peak) temperature of the mean temperature (right hand axis) (a), $x'/M < 8$, 0.025 mm heated wire. (b) $x'/M > 8$, 0.127 mm wire. Open circles are for peak temperature, filled circles and crosses are for the half width.

The thermal wakes were measured by means of conventional thermocouples and fast response resistance thermometers. The thermal fields were transversed in the y direction by means of a precision traversing mechanism and stepping motor.

RESULTS

The mean velocity, U , was set at 7 m/s and the velocity variance, $\overline{u^2}$, was found to follow the relation

$$\overline{u^2}/U^2 = 0.121 (x'/M)^{-1.4} \quad (3)$$

Single line source

Figure 2 shows the evolution of the mean center-line temperature, as well as the half width of the mean profile, for a single wire placed at $x_0/M=52$. The mean profiles were Gaussian; the half width is defined as half the width of the profile when its level is 50% of the maximum (center line value). The standard deviation for a Gaussian profile is 0.849 times the half width. The ordinate y'/M refers to the

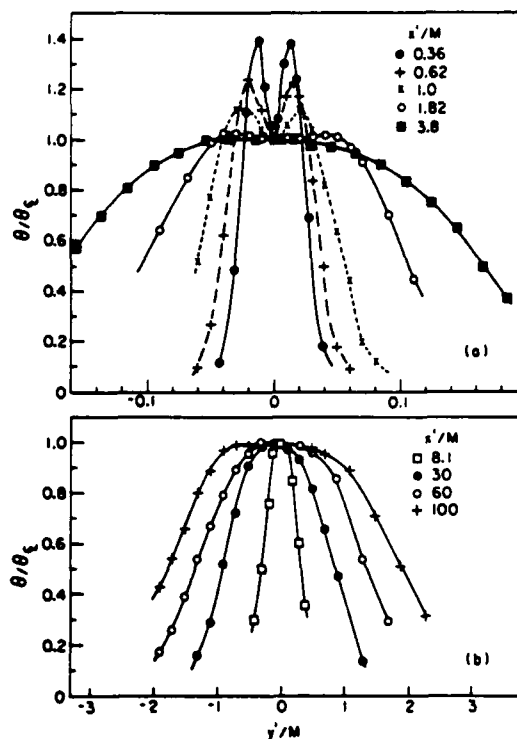


Fig. 3. rms temperature profiles normalized by the center-line rms values.

lateral distance from the line source (fig. 1). Up until 8 M, ie, approximately until the end of the linear spreading region, the fine (0.025 mm) wire was used; thereafter, in order to produce a larger signal, the 0.127 mm wire was used. The curves match well. The power in the fine wire was 4.4 watt/meter, that in the thicker wire was 45 watt/meter. The form of the curves is similar to that observed by Uberoi and Corrsin (1953). Note that the product of the half width and the peak (center line) temperature should be constant for a particular wire heating, as is observed.

Figure 3 shows the evolution of the rms θ profiles, normalized by their center line values, as a function of x'/M . As for fig. 2 the 0.025 mm wire was used until $x'/M=8.1$, thereafter the 0.127 mm wire was used. Notice that until approximately $x'/M=1.8$ the rms profiles are double peaked. The length of the arc of the flapping of the heated wake is comparable to its (molecular diffusive) spreading width for small distances from the source. Thus the largest gradients in temperature, and hence the highest values of rms θ will occur off the center line, producing the double peak. After about $x'/M=1.8$, the profiles become single peaked. However as will be shown in Warhaft 1983 (see also fig. 5 below), if the thermal source is placed closer to the grid ($x_0/M \leq 20$) a double peak re-emerges far downstream.

The evolution of θ rms/ T (center line values) is shown in figure 4(a). (for clarity the horizontal axis has also been amplified ten-fold for the data points up to $x'/M=8$). The peak of θ rms/ T is at about $x'/M=10$ (ie. approximately the end of the linear spreading region). Thereafter it appears to asymptote to a value of about 0.7. This is consistent with the values far downstream from the source observed by Uberoi and Corrsin (1953). The lower graph (fig. 4b) shows the evolution of the half width (50% of the center line value) of the rms profiles of fig. 3. Note that this half width is considerably larger than the mean profile half widths.

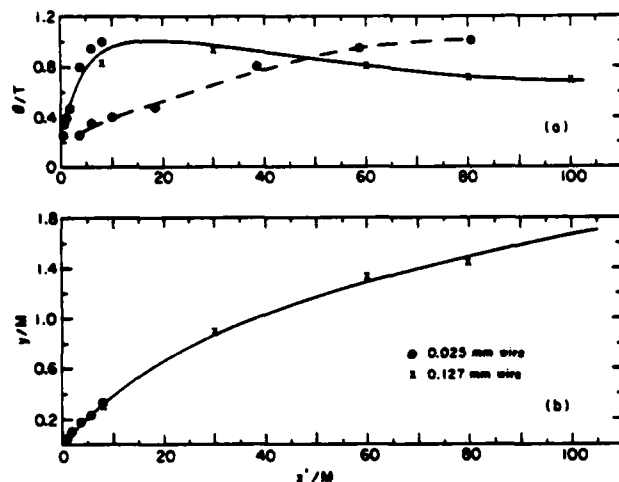


Fig. 4. (a) rms θ /mean T, center line values. For clarity, the horizontal axis has also been amplified ten-fold for the data points up to $x'/M=8$. (b) rms θ profile half width.

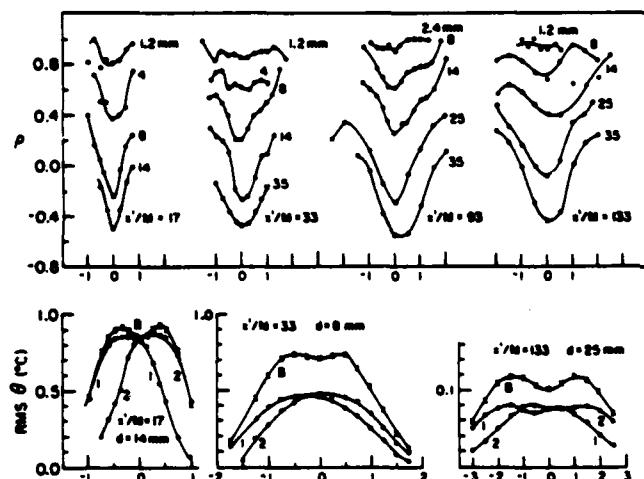


Fig. 5. Bottom graphs show rms θ profiles for a pair of wires operating separately (1 and 2) and together (B). Top graphs show ρ , inferred from graphs such as the bottom ones, for various d and x'/M . All horizontal axes are y/M . Wires are at $x_0/M = 20$.

Comparison of spreading rates of rms and mean profiles for values of x_0/M other than 52 will be given in Warhaft 1983.

The Interference of Multiple Line Sources

We consider first the interference of two line sources. Fig. 5 (lower curves) shows some examples of rms θ profiles for two wires (placed at $x_0/M = 20$) for different wire spacings and for the probe placed at different locations from the sources. The integral scale, λ , for $x_0/M = 20$ is $1.02 \times 10^{-2} m$. Curves 1 and 2 are for each wire operating separately, curve B is for each wire operating together. From such profiles, the upper curves of figure 5 were obtained by solving equation 1 for ρ . These curves show the variation of ρ as the field is traversed in the y direction for a particular value of x'/M . Notice that the curves have distinct minima at the points intermediate between the two wires ($y = 0$, fig. 1). From such families of curves at other x'/M and other spacings fig. 6 was produced. These correlation coefficients are for the probe location at $y = 0$, for various values of d and x'/M . Wires are at $x_0/M = 20$.

The evolution of ρ is clearly a function of d (or

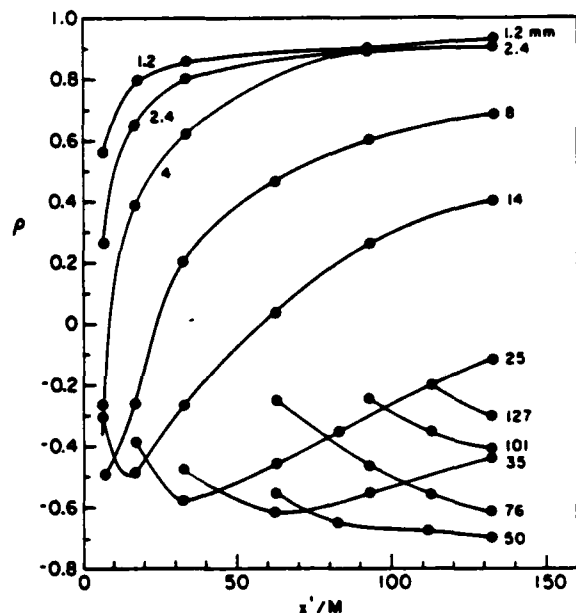


Fig. 6. ρ vs. x'/M for experiments such as shown in fig. 5. ρ is for the midpoint between the wires ($y=0$, fig. 1). The numbers are the wire spacing, d (mm).

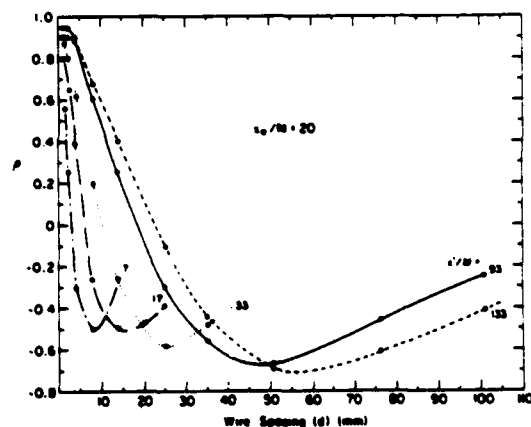


Fig. 7. Re-plot of fig. 6. ρ vs. d (wire spacing) for various values of x'/M (labeled on the graph).

more generally d/λ , see below). For very small d the cross correlation coefficient rapidly increases from -1 close to the wires to a value close to +1. (The evolution of ρ for very small d and small x'/M is described in Warhaft 1983.) Close to the wires the two wakes are separate and thus ρ should be -1 since the probe senses one wake or the other but not both at the same time nor the ambient air. However as the wakes merge together, ρ rises to a value of +1 (when they are completely mixed). For slightly larger d , this merging process occurs at a slower rate. For large d , (the effect is clear for $d > 8 mm$) ρ first decreases and then begins to increase. For these cases the sensor may initially sample one wake or the other (but not both). However it will mainly be sampling ambient air and ρ will be close to zero. As the two wakes begin to broaden (ie. as x'/M increases) less of the time will be spent sampling ambient air and the negative correlation will build up and should approach -1 as only one wake or the other is sampled. However mixing of the two wakes will also begin to occur and this has the effect of reversing the negative trend in ρ ; the mixing will drive ρ to +1 as for the small d case. Notice that for $d > 50 mm$ only the initial decrease in ρ

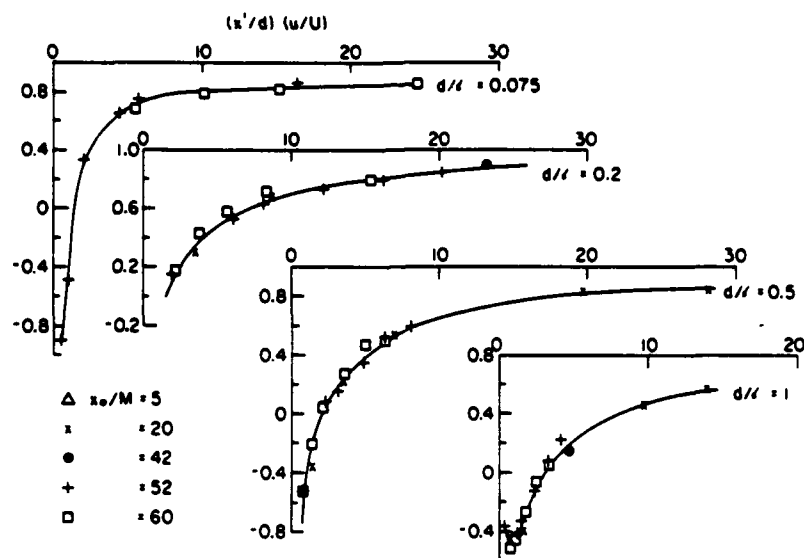


Fig. 8(a)

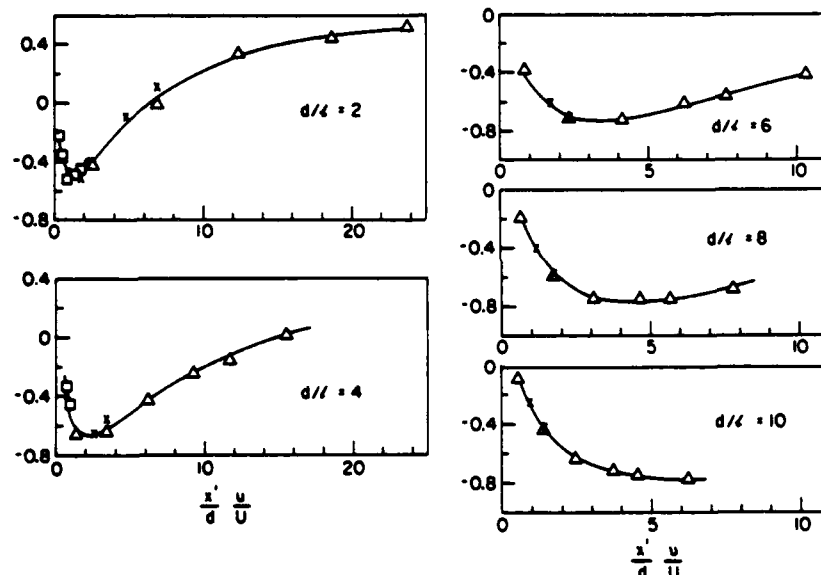


Fig. 8(b)

Fig. 8. ρ vs. normalized (convective) time $(x'/d)(u/U)$ for pairs of wires located at $x_0/M=5, 20, 42, 52$ and 60 . l is calculated at the x_0/M location of the wires. 8(a), d/l varying from 0.075 to 1 . 8(b), d/l varying from 2 to 10 .

is observed. Also, for these larger d , no meaningful value of ρ could be determined for small x'/M since there was no overlap of the rms profiles.

The effect of varying d but holding the probe at a particular downstream location is shown in fig. 7 which is a re-plot of fig. 6. As the wire separation is increased ρ decreases from its initial value near unity, however this trend reverses for large separation, for the reason described above. Note that as x'/M decreases, the reversal occurs for smaller d , as would be expected.

The evolution of the cross correlation coefficient ρ is a function of u/U , l , d and x' (in Warhaft 1983 it is shown that the wire diameter itself plays no role). Measurements of ρ such as those shown in figs. 6 and 7 were done for the pairs of wires placed at $x_0/M=5, 42, 52$ and 60 as well as $x_0/M=20$. Thus u/U and l

(the turbulence intensity and integral scale respectively, determined at the location of the wires) as well as x' and d were varied. Figure 8 summarizes the results of these experiments. The two dimensionless variables chosen have been d/l and $(x'/d)(u/U)$. This latter variable may be thought of as the time to the probe (x'/U) non-dimensionalized by a lateral convective time scale (u/d) . (Note that the turbulence is close to isotropic; $u-w$). The collapse of the data points is remarkable. The task of relating these curves to various turbulence models is described in Warhaft 1983. Notice, of course, that the form of the curves are similar to fig. 6.

Finally we show how a mandoline may be synthesised from a number of parallel line sources. Figure 9a shows the individual rms θ profiles for four line sources located at $x_0/M=20$, with wire spacing $1M$. Also shown on the figure is the effect of operating the line sources in various combinations, as well as the

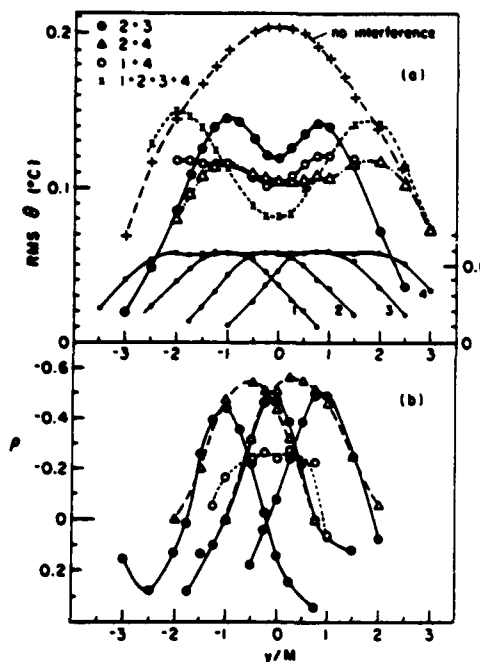


Fig. 9. Top graph. rms θ profiles measured at $x'/M=63$ for various combinations of four heated wires (labeled on the graph) spaced 1 M apart and located at $x_0/M=20$. The transverse locations of the wires are $y/M = -1.5, -0.5, +0.5$ and $+1.5$. Left hand axis is for the various combinations (wire 2 + wire 3 etc.), right hand axis is for the rms profiles of each wire (1,2,3 and 4) operating separately. Bottom graph shows ρ inferred from the top graph. Dots, pairs of wires 1 M apart (wires 1 & 2, 2 & 3, 3 & 4) triangles, pairs 2 M apart (wires 1 & 3, 2 & 4) open circles, the pair of wires 1 and 4 (3 M apart).

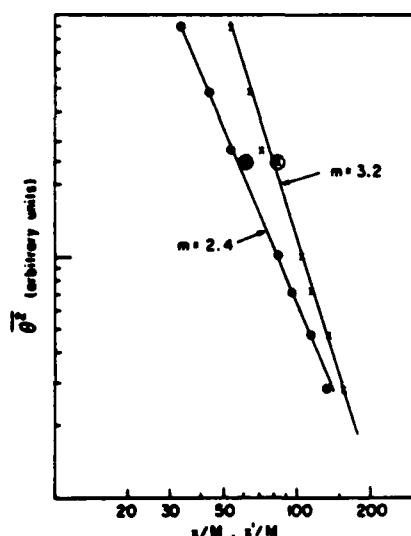


Fig. 10. $\overline{\theta^2}$ decay for a mandoline (wires 1 M spacing) at $x_0/M=20$. Crosses, $\overline{\theta^2}$ vs. x/M ; dots, $\overline{\theta^2}$ vs. x'/M . The circled cross and dot shows the value of $\overline{\theta^2}$ for only four wires of the mandoline operating (figure 9).

value of rms θ if no interference were present ($\rho=0$, equation 1). Note that if extra wires were added to the set (placed 1 M apart) for this downstream location ($x'/M=63$) the center line ($y/M=0$) value of the total rms θ would hardly be effected because the spread of the rms profile would be insufficient to reach $y=0$ (consider the addition of wire 5 placed at $y/M = 2.5$ for example). Thus the mandoline, for this x'/M , can be considered of consisting of four interfering wires only. (Closer to the source less wires will be needed, further away, more). Fig. 9b shows the cross correlation profiles for the data of fig. 9a. From these and the individual rms profiles, equation 2 could be solved for $\overline{\theta^2}$. Fig. 10 shows the decay of $\overline{\theta^2}$ for a full mandoline (all wires operating). Also shown is the value of $\overline{\theta^2}$ for $x'/M=63$ (figure 9a). It is clear that the interference of four wires at this location produces the same variance as a full mandoline.

The author wishes to thank Mr. D. Boxley for his careful assistance with the measurements. This work was funded by grants from the Engineering section and the Atmospheric Science section of the U.S. National Science Foundation. The respective grant numbers are MEA-8104733 and ATM 79-22006.

REFERENCES

- Durbin, P.A. 1980 "A Stochastic model of two-particle dispersion and concentration fluctuations in homogeneous turbulence." *J. Fluid Mech.* 100 pp 279-302.
- Sawford, B.L. 1983 "The effect of Gaussian particle-pair distribution functions in the statistical theory of concentration fluctuations in homogeneous turbulence." *Quart. J.R. Met. Soc.* 109 pp 339-354.
- Townsend, A.A. 1954 "The diffusion behind a line source in homogeneous turbulence." *Proc. Roy. Soc.* 224 A pp 487-512.
- Uberoi, M.S. and Corrsin, S. 1953 "Diffusion of heat from a line source in isotropic turbulence." N.A.C.A. Report, 1142.
- Warhaft, Z. 1983 "Interference of line sources in grid turbulence." To be submitted to *J. Fluid Mech.*
- Warhaft, Z. 1981 "The use of dual heat injection to infer scalar covariance decay in grid turbulence." *J. Fluid Mech.* 104 pp 93-109.
- Warhaft, Z. and Lumley, J.L. 1978 "An experimental study of the decay of temperature fluctuations in grid generated turbulence." *J. Fluid Mech.* 99 pp 545-573.

DIFFUSION BEHIND A LINE SOURCE IN GRID TURBULENCE

M. S. Anand and S. B. Pope

Sibley School of Mechanical and
Aerospace Engineering
Cornell University
Ithaca, New York 14853

ABSTRACT

The flow considered is the thermal wake downstream of a fine heated wire in grid turbulence. The inability of generally-applicable turbulent diffusion models and second-order closures to calculate the mean and variance of the temperature is reviewed. Calculations based on the transport equation for the joint probability density function (pdf) of velocity and temperature show good agreement with measurements of mean temperature but not with those of the variance. Better calculations of the variance are obtained with a method based on the joint pdf conditional on the lateral velocity at the source.

INTRODUCTION

The thermal wake downstream of a heated wire in grid turbulence has been the subject of several experimental (1-4) and theoretical studies (5-10, for example). The flow is of fundamental theoretical importance and is also relevant to the practical problem of the dispersion of heat and pollutants in the environment (11).

In comparison to free shear flows — jets, wakes, mixing layers — the thermal wake appears simple: the mean velocity is uniform and the turbulence is isotropic. But turbulence models that are applicable to free shear flows (e.g. $k-\epsilon$ and Reynolds-stress models) produce qualitatively incorrect results for the thermal wake (9). This is because the thermal wake thickness σ is, initially, much smaller than the integral length scale, and because we are interested in the wake at convection times that are much smaller than the integral time scale of the turbulence.

In this work, the thermal wake is studied using velocity-temperature joint pdf transport equations (12,13). It is found that the standard (unconditional) pdf method is successful in calculating the mean temperature field, but not the temperature variance. A second method — based on the joint pdf conditional on the lateral velocity at the heated wire — is successful in calculating the normalized variance profiles and calculates the absolute magnitude of the variance to within a factor of two. This level of accuracy is comparable with that obtained using two-particle dispersion models (4).

THERMAL WAKE

The thermal wake is sketched on Fig. 1. A fine heated wire of diameter d is placed normal to the flow, a distance x_0 downstream of a turbulence-generating grid of mesh size M . The mean velocity U is uniform and the turbulence intensity normal to the flow and the wire is found to vary according to the power law:

$$\langle w^2 \rangle / U^2 = A(x/M)^{-m} \quad (1)$$

In the measurements of Warhaft (3) — with which the calculations are compared — the conditions are: $U = 7.0$ m/s, $M = 25$ mm, $x_0/M = 52$, $A = 0.0714$, $m = 1.32$, $d = 0.025$ mm (for measurements up to $x_w/M = 8.1$), and $d = 0.127$ mm (for measurements beyond $x_w/M = 8.1$).

The wire is intended to be sufficiently fine that it does not significantly affect the mean or fluctuating velocity field. Although the wire is quite hot, the excess temperature rapidly falls to a few degrees Celsius. Thus, except in the immediate vicinity of the wire, the excess temperature is a conserved, passive scalar.

The principal quantities of interest are the mean $\langle \phi \rangle$ and variance $\langle \phi'^2 \rangle$ of the normalized excess temperature $\phi(x, t)$. (Angled brackets and primes denote means and fluctuations about the mean, respectively.) At any distance x_w downstream of the source (i.e. the heated wire), the profile of $\langle \phi \rangle$ is found to be Gaussian (1-4),

$$\langle \phi(x_w, z) \rangle = (\sigma\sqrt{2\pi})^{-1} \exp(-\frac{1}{2} z^2/\sigma^2) \quad (2)$$

The integral $\int \langle \phi(x_w, z) \rangle dz$ is a conserved quantity, and ϕ is normalized so that this integral is unity. Profiles of $\langle \phi^2 \rangle$ (but not of $\langle \phi'^2 \rangle$) also appear to be Gaussian (4).

There is an analogy (1) between the thermal wake and the temperature field resulting from the instantaneous production (at time $t=0$) of an excess temperature distribution along the plane $z=0$. Thermal wake statistics at (x_w, z) are similar to those at (t, z) resulting from the plane source, where $t = x_w/U$. The analogy depends upon the turbulence intensity $\langle u^2 \rangle^{1/2}/U$ being small and mean axial gradients being small in comparison with lateral gradients. In common with previous work, our calculations are of the statistically one-dimensional, time dependent evolution of the temperature field from the plane source in decaying homogeneous turbulence. The results at time t are compared with the thermal wake data of Warhaft at $x_w = Ut$. (Henceforth t is used interchangeably with x_w/U).

PREVIOUS WORK

Mean Temperature

A theory should predict a Gaussian mean temperature profile (Eq. 2) and should determine the evolution of the width of the profile $\sigma(t)$. In high Reynolds-number, non-decaying, homogeneous turbulence, there are three regimes:

$$\begin{aligned} \text{Molecular diffusion, } t < \Gamma / \langle w^2 \rangle: & \quad \sigma^2 = 2\Gamma t. \\ \text{Turbulent convection, } \Gamma / \langle w^2 \rangle < t < \tau: & \quad \sigma^2 = \langle w^2 \rangle t^2. \\ \text{Turbulent diffusion, } t > \tau: & \quad \sigma^2 = 2\Gamma_t t. \end{aligned}$$

Here Γ is the thermal diffusivity, τ is the Lagrangian integral time scale, and Γ_t is the turbulent diffusion coefficient. Taylor (5) neglected molecular diffusion and obtained an expression for σ in terms of the Lagrangian velocity autocorrelation function. This expression (which can readily be generalized to the case of decaying turbulence (4)) correctly accounts for the turbulent convection and diffusion regimes. The effect of molecular diffusion is simply to increase σ^2 by $2\Gamma t$ (2).

The exact equation for the mean of ϕ is

$$\frac{\partial \langle \phi \rangle}{\partial t} = \Gamma \frac{\partial^2 \langle \phi \rangle}{\partial z^2} - \frac{\partial \langle w\phi \rangle}{\partial z}. \quad (3)$$

Turbulence models attempt to approximate the scalar flux $\langle w\phi \rangle$ so that Eq. 3 can be solved for $\langle \phi \rangle$.

Turbulent diffusion models (mixing length, k - ϵ etc.) approximate the scalar flux by

$$\langle w\phi \rangle = -\Gamma_t \frac{\partial \langle \phi \rangle}{\partial z}. \quad (4)$$

As their name implies, these models are applicable only to the turbulent diffusion regime: early on ($t < \tau$) they predict far too rapid spreading. For example, according to the k - ϵ model (see e.g. 14) the turbulent diffusion coefficient is

$$\Gamma_t = \frac{C_u}{\sigma_f} k^2 / \epsilon, \quad (5)$$

where k is the turbulent kinetic energy ($k = 3/2 \langle w^2 \rangle$ in isotropic turbulence) and ϵ is the rate of dissipation

$$\epsilon = -dk/dt. \quad (6)$$

The model constants are taken to be $C_u = 0.09$ and $\sigma_f = 0.7$. With the turbulence decaying according to Eq. 1, the k - ϵ model yields (neglecting molecular diffusion)

$$\sigma^2 = \int_0^t 2\Gamma_t(t') dt' = \frac{3A^2 C_u}{m(2-m)\sigma_f} \left\{ \left(\frac{x}{M} \right)^{(2-m)} - \left(\frac{x_0}{M} \right)^{(2-m)} \right\}. \quad (7)$$

On Fig. 2, the broken line shows this predicted evolution of σ compared to Warhaft's data (triangles). It may be seen that Eq. 7 is qualitatively and quantitatively incorrect. At the first measurement station, the calculated width is over three times that measured.

Turbulent diffusion models can be made to work, by making Γ_t an explicit function of σ or t (9,10). But such ad hoc modifications are inconsistent with the principles of invariant modelling (15,16) and have little general utility.

Second-order closures experience the same problem (7,9). The correct evolution of σ can be obtained only by modifying the transport coefficient for the third moment $\langle w^3 \phi \rangle$ to be a function of the temperature field.

Temperature Variance

The exact equation for the variance of ϕ is

$$\frac{\partial \langle \phi'^2 \rangle}{\partial t} + \frac{\partial \langle w\phi'^2 \rangle}{\partial z} = \Gamma \frac{\partial^2 \langle \phi'^2 \rangle}{\partial z^2} - 2\langle w\phi' \rangle \frac{\partial \langle \phi \rangle}{\partial z} - 2\epsilon_\phi; \quad (8)$$

where the scalar dissipation is

$$\epsilon_\phi = \Gamma \left\langle \frac{\partial \phi'}{\partial x_1} \frac{\partial \phi'}{\partial x_1} \right\rangle. \quad (9)$$

The simplest modelling assumption for ϵ_ϕ is that the scalar-dissipation time scale $1/2\langle \phi'^2 \rangle / \epsilon_\phi$ is proportional to the mechanical-dissipation time scale k/ϵ : then ϵ_ϕ is given by

$$\epsilon_\phi = C_\phi \frac{1}{2} \langle \phi'^2 \rangle \epsilon / k. \quad (10)$$

The data of Warhaft and Lumley (17) suggest that C_ϕ is not a universal constant, but a value of $C_\phi = 2.0$ is commonly employed (e.g. 12).

The validity of Eq. 10 for the thermal wake can be tested rather directly. Let $I(t)$ be the integral of the scalar variance:

$$I \equiv \int_{-\infty}^{\infty} \langle \phi'^2 \rangle dz. \quad (11)$$

Then, from Eqs. 3 and 8 and the knowledge that the profile of $\langle \phi \rangle$ is Gaussian, we obtain

$$\frac{dI}{dt} = \bar{P} - C_\phi \frac{\epsilon}{k} I, \quad (12)$$

where

$$\bar{P} \equiv \left(\frac{1}{2} \frac{d\sigma^2}{dt} - \Gamma \right) / (2\sigma^3 \sqrt{\pi}). \quad (13)$$

It may be noted that a knowledge of $\sigma(t)$ is sufficient to determine the production term \bar{P} . In the next section a model that accurately determines σ is described (see the solid line on Fig. 2). Using this result (Eq. A7) $\bar{P}(t)$ was evaluated and then Eq. 12 was integrated numerically to yield $I(t)$. The result is compared with Warhaft's data on Fig. 3.

It may be seen from Fig. 3 that with the conventional value $C_\phi = 2.0$, the calculated integral variance I exceed the measured value by, typically, a factor of 7 to 12. With the higher value $C_\phi = 4.0$, this range is reduced to 4 to 7. Since $\sigma(t)$ given by Eq. A7 agrees extremely well with the data (see Fig. 2), the only significant assumption in the analysis is the modelling of the scalar dissipation, Eq. 10. The results shown on Fig. 3 clearly indicate, therefore, that this model is grossly in error for the thermal wake. If ϵ_ϕ were determined instead from a consistently-modelled transport equation (16) the result would be little different.

In light of these observations, Sykes, Levellen and Parker (7) replaced Eq. 10 with a model for ϵ_ϕ in terms of a scalar length scale, for which a modelled ordinary differential equation was solved. They were then able to obtain accurate calculations of the scalar variance, including the effect of the source size. While this method succeeded for the case considered, because of the way in which both $\langle w^2 \phi \rangle$ and ϵ_ϕ are modelled, the model does not appear to be applicable to the general case (i.e. more than one transported scalar (16), or more than one source (7)).

A completely different method of calculating the temperature variance is based on the relative dispersion of two fluid particles or, better, of two molecules. There has been considerable work on this method recently (see 8 for references) culminating in the comparison of theory and experiment by Stapountzis, Sawford, Hunt and Britter (4). The mean thermal wake width $\sigma(t)$ is calculated to within experiment error; the variance is calculated to within a factor of two; and normalized variance profiles agree well with the data.

UNCONDITIONAL PDF METHOD

Turbulent diffusion models are unsuccessful in calculating the mean wake thickness $\sigma(t)$ because the second moment $\langle w\phi' \rangle$ is approximated by a gradient diffusion model. Similarly, in second-order closures a gradient-diffusion model is used for the third moment $\langle w^2 \phi \rangle$ and consequently σ is not calculated correctly.

But gradient-diffusion models can be entirely avoided by making use of the velocity-scalar joint pdf equation.

For a general flow, $f(\underline{V}, \psi; \underline{x}, t)$ is the probability density of the joint events $\underline{U}(\underline{x}, t) = \underline{V}$ and $\phi(\underline{x}, t) = \psi$. The four new independent variables V_1, V_2, V_3, ψ form the velocity-temperature space. An exact equation for the joint pdf can be derived (12): for the flow under consideration, the equation for $f(\underline{V}, \psi; \underline{x}, t)$ is

$$\frac{\partial f}{\partial t} + V_3 \frac{\partial f}{\partial z} = - \frac{\partial}{\partial \psi} \{ f \langle \Gamma V^2 \phi | \underline{V}, \psi \rangle \} - \frac{\partial}{\partial V_1} \{ f \langle a_1 | \underline{V}, \psi \rangle \}, \quad (14)$$

where, for any function Q , $\langle Q | \underline{V}, \psi \rangle$ is the expectation of Q conditional upon the joint events $\underline{U} = \underline{V}$ and $\phi = \psi$. The fluid particle acceleration is

$$a_1 = \nu \frac{\partial^2 U_1}{\partial x_j \partial x_j} - \frac{1}{\rho} \frac{\partial p}{\partial x_1}, \quad (15)$$

where ν is the kinematic viscosity and ρ the density.

In the joint pdf equation only the terms on the right-hand side need to be modelled. It may be seen that the convective term $V_3 \partial f / \partial z$ is in closed form and hence no transport model is required. Stochastic models for the terms in $\nabla^2 \phi$ and a_1 have been described previously (12, 13). The joint pdf equation incorporating these models can be integrated to form transport equations for the scalar flux and scalar variance:

$$\begin{aligned} \frac{\partial}{\partial t} \langle w \phi \rangle + \frac{\partial}{\partial z} \langle w^2 \phi \rangle + \langle w^2 \rangle \frac{\partial}{\partial z} \langle \phi \rangle - \Gamma \frac{\partial^2}{\partial z^2} \langle w \phi \rangle \\ = -C_m \frac{\epsilon}{k} \langle w \phi \rangle, \end{aligned} \quad (16)$$

$$\begin{aligned} \frac{\partial}{\partial t} \langle \phi'^2 \rangle + \frac{\partial}{\partial z} \langle w \phi'^2 \rangle + 2 \langle w \phi \rangle \frac{\partial}{\partial z} \langle \phi \rangle - \Gamma \frac{\partial^2}{\partial z^2} \langle \phi'^2 \rangle \\ = -C_\phi \frac{\epsilon}{k} \langle \phi'^2 \rangle. \end{aligned} \quad (17)$$

These equations illustrate the effect of the model constants which were chosen to be $C_m = 2.9$ and $C_\phi = 2.0$.

The modelled joint pdf equation was solved by a Monte Carlo method (13) for the conditions of Warhaft's experiment. The profiles of $\langle \phi \rangle$ were found to be Gaussian and the development of $\sigma(t)$ (circles on Fig. 2) is in excellent agreement with the data. In

high-Reynolds number decaying turbulence ($\langle w^2 \rangle = x^{-m}$), σ can be expected to vary as $\sqrt{x_w}$, x_w , and $x_w^{(1-m/2)}$, respectively, in the three regimes — molecular diffusion, turbulent convection, turbulent diffusion. The calculations exhibit the correct variations in the first two regimes, and are consistent with the third regime. Neither the calculations nor the measurements extend far enough to show the third regime distinctly.

It may be seen that the equation for the variance derived from the modelled pdf equation (Eq. 17) is just the exact equation (Eq. 8) with the scalar dissipation modelled according to Eq. 10. Consequently, the integrated variance $I(t)$ obtained from the pdf equation is the same as that obtained previously (Eqs. 12-13, Fig. 3), and is greater than the measured value by, typically, a factor of 7-12.

Thus this unconditional pdf method is successful in calculating the mean spreading, but the calculated variance is grossly in error.

CONDITIONAL PDF METHOD

In order to obtain more accurate calculations of the temperature variance, we seek a more complete statistical description of the thermal wake. In the early stages, the random variable that has most influence upon the wake's development is w_0 — the lateral velocity at the source at time zero:

$$w_0 \equiv w(\underline{x}=0, t=0). \quad (18)$$

Indeed, at very early times, the temperature profile is completely determined by w_0 . It is a laminar wake of

thickness $\sqrt{2\Gamma t}$ that has been convected laterally a distance $w_0 t$.

We shall therefore consider statistical quantities conditioned on $w_0 = w$ — primarily $f(\underline{V}, \psi | w; \underline{x}, t)$, the joint probability of $\underline{U} = \underline{V}$ and $\phi = \psi$, conditional upon $w_0 \equiv w(\underline{x}=0, t=0) = w$. The unconditional joint pdf (at any \underline{x}, t) can readily be recovered by

$$f(\underline{V}, \psi) = \int_{-\infty}^{\infty} \tilde{f}(\underline{V}, \psi | \tilde{w}) g(\tilde{w}) d\tilde{w}, \quad (19)$$

where $g(\tilde{w})$ is the pdf of w_0 which (in grid turbulence) is known to be Gaussian (18):

$$g(\tilde{w}) = \frac{1}{\sqrt{2\pi \langle w_0^2 \rangle}} \exp\left(-\frac{1}{2} \frac{\tilde{w}^2}{\langle w_0^2 \rangle}\right). \quad (20)$$

The conditional mean profile is

$$\tilde{\phi} \equiv \langle \phi | \tilde{w} \rangle = \iint \psi \tilde{f}(\underline{V}, \psi | \tilde{w}) d\underline{V} d\psi, \quad (21)$$

and, again, the unconditional mean is recovered by

$$\langle \phi \rangle = \int \langle \phi | \tilde{w} \rangle g(\tilde{w}) d\tilde{w}. \quad (22)$$

(Here, and henceforth, the limits of integration $\pm \infty$ are not explicitly indicated. Note also that ϕ and ϕ' (defined below) depend on w as well as on \underline{x}, t).

The principal virtue of this approach is that fluctuations in ϕ can be decomposed into two parts: the difference between conditional and unconditional means $\langle \phi - \langle \phi \rangle \rangle$, and fluctuations about the conditional mean $\phi' \equiv \phi - \tilde{\phi}$. The unconditional variance can then be expressed as

$$\langle \phi'^2 \rangle = \int g(\tilde{w}) \langle \phi - \langle \phi \rangle \rangle^2 d\tilde{w} + \int g(\tilde{w}) \tilde{\phi}'^2 d\tilde{w}, \quad (23)$$

where the conditional variance is

$$\tilde{\phi}'^2 \equiv \langle \phi'^2 | \tilde{w} \rangle = \langle (\phi - \langle \phi | \tilde{w} \rangle)^2 | \tilde{w} \rangle. \quad (24)$$

The first contribution to $\langle \phi'^2 \rangle$ is due to the meandering or flapping of the wake (6, 4). The second contribution is due to fluctuations about the conditional mean.

The exact transport equation for \tilde{f} is

$$\begin{aligned} \frac{\partial \tilde{f}}{\partial t} + V_3 \frac{\partial \tilde{f}}{\partial z} = - \frac{\partial}{\partial \psi} \{ \tilde{f} \langle \Gamma V^2 \phi | \underline{V}, \psi, \tilde{w} \rangle \} \\ - \frac{\partial}{\partial V_1} \{ \tilde{f} \langle a_1 | \underline{V}, \psi, \tilde{w} \rangle \}. \end{aligned} \quad (25)$$

Since the conditional joint pdf contains two-time Lagrangian information, the modelling of the conditional expectations should be consistent with our knowledge of such statistics (19). The following model, which is based on Langevin's equation (20), is consistent with Kolmogorov's inertial range scaling laws:

$$\begin{aligned} \langle a_1 | \underline{V}, \psi, \tilde{w} \rangle = - \frac{1}{\rho} \frac{\partial}{\partial x_1} \langle p | \underline{V}, \psi, \tilde{w} \rangle \\ - 1/2(1 + C_L) \frac{\epsilon}{k} \{ V_1 - \langle U_1 | \tilde{w} \rangle \} - C_L \epsilon \frac{\partial \ln \tilde{f}}{\partial V_1}. \end{aligned} \quad (26)$$

And, according to Kolmogorov's second hypothesis, C_L is a universal constant.

For the scalar dissipation term, the model

$$-\frac{\partial}{\partial \psi} \{ \bar{f} \langle \nabla^2 \phi | \psi, \bar{\psi} \rangle \} = \nabla^2 \bar{f} + \bar{c}_\phi \frac{\partial}{\partial \psi} \{ \bar{f}(\psi - \bar{\psi}) \} / \bar{\sigma}^2, \quad (27)$$

is exact for the mean and variance (although it may be inaccurate for higher moments). And, although it proved inapplicable in the unconditional case, we hypothesize that the conditional scalar dissipation can be modelled by:

$$\bar{c}_\phi \equiv \langle \frac{\partial \phi}{\partial x_1} \frac{\partial \phi}{\partial x_1} | \bar{\psi} \rangle = C_\phi \frac{1}{2} \bar{\sigma}^2 \epsilon/k. \quad (28)$$

Equations 25-28 could be solved (for given $\bar{\psi}$) by a Monte Carlo method to yield \bar{f} . Then the unconditional pdf could be obtained from Eq. 19. Instead of following this approach, we obtain (in the Appendix) approximate analytical solutions.

The conditional mean profile of ϕ is Gaussian

$$\langle \phi | \bar{\psi} \rangle = \frac{1}{\sqrt{2\pi} \bar{\sigma}} \exp(-\frac{1}{2} (z - \bar{z})^2 / \bar{\sigma}^2). \quad (29)$$

Expressions are given in the Appendix for the conditionally-expected location of the center of the wake $\bar{z}(t)$ and its width $\bar{\sigma}$. The unconditional wake thickness σ , obtained from Eqs. 22 and 29, is shown as the full line on Fig. 2. Even though the constant value $C_L = 3.125$ was chosen with respect to this data, the agreement over the whole range of x_w/M lends support to the modelling. (C_L was not determined to four figures; rather the quantity $(2C_L)^{1/2} = 2.5$ was determined to two figures.)

We now turn our attention to the determination of the unconditional variance $\langle \phi'^2 \rangle$. As previously mentioned, Eq. 23, $\langle \phi'^2 \rangle$ can be decomposed into a contribution from the wake flapping

$$\langle \phi'^2 \rangle_{\text{flap}} \equiv \int g(\bar{\psi}) (\bar{\phi} - \langle \phi \rangle)^2 d\bar{\psi}, \quad (30)$$

and a contribution from fluctuations about the conditional mean

$$\langle \phi'^2 \rangle_c \equiv \int g(\bar{\psi}) \bar{\phi}^2 d\bar{\psi}. \quad (31)$$

Similarly, the integral variance I , Eq. 11, can be decomposed as

$$I = I_{\text{flap}} + I_c, \quad (32)$$

where I_{flap} and I_c are the integrals of $\langle \phi'^2 \rangle_{\text{flap}}$ and $\langle \phi'^2 \rangle_c$.

Since expressions for both $\langle \phi \rangle$ and $\bar{\phi}$ have been obtained, $\langle \phi'^2 \rangle_{\text{flap}}$ can be determined from Eq. 30, and I_{flap} by integrating the result: the results are given in the Appendix. The conditional integral variance I_c can be determined in the same way as I . It satisfies Eq. 12 (with I_c replacing I), with the production \bar{P} given by Eq. 13 with σ replacing $\bar{\sigma}$ (see Appendix). This equation was integrated numerically to determine I_c .

The calculated integral variance I and the flapping contribution I_{flap} are shown on Fig. 4 for two values of the model constant C_ϕ . It may be seen that up to $x_w/M = 1.0$, I_{flap} contributes more than 90% of the variance, whereas beyond $x_w/M = 10$ it contributes less than 25%. At the first two measurement locations ($x_w/M = 0.36$ and 0.62) the calculations are in excellent agreement with the data. By $x_w/M = 8.1$, where the influence of C_ϕ begins to appear, the calculated variance is about twice the measured value. With $C_\phi = 2.0$, the calculated variance is four times the measured value at $x_w/M = 100$, whereas with $C_\phi = 4.0$, the calculations never exceed the measurements by more than a factor of two. This level of agreement (at least with $C_\phi = 4.0$) is comparable with that obtained by Stapountzis et al.

(4). (It may be noted that these authors' calculations extend to $x_w/M = 20$ even though their measurements extend to $x_w/M = 85$. As with our calculation, it appears that the agreement between their theory and experiment deteriorates beyond $x_w/M = 10$.)

In order to calculate profiles of $\langle \phi'^2 \rangle$ we need one more piece of information. Assuming $\langle \phi'^2 \rangle$ to have a Gaussian profile (4) with variance $X\sigma^2$, then the profiles of $\langle \phi'^2 \rangle$ can be determined from σ , I and X . But from our analysis X is not known. If there were only flapping (i.e. $I_c = 0$), then X could be determined, since $\langle \phi'^2 \rangle_{\text{flap}}$ is known: the value of X obtained thus we denote by X_{flap} . In the early stages of the wake, flapping is the dominant contribution to I , and X_{flap} can be expected to be a good approximation to X . Figure 5 shows normalized rms profiles

$$\phi' / \phi'_{\text{flap}} \equiv (\langle \phi'^2 \rangle / \langle \phi'^2 \rangle_{\text{flap}})^{1/2}, \quad (33)$$

at the first three measuring stations based on the calculated values of σ , I and X_{flap} . It may be seen that there is good agreement with the data. The location and magnitude of the peak away from the plane of symmetry is calculated reasonably well.

At the measurement stations further downstream, the peak value of $\langle \phi'^2 \rangle$ is on the plane of symmetry and the profiles are approximately self similar. Figure 6 shows a comparison of the measured and calculated profiles at the last measurement station $x_w/M = 100$. Here, I_c is the dominant contribution to I , and it would be fortuitous if X_{flap} approximated X . It can be seen that the calculated profile (with $C_\phi = 2.0$) based on σ , I and $X_{\text{flap}} = 1.59$ is significantly narrower than the experimental profile: but with the value $X = 1.0$, the agreement is improved. Better agreement still is obtained with $C_\phi = 4.0$, $X = 1.39$.

DISCUSSION

Both the conditional and unconditional pdf methods are capable of describing the mean spreading of the thermal wake through all three stages of its development. This ability is due to the fact that convection appears in closed form in the pdf equations, and gradient-diffusion models are avoided.

The conditional pdf method succeeds in calculating the temperature variance (to within a factor of 2) whereas the unconditional method does not. The crucial difference between the two methods is revealed in the (unconditional) integral variance equation:

$$\frac{dI}{dt} = \bar{P} - 2\bar{c}_\phi, \quad (34)$$

where

$$\bar{c}_\phi \equiv \int_{-\infty}^{\infty} c_\phi dz. \quad (35)$$

The integral production \bar{P} is the same for both models (see Eq. 13). For the unconditional model, the integral dissipation is

$$\bar{c}_\phi = 1/2 C_\phi \frac{\epsilon}{k} I, \quad (36)$$

whereas for the conditional model it is

$$\bar{c}_\phi = 1/2 C_\phi \frac{\epsilon}{k} (I - I_{\text{flap}}) + \frac{\Gamma}{4\sqrt{\pi}} (\bar{\sigma}^{-3} - \sigma^{-3}). \quad (37)$$

Figures 3 and 4 show that the modelled terms (that contains C_ϕ) have no effect until beyond the first measurement station. The success of the conditional model in calculating the variance at $x_w/M = 0.36$ is due, therefore, to the last term in Eq. 37. (At this location, the unconditional model yields a variance larger by a factor of 3). The term—which is exact

(given σ and $\bar{\sigma}$)—is due to the steep gradients in the conditional mean profile. From a broader perspective, the success of the conditional model is due to its ability to separate the flapping of the wake (largely determined by w_0) from the more random spreading.

Several approximations are made in the Appendix in order to obtain analytic solutions. The errors thus introduced can be avoided by solving the modelled conditional pdf transport equation by a Monte Carlo method.

ACKNOWLEDGEMENT

We are grateful to Professor Z. Warhaft for making available his unpublished data. This work was supported in part by Grant No. DAA929-82-K0017 from the U.S. Army Research Office.

BIBLIOGRAPHY

1. Townsend, A.A., 1954, "The diffusion behind a line source in homogeneous turbulence." Proc. Roy. Soc. **224 A**, 487-512.
2. Uberoi, M.S. and Corrsin, S., 1953, "Diffusion of heat from a line source in isotropic turbulence." N.A.C.A. Report 1142.
3. Warhaft, Z., 1983, "Interference of line sources in grid turbulence." To be submitted to J. Fluid Mech.
4. Stapountzis, H., Sawford, B.L., Hunt, J.C.R. and Britter, R.E., 1983, "Structure of the temperature field downwind of a line source in grid turbulence." Submitted to J. Fluid Mech.
5. Taylor, G.I., 1921, "Diffusion by continuous movements." Proc. Lond. Math. Soc. **20**, 196-212.
6. Gifford, F., 1959, "Statistical properties of a fluctuating plume dispersal model." Adv. Geophysics, **6**, 117-137.
7. Sykes, R.I., Lawellen, W.S. and Parker, S.F., 1983, "A turbulent transport model for concentration fluctuations and fluxes." Submitted to J. Fluid Mech.
8. Sawford, B.L. and Hunt, J.C.R., 1983, "Effects of turbulence structure, molecular diffusion and source size on fluctuations of concentration in homogeneous turbulence." Submitted to J. Fluid Mech.
9. Deardorff, J.W., 1978, "Closure of second- and third-order rate equations for diffusion in homogeneous turbulence." Phys. Fluids, **21**, 525-530.
10. Libby, P.A. and Scragg, C.A., 1973, "Diffusion of heat from a line source downstream of a turbulence grid." AIAA J. **11**, 562-563.
11. Fischer, H.B., List, E.J., Koh, R.C.Y., Imberger, J. and Brooks, N.H., 1979, Mixing in inland and coastal waters, Academic Press.
12. Pope, S.B., 1981, "Transport equation for the joint probability density function of velocity and scalars in turbulent flow." Phys. Fluids **24**, 588-596.
13. Pope, S.B., 1983, "PDF methods for turbulent reactive flows." To be published in Prog. Energy Combust. Sci.
14. Launder, G.Z. and Spalding, D.B., 1972, Mathematical models of turbulence, Academic.
15. Lumley, J.L., 1978, "Computational modelling of turbulent flows." Adv. Appl. Mech. **18**, 123-176.

16. Pope, S.B., 1983, "Consistent modelling of scalars in turbulent flows." Phys. Fluids **26**, 404-408.
17. Warhaft, Z. and Lumley, J.L., 1978, "An experimental study of the decay of temperature fluctuations in grid generated turbulence." J. Fluid Mech. **99**, 545-573.
18. Tavoularis, S. and Corrsin, S., 1981, "Experiments in nearly homogeneous turbulent shear flow with a uniform mean temperature gradient. Part I." J. Fluid Mech. **104**, 311-341.
19. Monin, A.S. and Yaglom, A.M., 1975, "Statistical fluid mechanics." (Vol. 2, pp. 358-361) M.I.T. Press.
20. Wax, N. (ed.), 1954, "Noise and Stochastic processes." Dover.

APPENDIX

An analytic solution for the conditional mean $\langle \phi | w \rangle$ can be obtained from the modelled joint pdf equation (Eqs. 25-28) with three approximations. First, the conditional pressure gradient in Eq. 26 is neglected. This term is small and its neglect is an excellent approximation. Second, the scalar dissipation term (Eq. 27) is omitted. The principal justification here is that the scalar dissipation does not affect the mean directly. Third, the condition $w(x=0, t=0) = w$ is replaced by the (unlikely) condition $w(x, y, z=0, t=0) = w$ (all x and y). This is identical to the conventional assumption that dispersion can be approximated as a one-dimensional phenomenon.

With these approximations the modelled conditional joint pdf equation becomes

$$\frac{\partial \bar{f}}{\partial t} + v_1 \frac{\partial \bar{f}}{\partial x_1} = r \nabla^2 \bar{f} + \frac{1}{2} (1 + C_L) \frac{\epsilon}{k} \frac{\partial}{\partial v_1} \{ \bar{f} (v_1 - \langle U_1 | \bar{w} \rangle) \} + C_L \epsilon \frac{\partial^2 \bar{f}}{\partial v_1^2 \partial v_1} \quad (A1)$$

This is also the Fokker-Planck equation (20) for the random walk

$$\underline{x}(t+\Delta t) = \underline{x}(t) + \underline{U}(t)\Delta t + (6\Gamma\Delta t)^{1/2} \underline{\xi}, \quad (A2)$$

$$\underline{U}(t+\Delta t) = \underline{U}(t) \left[1 - \frac{1}{2} (1 + C_L) \frac{\epsilon}{k} \Delta t \right] + (2C_L \epsilon \Delta t)^{1/2} \underline{\xi}', \quad (A3)$$

(in the limit of $\Delta t \rightarrow 0$), where $\underline{\xi}$ and $\underline{\xi}'$ are standardized joint-normal random vectors. For the case considered, motion in all but the $z=x_3$ direction is irrelevant. The appropriate initial conditions are $z(t=0)=0$, $w(t=0)=w$.

From a standard analysis of the random walk (20) we deduce that the conditional mean profile $\langle \phi(z, t) | w \rangle$ is Gaussian (Eq. 29) with mean position

$$\bar{z}(\bar{w}, t) = \bar{w} t_0 [1 - (1 + t/t_0)^{-s}] / s, \quad (A4)$$

where $s \equiv 1/2 m(C_L + 1) - 1$ and $t_0 \equiv x_0/U$. The standard deviation of the Gaussian profile is

$$\bar{\sigma}^2 = 2\Gamma t + \Delta_0^2, \quad (A5)$$

where

$$\Delta_0^2 = 2 \langle w_0^2 \rangle t_0^2 \left\{ \frac{-(r+s)}{2s^2(r-s)} + \frac{(1+t/t_0)^{-r-s}}{r(r-s)} + \frac{(r+s)(1+t/t_0)^{-s}}{rs^2} - \frac{(1+t/t_0)^{-2s}}{2s^2} \right\}, \quad (A6)$$

and $r \equiv 1/2 m(C_L - 1) + 1$. From the conditional profile and Eq. 22, the unconditional wake width σ is determined to be

$$\sigma^2 = 2\Gamma t + \Delta^2, \quad (A7)$$

where

$$\Delta^2 = 2\langle w_0^2 \rangle t_0^2 \left[\frac{(1+t/t_0)^{r-s}}{r(r-s)} + \frac{(1+t/t_0)^{-s}}{rs} - \frac{1}{s(r-s)} \right]. \quad (A8)$$

From the conditional and unconditional mean profiles, the flapping contribution to $\langle \phi'^2 \rangle$ can be determined. Performing the integration in Eq. 30 yields

$$\langle \phi'^2 \rangle_{\text{flap}} = \frac{1}{2\pi} \left\{ \frac{\exp(-\frac{1}{2} z^2 / \sigma_*^2)}{\sqrt{2} \sigma \sigma_*} - \frac{\exp(-z^2 / \sigma^2)}{\sigma^2} \right\}, \quad (A9)$$

where

$$\sigma_*^2 = \frac{1}{2} \bar{\sigma}^2 + \langle w_0^2 \rangle t_0^2 [1 - (1+t/t_0)^{-s}]^2 / s^2. \quad (A10)$$

And, integrating over z , the integral variance due to flapping is found to be

$$I_{\text{flap}} = [1/\sigma - 1/\bar{\sigma}] / (2\sqrt{\pi}). \quad (A11)$$

Noting that the shape of the profile of $\bar{\phi}$ (though not its position) is independent of w , we assume, similarly, that the shape of the profile of ϕ'^2 is also independent of w . Then, the integral variance due to conditional fluctuations is, Eq. 31,

$$I_c = \int \langle (\phi - \bar{\phi})^2 | \bar{w} \rangle dz, \quad (A12)$$

where any value can be selected for \bar{w} . From the modelled conditional pdf equation, a modelled equation for I_c can be obtained. By exploiting the symmetries resulting from the choice $w = 0$ this equation can be reduced to

$$\frac{dI_c}{dt} = \bar{P}_c - C_\phi \frac{\bar{\epsilon}}{k} I_c, \quad (A13)$$

where

$$\bar{P}_c \equiv \left(\frac{1}{2} \frac{d\bar{\sigma}^2}{dt} - \Gamma \right) / (2\bar{\sigma}^3 \sqrt{\pi}). \quad (A14)$$

(It may be noted that these equations are the same (mutatis mutandis) as Eqs. 12 and 13 for the unconditional model.)

The solution described above applies to a line source. In the experiment, the heated wire is a source of finite size which Stapountzis et al. (4) suggest modelling as a Gaussian temperature profile of size $\sigma = 1.25 d$. Such an initial profile can be accommodated in the analysis simply by changing $2\Gamma t$ to $\sigma^2 + 2\Gamma t$ in Eqs. A5 and A7. The reported variance calculations were performed with $\sigma = 1.25d$, but, in the region of the measurements, this produced only a small change in I compared to calculations with $\sigma_0 = 0$.

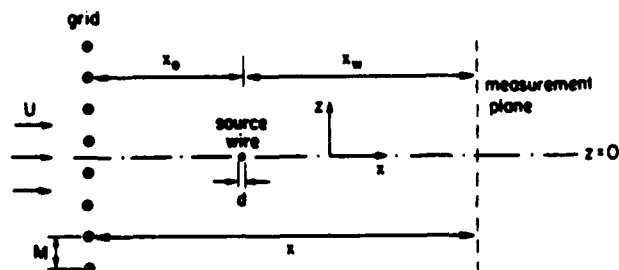


Fig. 1: Sketch of a heated wire downstream of a turbulence generating grid.

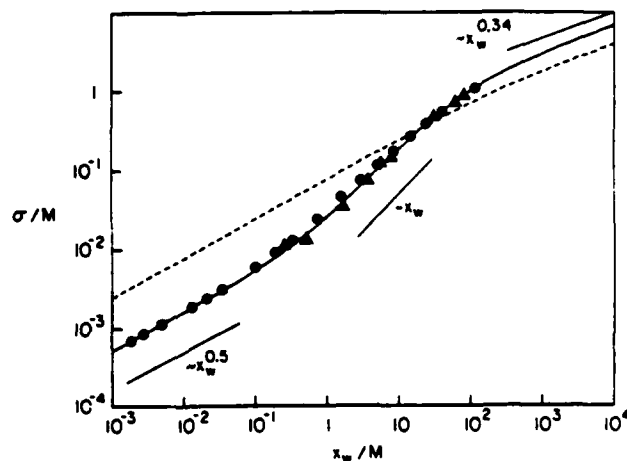


Fig. 2: Thermal wake thickness against distance from the wire.

----- $k-\epsilon$ model
 ● unconditional pdf method
 — conditional pdf method
 ▲ Experimental data (3)

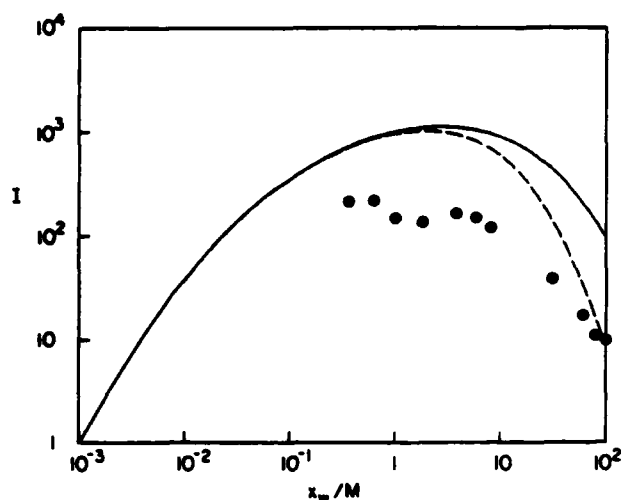


Fig. 3: Integral variance against distance from the wire.

— unconditional model $C_\phi = 2.0$.
 - - - unconditional model $C_\phi = 4.0$.
 ● from experimental data (3).

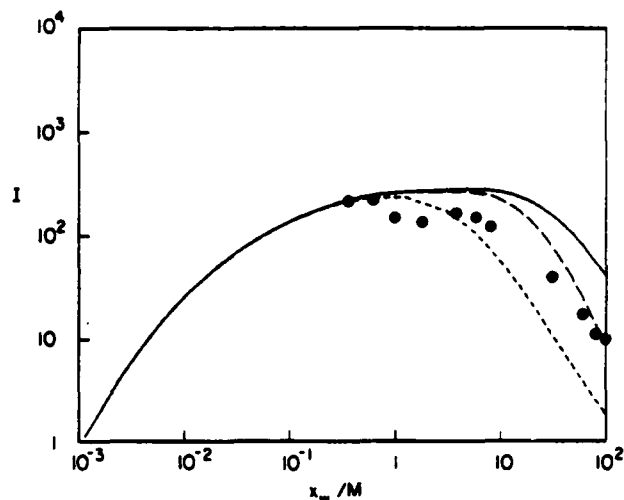


Fig. 4: Integral variance against distance from the wire.

— conditional pdf method $C_\phi = 2.0$.
 - - - conditional pdf method $C_\phi = 4.0$.
 - · - flapping contribution I_{flap}
 ● from experimental data (3).

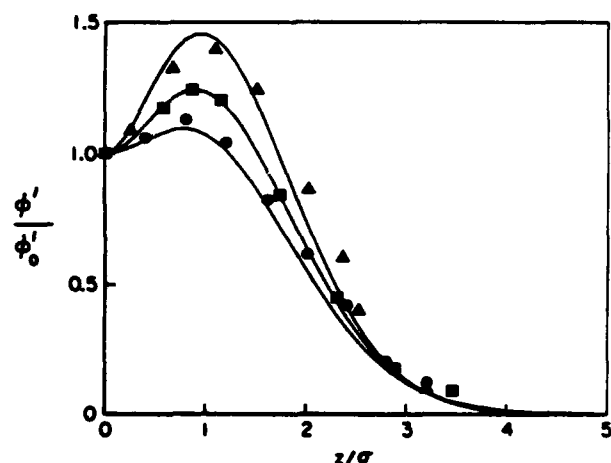


Fig. 5: Normalized standard deviation against cross-stream distance.

— conditional pdf method
 ▲, ■, ● data (3) at
 $x_w/M = 0.36, 0.62, 1.00$, respectively.

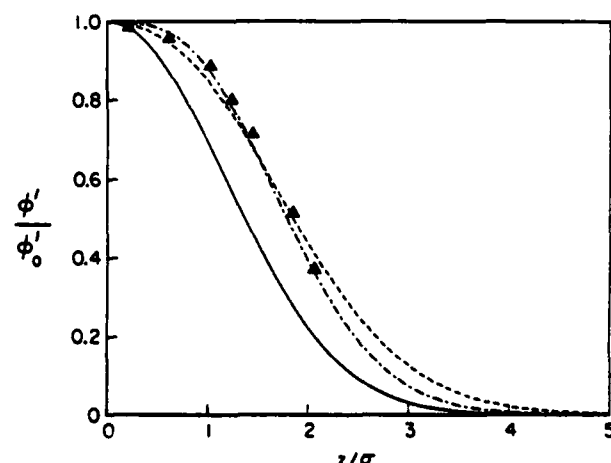


Fig. 6: Normalized standard deviation against cross-stream distance at $x_w/M = 100$: conditional pdf method

— $C_\phi = 2.0, X = X_{flap} = 1.59$.
 - - - $C_\phi = 2.0, X = 1.00$.
 - · - $C_\phi = 4.0, X = 1.39$.
 ▲ data (3).

Modelling of Scalar Transport in Homogeneous Turbulent Flows

by

W. P. Jones and P. Musonge
Department of Chemical Engineering and Chemical Technology
Imperial College, London SW7
England

ABSTRACT

The paper describes a second order closure for calculating the flux of passive scalar quantities in turbulent flow. One of the dominant terms appearing in the scalar flux balance equation for which a closure approximation is required is the fluctuating scalar-pressure gradient correlation. For this quantity a new approximation has been developed in terms of a time scale characteristic of the scalar field and linear combinations of the scalar flux and Reynolds stress. The characteristic time scale is obtained from solution of balance equations for the scalar variance and its "dissipation" rate. The constants appearing in the model have been chosen to reflect scalar turbulence data in a range of flows including strongly sheared nearly homogeneous flows, inhomogeneous equilibrium shear flows and decaying scalar (heated) grid turbulence. The model has been applied to the calculation of the scalar field in nearly homogeneous strongly sheared flow where it is shown to be capable of closely simulating the measured data.

NOMENCLATURE

b_{ij}	anisotropy tensor $\frac{2 \overline{u_i u_j}}{q^2/2} - \frac{2}{3} \delta_{ij}$
$C_{\theta 1}, C_{\theta 2}, C_{\theta 3}, C_{\theta 4}$	constants appearing in the $\overline{u_i \theta}$ equation
$C_{D 1}, C_{D 2}, C_{D 3}, C_{D 4}$	constants appearing in the ϵ_θ equation
$C_{\epsilon 1}, C_{\epsilon 2}$	constants appearing in the ϵ equation
p	fluctuating component of pressure
$q^2/2$	turbulence kinetic energy $= \frac{\overline{u_i u_i}}{2}$
r	time scale ratio $= \overline{\theta^2} \epsilon / \epsilon_\theta q^2$
r_e	value of r for equilibrium flows
t	time
u_i, u_i	mean and fluctuating components of velocity in direction x_i
$\overline{u_i \theta}$	scalar flux
x_i	Cartesian coordinate
ϵ	dissipation rate of turbulence energy
ϵ_θ	destruction or "dissipation" rate of scalar variance

ν	kinematic viscosity
ρ	fluid density
σ	molecular Prandtl or Schmidt number
τ	mechanical turbulence time scale $= q^2/2\epsilon$
τ_θ	scalar turbulence time scale $= \overline{\theta^2}/\epsilon_\theta$
ϕ, ϕ	mean and fluctuating component of scalar, e.g. temperature, mass fraction
$\overline{\theta^2}$	scalar variance

INTRODUCTION

The ability to predict the rate of turbulent transport of scalar quantities such as heat and mass is important in a wide range of practical applications. This requires the provision of a suitable model the construction of which can be approached at varying levels of complexity. Currently it appears that second order single point closure models in which all the second order moments (including the Reynolds stress tensor and scalar flux vector) are obtained from solution of their respective modelled transport equations represent about the simplest level at which most of the essential features of turbulent flows can be directly described. In general what would be required of a complete model of this type is that it should comprise a method of calculating both Reynolds stresses and turbulent scalar fluxes and should be able to cope with possible variations in fluid properties such as for example fluid density. However, the development of suitable models for the scalar field can best be carried out if first attention is restricted to passive scalars. In this case the scalar field has no influence on the velocity and then scalar transport can be studied in isolation from the Reynolds stress model.

This paper is concerned with the development of a second order closure to describe the transport of a passive scalar in nearly homogeneous turbulent flows both with and without mean scalar and mean velocity gradients. Such flows contain fundamental features of many scalar turbulent fields and as a consequence the model proposed should form the basis for calculating more complex flows. For high Reynolds and Peclet number homogeneous turbulent flow fields in the absence of buoyancy, to which the present work is restricted the scalar flux transport equation reduces to a form where a closure approximation is needed for one term only. This term is the fluctuating scalar-pressure gradient correlation and

represents so called "pressure-scrambling". A closure approximation has been formulated for this quantity in terms of linear combinations of the scalar fluxes and Reynolds stress (in the present context "known" quantities) and in which a time scale characteristic of the scalar field is required. This is obtained in terms of the scalar variance and its viscous destruction or "dissipation" rate. In homogeneous turbulent fields the scalar "dissipation" rate is the only unknown in the scalar variance equation and so the provision of a modelled form of the scalar destruction rate completes the present formulation.

As an aid to the modelling of "pressure scrambling" the formal solution of a Poisson equation can be used to relate the scalar-pressure gradient correlation to a volume integral involving two point correlations of the velocity and scalar fields. This volume integral comprises two parts, one involving only turbulence quantities and the other being a function of turbulence quantities times the mean rate of strain. A conventional approach - though not one which will be followed here - is then to develop closure approximations for these two contributions separately; for a review see Launder (1976). For the turbulence only part most workers have used Monin's (1965) linear relaxation model though more complex models have been proposed and used e.g. Lumley (1975); in practically all applications the necessary time scale has been assumed to be the mechanical turbulence time scale ($\equiv q^2/2\epsilon$). For the mean strain contribution two models have found popular use. These are the quasi-homogeneous model whereby the volume integral is modelled as a linear function of the scalar flux with the properties of the integral being used to eliminate (all) the constants and the proposal of Launder (1975) that the term be proportional to the mean strain part of the scalar flux generation rate. From these proposals Samaraweera (1978) has assembled two models which were then applied to a range of free flows with good results. However in this paper it is shown that when these two models are used to calculate scalar transport in the homogeneous shear flow of Tavoularis and Corrsin (1981) then the results obtained are extremely poor; a result which remains unchanged with the replacement of the mechanical turbulence time scale with a scalar field time scale. To overcome this, in addition to the current proposals a number of more complex formulations are possible. Prominent here is the work of Lumley (1978) who has attempted to construct more general models which satisfy the requirements of realizability (which the above and currently proposed model do not). However formulations satisfying all of the requirements of realizability are necessarily exceedingly complex involving as they must a number of invariant functions whose form must be determined from experiment. Since amongst other things realizability requires proper behaviour of the model as the turbulence becomes two dimensional (where there is little experimental data) the construction of suitable models and functions is a difficult task. It is not pursued in the present work: we prefer instead to attempt to construct a model which works over a more limited but practically important range of flows while acknowledging failure is likely if the turbulence approaches, for example, two-dimensionality.

The scalar field time scale used in the present work requires the scalar variance dissipation rate to be determined. About the simplest method of obtaining this is that adopted by Spalding (1971) where it is assumed to be given by

$$\epsilon_\theta = C_D (2\epsilon/q^2) \theta^2$$

and where the constant C_D is proportional to the ratio of the scalar and velocity field time scales. However it is extremely likely that the time scale ratio will be different in different flows and a more detailed model for ϵ_θ is then required; a model transport equation for ϵ_θ is needed. Newman, Launder, and Lumley (1981) have devised such an

equation for use in homogeneous fields without mean strain in which the source/sink terms depend on (in addition to the two time scales) the scalar variance production rate and the anisotropy of the velocity field. Good results were obtained when the model was applied to the range of scalar flows for which data was available. Elghobashi and Launder (1981) have also applied a simplified version of this model - in which the influence of the velocity field anisotropy was neglected - to the calculation of a thermal mixing layer developing in a uniform mean velocity field. However as they stand neither of these proposals is intended to apply to flows with mean strain; additional terms it appears then become necessary. For this reason a model equation for ϵ_θ applicable to flows with and without mean strain has been devised: for unstrained flows it is closely similar to the proposals above.

ANALYSIS

For a homogeneous turbulence field the set of balance equations describing the evolution of a passive scalar in an incompressible high turbulence Reynolds/Peclet number flow in the absence of buoyancy forces can be written in the form:

$$\frac{d \overline{u_i \theta}}{dt} + \overline{u_j \theta} \frac{\partial u_i}{\partial x_j} + \overline{u_i u_j} \frac{\partial \theta}{\partial x_j} = - \frac{\theta}{\rho} \frac{\partial p}{\partial x_i} \quad (1)$$

$$\frac{d \overline{\theta^2}}{dt} + 2 \overline{u_i \theta} \frac{\partial \theta}{\partial x_i} = - 2 \frac{\nu}{\sigma} \left(\frac{\partial \theta}{\partial x_j} \right)^2 \quad (2)$$

$$\frac{d \epsilon_\theta}{dt} = - 2 \frac{\nu}{\sigma} \frac{\partial \theta}{\partial x_i} \frac{\partial \theta}{\partial x_j} \frac{\partial u_i}{\partial x_j} - 2 \left(\frac{\nu}{\sigma} \right)^2 \left(\frac{\partial^2 \theta}{\partial x_i \partial x_j} \right)^2 \quad (3)$$

In writing the above equation set certain viscous terms negligible at high turbulence Reynolds numbers have been omitted and the assumption of local isotropy (Monin and Yaglom 1975) has been invoked with the consequence that terms such as $(\partial \theta / \partial x_j)(\partial u_i / \partial x_j)$ have been discarded. In order to establish values for the various constants which appear in the formulated model the equations describing the turbulence energy and its dissipation rate are needed. In the present work the following forms appropriate to homogeneous turbulent flows are adopted:

$$\frac{d q^2/2}{dt} = - \overline{u_i u_j} \frac{\partial u_i}{\partial x_j} - \epsilon \quad (4)$$

$$\frac{d \epsilon}{dt} = - 2 C_{\epsilon_1} \frac{\epsilon}{q^2} \overline{u_i u_j} \frac{\partial u_i}{\partial x_j} - 2 C_{\epsilon_2} \epsilon^2/q^2 \quad (5)$$

where $q^2/2 = \overline{u_i u_i}/2$ and where $C_{\epsilon_1} = 1.45$ and $C_{\epsilon_2} = 1.9$, (Morse, 1980).

The requirements of homogeneity imply that the mean scalar and mean velocity gradients must be uniform over the complete flow domain and are thus known. Hence in order to produce a closed set of equations closure approximations must be developed for the terms on the right hand side of (1) to (3) and in addition the characteristics of the velocity field including the Reynolds stress tensor must be known. In the context of a full second order closure the Reynolds stress would be obtained from solution of its own modelled balance equation. However in the present case where we are concerned only with the development of closure approximations for the scalar field it is immaterial whether the stress is obtained from measurement or calculation; that is providing the Reynolds stress model is capable of providing an accurate representation of the measurements. The Reynolds stress is therefore in the present work taken to be a "known" quantity.

The scalar flux equation (1) contains a single term which must be modelled; a correlation between the fluctuating scalar and the gradient of the pressure fluctuations - so called "pressure scrambling". For homogeneous flows the solution of a Poisson equation for the pressure can be used to relate this quantity to volume integral involving two point quantities, viz

$$\frac{\partial}{\partial x_i} \left(\frac{\partial \phi}{\partial x_j} \right) = \frac{1}{4\pi} \int_{\text{vol}} \left\{ \left(\frac{\partial^2 u_m u_m}{\partial x_l \partial x_l} \right) \frac{\partial \phi}{\partial x_i} + 2 \left(\frac{\partial u_l}{\partial x_m} \right) \left(\frac{\partial u_m}{\partial x_l} \right) \frac{\partial \phi}{\partial x_i} \right\} \frac{d \text{Vol}}{|\underline{x} - \underline{x}'|} \quad (a) \quad (b) \quad (6)$$

where the terms with and without primes denote values at \underline{x}' and \underline{x} , respectively. Equation (6) indicates that $(\partial/\partial \rho)(\partial \phi/\partial x_i)$ comprises two types of terms, one involving turbulence quantities only and another proportional to the mean strain. For these reasons the two terms have conventionally been modelled independently. The resulting complete closure approximation then consists of a term involving only turbulence quantities plus a function of the scalar flux (and sometimes the Reynolds stress) times the mean rate of strain, for example see Launder (1976), Lumley (1978). However an exact balance equation for the "turbulence only" component of the complete pressure scrambling term can be derived, Musonge (1983) and while this equation is too complicated to be of much direct use in modelling it does indicate that the contribution (a) in equation (6) depends both on the turbulence field and the mean scalar and mean velocity gradients. If it is accepted that both parts of the integral in equation (6) depend on the mean field then there is little or no advantage to be gained by modelling them separately and it is for this reason that the complete term is modelled collectively in the present work.

If it is assumed that the turbulence is quasi-steady then it seems reasonable to postulate that the dependence of $(\partial/\partial \rho)(\partial \phi/\partial x_i)$ can be expressed as:

$$-\frac{\partial}{\partial x_i} \left(\frac{\partial \phi}{\partial x_j} \right) = -C_{\phi 1} \frac{\overline{u_i \phi}}{\tau_{\phi}} + C_{\phi 2} b_{ij} q^2 \frac{\partial \phi}{\partial x_j} + d_{ijk} \frac{\partial u_j}{\partial x_k} \quad (7)$$

where b_{ij} is the anisotropy tensor and where d_{ijk} is a third rank linear tensor function of the scalar flux given by:

$$d_{ijk} = C_{\phi 3} \epsilon_{ij} \overline{u_k \phi} + C_{\phi 4} \epsilon_{ik} \overline{u_j \phi} + C_{\phi 5} \epsilon_{jk} \overline{u_i \phi}$$

The parameters $C_{\phi a}$ ($a=1,5$) are taken to be constants

and τ_{ϕ} is a time scale characteristics of the scalar field, here taken to be given by $\tau_{\phi} = \overline{\phi^2}/\epsilon_{\phi}$. In the absence of mean gradients equation (7) reduces to the approximation proposed by Monin (1954). It should also be noted that the constant $C_{\phi 5}$ plays no role in constant density flows. Equation (7) has been formulated in the belief that mean scalar gradients have no influence in isotropic turbulence and that $(\partial/\partial \rho)(\partial \phi/\partial x_i)$ should depend, at least to a first approximation, only linearly on turbulence quantities. To obtain values of the constants which appear in equation (7) measurements made in near equilibrium flows can be used. For this case convective and diffusive transport are negligible and production and dissipation rates are approximately equal. Applied to these flows on insertion of equation (7) into the scalar flux equation there results:

$$0 = -\overline{u_i u_j} \frac{\partial \phi}{\partial x_j} - \overline{u_j \phi} \frac{\partial u_i}{\partial x_j} - C_{\phi 1} \frac{\overline{u_i \phi}}{\tau_{\phi}} + C_{\phi 2} b_{ij} q^2 \frac{\partial \phi}{\partial x_j} + C_{\phi 3} \overline{u_j \phi} \frac{\partial u_i}{\partial x_j} + C_{\phi 4} \overline{u_j \phi} \frac{\partial u_i}{\partial x_j} \quad (8)$$

If, for situations where only $\frac{\partial u_1}{\partial x_2}$ and $\frac{\partial \phi}{\partial x_2}$ are none

negligible equation (8) is written for both the longitudinal (x_1) and lateral (x_2) directions after some manipulation there results:

$$C_{\phi 3} = -2 C_{\phi 1} \left(\frac{\overline{u_1 \phi}}{\tau_{\phi}} \right) \left(\frac{\overline{u_1 u_2}}{q^2} \right) - C_{\phi 2} \sigma_t + (1 + \sigma_t)$$

$$C_{\phi 4} = \frac{\overline{u_2 \phi}}{\overline{u_1 \phi}} \left\{ \sigma_t \frac{\overline{u_2^2}}{\overline{u_1 u_2}} - \frac{C_{\phi 2}}{2} \sigma_t \frac{q^2}{\overline{u_1 u_2}} \left(\frac{\overline{u_2^2}}{q^2} - \frac{1}{3} \right) - 2 C_{\phi 1} \frac{\overline{u_1 u_2}}{q^2} \right\}$$

where σ_t is the turbulent Prandtl number. If the following values of the various ratios representative of measurements in equilibrium flows:

$$\overline{u_1 u_2}/q^2 = -0.17 \quad ; \quad \overline{u_2^2}/\overline{u_1 u_2} = -1.45 \quad \text{Champagne, Harris, and Corrsin (1970)}$$

and

$$\overline{u_1 \phi}/\overline{u_2 \phi} = -1.2 \quad ; \quad \sigma_t = 0.7 \quad \text{Webster (1964)}$$

are inserted into the equation we obtain:

$$C_{\phi 3} = -0.408 C_{\phi 1} - 0.7 C_{\phi 2} + 1.7$$

$$C_{\phi 4} = -0.283 C_{\phi 1} - 0.309 C_{\phi 2} + 0.841$$

The remaining two constant values were estimated using free shear flow data, see Musonge (1973) with the result that the following set of constants were obtained

$$C_{\phi 1} = 1.9 \quad ; \quad C_{\phi 2} = -0.23 \quad C_{\phi 3} = 1.08 \quad \text{and} \quad C_{\phi 4} = 0.23$$

To complete the formulation a method must be devised for calculating the scalar field time scale which in the present case requires the scale dissipation rate to be determined. As was mentioned in the introduction there have been a number of previous attempts at devising model balance equations for ϵ_{ϕ} , though none of these formulations appear to be intended (in unmodified form) to be applicable to flows with mean strain. The strategy followed here follows the spirit of these previous attempts at formulating an ϵ_{ϕ} equation though there are some differences in detail. For the high Reynolds/Peclet number flows considered in the present work the following modelled form of the ϵ_{ϕ} equation is adopted:

$$\frac{d \epsilon_{\phi}}{dt} = -C_{D1} \frac{\epsilon_{\phi}^2}{\phi^2} - C_{D2} \frac{\epsilon_{\phi}}{q^2} \epsilon_{\phi} - C_{D3} \frac{\epsilon_{\phi}}{\phi^2} \overline{u_i \phi} \frac{\partial \phi}{\partial x_i} - C_{D4} \frac{\epsilon_{\phi}}{q^2} \overline{u_i u_j} \frac{\partial u_i}{\partial x_j} \quad (10)$$

where the coefficients C_{D1} , C_{D2} , C_{D3} and C_{D4} are

constants. For flows without mean strain equation (8) reduces to a form identical to that of Elghobashi and Launder (1981). In order to determine the constants

appearing in equation (10) use can be made of data obtained in decaying homogeneous scalar turbulence and the analysis of Béguier, Dekeyser and Launder (1978) of thermal turbulence data.

Experimental studies of decaying temperature fluctuations downstream of a heated grid, see Warhaft and Lumley (1978) and Sirivat and Warhaft (1982), have shown that the scalar to velocity field time scale ratio

$$r \equiv (\epsilon \theta^2) / (q^2 \epsilon_\theta)$$

remains approximately constant and equal to its initial value as the flow evolves. If it is assumed that r remains exactly constant in these flows then the present model can be reduced to:

$$\frac{dr}{dt} = 0$$

$$\frac{d\theta^2}{dt} = -2\epsilon_\theta$$

$$\frac{dq^2}{dt} = -2\epsilon$$

$$\frac{d\epsilon}{dt} = -2C_{\epsilon_2} \epsilon^2 / q^2$$

If C_{ϵ_1} is assigned the value of 1.9, Morse (1980) then solution of the above equations gives $C_{D_1} = 2.0$ and $C_{D_2} = 1.8$

The remaining two constants can be evaluated with the aid of data on inhomogeneous equilibrium flows - that is flows in which the scalar variance and turbulence energy production rates are approximately equal to their respective dissipation rates. Béguier et al (1978) have analysed flows of this type and concluded that in this situation the time scale ratio, r had a constant value of approximately 0.5. If to obtain an estimate of the constants turbulent transport is neglected then for equilibrium flows equation (10) becomes:

$$\frac{d\epsilon_\theta}{dt} = \frac{\epsilon^2}{\theta^2} \left[C_{D_3} - C_{D_1} + r_e (C_{D_4} - C_{D_1}) \right]$$

Using the definition of r together with equations (2), (4) and (5) we can also obtain

$$\frac{d\epsilon_\theta}{dt} = 2r_e (C_{\epsilon_1} - C_{\epsilon_2}) \frac{\epsilon^2}{\theta^2}$$

Using the quoted values for C_{ϵ_1} and C_{ϵ_2} together with

$r_e = 0.5$ the following relationship is obtained:

$$C_{D_4} = 4.9 - 2C_{D_3}$$

which leaves one constant and C_{D_3} still to be determined

Its value was selected by requiring that the complete scalar field model (with modelled diffusion terms included) produce that correct ratio of the spreading rates of the velocity and scalar fields in free jet/wake flows. By this means a provisional value of $C_{D_3} = 1$ was found to be adequate. The constants appearing in the scalar dissipation rate equation are thus assigned the values:

$$C_{D_1} = 2, \quad C_{D_2} = 1.8, \quad C_{D_3} = 1.0, \quad C_{D_4} = 0.9$$

and this completes the present formulation.

For the purposes of comparison with the present proposal two previously proposed and fairly extensively applied models are also considered. Samaraeera (1980) considered two models - denoted by

him as SF1 and SF2 - which when applied by him to a range of free shear flows gave good results. The two models are summarised below with the constants quoted as used by Samaraeera

SF1

$$-\frac{\theta}{\rho} \frac{\partial p}{\partial x_i} = -3.0 \frac{\epsilon}{q^2/2} \overline{u_i \theta} + 0.5 \overline{u_j \theta} \frac{\partial u_i}{\partial x_j}$$

SF2

$$-\frac{\theta}{\rho} \frac{\partial p}{\partial x_i} = -4.7 \frac{\epsilon}{q^2/2} \overline{u_i \theta} - 4.4 \frac{\epsilon}{q^2/2} b_{ij} + \frac{4}{5} \overline{u_j \theta} \frac{\partial u_i}{\partial x_j} - \frac{1}{5} \overline{u_j \theta} \frac{\partial u_j}{\partial x_i}$$

$$\text{with } b_{ij} = \frac{\overline{u_i u_j}}{q^2/2} - 2/3 \delta_{ij}$$

COMPARISON WITH EXPERIMENT

Before the equations describing the evolution of the scalar field can be solved the Reynolds stress field must be specified. In the experiment with which we are primarily concerned - that of Tavoularis and Corrsin (1981) - the components of the Reynolds stress were measured at locations covering the complete test section and these could have been curve fitted for use in the scalar field calculation. However, for reasons of convenience only this procedure was not adopted. The Reynolds stress field was calculated using the closure described by Jones and Musonge (1983) with the results corresponding to the continuous lines in figures 1 and 2; these were used in all subsequent scalar calculations. As the calculated components of the stress, including the turbulence energy are all in very close accord with the measured values - the maximum error is about 6% - no significant error in the scalar field can originate from this source. Thus any discrepancies which may subsequently arise between the measured and calculated scalar variance and scalar fluxes will reflect only inadequacies in the closure approximations adopted for "pressure-scrubbing" and the determination of the scalar dissipation rate. The resulting set of first order ordinary differential equations which arise when the present model is specialised to nearly homogeneous one dimensional flows have been solved by fourth order Runge-Kutta integration using measured initial values for the dependent variables.

Tavoularis and Corrsin (1981) have studied experimentally the nearly homogeneous turbulent velocity and scalar fields associated with a quasi-uniform mean shear rate and mean temperature gradient. In their experiment the turbulence energy production to dissipation rate had a roughly constant value of about 1.6 and the ratio of the scalar to turbulence energy time scales $r \equiv (\epsilon \theta^2) / (q^2 \epsilon_\theta)$ had a value of about 0.35. This latter value is significantly lower than the value found in most near equilibrium flows (where incidentally almost all scalar field models give good results). The results obtained when the present model is applied to the Tavoularis and Corrsin flow are shown in figures 3 to 5. The continuous lines represent calculations with the complete model (in which the scalar field time scale is calculated via the scalar dissipation rate equation) whereas the dashed lines represent the results obtained the scalar field time scale $\tau_\theta \equiv (\theta^2) / \epsilon_\theta$ set equal to mechanical time scale $q^2 / 2\epsilon$. This latter expression is that appropriate to equilibrium flows and has found common use in many scalar field closures though sometimes a constant of proportionality is introduced. In figure 3 the predicted and measured values of the turbulent Prandtl number defined by

$$\sigma_t = \frac{\overline{u_1 u_2} \frac{\partial \phi}{\partial x_2}}{\overline{u_2^2} \frac{\partial u_1}{\partial x_2}}$$

and the ratio of the longitudinal to lateral components of the scalar flux are shown over the complete test section. As can be readily observed the results obtained with the (two) mechanical and scalar field time scale model are in almost perfect agreement with the measurements whereas when the mechanical time scale only - the dashed line - is used the discrepancies are large; the predicted flux ratio increases to a value of about 2.7 compared with the measured value of 2.2 at the end of the test section. The absolute values of components of the flux and the scalar variance are shown in figure 4. Again consistent with the previous figure the fluxes and the variances are well predicted with two scale model with the maximum discrepancy between the measured and calculated fluxes being about 10% and that for the variance being about 13%. In contrast - again consistent with figure 3 - when only the mechanical time scale is used appreciable error occurs with discrepancies of the order 30% arising. Finally in figure 5 the predicted and measured variation of the correlation coefficients for the two components of the scalar flux and the scalar to mechanical time scale ratio over the test section are shown. Here only the complete (two time scale) model calculations are shown and these are again in good agreement with the measured values. In view of the maximum 6% discrepancy between the measured stress field and that used for the calculations (which is probably typical of the experimental uncertainty) the overall agreement displayed in figures 3 to 5 by the two scale model must be deemed satisfactory. In concluding this we must draw attention to the fact that the data of Tavoularis and Corrsin was influential in the choice of the model constants; any merit in the good agreement achieved must be therefore tempered by this fact.

From the results shown in figures 3 to 5 it is clear that the use of an independent scalar field time scale is necessary to bring agreement with experiment. It therefore seemed worthwhile to explore whether or not any of the simpler current models could be made to reproduce the presently considered measurements simply by replacing the mechanical time scale with the scalar time scale computed from the solution of equations (2) and (10). For this purpose the models used and denoted as SF1 and SF2 by Samaraweera (1978) have been used: both models have been found to perform well for a range of free shear flows. As for the previously discussed calculations the Reynolds stress field used was that displayed in figures 1 and 2 and the calculated results are shown in figures 6 to 8. Those shown in figures 6 and 7 represent the results obtained with models SF1 and SF2 in their original form and as used by Samaraweera (1978) while figure 8 shows the results when the mechanical time scale, $q^2/2\epsilon$, is replaced with that of the scalar field, namely ϕ^2/ϵ_ϕ . The results displayed in both cases are in exceedingly poor agreement with measurements. In figures 6 and 7 with both models SF1 and SF2 the predicted turbulent Prandtl number is about 0.3 over much of the flow compared with the measured value of 1.1 and both $u_1\phi$ and $-u_2\phi$ are overpredicted by an excess of 100% by the end of the test section. As a consequence the calculated values of the scalar variance are typically some 200-300% greater than the measured value at the end of the test section.

Some small improvement arises when the scalar field time scale is used, figure 8, with the computed turbulent Prandtl number now being about 0.6 over much of the flow. However both the scalar flux and scalar variance remain significantly in error with discrepancies of the order 100% arising at the end of the measuring section.

In view of the good performance of particularly model SF1 and to a lesser extent SF2 in free shear flows the results obtained here might at first sight seem slightly surprising. However the reasons for this can perhaps be understood if it is realised that in the Tavoularis and Corrsin flow that the turbulent Prandtl number, the flux ratio and the scalar to mechanical time scale ratio have values of approximately 1.1, -2.2 and 0.35, respectively. These are substantially different from those of 0.7, -1.1 and 0.5 found in near equilibrium flows and the data thus represents a stringent test of scalar flux models.

CONCLUDING REMARKS

The closure approximation formulated for the scalar-pressure gradient correlation appearing in the passive scalar flux balance equation has two components. These are (i) a general modelling in terms of linear combinations of the scalar flux and Reynolds stress and (ii) the use of a characteristic scalar field time scale obtained in the present work from solution of a modelled scalar "dissipation" rate equation. Both of these components have been shown to be necessary for the model to be capable of predicting both equilibrium and non-equilibrium scalar flows. The model necessary involves a number of empirical constants which have been chosen (without rigorous optimisation) by reference to a range of flow configurations which include decaying scalar grid turbulence, inhomogeneous near equilibrium free shear flows and the scalar field in the strongly sheared nearly homogeneous free shear flow of Tavoularis and Corrsin. In this latter flow appreciable departures from equilibrium arise and it thus represents a severe test of scalar flux models. When the proposed model is applied to the flow it closely simulates the measurements as it does also in the case of equilibrium free flows. Though not described here the model, with terms to account for flow inhomogeneities added, has been applied to a range of free flows, Musonge (1983). While the data available for comparison is limited and the scalar field predictions are sometimes contaminated by errors in the predicted velocity field characteristics the results were generally acceptable. However scalar field measurements and particularly those involving the components of the scalar flux and the variance are limited and these latter calculations do not therefore provide a stringent test of the proposed or indeed any other scalar flux model. More measurements particularly of the scalar-velocity correlations and scalar variance are therefore needed to fully determine the adequacy of the proposed model. It is also worth pointing out that the model has not so far been applied to the calculation of near wall flows and it may well be that further adjustments of the model and its constants will then be necessary.

ACKNOWLEDGEMENTS

One of the authors (PM) gratefully acknowledges the financial support provided by the Government of the United Republic of the Cameroon for the period during which this research was carried out.

BIBLIOGRAPHY

- Béguier, C., Dekeyser, I., and Launder, B. E., 1978, "Ratio of scalar and velocity dissipation time scales in shear flow turbulence", *Phys. of Fluids*, 21, 307.
- Champagne, F. H., Harris, V. B., and Corrsin, S., 1970, "Experiments on nearly homogeneous turbulent shear flow", *J. Fluid Mech.*, 41, 81.
- Elghobashi, S. and Launder, B. E., 1981, "Modelling the dissipation rate of temperature variance in a thermal boundary layer", 3rd Symp. on Turbulent Shear Flows, University of California, Davis.

Jones, W. P. and Musonge, P., "Closure of the Reynolds stress and scalar flux equations", in preparation.

Launder, B. E., 1975, "On the effects of a gravitational field on the turbulence properties of heat and momentum", J. Fluid Mech., 67, 569.

Launder, B. E., 1976, Heat and Mass Transport in Turbulence, Topics in App. Phys. 12, Ed. P. Bradshaw, Springer-Verlag.

Lumley, J. L., 1975, "Prediction methods for turbulent flows", Introduction Lecture Series 76, Von Karman Inst., Brussels.

Lumley, J. L., 1978, "Computational modelling of turbulent flows", Adv. in Appl. Mech., 18, Academic press, Inc.

Monin, A. S., 1954, "On the symmetry properties of turbulence in the surface layer of air", *IZV. Atm. and Oceanic Phys.*, 1, 45.

Monin, A. S. and Yaglom, A. M. (1975), Statistical Fluid Mechanics, MIT Press.

Musonge, P., 1983, "The prediction of free turbulent flows", Ph.D. Thesis, University of London.

Newman, G. R., Launder, B. E., Lumley, J. L., 1981, "Modelling the behaviour of homogeneous scalar turbulence", J. Fluid Mech., 111, 217.

Samaraweera, D. S. A., 1978, "Turbulent heat transport in two- and three-dimensional temperature fields", Ph.D. Thesis, University of London.

Sirivat, A. and Warhaft, Z., 1982, "The effect of a passive cross-stream temperature gradient on the evolution of temperature variance and heat flux in grid turbulence", J. Fluid Mech., 120, 475.

Tavoularis, S. and Corrsin, S., 1981, "Experiments in nearly homogeneous turbulence with a uniform mean temperature gradient", Part I. J. Fluid Mech., 104, 311.

Warhaft, Z. and Lumley, J. L., 1978, "An experimental study of the decay of temperature fluctuations in grid-generated turbulence", J. Fluid Mech., 88, 659.

Webster, C. A. G., 1964, "An experimental study of turbulence in a density stratified shear flow", J. Fluid Mech., 19, 221.

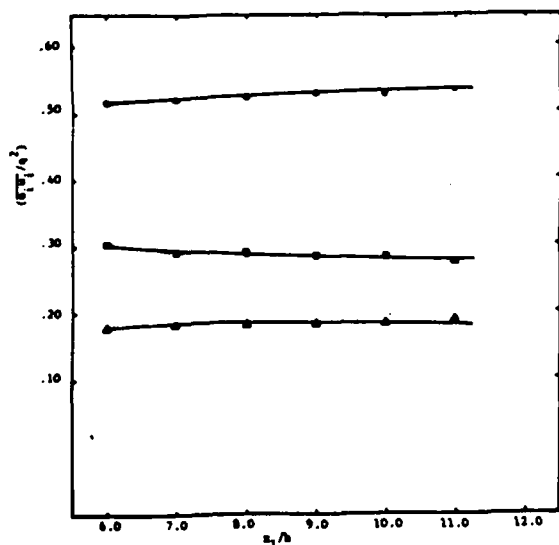


Figure 1 Normal stress variation in the nearly homogeneous flow of Tavoularis and Corrsin

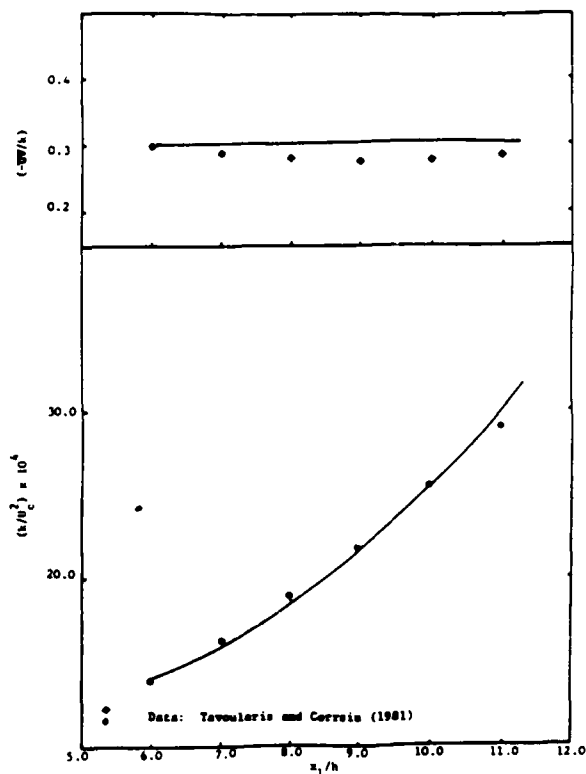


Figure 2 Shear stress and turbulence energy variation in the nearly homogeneous flow of Tavoularis and Corrsin

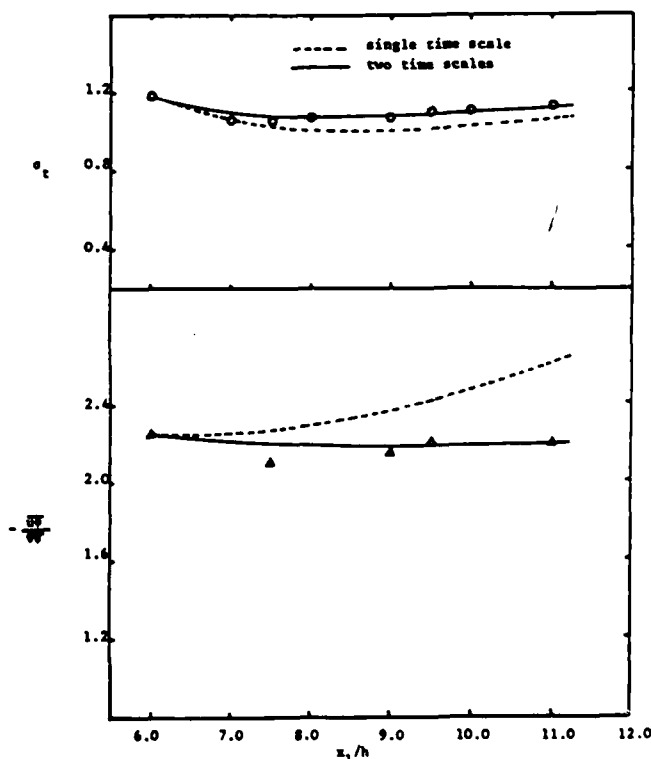


Figure 3 Predicted and measured Prandtl number and heat-flux ratio

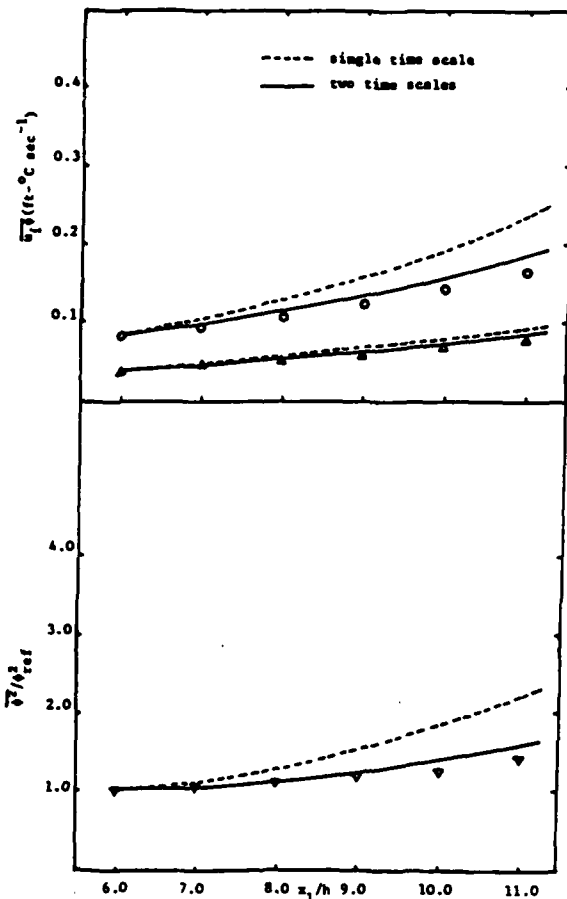


Figure 4 Predicted and measured heat-flux components and temperature variance

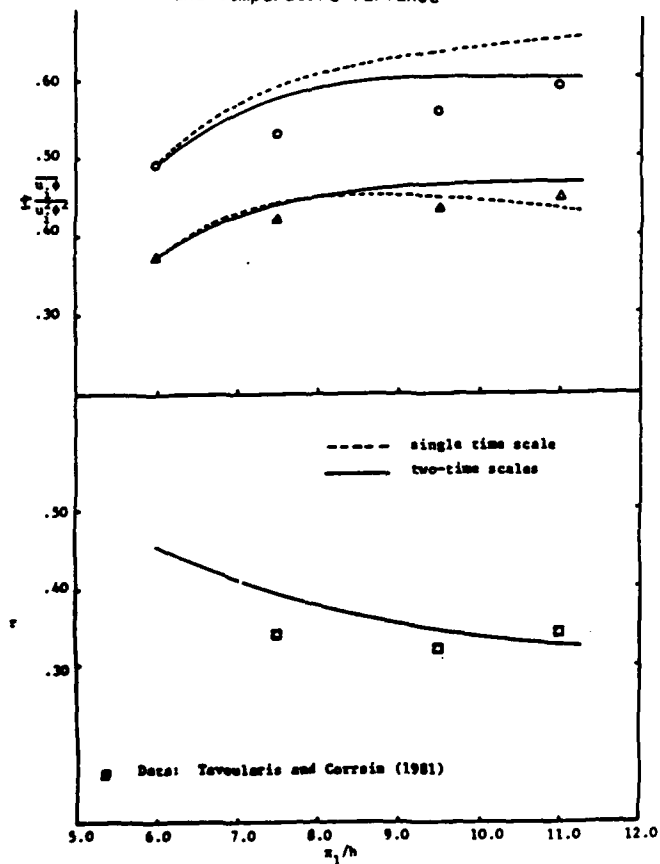


Figure 5 Predicted and measured correlation coefficients and time scale ratio

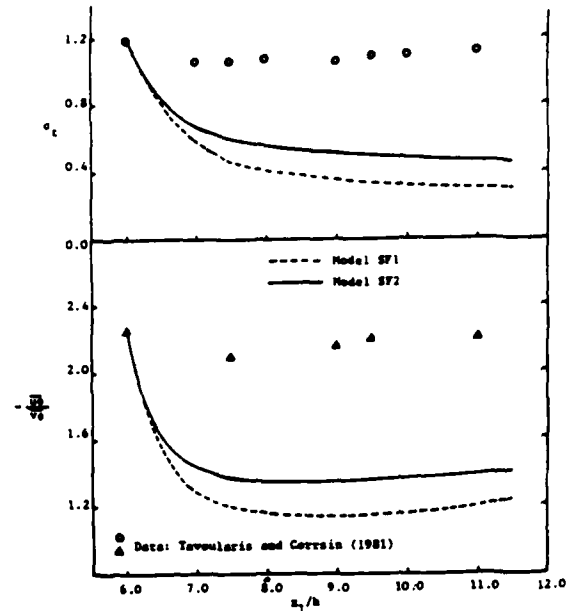


Figure 6 Prandtl and heat flux ratio distribution using models SF1 and SF2

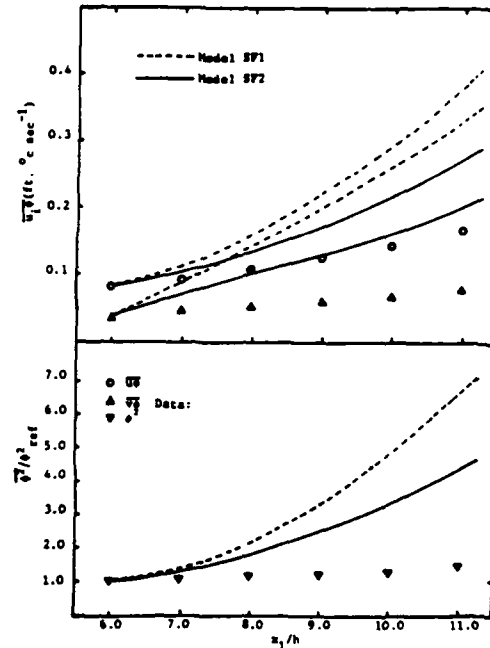


Figure 7 Heat flux components and temperature variance distribution using models SF1 and SF2

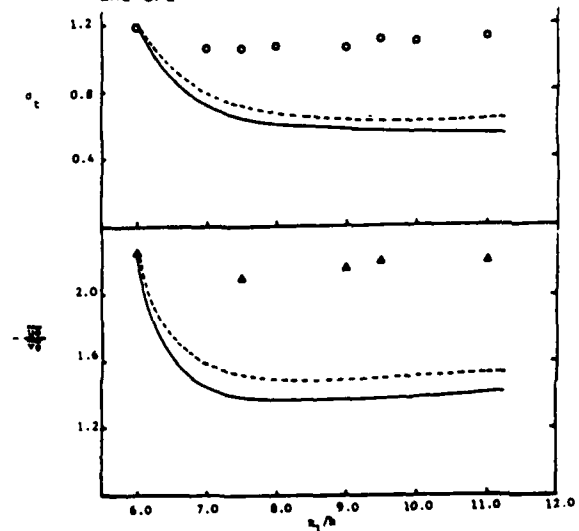


Figure 8 Prandtl number and heat flux ratio using models SF1 and SF2 with a scalar field

THE STRUCTURE OF TURBULENCE IN A NATURAL CONVECTION BOUNDARY LAYER

R. Cheesewright
Queen Mary College

and

A. Dastbaz
Queen Mary College
University of London

ABSTRACT

The paper reports on investigation into the structure of the turbulence in a natural convection boundary layer on an isothermal vertical surface, based on measurements of the temperature fluctuations. Two point correlations with probe separations in one or more of the three coordinate directions, were used to determine the extent to which the structure of the turbulence is similar to that found in forced flows. Spanwise correlations showed a structure, very similar to the streaks and bursts reported in forced flows, in the region near the wall, but further out the structure was different.

INTRODUCTION

The study of turbulent natural convection boundary layers has always lagged behind the study of the corresponding forced flows. Even today the important characteristics of the development of a turbulent natural convection boundary layer on an isothermal, vertical plane surface (such as the variation of the boundary layer thickness with distance along the surface) cannot be considered to be known. The profiles of mean velocity and mean temperature recently reported by Cheesewright and Ierokipiotis (1982) do at least satisfy an integral energy balance, unlike the earlier data of Cheesewright (1968), Smith (1972) and Doan (1977). However, they do not extend over a sufficiently large range of Grashof numbers to delineate the trends of development.

The setting up of experiments at large enough Grashof numbers is not easy and there is considerable interest in the use of numerical techniques, together with appropriate turbulence models, to provide the missing data. A number of different turbulence models are available from work on forced flows, but it is by no means certain that a model developed for use in forced flows will be satisfactory for natural convection flows since the structure of the turbulence in the two types of flow may be different. This situation suggests the need for experimental data on the structure of a turbulent natural convection boundary layer so that such data can be compared with the fairly extensive array of data which is already available for turbulent boundary layers in forced flows.

The work of Cheesewright and Doan (1978) was the first step in a study of the structure of the turbulence in a natural convection boundary layer. Two point correlations of the temperature fluctuations which were reported in that work gave some weight to the suggestion that the structure of the turbulence in natural convection flows was generally similar to that found in forced flows. The present work represents a second stage in the investigation begun by Cheesewright and Doan and to the authors' knowledge this is still the only study of the structure of a fully turbulent natural convection flow.

Studies of the structure of turbulent forced flows have used a range of different techniques from flow visualisation to the correlation of time derivatives of

velocity components. They have tended to concentrate on the velocity field since it is the velocity field which really comprises the turbulence and quantities such as the turbulent temperature fluctuations are secondary and result from the velocity field. In those studies which are known to have looked at the structure of the temperature fluctuations, the temperature behaved like a passive scalar, there being no feedback from the temperature field to the velocity field.

The measurement of velocities in a turbulent natural convection flow is particularly difficult. In the present experiment where the working fluid is air, the maximum mean velocity does not exceed 0.75 m/s, and these low velocities combined with the high level of turbulent fluctuations of temperature make accurate hot-wire anemometry particularly difficult. Recent mean velocity data measured with a laser-Doppler anemometer (Cheesewright and Ierokipiotis (1982)) have confirmed an earlier suspicion that, although the velocity profiles in a laminar natural convection boundary layer can be measured with a hot-wire anemometer, the velocities in the turbulent boundary layer are under-estimated by up to 25%. The reason for this error is not fully understood but it is believed that it is due to the support prongs of a typical hot-wire probe having a thermal time constant which is of the same order as the time constant associated with the large eddy structure of the turbulence. The temperature of the prongs is thus driven by the turbulent fluctuations of temperature in the flow and the interaction with the wire comes from the fact that at low velocities, a significant part of the energy supplied to the wire is lost by conduction to the prongs.

The nature of the above described problem with hot-wire anemometry suggests that the use of hot-wires to measure two point velocity correlations in a turbulent natural convection flow would almost certainly lead to serious errors. The alternative of using laser-Doppler anemometry is not really feasible because the provision of an optical system with two separate channels, one of which could be traversed relative to the other, while the whole system could be traversed to any point in the boundary layer would be very expensive.

The difficulties with velocity measurement gave rise to a decision to concentrate on the study of temperature fluctuations.

Before describing the experiments it is convenient to consider the current state of knowledge regarding the turbulent natural convection boundary layer.

Characteristics of a Turbulent Natural Convection Boundary Layer

The present work used air as a working fluid so that the thermal and flow regions in the boundary layer may be assumed to be of the same extent. For example, adjacent to the wall there will be a viscous sublayer and a conductive sublayer and the available data only clearly define the edge of the latter region but we will assume that the edge of the viscous sublayer is at the same distance from the wall.

It may be shown theoretically that the profile of mean temperature in the sublayer should be linear and this has been confirmed by experiment, but the corresponding cubic form of the mean velocity profile has not yet been confirmed.

George and Capp (1979) have suggested that the natural convection equivalent of the inertial sublayer is a buoyant sublayer and they have shown that the temperature and velocity in the region should vary with the inverse cube root and the cube root of the distance from the wall respectively. However, if we allow for a buffer layer between the viscous sublayer and the buoyant sublayer, the latter must be a much less extensive region than the inertial sublayer in a typical forced flow because it is bounded on the outer side by the peak in the mean velocity profile. Figure 1 shows an estimate of the extent of the various layers in the present flow, for which the edge of the viscous sublayer is at approximately 1.8 mm from the wall and the peak mean velocity is at 8-9 mm from the wall.

The presently available data do not entirely support the predictions of George and Capp in respect of the interrelation between the growth of the boundary layer thickness and the growth of the maximum mean velocity. However, this may be due to the experiments not having been carried to high enough values of the Grashof number.

Because George and Capp were able to show that the near wall region is not a constant stress layer, but a constant heat flux layer, they suggested velocity and length scales for that region which were different to the usual u_τ and v/u_τ . In order to facilitate comparison with forced flow data the present results have been made dimensionless against u_τ and v/u_τ rather than the new scales. The necessary values of τ_w have been taken from the work of Ierokipiotis (1983).

Interaction of the Temperature and Velocity Fields

In terms of the mean fields of temperature and velocity there is obviously complete interaction as the whole flow is driven by density differences arising from temperature differences. In terms of the turbulence the picture is not clear. Buoyancy 'source' terms appear in the conservation equations for both the kinetic energy of the turbulence and for the Reynolds stress ($u'v'$) but it has been suggested by some authors that these terms are negligible in a natural convection boundary layer on a vertical surface, although they are known to be significant in boundary layers on horizontal and inclined surfaces.

If the buoyant and shear stress 'source' terms in the kinetic energy equation are each integrated across the thickness of the boundary layer it is certainly true that the former is negligible, but if we look at the respective distributions across the layer there must be a significant region in which the buoyant 'source' term dominates. Approximate estimates of the distributions of the major turbulence terms have been made using a combination of modelling data by Leslie and Gibson (1982) and experimental data (where the latter is available), these estimates are shown in Figure 2.

It will be seen that there is a region just outside the viscous/conductive sublayer in which the shear stress 'source' term dominates, and a second region outside the peak in the mean velocity profile where the

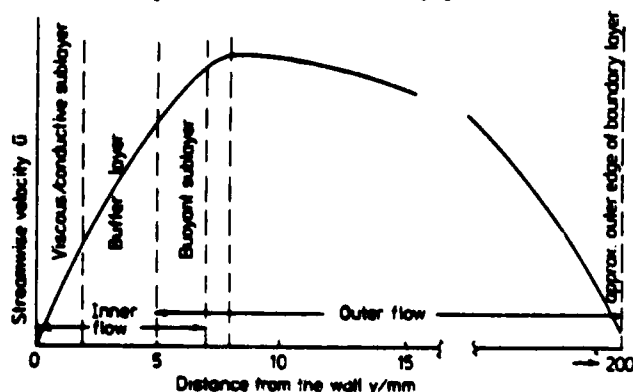


Figure 1 Regions of the Boundary Layer

same relationship is true. However, between these two regions the buoyant 'source' term dominates, since the shear stress 'source' passes through zero twice, once associated with the zero of the Reynolds stress and once associated with the zero of the gradient of mean velocity.

This review of the interaction between the temperature and velocity fields suggests that phenomena such as a span-wise structure of low speed streaks and the associated 'bursts', which originate at the outer edge of the viscous sublayer, may be expected to be relatively similar to corresponding phenomena found in forced flows. Structures which have their origin further out in the flow may be different.

EXPERIMENTAL DETAILS

The vertical plate 0.6 m wide and 2.75 m high, used to generate the natural convection boundary layer in this work was originally constructed by Cheesewright (1968) and with minor modifications it has since been used by Smith (1972) and Cheesewright and Doan (1978). The electrically heated plate is fitted with 0.25 m deep side walls over its whole length and spanwise traverses in the turbulent part of the boundary layer have shown no evidence of a lack of two-dimensionality in the mean fields, over the central 0.4 m of the plate. The plate surface was isothermal to better than $\pm 1^\circ\text{C}$ but it was not possible to eliminate a vertical stratification of 1.5 to 2.0 $^\circ\text{C}/\text{m}$ in the laboratory. All the experiments were made at a plate to ambient temperature difference of $20 \pm 1^\circ\text{C}$.

The low frequencies of the turbulence ($< 25\text{ Hz}$) allowed all the measurements to be made with 12.5 μm diameter chromel-alumel thermocouple probes. The traversing gear enabled one probe to be moved relative to the other in any of the three coordinate directions while the whole assembly could be moved to any point in the boundary layer. The two probes were always arranged so that their supports were in a streamwise plane but inclined at 45° to the upstream direction, one probe on each side. Thus, only in the most intense turbulence was the downstream probe in the wake of any part of the upstream probe, except the actual junction.

The thermocouple signals were amplified, filtered at 50 Hz and then digitised at 100 Hz with a resolution of 1/4096, which corresponded to approximately 0.025 $^\circ\text{C}$. The digital data was recorded on magnetic tape for later processing on a large main-frame computer. The amplification and digitisation system was calibrated before each experiment by utilising known signals in place of the actual thermal e.m.f.s.

The record lengths were typically 10 minutes and this together with the digitisation at 4 times the highest significant frequency of the turbulence meant that for any given experiment, sufficient data were available to give statistically significant results even when filtered, time delayed, cross-correlations were needed.

All the computation of correlations was done using fast fourier transform techniques although a few sets of

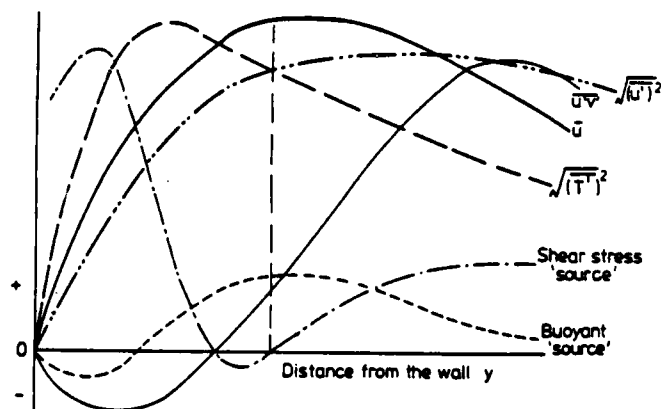


Figure 2 Estimated Distributions of Significant Quantities across the Boundary Layer (not to scale)

data were also submitted to the direct multiplication program used by Cheesewright and Doan, for comparison purposes. 'Box-car' filtering in the frequency domain was used to generate the filtered cross correlations.

When the spanwise correlation data was being examined in order to find the mean spacing and frequency of low speed streaks and bursts, the long period correlations proved to be inconclusive so the variable interval short period, time averaging technique developed by Gupta et al (1971) was used. After a number of trials an averaging period of 1.024 s was used in the estimation of the spacing and one of 10.24 s in the estimation of the frequency.

EXPERIMENTAL RESULTS

The notation used by Tritton (1967) is used to define the correlations and when reference is made to the 'fixed' probe it is always the one at the smallest x and y . The probe separations are thus always positive and the sign of the time delay is taken so that the sign of the convection velocity is consistent with the main co-ordinate system.

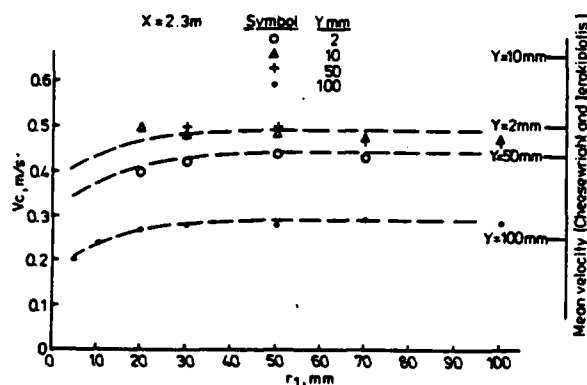


Figure 3 Streamwise Convection Velocities

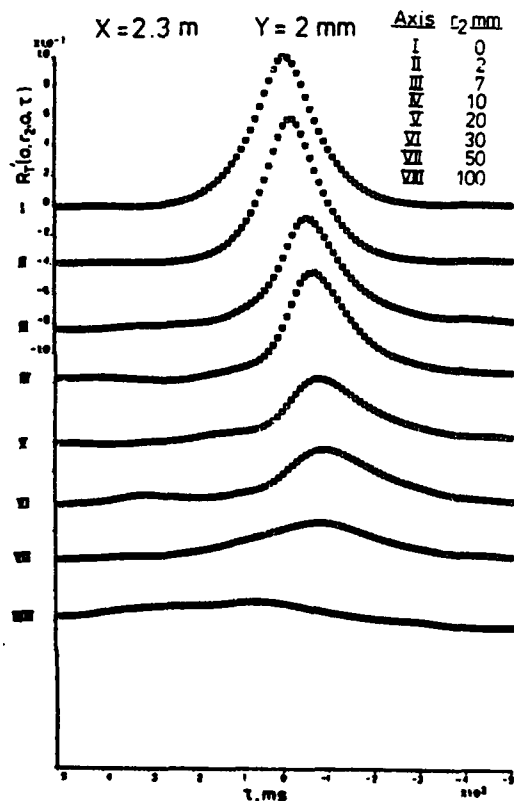


Figure 4 Space-time Correlations Normal to the Wall

Correlations with probe separation in the streamwise direction were in very close agreement with those reported by Cheesewright and Doan (1978) and are not shown here. However, it is of interest to consider the convection velocities implied by the streamwise space-time correlations. Figure 3 shows the velocities as a function of probe separation, for a number of different distances from the wall and the corresponding mean velocities are shown for comparison. It is notable that for $y > 25$ mm the convection velocities are greater than the local mean velocity.

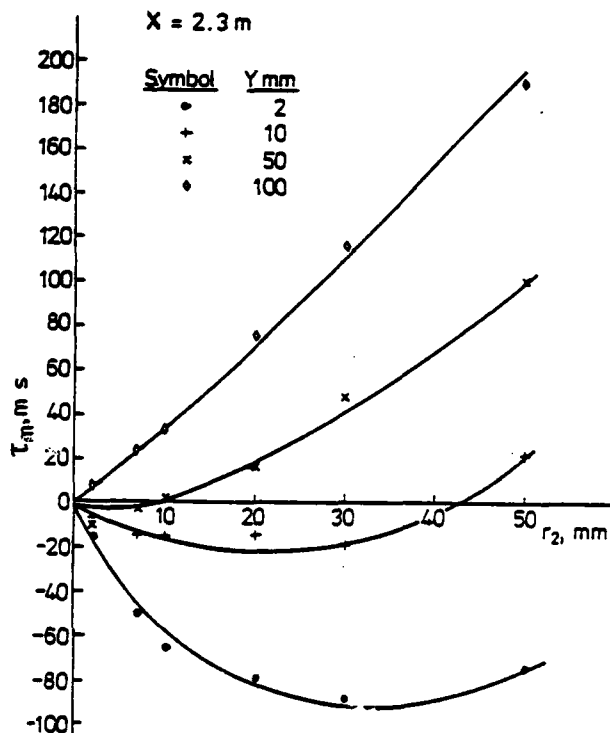


Figure 5 Optimum Time Delay Distributions Normal to the Wall

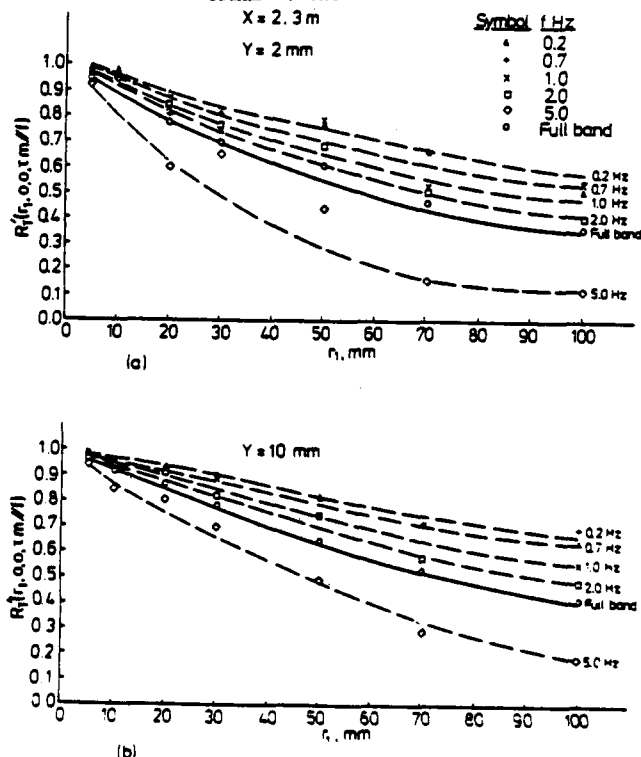


Figure 6 Filtered Space-time Correlations in the Streamwise Direction

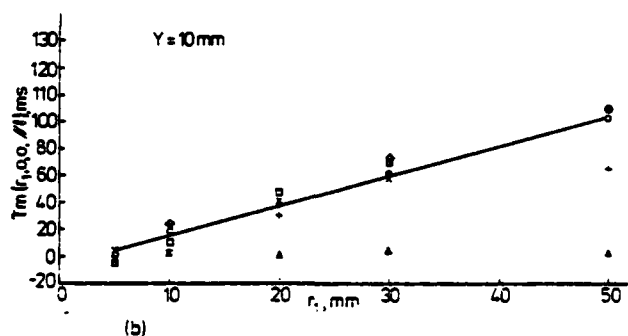
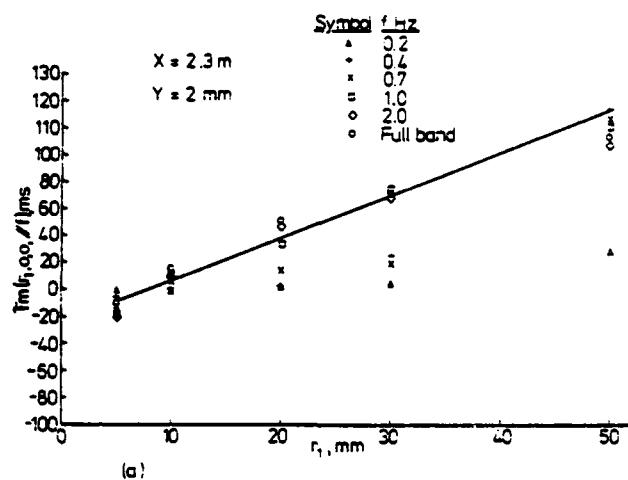


Figure 7 Optimum Time Delay as a Function of Frequency

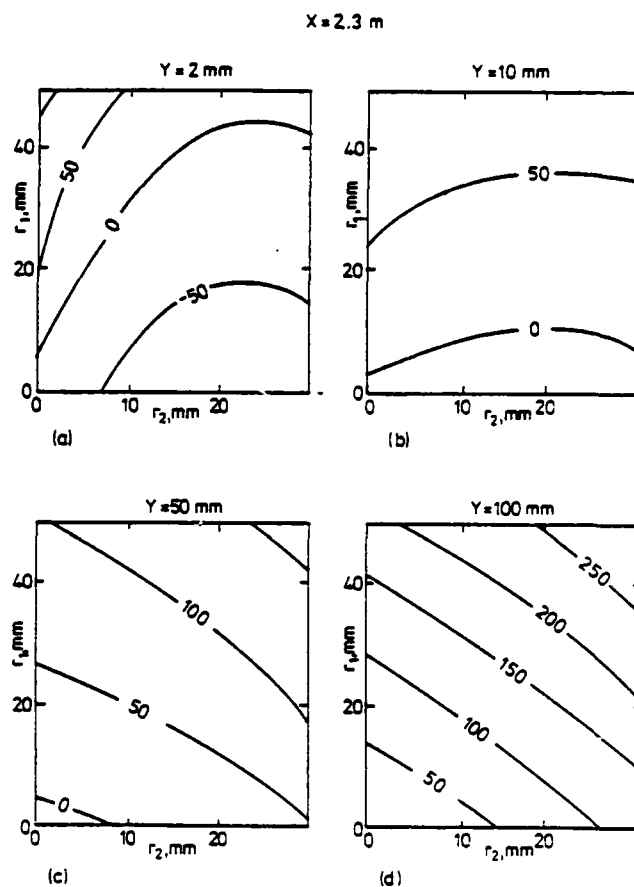


Figure 9 Iso-optimum Time Delay Contours

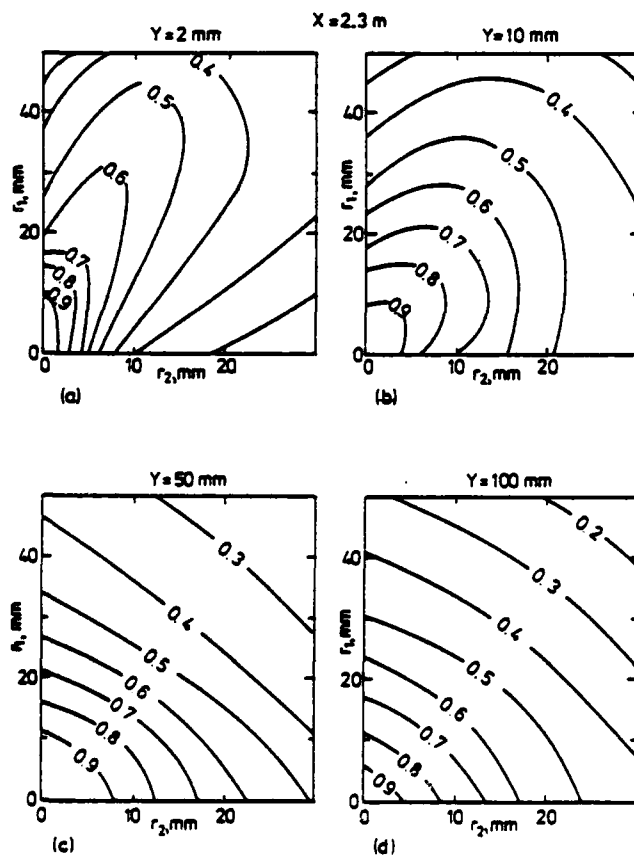


Figure 8 Iso-correlation Contours of Spatial Correlations

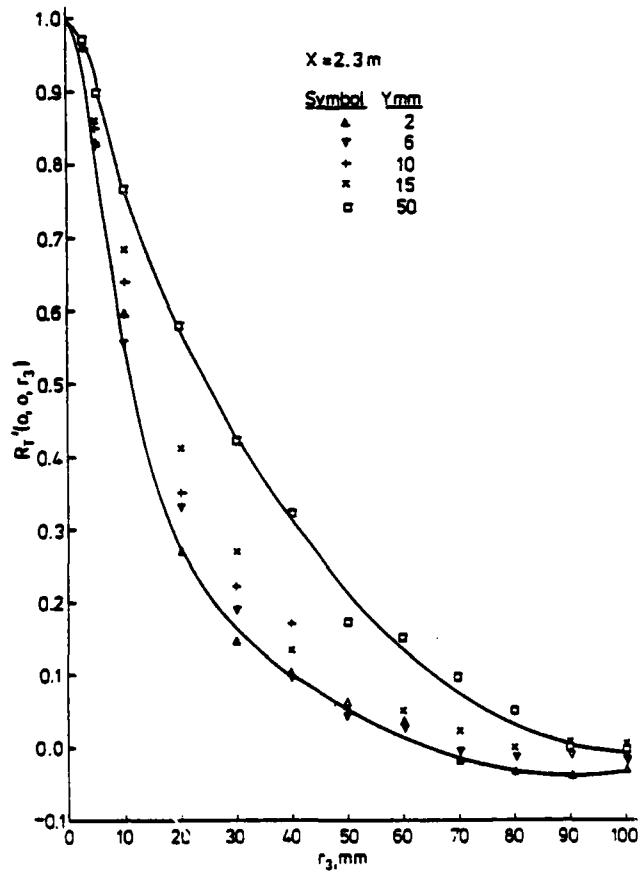


Figure 10 Spanwise Spatial Correlations

Data obtained with probe separations normal to the wall were subjected to time delayed correlation and a typical example is shown in Figure 4 for the fixed probe at 2 mm from the wall (at the outer edge of the viscous sublayer). The negative optimum time delay is suggestive of a structure inclined away from the wall and Figure 5 which shows the optimum time delay as a function of the fixed probe position and the separation confirms that this phenomenon is present only in the near wall region.

Following suggestions by Cheesewright and Doan (1978), the effect of filtering the correlations was investigated. Figure 6 shows filtered space-time correlations in the streamwise direction. These were computed using a fixed bandwidth of 0.2 Hz rather than a proportional bandwidth, but the results should not be significantly different. There is more scatter in the filtered correlation data but the trends are clearly evident, with larger correlations at lower frequencies (larger eddies). Filtered correlations normal to the wall showed a similar behaviour.

The optimum time delays for the filtered correlations were evaluated and, contrary to what has been suggested by a number of authors, they do not seem to show a consistent frequency dependence (Figure 7) except at the lowest frequency.

In order to explore the near wall structure of the flow further, correlations were made with both streamwise and normal separations and isocorrelation contours were constructed. Figure 8 shows smoothed isocorrelation contours of the spatial correlations and again there is a clear indication of a structure which propagates at an angle to the wall. The isocorrelation contours with optimum time delay are less revealing, but the smoothed optimum time delay contours shown in Figure 9 serve to further establish the structure.

The probability that the above observations were associated with low speed streaks and 'bursting' of the type observed in forced flows suggested an examination of spanwise correlations. An example of the correlations is shown in Fig. 10.

When the spanwise correlation data were subjected to short period averaging as suggested by Gupta et al (1971) much clearer indications of a spanwise structure emerged. Table 1 shows the estimated wavelength and period as a function of the distance from the wall, with the standard deviations of the estimates given in each case. The estimates of the wavelength were based on correlations of the order of 0.25, while those for the period were based on correlations of 0.2 so that in each case we may be confident that the results are statistically significant.

TABLE 1: Wavelength and Period of Spanwise Structure

Distance from the wall y/mm	6	8	10	15	20	40
Mean wavelength λ/mm	71	74	73	76	79	81
Standard deviation %	31	27	25	28	27	25
Mean period T_p/s	3.6	3.3	3.3	3.3	3.0	3.5
Standard deviation %	53	56	55	63	50	48

It is unfortunate that data were not obtained at smaller distances from the surface, but an extrapolation of the trend in the data suggests a wavelength of the order of 65 mm at the outer edge of the sublayer.

It may be noted here that the above data form only one part of an investigation of both the transitional and fully turbulent parts of the natural convection boundary layer which is fully reported in the PhD thesis of the second author (Dastbaz (1983)). The work relating to the transition region is expected to be reported at the 8th Australasian Fluid Mechanics Conference, Dec. 1983.

DISCUSSION

Very near the wall in a turbulent natural convection boundary layer, the flow is dominated by wall shear stress effects and it is not surprising therefore that the present investigation suggests that the near wall structure is similar to that found in forced flows. The pattern of 'short time averaged', spanwise correlations

is very similar to that found by Gupta et al (1971). However, the dimensionless wavelength is in the range 250 to 350 (the uncertainty in the value of the wall shear stress is rather large) but most probably near to the lower value. This compares with the value of 100 which is often quoted for forced flows.

In a similar way, the dimensionless period is of the order of 700 ($T_p \nu / u_\tau^2$) and again is different to values usually quoted for forced flows. Alternatively it has been argued that the period should scale with the parameters of the outer flow rather than with the wall parameters. $T_p u_{\text{max}}/8$ has a value of approximately 10 as compared with the value of 5 which is often quoted for forced flows. If the displacement thickness is used in place of the boundary layer thickness, the dimensionless period is approximately 23 as compared with the value of 32 quoted by Rao et al (1971) for forced flows.

It is interesting that the wavelength of the spanwise structure shows a small but steady increase with increasing distance from the wall, just as in forced flows, despite the fact that from $y = 10 \text{ mm}$ onwards ($y^+ = 35$) local conditions are certainly different to those in forced flows as may be seen by reference to Figures 1 and 2. This seems to imply that the major features of the structure must be associated with the viscous sublayer region.

At first sight there does not seem to be any indication in the data presented here, of unusual effects due to the characteristics of the flow which were highlighted in Figures 1 and 2. This lack of effect also extended to the spectra of the temperature fluctuations which were closely similar at all positions between 2 mm from the wall and 50 mm from the wall. There is however one feature which is peculiar to this flow and that is shown in Figure 3, where it may be seen that streamwise convection velocities in the outer flow are consistently greater than the local mean velocity. This may be explained if we consider the probable characteristics of the bursts which are implied by the spanwise correlation data.

Bursts would be expected to originate from near the outer edge of the viscous sublayer and the isocorrelation contours in Figure 8 suggest that the initial motion is inclined at an angle of 15 to 20° away from the wall. As a burst moves away from the wall it will be subjected to two accelerating influences, firstly it will be moving into a region of higher velocity and secondly it will comprise relatively hot fluid moving into a cooler region and therefore being accelerated by buoyancy forces. These two accelerating forces will continue to act on the fluid in a burst until it is some way beyond the peak in the mean velocity profile, but since in this region the velocity is decreasing with increasing distance from the wall, the force due to the influence of the local mean velocity will change sign and it will become a retarding force. By this time the fluid in the burst will be travelling faster than the local mean velocity.

It is not certain to the authors whether the shape of the optimum time delay contours (Figure 9) is due to the above described characteristics of the bursts or whether it is due to the existence of counter-rotating streamwise vortices which have often been associated with problems of streaks and bursts in forced flows.

CONCLUSIONS

1. The near wall structure of a turbulent natural convection boundary layer is closely similar to that in forced flows although the scales are different.
2. The structure of low speed streaks and bursts seems to be closely tied to conditions in the viscous sublayer and not much influenced by detailed conditions in the outer flow.
3. The outer flow consistently shows convection velocities which are greater than the local mean velocity.

REFERENCES

Cheesewright, R., 1968, "Turbulent Natural Convection from a Vertical Plane Surface", J. Heat Transfer, 90, 1.

Cheesewright, R., and Doan, K.S., 1978, "Space-Time Correlation Measurements in a Turbulent Natural Convection Boundary Layer", Int. J. Heat Mass Transfer, 21, 7, 911.

Cheesewright, R., and Ierokipiotis, E., 1982, "Velocity Measurements in a Natural Convection Boundary Layer", Proc. 7th Int. Heat Transfer Conf., Paper NC31, Munich.

Dastbaz, A., 1983, "The Structure of Turbulence in a Natural Convection Boundary Layer on a Vertical Flat Plate", Ph.D. thesis, Univ. of London.

Doan, K.S., 1977, "Contribution a l'etude de la Zone de Transition et de la Zone de Turbulence Etablie dans un Ecoulement de Convection Naturelle sur une Plane Verticale Isotherme", Thesis, Dr. es Sc., Univ. de Poitiers.

George, W.K., and Capp, S.P., 1979, "A Theory for Natural Convection Turbulent Boundary Layers next to Heated Vertical Surfaces", Int. J. Heat Mass Transfer, 22, 813.

Gupta, A.K., Laufer, J., and Kaplan, R.E., 1971, "Spatial Structure in the Viscous Sublayer", J. Fluid Mech., 50, 493.

Ierokipiotis, E., 1983, "A Study of the Development of a Turbulent Natural Convection Boundary Layer using Laser Doppler Anemometry", Ph.D. thesis (in preparation) Univ. of London.

Leslie, D.C., and Gibson, M.M., 1982, Unpublished work.

Rao, K.N., Narasimha, R., and Badri Narayanan, M.A., 1971, "The 'Bursting' Phenomenon in a Turbulent Boundary Layer", J. Fluid Mech., 48, 339.

Smith, R.R., 1972, "Characteristics of Turbulence in Free Convection Flow past a Vertical Flat Plate", Ph.D. thesis, Univ. of London

Tritton, D.J., 1976, "Some new Correlation Measurements in a Turbulent Boundary Layer", J. Fluid Mech., 28, 439.

HEAT TRANSFER MECHANISM AND ASSOCIATED TURBULENCE STRUCTURE IN THE NEAR-WALL REGION OF A TURBULENT BOUNDARY LAYER

Yoichiro Iritani, Nobuhide Kasagi and Masaru Hirata
Department of Mechanical Engineering
University of Tokyo, Bunkyo-ku, Tokyo 113, Japan

ABSTRACT

Heat transfer mechanism and associated turbulence structure in the near-wall region of a turbulent boundary layer have been investigated experimentally. With the aid of temperature-sensitive liquid crystal and hydrogen bubble method, the wall temperature fluctuation and the flow structure are visualized simultaneously to study directly the heat exchange between the fluid and the wall. The structure of temperature field near the wall is further studied by the measurement of cross correlation of temperature fluctuations in the spanwise and streamwise directions. All of these experimental results show that the turbulent temperature field near the wall has a feature very much similar to the flow structure in the viscous wall region, e.g., the streamwise elongated structure with a quasi-periodicity in the spanwise direction, and are compatible with what is known about the streamwise sublayer vortices previously studied.

NOMENCLATURE

Coh² square of coherence, Eq.(5)
F bursting frequency, 1/ms
f frequency, Hz
fv $=u^2/\nu$, Hz
k mass transfer fluctuation
N number of event
R correlation coefficient
T_B bursting period, s, Eq.(1)
t time, s
U_∞ free stream velocity, m/s
u velocity fluctuation in x-direction, m/s
u* friction velocity, m/s
v velocity fluctuation in y-direction, m/s
w velocity fluctuation in z-direction, m/s
x streamwise coordinate
y coordinate normal to the wall
z transverse coordinate
δ boundary layer thickness (0.99U_∞), mm
δ_T thermal boundary layer thickness, mm
δ* displacement thickness
θ momentum thickness, mm, or
temperature fluctuations, °C
λ spanwise spacing between streaks
ν kinematic viscosity, m²/s
σ standard deviation

Superscripts

()⁺ non-dimensionalized with u* and ν
()' root-mean-square value

Subscripts

()_l low-speed streaks
()_T high-temperature streaks
()_w at the wall

INTRODUCTION

In the wall region of a turbulent boundary layer, characteristic intermittent turbulence motions are the ejection of low-momentum fluid from the wall and the inrush of high-momentum fluid towards the wall (sweep), i.e., the bursting phenomena [1-3]. In the region further close to the wall, the fluid motion is much affected by the molecular viscosity and there appear so-called low- and high-speed streaks. Characteristic spatial and time scales of such streaks are known to be statistically deterministic [1-4], but the turbulent motions associated with streaky structures are also highly intermittent and non-isotropic. While the ejection and sweep motions during the bursting process have an important role upon not only turbulent momentum flux [2,5] but also turbulent heat flux [5,6], the relationship between the coherent streaky structure and the heat transfer mechanism has not been clear enough, due to the fact that the temperature field has been mainly studied by the point type measurement up to the present. Flow field and wall pressure fluctuation have been visualized to reveal many important features of wall turbulence [7] which are difficult to obtain by the point type measurement.

In this study, with the use of liquid crystal technique [8,9] combined with the hydrogen bubble method, the wall temperature fluctuation as well as the flow structure is visualized simultaneously to study directly the heat exchange between the wall and the fluid with an emphasis on streaky structures near the wall. In addition, the temperature fluctuations are measured by a conventional thermocouple probe to obtain the cross correlations in the spanwise and streamwise directions.

EXPERIMENTAL APPARATUS AND PROCEDURES

All the experiments have been carried out in a low-speed closed-loop water channel [10] and the measurement has been made in the 2m-long test section, shown in Fig.1, which is attached to the end of the nozzle (contraction ratio is 9:1) of the water channel. The test section is made of transparent plexiglas and has a cross-section of 0.3m x 0.3m. One of the vertical side walls of the channel is used as a working wall on which the turbulent boundary layer is developed. Pressure gradient in the streamwise direction is removed by a additional roof plate installed in the test channel. The cylindrical rod of 4mm in diameter is introduced at the inlet of the test channel to promote boundary layer transition.

The test plate for the visualization of wall temperature fluctuation shown in Fig.2 is installed at the position 1600mm downstream of the inlet of test section. Four stainless steel foils, each of them 300mm in length, 45mm in width and 30μm in thickness, are bonded by epoxy adhesive to the surface of a bakelite plate and connected electrically in series. Constant heat flux heating is achieved by A.C. supply into these foils. A liquid crystal sheet, which is composed of polyester sheet of 50μm thickness, liquid crystal layer and black paint [9,10], is attached flush on the heater, and the total thickness of these materials is about 100μm. Thus, the wall temperature fluctuation is visualized as a color change of liquid crystal. The upper limit of frequency range in this experiment, where the color change can be recognized, is estimated as about 2Hz [9], and is approximately equal to the frequency, where the spectrum of streamwise velocity fluctuation is one tenth of its maximum value [10].

The hydrogen bubble method is used for flow visualization. The cathode is a tungsten wire and the pulse interval of D.C. supply is controlled as 0.1 sec. Presently, transverse and vertical wires are used in the region about 1750mm downstream of the tripping rod. The transverse wire of 20μm in diameter is positioned perpendicular to the flow direction and parallel to the wall, while the vertical wire of 50μm in diameter is positioned perpendicular to the wall.

For the quantitative measurement of temperature fluctuation, copper-constantan thermocouples of 50μm in diameter are used. The frequency response is fast enough and is estimated to be flat up to about 120Hz. Signals obtained are recorded on a FM-type tape recorder, TEAC R210-B, through a DC amplifier and a 35Hz

low-pass filter. The resultant frequency response of this system is 35Hz ($=fv/2.47$). The analogue signals are digitized at a sampling rate of 100Hz, stored on the magnetic tapes, and successively processed by a mini-computer system, MELCOM 70/25. 'Fixed probe' and 'moving probe' are used. The location of the fixed probe is 1.75m downstream of the trip and right above the center line of the test plate. The moving probe is traversed relative to the fixed probe in the spanwise and streamwise directions, with the same distance from the wall as the fixed probe. A thermocouple is soldered on the backside surface of stainless steel foil heater to measure the wall temperature fluctuation. In this case, liquid crystal sheet is not attached on the heater surface to assure higher frequency limit than the liquid crystal technique.

Basic experimental conditions are shown in Table 1. The mean flow velocity is measured by the Pitot tube of a boundary layer type and an inclined U-tube manometer of two fluid type (water and benzene). The free stream turbulent intensity measured by a hot-film anemometer system, DISA 55M10, is about 2%, while the water temperature is kept at 20°C. At the location of measurement 1.75m downstream from the trip, the flow field is confirmed to be two-dimensional in the central 60mm region and the turbulent boundary layer is fully developed [10]. The friction velocity is determined by the Clauser's chart. In the present experiment, only the streamwise 300mm length of the test plate is heated with a uniform heat flux, and the thermal boundary layer thickness is 9.4mm ($y^+=87$) at the half length of the heated plate. Thus the thermal contamination is confined deep into the turbulent boundary layer so that the structure of near-wall region is mainly studied. Heating is always slight and the temperature can be recognized as a passive contaminant.

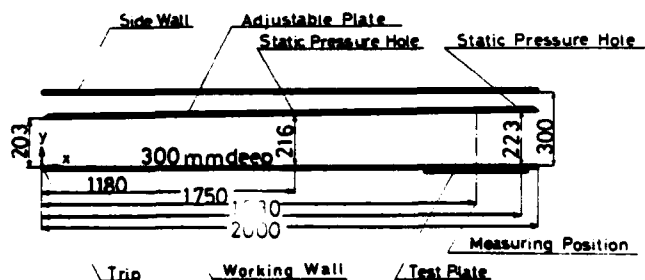


Figure 1. Schematic of the test section.

Table 1. Basic data of the turbulent boundary layer.

U_∞ m/s	δ mm	δ^+ mm	θ mm	$R_\theta = \frac{U_\infty \delta^+}{\nu}$	$R_\theta = \frac{U_\infty \theta}{\nu}$	$H = \frac{\delta^+}{\theta}$	u^+ m/s	S_τ mm
0.204	50	6.8	4.9	1370	990	1.4	$9.35 \cdot 10^3$	9.4

EXPERIMENTAL RESULTS AND DISCUSSION

Simultaneous Visualization of Flow Structure and Wall Temperature Fluctuation

A typical photograph of the simultaneous visualization is shown in Fig.3, where the location of transverse wire is at $y^+=6$. The streaky structures of high-speed fluid and low-speed fluid are observed appearing alternatively in the spanwise direction and being elongated in the streamwise direction. The wall temperature fluctuation visualized by the liquid crystal also indicates streaky pattern, and the thermal field consists of high-temperature streaks (black in Fig.3 but actually blue) and low-temperature streaks (white but actually orange). These thermal streaks are observed more or less periodically in the spanwise direction and elongated in the streamwise direction much same as the momentum streaks. The streamwise extent of these thermal streaks is about $1000-2000\nu/u^*$ and is by an order of magnitude longer than the spanwise spacing. In the 16mm motion pictures taken in this experiment, every thermal streak appears randomly in space and time and vanishes out after some timespan in which it moves downstream. It is qualitatively confirmed that the high-temperature streaks are mostly associated with the low-speed streaks and low-temperature streaks with the high-speed streaks.

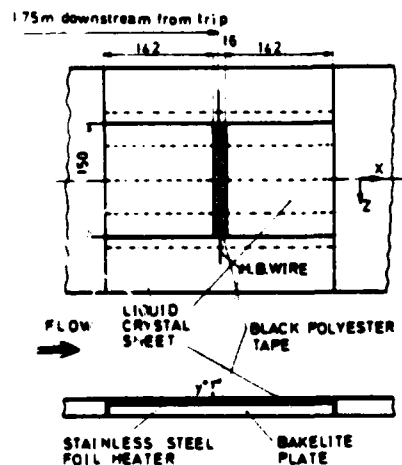


Figure 2. Test plate for the simultaneous visualization of wall temperature fluctuation and flow field.

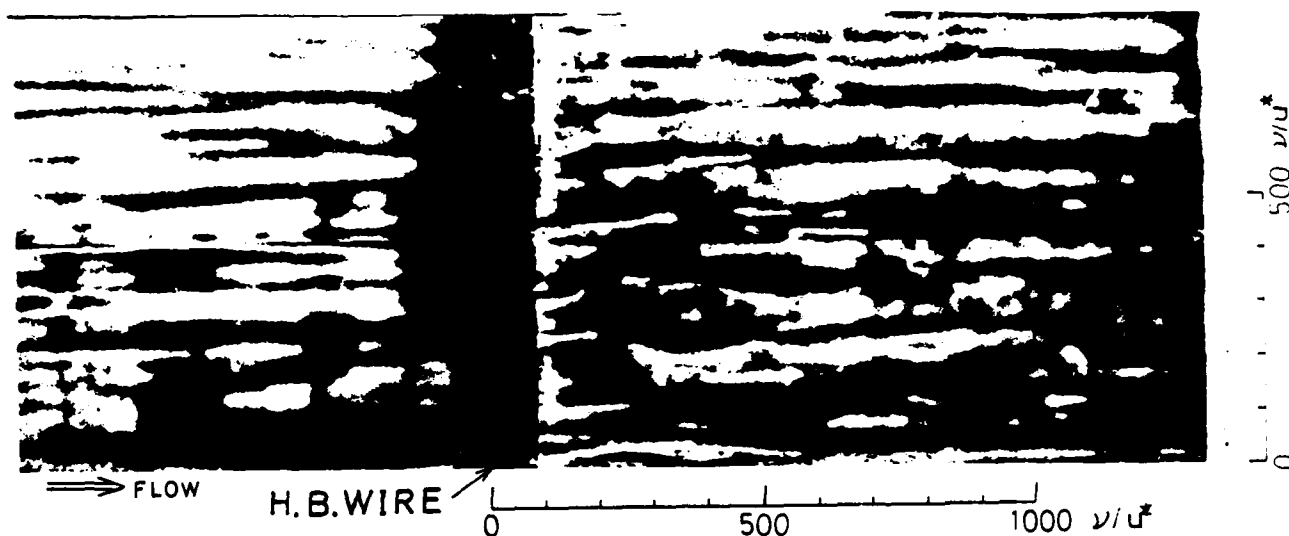
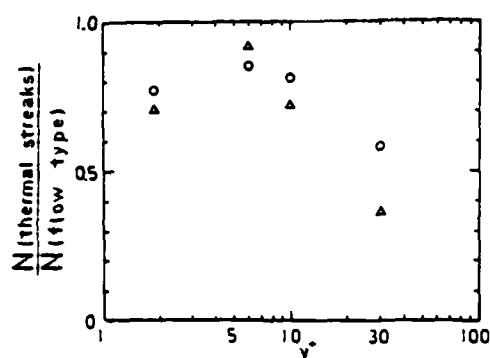


Figure 3. Simultaneous visualization of wall temperature fluctuation and flow field (A hydrogen bubble wire is located at $y^+ = 6$).



- "high-temperature streaks" associated with "low-speed streaks".
- △ "low-temperature streaks" associated with "high-speed streaks".

Figure 4. Correspondence between thermal streaks and momentum streaks as a function of a distance from the wall.

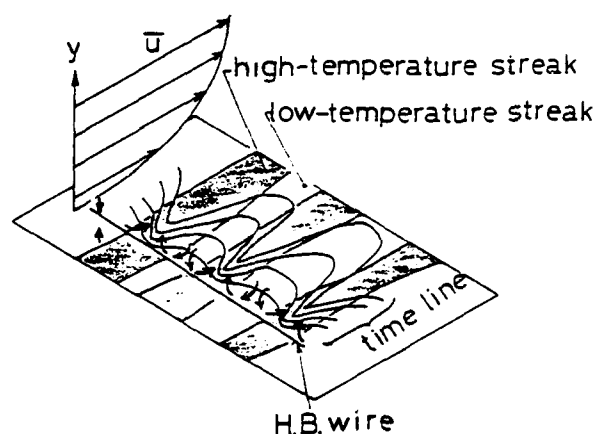


Figure 5. Conceptual model of the relationship between thermal streaks and momentum streaks.

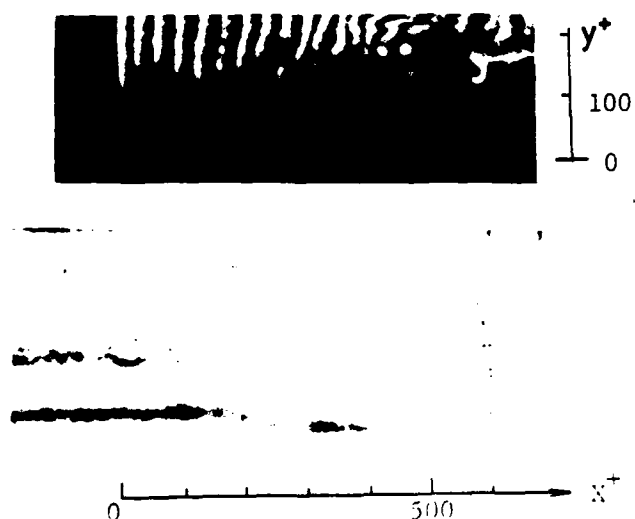


Figure 6-(a). Typical appearance of high-temperature streak associated with lift-up event.

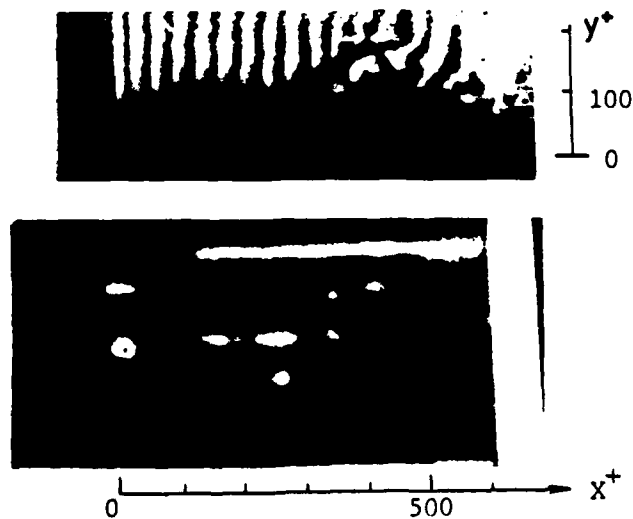


Figure 6-(b). Typical appearance of low-temperature streak associated with sweep event.

The correspondence between the thermal and momentum streaks is shown in Fig.4, as a function of a distance from the wall. These data have been obtained from 20-40 streaks in the 8 still photographs taken at each position over 2.16sec. ($=187v/u^*$) by using a motor-driven camera. These correspondence is remarkable in the region $y^+ \leq 10$ and more than 70% of the thermal streaks are uniquely associated with the prescribed momentum streaks. But these tight relationship fades out in the region $y^+ \geq 30$ due to the disappearance of streaky structures. These results agree with the observation that the center of the streamwise vortices associated with the bursting phenomena lies at approximately $y^+ = 20-30$ [11] (also see Fig.10). A conceptual model of the relationship between the coherent streaky structures and thermal streaks is presented in Fig.5.

Simultaneous observations of the wall thermal streaks and the flow pattern in the x-y plane are given by using the vertical hydrogen-bubble wire as shown in Fig.6. Fig.6-(a) indicates a typical pattern that the high-temperature streak is associated with the lift-up event [1], which is presently defined as the case that the lift-up motion of low-speed streak and the inflectional point of time lines appear within the area $x^+ = 100$ downstream of the wire. On the other hand, Fig.6-(b) indicates that the low-temperature streak is formed by the sweep event, i.e., the appearance of large fluid element toward the wall in the region $y^+ \leq 50$ within $x^+ = 100$ downstream of the wire. While 82 couples of photograph have been obtained, the high-temperature streaks have appeared with 70% of the total lift-up events, and the low-temperature streaks with 72% of the sweep events.

From the experimental results described above, the heat exchange between the wall and the fluid is considered primarily ruled by the streaky structures in the region at least $y^+ \leq 10$. Under the present constant heat-flux condition, the instantaneous local heat transfer coefficient is relatively small and large at the high- and low-temperature streaks, respectively. When the local inrush towards the wall is induced by the streamwise vortices [11-13], the local wall temperature is rapidly decreased, and this results in the formation of the elongated low-temperature streak with the streamwise convection of low-temperature high-momentum fluid. During this streamwise convection, the fluid is decelerated by the wall shear and, at the same time, heated by the wall heat flux, and this results in the high-temperature low-momentum streak which is eventually ejected from the wall by the streamwise vortices.

Spanwise Spacing of Streaks

The 16mm motion pictures with the transverse wire positioned at $y^+ = 4$ are analyzed on a screen of a motion analyzer. The spanwise spacing of low-speed streaks, λ_f , is sampled and measured in every 10 frames (at an interval of $0.417\text{sec} = 36v/u^*$). The total average spacing is $89v/u^*$, and the probability density distribution is well approximated by a lognormal distribution [3,10]. These experimental results are in good agreement with the values obtained in previous studies [1-4]. (In Ref.[4], measured values of λ_f have been summarized.)

In order to determine the spanwise spacing of the thermal streaks quantitatively, high- and low-temperature streaks are defined in the following manner as shown in Fig.7. A threshold is the border between green and orange-yellow, and is presently equal to 30.9°C . Uncertainty of $\pm 0.35^\circ\text{C}$, however, lies in identifying whether the local wall temperature is below or beyond this threshold. High-temperature streaks are defined as the regions where the temperature is higher than the threshold. The spanwise spacing of high-temperature streaks, λ_T , is defined as the distance between the centers of two neighboring high-temperature streaks. The time-averaged temperature of liquid crystal layer, \bar{T}_{LC} , depends on the heat flux given at the wall, while the free stream temperature is kept constant, $T_\infty = 20^\circ\text{C}$. Hence, the experimental results of

the mean and the standard deviation of λ_T are obtained for various heat fluxes, i.e., various wall temperatures, as shown in Fig.8. It is easily understood that the mean spacing between the thermal streaks thus defined is independent of the mean temperature level of the surface liquid crystal layer in the temperature range of \bar{T}_{LC} between the case of (C) and (D). The value measured is $81v/u^*$ and agrees well with that of momentum streaks, $89v/u^*$. It is noted that the probability density distribution can also be approximated as a lognormal distribution. Under the present experimental condition of constant wall heat-flux, the wall temperature fluctuation can be recognized straightforward as the fluctuation of local heat transfer coefficient. In other words, the heat transfer coefficient also has a quasi-periodicity of $\lambda_T = 81$ in the spanwise direction, but this result is different from the result of Shaw and Hanratty [14], where the mass transfer fluctuation has not been directly related to the momentum transport in the viscous sublayer (also see Fig.11).

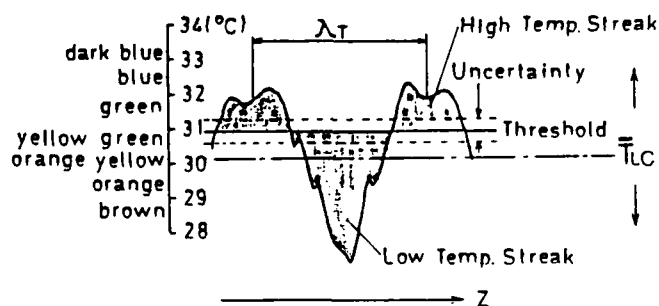


Figure 7. High- and low-temperature streaks defined by the threshold of color change.

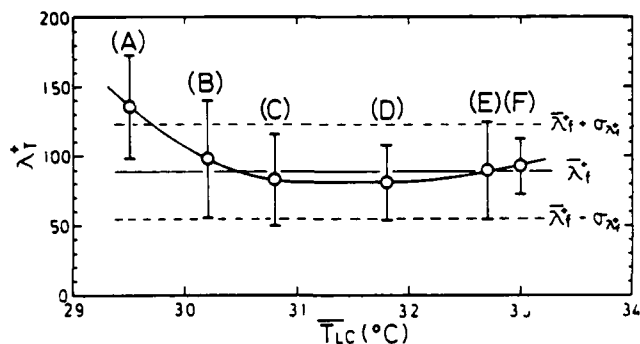


Figure 8. Mean spacing and its standard deviation of high-temperature streaks.

Frequency of the occurrence of Streaks

The visual break-up frequency of the low-speed streak [1] is counted in the motion pictures with the transverse wire located at $y^+ = 4$. The result is shown as a straight line in Fig.9, which indicates the frequency of $F = 80$ (1/ms). The passing frequency of low-temperature streak is also counted with the wall temperature range, where the measured spanwise spacing is constant as described previously. The results are also included in Fig.9, where a good agreement is obtained between the break-up frequency of the low-speed streak and the passing frequency of the low-temperature streak. These results again suggest that the turbulent motions of sublayer vortices, which lead to the formation of the low- and high-speed streaks, produce the similar pattern of wall temperature fluctuations show in Fig.3.

If the bursting period is defined by the following equation;

$$T_B = 1/F\lambda_f \quad (1)$$

then it is 1.3sec ($=112\nu/u^*$) in the present experiment and is in agreement with the values obtained previously [1,2,4].

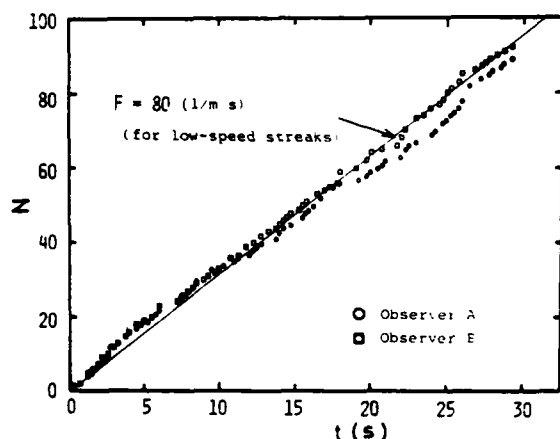


Figure 9. Comparison of the passing frequency of low-temperature streaks with the break-up frequency of low-speed streaks.

Temperature Fluctuation in the Viscous Wall Region

The structure of the temperature fluctuation is investigated by the analyses of cross correlations. The cross correlation coefficient between wall temperature fluctuations and fluid temperature fluctuations is defined as follows;

$$R_{\theta_w\theta} = \overline{\theta_w\theta}/\sigma_{\theta_w}\sigma_{\theta} \quad (2)$$

The result is shown in Fig.10 as a function of a distance from the wall. This figure also include the correlation coefficient of spanwise velocity fluctuations measured by Blackwelder and Eckelmann [11]. The temperature correlation shows a rapid decrease in the region of $y^+ \leq 10$ and gradually approaches zero without any negative value, in contrast to the spanwise velocity fluctuations. This discrepancy is considered primarily due to the difference between the measured variables, i.e., a scalar and a spanwise vector, respectively.

The spanwise and streamwise cross correlations are defined as;

$$R_{\theta\theta}(\Delta z) = \overline{\theta(z)\theta(z+\Delta z)}/\sigma_{\theta}(z)\sigma_{\theta}(z+\Delta z) \quad (3)$$

$$R_{\theta\theta}(\Delta x) = \overline{\theta(x)\theta(x+\Delta x)}/\sigma_{\theta}(x)\sigma_{\theta}(x+\Delta x) \quad (4)$$

The present result of spanwise correlation is shown in Fig.11 along with the related data obtained by previous works [12, 14, 15]. At the edge of viscous sublayer, $y^+ = 5.5$, there are a negative peak at the distance of $\Delta z^+ = 50$, and a positive small peak near around at $\Delta z^+ = 100$. Thus the quasi-periodicity with a period of about $\Delta z^+ = 100$ can be confirmed. As the distance from the wall increased, the distance which gives the first zero-crossing increases, and a negative correlation is hardly observed beyond $y^+ = 34$. The present data at $y^+ = 5.5$ are very much similar to the correlations of the spanwise velocity gradient fluctuation at the wall, but not so much to those of the streamwise velocity gradient. The data of the wall temperature fluctuations by Meek and Beer [15] and the mass transfer fluctuations by Shaw and Hanratty [14] are somewhat different from the present data.

The result of the streamwise correlation at $y^+ = 5.5$ is shown in Fig.12., where a positive correlation can be found as far as $\Delta x^+ = 100$. This length scale is qualitatively in agreement with the streamwise extent which has been visually confirmed by the liquid crystal technique (see Fig.3). It also agrees with the length scale suggested by Kreplin and Eckelmann [12]. The curve for the temperature fluctuations at $y^+ = 5.5$ is again similar to that for the spanwise velocity gradient rather than the streamwise velocity gradient, even though the data by Meek and Baer is considerably different from the present result. All of these results of spatial temperature correlations suggest not only the existence of streamwise sublayer vortices [11-14] but also their important role on the heat transfer mechanism in the viscous wall region.

In order to analyze the frequency range, of which the above cross correlations are composed, the coherence is obtained by using the following equation;

$$\text{coh}^2(f) = |\Theta_{12}|^2/\Theta_1\Theta_2 \quad (5)$$

In Eq.(5), Θ_{12} is a cross spectrum of θ_1 and θ_2 , while Θ_1 and Θ_2 are spectra of θ_1 and θ_2 , respectively. Numerical data reduction has been carried out by using FFT and Hanning filter. As a result, it can be said that the component of an order of the bursting frequency must be a main contributor to the coherent transport mechanism in the viscous sublayer.

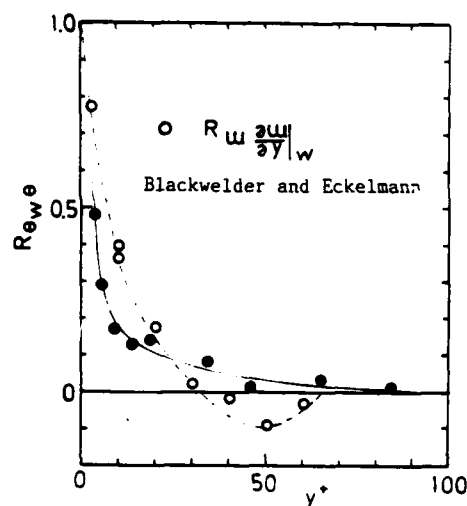


Figure 10. Spatial correlation of the temperature fluctuations with the separation normal to the wall.

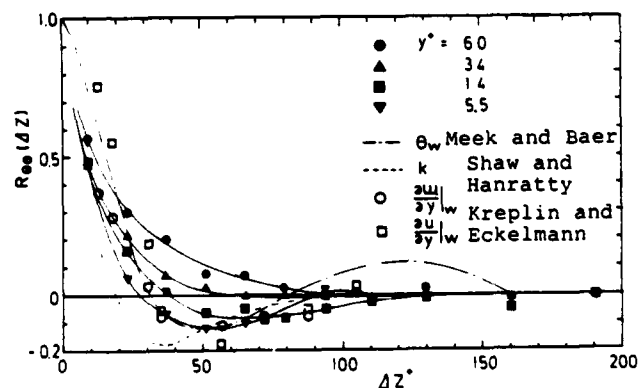


Figure 11. Spanwise correlations of the temperature fluctuations.

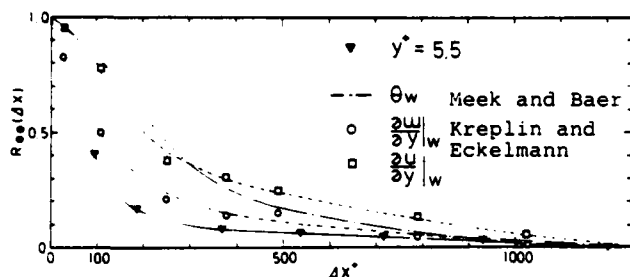


Figure 12. Streamwise correlations of the temperature fluctuations.

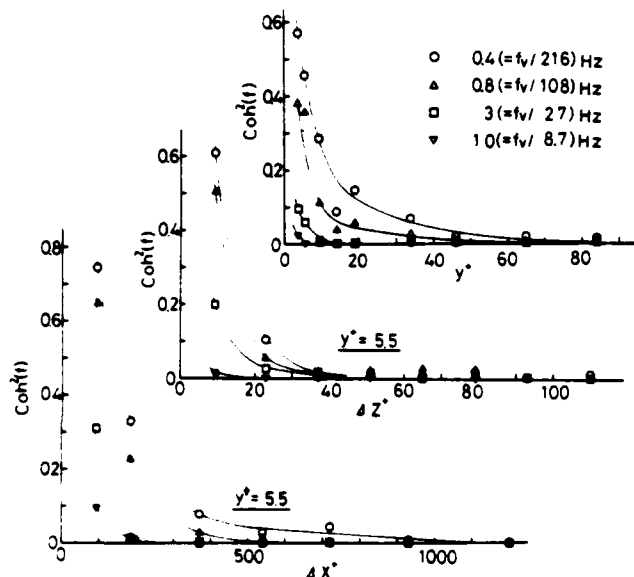


Figure 13. Coherence of the temperature fluctuation.

CONCLUSIONS

The relationship between the coherent structures and the temperature fluctuations in the near-wall region of a turbulent boundary layer has been investigated experimentally.

In the visual data obtained with the aid of the liquid crystal technique combined with the hydrogen bubble method, it is directly confirmed that the high-temperature streaks are mostly associated with the low-speed streaks and the low-temperature streaks with the high-speed streaks. In addition, quantitative agreements of the spacing and the frequency between thermal and momentum streaks are obtained.

In the viscous sublayer and the buffer layer, the fluctuating temperature field has a quasi-periodicity in the spanwise direction with a mean period of about λ_T^+ and has a much elongated scale in the streamwise direction, about $1100 \nu/u^*$, and these scales are consistent with the scale of streamwise vortices proposed by the previous studies. These coherent structures are composed of the frequency components of an order of the bursting frequency.

The turbulent motions presently studied lead to the formation of the streaky structures and also play an main role on the turbulent heat transfer in the viscous-wall region, at least $y^+ \leq 10$.

REFERENCES

- 1 Kline, S.J., Reynolds, W.C., Schraub, F.A., and Runstadler, P.W., 1967, "The Structure of Turbulent boundary Layers," J. Fluid Mech., 30, 741.
- 2 Kim, H.T., Kline, S.J., and Reynolds, W.C., 1971, "The Production of Turbulence near a Smooth Wall in a Turbulent Boundary Layer", J. Fluid Mech., 50, 133.
- 3 Smith, C.R., and Metzler, S.P., 1983, "The Characteristics of Low-Speed Streaks in the Near-Wall Region of a Turbulent Boundary Layer", J. Fluid Mech., 129, 27.
- 4 Hirata, M., Tanaka, H., Kawamura, H., and Kasagi, N., 1982, "Heat Transfer in Turbulent Flows", Proc. 7th Int. Heat Transfer Conf. 1, 32.
- 5 Perry, A.E. and Hoffmann, P. H., "An Experimental Study of Turbulent Convective Heat Transfer from a Flat Plate", J. Fluid Mech., 77, 355.
- 6 Zaric, Z., 1975, "Wall Turbulence Structure and Convection Heat Transfer", Int. J. Heat Mass Transfer, 18, 831.
- 7 Dinkelacker, A., Hessel, M, Meier, G.E.A., and Schewe, G., 1977 "Investigation of Pressure Fluctuations Beneath a Turbulent Boundary Layer by Means of an Optical Method", Phys Fluids, 20, S216.
- 8 Kasagi, N., 1980, "Liquid Crystal Applications in Heat Transfer Experiments", Report IL-27, Thermosciences Division, Mech. Engrg. Dept., Stanford University.
- 9 Kasagi, N., 1982, "Application of Temperature-Sensitive Liquid Crystals", J. Flow Visual. Soc. Japan, 2, 647 (in Japanese).
- 10 Iritani, Y., Kasagi, N., and Hirata, M., 1982, "Transport Mechanism in a Turbulent Boundary Layer ; 1st rept", Trans. JSME, Ser. B, 48, 2284 (in Japanese).
- 11 Blackwelder, R.F., and Eckelmann, H., 1979, "Streamwise Vortices Associated With the Bursting Phenomenon", J. Fluid Mech., 94, 577.
- 12 Kreplin, H.P., and Eckelmann, H., 1979, "Propagation of Perturbation in the Viscous Sublayer and Adjacent Wall Region", J. Fluid Mech., 95, 305.
- 13 Lee, M.K., Eckelman, L.D. and Hanratty, T.J., 1974, "Identification of Turbulent Wall Eddies through the Phase Relation of the Components of the Fluctuating Velocity Gradient", J. Fluid Mech., 66, 17
- 14 Shaw, D.A., and Hanratty, T.J., 1977, "Influence of Schmidt Number on the Fluctuations of Turbulent Mass Transfer a wall", AIChE J., 23, 160.
- 15 Meek, P. L., and Baer, D., 1970, "The Periodic Viscous Sublayer in Turbulent Flow", AIChE J., 16, 841.

THE STATISTICS OF THE PASSIVE SCALAR FIELD IN AN AXISYMMETRIC TURBULENT WAKE

B.A.Kolovandin, Yu.M.Dmitrenko and S.I.Gabrilovich

Heat and Mass Transfer Institute, 220728, Minsk, U.S.S.R.

ABSTRACT

Previous experiments (Kolovandin et al. 1983) revealed a sign reversal of streamwise velocity derivative skewness $S_{\partial u_1/\partial x_1}$ in the

outer part of turbulent wake, which was presumably attributed to the presence of large-scale orderly motions. This paper presents the third-order statistics of streamwise derivatives of velocity and temperature fluctuations measured in the temperature wake of ellipsoid. A qualitative analysis of simultaneous velocity and temperature fluctuation records is also made to identify a possible shape of the representative large-scale eddy structure.

INTRODUCTION

It is known (see, e.g., Tavoularis et al. 1978) that a negative skewness of streamwise velocity derivative $\partial u_1/\partial x_1$ is a ubiquitous feature of turbulence caused by generation of relatively small-scale turbulent velocity field vorticity ω_u by vortex stretching. One of the most intriguing results of our previous investigation (Kolovandin et al. 1983) was a positive sign of $S_{\partial u_1/\partial x_1}$ in the periphery region

of an axisymmetric wake. It has been assumed then that the vorticity "sink" effect of relatively small-scale turbulence is caused by the orderly structures. Further experiments revealed the existence of repeating features in the shape of streamwise velocity fluctuation signal in the outer region of the wake. The u_1 -signal in this region looks like a series of randomly arising positive peaks with different slopes at the leading and trailing edges. The net contribution of these peaks to the mean value of $(\partial u_1/\partial x_1)^3$ is positive, so it is reasonable to assume that they are responsible for the observed sign reversal of derivative skewness. The existence of repeatable features in the peak shape was attributed to the organized motion in the wake. (The results of the above experiments are not presented here and will be published elsewhere). To get more information on organized motion, it was decided to study some properties of the passive scalar (temperature) field in the wake.

This paper presents some results on the third-order statistics of streamwise derivatives of velocity and temperature fluctuations measured in the axisymmetric turbulent wake of an ellipsoid with temperature field generated by injection of a heated jet. It includes also

a qualitative analysis of simultaneous velocity and temperature fluctuation records made to identify some features of typical "eddies" responsible for the observed anomalous trend of velocity derivative skewness.

EXPERIMENTAL SETUP

The experimental facility used was essentially the same as that described by Kolovandin et al. (1983).

A turbulent axisymmetric wake was generated by an ellipsoid of revolution with the main axes ratio 6:1 and the midsection $d = 0.03$ m at $Re = U_\infty d/\nu = 1.88 \cdot 10^4$ ($U_\infty = 10$ m/s). The temperature field in the wake was generated by a hot jet injected into the region of the rear stagnation point of the ellipsoid. The temperature of the jet at $x = x_1/d = 0.1$ was about 60°C in excess of the ambient temperature. The measurements were made downstream of the ellipsoid within the range of the longitudinal coordinate $3 < x < 70$ at two jet velocities: "strong" injection ($C_d = 0.021$) and "weak" injection ($C_d = 0.0385$), where $C_d = 4 \int_0^\infty [U_1(U_1 - U_\infty) + u_1^2 - u_2^2] x_2 dx_2 / U_\infty^2 d^2$ is the drag coefficient.

Velocity fluctuations were measured with a standard DISA 55P11 5 μm dia. and 1.2 mm long hot wire probe operated by a DISA 55M01 constant temperature anemometer. Temperature fluctuations were measured with a DISA 55P31 1 μm dia. and 0.4 mm long "cold wire" operating at a constant current of 0.7 mA. Sensors of velocity and temperature probes were placed normal to the mean flow direction 0.6 mm apart. The compensation of temperature sensitivity of velocity sensor was made by summing up the weighted temperature and velocity signals using an analog summing device.

The velocity and temperature signals were amplified, differentiated and low-pass filtered before being digitized at a sampling rate of $2 \cdot 10^4$ samples/s. The streamwise derivatives of velocity and temperature were inferred from temporal derivatives using the Taylor hypothesis. The digitized signals from an 8 bit A/D converter were stored on 7.25 M byte magnetic discs. The data processing was carried out on M4030 computer.

DERIVATIVE STATISTICS

The measurements of the temperature derivative skewness $S_{\partial t/\partial x_1}$ were carried out in or-

der to verify the degree of the local isotropy of temperature field. As it follows from the previous measurements (see, e.g., Sreenivasan and Tavoularis, 1980; Tavoularis and Corrsin, 1981), the skewness of $\partial t / \partial x_1$, which for an isotropic field is equal to zero, is not such for a wide range of turbulent flows including quasi-homogeneous ones behind a heated grid. This may signify either a departure from the local isotropy of small-scale turbulence at moderate values of turbulent Reynolds and Peclet numbers, $R_\lambda (= q \lambda_u / \nu)$ and $R_t (= q \lambda_t / \alpha)$, (where $q^2 = u_1^2$ is the doubled kinetic energy of turbulence, λ_u and λ_t are the velocity and temperature microscales) in the case of homogeneous turbulence or be the consequence of the statistical nonstationarity of large-scale structures in the shear flows. For quasi-homogeneous flows it was shown that $S_{\partial t / \partial x_1} \neq 0$ if and only if both the transverse mean velocity and mean temperature gradients are non-zero and the sign of $S_{\partial t / \partial x_1}$ is determined by the relationship (Tavoularis and Corrsin 1981)

$$\text{sgn } S_{\partial t / \partial x_1} = - \text{sgn}(\partial U_1 / \partial x_2) \text{sgn}(\partial T / \partial x_2).$$

In order to verify this relationship in strongly nonhomogeneous turbulence, the measurements of the skewness of $\partial t / \partial x_1$ in a non-isothermal wake behind the ellipsoid of revolution were made for two different velocities of the injected jet. The downstream evolution of $S_{\partial t / \partial x_1}$ on the wake centerline (figure 1) shows that the skewness of $\partial t / \partial x_1$ corresponds to the sign of mean velocity gradient in the core of the flow under consideration: $S_{\partial t / \partial x_1} < 0$ for the jet and $S_{\partial t / \partial x_1} > 0$ for the wake. At a sufficiently large distance from the body, the value of $S_{\partial t / \partial x_1}$ increases, while the numbers R_λ and P_λ decrease. This fact is in agreement with the results of other investigations referred to in the paper by Sreenivasan and Antonia (1977). The transverse distribution of $S_{\partial t / \partial x_1}$, shown in figure 2, demonstrates the approach of the profile of $S_{\partial t / \partial x_1}(r)$ to some self-similar form at a sufficiently large distance downstream of the body. The data of figures 1 and 2 confirm the relationship of Tavoularis and Corrsin (1981) for the flow considered. As was shown earlier (Sreenivasan and Antonia 1977; Gibson et al. 1977 and a number of subsequent studies) the nonzero skewness of $\partial t / \partial x_1$ can be attributed to the presence of large-scale orderly structures in the shear flow (manifesting itself in a ramp-like temperature signal). However, as far as the authors know, a systematic dependence of the local nonhomogeneity of scalar field on such structures is lacking.

Along with $S_{\partial t / \partial x_1}$, the statistical parameters of velocity and temperature derivatives measured in the present experiment include

$$S_{\partial u_1 / \partial x_1} \text{ and } S_T = \frac{(\partial u_1 / \partial x_1)(\partial t / \partial x_1)^2}{(\partial u_1 / \partial x_1)^2 (\partial t / \partial x_1)^2}^{1/2}.$$

In local isotropic turbulence these quantities determine the rate of generation of mean-squared vorticity or velocity field ω_u^2 and the similar parameter for temperature field ω_t^2 , respectively. So it was interesting to see whether S_T would have the same trend as $S_{\partial u_1 / \partial x_1}$.

In order to ensure the highest possible accuracy in evaluation of the above parameters, preliminary investigations were carried out on the choice of the optimum frequency band and

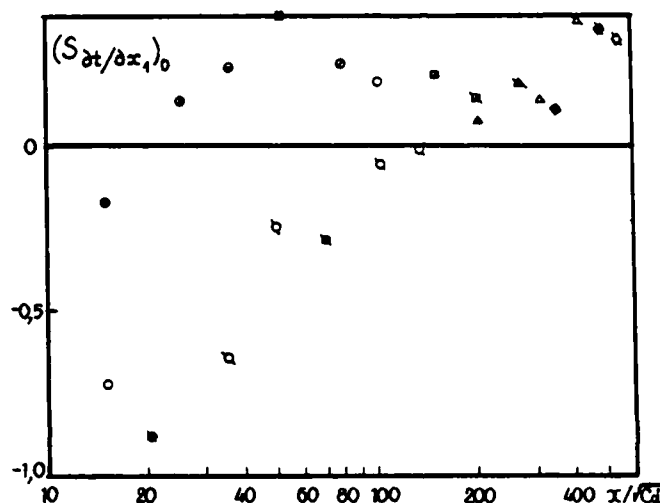


Figure 1. Downstream evolution of $S_{\partial t / \partial x_1}$ at $C_d = 0.0385$ and $C_d = 0.021$: \bullet , $x=3$; \circ , $x=5$; \blacksquare , $x=7$; \square , $x=10$; \bullet , $x=15$; \circ , $x=20$; \blacksquare , $x=30$; \square , $x=40$; \bullet , $x=50$; \circ , $x=60$; \blacksquare , $x=70$; \square , $x=80$ (crossed symbols correspond to $C_d = 0.021$).

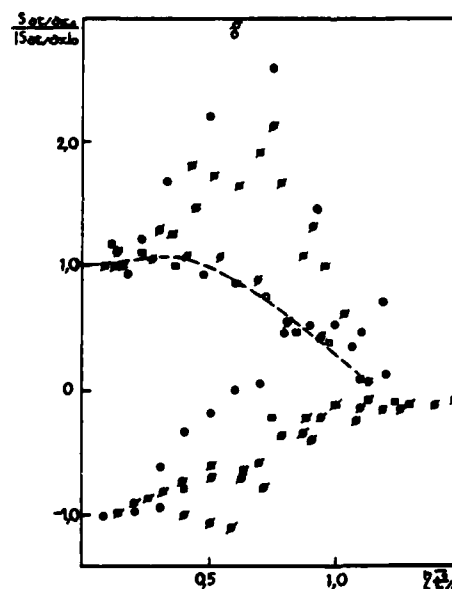


Figure 2. Radial profiles of $S_{\partial t / \partial x_1}$ normalized by the centerline values. $\eta/\ell_d = x_2/\ell_d$ is the dimensionless transverse coordinate, ℓ_d , radial distance at which the mean squared temperature \bar{t} equals a quarter of its axial value; —, self-similar form or the profile; the symbols as in figure 1.

averaging time for each measuring point in the cross-section. The averaging time increased towards the outer part of the wake. The duration of digital records (150 s in the outer region) was sufficient to ensure the stability of moments of the velocity and temperature derivatives. Corrections of the measured values for electronic noise were also made.

The transverse distribution of the parameter $S_{\partial u_1 / \partial x_1}$, presented in figure 3, gives a good evidence for its sign reversal: on the wake periphery $S_{\partial u_1 / \partial x_1}$ changes its negative sign to the opposite one. In the case of the local isotropy this would be indicative of the

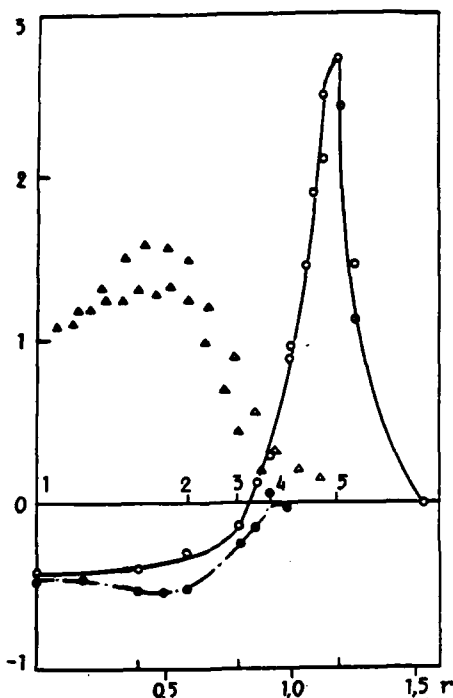


Figure 3. Radial distributions of $S_{\partial u_1 / \partial x_1}$ (o), S_T (•), R_λ (Δ) and R_λ (▲) at $x=20$. $r=x_2/d$ is the dimensionless coordinate. Numerals (from 1 to 5) on the r axis correspond to the points where an analysis of time histories is made.

vorticity sink of a relatively small-scale velocity field, i.e. the reverse transport of energy over the energy spectrum: from relatively small to larger vortices. At the same time, the radial distribution of S_T differs from that of $S_{\partial u_1 / \partial x_1}$ - it tends monotonically to zero towards the outer part of the wake, where the temperature fluctuations are absent. It should be noted that the observed behaviour of $S_{\partial u_1 / \partial x_1}$ is consistent with the experimental results reported by Reichert and Azad (1979), who detected the $S_{\partial u_1 / \partial x_1}$ sign reversal near the outer edge of the turbulent boundary layer developing over the inlet section of the tube. It seems to be the only information on this quantity distribution in the outer edges of turbulent shear flows. As to the parameter S_T , its behaviour in the wake core agrees with the reported experimental data for different types of flow (see, e.g., Van Atta 1974) at moderate R_λ and R_λ numbers, though the fact of its disappearance in the outer region at $R_\lambda \approx 50$ ($R_\lambda u_1^2 \lambda_u^{-1/2} \approx 30$), $R_\lambda \approx 10$ and $S_{\partial t / \partial x_1} \neq 0$ is also a curious one.

TIME HISTORIES AND EDDY STRUCTURE

Additional information on the eddy structure of the wake can be obtained from the analysis of the temperature field characteristics. This analysis was based on qualitative comparison of simultaneous traces of velocity and temperature fluctuation signals in some typical points of the flow chosen as follows:

- (1) Point 1 - at the wake centerline ($r = 0$);
- (2) Point 2 - at the wake core where essential decrease of $S_{\partial u_1 / \partial x_1}$ relative to its centerline value occurs ($r = 0.6$);
- (3) Point 3 - in the region where $S_{\partial u_1 / \partial x_1}$ is close to zero ($r = 0.8$);

- (4) Point 4 corresponds to the maximum transverse gradient of $S_{\partial u_1 / \partial x_1}$ ($r = 0.9$);
- (5) Point 5 corresponds to the positive extremum of radial $S_{\partial u_1 / \partial x_1}$ distribution ($r = 1.2$).

The positions of these points are shown in figure 3. Digital records of velocity and temperature were made at $x = x_1/d = 20$. At this section the dimensionless wake half-widths $\delta_{u_1^2/4} = \delta_{u_1^2/4}/d$ and $\delta_{t^2/4} = \delta_{t^2/4}/d$ based on radial u_1^2 and t^2 distributions are $\delta_{u_1^2/4} = 0.93$, $\delta_{t^2/4} =$

$= 0.81$. The section under consideration seems to be quite representative for such an analysis, with the S/N ratio being here still acceptable. Typical parts of the stored signals have been chosen and computer plotted. Because of the space limitations, only a few typical u_1 and t records are presented. In figure 4(a), for each pair of traces the point number and scale factor M are given, the latter being used prior to computer plotting when the amplitudes of the events are too small. The duration of each trace is 0.0256 s (1 division = 2.56 ms).

The time histories of figure 4(a) are useful to explain the observed $S_{\partial u_1 / \partial x_1}$ and S_T distribution trends as well as to infer the possible structure of large eddies. These traces show how the u_1 -signal changes from a fully stochastic on the wake axis (point 1) to an intermittent one with regularly shaped peaks at the wake periphery (points 4 and 5). As was noted, the positive sign of streamwise velocity derivative skewness, $S_{\partial u_1 / \partial x_1}$, can be explained by the existence of regular positive peaks in streamwise velocity signals in the outer region of the wake. Clear evidence of this was obtained from visual inspection of simultaneous computer plots of u_1 and $(\partial u_1 / \partial x_1)$, which are not presented here. An example of such a peak is given by the u_1 -trace for point 5 in figure 4(a). The trailing edge of the peak is somewhat steeper than the leading one thus causing the essential difference of $(\partial u_1 / \partial x_1)^3$ at the peak edges. Similar peaks can also be observed in points 3 and 4 but less pronounced, though their occurrence rate seems to be somewhat higher. As the measuring point moves towards the wake axis, the relative contribution of the positive peaks to $(\partial u_1 / \partial x_1)^3$ gradually decreases while that of turbulence increases. In point 3, the positive contribution of regular peaks is approximately the same as the negative contribution of relatively high-frequency stochastic fluctuations, so that in the point considered $S_{\partial u_1 / \partial x_1} \approx 0$. In the wake core $S_{\partial u_1 / \partial x_1}$ becomes negative, i.e. has the usual sign which is typical of turbulent flows.

In point 2, low-frequency negative velocity fluctuations appear in the u_1 -signal. First these were regarded to be fully stochastic, but later, when simultaneous two-point velocity traces had been examined, it became clear that there was a strong correlation between the negative peaks in the wake core and the positive ones on the wake periphery. An example of such correlation is given in figure 4(b), where the traces of the u_1 -fluctuations for points 4 and 2 are presented.

Examination of u_1 and t time histories shows that in the outer part of the wake the temperature fluctuations, if present, always accompany the velocity peaks. So it is natural to assume that S_T , being similar to $S_{\partial u_1 / \partial x_1}$, would also have the sign reversal in the wake

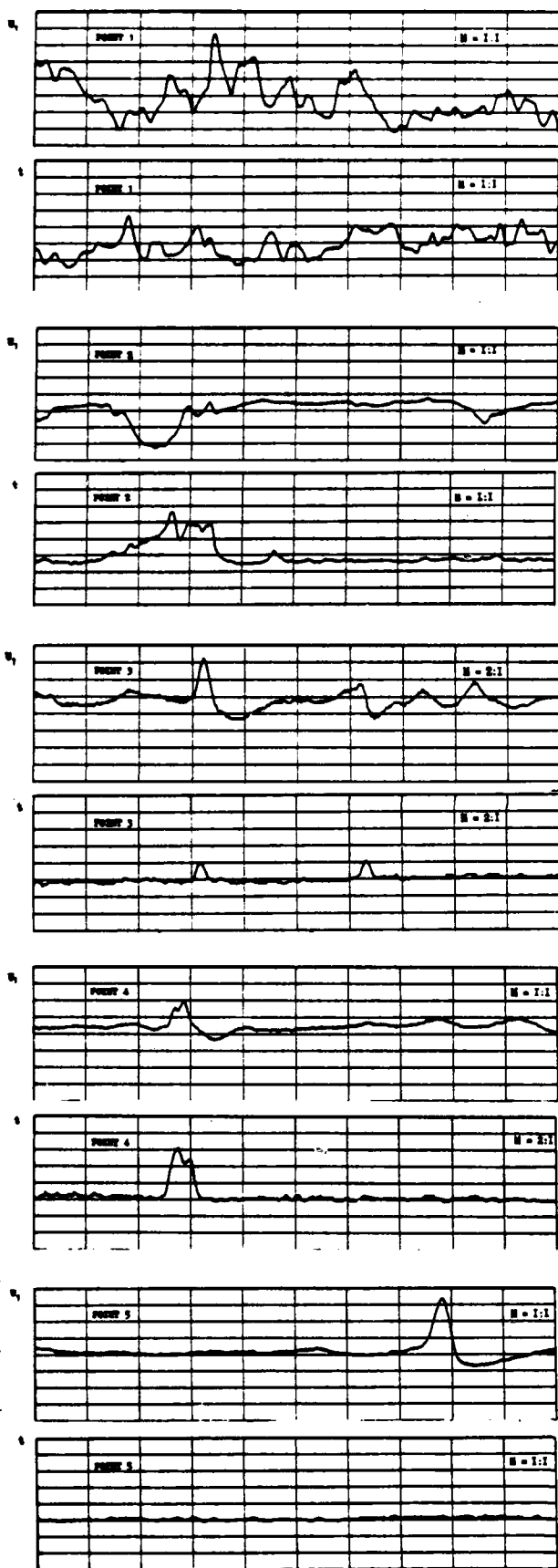


Figure 4(a). Digital plots of velocity and temperature fluctuations at various radial positions in the wake cross-section, $x = 20$.

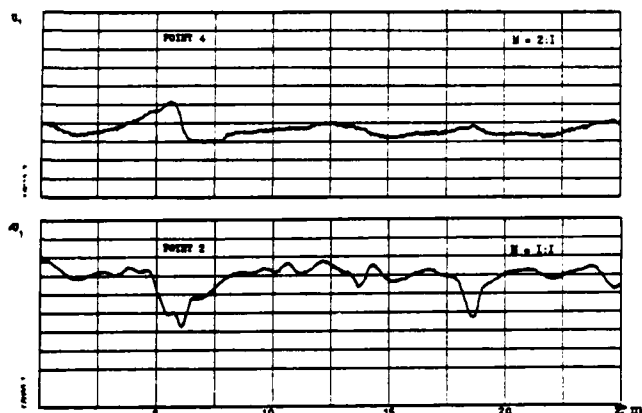


Figure 4(b). Two-point velocity traces at the wake cross-section, $x = 20$.

periphery. But the effect of the parameter S_T sign reversal is not pronounced enough in our experiments. ($S_T = 0.05$ only in point 4, see figure 3). In order to explain this fact, a large number of u_1 and t traces were carefully analyzed. It was found that in point 4 the regular velocity peaks are sometimes correlated with the positive large-scale temperature fluctuations, while sometimes the latter are absent at all. The case of the coincidence of these signals in point 4 is shown in figure 4(a). In point 5, the temperature fluctuations are not observed though distinct positive regular peaks are present. Thus, the contribution of these regular structures to S_T is negligible which results in the different behaviour of $S_{\partial u_1 / \partial x_1}$ and S_T .

The data on the value and sign of the parameters $S_{\partial u_1 / \partial x_1}$ and S_T , as well as the u_1 and t traces allow one to imagine the detected large-scale structures as torroid-like vortices, the generalized image of which is depicted in figure 5 (numerals 1-5 here correspond to the positions of the points in which the traces were registered):

- in point 2, located near the lower edge of the vortex core, the vortex generates (see the corresponding oscillogram) a negative velocity peak, which is due to the opposite direction of the longitudinal velocities of the main stream, U_1 , and of the vortex, \bar{u}_1 ; in this point, the positive temperature fluctuation is attributed to a more heated liquid being captured by the vortex from the wake axis region;
- in point 3, located nearly at the vortex core center, there develops a positive velocity peak with a smooth front caused by a slow increase of $\bar{u}_1(x_1)$ in the vortex core and a sharp trailing edge followed by a negative part of the fluctuation caused, probably, by the shape of the vortex "back";
- in point 4, located at the upper edge of the vortex core, the similar positive velocity peak $\bar{u}_1(r)$ causes a rise of temperature, with relatively small-scale temperature fluctuations being absent here, since the point considered is beyond the boundary of the thermal wake;
- in point 5, located at the edge of the outer shell of the vortex, the velocity fluctuations are due to regular vortices running past the point of observation; in this point, the stochastic velocity and temperature signals are not observed, i.e. turbulence is absent in the point considered.

Van Atta, C.W., 1974, "Influence of Fluctuations in Dissipation Rates on Some Statistical Properties of Turbulent Scalar Fields", Atmos. Ocean Fis., 10, 712.

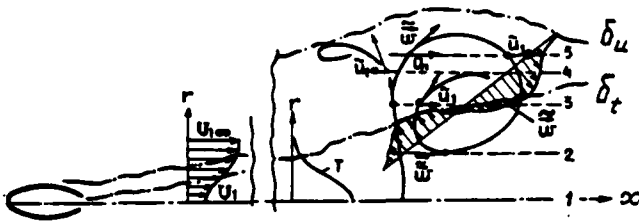


Figure 3. Sketch of a typical large-scale vortex in the wake of an axisymmetric body: \vec{u} is the velocity vector of the vortex; u_1 , the streamwise component of velocity generated by the vortex; T , the mean temperature; δ_u , the thickness of momentum wake; δ_t , the thickness of scalar wake.

CONCLUSIONS

All of the conclusions on the possible shape of the large-scale structure responsible for the observed trends in $S_{\partial u_1 / \partial x_1}$ and S_T distributions were based on the qualitative interpretation of u_1 and t plots. An additional quantitative analysis is clearly needed. It is believed that further valuable information can be gained from conditional sampling, multiprobe arrays and spatial correlation measurements.

ACKNOWLEDGEMENT

The authors are very indebted to Mrs. I. Labuda for her assistance in experimental data processing including software.

REFERENCES

- Gibson, G.H., Friehe, C.A., and McConnel, O., 1977, "Structure of Sheared Turbulent Fields", Phys. Fluids, 20, S156.
- Kolovandin, B.A., Luchko, N.N., and Dmitrenko, Yu.M., 1983, "The Turbulent Wake Behind an Axisymmetric Body and Its Interaction With the External Turbulence", in Structure of Complex Turbulent Shear Flows, Dumas, R. and Falachien, L., eds., Springer, 399.
- Reichert, J.K., and Azad, R.S., 1979, "Feature of a Developing Turbulent Boundary Layer Measured in a Bounded Flow", Can. J. Phys., 57, 477.
- Sreenivasan, K.R., and Antonia, R.A., 1977, "Skewness of Temperature Derivatives in Turbulent Shear Flows", Phys. Fluids, 20, 1986.
- Sreenivasan, K.R., and Tavoularis, S., 1980, "On the Skewness of the Temperature Derivative in Turbulent Flows", J. Fluid Mech., 101, 783.
- Tavoularis, S., Bennet, J.C., and Corrsin, S., 1978, "Velocity-Derivative Skewness in Small Reynolds Number, Nearly Isotropic Turbulence", J. Fluid Mech., 88, 63.
- Tavoularis, S., and Corrsin, S., 1981, "Experiments in Nearly Homogeneous Turbulent Shear Flow With a Uniform Mean Temperature Gradient. Pt. 2. The Fine Structure", J. Fluid Mech., 104, 349.

SESSION 18 - RECIRCULATING FLOWS

R. Adrian - Chairman

Turbulence Measurements Related To Heat Transfer In An Axisymmetric Confined Jet

With Laser Doppler Anemometer

K. Suzuki, S. Ida and T. Sato

Department of Mechanical Engineering
Kyoto University, Kyoto 606, Japan

ABSTRACT

Measurements of the turbulence in the recirculating flow region have been made for an axisymmetric confined jet. Based on the results of such experiments, discussions are given to the physical background of the fact previously found such that the maximum heat transfer occurs within the recirculating flow region. Some further discussions are also given to the structure of the turbulence in the recirculating flow region.

INTRODUCTION

The wall heat transfer was found to be very much augmented by the generation of recirculating flows by Krall and Sparrow (1966) for the tube flow in the downstream of an inserted orifice and by Kang et al (1979) for confined jets. Thus, it is of practical importance to study on the mechanism of wall heat transfer in such partially recirculating flows. The simultaneous visualization by Kang et al (1982) of surface flow and wall temperature revealed that the maximum heat transfer position does not necessarily coincide with the reattachment point of average flow stream line in the cases of partially separated flows. This was successfully predicted by Kang and Suzuki (1982) and Suzuki et al (1982) through the numerical prediction employing the $k-\epsilon$ two-equation model of turbulence for both of the two types of the flows studied by Krall and Sparrow and by Kang et al. From the results of these numerical computations, a conjecture was given for the physical background of this spatial separation between the maximum heat transfer position and the average flow reattachment point. The inactive viscous sublayer controlling the major part of heat transfer resistance was guessed to be activated by the near wall turbulence which was predicted to be highest in intensity within the recirculating flow region.

In the present study, the measurements of the turbulence in the recirculating flow regions have been initiated for the axisymmetric confined jet with the Laser Doppler Anemometer to prove the above mentioned conjecture and to get deeper insight into the heat transfer mechanism in the turbulent recirculating flow region. In this first stage of the experiments, attention has been paid only to the streamwise averaged and fluctuating velocity components. The present experimental data will also be compared with the numerical results and the experimental data reported previously.

EXPERIMENTAL APPARATUS AND PROCEDURE

An axisymmetric confined jet is a coaxial jet issued into a concurrent stream flowing in a circular tube. This is a kind of partially recirculating flow. When the momentum ratio between the central jet and the concurrent stream is high enough, a reversed flow appears near the tube wall at some distance from the central jet

nozzle. Turbulence measurements have been made in this recirculating flow region. The size of the recirculating flow region can easily be changed only by changing the above mentioned momentum ratio. This is the major reason why the confined jet has been chosen as the test flow in the present study.

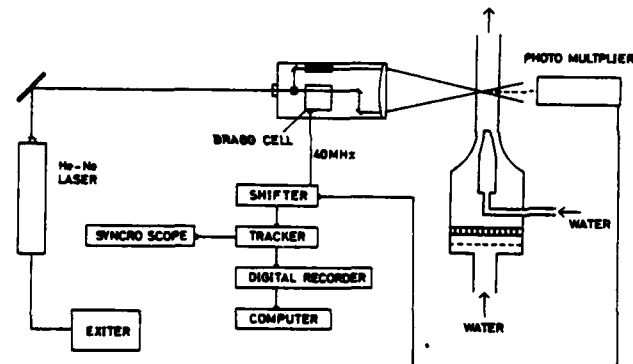


Figure 1 Outlines of Test tube and Measuring Devices

Ct	U_j m/s	U_f m/s	U^* m/s	Re^*
0.26	8.96	0.08	0.370	34200
0.50	8.94	0.17	0.368	34000
0.82	8.83	0.28	0.361	33300

Table 1 Experimental Conditions

The experimental apparatus used in the present study is schematically shown in Figure 1. Different from the previous studies, a water flow test loop was newly constructed for the present purpose and a small amount of milk was introduced into the water flow. Finely dispersed milk droplets serve as the scattering particles.

Experiments were made at the three flow rate conditions tabulated in Table 1. U_j and U_f in the table are respectively the outlet average velocity of central jet and the one of the concurrent stream. Ct is the Craya-Crte number, a similitude parameter of the flow pattern and heat transfer as shown by Becker et al (1963) and by Kang et al (1979), and is defined as follows:

$$Ct = \frac{U_k}{U^*}$$

$$U^* = \sqrt{U_d^2 - U_k^2/2}$$

$$U_k = \frac{1}{A_0} \int_{A_0} U \, dA$$

$$U_d = \frac{1}{A_0} \int_{A_0} (U^2 - U_k^2/2) \, dA$$

A_0 in the above general definitions of U_d and U_k is the cross sectional area of the tube at $X=0$, the outlet position of the nozzle. The values of the characteristic velocity U^* and the Reynolds number based on U^* and on the tube diameter D are also shown in Table 1. The tube inner diameter and the central nozzle outlet port diameter used in the present study are 120mm and 5 mm, respectively. In the case of the axisymmetric confined jet, the recirculating flow appears when $Ct < 0.7$. Therefore, the range of Ct chosen in this experiment covers the flow patterns both with and without recirculating flow.

In Figure 1 are also shown the outlines of the measuring system. 50mW He-Ne Laser was used as the light source. To detect the reversed flow velocity, 40MHz optical frequency shift was given first by making use of a Bragg cell to one of the two beams separated with a beam splitter. The intersection angle of the two beams was kept constant at 5.71 degree in air in all the experiments and the position of the beam intersection or the measurement control volume was determined by calculation following the geometrical optics.

The scattered light signal from the measuring control volume at the intersection of the two Laser beams was detected with a photomultiplier and the detected optically shifted signal was shifted down in frequency electronically with a frequency shifter DISA 55N10 by an appropriate magnitude in order to secure the linearity between the output signal and the flow velocity. The frequency signal was converted into voltage signal with a frequency tracker DISA 55N20. The output signal corresponding to the flow velocity and the "drop-out" signal from the tracker were recorded on a digital magnetic tape recorder. These digitized signals were afterward processed with a digital computer discarding the portion of the velocity signal in the drop-out phase. The discarded portion of the signal was less than twenty percent of the total length of the recorded signal.

The calibration of the measuring system was performed in the outlet flow from an orifice inserted into the same flow loop. The magnitude of an error caused by the signal broadening due to several possible causes was evaluated referring to Durst et al (1976). In this evaluation, the value of the dissipation rate of the turbulence kinetic energy computed with a scheme used by Kang and Suzuki (1978) was assigned to its required value. The level of such an error was confirmed to be a negligible order of magnitude.

NUMERICAL SCHEME

Experimental data will be compared with the corresponding numerical results computed with the $k-\epsilon$ two-equation model of turbulence. In this computation, a scheme used by Kang and Suzuki (1978, 1982) was used. This is a modified version of 2/E/FIX developed by Pun and Spalding (1976). The turbulence model used in this computation consists of the following two equations for k and ϵ .

$$\frac{\partial}{\partial x} (\rho U k) + \frac{1}{r} \frac{\partial}{\partial r} (\rho r V k) = \frac{\partial}{\partial x} \left(\frac{\mu_e}{\sigma_k} \frac{\partial k}{\partial x} \right) + \frac{1}{r} \frac{\partial}{\partial r} \left(r \frac{\mu_e}{\sigma_k} \frac{\partial k}{\partial r} \right) + G - \rho \epsilon$$

$$\frac{\partial}{\partial x} (\rho U \epsilon) + \frac{1}{r} \frac{\partial}{\partial r} (\rho r V \epsilon) = \frac{\partial}{\partial x} \left(\frac{\mu_e}{\sigma_\epsilon} \frac{\partial \epsilon}{\partial x} \right) + \frac{1}{r} \frac{\partial}{\partial r} \left(r \frac{\mu_e}{\sigma_\epsilon} \frac{\partial \epsilon}{\partial r} \right) + \frac{\epsilon}{k} (C_1 G - C_2 \rho \epsilon)$$

$$\mu_e = \mu + \mu_t = \mu + C_D \rho k^2 / \epsilon$$

$$G = \mu_e \left[2 \left(\frac{\partial U}{\partial x} \right)^2 + \left(\frac{\partial V}{\partial r} \right)^2 + \left(\frac{V}{r} \right)^2 + \left(\frac{\partial U}{\partial r} + \frac{\partial V}{\partial x} \right)^2 \right]$$

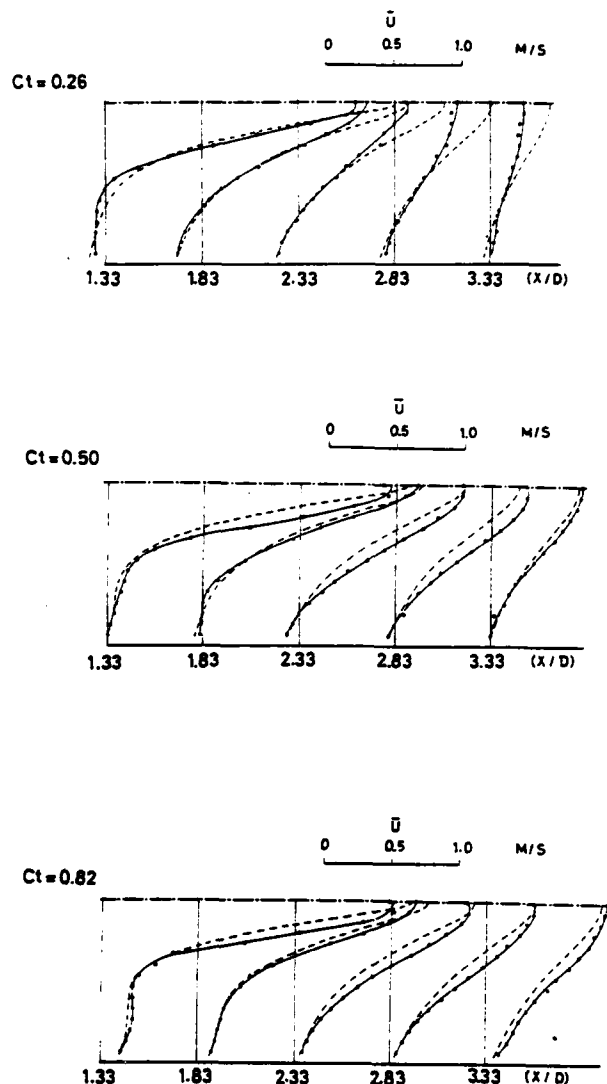


Figure 2 Radial Profile of Streamwise Averaged Velocity

The finite difference analogues of these equations were solved numerically together with those of the momentum equations for the axial and radial velocity components. For the computation of heat transfer, an additional equation for the enthalpy was also solved simultaneously.

EXPERIMENTAL RESULTS AND DISCUSSIONS

In Figure 2 is shown how the radial profile of the measured streamwise velocity develops with the axial distance from the nozzle. The abscissa of the figure is the axial distance downstream from the outlet port of the central jet nozzle, non-dimensionalized with the tube diameter D . In the case when $Ct = 0.82$, there appears no average flow reversal, but in other two cases of smaller Ct number, a recirculating flow region is found to exist. At $Ct = 0.50$, the reversed flow is found near the tube wall at the positions of $X/D = 1.83 - 2.83$. In the last case when $Ct = 0.26$, the reversed flow starts already from $X/D = 1.33$. The recirculating flow region expands upstream with the decrease of Ct value, agreeing with the experimental results with a pitot-tube by Becker et al (1963). The dashed curves in the figures show the computed results. As seen in the figures, the experimental and numerical results agree fairly well with each other.

in two cases of higher value of C_t number. The velocity decay in the central part of the jet delays in the computation in the case of the highest momentum ratio between the central jet and the concurrent stream ($C_t = 0.26$). This feature of the numerical results with the $k-\epsilon$ two-equation model of turbulence was previously pointed out by Kang and Suzuki (1978). In Figure 3 are compared the present results on the position where the axial velocity is zero with the counterparts given by Becker et al (1963). Fair agreement can be found between the two experimental results although the measuring means are different from each other. The predicted zero averaged velocity contour is indicated to agree rather better with the present results, for example, in a point that the front edge of the separation bubble is located upstream of the corresponding results by Becker et al.

The measured fluctuation intensity of the streamwise velocity u' is plotted in Figure 4 in the form normalized with the characteristic velocity U^* . The value of U^* is strongly related to the excess momentum of central jet. The central part of u' profile at $X/D = 1.33$ is of a shape akin to that for the free jet, in all the three cases of different C_t number, while it becomes almost flat in shape at the position of largest X/D . The dashed curves in Figure 4 show the value of $\sqrt{2k/3}$ computed with the scheme explained in the above. The numerical results qualitatively follow the experimental data shown in the figures. Quantitatively, the numerical results are lower than the experimental counterparts. One of the reasons for this is connected with a fact that the value of u' should be higher than $\sqrt{2k/3}$ in turbulent shear flows.

Paying attention to the u' value obtained at the points closest to the tube wall, $y = R - r = 4\text{mm}$, its axial distribution differs from one case to another depending on the value of C_t . In the case of $C_t = 0.82$ when no recirculating flow region appears, it increases toward the downstream almost monotonously. Against this case, in other two cases of lower C_t number, a different feature can be found for the axial variation of u' obtained at $y = 4\text{mm}$. Its value or the intensity of the near wall turbulence becomes maximum at some position in the measured range of X/D , where the average flow has been found reversed near the wall in Figure 2.

In Figure 5, comparison is made among the above mentioned profile of u' along $y = 4\text{mm}$, the profile of the Nusselt number reported by Kang et al (1979) and the profile of the computed value of $\sqrt{2k/3}$ again along $y = 4\text{mm}$. The presently measured u' profile is very similar in shape to the profile of local Nusselt number at any case of different C_t number. In the two cases when the average flow reversal has been found in Figure 2, the maximum intensity of the near wall turbulence is found to occur very close to the maximum heat transfer position or to the maximum position of computed value of $\sqrt{2k/3}$ along $y = 4\text{mm}$. This gives a proof for the conjecture mentioned in the introduction and the first aim of this study has

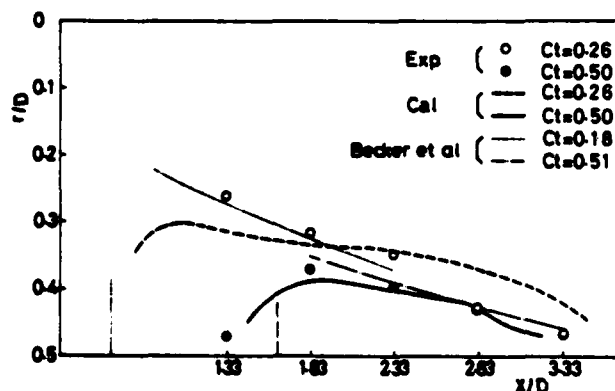


Figure 3 Position of Zero Axial Velocity

partially been accomplished. In order to clarify why the intensity of the near wall turbulence becomes maximum within the recirculating flow region, further systematic experiments are desired to be done in future, not only for the value of u' but also for the fluctuating intensities of other velocity components v' and w' .

Comparing the measured profile of u' and the computed profile of $\sqrt{2k/3}$ plotted in Figure 5 with each other, the measured value of u' is found about two times larger than the computed value of $\sqrt{2k/3}$. Since $k = (u'^2 + v'^2 + w'^2)/2$, the largest possible value of the ratio $u'/\sqrt{2k/3}$ is $\sqrt{3}$. This largest value occurs when both of the other two components v' and w' are equal to zero. Taking account this into consideration, the computed value of k is concluded to be smaller than actually expected value. More detailed discussion on this point would also require further informations about the values of v' and w' . The measurements of these quantities and of the Reynolds shear stress are now in progress.

The confined jet seems to be a simple turbulent flow from the view point that the flow pattern and the Nusselt number distribution are characterized by the similitude parameter C_t . However, this is not the case actually. The turbulent eddies generated in the jet shear layer are mingled with the ones entrained from the recirculating

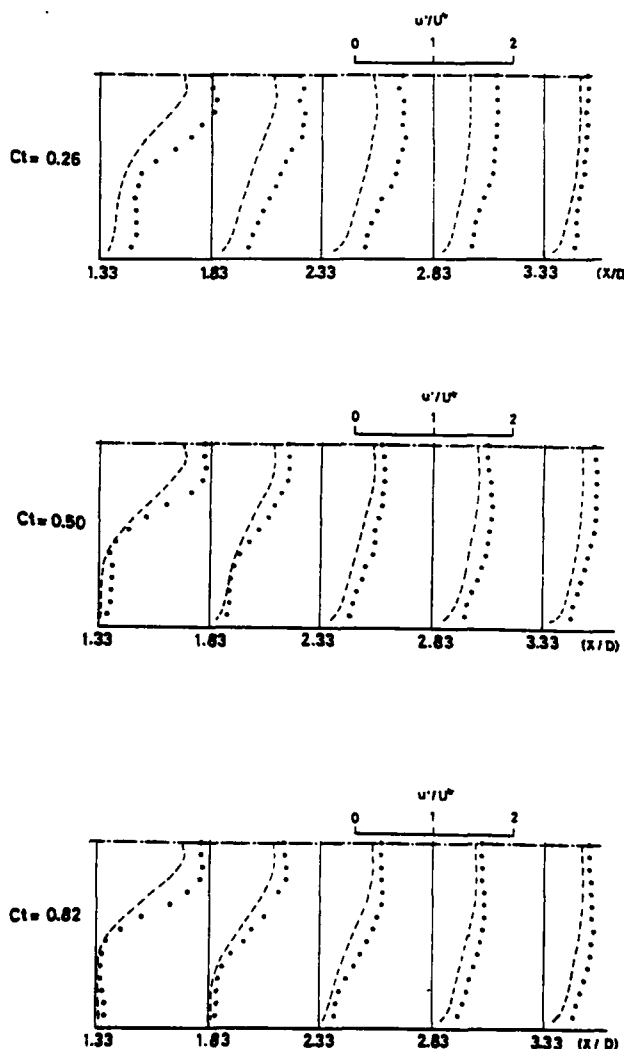


Figure 4 Radial Profile of Streamwise Velocity Fluctuation Intensity

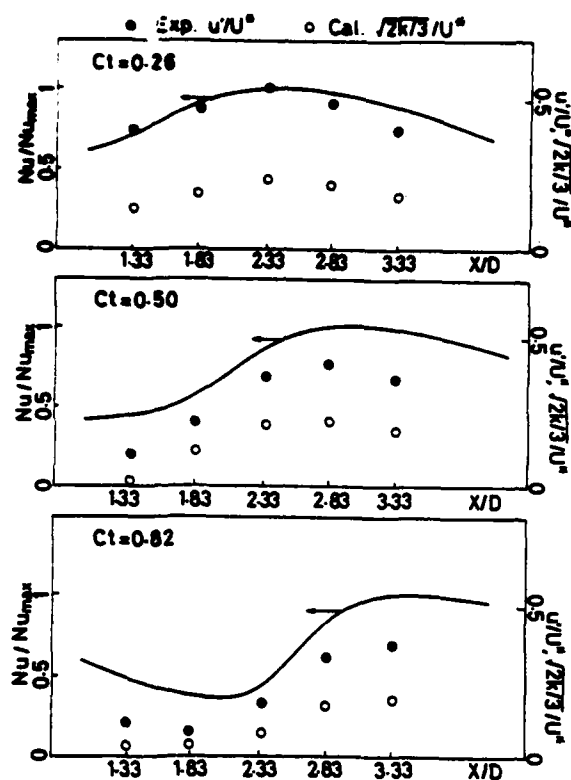


Figure 5 Distribution of Nusselt Number and The Profiles of u' and $\sqrt{k}/3$ along $y = 4\text{mm}$.

flow region. Some of them flows downstream and their structure changes gradually to the one pertinent for the tube flow. The remaining ones are brought to the near wall region again and are conveyed upstream by the reversed flow. In the course of this, the structure of these eddies should be deformed due to the wall interference. These cause non-equilibrium in the structure of the eddies existing in the confined jet flow. To get deeper insight into this non-equilibrium in the turbulence structure and its effect on the heat transfer mechanism, it may be worthwhile to analyze the presently obtained velocity signal from different view points. In the following, some results obtained so far in this line are discussed.

Simpson et al (1981) examined the velocity probability $P(u)$ and the flow reversal intermittency γ_{nu} for the separating turbulent boundary layer. These two quantities were also calculated in the present study from the recorded velocity signal and they are defined as follows:

$$\int_{-\infty}^{\infty} P(u/u') d(u/u') = 1$$

$$\gamma_{nu} = \int_{-\infty}^0 P(u/u') d(u/u')$$

The above definition of the velocity probability distribution with variable band width proportional to u' is introduced in order to secure the same accuracy for its shape among the cases of different level of fluctuation u' . γ_{nu} expresses the fraction of time that the flow velocity is negative or that the flow is reversed.

Figure 6 shows the map of the points where the velocity probability histograms were examined. The centre of each circle corresponds to such positions. The five points A, B, C, D and E are on the line $y = 4\text{mm}$ in all the three figures for different Ct number. When $Ct = 0.26$, one of the above mentioned points, the point E, and other four points F, G, H and I are chosen so that they are close to the positions of zero averaged axial velocity estimated from Figure 2. In the same manner, the three points F, G and H in the case of $Ct = 0.50$, are

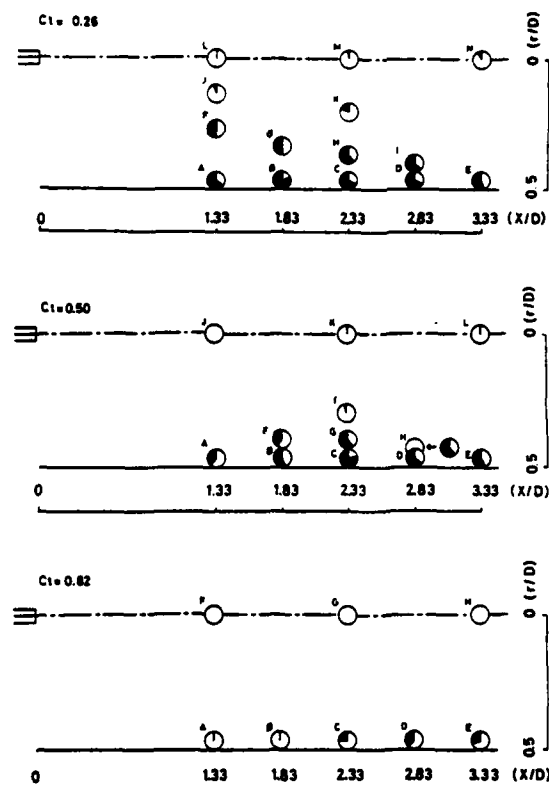


Figure 6 Spatial Distribution of Negative Velocity Probability

also chosen as the positions where U is nearly zero. The two points J and K in the case of $Ct = 0.26$ and one point I in the case of $Ct = 0.50$ represent the positions lying on the edge of the recirculating flow region. These points are also chosen based on the profiles shown in Figure 2.

As seen at the points H and I in the figure for the case of $Ct = 0.26$, the value of γ_{nu} is not necessarily 0.5 at the positions where the averaged axial velocity is zero. This suggests that the velocity probability histogram to be obtained there should be skewed in shape. This will be discussed later in more detail. At the points where the average flow is reversed, the value of γ_{nu} is larger than 0.5 but it is clearly less than unity. This means that the flow is not always reversed even at such positions. On the other hand, at the points where the average flow velocity is positive, the value of γ_{nu} is not zero so that the flow is sometime reversed. The oil mist flow visualization made by Kang et al (1982) actually reveals that the instantaneous separation point varies from time to time. The same would be true for the reattachment point too. All the points discussed above seem to suggest the intermittent evolvement of large eddies which can alter the flow direction from time to time. Such eddies were actually observed by Barchillon and Curtet (1964). The effect of such large eddies may extend even to the tube axis. This may explain such a fact that the value of γ_{nu} is not zero even on the axis. This is seen, for example, at the points M and N in the figure for the case of $Ct = 0.26$. But this is a feature found noticeably only in the case of $Ct = 0.26$. In the case of $Ct = 0.82$, γ_{nu} is found to be almost completely zero at the points F, G and H on the tube axis. In the case of $Ct = 0.50$, it is not zero at the three points on the axis J, K and L but is very close to zero.

The feature of the value of γ_{nu} lastly discussed may have the relation with the axial distribution of the intensity of the streamwise velocity fluctuation on the tube axis. The latter is shown in Figure 7 for the three cases of different Ct number. It is clearly seen that the distribution of u' along the tube axis for the case of $Ct = 0.26$ is quite different from those for other two cases of larger Ct number. Especially in the case of the

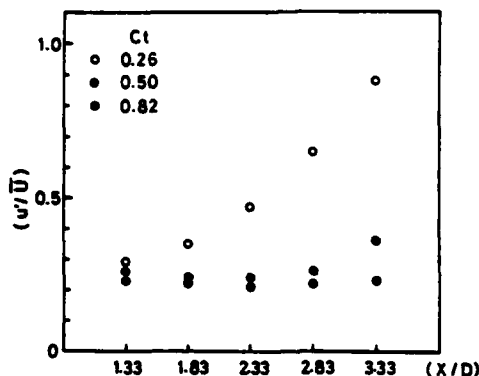


Figure 7 Axial Distribution of u'/U on the Axis

largest C_t number, the value of u'/U on the axis distributes almost uniformly and is close to the value usually accepted for the free jet.

In Figure 8, the velocity probability histogram $P(u/u')$ is plotted for all the observed positions of Y_{nu} in the case of $C_t = 0.26$. $P(u/u')$ is plotted in the figure against u itself so that, if the comparison is made among the histograms with the same scale for the abscissa, the area under the curve connecting the evaluated data of $P(u/u')$ is proportional to the intensity u' . In the figures, the values of the skewness

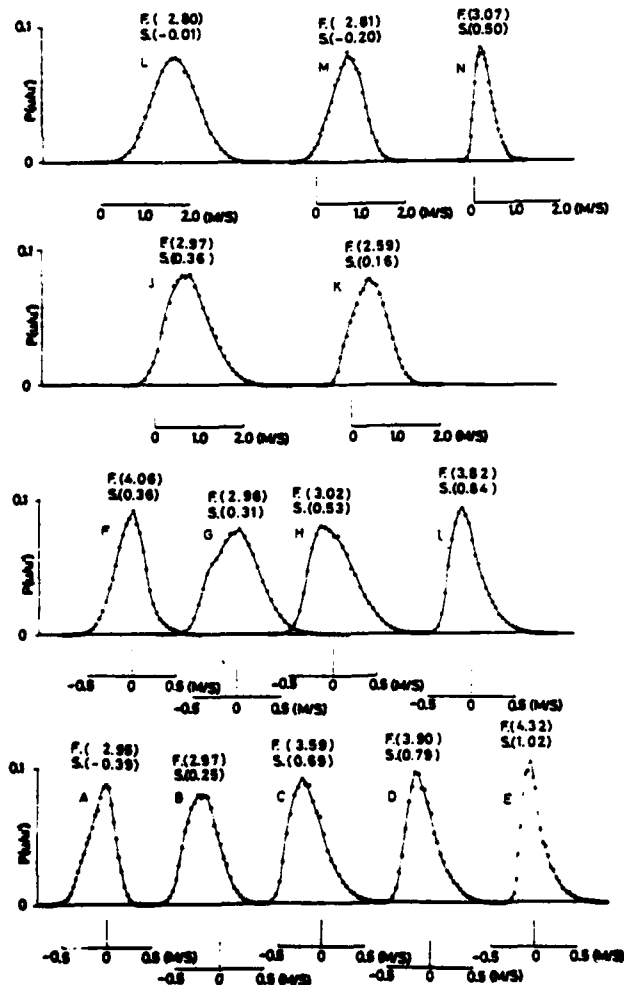


Figure 8 Examples of Velocity Probability Histogram ($C_t = 0.26$)

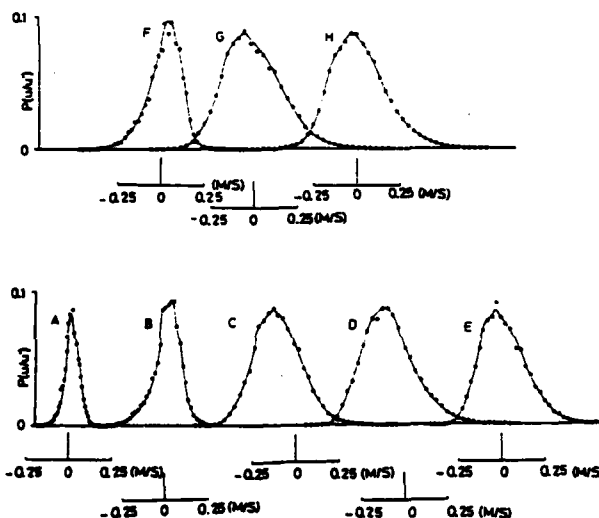
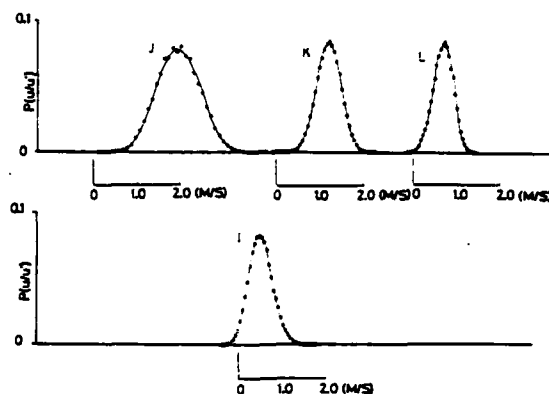


Figure 9 Examples of Velocity Probability Histogram ($C_t = 0.50$)

factor F and the flatness factor F calculated for each of the histogram are illustrated too. The flatness factor F and the skewness factor S are defined as follows:

$$F = \overline{u^4} / \overline{u'}^4, \quad S = \overline{u^3} / \overline{u'}^3$$

For Gaussian distribution, $F = 3.0$ and $S = 0.0$. Except at a few exceptional positions, the shape of each histogram is not Gaussian. For instance, while the histogram is almost Gaussian on the jet axis in the case of free jet as shown by Hetsroni and Sokolov (1971), the present result is clearly of skewed shape even for the positions on the axis except at the most upstream position L. Comparing the histograms obtained at the five points at $y = 4\text{mm}$, those at the most upstream and downstream positions A and E are remarkably skewed in shape. At the most upstream position, large negative velocity occurs more frequently than expected from the Gaussian distribution and the opposite occurs at the most downstream position. The same trends are also found among the results obtained at the positions where the average velocity is zero, i.e. positions F, G, H and I. The significance of these results is not clear yet but it may be connected somehow with the intermittently evolving large eddies suggested above. In connection with this, further effort to visualize the over-all flow pattern of confined jet is now under development.

In Figures 9 and 10 are shown other examples of velocity probability histograms for other two cases of $C_t = 0.50$ and 0.82 . The features similar to those pointed

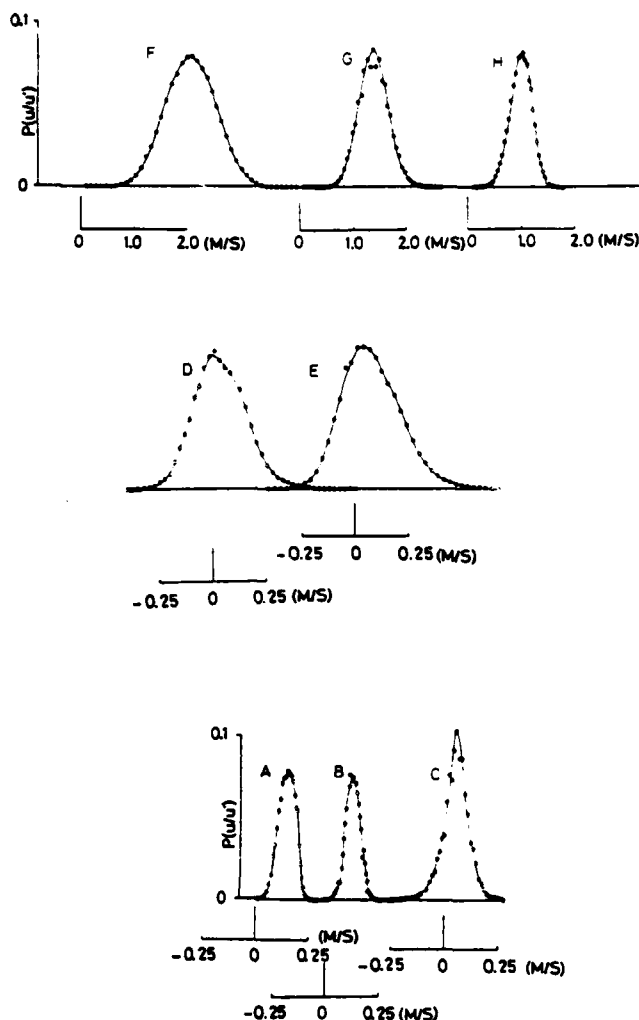


Figure 10 Examples of Velocity Probability Histogram ($C_t = 0.82$)

out in the above can be found among these results too. Especially interesting is that the velocity probability histogram is also skewed in shape at the flow reattachment point. There is a flow visualization technique, with a thin smoke wire located close to the wall, of determining the flow reattachment point by searching for the place such that the negative velocity and the positive velocity occur with equal probability. This technique is based on the assumption that the velocity probability histogram is Gaussian at such a point. The present result denies this assumption. Therefore, the utilization of this technique for the determination of the flow reattachment point can sometimes be false. The position of the flow reattachment point reported by Kang et al (1982) is around or a little upstream of $(X/D) = 3.5$. In this flow visualization, oil surface method was used and the position where the average wall shear stress is zero was taken to be the flow reattachment point. The above cited result for the reattachment point position seems to agree with the flow pattern shown in Figure 3. Thus, the oil surface method may be recommended preferably.

CONCLUDING REMARKS

A conjecture given previously for the physical background of the spatial difference between the maximum heat transfer position and the flow reattachment point has been partially proven. The level of the near wall turbulence has been found to be higher within the recirculating flow region. This may activate the inactive viscous or conductive sublayer. This reduces the heat transfer resistance there and leads to higher wall heat transfer within the recirculating flow region. The dis-

tribution of u' along $y = 4\text{mm}$ close to the wall agrees qualitatively well with the distribution of $\sqrt{2k/3}$ computed employing the $k-\epsilon$ two-equation model of turbulence. But they do not agree quantitatively and the computed values are estimated to be lower. For detailed discussion of this, further experiments on other fluctuating velocity components are desirable in future. Negative velocity intermittency factor is not zero at the positions where the average velocity is positive. This is true even on the axis when the recirculating flow is strong. The last suggests the possibility of intermittent evolution of large eddies in the recirculating flow region. The velocity probability histogram is noticeably skewed in shape at the flow reattachment point and at the separation point. The skewness of the velocity probability histogram is also found at other position, even on the jet axis. This feature may also be connected with the possible intermittent evolution of large eddies. To get clear picture on this, visualization of over-all flow pattern may be necessary.

REFERENCES

- Barchillon, M. and Curtet, R., 1964, "Some Details of the Structure of an Axisymmetric Confined Jet with Backflow", *J. Basic Eng.*, 86, 777.
- Becker, H.A., Hottel, H.C. and Williams, G.C., 1963, "Mixing and Flow in Ducted Turbulent Jets", *Proc. 9th Int. Symposium on Combustion*, 7.
- Durst, F., Melling, A. and Whitelaw, J.H., 1976, "Principles of Laser-Doppler-Anemometry", Academic Press.
- Hetsroni, G. and Sokolov, M., 1971, "Distribution of Mass, Velocity and Intensity of Turbulence in a Two-Phase Turbulent Jet", *J. Appl. Mech.*, 38-8, 315.
- Kang, Y. and Suzuki, K., 1978, "Numerical Study of Confined Jets. I. Prediction of Flow Pattern and Turbulence Quantities with a Two-equation Model of Turbulence", *Mem. Fac. Engng, Kyoto Univ.*, 40-2, 41.
- Kang, Y., Suzuki, K. and Sato, T., 1979, "Convective Heat Transfer in an Axisymmetric Confined Jet", *Studies in Heat Transfer* (ed. by T.F. Irvine), 103, Hemisphere.
- Kang, Y., Nishino, J., Suzuki, K. and Sato, T., 1982, "Application of Flow and Surface Temperature Visualization Techniques to a Study of Heat Transfer in Recirculating Flow Regions", *Flow Visualization II* (ed. by W. Merzkirch), 77, Hemisphere.
- Kang, Y. and Suzuki, K., 1982, "Numerical Study of Wall Heat Transfer in the Recirculating Flow Region of a Confined Jet", *Heat Transfer-Japanese Research*, 11-1, 44.
- Krall, K.M. and Sparrow, E.M., 1966, "Turbulent Heat Transfer in the Separated, Reattached and Redevelopment Region of a Circular Tube", *J. Heat Transfer*, 88, 131.
- Pun, W.M. and Spalding, D.B., 1976, "A General Computer Program for Two-Dimensional Elliptic Flows", *Imperial College Heat Transfer Sec. Report HTS/76/2*.
- Simpson, R.L., Chow, Y.T. and Shivaprasad, B.G., 1981, "The Structures of a Separating Turbulent Boundary Layer. Part 1. Mean Flow and Reynolds Stresses", *J. Fluid Mech.*, 113, 23.
- Suzuki, K., Sato, T., Kang, Y. and Sugimoto, T., 1982, "Circular Tube Turbulent Heat Transfer in the Downstream of an Orifice", *Heat Transfer-Japanese Research*, 11-1, 70.

LDA-MEASUREMENTS AND SOME THEORETICAL
ASPECTS OF SEPARATED FLOWS

D. Geropp
and
A. Leder

Institut für Fluid- und Thermodynamik
Universität -GH- Siegen, F.R.G.

ABSTRACT

Characteristic vortex and turbulence structures in separated flows behind two-dimensional drag bodies can be demonstrated by pressure- and especially LDA-measurements on the basis of the time-averaged approach for large Reynolds numbers. The typical pressure distributions which are always observed in the dead water can be explained by the vortex pair. In theory this quasi-stationary vortex pair can be interpreted as a supplementary virtual displacement body as demonstrated by panel calculations of potential theory. Finally a simple method, called "plate-model-method", is developed to calculate the drag coefficient of sharp-edged cylinders.

INTRODUCTION

The calculation of flows with large separated regions, also called 'dead water', by means of the Navier Stokes equations is impossible until now, especially for low viscosity or high Reynolds number flows. The turbulent boundary layer on the body but also the turbulent motions in dead water require additional physical information in form of empirical laws to help solve the NS-equations.

For the determination of drag and lift of airfoils with dead water calculation methods are already existing (e.g. Grashof (1973), Jacob (1976), Gross (1978), Pfeiffer and Zumwalt (1981)). They are based on a model proposed by Walz (1940), in which the dead water is considered as a finite, closed region. Because of limited physical knowledge about the structure of dead waters, this and other

similar models represent quite an abstraction of reality, particularly concerning the extent of the separated region, the pressure distribution as well as the turbulent and vortex motions. Therefore the calculation schemes based on this idea are often quite inexact. It appears that improvements may be made mainly in conjunction with intensive experiments, which until now are not submitted in a sufficient form.

The aim of the experimental and theoretical investigations presented by Leder (1983) and Geropp (1982) is to deliver more insight into the structure of separated flows and thereby to improve the dead water models for theoretical applications. They are restricted to two-dimensional incompressible separated flows behind flat plates, wedges, circular cylinders and airfoils at different angles of attack at large Reynolds numbers ($Re > 10^3$). Later on these investigations will be extended to three-dimensional cases, which in general are more interesting for technical applications.

EXPERIMENTAL ASSEMBLY AND MEASUREMENT TECHNIQUE

The measurements were performed in a low speed wind tunnel (22 kW fan-power). The open test section had an overall dimension of 460 x 460 mm². The turbulence-intensity of the channel reached an amount of 1 %, the velocity-range was 9 - 25 m/s. All investigated profiles (flat plate, circular cylinder, wedges and NACA 2412 airfoil) had a high number of pressure taps. With the help of endplates the flow field got an intrinsic two-dimensional character. The pressure distribution in the dead water region was measured with a small Prandtl tube, connected with a capacitive device.

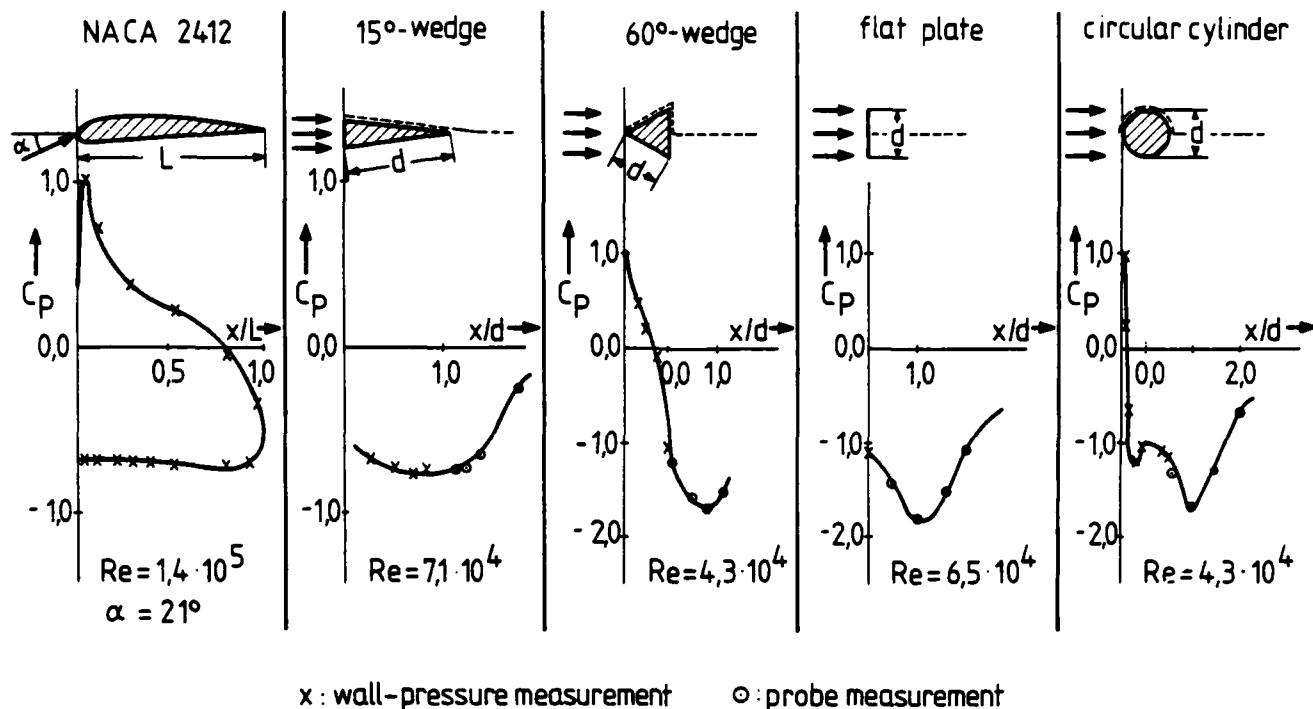


FIGURE 1. Pressure distributions in high Re-number flows.

To determine the time-averaged fluid flow velocity and direction as well as the turbulence energy inside the highly separated region a one-channel Laser-Doppler-System, operating in backscatter-mode, was used. A computer controlled the data sampling from the counter via buffer interface, the positioning of the measuring volume and the storing of results. The accuracy of the LDA measurements presented reaches a value of 10 % in the worst case (in the area of great velocity gradients).

EXPERIMENTAL RESULTS

Pressure measurements

At first pressure measurements were performed inside the dead water behind the investigated bodies. Also in the region of highly fluctuating velocity the results can be understood as time-averaged values because of the slowness of the probe. Fig. 1 shows the pressure distributions in two-dimensional flow for a NACA 2412 profile, a 15°- and 60°-wedge, a vertical flat plate and a circular cylinder. In all cases the pressure coefficient c_p is plotted against the position x/L respectively x/d . Caused by the high angle of attack ($\alpha = 21^\circ$, $c_{l_{\max}}$ occurs for this airfoil at $\alpha = 16^\circ$) a separated region is setting up over the suction side. The nearly constant pressure distribution is an indication of flow separation.

Near the trailing edge however a slight pressure minimum can be detected.

A qualitatively similar pattern is formed when blowing against the base side of the 15°-wedge. The pressure tap measurements along the wedge flank show a slight pressure minimum near the wedge tip projecting into the dead water.

In the cases of the 60°-wedge, the vertical flat plate, and the circular cylinder an analogous behavior of the pressure can be observed: inside the dead water a distinct pressure minimum occurs.

The appearance of the pressure minimum can be explained by the displacement effect of the dead water: the separated region is 'seen' by the external flow - in a similar manner like the rigid body contour - as a displacement body. The velocity of the inviscid external flow does not reach its maximum at the position of greatest cross-sectional dimension of the cylinder but approximately one body-width downstream. The static pressure of the external flow superposes the rigid wall as well as the dead water.

The calculation methods of Grashof (1973) and Jacob (1976) suppose that the pressure along the contour of the dead water remains constant. With this assumption they calculate the boundary of the separated region.

The results of the pressure measurements

clarify that the hypothesis of a constant dead water pressure is permissible for the airfoil, but not for bluff bodies. The question is now: which structure and extent has the dead water?

In this context we have to remember the characteristic flow structures as a function of Re-number for the case of a circular cylinder in cross flow.

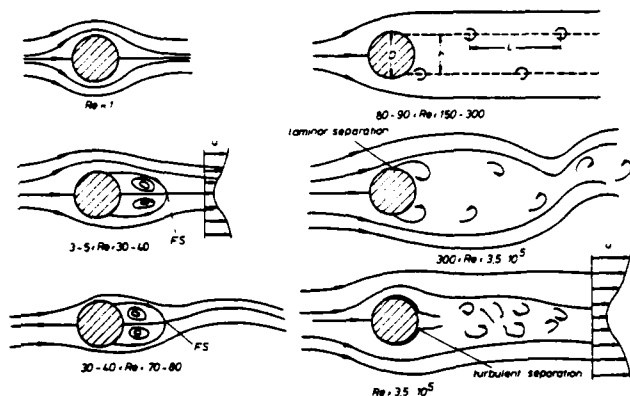


FIGURE 2. Influence of Re-number on the wake.

The single instantaneous pictures in fig. 2 show, that beginning above $Re > 5$ a first separation occurs forming a clearly defined laminar dead water which consists of a stationary vortex pair. Above $Re > 40$ first indications of an instable waving show up originating from the so called 'free stagnation point' (FS). In the region $Re \approx 150$ the vortices shed periodically from the cylinder forming the so called 'Kármán vortex street'. The flow is generally considered as laminar but instationary. Until $Re < 3,5 \cdot 10^5$ the attached flow is laminar. The vortices still shed periodically but now they are completely

turbulent and don't form a stable configuration. Above $Re > 3,5 \cdot 10^5$ the attached flow becomes turbulent. Therefore the separation point jumps to the backside of the cylinder. So the wake, resp. dead water, has a smaller cross-sectional dimension than at lower Re-numbers and is characterized by turbulent stochastic vortex motions. But also in this Re-number region stable vortex streets can appear as shown by satellite-pictures taken at $Re = 10^{10}$ leeward a hill at the island of Jan Mayen. The photographs were analyzed by Wenderoth (1979).

All considerations mainly depended on instantaneous pictures of the separated flows. Because, with the exception of Re-numbers < 40 , these flows show an unsteady behavior with periodical and mostly high frequency turbulent motions it is obvious that a quasistationary image of the dead water should be formed by the time-averaging method.

In such a manner it is possible to obtain steady vortex structures, which can be the base of a dead water model for theoretical considerations.

LDA-measurements

Time-averaged Velocity Fields. Fig. 3 shows the results of LDA-measurements of time-averaged velocity fields in separated flows behind a 60° -wedge with two different angles of attack and downstream of a NACA 2412 airfoil. Each vector is the result of 500 velocity measurements. For plotting each flow field more than 100.000 measurements had to be processed.

The example of the symmetrical flow field shows clearly, that beside the velocity gradient

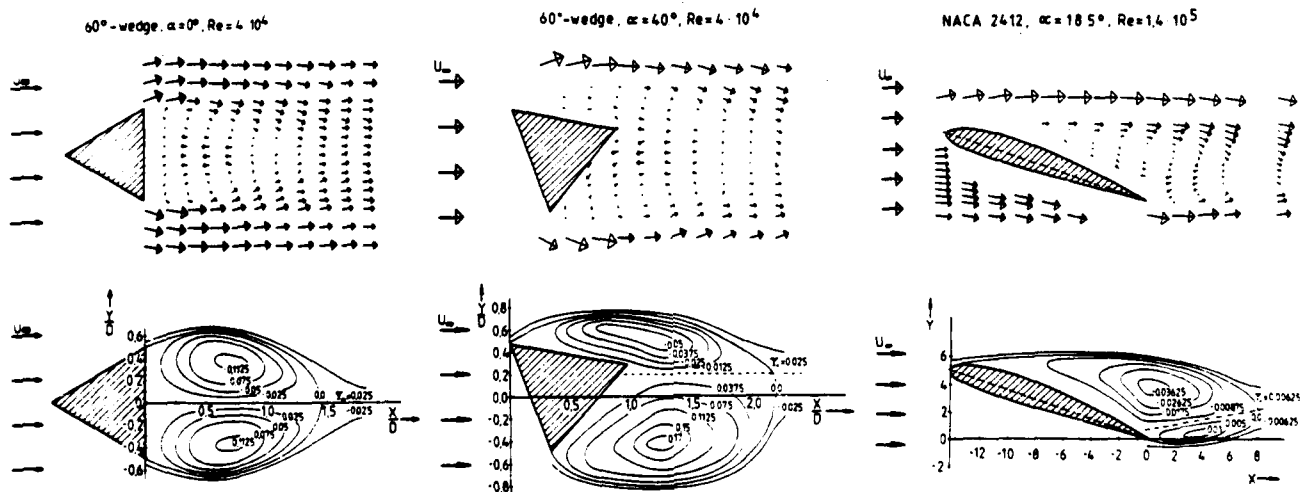


FIGURE 3. Time-averaged flow fields and mean streamlines.

in Y-direction there is also a gradient in X-direction. It is evident that downstream the separation point the external flow is accelerated along the dead water and delayed when transitioning into the wake depression. This corresponds with the pressure minimum in the dead water. A recirculating region can be seen which is part of two symmetrical vortices. Downstream the vortex pair a punctiform region appears with zero mean velocity which we call 'free stagnation point'.

This pairwise time-averaged vortex structure is characteristic for all investigated dead waters. The angle of attack changes the relative sizes and vorticities of vortices, as shown, fig. 3, in the cases of the wedge with $\alpha = 40^\circ$ and the inclined NACA airfoil.

To clarify the flow situations the lower half of the pictures represents the time-averaged streamlines, calculated by an integration of the measured velocity profiles. The plotted streamfunction ψ_0 is normalized with the free-stream velocity U_∞ and a characteristic length of the body, in the case of the wedge with the flank length D.

We define the zero-streamline as the effective dead water contour embedded in the inviscid external flow. The energy of the vortex pair is removed from the external flow, dissipates and is expressed as drag.

Distribution of Turbulence Energy. The results of the turbulence measurements are plotted in normalised form. The longitudinal fluctuation $\overline{u'^2}$ as well as the transversal component $\overline{v'^2}$ are plotted as a function of the dimensionless coordinate Y/D. $\overline{u'^2}$ and $\overline{v'^2}$ are normalised with the square of the free stream velocity U_∞ . Fig. 4 represents the distributions in the case of the 60° -wedge. In spite of the spreading of the measured values the curve shape is determined reliably because of the dense sequence of measuring points. The diagram illustrates that the turbulent motions show a characteristic behavior. In the external flow, far above the wedge, here at $Y/D = 2.5$, the turbulence energy is nearly zero. Approaching the wedge the turbulent motions grow strongly. The transversal fluctuations in the upper half of fig. 4 reach a maximum at $Y/D = 0.0$ along the axis of symmetry. The absolute extreme value appears at the point $Y/D = 0.0$ and $X/D = 1.5$, the free stagnation point. Further downstream the steep gradient decreases because of the intense

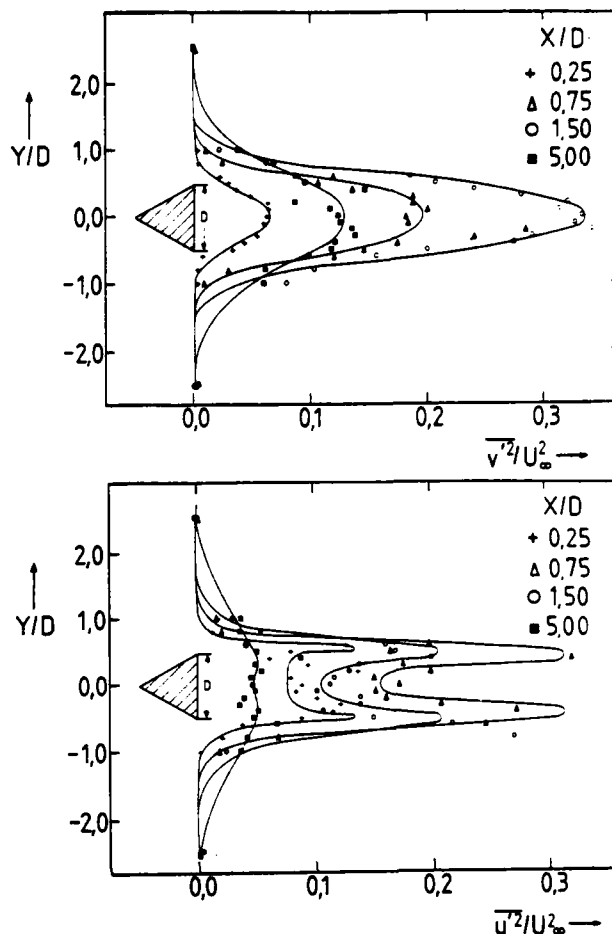


FIGURE 4. Fluctuating values $\overline{u'^2}$ and $\overline{v'^2}$ downstream the 60° -wedge, $\alpha = 0^\circ$, $Re = 4 \cdot 10^4$.

turbulent mixing. This is shown by the curve $X/D = 5.0$, plotted with black square-symbols. The lower half of fig. 4 shows, that the longitudinal component has a different behavior. $\overline{u'^2}$ reaches its maximum at $Y/D = 0.6$. For small X/D -values this locus lies inside the dead water, just below the streamline $\psi_0 = 0.0$. At the positions of the time-averaged vortex axes $\overline{u'^2}$ reach their absolute extreme values. Along the axis of symmetry the longitudinal fluctuations have a minimum.

If the angle of attack α changes, the flow field becomes asymmetric. Fig. 5 represents the case of the 60° -wedge with $\alpha = 40^\circ$. In conjunction with the flow field the distribution of the turbulence energy becomes asymmetric. Qualitatively the same conclusions can be drawn: the absolute extreme value in $\overline{v'^2}$ again appears at the free stagnation point whilst the longitudinal fluctuations reach the extreme value at the time-averaged positions of the vortex axes.

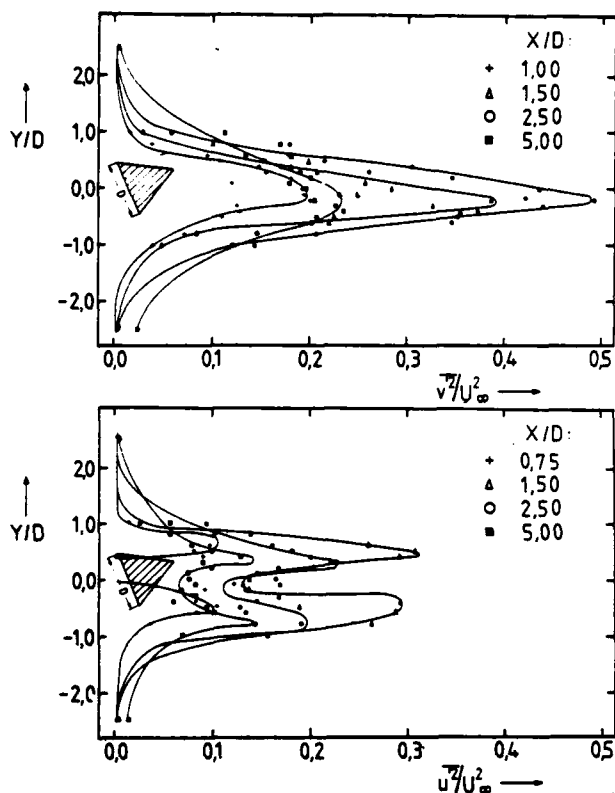


FIGURE 5. Fluctuating values $\overline{u'^2}$ and $\overline{v'^2}$ downstream the 60°-wedge, $\alpha = 40^\circ$, $Re = 4 \cdot 10^4$.

THEORETICAL CONSIDERATIONS

In the following some approaches for dead water models should be considered in which the illustrated experimental results are approximately taken into account.

Dead Water as Displacement Body

As shown in fig. 6 for the example of a circular cylinder the displacement effect of the dead water can be simulated by the zero-streamline as a virtual auxiliary body contour. The pressure distribution around the contour is calculated by a panel-method applying the potential theory. The measured pressure distribution is compared with the one calculated by the panel-method. The calculated and measured pressure data agree very well directly at the cylinder but the pressure minimum in the dead water is simulated with less accuracy. The reasons are dissipative effects in the separated flow which are not taken into account by the panel-method.

Fig. 7 shows corresponding results for the example of the 15°-wedge cylinder. It also proves that the model conception of a dead water

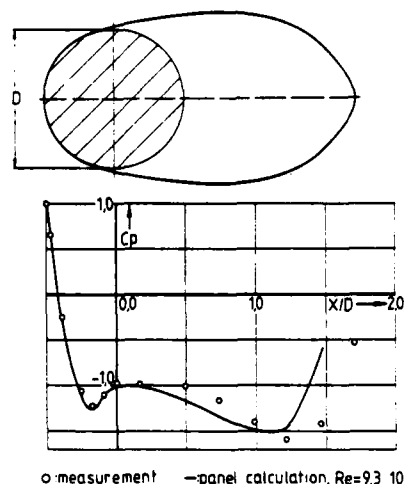


FIGURE 6. Measured and calculated pressure distribution for a circular cylinder.

simulating a virtual displacement body is practicable. But it is necessary to correct the dead water contour. Especially it is purposeful to consider the displacement effect of the shear layers outside the zero-streamline.

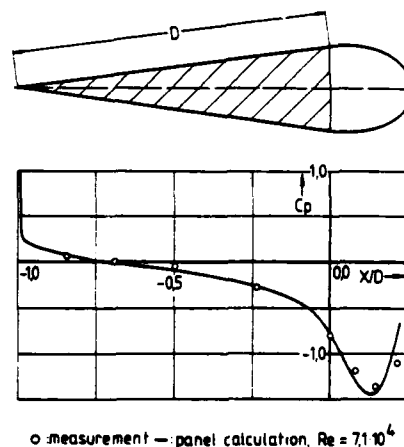


FIGURE 7. Measured and calculated pressure distribution for a 15°-wedge, $\alpha = 0^\circ$.

Drag Calculation for Sharp-Edged Bodies

The present LDA-measurements clarified that the dead water motions behind bluff sharp-edged bodies are very similar to the motions behind a flat plate with a corresponding angle of attack. With this observation a simple method for calculating the drag of sharp-edged cylinders can be developed.

This calculation method, called "plate-model method", is explained in fig. 8. The measured drag coefficient c_w for the flat plate and its constituting parts c_{wA} and c_{wT} are plotted as a function of the angle of attack α (left side). c_{wA} is that part of c_w which

results from the pressure distribution produced by the stagnation flow in front of the flat plate, the c_{WT} -part results from the pressure distribution in the dead water on the back of the flat plate.

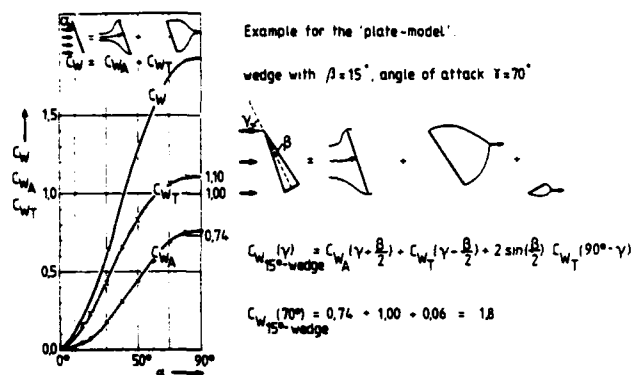


FIG. 8. Calculation example for the 'plate-model'.

Fig. 8 shows the drag part c_{WT} to be larger than c_{wA} . It is obvious that the largest drag of flat plate exists at $\alpha = 90^\circ$ decreasing steadily to $\alpha = 0^\circ$. In this case only friction drag exists provided that the flat plate is very thin. The resulting c_w -value is approximately zero considering the scale used in this diagram.

In analogy to this superposition of two drag parts the c_w -coefficient of sharp-edged cylinders can be determined. First the surface of the body considered should be split up into single flat plates as shown in fig. 8 for the example of the 15° -wedge cylinder with an angle of attack of 70° . In the next step the c_w -parts for each single flat plate are taken from the diagram in fig. 8. Doing this the position of each wedge flank to stagnation flow and the wedge angle β itself must be taken into account. The superposition of all c_w -parts results in the drag coefficient.

The angle of smooth stream is relevant when deciding up to which angle the c_{wA} - or c_{wT} -function of fig. 8 has to be taken. Varying the angles of attack from 0° up to 180° the upper wedge flank of the 15° -wedge cylinder is turned to the dead water above the angle $\gamma = 7.5^\circ$. It must be remarked that the c_w -values in fig. 8 are related to flat plates with unit length. Since the flank length of the wedge is chosen as a reference the factor " $2 \sin(\beta/2)$ " must be chosen for the base side. The efficiency of the plate-model method is tested by the following examples.

In fig. 9 the c_w -coefficients of 15° -, 60° -

120° -wedge cylinders are plotted against the angle of attack.

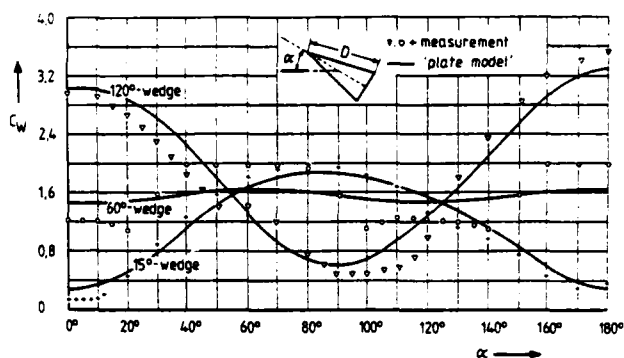


FIGURE 9. Measurements and 'plate-model' calculations for wedges (relative value: length D).

The symbols indicate values measured by Krämer (1964). The solid curves indicate the calculated results. The comparison of measurement and calculation attests the applicability of this new method. Small differences caused of angles near smooth incident flow can be explained because in reality separated bubbles are occurring. The plate-model method cannot consider these effects.

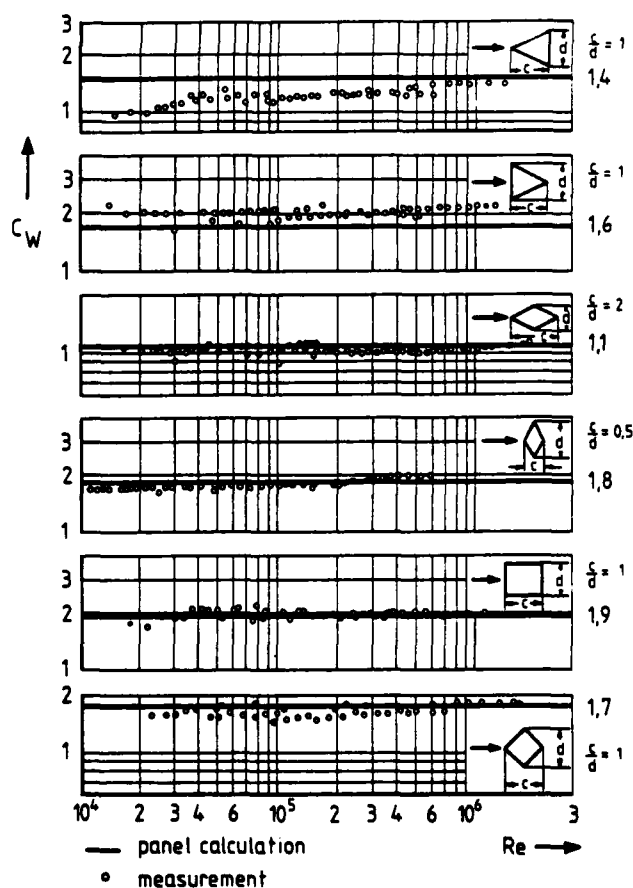


FIGURE 10. Measurements and 'plate-model' calculations for sharp-edged cylinders (relative value: length d).

Also this method cannot take into account the dependence on Re-number because the separation points are fixed by the sharp edge of the flat plate. Therefore the plate-model method is restricted to c_w -calculations of sharp-edged bodies. In figure 10 measurements of Delany and Sorensen (1953) for a wedge, cylinders with rhomboidal and quadratic cross-sections with different angles of attack indicate this fact. It is evident that the c_w -values calculated with the plate-model method are corresponding very well with measurements.

Free Stagnation Point

Finally it is interesting to note the distance B of the so called free stagnation point (fig. 11) behind the body as a function of the Re-number. It characterises the extent of the dead water as defined by the zero-streamline.

In figure 11 measuring results from Taneda (1956) and Leder and Geropp (1982) are plotted for the case of a circular cylinder. There is a distinguished maximum at about $Re \approx 2 \cdot 10^2$ where first indications of turbulence in the Kármán vortex street are known to appear. With increasing Re-numbers the length B decreases in spite of the growth of turbulence. Above $Re \approx 10^3$ the value of the laminar case at $Re \approx 30$ is reached again. This process looks like a relaminarisation of vortex formations in the dead water. In reality the experiments show increasing turbulent fluctuations and eddy viscosities for larger Re-numbers. Indeed the pairwise vortex structure in the dead water may be denoted as "quasi-laminar" at high external flow Re-numbers, if an "effective Re-number" with a constant turbulent eddy viscosity is accepted as the governing physical parameter.

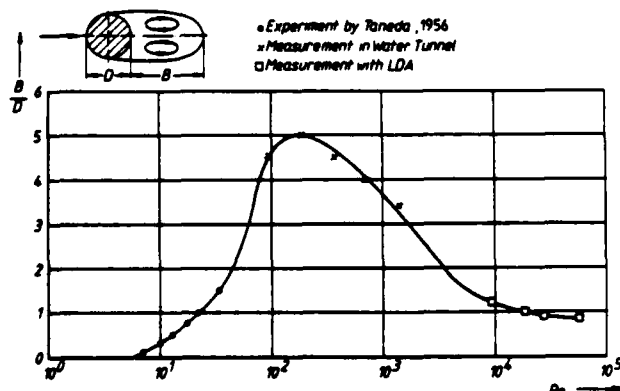


FIGURE 11. Distance of the "free stagnation point" downstream the circular cylinder.

Similar relations are observed in flows of a single vortex or in two-dimensional wakes, where the turbulent eddy viscosity is constant, too. Fig. 11 demonstrates that the dead water length $B/D \approx 10$ for $Re \approx 10^4 - 10^5$ corresponds to the laminar case with $Re \approx 30$.

It can be concluded that at high Re-numbers similar turbulent structures of quasi-laminar character will also occur in other separated flows and dead waters than those behind circular cylinders considered so far. Further investigations are planned in this direction.

CONCLUSIONS

Summarizing the most important findings of these investigations presented in this paper:

- The pairwise occurring, time-averaged vortex structure is characteristic for all investigated dead waters. The zero-streamline enveloping the vortex pair can be understood as a displacement contour for the external flow. Accordingly there are typical pressure distributions in the dead water with a pronounced pressure minimum. This fact is opposed to the pressure constancy assumed until now.
- The distributions of turbulence energy in dead waters are similar. They are anisotropic. Characteristic maxima and minima in this region are evident.
- The effect of dead water on the pressure distribution on the body can be theoretically represented by a virtual displacement contour.
- The dead waters behind sharp-edged cylinders are similar to those of flat plates with corresponding angles of attack.

REFERENCES

- Delany, N.K., Sorensen, N.E., 1953, NACA TN 3038.
 Geropp, D., 1982, in "Recent Contributions to Fluid Mech.", Ed.: W.Haase, Springer-Verlag.
 Grashof, J., 1973, Diss., TH Karlsruhe.
 Gross, L.W., 1978, AIAA 16th Aerosp.Sci. Meet. Huntsville, Alabama, Jan. 16-18.
 Jacob, K., 1976, DLR FB 76 - 36.
 Krämer, K., 1964, AVA-Bericht Nr. 30.
 Leder, A., Geropp, D., 1982 ZAMM 63, Heft 4/5.
 Leder, A., 1983, Diss. Uni-GH-Siegen.
 Pfeiffer, N.J., Zumwalt, G.W., 1981, AIAA 20, 3, p.376 - 382.
 Taneda, S., 1956, J.Phys.Soc.Japan, 11, p.302-307.
 Walz, A., 1940, Jb.d.dt.Luftf.-Forsch. I, p.265-277.
 Wenderoth, O., 1979, Diss. TH Karlsruhe.

MASS AND MOMENTUM TURBULENT TRANSPORT EXPERIMENTS WITH CONFINED COAXIAL JETS

B. V. Johnson
United Technologies Research Center
East Hartford, Connecticut 06108

and

J. C. Bennett
University of Connecticut
Storrs, Connecticut 06108

ABSTRACT

An experimental study of mixing downstream of coaxial jets discharging into an expanded circular duct was conducted to obtain data for the evaluation and improvement of turbulent transport models. A combination of turbulent momentum transport rate and two components of velocity data were obtained from simultaneous measurements with a two-color LV system. A combination of turbulent mass transport rate, concentration and velocity data were obtained from simultaneous measurements with laser velocimeter (LV) and laser induced fluorescence (LIF) systems.

INTRODUCTION

Computational procedures to predict combustion (and other mixing) processes are being developed and refined by a number of researchers (e.g., see Ref. 1 and surveys in Refs. 2 and 3). These computational procedures predict the velocity, species, concentration temperature and reaction rate distribution within the combustors. Because combustors of practical interest have turbulent flow, the calculation procedures usually include mathematical models for the turbulent transport of mass (or species), momentum and heat. However, the prediction of these mixing processes with improper turbulent transport models result in inadequate predictions of streamline location and scalar concentration distribution.

The data used to formulate and validate the turbulent transport models have been obtained primarily from velocity and momentum transport measurements because only a limited amount of concentration and mass transport data is available. The mass (species) transport data presently available for recirculating flows like those occurring in combustors are not sufficient to determine where inadequacies exist in the present models or to formulate improvements for the models. One reason for this situation is that the methods used prior to the mid-1970's for simultaneously obtaining turbulent mass (species) and momentum transport data often have been indirect, requiring compromising assumptions or require probes unsuitable for recirculating flows. To overcome these limitations, new optical techniques have been developed to simultaneously measure a scalar quantity and velocity and, therefore, to obtain mass transport data. These techniques include fluorescence of a trace material in water or gases to measure concentration, Mie scattering of a trace material to measure concentration, fluorescence of gas molecules to measure species and temperature, and Rayleigh scattering from gas molecules to measure temperature (e.g., surveys in Refs. 4 and 5). All these techniques use lasers as a light source and have been used recently (since 1979) with laser velocimetry to obtain combined scalar/velocity measurements. The

fluorescence of dye in water was selected as an appropriate technique for this mass and momentum turbulent transport study with constant density fluids.

A preliminary effort at UTRC to obtain quantitative concentration measurements with fluorescent dye in 1975 was described by Owen (paper 28 of Ref. 5). The current effort makes use of improved optics, data handling capabilities and operative procedures. Initial results from the current effort were presented in Ref. 6. The experimental capabilities for the present study were expanded to include measurement of the mass transport in the z - r and z - θ planes. The current application of the combined LV/LIF measurement techniques along with the available data handling procedures provides an opportunity to obtain data which can be used to evaluate a number of computational methods and turbulent transport models. Results from the present experiment can be used to evaluate (1) the two-equation turbulence model, (2) the Reynolds stress transport model and (3) the probability density function formulation for predicting turbulent transport and concentration fluctuations.

The present study was initiated with a flow visualization phase to qualitatively determine the effects of velocity ratio, U_i/U_o , and the Reynolds number on the flow characteristics within the duct (Ref. 7). Results from the study were also used to determine the streamwise locations for obtaining detailed velocity, concentration, and mass transport rate measurements. A sketch of the shear regions, which existed for the flow condition measured, is shown in Fig. 1. The four major shear regions are: a wake region immediately downstream of the inner jet inlet duct; a shear region further downstream between the inner and annular jets, a recirculation zone, a reattachment zone. The high speed motion pictures showed (a) the turbulent eddy structure of the annular jet accelerating the slower moving inner jet which also produced large counter gradient scalar transport and (b) the coupling of some large scale eddies between the annular jet and the recirculation zone and between the annular jet and inner stream. The quantitative results will be related to these shear regions and mixing phenomena.

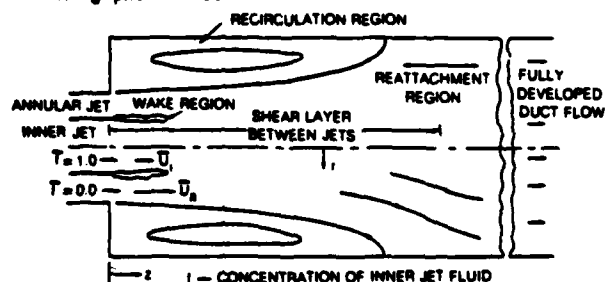


Fig. 1 Shear regions of coaxial jets in an enlarged duct

The complete results from this experiment are described in a limited distribution report (Ref. 8). The statistical characteristics of the mixing process, i.e., the mean values, the rms deviation, skewness and kurtosis of the velocity, concentration and turbulent transport probability density functions, are discussed in Ref. 9. The present paper focuses on the interaction between the momentum and scalar transport processes and the overall results from the experiment.

DESCRIPTION OF EXPERIMENT

Measurement Techniques

The experimental method employed a laser velocimeter (LV) to obtain velocity data, a laser induced fluorescence (LIF) technique to obtain concentration data, and a microcomputer to control the data acquisition and to store and reduce the data. Commercially manufactured equipment was used for the optics and most of the electronic components. For the LV/LIF measurements the equipment was arranged as shown in Fig. 2. The light source used was the 0.488 μm line with a 1-mm-dia. beam from a Spectra-Physics argon ion laser. The laser was operated in the constant light amplitude mode with a power of 0.4 Watt. Fluctuations in the light intensity were estimated to be less than 1 percent. The LV optics were arranged to use the dual-beam laser-Doppler velocimeter system. The sending optics consisted of a beam splitter, Bragg cell, 2.27x beam expander, and a 378 mm focal length lens. The collection optics were arranged for forward scattering. The input to the photomultiplier was optically filtered to receive only 0.488 μm light. The photomultiplier signal was mixed to achieve a 1.0 MHz signal for zero velocity. These optical components were manufactured by TSI. The mixed signal was processed with a SCIMETRICS signal processor and the acceptable signals were fed through an electronic interface to a Digital Equipment Corporation (DEC) PDP 11/10 computer. The DISA 55X00 laser velocimeter system and the 0.5145 and 0.488 μm lines of the laser were used in the direct backscatter mode for the simultaneous two velocity measurements.

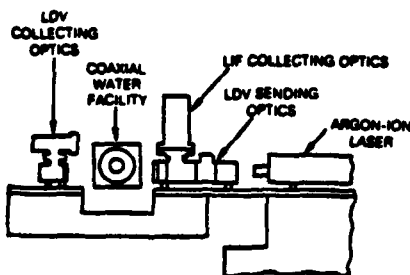


Fig. 2 Sketch of optics arrangement

The circular duct test section was enclosed in a rectangular, glass walled optical box filled with water to reduce beam direction distortion as the laser beams passed from air through the glass wall of the duct and into the test section water. A ray tracing program was used to determine that the radial displacement of the probe volume was less than 0.03 mm and the offset of the measurement direction from radial was less than 0.05 deg for $r/R_0 < 0.9$. The LV probe volume was calculated to have dimensions of 0.12 mm diameter and 2.3 mm length and 24 fringes.

The LIF measurement technique used fluorescein dye as a trace element in the inner jet of the coaxial flow streams. This dye absorbs light at 0.488 μm and emits light with highest intensities at wavelengths between 0.5 and 0.6 μm . Direct backscattering, light-collection optics were used for the LIF system. The light was focused through a Kodak No. 15 Wratten filter onto a photomultiplier tube. The photomultiplier tube current was converted to voltage, was filtered with a 2 KHz low pass filter and was fed into a 12 bit analog-to-digital converter in the computer.

The LIF data were digitized 24 microseconds after the LV data sample was obtained. The time between the LV and LIF data acquisition was less than 0.25 and 0.02 times the minimum transit time across the probe volume diameter and length, respectively. Therefore, no correction to the LV or LIF data was necessary for this short time period.

One thousand pairs of data samples were obtained at each data acquisition point (250 in slow moving regions). The LV data acquisition rate was slowed, by controlling the signal processor A+ start signal to less than 10 per sec, to prevent the data from being acquired too fast and probably biasing the measurements with short-term statistics (Ref. 10). The data were stored on flexible disks and are available for future additional data processing.

Flow Conditions

The geometry for the experiment is shown in Fig. 3. This configuration with coaxial jets discharging into an enlarged circular duct is similar to the configuration used in previous momentum transport experiments (e.g., Ref. 11). The configuration had ratios of annular jet diameter to inner jet diameter (R_2/R_i) and outer wall diameter to inner jet diameter (R_0/R_i) of approximately 2 and 4. The inner jet, annular jet, and total flows through the system were held constant at 23.5, 200.0 and 223.5 l/min, respectively.

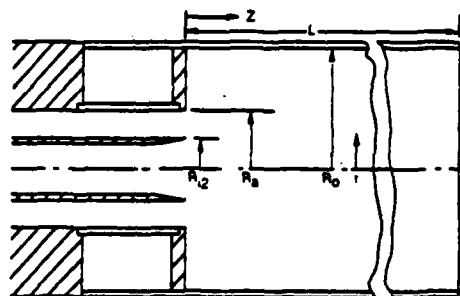


Fig. 3 Sketch of inlet and test section; $L = 1016$ mm, $R_{i1} = 12.5$ mm, $R_{i2} = 15.3$ mm, $R_a = 29.5$ mm, $R_0 = 61.0$ mm

The water temperature varied from 50 to 70 C causing the duct Reynolds numbers, UD/ν to vary from 30,000 to 40,000. (These Reynolds numbers are an order of magnitude above the transitional range.) In reducing the data, the turbulent transport characteristics were assumed to be independent of the Reynolds number. All the turbulent mass transport data and most of the velocity data were obtained over a one-month period when the water temperature varied less than 3C from the average value and the Reynolds number varied less than 5 percent. For a typical two hour test period, the water temperature varied less than 1C.

Axial velocity and turbulent kinetic energy profiles 13 mm downstream of the inlet plane are shown in Fig. 4. This was the nearest upstream location to the inlet plane where all LV and LIF measurements could be obtained. Each symbol represents a different azimuthal location. The results form a single profile and show the flow is axisymmetric in the inlet region. The turbulent kinetic energy results were obtained from u' , v' and w' profiles.

DISCUSSION OF RESULTS

The objective of this study was the acquisition, reduction, and analysis of velocity, concentration, mass transport rate and momentum transport rate measurements at seven axial locations within the duct test section. Data obtained at one of seven axial stations will be used to illustrate the principal results. Summary of the profiles obtained at all locations will be presented as isograms.

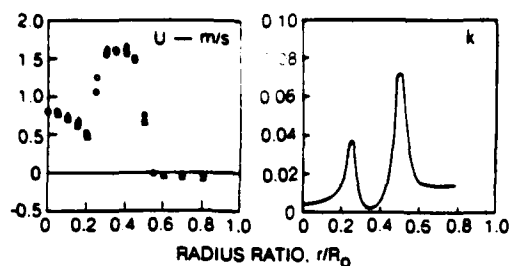


Fig. 4 Axial velocity and turbulent kinetic energy profiles at $z/R_0 = 0.2$ ($z = 13$ mm) from inlet plane

Velocity

The mean velocity profile at $z/R_0 = 1.67$ (Fig. 5a) shows large velocity gradients at $r/R_0 = 0.2$ where the annular jet is accelerating the inner jet fluid and at $r/R_0 = 0.6$ where the annular jet is also driving an annular recirculation cell. The maximum negative velocity in the recirculation cell are approximately 0.3 m/s which is 20 percent of the peak driving velocity and consistent with previous results in recirculating zones. The fluctuating rms axial velocity profiles (Fig. 5b) shows peak values of u' in the high shear regions. The values of v' and w' were 60 to 80 percent of the u' values in the peak shear regions and approximately equal to the u' value in the low axial velocity gradient and shear regions. Iso-grams of the mean axial velocity (U), the mean radial velocity (V), and the turbulent kinetic energy (k) are presented in Fig. 6a-c. Note the length scales, r/R_0 and z/R_0 , on the isogram are chosen unequal to show the variations more clearly. The axial velocity isogram, $U = 0$, shows the axial extent of the recirculation cell and the approximate outline of the cell. The two velocity isograms, $U = 0.75$, bounded by $z/R_0 < 2.0$ and $r/R_0 < 0.25$ and the lower velocities between them are due to the inner jet being decelerated by the wake region between the inner and annular jet and then being accelerated by the annular stream. The radial velocity (V) isogram (Fig. 6b) shows (a) low positive velocities at $z/R_0 = 0.5$ and $r/R_0 = 0.1$ due to the deceleration of the inner jet by the wake region, (b) negative values at $r/R_0 = 0.2$ and $z/R_0 = 1.5$ as the annular jet is accelerating the inner jet fluid, (c) all positive values at $z/R_0 > 4.1$ as the jets begin to fill the enlarged duct downstream of the recirculation cell and (d) negative velocities in the recirculation cell at $r/R_0 = 0.75$ and $z/R_0 = 1.0$. The turbulent intensities at these locations were 5 to 8 percent and consistent with values expected at the center of developed duct flow. Note the peak values of k occur near the recirculation zone reattachment location and may be due to general unsteadiness of the flow in this region. Note the growth of turbulent energy in the

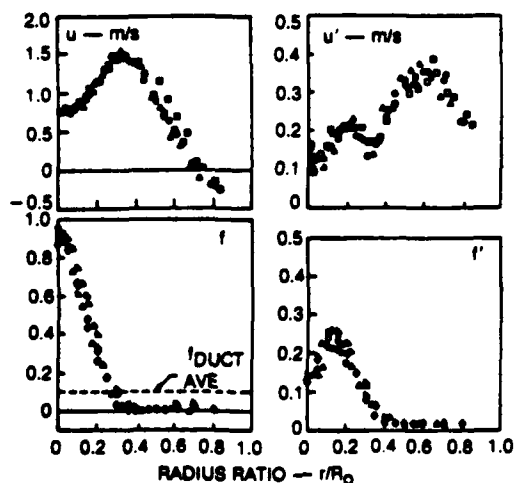


Fig. 5 Mean and RMS fluctuating axial velocity and concentration profiles at $z/R_0 = 1.67$

direction of the flow in the high shear region and the decrease in the direction of the flow in the recirculation zone, $r/R_0 > 0.8$ and $z/R_0 < 3.0$.

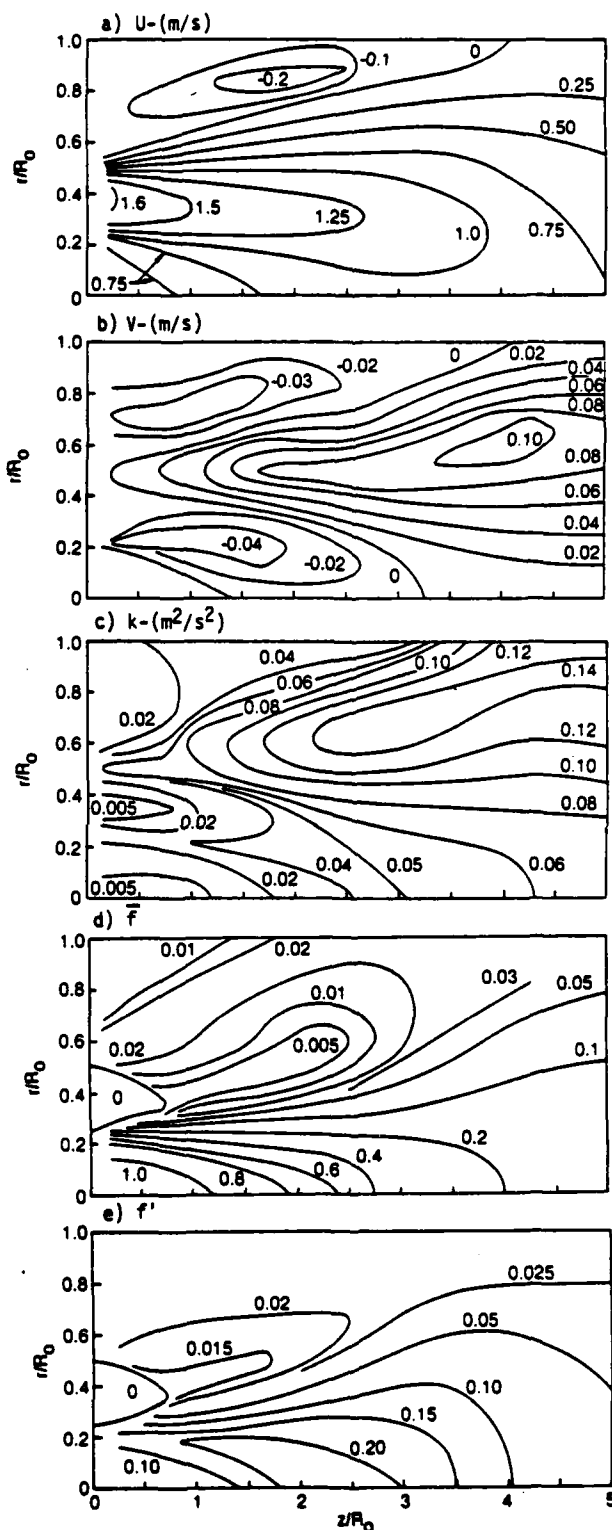


Fig. 6 Iso-grams of axial velocity (U), radial velocity (V), turbulent kinetic energy (k), mean inner jet concentration (f) and RMS fluctuating inner jet concentrations (f')

Concentration

The mean inner jet concentration profile at $z/R_0 = 1.67$ (Fig. 5c) shows peak values near 0.9 at $r/R_0 = 0$ and near zero values at $r/R_0 = 0.4$. This axial loca-

tion is a short distance downstream of the central core regions for both the inner jet and the annular jet. The rms fluctuating concentration profile shows values of 0.14 at $r/R_0 = 0$ and approximately 0.01 near $r/R_0 = 0.5$. At $r/R_0 = 0$ most of the concentration values were 1.0 with lower values (0.3 to 0.5) occurring occasionally. At $r/R_0 = 0.5$, the measured concentration fluctuations were close to the noise levels in the photomultiplier, i.e., $f' = 0.01$. The mean concentration contours (Fig. 6d) show the decrease in the inner stream concentration along the centerline from a value of 1.0 at $z/R_0 = 1.0$ (the downstream end of the inner jet core) toward the volume flow averaged value of 0.105 at $z/R_0 > 5.0$. However, note the concentration gradients are primarily in the radial direction. The $f = 0.2$ isoconcentration line occurs along the $r/R_0 = 0.25$ radius for $z/R_0 < 3.0$. Note also the concentration profiles in the recirculation zone, $r/R_0 > 0.8$ and $z/R_0 < 3.0$. These concentration contours also decrease in the direction of the mean flow (compare with velocity isograms, Fig. 6a). The accuracy of the inner jet concentration measurements was approximately 1 percent. Thus, the contours for $f < 0.05$ are best estimates based on the data profiles and the author's judgement. The rms concentration fluctuation profiles show peak values in the region near $r/R_0 = 0.1$ and $z/R_0 = 2.0$ where the concentration gradients are high and the turbulent kinetic energy is increasing with z/R . Note that ratio f'/f was greater than 1 in the recirculation zone and attributed to filaments of high concentration inner jet fluid.

Turbulent Transport

R-Z Momentum Transport. A radial profile of \overline{uv} at $z/R_0 = 1.67$ (Fig. 7a) shows the inward turbulent transport of momentum for $r/R_0 > 0.35$ where the annular jet is accelerating the inner jet fluid and the outward turbulent transport of momentum for $r/R_0 < 0.35$ where the annular jet is driving the recirculation cell. Note that the location, $r/R_0 = 0.35$, where $\overline{uv} = 0$ corresponds to the peak of the axial velocity profile in Fig. 5a. Results from the seven radial profiles are summarized in the isograms (Fig. 8a); the nature of the turbulence structure which produces the momentum transport is shown in the isogram of the R_{uv} correlation coefficient (Fig. 8b). The results can be related to the shear region shown in Fig. 1: (a) $\overline{uv} > 0$ in the inner jet core region where the inner jet is accelerating the wake flow; (b) $\overline{uv} < 0$ where the annular jet is accelerating the wake flow and the inner jet fluid; (c) $\overline{uv} > 0$ where the annular jet is driving the recirculation cell and (d) $\overline{uv} > 0$ downstream of the reattachment zone where the flow is beginning to develop into duct flow. At the furthest downstream location, $z/R_0 = 5$, the shear stress was approximately linear as expected for developed pipe flow. However, the stresses were factors of 30 to 50 greater than those for fully developed pipe flow. Thus the flow at this location was far from equilibrium. The correlation coefficients show low values, i.e., 0.1 where $\overline{uv} > 0$ and the inner jet is accelerating the wake region. The prediction of this region has also been troublesome (Ref. 14). The peak correlation coefficients in the free shear regions on the inside and outside of the annular stream are high, i.e., $R_{uv} = -0.45$ and 0.50.

Radial Mass Transport. The measured radial mass transport rate profiles at $z/R_0 = 1.67$ (Fig. 7a) is associated with the radial gradient of the mean concentration profiles. The peak outward mass transport occurred at $r/R_0 = 0.15$ which is also the radial location of the peak concentration gradient. The transport at $r = 0$ approaches 0 as expected for axisymmetrical profiles. The negative (inward) mass transport for $r/R_0 > 0.4$ is due to the turbulent transport of inner jet fluid from the recirculation cell. The isogram of the radial mass transport and the correlation coefficients R_{vf} are presented in Figs. 8c and 8d. The greatest transport rate and correlation coefficients occur at $r/R_0 = 0.2$ and $z/R_0 = 2.0$. The peak correlation coefficient is high, i.e., 0.5 in the

shear region between the inner and annular jets. Note the mass transport is outward and the momentum transport is inward at this location. However in the recirculation zone, $r/R_0 = 0.7$ and $z/R_0 = 2.0$, the correlation coefficients are low, i.e., -0.12. This may be due to the less structured transport process in the recirculation zone. Note that at $r/R_0 = 0.3$ and $z/R_0 = 2.0$, the correlation coefficient for the radial mass transport is $0.3 < R_{vf} < 0.4$ though the momentum turbulent transport is zero, i.e., $\overline{uv} = R_{uv} = 0$.

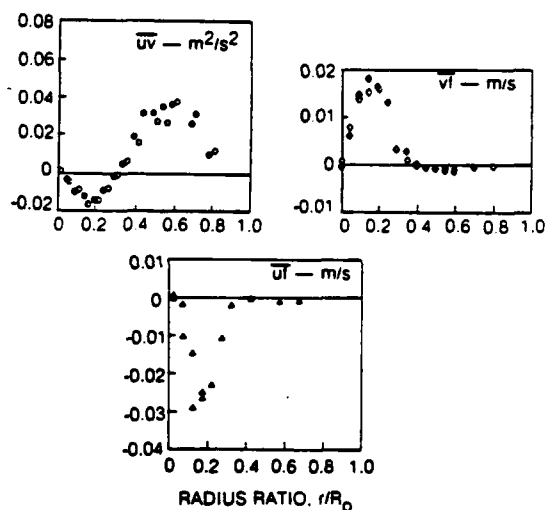


Fig. 7 Momentum turbulent transport (\overline{uv}), radial mass turbulent transport (\overline{vf}) and axial mass turbulent transport (\overline{uf}) at $z/R_0 = 1.67$

Axial Mass Transport. Turbulent scalar (mass) transport is generally associated with the scalar (concentration) gradients and a transport diffusion coefficient, $m_1 = \epsilon_1(\partial f/\partial x)$. (A recent evaluation of gradient transport models is given in Ref. 13.) However, for some classes of flows with turbulent transport, notably atmospheric transport of heat, the scalar transport can be opposite the direction of the scalar gradient. This class of scalar transport is denoted "countergradient" transport and requires a "Reynolds stress" formulation to calculate the scale (mass) transport rate (e.g., Ref. 12). Some of the axial mass transport rate measurements obtained in this study fall into the "countergradient" diffusion transport category. Discussion of these flows will relate the measured axial mass transport to the velocity shear field which produces the mass transport mechanism.

The axial mass transport profile at $z/R_0 = 1.67$ (Fig. 7c) shows the large negative mass turbulent transport which occurred in the central region of the test section, $z/R_0 < 4$. Isograms of \overline{uf} and R_{uf} constructed from profiles are shown in Figs. 8e and 8f. Note that the peak absolute values of the axial transport rates were higher than the values for the radial transport (Fig. 8c) even though the peak radial concentration gradients were more than ten times the axial concentration gradients.

The peak correlation coefficients, R_{uf} , were -0.55 to -0.60, greater than those for the radial mass transport or the momentum transport. A comparison of the correlation coefficients R_{uv} , R_{vf} and R_{uf} shows the peak values for R_{uv} occur at $z/R_0 = 1.0$ whereas those for R_{vf} and R_{uf} occur at $z/R_0 = 2.0$. Thus, the turbulent structure generated by the shear persists after the momentum transport has occurred and continues to produce large scalar transport.

The countergradient transport process can be explained by considering the shape of the axial velocity profiles in the countergradient transport region (Fig. 5a) and the eddy structure associated with the momentum transport. In the region where the inner

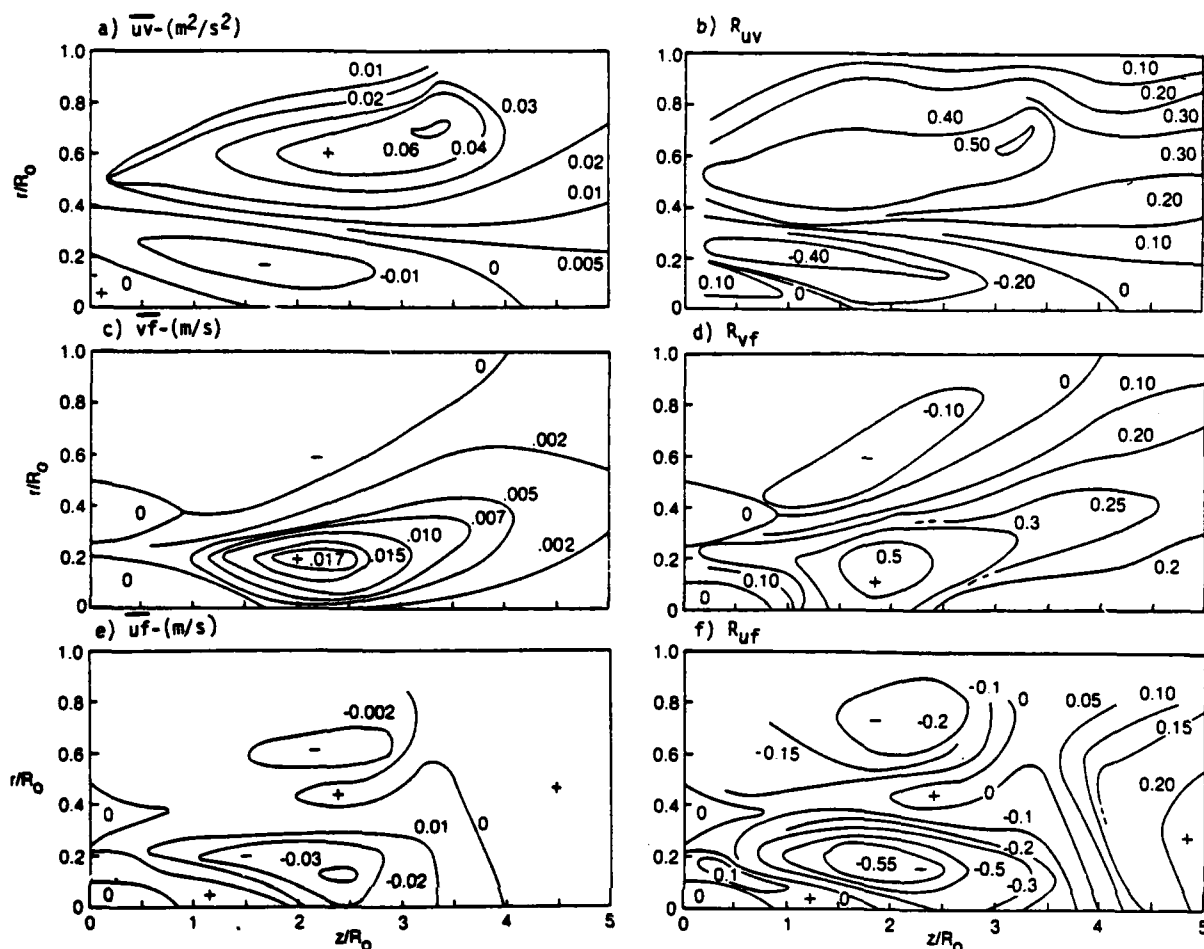


Fig. 8 Isograms of turbulent transport rates and correlation coefficients
 $R_{uv} = \overline{uv}/u'v'$; $R_{vf} = \overline{vf}/v'f'$; $R_{uf} = \overline{uf}/u'f'$

jet was being accelerated by the annular jet, the large eddies in that velocity shear layer near the centerline were "rolling" with the negative fluctuating axial velocities near the inner jet fluid. The result was that the preferred rotational orientation of these eddies retarded the flow in the streamwise direction and resulted in $\overline{uf} < 0$ and hence countergradient mass transport. The regions with countergradient, $\overline{uf} < 0$, and gradient, $\overline{uf} > 0$, axial mass turbulent transport and positive and negative axial velocity accelerations are shown in Figs. 8e and 8e. The region with the countergradient mass turbulent transport ($\overline{uf} < 0$) was larger than the region where the flow from the inner jet was accelerated by the flow from the annular jet ($\overline{uv} < 0$). The larger size of the scalar countergradient turbulent transport region may be due to the response time or distance required to change the character of the turbulent structure.

The countergradient axial mass turbulent transport may be an appreciable portion of the mean convective mass transport. For example, at $z/R_0 = 1.67$ and $r/R_0 = 0.2$, the values of \overline{uf} and Uf are -0.025 and 0.336 , respectively; thus $\overline{uf}/Uf = -0.074$. In the high countergradient axial mass transport region, the ratio of \overline{uf}/Uf ranged from -0.05 to -0.10 , an appreciable percentage of the total inner jet mass flux.

Thus, it is apparent that the local turbulent transport coefficients are not isotropic. Further analysis of the experimental results and comparisons with predictions will be required to determine the extent of deficiencies in the turbulent transport models. The impact of these deficiencies on the numerical predictions and the effects of improved turbulent transport modeling on the predictions.

CONCLUSIONS

The velocity, concentration, and transport rate distributions measured downstream of coaxial jets discharging into an expanded circular duct show region-to-region variations in the transport processes. The accurate prediction of the phenomena measured is a difficult task which will probably require improvements in both the currently-used transport models and mathematical models. Following are the principal results from this study:

1. The turbulent momentum transport rate measurements in the r - z plane documented the local momentum fluxes due to turbulent mixing.
2. Countergradient turbulent axial mass transport was measured in the shear region between jets. The peak axial mass transport rates were greater than the peak radial mass transport rates even though the axial concentration gradients were less than one-tenth the radial gradients.
3. The countergradient turbulent axial mass transport was related to the general direction of the eddies between the inner and annular jets. The countergradient axial mass transport occurred when the annular jet was accelerating the inner jet fluid.
4. The turbulent structure produced by the velocity field caused high radial and axial mass transport rates at downstream locations where the momentum turbulent transport had decreased.

ACKNOWLEDGMENT

The experiments were conducted in the Gas Dynamics and Thermophysics Laboratory of the United Technologies Research Center. The experimental data, presented herein, were obtained under Contract NAS3-22771 from the NASA Lewis Research Center with Dr. C. J. Marek as Project Manager.

REFERENCES

1. Gerstein, M. (Ed.): Fundamentals of Gas Turbine Combustion, NASA Conference Publication 2087, 1979.
2. Hudson, D. W.: "Combustion Modeling Needs for the 80's." AIAA Preprint 80-1288.
3. Mellor, A. M.: "Turbulent Combustion Interaction Models for Practical High Intensity Combustors;" Seventeenth Symposium on Combustion, p. 377, Combustion Institute, 1979.
4. Demetriades, A.: "Probes for Multivariant Flow Characteristics," Proceedings of the Dynamic Flow Conference, 1978.
5. ———: Application of Non-Intrusive Instrumentation in Fluid Flow Research, AGARD Conference Proceedings, No. 193, May 1976.
6. Johnson, B. V. and J. C. Bennett: "Velocity and Concentration Characteristics and Their Cross Correlations for Coaxial Jets in a Confined Sudden Expansion - Part I Experiments; pp. 145-160, ASME, 1981.
7. ———: Film Supplement to Ref. 8. NASA Lewis Research Center Loan Film C-303 (Sound, Color, 18 mins.).
8. Johnson, B. V. and J. C. Bennett: Mass and Momentum Turbulent Transport Experiments with Confined Coaxial Jets, NASA Contractor Report NASA CR-165574, UTRC Report R81-915540-9, November 1981.
9. Johnson, B. V. and J. C. Bennett: Statistical Characteristics of Velocity Concentration, Mass Transport and Momentum Transport for Coaxial Jet Mixing in a Confined Duct. ASME Preprint 83-GT-39. To be published ASME Journal of Power, 1984.
10. McLaughlin, D. K. and W. G. Tiederman: Biasing Correcting for Individual Realization of Laser Anemometer Measurements in Turbulent Flows, Physics of Fluids, Vol. 16, pp. 2082-2088, 1973.
11. Habib, M. A. and J. H. Whitelaw: Velocity Characteristics of Confined Coaxial Jets With and Without Swirl. ASME Journal of Fluids Engineering, Vol. 102, pp. 47-53.
12. Lumley, J. L.: "Computational Modeling of Turbulent Flows." Advances in Applied Mechanics, Vol. 18, Academic Press, 1978.
13. Sreenivasan, K. R., Tavoularis, S., and S. Corrsin: "A Test of Gradient Transport and its Generalizations", Turbulent Shear Flows 3, Springer-Verlag, 1982.
14. Syed, S. A. and Sturgess, G. J.: "Velocity and Concentration Characteristics and Their Cross Correlations for Coaxial Jets in a Confined Sudden Expansion - Part II - Predictions", Fluid Mechanics of Combustion Systems, pp. 161-168, ASME, NY 1981.

TURBULENT FLOW DOWNSTREAM OF A BACKWARD-FACING STEP

J.O. Ilegbusi
Imperial College
London, UK

and

D.B. Spalding
Imperial College
London, UK

ABSTRACT

A brief account is given of a numerical and experimental study of turbulent flow downstream of a backward-facing step. The former involves the application of the latest version of the k-W model of turbulence, k being the specific kinetic energy of the fluctuating motion, and W the time-mean square of the vorticity fluctuations.

The experimental investigation comprises a new flow-visualization technique in which the test body is pulled through partially-dyed fluid. The result of its preliminary application is presented.

NOMENCLATURE

C_{pwall}	Wall-static pressure coefficient
E	Constant in near-wall description of velocity profile (≈ 9.0)
g	Gravitational acceleration
H	Step height
k	Turbulence kinetic energy
l	Length scale of turbulence fluctuation ($\approx k^2/W$)
L	Body length
Re_v	Reynolds number based on the laminar sublayer
t	Time
U	Axial velocity component
U_0	Reference velocity (≈ 18.2 m/s)
V	Cross-stream velocity component
W	Time-mean square vorticity fluctuation
X	Streamwise coordinate
X_R	Recirculation length
y	Cross-stream coordinate
y_v	Laminar sublayer thickness
$-UV$	Specific turbulent shear stress
κ	Von-Karman constant (≈ 0.435)
ρ	Density
τ	Shear stress
τ_s	Shear stress at the wall
σ	Prandtl/Schmidt number
μ	Absolute viscosity

INTRODUCTION

When a fluid flows steadily past a backward-facing step, a recirculation occurs, having appreciably higher levels of turbulence energy and stress than exist in the upstream or far-downstream regions. The governing equations are elliptic in nature.

In recent years, various turbulence models have been applied to such recirculating flows. The more successful ones are those which take account of one important feature, namely that the turbulent motions adjacent to the surface are not produced solely by the local shear stress, but by stresses which exist at an upstream location in the flow field. The turbulence

energy is transported from the generation area to the surface by convection and diffusion.

Two such turbulence models are the k- ϵ model of Harlow and Nakayama (1968), and the k-W model of Spalding (1969). Both these models have been modified since their inception e.g. in the case of k- ϵ by Jones and Launder (1972), and by Launder and Spalding (1974), and in the case of k-W by Gibson and Spalding (1972) and Ilegbusi and Spalding (1983). The present paper focusses attention on the last-mentioned modification, and carries it somewhat further.

The k- ϵ and k-W turbulence models both need boundary conditions which represent the way in which the shear stress at the wall depends upon nearby velocities and on the diffusion of turbulence kinetic energy. One such condition, proposed by Spalding (1967) and recently extended by Chieng and Launder (1980) in respect of the k- ϵ model, is here employed for the k-W model.

The above-mentioned work by Ilegbusi and Spalding (1983) has shown the k-W model to perform satisfactorily in several circumstances, including:- turbulent pipe-flow; flow over a flat plate with intense heat transfer and with intense mass transfer through the surface; flow and heat transfer downstream of an abrupt pipe-expansion; flow in a plane jet; flow in a mixing layer; and flow in a round jet.

In the present paper, this model is applied to the prediction of the flow investigated by Kim et al (1978) and reported at the 1981 Stanford Conference on Complex Turbulent Flows. This concerns flow downstream of a backward-facing step in the wall of a duct.

It will be shown that the k-W model can perform quite well in these circumstances also.

It is interesting to determine whether the k-W model represents the flow better or worse than does the k- ϵ model, when that is applied with precisely the same initial and boundary conditions, and with an identical grid and solution algorithm. Therefore the corresponding k- ϵ calculations have been performed for comparison and are reported below. It may be concluded that there is little to choose between the two models from the point of view of agreement with experiment.

The paper goes beyond the experimental investigation by providing some typical profiles of the velocity components and of k, W and the length-scale based on the new k-W model. These predictions, as well as being interesting in themselves, also provide a body of material which future modellers and/or experimenters may wish to compare with their own results.

The paper also describes briefly a new experimental flow-visualization technique, and the result of its pre-

liminary application to flow downstream of a backward-facing step. The procedure involves the known practice of pulling the test body through a fluid at rest; but it has the novel feature of using two fluids, one above the other, and making their flow-induced intermingling visible by use of a dye.

MATHEMATICAL FORMULATION OF THE k-W MODEL

Because the k-W model has had less public exposure than the k-ε one, it may be useful to present briefly the relevant equations, as follows. For the k-ε equations, on the other hand, the reader is referred to papers already cited.

Differential Equations

The conservation equations for k and W are:

$$\frac{Dk}{Dt} = \rho^{-1} [\text{div}(\frac{\mu}{\sigma_k} \text{grad } k) + S_k] \quad (1)$$

$$\frac{DW}{Dt} = \rho^{-1} [\text{div}(\frac{\mu}{\sigma_W} \text{grad } W) + S_W] \quad (2)$$

time-dependence turbulence- source
and bulk diffusion
transport transport

The source term for k is expressed as:

$$S_k = G_k - C_D \rho k W^{\frac{1}{2}} \quad (3)$$

in which the generation term G_k can be expressed in cartesian-tensor form as:

$$G_k = \mu_t (\frac{\partial u_i}{\partial x_j} + \frac{\partial u_j}{\partial x_i}) \frac{\partial u_i}{\partial x_j} \quad (4)$$

No compressible-flow adjustment is employed in the present work.

The eddy viscosity, μ_t , takes the form:

$$\mu_t = C_\mu \rho k W^{-\frac{1}{2}} \quad (5)$$

The source term for W is expressed as:

$$S_W = k^{-1} W (C_3 G_k - C_2 \rho k W^{-\frac{1}{2}}) + C_1 \mu_t (|\text{grad } \Omega|)^2 - C_4 \rho W^{\frac{1}{2}} (|\text{grad}(kW^{-\frac{1}{2}})|)^{C_5} \quad (6)$$

in which Ω is the major component of the vorticity of the mean motion.

The first term on the right of equation (6) is similar to S_k , the second is a relatively small term, and the last is the term which was missing from k-W publications by the present authors before 1982.

The Turbulence-Model Constants

The complete set of constants used in the current k-W model is given in Table 1 below.

C_μ	C_D	C_1	C_2	C_3	σ_k	σ_W	C_4	C_5
1.0	0.09	3.5	0.17	1.04	1.0	1.0	2.97	2.0

Table 1. The values of the constants

The first seven constants of the set were established by earlier work on the original version (Spalding 1972) while the remaining two, namely C_4 and C_5 of the new model, were deduced in a previous paper (Ilegbusi and Spalding, 1983).

Boundary Conditions at the Wall

The restriction of equations (1) and (2) to regions of high turbulence Reynolds number precludes specification of k and W at the wall; and the conventional log-law wall-function does not hold in the separation region, because larger scale turbulence diffusion seems to be the main mechanism bringing turbulence energy to the wall.

For this reason therefore, a wall function has been employed, which is similar to that used by Chieng and Launder (1980) for the k-ε model. This approach extends the works of Spalding (1967) and Launder and Spalding (1974).

The near-wall model is shown in Figure 1. The flux of momentum to the wall is supposed to obey the relation:

$$\frac{Uk_v^{\frac{1}{2}}}{(\tau_s/\rho)} = \frac{1}{\kappa^*} \ln E^* \frac{yk_v^{\frac{1}{2}}}{v} \quad (7)$$

wherein

$$\kappa^* = \kappa C_D^{\frac{1}{2}} \quad (8)$$

and

$$E^* = E C_D^{\frac{1}{2}} \quad (9)$$

The drag law for non-equilibrium flow is obtained by inverting equation (7) and evaluating the resultant at node P to give:

$$\tau_s = \kappa^* \rho U_P k_v^{\frac{1}{2}} / (\ln E^* y_P k_v / v) \quad (10)$$

Equations (7) and (10) are similar to those of Launder and Spalding (1974) except that the kinetic-energy term k is here evaluated at the edge of the laminar sublayer rather than at node P.

The turbulence kinetic energy k_v is obtained by extrapolating the line through k_P and k_E (Figure 1) to $y = y_v$, thus:

$$k_v = k_P + (y_P - y_v) (k_E - k_P) / (y_E - y_P) \quad (11)$$

k_P is calculated from a balance of turbulence energy generation, dissipation, diffusion and convection in the computational cell surrounding the near-wall node. The thickness of the laminar sublayer y_v and the mean velocity at the location are obtained from:

$$y_v = Re_v / k_v^{\frac{1}{2}} \quad (12)$$

and

$$U_v = Re_v (\tau_s / \rho) k_v^{\frac{1}{2}} \quad (13)$$

wherein Re_v is the sublayer Reynolds number assumed to be 20.

Further details of the above treatment can be found in Ilegbusi (1983).

The mean-square vorticity fluctuation, W, is deduced from k from the relation:

$$W = \kappa^{-2} C_D^{-\frac{1}{2}} k_P / y^2 \quad (14)$$

This serves as the third boundary condition.

COMPUTATIONAL DETAILS OF SUDDEN-ENLARGEMENT CALCULATION

Initial and Boundary Conditions of Particular Problem

At the inlet section, the measured velocity and turbulence intensity are prescribed. The boundary-layer thicknesses at the two bounding walls there are assumed equal.

At the exit boundary, a constant-pressure condition is imposed.

Grid. A partial layout of the grid network in the calculation domain is shown in Figure 2. A total of 30 cross-stream grids are used to span 4.5 inches, out of which 14 nodes are used for the 1.5-inch step. The first interior node is 0.18 inch (0.12 step height) from the step-side wall. The smallest axial grid spacing is 0.3 inch and a total of 42 axial nodes are used.

Effect of grid-refinement studies

Table 2 shows the effect of the above and of five other grids on the turbulence-energy distribution at a location 5.33 step heights beyond the step and within the recirculation region. The first three columns show the effect of forward-step size while the last three show the effect of cross-stream grids. It can be seen by reading along the rows that the 30x42 grid described above can be considered sufficiently refined. This is the one employed for the computations to be presented.

grid	20x30	20x42	20x47	25x42	30x42	36x42
y/H	$k/U_0^2 \times 10^2$					
0.18	2.201	2.210	2.216	2.229	2.244	2.248
0.30	2.795	2.840	2.850	2.855	2.860	2.863
0.51	3.608	3.617	3.622	3.637	3.669	3.672
0.63	3.942	3.949	3.953	3.958	3.961	3.964
0.75	3.968	3.978	3.985	3.996	4.005	4.058
0.87	3.686	3.762	3.770	3.864	3.898	3.910
0.95	3.255	3.513	3.520	3.591	3.602	3.606
1.065	2.641	2.708	2.716	2.726	2.744	2.747
1.125	1.988	2.116	2.121	2.130	2.139	2.139

Table 2. Effect of grid numbers on the turbulence kinetic energy, k/U_0^2

k-ε calculation

In addition to the k-W model described, the comparable computations have been performed with the k-ε model as described by Launder & Spalding (1974).

These employ exactly the same boundary and internal conditions and grid as those presented above for the k-W model.

Computer Program

All computations have been performed by means of the PHOENICS program of Spalding (1981).

PREDICTIONS OF THE SUDDEN-ENLARGEMENT FLOW RESULTS

The results are displayed in figures 3 to 8 and in Tables 3 and 4. Also shown in the figures are the experimental data of Kim et al (1978). Figures 3 to 6 include in addition the predictions with the k-ε

model, while Figure 8 includes the comparable measurements of Tropea and Durst (1980). X_R in Figure 8 is the recirculation length which, for the prediction, is taken as the distance from the step to the point

y/H	$\frac{U}{U_0}$	$\frac{V}{U_0} \times 10^2$	$\frac{k}{U_0^2} \times 10^2$	$\frac{W}{\partial U / \partial y}$	$\frac{\ell}{3H} \times 10^2$
0.18	-0.056	-1.400	2.244	5.058	1.590
0.30	0.0096	-2.300	2.860	4.192	2.410
0.51	0.138	-3.967	3.669	3.265	2.788
0.63	0.226	-4.796	3.961	3.053	2.724
0.75	0.327	-5.529	4.055	2.898	2.560
0.87	0.439	-6.129	3.898	2.723	2.345
0.945	0.518	-6.415	3.602	2.190	2.190
1.065	0.651	-6.668	2.744	2.476	1.924
1.125	0.718	-6.669	2.139	2.489	1.779

Table 3. Predicted normalised values of flow variables at axial location 5.33 step-heights beyond the step

where the mean streamline is re-anchored to the wall.

y/H	$\frac{U}{U_0}$	$\frac{V}{U_0} \times 10^2$	$\frac{k}{U_0^2} \times 10^2$	$\frac{W}{\partial U / \partial y}$	$\frac{\ell}{3H} \times 10^2$
0.18	-0.135	-1.304	2.008	5.288	1.562
0.30	0.190	-2.126	2.537	4.536	2.521
0.51	0.291	-3.416	3.188	3.492	3.144
0.63	0.357	-4.016	3.394	3.236	3.185
0.75	0.430	-4.493	3.425	3.043	3.107
0.87	0.508	-4.823	3.244	2.850	2.958
0.945	0.562	-4.548	2.987	2.708	2.837
1.065	0.649	-4.985	2.339	2.589	2.609
1.125	0.693	-4.931	1.914	2.575	2.476

Table 4. Predicted normalised values of flow variables at axial location 8 step-heights beyond the step

DISCUSSION

Comparison with Experiment

(i) **Pressure.** The predicted static-pressure distribution along the no-step side wall in Figure 3 compares well with the measurement for the k-W model. The predictions in Figure 4 for the stepped wall show a decrease in C_p for the region up to 2.2H (H being the step height) downstream of the step, compared with 3.4H deduced from the data. However, except for the immediate neighbourhood of the reattachment (7.2H for the k-W model), the difference between prediction and measurement is within the experimental uncertainty.

(ii) **Mean velocity.** In Figure 5, the mean velocity seems to be fairly well predicted. In the first section, which lies within the recirculation region, the peak reverse flow velocity is slightly underpredicted. The recovery of the flow

beyond the separation region appears to be fairly well reproduced at the remaining two sections.

(iii) Shear Stress. The predicted shear-stress distributions in Figure 6 are in fair accord with the measurements. The stress first increases monotonically to its peaks (at about $y/H=0.9$ for the data and 0.94 for the k-W model) before descending to zero at the axis. The variations become more gradual with increase in stream-wise distance.

The difference between predicted and measured peak shear-stresses in the three sections considered ranges from -4% to $+21\%$ for the k-W model.

The maximum shear stresses along the channel in Figures 7 and 8 are well predicted beyond the recirculation region. This result is consistent with the observed features in Figure 6. The prediction in Figure 7 drops sharply from a maximum value near the step, exhibits a kink at $1.3H$ and rises to a second maximum at about $5H$ beyond the step.

Figure 8 shows that the prediction agrees with the data of Tropea and Durst (1980) in the separation region. The data of Kim et al (1980) there may be too low, perhaps because of the use of an x-array hot-wire in their measurements.

Comparison with k- ϵ predictions

(i) Pressure. The static pressures appear in Figures 3 and 4 to be better predicted with the k-W model, especially for the non-stepped wall.

(ii) Mean velocity. The predicted mean-velocity distribution with the k- ϵ model (Figure 5) compares well with both the k-W predictions and the data. However, the k- ϵ underpredicts the peak reverse flow velocity in the first section (which lies in the recirculation region) by about 40%. In addition, the k- ϵ model predicts a slower recovery of the flow than the k-W and the data in the remaining two sections.

(iii) Shear stress. The k- ϵ model predictions in Figure 6 have the same trend as both the k-W predictions and the data. The peak shear-stresses occur at $y/H=0.91$ for the k- ϵ compared to 0.94 for the k-W.

In the three sections considered, the k-W model appears to have a more gradual return to the free-stream levels than the k- ϵ model.

The difference between predicted and measured peak shear-stresses in these sections ranges from -17.5% to -1% for the k- ϵ model as compared to -4% to $+21\%$ for the k-W.

Further Predictions

Tables 3 and 4 show that the maximum turbulence energy occurs in the high-shear regions away from the walls. The cross-stream velocities, V , are all negative, showing the expected flow towards the stepped wall located at $y=0$.

The normalised frequency $W^2/|\partial U/\partial y|$ shown in the three tables exhibits a maximum near the stepped wall and decreases progressively towards the core. The normalised length scale, $l/3H$, on the other hand, rises gradually from the stepped wall, reaches a maximum and then decreases progressively towards the core. The tables also reveal that the magnitude of the length scale increases with downstream distance, thus showing the predominance of large-scale motions beyond the recirculation region.

THE EXPERIMENTAL INVESTIGATION

The principle of the flow-visualization experiment

Wind tunnels and water channels are expensive to build and to run. It is much cheaper, and can be very instructive, to pull the flow-creating body through fluid at rest, as is routinely performed in "towing tanks" for ship research.

The present technique is of the pulling-through-fluid kind; but it has the novel feature of using two fluids, one above the other, and making their flow-induced intermingling visible by the use of a dye.

The two fluids are at first kept separate by a small difference of density, sufficient to maintain a perfectly horizontal and well-defined interface, but not so great as to influence the flow generated by the movement of the test body. This latter condition simply requires the Froude number U^2/gL greatly to exceed the ratio $\Delta\rho/\rho$; where ρ stands for density and $\Delta\rho$ is therefore the density difference.

The body is at first immersed at rest within the lower fluid, which is coloured with a dye. A steady upward force is then suddenly applied to it, so that it rises, steadied by suitable guides, attaining a uniform velocity before it breaks through the interface.

As the body emerges from the lower fluid, it is seen to carry with it, in its boundary layer and wake, significant quantities of the lower fluid. Entrainment of clear (upper) fluid into the boundary layer and wake progressively dilutes the dye, with obvious visible consequences.

A succession of photographs enables the various states of mixing to be recorded.

Application

The new technique has been used to study flow behind a wedge and behind a bar (Ilegbusi, 1983). Here, its application to the downstream of a backward-facing step is described.

The configuration has a test-section inlet height of 7.62 cm with the step height of 2.54 cm, thus giving an expansion ratio of 1.5. The axial length from inlet to step is 8 step-heights, while that from step to exit is 10.

Two measures have been adopted which, together, ensure that the boundary layers on the surfaces of the wedge are both thick and turbulent: a wire gauze has been affixed to the leading edge, with its plane at right-angles to the motion; and the step-side wall has been roughened with sandpaper.

Figure 9 shows a succession of photographs taken during the rise of the body. The boundary layers and wake are clearly visible and it is evident that the oscillatory character of the latter has not been completely damped by the wall. This observation lends support to the intermittent nature of turbulence.

RELATION OF THE EXPERIMENTS TO THE THEORETICAL MODELS

Although intended to provide a set of measurements with which the turbulence model predictions could be compared, the observations reported above have had a more far-reaching effect; for they have made inescapably obvious the feature of turbulence which both the k-W and k- ϵ models leave out of account, namely its intermittency.

So universally is this character of turbulence revealed by sufficiently careful measurements that it is surprising only that turbulence models of the present kind predict the mean-flow properties as well as they do. Refinements which still disregard inter-

mittency no longer seem to be worthwhile.

Accordingly, the attention of the authors is now moving towards the use of a two-fluid model (see e.g. Spalding, 1982a, 1982b, 1983) which has the ability to predict intermittency and its effects on the fluctuating and time-mean character of the flow. Reports on the preliminary results of this work are in preparation.

CONCLUSIONS

A revised version of the k-W model of turbulence has been successfully applied to turbulent flow downstream of a backward-facing step. The results have been compared with predictions based on the k-ε model and with the measurements of Kim et al (1978). The k-W and k-ε models perform equally well in simulating the experimental data.

A novel experimental technique of the pulling-through-fluid kind has been described and applied to flow downstream of a backward-facing step. This has made the intermittent nature of the turbulence inescapably obvious, and stimulated new efforts to include this feature in future turbulence models.

ACKNOWLEDGEMENTS

The thanks of the authors are due to Mrs F Oliver for the preparation of the typescript and to Mr FJ King for his assistance with the construction of the apparatus and with the photography.

REFERENCES

- Chiang, C.C., and Launder, B.E., 1980, "On the Calculation of Turbulent Heat Transfer Downstream from an abrupt Pipe Expansion", Numerical Heat Transfer, Vol. 3, pp. 189-207.
- Gibson M.M., and Spalding D.B., 1972, "Two-equation Model of Turbulence Applied to the Prediction of Heat and Mass Transfer in Wall Boundary Layers", ASME 72-HT-15, New York, pp. 1-8.
- Harlow, F.H., and Nakayama, P.I., 1968, "Transport of Turbulence Energy Decay Rate", Los Alamos Sc. Lab., University of California, Report LA-3854.
- Ilegbusi, J.O., 1983, "A revised Two-equation model of Turbulence", PhD Thesis, University of London.
- Ilegbusi J.O. and Spalding D.B., 1983, "An improved version of the k-W model of Turbulence", paper to be presented at the National Heat Transfer Conference, Seattle, USA, July 24-28.
- Jones W.P. and Launder B.E., 1972, "The Prediction of Laminarization with a 2-equation Model of Turbulence", Int. J. Heat and Mass Transfer, 15, p. 301.
- Kim, J., Kline, S.J. and Johnston, J.P., 1978, "Investigation of Separation and Reattachment of a Turbulent Shear Layer: Flow over a Backward-facing step", Report MD-37, Department of Mechanical Engineering, Stanford University.
- Launder B.E. and Spalding, D.B., 1974, "The Numerical Computation of Turbulent Flows", Computer Methods in Applied Mechanics and Engineering, Vol. 3, pp. 269-89.
- Spalding, D.B., 1967, "Heat Transfer from Turbulent Separated Flows", J. Fluid Mech., Vol. 27, p. 97.
- Spalding, D.B., 1969, "The Prediction of Two-Dimensional, Steady, Turbulent, Elliptic Flows", Imperial College, Mech. Engg. Dept., Rep. EF/TN/A/16 also Report NTS/69/23.
- Spalding, D.B., 1981, "A General Purpose Computer Program for Multi-dimensional One and Two-phase Flow", presented at Lehigh IMACS Conference, July, published in Mathematics and Computers in Simulation XIII 1981, pp. 267-276.
- Spalding, D.B., 1982a, "Computers, Turbulence and 2-Phase Flow", CFDU, Imperial College, London, Report CFD/82/3.
- Spalding D.B., 1982b, "Chemical Reaction in Turbulent Fluids", CFDU, Imperial College, London, Report CFD/82/8.
- Spalding, D.B., 1982c, "Representation of combustion in computer models of spark ignition", CFDU, Imperial College, London, Report CFD/82/18.
- Spalding D.B., 1983, "Turbulence Modelling - a State-of-the-art Review", CFDU, Imperial College, London, Report CFD/83/3.
- Tropea, C. and Durst, F., 1981, "Evaluators' Comment", 1981 AFOSR-IFP Stanford Conference on Complex Turbulent Flows.

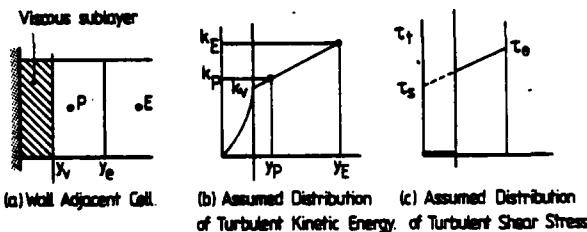


FIGURE 1. Near-Wall Physical Model.

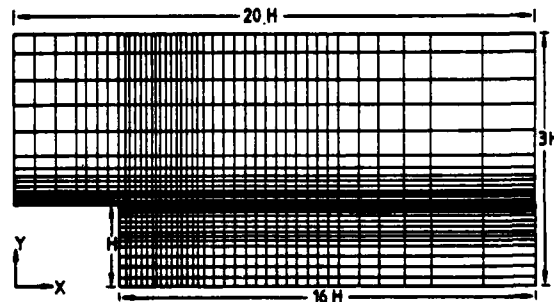


FIGURE 2. Calculation domain and partial layout of the grid network for backward-facing step (Kim et al, 1978).

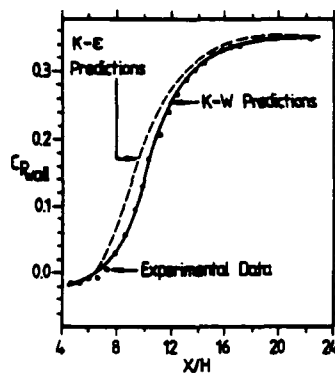


FIGURE 3. Wall-static pressure distribution along the wall opposite a backward-facing step. (Data of Kim et al, 1978).

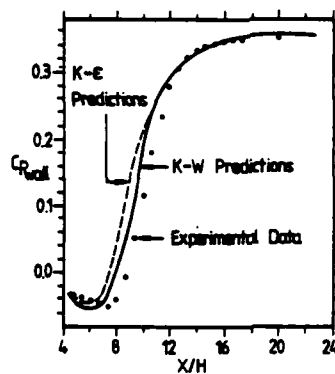


FIGURE 4. Wall-static pressure distribution along the stepped wall (Data of Kim et al, 1978).

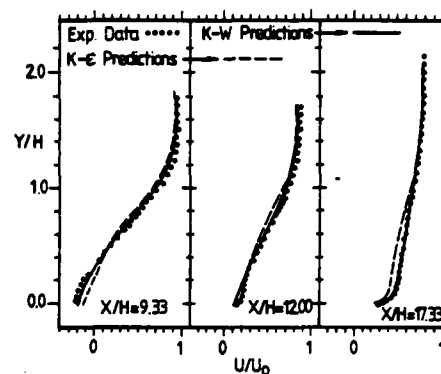


FIGURE 5. Mean-velocity distribution at three streamwise locations (Data of Kim et al, 1978).

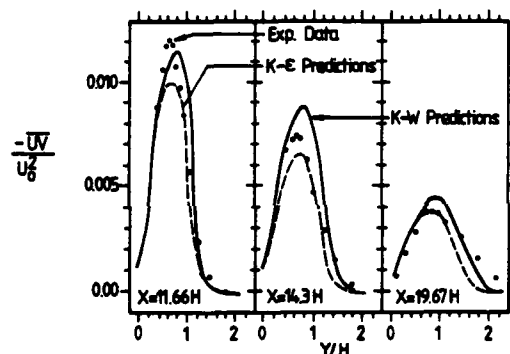


FIGURE 6. Turbulence shear-stress distribution at three streamwise locations (Data of Kim et al, 1978).

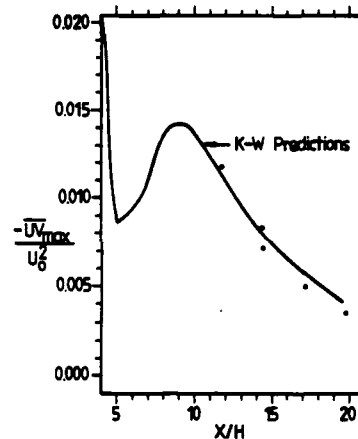


FIGURE 7. Streamwise distribution of maximum shear stress (Data of Kim et al, 1978).

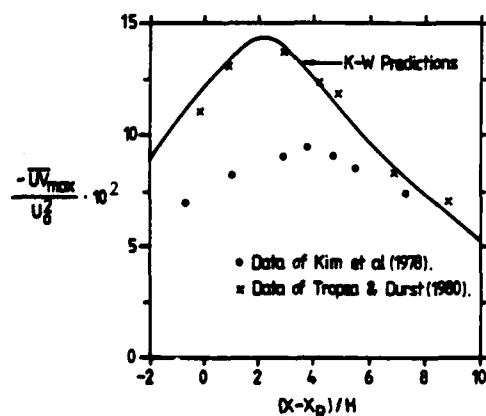


FIGURE 8. Streamwise distribution of maximum shear stress. (X_R = Recirculation length; Predicted value = 7.2H)

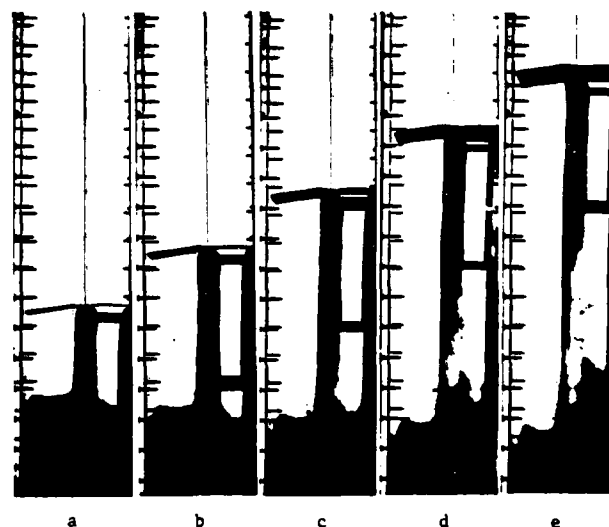


Figure 9. Photographs of Turbulent Flow in a backward-facing step.

IMPROVEMENTS TO THE $k-\epsilon$ MODEL FOR CALCULATIONS OF TURBULENT RECIRCULATING FLOW

A.M. Gooray
Xerox Corporation
Rochester, N.Y. 14644

and

C.B. Watkins and W. Aung
Department of Mechanical Engineering
Howard University
Washington, D.C. 20059

ABSTRACT

Improvements to the $k-\epsilon$ model of turbulence for numerical computation of recirculating flow beyond rearward-facing steps and pipe expansions are presented. The improvements involve sensitizing the models to the effects of streamline curvature and wall-damped pressure-strain interaction, through functionalizing C_μ . A procedure consisting of a sequence of two computational passes is performed to obtain optimal results over the entire flow field. Both the standard and the low-Reynolds number versions of the $k-\epsilon$ model are used in this procedure. Results obtained by applying the improved model to simulate four previous experimental investigations are presented and compared with the experimental data.

NOMENCLATURE

C_p	pressure coefficient
H	step or expansion height
k	turbulent kinetic energy
p	time mean pressure
Re	Reynolds number based on mean inlet velocity and step height for back step or downstream pipe diameter for pipe expansion
u	mean velocity in the streamwise or x direction
u_τ	friction velocity $(= (\tau_w/\rho)^{1/2} = (C_\mu^{1/2} k_p)^{1/2})$
U_o	free-stream mean velocity
x	distance along the main flow direction
x^+	dimensionless value of x $(= u_\tau x/\nu)$
x_R	reattachment distance
y^+	dimensionless value of y $(= u_\tau y/\nu)$

Greek Symbols

δ_u	momentum boundary layer thickness
ϵ	dissipation rate of turbulent energy
ν	kinematic viscosity
ρ	density
τ_w	wall shear stress
p	values at the first near-wall grid in standard $k-\epsilon$ model

w wall values

INTRODUCTION

The numerical computation of turbulent recirculating flow is an important area of contemporary engineering research. Such calculations are far from routine since recirculating turbulent flows are complex fluid-dynamic phenomena. Among two-dimensional recirculating flows, the rearward-facing step is the simplest flow of practical significance in which the reattachment point is not predetermined. Axisymmetric flow through a pipe expansion is qualitatively similar and also is of great practical importance.

The early studies of Abbot and Kline (1962) identify four distinct and dissimilar flow regions or zones downstream of the rearward-facing step. However, the classical division of the flow into two zones is adequate for most engineering studies. Figure 1 shows this classical division. The first zone downstream of the step contains the recirculating pattern of flow near the wall moving upstream and near the dividing streamline moving downstream. In the second zone, beyond reattachment, the flow redevelops to a reestablished turbulent boundary layer.

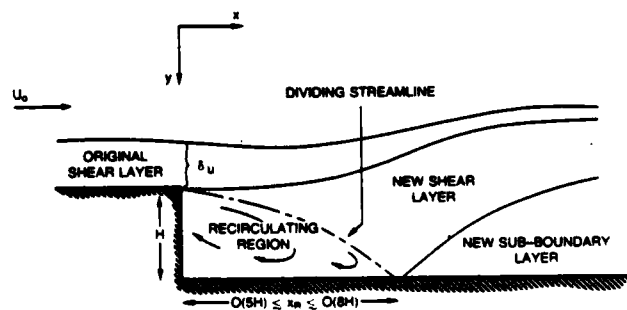


Fig. 1 General Behavior of Reattaching Flow

Recirculating flows in simple two-dimensional or axisymmetric geometries have recently been reviewed by Eaton and Johnson (1980), Aung (1983), and Gooray (1982a). Most studies report reattachment lengths varying from about four-and-one-half to nine step heights downstream of separation. The accurate prediction of reattachment length is an important goal in computations of recirculating flows. Reattachment length can depend on many physical factors. However, in turbulent flow, when reattachment distance is normalized by step height, Reynolds

number has no effect. Narayan, et al. (1974) examined the effects of approach boundary layer thickness on reattachment length. Their experimental results indicate that the effects are slight, particularly where the boundary layer thickness is less than one-and-one-half times the step height. Increasing the level of free stream turbulence has been found to decrease reattachment length (Etheridge and Kemp 1978).

The standard k- ϵ model of turbulence (Launder and Spalding (1974) has been frequently applied to numerical computation of flows beyond rearward-facing steps and sudden pipe expansions, cf Gooray, et al. (1981) and Chieng and Launder (1980). However, Hanjalic and Launder (1980) and Leschziner and Rodi (1981) have cited deficiencies in the standard k- ϵ model and indicated the need for including such effects as normal strains, pressure-strain interaction with wall damping, and streamline curvature. Experimental measurements attest to the importance of these effects (Chandrusda and Bradshaw 1981; Bradshaw 1973).

The present paper describes the numerical computation of flows beyond rearward-facing steps and sudden pipe expansions using an improved version of the standard k- ϵ model of turbulence. The improvements are based on the development of a generalized expression for the C_μ term in the k- ϵ model through incorporation of algebraic Reynolds stress modeling. As a result of this modification, the turbulence model is sensitized to account for the effects of streamline curvature and pressure-strain interaction with wall damping.

In order to further improve the present results in the vicinity of reattachment and beyond, the Jones and Launder (1972) low-Reynolds number version of the k- ϵ model was applied in the redevelopment region downstream of reattachment. A generalized expression for C_μ is also derived to improve the low-Reynolds number model in the redevelopment region. In the case of computations for the present geometries, a two-pass procedure (Gooray, et al. 1982b) is used to patch the two versions of the model together. In this procedure the improved standard k- ϵ model is applied to the entire flow region to predict the reattachment point. Then, with the reattachment point known, a second computational pass is performed with the improved standard k- ϵ model applied upstream of reattachment and the improved low-Reynolds version of the model applied downstream.

In companion studies (Gooray, et al. 1983a; Gooray, et al. 1983b) to the present research, the improved method was applied to predict heat transfer rates for the present geometries and for surface cavities. In these studies generalized expressions were also derived for the turbulent Prandtl number.

TURBULENCE MODEL

The standard k- ϵ model of turbulence is applied to the time-averaged Navier-Stokes equations wherein the Boussinesq approximation is used to express viscous diffusion in terms of an effective viscosity. The effective viscosity is represented as the sum of molecular and turbulent contributions, where

$$\mu_{eff} = \mu + \mu_t \quad (1)$$

The turbulent viscosity μ_t is computed from the turbulent kinetic energy k and its rate of dissipation ϵ , where

$$\mu_t = C_\mu \rho k^2 / \epsilon \quad (2)$$

and C_μ is normally assumed a constant. Transport equations for k and ϵ complete the closure. The resulting set of equations in a form appropriate for the numerical solution of two-dimensional or axisymmetric flow are not reproduced here but are given in a number of sources, cf Gooray, et al. (1981).

Some investigators (Leschziner and Rodi 1981; Humphrey and Pourahmadi 1980) have obtained more realistic turbulence models by deriving functional expressions for C_μ . This approach is followed here with the general outline of the present derivation given. The complete algebraic details are given in

Gooray (1982a). The derivation proceeds from the turbulence model based on algebraic approximations to the Reynolds stress transport equations. Closure of this algebraic stress model with wall damping terms retained, as described by Hanjalic and Launder (1976), results in the following set of algebraic equations for the stress components, $u_i u_j$

$$\frac{u_i u_j}{k} = \frac{\Lambda}{\epsilon} (P_{ij} - \frac{2}{3} P \delta_{ij}) + \frac{\Lambda''}{\epsilon} (P_{ij} - D_{ij}) + \frac{2}{3} \delta_{ij} \quad (3)$$

where D_{ij} involves products of mean gradients and the $u_i u_j$, and where $P = 1/2 P_{ij}$ is the rate of production of turbulent energy (a term in the k transport equation, See Appendix). The following definitions also apply

$$\Lambda' \equiv (1 - C_{s2}) / [\frac{P}{\epsilon} - 1 + C_{s1} - C_{slw} f(l/x_2)] \quad (4)$$

and

$$\Lambda'' \equiv C_{s2w} f(l/x_2) \Lambda' / (1 - C_{s2}) \quad (5)$$

In (4) and (5) the near-wall function $f(l/x_2)$ is modeled so as to take on a value of unity near a wall and zero remote from a wall. It is modeled so as to reflect the importance of both side and bottom walls in the corner region of Fig. 1 so that

$$f(l/x_2) = \frac{1}{C_w} \frac{k^{3/2}}{\epsilon} \left\{ \left[\frac{1}{(D/2-y)} \right]^{1/2} + \left[\frac{1}{x} \right]^{1/2} \right\}^2 \quad (6)$$

where, $1/x = 0$ for $(D/2-y) < d/2$ and D and d are the large and small channel widths or diameters, respectively. The C 's are empirical constants given in Gooray, et al. (1983b) and tabulated in the Appendix.

To include the effects of streamline curvature in the analysis the procedure of Leschziner and Rodi (1981) is followed. Using this procedure, with some degree of approximation (3) are expressed in streamline coordinates (s, n) where coordinate s is along the streamline and n is normal to the streamline. By lengthy algebraic elimination, a unique expression for the Reynolds shear stress, $u_s u_n$ can be obtained. The final expression is

$$-u_s u_n = \frac{2}{3} \frac{k^2}{\epsilon} (\Lambda' \frac{P}{\epsilon} - 1) (\frac{\partial u_s}{\partial n} - \frac{u_s}{R_c}) / S_4 \quad (7)$$

in which,

$$S_4 = 1 + \frac{k^2}{\epsilon^2} \left[8 \Lambda'^2 \frac{u_s}{R_c} S_1 + 4 \Lambda'' S_2 (3 \Lambda' \frac{u_s}{R_c} + \Lambda'' \frac{\partial u_s}{\partial n} + \Lambda'' S_2) \right] \quad (8)$$

and,

$$S_1 = \partial u_s / \partial n + u_s / R_c ; S_2 = \partial u_s / \partial n + 3 u_s / R_c \quad (9)$$

R_c is the radius of streamline curvature.

The expression for C_μ results from comparing (7) with the Boussinesq approximation from the shear stress in streamline coordinates. The result is

$$C_\mu = -\frac{2}{3} \Lambda' (\Lambda' \frac{P}{\epsilon} - 1) / S_4 \quad (10)$$

Equation (10) reduces to the more restrictive formulation of Leschziner and Rodi (1981) if equilibrium of turbulence energy is assumed and if "wall damping" corrections in the pressure-strain terms are ignored, i.e. $P/\epsilon = 1$ and $\Lambda'' = 0$.

Equation (10) was not used with the low-Reynolds number version of the k- ϵ model for the redevelopment region in the two-pass procedure. Instead, a similar but more algebraically complex functionalized relation was obtained from the Reynolds shear expression in x-y

coordinates. This relation is given in the Appendix.

NUMERICAL METHODS

The numerical computations of the present research were carried out using a modified version of the TEACH-T computer code (Gosman 1976). The modifications included replacement of the original hybrid interpolation scheme by the quadratic interpolation or "QUICK" scheme of Leonard (1979), since grid independent results can be obtained more readily with the QUICK scheme. In applying the iterative line solution algorithm of TEACH-T to the QUICK scheme, care must be exercised to avoid convergence difficulties associated with the lack of diagonal dominance of the system of discretized equations. The present research accomplishes this by partial linearization of the source terms in these equations, thus permitting their implicit evaluation.

Conventional wall functions (Lauder & Spalding 1974) were applied in the calculations involving the standard model, although recent research (Johnson and Launder 1982) suggests that further improvement in results can be achieved by modifying the standard wall treatment. Further details of the present numerical methods and the prescribed numerical boundary conditions are given by Gooray (1982a).

RESULTS AND DISCUSSION

The present improvements to the k- ϵ model were applied to the two-dimensional rearward-facing step or pipe expansion flows studied in four experimental investigations by previous researchers (Aung and Goldstein 1972; Moss and Baker 1980; Eaton and Johnson 1980; Zemanick and Dougall 1970). The emphasis herein is placed on comparisons between numerical and experimental hydrodynamic data. Comparisons with heat transfer data and with previous k- ϵ formulations are given by Gooray, et al. (1983b).

Figure 2 shows a typical non-uniform grid distribution used with the improved standard model in the present study. For most of the calculations, the dimensionless coordinate of the first grid point away from the wall y^+ was approximately 15. For a typical non-uniform grid size of 25 by 28, convergence was obtained after about 250 iterations with CPU times on an IBM 3033S averaging around four minutes.

One way of testing the validity of turbulence models is to check the accuracy and consistency of the reattachment length predicted using them. Consequently, in the present study various numerical experiments were undertaken to assess the reliability of predictions of reattachment lengths.

Table 1 summarizes reattachment lengths computed by including the various improvements in the standard

version of the k- ϵ model discussed previously and compares them with experimental values for the experiments simulated. In the table, the expression "partially functionalized C_μ " refers to exclusion of wall damping corrections and imposing the equilibrium of turbulence energy assumption as the formulation of Leschziner and Rodi (1981). "Fully improved C_μ " refers to (10). The results indicate that employing the fully improved expression for C_μ yields reattachment lengths consistent with the experimental data, except for the data of Aung and Goldstein (1972). However, the reason for over prediction of the Aung and Goldstein measured value is explainable. In their experiments, the boundary layer trip was located at eleven trip-heights upstream of the step, which results in the persistence of a higher level of turbulence intensity at the step, thus influencing the length of the recirculating zone. Numerical experiments conducted to simulate this effect tend to substantiate this explanation.

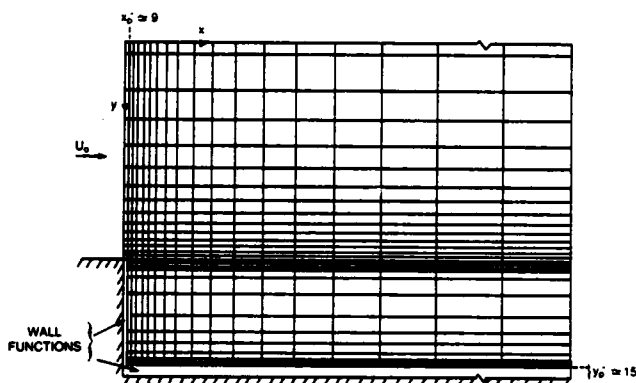


Fig. 2 Typical Grid Distribution

In another numerical experiment, calculations were performed using step heights of four, six and eight millimeters in a typical flow over a rearward-facing step (Aung and Goldstein 1972), for the purpose of examining the effect of step height on reattachment length. The computed value of x_R/H remained constant for all three cases. These results were obtained by using both the original standard k- ϵ model and the fully improved model.

As described in the introductory section of this paper, the second pass of the two-pass procedure employs

TABLE 1. SUMMARY OF FIRST-PASS PREDICTED REATTACHMENT LENGTHS

Geometry	Experimental values of x_R/H	Predictions of Reattachment Length, x_R/H		
		$C_\mu = 0.09$	C_μ functionalized	C_μ partially functionalized
Rearward-facing Step	4.5-5.0 Aung and Goldstein (1972)	4.5	5.8	5.2
Rearward-facing Step	5.7-6.0 Moss and Baker (1980)	4.9	6.0	5.3
Rearward-facing Step	7.97 Eaton and Johnson (1980)	5.1	7.5	5.9
Pipe Expansion	6-9 Zemanick and Dougall (1970)	6.4	8.4	7.1

the low-Reynolds number version of the $k-\epsilon$ model. Since, instead of utilizing wall functions, this version permits computation all the way to the wall, more accurate flow field predictions downstream of reattachment can be achieved with it. (The low-Reynolds number version's performance is poor upstream of reattachment) since it was developed for a boundary-layer flow). The improved downstream results also slightly influence and improve the results upstream of reattachment. Except for Table 1, the data presented herein were all obtained using the two-pass procedure. Table 2 compares, for two flows, the reattachment lengths computed from: a single pass with the improved standard model (as in Table 1), the two-pass procedure, and a three-pass calculation where the reattachment point estimate from the second pass was used to recycle the second-pass. It is fair to say that the single pass reattachment length results are not significantly improved in subsequent passes. Further refinement in Table 2 is impossible since in the terminal pass the interpolated location of the reattachment point does not move beyond a grid line on the fixed grid used.

TABLE 2

EFFECTS OF MULTIPLE PASSES ON REATTACHMENT LENGTH

GEOMETRY	x_R/H	No. of Passes
Rearward-facing Step	5.8	1
	6.1	2
	6.1	3
Pipe Expansion	8.4	1
	8.6	2
	8.7	3

Typical computed velocity profiles are shown in Fig. 3 where they are compared with the experimental data of Moss and Baker (1980). A similar comparison with the data of Eaton and Johnston (1980) is given in Fig. 4. In both cases, the agreement between computation and experiment is fairly good.

Figures 5 and 6 depict typical computed and experimental (Eaton and Johnston 1980) surface pressure coefficient variation in the cross stream (y) and streamwise (x) directions, downstream of the step. Again, the agreement is fairly good.

Figure 7 is a plot of the streamwise variation of the peak value of k (maximum value obtained by traversing the flow in the cross stream direction) for simulation of the Moss and Baker (1980) experiments. As was the case with the mean flow variables, the computed results for this turbulence quantity agree reasonably well with the experimental measurements.

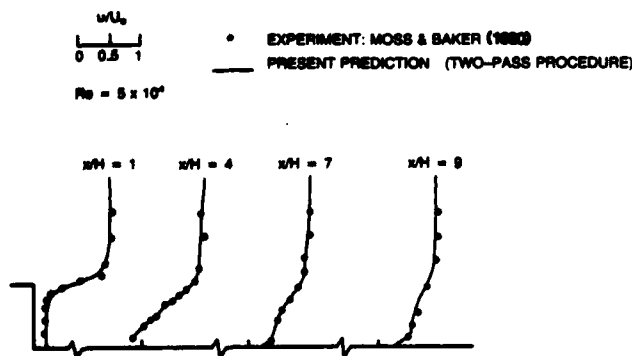


Fig. 3 Streamwise Mean Velocity Downstream of Step

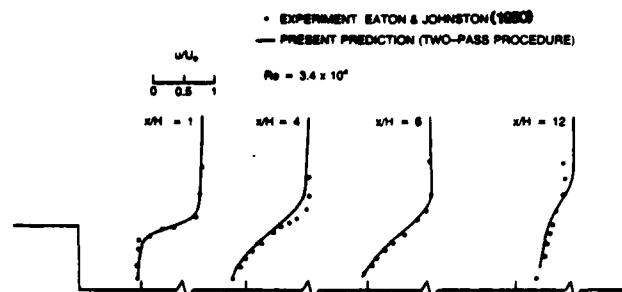


Fig. 4 Streamwise Mean Velocity Downstream of Step

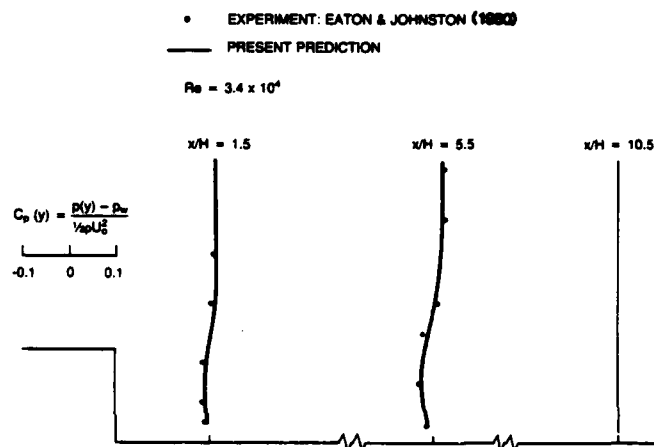


Fig. 5 Cross Stream Pressure Variation

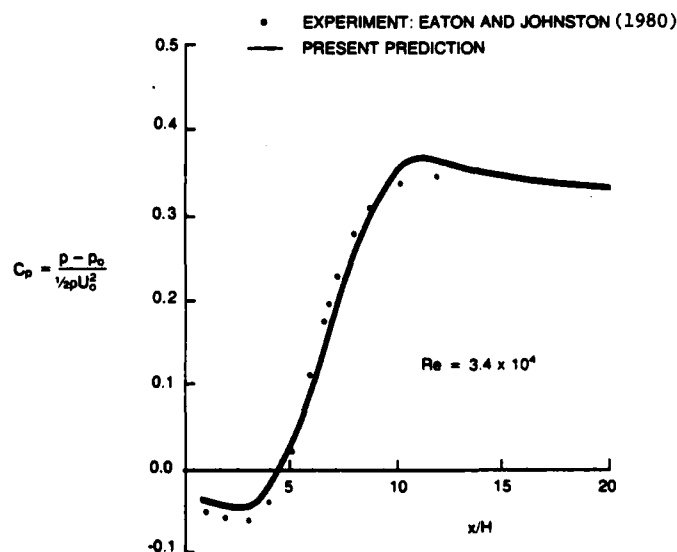


Fig. 6 Streamwise Pressure Variation

CONCLUSIONS

The present results indicate that the $k-\epsilon$ model of turbulence, improved by including the effects of stream-line curvature and wall-damped pressure-strain inter-

action, and applied in a two-pass computational procedure is capable of reasonably accurate recirculating flow predictions. Computed reattachment lengths, mean

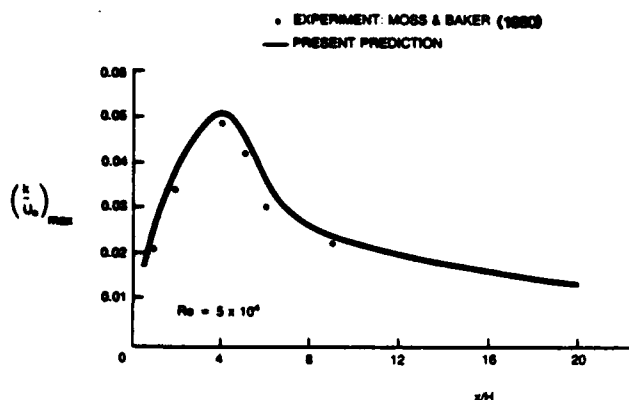


Fig. 7 Streamwise variation of Peak Turbulent Kinetic Energy

flow variables, and turbulent kinetic energy, for flow beyond rearward-facing steps and sudden pipe expansions agree reasonably well with experimental data. Therefore, for engineering calculations in these flows, the $k-\epsilon$ model is a viable alternative to more complex higher-order closure schemes.

The method developed has potential for future refinement, for example, by adding the wall function modifications developed by Johnson and Launder (1982). However, due to the inherent limitations of $k-\epsilon$ representations of turbulence, it is uncertain at this time if the present methodology can also be successfully applied other geometries of engineering interest and further research is needed.

ACKNOWLEDGEMENT

The first two authors were partially supported by the Office of Naval Research, under Contract N0014-80-C-0545, Work Unit No. NR 094-444.

REFERENCES

- Abbott, D.E. and Kline, S.J., 1962, "Experimental Investigation of Subsonic Turbulent Flow over Single and Double Backward Facing Steps", *J. Basic Eng. Trans. ASME*, 84, 317.
- Aung, W., 1983, "Separated Forced Convection", *Proc. ASME-JSME Thermal Eng. Joint Conf.*, Hon., Hawaii, Vol. II, 489.
- Aung, W. and Goldstein, R.J., 1972, "Heat Transfer in Turbulent Separated Flow Downstream of a Rearward-Facing Step", *Isr. J. Technol.*, 10, 35.
- Chandrauda, C. and Bradshaw, P., 1981, "Turbulence Structure of a Reattaching Mixing Layer", *J. Fluid Mech.*, 110, 171.
- Chiang, C.C. and Launder, B.E., 1980, "On the Calculation of Turbulent Heat Transport Downstream from an Abrupt Pipe Expansion", *Numer. Heat Transfer*, 3, 189.
- Eaton, J.K. and Johnston, J.P., 1980, "Turbulent Flow Reattachment: An Experimental Study of the Flow and Structure Behind a Backward-Facing Step", *Report MD-39*, Thermo. Div., Dept. of M.E., Stanford Univ.
- Etheridge, D.W., and Kemp, P.H., 1978, "Measurements of Turbulent Flow Downstream of a Rearward-Facing Step", *J. Fluid Mech.*, 86, 3, 545.
- Gooray, A.M., Watkins, C.B. and Aung, W., 1981, "Numerical Calculations of Turbulent Heat Transfer Downstream of a Rearward-Facing Step", *Proc. 2nd Int. Conf. on Num. Methods in Laminar and Turbulent Flow*, Venice, Italy, Pineridge Press, Swansea U.K., 639.
- Gooray, A.M., 1982a, "Numerical Calculations of Turbulent Recirculating Heat Transfer Beyond Two-Dimensional Back-Steps and Sudden Pipe Expansions", Ph.D. Dissertation, Dept. of M.E., Howard Univ., Wash., D.C., (See also by Watkins, C.B. & Gooray, A.M., same title, Final Report ONR Contract No. N0014-80C-0545, Howard Univ., Aug. 82).
- Gooray, A.M., Watkins, C.B. and Aung, W., 1982b, "k- ϵ Calculations of Heat Transfer in Redeveloping Turbulent Boundary Layers Downstream of Reattachment", *ASME Paper 82-HT-77*, AIAA/ASME Fluids, Plasma, Thermophysical and Heat Transfer Conf.
- Gooray, A.M., Watkins, C.B. and Aung, W., 1983a, "Numerical Calculation of Heat Transfer in Turbulent Recirculating Flow Over an Open Surface Cavity", *Proc. ASME-JSME Thermal Eng. Joint Conf.*, Hon., Hawaii, Vol. III, 79.
- Gooray, A.M., Watkins, C.B. and Aung, W., 1983b, "Computations of Turbulent Heat Transfer Beyond Rearward-Facing Steps and Sudden Pipe Expansions", to be presented at the Natl. Heat Transfer Conf., Seattle, Wash.
- Gosman, A.D., 1976, "The TEACH-T Computer Program Structure", *Flow Heat and Mass Transfer in Turbulent Recirculating Flows - Prediction and Measurement*, Notes from seminar presented at McGill University, Canada.
- Hanjalic, K. and Launder, B.E., 1976, "Contribution Towards a Reynolds Stress Closure for Low Reynolds Number Turbulence", *J. Fluid Mech.*, 74, 593.
- Hanjalic, K. and Launder, B.E., 1980, "Sensitizing the Dissipation Equation to Irrotational Strains", *J. Fluids Eng., Trans. ASME*, 102, 34.
- Humphrey, J.A.C. and Pourahmadi, F., 1980, "A Generalized Algebraic Relation for Predicting Developing Curved Channel Flow with a $k-\epsilon$ Model of Turbulence", *Third Symp. on Turbulent Shear Flow*, Univ. of California, Davis.
- Johnson, R.W. and Launder, B.E., 1982, "Discussion of On the Calculation of Turbulent Downstream from an Abrupt Pipe Expansion", *Numer. Heat Transfer*, 5, 493.
- Jones, W.P. and Launder, B.E., 1972, "The Prediction of Laminarization with a Two-Equation Model of Turbulence", *Int. J. Heat & Mass Transfer*, 15, 301.
- Launder, B.E. and Spalding, D.B., 1974, "The Numerical Computation of Turbulent Flows", *Comput. Methods Appl. Mech. Eng.*, 3, 269.
- Leonard, B.P., 1979, "A Stable and Accurate Convective Modeling Procedure Based on Quadratic Upstream Interpolation", *Comput. Methods Appl. Mech. Eng.*, 19, 59.
- Leschziner, M.A. and Rodi W., 1981, "Calculation of Annular and Twin Parallel Jets Using Various Discretization Schemes and Turbulence Model Variations", *J. Fluids Eng.*, 103, 352.
- Moss, W.D. and Baker, S., 1980 "Re-circulating Flows Associated with Two-Dimensional Steps", *Aeronaut. Q.*, 31, 3.
- Narayana, B., et. al., 1974, "Similarities in Pressure Distribution in Separated Flow Behind Backward-Facing Steps", *Aeronaut. Q.*, 25, 4, 305.

24. Zemanick, P.P. and Dougall, R.S., 1970, "Local Heat Transfer Downstream of Abrupt Circular Channel Expansion", J. Heat Transfer Trans. ASME, 92, 53.

TABLE 2

Values of Empirical Coefficients Used in Turbulence Model

APPENDIX

The functionalized expression for C_μ in the redevelopment region is

$$C_\mu = \frac{\Lambda''}{Ak} \frac{1}{C_\ell} \left[F \left(\frac{A}{\beta} + \frac{C}{A} \right) + \frac{2}{3} k B \left(\frac{1}{\beta A} + \frac{C}{A} \right) + \frac{A}{\alpha} \left(F + \frac{2}{3} k B \right) \right] \quad (11)$$

In the above equation

$$C_\ell = \left[\frac{k}{\epsilon} \frac{v}{y} \left(\frac{1 - C_{s2} + C_{s2w}^f}{\frac{P}{\epsilon} + C_{s1} - C_{s1w}^f} \right) \right]^j \quad (12)$$

where $j=0$ applies to the rearward-facing step and $j=1$ to the pipe expansion. Also in (11)

$$A = - \frac{\Lambda''}{\Lambda' + \Lambda''} ; B = \frac{\Lambda' P}{\epsilon} - 1 ; C = \frac{1 - \beta}{A \alpha \beta} \quad (13)$$

$$E = C_\ell - \frac{1}{2} \frac{2k\Lambda''}{\epsilon A} \frac{\partial u}{\partial y} \left[\frac{A(\alpha + \beta)}{\alpha \beta} + \frac{1 - \beta}{A \alpha \beta} \right] \quad (14)$$

$$F = \frac{1}{3} k \frac{B}{E} \left(\frac{\partial u}{\partial y} \right)^2 \left(\frac{2k\Lambda''}{\epsilon A} \right)^2 \left(\frac{1 + A}{\alpha \beta} + \frac{1 - \beta}{A \alpha \beta} \right) \quad (15)$$

$$\alpha = 1 + 2 \frac{\Lambda' k}{\epsilon} \frac{\partial u}{\partial x} \quad (16)$$

$$\beta = 1 - \frac{2k}{\epsilon} \Lambda'' \frac{\partial u}{\partial y} \quad (17)$$

In the preceding equations

$$P = \nu_t G / \rho \quad (18)$$

where

$$G \equiv 2 \left[\left(\frac{\partial u}{\partial x} \right)^2 + \left(\frac{\partial v}{\partial y} \right)^2 + j \left(\frac{v}{y} \right)^2 \right] + \left(\frac{\partial u}{\partial y} + \frac{\partial v}{\partial x} \right)^2 \quad (19)$$

The values of the empirical coefficients, i.e. the "C's", used in the present calculations are shown in Table 2.

Coefficient	Variable Modeled	Value
C_μ	Turbulent Viscosity	functionalized
C_{s1}	Pressure Strain Effects	2.6
C_{s2}		0.22
C_{s1w}		0.75
C_{s2w}		0.3
C_w	Wall Damping Contributions	2.44

SESSION 19 - RECIRCULATING FLOWS II

R. Dumas - Chairman

Background and Objectives

SS and KP employed the two-equation model for the turbulent kinetic energy k and its dissipation rate ϵ (Launder and Spalding 1974). This model in its standard version does not account for streamline curvature effects. Its predictions overestimated the extent of the recirculation region in the APL CBCC compared with the laser Doppler anemometry (LDA) data of Lightman et al. (1980). This was in contrast to the experience of several previous studies of turbulent recirculating flows where significant underprediction was observed (e.g., see Pope and Whitelaw 1976; Militzer et al. 1977; Gosman et al. 1979; Durst and Rastogi 1980). Also, SS and KP overpredicted the central jet CO_2 mass flow rate required to eliminate the centerline reverse air flow. Another aspect in which the prediction was deficient concerned the axial distribution of the centerline rms axial velocity component.

It is known that the turbulent shear stress and the degree of anisotropy between the normal stresses are very sensitive to streamline curvature (Bradshaw 1973). Thus, the presence of large curvature in the CBCC may have contributed in part to the discrepancy between the measurement and prediction. Accordingly, the main objective of the present study was to examine the influence of curvature corrections in the prediction. Recent availability of extensive isothermal LDA data from UCI, as well as LDA (Lightman et al. 1983) and CO_2 concentration (Bradley et al. 1982) data from APL has facilitated this inquiry.

The calculations with standard $k-\epsilon$ model underpredicted the centerline recirculation length in the UCI CBCC. The introduction of a curvature correction, along the lines suggested by Leschziner and Rodi (1981, hereafter denoted by LR), resulted in only a partial improvement of the prediction. Therefore, the second objective was to examine the impact of the diffusion-equation modification considered in LR. A final objective was the comparison of the predictions with the newer APL data to elucidate the distinctions between the small- and large-scale CBCC.

Scope. This paper deals with the isothermal flow-field predictions. As in SS and KP, present work employs the TEACH computational procedure (Gosman and Ideriah 1976), and the standard features of the numerics thereof. An additional feature considered here is the power-law differencing scheme (Patankar 1980) in place of the hybrid upwind scheme. While both the APL and the UCI configurations were studied, only a limited parametric range of the flowfield conditions investigated is reported.

NUMERICAL COMPUTATIONS

The details concerning the application of the TEACH procedure to the CBCC flowfields are available in Krishnamurthy et al. (1983) and in KP and therefore are not repeated here.

Computational Details

The lower part of Figure 1 shows the present computational domain and the grid-point distribution. The grid consists of 41 axial nodes and 39 radial nodes with a nonuniform spacing in both directions to ensure adequate spatial resolution in flowfield regions with large gradients of the flow variables. The calculations with this grid require about 170,000 words of memory on the CDC CYBER computer. The converged solutions are attained in less than 900 iterations, with each iteration taking less than a second of computer time.

The results herein correspond to the conditions shown in Table 1, with uniform inlet profiles for the mean axial velocity, corresponding to \bar{W}_A in the annular jet and \bar{W}_F in the central jet. The Reynolds number Re_A of the air flow is based upon D and the reference velocity \bar{W}_A in the duct. The Reynolds number Re_F of the CO_2 flow is based upon d and \bar{W}_F .

Turbulence Model

The turbulent eddy viscosity μ_t (the effective viscosity μ_{eff} appearing in the governing equations is given by $\mu_t + \mu$ where μ is the laminar viscosity) in the $k-\epsilon$ model is obtained from $\mu_t = c_\mu \rho k^2/\epsilon$, where ρ is the mass density and c_μ is a constant equal to 0.09.

TABLE 1
FLOWFIELD CONDITIONS

CBCC	Temp. K	\bar{W}_d m/s	\bar{W}_A m/s	Air Mass Flow kg/s $\times 10^{-2}$	Re_A $\times 10^{-5}$	\bar{W}_F m/s	CO_2 Mass Flow kg/s $\times 10^5$	Re_F $\times 10^{-4}$
APL	300	32.91	46.76	200	3.08	51.19	167 (6)	2.44
						136.5	444 (16)	6.50
UCI		7.5	11.68	1.86	0.153			
		15.0	23.35	3.72	0.306	24.82	5.93 (0.213)	0.32

Isotropy is assumed in obtaining k from the rms velocity components, according to $k = (3/2)w^2$, where w is the axial rms velocity component. The inlet profile of k is given by $0.03 \bar{W}_A^2$ for the annular jet and by $0.03 \bar{W}_F^2$ for the central jet (see SS and KP). The required inlet profile for ϵ is specified as discussed below.

Inlet Turbulence-Length Scale. As in KP, we obtain the inlet profile of ϵ from $\epsilon = k^3/2l$, where the inlet turbulence-length scale l is given by $l = \lambda \delta$. Here λ is a specified constant and δ is a characteristic reference length given by $(D_0 - D)/2$ for the annular jet and $d/2$ for the central jet. KP used 0.3333 and 0.5556 for λ . The former value is equivalent to 0.3 used in SS (since they employ $\epsilon = c_\mu k^3/2l$) and the latter value is used in LR. Present results are based upon $\lambda = 0.5556$.

Streamline Curvature Correction. Curvature modifications to turbulence models have been attempted by a number of researchers (e.g., see LR; Humphrey and Pourahmadi 1981; Rodi and Scheuerer 1982; and the references cited in them). A majority of these modifications have been concerned with the $k-\epsilon$ model. Present numerical investigation has introduced a curvature-dependent (and hence nonconstant) c_μ into the standard $k-\epsilon$ model. Following LR, we have

$$c_\mu = -K_1 K_2 / [1 + 8K_1^2 (k/\epsilon)^2 \left(\frac{\partial W}{\partial n} + \frac{W}{R_c} \right) \frac{W}{R_c}],$$

where R_c is the local radius of curvature of a streamline, the subscripts s and n denote the coordinates along and normal to the streamline, and K_1 and K_2 are constants equal to 0.267 and -0.489 respectively. Although an element of arbitrariness in LR is noted by So (1982), the discussion therein emphasizes the utility of the formulation of LR which is retained here. Also, as in LR, the calculations impose an arbitrary positive lower bound of 0.025 on c_μ .

ϵ Modification. We employ the preferential modification of dissipation proposed in LR for recirculating flowfields. Although additional work is necessary in view of the ad hoc nature of this modification, its inclusion throws some light on the observed distinction between the small- and large-scale CBCC.

RESULTS AND DISCUSSION

Pertinent Results from SS and KP

To set the present results in context, we show in Figure 2 the earlier results from SS and KP. With identical values of λ (0.03 in SS), the two (grid A in KP) show good agreement in their degrees of underprediction of the forward stagnation points (FSP) and overprediction of the rear stagnation points (RSP) (the FSP occurs where the central jet loses its forward momentum entirely and the RSP is the usual end of the recirculation zone).

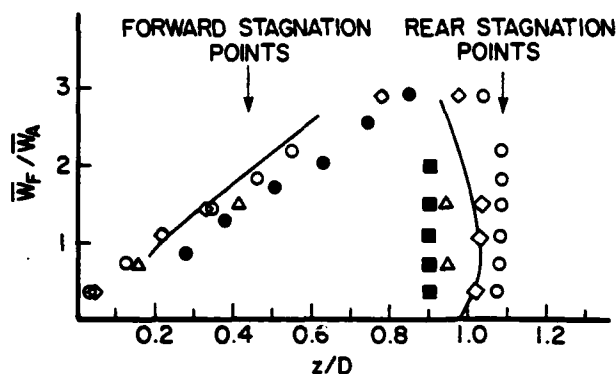


Figure 2. Measured and predicted centerline stagnation points for APL CBCC. \bullet , \blacksquare LDA results: Lightman et al. (1980). The predictions are based upon hybrid upwind differencing scheme. —: SS (39 x 39), $\lambda = 0.3333$; \diamond : KP, grid A (41, 34), $\lambda = 0.3333$; \circ : KP, grid B (41, 34), $\lambda = 0.3333$; \triangle : KP, grid B (41, 34), $\lambda = 0.5556$, with curvature correction. Grid B had more nodes in the annular region than grid A.

The measurements showed that for $\bar{W}_A = 47$ m/s and $\bar{W}_F = 135$ m/s (corresponding respectively to an air mass flow of 2 kg/s and CO_2 mass flow of 16 kg/hr in the APL CBCC), \bar{W} was nonnegative on the centerline. Indeed, the minimum CO_2 mass flow which eliminated the centerline-flow reversal was inferred from the measurements to be 14.7 kg/hr in SS. The predictions, however, indicate the occurrence of the centerline reverse flow (with both stagnation points present) at 16 kg/hr.

Curvature Correction. The preliminary results in KP for streamline curvature correction are shown for two CO_2 flow rates (viz., 4 and 8 kg/hr). It must be noted that the increase in λ from 0.3333 to 0.5556 has masked the effect of the correction. SS and KP have observed, however, that the increase in λ (without the correction) moves monotonically both the stagnation points upstream, thereby resulting in greater underprediction of the FSP. With the correction, the FSP moves farther downstream towards the measured value. The degree of overprediction of the RSP is seen greatly reduced with the larger λ and the curvature correction. Finally, the prediction with the correction has eliminated the centerline-flow reversal at the CO_2 flow of 16 kg/hr.

Unlike the good agreement for the centerline stagnation points, the centerline peak negative mean axial velocity \bar{W}_m was overpredicted with the curvature correction. Since KP had not isolated the influence of λ , hybrid upwind differencing (and the propensity for numerical diffusion therein) and the arbitrarily modified grid B, it was essential to examine the effect of the curvature correction more systematically.

UCI Configuration

Figure 3 compares the present predictions with the measurements. We note that the standard model underpredicts both the stagnation points by about 30%, a result in agreement with other studies. Considerable improvement is seen when the curvature correction to c_{μ} is introduced. However, the stagnation points and \bar{W}_m are still underpredicted. With the ϵ -equation modification in addition to the curvature correction, excellent agreement is seen for $0 < z/D < 1.6$. Farther downstream, the measured recovery is greater than given by all the predictions.

Comparison of rms Velocity. The results seen in Figure 4 do not confirm the good agreement observed for the mean axial velocity. In fact, the predictions are very poor especially for $z/D < 1.3$. The somewhat better agreement seen for $2 < z/D < 3$ is not consistent with the greater disparity noted for the mean velocity. Of course, a major problem in the predictions is the assumption of isotropy, which is known to be invalid in the near wake. Furthermore, good agreement for \bar{W} and poor agreement for w appear to be characteristic of complex turbulent flows (e.g., see Wood and Bradshaw 1982).

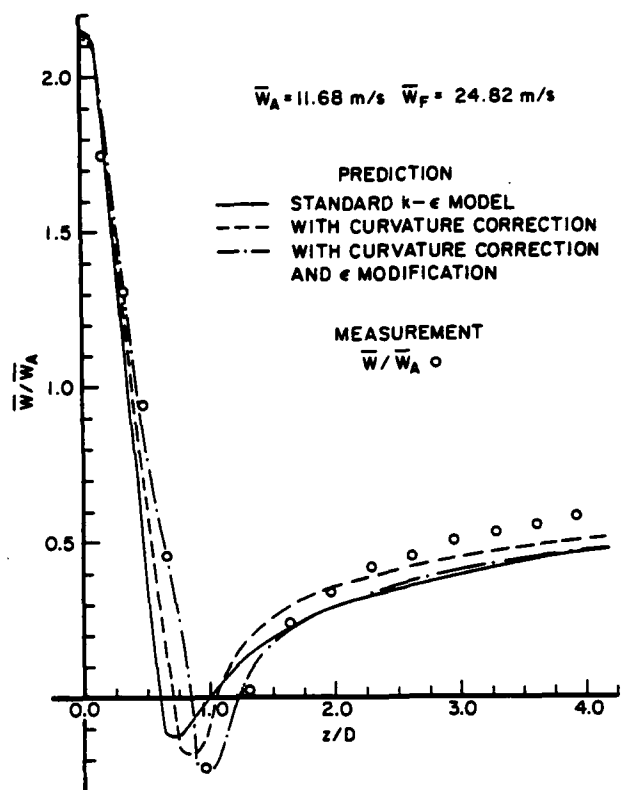


Figure 3. Measured (Brum et al. 1982) and predicted centerline mean axial velocity for UCI CBCC.

Radial Distributions. The predicted radial profiles at four axial locations in Figures 5 and 6 include both the c_{μ} and ϵ modifications. Good agreement is seen and the comparison is particularly striking at the axial

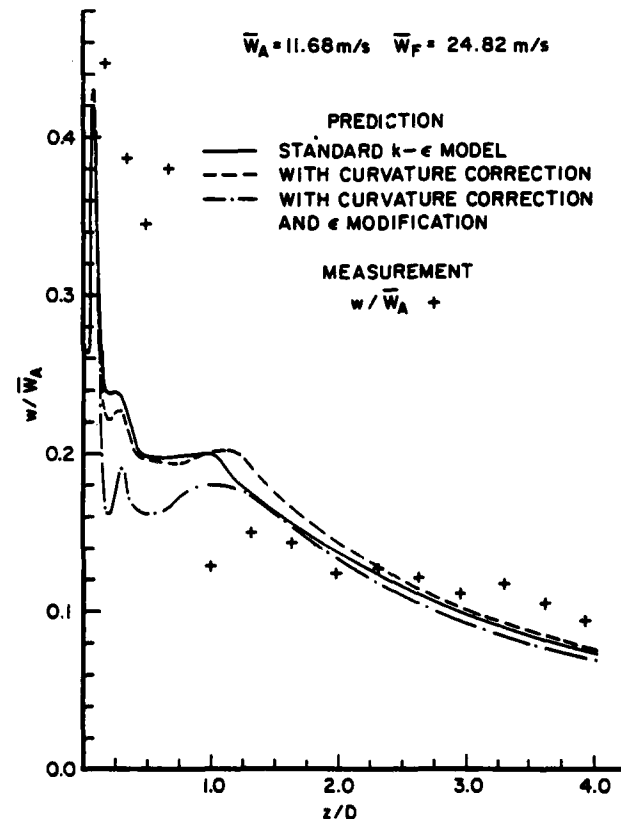


Figure 4. Measured (Brum et al. 1982) and predicted centerline rms axial velocity for UCI CBCC.

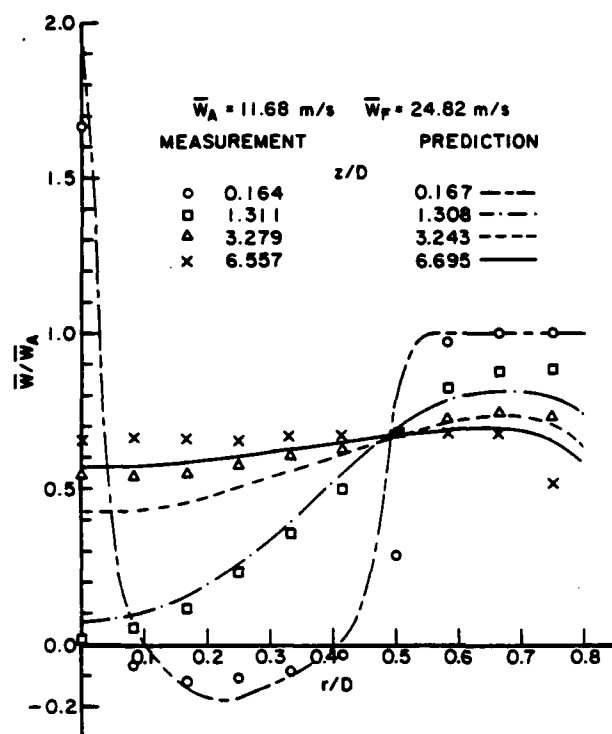


Figure 5. Mean velocity radial profiles for UCI CBCC. Measurement (Brum et al. 1982).

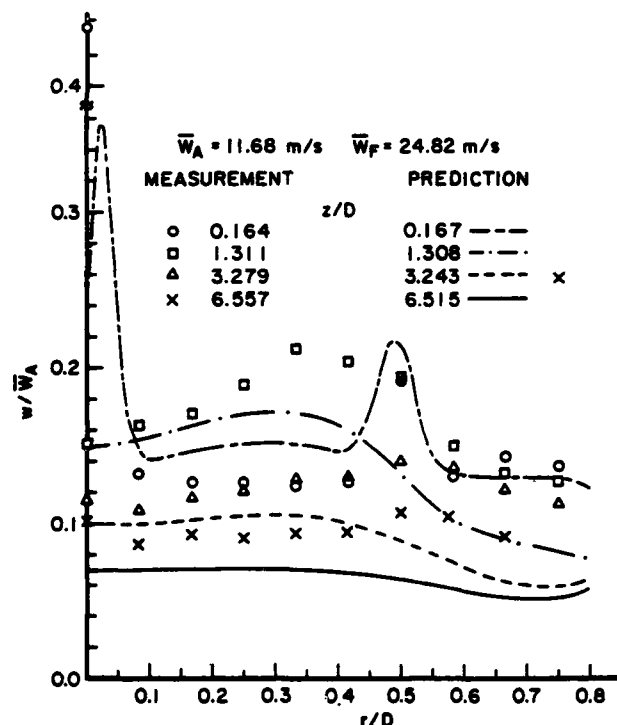


Figure 6. Measured (Brum et al. 1982) and predicted rms velocity radial profiles for UCI CBCC.

location well within the recirculation region ($z/D \sim 0.17$) and at the one near the RSP ($z/D \sim 1.31$).

Flowfield Without the Central Jet. There is a marked difference in Figure 7 where the central jet is absent. The RSP is underpredicted by about 10% but the predicted magnitude and the axial location of \bar{w}_m differ by a factor of 2 from the measured values. The rms component, however, shows better agreement between the prediction and the measurement. This behavior is clearly different from that of the nonzero central jet seen in

Figures 3 and 4. A parametric dependence emerging from these observations appears to emphasize the *ad hoc* nature of the modifications examined.

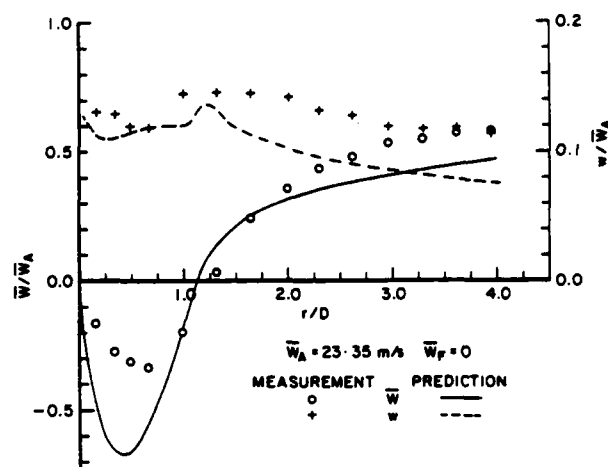


Figure 7. Measured (Brum et al. 1982) and predicted centerline velocity profiles for UCI CBCC.

APL Configuration

The centerline profiles of \bar{w} and w for the large-scale CBCC are seen in Figures 8 through 10 for three different values of \bar{w}_F . The predictions of the standard k- ϵ model and those with the correction for curvature (with and without the ϵ modification) are compared with the LDA data of Lightman et al. (1983).

Measurements. The experimental data for the mean velocity differ from the earlier results (Lightman et al. 1980). The locations of the RSP are at a z/D of 1 instead of 0.9 (see Figure 2). Figure 10 indicates a small region of centerline-flow reversal ($0.75 < z/D < 0.975$). The newer data thus show better agreement with the predictions in SS and KP. Indeed, for the case of zero CO_2 flow, the RSP result of SS even shows a small underprediction.

Figure 9 shows the FSP to occur at $z/D = 0.28$ which more closely agrees with SS and KP in Figure 2 than the earlier experimental data. A crucial difference in the two measurements which contributes to the appreciable difference in the observed FSP location is the central-jet exit configuration. Recent experiments employed a well-designed nozzle, thereby ensuring a uniform \bar{w}_F . Earlier experiments involved a straight tube 15 diameters in length upstream of the exit plane, resulting in a nonuniform \bar{w}_F . While this difference accounts for the decrease in the FSP location, the reason for the increase in the RSP location is not clear.

Predictions. In terms of the present predictions, a number of observations can be made. Calculations with c_μ and ϵ modifications are clearly inferior for all three CO_2 flows in all respects. The fact that the three predictions do not differ significantly for 16 kg/hr reflects that the central jet essentially breaks through the recirculation region and does not suffer the large streamline curvature effects associated with the recirculating flow. At the lower CO_2 flows, the dissipation modification significantly decreases the rms velocity. For the mean velocity, the zero CO_2 case shows good agreement for the RSP and very poor agreement for the velocity profile in the reverse-flow region. For the 6 kg/hr CO_2 case, while the magnitude of \bar{w}_m agrees reasonably well with the measured value, its location, as well as the locations of FSP and RSP, are all considerably overpredicted.

The differences in the predictions based upon standard c_μ and curvature-corrected c_μ are not clear cut. At 16 kg/hr, the uncorrected prediction for \bar{w} is superior, while the correction yields better w prediction, especially near the RSP (as may be anticipated). At 6 kg/hr, the correction again predicts w better near the RSP. For \bar{w} , except for the location of the RSP, the curvature correction appears to show better agreement with the measurement than the standard model. Both calculations underpredict the location of \bar{w}_m ; the magnitude is underpredicted by the standard model and

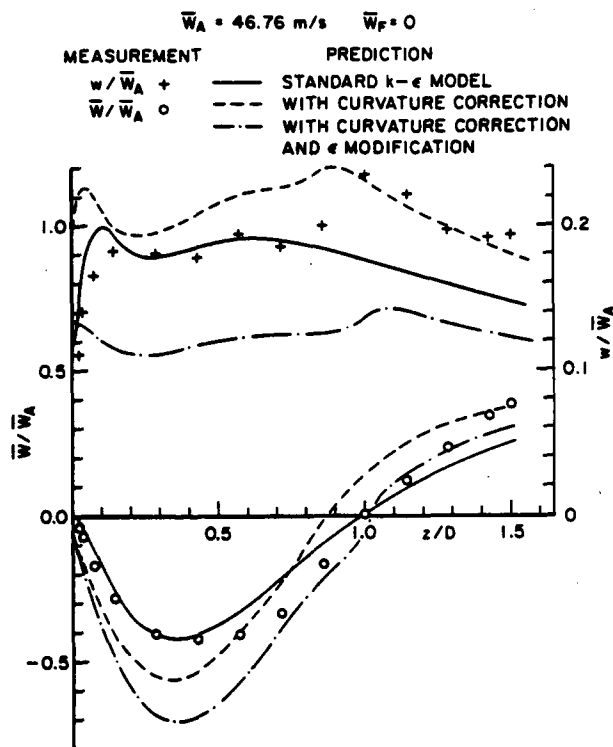


Figure 8. Centerline velocity profiles for APL CBCC. Air flow 2 kg/s and zero CO_2 flow. +, o: Lightman et al. (1983).

overpredicted by the curvature correction. For the zero CO_2 flow case, the uncorrected prediction appears to be better overall.

CO_2 Concentrations. Comparison of the predictions with the measurements (Bradley et al. 1982) of CO_2 mole fractions seen in Figures 11 and 12 leads to similar

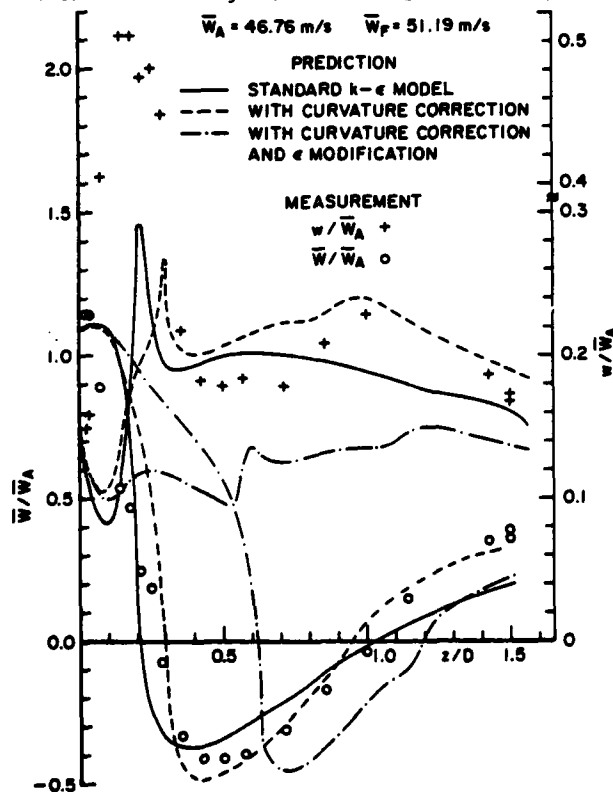


Figure 9. Centerline velocity profiles for APL CBCC. Air flow 2 kg/s and CO_2 flow 6 kg/hr. +, o: Lightman et al. (1983).

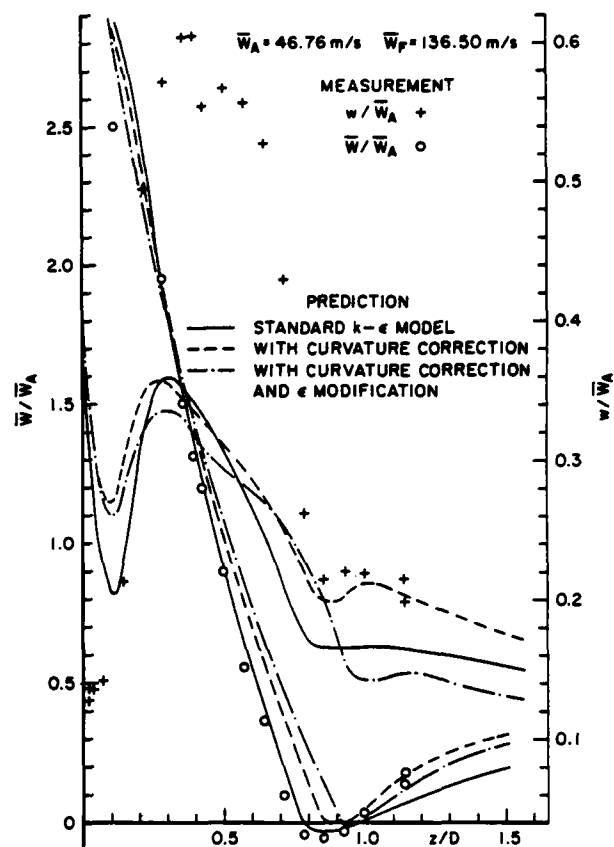


Figure 10. Centerline velocity profiles for APL CBCC. Air flow 2 kg/s and CO_2 flow 16 kg/hr. +, o: Lightman et al. (1983).

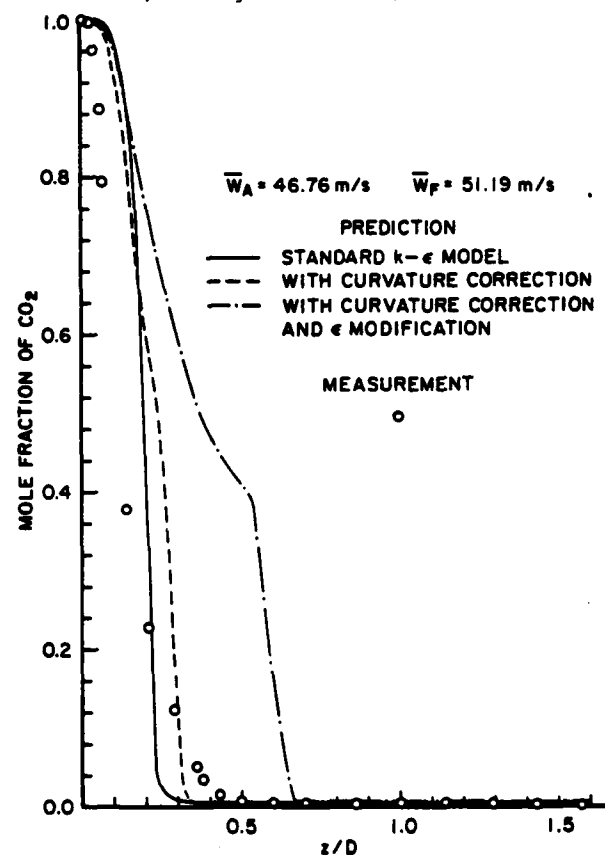


Figure 11. Centerline CO_2 mole fraction for APL CBCC. See Figure 9 for flow rates. o: Bradley et al. (1982).

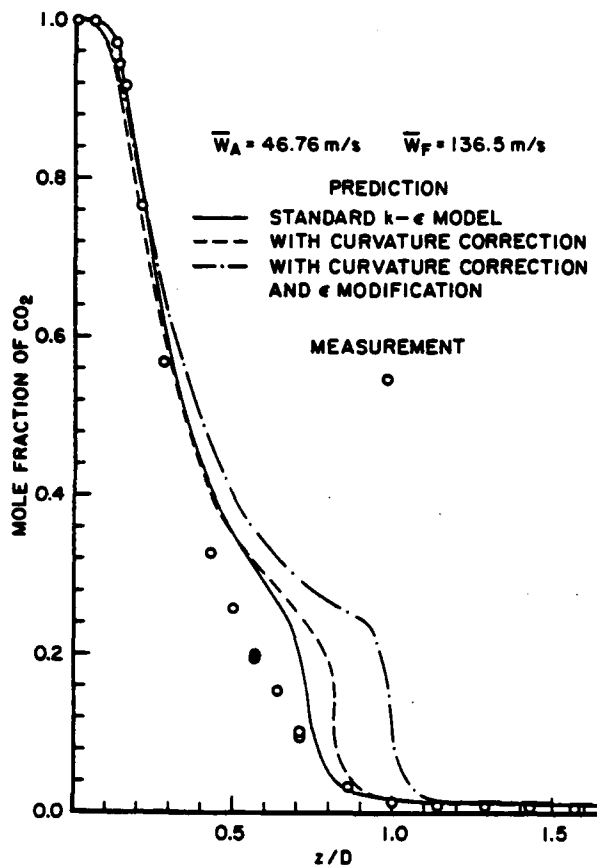


Figure 12. Centerline CO_2 mole fraction for APL CBCC. See Figure 10 for flow rates. O: Bradley et al. (1982).

conclusions regarding the calculations. The prediction of the standard model is clearly superior at the higher CO_2 flow rate. At 6 kg/hr, the standard model and the curvature correction do not appear to differ appreciably from each other. The predictions with the modifications of c_μ and ϵ show much slower decay of CO_2 centerline concentration than do the measurements and other predictions. This behavior is consistent with the significant underprediction of w and the slower decay of W (noted especially for 6 kg/hr in Figure 9).

CONCLUSIONS

The numerical computations based upon the Reynolds-averaged equations and $k-\epsilon$ turbulence model have demonstrated that the CBCC represents a highly complex turbulent flow. The predictions with the standard $k-\epsilon$ model, as well as ad hoc modifications to account for the streamline curvature and the preferential influence of normal stresses on dissipation are compared with the measurements in a large-scale and a small-scale CBCC. Significant differences between the predictions are noted, especially for the dissipation-equation modification which results in much greater dissipation in the large-scale CBCC. The introduction of the curvature-corrected c_μ results in better predictions for certain flowfield regions but exhibits a dependence on the annular and central flow rates.

ACKNOWLEDGMENTS

This research was sponsored by Air Force Wright Aeronautical Laboratories, Aero Propulsion Laboratory, Wright-Patterson Air Force Base, Ohio, under Contract No. F33615-82-K-2252. Dr. W. M. Roquemore is the Air Force Technical Monitor. Authors express their appreciation to him, to Dr. A. J. Lightman (UDRI) and to Professor G. S. Samuelson (UCI) for making available the APL and UCI experimental data. The assistance of Ms. K. Glaser and Ms. J. Memering in data reduction and of Ms. A. Cochran, Ms. A. Kite, and Ms. L. Knox in the preparation of the manuscript is gratefully acknowledged.

REFERENCES

- Bradley, R.P., Roquemore, W.M., Stutrud, J.S., Reeves, C.M. and Obringer, C.A. 1982, "Second Data Set for APL Research Combustor," Air Force Wright Aeronautical Laboratories, Aero Propulsion Laboratory.
- Bradshaw, P. 1973, "Effects of Streamline Curvature on Turbulent Flow," AGARDograph No. 169.
- Bradshaw, P. 1975, "Review-Complex Turbulent Flows," J. Fluids Engng. 97, 146.
- Brum, R.D., Ikioka, L.M. and Samuelson, G.S. 1982, "Assessment of Candidate Combustor Configurations as Test Beds for Modeling Complex Flow," ASME-82-HT36.
- Durst, F. and Rastogi, A.K. 1980, "Turbulent Flow Over Two-Dimensional Fences," in *Turbulent Shear Flows 2*, Springer-Verlag.
- Gosman, A.D., Khalil, E.E. and Whitelaw, J.H. 1979, "The Calculation of Two-Dimensional Turbulent Recirculating Flows," in *Turbulent Shear Flows 1*, Springer-Verlag.
- Gosman, A.D. and Ideriah, F.J.K. 1976, "TEACH-T: A General Computer Program for Two-Dimensional Turbulent Recirculating Flows," Imperial College, Department of Mechanical Engineering Report.
- Humphrey, J.A.C. and Pourahmadi, F. 1981, "A Generalized Algebraic Relation for Predicting Developing Curved Channel Flow with a $k-\epsilon$ Model of Turbulence," in *Proc. Turbulent Shear Flows 3 Symp.* Davis, California.
- Krishnamurthy, L. 1981, "Isothermal Flowfield Predictions of Confined Coflowing Turbulent Jets in an Axisymmetric Bluff-Body Near Wake," AFWL-TR-81-2036.
- Krishnamurthy, L. and Park, S.O. 1983, "Isothermal Predictions of Recirculating Turbulent Flowfields of Confined Dual Coaxial Jets Behind an Axisymmetric Bluff Body," ASME-83-FE-14.
- Krishnamurthy, L., Wahrer, D.J. and Cochran, H.S. 1983, "Similarity Considerations of Isothermal Turbulent Recirculating Flowfields in Axisymmetric Bluff-Body Near Wakes," AIAA-83-1203.
- Krishnamurthy, L., Park, S.O., Wahrer, D.J. and Cochran, H.S. 1983, "Laser Diagnostic Development and Measurement and Modeling of Turbulent Flowfields of Jets and Wakes," AFWL-TR-83-2044, Part II.
- Launder, B.E. and Spalding, D.B. 1974, "The Numerical Computation of Turbulent Flows," *Comp. Meth. Appl. Mech. Engng.* 3, 269.
- Leschziner, M.A. and Rodi, W. 1981, "Calculation of Annular and Twin Parallel Jets Using Various Discretization Schemes and Turbulence-Model Variations," J. Fluids Engng. 103, 352.
- Lightman, A.J., Richmond, R.D., Magill, P.D., Krishnamurthy, L., Roquemore, W.M., Bradley, R.P., Stutrud, J.S. and Reeves, C.M. 1980, "Velocity Measurements in a Bluff-Body Diffusion Flame," AIAA-80-1544.
- Lightman, A.J., Magill, P.D. and Andrews, R.J. 1983, "Laser Diagnostic Development and Measurement and Modeling of Turbulent Flowfields of Jets and Wakes," AFWL-TR-83-2044, Part I.
- Miltzer, J., Nicoll, W.B. and Alpay, J.A. 1977, "Some Observations on the Numerical Calculations of the Recirculation Region of Twin Parallel Symmetric Jet Flow," in *Proc. Turbulent Shear Flows 1 Symp.* University Park, Pennsylvania.
- Patankar, S.V. 1980, *Numerical Heat Transfer and Fluid Flow*, McGraw-Hill.
- Pope, S.B. and Whitelaw, J.H. 1976, "The Calculation of Near-Wake Flows," J. Fluid Mech. 73, 9.
- Rodi, W. and Scheuerer, G. 1982, "Calculations of Curved Shear Layers with Two-Equation Turbulence Models," SFB80/T/211, University of Karlsruhe.
- Roquemore, W.M., Bradley, R.P., Stutrud, J.S., Reeves, C.M., and Krishnamurthy, L., 1980, "Preliminary Evaluation of a Combustor for Use in Modeling and Diagnostics Development," ASME-80-GT-93.
- So, R.M.C. 1982, Discussion on Reference 14, J. Fluids Engng. 104, 263.
- Sturgess, G.J. and Syed, S.A. 1982, "Widely Spaced Co-Axial Jet, Diffusion-Flame Combustor: Isothermal Flow Calculations Using the Two-Equation Turbulence Model," AIAA-82-0113.
- Wood, D.H. and Bradshaw, P. 1982, "A Turbulent Mixing Layer Constrained by a Solid Surface. Part 1. Measurements Before Reaching the Surface," J. Fluid Mech. 122, 57.

AN EXPERIMENTAL INVESTIGATION OF THE TURBULENT SHEAR FLOW DOWNSTREAM OF A NORMAL FLAT PLATE
WITH A LONG SPLITTER PLATE-MODIFICATION OF A MODEL

R. Ruderich and H. H. Fernholz

Bermann-Föttinger-Institut für Thermo- und Fluidodynamik
der Technischen Universität Berlin

ABSTRACT

Flow visualization studies and measurements by means of pulsed-wire and hot-wire techniques lead to a better understanding of the complex turbulent flow downstream of a normal plate with a long splitter plate in its plane of symmetry.

INTRODUCTION

The flow downstream of a normal flat plate with a sharp beveled edge and a long splitter plate in its plane of symmetry has been investigated. The simple flow model which is generally accepted to describe this nominally two-dimensional flow consists of a separated free shear layer, a recirculation region adjacent to the normal plate, followed by a reattachment region downstream of which the attached shear layer develops into a turbulent wall boundary layer. Despite the importance of this flow configuration for the investigation of relatively steady and defined recirculation regions with reattachment of the flow, it has received relatively little attention compared with the flow downstream of a step (e.g. Eaton & Johnston 1980), that over a fence perpendicular to a wall (e.g. Ranga Raju et al. 1976) or finally with the important problem of the effects of wake splitter plates on bluff-body flow (e.g. Apelt & West 1975).

The flow configuration consisting of a normal plate and a "long" splitter plate avoids upstream effects of the free wake behind short splitter plates and is not influenced by the state and thickness of an approaching boundary layer. In the limit of decreasing fence height one obtains a blunt plate where a separation bubble may form at the leading edge with reattachment of the flow downstream*. Separation of the free shear layer is fixed.

All experimental investigations mentioned above, run into considerable difficulties when profiles of mean velocity and turbulence quantities in the recirculation and reattachment region have to be measured. This is due to a high level of turbulence and to mean and instantaneous reverse flow. So we have supplemented hot-wire with pulsed-wire measurements both in the flow and at the wall, the latter to check surface-fence measurements and to obtain both mean and fluctuating values of skin friction.

The present investigation has three principle aims: to improve our understanding of the rather complex flow downstream of a normal plate with a long splitter plate, to investigate the importance of three-dimensional effects in a nominally two-dimensional flow, and to gather more reliable measurements (Chandrsuda & Bradshaw 1981) of mean velocity, turbulent intensities and skin friction in the recirculation region.

* Earlier experiments of these latter flow configurations were performed, for example by Arie & Rouse (1956), Ranga Raju & Garde (1970), Smits (1982), and by Billier & Cherry (1981) and Kiya et al. (1982).

Since turbulent intensities often reach very high levels it was interesting to compare profile data with the two techniques. In flow regions with high levels of turbulence and little or no reverse flow hot-wire data, which were corrected according to Tutu & Chevray (1975) or Vagt (1979), agreed very well with pulsed-wire measurements.

More emphasis will be laid on a description of the separated shear layer and on the flow downstream of reattachment in a further paper.

EXPERIMENT

The experiments were carried out in an open-return suction tunnel described by Fernholz et al. (1982) with a working section measuring $0,49 \text{ m} \times 0,50 \text{ m}$ and a length of about 6 m. The normal plate (fence) was steel with a smoothly polished surface having a thickness of 6 mm with the edges machined to a sharp 30° bevel. The fence height h_f above the splitter plate (6 mm thick and 1.50 m long) was 22 mm, providing an aspect ratio of about 22. The total height h of the fence was 50 mm which gives a blockage ratio h/H of 0.10. The base pressure coefficient $C_{pb} = (P_b - P_\infty) / (0.5 \rho_\infty u_\infty^2)$ for this flow configuration is -1.044 and agrees very well with data reported by Smits (1980). No end plates were used in this experiment, since both plates span the tunnel width.

The undisturbed upstream velocity distribution was uniform with a maximum deviation of $\pm 1\%$ from the mean velocity on the tunnel centerline. The turbulence level across the tunnel is approximately constant with $T_u = 0.6\%$. Symmetry of the flow on both sides of the splitter plate which was located on the centerline of the working section was confirmed by pressure measurements in front of the normal plate at different vertical and spanwise positions.

DISCUSSION OF THE FLOW PATTERN

Flow visualization studies were performed using kerosene smoke illuminated by a rotating 3 watt laser beam (Mending & Fiedler 1980) in different planes of the flow field and by using a suspension of lampblack in paraffin on the splitter plate and on the tunnel side walls.

The separation of the flow at the sharp edge of the fence leads to the development of a free shear layer, the flow structure of which becomes finer with increasing Reynolds number as is shown in figures 1 a ($Re_{hf} = 1.5 \times 10^3$) and 1 b ($Re_{hf} = 1.4 \times 10^4$). The flow direction is from left to right, and the photograph was taken in the center xy-plane. The scale in flow direction is about 14 fence heights. The subsequent discussion refers only to flow conditions at the higher of the two Reynolds numbers where the flow structure shows no apparent further changes with Reynolds number. Details of the flow structure as we have seen it at different times and Reynolds numbers are collected in a schematic picture of instantaneous streamlines by Smits (1980).

Figure 2 shows the oil-flow picture on the splitter plate revealing a spanwise almost straight limiting streamline on the wall (cf. the skin friction distribution in figure 5), a recirculation region, a reattachment region and, furthest downstream, the upstream region of the developing wall boundary layer. Reattachment occurs within a range $x/h_f = 17.2 \pm 0.5$ ($x/h = 7.6$) on the centerline of the splitter plate, curving upstream towards the side walls. This is in excellent agreement with Smits (1982). The reattachment process appears to be unsteady, having a low frequency, however. Wall streamlines converge slightly towards the centerline in the recirculation region (seen from downstream) and are fairly parallel downstream of reattachment.

The description of the flow pattern deals first with the center region, covering approximately 40 % of the span, and then with the corner regions adjacent to the tunnel side walls (schematic flow picture figure 3). Immediately downstream of the fence and next to the surface of the splitter plate the flow is in downstream direction, forming a vortex with "triangular" shape and the axis in spanwise direction. It extends from the normal plate down to a limiting wall streamline - sometimes called reattachment - on the splitter plate. This vortex was visualized at lower Reynolds numbers (not shown here).

The limiting streamline separates the fluid from upstream and from downstream and connects an attachment (saddle) point (Hunt et al. 1978) at $x/h_f = 3.2$ on the centerline of the splitter plate with two "standing" vortices located at $x/h_f = 3.2$ and $z = \pm 9.10 \cdot h_f$, respectively. According to de Brederode & Bradshaw (1972) who observed such vortices downstream of a step they are nodal points of separation and finite circulation. Each vortex has its axis normal to the splitter plate close to the surface and it is curved in downstream direction as one moves away from the wall. The sense of rotation is such that the flow is in downstream direction on the side of the vortex where it faces the tunnel side wall. Downstream of the limiting streamline there is a large recirculation region with a length L of approximately 14 fence heights. At the junction of the normal plate with the boundary layer of the tunnel side wall a rather "flat" horseshoe vortex is formed (see oil flow pattern in figure 4 and a very similar streamline picture in front of a circular cylinder shown by Baker 1980) with its legs on the upper and lower side of the splitter plate, respectively. Immediately downstream of the normal plate the flow on the side wall is in downstream direction over the full height of the normal plate until it meets with a separation point in the corner of the side wall and the splitter plate. Downstream of this separation point we observe the elliptical footprint of a vortex with its axis normal to the side wall which transports fluid from downstream along the corner and again in downstream direction along a line inclined at about 10° against the xz -plane. Side-wall vortex and corner vortex merge with the horseshoe vortex and interact with the separated shear layer thus causing a complex three-dimensional flow field in the corner region, which makes the reattachment region on the splitter plate curve in upstream direction.

We were surprised to notice that the influence of the corner vortex on the three-dimensional behaviour of the flow in the recirculation region became even greater when the height of the fence was reduced to half its original height ($h_f = 11$ mm). The corner vortex disappeared completely, however, when the normal plate was removed and only the splitter plate with a blunt edge (6 mm thick) remained. In this latter case the wall streamlines were parallel and the flow nominally two-dimensional over 80 % of the span (the oil-flow photograph is not shown here).

MEASUREMENTS ON THE SPLITTER PLATE

Before we discuss the spanwise behaviour of the flow further, measurements of static pressure, mean and fluctuating skin friction along the centerline are presented in figure 5. Static pressure was measured by means of pressure tappings in the wall (0.60 mm diameter) and a Statham pressure transducer. It is plotted in the form of a pressure coefficient $c_p = (p_{st} - p_{ref}) / 0.5 \rho u_\infty^2$

where u_∞ is the velocity in the undisturbed flow and p_{ref} approximately p_∞ .

As may be seen from figure 5 separation occurs upstream of the pressure minimum and reattachment just before the pressure reaches a plateau with a slight negative gradient further downstream (cf. Smits 1982). It is interesting to note that we find the same trend as Smits (1980) in that the distance along the splitter plate to the point of maximum pressure made dimensionless by the bubble length increases versus blockage ratio.

Skin friction was measured by means of a pulsed-wire wall probe (Ginder & Bradbury 1973) which was calibrated against a Preston tube in a ZPG turbulent boundary layer. The skin-friction distribution, plotted as $\bar{c}_f = 2\tau_w / \rho u_\infty^2$, shows a change from positive to negative at $x/h_f = 3.2$, a minimum of $-3 \cdot 10^{-3}$ in the range $10 \leq x/h_f \leq 12$ and reattachment at about $x/h_f = 17$. Downstream of reattachment there is a sharp increase of c_f reaching a plateau with a value $c_f = 3.8 \cdot 10^{-3}$ at about $x/h_f = 36$ which is only 30 % higher than the value in the recirculation region. Probability density distributions of c_f show a high narrow Gaussian distribution at separation and a wider (double that width) distribution at reattachment.

The distribution of the r.m.s. value of the fluctuating skin friction coefficient shows a flat peak in the region of minimum mean skin friction and then falls to a roughly constant value.

Although we have seen that there must be strong three-dimensional effects in the junction of the splitter plate with the side wall, the flow in the center region of the splitter plate should be approximately two-dimensional according to de Brederode (1975) if the aspect ratio is larger than ten. A check of this statement appeared to be necessary and may be carried out best by measurements of flow quantities in spanwise direction, such as skin friction, mean and fluctuating velocities. Figure 6 shows the spanwise skin-friction distribution in the recirculation region ($x/h_f \approx 9$), just downstream of reattachment ($x/h_f \approx 24$) and in the developing boundary layer ($x/h_f \approx 46$). As may be expected from the oil-flow pattern there is hardly any variation over ± 20 % of the span on both sides of the centerline in the middle of the recirculation region. This is due to the fairly straight separation and reattachment lines in this region which assure uniform starting conditions for the upstream near-wall flow in the separation bubble. Since the reattachment line is further upstream towards the tunnel side wall, the reverse-flow region is shorter and skin friction downstream correspondingly higher, increasing to a value 30 % higher than on the centerline. This considerable increase towards the side wall is reduced to about 14 % twenty-two fence heights further downstream showing an almost uniform spanwise distribution. In all three cases the symmetry of the skin-friction distribution is remarkable.

In spanwise direction we have also measured the distribution of the mean velocity \bar{u} and the Reynolds normal stress u'^2 in the recirculation region ($x/h_f \approx 9$) at two positions above the splitter plate (figure 7). The mean velocity values are constant within ± 5 % over the width of the c_f -plateau, falling to 60 % of the centerline value at the $y/h_f = 0.66$ position and increasing to 160 % at $y/h_f = 2.2$ towards the side walls. Reynolds normal stress u'^2 was within ± 5 % of the centerline value over most of the span, decreasing only in the outer flow by 30 % towards the side walls. Again the distributions are almost symmetrical but they confirm strong three-dimensional effects off the centerline.

These measurements were supplemented by distributions of the reverse-flow factor χ (e.g. Simpson 1976) defined as the ratio of the number of samples of the instantaneous velocity u smaller than zero and the total number of samples in percent, measured here by a pulsed wire. Figure 8 shows that χ is approximately 92 % in the center part of the flow close to the splitter plate with a sharp decrease to 78 % near the side walls. This indicates that about 20 % of the samples outside the center region represent flow in downstream direction.

PROFILE MEASUREMENTS

Velocity measurements were performed using the pulsed-wire technique (Bradbury & Castro 1971) with a probe designed by Dengel & Vagt (1982) taking 5000 to 10 000 samples per data point, and conventional hot-wire anemometry (Prosser) with single normal and X-wire probes. The integration time was about 50 seconds. Figure 9 shows measurements of mean and fluctuating velocities by means of both techniques and the respective χ -distribution obtained by the pulsed wire plotted against y/h_F . These profiles are characteristic of the flow in the recirculation region.

In figure 10 the same data are plotted against y in a semi-logarithmic scale in order to enlarge the near-wall region. Mean velocity measurements (single normal wire) are presented in raw and corrected form (open and full circles) in the outer region and in corrected form in the recirculation region where the flow was unidirectional, indicated by values for χ of approximately 10 or 100 %. Corrections for the high turbulence level, carried out according to Vagt (1979), were at most 11 %. The correction procedure was slightly modified, however, in that w'^2 was substituted by u'^2 . In the flow region where χ was between 0 and 100 % differences between hot-wire and pulsed-wire measurements (open triangles) were large, with hot-wire data too high due to rectification effects and the large transverse fluctuations. The cross-over point where the mean velocity component \bar{u} changes sign is located at $y/h_F = 1.50$.

The importance of the reverse flow factor lies in the fact that it determines the range within which hot-wire measurements, both for \bar{u} and u'^2 , are erroneous, i.e. where hot-wire anemometry measures systematically wrong. Hot-wire r.m.s. values (full squares) were corrected according to Tutu & Chevray (1975) - although this is correct only under very specific conditions - and showed very good agreement with pulsed-wire data (full triangles) up to turbulence levels of 42 %. As for the velocity level in the recirculation region, the mean velocity reaches 30 % of the maximum velocity in the shear layer and the r.m.s. value is about 50 % of the maximum and almost constant over y .

Figure 11 shows the dimensionless distance above the splitter plate to the point of zero velocity which could be easily determined from the pulsed-wire measurements. The maximum value is $(y/h_F)_{u=0}^{max} = 1.7$ at $x/h_F = 4$. Smits (1982) suggested this to be a length characteristic of the height of the recirculation region. It is slightly dependent on blockage ratio.

Furthermore we have plotted maximum values of the two Reynolds normal stresses u'^2 and v'^2 and of the Reynolds shear stress $u'v'$ as a function of x/h_F along the centerline. The distributions u'^2 , v'^2 and $(u'v')_{max}$ are furthest away from the wall at $x/h_F \approx 9$ which is roughly in the middle of the recirculation region where-as the maximum location of $(u'^2)_{max}$ is just downstream of separation. The minimum locations of $(u'^2)_{max}$ and $(v'^2)_{max}$ are close to the reattachment region. The distribution of $(-u'v'/\bar{u}^2)_{max}$ is comparable with data in similar flows provided by Chandrsuda & Bradshaw (1981). We have chosen \bar{u}_{max} as the normalization velocity which reaches its maximum velocity difference $\Delta \bar{u} = \bar{u}_{max} - \bar{u}_{min}$, the ratio of $(-u'v'/(\Delta \bar{u})^2)_{max}$ would have been smaller - 0.012 - and even closer to 0.01 found for the curved mixing layer.

Figure 12 shows mean velocity measurements through the recirculation and reattachment regions into the redevelopment region. Full circles indicate pulsed-wire data and open circles hot-wire data, the latter being corrected for high turbulence effects according to Vagt (1979), with w'^2 again being substituted by u'^2 .

The uncertainty range of these measurements varies according to the flow region but it is estimated to be 5 % in the recirculation region and 2 % outside of it. Mean velocity measurements were also plotted in inner layer coordinates u^+ against y^+ (figure 13) and indicate the dip below the standard logarithmic law which Bradshaw & Wong (1972) showed to persist to a downstream distance of about fifty step heights and which is explained by the "constant" length scale of the free mixing layer which has not adjusted to the length scale of the wall bounded flow (Chandrsuda & Bradshaw 1981). Skin friction was measured by a pulsed-wire wall probe which

is independent of the logarithmic law. There is a clear development towards a logarithmic law of the wall in downstream direction but there is no agreement yet 30 step heights downstream of reattachment. Measurements agree, however, with the linear law in the viscous sub-layer, even relatively close to reattachment. From 24 step heights downstream of reattachment measurements of skin friction performed by means of a Preston tube, a surface fence and a pulsed-wire wall probe are within 10 % of each other. The constants used for the logarithmic law were $K = 0.40$ and $B = 5.10$ (Coles 1956).

CONCLUSIONS

The flow downstream of a normal plate with a long splitter plate shows highly three-dimensional features in the vicinity of the tunnel side walls despite an aspect ratio of twenty-two. Between the normal plate and reattachment the flow is rather complex due to relatively large, though weak vortices and due to a large recirculation region. Although time-averaged measurements and wall-flow visualization provide a plausible insight into the flow, it is arguable how well this agrees with the time flow picture which one observes when looking at the flow by means of instantaneous flow visualization. For future work two problems are of special interest: (a) What is the spanwise extent and influence of the vortices one observes in the shear layer downstream of the sharp edge of the normal plate and (b) what is the influence of a periodically forming, large turbulence pattern (vortex?) on the movement of the reattachment line.

REFERENCES

- Apelt, C.J., and West, G.S., 1975, "The effects of splitter plates on bluff-body flow in the range $10^4 < R < 5 \times 10^4$ ", *J. Fluid Mech.*, 71, 145-160.
- Arie, M., and Rouse, H., 1956, "Experiments on two-dimensional flow over a normal wall", *J. Fluid Mech.*, 1, 129-141.
- Baker, C.J., 1980, "The turbulent horseshoe vortex", *J. Wind Engng. Indust. Aero.*, 6, 9-23.
- Bradbury, L.J.S., and Castro, I.P., 1971, "A pulsed-wire technique for velocity measurements in highly turbulent flows", *J. Fluid Mech.*, 49, 657-691.
- Bradshaw, P., and Wong, F.Y.F., 1972, "The reattachment and relaxation of a turbulent shear layer", *J. Fluid Mech.*, 52, 113-135.
- De Brederode, V.A.S.L., 1975, "Three-dimensional effects in nominally two-dimensional flow", Ph.D.thesis, Imperial College, London University.
- Chandrsuda, C., and Bradshaw, P., 1981, "Turbulence structure of a reattaching mixing layer", *J. Fluid Mech.*, 110, 171-194.
- Dengel, P., and Vagt, J.-D., 1982, "A comparison between hot-wire and pulsed-wire measurements in turbulent flows", *Bermann-Föttinger-Institut für Thermo- und Fluidodynamik, TU Berlin, Institutsbericht 01/82*.
- Eaton, J.K., and Johnston, J.P., 1980, "A review of research on subsonic turbulent flow reattachment", *AIAA Paper 80-1438*.
- Fernholz, H.E., Graham, J.M.R., and Vagt, J.D., 1982, "A wind tunnel for unsteady turbulent shear flows: Design and flow calculation", *Z.F.W.*, 6, 408-416.
- Ginder, R.B., and Bradbury, L.J.S., 1973, "Preliminary investigation of a pulsed-gauge technique for skin friction measurements in highly turbulent flows", *ARC Paper 34448*.
- Hillier, R., and Cherry, N.J., 1981, "Pressure fluctuations under a turbulent shear layer", III. *Symp. Turbulent Shear Flows*, Davis, 16.23 - 16.29.
- ^{*} value, $1.39 \bar{u}_m$, at $x/h_F = 8.95$. Had one used the maximum

Hunt, J.C.R., Abell, C.J., Peterka, J.A., and Woo, H., 1978, "Kinematical studies of the flow around free or surface-mounted obstacles; applying topology to flow visualization", *J. Fluid Mech.*, 86, 179-200.

Kiya, M., Sasaki, K., and Arie, M., 1982, "Discrete vortex simulation of a turbulent separation bubble", *J. Fluid Mech.*, 120, 219-244.

Mensing, P., and Fiedler, H., 1980, "Eine Methode zur Sichtbarmachung von hochturbulenten Luftströmungen mit großen Reynoldszahlen", *ZfV* 4, 366-368.

Ranga Raju, K.G., and Garde, R.J., 1970, "Resistance of an inclined plate placed on a plane boundary layer in a two-dimensional flow", *J. Basic Eng.*, 92, 21-31.

Ranga Raju, K.G., Loeser, J., and Plate, E.J., 1976, "Velocity profiles and fence drag for a turbulent boundary layer along smooth and rough flat plates", *J. Fluid Mech.*, 76, 383-399.

Simpson, R.L., 1976, "Interpreting laser and hot-film anemometer signals in a separating boundary layer", *AIAA J.*, 14, 124-126.

Smits, A.J., 1980, "A visual study of a separation bubble", *Proc. Inter. Symp. on Flow Visualization*, Bochum, pp. 204-208.

Smits, A.J., 1982, "Scaling parameters for a time averaged separation bubble", *J. Fluids Eng.*, 104, 178-184.

Tutu, N.K., and Chevray, R., 1975, "Cross-wire anemometry in high intense turbulence", *J. Fluid Mech.*, 71, 785-800.

Vagt, J.D., 1979, "Hot-wire probes in low speed flow", *Progress in Aerospace Sci.*, 18, 271-325.

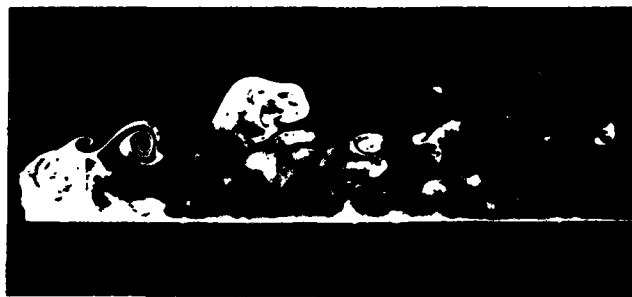


Fig. 1a Flow in the centerline xy-plane
($Re_{hf} = 1.5 \times 10^3$)



Fig. 1b Flow in the centerline xy-plane
($Re_{hf} = 1.4 \times 10^4$)

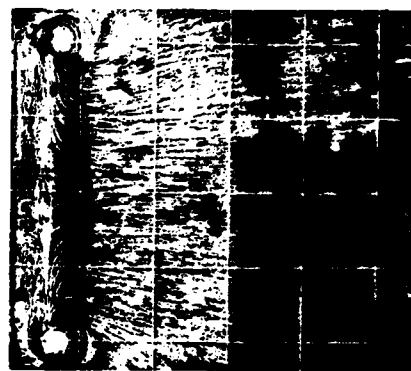


Fig. 2 Oil flow on the splitter plate
($Re_{hf} = 1.4 \times 10^4$)

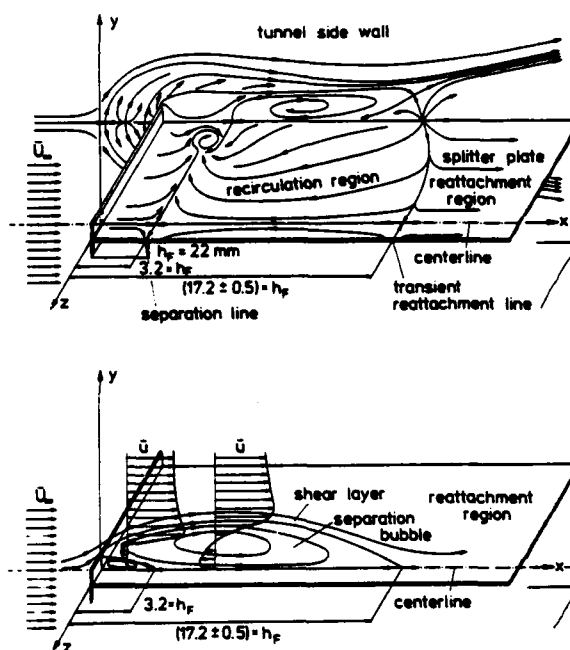


Fig. 3 Schematic diagram of the mean flow downstream of a normal plate with a long splitter plate.
($Re_{hf} = 1.4 \times 10^4$)

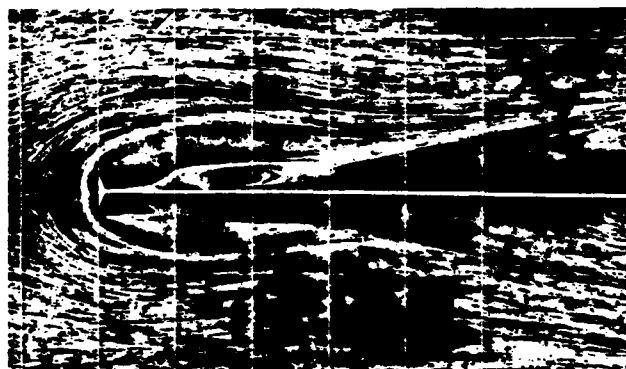


Fig. 4 Oil flow on the tunnel side wall
($Re_{hf} = 1.4 \times 10^4$)

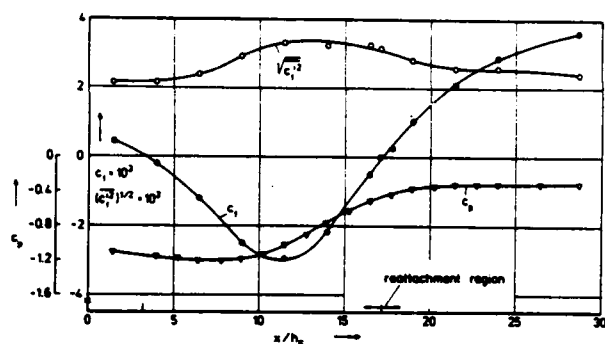


Fig. 5 Distributions of static pressure, mean skin friction, and skin-friction intensity downstream of a normal plate along the centerline of the splitter plate ($Re_{h_F} = 1.4 \times 10^4$)

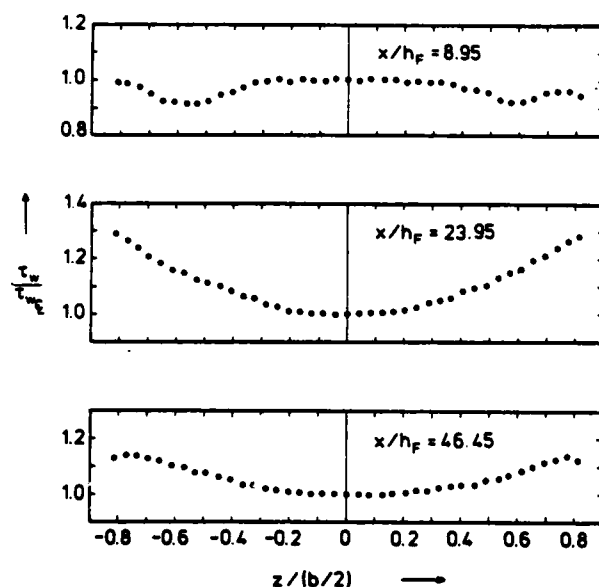


Fig. 6 Skin friction distribution in spanwise direction on the splitter plate at different positions x/h_F along the centerline ($b/2 = 245$ mm, $h_F = 22$ mm, Preston tube 1 mm dia.)

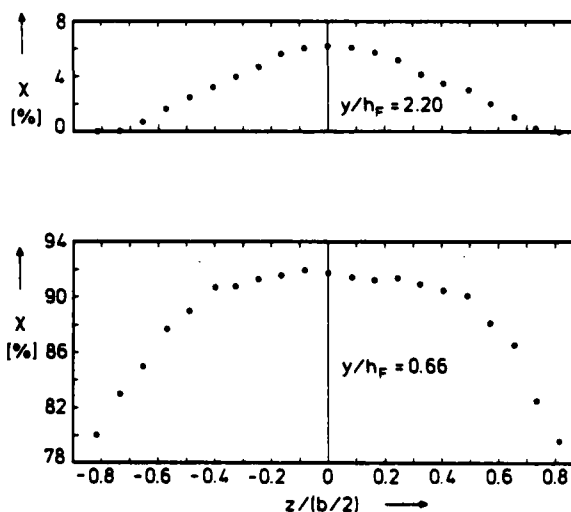
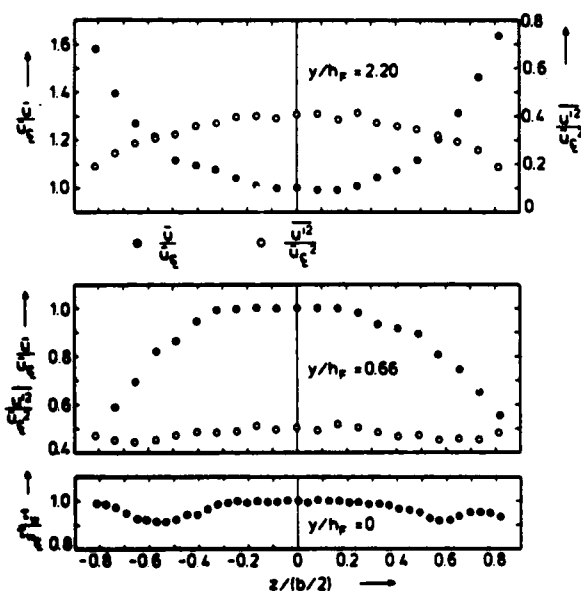


Fig. 8 Distribution of the reverse flow parameter X in spanwise direction at $x/h_F = 8.95$ and two positions y above the splitter plate ($Re_{h_F} = 1.4 \times 10^4$)

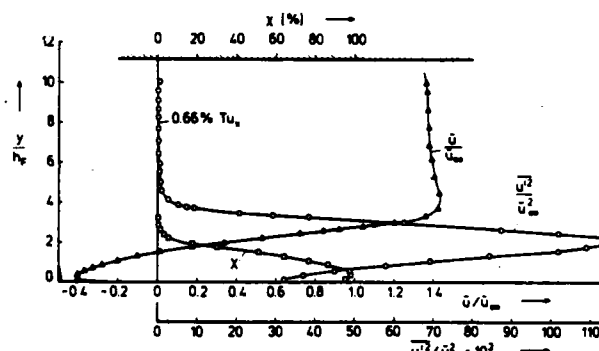


Fig. 9 Mean velocity and Reynolds normal stress distributions in the separation bubble ($x/h_F = 8.95$, $Re_{h_F} = 1.4 \times 10^4$; pulsed-wire and hot-wire measurements)

Fig. 7 Distribution of mean skin friction, mean velocity and Reynolds normal stress in spanwise direction at $x/h_F = 8.95$, the latter at two positions above the splitter plate ($Re_{h_F} = 1.4 \times 10^4$)

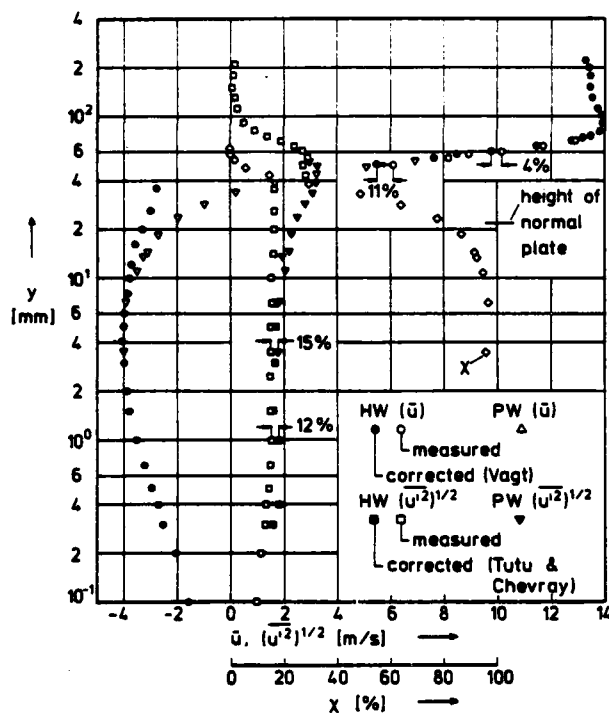


Fig. 10 Distribution of mean velocity \bar{u} , fluctuating velocity $(u'^2)^{1/2}$, and reverse flow factor X in the recirculation region (centerline, $Re_{h_F} = 1.4 \times 10^4$, $x/h_F = 8.95$)

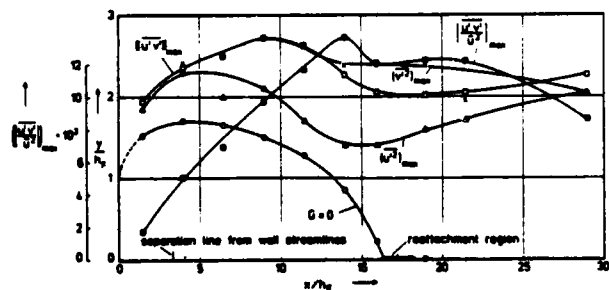


Fig. 11 Location of maximum values of Reynolds shear and normal stresses downstream of a normal plate along the centerline of a splitter plate ($Re_{h_F} = 1.4 \times 10^4$)

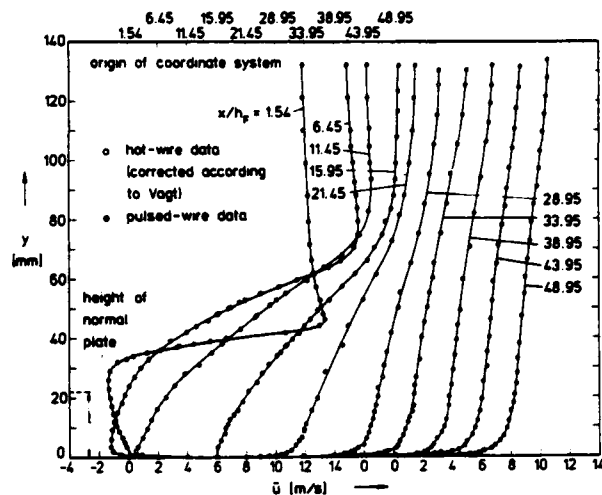


Fig. 12 Mean velocity distribution downstream of the normal plate along the centerline of the splitter plate ($Re_{h_F} = 1.4 \times 10^4$)

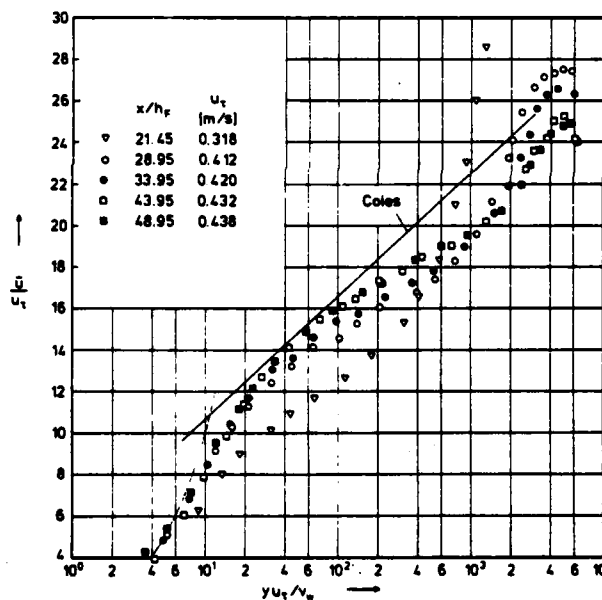


Fig. 13 Comparison of the law of the wall with velocity profiles in a wall-bounded turbulent shear flow downstream of reattachment ($Re_{h_F} = 1.4 \times 10^4$). u_τ from pulsed-wall probe

UNSTEADY MEASUREMENTS IN SEPARATED-AND-REATTACHING FLOWS

R. Hillier, M.E.M.P. Latour and N.J. Cherry*

Department of Aeronautics, Imperial College,
London, England

ABSTRACT

This paper presents preliminary details of an experimental study of a series of two-dimensional separated and reattaching flows, where separation is forced to occur at a sharp edge in each case. Data are confined to cases with a non-turbulent approach stream. Measurements include spectral data for streamwise velocity fluctuations in the irrotational region at the shear layer edge, which provide a convenient measure of the large scale shear layer structure, and also smoke flow visualisations which illustrate the various phases in the irregular shedding of vorticity from the bubble.

NOMENCLATURE

C_p, C_{ps}, C_{pR}	Pressure coefficient; values at separation and reattachment respectively.
\tilde{C}_p	Reduced pressure coefficient, $\frac{C_p - C_{ps}}{1 - C_{ps}}$
D	maximum model thickness
L_R	time mean reattachment length determined from surface oil flows.
U_s	Separation velocity = $\sqrt{1 - C_{ps}}$ U_∞ .
X	Streamwise distance measured from separation.

INTRODUCTION

Despite the large number of experiments which have been conducted in separated-and-reattaching flows there is still relatively little known about the unsteady flow structure for even the simplest of two-dimensional geometries. This largely results from difficulties with instrumentation, since conventional hot-wire anemometry is not possible in a large part of the flow field. Measurements using pulsed wire (e.g. Moss and Baker, 1980) or laser anemometry (Etheridge and Kemp, 1978) or surface probes for instantaneous surface skin friction or flow direction (Westphal, Eaton and Johnston, 1981; Castro and Dianat, 1982) are still scarce and often may be prone to their own particular difficulties of operation or interpretation. A knowledge of the unsteady processes is essential, however, both to improve the physical understanding of the flow phenomena and also to provide comparative data against which can be tested calculation methods. As part of the current programme of work it is intended eventually to apply the discrete vortex method to the various configurations studied here, since this has already had some success (e.g. Ashurst, 1979; Kija et al, 1982) in calculating reattaching flows.

The purpose of the present study was to investigate the various configurations shown in Figure 1 where the

angle of the separating shear layer is varied. In earlier papers Roshko and Lau (1965), amongst others, demonstrated a good collapse of mean pressure data (in appropriate reduced co-ordinates) between a variety of two-dimensional configurations, and Mabey (1971) suggested that the dominant frequencies for the irregular shedding of vorticity from the reattachment zone correlate well when normalised by the time averaged reattachment length. The intention here was to explore further the similarities in flowfield between the various configurations.

Some data for these geometries have already been presented and will be reviewed only briefly. For geometry A, the rectangular separation body, Hillier and Cherry (1981) observed a significant low frequency motion best revealed as a flapping of the shear layer near separation and a modulation of shedding characteristics at reattachment; a broad band shedding from reattachment of vortical structures with an average spacing of about 65% of the mean reattachment length; and fairly low spanwise correlations for pressure fluctuations. Preliminary measurements on models B and E, reported by Cherry, Hillier and Latour (1982) showed that the low frequency fluctuations persist for these configurations as well, with a characteristic time scale in which shear layer disturbances could convect several bubble lengths. Other workers have also reported them, notably Eaton and Johnson (1981) for the rearward facing step and also McGuinness (1978) for an internal flow and Kija, Sasaki and Arie (1982) for essentially the same configuration as the present model A, so that a low frequency motion appears to be an integral part of cavity flows.

EXPERIMENTAL EQUIPMENT AND PROCEDURE

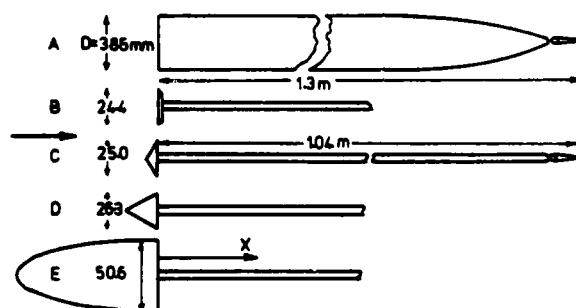


Figure 1. THE TEST GEOMETRIES

* Present address: Central Electricity Research Laboratories.

The models investigated here are the sequence shown in Figure 1, with shear layer separation occurring at a sharp two-dimensional edge in each case. These models comprise the rectangular forebody of geometry A and several forebody/splitter-plate combinations which are designed to vary the initial separation angle of the shear layer from 90° (normal flat plate B), through 60° and 30° (C and D), to a zero separation angle rearward step E formed by a 2 : 1 length/thickness ratio semi-ellipse. In each case the total model length was considerably greater than the mean bubble length so that periodic shedding, through interaction of the shear layers from either edge of the forebody, is prevented. Model A was terminated by a streamlined trailing edge and all the models were fitted with a trailing edge flap for circulation control so that asymmetric pressure distributions top-to-bottom could be generated. Unless stated otherwise all data presented here are for the symmetrical zero incidence case however, achieved by first locating the model at as close to zero incidence as possible, and then using the flap to minimise any residual pressure difference between several pairs of matching tappings (top-to-bottom) in the recirculation region. Generally data can be expected to be accurate within about ± 0.015 in C_p . The experiments were conducted in nominally smooth stream conditions ($< 0.1\%$ turbulence intensity) with end plates employed for all tests; both the present experiments and also Brederode's (1975) work have shown that absence of end plates can cause a serious artificial extension of the bubble by ventilation of the tunnel wall boundary layer into the cavity region. Model A spanned the 0.61m width of a 0.61m x 1.02m wind tunnel, giving a solid blockage of 3.79%. The data presented for this model were obtained at an aspect ratio of 13.2 (span between end plates/model thickness) but tests showed no systematic variations in data for aspect ratios down to 9. The test Reynolds number was 3×10^4 based upon the model thickness, giving a laminar shear layer at separation with a momentum thickness of order 0.0015D. Transition in the shear layer was completed by about 0.35D or 7% of the mean bubble length (see Hillier and Cherry 1981). The data for the remaining models were taken in a tunnel of 0.91m x 0.91m section, enabling higher aspect ratios to be employed. Fairly comprehensive checks on aspect ratio effects (Cherry, 1982; Latour, 1983) suggest that these are unlikely to be very significant at the values employed. Geometries B, C and D again produce very thin laminar boundary layers, but with early subsequent transition; they were tested at a Reynolds number (based upon model thickness) of 3.8×10^4 . For the rearward step model, geometry E, natural transition would occur on the forebody. This generally appeared to occur asymmetrically top-to-bottom and caused, or was coupled with, asymmetry in splitter plate pressure distribution and hence a mean circulation about the model. This problem was eliminated by the use of trip wires on the forebody for all tests; the turbulent boundary layer separation data have not yet been fully analysed but give a probable momentum thickness θ at separation of 0.8mm (0.5% L_R).

MEAN PRESSURE DATA

Table 1 presents the measured data for the mean pressure at separation C_{ps} (i.e. strictly the extrapolation of the splitter plate pressure distribution to $X = 0$) and at reattachment C_{pr} (both uncorrected for blockage), together with the time-mean reattachment length from separation on the centre-line L_R (normalised by the model or forebody thickness D) as determined from surface oil flows.

TABLE 1

Model	% solid blockage (based on D)	C_{ps}	C_{pr}	L_R/D	\bar{C}_{pr}
A	3.8	-0.74	-0.18	4.89	0.32
B	2.5	-0.62	-0.1	8.84	0.32
C	2.5	-0.58	-0.07	8.00	0.32
D	2.5	-0.55	-0.05	5.26	0.32
E	5	-0.39	0.00	3.0	0.28

Observation of similarity in pressure distribution shape in the bubble region has led to various attempts to produce a more universal correlation of mean pressure data (e.g. Norbury and Crabtree (1955), Roskho and Lau (1965)). Following Roshko and Lau (1965), in Figure 2 the reduced pressure recovery coefficient \bar{C}_p is plotted against X/L_R ,

$$\text{where } \bar{C}_p = \frac{C_p - C_{ps}}{1 - C_{ps}}$$

and X is measured from separation.

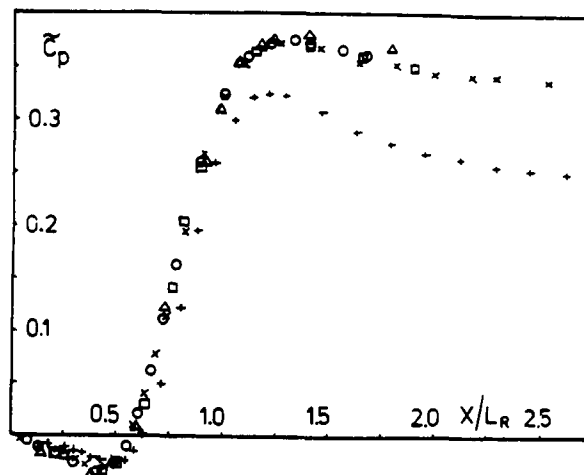


Figure 2. DISTRIBUTION OF REDUCED PRESSURE \bar{C}_p .
MODEL A, Δ ; B, \circ ; C, \square ; D, \times ; E, $+$.

This produces an excellent correlation of data within the cavity region (that is $X/L_R < 1.0$) for geometries A to D, indeed better than that actually implied in the source paper, both in terms of the shape of the distribution and also in the recovery to reattachment C_{pr} which is included in Table 1. The constancy of C_{pr} indicates the importance of the separation dynamic head in controlling the pressure recovery to reattachment. Indeed, deliberate offset of the trailing edge flap still produced a good correlation of data despite significant changes in the pressure level itself. The rearward step geometry E shows a slightly lower value of C_{pr} , which possibly reflects the fact that although the sequence of geometries A to E was designed to produce a progressive variation in the initial shear layer separation angle (and hence also in the overall shear layer curvature), geometry E also shows a marked relative increase in separation boundary layer thickness compared with the other cases. In Chandrsuda's (1976) experiment, which seems to give the thinnest separation boundary layer thickness of those rearward step data available and is therefore perhaps better for comparison with the sequence of geometries A to D, a value of 0.32 is obtained. There are numerous other studies of rearward steps in the literature (see Eaton and Johnston (1981) for a review), giving a wide range of values for C_{pr} which must reflect to some extent the differences in measurement technique, accuracy, etc. There is certainly still considerable evidence that C_{pr} reduces with increasing separation boundary layer thickness, as shown for example by the correlation of Le Balleur and Mirande (1975), and our present measurements are in fact consistent with this.

SPECTRA OF VELOCITY FLUCTUATIONS AT THE SHEAR LAYER EDGE

The velocity measurements presented here are confined to the shear layer edge in the region of more-or-less irrotational velocity fluctuations. Figures 3, 4 and 5 show streamwise velocity spectra for models A, B and E, taken along loci of 2%, 3% and 3% local turbulence intensities respectively. Qualitatively the spectral developments are similar, that is a steady fall in characteristic frequencies from separation to about

50% of the bubble length, which shows the progressive growth of shear layer scales, followed by the establishment of a fixed frequency for the irregular broad band shedding of vorticity from the bubble. In the central

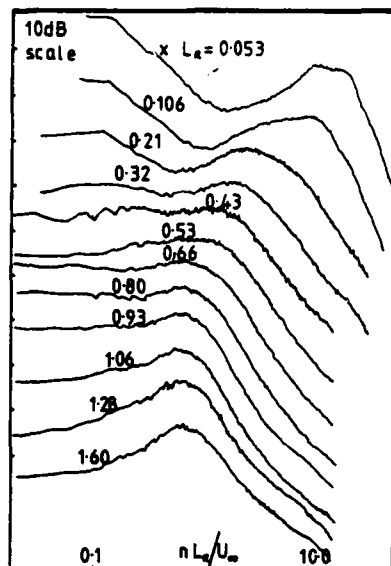


Figure 3. SPECTRA FOR STREAMWISE VELOCITY FLUCTUATIONS ON MODEL A. TRAVERSE LOCUS OF 2 1/2% LOCAL INTENSITY

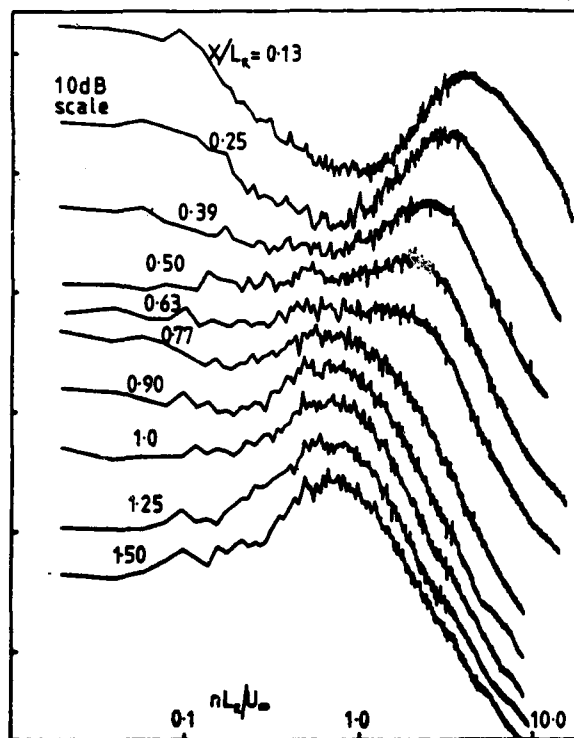


Figure 4. SPECTRA FOR STREAMWISE VELOCITY FLUCTUATIONS ON MODEL B. TRAVERSE LOCUS OF 3% LOCAL INTENSITY

region of the bubble an overlap between the two is just detectable. Figure 6 compares the spectra some distance downstream of reattachment, where it is seen that the values for the peak spectral density occur in the frequency range 0.6 - 0.8 for nL_R/U_∞ , which is comparable to the value initially suggested by Mabey (1971). Clearly the free stream velocity (rather than the separation velocity U_s perhaps) and the reattachment length L_R may not be the most appropriate scales for generating a dimensionless frequency.

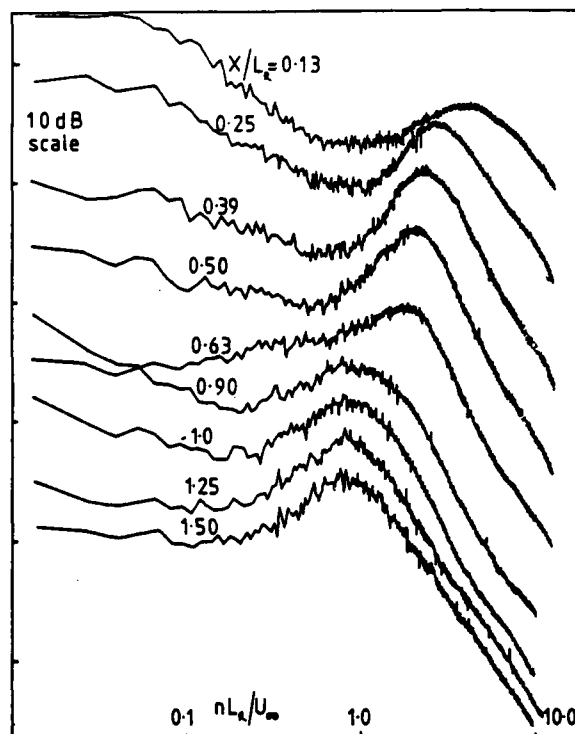


Figure 5. SPECTRA FOR STREAMWISE VELOCITY FLUCTUATIONS ON MODEL E. TRAVERSE LOCUS OF 3% LOCAL INTENSITY.

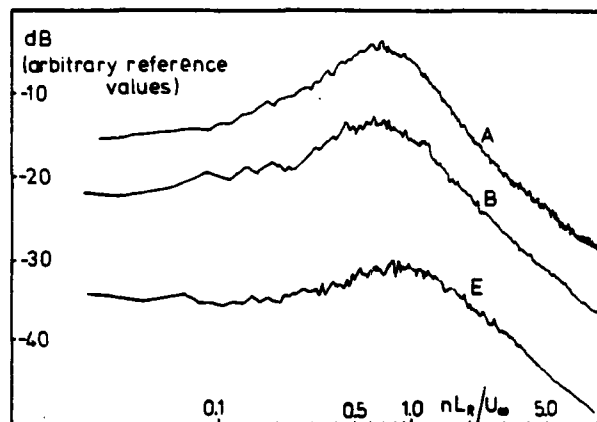


Figure 6. COMPARISON OF VELOCITY SPECTRA DOWNSTREAM OF REATTACHMENT FOR MODELS A, B AND E.

In particular the reattachment shear layer thickness for Model E was noticeably thinner than the other two, as shown by the mean velocity profiles in Figure 7, so that a characteristic shear layer thickness may eventually prove to be the more appropriate physical scale. This figure incidentally includes data from Chandrusda (1976) for a very thin separating shear layer.

Figure 8 presents the variation with streamwise distance of the frequency $n_{0.5}$ which divides each spectra into two halves of equal energy. Here we have chosen to normalise the frequency by the separation velocity, which tends to spread out the post-reattachment data compared with (say) Figure 6 but does then allow inclusion of the data of McGuinness (1978), for the internal separation at a pipe inlet.

In the initial growth region (say $X/L_R < 0.6$) the difference in Figure 8 between configuration A and configurations B/E is rather surprising since it had been supposed that the separation velocity U_s would be the

AD-A135 034

SYMPOSIUM ON TURBULENT SHEAR FLOWS (4TH) HELD AT
KARLSRUHE UNIVERSITY (GERMANY FR) 12-14 SEPTEMBER 1983
(U) KARLSRUHE UNIV (GERMANY F R) SEP 83

7/7

UNCLASSIFIED

F/G 20/4

NL

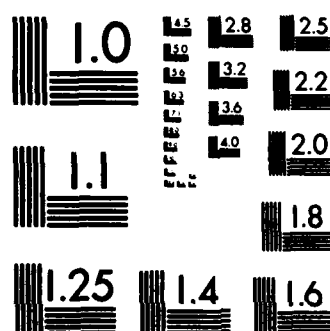
RECEIVED

END

FILED

1-84

DTI



MICROCOPY RESOLUTION TEST CHART
NATIONAL BUREAU OF STANDARDS-1963-A

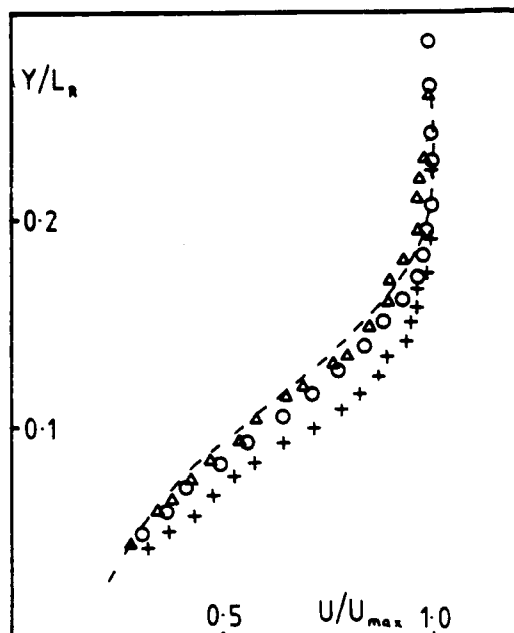


Figure 7. MEAN VELOCITY PROFILES AT REATTACHMENT FOR MODELS. THE MEAN VELOCITY IS NORMALISED BY ITS MAXIMUM VALUE. MODEL A, Δ ; MODEL B, \circ ; MODEL E, $+$; CHANDRUSDA (1976), ----.

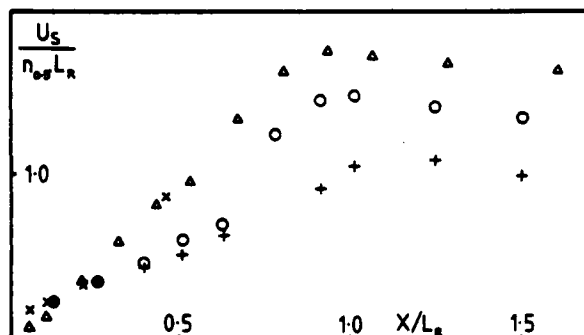


Figure 8. VARIATION OF THE HALF ENERGY FREQUENCY WITH DISTANCE X FROM SEPARATION. MODEL A, Δ ; B, \circ ; E, $+$; MCGUINNESS (1978), X.

most plausible normalising velocity here. The differences appear unlikely to be due to the probe reference positions chosen (2% local intensity for configuration A, 3% for configurations B and E), and must be attributable to the detailed differences in the initial shear layer history due to effects such as curvature, the pre-separation transition for configuration E, and the fact that for configurations B and E the initial shear layer is relatively much more isolated from the surface than for configuration A. It was not possible, of course, to use a hot wire to measure profiles through the full shear layer thickness in the cavity region, but some such thickness together with perhaps the average large scale disturbance convection velocity are likely to be more appropriate normalising quantities. All these points are still the subject of the present investigation. At reattachment and downstream the differences are the cause of less concern, since it has already earlier been remarked that neither U_s nor L_R is necessarily the obvious normalising parameter. The reattachment spectra of Figures 3, 4 and 5 are broad band and the shedding is generally an irregular process, although quasi-periodic bursts of several cycles duration are evident in velocity signals as remarked earlier by

Hillier and Cherry for configuration A. It is unclear whether these are a natural feature of a high Reynolds number flow, or whether they still reflect the history of the shear layer transition since the mixing layer experiments of Browand and Troutt (1980) imply that the shear layer reattachment structure is likely still to be weakly dependent upon the transition process. Figures 9a, b, c present smoke flow visualisations of model A, taken using a high intensity strobe flash illumination of a thin segment of flow field. These illustrate various shedding phases observed which, qualitatively, appear also to be typical of the other configurations. In Figure 9a vorticity sheds from the bubble as a series of more-or-less discrete turbulent structures with streamwise spacings of order 60% to 80% L_R which corresponds to the pseudo-periodic shedding phase. Figures 9b and 9c are less regular and illustrate, respectively, a very vigorous shedding of large scale structures and a "quiescent" phase characterised by the absence of large scale disturbances and a noticeable "necking" of the shear layer downstream of reattachment. It is suggested that the low frequency motions remarked upon earlier perhaps correspond to the relaxation time for the flow to change between these typical shedding phases.

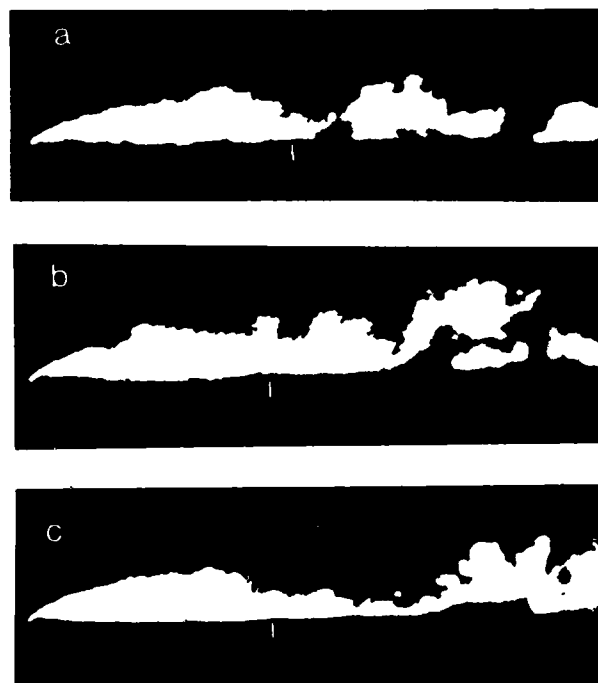


Figure 9. SMOKE FLOW VISUALISATIONS FOR MODEL A. THE TIME-AVERAGED REATTACHMENT POSITION IS MARKED

Flow visualisation studies for the flat plate/splitter plate combination have shown the shedding from reattachment of large scale vortical structures and the same necking phenomenon (Savill (1983), Gartshore and Savill (1982)).

SPANWISE CORRELATIONS

There are relatively few measurements of spanwise correlations in separated-and-reattaching flows, despite the obvious importance of unsteady three-dimensional effects both in the initial shear layer development downstream of reattachment and also in the dynamics of the reattachment process. In the present experiments spanwise correlations of streamwise velocity fluctuations were made at the shear layer edge, in the same nearly-

irrotational region as for the earlier spectral data.

Figure 10 presents data at reattachment for models A, B and E. Within measurement accuracy these correlations were unchanged by a doubling of Reynolds number, so that the spanwise structure at reattachment appears to show little or no dependence upon the initial transition behaviour. In Figure 10 the spanwise separation Z of the hot-wires is normalised by the reattachment shear layer vorticity thickness δ_w , which produces a satisfactory correlation between the various configurations. The figure also includes the data of Browand and Troutt (1980) which were measured on the low velocity side of a plane mixing layer (with 8 : 1 velocity ratio) at a location corresponding to about 2% irrotational velocity fluctuations and sufficiently far from the origin for transitional effects to have disappeared. These show generally a slightly larger

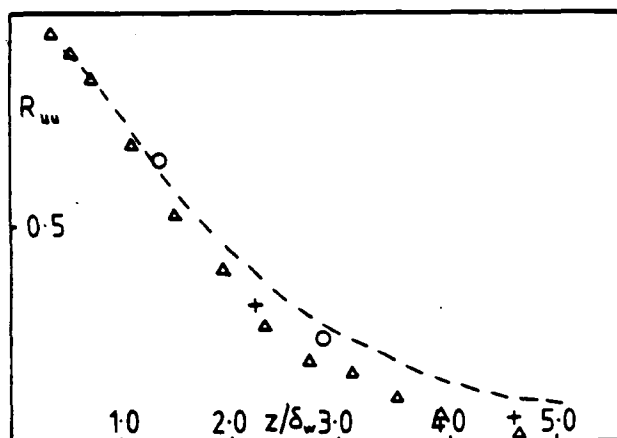


Figure 10. SPANWISE CORRELATION MEASUREMENTS AT REATTACHMENT; Δ , MODEL A; \circ , MODEL B; $+$, MODEL E. HOT WIRE LOCATION AS FOR SPECTRAL DATA. DATA FROM BROWAND AND TROUTT (1980), -----.

scale than was found for the present experiments with a somewhat more pronounced low correlation tail at large hot wire separations. The development of the lateral correlation scale with distance from separation is shown in Figure 11 for configuration A. This shows a

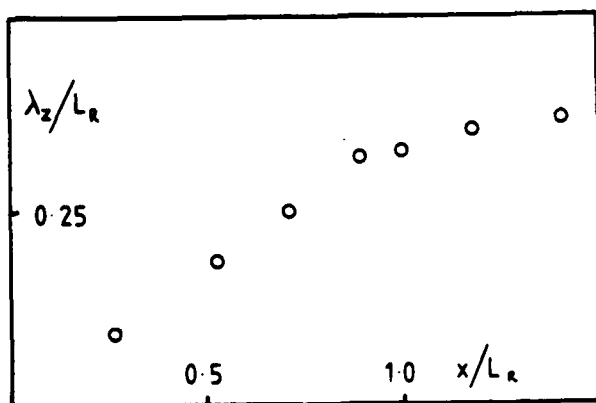


Figure 11. STREAMWISE DEVELOPMENT OF LATERAL CORRELATION SCALE FOR CONFIGURATION A.

surprisingly linear development up to the time-averaged reattachment position, beyond which the growth rate is much reduced. There appears to be no strong extra three-dimensionalising effect of reattachment (at least for the larger shear layer scales monitored here) and the implication of the continuous growth prior to

reattachment would be that the separated shear layer achieves a near fully developed stage shortly after separation.

CONCLUDING REMARKS

At least three distinct phenomena appear to be involved in the evolution of the shear layer from separation to reattachment. In the initial half of the bubble there is a fall in characteristic frequency, showing the progressive increase of shear layer scale as the shear layer develops in the relative isolation from the reattachment surface. From the mid-bubble position onwards the development of shear layer structures becomes increasingly influenced by the presence of the reattachment surface and the spectra eventually become dominated by the large scale (on average) shedding of vorticity from the bubble. Superimposed on the whole bubble motion is a low frequency phenomenon, which probably corresponds to a bubble growth/decay process as it varies between the various shedding phases noted earlier. Since spanwise correlation scales are less than the time-averaged reattachment length it is likely that several different shedding phases may exist simultaneously across the span of the model.

This paper is a preliminary report on a current study. Further measurements will concentrate on providing more detail of the unsteady structure, through space-time correlations and spectral data.

ACKNOWLEDGEMENTS

Part of this work was supported by the Building Research Establishment and is contributed by permission of the Director, BRE.

N.J. Cherry was supported by a S.E.R.C. Case Award.

REFERENCES

1. Ashurst, W.T. "Calculation of Plane Sudden Expansion Via Vortex Dynamics". Sandia Lab. Rep. SAND 79-8679, 1979.
2. Brederode, V.A.S.L. "Three Dimensional Effects in Nominally Two-Dimensional Flows". Ph.D. Thesis, University of London, 1975.
3. Browand, F.K. and Troutt, T.R. "A Note on Spanwise Structure in the Two-Dimensional Mixing Layer". Journal of Fluid Mechanics, Vol. 97, 1980, p. 771.
4. Castro, I.P. and Dianat, M. "Surface Flow Patterns on Rectangular Bodies in Thick Boundary Layers". Proc. 5th Coll. Ind. Aero., Aachen, 1982.
5. Chandrsuda, C. "A Reattaching Turbulent Shear Layer in Incompressible Flow". Ph.D. Thesis, London University, 1976.
6. Cherry, N.J. "The Effects of Stream Turbulence on a Separated Flow with Reattachment". Ph.D. Thesis, University of London, 1982.
7. Cherry, N.J., Hillier, R. and Latour, M.E.M.P. "The Unsteady Structure of Two-Dimensional Separated-and-Reattaching Flow". Proc. 5th Coll. Ind. Aero., Aachen, 1982.
8. Eaton, J.K. and Johnston, J.P. "Low Frequency Unsteadiness of a Reattaching Turbulent Shear Layer". 1981, 3rd Symposium Turbulent Shear Flows, Davis, California.
9. Eaton, J.K. and Johnston, J.P. "A Review of Subsonic Turbulent Flow Reattachment". AIAA J. Vol. 19, No. 9, 1981, p. 1093.
10. Etheridge, D.W. and Kemp, P.H. "Measurements of Turbulent Flow Reattachment". AIAA J. Vol. 19, No. 9, 1978, p. 1093.
11. Gartshore, I.P. and Savill, M. "Some Effects of Free Stream Turbulence on the Flow Around Bluff Bodies". Euromech 160, Berlin, 1982.
12. Hillier, R. and Cherry, N.J. "Pressure Fluctuations Under a Turbulent Shear Layer". 1981, 3rd Symposium Turbulent Shear Flows, Davis, California.
13. Kiya, M., Sasaki, K., and Arie, M. "Discrete Vortex Simulation of a Turbulent Separation Bubble". J.F.M., Vol. 20, 1982, P. 129.
14. Latour, M.E.M.P. Ph.D. Thesis, University of London,

1983.

15. Le Balleur, J-C and Mirande, J. "Étude Expérimentale et Théorique du Recollement Bidimensionnel Turbulent Incompressible", ONERA TP 1975-16, 1975.
16. Mabey, D.G. "Pressure Fluctuations caused by Separated Bubbles at Subsonic Speeds". Royal Aircraft Establishment, Tech. Report 71160, 1971.
17. McGuinness, M.D. "Flow with a Separation Bubble: Steady and Unsteady Aspects". Ph.D. Thesis, University of Cambridge, 1978.
18. Moss, W.D. and Baker, S. "Recirculating Flows Associated with Two-Dimensional Steps". Aero. Quarterly, XXXI, August 1980, p. 151.
19. Norbury, J.F. and Crabtree, L.F. "A Simplified Model of Incompressible Flow Past Two-Dimensional Aerofoils with a Long Bubble Type of Separation". RAE Tech. Note Aero. 2352, 1955.
20. Roshko, A. and Lau, J.K. "Some Observations on Transition and Reattachment of a Free Shear Layer in Incompressible Flow". Proc. Heat Transfer Fluid Mech. Inst. Vol. 18, 1965, p. 157.
21. Savill, M. Cambridge University, Private Communication, 1982.
22. Westphal, R.V., Eaton, J.K., and Johnston, J.P. "A New Probe for Measurement of Velocity and Wall Shear Stress in Unsteady Reversing Flow". ASME J. of Fluid Eng., Vol. 103, 1981, P. 478.

VELOCITY FIELD AROUND A DISK

by

D.F.G. Durão and F.C. Firmino
Instituto Superior Técnico
Mech. Engineering Department
1096 Lisbon codex - Portugal

ABSTRACT

Measurements of the mean velocity and turbulence characteristics were obtained with a direction-sensitive laser-Doppler anemometry in the wake of two different disks located in the centre line of a jet exiting from a tube. The work includes profiles of the axial and radial mean velocity components and rms values of the three fluctuating velocity components and shear stress. In an effort to detect the presence and magnitude of predominant frequencies, velocity probability distributions and turbulence energy spectra were also obtained.

The results indicate a length of the recirculation region equal to 1.35 disk diameters for a 10 mm diameter baffle, increasing with disk diameter, independent of initial velocity and slightly decreasing with the increase of the distance from the jet exit to the baffle.

1. INTRODUCTION

Available information on the mean velocity and turbulence characteristics of wake flows with recirculation is limited and the present paper reports measurements obtained with a laser Doppler anemometer (LDA) in and around the region of recirculating flow behind disks located in the centre line of a jet.

The present geometry is similar to that existing in flame stabilizers used, for instance, in small furnaces where a region of low velocity and high mixing is created preventing blow-off. References (1) to (8) report previous related investigations and the results of (6), (7) and (8) were obtained with LDA. Carmody (1964), using hot wire anemometry and small values of d/D , i.e. blockage indicates lengths of the recirculation zones behind disks equal to 2.5 disk diameters; Fugii et al. (1978) give the value of 1.88 when measuring with the disk with a 60 degrees inclination in respect to the main flow and a blockage of 50% still in confined flows. Winterfeld (1965) quotes recirculation length of 2.0 disk diameters for blockages of 4% and 25% and Taylor (1981) refers the values of 1.75 and 2.20 for blockages of 25% and 50% respectively. Calvert (1967) noticed the presence of periodic oscillations corresponding to a Strouhal number of 0.19 and values of the drag coefficients and pressure on the base of the disk are reported by Humphries and Vicent (1976).

The measurements of Davis and Baer (1971) and Durão and Whitelaw (1978) were obtained in free annular jets from a nozzle and show lengths of the recirculation zone equal to 1.52 and 1.45 disk diameters respectively diminishing with the increase of blockage. Numerical predictions of this type of flow were carried out by Pope and Whitelaw (1976) and McGuirk and Taylor (1982). References (2), (8) and (11) also present measurements obtained with cone-shaped baffles.

The present report introduces measurements of the axial and radial mean velocity components, U and V , rms values of the three fluctuating components of velocity, u' , v' and w' and shear stress, uv . To complement

this work with information on the existence of periodic oscillations velocity probability distributions and turbulence energy spectra were also obtained. The baffles of diameter d , could be located at different distances from the jet-exit plane, x_1 , for different values of the initial maximum velocity, U_0 . The influence of d , x_1 and U_0 in the characteristics of the flow was identified.

The experimental set up and measuring procedure are described in the next section and the results are analysed and discussed in the following section; the paper finishes with main conclusions.

2. EXPERIMENTAL SYSTEM

A brief description of the experimental set up is presented in subsection 2.1; subsection 2.2 deals with the optical and signal processing arrangements and the experimental precision is referred in 2.3. More details about the experimental system is given in reference (12).

2.1 Flow Configuration

Disks of 15.0 and 10.0 mm of diameter (d_1 and d_2 respectively), and 1.5 mm of thickness, machined with sharp edges were located in the centre line of a jet exiting from a tube with 42 mm inner diameter, D , and 48 diameters long. Experiments confirmed that in the absence of the baffles, at the exit of the tube the velocity characteristics were those associated with fully developed pipe flow. The disks were supported from upstream mounted on 5 mm diameter and 600 mm long rods hold to the tube with two sets of three, 2 mm diameter screws. They could be positioned at different distances from the jet exit plane, x_1 and during the present work results were obtained with x_1 equal to 10 and 75 mm. Along the 100 mm near to the disk, the supporting rod had been machined smoothly to a 4 mm diameter. The tube and the axisymmetric baffle arrangement were fixed rigidly to a three-dimensional traversing mechanism (x, r, z). The detailed measurements presented in this report were undertaken only after symmetry of the flow had been established by measuring profiles of mean velocity 90° apart at downstream distances corresponding to x/d equal to 0, 1 and 6 and ensuring that each set of four profiles agreed to within 1%. Subsequently two initial velocities were used for detailed measurements, 8.2 and 10.6 m/s.

2.2 Optical and Signal Processing Arrangements

The measurements were obtained with a laser-Doppler anemometer of the forward scattering type operating in the dual beam mode and comprised a 2W Spectra-Physics model 165 Argon laser, an OEI optical unit with two Bragg cells driven by an OEI power supply to frequency-shift the beams and a 310 mm focal length lens. The collecting optics included an 150 mm focal length lens and a OEI-810 photomultiplier with a resistor-pre-amplifier unit. The measuring control volume was fixed, the laser wave length and power were 488 nm and around 100 mW respectively and the distance between two consecutive fringes was 3.036 μ m. A particle generator as described in reference

(13) was used to increase the number of light scattering centre in the flow. The signal to noise ratio of Doppler bursts was in average in the order of 20 db.

The photomultiplier output signal was filtered and subsequently fed to a home-made FS02 frequency counter, see reference (14), with a dual facility of analogue and digital outputs and a minimum cycle time of 76 microseconds. The frequency comparator circuit of the counter accepted for further processing, Doppler bursts with a difference in frequency between the 8 and 16 measured cycles of less than 0.5%, guaranteeing the absence of significant errors in the measurement of frequency. The amplitude discrimination level was monitored through the counter. Both digital and analogue outputs were analysed by an Apple II microprocessor: the former to obtain the mean, rms and probability distribution of velocity from at least 10000 frequency values and the latter to measure the power spectral density from 100 blocks of 512 values, first stored on a 7700 Racal magnetic tape recorder and latter analysed with a fast Fourier transform program as reported in reference (12). A 9872B Hewlett-Packard plotter was used to produce the graphs and a 43 Teletype to list out the data.

2.3 Precision

The three-dimensional traversing mechanism introduces errors of 0.05 mm in the axial direction and of 0.025 mm in the other two directions.

Based upon the number of frequency values considered for each measurement, never below 10000, and according to Yanta (1973), the error in the mean and rms results is below 1%.

Considering the bias associated with LDA, and the significance of the errors due to correlations between velocity and signal quality, see references (16) and (17), and velocity and particle concentration, see references (18) and (19), the uncertainty is not only related to the discrimination level used in the instrumentation but also to the flow turbulence intensity. In the present study the uncertainties in the mean and rms values were estimated to be in average 3 and 5 percent respectively. The shear stress values were obtained from the subtraction of two sets of rms measurements and the average error associated rounds 10%. Tests made to the mean velocity profiles indicate a conservation of momentum in average within 3%.

3. RESULTS AND DISCUSSION

The results are presented in the next two subsections: 3.1 reports the mean flow patterns and the turbulence characteristics, including the normal and shear stresses, velocity probability distributions and turbulence energy spectra are introduced in subsection 3.2.

3.1 Mean Velocity Field

Figure 1 presents for the two disks of 10 and 15 mm diameter and x_1 equal to 10 mm, the axial and radial components of the mean velocity 5 mm upstream of the disk and shows that the value of the V-component and the distance from the centre line to the location of maximum velocity increase with blockage. These profiles may also be useful as upstream boundary conditions, to those that will be testing computer codes and turbulence models with the present experimental results.

Figure 2 and 3 show, for $x_1 = 10$ mm and $U_0 = 8.2$ m/s, radial profiles of the axial and radial mean velocities respectively. Figure 4 gives the mean flow patterns obtained from the two velocity components; the arrows are proportional to velocity. The measurements characterize the development of the flow in the wake of the bluff bodies: a region of recirculating flow where the mean velocity is negative, a region where the flow is accelerating until a maximum velocity is reached at the centre line and a downstream region where the velocity decreases in a way similar to that of a free jet. Both U and V profiles at $x = 90$ mm do not present visible differences due to disk diameter and at $x = 120$ mm ($x/d_1 = 6$, $x/d_2 = 12$) the axial mean velocity profiles if normalized with the centre line velocity and plotted against radial distance normalized with the width of the jet corresponding to the location of half the centre line

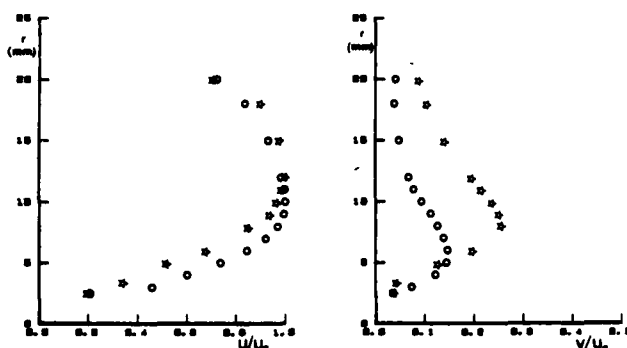


Fig. 1. Radial profiles of the axial and radial mean velocities. $x_1 = 10$ mm; $U_0 = 8.2$ m/s. $\circ d = 10$ mm; $\times d = 15$ mm.

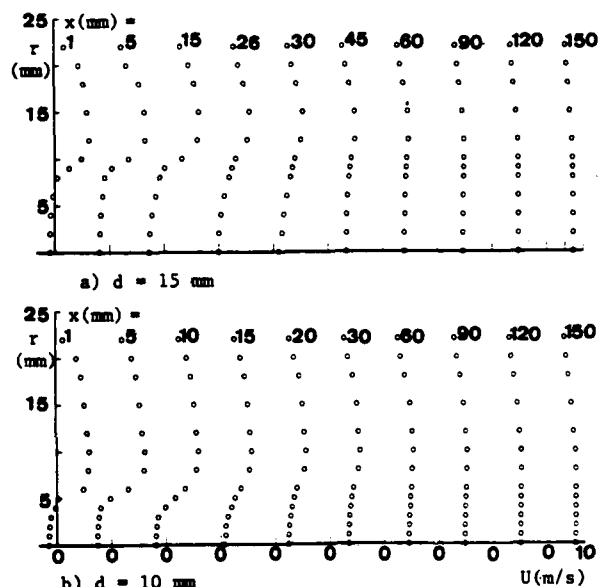


Fig. 2. Radial profiles of the axial mean velocity. $x_1 = 10$ mm; $U_0 = 8.2$ m/s.

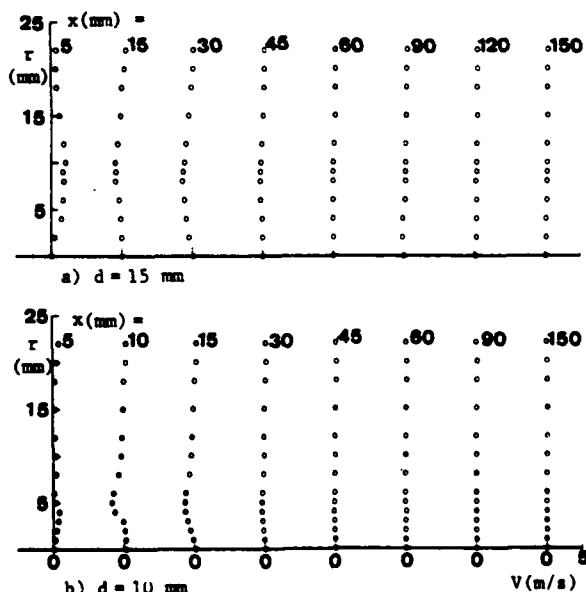


Fig. 3. Radial profiles of the radial mean velocity. $x_1 = 10$ mm; $U_0 = 8.2$ m/s.

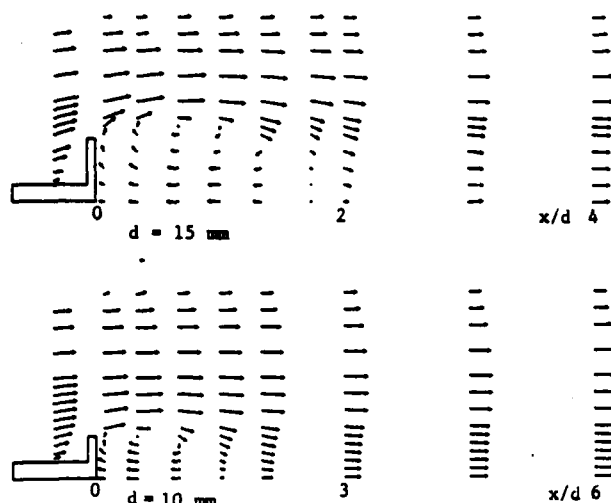


Fig. 4. Mean Flow pattern

velocity, are not significantly different from that associated with fully developed free jets, confirming the rapid spreading, mixing and development of these wake flows. Immediately downstream of the disks, in contrast to the results obtained with the annular jets, the width of the recirculation regions increases, having maximum values around $x/d = 0.5$ of $2r/d = 1.13$ and 1.10 for disks of 15 and 10 mm diameter respectively. The corresponding recirculation zone lengths at the centre line are $1.75 d_1$ and $1.32 d_2$; slightly larger negative velocities are associated with larger disks.

The profiles of the radial velocity in figure 3 show that in and around the recirculation region the radial velocity is of significance with a positive sign at $x = 5$ mm changing to negative with downstream distance and to close-to-zero still further downstream. The location of zero axial and radial velocities, i.e. the locus of the circle through the centre of the toroidal vortex, is at $x/d = 0.65$ and $2r/d = 1.2$ for the case of $d = 15$ mm and $x/d = 0.5$ and $2r/d = 1$ for the case of $d = 10$ mm.

Figure 5 presents profiles of the centre line mean velocity, U_{cl} , for different values of U_0 and x_1 . It confirms that the increase of baffle diameter increases the recirculation zone and the values of the maximum positive and negative velocities. The increase in x_1 slightly diminishes the length of the recirculation region which is not dependent on the value of U_0 . U_0 and x_1 seem to have no significant effect on the maximum values of velocity.

If the present measurements are compared with those of previous authors, even considering the inaccuracies that in some cases previous results may have, it is clear that the geometry of the flow has a considerable influence, for instance, on the length of the region of recirculation and extrapolations from one arrangement to another must be carried out with great care.

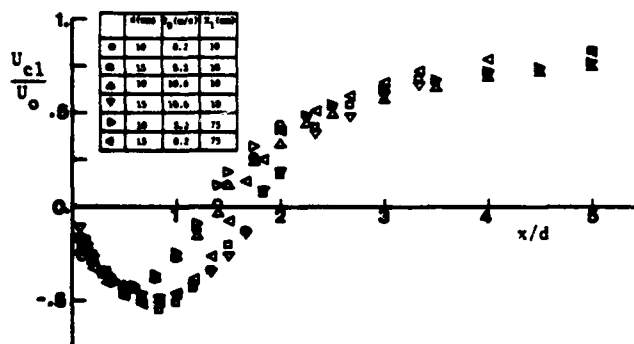


Fig. 5. Centre line profiles of mean velocity.

3.2 Turbulent Field

Figures 6, 7 and 8 show for the same conditions of figure 2, radial profiles of the rms values of the axial, radial and tangential components of velocity, respectively. For the smaller disk figure 9 gives the corresponding isolines obtained with linear interpolation. It can be seen that the turbulent field has a large dependence on the baffle dimensions but most of the differences result from the variations existing in the mean velocity field. In general the larger disk shows higher turbulence intensity values. The radial and also the tangential velocity fluctuations have their maximum value slightly downstream the mean stagnation point. In a large region around this point both fluctuations are much larger than the axial fluctuations, confirming that the turbulence is strongly anisotropic. Along the centre line this region extends from the location of maximum negative mean

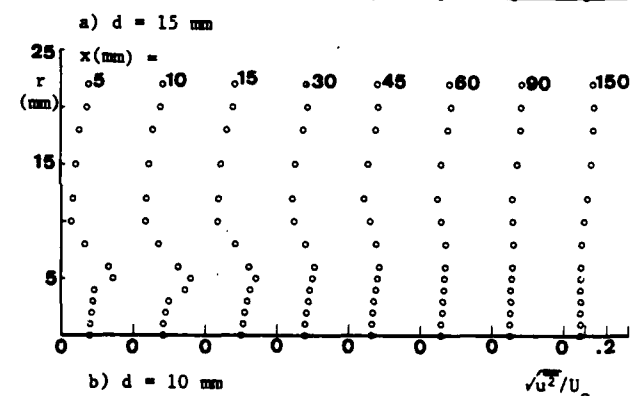
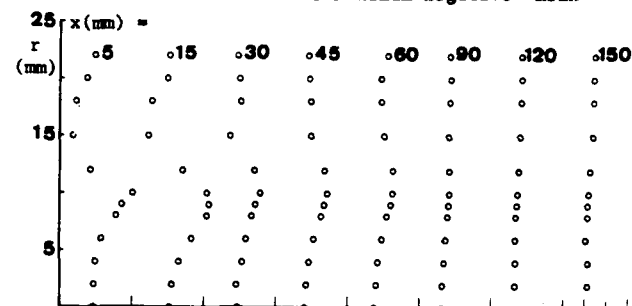


Fig. 6. Radial profiles of the axial velocity fluctuations. $x_1 = 10$ mm; $U_0 = 8.2$ m/s.

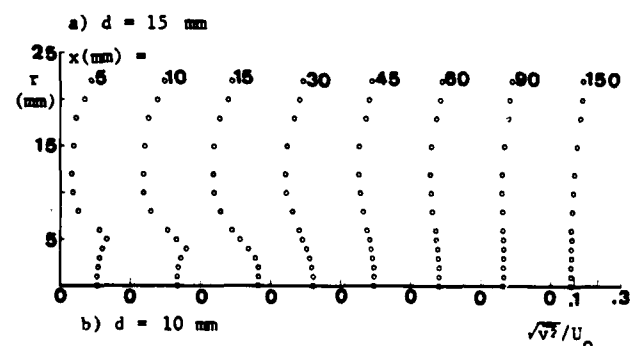
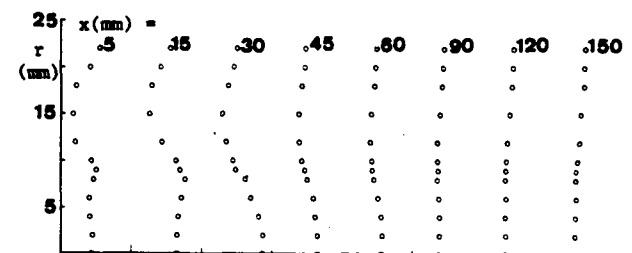


Fig. 7. Radial profiles of the radial velocity fluctuations. $x_1 = 10$ mm; $U_0 = 8.2$ m/s.

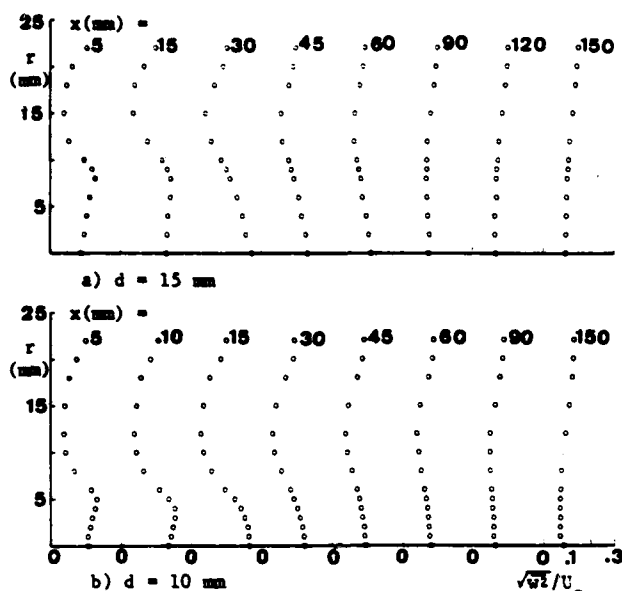


Fig. 8. Radial profiles of the tangential velocity fluctuations. $x_1 = 10$ mm; $U_0 = 8.2$ m/s.

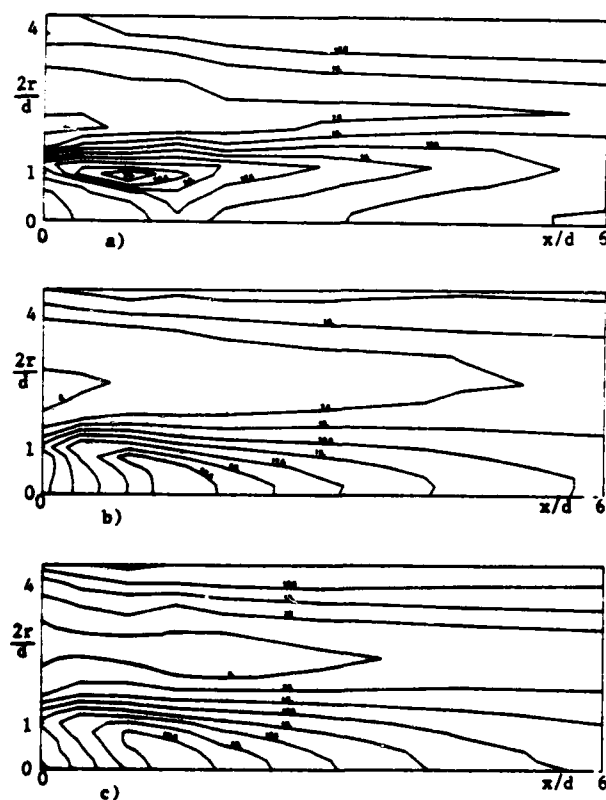


Fig. 9. Isolines of a) $\sqrt{u'}/U_0$, b) $\sqrt{v'}/U_0$ and c) $\sqrt{w'}/U_0$. $d = 10$ mm; $x_1 = 10$ mm; $U_0 = 8.2$ m/s.

velocity ending at x/d equal to 9. The maximum value of the axial fluctuations is slightly higher than the other two, of the v and w fluctuations, but localized just downstream the locus of the circle through the center of the toroidal vortex. In the center line the maximum value of the axial fluctuations also occurs close to the location of zero mean velocity; further downstream, close to the point of maximum mean velocity the turbulence intensity reaches a minimum value of around 15%.

In the recirculation region the turbulence intensity is never less than around 30% and in spite of the decrease in the magnitude of the mean axial velocity, the

rms of the u -fluctuations increases from the centre line to the edge. Outside this region, the axial fluctuations continue to increase rapidly in the axial direction, reach a maximum value and, at still larger radii, fall to a minimum, close to the location of maximum mean velocity, which increases very rapidly with downstream distance. From the centre line to the edge of the recirculation zone the radial and tangential stresses exhibit a much less pronounced increase than that noticed in the axial normal stress; further away from the centre line, the general behaviour of all the normal stresses is similar although their magnitude differ and the locations of maxima and minima are not coincident. Downstream the recirculation zone, the three normal stresses tend to diminish and at $x = 150$ mm the presence of the recirculation region starts to be unrecognizable and their variation starts to be similar to that of free turbulent jets.

From the values presented, the turbulence kinetic energy can be evaluated by adding the three normal stresses. This is relevant to turbulence models which make use of the corresponding conservation equation, but the present flow is far from isotropic and conservation equations for each of the normal stresses seem to be required to represent the detail of the present flow, except perhaps in the far downstream region.

Figure 10 shows values of the shear stress for the same conditions of previous figures. They were obtained by subtracting two sets of measurements made with the plane of the two laser beams inclined $+45^\circ$ and -45° with reference to the x -direction and the errors involved may be significant. The radial profiles show, in the

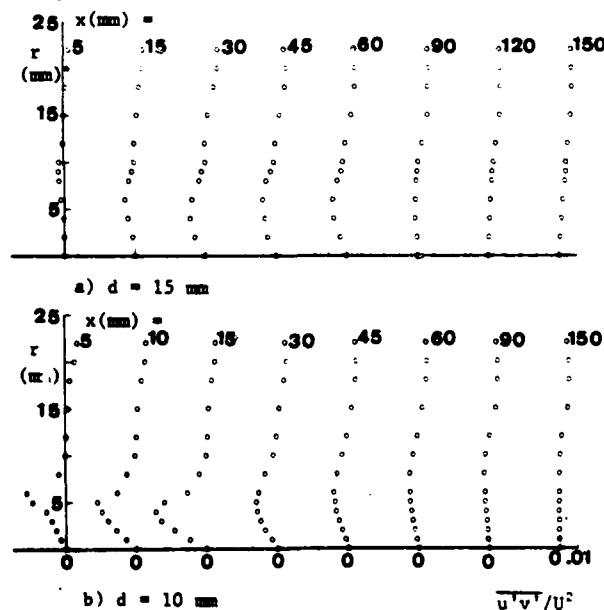


Fig. 10. Radial profiles of the shear stress. $x_1 = 10$ mm; $U_0 = 8.2$ m/s.

recirculation zone and further downstream large regions of negative shear which can be detected as far as $x/d_2 = 15$. The results tend to indicate that the locations of zero shear do not, in general, coincide with those of zero mean velocity gradient or turbulence kinetic energy.

As shown in figure 11 the velocity probability distributions of the axial component of velocity measured along the centre line, including those obtained inside the recirculation region and close to the stagnation point, were near Gaussian in nature varying mainly with the rms value and mean velocity. However, when measuring radially at $x/d = 1$, bimodal distributions were detected close to the centre of the toroidal vortex, as shown in figure 12, suggesting the presence of predominant oscillations coexisting with the turbulent fluctuations. The distribution measured in the recirculation zone, $2r/d = 0.4$ as those obtained along the centre line, continues to be near Gaussian. Those obtained close to the point of maximum velocity, $2r/d$ equal to 1.6 and 2.4,

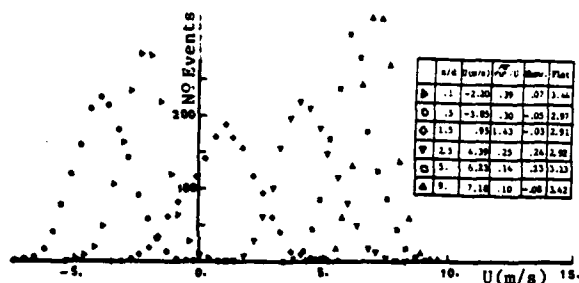


Fig. 11. Probability distributions of the axial velocity component measured along the centre line.
 $d = 10 \text{ mm}$; $x/d = 1$; $x_1 = 10 \text{ mm}$; $U_0 = 8.2 \text{ m/s}$.

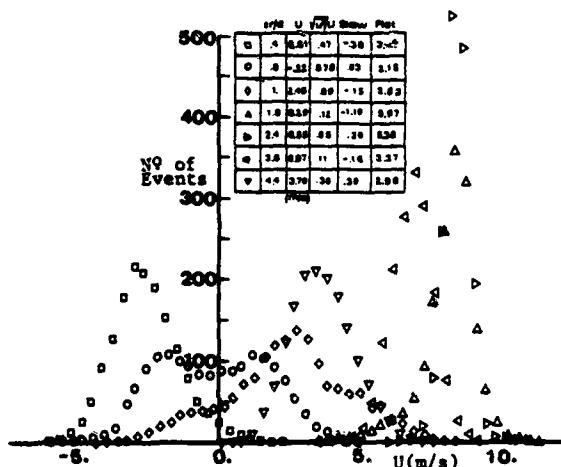


Fig. 12. Probability distributions of the axial velocity component obtained with the disk at different radii.
 $d = 10 \text{ mm}$; $x/d = 1$; $x_1 = 10 \text{ mm}$; $U_0 = 8.2 \text{ m/s}$

are spiky. The figure also gives values of skewness and flatness. The inaccuracy of these values is significant but the overall pattern is correct and allows to interpret the mixing mechanism existing at this downstream plane.

To measure the frequency of the periodic instabilities noticed already in the velocity probability distributions, energy spectra of the analogue output of the counter were attempted. Special measuring conditions were created to increase the particle arrival rate and figure 13 shows the result with the ordinate normalized to have the total energy equal to unity. The microcomputer needed several hours to analyse all the frequency results measured for a period of around three minutes and stored in the magnetic tape for overnight processing. The inaccuracies increase towards the lower frequencies but a peak is detectable at around 150 Hz. The corresponding Strouhal number based on disk diameter and initial velocity, is 0.18, value close to that reported by Calvert (3), 0.19.

4. CONCLUSIONS

The experimental investigation lead to the following more important conclusions:

- (1) Recirculation lengths of 1.75 and 1.35 baffle diameter were measured with disks of 15 and 10 mm diameter respectively. The recirculation zone is independent of initial velocity and slightly decreases with the increase of the distance from the jet exit to the stabilizer.
- (2) The locations of zero axial mean velocity, which occur at the border of the recirculation

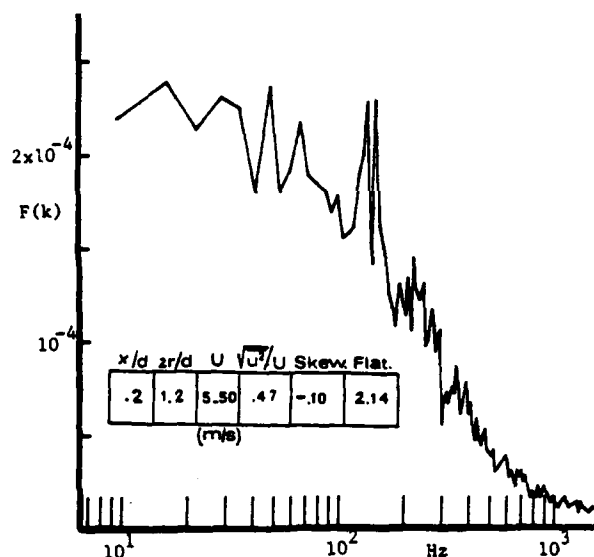


Fig. 13. Turbulence energy spectra.
 $d = 10 \text{ mm}$; $x/d = .2$; $2r/d = 1.2$; $x_1 = 10 \text{ mm}$; $U_0 = 8.2 \text{ m/s}$.

region do not coincide with those of zero values of radial mean velocity except at the circle through the centre of the toroidal vortex.

- (3) The turbulence intensity in the recirculation region is never below 30% and strongly anisotropic. In general, larger velocity fluctuations were associated with the larger disk. The locations of zero shear stress did not coincide always with those of zero velocity gradient or turbulence kinetic energy.
- (4) In a large region around the centre line, the radial and tangential fluctuations are much larger than the axial fluctuations. The maximum value of the axial fluctuations is located off axis shortly after the center of the toroidal vortex.
- (5) Bimodal velocity probability distributions and the corresponding peak in the turbulence energy spectra were detected in the wake associated to a Strouhal number of 0.18. Most of the recirculation zone do not reveal this periodic instabilities.

ACKNOWLEDGEMENTS

The authors want to thank Prof. F. Durst and Mr. G. Pita for useful discussions. The experiments were partially supported by the Stiftung Volkswagenwerk and made at the Centro de Termodinâmica Aplicada e Mecânica dos Fluidos da Universidade Técnica de Lisboa (CTAMFUTL).

REFERENCES

1. Carmody, T., 1964, "Establishment of the Wake Behind a Disc", Trans. ASME: J. Basic Eng., 86, 869.
2. Winterfeld, G., 1965, "On Processes of Turbulence Exchange Behind Flame Holders", Proc. 10th Symp. (Int) on Combustion, 1265.
3. Calvert, J.R., 1967, "Experiments on the Low-Speed Flow Past Cones", J. Fluid Mech., 27, 273.
4. Davis, T.W. and Beer, J.M., 1971, "Flow in the Wake of Bluff-Body Flame Stabilisers", Proc. 13th Symp. (Int.) on Combustion, 637.
5. Humphries, W. and Vicent, J.H., 1976, "Experiments to Investigate Transport Processes in the Near Wakes of Disks in Turbulent Air Flow", J. Fluid Mech., 75.

6. Fujii, S., Gomi, M. and Eguchi, K., 1978, "Cold Flow Tests of a Bluff-Body Flame Stabilizer", Trans. ASME: J. Fluid Eng., 100, 323.
7. Durão, D.F.G. and Whitelaw, J.H., 1978, "Velocity Characteristics of the Flow in the Near Wake of a Disk", J. Fluid Mech., 85, 369.
8. Taylor, A.M.K.P., 1981, "Confined, Isothermal and Combusting Flows Behind Axisymmetric Baffles", Ph.D. thesis, Univ. of London.
9. Pope, S.B. and Whitelaw, J.H., 1976, "The Calculation of Near-Wake Flows", J. Fluid Mech., 73, 1, 9.
10. McGuirk, J.J., Taylor, A.M.K.P., 1982, "The Assessment of Numerical Diffusion in Upwind Difference Calculations of Turbulent Recirculating Flows", 3rd Turbulent Shear Flows Symposium, Springer-Verlag, 206.
11. Durão, D.F.G. and Firmino, F.C., 1983, "Velocity Characteristics of the Flow Around Disks and Cones", ASME, paper 1504-CD.
12. Firmino, F.J.C., 1983, "Experimental Study of the Aerodynamics of Flame Stabilizers", M.Sc. thesis, Tech., Univ. Lisbon - IST.
13. Melling, A. and Whitelaw, J.H., 1973, "Seeding of Gas Flow for Laser Anemometry", DISA inf. 15, 5.
14. Durão, D.F.G., Laker, J., Taylor, A.M.K.P. and Yanneskis, M., 1982 "Operation and Performance of the Fluids Section FS02 Frequency Counter", Imperial College, Fluids Section Rept.
15. Yanta, W.J., 1973, "Turbulence Measurements with a Laser Doppler Velocimeter", Naval Ord. Lab., White Oak, rep. NOLTR73-94.
16. Durão, D.F.G. and Whitelaw, J.H., 1980, "Bias Effects in Laser Doppler Anemometry", J. Phys. E: Sci. Inst., 13, 442.
17. Durão, D.F.G., Founti, M.A., Laker, J., Pita, G., Velho, A. and Whitelaw, J.H., 1982, "Some Consequences of Bias Effects in Laser Doppler Velocimetry", Proc. Int. Symp. LDA Appl. to Fluid Mech., paper 16.1.
18. McLaughlin, D.K. and Tiederman, W.G., 1973, "Biasing Correction for Individual Realisation of Laser Anemometer Measurements in Turbulent Flows", The Physics of Fluids, 16, 12, 2082.
19. Edwards, R.V., 1981, "A New Look at Particle Statistics in Laser-Anemometer Measurements", J. Fluid Mech., 105, 317.

THE TURBULENT STRUCTURE OF SWIRLING FLOW IN A SUDDEN EXPANSION

W. L. H. Hallett,
Mech. Eng. Dept., University of Ottawa,
Ottawa, Canada

and

R. Günther,
Lehrstuhl für Feuerungstechnik, Universität Karlsruhe,
Karlsruhe, W. Germany

ABSTRACT

Measurements of turbulent velocity fluctuations, shear stresses, and the concentration fluctuations of a tracer gas are reported for a swirling air flow in a stepped sudden expansion. Tests were conducted at three different swirl intensities, giving two flow regimes: a vortex breakdown flow at high swirl, and an unsteady precessing flow at low swirl. Shear stresses and time-mean concentration data indicated mixing at all swirl levels to be about equally fast, but concentration fluctuation measurements showed a large unmixedness at low swirl, corresponding to the large scale motion of the precessing flow.

NOMENCLATURE

I	- axial momentum flux
k	- turbulent kinetic energy
L_E, L_K	- velocity and concentration macro length scales
Q	- volumetric flow rate
r	- radius
R	- wall radius of test section
u_R	- $Q/\pi R^2$ - reference velocity
u	- axial velocity
v	- radial velocity
w	- tangential velocity
θ	- swirl parameter in swirl generator
θ_T	- swirl parameter in throat
ρ	- density
Ω	- angular momentum flux

INTRODUCTION

Swirling flows are widely used to achieve high mixing intensities in combustors and reactors. Of particular importance for such applications is the occurrence of a central recirculation zone or "vortex breakdown", which appears when a flow of sufficiently high swirl exits into a duct or furnace of larger cross-section. In general, the additional velocity gradients generated by the tangential velocity component in a swirling flow result in higher turbulence levels than in an equivalent non-swirling flow; vortex breakdown further enhances turbulence production and mixing, and also provides aerodynamic flame stabilization.

In spite of the industrial importance of vortex breakdown flows, little experimental data on their turbulence properties is available, apart from free jet measurements by Hösel /1/ and Hellat /2/, and data from the double swirl combustor of Gouldin et al /3,4/. The purpose of the present work was therefore to measure turbulence quantities and assess mixing in a breakdown flow and compare them to those in flows at lower swirl without breakdown.

EXPERIMENTAL EQUIPMENT

The geometry of the model in which experiments were carried out (Fig. 1) typifies a simple combustor, in which fuel is injected through a central nozzle into the mixing region downstream of the stepped sudden expansion. Swirl of variable intensity was produced by a swirl generator of the tangential inlet type. The model itself consisted of plexiglas tubes of various diameters with numbered ports for the insertion of probes; the port spacing was 0.5 R. A nozzle (Fig. 2), located as shown in Fig. 1, served to introduce tracer gases into the main air stream for mixing experiments. Attention was concentrated on the main mixing region downstream of the expansion, extending roughly from station 6 to station 10.

Measurements of the local time-mean velocity components were made with a five-hole Pitot probe with a head diameter of 2.2 mm, while hot-wire probes were used to determine the turbulent velocity fluctuations and shear stresses. Since swirling flows are three-dimensional, all six components of the turbulent stress tensor were required.

The very high turbulence intensities encountered in this flow (average about 60%) precluded the use of conventional series expansion hot-wire signal analyses. Use was therefore made of an approximate method based on one proposed by Acrivelllis /5/, in which the resultant of the time-mean velocities at a particular wire orientation is equated to the DC component of the linearized hot-wire signal, and that of the fluctuating components to the mean square signal. This results in measured mean velocities being too high, and turbulent stresses too low, although the sums of mean and fluctuating components are given correctly. Estimates of this error were made, using series expansions at low turbulence intensity and extrapolating the results to high levels using the "rotating vector" model for the velocity fluctuations proposed by Schollmeyer /6/. Depending on the relative magnitudes assumed

for the different fluctuating velocity components, the error in the measured RMS velocity fluctuation was estimated at 10-15%; this error was nearly independent of turbulence intensity /7/.

The actual hot-wire measurement procedure, described in detail in /7/, involved the use of 90° and 45° probes at a total of 7 different wire orientations. Probes were inserted radially into the flow, and a system of rotating the probe system to correspond to the local flow direction was adopted to ensure that the wires did not lie in the wakes of their support pins.

Measurements of the local time-average concentration of the nozzle fluid were made using natural gas (81% CH₄) as a tracer and sampling probes connected to infra-red gas analyzers. Concentration fluctuations were determined using helium as a tracer. An aspirating probe with a hot wire mounted inside, responding to the change in thermal conductivity of the air due to the presence of the helium, recorded the instantaneous tracer concentration /7,8/. This probe could resolve concentration fluctuations of up to 200 Hz in frequency.

The chief similarity parameter for swirling flows is the swirl number, defined as

$$\Theta = \frac{\Omega}{R\dot{m}} = \frac{\int_0^R \rho u w r^2 dr}{R \int_0^R \rho u^2 r dr} \quad (1)$$

Experiments were performed at three different swirl levels, characterized by the swirl number Θ in the swirl generator as determined from the swirler geometry. Values of $\Theta = 1.10$, 1.60 and 2.06 were set, yielding actual swirl numbers in the throat Θ_T (determined by integration of measured velocity profiles) of 0.23, 0.32 and 0.41 (based on the throat diameter). The Reynolds number for the turbulence measurements was 48000, based on the diameter $2R$ (Fig. 1). Measured velocities were made dimensionless with the reference velocity

$$u_R = Q/\pi R^2. \quad (2)$$

THE TURBULENT FLOW FIELD

Fig. 3 shows time-mean velocity profiles downstream of the throat as measured with the five-hole probe. At the highest swirl ($\Theta = 2.06$) vortex breakdown occurs immediately on leaving the throat, forming a recirculation zone extending as far as station 10, just over one test section diameter $2R$ from the throat. Despite the size of the backflow-region, only about 10% of the total mass flow recirculates. Characteristic for a breakdown are the large radial velocities at station 6 and the rapid formation of the recirculation "bubble". At lower swirl numbers ($\Theta = 1.60$) no breakdown occurs, and the flow maintains its forward motion throughout the test section. In all cases the flow separates from the wall on leaving a small recirculating wake behind the step. The results for $\Theta = 1.10$ were similar to those for $\Theta = 1.60$ except that the velocity profiles changed shape more slowly. The critical swirl number for the onset of breakdown was found to be $\Theta = 1.8-1.9$ ($\Theta_T = 0.37-0.39$).

The flows studied at the two lower swirl numbers were found to be unsteady, and spectrum analysis of hot-wire signals indicated the presence of a low frequency oscillation. Flow visualization with smoke showed that the entire flow emerging as a jet from the throat was precessing as a body around the test section axis. This phenomenon has yet to be studied in detail, but appears to be some sort of rotating Coanda effect, in which the jet

draws itself to the wall through self-entrainment and is caused to precess by the swirl /7, 9/. This motion was accompanied by the shedding of large eddies from the wake behind the step of the expansion. At $\Theta = 1.10$ the precession was strong and regular, but became weaker as the critical swirl number for breakdown was approached; at $\Theta = 1.60$, for example, frequency analysis showed no trace of it after station 9.

Fig. 4 gives the measured profiles of the turbulent kinetic energy k

$$k = \frac{1}{2} (\overline{u'^2} + \overline{v'^2} + \overline{w'^2}) \quad (3)$$

while Fig. 5 shows the proportion of k contained in the periodic component of the flow at low swirl. At station 6 the locations of the strongest fluctuations correspond closely with the steep velocity gradients between the forward flow and the wake flow behind the step, and (at $\Theta = 2.06$) on the boundary of the central recirculation zone (Fig. 3). However, at station 7 the radial outflow and intense turbulent mixing have already moved these maxima away from the areas of the strongest velocity gradients. The central recirculation is seen to transport flow of low turbulence intensity stream. Further downstream the velocity gradients are rapidly smoothed out, leading to a sharp decrease in turbulence production; transport and dissipation now dominate the energy budget. Since a high velocity results in a short residence time and hence less dissipation of energy, the profiles of turbulent energy have assumed shapes very similar to those of the axial velocity by station 8. The departures from this near the wall are due to production in the boundary layer and to the precession. The precession is partly responsible for the continued high energy at $\Theta = 1.10$, while the turbulence energy for $\Theta = 1.60$ drops to the level of $\Theta = 2.06$ after the precession has died down at station 9.

The local turbulence intensity T , defined as

$$T = 2 \cdot \sqrt{k} / (\overline{u^2} + \overline{v^2} + \overline{w^2})^{1/2} \quad (4)$$

in all cases averaged about 60% throughout the test section, and varied little from station to station, except at station 6, where the large velocities reduced it to 25-30%. These high values are in part due to the large velocity gradients associated with the expansion, but also to irregular fluctuations in the shape of the central recirculation zone at high swirl, and to a large degree to the precession at low swirl. Comparable turbulence intensities have been measured in strongly swirling free jets /2/. Gouldin et al /3,4/ reported much lower values, of the order of 30% or less, for their swirl combustor; however, theirs was not a sudden expansion flow but two co-flowing streams.

Figs. 6 and 7 show measured turbulence quantities for $\Theta = 2.06$ and $\Theta = 1.60$. At low swirls the precession caused noticeable errors in these quantities, particularly in the shear stresses, which are most sensitive to measurement error. For this reason no results are presented for $\Theta = 1.10$, and no shear stresses for $\Theta = 1.60$. As a test of the validity of the measurements, the Reynolds equations require that on the axis

$$\overline{v'^2} = \overline{w'^2}; \quad \overline{u'v'} = \overline{v'w'} = 0 \quad (5)$$

The results shown in Figs. 6 and 7 fulfill these conditions, with the single exception of station 7 of $\Theta = 1.60$; the rejected measurements, however, all showed large (and physically unrealistic) negative shear stresses near the axis. These errors are thought to result from the interaction of the precession with probe

disturbances.

Near the throat the turbulence is decidedly anisotropic, the axial velocity component u'' being roughly twice the other two (Fig. 6,7). The predominance of this component may be traced to the fact that the axial velocity is also the greatest time mean component and exhibits the steepest gradients. The u'' component possesses the largest portion of the total kinetic energy and steadily feeds it to v'' and w'' ; these then become fairly uniform and decay quite slowly, while u'' drops rapidly to their level. At lower swirl ($\theta = 1.60$) the larger mean axial velocity near the axis decreases residence time and dissipation, maintaining u'' at a higher level. The precession also contributes to this; its action may be visualized as a to-and-fro motion of the mean velocity profiles. In interpreting the behaviour of w'' , it should be recalled that the appropriate gradient is $\delta(w/r)/\delta r$ - a forced vortex has no shear.

The shear stresses $u''v''$ and $v''w''$, representing radial transport of axial and tangential momentum respectively, also give qualitative information on turbulent mass transfer in the radial direction. Both quantities exhibit very similar behaviour. At $\theta = 2.06$ large rates of transport both outward to the outer separated flow region and inward to the central recirculation are evident at stations 6 and 7 (Fig. 6). The magnitude of these stresses indicate that very rapid mixing should be possible in this region. As the fluctuating velocity components begin to approach isotropy at station 8, however, the radial stresses drop very rapidly. This suggests that if mixing is not substantially complete by station 8, the remaining mixing will occur very slowly. Much the same pattern was observed at lower swirls, and the stresses measured were very similar in magnitude. The third shear stress, $u''w''$, represents an axial transport of tangential momentum, and is of no significance for the mixing of the nozzle fluid.

The measured turbulent shear stress can be compared to those for free swirling jets by treating the throat as the jet nozzle. Experiments by Hellat /2/ and Hösel /1/ show that shear stresses increase with swirl, the present results corresponding roughly to a free jet with $\theta_t \approx 1$; the enclosed flow therefore has a higher exchange rate than a free jet at the same swirl number.

MIXING AND CONCENTRATION FLUCTUATIONS

The high mixing intensities predicted from the shear stresses at station 6 and 7 were confirmed by tracer gas experiments. Measurements of local time-mean concentrations showed that a uniform distribution of nozzle fluid concentration over the flow cross-section had been achieved by station 10 (1.1 diameters from the throat) at $\theta = 2.06$, and by station 11 at lower swirl. The time mean mixing experiments would thus suggest that mixing rates were nearly independent of swirl level. Measurements of tracer concentration fluctuations, however, revealed marked differences in the quality of mixing, which are evident in the turbulence intensities of the concentration fluctuations (Fig. 8). Large fluctuation intensities are recorded at low swirl (up to 60% for $\theta = 1.10$), indicating a large "unmixedness" at the point where time mean measurements indicated substantially complete mixing. Oscilloscope traces of the concentration signal showed large irregular fluctuations super-imposed on a slower, more regular oscillation of the mean concentration, patterns associated with eddy

shedding and precession respectively. As the precession becomes weaker and disappears with increasing swirl, the unmixedness is sharply reduced. With vortex breakdown ($\theta = 2.06$) the concentration signal exhibited a much finer structure with no large scale or periodic fluctuations.

These results allow mixing at low swirl to be separated into a coarse mixing through precession and large scale eddy shedding, and a finer mixing by the actual turbulence. The "true" turbulent mixing decreases in intensity at lower swirl levels, as would be expected from results for free swirling jets /1,2/, while the contribution of the precession rises, so that the measured time-mean mixing remains nearly constant. The turbulent shear stresses and the time mean mixing experiments thus give a very incomplete picture of the state of mixing at low swirl. The role of the vortex breakdown in improving the quality of mixing is two fold: it stabilizes the flow, preventing large scale unsteady motion and coarse mixing, while relatively long residence time of the fluid in this zone allows ample time for dissipation and reduction of eddy length scales.

In accordance with the observed sharp drop in turbulent shear stresses after station 8, the reduction of the unmixedness remaining at station 10 requires a considerable distance, and in the precessing flows concentration fluctuations are still measurable at station 15, 3 diameters from the throat (Fig. 8).

Fig. 9 compares eddy macro length scales for velocity and concentration fluctuations at $\theta = 2.06$ as measured by correlation of the hot-wire signals. The velocity length scale L_v rises towards the wall as a result of production in the boundary layer. The concentration length scale L_K increases above the velocity scale as concentration eddies coalesce; in the limit as mixing goes to completion, L_K becomes infinite. No meaningful length scales could be measured at $\theta = 1.60$ and 1.10 because of the precession.

CONCLUSIONS

(1) Turbulence in a swirling flow immediately downstream of a sudden expansion is highly anisotropic, the axial velocity fluctuations being initially much larger than the other components. Transport of turbulent kinetic energy plays a strong role, so that regions of maximum turbulent exchange do not always coincide with velocity gradients. The turbulent shear stresses, initially very high, drop sharply about a half test section diameter downstream of the expansion.

(2) In a flow with a periodic disturbance or large-scale eddy shedding, predictions of mixing or combustion based on measured turbulent shear stresses or time-mean mixing experiments may be erroneous. The bulk motion in such flows produces only a coarse mixing and a large unmixedness, and is probably undesirable in technical applications.

REFERENCES

- /1/ Hösel, W., 1978, "Drallstrahlenuntersuchungen mit einem weiterentwickelten Laser-Doppler-Verfahren", SFB 80, Universität Karlsruhe, Report SFB 80/E/120.
- /2/ Hellat, J., 1979, "Turbulente Strömung und Mischung in Erdgas-Diffusionsflammen mit Luftdrall", Dissertation Karlsruhe.
- /3/ Gouldin, F.C., and S.-L. Lee, 1980, "Velocity Measurements in a Swirl-stabilized Combustor", U.S. Dept. of Energy Report E80-08.

/4/ Vu, B.T., and F.C. Gouldin, 1980, "Flow Measurements in a Model Swirl Combustor", AIAA 18th Aero. Sci. Meeting, Paper 80-0076.

/5/ Acrivlellis, M., 1978, "An Improved Method for determining the Flow Field of Multi-Dimensional Flows of any Turbulence Intensity", DISA Info 23, p. 11.

/6/ Schollmeyer, H., 1975, "Hitzdrahtkorrekturen bei großem Turbulenzgrad", VDI-Zeitschrift 117, p. 483.

/7/ Hallett, W.L.H., 1981, "Zur Strömung und Mischung in einer eingeschlossenen Drallströmung mit Querschnittsänderungen", Dissertation Karlsruhe.

/8/ Hallett, W.L.H., 1981, "Eine Spurengas-methode zur Aufenthaltszeitmessung in Gasströmungen", Verfahrenstechnik 15, p. 157.

/9/ Hallett, W.L.H., and R. Günther, "Flow and Mixing in Swirling Flow in a Sudden Expansion", submitted to Can. J. Chem. Eng.

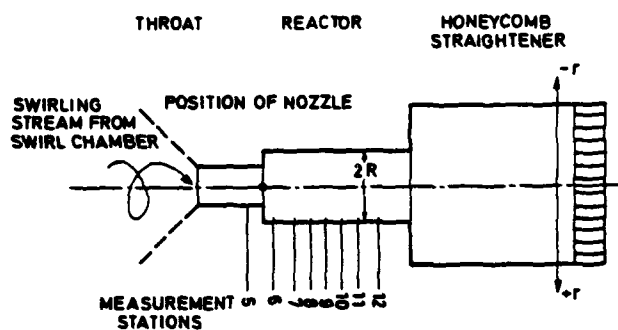


Fig. 1. CROSS-SECTIONAL SKETCH OF EXPERIMENTAL MODEL, SHOWING MEASURING PORTS FOR THE INSERTION OF PROBES

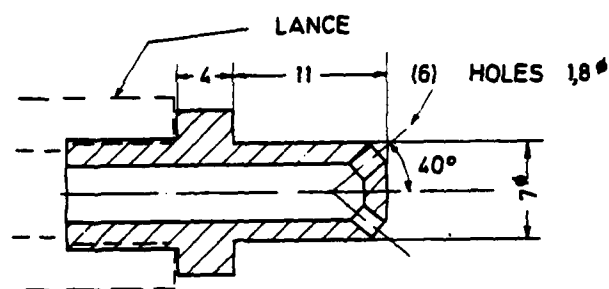


Fig. 2. NOZZLE FOR THE INJECTION OF TRACER GAS

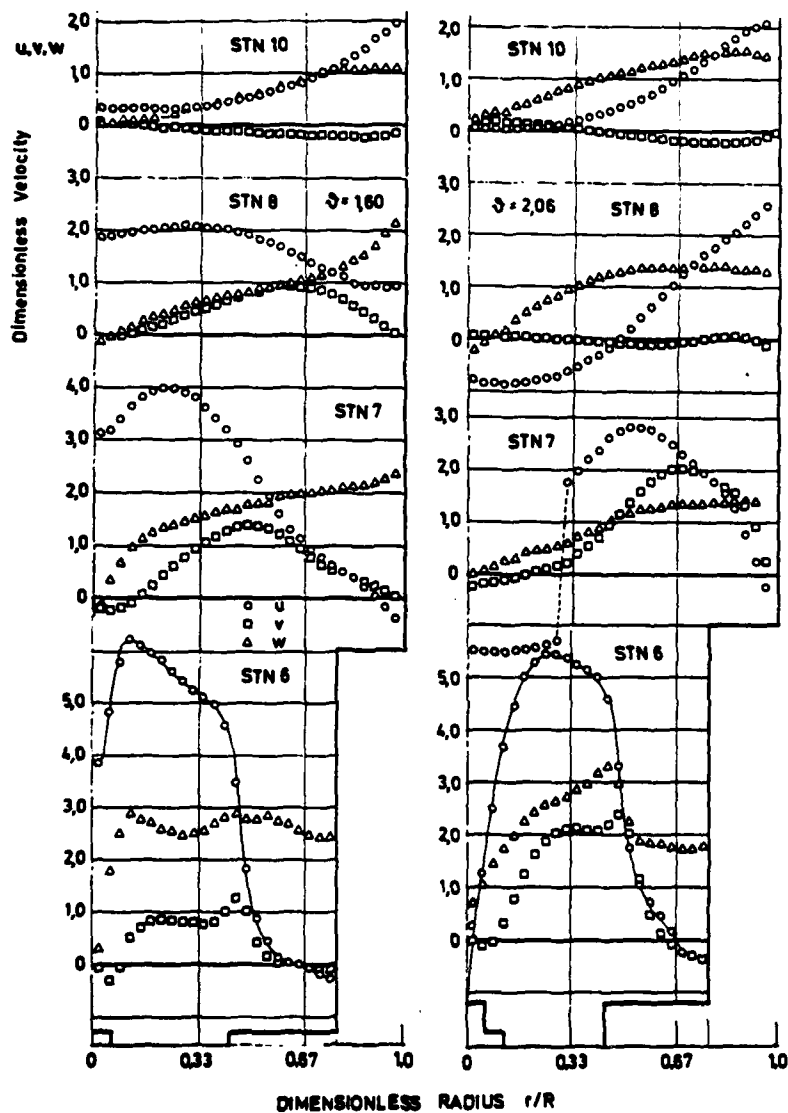


Fig. 3. PROFILES OF TIME MEAN VELOCITY COMPONENTS u , v and w AT VARIOUS STATIONS, NORMALIZED WITH U_R (a) $\theta=1.60$; (b) $\theta=2.06$

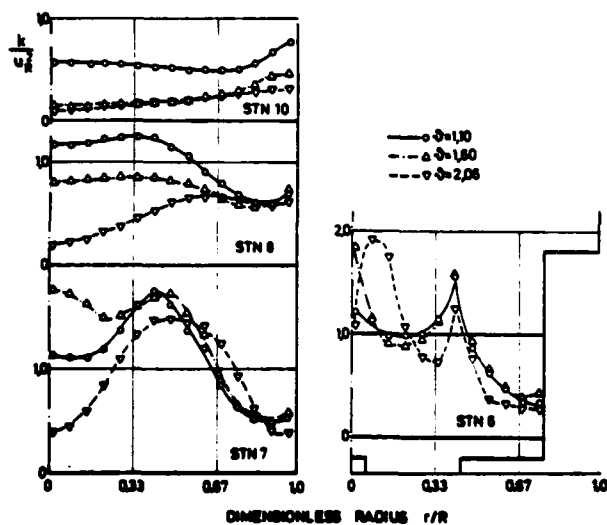


Fig. 4. PROFILES OF THE DIMENSIONLESS TURBULENT KINETIC ENERGY k

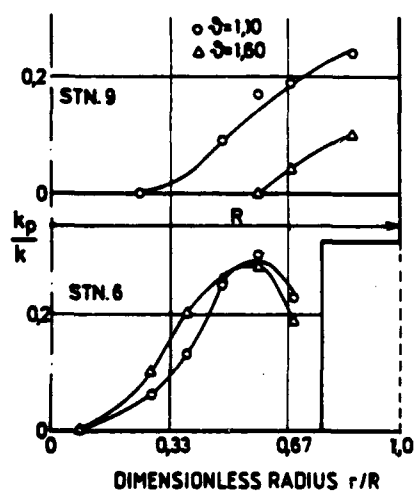


Fig. 5. ENERGY CONTENT k_p OF THE PERIODIC COMPONENT AS A FRACTION OF THE TOTAL TURBULENT KINETIC ENERGY k

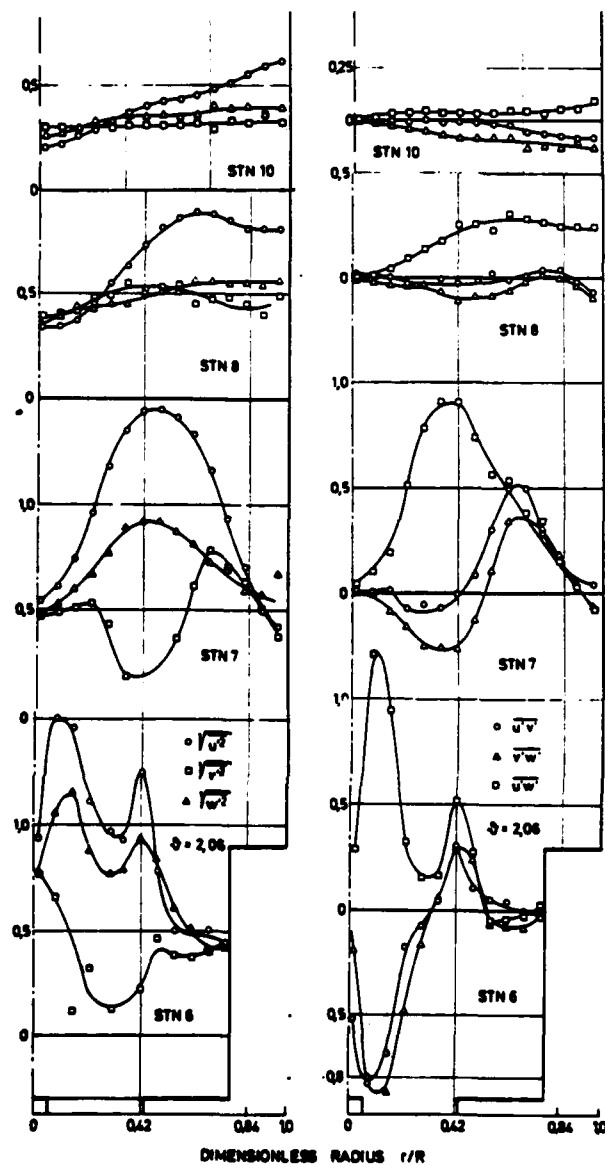


Fig. 6. TURBULENT VELOCITY FLUCTUATIONS (LEFT) AND SHEAR STRESSES (RIGHT) FOR $\Theta = 2.06$, NORMALIZED RESPECTIVELY WITH u_R AND u_R^2

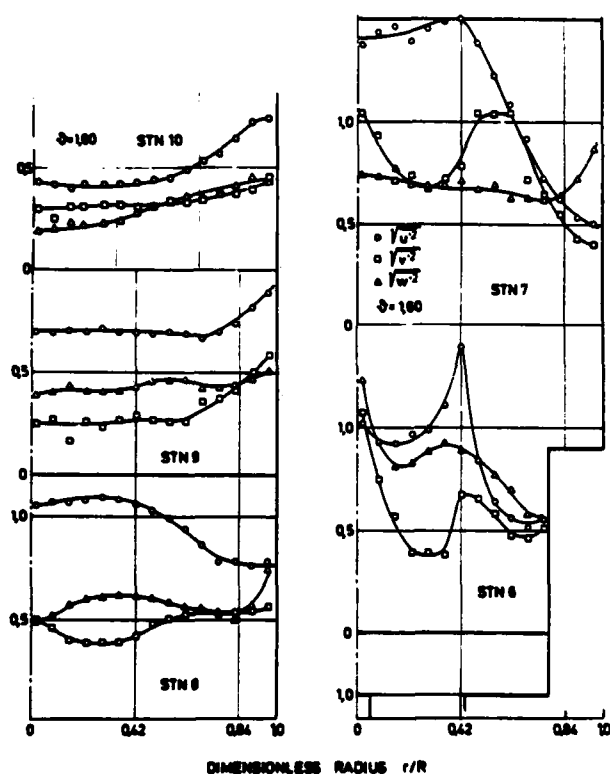


Fig. 7. TURBULENT VELOCITY FLUCTUATIONS FOR $\theta = 1.60$, NORMALIZED WITH u_R

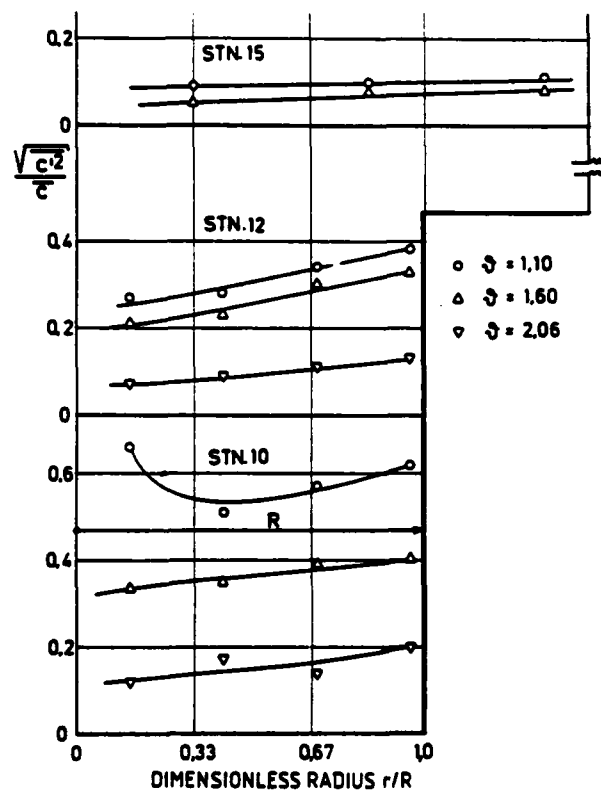


Fig. 8. TURBULENCE INTENSITY OF NOZZLE FLUID CONCENTRATION FLUCTUATIONS

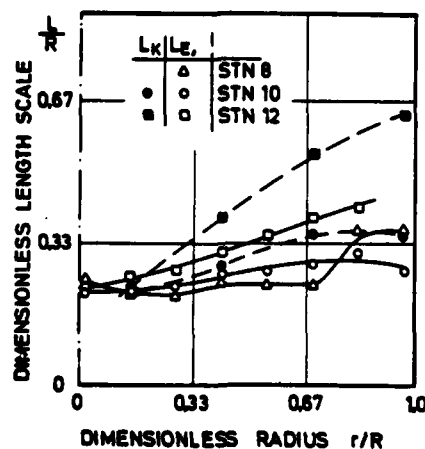


Fig. 9. MACRO (INTEGRAL) LENGTH SCALES OF VELOCITY FLUCTUATIONS L_E AND CONCENTRATION FLUCTUATIONS L_K

END

FILMED

1-84

DTIC